Transactions of the ASME

Technical Editor, **L. B. FREUND**

Division of Engineering
Brown University
Providence, R.I. 02912

The Journal of Applied Mechanics (ISSN 0021-8936) is published quarterly for $100 per year by The American Society of Mechanical Engineers, 345 East 47th Street, New York, NY 10017. *Second class postage paid at New York, NY and additional mailing offices.* POSTMASTER: Send address changes to The Journal of Applied Mechanics, c/o THE AMERICAN SOCIETY OF MECHANICAL ENGINEERS, 22 Law Drive, Box 2300, Fairfield, NJ 07007-2300.
CHANGES OF ADDRESS must be received at Society headquarters seven weeks before they are to be effective. Please send old label and new address.

PRICES: To members, $24.00, annually; to nonmembers, $100.00.
Add $6.00 for postage to countries outside the United States and Canada.

STATEMENT from By-Laws. The Society shall not be responsible for statements or opinions advanced in papers or . . . printed in its publications (B7.1, Par. 3).

INDEXED by the Engineering Information

Journal of Applied Mechanics

Published Quarterly by The American Society of Mechanical Engineers

VOLUME 53 • NUMBER 2 • JUNE 1986

TECHNICAL PAPERS

(Contents continued on Inside Back Cover)

CONTENTS (CONTINUED)

BRIEF NOTES

BOOK REVIEWS

ERRATA

P. G. Hodge, Jr.
Department of Aerospace Engineering and Mechanics,
University of Minnesota,
Minneapolis, MN 55455

K.-J. Bathe
Department of Mechanical Engineering,
Massachusetts Institute of Technology,
Cambridge, MA 02139

E. N. Dvorkin
Universidad de Buenos Aires,
Facultad de Ingeniera,
Buenos Aires, Argentina

Causes and Consequences of Nonuniqueness in an Elastic/Perfectly-Plastic Truss

A complete solution to collapse is given for a three-bar symmetric truss made of an elastic/perfectly-plastic material, using linear statics and kinematics, and the solution is found to be partially nonunique in the range of contained plastic deformation. The introduction of a first-order deviation from symmetry and/or the inclusion of first-order nonlinear terms in the equilibrium equations is found to restore uniqueness. The significance of these effects is analyzed and discussed from mathematical, physical, modelling, computational, and engineering points of view.

1 Introduction

In the linear theory of elasticity the solution to a "well-defined boundary-value problem" is known to exist and be unique. However, for an elastic/perfectly-plastic material neither of these facts is obvious. Indeed, if the load is equal to the so-called "yield-point load" the solution ceases to be unique; beyond this load no solution exists.

The mathematical description of a boundary-value problem for an elastic/perfectly-plastic material involves partial differential equations and nonlinear constitutive relations. Further, if actual answers are required, it is necessary to approximate the structure with a numerical model. Thus the difficulty in combining mathematical rigor and physical intuition in the discussion of such questions as uniqueness is compounded by the necessity of distinguishing between the true nature of the continuum model and aspects introduced by the numerical model.

However, many features of the general continuum are present in much simpler structures where they can be more clearly discussed. As an illustration of this approach, the present paper is concerned with a particular simple three-bar plane truss.

We begin by defining a "well-defined equilibrium problem" for trusses as one in which the applied forces and displacements at the joints are such that:

(*a*) overall equilibrium is not violated;
(*b*) overall displacement constraints prescribe a unique allowable rigid-body motion (usually zero);
(*c*) at each joint in each of two independent directions either the displacement or the applied load is prescribed.

It is not difficult to prove that the solution to any well-defined equilibrium elasticity problem is unique. Indeed, if two solutions exist and are denoted by primes and double primes, then it follows from the principle of virtual work that

$$\Sigma_{\text{bars}}(F_i' - F_i'')(e_i' - e_i'') = \Sigma_{\text{joints}}(\mathbf{P}_j' - \mathbf{P}_j'')\cdot(\mathbf{u}_j' - \mathbf{u}_j'') \quad (1)$$

where F_i and e_i are the bar force and elongation, respectively, and $\mathbf{P}_j$ and $\mathbf{u}_j$ are the respective force and displacement vectors at joint j. If each solution satisfies condition (*c*) above and we write the scalar product in terms of components in the independent prescription directions, then either $P' = P''$ or $u' = u''$ in each term on the right. Further, if each bar is elastic, then

$$F_i = k_i e_i \quad (2)$$

where the stiffness k_i is positive. Thus equation (1) becomes

$$\Sigma_{\text{bars}} k_i (e_i' - e_i'')^2 = 0 \quad (3)$$

which clearly requires that each $e_i' = e_i''$ and hence each $F_i' = F_i''$. Equilibrium equations then show each $\mathbf{P}_j' = \mathbf{P}_j''$, and truss kinematics plus condition (*b*) above lead to each $\mathbf{u}_j' - \mathbf{u}_j'' = 0$. Therefore, the solution is unique.

Let us generalize the material behavior of equations (2) to an "elastic/perfectly-plastic" truss where each bar behaves elastically under small bar forces but can elongate indefinitely when F_i reaches a certain limiting value Y_i with similar behavior in compression. Thus during any sufficiently small time interval each bar is

EITHER
Elastic $\quad (F_i^2 < Y_i^2 \quad \text{AND } \Delta F_i = k_i \Delta e_i) \quad (4a)$
OR Plastic $\quad (F_i^2 = Y_i^2 \qquad F_i \Delta e_i \geq 0) \quad (4b)$

Consider first any well-posed equilibrium boundary-value problem where any prescribed displacements are zero and the loads $\mathbf{P}_j$ are such that every bar is elastic. Clearly the same unique solution will hold as in the ideally elastic truss.

Now consider this same truss under the set of loads $\lambda \mathbf{P}_j$ where λ is slowly increased from $\lambda = 1$. So long as $F_i^2 < Y_i^2$ for each bar, the truss will remain fully elastic and the unique solution will increase in proportion to λ. However, for some critical value λ_e one or more bars will have their force

Contributed by the Applied Mechanics Division for presentation at the Winter Annual Meeting, Anaheim, CA, December 7–12, 1986, of the American Society of Mechanical Engineers.

Discussion on this paper should be addressed to the Editorial Department, ASME, United Engineering Center, 345 East 47th Street, New York, N.Y. 10017, and will be accepted until two months after final publication of the paper itself in the JOURNAL OF APPLIED MECHANICS. Manuscript received by ASME Applied Mechanics Division, November 27, 1984; final revision August 1, 1985. Paper No. 86-WA/APM-8.

$F_i = \pm Y_i$ and for larger values of λ some bars will be plastic. For a truss with a sufficient degree of indeterminancy enough bars remain elastic to support further increases in λ, but eventually a second critical value λ_L is reached at which the truss becomes a mechanism and no further load increases are possible.

Clearly the displacements of a mechanism motion are not unique, but the situation with regard to uniqueness is not as clear in the range of "contained plastic deformation" when $\lambda_e < \lambda < \lambda_L$. When even one bar reaches yield, the uniqueness proof above breaks down, since any two solutions which included plastic behvior for that bar would furnish $F_i' = F_i''$ but give no information about either e_i' or e_i''. In most examples and applications it turns out that uniqueness does hold in the range of contained plastic deformation, but extremely simple counter examples can be constructed in which more than one displacement solution exists for all loads with $\lambda > \lambda_e$.

In Section 2 we shall review a simple example of a 3-bar truss (Hode and White, 1980). In particular, we will note that any of several infinitesimal changes in the definition of the problem would render the solution unique up to $\lambda = \lambda_L$. In Sec. 3 we will examine one such variation by introducing an additional horizontal load αP, and we will study the limiting case as α tends to zero.

Section 4 will show that if we require equilibrium in the deformed position, rather than in the original configuration as is normally done in a linear analysis, then the change in predicted values can be expressed in terms of the small parameter $\beta = \sigma_y/E$ which is determined by the physical properties of the bar materials. The original problem now has a unique solution, but as α tends to zero in the varied problem, the predictions are quite different than in Section 3.

In Section 5 we attempt to solve the above models by the prepared computer program ADINA (1981). Finally, the paper concludes with a discussion of the relation between the various model solutions and the physical behavior to be expected from a "real" truss.

2 Nonunique 3-Bar Truss

The 3-bar truss in Fig. 1 has been used to point out many interesting facets of elastic/plastic truss behavior (Hodge and White, 1980; Hodge, 1958; Prager, 1948; Freudenthal, 1954). All bars have the same Young's modulus E and cross-sectional area A, but the yield stress for the diagonal bars is σ_y whereas that for the vertical bar is 3 σ_y. We begin by using an asterisk to define all real physical variables and defining dimensionless quantities as follows:

$$\beta = \sigma_y/E \qquad P = P^*/A\sigma_y \qquad F_i = F_i^*/A\sigma_y$$
$$u = u^*/\beta H \qquad v = v^*/\beta H \qquad e_i = e_i^*/\beta H \tag{5}$$

where H is defined in Fig. 1.

The static and kinematic equations are trivial and can be written in incremental form as

$$\Delta F_1 - \Delta F_3 = 0 \tag{6a}$$
$$\Delta F_1 + \Delta F_3 + \sqrt{2}\Delta F_2 = \sqrt{2}\Delta P \tag{6b}$$
$$\Delta e_1 = (\Delta v + \Delta u)/\sqrt{2} \quad \Delta e_2 = \Delta v \quad \Delta e_3 = (\Delta v - \Delta u)/\sqrt{2} \tag{7}$$

Equations (4) and (7) can be combined for each bar to obtain

Bar 1 Elastic $-1 < F_1 < 1$ $\Delta F_1 = (\Delta v + \Delta u)/2$ (8a)

Plastic $F_1 = \pm 1$ $\Delta F_1 = 0$ $F_1(\Delta v + \Delta u) > 0$ (8b)

Bar 2 Elastic $-3 < F_2 < 3$ $\Delta F_2 = \Delta v$ (8c)

Plastic $F_2 = \pm 3$ $\Delta F_2 = 0$ $F_2 \Delta v > 0$ (8d)

Bar 3 Elastic $-1 < F_3 < 1$ $\Delta F_3 = (\Delta v - \Delta u)/2$ (8e)

Plastic $F_3 = \pm 1$ $\Delta F_3 = 0$ $F_3(\Delta v - \Delta u) > 0$ (8f)

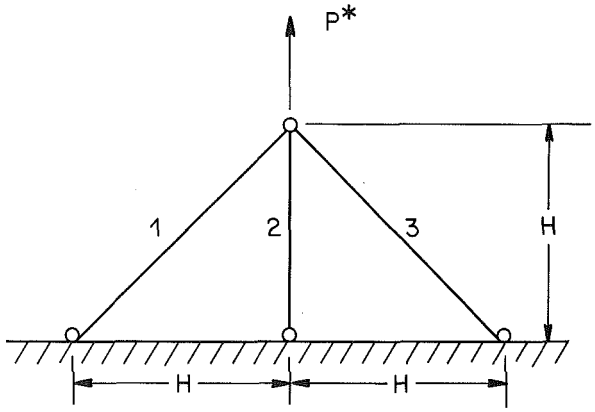

Fig. 1 Three-bar truss with vertical load

As the load P is slowly increased from zero, all three bars will start from zero force and be elastic, hence we can use the integrated form of equations (6) and (8*a*,*c*,*e*) to obtain

Stage 1

$$u = 0 \quad v = F_2 = (2 - \sqrt{2})P \quad F_1 = F_3 = (1 - 1/\sqrt{2})P \tag{9}$$

In view of the different yield stresses, the diagonal bars will yield first, and the limit of Stage 1 is

Stage 1L

$$P = 2 + \sqrt{2} \quad u = 0 \quad v = F_2 = 2 \quad F_1 = F_3 = 1 \tag{10}$$

As the load P is further increased both diagonal bars will yield, hence we use equations (8*b*, *c*, *f*) with equations (6). However, these equations are not independent since equations (8*b*, *f*) show that $\Delta F_1 = \Delta F_3 = 0$ which automatically satisfies equation (6*a*). The five equations (8*b*, *c*, *f*) and (6 *a*, *b*) do provide unique values for the increments of forces and vertical displacement, but only provide bounds for the horizontal displacement:

Stage 2

$$\Delta F_1 = \Delta F_3 = 0 \quad \Delta F_2 = \Delta v = \Delta P \quad -\Delta P \le \Delta u \le \Delta P \tag{11}$$

Adding these increments to equations (10) and determining P so that $F_2 = 3$, we obtain the limiting solution

Stage 2L

$$P = 3 + \sqrt{2} \quad F_1 = F_3 = 1 \quad F_2 = v = 3 \quad -1 \le u \le 1 \tag{12}$$

At this load all bars are plastic. Equations (8*b*, *d*, *f*) now automatically satisfy both of (6) with $\Delta P = 0$, hence the mechanism motion at the yield-point load has two degrees of freedom with Δu and Δv subject only to inequalities

Stage 3 (mechanism)

$$P = 3 + \sqrt{2} \quad F_1 = F_3 = 1 \quad F_2 = 3$$
$$\Delta v \ge 0 \quad -\Delta v \le \Delta u \le \Delta v \tag{13}$$

The nonuniqueness of the motion in Stage 3 has been long known and is implied in the very name of mechanism. However, the nonuniqueness in Stage 2, when the truss is still capable of handling increased load is a more subtle phenomenon. It can be examined from mathematical, physical, computational, or modelling points of view.

Mathematically, it occurs because the simultaneous occurance of yield in two bars at stage 1L leads to the homogeneous equilibrium relation (equation (6*a*)) becoming redundant in Stage 2. Thus the total system of 5 equations becomes singular and cannot be solved uniquely.

Physically, we could think of the general motion permitted in Stage 2 as a combination of a vertical motion $\Delta v = \Delta P$ which stretches each plastic bar by an amount $\Delta v/\sqrt{2}$, together with a horizontal motion Δu. If Δu were positive, this latter

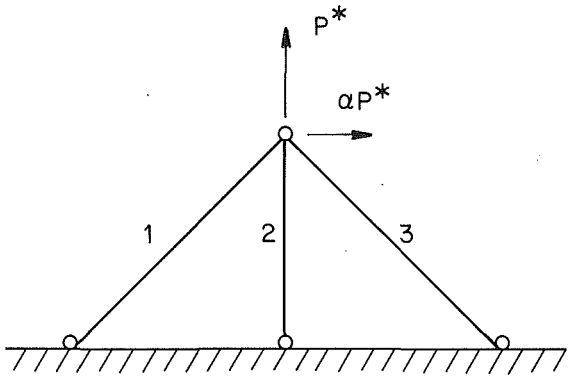

Fig. 2 Truss with small horizontal load component

motion by itself would compress bar 3 which would not be permissible at tensile yield. However, the physical requirement of extension applies only to the total motion which includes a positive Δv, hence the only restriction is given by the inequalities in equation (11). The computational aspects will be discussed in Section 5.

From a modelling viewpoint, any of several infinitesimal changes in the model will remove the singularity, produce a unique value for u, and create at most infinitesimal changes in the other variables. If the symmetry of the problem is changed ever-so-slightly by an alteration of area, stiffness, strength, load, or node position, then bar 1, say, will become plastic while bar 3 is still just short of yield. Then Stage 3 would use equations (8*b*, *c*, *e*); equation (6*a*) would no longer be an identity, but would contribute the information $\Delta F_3 = 0$; equation (8*e*) would then provide the unique solution

$$\Delta u = \Delta v \tag{14}$$

Further, since $\Delta F_3 = 0$, Stage 2 would continue as before until bar 2 yielded. The resulting mechanism motion would have one degree of freedom with bar 3 rotating as a rigid body subject to equation (14) corresponding to the right-hand limit of the last inequality in equation (13).

However, if the change from symmetry is in the opposite sense, bar 3 will yield while bar 1 remains elastic and equation (14) will be replaced by

$$\Delta u = -\Delta v \tag{15}$$

corresponding to the left-hanf inequality in equation (13).

Another possibility is to allow for infinitesimal strain hardening. If both bars 1 and 3 harden equally, the symmetric solution $\Delta u = 0$ will become unique, but if there is any difference in the hardening of bars the solution will still be unique but any value of u satisfying equation (11) may be obtained by a suitable ratio of the hardening coefficients.

Uniqueness of solution will also result if we account for the additional stiffening effect of the bars produced by their elastic elongation. However, we will postpone discussion of this effect until we have examined in detail the consequences of altering symmetry in a specific manner in the next section.

3 Truss with Small Horizontal Load Added

Let us suppose that as before the truss geometry in Fig. 1 is precisely symmetric, that bars 1 and 3 are identical in all their measurements and properties, and that there is absolutely no strain hardening. However, let us allow for a minute deviation in the direction of the applied load. Thus instead of the problem in Fig. 1, we consider the truss problem in Fig. 2, where α is a small, dimensionless parameter; for definiteness we take $\alpha > 0$.

Equations (6*b*) and (8) are still applicable, but equation (6*a*) is replaced by

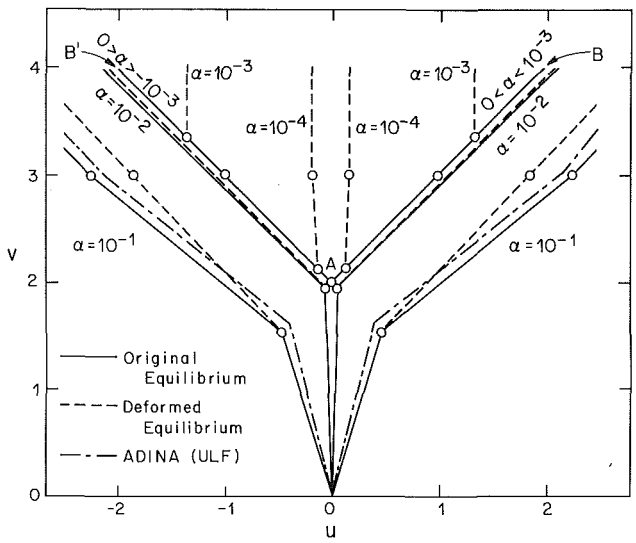

Fig. 3 Motion of loaded point

$$\Delta F_1 - \Delta F_3 = \sqrt{2}\alpha \Delta P \tag{16}$$

The fully elastic solution is obtained from equation (6*b*), (16), and (8*a*,*c*,*e*):

Stage 1

$$u = \sqrt{2}\alpha P \qquad v = F_2 = (2 - \sqrt{2})P$$
$$F_1 = (1 - 1/\sqrt{2} + \alpha/\sqrt{2})P \qquad F_3 = (1 - 1/\sqrt{2} - \alpha/\sqrt{2})P \tag{17}$$

For any positive α, bar 1 yields first with the following values:

Stage 1*L*

$$P = (2 + \sqrt{2})[1 - (\sqrt{2} + 1)\alpha]$$
$$u = 2(\sqrt{2} + 1)\alpha \qquad v = F_2 = 2 - 2(\sqrt{2} + 1)\alpha \tag{18}$$
$$F_1 = 1 \qquad F_3 = 1 - 2(\sqrt{2} + 1)\alpha$$

where we have kept only first-order terms in α.

With bar 1 plastic we use the equations (8*b*, *c*, *e*), (6*b*), and (16) to obtain the incremental solution:

Stage 2

$$\Delta u = [1 + (1 + 2\sqrt{2})\alpha]\Delta P \qquad \Delta v = \Delta F_2 = (1 + \alpha)\Delta P$$
$$\Delta F_1 = 0 \qquad \Delta F_3 = -\sqrt{2}\alpha \Delta P \tag{19}$$

We note that ΔF_3 is negative, and hence for α reasonably small bar 3 will remain elastic. Therefore, Stage 2 ends when bar 2 becomes plastic:

Stage 2*L*

$$\Delta P = 1 + (2\sqrt{2} + 1) \qquad P = 3 + \sqrt{2} - (3 + \sqrt{2})\alpha$$
$$u = 1 + 2(3\sqrt{2} + 2)\alpha \qquad v = F_2 = 3 \tag{20}$$
$$F_1 = 1 \qquad F_3 = 1 - (3\sqrt{2} + 2)\alpha$$

In Stage 3 bars 1 and 2 are plastic. Equations (6*b*), (8*b*, *d*, *e*), and (16) cannot be solved for a prescribed P but require the following:

Stage 3 (mechanism)

$$\Delta P = \Delta F_1 = \Delta F_2 = \Delta F_3 = 0 \qquad \Delta v = \Delta u \geq 0 \tag{21}$$

Clearly this is a mechanism motion under the yield-point load $P_L = (3 + \sqrt{2})(1 - \alpha)$.

The solid curves in the right half of Fig. 3 show the motion of the loaded point for various α. To the scale used values of $\alpha < 10^{-3}$ will not be any different than $\alpha = 10^{-3}$. In particular, the curve OAB will also be the limit curve as α tends to zero from above.

The preceding analysis is for the case $\alpha > 0$. Clearly, if $\alpha < 0$, i.e., if the horizontal component is directed to the left, the

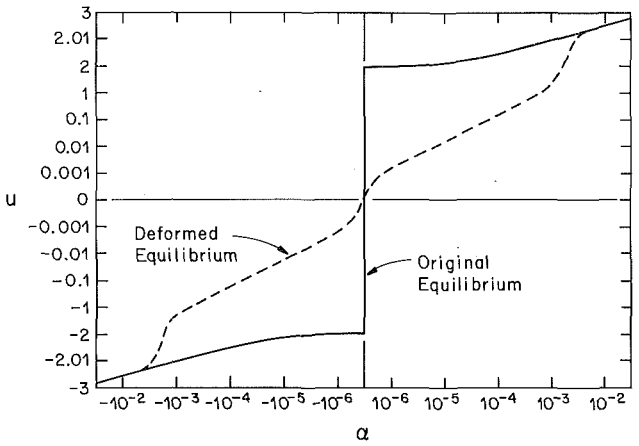

Fig. 4 Horizontal displacement as a function of α for $v = 4$

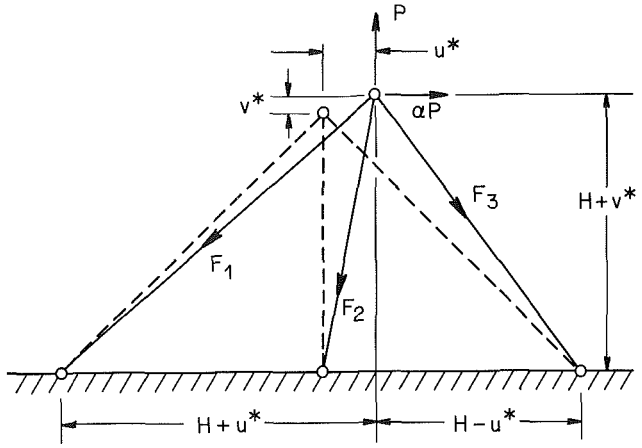

Fig. 5 Equilibrium of deformed truss

roles of bars 1 and 3 will be interchanged and the sign of u will be reversed. In particular, we obtain curve OAB′ as the limit curve when α tends to zero from below.

Both OAB and OAB′ are admissible curves for the nonunique solutions obtained in Section 2 where α is set equal to zero at the outset. Indeed, any curve in the open wedge B′AB whose slope satisfies $dv \geq |du|$ is an admissible nonunique solution to that ideal problem.

The solid curve in Fig. 4 shows the horizontal displacement u as a function of α when the vertical displacement is $v = 4$. Note that both scales are nonlinear. It is clear from either Fig. 3 or Fig. 4 that the motion is unique for any fixed positive value of α, hence the horizontal displacement u is a unique function of the load P. Furthermore, as the parameter α tends to zero, this motion will approach a unique limit which is very close to its value when $\alpha = 10^{-3}$. The same statements apply to negative values of α, but the two limits are distinctly different. Finally, a direct analysis with $\alpha = 0$ leads to a nonunique solution which includes all possibilities between the two above limits. These points will be commented on further in Section 6.

4 Deformed Equilibrium Approach

The geometrically linear theory used in the two preceding sections is based on the neglect of various small quantities. However, as we have seen, small values of the horizontal load parameter α can have a large effect on the motion of the truss vertex. Therefore, it seems natural to ask if any of the neglected small effects might have large consequences. In particular, we consider the change in effective stiffness due to small displacements. Since Fig. 1 can be treated as the special case $\alpha = 0$, we examine this effect for the truss in Fig. 2 by replacing the equilibrium relations (equations (16) and (6*b*)) with equilibrium requirements derived from Fig. 5. Using the same dimensionless variables and keeping only first order terms in the small parameter β, we obtain

$$\begin{aligned} &\Delta F_1 - \Delta F_3 + (\beta/2)[(F_3 + F_1 + 2\sqrt{2}F_2)\Delta u \\ &\qquad + (F_3 - F_1)\Delta v] = \sqrt{2}\alpha\Delta P \\ &\Delta F_1 + \Delta F_3 + \sqrt{2}\Delta F_2(\beta/2)[(F_3 - F_1)\Delta u \\ &\qquad + (F_3 + F_1)\Delta v] = \sqrt{2}\Delta P \end{aligned} \tag{22}$$

For simplicity, we continue to use the linear equations (8); the introduction of nonlinear terms there would not change the qualitative results.

Strictly speaking, equations (22) are nonlinear differential equations. Since the nonlinear terms are all multiplied by the small parameter β, we shall linearize them by using appropriate constant values for the forces in the terms multiplied by β. In effect, we replace the differential equation by taking a single linear difference equation for each stage of the solution.

We regard both α and β as small compared to unity and neglect all terms α^2, $\alpha\beta$, β^2, etc. Therefore, we need only the zero-order terms for the forces in equations (22). At the end of Stage 1, it follows from equations (18) that the zero-order forces are $F_1 = F_3 = 1$, $F_2 = 2$. since all $F_i = 0$ at the beginning of the stage, their average values during Stage 1 are

$$F_1 = F_3 = \tfrac{1}{2} \quad F_2 = 1 \tag{23}$$

The solution of equations (22) and (8*a*, *c*, *e*) with F_i given by equation (23) is

Stage 1

$$\begin{aligned} &\Delta u = \sqrt{2}\alpha\Delta P \quad \Delta v = \Delta F_2 = \sqrt{2}(\sqrt{2}-1)[1-(\sqrt{2}-1)\beta/2]\Delta P \\ &\Delta F_1 = [(\sqrt{2}-1)/\sqrt{2}][1-(\sqrt{2}-1)\beta/2+(\sqrt{2}+1)\alpha]\Delta P \\ &\Delta F_3 = [(\sqrt{2}-1)/\sqrt{2}][1-(\sqrt{2}-1)\beta/2-(\sqrt{2}+1)\alpha]\Delta P \end{aligned} \tag{24}$$

The stage ends when bar 1 becomes plastic at the load

Stage 1*L*

$$P = (2+\sqrt{2})[1+(\sqrt{2}-1)\beta/2-(\sqrt{2}+1)\alpha] \tag{25}$$

With this load, the forces and displacements at Stage 1*L* all have the same values as in equations (18) for the geometrically linear theory (to within first-order terms).

In Stage 2, bar 1 is plastic and, to zero-order terms, $F_1 = F_3 = 1$ throughout the stage. Therefore, using (8*b*, *c*, *e*) we can write equation (22) as

$$\begin{aligned} &[1+2\beta(1+\sqrt{2}F_2)]\Delta u - \Delta v = 2\sqrt{2}\alpha\Delta P \\ &-\Delta u + [(1+2\sqrt{2})+2\beta]\Delta v = 2\sqrt{2}\Delta P \end{aligned} \tag{26}$$

where we have not yet assigned a value to F_2, but have treated it as a constant. To within first-order terms the solution of equation (26) is

Stage 2

$$\Delta u = \{1+(1+2\sqrt{2})\alpha - [(2+\sqrt{2})+(1+2\sqrt{2})F_2]\beta\}\Delta P \tag{27a}$$

$$\Delta v = \Delta F_2 = [1+\alpha-(\sqrt{2}+F_2)\beta]\Delta P \tag{27b}$$

$$\Delta F_1 = 0 \qquad \Delta F_3 = [(1+\sqrt{2}F_2)\beta - \sqrt{2}\alpha]\Delta P \tag{27c,d}$$

The essential difference between equations (27) and equations (19) for the linear case is that now F_3 will increase for sufficiently small α so that it is not clear whether bar 2 or bar 3 will be the next to yield. Therefore, we consider the two cases separately. If bar 2 yields next, the final value of F_2 is $F_2 = 3$ hence its average value during the stage is $F_2 = 2.5$. The solution at the end of the stage is then

Stage 2*LA*

$$\Delta P = 1+(2\sqrt{2}+1)\alpha+(\sqrt{2}+5/2)\beta \tag{28a}$$

$$\Delta F_3 = (1+5\sqrt{2}/2)\beta - \sqrt{2}\alpha \tag{28b}$$

$$F_1 = 1 \quad F_2 = 3 \quad P = 3+\sqrt{2} \quad u = 1 \quad v = 3 \tag{28c}$$

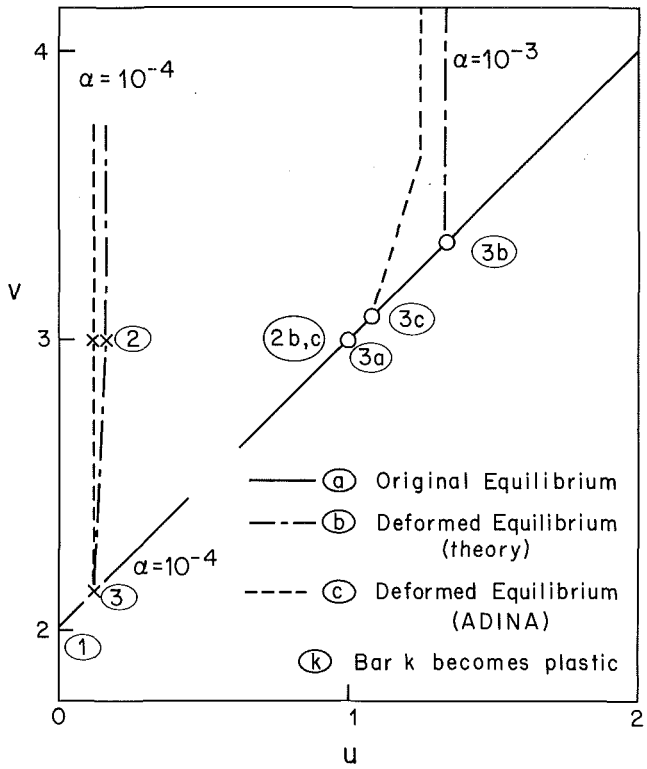

Fig. 6 Comparison of computational and theoretical results

$$F_3 = 1 + (1 + 5/\sqrt{2})\beta - (3\sqrt{2} + 2)\alpha \le 1 \tag{28d}$$

$$t \equiv \alpha/\beta \ge (13 - 2\sqrt{2})/14 = 0.727 \tag{28e}$$

In equations (28) we have listed only the zero order terms for P, u, and v, but the first order terms are important for F_3, since this solution is valid only if $F_3 \le 1$, thus leading to inequality (28) on the ratio $t = \alpha/\beta$ which may be of any magnitude.

In Stage 3*A*, bars 1 and 2 are at yield and equations (22) and (8*b*, *d*, *e*) lead to

$$\Delta F_3 = (\Delta v - \Delta u)/2 \tag{29a}$$

$$\Delta u - \Delta v + \beta[(F_3 + 1 + 6\sqrt{2})\Delta u + (F_3 - 1)\Delta v] = 2\sqrt{2}\alpha\Delta P \tag{29b}$$

$$\Delta v - \Delta u + \beta[(F_3 - 1)\Delta u + (F_3 + 1)\Delta v] = 2\sqrt{2}\Delta P \tag{29c}$$

For bar 3 to reach yield will require only a first order increase in F_3, hence to order zero $\Delta u = \Delta v$ and equation (29*c*) shows that ΔP is of order greater than zero. Therefore, keeping only the leading terms in each equation (29) we see that for bar 3 to reach yield

$$\Delta F_3 = (\Delta v - \Delta u)/2 = (3\sqrt{2} + 2)\alpha - (5/\sqrt{2} + 1)\beta \tag{30a}$$

Since this is first order, equation (29*c*) shows that ΔP is also of first order. Keeping only the leading terms in equations (29), we obtain

$$\Delta u - \Delta v + \beta[(2 + 6\sqrt{2})\Delta u] = 0 \tag{30b}$$

$$\Delta u - \Delta v + \beta(2)\Delta v = 2\sqrt{2}\Delta P \tag{30c}$$

which leads to

Stage 3*LA*

$$\Delta u = \Delta v = (1/34)[(32 + 6\sqrt{2})t - (28 + \sqrt{2})]$$

$$u = (1/34)[(32 + 6\sqrt{2})t + (6 - \sqrt{2})]$$

$$v = (1/34)[(32 + 6\sqrt{2})t + (74 - \sqrt{2})]$$

$$F_1 = 1 \quad F_2 = 3 \quad F_3 = 1 \quad P = 3 + \sqrt{2} \tag{31}$$

to zero order terms.

The final stage occurs when all bars are plastic. Equations (8*b*, *d*, *f*) and (22) now lead simply to

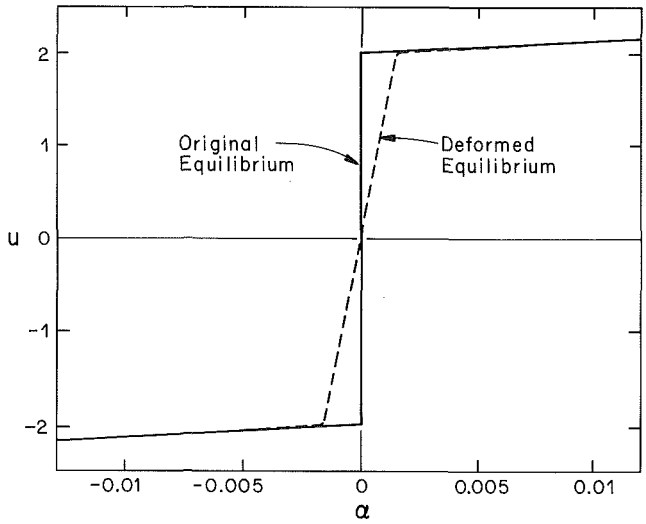

Fig. 7 Horizontal displacement as a function of α for $v = 4$

Stage 4

$$\Delta u = (t/17)(6 - \sqrt{2})\Delta P$$

$$\Delta v = \sqrt{2}\Delta P/\beta \tag{32}$$

Thus, although we do not have a mechanism in the sense of linear plasticity, only a first order increase in ΔP is required to produce a zero-order vertical displacement.

Returning now to the case where bar 3 yields before bar 2, we do not know the final value of F_2, but we can denote it (to zero-order terms) by $2 + \Delta F_2$. Therefore, the average value called for in equations (27) will be

$$F_2 = 2 + \Delta F_2/2 = 2 + \Delta P/2 \tag{33}$$

where the last step follows from equation (27*b*). It then follows from equation (27*d*) that when bar 3 yields

$$\Delta F_3 = \{[1 + \sqrt{2}(2 + \Delta P/2)]\beta - \sqrt{2}\alpha\}\Delta P = 2(\sqrt{2} + 1)\alpha \tag{34}$$

This is a quadratic equation for ΔP whose solution is

Stage 2*LB*

$$\Delta P = [4.5 + 2\sqrt{2} + \sqrt{2}t + t^2]^{1/2} - (2 + 1/\sqrt{2} - t) \tag{35a}$$

$$\Delta u = \Delta v = \Delta F_2 = \Delta P \quad F_2 = 2 + \Delta P \tag{35b}$$

where we have listed only the zero-order terms. In order for this solution to be valid, ΔF_2 cannot exceed 1, and it is readily verified that this requirement leads to the reverse of inequality (28):

$$t \le (13 - 2\sqrt{2})/14 \tag{35c}$$

In Stage 3*B*, bars 1 and 3 yield, and equations (22) and (8*b*, *c*, *f*) produce

$$\Delta F_2 = \Delta v$$

$$\beta(1 + \sqrt{2}F_2)\Delta u = \sqrt{2}\alpha\Delta P \tag{36}$$

$$(\sqrt{2} + \beta)\Delta v = \sqrt{2}\Delta P$$

In view of equations (35*a*), the value of F_2 to be used in equation (36) is

$$F_2 = (1/2)[3 - 1/\sqrt{2} + t + (4.5 + 2\sqrt{2} + \sqrt{2}t + t^2)^{1/2}] \tag{37}$$

The solution (equation (36) when ΔF_2 is sufficient to bring F_2 to its yield value of 3) is

Stage 3*LB*

$$\Delta v = \Delta F_2 = \Delta P = 3 + 1/\sqrt{2} - t - (4.5 + 2\sqrt{2} + \sqrt{2}t + t^2)^{1/2}$$

$$\Delta u = 2t\Delta P/[3 + 1\sqrt{2} + t + (4.5 + 2\sqrt{2} + \sqrt{2}t + t^2)^{1/2}]$$

Since all three bars are now at yield, the incremental solution for Stage 4 is again given by equations (32).

The dashed curves in Figs. 3 and 4 show the displacements

according to the nonlinear geometry model with $\beta = 10^{-3}$. As α tends to zero the displacements do move continuously with u being positive for $\alpha > 0$, zero for $\alpha = 0$, and negative for $\alpha < 0$. We shall comment more fully on the similarities and differences between the two solutions in the conclusions.

5 ADINA Solutions

The truss in Figs. 1 and 2 was run on the structural program ADINA (1981) for $\alpha = 0$ (no horizontal load as in Fig. 1) and for $\alpha = 10^{-6}$, 10^{-5}, 10^{-4}, 10^{-3}, 10^{-2}, and 10^{-1}. Default options were used for most of the parameters in ADINA, except as noted in the following discussion. All problems were run twice; once with a "material-nonlinear-only" (MNO) code corresponding to the analysis in Sections 2 and 3, and once with an "updated-Lagrangian-formulation" (ULF) code similar to the analysis in Section 4. Descriptions of these methods may be found in Bathe (1982).

For the case $\alpha = 0$ the MNO program only gave results up to the load $P = 3.415$, at which point it stopped with the message "NONPOSITIVE PIVOT FOR EQUATION 1 . . .COLLAPSE LOAD OF THE MODEL HAS BEEN REACHED." A load increment $P = 0.001$ was used, and the final values were

$$P = 3.415 \quad u = 0 \quad v = 2.00078$$
$$F_1 = F_3 = 1.00000 \quad F_2 = 2.0078 \tag{38}$$

with bars 1 and 3 being listed as PLASTIC. Clearly these values are an excellent approximation to those given in equation (10) for Stage 1L, but they do not represent the collapse load given in equation (12).

The reason that the computer solution stops here is easy to see. ADINA, like most finite-element programs, essentially substitutes the appropriate equations (8) in equations (6) and then solves the resulting set of linear equations for Δu and Δv. However, for the next load increment we must use equations (8b, d, e) for which equations (6) become

$$0 \cdot \Delta u + 0 \cdot \Delta v = 0$$
$$0 \cdot \Delta u + \sqrt{2} \cdot v = \sqrt{2} P \tag{39}$$

Although these equations do contain the useful information $\Delta v = \Delta P$ given in equation (11), the stiffness matrix (the matrix of coefficients on the left-hand side of equation (39)) is singular. Therefore, standard methods of automatic solution will not produce the solution in equation (12). Such a singular matrix always occurs at the yield-point (collapse) load and its occurance due to nonuniqueness was evidently not allowed for when ADINA was written.

For $\alpha = 10^{-6}$, the MNO program stops with the same message and values, except that $u = 0.241477 \times 10^{-4}$. Evidently the small horizontal load gets "lost" in the computations leading to the stiffness matrix.

Two variations were experimented with to overcome this difficulty. When load steps near 3.414 were reduced to 0.0001, bar 1 became plastic at $P = 3.4143$. Although it took 19 iterations for this solution to converge, the program then continued with only one iteration per step until the load was $P = 4.415$ when it stopped with the message "ITERATION LIMIT REACHED WITH NO CONVERGENCE."

The other variation used an optional iteration method known as Broyden-Fletcher-Goldfarb-Shanno (BFGS) instead of the modified Newton method which is the default option (Bathe, 1982, Sec. 8.6). With BFGS, we obtained the same loads, but it took only 3 iterations to pass $P = 3.4143$, and when the program stopped at the collapse load the message was again "NONPOSITIVE PIVOT . . . . ".

For $\alpha = 10^{-5}$, the MNO program predicted that only bar 1 became plastic at $P = 3.415$ and continued to the load 4.414 with the values

$$P = 4.414 \quad u = 0.999955 \quad v = 2.99983$$
$$F_1 = 1.00000 \quad F_2 = 2.99983 \quad F_3 = 0.999938 \tag{40}$$

in excellent approximation to equations (20). The program then stopped with the message "ITERATION LIMIT REACHED WITH NO CONVERGENCE." The iteration limit was 9999 and the previous maximum number of iterations required was 17 when bar 1 became plastic.

Similar results were obtained for all $\alpha \geq 10^{-4}$. In all cases the numbers produced by ADINA using the MNO model were in excellent agreement with the formulas in Sections 2 and 3.

Using ULF with $\alpha = 0$ we did not encounter any singularities and the program ran all the way to $P = 4.5$, the largest load requested. The displacement u was always identically zero, and bars 1 and 3 both became plastic at $P = 3.415$. The solution at $P = 3.415$ took only 3 iterations, but at $P = 4.415$ it took over 4000 iterations before the solution was found for all three bars plastic, and from then on it took about 20 iterations per step. All numbers were in close agreement with the results of Section 4 with $\alpha = 0$. When we ran the same program with BFGS iteration, the same numbers were obtained but the maximum number of iterations was three.

Figure 6 compares the motion of the loaded vertex according to the ADINA results and the theory in Sections 2 through 4 for $\alpha = 10^{-3}$ and $\alpha = 10^{-4}$. According to the MNO model bar 3 never does become plastic and the mechanism motion is simply $\Delta u = \Delta v$ once $P = 4.414$. ADINA gives the same results up to collapse of $P = 4.414$ but does not, of course, predict the mechanism motion.

For the ULF model when $\alpha = 10^{-3}$ equations (29) for Stage 3 apply only during a load increment $\Delta P = 0.0015$. Since the load step used in ADINA was only 0.001, it is perhaps not surprising that the predicted horizontal displacements are noticeably different, as shown in Fig. 6. It is not clear whether this is due to the numerical approximations in ADINA or to the approximate integration assumed in interpreting the difference equations in Section 4.

A lesser difference is observed for $\alpha = 10^{-4}$, as shown in Fig. 6. For $\alpha = 10^{-5}$ and $\alpha = 10^{-6}$, the predicted values of u are too small to appear on the scale of Fig. 6.

For $\alpha = 10^{-2}$ the results predicted by ADINA lie very close to the corresponding curve in Fig. 3.

Finally, for $\alpha = 10^{-1}$, ADINA's results are noticeably different from those predicted in Section 4, as indicated by the dot-dash curve in Fig. 3. Since the latter equations were all linearized with respect to α, it is to be expected that they may be significantly in error for α as large as 0.1. For example, a neglected term in α^2 might be considerably larger than a considered term in β.

6 Conclusions

The primary purpose of the present investigation was to examine the true significance of the nonunique solution predicted for the truss in Fig. 1. We considered first the effect of a small misalignment of load as evidenced by a horizontal component αP. The solution now was not only unique for all nonzero α, but approached a unique limit as α tended to zero through either all-positive or all-negative values. However, these limits were different, so that in effect the nonunique solution at $\alpha = 0$ has simply been replaced by a discontinuity at $\alpha = 0$. Further, it seems evident that similar results would have been obtained had we varied various other physical parameters such as yield stress or Young's modulus or geometrical quantities such as node position or cross-sectional area.

The inclusion of nonlinear geometric terms in the equilibrium equations represents a quite different philosophical approach. Whereas previously we had *added* a small perturbation to the model, in effect allowing for experimental error, we now *restored* a nonlinear effect which

normally exerts an entirely negligible effect on the solution. The results were to make all transitions smooth and unique. As α tended to zero from either direction the horizontal displacement also tended to zero, and a direct solution with $\alpha = 0$ encountered no singularity but gave the unique solution $u = 0$. Thus our implicit faith in the uniqueness and continuity of nature is confirmed, and the apparent singular behavior described in Sections 3 and 4 is merely the result of an oversimplified model of reality.

However, the answer above is really a mathematician's answer, and perhaps gives a misleading picture of reality to the engineer. Figure 4 was drawn with nonlinear scales to emphasize the difference between the discontinuous nonunique features of the MNO model and the unique continuous ULF model. Figure 7 shows the same information on a linear scale. Although the dashed curve for the ULF model is actually continuous through $\alpha = 0$, a variation of α from -0.005 to $+0.005$ essentially changes u from -2.0 to $+2.0$, whereas except near $\alpha = 0$ a change of 0.01 in α only produces a change of 0.3 in u. Thus, two experiments designed to have $\alpha = 0$ might well produce experimental values of $+2$ and -2 in u due to an error of half of one percent.

From another viewpoint, $\alpha = 10^{-3}$ represents deviation of less than 0.06 from the vertical in the load direction. According to Fig. 3, at stage $2L$ when the yield-point load is reached, $u = 1$ and $v = 3$ so that the total deviation of the loaded point from the vertical is more than 18 deg or some 300 times that of the load deviation.

In conclusion, for this simple example and considering variations in only one of the many parameters, we have shown that the linear equilibrium equations in the undeformed position produce a discontinuity and nonuniqueness which is mathematically disturbing but which is a very good approximation to physical reality. The nonlinear equilibrium equations in the deformed position produce a mathematically unique continuous solution, but one which exhibits such large changes over such a small range that the solution would be regarded as discontinuous from a practical engineering view point.

One must always be cautious about generalizing from a particular example. However, it is usually true that any phenomenon which is found in a simple example should be regarded as a possibility in a more general situation, whereas a particular technique which works in a particular case may or may not apply more generally.

If uniqueness of solution is important, it should not be assumed without evidence beyond the elastic limit. In particular, if an all-purpose computer program gives a message of termination, the possibility that the yield-point load is not yet reached should at least be considered. An empirical method of approach would be to introduce various small parameters of arbitrary sign and observe if any of them produce large effects on the solution.

The use of a numerical method which accounts for nonlinear geometric effects will almost certainly give better behaved results, but even here it would be wise to ask questions about the possibility of small changes in the problem making large differences in the results. Finally, one should always interpret the physical significance of any predicted anomalous effects. If a small change in input data truly produces a large change in an important output result, then the proposed structure is probably not a satisfactory one.

References

ADINA, 1981, "A Finite Element Program for Automatic Dynamic Incremental Nonlinear Analysis," ADINA Engineering Report AE 82-1, Watertown, Mass.

Bathe, K. J., 1982, *Finite Element Procedures in Engineering Analysis*, Prentice-Hall, Englewood Cliffs, N.J.

Freudenthal, A. M., 1954, "Effect of Rheological Behavior on Thermal Stresses," *Journal of Applied Physics*, Vol. 25, pp. 1110–1117.

Hodge, P. G., Jr., 1958, "The Practical Significance of Limit Analysis," *Journal of the Aero/Space Sciences*, Vol. 25, pp. 724–725.

Hodge, P. G., Jr. and White, D. L., 1980, "Examples of Nonuniqueness in Contained Plastic Deformation," ASME JOURNAL OF APPLIED MECHANICS, Vol. 47, pp. 273–277.

Prager, W., 1948, "Problem Types in the Theory of Perfectly Plastic Materials," *Journal of the Aeronautical Sciences*, Vol. 15, pp. 337–341.

G. I. N. Rozvany
Reader, Department of Civil Engineering,
Monash University,
Clayton, Victoria, Australia, 3168
Professor of Structural Engineering,
Universitat Essen,
4300 Essen 1, West Germany

T. G. Ong
Research Associate,
Department of Civil Engineering,
Monash University,
Clayton, Victoria, Australia, 3168

B. L. Karihaloo
Professor and Head,
Department of Civil Engineering & Surveying,
University of Newcastle,
N.S.W., Australia, 2308
Mem. ASME

A General Theory of Optimal Elastic Design for Structures With Segmentation

Optimal plastic design of segmented structures is reviewed and then general static-kinematic optimality criteria are introduced for segmented elastic structures. The proposed theory is illustrated with beam and plate examples and the results are checked by independent calculations.

Introduction

Using Prager's terminology, a structure may be divided into *segments*, over which the variation of the cross section is restricted to multiples of a prescribed function termed *shape function*. The simplest examples of segmented structures are beams, plates and shells of segmentwise constant cross section or thickness. However, the variation of the cross section over some segments may be governed, for example, by a linear or quadratic shape function resulting in a uniform taper or uniformly varying taper. At segment boundaries, sudden changes (steps) may occur in cross-sectional dimensions. Owing to savings in labour costs, segmented structures are often more economical than structures with freely varying cross sections.

Whilst a comprehensive optimization theory for *plastically designed segmented structures* was developed in the seventies, the aim of this paper is to extend the same ideas to *segmented elastic structures* having stress and deflection constraints. All theories discussed are based on *static/kinematic optimality criteria* which, in effect, convert a problem of structural optimization into a problem of structural analysis. This is done by regarding certain Lagrangian functions in the underlying variational problems as fictitious deflection fields and their derivatives as strain components. Euler-Lagrange equations can then be converted into optimal strain-stress relationships which, together with static and kinematic admissibility, furnish the optimal solution. The above idea was first introduced by Prager and Shield (1967) who used energy principles instead of variational formulation.

Contributed by the Applied Mechanics Division for publication in the JOURNAL OF APPLIED MECHANICS.

Discussion on this paper should be addressed to the Editorial Department, ASME, United Engineering Center, 345 East 47th Street, New York, N.Y. 10017, and will be accepted until two months after final publication of the paper itself in the JOURNAL OF APPLIED MECHANICS. Manuscript received by ASME Applied Mechanics Division, July 3, 1984; final revision, July 5, 1985.

Review of Optimality Conditions for Plastically Designed Segmented Structures

In one of the earliest papers on optimal *plastic* design, Foulkes (1954) introduced an *optimality criterion* for segmentwise prismatic beams. Foulkes' theorem states that for minimum weight the sum of absolute values of plastic hinge rotations within each segment must be proportional to the segment length. Sheu and Prager (1969) extended the same concept to plates of segment-wise constant thickness and Rozvany (1973; 1976, pp. 97–102) introduced a general theory of optimal plastic design for structures in which each segment has a prescribed shape. The above theory is based on an extension of a fundamental optimality criterion by Prager and Shield (1967) whose notation and terminology are used below.

The considered class of plastic design problems can be stated as

$$\min_{\mathbf{Q}^s}\Phi=\int_D \bar{\psi}(\mathbf{x})d\mathbf{x},\ \bar{\psi}\geq\psi(\mathbf{Q}),$$

$$\text{on } D_i{:}\bar{\psi}=\Lambda_i\gamma_i(\mathbf{x})(i=1,2,\ldots,n), \tag{1}$$

where $\mathbf{Q}$ is the "generalised stress vector" (containing stresses or stress resultants), ^{s} denotes statical admissibility, Φ is the total "cost" (e.g., total structural weight), $\bar{\psi}$ is the design value of the "specific cost", $\psi(\mathbf{Q})$ is the "specific cost function" representing the minimum cost requirement for a state of stress $\mathbf{Q}$ at a point or cross section, D is the structural domain containing the segments D_i $(i=1,2,\ldots,n)$ and referred to coordinates $\mathbf{x}$, Λ_i are unspecified constants and $\gamma_i(\mathbf{x})$ are given "shape functions".

To illustrate the above class of problems with a simple example, consider the plastic design of a uniformly loaded built-in beam (Fig. 1*a*). In plastic design, any statically admissible moment diagram ($\mathbf{Q}^s=M^s$) can be adopted and then the yield moment capacity M_y must fulfill the condition $M_y\geq|M^s|$. All

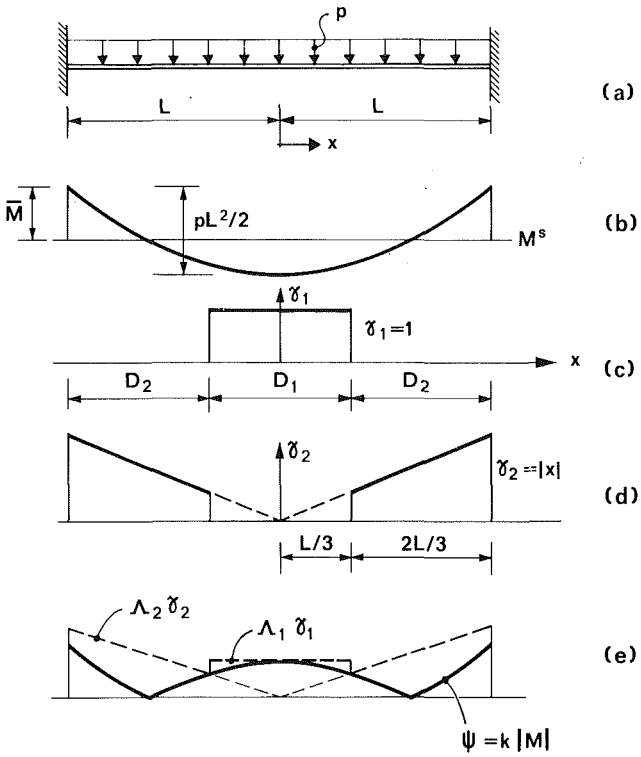

Fig. 1 Example of a segmented structure

symmetric statically admissible moment diagrams for the above problem are given in Fig. 1*b* in which the end moment value $\bar{M}$ can be chosen freely. Figures 1*c* and 1*d* show the two shape functions $[\gamma_1(x)$ and $\gamma_2(x)]$ to be used over the segments D_1 and D_2, respectively. If the "specific cost" $\bar{\psi}$ in this case is the beam volume per unit length (i.e., the cross-sectional area) then the design values of $\bar{\psi}$ will be $\Lambda_2\gamma_2 = \Lambda_2 |x|$ over the outer segments D_2 and $\Lambda_1\gamma_1 = \Lambda_1$ over the inner segment D_1 (Fig. 1*e*). Assuming finally that the beam has a given depth d, a variable width b and a yield stress of σ_y, the yield moment will be $M_y = bd^2\sigma_y/4$ and the corresponding cross-sectional area $\bar{\psi} = bd = kM_y$ with $k = 4/d\sigma_y$. Since $M_y \geq |M^s|$, it follows that $\bar{\psi} = \Lambda_i\gamma_i(x) = kM_y \geq \psi = k|M^s|$ where ψ is the cross-sectional area *requirement* for a given beam bending moment M. A feasible design in which the above inequality is satisfied as an equality at $x = 0$ and $x = \pm L/3$, is shown in Fig. 1*e*.

The optimal solution of the problem in equation (1) has been shown (Rozvany, 1973, 1976) to satisfy the following optimality criteria:

$$\text{on } D_i\text{: } \mathbf{q}^k = \lambda_i(\mathbf{x})\mathbf{G}[\psi(\mathbf{Q}^s)], \int_{D_i} \gamma_i(\mathbf{x})d\mathbf{x} = \int_{D_i} \gamma_i(\mathbf{x})\lambda_i(\mathbf{x})d\mathbf{x},$$

$$\text{at } \mathbf{x}\text{: } \lambda_i(\mathbf{x}) > 0 \text{ only if } \bar{\psi}(\mathbf{x}) = \psi[\mathbf{Q}(\mathbf{x})], \tag{2}$$

where $\lambda_i(\mathbf{x})$ is always non-negative, $\mathbf{q}$ is the generalised strain vector "associated with" $\mathbf{Q}$, the superscript^k denotes kinematic admissibility and $\mathbf{G}$ is the subgradient operator. For differentiable functions $\psi(\mathbf{Q})$, $\mathbf{G}[\psi(\mathbf{Q})] = (\partial\psi/\partial Q_1, \ldots, \partial\psi/\partial Q_m)$ but at slope discontinuities (see Point A in Fig. 2*a*) $\mathbf{G}[\psi(\mathbf{Q})]$ is non-unique and may take on *any* convex combination of the adjacent slopes (Rozvany, 1976, 1981).

In Prager's terminology (Prager, 1974), the stress vector $\mathbf{Q}$ is "associated" with $\mathbf{q}$ if $\mathbf{Q}\cdot\mathbf{q}$ (scalar product) is the (internal) work produced by $\mathbf{Q}$ and the virtual strains $\mathbf{q}$. For example, a bending moment for a beam is associated with the beam curvature in the same plane. The strains $\mathbf{q}(\mathbf{x})$ in equation (2) and the corresponding ("Pragerian") displacements $\mathbf{u}$ $(\mathbf{x})$ are in general fictitious quantities used for solving an extremum problem via a physical analogy. However, in the above problem $\mathbf{u}$ $(\mathbf{x})$ represents one feasible collapse velocity field for the optimal structure. By the inequality condition under equation

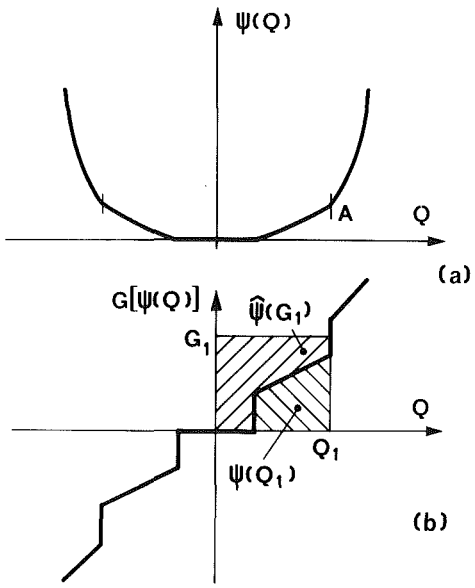

Fig. 2 Example of specific cost function, subgradient and complementary cost

(2), the generalised functions λ_i are in general only non-zero at isolated points and hence they usually consist of series of impulses (Dirac distributions).

Mathematical aspects of such solutions were discussed by Strang and Kohn (1983). A simple example of a specific cost function $\psi(Q)$ and its subgradient $G[\psi(Q)]$ is given in Fig. 2 in which $\psi(Q)$ depends on a single stress component (Fig. 2*a*) and its graph consists of a horizontal segment and four parabolic segments. At each slope discontinuity (cusp) of $\psi(Q)$ the subgradient $G[\psi(Q)]$ has a discontinuity (step) (Fig. 2*b*).

More recently (Rozvany, 1984, 1985), the dual of the problem in equation (1) was also determined for convex *symmetric* specific cost functions of a single variable and structures with segment-wise constant cross section ($\gamma_i = 1.0$):

$$\Phi_{\min} = \max_{u^k, q^k} \bar{\Phi} = \int_D pu\, dx - \sum_i L_i\hat{\psi}(|q|_{av})_i,$$

$$(|q|_{av})_i = \int_{D_i} |q|\, dx/L_i, \tag{3}$$

where $p(x)$ is the load, L_i is the length (or area) of D_i and $\hat{\psi}$ is the *complementary cost* (Rozvany, 1981) defined as (Fig. 2*b*)

$$\hat{\psi}(G_1) = Q_1G_1 - \psi(Q_1),\ G_1 = G[\psi(Q_1)]. \tag{4}$$

$u(x)$ is the ("Pragerian") deflection related to the strains q.

Primal-dual formulation has the advantage that an upper bound on the optimum cost can be obtained from any statically admissible stress field and a lower bound from any kinematically admissible strain field. Moreover, the same optimal solution can be checked on the basis of two independent calculations.

Considering *piece-wise prismatic beams* with a specific cost function $\psi = k|M|$ where k is a given constant and M is the bending moment, the shape functions in equation (2) become $\gamma_i = 1.0$ and then equations (2) and (3) reduce to

$$\text{on } D_i\text{: } \kappa^k = \lambda_i(x)k \text{ sgn } M, \quad L_i = \int_{D_i} \lambda_i(x)dx, \tag{5}$$

$$\text{at } x\text{: } \lambda_i(x) > 0 \quad \text{only if } \Lambda_i(x) = k|M(x)|,$$

$$\Phi_{\min} = \max_{u^k, \kappa^k} \int_D pu\, dx,\ |\kappa| \leq k, \tag{6}$$

where λ_i are nonnegative quantities, $\bar{\psi}_i = \Lambda_i = \text{const.}$ on D_i, $\kappa = -d^2u/dx^2$ is the beam curvature and u is the "associated"

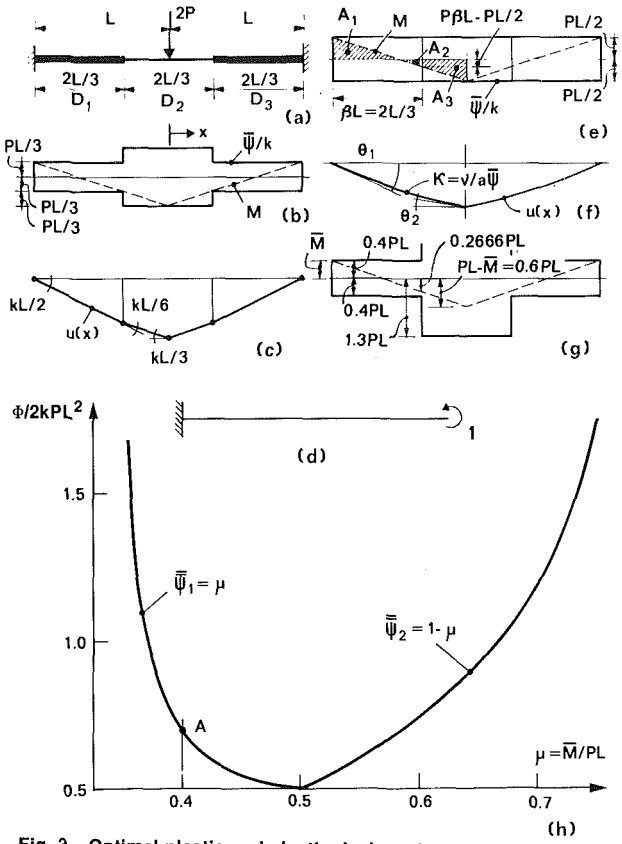

Fig. 3 Optimal plastic and elastic design of a segmented beam

beam deflection. The conditions in equations (5) and (6) constitute Foulkes' theorem (Foulkes, 1954) and its dual (Rozvany, 1984, 1985). The inequality in equation (6) is due to the fact that for $\psi = k\,|M|$, equation (4) gives $\hat{\psi} = 0$ for $\kappa \le k$ and $\hat{\psi} = \infty$ for $\kappa > k$.

Example. Considering the optimal plastic design of the beam with three prismatic segments in Fig. 3*a*, the solution satisfying the conditions (5) and (6) is given in Figs. 3*b* and 3*c*. Note that by equation (6) the generalised functions $\lambda_1(x)$ and $\lambda_2(x)$ can only be nonzero at $x = 0$, $x = L/3$ and $x = L$ because the condition $\bar{\psi} = \psi(x)$ is fulfilled only at the above x-values. Moreover, by equation (5) the integral of the λ_i functions must equal the segment length $L_i = 2L/3$ for all segments and kinematic admissibility requires that the integral of the curvature κ over the beam length equals zero. It follows that λ_1 consists of two impulses (having the magnitudes $L/2$ and $L/6$) and λ_2 of one impulse (magnitude: $2L/3$). Note that a curvature impulse becomes a concentrated rotation (cusp) whose sign by equation (5) is determined by the bending moment at that point. Both primal [equation (1) and Fig. 3*b*] and dual [equation (6) and Fig. 3*c*] formulations furnish the same total cost:

$$\Phi_{min} = \int_D \bar{\psi} dx = \int_D pu\, dx = 2Pu_{\max} = 8kPL^2/9. \tag{7}$$

Optimality Conditions for Redundant Elastic Structures with Stress and Displacement Constraints

An elastic structure may be subject to two types of kinematic constraints:

(*a*) physical kinematic constraints associated with (*i*) redundant supports and (*ii*) compatibility conditions for multidimensional structures (e.g., plates);

(*b*) operational kinematic constraints representing prescribed displacements in the design process.

Whereas *physical* kinematic constraints always consist of equalities, *operational* ones may consist of inequalities or equalities.

Both types of constraints can be handled by the proposed procedure. Applying a unit force or couple at the α^{th} prescribed deflection or rotation, respectively, let the generalised stress field equilibrating such "unit dummy load" be $\bar{\mathbf{Q}}_\alpha$. A deflection constraint may refer to some weighted combination of deflections and hence the unit dummy load may be replaced by any virtual load $\bar{p}$ (**x**). It is important to note that in any feasible solution the "virtual stresses" $\bar{\mathbf{Q}}_\alpha$ need to be statically admissible only, but in an optimal solution kinematic admissibility of the corresponding strains $\bar{\mathbf{q}}_\alpha$ is also required (see proof in the Appendix). On the other hand, the "real" stresses and strains (**Q**, **q**) must be both statically and kinematically admissible in all feasible solutions. However, the variational formulation does not have to include kinematic admissibility of the real strains **q** because this latter condition is automatically furnished by optimality over the set of all statically admissible stress fields ($\mathbf{Q}^s$ and $\bar{\mathbf{Q}}^s_\alpha$) (see the Appendix). Then by the principle of virtual work the displacement constraint can be expressed as

$$\int_D \left(\sum_{j=1}^{n} \sum_{k=1}^{n} Q_j \cdot \bar{Q}_{k\alpha}/S_{jk} \right) d\mathbf{x} = d_\alpha$$

$$\text{or} \int_D \left(\sum_{j=1}^{n} \sum_{k=1}^{n} Q_j \cdot \bar{Q}_{k\alpha}/S_{jk} \right) d\mathbf{x} \le d_\alpha \tag{8}$$

where $\mathbf{Q}(\mathbf{x}) = (Q_1, Q_2, \ldots, Q_n)$ is the stress field induced by the external load and Q_j/S_{jk} is the contribution of Q_j to the strain component q_k, $S_{jk}(\mathbf{x})$ is a specific stiffness component, and d_α are prescribed displacements. Note that d_α is zero for redundant reactions. Denoting the design value of the specific cost by $\bar{\psi}(\mathbf{x})$, the specific cost requirement (due to stress constraints) by $\psi(\mathbf{Q})$, the shape function for the segment D_i by $\gamma_i(\mathbf{x})$, and the stiffness-specific cost relation by $S_{jk} = S_{jk}(\bar{\psi})$, the optimality conditions for *any* segmented elastic structure become:

$$\int_{D_i} \gamma_i(\mathbf{x}) d\mathbf{x} = \int_{D_i} \gamma_i(\mathbf{x}) \lambda_i(\mathbf{x}) d\mathbf{x}$$
$$+ \int_{D_i} \sum_\alpha \nu_\alpha \sum_{j=1}^{n} \sum_{k=1}^{n} \frac{Q^s_j \bar{Q}^s_{k\alpha}}{S_{jk}^2} \frac{\partial S_{jk}}{\partial \bar{\psi}} \gamma_i(\mathbf{x}) d\mathbf{x} \quad \text{(for all } i\text{)} \tag{9}$$

$$\text{on } D_i\text{: } \bar{q}^k_j(\mathbf{x}) = \lambda_i(\mathbf{x}) \frac{\partial \psi}{\partial Q^s_j} + \sum_\alpha \nu_\alpha \sum_{k=1}^{n} \frac{\bar{Q}^s_{k\alpha}}{S_{jk}}$$
$$(j = 1, 2, \ldots, n) \tag{10}$$

$\lambda_i(\mathbf{x}) > 0$ only if $\bar{\psi}(\mathbf{x}) = \psi[\mathbf{Q}(\mathbf{x})]$,

$$\nu_\alpha > 0 \text{ only if } \int_D \left(\sum_{j=1}^{n} \sum_{k=1}^{n} Q_j \cdot \bar{Q}_{k\alpha}/S_{jk} \right) d\mathbf{x} = d_\alpha \tag{11}$$

where $\bar{\mathbf{q}}(\mathbf{x})$ is the "associated" strain vector, $\lambda_i(x)$ are non-negative functions and ν_α are non-negative constants. At slope discontinuities of $S_{jk}(\bar{\psi})$ and $\psi(\mathbf{Q})$, partial derivatives are replaced by subgradients (**G**).

Proof of the above optimality criteria and some duality theorems are given in the Appendix. Note that the above formulation does not take into consideration stress concentrations at sudden changes of cross section because it is assumed that such changes are locally "rounded" to eliminate high stresses at segment boundaries.

First Application: Segmentwise Prismatic Redundant Beam with a Stress Constraint

Let the specific cost function be $\psi = k\,|M|$, the stiffness

function $S = a\,\bar{\psi}$ where k and a are given constants. The shape functions for the above problem are $\gamma_i = 1$, while the stress vectors for a single redundant reaction become $\mathbf{Q}(x) = M(x)$ and $\bar{\mathbf{Q}}_\alpha(x) = \bar{\mathbf{Q}}_1(x) = \bar{M}(x)$ which denote bending moments equilibrating the external load and unit dummy (virtual) load, respectively. The strain vector becomes the curvature $\bar{q}_\alpha = \bar{\kappa} = -d^2u/dx^2$ where $u(x)$ is the "associated" (Prager and Shield, 1967) beam deflection. Then equations (9) and (10) reduce to

$$L_i = \int_{D_i} \lambda_i(x)dx + \int_{D_i} (\nu M\bar{M}/a\bar{\psi}_i^2)dx \text{ (for all } i) \tag{12}$$

$$\text{on } D_i: \quad \kappa = \lambda_i(x)k\, sgn M(x) + \nu\bar{M}/a\bar{\psi}_i \tag{13}$$

Moreover, by equation (*A*6, Appendix) with $m = n = 1$, $\Phi_{\min}$ can also be calculated from the dual expression

$$\Phi_{min} = \int_D pu\, dx \tag{14}$$

Example. Consider again the problem in Fig. 3*a* but with the elastic kinematic admissibility constraint $\int_D (M\bar{M}/S)dx = 0$ where $\bar{M}(x) = 1.0$ is caused by a unit couple at one clamped support (to assure zero rotation at that support, see Fig. 3*d*). The optimal solution and the corresponding associated deflection field $u(x)$ are shown in Fig. 3*e* and 3*f*. Then equation (12) and Fig. 3*e* imply

$$\theta_1/k = L_1 - \int_{D_1} (\nu M/a\bar{\psi}^2)dx = L_1 - \nu(A_2 - A_1)/a(kPL/2)^2$$
$$= \beta L + 2\nu(1-\beta)\beta/ak^2P \tag{15}$$

since $A_1 = PL^2/8$ and $A_2 = P(\beta L - L/2)^2/2$ in Fig. 3*e*. Similarly, for D_2 in Fig. 3*e*, equation (12) furnishes

$$\theta_2/k = (1-\beta)L - \nu A_3/a(kPL/2)^2 = (1-\beta)L - 2\nu\beta(1-\beta)/ak^2P \tag{16}$$

since $A_3 = P\beta L^2(1-\beta)/2$. The "distributed" curvature of $\nu/a\bar{\psi}$ in Fig. 3*f* is given by equation (13). Finally, kinematic admissibility requires:

$$\int_0^L \kappa\, dx = 0 = -\theta_1 + 2\nu/akP + \theta_2 \tag{17}$$

Equations (15)–(17) furnish

$$\theta_1 = kL/2 + \nu/akP, \quad \theta_2 = kL/2 - \nu/akP,$$

$$u_{\max} = \theta_1 L - (\nu/a\bar{\psi})L^2/2 = \left(\frac{kL}{2} + \frac{\nu}{akP}\right)L - \frac{2\nu}{akPL}\cdot\frac{L^2}{2} = kL^2/2. \tag{18}$$

Then equation (14) implies $\Phi_{\min} = PkL^2$ which agrees with the total primal "cost" of the solution in Fig. 3*e*. Note that the latter solution satisfies all optimality conditions not only for $\beta = 2/3$ but for any other β value within the range $0 \le \beta \le 1.0$.

Check by Independent Calculations. Denoting for any statically admissible solution the end moments by $-\bar{M}$ and introducing the notation $\mu = \bar{M}/PL$, $\bar{\bar{\psi}}_i = \bar{\psi}_i/PL$ $(i = 1,2)$, elastic compatibility ($\int_0^L (M/S)\,dx = 0$) implies for $\beta = 2/3$

$$[\bar{M}^2/2P - (2L/3 - \bar{M}/P)^2P/2]/a\bar{\psi}_1 = [(L - \bar{M}/P)^2P/2$$
$$-(2L/3 - \bar{M}/P)^2P/2]/a\bar{\psi}_2,\ (12\mu - 4)\bar{\bar{\psi}}_2 = (5 - 6\mu)\bar{\bar{\psi}}_1. \tag{19}$$

Clearly a beam which is understressed throughout ($\bar{\psi} > k\,|M|$) cannot be optimal. It is therefore sufficient to consider solutions with either $\bar{\bar{\psi}}_2 = 1 - \mu$ or $\bar{\bar{\psi}}_1 = \mu$. Substituting, in turn, these values into equation (19), the total cost values $\Phi/2kPL^2$ are shown in Fig. 3*h*. Clearly, $\mu = 1 - \mu = 0.5$ gives the optimal solution as in Figs. 3*e* and 3*f*.

Check on Uniqueness of the Solution. It is easy to check that for *any* nonoptimal solution the optimality conditions in equations (11)–(13) are *not* satisfied. Considering the design in Fig. 3*g*, for example (see point *A* in Fig. 3*h*), equation (11) requires $\lambda_2(x) \equiv 0$ on D_2 (since $\bar{\psi}_i > k\,|M|$). As in this case $\lambda_1(x)$ consists of a single impulse, equation (12) implies

$$\theta_2/k = \int_{D_1} \lambda_2(x)dx = 0 = L/3 - \nu(1/3)L[(0.6 + 0.2666)/2]PL/a(1.3\ kPL)^2,\ \nu = 3.9\ ak^2PL,$$

$$\theta_1/k = \int_D \lambda_1(x)dx = 2L/3 + \nu(2/3)L[(0.4 - 0.2666)/2]PL/a(0.4\ kPL)^2 = 1.75L,\ \int_D \nu/a\bar{\psi}dx = \int_{D_1} [\nu/(1.3\ kPLa)]dx + \int_{D_2} [\nu/(0.4\ kPLa)]dx = 7.5kL \tag{20}$$

which by equation (13) violates the kinematic condition

$$\int_0^L \kappa\, dx = 0.$$

Second Application: Circular Elastic Plate of Segmentwise Constant Thickness With Stress and Deflection Constraints

Consider a simply supported elastic plate of unit radius and uniform loading $p = 1$ whose thickness is constant over the segments D_1 $(0 \le r \le 0.5)$ and $D_2 (0.5 \le r \le 1)$. The deflection at the plate centre $(r = 0)$ is to be d. After suitable nondimensionalisation, we adopt the specific cost and stiffness functions:

$$\psi = \max(|M_r|^{1/2}, |M_\theta|^{1/2}),\ S_i = \bar{\psi}_i^3 \tag{21}$$

where M_r and M_θ are the radial and circumferential moments. It will be assumed that Poisson's ratio takes on a zero value, but the formulation in equations (9)–(11) can easily handle problems with nonzero Poisson's ratio. For zero Poisson's ratio, $Q_1 = M_r$ and $Q_2 = M_\theta$ we have $S_{11i} = S_{22i} = S_i$ and $S_{12} = S_{21} = 0$. Adopting $\gamma_i = 1$, equations (9) and (10) then reduce to

$$A_i = 2\pi\int_{D_i} \left[\lambda_i(r) + \nu\left(\frac{M_r\bar{M}_r}{S_i^2} + \frac{M_\theta\bar{M}_\theta}{S_i^2}\right)\frac{\partial S_i}{\partial\bar{\psi}_i}\right] r\, dr (i = 1,2) \tag{22}$$

$$\bar{\kappa}_r = -u'' = \lambda_i\frac{\partial\psi}{\partial M_r} + \frac{\nu\bar{M}_r}{S_i} \quad (i = 1,2)$$

$$\bar{\kappa}_\theta = -u'/r = \lambda_i\frac{\partial\psi}{\partial M_\theta} + \frac{\nu\bar{M}_\theta}{S_i} \tag{23}$$

where A_i is the area of the segment D_i and S_i is the plate stiffness per unit width over the segment D_i.

Denoting the plate deflection by $w(r)$, the usual elastic plate equations $S_i[(rw')'/r]' = r/2$, $M_\theta = -S_iw'/r$, $M_r = -S_iw''$ together with boundary and continuity conditions furnish:

(for $0 \le r < 0.5$)

$$M_r = C - 3r^2/16, \quad M_\theta = C - r^2/16$$

(for $0.5 < r \le 1$)

$$M_r = B - 3r^2/16 - E/r^2,\ M_\theta = B - r^2/16 + E/r^2,$$

with

$$C = (3 + 93\alpha)/[64(3 + 5\alpha)],$$
$$B = (47 + 49\alpha)/[64(3 + 5\alpha)],$$
$$E = 11(1-\alpha)/[64(3 + 5\alpha)],\ \alpha = S_1/S_2 \tag{24}$$

Case I Both Segments Understressed

Since in this case $\psi(M_\theta, M_r) < \bar{\psi}$ for $0 \le r \le 1$, equation (11) implies that $\lambda_1 \equiv 0$ and $\lambda_2 \equiv 0$ throughout and hence only the second term in equations (23) is nonzero. This means that

$u(r)/v$ becomes the elastic deflection field for the unit dummy load (unit force at $r=0$) while $\bar{M}_r$ and $\bar{M}_\theta$ are the elastic plate moments for the same load. The equilibrium conditions $[(ru')'/r]'/v = 1/2\pi r$, $\bar{M}_r = -S_i u''/v$, $\bar{M}_\theta = -S_i u'/vr$ and boundary/continuity conditions furnish

(for $0 \le r < 0.5$)

$$\bar{M}_r = [F-(1/2)-(ln\, r)/2]/2\pi$$
$$\bar{M}_\theta = [F-(ln\, r)/2]/2\pi$$

(for $0.5 < r \le 1$)

$$\bar{M}_r = [G(1-r^2)/r^2-(ln\, r)/2]/2\pi$$
$$\bar{M}_\theta = [(1/2)-G(1+r^2)/r^2-(ln\, r)/2]/2\pi$$

with

$$F=\frac{3(1-\alpha)ln(1/2)+8\alpha}{2(3+5\alpha)}$$
$$G=[F-(1/2)]/3 \tag{25}$$

Then by equation (22) with $\lambda_i \equiv 0$ and equations (21), (24) and (25)

$$\frac{\pi}{4} = \frac{3v(2\pi)}{S_1^{4/3}}\int_0^{1/2}(M_r\bar{M}_r+M_\theta\bar{M}_\theta)rdr$$
$$= \frac{3v}{S_1^{4/3}}\left\{\frac{1}{8192}[16ln(1/2)+8-32F] - \frac{C}{32}[4ln(1/2)-8F]\right\}, \tag{26}$$

$$\frac{3\pi}{4} = \frac{3v(2\pi)}{S_2^{4/3}}\int_{1/2}^{1}(M_r\bar{M}_r+M_\theta\bar{M}_\theta)rdr$$
$$= \frac{3v}{S_1^{4/3}}\left\{-\frac{15}{1024}-\frac{ln0.5}{512}+\frac{B}{8}[ln(1/2)+3+6G]+3EG - [Eln(1/2)]/2+3G/256\right\}. \tag{27}$$

Equations (26) and (27) then furnish

$$\alpha_{opt} = (S_1/S_2)_{opt} = 6.34373859 \tag{28}$$

The optimal values of S_1 and S_2 can be calculated from equation (28) and the condition $w(0)=d$. Since $M_\theta = -S_i w'/r$ and $w'(0)=0$ the value of d can be expressed from equation (24) as

$$S_1 d = S_1 w(0) = \int_0^{1/2} M_\theta r dr + \alpha\int_{1/2}^{1} M_\theta r dr$$
$$= (C+3\alpha B)/8-(1+15\alpha)/1024-\alpha E ln(1/2)$$
$$= \frac{3+418\alpha+219\alpha^2-176\alpha(1-\alpha)ln(1/2)}{1024(3+5\alpha)} \tag{29}$$

However, by equation (11) the above solution is only valid if $\lambda_i \equiv 0$ $(i=1,2)$ implying $\psi < \bar{\psi}$ (for $0 \le r \le 1$).

Case II The Inner Segment is Understressed and the Outer Segment Fully Stressed

It can be checked readily that for the quadratic moment fields in the inner region [equation (24)] and the stiffness ratio in equation (28), only the *outer* region can be fully stressed (at $r=0.5$), since for Case I the ratio $M_r(0)/M_r(1/2)$ is always smaller than $(6.34373859)^{2/3}$. The condition $\bar{\psi} = \psi(M_r, M_\theta) = \max(|M_r|^{1/2}, |M_\theta|^{1/2})$ can only be brought about by $\bar{\psi} = |M_r|^{1/2}$ for the following reasons. The fully stressed state for the circumferential moment ($\bar{\psi} = |M_\theta|^{1/2}$) would, by equations (11) and (23), imply an impulse in $\bar{\kappa}_\theta = -u'/r$. The latter, however, would cause a *step* in $u(x)$ which would be associated with two infinite impulses (of opposite sign) in $\bar{\kappa}_r = -u''$. The latter would clearly violate the first equation under (23) and equation (22), as well as the non-negativity condition for $\lambda_i(r)$. It follows that in Case II we must have $\bar{\psi}_2 = |M_r(0.5)|^{1/2}$. Then by equations (21) and (24), we have

$$C-(3/64) = S_2^{2/3} \tag{30}$$

This condition, together with equation (29) furnishes the optimal values of S_1 and S_2 for this case.

Case III Both Segments Fully Stressed

As we increase the value of the prescribed deflection d, we reach the case when the inner segment becomes also fully stressed with $\bar{\psi}_1 = |M_r(0)|^{1/2}$. Then equation (24) implies

$$C = S_1^{2/3} \tag{31}$$

which, together with equations (29) and (30), furnishes the unique deflection value

$$d_{max} = 0.97967086. \tag{32}$$

At any prescribed deflection d with $d > d_{max}$ the plate would be overstressed and hence d_{max} is the maximum feasible value of a prescribed deflection (in an equality form). However, the above solution would be valid for any prescribed deflection with $d > 0.9797086$ if the deflection constraint were to be specified as *inequality* constraints (prescribing the maximum permissible deflection value).

Check by Independent Calculation

The total plate volume is given by

$$\Phi/2\pi = \int_0^{1/2} S_1^{1/3} r dr + \int_{1/2}^{1} S_2^{1/3} r dr = S_1^{1/3}/8 + 3S_2^{1/3}/8. \tag{33}$$

For any value of $\alpha = S_1/S_2$ and d, the value of Φ can then be calculated from equations (29) and (33). The results are given in Fig. 4 in which the stress constraints in equation (30) (Curve *ZUSRT*) are also indicated. It can be seen that for understressed solutions (area above the curve *ZUSRT*), the minimum volume occurs along the line segment *QR*, with the d-value given in equation (28). In Case II, the optimal solutions are given by (the interior of) curve *SR* and in Case III by the point *S*. The boundary segments *SRT*, *SU* and *UZ* of the feasible region (Fig. 4) correspond to $\bar{\psi}_2 = |M_r(1/2)|^{1/2}$, $\bar{\psi}_1 = |M_r(0)|^{1/2}$ and $\bar{\psi}_2 = |M_\theta(1/2)|^{1/2}$, respectively.

Conclusions

1 A general theory of optimal design for elastic structures with segmentwise prescribed shape was presented. The proposed technique is based on *static-kinematic optimality* criteria, and can be regarded as a generalised combination of methods proposed by Foulkes (1954) and Prager and Shield (1967).

2 The above technique converts an optimization problem into a problem of structural analysis. Whereas in *optimal plastic design* only one static/kinematic analysis was necessary (for the "associated" or "Pragerian" field), in *optimal elastic design* two such analyses are required (one for the associated field and one for the elastic stresses/strains).

3 The optimality conditions for elastic systems include a *local stress-strain relationship* for the associated field which depends on both the elastic stresses in the optimal structure and on the associated strains (caused by the virtual loads used in the deflection constraints). In addition, a *global condition* must be fulfilled *for each segment*. The latter involves the integral of some strain terms which must equal the length or area of the segment (for segmentwise constant cross section) or the integral of the shape function for that segment (general case).

4 Further extensions of this theory could readily handle allowance for selfweight (see Karihaloo and Hemp, 1983; Rozvany and Wang, 1984) optimization of the location of segment boundaries and supports (see Masur, 1974; Prager and Roz-

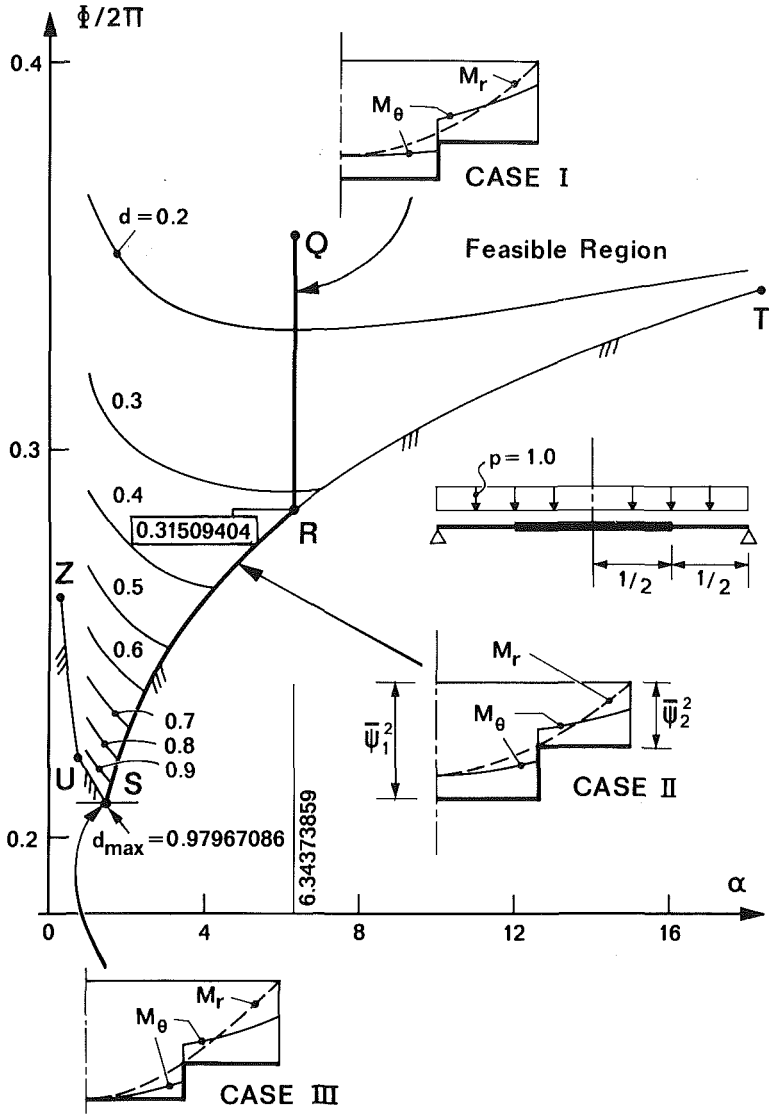

Fig. 4 Optimal elastic design of a simply supported elastic plate with a deflection constraint

vany, 1975) as well as elastic structures other than beams and plates.

5 By making the segments of infinitesimal length, the theory presented herein reduces to that for elastic structures with continuously variable cross section (Rozvany, 1977, 1978).

6 In the very special case when (i) all segments are controlled by a deflection constraint, (ii) there is only one stress component, (iii) the cost and stiffness functions are linear, and (iv) the structure is statically determinate, the proposed optimality conditions reduce to those of Prager (1971).

7 In the beam example given, the optimal elastic design is 12.5 percent heavier than the corresponding optimal plastic design.

8 In the plate example, the form of the optimal solution depends on the relative magnitude of the prescribed deflection. Consequently, either both segments, or only one segment, or neither segment is controlled by the stress constraint.

References

Foulkes, J., 1954, "The Minimum Weight Design of Structural Frames," *Proceedings of the Royal Society, London*, Ser. A, Vol. 223, pp. 482–494.

Karihaloo, B. L., and Hemp, W. S., 1983, "Maximum Strength/Stiffness Design of Structural Members in the Presence of Selfweight," *Proceedings of the Royal Society, London*, Ser. A, Vol. 389, pp. 119–132.

Masur, E. F., 1974, "Optimal Structural Design for a Discrete Set of Available Structural Members, *Computer Methods in Applied Mechanics and Engineering*, Vol. 3, pp. 195–207.

Prager, W., 1974, *Introduction to Structural Optimization*, Springer-Verlag, Vienna.

Prager, W., and Shield, R. T., 1967, "A General Theory of Optimal Plastic Design," ASME Journal of Applied Mechanics, Vol. 34, pp. 184–186.

Prager, W., 1971, "Optimal Design of Statically Determinate Beams for Given Deflection," *International Journal of Mechanical Sciences*, Vol. 13, pp. 893–895.

Prager, W., and Rozvany, G. I. N., 1975, "Plastic Design of Beams: Optimal Location of Supports and Steps in the Yield Moment," *International Journal of Mechanical Sciences*, Vol. 17, pp. 627–631.

Rozvany, G. I. N., 1973, "Optimal Plastic Design for Partially Preassigned Strength Distribution," *Journal of Optimization Theory and Applications*, Vol. 11, pp. 421–436.

Rozvany, G. I. N., 1976, *Optimal Design of Flexural Systems*, in English: Pergamon, Oxford; in Russian: Stroijdat, Moscow, 1980.

Rozvany, G. I. N., 1977, "Elastic versus Plastic Optimal Strength Design," ASCE *Journal of Engineering Mechanics*, Vol. 103, pp. 210–214.

Rozvany, G. I. N., 1978, "Optimal Elastic Design for Stress Constraints," *Computers and Structures*, Vol. 8, pp. 455–463.

Rozvany, G. I. N., 1981, "Variational Methods and Optimality Criteria," *Proceedings, NATO ASI Optimization of Distributed Parameter Structures*, Haug, E. J., and Cea, J., eds., Sijthoff and Noordhoff, Alphen aan de Rijn, pp. 112–151.

Rozvany, G. I. N., 1984, "The Dual of Extended Prager-Shield and Foulkes' Optimality Criteria," ASCE *Journal of Engineering Mechanics*, Vol. 110, pp. 1778–1785.

Rozvany, G. I. N., 1985, "Generalisations of Heyman's and Foulkes' Theorems Using Dual Formulation," *International Journal of Mechanical Sciences*, Vol. 27, pp. 347–360.

Rozvany, G. I. N., and Wang, C.-M., 1984, "Optimal Layout Theory: Allowance for Selfweight," ASCE *Journal of Engineering Mechanics*, Vol. 110, pp. 66–83.

Sheu, C. Y., and Prager, W., 1969, "Optimal Plastic Design of Circular and Annular Sandwich Plates with Piece-wise Constant Cross-Section," *Journal of the Mechanics and Physics of Solids*, Vol. 17, pp. 11–16.

Strang, G., and Kohn, R., 1983, "Hencky-Prandtl Nets and Constrained Michell Trusses," *Computer Methods in Applied Mechanics and Engineering*, Vol. 36, pp. 207–222.

APPENDIX

Proof of Optimality Conditions and Duality Theorems

The considered problem can be formulated as

$$\min\Phi = \sum_i \int_{D_i} \Big\{\Lambda_i\gamma_i(x) + \lambda_i[-\Lambda_i\gamma_i(x) + \psi(\mathbf{Q}) + s_i] + \mathbf{u}[\mathbf{E}(\mathbf{Q},\mathbf{p})] + \sum_\alpha \mathbf{w}_\alpha[\mathbf{E}(\bar{\mathbf{Q}},\bar{p}_\alpha)] + \sum_\alpha \nu_\alpha\Big[\sum_{j=1}^{n}\sum_{k=1}^{n^\alpha}\frac{Q_j\bar{Q}_{k\alpha}}{S_{jk}(\Lambda_i\gamma_i)} + s_\alpha\Big]\Big\}d\mathbf{x} - \sum_\alpha \nu_\alpha d_\alpha \quad (A1)$$

where Λ_i are unknown constants, λ_i, $\mathbf{u}$ and $\mathbf{w}_\alpha$ Lagrangian functions, ν_α Lagrangian multipliers, $s_i(x)$ slack functions, s_α slack variables, and $\mathbf{E}(\ ) = 0$ equilibrium equations. Other symbols were defined earlier (see equations (8)–(11)). Then necessary minimality conditions with respect to variations of Λ_i, $\mathbf{Q}$ and s_i furnish the optimality conditions in equations (9)–(11). It was shown earlier [Rozvany, 1976, p. 58] that for the variation of Q_j, the equilibrium equations produce a term in the Euler-Lagrange equations which represents the "associated" kinematically admissible strain component $\bar{q}_j^k$.

Considering now variations of the virtual stress components $\bar{Q}_{k\alpha}$, we obtain the Euler-Lagrange equations

$$q_{k_\alpha}/\nu_\alpha = \sum_j Q_j/S_{jk} (k = 1,2, \ldots, n) \quad (A2)$$

which has the same RHS for any α-value. Since q_{k_α}/ν_α are kinematically admissible strains associated with the elastic deflections $w(\mathbf{x})$ for the external load, it can be seen from equation (A2) that *the optimcal solution automatically satisfies the elastic compatibility equations* and hence it is not necessary to incorporate the latter in the variational problem (eqn. (A1)). This conclusion was verified on specific types of multidimensional structures (e.g., elastic plates). Note also that in *structural analysis*, the virtual stress fields $\bar{Q}_\alpha$ need to be only statically admissible. By virtue of equation (10), however, the strains produced by $\bar{Q}_\alpha$ in *optimization problems* must also satisfy kinematic conditions.

Dual formulae for calculating the minimum total cost $\Phi_{\min}$ can be readily obtained for various subclasses of problems. For example, for a single deflection constraint ($\bar{p}$ = unit load), $\gamma_i = 1$ (for all i), $S_i = \bar{\psi}_i^n$, $Q_i = \max_{j,D_i} |Q_j| = \bar{\psi}_i^m$, we have

$$\bar{\psi}_i\frac{\partial S_i}{\partial\bar{\psi}_i} = nS_i, Q_i\frac{\partial\bar{\psi}_i}{\partial Q_i} = \frac{\bar{\psi}_i}{m} \quad (A3)$$

and by the principle of virtual work,

$$\int_D \bar{\mathbf{p}}\mathbf{w}d\mathbf{x} = d = \int_D \sum_k \bar{\mathbf{Q}}_k\mathbf{q}_k d\mathbf{x},$$

$$\int_D \mathbf{p}\mathbf{u}d\mathbf{x} = \int_D \sum_j \mathbf{Q}_j\bar{\mathbf{q}}_j d\mathbf{x} \quad (A4)$$

where d is the prescribed deflection, $w(\mathbf{x})$ is the elastic displacement and $u(\mathbf{x})$ is the associated displacement.

Then equations (9), (10), (A2), (A3) and (A4) imply:

if all segments are understressed:

$$\Phi_{\min} = n\nu d = n\int_D pud\mathbf{x} \quad (A5)$$

if all segments are fully stressed:

$$\Phi_{\min} = \nu(n-m)d + m\int_D pud\mathbf{x} \quad (A6)$$

The validity of the expressions in (A5) and (A6) has been checked on the beam and plate examples presented.

Linear Analysis of Uniformly Stressed, Orthotropic Cylindrical Shells

J. F. Wilson
Professor,
School of Engineering,
Duke University,
Durham, NC 27706.
Mem. ASME

G. Orgill
Senior Research Engineer,
Exxon Production Research Co.,
Houston, TX 77252.

Within the framework of classical elasticity, the nonbuckled deformations are calculated for orthotropic, right circular, thin-walled cylinders under uniform load conditions. The principle direction of orthotropy follows parallel constant angle helices. Nondimensional system parameters involving four material constants and three loading conditions (internal pressure, longitudinal load, and pure torque) are identified. Through parametric studies deformation patterns are calculated that are unique to orthotropy. Numerical examples illustrate that the proper selection of cylinder orthotropy can lead to designs with optimal deformations or load-carrying capacity. Results may be used for the design of robotic actuators driven by internal pressure.

Introduction

Improvement in the mechanical performance of cylindrical or nearly cylindrical shell-type structures may be achieved by adding reinforcement or by making small modifications in the basic structural geometry. For instance, the high pressure capacity of fire hoses is due to the reinforcing effect of the helical fibers in the rubber walls. In other cases, the buckling resistance to longitudinal loading of thin-walled cylindrical columns can be greatly improved by the use of a fluted design, or a periodic variation of the radius around the circumference. On the other hand, there are cases where high deformations are desirable as, for instance, in cylindrical bellows used as pipeline expansion joints. Here, length changes of up to 100 percent may be achieved by the use of axisymmetric, periodic corrugations along the length of a basic cylindrical shape (Wilson, 1984). Thus, the most flexible directions of the bellows and the thin-walled fluted column are orthogonal.

The purpose of this paper is to present a unified continuum model of such thin-walled, cylindrical shells using directional material properties. Such continuum models are especially efficient for calculating overall, nonbuckling, elastic deformations for fiber-reinforced cylinders (Verma and Rana, 1983), and for uniformly loaded, anisotropic, cylindrical shells as discussed by Reissner (1970) and Reissner and Tsai (1974). In the present study, classical elasticity is employed to predict the nonbuckled deformations for uniform, orthotropic right circular cylinders with thin walls, subjected to three types of uniform loads: a torque T effecting rotation about the longitudinal axis, a longitudinal load P, and an internal pressure p. Strains along the geometric axes of symmetry are presented as functions of nondimensional system parameters involving these loads (applied separately and in combination), the cylinder geometry, four material properties, and the constant helix angle θ_o that defines the direction of maximum stiffness. See Fig. 1. This continuum model may describe the overall deformation characteristics of fiber-reinforced tubes as well as tubes with corrugations at arbitrary helix angles, as long as the cylindrical shape is maintained under load. Results may be used in future designs of robotic actuators that twist (40 deg $< \theta_o <$ 80 deg) or that only lengthen as for bellows ($\theta_o = 0$) when subjected to internal pressure.

Constitutive Relationships

Following the development of Lekhnitskii (1963), the constitutive law for an orthotropic, elastic solid that relates the six strain components to the six stress components is given by

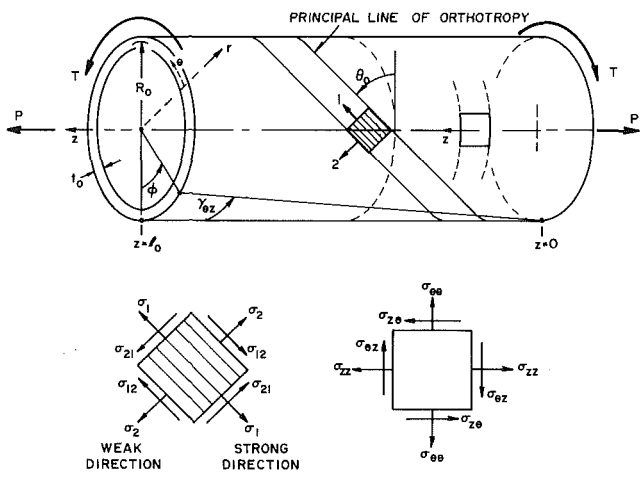

Fig. 1 Definition of the orthotropic cylinder

Contributed by the Applied Mechanics Division for publication in the JOURNAL OF APPLIED MECHANICS.

Discussion on this paper should be addressed to the Editorial Department, ASME, United Engineering Center, 345 East 47th Street, New York, N.Y. 10017, and will be accepted until two months after final publication of the paper itself in the JOURNAL OF APPLIED MECHANICS. Manuscript received by ASME Applied Mechanics Division, June 18, 1985; final revision, November 18, 1985.

$$\begin{bmatrix} \epsilon_{11} \\ \epsilon_{22} \\ \epsilon_{33} \\ \gamma_{12} \\ \gamma_{13} \\ \gamma_{23} \end{bmatrix} = \begin{bmatrix} \frac{1}{E_{11}} & -\frac{\nu_{21}}{E_{22}} & -\frac{\nu_{31}}{E_{23}} & 0 & 0 & 0 \\ -\frac{\nu_{12}}{E_{11}} & \frac{1}{E_{22}} & -\frac{\nu_{32}}{E_{33}} & 0 & 0 & 0 \\ -\frac{\nu_{13}}{E_{11}} & -\frac{\nu_{23}}{E_{22}} & \frac{1}{E_{33}} & 0 & 0 & 0 \\ 0 & 0 & 0 & \frac{1}{G_{12}} & 0 & 0 \\ 0 & 0 & 0 & 0 & \frac{1}{G_{13}} & 0 \\ 0 & 0 & 0 & 0 & 0 & \frac{1}{G_{23}} \end{bmatrix} \begin{bmatrix} \sigma_{11} \\ \sigma_{22} \\ \sigma_{33} \\ \sigma_{12} \\ \sigma_{13} \\ \sigma_{23} \end{bmatrix} \tag{1}$$

Equation (1) is written with respect to the principal axis (1,2,3). The 6×6 material matrix, whose elements are designated as a_{ij}, is determined by experiments. The strains and stresses of equation (1) are redefined using single subscription, or

$$\epsilon_{11}=\epsilon_1, \quad \epsilon_{22}=\epsilon_2, \quad \epsilon_{33}=\epsilon_3 \tag{2a}$$
$$\gamma_{12}=\epsilon_4, \quad \gamma_{13}=\epsilon_5, \quad \gamma_{23}=\epsilon_6$$
$$\sigma_{11}=\sigma_1, \quad \sigma_{22}=\sigma_2, \quad \sigma_{33}=\sigma_3 \tag{2b}$$
$$\sigma_{12}=\sigma_4, \quad \sigma_{13}=\sigma_5, \quad \sigma_{23}=\sigma_6$$

Using this notation, equations (1) become

$$\epsilon_i=\sum_{j=1}^{6} a_{ij}\sigma_j \tag{3}$$

Recognizing that the total elastic energy for the orthotropic solid is invariant with respect to the coordinate system, the elements a'_{ij} of the material matrix in the (r,θ,z) coordinate system can be written in terms of a_{ij} of the (1,2,3) coordinate system. That is

$$a'_{ij}=\sum_{m=1}^{6}\sum_{n=1}^{6} a_{mn}q_{mi}q_{nj} \qquad i,j=1,2,\ldots 6 \tag{4}$$

where q_{ij} represents the direction cosines of the (1,2,3) system with the (r,θ,z) coordinate system. As shown in Fig. 1, the relationship is simply one of rotation of the (1,2) axis to the (θ,z) axis by an angle of $-\theta_o$ in the plane $r=$ constant. The values of q_{ij} for this rotation are listed in Table 1.

In the transformed coordinate system, the constitutive law is

$$\epsilon'_i=\sum_{j=1}^{6} a'_{ij}\sigma'_j \tag{5}$$

which is expressed in cylindrical coordinates as follows:

$$\begin{bmatrix} \epsilon_{\theta\theta} \\ \epsilon_{zz} \\ \epsilon_{rr} \\ \gamma_{zr} \\ \gamma_{\theta r} \\ \gamma_{\theta z} \end{bmatrix} = \begin{bmatrix} a'_{11} & a'_{12} & a'_{13} & 0 & 0 & a'_{16} \\ a'_{21} & a'_{22} & a'_{23} & 0 & 0 & a'_{26} \\ a'_{31} & a'_{32} & a'_{33} & 0 & 0 & a'_{36} \\ 0 & 0 & 0 & a'_{44} & a'_{45} & 0 \\ 0 & 0 & 0 & a'_{54} & a'_{55} & 0 \\ a'_{61} & a'_{62} & a'_{63} & 0 & 0 & a'_{66} \end{bmatrix} \begin{bmatrix} \sigma_{\theta\theta} \\ \sigma_{zz} \\ \sigma_{rr} \\ \sigma_{zr} \\ \sigma_{\theta r} \\ \sigma_{\theta z} \end{bmatrix} \tag{6}$$

For the types of uniform loading considered here, the shear stresses $\sigma_{\theta r}$ and σ_{zr} may be approximated as zero, an assumption consistent with the elastic theory of thin-walled cylinders (Timoshenko and Woinowsky-Krieger, 1959). From equation (6), the remaining stress-strain relations are thus

$$\begin{bmatrix} \epsilon_{\theta\theta} \\ \epsilon_{zz} \\ \epsilon_{rr} \\ \gamma_{\theta z} \end{bmatrix} = \begin{bmatrix} a'_{11} & a'_{12} & a'_{13} & a'_{16} \\ a'_{21} & a'_{22} & a'_{23} & a'_{26} \\ a'_{31} & a'_{32} & a'_{33} & a'_{36} \\ a'_{61} & a'_{62} & a'_{63} & a'_{66} \end{bmatrix} \begin{bmatrix} \sigma_{\theta\theta} \\ \sigma_{zz} \\ \sigma_{rr} \\ \sigma_{\theta z} \end{bmatrix} \tag{7}$$

The elements a'_{ij} of the material matrix of equation (7) are calculated from equation (4) with a_{ij} and q_{ij} given by equation (1) and Table 1, respectively. The results are as follows[1]:

$$a'_{11}=\frac{1}{E_{11}}\cos^4\theta_o+\left(\frac{1}{G_{12}}-\frac{2\nu_{12}}{E_{11}}\right)\sin^2\theta_o\cos^2\theta_0+\frac{1}{E_{22}}\sin^4\theta_o \tag{8}$$

$$a'_{22}=\frac{1}{E_{11}}\sin^4\theta_o+\left(\frac{1}{G_{12}}-\frac{2\nu_{12}}{E_{11}}\right)\sin^2\theta_o\cos^2\theta_o+\frac{1}{E_{22}}\cos^4\theta_o \tag{9}$$

$$a'_{33}=\frac{1}{E_{33}} \tag{10}$$

$$a'_{12}=a'_{21}=\left(\frac{1}{E_{11}}+\frac{1}{E_{22}}+\frac{2\nu_{12}}{E_{11}}-\frac{1}{G_{12}}\right)\sin^2\theta_o\cos^2\theta_o-\frac{\nu_{12}}{E_{11}} \tag{11}$$

Table 1 Elements of q_{ij} for axis rotation

i \ j	1	2	3	4	5	6
1	$\cos^2\theta_o$	$\sin^2\theta_o$	0	0	0	$\sin2\theta_o$
2	0	0	0	0	0	$-\sin2\theta_o$
3	0	0	1	0	0	0
4	0	0	0	$\cos\theta_o$	$-\sin\theta_o$	0
5	0	0	0	$\sin\theta_o$	$\cos\theta_o$	0
6	$-\frac{1}{2}\sin2\theta_o$	$\frac{1}{2}\sin2\theta_o$	0	0	0	$\cos2\theta_o$

[1] Note that ϕ as defined by Lekhnitskii (1963) is interpreted as $-\theta_o$ in Equations (8)–(17). Also, Equation (9) reflects a correction of the results reported in this reference.

$$a'_{23}=a'_{32}=-\frac{\nu_{23}}{E_{22}}\cos^2\theta_o-\frac{\nu_{31}}{E_{33}}\sin^2\theta_o \tag{12}$$

$$a'_{13}=a'_{31}=-\frac{\nu_{23}}{E_{22}}\sin^2\theta_o-\frac{\nu_{31}}{E_{33}}\cos^2\theta_o \tag{13}$$

$$a'_{66}=\left(\frac{4}{E_{11}}+\frac{4}{E_{22}}+\frac{8\nu_{12}}{E_{11}}-\frac{4}{G_{12}}\right)\sin^2\theta_o\cos^2\theta_o+\frac{1}{G_{12}} \tag{14}$$

$$a'_{16}=a'_{61}=\left[\frac{2}{E_{11}}\cos^2\theta_o-\frac{2}{E_{22}}\sin^2\theta_o-\left(\frac{1}{G_{12}}-\frac{2\nu_{12}}{E_{11}}\right)\cdot\right.$$
$$\left.\cdot(\cos^2\theta_o-\sin^2\theta_o)\right]\sin\theta_o\cos\theta_o \tag{15}$$

$$a'_{26}=a'_{62}=\left[\frac{2}{E_{11}}\sin^2\theta_o-\frac{2}{E_{22}}\cos^2\theta_o+\left(\frac{1}{G_{12}}-\frac{2\nu_{12}}{E_{11}}\right)\cdot\right.$$
$$\left.\cdot(\cos^2\theta_o-\sin^2\theta_o)\right]\sin\theta_o\cos\theta_o \tag{16}$$

$$a'_{36}=a'_{63}=\left(\frac{-2\nu_{31}}{E_{33}}+\frac{2\nu_{23}}{E_{22}}\right)\sin\theta_o\cos\theta_o \tag{17}$$

Evaluation of Material Constants

There are seven material constants that appear in equations (8)–(17), namely E_{11}, E_{22}, E_{33}, ν_{12}, ν_{23}, ν_{31} and G_{12}. It is necessary to determine how these constants are related to each other and then to devise meaningful tests to measure them. To insure that the strain energy is a single valued function of the strain displacements, the material matrix of equation (1) must be symmetric. That is

$$E_{11}\nu_{21}=E_{22}\nu_{12} \tag{18}$$

$$E_{22}\nu_{32}=E_{33}\nu_{23} \tag{19}$$

$$E_{33}\nu_{13}=E_{11}\nu_{31} \tag{20}$$

Consider a tensile test for which the specimen's longitudinal axis coincides with the longitudinal or z axis of an orthotropic cylinder, given that $\theta_o=90$ deg. For a uniform, applied stress $\bar{\sigma}_{zz}$ where $\sigma_{\theta\theta}=\sigma_{rr}=\sigma_{\theta z}=0$, it follows from equations (7)–(20) that the strains are

$$\epsilon_{\theta\theta}=-\frac{\nu_{12}}{E_{11}}\bar{\sigma}_{zz}=-\frac{\nu_{21}}{E_{22}}\bar{\sigma}_{zz} \tag{21}$$

$$\epsilon_{zz}=\frac{1}{E_{11}}\bar{\sigma}_{zz} \tag{22}$$

$$\epsilon_{rr}=-\frac{\nu_{31}}{E_{33}}\bar{\sigma}_{zz}=-\frac{\nu_{13}}{E_{11}}\bar{\sigma}_{zz} \tag{23}$$

Equation (22) shows that E_{11} is the equivalent of Young's modulus along the 1 axis. Now suppose that for $\theta_o=90$ deg the orthotropic tube corresponds to a fluted, thin-walled cylindrical column of a homogeneous, isotropic material with Young's modulus E and Poisson's ratio ν. This fluted column test specimen thus exhibits the same stress-strain behavior of the isotropic material in both the 1 (or z) direction and in the 3 (or r) direction. The following definitions of the orthotropic constants are consistent with equations (21)–(23).

$$E=E_{11}=E_{33} \tag{24}$$

$$\nu=\nu_{31}=\nu_{13}=\nu_{12} \tag{25}$$

Consider a second tensile test for which the specimen's longitudinal axis again corresponds with the z axis of an orthotropic cylinder, but now let $\theta_o=0$ deg. Again, the only nonzero stress is the applied, uniform tensile stress $\bar{\sigma}_{zz}$. It follows from equations (7)–(20), (24), and (25) that

$$\epsilon_{\theta\theta}=-\frac{\nu}{E}\bar{\sigma}_{zz}=-\frac{\nu_{21}}{E_{22}}\bar{\sigma}_{zz} \tag{26}$$

$$\epsilon_{zz}=\frac{1}{E_{22}}\bar{\sigma}_{zz} \tag{27}$$

$$\epsilon_{rr}=-\frac{\nu_{23}}{E_{22}}\bar{\sigma}_{zz}=-\frac{\nu_{32}}{E}\bar{\sigma}_{zz} \tag{28}$$

Observing equation (27), it is seen that the modulus of elasticity in the 2 (or z) direction is E_{22}. Now let

$$E'=E_{22} \tag{29}$$

$$\nu'=\nu_{21}=\nu_{23} \tag{30}$$

which define, respectively, the effective Young's modulus and Poisson's ratio for a bellows, consistent with the assumption that $\epsilon_{\theta\theta}=\epsilon_{rr}$ in this tensile test. It follows, using equations (24), (25), (29), (30), that equations (18)–(20) are satisfied if

$$\nu=\nu_{32},\quad E\nu'=E'\nu \tag{31}$$

In a third test, a pure shear stress $\sigma_{\theta z}$ is applied to an orthotropic cylinder for which $\theta_o=0$. This corresponds to the application of a pure torque that rotates a bellows about its longitudinal axis. As for the previous two tests, the cylinder is orthotropic only because of its corrugations, since it is constructed of an isotropic material with elastic constants E, ν and shear modulus G. Torsion tests on such a bellows reported by Dahl (1953) show that

$$\gamma_{\theta z}=\frac{\sigma_{\theta z}}{G} \tag{32}$$

which indicates that the rotation and shearing stress are those predicted by the theory of thin-walled tubes without corrugations. When equation (32) is compared with the stress-strain law given by equations (7)–(17) in this case, it is seen that

$$G=G_{12} \tag{33}$$

In summary, there are four independent material constants needed to describe the stress-strain behavior of a cylinder with corrugated walls made of an isotropic material, but modeled as an orthotropic, smooth-walled tube. The stiffest direction (modulus E) follows the corrugation lines forming constant angle helices. Orthogonal to the helices is the weakest direction (modulus E'). The independent material constants are E, E', G and ν. Given uniform stresses $\sigma_{\theta\theta}$, σ_{zz}, σ_{rr}, and $\sigma_{\theta z}$, the uniform strains are calculated from equation (7). Using equations (24), (25), (29–31) and (33), equations (8)–(17) give the elements of the material matrix as follows.

$$a'_{11}=\frac{1}{E}\cos^4\theta_o+\left(\frac{1}{G}-\frac{2\nu}{E}\right)\sin^2\theta_o\cos^2\theta_o+\frac{1}{E'}\sin^4\theta_o \tag{34}$$

$$a'_{22}=\frac{1}{E}\sin^4\theta_o+\left(\frac{1}{G}-\frac{2\nu}{E}\right)\sin^2\theta_o\cos^2\theta_o+\frac{1}{E'}\cos^4\theta_o \tag{35}$$

$$a'_{33}=\frac{1}{E} \tag{36}$$

$$a'_{12}=a'_{21}=\left(\frac{1}{E}+\frac{1}{E'}+\frac{2\nu}{E}-\frac{1}{G}\right)\sin^2\theta_o\cos^2\theta_o-\frac{\nu}{E} \tag{37}$$

$$a'_{23}=a'_{32}=-\frac{\nu}{E} \tag{38}$$

$$a'_{13}=a'_{31}=-\frac{\nu}{E} \tag{39}$$

$$a'_{66}=\left(\frac{4}{E}+\frac{4}{E'}+\frac{8\nu}{E}-\frac{4}{G}\right)\sin^2\theta_o\cos^2\theta_o+\frac{1}{G} \tag{40}$$

$$a'_{16}=a'_{61}=\left[-\frac{2}{E'}\sin^2\theta_o+\frac{2}{E}\cos^2\theta_o-\left(\frac{1}{G}-\frac{2\nu}{E}\right)\cdot\right.$$

$$\cdot(\cos^2\theta_o - \sin^2\theta_o)\Big]\sin\theta_o\cos\theta_o \tag{41}$$

$$a'_{26} = a'_{62} = \Big[-\frac{2}{E'}\cos^2\theta_o + \frac{2}{E}\sin^2\theta_o + \Big(\frac{1}{G} - \frac{2\nu}{E}\Big)\cdot (\cos^2\theta_o - \sin^2\theta_o)\Big]\sin\theta_o\cos\theta_o \tag{42}$$

$$a'_{36} = a'_{63} = 0 \tag{43}$$

These results can be used to calculate the strains, displacements, and rotations of the cylinder for the special cases of loading discussed below.

Equilibrium and Compatibility

As shown in Fig. 1, the thin-walled cylinder is subjected to three types of uniform loads: an internal pressure p, a longitudinal load P centered on the z axis, and a pure torque T causing rotation about the z axis. Since there are no boundary or edge constraints, the resulting uniform stresses may be derived using equilibrium conditions and elementary methods. In terms of the mean radius R_o and shell thickness t_o, which are essentially constant during loading, the stresses are:

$$\sigma_{zz} = \frac{pR_o}{t_o} \tag{44}$$

$$\sigma_{\theta\theta} = \frac{P}{2\pi R_o t_o} + \frac{pR_o}{2t_o} \tag{45}$$

$$\sigma_{\theta z} = \frac{T}{2\pi R_o^2 t_o} \tag{46}$$

Consistent with the thin-wall assumption, the radial stress is negligible, or $\sigma_{rr} = 0$.

Since these stresses and their corresponding strains, as given by equations (7) and (34–43), are all uniform, they are all independent of the cylindrical coordinates (r,θ,z). Thus the 81 St. Venant strain compatibility conditions are automatically satisfied (Sokolnikoff, 1956).

Strain-Displacement Relations

The general strain-displacement equations in polar-cylindrical coordinates given by Sokolnikoff (1953) are simplified as follows to express the condition that there are no variations in displacement in the θ or circumferential direction.

$$\epsilon_{rr} = \frac{\partial U_r}{\partial r} \tag{47}$$

$$\epsilon_{\theta\theta} = \frac{1}{r}\frac{\partial U_\theta}{\partial \theta} + \frac{U_r}{R} = \frac{U_r}{r} \tag{48}$$

$$\epsilon_{zz} = \frac{\partial U_z}{\partial z} \tag{49}$$

$$\gamma_{\theta z} = \frac{\partial U_\theta}{\partial z} + \frac{1}{r}\frac{\partial U_z}{\partial \theta} = \frac{\partial U_\theta}{\partial z} \tag{50}$$

Here, U_r, U_θ, and U_z are, respectively, the displacements in the r, θ, and z directions.

Following a procedure of Reissner (1970), these relationships can be integrated in terms of three functions $f_1(r,z)$, $f_2(z)$, and $f_3(z)$ which are to be determined. From equation (47):

$$U_r = r\epsilon_{rr} + f_1(r,z) \tag{51}$$

It follows from equations (48) and (51) that:

$$f_1(r,z) = r(\epsilon_{\theta\theta} - \epsilon_{rr}) \tag{52}$$

From the last two equations, then,

$$U_r = r\epsilon_{\theta\theta} = R_o\epsilon_{\theta\theta} \tag{53}$$

where $r = R_o$ for a thin-walled cylinder.

From equation (49):

$$U_z = z\epsilon_{zz} + f_2(z) \tag{54}$$

where the second function of integration, $f_2(z)$, is independent of r since the cylinder wall is very thin and any variations across this thickness have no significant effect on the longitudinal deformation. Further, by imposing the condition of no rigid body motion, where $U_z = 0$ at $z = 0$, and noting that U_z can be at most a linear function of z, then it is apparent that $f_2(z) = 0$. Thus equation (54) thus yields the position $\xi = z + U_z$ of a material point originally at point z measured from one end of the cylinder, or

$$\xi = (1 + \epsilon_{zz})z \tag{55}$$

The circumferential displacement is obtained by integrating equation (50) and then using equation (55). That is

$$U_\theta = \xi\gamma_{\theta z} + f_3(z) \tag{56}$$

Here the function of integration is again independent of r, which is consistent with the thin-wall assumption. By imposing the condition of no rigid body rotation where $U_\theta = 0$ at $z = 0$, and noting that U_θ can at most be a linear function in z, it is evident that $f_3(z) = 0$. Therefore, $U_\theta = \xi\gamma_{\theta z}$.

In summary, the radial, circumferential, and longitudinal displacements are given in terms of the strains, the mean radius, and the z coordinate only, or

$$U_r = R_o\epsilon_{\theta\theta};\quad U_\theta = (1 + \epsilon_{zz})z\gamma_{\theta z};\quad U_z = z\epsilon_{zz} \tag{57}$$

It is noted that U_θ and U_z are the same displacements assumed [2] for the solid orthotropic cylinder rotating about the z axis.

A further displacement of practical interest is the angle of rotation ϕ for a cross section of the cylinder at the coordinate z. Within the limits of linear theory, $\phi = U_\theta/R_o$. Thus, from equation (57):

$$\phi = \frac{z}{R_o}(1 + \epsilon_{zz})\gamma_{\theta z} \tag{58}$$

Parametric Studies

All of the calculations for the parametric studies that follow are based on equation (7), the stresses of equations (44)–(46), and the elements of the material matrix given by equations (34)–(43). The specific values of $E/G = 3$ and $\nu = 0.5$ were chosen since they are characteristic of the polymeric and rubber-like materials to be used in future applications.

Effects of Loading Without Constraint. In the first series of parametric studies, the separate effects of each loading, p, P, and T on the homogeneous strains $\gamma_{\theta z}$ and ϵ_{zz} were investigated for an unconstrained cylinder. The goal was to determine peak strains as a function of the appropriate nondimensional system parameters.

The three nondimensional parameters involving the shear strain $\gamma_{\theta z}$ are defined by the ordinates of Figs. 2 through 4, in which the only nonzero load is p, P, and T, respectively. For the isotropic case $(E/E' = 1)$, all three of these figures show no shear strain variations with the helix angle θ_o, a result that could be anticipated. For p loading only (Fig. 2) and for P loading only (Fig. 3) the negative ordinates indicate that $\gamma_{\theta z}$ is negative, or that the cylinder "unwinds" because of orthotropy $(E/E' > 1)$. For T loading only (Fig. 4), the positive ordinate indicates that the cylinder "winds up" if T is applied as shown in Fig. 1. The interesting result is that the *peak* value of each respective shear strain parameter occurs at a distinctly different value of θ_o. That is:

$$\text{peak}\Big(\frac{Et_o\gamma_{\theta z}}{pR_o}\Big) \text{ occurs for } \theta_o = 53 \text{ deg}$$

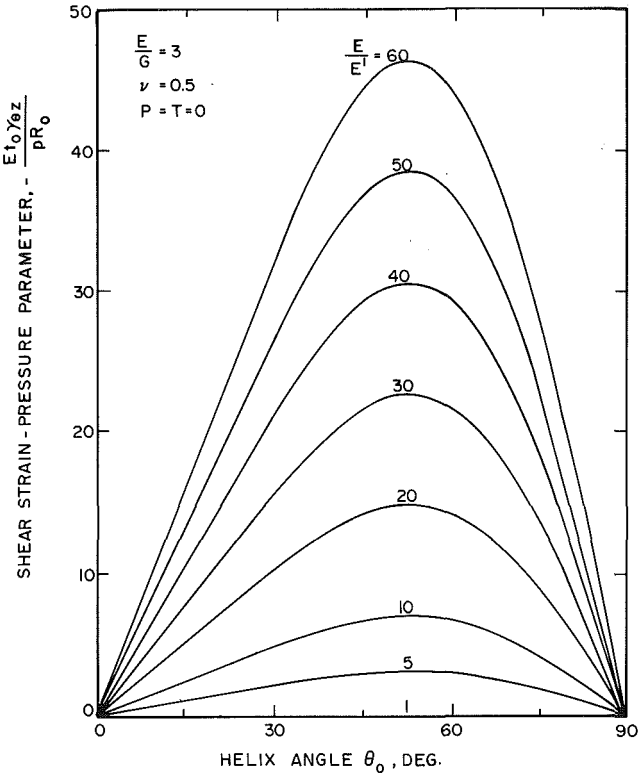

Fig. 2 Unrestrained twisting due to internal pressure

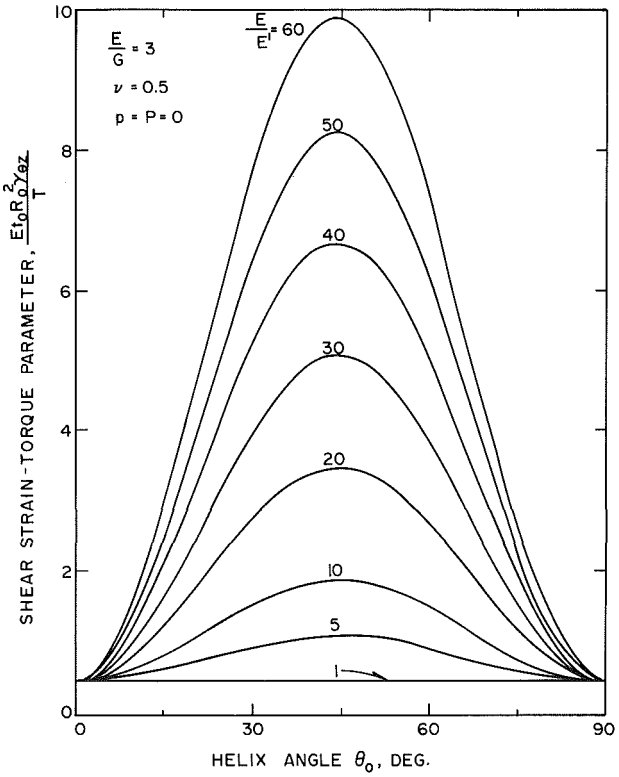

Fig. 4 Unrestrained twisting due to a pure torque

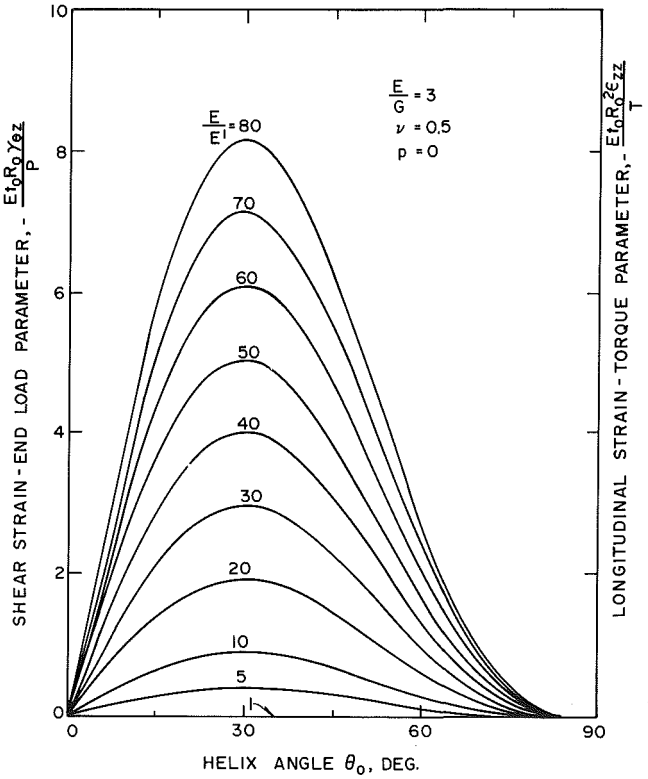

Fig. 3 Unrestrained twisting due to longitudinal load (left ordinate) and unrestrained longitudinal strain due to pure torque (right ordinate)

$$\text{peak}\left(\frac{Et_oR_o\gamma_{\theta z}}{P}\right) \text{ occurs for } \theta_o = 30 \text{ deg}$$

$$\text{peak}\left(\frac{Et_oR_o^2\gamma_{\theta z}}{T}\right) \text{ occurs for } \theta_o = 45 \text{ deg}$$

For each load type, there is no shift in these respective values of θ_o for $1 < E/E' \leq 100$.

The three nondimensional parameters involving the longitudinal strain ϵ_{zz} are defined by the ordinates of Figs. 5, 6 and 3 (right ordinate), given that p, P, and T are the only nonzero loads, respectively. For the isotropic case ($E/E' = 1$), ϵ_{zz} is zero for two load cases: with the p load as a direct consequence of choosing ν as 0.5, and with the T load as expected from elementary solutions. With orthotropy, the peak values of the longitudinal strain parameters are as follows:

$$\text{peak}\left(\frac{Et_o\epsilon_{zz}}{pR_o}\right) \text{ occurs for } \theta_o = 0$$

$$\text{peak}\left(\frac{Et_oR_o\epsilon_{zz}}{P}\right) \text{ occurs for } \theta_o = 0$$

$$\text{peak}\left(\frac{Et_oR_o^2\epsilon_{zz}}{T}\right) \text{ occurs for } \theta_o = 30 \text{ deg}$$

From Figs. 5 and 6 it is observed that the values of these parameters are only somewhat depressed for $0 < \theta_o \leq 15$ deg, but that this depression increases more rapidly as E/E' increases. From Fig. 3 (right ordinate) the longitudinal strain is seen to be negative, indicating the tendency of the orthotropic cylinder to shorten as it winds up under a positive torsion load.

Effects of Radial and End Constraint. While the studies above dealt with strain behavior for loadings applied one at a time, one can imagine a multitude of practical cases involving combined loads. Consider now one such case where an orthotropic cylinder is required to operate in close proximity with other mechanical parts. To avoid longitudinal and radial or circumferential expansions when pressurized, suppose that the unloaded orthotropic cylinder just fits within the confines of a rigid, closed-end tube. Under loading, then:

$$\epsilon_{zz} = \epsilon_{\theta\theta} = 0 \tag{59}$$

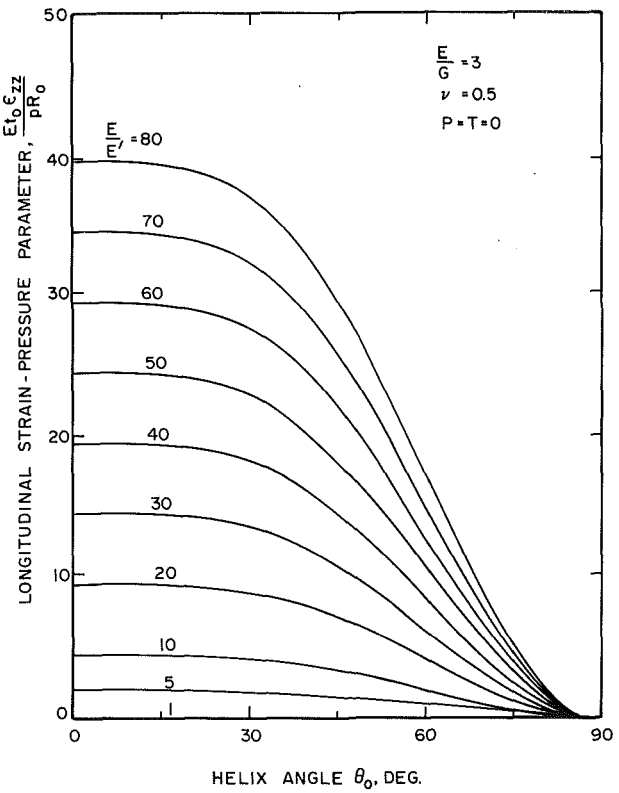

Fig. 5 Unrestrained longitudinal strain due to internal pressure

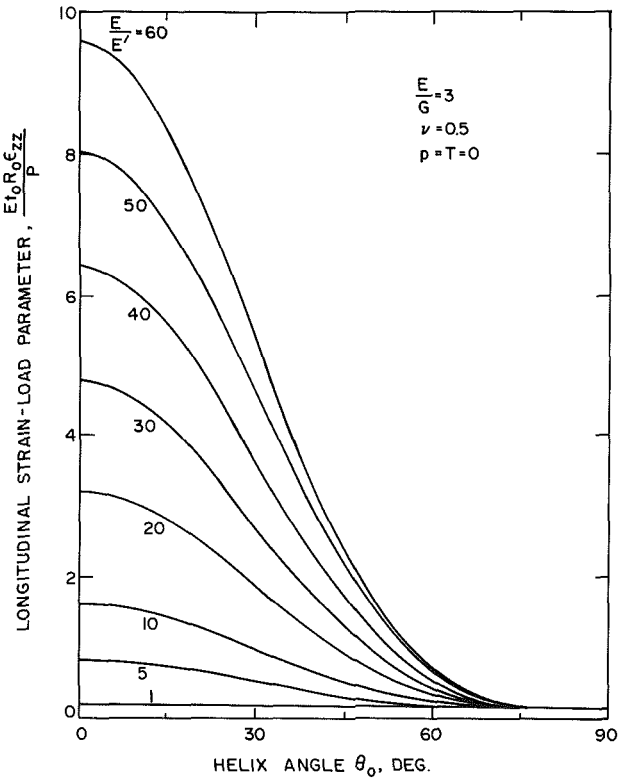

Fig. 6 Unrestrained longitudinal strain due to longitudinal load

The confining tube has frictionless walls where its design allows for the application of a torque T to the orthotropic cylinder. The confining tube does not inhibit torsion. From equations (7) and (44–46), the two constraints of equation (59) become:

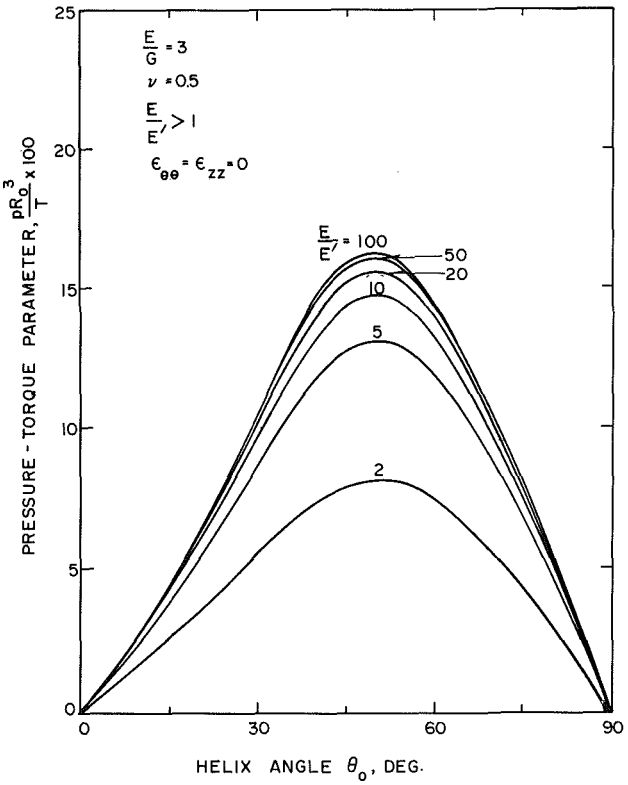

Fig. 7 Pressure-torque behavior for the fully confined cylinder

$$\left(a'_{12}+\frac{1}{2}a'_{22}\right)\frac{pR_o}{t_o}+a'_{22}\frac{P}{2\pi R_o t}+a'_{26}\frac{T}{2\pi R_o^2 t_o}=0 \tag{60}$$

$$\left(a'_{11}+\frac{1}{2}a'_{12}\right)\frac{pR_o}{t_o}+a'_{12}\frac{P}{2\pi r_o t}+a'_{16}\frac{T}{2\pi R_o^2 t_o}=0 \tag{61}$$

The compatible equation relating the loadings p and T is found by eliminating P between equations (60) and (61), or

$$\frac{T}{pR_o^3}=2\pi\left(\frac{a'_{12}a'_{12}-a'_{11}a'_{22}}{a'_{16}a'_{22}-a'_{12}a'_{26}}\right)=S \tag{62}$$

The pressure-longitudinal load parameter is found by eliminating T between equations (60) and (61). In terms of S of equation (62), this is

$$\frac{P}{pR_o^2}=-2\pi\left(\frac{a'_{12}}{a'_{22}}+\frac{1}{2}+\frac{a'_{26}}{a'_{22}}S\right) \tag{63}$$

The results of equations (62) and (63) are shown in Figs. 7 and 8. Figure 7 shows that the pressure-torque parameter, the inverse of equation (62), has a peak value at $\theta_o=50$ deg for all $E/E'>1$. For an imposed torque, this gives the maximum required cylinder pressure for full cylinder confinement. Figure 8 (the right ordinate) shows that the end load-pressure parameter defined by equation (63) is independent of E/E' if that ratio exceeds unity. For a fixed pressure level p, the compatible end load P always decreases with θ_o to maintain full cylinder confinement. It is noted that the isotropic cylinder is not shown in Fig. 8 (the right ordinate) since the only way that full cylinder confinement can be met for $E/E'=1$ is that $P=p=0$. For this latter set of conditions, it is recalled that a nonzero value for T always implies full cylinder confinement; that is, equation (59) is satisfied.

Using the results of equations (62) and (63) it is possible to calculate the helix angle that will minimize the rotation ϕ (minimize $\gamma_{\theta z}$) at a given pressure level. The conclusion in this case, based on the results of Fig. 8, left ordinate, is that $\theta_o=53$ deg will produce a minimum ϕ for all $E/E'>1$.

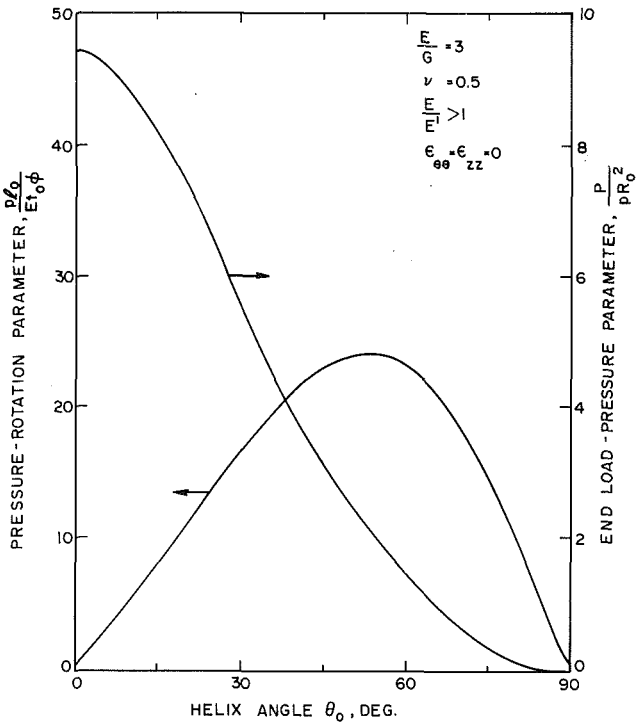

Fig. 8 Rotation (left ordinate) and longitudinal load (right ordinate) for a pressurized and fully confined cylinder

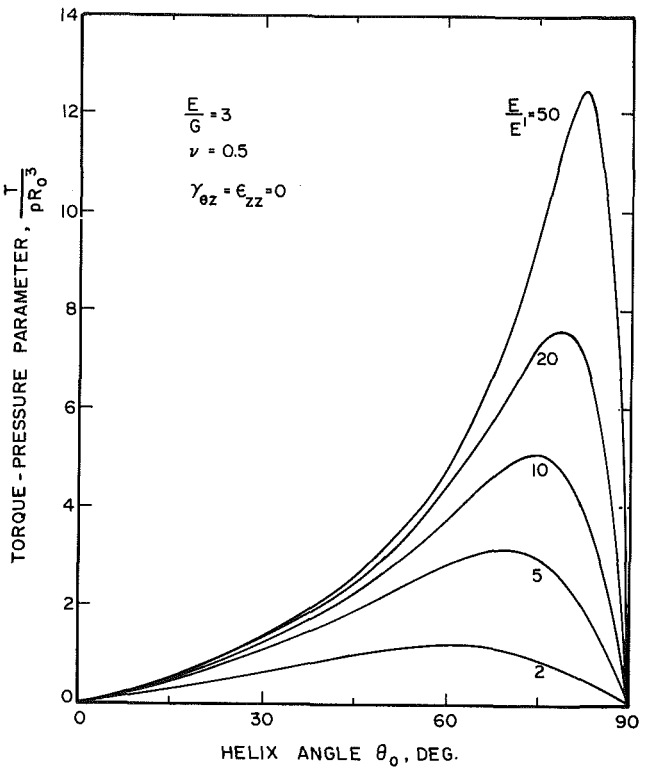

Fig. 9 Torque required to suppress rotation and longitudinal strain in a pressurized cylinder

Effects of Torsional and End Constraint. Consider now the special case where the orthotropic cylinder is fully restrained from rotation and also from longitudinal displacement. That is

$$\gamma_{\theta z} = \epsilon_{zz} = 0 \tag{64}$$

With equations (7) and (34)–(46) these two constraint equations are:

$$\left(a'_{12} + \frac{1}{2}a'_{22}\right)\frac{pR_o}{t_o} + a'_{22}\frac{P}{2\pi R_o t_o} + a'_{26}\frac{T}{2\pi R_o^2 t_o} = 0 \tag{65}$$

$$\left(a'_{16} + \frac{1}{2}a'_{26}\right)\frac{pR_o}{t_o} + a'_{26}\frac{P}{2\pi R_o t_o} + a'_{66}\frac{T}{2\pi R_o^2 t_o} = 0 \tag{66}$$

By eliminating P between equations (65) and (66), the torque-pressure parameter is deduced as:

$$\frac{T}{pR_o^3} = -2\pi\left(\frac{a'_{16}a'_{22} - a'_{26}a'_{12}}{a'_{22}a'_{66} - a'_{26}a'_{26}}\right) = S' \tag{67}$$

The compatible end load-pressure parameter is found by eliminating T between the same two equations. In terms of S' of equation (67), this is

$$\frac{P}{pR_o^2} = -2\pi\left(\frac{a'_{12}}{a'_{22}} + \frac{1}{2} + \frac{a'_{26}}{a'_{22}}S'\right) \tag{68}$$

The results of these studies are shown in Figs. 9 and 10. For a constant pressure p and a fixed modulus ratio E/E', it is observed that both the applied torque T and end load p reach peaks that are highly dependent on the helix angle. For instance, if the orthotropic cylinder were to be used as an efficient torque-exerting device, we would pick $\theta_o = 60$ deg if $E/E' = 2$, but would pick $\theta_o = 80$ deg if $E/E' = 50$. However, if this cylinder were to be used as a longitudinal or end loading device, we would choose $\theta_o = 62$ deg for $E/E' = 50$. These results are contingent, of course, on the requirement that all rotations and longitudinal motions be completely suppressed.

There are three observations for this case where $\theta_o = 90$ deg and $p > 0$. First, no end load is required for the longitudinal strain to vanish, which is a direct consequence of having chosen $\nu = 0.5$. Second, no torque is required and $\gamma_{\theta z}$ is automatically zero, a result that agrees with intuition. Third, a straightforward calculation of the circumferential strain reveals that $\epsilon_{\theta\theta}$ reaches its peak value when $\theta_o = 90$ deg, for all $E/E' > 1$.

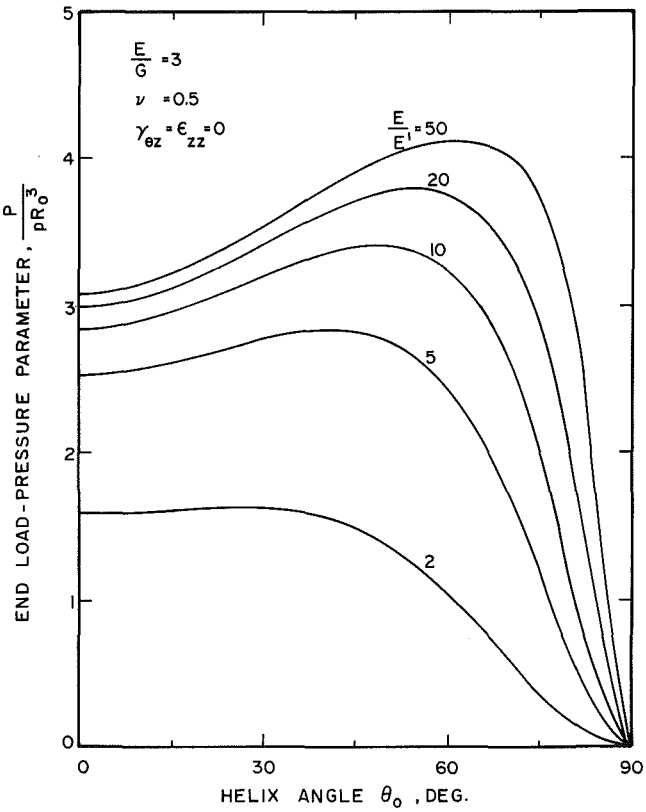

Fig. 10 End load required to suppress longitudinal strain and rotation in a pressurized cylinder

Design Examples

The following examples show the utility of the above parametric studies in the design of special purpose configurations. The finite length cylinders are assumed to be fitted with end caps that have negligible radial stiffness so that homogeneous stresses are maintained throughout. The material and geometric properties common to all three design examples discussed below are as follows: $E = 1.5 \times 10^7$ N/m^2; $E' = 1.5 \times 10^6$ N/m^2; $G = 5 \times 10^6$ N/m^2; $\nu = 0.5$; $t_o = 1.5$ mm; $R_o = 15$ mm; $l_o = 50$ mm.

In the first design, $\theta_o = 30$ deg and the maximum allowable internal pressure is $p = 1.9 \times 10^5$ N/m^2. What is the maximum torque T that such a cylinder can exert to loosen a bolt, for instance? With $E/E' = 10$, the value of the shear strain-pressure parameter for unconstrained rotation ($T = 0$) is given in Fig. 2 as -4.87, from which $\gamma_{\theta z} = -0.62$ rad. The maximum torque capacity is then the value of T for which $\gamma_{\theta z} = +0.62$ rad., corresponding to complete suppression of rotation. With this shear strain and the ordinate of Fig. 4, for which the shear strain-torque parameter is 1.55 at $\theta_o = 30$ deg and $E/E' = 10$, the maximum possible torque is thus calculated as $T = 2.02$ N-m.

For this first design, what is the length change in the cylinder for this maximum torque condition? From Fig. 5, the longitudinal strain-pressure parameter is 4.2, for which $\epsilon_{zz} = 0.53$ for unconstrained rotation ($T = 0$). For fully constrained rotation ($\gamma_{\theta z} = 0$) let $T = 2.02$ N-m. The corresponding value of longitudinal strain from the right ordinate of Fig. 3 is calculated, or $\epsilon_{zz} = -0.37$. By superposition, the net result is $\epsilon_{zz} = 0.16$, the length change of the cylinder is $U_z = 8$ mm and the final cylinder length is $\xi = 58$ mm, which are found from equations (57) and (55), respectively, for $z = l_o = 50$ mm.

In the second design, the maximum allowable internal pressure is again $p = 1.9 \times 10^5$ N/m^2. What value of θ_o will produce the maximum end load P? The procedure is to allow the cylinder to expand freely in the longitudinal direction with a strain ϵ_{zz} compatible with Fig. 5; and then for the same θ_o to apply a compressive load P compatible with Fig. 6 where this load completely nullifies the previous strain ϵ_{zz}. This is equivalent to finding the value of θ_o that maximizes the ratio Y_5/Y_6, or the ratio of ordinates of these two respective Figures. In these terms, the peak compressive value of P is given by

$$P = \left(\frac{Y_5}{Y_6}\right)_{\max} pR_o^2 = 341 \text{ N} \tag{69}$$

corresponding to $\theta_o = 58$ deg.

In the third design, the applied torque and the longitudinal strain are zero. What value of θ_o will produce the maximum cylinder rotation at an arbitrary internal pressure? In this case, $\gamma_{\theta z}$ is the sum of two components: that due to the internal pressure (Fig. 2) and that due to the longitudinal load (Fig. 3, left ordinate). In terms of the ordinates Y_2 and Y_3 of these respective Figs., as well as the ordinates Y_5 and Y_6, the total shear strain reduces to:

$$\gamma_{\theta z} = \left(-Y_2 + \frac{Y_3 Y_5}{Y_6}\right)\frac{pR_o}{Et_o} \tag{70}$$

In equation (70), the value of P was eliminated from Y_3 by the multiple Y_5/Y_6. Using a trial and error procedure, the peak value of the bracket term in equation (70) was calculated as -4.94, for which $\theta_o = 67$ deg. If the internal pressure is $p = 3.8 \times 10^4$ N/m^2, then the corresponding shear strain is $\gamma_{\theta z} = -0.125$ rad; and the rotational displacement and angle of rotation at $z = l_o$, calculated from equations (57) and (58), are $U_\theta = -6.25$ mm and $\phi = -0.42$ rad, respectively.

Summary and Conclusions

Within the limits of linear theory, the deformation behavior of uniformly stressed, orthotropic cylindrical shells is described by several nondimensional parameters involving four independent material constants E, E', G, ν, and three loads: internal pressure, longitudinal load and pure torque. It is assumed that buckling is absent and that the cylinder is sufficiently constrained so that the cylindrical shape is always maintained. As shown in Fig. 1, the principal directions of orthotropy follow constant angle helices. The more important findings of the parametric studies, unique to this type of orthotropy, are summarized as follows:

(1) Longitudinal loading P and/or internal pressure p effects twisting about the longitudinal axis.

(2) For P loading only, maximum twisting deformation occurs for an orthotropy angle of $\theta_o = 30$ deg; but for p loading only, this occurs when $\theta_o = 53$ deg.

(3) For a pure torque T, maximum twisting deformation occurs when $\theta_o = 45$ deg.

(4) A pure torque T produces a change in cylinder length, which is not the case for isotropic cylinders.

(5) The cylindrical strains $\gamma_{\theta z}$, $\epsilon_{\theta\theta}$ and ϵ_{zz} are all amplified for a given set of loads (p, P, T) as the magnitude of the orthotropy increases, that is, as E/E' increases, given that the geometry and other material constants remain fixed.

(6) The maximum longitudinal strain ϵ_{zz} for P and p loading occurs for $\theta_o = 0$; but ϵ_{zz} is maximum for T loading when $\theta_o = 30$ deg.

(7) The design examples show that the proper selection of cylinder orthotropy (θ_o and E/E') can lead to optimal deformations or load-carrying capacity. Such designs, however, are highly sensitive to both the type of loading and strain constraint conditions.

The results of these studies are important to the design of versatile and efficient pressure-controlled actuators made of rubber-like materials that can sustain relatively high strains. Orthotropy may be achieved by corrugations of the wall. Robotics is a logical field of application for such actuators.

Acknowledgment

This study was sponsored by the US Defense Advanced Research Projects Agency under Contract No. MDA903 -84-C-0243. The support and encouragement of William E. Isler, project monitor, is greatly appreciated.

References

Dahl, N. C., 1953, "Toroidal-Shell Expansion Joints," ASME JOURNAL OF APPLIED MECHANICS, Vol. 20, pp. 497–503.

Lekhnitskii, S. G., 1963, *Theory of Elasticity of an Anisotropic Elastic Body*, Translated from Russian by P. Fern, Holden-Day, Inc., San Francisco, CA.

Reissner, E., 1970, "On Uniform Stress and Strain in Axially Homogeneous Cylindrical Shells," *International Journal of Solids and Structures*, Vol. 6, pp. 133–138.

Reissner, E., and Tsai, W. T., 1974, "Pure Bending, Stretching, and Twisting of Anisotropic Cylindrical Shells," ASME JOURNAL OF APPLIED MECHANICS, Vol. 41, pp. 168–174.

Sokolnikoff, I. S., 1956, *Mathematical Theory of Elasticity*, 2nd Edition, McGraw-Hill, New York.

Timoshenko, S. P., and Woinowsky-Krieger, S., 1959, *Theory of Plates and Shells*, 2nd Edition, McGraw-Hill, New York.

Verma, P. D. S., and Rana, O. H., 1983, "Rotation of a Circular Cylindrical Tube Reinforced by Fibres Lying Along Helices," *Mechanics of Materials*, Vol. 2, pp. 353–359.

Wilson, J. F., 1984, "Mechanics of Bellows: A Critical Review," *International Journal of Mechanical Sciences*, Vol. 26, No. 11/12, pp. 593–605.

Finite Deformations of Nonlinear, Orthotropic Cylindrical Shells

G. Orgill
Senior Research Engineer,
Exxon Production Research Co.,
Houston, TX 77252

J. F. Wilson
Professor,
School of Engineering,
Duke University,
Durham, NC 27706
Mem. ASME

The nonbuckling finite deformations of an orthotropic, thin wall cylinder are investigated. The cylinder is made of a nonlinear material and subjected to internal pressure, end load and torque. Initially the stresses and strains in the cylinder are assumed to be axially homogeneous. The model is then extended to include axially nonhomogeneous stresses and strains that may arise due to particular displacement boundary conditions such as radial confinement at the edges. The loads are applied to the cylinder incrementally, the finite strains are computed, and adjustments are made in cylinder dimensions and the constitutive law to account for geometric and material nonlinearities. Parametric studies show how the deformation behavior is influenced by the orientation of the angle of material orthotropy. Results may be applied to the design of pressure controlled robotic actuators and manipulators.

Introduction

The behavior of cylindrical shells under a variety of loading combinations and boundary conditions has been the subject of intense study. The literature is replete with classical and numerical solutions involving stress, deformation, and buckling mechanisms. Most of the work to date, however, involves isotropic, linear, elastic materials where deformation are assumed to be small. Wilson and Orgill (1986) presented numerical results for small deformations of an orthotropic thin-wall right cylinder made of a linear, elastic material. Verma and Rana (1983) investigated displacements of a rotating concrete cylinder with steel reinforcing rods wound around the cylinder as helices. Reissner (1970) calculated the general expressions for stress and strain in anisotropic, thin walled cylinders and Lekhnitskii (1963) solved several problems involving linear elastic orthotropic solids. However, the work involving finite deformations of cylindrical shells, even for linear elastic isotropic materials, is sparse. The classical text of Green and Adkins (1970) discusses finite deformation analysis for shells from a general viewpoint. Leonard (1967) solved the particular problem of large deformations resulting from inflating a flexible isotropic shell of revolution. Presently there are several commercial computer codes employing numerical techniques to solve finite deformation, cylindrical shell problems.

As the use of rubber and other polymeric materials become increasingly popular in structural design, an analysis is needed that accounts for both geomtric nonlinearities arising from finite deformations and material nonlinearities. In applications using such materials, it may be desirable to incorporate helical reinforcement in the cylindrical shell or to model helical corrugations as orthotropy of a continuum. A procedure that accounts for such material and geometric nonlinearities, as well as material orthotropy along parallel helices oriented at a constant angle to the cylinder's longitudinal axis, is developed herein. See Fig. 1. Parametric studies show how the selection of the orthotropic properties will affect the deformation patterns and how proper selection of such properties can result in an optimal deformation or load-carrying capacity. First, the problem of axially homogeneous stress and strain is considered. These results are then extended to include nonaxially homogeneous stress and strain that arise due to end constraints. The assumption is made throughout this study that the stress and strain in the circumferential direction are homogeneous and that the cylinder maintains a circular cross-section as it deforms. Buckling loads and post-buckling behavior are not considered.

The loads on the cylinder are internal pressure, an end load applied along the longitudinal axis of the cylinder, and a pure torque about the longitudinal axis of the cylinder, applied separately or in combination. An incremental analysis technique is used in which small increments of load are applied to the cylinder at each step and the incremental strain is computed by assuming linearity over that small range. The change in section properties such as wall thickness and radius are computed from the strain increments at each step, thus accounting for the geometric nonlinearities. In addition the material properties, assumed to be known functions of strains, are updated as well. After each increment of load is applied, the section properties and material properties are recomputed. The procedure continues in this fashion until the desired load level is attained.

Part I Axially Homogeneous Stresses and Strains

Incremental Stresses. The stresses and strains are assumed to be axially homogeneous, which is possible if both ends of the cylinder are capped with flexible membranes. For increments of internal pressure Δp, end load ΔP, and torque ΔT, the incremental stresses at load step n are derived from elementary theory. These are:

Contributed by the Applied Mechanics Division for publication in the JOURNAL OF APPLIED MECHANICS.

Discussion of this paper should be addressed to the Editorial Department, ASME, United Engineering Center, 345 East 47th Street, New York, N.Y. 10017, and will be accepted until two months after final publication of the paper itself in the JOURNAL OF APPLIED MECHANICS. Manuscript received by ASME Applied Mechanics Division, October 21, 1985; final revision, November 18, 1985.

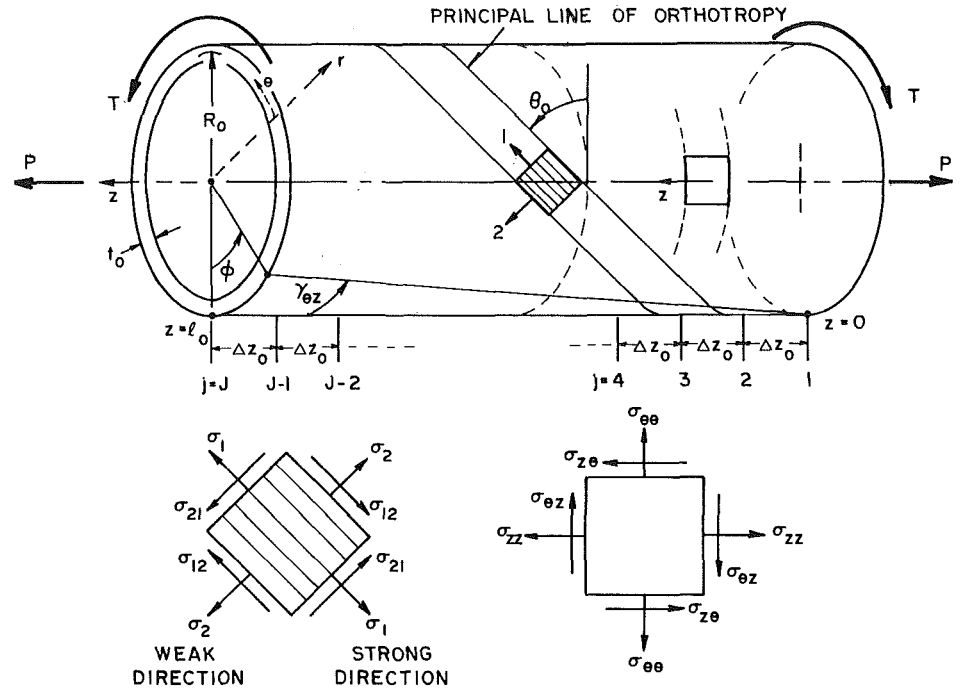

Fig. 1 Cylinder geometry, coordinates, and loading

$$\Delta\sigma_{\theta\theta n} = \frac{\Delta p\, R_i}{t_i} \tag{1}$$

$$\Delta\sigma_{zzn} = \frac{\Delta p\, R_i}{2t_i} + \frac{\Delta P}{2\pi\, R_i\, t_i} \tag{2}$$

$$\Delta\sigma_{rrn} = 0 \tag{3}$$

$$\Delta\sigma_{\theta zn} = \frac{\Delta T}{2\pi R_i^2\, t_i} = \frac{\Delta T}{Z_i} \tag{4}$$

where $n = i + 1 = 1, 2, 3, \ldots$
Here Z_i is the polar section modulus, and R_i and t_i are, respectively, the mean radius and thickness of the cylinder at load step n. The radial stress $\Delta\sigma_{rrn}$ is vanishingly small, consistent with the thin wall assumption.

Constitutive Relationships and Strain Transformations. Consider the thin-walled right circular cylinder of Fig. 1, with the orthotropy defined by the constant helix angle θ_i. The initial condition $i = 0$ is the no load condition. At load step $n = i + 1$, the incremental strain vector $\Delta\epsilon_n$ is related linearly to the incremental stress vector $\Delta\sigma_n$ through the 4×4 coefficient matrix $\mathbf{A}_i$, assuming sufficiently small load increments. That is:

$$\Delta\boldsymbol{\epsilon}_n = \mathbf{A}_i\, \Delta\boldsymbol{\sigma}_n \quad (i = n-1 = 0,1,2, \ldots) \tag{5}$$

$$\Delta\boldsymbol{\epsilon}_n^T = [\Delta\epsilon_{\theta\theta}\ \Delta\epsilon_{zz}\ \Delta\epsilon_{rr}\ \Delta\gamma_{\theta z}]_n \tag{6}$$

$$\Delta\boldsymbol{\sigma}_n^T = [\Delta\epsilon_{\theta\theta}\ \Delta\sigma_{zz}\ 0\ \Delta\sigma_{\theta z}]_n \tag{7}$$

and T denotes transpose.

The general classical constitutive equations for $\mathbf{A}_i$ as discussed by Lekhnitskii (1963) were reduced for the present problem by Wilson and Orgill (1986). The components of $\mathbf{A}_i$ are as follows, where the subscripts denote, respectively, the row position, the column position, and the load step.

$$a_{11_i} = \frac{\cos^4\theta_i}{E_i} + \left(\frac{1}{G_i} - \frac{2\nu}{E_i}\right)\sin^2\theta_i\, \cos^2\theta_i + \frac{\sin^4\theta_i}{E_i'} \tag{8a}$$

$$a_{22_i} = \frac{\sin^4\theta_i}{E_i} + \left(\frac{1}{G_i} - \frac{2\nu}{E_i}\right)\sin^2\theta_i\, \cos^2\theta_i + \frac{\cos^4\theta_i}{E_i'} \tag{8b}$$

$$a_{33_i} = \frac{1}{E_i} \tag{8c}$$

$$a_{12_i} = a_{21_i} = \left(\frac{1}{E_i} + \frac{1}{E_i'} + \frac{2\nu}{E_i} - \frac{1}{G_i}\right)\cos^2\theta_i\, \sin^2\theta_i - \frac{\nu}{E_i} \tag{8d}$$

$$a_{23_i} = a_{32_i} = a_{13_i} = a_{31_i} = -\frac{\nu}{E_i} \tag{8e}$$

$$a_{44_i} = \left(\frac{4}{E_i} + \frac{4}{E_i'} + \frac{8\nu}{E_i} - \frac{4}{G_i}\right)\sin^2\theta_i\, \cos^2\theta_i + \frac{1}{G_i} \tag{8f}$$

$$a_{14_i} = a_{41_i} = \left[-\frac{2}{E_i'}\sin^2\theta_i + \frac{2}{E_i}\cos^2\theta_i - \left(\frac{1}{G_i} - \frac{2\nu}{E_i}\right)(\cos^2\theta_i - \sin^2\theta_i)\right]\cdot\sin\theta_i\, \cos\theta_i \tag{8g}$$

$$a_{24_i} = a_{42_i} = \left[-\frac{2}{E_i'}\cos^2\theta_i + \frac{2}{E_i}\sin^2\theta_i + \left(\frac{1}{G_i} - \frac{2}{E_i}\right)(\cos^2\theta_i - \sin^2\theta_i)\right]\cdot\sin\theta_i\, \cos\theta_i \tag{8h}$$

$$a_{34_i} = a_{43_i} = 0 \tag{8i}$$

In equations (8), E_i and E_i' are the tangent moduli measured in simple tensile tests and correspond to the slopes of the stress-strain curves for principal strains ϵ_{11i} and ϵ_{22i} in the 1 and 2 directions, respectively. Similary, G_i is the tangent modulus for a simple shear test at the principal shear strain γ_{12i}. Poisson's ratio ν is taken as invarient with respect to strain levels ϵ_{11i} and ϵ_{22i} as observed experimentally for rubber by Goodyear (1949). As shown later, the angle of orthotropy θ_i changes with load increment.

The uniaxial stress-strain behavior with respect to the principle directions of orthotropy is assumed in the following form:

$$\sigma_{11} = E_o\, \epsilon_{11} + B\, \epsilon_{11}^3 + C\, \epsilon_{11}^5 \tag{9}$$

$$\sigma_{22} = E_0'\, \epsilon_{22} + B'\, \epsilon_{22}^3 + C'\, \epsilon_{22}^5 \tag{10}$$

and the behavior in simple shear with respect to these principal directions is of the same form, or

$$\sigma_{12} = G_0' \gamma_{12} + B_g \gamma_{12}^3 + C_g \gamma_{12}^5 \tag{11}$$

where the coefficients of the strain are measured constants. The tangent moduli with respect to the strains at level i in this 1-2 coordinate system, found by differentiating equations (9)–(11), are:

$$E_i = E_o + 3B \epsilon_{11i}^2 + 5C \epsilon_{11i}^4 \tag{12}$$

$$E_i' = E_o' + 3B' \epsilon_{22i}^2 + 5C' \epsilon_{22i}^4 \tag{13}$$

$$G_i = G_o' + 3B_g \gamma_{12i}^2 + 5C_g \gamma_{12i}^4 \tag{14}$$

These tangent moduli are used to compute the elements of $\mathbf{A}_i$ given by equations (8) for orientation θ_i.

The principal strains of equations (12)–(14) are related to the strains at load level i in the cylindrical system through the well-known transformation equations (Popov, 1981) given by:

$$2\epsilon_{11i} = \epsilon_{\theta\theta i} + \epsilon_{zzi} + (\epsilon_{\theta\theta i} - \epsilon_{zzi})\cos 2\theta_i + \gamma_{\theta zi} \sin 2\theta_i \tag{15a}$$

$$2\epsilon_{22i} = \epsilon_{\theta\theta i} + \epsilon_{zzi} + (\epsilon_{zzi} - \epsilon_{\theta\theta i})\cos 2\theta_i - \gamma_{\theta zi} \sin 2\theta_i \tag{15b}$$

$$\gamma_{12i} = (\epsilon_{zzi} + \epsilon_{\theta\theta i})\sin 2\theta_i + \gamma_{\theta zi} \cos 2\theta_i \tag{15c}$$

Geometric Nonlinearities. If the initial wall thickness is t_o, then after the first load increment is applied there will be a corresponding incremental radial strain $\Delta\epsilon_{rr1}$. The updated wall thickness after the first load increment

$$t_1 = t_o(1 + \Delta\epsilon_{rr1}) \tag{16}$$

Similary, after the second load increment, the updated wall thickness is:

$$t_2 = t_1(1 + \Delta\epsilon_{rr2}) \tag{17}$$

Between two successive load increments, it follows that the updated wall thickness is:

$$t_i = t_{i-1}(1 + \Delta\epsilon_{rri}) \tag{18}$$

In terms of the inital wall thickness t_o, equation (18) becomes:

$$t_i = t_o \prod_{k=1}^{i} (1 + \Delta\epsilon_{rrk}) \equiv t_o \, F_{ti} \tag{19}$$

The factor F_{ti} represents the deviation of t_i from t_o after load step i. The closer F_{ti} is to unity, the less the solution is affected by geometric nonlinearity.

A similar argument is made for changes in the mean radius. Equation (18), rewitten in terms of the mean radius and the incremental circumferential strain, is

$$R_i = R_{i-1}(1 + \Delta\epsilon_{\theta\theta i}) \tag{20}$$

Likewise, R_i can be expressed in terms of R_o, the mean radius of the cylinder under zero load, or

$$R_i = R_o \prod_{k=1}^{i} (1 + \Delta\epsilon_{\theta\theta k}) \equiv R_o \, F_{ri} \tag{21}$$

Here, F_{ri} represents the deviation of R_i from R_o after load step i.

Based on the cross-sectional area of a thin ring given by $A_i = 2\pi R_i t_i$, the updated expressions for the area become:

$$A_i = A_{i-1}(1 + \Delta\epsilon_{\theta\theta i})(1 + \Delta\epsilon_{rri}) \tag{22}$$

$$A_i = 2\pi R_o t_o \prod_{k=1}^{i} (1 + \Delta\epsilon_{\theta\theta k})(1 + \Delta\epsilon_{rrk}) \equiv 2\pi R_o t_o F_{ai} \tag{23}$$

Likewise, the updated values of the polar section modulus, initially given by $Z_o = 2\pi R_o^2 t_o$, are:

$$Z_i = Z_{i-1}(1 + \Delta\epsilon_{\theta\theta i})^2(1 + \Delta\epsilon_{rri}) \tag{24}$$

$$Z_i = 2\pi R_o^2 t_o \prod_{k=1}^{i} (1 + \Delta\epsilon_{\theta\theta k})^2(1 + \Delta\epsilon_{rrk}) \equiv 2\pi R_o^2 t_o F_{pi} \tag{25}$$

The corresponding expressions for changes in length of the cylinder are:

$$l_i = l_{i-1}(1 + \Delta\epsilon_{zzi}) \tag{26}$$

$$l_i = l_o \prod_{k=1}^{i} (1 + \Delta\epsilon_{zzi}) \equiv l_o \, F_{zi} \tag{27}$$

Computation of Strains. The total strains are needed in order to update values of the material properties E_i, E_i', and G_i and to compute cylinder displacements. Expressions for these strains are now deduced. Consider the relationship between the wall thicknesses t_1 and t_o given in equation (16). The total radius strain after the first load increment is:

$$\epsilon_{rr1} = \frac{t_1 - t_o}{t_o} = \frac{t_o(1 + \Delta\epsilon_{rr1})}{t_o} = \Delta\epsilon_{rr1} \tag{28}$$

and after the second load increment is:

$$\epsilon_{rr2} = \frac{t_2 - t_o}{t_o} = \frac{t_o(1 + \Delta\epsilon_{rr1})(1 + \Delta\epsilon_{rr2}) - t_o}{t_o}$$

$$= (1 + \Delta\epsilon_{rr1})(1 + \Delta\epsilon_{rr2}) - 1 \tag{29}$$

After i increments of load it follows that

$$\epsilon_{rri} = \frac{t_o \prod_{k=1}^{i} (1 + \Delta\epsilon_{rrk}) - t_o}{t_o} = F_{ti} - 1 \tag{30}$$

The total strains in the circumferential and longitudinal directions, obtained in a similar manner, are given by:

$$\epsilon_{\theta\theta i} = F_{ri} - 1 \tag{31}$$

$$\epsilon_{zzi} = F_{zi} - 1 \tag{32}$$

The total shearing strain $\gamma_{\theta zi}$ is simply the sum of the incremental shear strains, as there are no length changes involved. After i increments of load, this is

$$\gamma_{\theta zi} = \sum_{k=1}^{i} \Delta\gamma_{\theta zk} \tag{33}$$

The end rotation ϕ_i of the cylinder may be expressed in terms of shear strain. For the first and second load increments, the respective rotations are

$$\phi_1 = \Delta\phi_1 = \frac{l_o}{R_o} \Delta\gamma_{\theta z1} \tag{34}$$

$$\Delta\phi_2 = \frac{l_1}{R_1} \Delta\gamma_{\theta z2} \tag{35}$$

The total rotation after two increments of load is the sum of equations (34) and (35), or

$$\phi_2 = \frac{l_o}{R_o} \Delta\gamma_{\theta z1} + \frac{l_1}{R_1} \Delta\gamma_{\theta z2}$$

$$= \frac{l_o}{R_o} \left(\Delta\gamma_{\theta z1} + \frac{(1 + \Delta\epsilon_{zz1})}{(1 + \Delta\epsilon_{\theta\theta 1})} \Delta\gamma_{\theta z2} \right) \tag{36}$$

Extending equation (36) to i increments of load leads to:

$$\phi_i = \frac{l_o}{R_o} \left(\sum_{k=1}^{i} \Delta\gamma_{\theta zk} \prod_{m=1}^{i-1} \left(\frac{1 + \Delta\epsilon_{zzm}}{1 + \Delta\epsilon_{\theta\theta m}} \right) \right)$$

$$= \frac{l_o}{R_o} \cdot \frac{F_{z(i-1)}}{F_{r(i-1)}} \sum_{k=1}^{i} \Delta\gamma_{\theta zk} \tag{37}$$

Deformations for Single-Turn Orthotropy. Consider the segment of an unloaded cylinder with radius R_o and length l_o'. The length is selected such that a line parallel with the principal directon of orthotropy makes exactly one turn about the cylinder as shown in Fig. 2. This condition is expressed as:

$$l_o' = 2\pi R_o \tan\theta_o \tag{38}$$

After the first load increment, l_o', R_o, and θ_o change. The

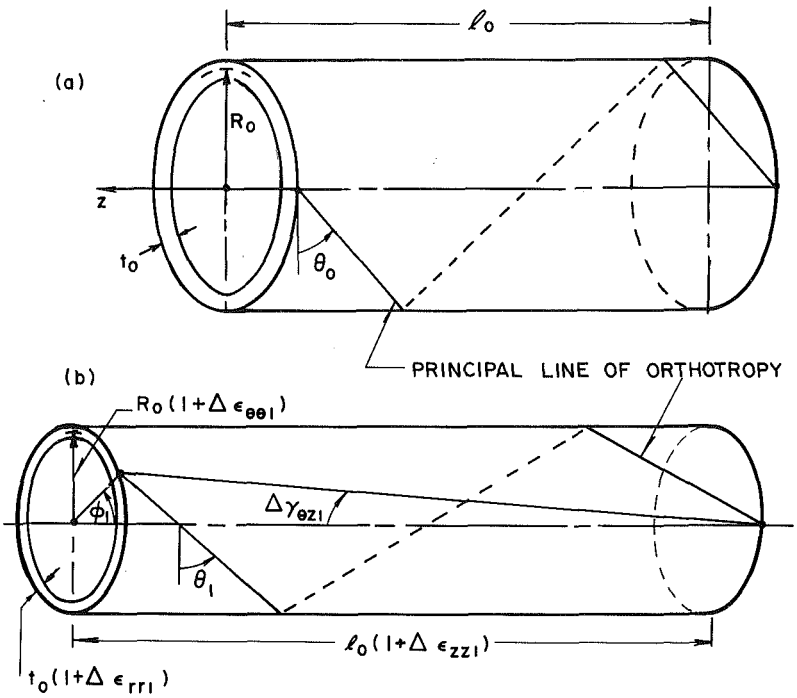

Fig. 2 Cylinder with a single turn helix: before loading (*a*), and after one load step (*b*)

Table 1 Load increments required for a solution error of less than 5 percent (linear material)

Maximum Value of Load Parameter		E_i/E_i'	E_i/G_i	Increment in Load Parameter
$\frac{p\,R_o}{E_o t_o}$	$=0.08$	10	3	0.001
	$=0.01$	50	3	0.001
$\frac{T}{E_o t_o R_o^2}$	$=0.07$	10	3	0.005
	$=0.25$	50	3	0.002
$\frac{P}{E_o t_o R_o}$	$=0.40$	10	3	0.001
	$=0.16$	50	3	0.001

resulting change in geometry is given by equations (20), (26), (34), and (38), or

$$l_1' = (2\pi+\phi_1)R_1\tan\theta_1 = l_o'(1+\Delta\epsilon_{zz1})$$
$$= \left(2\pi+\frac{l_o'}{R_o'}\Delta\gamma_{\theta z1}\right)R_o(1+\Delta\epsilon_{\theta\theta 1})\tan\theta_1 \tag{39}$$

It follows that the length for steps $i-1$ and i are given as:

$$l_{i-1}' = (2\pi+\phi_{i-1})R_{i-1}\tan\phi_{i-1} \tag{40}$$

$$l_i' = (2\pi+\phi_i)R_i\tan\theta_i$$
$$= \left(2\pi+\phi_{i-1}+\frac{l_{i-1}}{R_{i-1}}\Delta\gamma_{\theta zi}\right)R_i\tan\theta_i \tag{41}$$

Using equations (40) and (41), a recursion relationship to compute θ_i is deduced as:

$$\theta_i = \tan^{-1}\left(\frac{1+\Delta\epsilon_{zzi}}{1+\Delta\epsilon_{\theta\theta i}}\cdot\frac{1}{\cot\theta_{i-1}+\Delta\gamma_{\theta zi}}\right) \tag{42}$$

Increment Selection and Convergence. The selection of the appropriate load increment will depend on the initial angle θ_o, the ratio of the elastic moduli E_i/E_i' and E_i/G_i, the magnitude of the load, and the type of loading. As the load increment is increased, the computational effort is decreased, but the solution error is increased. The solution error after loading step i is defined as

$$\text{Percent Error} = \frac{100\|\epsilon_i-\epsilon^*\|_2}{\|\epsilon^*\|_2} \tag{43}$$

where ϵ_i is the total strain vector with components $\epsilon_{\theta\theta i}$, ϵ_{zzi}, ϵ_{rri} and $\gamma_{\theta zi}$. The vector ϵ^* is the exact total strain vector for the corresponding loading level containing the four strain components. The percent error is the Euclidean norm of the residual vector divided by the Euclidean norm of the exact solution. The exact solution is obtained by choosing increasingly smaller loading increments until the solution converges.

Typical results of such studies are shown in Table 1 which gives values of load increments that can be used over the range of angle $0 \le \theta_o \le 90$ deg. These load increments were selected so that the percent error as defined never exceeds 5 percent if the values of the total nondimensional load parameters do not exceed their listed values. The maximum internal pressure, applied torque, and longitudinal load are p, T, and P, respectively. The material is linear for these cases, where the only nonzero constants of equations (12)–(14) are E_o, E_o', and G_o'.

Part II Nonaxially Homogeneous Stresses and Strains

Certain edge constraints give rise to nonuniform stresses

and strains in the loaded orthotropic cylinder. To account for such nonhomogeneity along the length, the cylinder is divided into $J-1$ segments each of length Δz_o given by

$$\Delta z_o = \frac{l_o}{J-1} \tag{44}$$

The incremental and total stresses and strains are computed at each point $j = 1, 2, \ldots J$ as shown in Fig. 1. The boundary conditions are incorporated when the strains are integrated numerically for the deformations. The computational procedure follows closely that of the axially homogeneous case of Part I. However, quantities such as $\Delta\epsilon_{\theta\theta i}$, F_{ti}, etc., are now vector quantities of dimension J with components $\Delta\epsilon_{\theta\theta ij}$, F_{tij}, etc. The added index j denotes the length from the coordinate origin as shown in Fig. 1.

Incremental Stresses. The equation of equilibrium for an element of a thin-wall shell of revolution at location j and after loading step i, deduced by Timoshenko and Woinowsky-Kreiger (1959), is

$$\frac{\sigma_{\theta\theta ij}}{R_{ij}} + \frac{\sigma_{\psi\psi ij}}{\rho_{ij}} = \frac{p_i}{t_{ij}} \tag{45}$$

Here $\sigma_{\psi\psi ij}$ is the meridional stress in the shell, ρ_{ij} is the radius of curvature in the meridional direction, $\sigma_{\theta\theta ij}$ is the circumferential stress in the shell, R_{ij} is the shell radius, p_i is the total internal pressure, and t_{ij} is the wall thickness. If the load increment is sufficiently small, equation (44) can be rewritten in terms of section properties of the previous step, or

$$\frac{\sigma_{\theta\theta ij}}{R_{(i-1)j}} + \frac{\sigma_{\psi\psi ij}}{\rho_{(i-1)j}} \approx \frac{p_i}{t_{(i-1)j}} \tag{46}$$

The meridional stress (Timoshenko and Woinowsky-Kreiger, 1959) is

$$\sigma_{\psi\psi ij} = \frac{p_i\ \pi R^2_{(i-1)j}}{2\pi R_{(i-1)j}\ t_{(i-1)j}} = \frac{p_i R_{(i-1)j}}{2t_{(i-1)j}} \tag{47}$$

By combining equations (46) and (47), the circumferential stress becomes

$$\sigma_{\theta\theta ij} = \frac{p_i R_{(i-1)j}}{t_{i-1}}\left(1 - \frac{R_{(i-1)j}}{2\rho_{(i-1)j}}\right) \tag{48}$$

Expressions for the incremental stresses for load step $i-1$ follow from equations (47) and (48), or

$$\Delta\sigma_{\psi\psi ij} = \frac{\Delta p\ R_{(i-1)j}}{2t_{(i-1)j}} \tag{49}$$

$$\Delta\sigma_{\theta\theta ij} = \frac{\Delta p\ R_{(i-1)j}}{t_{(i-1)j}}\left(1 - \frac{R_{(i-1)j}}{2\rho_{(i-1)j}}\right) \tag{50}$$

Equations (49) and (50) are similar to the internal pressure components of stress given for the axially homogeneous case in equations (1) and (2). Note that for the homogeneous stress case, $\rho_{(i-1)j} \to \infty$ and $\sigma_{\psi\psi ij} = \sigma_{\theta\theta ij}/2$.

To compute strains and deformations in the cylindrical coordinate system, it is necessary to transform $\sigma_{\psi\psi ij}$ to that coordinate system. Using the stress-transformation equations, (Popov, 1981) yields

$$\sigma_{zzij} = \sigma_{\psi\psi ij}\left[\frac{1}{2} - \frac{\cos 2\alpha_{(i-1)j}}{2}\right] \tag{51}$$

where $\alpha_{(i-1)j}$, the angle that the wall of the cylinder makes with the longitudinal axis, is defined as the gradient of the radial deformation, or

$$\tan\alpha_{(i-1)j} = \frac{\partial u_{r(i-1)j}}{\partial z} \tag{52}$$

In employing the stress transformation of equation (51), it is assumed that alpha is sufficiently small so that the radial stresses in the cylindrical coordinate system are small, contributing a negligible amount to the cylinder deformation.

While the discussion in this section has dealt only with stress and deformation due to internal pressure, results can be developed analogously for end load and pure torque, as well as for various combinations of these three types of loads.

Constitutive Relationships, Material and Geometric Nonlinearity. The incremental constitutive law given by equations (5)–(8), along with the material nonlinearity of equations (12)–(14) and the transformations of equations (15), are assumed to be valid not only at each load step i but also at each length location j. With this notation, equations (5)–(8) become

$$\begin{bmatrix} \Delta\epsilon_{\theta\theta nj} \\ \Delta\epsilon_{zznj} \\ \Delta\epsilon_{rrnj} \\ \Delta\epsilon_{\theta znj} \end{bmatrix} = \begin{bmatrix} a_{11ij} & a_{12ij} & a_{13ij} & a_{14ij} \\ a_{21ij} & a_{22ij} & a_{23ij} & a_{24ij} \\ a_{31ij} & a_{32ij} & a_{33ij} & a_{34ij} \\ a_{41ij} & a_{42ij} & a_{43ij} & a_{44ij} \end{bmatrix} \begin{bmatrix} \Delta\sigma_{\theta\theta nj} \\ \Delta\sigma_{zznj} \\ \Delta\sigma_{rrnj} \\ \Delta\sigma_{\theta znj} \end{bmatrix} \tag{53}$$

$n = i + 1 = 1, 2, 3, \ldots$
$j = 1, 2, 3, \ldots J$

Note the components of the coefficient matrix of equation (53) are still given by equations (8) where each parameter with the subscript i now has the added subscript j. In equations (12)–(15), the simple subscript i is also replaced by ij.

The geometric properties, except for length change, are deduced from equations (19), (21), and (25), i being replaced by ij. The change in length along the longitudinal axis for a segment bounded by points j and $j+1$ is given by

$$\Delta z_{ij} = \Delta z_o + u_{zi(j+1)} - u_{zij} \equiv \Delta z_o\, F_{zij} \tag{54}$$

where Δz_o is given by equation (44) and where $u_{zi(j+1)}$ and u_{zij} are the total displacements measured relative to the initial points j and $j+1$ when the cylinder is without load ($i=0$).

Computation of Strain, Rotation and Orthotropy Angle. The total strains can be computed either from the incremental strains or from the displacements. The radial, circumferential and shear strain at load level i and position j, expressed as ϵ_{rrij}, $\epsilon_{\theta\theta ij}$, and $\gamma_{\theta zij}$, respectively, are given explicitly by equations (30), (31), and (33), where ij replaces i.

An efficient method for calculating ϵ_{zzij}, the longitudinal strain, is by the finite difference method used by Utku (1981). If u_{zij} denotes a segment displacement, then

$$\delta_{zzij} = \frac{u_{zi(j+1)} - u_{zi(j-1)}}{\Delta z_{i(j-1)} + \Delta z_{ij}} \tag{55}$$

The average longitudinal strain for the whole cylinder of initial length l_o is

$$\bar{\epsilon}_{zzij} = \frac{1}{l_o}\ (u_{zij} - u_{zi1}) \tag{56}$$

where $J-1$ is the number of length segments.

The end rotation ϕ_{ij} of the cylinder segment between locations j and $j+1$ can be computed from equation (37), after the subscript j is added where appropriate; or from the expression involving the incremental circumferential displacement $\Delta u_{\theta ij}$ given by

$$\phi_{ij} = \phi_{(i-1)j} + \frac{\Delta u_{\theta ij}}{R_{(i-1)j}} \tag{57}$$

The angle of orthotropy θ_{ij} in each of the $J-1$ longitudinal segnents is given by equation (42) where each subscript i or $(i-1)$ is replaced by ij or $(i-1)j$, respectively.

Computation of Displacements and Curvature. The computation of displacements u_r, u_z and u_θ in the case of axially homogeneous strain is a straightforward application of the strain-displacement equations (Wilson and Orgill, 1986). However, when the strains are axially nonhomogeneus, displacements are more difficult to compute and in general must be obtained numerically. The results that follow will be based on the finite difference method discussed by Utku (1981) and Carnahan, et al. (1964).

From the strain-displacement equations given by

Sokolnikoff (1956), the incremental radial displacement becomes

$$\Delta u_{rij} = R_{(i-1)j}\,\Delta\epsilon_{\theta\theta ij} \tag{58}$$

The incremental displacement is then added to the total displacement from the previous load step to obtain the total radial displacement at step i for segment j, or

$$u_{rij} = u_{r(i-1)j} + \Delta u_{rij} \tag{59}$$

Computation of the incremental longitudinal displacement is obtained from the strain-displacement equations by integrating the incremental longitudinal strain given by

$$\Delta u_{zi(j+1)} - \Delta u_{zi(j-1)} = [\Delta z_{(i-1)j} + \Delta z_{(i-1)(j-1)}]\Delta\epsilon_{zzij} \tag{60}$$

As j varies from 1 to J in equation (60), a tridiagonal system of linear equations is found. These equations are solved simultaneously for the incremental displacements Δu_{zij}. The total longitudinal displacement at step i is once again computed by adding the incremental displacement to the total longitudinal displacement at the previous step.

$$u_{zij} = u_{z(i-1)j} + \Delta u_{zij} \tag{61}$$

The computation of the circumferential displacement is obtained from the strain-displacement equations by integrating the incremental shear strain. The integration results in expressions similar to equation (60) and (61) for the longitudinal displacement. The incremental circumferential displacement and total circumferential displacement are, respectively:

$$\Delta u_{\theta i(j+1)} - \Delta u_{\theta i(j-1)} = [\Delta z_{(i-1)j} + \Delta z_{(i-1)(j-1)}]\Delta\gamma_{\theta zij} \tag{62}$$

$$u_{\theta ij} = u_{\theta(i-1)j} + \Delta u_{\theta ij} \tag{63}$$

With these displacements it is possible to compute α_{ij}, the angle between the meridional direction and the longitudinal axis of the cylinder; and ρ_{ij}, the radius of curvature in the meridional direction. The angle α_{ij} is used in transforming stress from the meridional direction to the longitudinal direction as given in equation (51). Equation (52) expresses α_{ij} in terms of the derivative of u_{rij} in the z direction. In finite difference form, the first and second derivatives of this displacement are as follows.

$$\frac{\partial u_{rij}}{\partial z} = \frac{-u_{ri(j-1)} + u_{ri(j+1)}}{\Delta z_{(i-1)j} + \Delta z_{(i-1)(j-1)}} = \tan\alpha_{ij} \tag{64}$$

$$\frac{\partial^2 u_{rij}}{\partial z^2} = \frac{2\left[u_{ri(j-1)} + u_{ri(j+1)} - 2u_{rij} + \dfrac{\partial u_{rij}}{\partial z}(\Delta z_{(i-1)(j-1)} - \Delta z_{(i-1)})\right]}{\Delta z^2_{(i-1)(j-1)} + \Delta z^2_{(i-1)j}} \tag{65}$$

The radius of curvature is computed from the following familar form, together with equations (64) and (65).

$$\rho_{ij} = \frac{\left[1 + \left(\dfrac{\partial u_{rij}}{\partial z}\right)^2\right]^{3/2}}{\dfrac{\partial^2 u_{rij}}{\partial z^2}} \tag{66}$$

A comprehensive treatment of the finite difference representation of displacement boundary conditions that satisfy various end restraints at $j = 1$ and J is given by Carnahan, et al. (1964). A particular example is presented below.

For suitable convergence, it is important to select a sufficient number of cylindrical segments $J-1$ to accurately represent the cylinder's overall shape. As equations (60) and (61) are integrated to yield the displacement, the error in the result will decrease as J is increased. However, if J is too large, the accuracy of the derivatives computed by equations (64) and

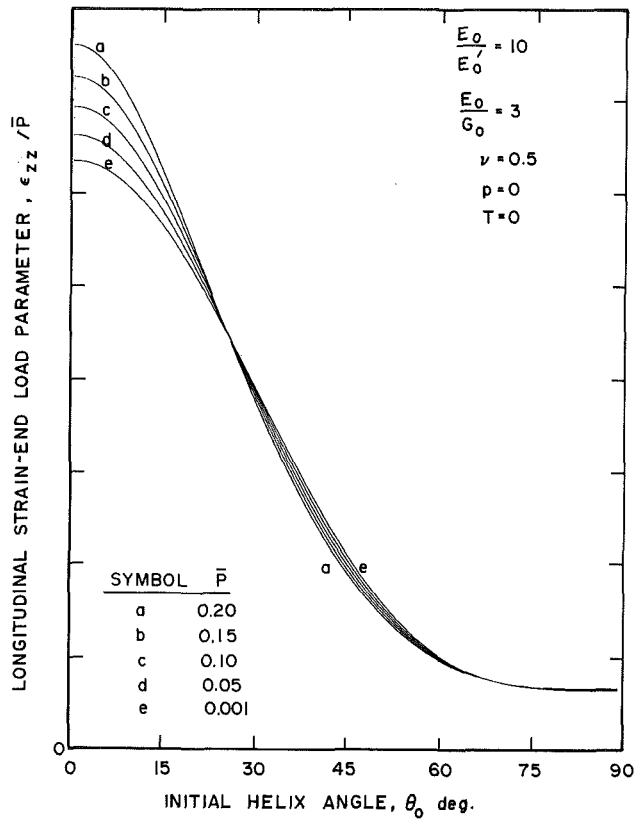

Fig. 3 Effect of axial load and orthotropy on axial strain (axially homogeneous case)

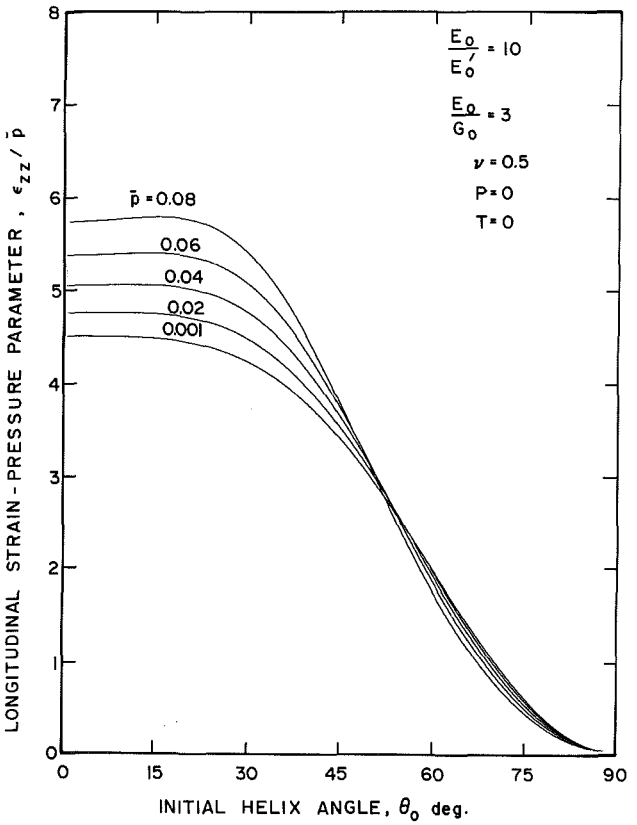

Fig. 4 Effect of internal pressure and orthotropy on axial strain (axially homogeneous case)

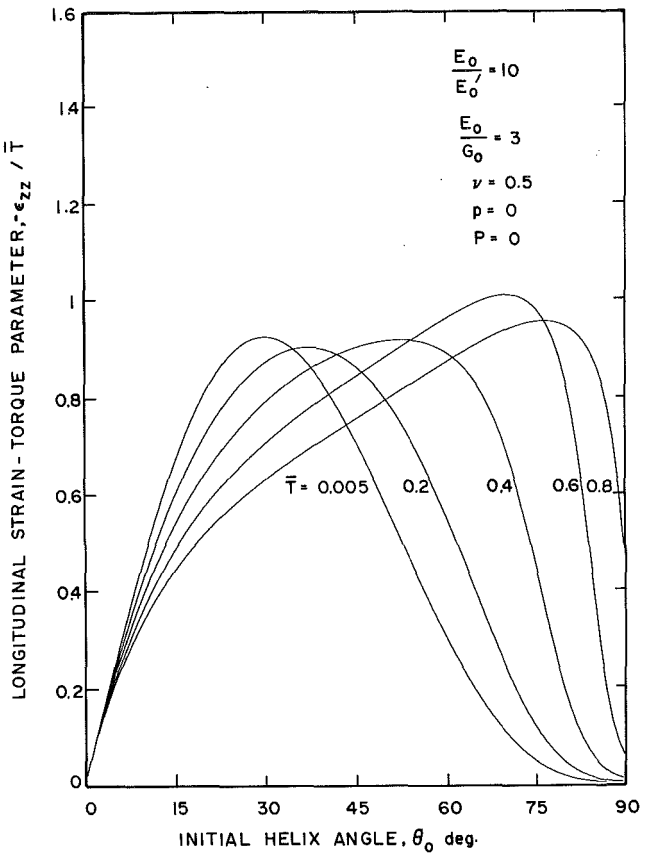

Fig. 5 Effect of pure torque and orthotropy on axial strain (axially homogeneous case)

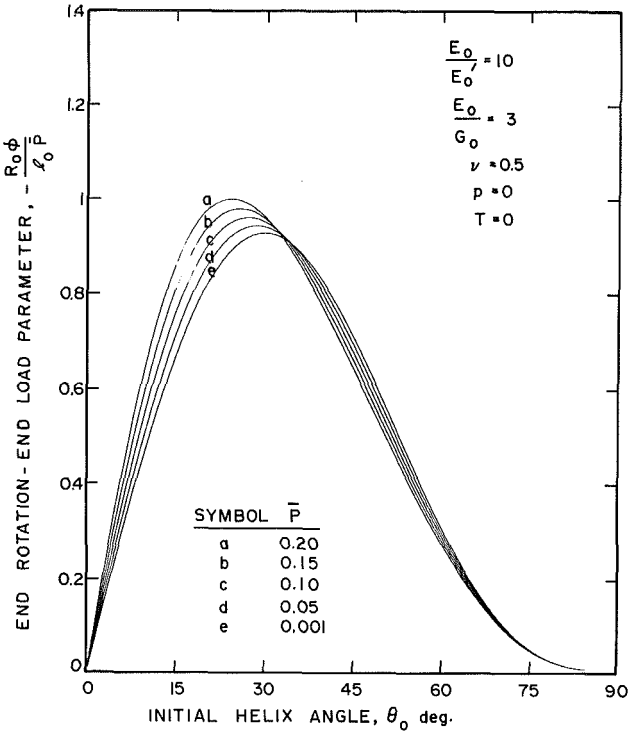

Fig. 6 Effect of axial load and orthotropy on end rotation (axially homogeneous case)

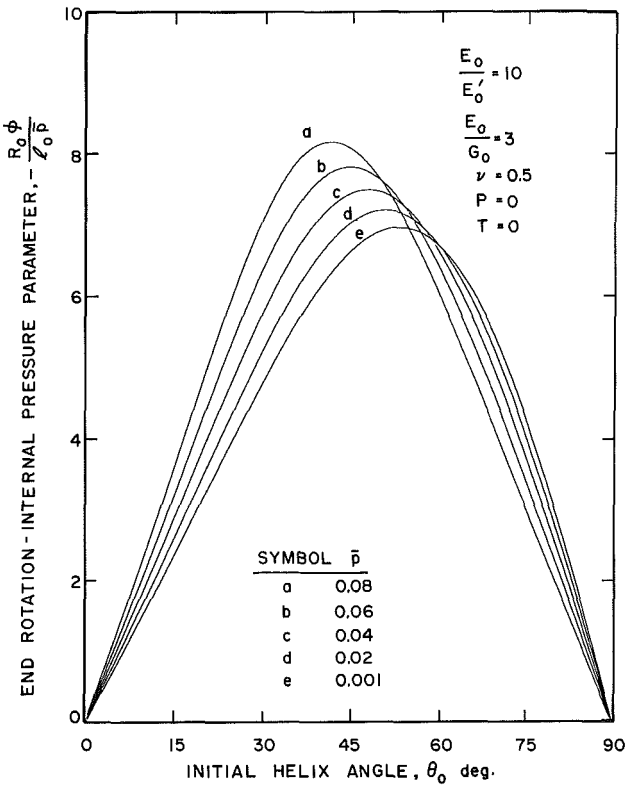

Fig. 7 Effect of internal pressure and orthotropy on end rotation (axially homogeneous case)

(65) may actually decrease. It was found that the selection of the number J is tempered by the initial cylinder geometry, the orthotropy angle θ_o, the material constants, the type and magnitude of loading, and the computational effort.

Parametric Studies. A Fortran IV computer code was written to carry out the calculations for the finite deformation behavior of both the homogeneous and nonhomogeneous types of cylinders. Selected parametric studies for both types are now presented. For cases where the material is linear and only one of the three loads is present (longitudinal load P, internal pressure p, or pure torque T), the deformations depend on the following appropriate independent nondimensional load parameters and three geometric parameters.

$$\bar{P}=\frac{P}{E_oR_ot_o}\ ;\ \bar{p}=\frac{pR_o}{E_ot_o}\ ;\ \bar{T}=\frac{T}{E_oR_o^2t_o}\ ;\ \theta_o;\ \frac{R_o}{t_o}\ ;\ \frac{l_o}{R_o} \tag{67}$$

In the selected examples, the deformations were found to be very sensitive to the independent parameter θ_o, the initial angle of orthotropy. Therefore, θ_o was taken as the abscissa in the presentation of the graphical results. The last two geometric parameters of (67) affect deformations only in axial nonhomogeneous problems.

The first type of cylinder has axially homogeneous stresses and strains and is made of an orthtropic, linear elastic material with the following properties:

$$E_i/E_i'=E_o/E_o'=10;\quad E_i/G_i=E_o/G_o=3$$
$$B=B'=B_g=C=C'=C_g=0;\quad \nu=0.5 \tag{68}$$

The results for this cylinder are presented in Figs. 3-8.

Figures 3, 4, and 5 shows the behavior of the finite longitudinal strain ϵ_{zz} with the loading P, p, and T, respectively. For longitudinal loading, it is deduced from Fig. 3 that for $\theta_o = 27$ deg and $\theta_o > 60$ deg, the curves coalesce and ϵ_{zz} is linear with P. For $0 < \theta_o < 27$ deg, however, the cylinder acts as a "soft" spring in the axial direction, since as P increases, ϵ_{zz} becomes proportionally larger. For $27 < \theta_o < 60$ deg, however, the reverse is true but is less pronounced, where the cylinder behaves as a "hard" spring. However, for internal pressure loading, Fig. 4, linear behavior is found for $\theta_o = 52$

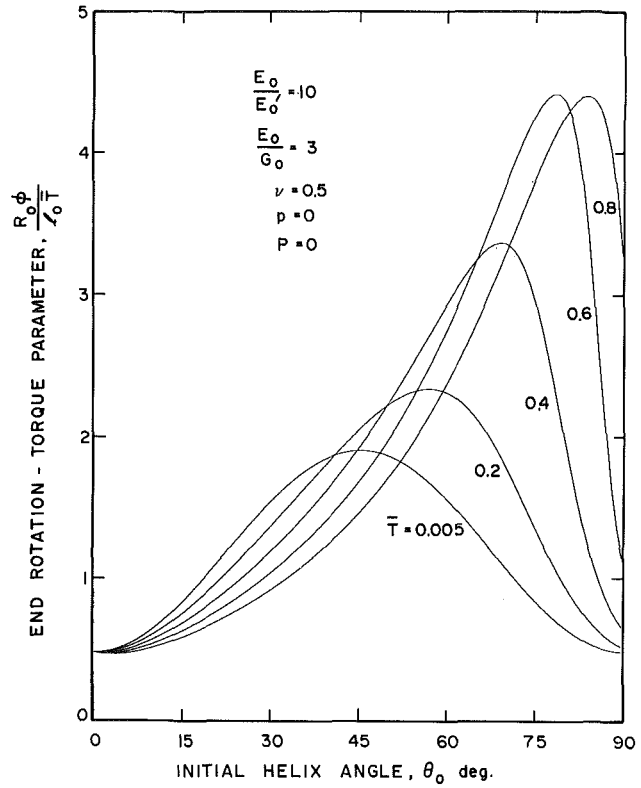

Fig. 8 Effect of torque and orthotropy on end rotation (axially homogeneous case)

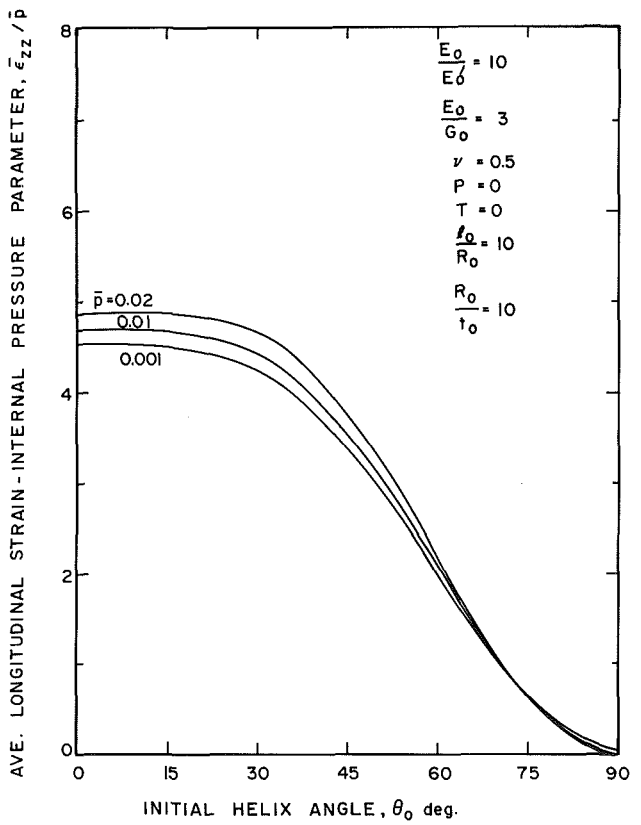

Fig. 9 Effect of internal pressure and orthotropy on axial strain (axially nonhomogeneous case)

deg, with soft spring behavior for smaller values and hard spring behavior (but less pronounced) for larger values of θ_o. Except near the extreme values of θ_o, the behavior of axial

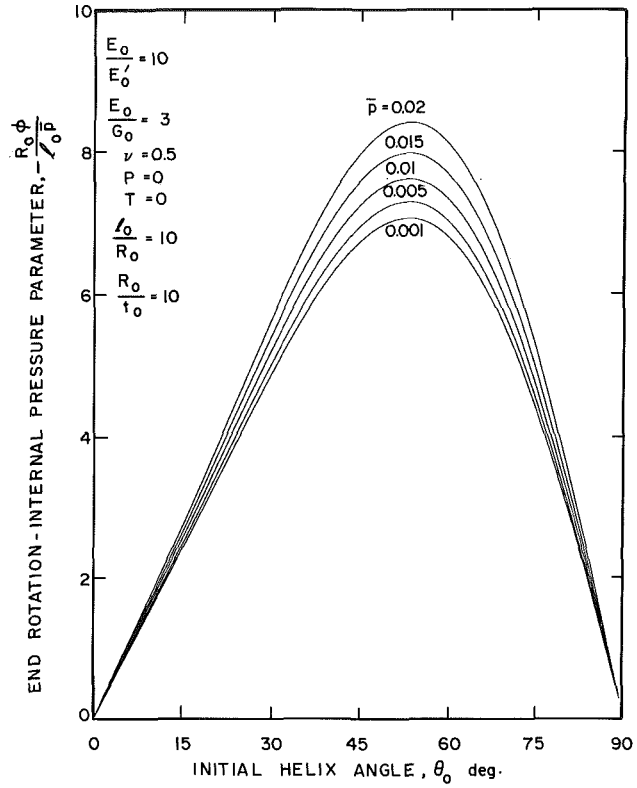

Fig. 10 Effect of internal pressure and orthotropy on end rotation (axially nonhomogeneous case)

strain with pure torque is more complex, as shown in Fig. 5. For θ_o up to 3 deg, the behavior is linear; and from that point to 30 deg the cylinder "winds together" where, as T increases, changes in ϵ_{zz} are proportionally smaller. However, for θ_o near 80 deg, as T increases, ϵ_{zz} becomes proportionally larger, and the cylinder winds together more and more easily, within small changes for θ_i. It is noted that θ_i decreases as the cylinder winds together.

Figures 6, 7, and 8 show the behavior of ϕ, the finite angle of rotation about the longitudinal axis of the cylinder, with loading P, p, and T, respectively. The negative ordinate in Figs. 6 and 7 indicates that the cylinder unwinds with the application of load. The change from a soft or flexible configuration to a hard one at $\theta_o = 30$ deg is apparent in Fig 6; but for pressure loading this change is less distinct and occurs when θ_o is between 50 and 60 deg, as shown in Fig. 7. The effect of pure torque on ϕ for θ_o up to about 30 deg is clear from Fig. 8: as T increases, ϕ becomes proportionally larger, and the cylinder winds together and becomes shorter.

The second type of cylinder selected for study has axially nonhomogeneous stresses and strains, but has the same material constants as for the study just completed. That is, the material is orthotropic, linear and elastic with the properties defined by equations (68). For axial nonhomogeneity, the initial geometry (l_o, R_o, t_o) and number of points J along the length affect the deformation patterns. These particular quantities were chosen as follows:

$$l_o/R_o = 10; \quad R_o/t_o = 10; \quad J = 11 \tag{69}$$

The boundary conditions for the second type of cylinder were chosen to simulate a fully clamped condition at one end, $j = 1$, and zero radial displacement at the the end, $J = 11$. However, the longitudinal displacement and twisting angle were chosen to be unrestrained at $J = 11$. These conditions are:

$$u_{z1} = u_{\theta 1} = u_{r1} = u_{rJ} = 0 \tag{70}$$

The results for this second type of cylinder are presented in Figs. 9, 10, and 11 in which the only loading is internal

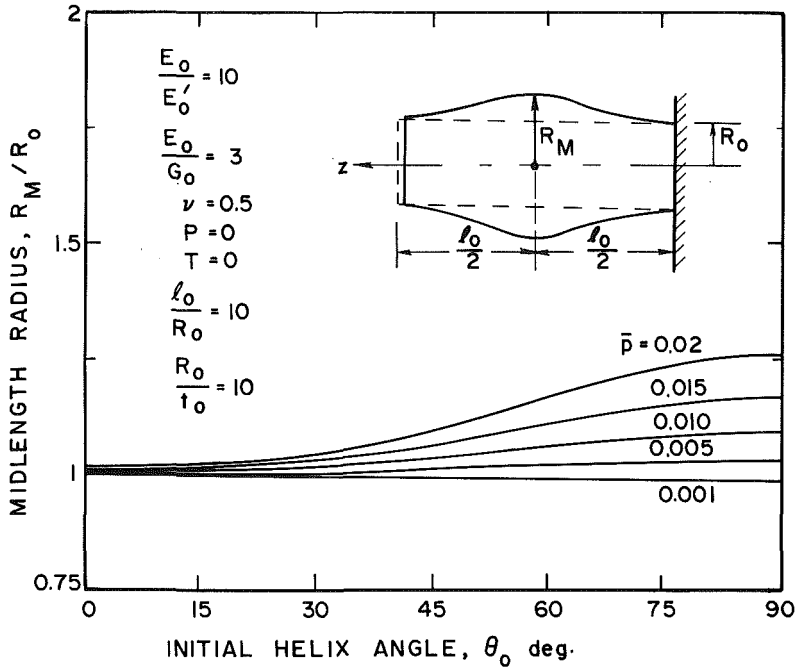

Fig. 11 Effect of internal pressure and orthotropy on midlength radial expansion (axially nonhomogeneous case)

pressure. For the range of $\bar{p}$ that overlaps ($0.001 \leq \bar{p} \leq 0.02$), it is observed that the curves of Fig. 9 for the average longitudinal strain $\bar{\epsilon}_{zz}$ are identical to those of Fig. 4 for the homogeneous strain ϵ_{zz}. For this range, then, the end boundary constraints have a negligible effect on the total longitudinal deformation. However, for the range of $\bar{p}$ that overlaps ($0.001 \leq \bar{p} \leq 0.02$), the total end rotations ϕ of Fig. 10 differ from the counterpart results of Fig. 7 (boundaries unconstrained), where these rotations become more dissimilar as θ_o is increased beyond 15 deg. Compared to the constrained case, the geometric changes along the length of an unconstrained cylinder are always more pronounced. The last study, Fig. 11, shows the nonlinear variation in midlength radius R_M, with internal pressure. Such calculations are of particular importance for axially nonhomogeneous deformations because they serve as a way to check the limits of vaidity of the present analysis. That is, since out-of-plane stresses, strains, and deformations were ignored, then the angle α_{ij} needs to be sufficiently small for the results of Figs. 9, 10, and 11 to be valid, or $\cos \alpha_{ij} \simeq 1$, $\sin \alpha_{ij} \simeq \alpha_{ij}$. For instance, if $\bar{p} = 0.02$ and $\theta_o = 75$ deg, then $R_M/R_o = 1.25$ from Fig. 11. Let α_{ij} be approximated from equation (52) as follows.

$$\alpha_{ij} \simeq \tan^{-1}\left(\frac{\Delta u_r}{\Delta z}\right) = \tan^{-1}\left(\frac{R_M - R_o}{0.5\, l_o}\right)$$

$$= \tan^{-1}\left(\frac{1.25\, R_o - R_o}{5\, R_o}\right) = 2.86 \text{ deg} \qquad (71)$$

Therefore, α_{ij} is sufficiently small to justify the present analysis of Part II.

Acknowledgment

This study was sponsored by the US Defense Advanced Research Projects Agency under Contract No. MDA903-84-C-0243. Senol Utku is acknowledged for his helpful technical advice.

References

Carnahan, B., Luther, H. A., and Wilkes, J. O., 1964, *Applied Numerical Methods*, Wiley, New York.

Goodyear, Tire and Rubber Co., 1949, *Handbook of Molded and Extruded Rubber*, 1st ed., Akron, Ohio.

Green, A. E., and Adkins, J. E., 1970, *Large Elastic Deformations*, 2nd ed., Clarendon Press, Oxford, England.

Lekhnitskii, S. G., 1963, *Theory of Elasicity of an Anisotropic Body*, translated from Russian by P. Fern, Holden-Day Inc., San Francisco.

Leonard, J. W., 1967, "Inflatable Shells: In-Service Phase," *Journal of Engineering Mechanics*, ASCE Vol. 93.

Popov, E. P., 1981, *Mechanics of Materials*, 2nd ed., Prentice-Hall, New York.

Reissner, E., 1970, "On Uniform Stress and Strain in Axially Homogeneous Cylindrical Shells," *International Journal of Solids and Structures*, Vol. 6, pp. 133–138.

Sokolnikoff, I. S., 1956, *Mathematical Theory of Elasticity*, 2nd ed., McGraw-Hill, New York.

Timoshenko, S. P., and Woinowsky-Kreiger, S., 1959, *Theory of Plates and Shells*, 2nd ed., McGraw-Hill, New York.

Utku, S., 1981, *Numerical Solutions of Partial Differential Equations*, Dept. of Civil Engineering and Dept. of Computer Science, Duke University, Durham, NC.

Verma, P. D. S., and Rana, O. K., 1983, "Rotation of a Circular Cylindrical Tube Reinforced by Fibers Lying Along Helices," *Mechanics of Materials*, Vol. 2, pp. 353–359.

Wilson J. F., and Orgill, G., 1986, "Linear Analysis of Uniformly Stressed, Orthotropic Cylindrical Shells," ASME *Journal of Applied Mechanics*, Vol. 53, pp. 249–256.

R. Fosdick
Department of Aerospace Engineering and Mechanics,
University of Minnesota,
Minneapolis, Minn. 55455

P. Villaggio
Istituto di Scienza delle Costruzioni,
56100 Pisa, Italy

Influence of the Bending Stiffness on the Shape of a Belt in Steady Motion

The equilibrium and steady forms of a pulley belt are determined. We consider large displacements of the central line of the belt for a special class of nonlinear stress-strain relations which includes the usual linear elastic case. If the centrifugal force on the belt is neglected, it is possible to obtain an explicit solution; if the centrifugal force is taken into account, but it is not very large, an approximate, but still explicit, solution can be derived.

1 Introduction

It is commonly known that when a belt transmits a rotatory motion to a pulley there is a loss of mechanical energy due not only to friction, but also to the flexural rigidity of the belt. In the example sketched in Fig. 1, in which a belt with a rectangular cross section imparts a clockwise rotation to a wheel, the tension S_1 in the ongoing branch is less than the tension S_2 in the exit branch. When the belt connects two identical pulleys, both of its branches (if long enough) tend to assume asymptotically the positions of two straight lines at different distances, $(R+e_1)$ and $(R+e_2)$, from the mean line through the pulley centers, one of which is at O.

This fact was considered for the first time by Coulomb (1785) who, on the basis of experimental observations, proposed the following law for e_1 and e_2:

$$e_1+e_2=\delta^n\left(a+\frac{b}{S_\infty}\right), \tag{1.1}$$

where δ is the thickness of the belt, $S_\infty = 1/2(S_1+S_2)$, and a, b, n are constants to be determined empirically. Coulomb's formula was subsequently simplified by Eytelwein (1808) to

$$e_1+e_2=c\delta^2, \tag{1.2}$$

where c is another constant. In 1927, however, Hamel (1927) attempted to give a theoretical justification of the old experimental formulae by considering the belt as an elastic rod in equilibrium pulled by two normal forces at the ends and supported partially by contact with a rigid circle. Hamel considered the extent of the arc where the belt remains in contact with the wheel as an unknown, offering in this way one of the first examples of a unilateral constraint problem in elasticity theory. He found the theoretical values of e_1 and e_2, however the conditions of continuity at the end of the arc of contact imposed by Hamel were incorrect and, consequently, his solution was not completely satisfactory.

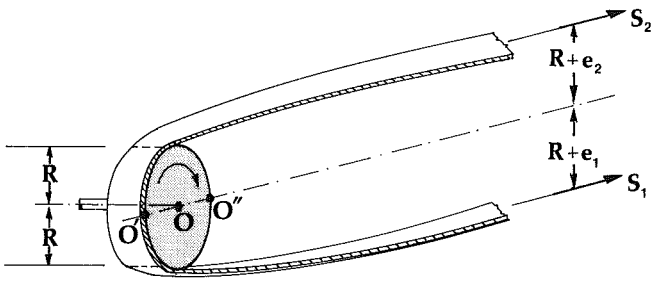

Fig. 1

In this paper we propose a revised and generalized version of Hamel's original theory. In addition to Hamel's linear elastic model, we shall also consider the influence of some nonlinear effects that, even in the most common cases, are not negligible. Since the relative displacements of the parts of the belt need not be small while the strains, themselves, are supposedly small, we shall apply Kirchhoff's theory of thin rods. In addition, we shall assume that the material of the belt is elastic, but not necessarily linearly elastic, and consider a special class of stress-strain laws that describe the behavior of highly tensioned belts. The equations describing this model are nonlinear, but they will be solved in full generality to find the equilibrium configuration of the belt in the absence of gravity. The analysis then will be extended to the case in which the pulley has a steady angular speed around its axis and the mass and the inertia of the belt are no longer negligible; gravity will again be neglected.

In agreement with Hamel's result, if the material is linearly elastic, the two branches of the belt assume a straight configuration, parallel to the mean axis through O, at *infinite* distances from the pulley. However, within the class of *nonlinear* elastic materials of this work, we find that such a parallel rectilinear configuration for the branches of the belt is assumed after *finite* distances from the pulley.

2 The Solution: Inertia Neglected

Let us consider a circle of radius R which represents the middle section of a pulley, and a curve $A'ABB'$ which represents the axis of a thin plane belt partially wound around

Contributed by the Applied Mechanics Division for publication in the JOURNAL OF APPLIED MECHANICS.
Discussion on this paper should be addressed to the Editorial Department, ASME, United Engineering Center, 345 East 47th Street, New York, N.Y. 10017, and will be accepted until two months after final publication of the paper itself in the JOURNAL OF APPLIED MECHANICS. Manuscript received by ASME Applied Mechanics Division, February 21, 1985; final revision, September 3, 1985.

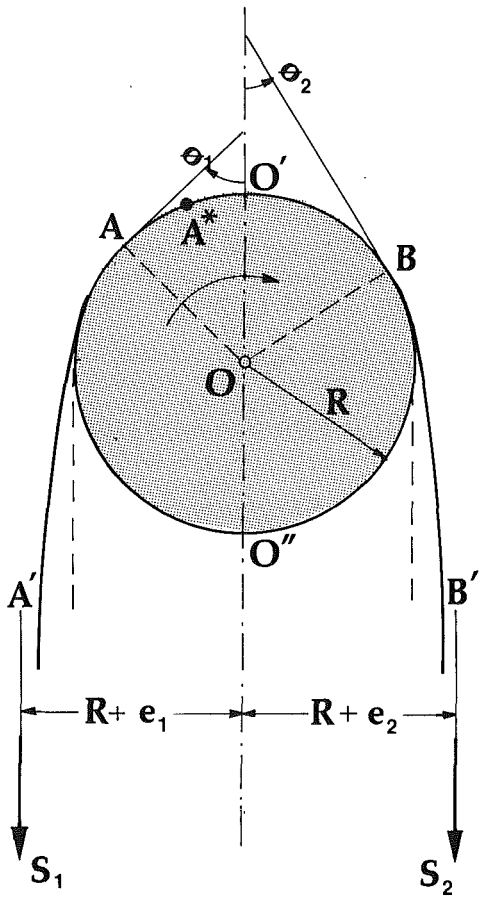

Fig. 2

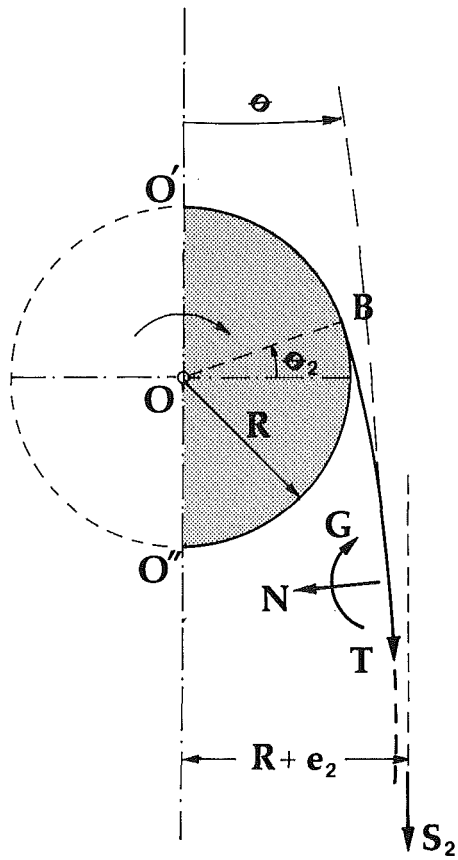

Fig. 3

the boundary of the circle as shown in Fig. 2. We assume that the belt connects to a widely spaced identical pulley. Let us distinguish three parts of the belt; the ingoing arc $A'A$, the arc AB lying on the circle, and the outgoing arc BB'. The points A and B, which define the boundaries of the region of contact, are unknown. It is also not known in advance that the contact set AB is composed of a single arc, but, if the belt is sufficiently flexible, the assumption that it is seems reasonable. The arcs AA' and BB', regarded as being of infinite length, tend to assume the distances $R + e_1$ and $R + e_2$, respectively, from the central axis $O'O''$. Furthermore, the deflections e_1 and e_2, which are due to the stiffness of the belt, are unknown. The tensions in the two branches of the belt are denoted by S_2 and S_1, as in Fig. 2. Of these, S_1 is known while S_2 is unknown.

It is assumed that the wheel experiences a reactive torque M due to transmission. In order to describe the equilibrium of each portion of the belt in classical terms (Love, 1927, Section 262), we first consider the arc BB' in Fig. 2, the points of which are distinguished by the arc distance s from the section at O'. We call G(s) the flexural couple (Fig. 3), T(s) the tension, and N(s) the shearing force, oriented as shown in Fig. 3. Let θ be the angle that the tangent to the curve, drawn in the sense in which s increases, makes with the axis $O'O''$.

The equations of equilibrium for the arc BB' can be expressed in the forms

$$T=S_2\cos\theta, \quad N=S_2\sin\theta, \quad \frac{dG}{ds}+N=0. \tag{2.1}$$

In the following, we shall introduce the quantity $\kappa \equiv -d\theta/ds$ which represents the curvature of the strained axis at the current section where the stress resultants G, T, and N are acting. In order to relate G to κ we first let σ_{zz} denote the normal stress acting perpendicular to the cross section of the belt, and let ϵ_{zz} be the corresponding strain. Let x and y be the principal axes of the cross section at its centroid, and take z to be the axis of T, x the axis of N, and y the axis of the flexural couple G (as shown in Fig. 3). If the belt is sufficiently thin, the strain ϵ_{zz} is given by

$$\epsilon_{zz}=-\kappa x=\frac{d\theta}{ds}x. \tag{2.2}$$

As to the stress-strain law, a relation that is suggested by certain experiments (Bach, 1920, and Pöschl, 1928, Section 39) is of the form

$$\sigma_{zz}=E\epsilon_{zz}^n, \tag{2.3}$$

where E is a constant and $n = 1,3,5, \ldots$. On combining (2.2) and (2.3) we obtain the stress-couple G:

$$G=\iint_A -x\sigma_{zz}dxdy=-D_n\left[\frac{d\theta}{ds}\right]^n,$$

where

$$D_n=E\iint_A x^{n+1}dxdy,$$

and where the integration is carried out over the cross-sectional area A of the belt.

Thus, by substituting this expression for G into the equations (2.1), we arrive at the differential equation

$$D_n\frac{d}{ds}\left[\left[\frac{d\theta}{ds}\right]^n\right]-S_2\sin\theta=0, \quad s_2<s<\infty, \tag{2.4}$$

where s_2 denotes the arc length of the point B measured from O'. If (2.4) is multiplied by $d\theta/ds$ and written in the equivalent form

$$\frac{d}{ds}\left[\frac{n}{n+1}D_n\left[\frac{d\theta}{ds}\right]^{n+1}+S_2\cos\theta\right]=0,$$

we obtain the first integral

$$\frac{n}{n+1} D_n \left[\frac{d\theta}{ds}\right]^{n+1} + S_2 \cos\theta = \text{const.}, \tag{2.5}$$

where the constant is determined by the assumed conditions that θ and $d\theta/ds$ vanish simultaneously as $s \to \infty$. Thus,

$$\frac{n}{n+1} D_n \left[\frac{d\theta}{ds}\right]^{n+1} = S_2(1-\cos\theta) = 2S_2 \sin^2\frac{\theta}{2}. \tag{2.6}$$

This equation can be solved with respect to $d\theta/ds$ to obtain

$$\frac{d\theta}{ds} = -\sqrt[n+1]{2\,\frac{n+1}{n}\,\frac{S_2}{D_n}\sin^2\frac{\theta}{2}}, \tag{2.7}$$

where only the negative root has been considered since θ must decrease with s. By separating the variables in the equation (2.7), we then reach

$$\frac{d\theta}{\sin^{2/n+1}\frac{\theta}{2}} = -\sqrt[n+1]{2\,\frac{n+1}{n}\,\frac{S_2}{D_n}}\,ds, \quad (n=1,3,5,\ldots). \tag{2.8}$$

For $n = 1$, the solution of (2.8) which satisfies $\theta(s_2) = \theta_2$ is given by

$$\tan\frac{\theta}{4} = \tan\frac{\theta_2}{4}\, e^{\sqrt{S_2/D_1}\,(s-s_2)}, \quad s_2 \leqq s < \infty. \tag{2.9}$$

For $n = 3,5,7, \ldots$, the solution of (2.8) which satisfies the boundary condition $\theta(s_2) = \theta_2$ has the form (Gradshteyn and Ryzhyk, 1965, Section 8.39)

$$B_{\sin^2\theta/2}\left[\frac{n-1}{2(n+1)}, \frac{1}{2}\right] = B_{\sin^2\theta_2/2}\left[\frac{n-1}{2(n+1)}, \frac{1}{2}\right] - \sqrt[n+1]{2\,\frac{n+1}{n}\,\frac{S_2}{D_n}}\,(s-s_2),$$

$$s_2 \leqq s < \infty, \tag{2.10}$$

where $B_x(p,q)$ denotes the incomplete beta function.

In both (2.9) and (2.10) θ_2 is still unknown and must be determined by the condition that, at $s = s_2$, $d\theta/ds = -1/R$. Thus, equation (2.7) yields

$$\theta_2 = 2\arcsin\sqrt{\frac{1}{R^{n+1}}\,\frac{n}{2(n+1)}\,\frac{D_n}{S_2}}. \tag{2.11}$$

If $\sqrt{\frac{1}{R^{n+1}}\,\frac{n}{2(n+1)}\,\frac{D_n}{S_2}} \leqq 1$, there exists only one value of θ_2, for $0 \leqq \theta_2 \leqq \pi$, which satisfies (2.11). This means that, if the ratio $D_n/R^{n+1}S_2$ is too large, the belt fails to wind upon the pulley, a feature already noted by Wang (1981).

From (2.8) it is possible to derive the value of $R + e_2$, the distance of the asymptote of the outgoing branch of the belt from the axis $O'O''$ (Fig. 3). In fact, this distance is given by the following geometric relation:

$$R + e_2 = R\cos\theta_2 + \int_{s_2}^{\infty} \sin\theta\, ds.$$

Thus, recalling (2.8), we have

$$R + e_2 = R\cos\theta_2 + \left[\frac{n}{2(n+1)}\,\frac{D_n}{S_2}\right]^{\frac{1}{n+1}} \int_0^{\theta_2} \frac{\sin\theta\, d\theta}{\sin^{2/n+1}\frac{\theta}{2}},$$

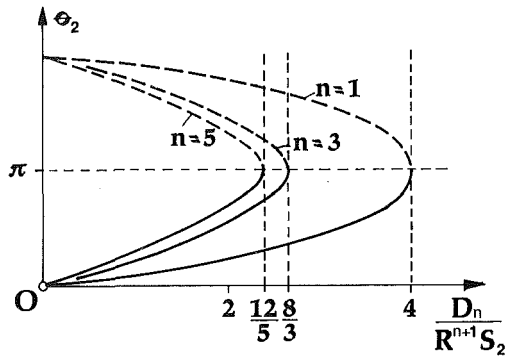

Fig. 4

and by using (2.11) to obtain $\cos\theta_2$ and by calculating the integral, we obtain

$$R + e_2 = R + \frac{D_n}{(n+1)R^n S_2}. \tag{2.12}$$

The same considerations as given above also hold for the ingoing branch of the belt. Thus, suppose s now denotes the arc length as measured from O', s_1 represents the arc length form O' to A, and θ_1 is the angle that the tangent at A, drawn in the sense of increasing s, makes with the axis $O'O''$ (Fig. 2). Then, in the same way as before, the angle θ, made by the tangent at any point of the arc AA' with the axis $O'O''$, is given by two equations like (2.9) and (2.10) where S_2 is replaced by S_1. The angle θ_1 is then determined by the condition $d\theta/ds = -1/R$ at s_1, and, analogous to (2.11), we get

$$\theta_1 = 2\arcsin\sqrt{\frac{1}{R^{n+1}}\,\frac{n}{2(n+1)}\,\frac{D_n}{S_1}}. \tag{2.13}$$

Also for the ingoing branch it follows as above that the distance $R + e_1$ of the asymptote from the axis $O'O''$ is given by

$$R + e_1 = R + \frac{D_n}{(n+1)R^n S_1}.$$

In order to complete the analysis of equilibrium it is necessary to consider the arc AB. The equilibrium of $O'B$ is described by the equations

$$\frac{dN}{ds} + T\kappa + X = 0, \quad \frac{dT}{ds} - N\kappa + Z = 0, \quad \frac{dG}{ds} + N = 0, \tag{2.14}$$

where Z and X, respectively, are the tangential and normal forces per unit of length exerted by the wheel on the belt. If conditions are appropriate for impending motion between the belt and the pulley, the belt tending to overtake the motion of the resisting pulley, then, on $O'B$, Z and X are related by the equation

$$Z = -f|X|, \tag{2.15}$$

where f is the coefficient of friction, herein assumed constant.

On the arc $O'B$ we have $\kappa = 1/R$ = constant. Thus, also $G = D_n/R^n$ is a constant and the last of (2.14) yields $N = 0$. Using (2.15) and solving the first two of (2.14) with respect to T, we first see that $X = -T/R$, so that $X < 0$, which represents a true pressure between the pulley and the belt, for $T > 0$, and then

$$\frac{dT}{ds} = f\frac{T}{R}.$$

Whence, as $T(s_2) = S_2\cos\theta_2$, by (2.1), it follows that

$$T = S_2\cos\theta_2 e^{-f(s_2-s)/R}, \quad 0 \leqq s \leqq s_2. \tag{2.16}$$

Similar considerations apply to the arc $O'A$, with the conclusion that the tension is given by

$$T = S_1\cos\theta_1 e^{f(s_1-s)/R}, \quad 0 \leqq s \leqq s_1. \tag{2.17}$$

Since the tension must be continuous at O', it is necessary to satisfy the condition

$$S_1\cos\theta_1 e^{fs_1/R} = S_2\cos\theta_2 e^{-fs_2/R}. \tag{2.18}$$

This equation must be combined with the equation which expresses the balance of moment of momentum around O for the system, i.e.,

$$S_2(R+e_2) = S_1(R+e_1) + M. \tag{2.19}$$

If we now substitute in this equation the values of $R + e_2$ and $R + e_1$ as calculated above, it follows immediately that $S_2 = S_1 + M/R$. Then, the angles θ_2 and θ_1 are determined by (2.11) and (2.13).

We emphasize that the formula (2.18) is valid when the pulley offers its maximal resisting torque. If M is less than this limiting value, the arc of effective contact, along which friction acts, apparently is no longer AB, but consists of a shorter arc A^*B, where A^* (cf. Fig. 2) is interior to AB. (See, for example, Dubbel, 1984, p. 809.)

In order to assess the influence of the stress-strain law (2.3) on the value of θ_2, we show in Fig. 4 the qualitative behavior of the function (2.11) for $n = 1,3,5, \ldots$, assuming the ratio $D_n/R^{n+1}S_2$ as variable. Each curve in this figure has a proper interval of definition (always greater than two), and it is evident that the discrepancies between the different solutions tend to decrease as n increases, that is, when the nonlinearity grows.

3 Influence of Inertia

An approximate solution to the above belt problem can be obtained when the inertia of the belt is considered, but the assumption of steady, slow motion is maintained. In order to describe this, we let ρ denote the mass density of the belt, A the area of its cross section, and J the moment of inertia of its cross section with respect to the y axis. The balance equations for the arc BB' then become

$$\frac{dT}{ds} - N\kappa = 0, \quad \frac{dN}{ds} + T\kappa = -\rho A v^2 \frac{d\theta}{ds},$$

$$\frac{dG}{ds} + N = -\rho J v^2 \frac{d^2\theta}{ds^2}, \tag{3.1}$$

where v is the steady (constant) speed of the belt. Setting

$$H = \rho A v^2, \quad C = \rho J v^2,$$

and recalling that $\kappa = -d\theta/ds$, we may rewrite the first two of (3.1) as

$$\frac{dT}{d\theta} + N = 0, \quad \frac{dN}{d\theta} - T = -H.$$

Thus, observing that for $\theta = 0$ we have $N = 0$ and $T = S_2$, we obtain

$$T = H + (S_2 - H)\cos\theta, \quad N = (S_2 - H)\sin\theta. \tag{3.2}$$

The third of (3.1) then yields

$$-D_n \frac{d}{ds}\left[\left[\frac{d\theta}{ds}\right]^n\right] + (S_2 - H)\sin\theta = -C\frac{d^2\theta}{ds^2},$$

a first integral of which is given by

$$\frac{n}{n+1} D_n\left[\frac{d\theta}{ds}\right]^{n+1} + (S_2 - H)\cos\theta - \frac{1}{2} C\left[\frac{d\theta}{ds}\right]^2 = \text{const.} \tag{3.3}$$

Since θ and $d\theta/ds$ must vanish simultaneously as $s \to \infty$, (3.3) becomes

$$\frac{n}{n+1} D_n\left[\frac{d\theta}{ds}\right]^{n+1} - \frac{1}{2} C\left[\frac{d\theta}{ds}\right]^2 = (S_2 - H)(1-\cos\theta)$$

$$= 2(S_2 - H)\sin^2\frac{\theta}{2}. \tag{3.4}$$

Now, contrary to the situation when inertia was neglected, the last equation can be solved explicitly with respect to $d\theta/ds$ only for $n = 1$ and $n = 3$. However, an approximate solution, valid for any n, can be found if the motion is sufficiently slow in the sense that

$$\frac{1}{2} C\left[\frac{d\theta}{ds}\right]^2 \ll \frac{n}{n+1} D_n\left[\frac{d\theta}{ds}\right]^{n+1}.$$

Putting

$$\frac{d\theta}{ds} = -\sqrt[n+1]{2\frac{n+1}{n}\frac{S_2 - H}{D_n}\sin^2\frac{\theta}{2}}\,(1+\epsilon(\theta)) \tag{3.5}$$

into (3.4), and disregarding the terms of order higher than one in ϵ, we readily find that

$$\epsilon(\theta) = \frac{1}{2n}\frac{C}{D_n}\left[2\frac{n+1}{n}\frac{S_2 - H}{D_n}\sin^2\frac{\theta}{2}\right]^{-\frac{n-1}{n+1}},$$

and hence, from (3.5), that

$$\frac{d\theta}{ds} = -\sqrt[n+1]{2\frac{n+1}{n}\frac{S_2 - H}{D_n}\sin^2\frac{\theta}{2}}$$

$$\cdot\left[1 + \frac{1}{2n}\frac{C}{D_n}\left[2\frac{n+1}{n}\frac{S_2 - H}{D_n}\sin^2\frac{\theta}{2}\right]^{-\frac{n-1}{n+1}}\right]. \tag{3.6}$$

Thus, by separating the variables and using the approximate expression $(1+\epsilon)^{-1} = 1 - \epsilon$, we obtain

$$\frac{d\theta}{\sin^{2/n+1}\frac{\theta}{2}}\left[1 - \frac{1}{2n}\frac{C}{D_n}\left[2\frac{n+1}{n}\frac{S_2 - H}{D_n}\sin^2\frac{\theta}{2}\right]^{-\frac{n-1}{n+1}}\right]$$

$$= -\sqrt[n+1]{2\frac{n+1}{n}\frac{S_2 - H}{D_n}}\,ds, \quad (n = 1,3,5, \ldots), \tag{3.7}$$

where, in addition, the initial condition $\theta(s_2) = \theta_2$ holds.

For $n = 1$, the solution of (3.7) is given by

$$\tan\frac{\theta}{4} = \tan\frac{\theta_2}{4}\exp\left[-\sqrt{\frac{S_2 - H}{D_1}}\frac{1}{1 - \frac{1}{2}\frac{C}{D_1}}(s - s_2)\right]. \tag{3.8}$$

For $n = 3,5,7, \ldots$ it is again possible to obtain the explicit solution of (3.7) in the form

$$B_{\sin^2\theta/2}\left[\frac{n-1}{2(n+1)}, \frac{1}{2}\right] - B_{\sin^2\theta_2/2}\left[\frac{n-1}{2(n+1)}, \frac{1}{2}\right]$$

$$-\frac{1}{2n}\frac{C}{D_n}\left[2\frac{n+1}{n}\frac{S_2 - H}{D_n}\right]^{-\frac{n-1}{n+1}}\int_{\theta_2}^{\theta}\frac{d\theta}{\sin^{2n/n+1}\frac{\theta}{2}}$$

$$= -\sqrt[n+1]{2\frac{n+1}{n}\frac{S_2 - H}{D_n}}\,(s - s_2), \quad s_2 \leqq s < \infty. \tag{3.9}$$

The unknown angle θ_2 must be determined by the condition

$$\frac{d\theta}{ds} = -\frac{1}{R} \quad \text{at} \quad s = s_2.$$

Neglecting the terms of order higher than one in $\epsilon(\theta)$, we find, from (3.6),

$$\frac{1}{R} \approx \sqrt[n+1]{2\frac{n+1}{n}\frac{S_2 - H}{D_n}\sin^2\frac{\theta_2}{2}}\left[1 + \frac{1}{2n}\frac{C}{D_n}R^{n-1}\right],$$

and, therefore,

$$\theta_2 = 2 \arcsin \sqrt{\frac{\frac{1}{R^{n+1}} \frac{n}{2(n+1)} \frac{D_n}{S_2 - H}}{\left[1 + \frac{1}{2n} \frac{C}{D_n} R^{n-1}\right]^{n+1}}}. \tag{3.10}$$

The distance of the asymptote of the outgoing branch of the belt from the axis $O'O''$ (Fig. 3) is determined by the relation

$$R + e_2 = R\cos\theta_2 + \int_{s_2}^{\infty} \sin\theta \, ds,$$

where, now, $\cos\theta_2$ is given by (3.10) and ds can be expressed in terms of $d\theta$ through (3.7). The result of this computation is

$$R + e_2 = R + \frac{D_n}{(n+1)R^n (S_2 - H)} \left[1 + \frac{CR^{n-1}}{2nD_n}\right]^{-(n+1)} - \frac{C}{2(S_2 - H)} \left[1 + \frac{CR^{n-1}}{2nD_n}\right]^{-1}. \tag{3.11}$$

With the same procedure as employed above it is possible to find θ_1, the angle of first contact of the ingoing branch, in terms of S_1:

$$\theta_1 = 2 \arcsin \sqrt{\frac{\frac{1}{R^{n+1}} \frac{n}{2(n+1)} \frac{D_n}{S_1 - H}}{\left[1 + \frac{1}{2n} \frac{C}{D_n} R^{n-1}\right]^{n+1}}}.$$

The distance of the asymptote of the ingoing branch of the belt from the axis $O'O''$ is given by a formula like (3.11) where S_2 is replaced by S_1.

The equilibrium equations for the arc $O'B$ are

$$\frac{dN}{ds} + T\kappa + X = -H \frac{d\theta}{ds}, \quad \frac{dT}{ds} - N\kappa + Z = 0,$$

$$\frac{dG}{ds} + N = -C \frac{d^2\theta}{ds^2}. \tag{3.12}$$

Since in this interval $\kappa = -d\theta/ds = 1/R$ = constant, the bending moment $G = D_n/R^n$ is constant and the last equation of (3.12) gives $N = 0$. Then, the first of (3.12) gives

$$X = \frac{1}{R}(H - T),$$

which shows that there is a true pressure between the pulley and the belt only if $T > H$. When such is the case, we may again consider the situation of impending motion between the belt and the pulley, as before, and apply the relation (2.15) in order to reduce the first two of (3.12) to

$$\frac{dT}{ds} = \frac{1}{R} f(T - H).$$

The solution of this differential equation which, according to $(3.2)_1$, is such that $T(s_2) = H + (S_2 - H)\cos\theta_2$ is given by

$$T - H = (S_2 - H)\cos\theta_2 e^{-f(s_2 - s)/R}, \tag{3.13}$$

and, in a similar manner, it follows that the expression for T on the arc $O'A$ is

$$T - H = (S_1 - H)\cos\theta_1 e^{f(s_1 - s)/R}. \tag{3.14}$$

Since T is continuous at O', it follows that

$$(S_1 - H)\cos\theta_1 e^{fs_1/R} = (S_2 - H)\cos\theta_2 e^{-fs_2/R}. \tag{3.15}$$

By combining this equation with the equation of balance of moment of momentum about O, it is possible to derive S_2 as a function of S_1. The dependence of θ_2 on the stress-strain law (2.3) is still elucidated by a diagram like that drawn in Fig. 4. Of course, as remarked above, this solution is valid only if $T \geqq H$ and this will require $S_1 \geqq H$.

It may be interesting to observe that, for $n = 1$, θ tends exponentially to zero as s tends to infinity, while, for $n = 3,5, \ldots$, θ vanishes at a finite value of s, after which the belt remains straight.

Acknowledgment

The authors wish to thank Millard Beatty for many useful comments and suggestions.

References

Bach, 1920, *Maschinenelemente*, Berlin.

Coulomb, C. A., 1785, "Theories des machines simples en ayand égard au frottement de leurs parties," *Acad. Roy. Sc. Mem. Math. Phys. X*, p. 16.

Dubbel, H., 1984, *Handbuch der Maschinenkonstrucktion*, Springer, Berlin-Heidelberg-New York.

Eytelwein, J. A., 1808, *Handuch der Statik Fester Korper*, Bd. II, Berlin.

Gradshteyn, I. S., and Ryzhyk, I. M., 1965, *Tables of Integrals, Series, and Products*, Academic Press, New York-London.

Hamel, G., 1927, "Uber Seilsteifigkeit," *Zeit. Angew. Math. Mech.*, Vol. 7, No. 2, pp. 113-119.

Love, A. E. H., 1927, *A Treatise on the Mathematical Theory of Elasticity*, 4th Ed., The University Press, Cambridge.

Poschl, T., 1928, "Der Stoss," *Handbuch der Physik*, Bd. VI, Springer, Berlin.

Wang, C.-Y., 1981, "Winding a Long Elastic Sheet," *Acta Mechanica*, Vol. 39, pp. 297-301.

Combined Loading of a Fully Plastic Ligament Ahead of an Edge-Crack

C. F. Shih
Division of Engineering,
Brown University,
Providence, R.I. 02912

J. W. Hutchinson
Division of Applied Sciences,
Harvard University,
Cambridge, Mass. 02138

Complete, accurate numerical results are given for the solution to the problem of a semi-infinite crack aligned perpendicularly to the free-edge of a semi-infinite half space in which the ligament is subject to arbitrary combinations of bending and tension or compression. The material is an incompressible, pure power-law deformation theory solid. Conditions of plane strain are assumed. Approximate solutions are proposed for predominantly bending loadings and also for predominantly stretching loadings.

1 Introduction

Accurate numerical results will be presented for the basic problem of a semi-infinite crack approaching the free edge of a semi-infinite plane, as depicted in Fig. 1. The remote stresses acting on the upper-half plane are equivalent to a net load per unit thickness P and a net moment per unit thickness M taken about the origin in the sense shown. This is a Mode I problem, and attention is directed to the plane strain problem with $\epsilon_{33}=\epsilon_{13}=\epsilon_{23}=0$. The study is carried out within the context of small strain theory, and the material of the cracked body is taken to be described by J_2 deformation theory for an incompressible pure power-law stress-strain behavior. In uniaxial tension the material deforms according to

$$\epsilon/\epsilon_o=(\sigma/\sigma_o)^n \tag{1.1}$$

where σ_o and ϵ_o are the reference stress and strain. Under multi-axial stress states, σ_{ij}, the strain is

$$\epsilon_{ij}/\epsilon_o=\frac{3}{2}(\sigma_e/\sigma_o)^{n-1}s_{ij}/\sigma_o \tag{1.2}$$

Here, s_{ij} is the stress deviator and $\sigma_e=(3s_{ij}s_{ij}/2)^{1/2}$ is the effective stress. (In earlier papers on pure power-law problems we have introduced an additional convenient scale factor α multiplying the right hand sides of (1.1) and (1.2). In this paper α has been absorbed into ϵ_o).

Approximate solutions to semi-infinite crack problems have been used to model the effect of deep part-through cracks in plates subject to combined tension and bending. In particular, such solutions play a central role in the development of the line-spring model for analyzing the effect of surface cracks in pressure vessel walls (Rice, 1972, and Parks and White, 1982).

This paper begins with the derivation of some fairly general relationships for arbitrary small strain deformation theory materials and then proceeds to specialize them to the power-law material. Numerical results are presented for quantities of interest over the full range of combined loading. The effect of shifting the origin about which the moment is defined is also discussed, and approximate analytical solutions are proposed.

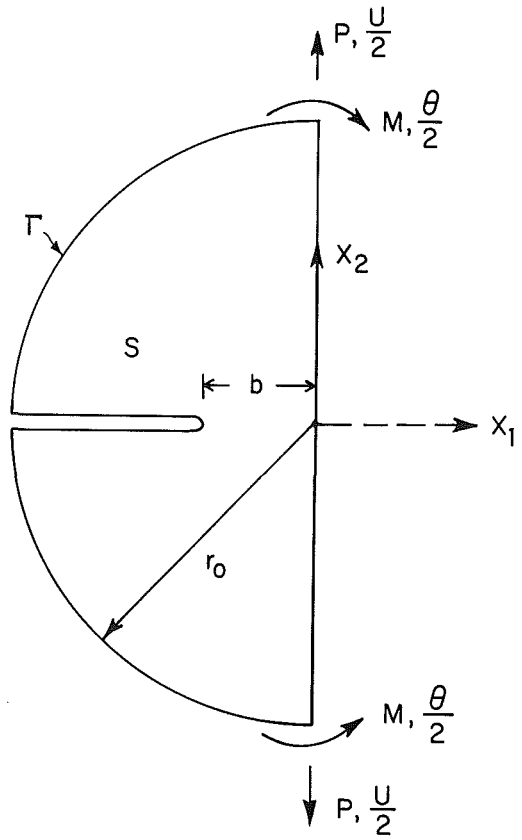

Fig. 1 Conventions

Contributed by the Applied Mechanics Division for presntation at the Winter Annual Meeting, Anaheim, CA, December 7–12, 1986, of the American Society of Mechanical Engineers.

Discussion on this paper should be addressed to the Editorial Department, ASME, United Engineering Center, 345 East 47th Street, New York, N.Y. 10017, and will be accepted until two months after final publication of the paper itself in the JOURNAL OF APPLIED MECHANICS. Manuscript received by ASME Applied Mechanics Division, April 23, 1985. Paper No. 86-WA/APM-1.

2 Some General Relationships for Finite and Infinite Geometries

At this stage, consider a body characterized by a general deformation theory in which $w(\epsilon)$ is the strain energy density and $\phi(\sigma)$ is the complementary stress energy density so that

$$\sigma_{ij}=\frac{\partial w}{\partial \epsilon_{ij}},\quad \epsilon_{ij}=\frac{\partial \phi}{\partial \sigma_{ij}} \text{ and } \sigma_{ij}\epsilon_{ij}=\phi+w \tag{2.1}$$

Consider a body occupying a finite region S, such as that in Fig. 1, and let Γ denote the portion of the body of S in the upper-half plane other than the traction-free crack faces and the traction-free edge along $x_1=0$. Prescribe in-plane displacements on Γ

$$u_\alpha=\frac{U}{2}\delta_{\alpha 2}+\frac{\Theta}{2}e_{\alpha\beta}x_\beta \tag{2.2}$$

where the sense of Θ is shown in Fig. 1 and $\delta_{\alpha\beta}$ is the Kronecker delta and $e_{\alpha\beta}$ is the permutation symbol. Opposite-signed prescriptions are made in the lower-half plane.

The force-like variables P and M are identified most directly through the external virtual work expression as

$$2\int_\Gamma T_\alpha \delta u_\alpha ds=\left(\int_\Gamma T_2 ds\right)\delta U + \left(\int_\Gamma e_{\alpha\beta}x_\beta T_\alpha ds\right)\delta\Theta \equiv P\delta U+M\delta\Theta \tag{2.3}$$

where $T_\alpha=\sigma_{\alpha\beta}n_\beta$ is the traction vector. In both (2.2) and (2.3) the origin of the coordinates (x_1, x_2) is taken at the free edge as shown in Fig. 1. Other choices are possible and may be preferred for certain purposes. The effect of shifting the origin of the coordinates is discussed in Section 5.

By (2.1) and the principle of virtual work,

$$PdU+Md\Theta=\int_S \sigma_{\alpha\beta}d\epsilon_{\alpha\beta}dS=\int_S dwdS \tag{2.4}$$

Thus, with the overall strain energy defined as

$$W(U,\Theta)=\int_S w dS \tag{2.5}$$

it follows that

$$P=\frac{\partial W}{\partial U} \text{ and } M=\frac{\partial W}{\partial \Theta} \tag{2.6}$$

The complementary connections may be derived similarly as

$$U=\frac{\partial \Phi}{\partial P} \text{ and } \Theta=\frac{\partial \Phi}{\partial M} \tag{2.7}$$

where

$$\Phi(P,M)=\int_S \Phi dS \tag{2.8}$$

In addition,

$$PU+M\Theta=W+\Phi \tag{2.9}$$

Now imagine that the stress-strain behavior of the material is such that W and Φ are well defined in the limit as the outer contour Γ is expanded to infinity (e.g., $r_o\to\infty$ in Fig. 1). For the power-law material (1.2) this limit is well defined as long as $n>1$. However, a linear material ($n=1$) is excluded from consideration unless $P=0$. By dimensional considerations similar to those first exploited by Rice et al. (1973), it necessarily follows that the functional dependence of W for the semi-infinite crack problem on the uncracked ligament, b, U and Θ is of the form

$$W=b^2F(U/b,\Theta) \tag{2.10}$$

where F depends implicitly on material properties.

The energy release rate, J, for the semi-infinite body is

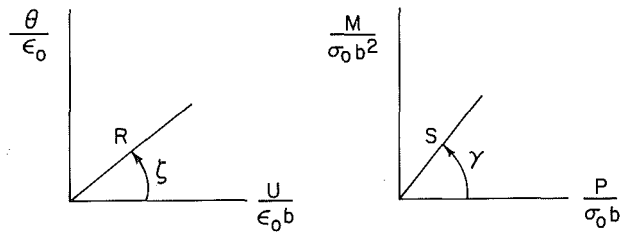

Fig. 2 Nondimensional displacement and load variables

$$J=\frac{dW}{db}=2bF-U\frac{\partial F}{\partial(U/b)}=\frac{2W}{b}-\frac{PU}{b} \tag{2.11}$$

where $P=b\partial F/\partial(U/b)$ from (2.6), and (2.10) has been used.

It has become fairly common practice (Turner, 1980) to write the relationship between J and W under combined bending and tension loadings as

$$J=\eta W/b \tag{2.12}$$

so that, from (2.11), the "eta factor" is given precisely by

$$\eta=2-PU/W \tag{2.13}$$

For either P or U vanishing, $\eta=2$. As an approximation, η has been taken to be 2 for load combinations typical of several "bend-type" geometries, but this approximation is of dubious accuracy in general. For example, when either $M=0$ or $\Theta=0$ one finds using (2.9) that

$$\eta=1-\Phi/W \tag{2.14}$$

which is necessarily less than unity since Φ and W are each inherently positive. For a pure-power-law material this becomes $\eta=(n-1)/n$.

3 Relations Among J, P, M and Θ for Semi-infinite Crack in a Power-Law Material

Because the equilibrium equations and the strain-displacement equations are linear, the dimensional forms for W and Φ from the solution for the pure power-law material (1.2) are

$$W=\sigma_o\epsilon_o b^2 f_W[U/(\epsilon_o b),\Theta/\epsilon_o] \tag{3.1}$$

$$\Phi=\sigma_o\epsilon_o b^2 f_\phi[P/(\sigma_o b),\ M/(\sigma_o b^2)] \tag{3.2}$$

where f_W and f_ϕ are dimensionless functions of the arguments indicated. Moreover, it also follows from the linearity of the equilibrium and strain-displacement equations and the character of the stress-strain law (1.2) that f_W and f_ϕ satisfy

$$f_W[-U/(\epsilon_o b),-\Theta/\epsilon_o]=f_W[U/(\epsilon_o b),\Theta/\epsilon_o] \tag{3.3}$$

$$f_\phi[-P/(\sigma_o b),-M/(\sigma_o b^2)]=f_\phi[P/(\sigma_o b),M/(\sigma_o b^2)] \tag{3.4}$$

Of course, contact between the crack faces is disregarded in writing these relations. Our interest is restricted to the range of variables such that the crack faces are not in contact; nevertheless, for mathematical purposes it is useful to produce the solution over the full range of the variables under the ficitious assumption that the crack faces may overlap.

From the equations listed in the previous section it is seen that knowledge of either f_W for f_ϕ fully determines the relationships among J, P, M, U and Θ. There are various ways to present the numerical results for f_W or f_ϕ, but the pure power character of the stress-strain law favors the following approach. Let

$$R=\left[\left(\frac{U}{\epsilon_o b}\right)^2+\left(\frac{\Theta}{\epsilon_o}\right)^2\right]^{1/2} \text{ and } \zeta=\arctan\left[\frac{\Theta/\epsilon_o}{U/(\epsilon_o b)}\right] \tag{3.5}$$

be polar coordinates in the plane of $U/\epsilon_o b$ and Θ/ϵ_o as in-

Table 1 Normalized functions for $n = 3$

ζ	γ	η	f	f'	g	k	h	h'
0.0	31.1	0.667	0.693	0.557	0.462	1.079	1.71E-01	-4.12E-01
5.0	31.6	0.735	0.739	0.492	0.543	1.101	1.68E-01	-3.35E-01
10.0	31.9	0.799	0.778	0.418	0.622	1.119	1.66E-01	-2.67E-01
15.0	32.4	0.861	0.811	0.340	0.698	1.134	1.64E-01	-2.05E-01
20.0	32.9	0.921	0.837	0.255	0.771	1.145	1.62E-01	-1.48E-01
25.0	33.3	0.980	0.856	0.167	0.838	1.153	1.61E-01	-9.45E-02
30.0	33.9	1.040	0.867	0.080	0.901	1.158	1.61E-01	-4.43E-02
35.0	34.5	1.100	0.870	-0.010	0.956	1.160	1.60E-01	5.71E-03
40.0	35.0	1.160	0.865	-0.100	1.003	1.157	1.61E-01	5.60E-02
45.0	35.5	1.222	0.852	-0.190	1.041	1.152	1.61E-01	1.08E-01
50.0	36.1	1.286	0.832	-0.275	1.070	1.143	1.63E-01	1.61E-01
55.0	36.7	1.354	0.804	-0.355	1.089	1.130	1.65E-01	2.18E-01
60.0	37.3	1.425	0.770	-0.429	1.097	1.113	1.67E-01	2.80E-01
65.0	37.9	1.501	0.729	-0.497	1.095	1.092	1.71E-01	3.49E-01
70.0	38.6	1.582	0.683	-0.556	1.081	1.068	1.75E-01	4.28E-01
75.0	39.3	1.671	0.633	-0.606	1.057	1.038	1.81E-01	5.21E-01
80.0	40.1	1.769	0.578	-0.644	1.023	1.004	1.90E-01	6.33E-01
85.0	41.1	1.878	0.521	-0.669	0.978	0.964	2.01E-01	7.75E-01
90.0	42.2	2.000	0.462	-0.679	0.924	0.916	2.18E-01	9.62E-01
95.0	43.6	2.135	0.403	-0.673	0.860	0.861	2.44E-01	1.22E+00
100.0	45.3	2.282	0.345	-0.649	0.787	0.795	2.87E-01	1.62E+00
105.0	47.8	2.429	0.290	-0.601	0.705	0.715	3.70E-01	2.30E+00
110.0	51.5	2.544	0.241	-0.524	0.612	0.615	5.62E-01	3.67E+00
115.0	58.2	2.541	0.200	-0.406	0.508	0.486	1.19E+00	7.29E+00
116.0	60.3	2.514	0.193	-0.377	0.485	0.456	1.48E+00	8.69E+00
117.0	62.7	2.474	0.187	-0.346	0.462	0.426	1.89E+00	1.05E+01
118.0	65.6	2.423	0.181	-0.313	0.438	0.395	2.48E+00	1.29E+01
119.0	69.1	2.357	0.176	-0.278	0.414	0.363	3.36E+00	1.59E+01
120.0	73.4	2.277	0.171	-0.241	0.390	0.332	4.69E+00	1.98E+01
121.0	78.6	2.184	0.167	-0.204	0.365	0.302	6.69E+00	2.44E+01
122.0	84.7	2.083	0.164	-0.167	0.342	0.275	9.53E+00	2.91E+01
122.8	90.0	2.000	0.162	-0.139	0.324	0.257	1.24E+01	3.15E+01
123.0	91.8	1.974	0.161	-0.131	0.319	0.252	1.34E+01	3.25E+01
124.0	100.0	1.858	0.160	-0.095	0.296	0.233	1.81E+01	3.22E+01
125.0	109.4	1.736	0.158	-0.059	0.275	0.219	2.29E+01	2.56E+01
126.0	120.0	1.606	0.157	-0.022	0.253	0.211	2.64E+01	1.11E+01
127.0	131.9	1.462	0.157	0.018	0.230	0.211	2.66E+01	-9.14E+00
128.0	144.2	1.307	0.158	0.061	0.207	0.220	2.27E+01	-2.63E+01
129.0	155.8	1.143	0.160	0.107	0.182	0.238	1.65E+01	-3.33E+01
130.0	166.0	0.972	0.162	0.157	0.157	0.267	1.06E+01	-3.09E+01
131.0	174.3	0.804	0.165	0.207	0.133	0.302	6.58E+00	-2.48E+01
132.0	180.7	0.648	0.169	0.257	0.110	0.342	4.13E+00	-1.88E+01
133.0	185.7	0.505	0.174	0.305	0.088	0.383	2.69E+00	-1.41E+01
134.0	189.8	0.377	0.180	0.352	0.068	0.426	1.82E+00	-1.07E+01
135.0	193.1	0.264	0.186	0.399	0.049	0.470	1.28E+00	-8.19E+00
140.0	201.7	0.000	0.229	0.567	0.000	0.644	4.44E-01	-3.29E+00
145.0	205.0	0.018	0.283	0.655	0.005	0.756	2.89E-01	-2.01E+00
150.0	206.8	0.118	0.342	0.698	0.040	0.834	2.36E-01	-1.44E+00
155.0	207.9	0.230	0.404	0.711	0.093	0.892	2.12E-01	-1.12E+00
160.0	208.8	0.333	0.466	0.710	0.155	0.943	1.96E-01	-8.97E-01
165.0	209.5	0.429	0.527	0.690	0.226	0.985	1.87E-01	-7.33E-01
170.0	210.1	0.515	0.586	0.658	0.302	1.021	1.80E-01	-6.04E-01
175.0	210.6	0.594	0.642	0.613	0.381	1.052	1.74E-01	-5.00E-01
180.0	211.1	0.667	0.693	0.557	0.462	1.079	1.71E-01	-4.12E-01

Table 2 Normalized functions for $n = 5$

ζ	γ	η	f	f'	g	k	h	h'
0.0	30.2	0.800	0.911	0.636	0.729	1.265	4.46E-02	-1.56E-01
5.0	30.5	0.859	0.963	0.551	0.827	1.280	4.38E-02	-1.25E-01
10.0	30.8	0.914	1.007	0.460	0.921	1.293	4.31E-02	-9.86E-02
15.0	31.2	0.968	1.043	0.363	1.009	1.303	4.26E-02	-7.43E-02
20.0	31.6	1.019	1.070	0.263	1.091	1.311	4.22E-02	-5.19E-02
25.0	32.0	1.071	1.089	0.160	1.166	1.316	4.19E-02	-3.09E-02
30.0	32.5	1.123	1.098	0.057	1.233	1.319	4.17E-02	-1.09E-02
35.0	33.0	1.175	1.099	-0.045	1.291	1.319	4.17E-02	8.60E-03
40.0	33.6	1.229	1.090	-0.147	1.340	1.316	4.19E-02	2.82E-02
45.0	34.1	1.284	1.073	-0.248	1.378	1.311	4.22E-02	4.88E-02
50.0	34.6	1.341	1.047	-0.346	1.404	1.303	4.28E-02	7.07E-02
55.0	35.1	1.402	1.013	-0.439	1.419	1.292	4.35E-02	9.43E-02
60.0	35.8	1.466	0.971	-0.524	1.423	1.277	4.47E-02	1.21E-01
65.0	36.4	1.536	0.921	-0.602	1.415	1.259	4.63E-02	1.51E-01
70.0	37.1	1.611	0.866	-0.671	1.394	1.237	4.84E-02	1.87E-01
75.0	37.9	1.692	0.805	-0.731	1.362	1.211	5.10E-02	2.32E-01
80.0	38.7	1.783	0.739	-0.780	1.317	1.180	5.46E-02	2.88E-01
85.0	39.6	1.885	0.669	-0.815	1.261	1.144	5.97E-02	3.64E-01
90.0	40.7	2.000	0.597	-0.834	1.194	1.099	6.77E-02	4.73E-01
95.0	41.9	2.130	0.524	-0.838	1.116	1.048	7.91E-02	6.33E-01
100.0	44.0	2.269	0.452	-0.805	1.024	0.970	1.08E-01	9.64E-01
105.0	45.9	2.420	0.383	-0.768	0.928	0.895	1.49E-01	1.49E+00
110.0	48.9	2.557	0.319	-0.691	0.815	0.790	2.62E-01	2.84E+00
115.0	55.9	2.552	0.265	-0.531	0.677	0.619	9.45E-01	9.45E+00
116.0	57.9	2.528	0.256	-0.494	0.648	0.582	1.32E+00	1.28E+01
117.0	60.3	2.491	0.248	-0.453	0.618	0.542	1.96E+00	1.79E+01
118.0	63.3	2.438	0.240	-0.408	0.586	0.499	3.10E+00	2.63E+01
119.0	67.0	2.369	0.234	-0.359	0.554	0.455	5.24E+00	4.02E+01
120.0	71.8	2.281	0.228	-0.306	0.520	0.410	9.53E+00	6.40E+01
121.0	77.8	2.180	0.223	-0.252	0.486	0.368	1.81E+01	1.02E+02
122.0	85.0	2.070	0.219	-0.199	0.454	0.330	3.42E+01	1.55E+02
122.6	90.0	2.000	0.217	-0.167	0.434	0.309	4.95E+01	1.79E+02
123.0	93.6	1.953	0.216	-0.146	0.422	0.298	6.20E+01	2.10E+02
124.0	103.7	1.831	0.214	-0.095	0.392	0.274	1.01E+02	2.25E+02
125.0	115.0	1.704	0.213	-0.045	0.363	0.259	1.40E+02	1.48E+02
126.0	127.6	1.569	0.213	0.007	0.334	0.255	1.54E+02	-2.60E+01
127.0	141.0	1.421	0.213	0.064	0.303	0.264	1.27E+02	-1.90E+02
128.0	153.9	1.262	0.215	0.125	0.271	0.287	7.76E+01	-2.26E+02
129.0	165.2	1.095	0.218	0.191	0.238	0.324	3.79E+01	-1.67E+02
130.0	174.6	0.922	0.221	0.262	0.204	0.373	1.64E+01	-9.70E+01
131.0	182.0	0.750	0.227	0.336	0.170	0.432	6.97E+00	-5.16E+01
132.0	187.7	0.587	0.233	0.411	0.137	0.497	3.09E+00	-2.72E+01
133.0	192.3	0.434	0.241	0.487	0.105	0.567	1.46E+00	-1.47E+01
134.0	196.0	0.293	0.250	0.565	0.073	0.640	7.29E-01	-8.24E+00
135.0	199.1	0.165	0.261	0.644	0.043	0.716	3.87E-01	-4.78E+00
140.0	205.3	0.010	0.329	0.859	0.003	0.946	9.20E-02	-1.20E+00
145.0	206.5	0.158	0.406	0.895	0.064	1.019	7.25E-02	-8.01E-01
150.0	207.5	0.285	0.485	0.913	0.138	1.082	6.04E-02	-5.68E-01
155.0	208.1	0.401	0.564	0.903	0.226	1.128	5.47E-02	-4.38E-01
160.0	208.6	0.502	0.642	0.875	0.322	1.165	5.12E-02	-3.49E-01
165.0	209.1	0.590	0.716	0.832	0.422	1.196	4.88E-02	-2.84E-01
170.0	209.5	0.667	0.787	0.779	0.525	1.224	4.68E-02	-2.32E-01
175.0	209.9	0.737	0.852	0.712	0.627	1.246	4.56E-02	-1.91E-01
180.0	210.2	0.800	0.911	0.636	0.729	1.264	4.46E-02	-1.56E-01

dicated in Fig. 2. Because f_W is homogeneous of degree $N+1$ in $U/\epsilon_o b$ and Θ/ϵ_o, one can further specialize (3.1) to

$$W = \sigma_o \epsilon_o b^2 R^{N+1} f(\zeta, N) \tag{3.6}$$

where f is a dimensionless function of $N \equiv 1/n$ and ζ which by (3.3) has the periodicity

$$f(\zeta + \pi, N) = f(\zeta, N) \tag{3.7}$$

Thus, knowledge of $f(\zeta, N)$ completely determines the relations among all variables of interest. In particular, from (2.6)

$$P = \sigma_o b R^N [(N+1) f \cos\zeta - f' \sin\zeta] \tag{3.8}$$

$$M = \sigma_o b^2 R^N [(N+1) f \sin\zeta + f' \cos\zeta] \tag{3.9}$$

where $f' = \partial f(\zeta, N)/\partial\zeta$. From (2.11) it follows that

$$J = \sigma_o \epsilon_o b R^{N+1} \{[2 - (N+1)\cos^2\zeta] f + f' \sin\zeta \cos\zeta\} \tag{3.10}$$

$$\equiv \sigma_o \epsilon_o b R^{N+1} g(\zeta, N) \tag{3.11}$$

and then, from (2.13), that

$$\eta(\zeta, N) = g/f = 2 - (N+1)\cos^2\zeta + (f'/f)\sin\zeta\cos\zeta \tag{3.12}$$

Alternatively, if P and M are preferred as independent variables, let

$$S = \left[\left(\frac{P}{\sigma_o b}\right)^2 + \left(\frac{M}{\sigma_o b^2}\right)\right]^{1/2} \text{ and } \gamma = \arctan\left[\frac{M/(\sigma_o b^2)}{P/(\sigma_o b)}\right] \tag{3.13}$$

Now, since f_ϕ is homogeneous of degree $n+1$ in P and M,

$$\Phi = \sigma_o \epsilon_o b^2 S^{n+1} h(\gamma, n) \tag{3.14}$$

where $h(\gamma + \pi, n) = h(\gamma, n)$. From (2.7),

$$U = \epsilon_o b S^n [(n+1) h \cos\gamma - h' \sin\gamma] \tag{3.15}$$

$$\Theta = \epsilon_o S^n [(n+1) h \sin\gamma + h' \cos\gamma] \tag{3.16}$$

where $h' = \partial h(\gamma, n)/\partial\gamma$.

The relations between the polar load variables and the polar displacement variables follow directly from (3.8) and (3.9) as

$$S = R^N [(N+1)^2 f^2 + (f')^2]^{1/2} \equiv k(\zeta, N) R^N \tag{3.17}$$

and

$$\gamma = \arctan\left\{\frac{(N+1) f \sin\zeta + f' \cos\zeta}{(N+1) f \cos\zeta - f' \sin\zeta}\right\} \tag{3.18}$$

Finally, from the fact that $\Phi = NW$, it follows that

$$h = N f k^{-(N+1)/N} \tag{3.19}$$

and

$$J = \sigma_o \epsilon_o b (S/k)^{n+1} g \tag{3.20}$$

4 Numerical Results

As has already been emphasized, all information regarding the relationships among M, Θ, P, U and J is contained in the function $f(\zeta, N)$. This function has been computed numerically using a finite element method specially designed for incompressible materials as has been described in prior publications (Shih and Needleman, 1984a, 1984b). Details peculiar to the present problem are discussed in the Appendix. In addition, a number of consistency checks on the numerical solution are also discussed in the Appendix. These checks give some indication of the accuracy of the computed quantities.

The numerical data is presented in Tables 1–3. Values of f, f', g, h, h', η, γ and k are given at 5 deg intervals of ζ for $n = 3$, 5, and 10. Within the range of ζ from 115 deg to 135 deg, γ changes rapidly so values are given for each 1 deg interval of ζ within this range. This range spans pure bending (i.e., $P = 0$, $\gamma = 90$ deg), and data for $\gamma = 90$ deg is also included in

Table 3 Normalized functions for $n = 10$

ζ	y	η	f	f'	g	k	h	h'
0.0	29.5	0.900	1.072	0.667	0.965	1.355	3.79E-03	-2.36E-02
5.0	29.8	0.952	1.126	0.571	1.073	1.364	3.70E-03	-1.87E-02
10.0	30.1	1.002	1.172	0.471	1.174	1.372	3.61E-03	-1.45E-02
15.0	30.4	1.049	1.208	0.366	1.268	1.378	3.54E-03	-1.07E-02
20.0	30.8	1.096	1.236	0.258	1.354	1.383	3.48E-03	-7.27E-03
25.0	31.2	1.142	1.253	0.150	1.431	1.387	3.44E-03	-4.10E-03
30.0	31.7	1.189	1.262	0.041	1.500	1.388	3.41E-03	-1.11E-03
35.0	32.3	1.237	1.261	-0.066	1.559	1.388	3.42E-03	1.80E-03
40.0	32.8	1.287	1.250	-0.173	1.608	1.386	3.45E-03	4.77E-03
45.0	33.4	1.337	1.230	-0.278	1.645	1.382	3.51E-03	7.94E-03
50.0	33.9	1.389	1.202	-0.382	1.669	1.376	3.60E-03	1.14E-02
55.0	34.5	1.445	1.164	-0.479	1.682	1.367	3.74E-03	1.54E-02
60.0	35.1	1.504	1.118	-0.570	1.682	1.356	3.93E-03	2.01E-02
65.0	35.8	1.568	1.065	-0.655	1.669	1.342	4.19E-03	2.58E-02
70.0	36.5	1.637	1.004	-0.731	1.644	1.325	4.55E-03	3.32E-02
75.0	37.2	1.713	0.937	-0.799	1.606	1.304	5.04E-03	4.30E-02
80.0	38.0	1.798	0.865	-0.856	1.555	1.280	5.73E-03	5.67E-02
85.0	38.8	1.892	0.788	-0.903	1.491	1.252	6.65E-03	7.62E-02
90.0	40.1	2.000	0.708	-0.924	1.416	1.208	8.84E-03	1.15E-01
95.0	41.1	2.123	0.627	-0.945	1.331	1.170	1.12E-02	1.68E-01
100.0	42.3	2.264	0.544	-0.944	1.231	1.118	1.60E-02	2.77E-01
105.0	44.6	2.410	0.463	-0.896	1.117	1.031	3.31E-02	6.39E-01
110.0	47.7	2.544	0.388	-0.813	0.988	0.919	9.88E-02	2.07E+00
115.0	53.6	2.575	0.324	-0.652	0.834	0.743	8.46E-01	1.70E+01
116.0	55.5	2.555	0.313	-0.609	0.799	0.699	1.60E+00	3.12E+01
117.0	57.8	2.520	0.303	-0.559	0.762	0.650	3.44E+00	6.36E+01
118.0	60.7	2.468	0.293	-0.503	0.724	0.597	8.51E+00	1.46E+02
119.0	64.5	2.396	0.285	-0.440	0.683	0.541	2.48E+01	3.82E+02
120.0	69.4	2.305	0.278	-0.372	0.641	0.482	8.61E+01	1.15E+03
121.0	75.9	2.196	0.272	-0.301	0.597	0.424	3.40E+02	3.76E+03
122.0	84.1	2.076	0.267	-0.229	0.555	0.373	1.38E+03	1.18E+04
122.6	90.0	2.000	0.265	-0.187	0.531	0.346	3.08E+03	2.17E+04
123.0	94.5	1.947	0.264	-0.158	0.514	0.331	5.12E+03	3.06E+04
124.0	107.3	1.809	0.262	-0.086	0.474	0.301	1.44E+04	4.73E+04
125.0	122.0	1.665	0.261	-0.015	0.435	0.288	2.35E+04	1.34E+04
126.0	137.5	1.514	0.261	0.059	0.396	0.293	1.88E+04	-4.21E+04
127.0	152.2	1.353	0.263	0.136	0.356	0.320	7.36E+03	-3.80E+04
128.0	164.6	1.187	0.266	0.217	0.316	0.365	1.75E+03	-1.43E+04
129.0	174.5	1.017	0.271	0.303	0.275	0.425	3.34E+02	-3.73E+03
130.0	182.2	0.848	0.277	0.392	0.235	0.497	6.11E+01	-8.66E+02
131.0	188.1	0.684	0.284	0.484	0.194	0.577	1.22E+01	-2.07E+02
132.0	192.8	0.530	0.294	0.577	0.156	0.661	2.77E+00	-5.45E+01
133.0	196.5	0.390	0.305	0.671	0.119	0.750	7.21E-01	-1.59E+01
134.0	199.5	0.263	0.317	0.766	0.083	0.842	2.12E-01	-5.11E+00
135.0	202.1	0.150	0.331	0.862	0.050	0.936	6.89E-02	-1.79E+00
140.0	206.8	0.092	0.420	1.076	0.039	1.171	7.40E-03	-1.90E-01
145.0	207.0	0.290	0.512	1.060	0.148	1.201	6.84E-03	-1.41E-01
150.0	207.7	0.421	0.605	1.053	0.255	1.246	5.38E-03	-9.36E-02
155.0	208.1	0.536	0.695	1.017	0.373	1.273	4.90E-03	-7.17E-02
160.0	208.5	0.630	0.782	0.971	0.493	1.298	4.46E-03	-5.53E-02
165.0	208.6	0.711	0.864	0.907	0.615	1.314	4.28E-03	-4.49E-02
170.0	208.9	0.781	0.940	0.835	0.735	1.330	4.09E-03	-3.64E-02
175.0	209.3	0.843	1.010	0.757	0.852	1.344	3.90E-03	-2.92E-02
180.0	209.5	0.900	1.072	0.667	0.965	1.355	3.80E-03	-2.36E-02

the Tables. Use of the data can be illustrated by two special cases.

Pure Stretching ($\Theta = 0$). Pure stretching is defined with $\Theta = 0$ and $U > 0$ so that $\zeta = 0$ deg and $R = U/(\epsilon_o b)$. Then

$$J = \sigma_o \epsilon_o b (U/\epsilon_o b)^{N+1} g(0, N) \tag{4.1}$$

where $g(0, 1/3) = 0.462$, $g(0, 1/5) = 0.729$, and $g(0, 1/10) = 0.965$. The corresponding values of P and M can be obtained from (3.8) and (3.9). Note that $\gamma \simeq 30$ deg in pure stretching, and, from (2.14), $\eta = 1 - N$.

Pure Bending. In pure bending, $P = 0$ and $M > 0$ so that $\gamma = 90$ deg and $S = M/(\sigma_o b^2)$. By (3.20)

$$J = \sigma_o \epsilon_o b \left(\frac{M}{k \sigma_o b^2} \right)^{n+1} g \tag{4.2}$$

The values of k and g associated with $\gamma = 90$ deg are included in the Tables, as are h and h', which allow one to determine U and Θ from (3.15) and (3.16). Equation (4.2) can be rewritten in the form given by Shih and Needleman (1984a) as

$$J = \sigma_o \epsilon_o b h_1(n) (M/M_o)^{n+1} \tag{4.3}$$

where, for all n, the reference moment is

$$M_o = \mu_2 \sigma_o b^2 \quad (\mu_2 = 0.364) \tag{4.4}$$

The results from Shih and Needleman (1984a) for a deeply-cracked strip with a ligament to width ratio of 1/8 are $h_1(3) = 1.30$, $h_1(5) = 1.16$ and $h_1(10) = 0.97$. The corresponding results converted from (4.2) using the values in the Tables are $h_1(3) = 1.31$, $h_1(5) = 1.15$ and $h_1(10) = 0.92$. In pure bending $\eta = 2$.

The overall strain energy W is equal to the work of the combined loads through their respective displacement quantities. If the loads are increased so that M and P maintain a fixed proportion, the deformation theory W is also exactly equal to

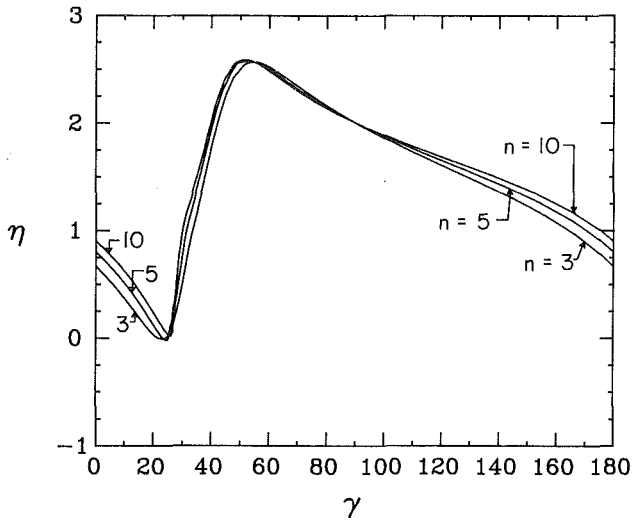

Fig. 3(*a*) The eta-factor as a function of γ

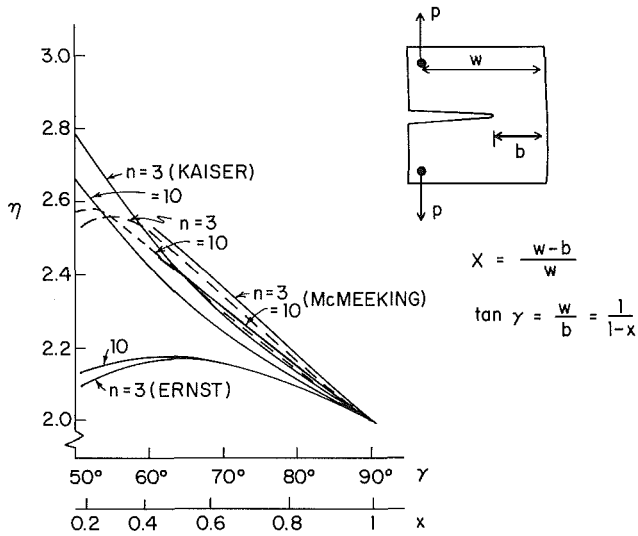

Fig. 3(*b*) The eta-factor as a function of γ for the range appropriate to a compact specimen

the work done on the body if the material is described by a pure-power flow theory (i.e., an incremental plasticity theory). The significance of the "eta factor," η, defined in (2.12) is that it permits the determination of J directly from the work done on a specimen by the applied loads. Curves of the eta factor are presented in Figs. 3*a* and 3*b*. In Fig. 3*a*, η is plotted as a function of γ for $n = 3$, 5 and 10 over the full range of loadings. The same variation of η is shown in Fig. 3*b* for $n = 3$ and 10 for γ between 50 deg and 90 deg, corresponding to the range of γ appropriate to standard compact tension specimens. Predictions from the present calculations are shown as dashed line curves in Fig. 3*b*. Predictions for η from other investigators are also shown and will be discussed below. To apply the deeply-cracked solution to a compact tension specimen, we let $M = Pw$ where w is the distance between the line of action of the load P and the back face of the specimen. Thus, $\tan \gamma = w/b$. The parameter $x = (w - b)/w$ is frequently used to characterize the geometry of the compact tension specimen. It is related to γ by $\tan \gamma = 1/(1 - x)$, and the variation of η with x is also included in Fig. 3*b*.

A typical value of x for a compact tension specimen is 1/2 corresponding to $\gamma = 63.4$ with $\eta = 2.46$ for $n = 3$ and $\eta = 2.42$ for $n = 10$, according to the present calculations. These values are substantially above the pure bending value, $\eta = 2$. Several investigators have developed approximations for η to account

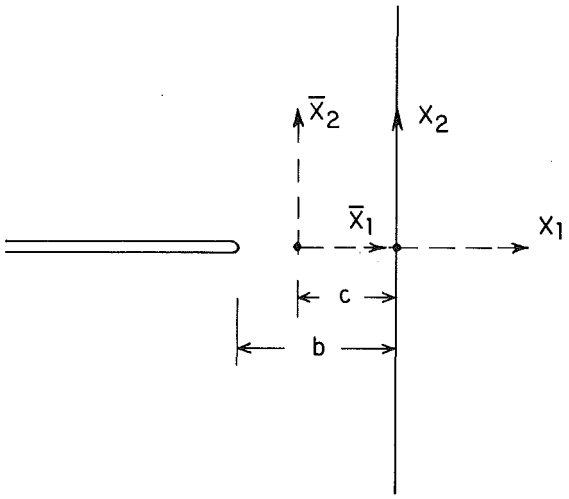

Fig. 4 Conventions for shift of origin

for combined loading effects present in the compact tension specimen, including Ernst (1983), Kaiser (1985), and McMeeking (1984). In each case, the approximation for the plastic part of J leads to an expression of the form

$$J=\eta_1 b^{-1}\int_0^{\Delta} P d\Delta+\eta_2 b^{-1}\int_0^{P}\Delta dP \tag{4.5}$$

where η_1 and η_2 depend on x or γ (but not on n) and Δ denotes the plastic part of the overall load-point displacement. For the pure power law material, this expression reduces to

$$J=(\eta_1+\eta_{2/n})b^{-1}W\equiv\eta b^{-1}W \tag{4.6}$$

We have used the variations of η_1 and η_2 with x given by Ernst (1983), Kaiser (1985), and McMeeking (1984) to plot the curves of η in Fig. 3*b* for the pure power material. Ernst's results for η are about 13 percent below the present predictions for $x=1/2$. McMeeking's results are exceedingly close to those obtained here over the range $0.4\le x\le 1$ for which he tabulates his η_1 and η_2. This suggests that the more general formula (4.5), which is not tied to the power law material, may be used with confidence with McMeeking's values of η_1 and η_2. Kaiser's predictions for η are also in reasonable accord with those obtained over this same range. However, outside this range his predictions deviate substantially from the present ones, as is already evident in Fig. 3*b*. We also note that Ernst's results become significantly in error in the vicinity of $\gamma=26$ deg, which is his "pure tension" limit. Ernst's notion of a pure tension limit is tied to the approximate form of the stress distribution he assumes. His approximation in this limit assumes the stress is uniform across the ligament so that P acts through the mid-point of the ligament. Unlike the special states of pure stretching and pure bending which are defined precisely, the "pure tension" state does not appear to have a precise meaning outside the context of his approximation.

5 Shift of Origin

For some applications another choice of origin may be preferred, and two other particular choices will be illustrated. Consider a second set of coordinates $(\bar{x}_1, \bar{x}_2)$ with $\bar{x}_2=x_2$ and $\bar{x}_1=x_1+c$, as shown in Fig. 4. The quantities P and Θ are invariant with respect to this coordinate shift, but denote the moment about the new origin ($\bar{x}_1=0$, $\bar{x}_2=0$) by $\bar{M}$ where from moment equilibrium

$$\bar{M}=M-cP \tag{5.1}$$

The remote displacements are rewritten as

$$u_\alpha=\frac{\bar{U}}{2}\delta_{\alpha 2}+\frac{\Theta}{2}e_{\alpha\beta}\bar{x}_\beta \tag{5.2}$$

where, by comparison with (2.2), it is readily established that

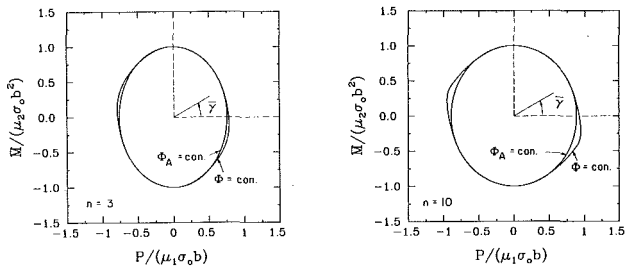

Fig. 5 Contours of constant Φ for choice of origin at the axis of rotation for pure bending as specified by equation (5.8)

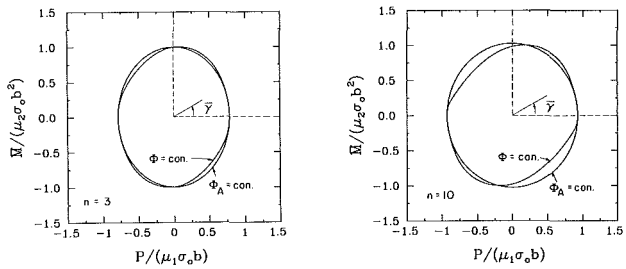

Fig. 6 Contours of constant Φ for choice of origin such that $\bar{M}=0$ when $\Theta=0$ according to equation (5.9)

$$\bar{U}=U+c\Theta \tag{5.3}$$

In deriving the relations of Sections 2 and 3 we could have equally well used the variable pairs $(\bar{U}, \Theta)$ and $(P, \bar{M})$ associated with $c\neq 0$. With the exception of the expressions for J, the formulas connecting the variables remain unchanged. However, given the fact that results have been presented for the choice $c=0$, it is probably simplest to use these results together with (5.1) and (5.3) to shift to a set of coordinates with $c\neq 0$. The alternative is to form a new table of functions (f, f', etc.) for the new choice from the functions presented for $c=0$.

The form of formula (2.11) for J is not preserved under a shift of origin. By (5.3), (2.11) becomes

$$J=\frac{2W}{b}-\frac{P(\bar{U}-c\Theta)}{b} \tag{5.4}$$

and (2.13) is

$$\eta=2-P(\bar{U}-c\Theta)/W \tag{5.5}$$

To determine numerical results for J in terms of shifted variables, $(P, \bar{M})$ or $(\bar{U}, \Theta)$, it is probably easiest to use the relations (5.1) and (5.3) to transform to (P, M) or (U, Θ) and then use Tables 1-3.

Origin at the "Axis of Rotation" for Pure Bending. As an illustration, choose c such that $\bar{U}=0$ when $P=0$. That is, the origin is located such that in pure bending the remote displacements in the upper-half plane are given by

$$u_\alpha=\frac{\Theta}{2}e_{\alpha\beta}\bar{x}_\beta \tag{5.6}$$

By (5.3) and (3.5), $\bar{U}=0$ requires

$$\frac{c}{b}=-\frac{U}{\Theta b}=-\frac{1}{\tan\zeta} \tag{5.7}$$

where the value of ζ is that associated with $\gamma=90$ deg (i.e., $P=0$). From Table 1, we obtain

$$c/b=\begin{cases}0.644 & (n=3)\\ 0.640 & (n=5)\\ 0.639 & (n=10)\end{cases} \tag{5.8}$$

The slip-line field for the perfectly-plastic material from the analysis of Green and Hundy (1956) gives $c/b=0.631$. This choice of origin will be considered again in the next section in

connection with an approximation for predominantly bending behavior.

Choice of Origin such that $\bar{M}=0$ in Pure Stretching. As a second illustration, choose c such that $\bar{M}=0$ when $\Theta=0$. That is, choose the origin so that the moment about this origin vanishes under pure stretching. By (5.1), this gives $c/b=M/(bP)$ for $\zeta=0$ deg. From (3.8) and (3.9), one obtains

$$\frac{c}{b}=\frac{f'(0)}{(N+1)f(0)}=\begin{cases}0.603 & (n=3)\\ 0.582 & (n=5)\\ 0.566 & (n=10)\end{cases} \tag{5.9}$$

This choice will be used in developing an approximation for predominantly stretching behavior.

6 Two Approximations

Predominantly Bending States. Take the origin at the axis of rotation for pure bending as specified by (5.7) and (5.8). With $\bar{M}$ measured about this choice of origin, contours of constant ϕ are shown in Fig. 5 for $n=3$ and $n=10$. For the power-law material these contours are self-similar, and the particular contour shown was chosen such that the vertical intercept is unity. The nondimensional load variables used in the plot are

$$\frac{P}{\mu_1\sigma_o b} \text{ and } \frac{\bar{M}}{\mu_2\sigma_o b^2} \tag{6.1}$$

Here, $\mu_2=0.364$ so that $\mu_2\sigma_o b^2$ is the Green-Hundy (1956) limit load for the perfectly-plastic problem in pure bending. We take $\mu_1=2/\sqrt{3}$ so that $\mu_1\sigma_o b$ would be the limit load in pure stretching, if the stress state for this perfectly-plastic problem were plane strain tension across the entire ligament. It is not certain that this is the correct limiting state; nevertheless, this choice for μ_1 is suitable for the normalization. The two contours in Fig. 5 were derived from the numerical results given in Tables 1 and 3. (The limit of these contours as $n\to\infty$ is the limiting yield surface under the combined loads.)

By virtue of the choice of origin such that $\bar{U}=\partial\Phi/\partial P=0$ when $P=0$, it follows that the contour of $\Phi=$ con. in Fig. 5 must intercept the vertical $\bar{M}$ axis with zero slope, as can be seen. We construct an approximation in the range of predominantly bending states (i.e., $|\bar{M}/(\mu_2\sigma_o b^2)|>|P/(\mu_1\sigma_o b)|$), by choosing an ellipse to approximate the contour of $\Phi=$ con. in such a way that the curvature, as well as the intercept and slope, matches that of the actual contour at the vertical intercept. The result can be seen in Fig. 5, and the specification of the approximation is as follows.

With Φ_A denoting the approximate ϕ, we take

$$\Phi_A=\frac{\epsilon_o\sigma_o b^2}{(n+1)}\left\{c_1(n)\left(\frac{P}{\mu_1\sigma_o b}\right)^2+c_2(n)\left(\frac{\bar{M}}{\mu_2\sigma_o b^2}\right)^2\right\}^{(n+1)/2} \tag{6.2}$$

This choice ensures that the approximating contour intercepts the $\bar{M}$ axis with zero slope; $c_2(n)$ is chosen so that $\Phi_A=\phi$ when $P=0$. We determined $c_1(n)$ by requiring that $\Phi_A=\phi$ at an angle $\bar{\gamma}$ about 30 from the horizontal axis in the first quadrant of the plane in Fig. 5. This simple procedure leads to a very small error in the curvature of the approximating contour at $P=0$ but slightly extends the range of the approximation so that it is accurate everywhere in the first quadrant except in the vicinity of $M=0$, as can be seen in Fig. 5. The values of c_1 and c_2 so determined are

$$\begin{aligned} c_1(3)&=1.2141 \quad & c_2(3)&=0.9329\\ c_1(5)&=0.9663 \quad & c_2(5)&=0.8838\\ c_1(10)&=0.8433 \quad & c_2(10)&=0.8828\end{aligned} \tag{6.3}$$

and the corresponding locations of the origin to which $\bar{M}$ is referred are given by (5.8).

Let H^2 denote the quadratic terms within the brackets in (6.2), so that

$$\Phi_A=\sigma_o\epsilon_o b^2 H^{n+1}/(n+1) \tag{6.4}$$

It follows then that the associated approximate displacement quantities are

$$\begin{aligned}\bar{U}&=\partial\Phi_A/\partial P=\epsilon_o b H^{n-1}(c_1/\mu_1)P/(\mu_1\sigma_o b)\\ \Theta&=\partial\Phi_A/\partial\bar{M}=\epsilon_0 H^{n-1}(c_2/\mu_2)\bar{M}/(\mu_2\sigma_o b^2)\end{aligned} \tag{6.5}$$

Moreover, the associated approximate overall strain energy $W_A=n\Phi_A$ is readily found to be

$$W_A=\sigma_o\epsilon_o b^2 n L^{(n+1)/n} \tag{6.6}$$

where

$$L^2=\frac{\mu_1^2}{c_1(n)}\left(\frac{\bar{U}}{\epsilon_o b}\right)^2+\frac{\mu_2^2}{c_2(n)}\left(\frac{\Theta}{\epsilon_o}\right)^2 \tag{6.7}$$

Using the connections $P=\partial W_A/\partial\bar{U}$ and $\bar{M}=\partial W_A/\partial\Theta$, one can derive the associated load variables in terms of U and Θ.

With these results in hand, the approximation for J follows immediately from (5.4) i.e.,

$$J_A=[2W_A-P(\bar{U}-c\Theta)]/b=[2n\Phi_A-P(\bar{U}-c\Theta)]/b \tag{6.8}$$

where $\bar{U}$ and Θ are obtained from (6.5) if P and $\bar{M}$ are prescribed or P and $\bar{M}$ are obtained from (6.6) if $\bar{U}$ and Θ are prescribed. We have compared J_A with the "actual" J given by the full numerical results over the full range of angle $\bar{\gamma}$ measured from the P axis in Fig. 5. For

$$30 \text{ deg}\le\bar{\gamma}\le 100 \text{ deg} \tag{6.9}$$

J_A differs from J by less than 1 percent for $n=3$ and by less than 3 percent for $n=10$. For the range

$$15 \text{ deg}\le\bar{\gamma}\le 125 \text{ deg} \tag{6.10}$$

J_A differs from J by no more than 6 percent for both $n=3$ and $n=10$. The approximation does become inaccurate in the vicinity of the P axis. With $\bar{M}=0$, the J_A differs from J by 16 percent for $n=3$ and 12 percent for $n=10$. Thus, this approximation is only recommended for use in the range (6.9) or possibly (6.10).

Predominantly Stretching States. Now take the origin as specified by (5.9) such that $\bar{M}=0$ when $\Theta=0$. Contours of $\Phi=$ con. with this choice of origin are shown in Fig. 6. The same nondimensional load variables (6.1) are used except, of course, now $\bar{M}$ is taken with respect to the new choice of origin. The same constant value of Φ as was used in Fig. 5 is used in plotting Fig. 6. Since $\Theta=\partial\Phi/\partial\bar{M}=0$ at the intercept with the P axis, the contour necessarily has an infinite slope there, as can be seen.

The approximation for predominantly stretching states (i.e., $|P/(\mu_1\sigma_o b)|>|\bar{M}/(\mu_2\sigma_o b^2)|$) is obtained in the same way as in the previous instance, except that now the ellipse is chosen so that it approximates the contour in the vicinity of the P axis. The functional form of the approximation is precisely that given above. All of equations (6.2) through (6.8) carry over, except that the coefficients c_1 and c_2 in (6.3) will be different. In this approximation, $c_1(n)$ is determined by requiring $\Phi_A=\Phi$ for $\bar{M}=0$ and $c_2(n)$ is chosen to provide a good approximation to the curvature at the intercept with the P axis. Here we chose $c_2(n)$ such that $\Phi_A=\Phi$ at $\bar{\gamma}\simeq 15$ deg, where now $\bar{\gamma}$ is defined as the angular measure from the P axis in Fig. 6. The resulting coefficients are

$$\begin{aligned} c_1(3)&=1.1267 \quad & c_2(3)&=0.9321\\ c_1(5)&=0.8625 \quad & c_2(5)&=0.8882\\ c_1(10)&=0.7408 \quad & c_2(10)&=0.8051\end{aligned} \tag{6.11}$$

As is clear from the contours in Fig. 6, the range of validity of this approximation is not nearly as extensive as in the previous case. For

$$0 \text{ deg}\le\bar{\gamma}\le 15 \text{ deg} \tag{6.12}$$

the error in J_A, compared to our numerical results for J, does not exceed 4 percent when $n=3$ nor 6 percent when $n=10$. But

outside this range the approximation becomes increasingly inaccurate, and thus its use is only recommended for the range (6.12). Together, the two approximations, for predominantly bending states and predominantly stretching states, do span essentially the entire range of practical interest.

Acknowledgment

The work of J. W. Hutchinson was supported in part by the National Science Foundation under Grant MEA-82-13925 and by the Division of Applied Sciences, Harvard University. The work of C. F. Shih was supported by the Electric Power Research Institute through Grant RP1757-17-1 and the US Department of Energy through Grant DE-AC02-80-ER10556. The computations reported on here were carried out on a VAX-11/780 computer at the Brown University, Division of Engineering, Computational Mechanics Computer Facility. This facility was made possible by grants from the US National Science Foundation (Grant ENG78-19378), the General Electric Foundation and the Digital Equipment Corporation.

References

Ernst, H. A., 1983, "Unified Solution for J Ranging Continuously from Pure Bending to Pure Tension," in *ASTM STP 791*, American Society for Testing and Materials, pp. I-499–I-519.

Green, A. P., and Hundy, B. B., 1956, "Initial Plastic Yielding in Notch Bend Tests," *Journal of the Mechanics and Physics of Solids*, Vol. 4, pp. 128–144.

Kaiser, S., 1985, "The J-Integral and Tearing Modulus for a SEN Specimen under Bending and Tension," *Engineering Fracture Mechancis*, Vol. 22, pp. 737–749.

Li, F. Z., Shih, C. F., and Needleman, A., 1985, "A Comparison of Methods for Calculating Energy Release Rates," *Engineering Fracture Mechanics*, Vol. 21, pp. 405–421.

McMeeking, R. M., 1984, "Estimates of J-Integral for Elastic-Plastic Specimens in Large Scale Yielding," *ASME Journal of Engineering Materials and Technology*, Vol. 106, pp. 278–284.

Parks, D. M., and White, C. S., 1982, "Elastic-Plastic Line Spring Finite Element for Surface-Cracked Plates and Shells," *Journal of Pressure Vessel Technology*, Vol. 184, pp. 287–292.

Rice, J. R., 1972, "The Line Spring Model for Surface Flaws," in *The Surface Crack: Physical Problems and Computational Solutions*, Swedlow, ed., ASME, pp. 171–186.

Rice, J. R., Paris, P. C., and Merkle, J. G., 1973, "Some Further Results of J-Integral Analysis and Estimates," in *ASTM STP 536*, American Society for Testing and Materials, pp. 231–245.

Shih, C. F., and Needleman, A., 1984a, "Fully Plastic Crack Problems: Part I – Solutions by a Penalty Method," ASME JOURNAL OF APPLIED MECHANICS, Vol. 51, pp. 48–56.

Shih, C. F., and Needleman, A., 1984b, "Fully Plastic Crack Problems: Part II – Application of Consistency Checks," ASME JOURNAL OF APPLIED MECHANICS, Vol. 51, pp. 57–64.

Turner, C. E., 1980, "The Ubiquitous η Factor," in *ASTM STP 700*, American Society for Testing and Materials, pp. 314–337.

Young, D. M., and Gregory, R. T., 1972, *A Survey of Numerical Mathematics*, Vols. I and II, Addison-Wesley, Reading, Mass.

APPENDIX

Finite Element Analysis of Fully Plastic Crack Problems

Penalty Formulation, Element Choice and Mesh Design. The numerical solutions for the deeply cracked panel presented in Section 4 were obtained by a finite element reduced integration penalty method (Shih and Needleman, 1984a). Fully plastic solutions obtained by the method have been shown to satisfy rather stringent consistency relations (Shih and Needleman, 1984b). We employed the 9-noded Lagrangian element to model the geometry depicted in Fig. 1. The volumetric stiffness matrix is obtained by 2 by 2 (reduced) integration while the deviatoric stiffness matrix is obtained by 3 by 3 (regular) integration. Hydrostatic stresses are computed at the 2 by 2 Gauss points and deviatoric stresses at the 3 by 3 Gauss points. To obtain the total stress at the 3 by 3 Gauss points, we used Lagrangian bilinear shape functions in conjunction with the values of hydrostatic stress at the 2 by 2 Gauss points to determine the hydrostatic stress at the 3 by 3 Gauss points.

With reference to the geometry in Fig. 1 we modelled only the upper-half plane since the problem possesses reflective symmetry about the crack plane. We experimented with r_o/b ratios of 4, 5, 10, and 20 and total number of elements ranging from 24 to 120. We found that the solutions for $n=3$, 5, 10 did not change with r_o/b ratios when the ratio is 5 or greater. Based on these studies we settled on a mesh with 40 elements and $r_o/b=5$. The ring of elements surrounding the crack tip is formed with a singular plastic (9-noded) wedge element. This element choice and mesh design in conjunction with selective/reduced integration has been shown to give accurate solutions (Shih and Needleman, 1984a, 1984b).

Parameter Tracking. The solution to the nonlinear boundary value problem is obtained by the Newton-Raphson method. The iterative method is second order convergent if a close initial estimate of the solution is available. This initial estimate is generated by parameter tracking (Shih and Needleman, 1984a). Our numerical procedure begins by obtaining the solutions for $n=3$, 5, 10 for a particular combination of displacements, say $R=1$ and $\zeta=0$. The solution for $n=3$, $R=1$ and $\zeta=0$ is then employed as the initial estimate in the Newton-Raphson iterations for a slightly different value of ζ (the value of n and R are held fixed). A typical solution converges within 5 to 7 iterations. In this manner solutions for the complete range of displacement combinations are obtained with ζ serving as the tracking parameter. Solutions are obtained at ζ increments of 5 degrees; smaller increments are used in the range where the solutions change rapidly with respect to ζ as indicated in Tables 1 to 3.

Function Evaluations and Spline Fitting. Several quantities of interest can be evaluated directly from the field solutions which are obtained at distinct combinations of remotely applied displacements parameterized by ζ. In particular the total strain energy W is obtained by summing the element strain energy as defined by (2.5). Using (3.6), the values of f are then known at distinct values of ζ. To evaluate the derivative of f with respect to ζ the following approach is taken. We employ the natural cubic spline (Young and Gregory, 1972) to interpolate the distinct values of f and ζ. Values of f and f' at any value of ζ can then be determined directly from the spline functions (note that first and second derivatives of the spline interpolation function are continuous everywhere, Young and Gregory, 1972). Noting the periodicity of f (3.7) and of f', we have given values corresponding to ζ ranging from 0 to 180 deg. The values of the other functions listed in the tables are obtained by using the appropriate formulas given in Section 3 in conjunction with the tabulated values of f and f'.

Consistency Checks. We carried out several consistency checks. In one check, we calculated P and M using (3.8) and (3.9) and the tabulated values of f and f'. These values were found to be within 1 percent of the P's and M's calculated using (2.3) and the equivalent nodal forces associated with the nodes on the remote boundary Γ. We also evaluated the value of the J-integral using a volume integral (area integral in the case of two-dimensional problems) expression (Li et al., 1985) and the finite element field quantities evaluated at the 3 by 3 Gauss points. The J values associated with various (area) domains differed by less than 1 percent from the value determined from (3.11). For the constitutive relations considered in this paper (1.2) the surface of constant W (3.1) and Φ(3.2) must be convex in their respective displacement and force planes indicated in Fig. 2. A check of the values of f, f' and h, h' given in the tables showed that they satisfy the geometrical requirements associated with convexity. Finally, we add that the convergence of the rotation points (5.8) towards the Green and Hundy slip-line rotation point (1956) is an independent verification of the accuracy of the fully plastic solutions.

A Curved C^0 Shell Element Based on Assumed Natural-Coordinate Strains

K. C. Park[1]
Mem. ASME

G. M. Stanley
Mechanics & Materials Engineering Laboratory,
Lockheed Palo Alto Research Laboratory,
Palo Alto, California 94304

A curved C^0 shell element is presented, which corrects several deficiencies in existing quadratic shell elements. The improvements realized in the present element include rank sufficiency without transverse shear locking, consistent membrane strain interpolation that admits inextensional bending without reduced integration, and adequate representation of curvature effects to capture the important membrane-bending coupling. The element can be constructed either by a nine-point integration rule or by a four-point integration rule with the proper rank compensating terms. Numerical experiments with the present element on several benchmark problems indicate that the element yields accurate and reliable solutions without any ostensible deficiency. The element is recommended for production analysis of shell structures.

1 Introduction

Structural engineers often prefer simple elements in performing plate and shell analyses, which leads to the adoption of triangular or four-node elements for most circumstances. This popularity is reflected in recent developments of four-node C^0 elements by Hughes et al. (1977, 1981), MacNeal (1978, 1982), Wempner et al. (1982), Crisfield (1983) and Dvorkin and Bathe (1984).

In order to make four-node elements more efficient while retaining all of their desirable properties intact, an element synthesis technique was developed that led to the formulation of a rank-sufficient one-point integrated quadrilateral plate element (Park and Flaggs, 1985) and a shell element (Park et al., 1985) which, unlike uniformly reduced-integrated elements, maintains the accuracy of fully integrated (four-point rule) elements. The four-node shell element is a strong candidate for production applications in which the strains vary *smoothly*.

There are circumstances, however, where curved elements are considered to be advantageous. These include shell structures in which the stresses vary rapidly or in which inextensional bending deformations dominate the solution, and for modeling curved boundaries and free edges by distorted element shapes as in curved panels with holes and stiffeners. For these problems, the performance of existing 8 and 9-node quadratic shell elements has been disappointing (Bathe et al., 1983), and as a result analysts have been forced to utilize the substantially more expensive 16-node elements (Ramm and Sattele, 1981). This has motivated the present authors to reexamine existing quadratic plate and shell elements, correct the deficiencies and provide a quadratic shell element as an advantageous alternative to 4 and 16-node elements. Although the improvements presented in the paper are applicable to other types of shell elements, we focus on the 9-node Lagrange shell element for reasons discussed below.

The first candidate quadratic shell element considered was the 8-node Serendipity element (Ahmad et al., 1970). Although the locking-free transverse shear strain interpolation procedure presented in Park (1985) is applicable to this element, it was concluded that the resulting element would be too stiff without introducing a bubble function as shown by Crisfield (1984). In addition, the corresponding membrane strain would have to be augmented by a similar bubble function. This not only complicates the element formulation, but yields a rank-deficient membrane stiffness matrix when the 4-point Gaussian integration rule is used. There is another unsettling aspect of the 8-node element: in shell dynamics, where the membrane response becomes important, it is better to have membrane degrees of freedom that lie on a uniform lattice. It is believed that the absence of the translational degrees of freedom at the center of the Serendipity element will force the energy associated with the membrane strains to be numerically dispersed to the side nodes. This numerical dispersion within the element is not desirable, especially in wave propagation problems. It is noted that the heterosis element (Hughes, 1978) adopts the same shape functions for the translational degrees of freedom as those of the Serendipity element.

Precursors of the present element may be traced to the following works: Hrennikoff (1941) for his adoption of a framework analogy to solve elasticity problems; Turner, Clough, Martin, and Topp (1956) for their assumed strain approach; Taig (1961) for his isoparametric (iso-P) representation of quadrilateral shapes; Wilson (1963) and Argyris (1964) for their boundary stress-strain modeling along flat triangular element sides; Fraeijs de Veubeke for his limitation principle

[1]Presently: Professor, Department of Mechanical Engineering, University of Colorado, Boulder, CO 80309

Contributed by the Applied Mechanics Division for publication in the JOURNAL OF APPLIED MECHANICS.

Discussion on this paper should be addressed to the Editorial Department, ASME, United Engineering Center, 345 East 47th Street, New York, N.Y. 10017, and will be accepted until two months after final publication of the paper itself in the JOURNAL OF APPLIED MECHANICS. Manuscript received by ASME Applied Mechanics Division, March 15, 1985; final revision, August 1, 1985.

(1965); Bogner, Fox, and Schmit (1965) and Clough and Felippa (1968) for their recognition of the importance of polynomial completeness for element convergence; Ergatoudis, Irons, and Zienkiewicz (1968) and Ahmad, Irons, and Zienkiewicz (1970) for their introduction of curved isoparametric elements; Wempner, Oden and Kross (1968) for their introduction of the discrete Kirchhoff condition for thin shells; and Irons (1976) for his courageous yet necessary departure from the standard iso-P formulation in the development of the semi-loof element. The derivation of the present element has also been influenced by recent studies by Wempner et al. (1982), McNeal (1982), Crisfield (1983), Dvorkin and Bathe (1984), and Pian (1984) (these works may be collectively viewed as additional modifications of the standard iso-P formulations); Parish (1979) for his extensive evaluation of the standard iso-P 9-node shell element; and Hughes and Liu (1981) for their thick-shell formulation. Finally, a lucid physical presentation of practical shell theories by Calladine (1983) provided an impetus for developing the present curved C^0 shell element for application to both thick and thin shell problems.

The derivation of the present element begins with the representation of the strains along the four element sides ($\xi = \pm 1$, $\eta = \pm 1$) and the two interior coordinate lines ($\xi = 0$, $\eta = 0$). These six natural-coordinate lines will be subsequently called *the reference lines*, which is an adaptation of Hrennikoff's framework concept. The strains along the reference lines are then linearly interpolated. The natural-coordinate strains at an interior point of the element are then obtained by quadratic interpolation of the strains among three of the six reference lines depending upon the component. Finally, the local-Cartesian strains, which are required at numerical integration points for evaluating the element stiffness and internal force arrays, are obtained by tensorial transformation of the natural-coordinate strain components instead of the standard iso-P derivative transformations. The procedure of assuming *natural*-coordinate strains and transforming tensorially to local-Cartesian coordinates has been found to play a key role in improving element performance when the mesh is distorted or curved.

The present element formulation thus prevents membrane and transverse shear locking, and improves in-plane bending performance by carefully constructing the strain components along the six reference lines. Furthermore, spurious mechanisms are eliminated at the outset by adopting full 9-point integration, or alternatively by adopting reduced (4-point) integration augmented with consistent rank compensating terms, as determined from the symbolic element synthesis procedures presented in Park and Flaggs (1984a, 1984b, 1985) and in Park (1984). Hence, unlike quadratic C^0 elements based on the standard iso-P formulation, e.g., Zienkiewicz (1971) and Irons and Ahmad (1980), the present element does not suffer from membrane or transverse shear locking when full integration is employed, or from spurious mechanisms when reduced integration is augmented with the appropriate rank compensation.

2 Natural-Coordinate Strains and Their Cartesian Transformation

The derivation of the strain-displacement relationships for the present element follows much of the conventional isoparametric approach with two important exceptions. First in the derivation of the natural-coordinate-based strains, the simple iso-P differentiation procedure to obtain displacement gradients is abandoned. Instead, the assumed strain interpolation approach presented in Park (1985) is adopted to represent the natural strain states along the six reference lines. This yields improved representations of membrane, in-extensional bending and transverse-shear strain states along the curved lines. The natural-coordinate-based strains in the interior of the element are then obtained by quadratic interpolation of the strains among the six reference lines. Second, we abandon the use of the isoparametric Jacobian matrix to transform the natural-coordinate-based derivatives of local-Cartesian displacement components to local-Cartesian *derivative* components. Instead, in the present formulation the local-Cartesian strain components at each integration point are obtained directly by a tensor transformation of the natural-coordinate strains themselves. This has been found to improve element performance substantially when the element is distorted. To this end, we now present the definitions of the natural and local-Cartesian coordinate systems, as well as the natural coordinate-based strains and their tensor transformation to the local-Cartesian system.

The position vector, $\mathbf{r}$, to the middle surface of the quadratic element may be expressed by

$$\mathbf{r} = x(\xi,\eta)\mathbf{e}_x + y(\xi,\eta)\mathbf{e}_y + z(\xi,\eta)\mathbf{e}_z \tag{1}$$

where

$$\mathbf{e} = [\mathbf{e}_x, \mathbf{e}_y, \mathbf{e}_z]^T \tag{2}$$

are the unit vectors in a *local* Cartesian coordinate system whose coordinates, (x, y, z), are interpolated by the two-dimensional quadratic Lagrange shape functions:

$$(x,y,z) = \sum_{i=1}^{9} N_i(\xi,\eta)(x_i,y_i,z_i) \tag{3}$$

in which (x_i, y_i, z_i) are the nodal coordinate values as shown in Fig. 1.

The unit basis vectors for the natural coordinate system, $\mathbf{a}_\xi$ and $\mathbf{a}_\eta$, are given by

$$\mathbf{a}_\xi = \frac{1}{A_\xi}\frac{\partial \mathbf{r}}{\partial \xi}, \quad \mathbf{a}_\eta = \frac{1}{A_\eta}\frac{\partial \mathbf{r}}{\partial \eta} \tag{4}$$

in which A_ξ and A_η are the first fundamental coefficients given by

$$A_\xi = \left(\frac{\partial \mathbf{r}}{\partial \xi}\cdot\frac{\partial \mathbf{r}}{\partial \xi}\right)^{\frac{1}{2}}, \quad A_\eta = \left(\frac{\partial \mathbf{r}}{\partial \eta}\cdot\frac{\partial \mathbf{r}}{\partial \eta}\right)^{\frac{1}{2}} \tag{5}$$

The unit vector $\mathbf{a}_\zeta$ that is normal to $(\mathbf{a}_\xi, \mathbf{a}_\eta)$ is then obtained by

$$\mathbf{a}_\zeta = \frac{\mathbf{a}_\xi \times \mathbf{a}_\eta}{|\mathbf{a}_\xi \times \mathbf{a}_\eta|} \tag{6}$$

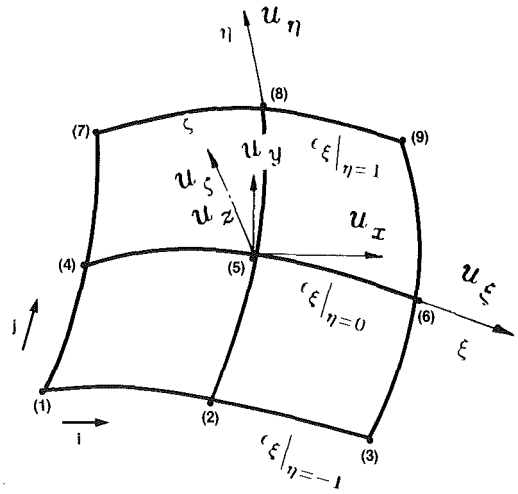

$$\epsilon_{\xi\xi} = N_1(\eta)\cdot\epsilon_\xi\big|_{\eta=-1} + N_2(\eta)\cdot\epsilon_\xi\big|_{\eta=0} + N_3(\eta)\cdot\epsilon_\xi\big|_{\eta=1}$$

Fig. 1 Six reference lines in nine-node element and assumed natural-coordinate strain, $\epsilon_{\xi\xi}$

Now, with respect to the local-Cartesian coordinate system, **e**, the shell displacement vector will be defined (by hypothesis) in the following manner

$$\mathbf{U}=(u_x+z\alpha_x)\mathbf{e}_x+(u_y+z\alpha_y)\mathbf{e}_y+u_z\mathbf{e}_z, \quad z=\zeta h/2 \tag{7}$$

where both the translations, u_x, u_y and u_z, and the rotations, α_x and α_y, are assumed to depend only on the natural surface coordinates, (ξ, η), and h is the shell thickness (see Fig. 1 for definitions of these quantities). The *covariant* displacement components along the three natural coordinate lines are obtained by projecting **U** onto the natural coordinate directions, i.e.,

$$U_\xi=\mathbf{U}\cdot\mathbf{a}_\xi, \quad U_\eta=\mathbf{U}\cdot\mathbf{a}_\eta, \quad U_\zeta=\mathbf{U}\cdot\mathbf{a}_\zeta \tag{8}$$

Throughout the present development we will adopt the convention that the unit normal vector for the **e** basis ($\mathbf{e}_z$) and the one for the **a** basis ($\mathbf{a}_\zeta$) coincide; in other words, ($\mathbf{e}_x$, $\mathbf{e}_y$) and ($\mathbf{a}_\xi$, $\mathbf{a}_\eta$) are coplanar. This convention leads to the following transformation

$$\mathbf{a}=\mathbf{T}^{-1}\mathbf{e} \tag{9}$$

where

$$\mathbf{a}=[\mathbf{a}_\xi,\mathbf{a}_\eta,\mathbf{a}_\zeta]^T \tag{10}$$

and the transformation matrix **T** is given by

$$\mathbf{T}=\begin{bmatrix} t_{x\xi} & t_{x\eta} & 0 \\ t_{y\xi} & t_{y\eta} & 0 \\ 0 & 0 & 1 \end{bmatrix}$$

$$=\frac{1}{|\mathbf{a}_\xi\times\mathbf{a}_\eta|}\begin{bmatrix} \mathbf{e}_y\cdot\mathbf{a}_\eta & -\mathbf{e}_y\cdot\mathbf{a}_\xi & 0 \\ -\mathbf{e}_x\cdot\mathbf{a}_\eta & \mathbf{e}_x\cdot\mathbf{a}_\xi & 0 \\ 0 & 0 & |\mathbf{a}_\xi\times\mathbf{a}_\eta| \end{bmatrix} \tag{11}$$

With the above definitions, the covariant strain components with respect to a *fixed* natural coordinate basis are given by (see, e.g., Prager, 1973):

$$\epsilon_{\xi\xi}=\frac{1}{A_\xi}\frac{\partial U_\xi}{\partial\xi}, \quad \epsilon_{\eta\eta}=\frac{1}{A_\eta}\frac{\partial U_\eta}{\partial\eta},$$

$$2\epsilon_{\xi\eta}=\frac{1}{A_\xi}\frac{\partial U_\eta}{\partial\xi}+\frac{1}{A_\eta}\frac{\partial U_\xi}{A_\eta} \tag{12}$$

$$2\epsilon_{\xi\zeta}=\frac{1}{A_\xi}\frac{\partial U_\zeta}{\partial\xi}+\frac{\partial U_\xi}{\partial\zeta}, \quad 2\epsilon_{\eta\zeta}=\frac{1}{A_\eta}\frac{\partial U_\zeta}{\partial\eta}+\frac{\partial U_\eta}{\partial\zeta}$$

Finally, the local-Cartesian strain components are obtained by the following tensor transformation

$$\begin{bmatrix} \epsilon_{xx} & \epsilon_{xy} & \epsilon_{xz} \\ \epsilon_{yx} & \epsilon_{yy} & \epsilon_{yz} \\ \epsilon_{zx} & \epsilon_{zy} & \epsilon_{zz} \end{bmatrix}=\mathbf{T}\begin{bmatrix} \epsilon_{\xi\xi} & \epsilon_{\xi\eta} & \epsilon_{\xi\zeta} \\ \epsilon_{\eta\xi} & \epsilon_{\eta\eta} & \epsilon_{\eta\zeta} \\ \epsilon_{\zeta\xi} & \epsilon_{\zeta\eta} & \epsilon_{\zeta\zeta} \end{bmatrix}\mathbf{T}^T \tag{13}$$

Remark 1. Throughout the present formulation, it should be understood that the natural-coordinate basis vectors, (a_ξ, a_η, a_ζ), are assumed to be *fixed* when subjected to differentiation with respect to (ξ, η). This definition should not be confused with the *curvilinear* coordinate systems that are adopted in most shell theories.

The task of discretizing curved structures is now, *via* the above strain tensor transformation, reduced to approximating the natural-coordinate displacement derivatives that appear in equation (12). This is addressed in the next section.

3 Strain-Displacement Interpolation Along the Six Reference Lines

In the preceding section, it has been shown that the natural-coordinate-based strain-displacement relationships given by equation (12) require eight displacement derivatives with respect to natural coordinates (ξ, η). To simplify the subsequent derivation, we introduce the following notational changes from equations (7) and (8):

$$U_\xi=u+z\alpha, \quad U_\eta=v+z\beta, \quad U_\zeta=w \tag{14}$$

where u, v, and w are the translations expressed in the natural-coordinate basis at (ξ, η), and the rotations α and β are defined to cause *relative* displacements of the unit normal along the two natural coordinate directions, (ξ, η). With these new definitions, the strains in the natural coordinate system become

$$\epsilon_{\xi\xi}=\epsilon_{\xi\xi}+z\kappa_{\xi\xi}, \quad \epsilon_{\xi\xi}=\frac{1}{A_\xi}\frac{\partial u}{\partial\xi}, \quad \kappa_{\xi\xi}=\frac{1}{A_\xi}\frac{\partial\alpha}{\partial\xi}$$

$$\epsilon_{\eta\eta}=\epsilon_{\eta\eta}+z\kappa_{\eta\eta}, \quad \epsilon_{\eta\eta}=\frac{1}{A_\eta}\frac{\partial v}{\partial\eta}, \quad \kappa_{\eta\eta}=\frac{1}{A_u}\frac{\partial\beta}{\partial\eta}$$

$$2\epsilon_{\xi\eta}=\epsilon_{\xi\eta}+z\kappa_{\xi\eta}, \quad \epsilon_{\xi\eta}=\frac{1}{A_\xi}\frac{\partial v}{\partial\xi}+\frac{1}{A_\eta}\frac{\partial u}{\partial\eta} \tag{15}$$

$$\kappa_{\xi\eta}=\frac{1}{A_\xi}\frac{\partial\beta}{\partial\xi}+\frac{1}{A_\eta}\frac{\partial\alpha}{\partial\eta}$$

$$2\epsilon_{\xi\zeta}=\gamma_{\xi\zeta}, \quad \gamma_{\xi\zeta}=\alpha+\frac{1}{A_\xi}\frac{\partial w}{\partial\xi}$$

$$2\epsilon_{\eta\zeta}=\gamma_{\eta\zeta}, \quad \gamma_{\eta\zeta}=\beta+\frac{1}{A_\eta}\frac{\partial w}{\partial\eta}$$

where it is assumed that A_ξ and A_η are independent of z (or ζ) and may be evaluated at the midsurface ($\zeta = 0$).

The derivation of the *element* approximations to the eight strain quantities in equation (15) proceeds as follows. First, the strain along constant η and ξ lines will be derived by satisfying constant and linearly varying strain states, and by introducing a curvature correction scheme to improve membrane-bending coupling. The strains at the interior of the element will then be interpolated quadratically from the one-dimensional approximations.

For example, the natural-coordinate membrane strain, $\epsilon_{\xi\xi}$, will be obtained as

$$\epsilon_{\xi\xi}=N_1(\eta)\cdot\epsilon_\xi(\xi)\,|_{n=-1}+N_2(\eta)\cdot\epsilon_\xi(\xi)\,|_{n=0}+N_3(\eta)\cdot\epsilon_\xi(\xi)\,|_{\eta=1} \tag{16}$$

where $N_i(\eta)$ are the one-dimensional quadratic Lagrange shape functions along the natural-coordinate η-lines and $\epsilon_\xi\,|_{\eta=-1,0,1}$ are the membrane strains along the $\eta = -1,0,1$ lines, respectively.

3.1 Transverse Shear Strains Along the Reference Lines. Locking (or over-stiffening) due to inadequate discretization of the transverse-shear strain energy in C^0 elements has long been recognized (Zienkiewicz, Taylor, and Too, 1971, and Pawsey and Clough, 1971) as a serious pathology of C^0 elements. The conventional means for alleviating the transverse shear locking phenomenon has been to under-integrate the transverse-shear strain energy, a numerical trick that often gives rise to spurious mechanisms. We shall now show that full integration does not cause locking provided the transverse-shear strains along the natural coordinate lines are *consistently* approximated. To this end, we approximate the transverse-shear strain, $\gamma_{\xi\zeta}$ by

$$\gamma_{\xi\zeta}=N_1(\eta)\cdot\gamma_\xi(\xi)\,|_{\eta=-1}+N_2(\eta)\cdot\gamma_\xi(\xi)\,|_{\eta=0}+N_3(\eta)\cdot\gamma_\xi(\xi)\,|_{\eta=1} \tag{17}$$

where $\gamma_\xi(\xi)\,|_{\eta=-1,0,1}$ are the transverse-shear strains along the $\eta = -1,0,1$ lines, given by

$$\gamma_\xi \Big|_{\eta=\text{const}} = \left(\alpha + \frac{1}{A_\xi}\frac{\partial w}{\partial \xi}\right)\Big|_{\eta=\text{const}} \tag{18}$$

Recently, the causes of both the locking and spurious mechanisms associated with discretization of the transverse-shear strain energy were analyzed by symbolic Fourier analysis procedures (Park and Flaggs, 1984b and 1985). The analysis revealed that rank deficiencies emanate from the reduced integration of the quadratic interpolation shape functions, $N_i(\eta)$ in equation (17), whereas locking is caused by an inconsistent approximation of the γ_ξ's along "η = *const*" lines. In the present formulation, therefore, we will adopt full integration in order to preserve rank sufficiency while avoiding locking by a consistent interpolation of the transverse-shear strains along the natural coordinate lines.

The consistency condition requires that, whenever the strain-displacement relations make use of the displacements themselves and not their derivatives, the corresponding displacement components be modified to vary linearly instead of obeying the original quadratic iso-P interpolation. For example, to avoide transverse-shear locking without reduced integration, the interpolation of the rotation component, α, in equation (18) is modified as follows. If the rotation, α, were allowed to vary quadratically, the corresponding transverse displacement, w, would have to vary cubically, viz.,

$$w = \sum_{i=1}^{3} N_i(\xi) w_i + \xi(1-\xi^2)\Delta w \tag{19}$$

where Δw may be viewed as a hierarchical displacement.

Substituting the above modified interpolation for w into the transverse-shear strain expression (18), for γ_ξ, and constraining the transverse-shear strain to be linear along ξ, one obtains for the hierarchical displacement

$$\Delta w = \frac{1}{6}(\alpha_1 - 2\alpha_2 + \alpha_3)$$

Finally, collecting the constant and linear terms and rearranging the resulting expression for the transverse-shear strain, one obtains the following modified approximation for α

$$\alpha \Big|_{\eta=\text{const}} = \left(\frac{1}{6} - \frac{\xi}{2}\right)\alpha_1 + \frac{2\alpha_2}{3} + \left(\frac{1}{6} + \frac{\xi}{2}\right)\alpha_3 = \sum_{i=1}^{3} \bar{N}(\xi)_i \alpha_i \tag{20}$$

A similar approach was successfully used in the development of plate bending elements by Crisfield (1984).

To complete the derivation of the transverse-shear strains along the natural coordinate lines, the term $(1/A_\xi)(\partial w/\partial \xi)$ in equation (18) needs to be modified further in order to maintain consistently both the constant and linearly varying transverse shear strain states. We shall defer this step to a later section as the necessary modifications follow a similar procedure to that used for the interpolation of membrane strains, which are presented below.

Remark 2. The preceding derivation for the assumed transverse shear strains, if specialized to a rectangular four-node case, would result in the same expressions as those already derived in MacNeal (1978), Hughes and Tedzduyar (1981), and Dvorkin and Bathe (1984). However, equation (17) differs from these formulations in that it is associated with direction cosines obtained by interpolating the natural-coordinate basis vectors at the nodes rather than with those computed directly from the isoparametric Jacobian matrix. Specifically, the natural-coordinate basis vectors at the interior of the element, defined by equations (4) and (6), are obtained for the 9-node element *via*

$$\mathbf{a}(\xi,\eta) = \sum_{i=1}^{9} N_i(\xi,\eta)\mathbf{a}_i \tag{21}$$

where $\mathbf{a}_i$ are the natural-coordinate basis vectors at the nodes. It is important for these *interpolated* basis vectors to be used at element integration points in the construction of the transformation matrix, $\mathbf{T}$ (equation (11)), for proper transformation of the strains from natural-coordinate to local-Cartesian bases (equation (13)).

3.2 Membrane Strains Along the Reference Lines. Several approaches have been proposed for improved interpolation of membrane strains for curved elements. A recent article by Belytschko et al. (1985) reviews various membrane modeling approaches and discusses in detail three major approaches: reduced integration by Parisch (1979) and Stolarski and Belytschko (1983), mixed formulations by Lee and Pian (1978) and Noor and Peters (1981), and the so-called mode decomposition technique by Stolarski et al. (1984), among others. In the present formulation, we adopt a generalization of Hrennikoff's method (1941) in that the membrane strains are assumed to vary linearly along the element's six reference natural-coordinate lines. In so doing, the assumed membrane strains are to satisfy two requirements: the direction of the covariant membrane strains must remain tangent to the curved

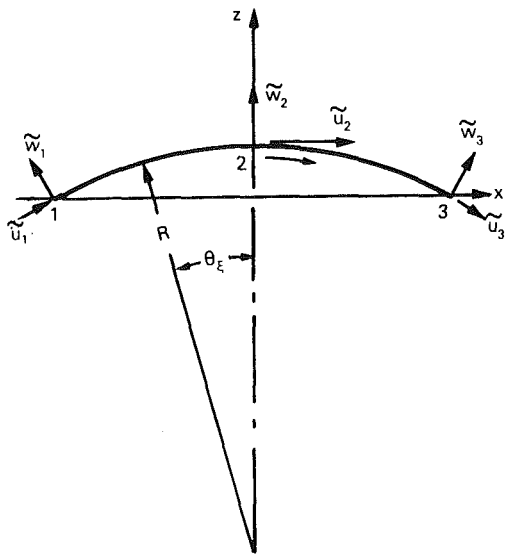

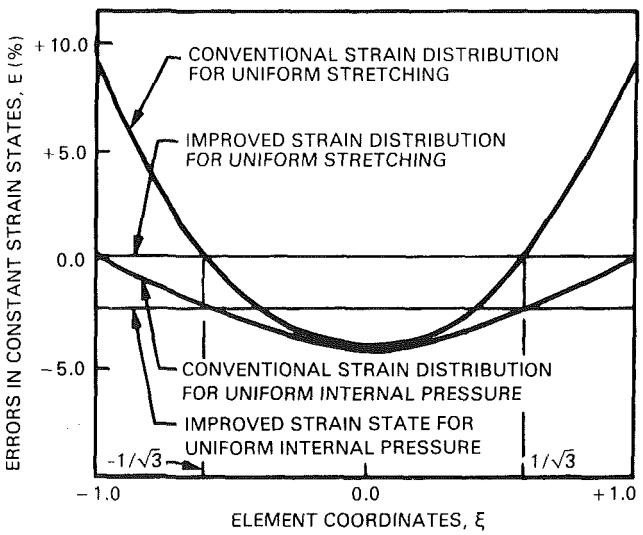

Fig. 2 Improved membrane strain modeling along a reference curved side

line, and the curvature term associated with the *curvilinear coordinate* definition of strain must itself admit a linear variation. Realization of these two requirements mitigates membrane locking and improves inextensional bending performance for thin shells, as explained below.

If one employs the standard iso-P approach to interpolate the membrane strain, ϵ_ξ, along a ξ-coordinate reference line, one obtains for a quadratic element

$$\epsilon_\xi^{std}(\xi) = \frac{1}{2A_\xi}(u_3 - u_1) + \frac{\xi}{A_\xi}(u_3 - 2u_2 + u_1) \tag{22}$$

where the u_i's are the three nodal displacements along the reference line, all pointing in the direction of the tangent, $\mathbf{a}_\xi$, at the evaluation point, ξ. Figure 2 shows the actual membrane strain distribution along a circular arch that is subjected to two constant strain states: under a uniform pressure and due to a uniform stretching around a frictionless rigid mandrel, respectively. Note that the membrane strain states computed by equation (22) are in error for both cases, except at certain points. In particular, the strain at the element center, which is one of the three full-integration points, is far less accurate than at the two Barlow points (1976), $\xi = \pm 1/\sqrt{3}$. This inadequacy was investigated in Park (1985), which led to the improved strain interpolation summarized below.

We search for points along the natural coordinate lines at which the standard strain interpolations, e.g., equation (22), yield accurate representations of the constant strain states. These happen to be the two reduced-integration (or Barlow) points. We then assume that the membrane strain is distributed linearly along the ξ coordinate line, while still satisfying the constant strain states. This leads to the following interpolation formula

$$\epsilon_\xi(\xi) = \epsilon_0 + \xi \cdot \epsilon_1 \tag{23}$$

where

$$\epsilon_0 = \frac{1}{2}(\epsilon_\xi^{std}(\sqrt{1/3}) + \epsilon_\xi^{std}(-\sqrt{1/3})),$$
$$\epsilon_1 = \frac{\sqrt{3}}{2}(\epsilon_\xi^{std}(\sqrt{1/3}) - \epsilon_\xi^{std}(-\sqrt{1/3})) \tag{24}$$

It must be noted that the membrane strain, ϵ_ξ, in equation (23) is assumed to be tangent everywhere along the ξ-coordinate line. That is, while both ϵ_0 and ϵ_1 are *fixed*, both the *magnitude* and *direction* of ϵ_ξ *vary linearly* with ξ.

Remark 3. The membrane over-stiffening phenomenon that is frequently encountered in curved elements emanates from poor modeling of the membrane strain states at the integration points. One of the important consequences of the above interpolation is that the constant and linearly varying strain states are correctly modeled regardless of whether a two or three-point Gaussian quadrature rule is adopted.

In order to appreciate how the present strain interpolation along ξ-lines captures membrane behavior, and to identify ways in which it may be further improved, let us compare the present approximation with the classical strain-displacement relation for a circular arch. In classical shell theories, the effect of curvature on the membrane strain in a circular arch with radius R is explicitly represented by

$$\epsilon_\xi = \frac{1}{A_\xi}\frac{\partial \tilde{u}}{\partial \xi} + \frac{\tilde{w}}{R} \tag{25}$$

where $\tilde{u}$ and $\tilde{w}$ are expressed in a natural coordinate basis, $(\tilde{\mathbf{a}}_\xi, \tilde{\mathbf{a}}_\eta, \tilde{\mathbf{a}}_\zeta)$, that *varies* along the ξ-line (see Fig. 2*a*). Recall that, in contrast, the original natural coordinate basis vectors, $(\mathbf{a}_\xi, \mathbf{a}_\eta, \mathbf{a}_\zeta)$, are assumed to be *fixed* with respect to natural-coordinate differentiation. Therefore, in the present membrane-strain interpolation (equation (23)), the curvature effect is captured *implicitly* through the transformation of the nodal displacements from the *nodal bases* to the integration-point basis. For example, the displacement at node i corresponding to the tangent direction, $\mathbf{a}_\xi$, at the point ξ is given by

$$u_i(\xi) = \mathbf{a}_\xi(\xi) \cdot \mathbf{u}_i = \mathbf{a}_\xi(\xi)^T \begin{bmatrix} \tilde{\mathbf{a}}_{\xi i}^T \\ \tilde{\mathbf{a}}_{\eta i}^T \\ \tilde{\mathbf{a}}_{\zeta i}^T \end{bmatrix}^{-1} \begin{Bmatrix} \tilde{u}_i \\ \tilde{v}_i \\ \tilde{w}_i \end{Bmatrix} \tag{26}$$

where $(\tilde{\mathbf{a}}_{\xi i}, \tilde{\mathbf{a}}_{\eta i}, \tilde{\mathbf{a}}_{\zeta i})$ are the natural-coordinate basis vectors at node i.

It was shown in Park (1985) that the present membrane strain interpolation models the curvature term, $\tilde{w}/R$, at the center node ($i=2$) of a ξ reference line by

$$\frac{\tilde{w}}{R} \approx \frac{1}{R}\frac{\sin(\theta_\xi)}{\theta_\xi}\tilde{w}_2', \quad \tilde{w}_2' = \frac{\tilde{w}_3 + \tilde{w}_2 + \tilde{w}_1}{3} \tag{27}$$

in which θ_ξ is the angle between the tangent at the center node and the tangent at the Barlow point (see Fig. 2). Note that $\tilde{w}_i$ is the *normal* displacement component at node i.

The above examination of the interpolation formula (equation (23)) reveals that the curvature effect, viz., $\tilde{w}/R$, is modeled by a uniform averaging of the three normal displacements. In other words, the $\tilde{w}$ term in the natural-coordinate-based strain, ϵ_ξ, is approximated by a constant, whereas the approximation of the first term in equation (25), $\partial \tilde{u}/\partial \xi$, varies linearly with ξ. This inconsistency is analogous to the transverse-shear strain, γ_F, (equation 18) for which the standard Iso-P interpolation led to a constant α and a linearly varying $\partial w/\partial \xi$. Therefore, employing the same consistency consideration that was invoked to derive locking-free interpolation of the transverse-shear strain, the desirable representation of $\tilde{w}$ in the term $\tilde{w}/R$ becomes (see equation (20))

$$\tilde{w}'(\xi) = \left(\frac{1}{6} - \frac{\xi}{2}\right)\tilde{w}_1 + \frac{2}{3}\tilde{w}_2 + \left(\frac{1}{6} + \frac{\xi}{2}\right)\tilde{w}_3 \tag{28}$$

which yields at the three nodes

$$\tilde{w}_1' = \frac{4\tilde{w}_1 + 4\tilde{w}_2 - 2\tilde{w}_3}{6}, \quad \tilde{w}_2' = \frac{\tilde{w}_3 + 4\tilde{w}_2 + \tilde{w}_1}{6},$$
$$\tilde{w}_3' = \frac{-2\tilde{w}_1 + 4\tilde{w}_2 + 4\tilde{w}_3}{6} \tag{29}$$

The above formulas give an improved representation of curvature effects, realized by replacing $\tilde{w}_i$ in equation (26) by $\tilde{w}_i'$, that is

$$u_i(\xi) \leftarrow \mathbf{a}_\xi(\xi)^T \begin{bmatrix} \tilde{\mathbf{a}}_{\xi i}^T \\ \tilde{\mathbf{a}}_{\eta i}^T \\ \tilde{\mathbf{a}}_{\zeta i}^T \end{bmatrix}^{-1} \begin{Bmatrix} \tilde{u}_i \\ \tilde{v}_i \\ \tilde{w}_i' \end{Bmatrix} \tag{30}$$

In order to obtain the final interpolation formula for the membrane strain along a ξ-line, first, equation (30) is substituted into equation (22). Second, equation (22) is evaluated at the Barlow points ($\pm\sqrt{1/3}$) and substituted into the modified strain interpolation expressions, (23)–(24). Finally, the strain-displacement relation for $\epsilon_F(\xi)$ emerges as

$$\epsilon_\xi = \sum_{i=1}^{3} \{ b_i^{\xi u}\tilde{u}_i + b_i^{\xi v}\tilde{v}_i + b_i^{\xi w'}\tilde{w}_i \} \tag{31}$$

where

$$b_1^{\xi u} = \frac{1}{\Delta s_\xi}(c_{l1}t_{uu}^{l1} + c_{r1}t_{uu}^{r1})$$
$$b_1^{\xi v} = \frac{1}{\Delta s_\xi}(c_{l1}t_{uv}^{l1} + c_{r1}t_{uv}^{r1}) \tag{32}$$
$$b_1^{\xi w'} = \frac{1}{\Delta s_\xi}(c_{l1}'t_{uw}^{l1} + c_{r1}'t_{uw}^{r1})$$

in which Δs_ξ is the curved beam length along the η = constant reference line, and c_{l1}, c_{r1}, c'_{l1} and c'_{r1} are given by

$$c_{l1} = -\left(\frac{1}{2}+\frac{1}{\sqrt{3}}\right)+\left(1+\frac{\sqrt{3}}{2}\right)\xi,$$

$$c_{l2} = -2\left(\xi-\frac{1}{\sqrt{3}}\right),\ c_{l3} = \left(\frac{1}{2}-\frac{1}{\sqrt{3}}\right)+\left(1-\frac{\sqrt{3}}{2}\right)\xi \quad (33)$$

$$c_{r1} = -\left(\frac{1}{2}-\frac{1}{\sqrt{3}}\right)+\left(1-\frac{\sqrt{3}}{2}\right)\xi,$$

$$c_{r2} = -2\left(\xi+\frac{1}{\sqrt{3}}\right),\ c_{r3} = \left(\frac{1}{2}+\frac{1}{\sqrt{3}}\right)+\left(1+\frac{\sqrt{3}}{2}\right)\xi \quad (34)$$

$$c'_{l1} = \frac{1}{6}(4c_{l1}+c_{l2}-2c_{l3}),\ c'_{l2} = \frac{4}{6}(c_{l1}+c_{l2}+c_{l3}),$$

$$c'_{l3} = \frac{1}{6}(-2c_{l1}+c_{l2}+4c_{l3}) \quad (35)$$

$$c'_{r1} = \frac{1}{6}(4c_{r1}+c_{r2}-2c_{r3}),\ c'_{r2} = \frac{4}{6}(c_{r1}+c_{r2}+c_{r3}),$$

$$c'_{r3} = \frac{1}{6}(-2c_{r1}+c_{r2}+4c_{r3}) \quad (36)$$

and the coordinate transformation matrix components, t_{uu}, etc., relate the displacements expressed in the natural coordinate bases at the element nodes to the natural coordinate bases at the two (right and left) Barlow points, $\xi = \pm 1/\sqrt{3}$, designated by r and l, respectively, e.g.,

$$\begin{Bmatrix} \tilde{u}_i^l \\ \tilde{v}_i^l \\ \tilde{w}_i^l \end{Bmatrix} = \begin{bmatrix} t_{uu}^{li} & t_{uv}^{li} & t_{uw}^{li} \\ t_{vu}^{li} & t_{vv}^{li} & t_{vw}^{li} \\ t_{wu}^{li} & t_{wv}^{li} & t_{ww}^{li} \end{bmatrix} \begin{Bmatrix} \tilde{u}_i \\ \tilde{v}_i \\ \tilde{w}_i \end{Bmatrix} \quad (37)$$

where $\tilde{u}_i^l$ is the component of the displacement vector at node i pointing in the $\tilde{\mathbf{a}}_\xi$ direction at $\xi = -1/\sqrt{3}$. The remaining terms needed for the right (r) Barlow point and for reference-line nodes 2 and 3 can be similarly obtained by following the above procedure.

4 Natural-Coordinate Strains in the Element Interior

The strain-interpolations along the six reference lines presented in the preceding section can now be used to interpolate the natural-coordinate strains to the *interior* of a generally shaped 9-node element.

4.1 Natural-Coordinate Membrane Strains. The two membrane strains, $\epsilon_{\xi\xi}$ and $\epsilon_{\eta\eta}$, can be obtained by quadratic interpolation of equation (31) in the same manner as was done for $\gamma_{\xi\zeta}$ in equation (17). However, to satisfy correct in-plane bending deformation modes, $\epsilon_{\xi\eta}$ must be interpolated in a special manner. To accomplish this special discretization, let us recall from equation (15) that

$$\epsilon_{\xi\eta} = \frac{1}{A_\xi}\frac{\partial v}{\partial \xi}+\frac{1}{A_\eta}\frac{\partial u}{\partial \eta} \quad (38)$$

The above expression for $\epsilon_{\xi\eta}$ implies that, since the two natural-coordinate derivatives, $\partial v/\partial\xi$ and $\partial u/\partial\eta$, are to vary linearly along the ξ-and η-lines, respectively, so must their interpolations in the complementary directions. This homogeneity requirement is satisfied if $N_i(\xi)$ and $N_i(\eta)$ are replaced by $\bar{N}_i(\xi)$ and $\bar{N}_i(\eta)$ (see equation (20)), respectively, to yield

$$\epsilon_{\xi\eta} = \sum_{j=1}^{3}\bar{N}_j(\eta)\frac{1}{A_\xi}\,v_{,\xi}\Big|_{\eta=(j-2)} + \sum_{i=1}^{3}\bar{N}_i(\xi)\frac{1}{A_\eta}\,u_{,\eta}\Big|_{\xi=(i-2)} \quad (39)$$

where $v_{,\xi}\,|_{\eta=(j-2)}$ and $u_{,\eta}\,|_{\xi=(i-2)}$ are the derivatives of (v, u) with respect to (ξ, η) along the constant-(η, ξ) reference lines, respectively.

With the above special treatment of $\epsilon_{\xi\eta}$, the resulting natural-coordinate membrane strain-displacement relations may be written as follows

$$\boldsymbol{\epsilon}^N = \sum_{a=1}^{9}(\tilde{\mathbf{B}}_a^{\epsilon u}\tilde{u}_a + \tilde{\mathbf{B}}_a^{\epsilon v}\tilde{v}_a + \tilde{\mathbf{B}}_a^{\epsilon w}\tilde{w}_a),\ \boldsymbol{\epsilon}^N = \{\epsilon_{\xi\xi}, \epsilon_{\eta\eta}, \epsilon_{\xi\eta}\}^T \quad (40)$$

in which, with the nodal subscript relation, $a = 3(j-1)+i$ (see Fig. 1), the strain-displacement matrix components are explicitly given by

$$\tilde{\mathbf{B}}_a^{\epsilon u} = \begin{bmatrix} N_j(\eta)b_i^{\xi u} \\ N_i(\xi)b_j^{\eta u} \\ \bar{N}_i(\xi)b_j^{\eta u}+\bar{N}_j(\eta)b_i^{\xi u} \end{bmatrix} \quad (41)$$

$$\tilde{\mathbf{B}}_a^{\epsilon v} = \begin{bmatrix} N_j(\eta)b_i^{\xi v} \\ N_i(\xi)b_j^{\eta v} \\ \bar{N}_i(\xi)b_j^{\eta v}+\bar{N}_j(\eta)b_i^{\xi v} \end{bmatrix} \quad (42)$$

$$\tilde{\mathbf{B}}_a^{\epsilon w} = \begin{bmatrix} N_j(\eta)b_i^{\xi w'} \\ N_i(\xi)b_j^{\eta w'} \\ \bar{N}_i(\xi)b_j^{\eta w'}+\bar{N}_j(\eta)b_i^{\xi w'} \end{bmatrix} \quad (43)$$

where the b_i's were defined in equation (32).

4.2 Natural-Coordinate Bending Strains. The natural-coordinate bending strains are constructed in a similar manner to the membrane strains, except in terms of the rotational quantities, $\tilde{\alpha}$ and $\tilde{\beta}$, and without the need for the *curvature corrections* used in equation (28). Thus,

$$\boldsymbol{\kappa}^N = \sum_{a=1}^{9}(\tilde{\mathbf{B}}_a^{\kappa\alpha}\tilde{\alpha}_a + \tilde{\mathbf{B}}_a^{\kappa\beta}\tilde{\beta}_a),\ \boldsymbol{\kappa}^N = \{\kappa_{\xi\xi}, \kappa_{\eta\eta}, \kappa_{\xi\eta}\}^T \quad (44)$$

where

$$\tilde{\mathbf{B}}_a^{\kappa\alpha} = \begin{bmatrix} N_j(\eta)b_i^{\xi u} \\ N_i(\xi)b_j^{\eta u} \\ \bar{N}_i(\xi)b_j^{\eta u}+\bar{N}_j(\eta)b_i^{\xi u}) \end{bmatrix} \quad (45)$$

$$\tilde{\mathbf{B}}_a^{\kappa v} = \begin{bmatrix} N_j(\eta)b_i^{\xi v} \\ N_i(\xi)b_j^{\eta v} \\ \bar{N}_i(\xi)b_i^{\eta v}+\bar{N}_j(\eta)b_i^{\xi v}) \end{bmatrix} \quad (45)$$

4.3 Natural-Coordinate Transverse-Shear Strains. As shown in equation (20), the rotational displacements, α and β, must vary linearly along the constant-η and ξ lines, respectively, in order to yield a locking-free transverse-shear strain field. In addition, care must be exercised so that the curvature effects due to $\tilde{u}$ and $\tilde{v}$ (in the corresponding *curvilinear* strain-displacement relations) also vary linearly. The incorporation of these curvature effects (which is analogous to the procedure used for the membrane-strains) yields the following natural-coordinate transverse-shear strain interpolation formula:

$$\boldsymbol{\gamma}^N = \sum_{a=1}^{9}(\tilde{\mathbf{B}}_a^{\gamma u}\tilde{u}_a + \tilde{\mathbf{B}}_a^{\gamma v}\tilde{v}_a + \tilde{\mathbf{B}}_a^{\gamma w}\tilde{w}_a + \tilde{\mathbf{B}}_a^{\gamma\alpha}\tilde{\alpha}_a + \tilde{\mathbf{B}}_a^{\gamma\beta}\tilde{\beta}_a),$$

$$\boldsymbol{\gamma}^N = \{\gamma_{\xi\zeta}, \gamma_{\eta\zeta}\}^T \quad (47)$$

where

$$\tilde{\mathbf{B}}_a^{\gamma u} = \begin{bmatrix} N_j(\eta) b_i^{\xi u\prime} \\ N_i(\xi) b_j^{\eta u\prime} \end{bmatrix} \tag{48}$$

$$\tilde{\mathbf{B}}_a^{\gamma v} = \begin{bmatrix} N_j(\eta) b_i^{\xi v\prime} \\ N_i(\xi) b_j^{\eta v\prime} \end{bmatrix} \tag{49}$$

$$\tilde{\mathbf{B}}_a^{\gamma w} = \begin{bmatrix} N_j(\eta) b_i^{\xi w} \\ N_i(\xi) b_j^{\eta w} \end{bmatrix} \tag{50}$$

$$\tilde{\mathbf{B}}_a^{\gamma \alpha} = \begin{bmatrix} N_j(\eta) \bar{N}_i(\xi) \\ 0 \end{bmatrix} \tag{51}$$

$$\tilde{\mathbf{B}}_a^{\gamma \beta} = \begin{bmatrix} 0 \\ N_i(\xi) \bar{N}_j(\eta) \end{bmatrix} \tag{52}$$

Remark 4. The present formulation is easily extended to the sixteen-node C^0 element if one adopts the following modifications. First, the consistent interpolations for (α,β), and the curvature terms, $(\tilde{w}/R,\ \tilde{u}/R,\ \tilde{v}/R)$ are modified according to (Park, 1985), e.g., for $\tilde{u}'$:

$$\tilde{u}' = \frac{(-1+6\xi+9\xi^2)}{16}\tilde{u}_1 + \frac{(9-42\xi-9\xi^2)}{16}\tilde{u}_2 + \frac{(9+42\xi-9\xi^2)}{16}\tilde{u}_3 + \frac{(-1-6\xi+9\xi^2)}{16}\tilde{u}_4 \tag{53}$$

Second, the strains along the four element sides ($\xi = \pm 1$, $\eta = \pm 1$) and the four interior natural coordinate lines ($\xi = \pm 1/3$, $\eta = \pm 1/3$) are assumed to vary quadratically. Finally, the natural coordinate strains in the interior of the element are obtained by *cubic* interpolation of the strains along the *eight* reference natural coordinate lines. Similarly, the natural-coordinate-based formulation of the four-node C^0 plate/shell element (Park et al., 1985) can be obtained by appropriate adaptation of the present formulation.

This completes the derivation of the natural coordinate strains at an interior point of the quadratic element. However, to evaluate the strain energy at numerical integration points and thus obtain the element stiffness and internal force arrays, some additional transformations are required. These are addressed in the next section.

5 Element Stiffness, Internal Force, and Geometric Stiffness

There are two avenues for evaluating the strain energy based on the natural-coordinate strain-displacement relations given above. The first is to adopt a conjugate natural-coordinate *stress* tensor, as was employed by Dvorkin and Bathe (1984). Although this approach appears to be straightforward, it requires the transformation of the Cartesian *constitutive* tensor to the element natural coordinate system, which can become quite costly for nonlinear shell analysis. Furthermore, natural-coordinate components are not particularly "natural" for engineering purposes. Thus, in the present formulation, the conventional Cartesian constitutive relations are preserved by transforming the assumed natural-coordinate *strains* to the local-Cartesian coordinate system defined at each numerical integration point. Note that the precise orientation of the in-plane local-Cartesian axes is *arbitrary*; that is, except for the *normal* axis, which is the same for the two bases, the above assumed natural-coordinate strain approximations are *invariant* with respect to the choice of the local-Cartesian basis.

5.1 Cartesian Strain-Displacement Matrix. The local-Cartesian strain-displacement matrix needed to compute the element strains, stresses, stiffness matrix and internal force vector, can now be obtained with the tensor transformation given in equations (11) and (13). After some rearrangement, the local-Cartesian membrane, bending and transverse-shear strains are obtained from the corresponding natural-coordinate strains *via* the following matrix-vector products:

$$\begin{Bmatrix} \epsilon_{xx} \\ \epsilon_{yy} \\ \epsilon_{xy} \end{Bmatrix} = \begin{bmatrix} t_{x\xi}^2 & t_{x\eta}^2 & t_{x\xi}t_{x\eta} \\ t_{y\xi}^2 & t_{y\eta}^2 & t_{y\xi}t_{y\eta} \\ 2t_{x\xi}t_{y\xi} & 2t_{x\eta}t_{y\eta} & t_{x\xi}t_{y\eta}+t_{x\eta}t_{y\xi} \end{bmatrix} \begin{Bmatrix} \epsilon_{\xi\xi} \\ \epsilon_{\eta\eta} \\ \epsilon_{\xi\eta} \end{Bmatrix}$$

$$\begin{Bmatrix} \kappa_{xx} \\ \kappa_{yy} \\ \kappa_{xy} \end{Bmatrix} = \begin{bmatrix} t_{x\xi}^2 & t_{x\eta}^2 & t_{x\xi}t_{x\eta} \\ t_{y\xi}^2 & t_{y\eta}^2 & t_{y\xi}t_{y\eta} \\ 2t_{x\xi}t_{y\xi} & 2t_{x\eta}t_{y\eta} & t_{x\xi}t_{y\eta}+t_{x\eta}t_{y\xi} \end{bmatrix} \begin{Bmatrix} \kappa_{\xi\xi} \\ \kappa_{\eta\eta} \\ \kappa_{\xi\eta} \end{Bmatrix} \tag{54}$$

$$\begin{Bmatrix} \gamma_{zx} \\ \gamma_{zy} \end{Bmatrix} = \begin{bmatrix} t_{x\xi} & t_{x\eta} \\ t_{y\xi} & t_{y\eta} \end{bmatrix} \begin{Bmatrix} \gamma_{\zeta\xi} \\ \gamma_{\zeta\eta} \end{Bmatrix}$$

Finally, substitution of (40), (44), and (47) into (54) followed by transformation of the nodal displacements from the natural-coordinate bases to the *global* bases used for the assembled structure (which may be either fixed Cartesian or shell-oriented), leads to the following standard format for the element strain-displacement matrix:

$$\begin{Bmatrix} \boldsymbol{\epsilon} \\ \boldsymbol{\kappa} \\ \boldsymbol{\gamma} \end{Bmatrix} = \sum_{a=1}^{9} \begin{bmatrix} \mathbf{B}_a^m \\ \mathbf{B}_a^b \\ \mathbf{B}_a^s \end{bmatrix} \mathbf{d}_a \tag{55}$$

where

$$\mathbf{d}_a = \{u_a^G, v_a^G, w_a^G, \alpha_a^G, \beta_a^G\}^T, \quad \mathbf{B}_a^{(\cdot)} = \mathbf{T}_{LN}\tilde{\mathbf{B}}_a^{(\cdot)}\mathbf{T}_{N_aG} \tag{56}$$

in which $\mathbf{d}_a$ is the global generalized displacement vector at element node a; $\tilde{\mathbf{B}}_a^{(\cdot)}$ are the natural-coordinate strain-displacement matrices for membrane, bending and transverse-shear components, whose submatrices are given by equations (41)–(43), (45)–(46), and (48)–(52); $\mathbf{T}_{LN}$ is the strain transformation from natural-coordinate to local-Cartesian bases at integration points (from equation (54)); and $\mathbf{T}_{N_aG}$ is the displacement transformation from global to the natural-coordinate basis at node a.

5.2 The Element Linear Stiffness Matrix, $\mathbf{K}_l$. The element linear stiffness matrix in the Global (assembled-structure) coordinate system is, for the case of a symmetrically layered shell, composed of independent membrane, bending and transverse-shear contributions, i.e.,

$$\mathbf{K}_l = \mathbf{K}^m + \mathbf{K}^b + \mathbf{K}^s \tag{57}$$

where $\mathbf{K}^{(m,b,s)}$ are defined in terms of the strain-displacement matrices in equation (55) as

$$\mathbf{K}^m = \int_S [\mathbf{B}^m]^T[\mathbf{C}^m][\mathbf{B}^m]dS \tag{58}$$

$$\mathbf{K}^b = \int_S [\mathbf{B}^b]^T[\mathbf{C}^b][\mathbf{B}^b]dS \tag{59}$$

$$\mathbf{K}^S = \int_S [\mathbf{B}^s]^T[\mathbf{C}^s][\mathbf{B}^s]dS \tag{60}$$

in which the $\mathbf{C}$'s are the corresponding integrated material constitutive matrices. Note that all integrals are performed over the current element reference-surface area.

5.3 The Element Internal Force Vector, f. For use in nonlinear analysis, the element internal force vector is obtained by

$$\mathbf{f}=\int_S [\mathbf{B}^m]^T\{\mathbf{n}\}dS+\int_S [\mathbf{B}^b]^T\{\mathbf{m}\}dS+\int_S [\mathbf{B}^s]^T\{\mathbf{q}\}dS \tag{61}$$

where

$$\mathbf{n}=\{n_{xx},n_{xy},n_{yy}\}^T \tag{62}$$

$$\mathbf{m}=\{m_{xx},m_{xy},m_{yy}\}^T \tag{63}$$

$$\mathbf{q}=\{q_{xz},q_{zy}\}^T \tag{64}$$

are membrane (force), bending (moment), and transverse-shear (force) stress resultants, respectively, with the conventional thin-shell definitions.

5.4 The Element Geometric Stiffness Matrix, $\mathbf{K}_g$. The element geometric stiffness matrix can be constructed in the following specially-ordered form (see, e.g., Zienkiewicz, 1971):

$$\mathbf{K}_g=\int_V \begin{bmatrix} \mathbf{k}_m & 0 & 0 & \mathbf{k}_b+\mathbf{k}_s & 0 \\ & \mathbf{k}_m & 0 & 0 & \mathbf{k}_b+\mathbf{k}_s \\ & & \mathbf{k}_m & 0 & 0 \\ & Symm. & & \mathbf{k}_{s'}+\mathbf{k}_{b'} & 0 \\ & & & & \mathbf{k}_{s'}+\mathbf{k}_{b'} \end{bmatrix} dV \tag{65}$$

where each row partition corresponds to a particular displacement component evaluated at all nine of the element's nodes, i.e., $\{\mathbf{u}_a^G\}_{a=1,9}$, $\{\mathbf{v}_a^G\}_{a=1,9}$, etc., and

$$\mathbf{k}_m=[\mathbf{B}^{xu}]^T\sigma_{xx}[\mathbf{B}^{xu}]+[\mathbf{B}^{yv}]^T\sigma_{yy}[\mathbf{B}^{yv}] +[\mathbf{B}^{xu}]^T\sigma_{xy}[\mathbf{B}^{yv}]+[\mathbf{B}^{yv}]^T\sigma_{xy}[\mathbf{B}^{xu}] \tag{66}$$

$$\mathbf{k}_s=[\mathbf{B}^{xu}]^T\sigma_{xz}[\mathbf{B}^{\alpha}]+[\mathbf{B}^{yu}]^T\sigma_{yz}[\mathbf{B}^{\beta}] \tag{67}$$

$$\mathbf{k}_b=z\mathbf{k}_m,\quad \mathbf{k}_{b'}=z^2\mathbf{k}_n,\quad \mathbf{k}_{s'}=z\mathbf{k}_s \tag{68}$$

in which $\mathbf{B}^{xu}$ is the interpolation matrix for the derivative of u_x with respect to x, $\mathbf{B}^{\alpha}$ is the interpolation matrix for α_x, etc.

In the actual element implementation, these local-Cartesian derivatives are obtained from the natural-coordinate derivatives (which are assumed in a manner similar to that employed for the strains) via the transformation

$$\begin{Bmatrix} u_{x,x} \\ u_{y,x} \\ u_{x,y} \\ u_{y,y} \\ u_{z,x} \\ u_{z,y} \end{Bmatrix} = \begin{bmatrix} t_{x\xi}^2 & t_{x\eta}t_{x\xi} & t_{x\xi}t_{x\eta} & t_{x\eta}^2 & 0 & 0 \\ t_{y\xi}t_{x\xi} & t_{y\eta}t_{x\xi} & t_{y\xi}t_{x\eta} & t_{y\eta}t_{x\eta} & 0 & 0 \\ t_{x\xi}t_{y\xi} & t_{x\eta}t_{y\xi} & t_{x\xi}t_{y\eta} & t_{x\eta}t_{y\eta} & 0 & 0 \\ t_{y\xi}^2 & t_{y\eta}t_{y\xi} & t_{y\xi}t_{y\eta} & t_{y\eta}^2 & 0 & 0 \\ 0 & 0 & 0 & 0 & t_{x\xi} & t_{x\eta} \\ 0 & 0 & 0 & 0 & t_{y\xi} & t_{y\eta} \end{bmatrix} \begin{Bmatrix} u_{,\xi} \\ v_{,\xi} \\ u_{,\eta} \\ v_{,\eta} \\ w_{,\xi} \\ w_{,\eta} \end{Bmatrix} \tag{69}$$

A similar transformation may be employed for the derivatives of the rotations, α_x and α_y.

Remark 5. It should be noted that the present formulation can be applied to general nonlinear analysis by adopting either a *corotational* procedure (e.g., Rankin and Brogan, 1984) for the small-strain case or an *updated-Lagrange* approach (e.g., Stanley, 1985) for the large-strain case.

6 Reduced-Integrated Implementation of the Present Element

The element derived in the preceding sections can be implemented either by invoking the full (nine-point) integration rule, or by the reduced (four-point) rule if augmented with proper rank-compensation terms. However, while this strategy is satisfactory for the linear stiffness matrix, $\mathbf{K}_l$, it is recommended that the four-point rule be adopted for calculating the *geometric* stiffness matrix, $\mathbf{K}_g$. Pending a consistent approximation of the geometric stiffness matrix, which must await a thorough symbolic investigation, we offer the following comment.

For quadrilateral elements, the stresses at the Barlow (or reduced integration) points are more accurate than those at the full integration points. Since the geometric stiffness matrix may be viewed as an *initial stress* matrix, the Barlow-point stresses are preferred over the fully integrated ones for geometric stiffness formation. Moreover, note that the strains that are conjugate to the Barlow-point initial stresses are also those evaluated at the Barlow points. Such preferred conjugate pairing appears to be akin to Fraeijs de Veubeke's limitation principle (1965).

In the remainder of this section, a step-by-step procedure is presented for proper rank compensation of the reduced-integrated linear stiffness matrix. We start with an illustration: rank compensation of the reduced-integrated mass matrix for a straight quadratic bar element. We will then show how this simple compensation scheme can be extended to the two-dimensional (shell) case.

6.1 Compensating the Reduced-Integrated Mass Matrix for a Quadratic Bar Element. To show how reduced integration affects rank deficiency, we introduce a straight quadratic bar element, whose mass matrix may be expressed as

$$\mathbf{M}=\int_l \mathbf{N}^T\mathbf{N}dl \tag{70}$$

where $\mathbf{N}=[N_1(\xi),N_2(\xi),N_3(\xi)]$ is the vector of quadratic nodal shape functions. If a three-point (full) numerical integration scheme is employed, the resulting mass matrix is

$$\mathbf{M}^f=\frac{l}{30}\begin{bmatrix} 4 & 2 & -1 \\ 2 & 16 & 2 \\ -1 & 2 & 4 \end{bmatrix} \tag{71}$$

Alternatively, if a two-point (reduced) integration rule is employed, the mass matrix becomes

$$\mathbf{M}^r=\frac{l}{18}\begin{bmatrix} 2 & 2 & -1 \\ 2 & 8 & 2 \\ -1 & 2 & 2 \end{bmatrix} \tag{72}$$

Thus, the difference between the fully integrated and the reduced-integrated mass matrices for the bar element is given by

$$\Delta\mathbf{M}=\frac{l}{45}\begin{bmatrix} 1 & -2 & 1 \\ -2 & 4 & -2 \\ 1 & -2 & 1 \end{bmatrix} \tag{73}$$

A symbolic analysis has revealed that this "perturbation" mass matrix, $\Delta\mathbf{M}$, may also be obtained by integrating

$$\Delta\mathbf{M}=\frac{1}{45}\int_l \left[\frac{\partial^2\mathbf{N}}{\partial\xi^2}\right]^T\left[\frac{\partial^2\mathbf{N}}{\partial\xi^2}\right]dl \tag{74}$$

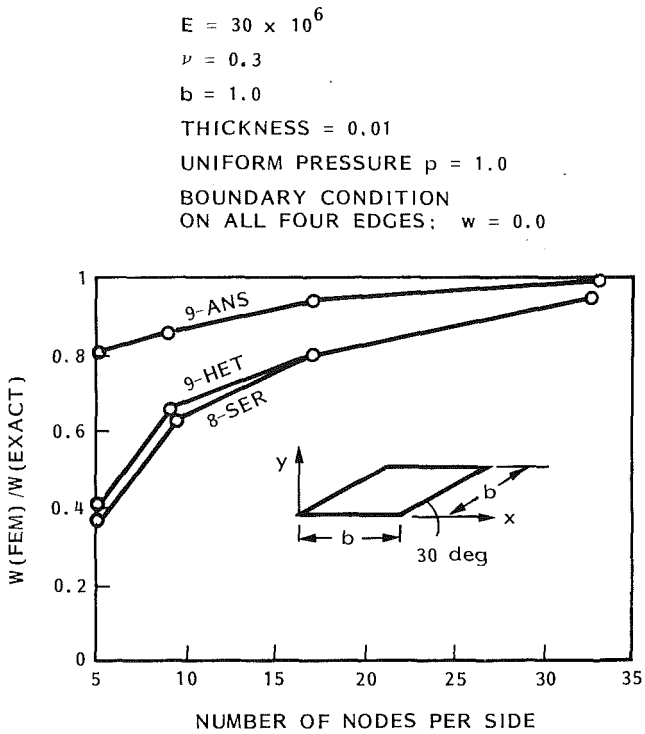

Fig. 3 Finite element solutions of rhombic plate problem

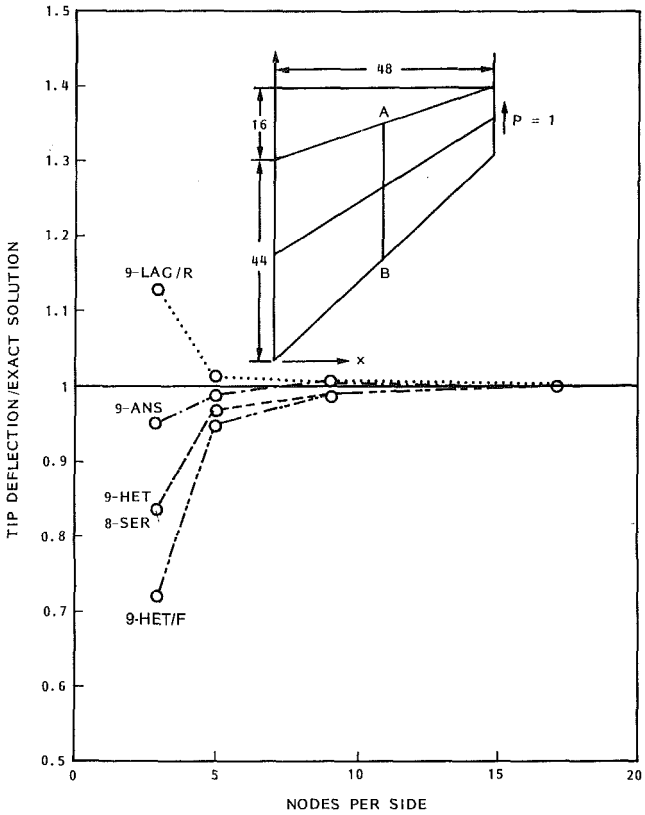

Fig. 4 Distorted plate under unit membrane edge load

with the *two-point* rule. It is this interesting result that forms the basis for constructing the proper rank-compensation for the reduced-integrated shell element stiffness matrix.

6.2 The Proper Compensation for the Reduced-Integrated Shell Stiffness Matrix. Recall that the present element strain-displacement relations are obtained by quadratically interpolating the strains between the element sides and the centroidal natural coordinate lines. Note that the strains *along* these reference lines are linearly varying. Hence, the deficiencies due to reduced integration stem solely from the quadratic interpolation used along the complementary directions. For example, the natural coordinate bending strain component, $\kappa_{\xi\xi}$, is expressed as (see equations (45)–(46)):

$$\kappa_{\xi\xi} = \sum_{j=1}^{3}\sum_{i=1}^{3} (N_j(\eta) b_i^{\xi u} \tilde{\alpha}_a + N_j(\eta) b_i^{\xi v} \tilde{\beta}_a), \tag{75}$$

with

$$a = 3(j-1)+i$$

It is emphasized that the terms, $b_i^{\xi u}$ and $b_i^{\xi v}$ vary linearly with respect to ξ. Hence, the only part that is affected by reduced integration is the quadratic term, $N_j(\eta)$. This observation suggests that we can apply the one-dimensional compensation obtained for the quadratic bar directly to the present two-dimensional case.

The fully integrated bending stiffness matrix, $\mathbf{K}^{bf}$, can thus be obtained as the sum of two reduced-integrated parts, viz,:

$$\mathbf{K}^{bf}|_{(3\times 3)} = \mathbf{K}^{br}|_{(2\times 2)} + \Delta\mathbf{K}^{bc}|_{(2\times 2)} \tag{76}$$

where

$$\Delta\mathbf{K}^{bc} = \int_S [\Delta\mathbf{B}^b]^T [\mathbf{C}^b][\Delta\mathbf{B}^b] dS \tag{77}$$

in which $[\Delta\mathbf{B}^b]$ is defined by

$$\Delta\kappa = \sum_{a=1}^{9} \Delta\mathbf{B}_a^b \mathbf{d}_a \tag{78}$$

where

$$\Delta\kappa = \begin{Bmatrix} \Delta\kappa_{xx} \\ \Delta\kappa_{yy} \\ \Delta\kappa_{xy} \end{Bmatrix}$$

$$= \frac{1}{\sqrt{45}} \begin{bmatrix} t_{x\xi}^2 & t_{x\eta}^2 & t_{x\xi}t_{x\eta} \\ t_{y\xi}^2 & t_{y\eta}^2 & t_{y\xi}t_{y\eta} \\ 2t_{x\xi}t_{y\xi} & 2t_{x\eta}t_{y\xi} & t_{x\xi}t_{y\eta}+t_{x\eta}t_{y\xi} \end{bmatrix} \begin{Bmatrix} \dfrac{\partial^2 \kappa_{\xi\xi}}{\partial\eta^2} \\ \dfrac{\partial^2 \kappa_{\eta\eta}}{\partial\xi^2} \\ 0 \end{Bmatrix} \tag{79}$$

Note the absence of any contribution from $\kappa_{\xi\eta}$, as it is already accurately obtained with reduced integration. The remaining rank compensation matrices for the membrane and transverse-shear stiffnesses, i.e., $\Delta\mathbf{K}^m$ and $\Delta\mathbf{K}^s$, can be similarly obtained.

Remark 6. The canonical hour-glass modes in the natural-coordinate system for the present element can now be identified by considering the following: First, the proper hour-glass mode, $\mathbf{h}_\xi$, for annihilating the rank deficiency associated with the natural derivative, $(\partial/\partial\xi)$, can be explicitly expressed as

$$\mathbf{h}_\xi = \left\{ \frac{(2\xi-1)}{l_{\xi 1}}, \frac{4\xi}{l_{\xi 1}}, \frac{(2\xi+1)}{l_{\xi 1}}, \frac{2(1-2\xi)}{l_{\xi 2}}, \frac{-8\xi}{l_{\xi 2}}, \frac{2(1+2\xi)}{l_{\xi 2}}, \frac{(2\xi-1)}{l_{\xi 3}}, \frac{4\xi}{l_{\xi 3}}, \frac{(2\xi+1)}{l_{\xi 3}} \right\}^T \tag{80}$$

Similarly, the proper hour-glass mode, $\mathbf{h}_\eta$, for annihilating the rank deficiency associated with the natural derivative, $(\partial/\partial\eta)$, can be expressed as

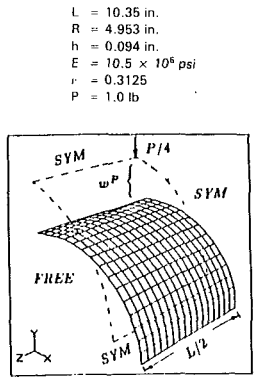

Problem Definition for Pinched Cylinder

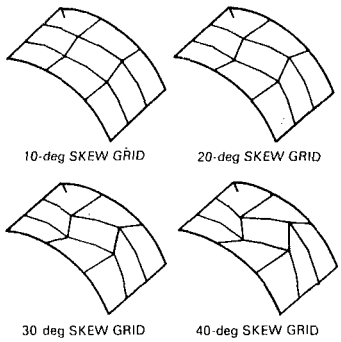

Progressively Distorted Mesh for Pinched Cylinder Problem

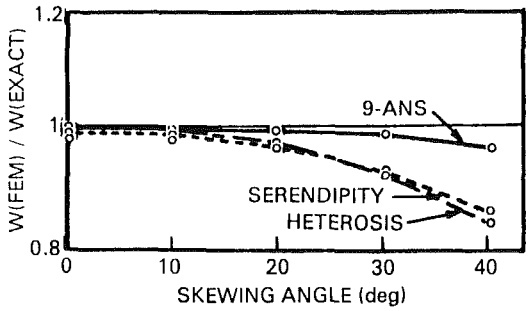

Fig. 5 Effect of mesh distortions for pinched cylinder problem

$$\mathbf{h}_\eta = \left\{ \frac{(2\eta-1)}{l_{\eta 1}}, \frac{2(1-2\eta)}{l_{\eta 2}}, \frac{(2\eta-1)}{l_{\eta 3}}, \frac{4\eta}{l_{\eta 1}}, \frac{-8\eta}{l_{\eta 2}}, \frac{4\eta}{l_{\eta 3}}, \frac{(2\eta+1)}{l_{\eta 1}}, \frac{2(1+2\eta)}{l_{\eta 2}}, \frac{(2\eta+1)}{l_{\eta 3}} \right\}^T \tag{81}$$

where $l_{l(\xi,\eta)i}$ are the natural coordinate side lengths (see Fig. 2). These two hour-glass modes vary linearly along the natural coordinate lines and are fundamentally different from those identified in Parisch (1979) and Belytschko et al. (1984). Finally, the corresponding local-Cartesian hour-glass modes are easily obtained from $\mathbf{h}_\xi$ and $\mathbf{h}_\eta$ by coordinate transformations.

Remark 7. The rank compensating operator presented in Park and Flaggs (1985) for a four-node element can be easily adapted to the present natural-coordinate strain formulation. For example, the rank-compensating bending strain, $\Delta\boldsymbol{\kappa}$, for the four-node element can be obtained from the transformation

$$\Delta\boldsymbol{\kappa}^{(4)} = \frac{1}{\sqrt{3}} \begin{bmatrix} t_{x\xi}^2 & t_{x\eta}^2 & t_{x\xi}t_{x\eta} \\ t_{y\xi}^2 & t_{y\eta}^2 & t_{y\xi}t_{y\eta} \\ 2t_{x\xi}t_{y\xi} & 2t_{x\eta}t_{y\xi} & t_{x\xi}t_{y\eta}+t_{x\eta}t_{y\xi} \end{bmatrix} \begin{bmatrix} \dfrac{\partial \kappa_{\xi\xi}}{\partial \eta} \\ \dfrac{\partial \kappa_{\eta\eta}}{\partial \xi} \\ 0 \end{bmatrix} \tag{82}$$

Furthermore, the two hour-glass modes for the four-node element in terms of natural-coordinates are simply

$$\mathbf{h}_\xi^{(4)} = \left\{ \frac{1}{2l_{\xi 1}}, -\frac{1}{2l_{\xi 1}}, -\frac{1}{2l_{\xi 2}}, \frac{1}{2l_{\xi 2}} \right\}^T \tag{83}$$

Table 1 Results for the inextensional bending of Fig. 5

	Radial deflection at loaded point for subdivision			
Element	2×2	4×4	8×8	16×16
4-LAG	0.0703	0.1002	0.1100	
4-ANS	0.0703	0.1002	0.1099	0.1128
9-HET	0.1184	0.1126	0.1136	0.1137
9-LAG/F	10^{-10}	*	*	10^{-10}
8-SER	0.0963	0.1107	0.1133	0.1137
4-STG	0.0973	0.1072	0.1116	0.1131
9-ANS	0.1055	0.1123	0.1136	0.1138

$$\mathbf{h}_\eta^{(4)} = \left\{ \frac{1}{2l_{\eta 1}}, -\frac{1}{2l_{\eta 2}}, -\frac{1}{2l_{\eta 1}}, \frac{1}{2l_{\eta 2}} \right\}^T \tag{84}$$

7 Performance Evaluation of the Present Element

The present element has been implemented in a stand-alone shell element processor within the NICE architecture (Felippa, 1981) and evaluated numerically. Element patch tests were performed for both plane stress and plate bending problems under constant strain states. The results indicate that the element passes the patch test when the element sides are straight but fails the test (weakly) when the element sides are parabolically curved *in-plane*. Nevertheless, the curved-sided solutions do converge monotonically as the grid is refined. For cylinders subjected to uniform internal pressure, the element also passes the patch test exactly if the element sides have no in-plane curvature.

Of the many problems analyzed with the present element, we present four examples: bending of a rhombic plate, a plane stress problem with a distorted mesh, a pinched cylinder problem with progressive mesh distortion, and classical buckling of a thin cylindrical shell with both regular and distorted grids. As we shall see, the present element performs reliably for all of these problems; the element possesses correct rank without problem-dependent hour-glass mode control, remains free from both transverse-shear and membrane locking, and is least sensitive to element mesh distortion in comparison with the other quadratic C^0 elements tested. In the numerical experiments that follow, the present element is designated as *9-ANS*. The other elements compared in the present study include the serendipity element (*8-SER*) and the heterosis element (*9-HET*)—both of which require reduced integration of membrane and transverse-shear strains and hence may suffer from rank deficiency for certain applications, especially in dynamics. The two four-node elements included for comparison purposes are: a modified version of the symbolically synthesized element (Park and Flaggs, 1985) designated as *4-ANS* (which appears to be similar to the element developed by Dvorkin and Bathe (1984)) and a C^1 element that is employed extensively by users of the STAGS code, designated *4-STG*. In all of these elements, the geometric stiffness matrix, K_g, is constructed by reduced integration unless otherwise noted.

7.1 Bending of a Rhombic Plate. Figure 3 presents the problem definition of a rhombic plate that is subjected to a uniform pressure with simply supported boundaries. Illustrated in the same figure are the mesh convergence curves of the present element (*9-ANS*) and two other C^0 plate bending elements. Observe that the present element is far less sensitive to the severe (intrinsic) mesh distortion of this problem than other elements. The robust performance of the *9-ANS* element is believed to be a direct consequence of the natural-coordinate formulation of the strain-displacement relations, which constitutes a significant departure from the standard isoparametric approach.

7.2 Cook's Plane Stress Problem. To assess the membrane performance of the present element for a flat surface, the plane stress problem suggested by Cook (1973), and shown in Fig. 4, was analyzed. The convergence curves for several

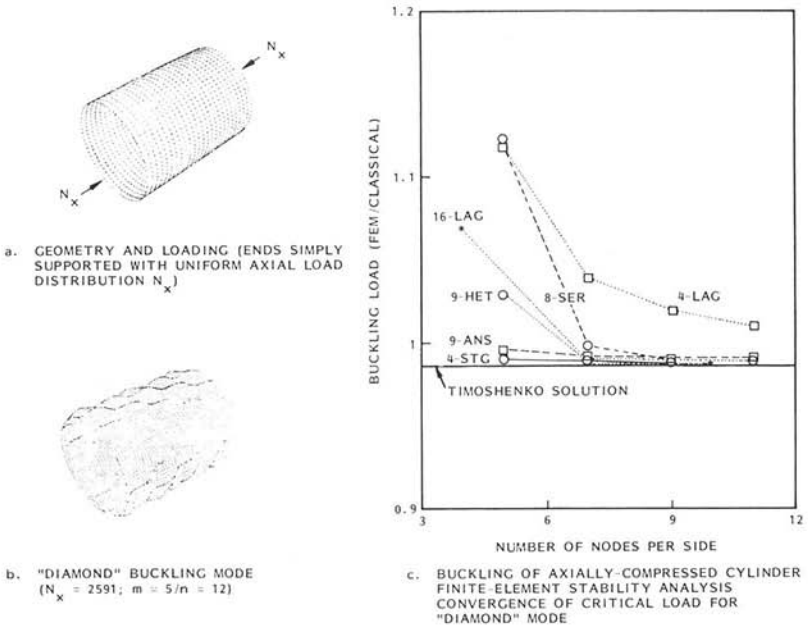

Fig. 6 Finite element solutions of cylindrical shell buckling

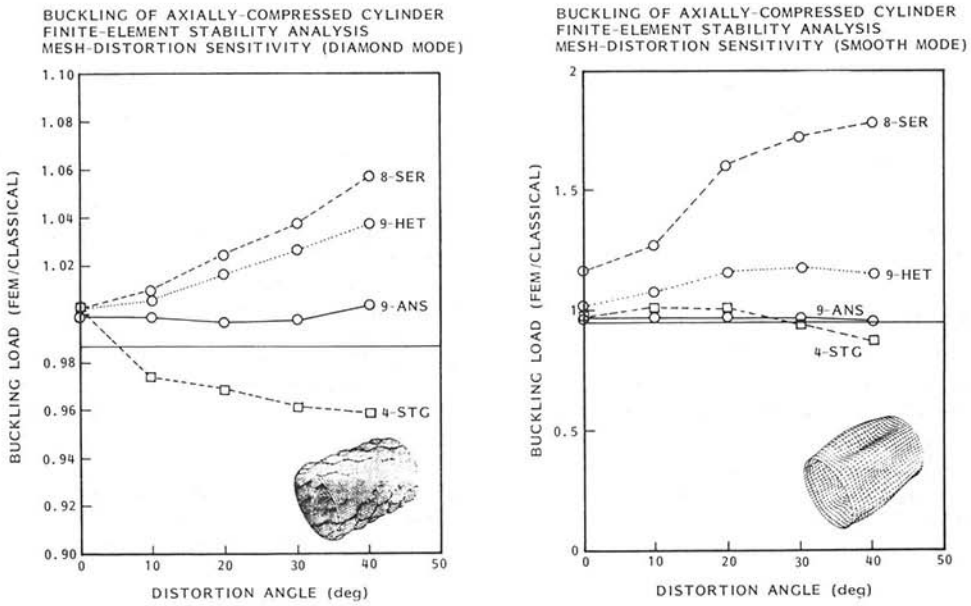

Fig. 7 Mesh distortion sensitivity for buckling analysis

elements are also presented therein. The results show that while all of the elements tested converge to the same answer, the *9-ANS* element yields a far more accurate solution for coarse grids than both the serendipity (*8-SER*) and heterosis (*9-HET*) elements. Note also that the present *9-ANS* element is constructed with full integration whereas the 8-SER and 9-HET elements must employ selective reduced integration to avoid membrane locking (and, for other problems, transverse-shear locking). For example, the stiffening effect of full membrane integration on the heterosis element is depicted in Fig. 4 by the curve labeled 9-HET/F.

7.3 Pinched Cylinder Problem. This problem was selected for two purposes: to evaluate how well the present element captures inextensional deformation in shells, and to assess the effect of element distortion on curved surfaces. Figure 5*a* presents the problem statement. The convergence characteristics of various elements for rectangular grids are summarized in Table 1. We emphasize that the heterosis (9-HET) and the Serendipity (8-SER) elements must employ reduced integration for both membrane and transverse-shear strains in order to avoid locking. This is dramatically illustrated in this problem by the membrane locking of the fully integrated 9-node Lagrange element, labeled *9-LAG/F*.

To examine how well the 9-ANS element performs for inextensional bending when the element is distorted, the mesh was progressively distorted as shown in Fig. 5*b*. The superior performance of the present *9-ANS* element as compared with the *8-SER* and *9-HET* elements is evident from Fig. 5*c*.

7.4 Classical Buckling of a Cylindrical Shell. Figure 6*a* shows a thin medium-length perfect cylinder ($L/R = 3$, $R/h = 300$) under axial compression with simply supported boundaries. The finite element solution of this apparently simple problem is often surprising to the unsuspecting analyst, due to the inherent multiplicity of closely spaced eigenvalues that are nevertheless associated with vastly different buckling mode shapes. One of the many classical buckling modes and

corresponding eigenvalues is shown in Fig. 6*b*: a *diamond pattern* mode. Note that this typically observed mode ($m = 5/n = 12$), a *smoothly varying* mode ($m = 1/n = 6$), and an *axisymmetric* mode ($m = 27/n = 0$), all correspond to practically identical axial load levels (where m is the number of axial half-waves and n is the number of circumferential whole-waves). Although these classical buckling solutions for a perfect cylinder always overestimate the load-carrying capacity of a real cylinder, the same modes may participate to varying degrees in the fully nonlinear analysis of an imperfect cylindrical shell, and hence must be properly represented in the numerical model.

In the numerical model studied, only 60 deg by one-half the length of the full cylinder is represented. Simple supports and symmetry conditions are imposed at the two axial ends, respectively, with symmetry conditions imposed at both the 0 and 60 deg boundaries. Such a model is extensive enough to capture most of the interesting mode shapes at modest expense. In particular, the convergence curves for the diamond mode (see Fig. 6*b*) are reported in Fig. 6*c*. For this buckling mode the superior performance of the present element (*9-ANS*) is in part due to the improved curvature representation that was detailed in equations (24)–(31).

To test the effect of mesh distortion on element buckling load predictions, a (7×7)-grid was progressively skewed in the same manner as in the pinched cylinder case (see Fig. 5*b*). The convergence characteristics of several elements under progressive mesh distortion are illustrated in Fig. 7 for both the *diamond* and the *smooth* modes. Once again, the superior robustness of the *9-ANS* element is confirmed.

8 Discussions and Conclusions

A curved C^0 shell element that corrects several deficiencies in existing quadratic shell elements has been presented. The element passes the patch test—provided the element sides do not have *in-plane* curvature—for arbitrary quadrilateral element shapes. The improved performance of the present element has been realized by the adoption of linearly interpolated strain fields along the *six reference lines* (ξ, $\eta = 0, \pm 1$); the construction of the element interior-strain fields by quadratic interpolation of the strains between the reference lines; improved modeling of curvature effects for both membrane and transverse-shear strains; and tensorial transformation of the natural-coordinate *strains* to a local-Cartesian system, rather than using the standard isoparametric approach of employing only the Jacobian (derivative) transformation. The element thereby possesses correct rank without transverse-shear locking, consistent membrane strain interpolation that admits accurate membrane *and* inextensional bending deformation without reduced integration, and, finally, robustness in the presence of severe mesh distortion.

The present element can also be implemented with *reduced* integration if it is augmented with the proper (symbolically synthesized) compensating parts described in Section 6 of the paper. Note that since the reduced-integrated version of the present element maintains the same accuracy as the fully integrated version, it thus differs fundamentally from the hourglass controlled reduced-integrated elements that have been suggested by Parish (1979) and Belytschko et al. (1984). Numerical experiments with the present element demonstrate that the element maintains its robustness for a variety of applications and is extremely resistant to mesh distortion; hence it is recommended for production applications.

Acknowledgments

This work was sponsored under the Discrete Element Technology Project of Lockheed's Independent Research Program. The authors thank Dr. Norm Cyr, Mr. Gordon Ferguson, and Dr. S. Nagarajan for their encouragement throughout the course of the present work.

References

Ahmad, S., Irons, B. M., and Zienkiewicz, O. C., 1970, "Analysis of Thick and Thin Shell Structures by Curved Elements," *Int. J. Num. Meth. Engr.*, Vol. 2, pp. 419–451.

Argyris, J. H., 1964, *Recent Advances in Matrix Methods of Structural Analysis*, Pergamon Press, New York.

Barlow, J., 1976, "Optimal Stress Locations in Finite Element Models," *Int. J. Num. Meth. Engr.*, Vol. 10, pp. 243–251.

Bathe, K. J., Dvorkin, E., and Ho, L. W., 1983, "Our Discrete Kirchhoff and Isoparametric Elements for Nonlinear Analysis – An Assessment," *Comp. & Struct*, Vol. 16, pp. 89–98.

Belytschko, T., Ong, S.-J., and Liu, W. K., 1984, "A Consistent Control of Spurious Singular Modes in the 9-Node Lagrangian Element for the Laplace and Mindlin Plate Equations," *Comp. Meth. Appl. Mech. & Engr.*, Vol. 44, pp. 269–295.

Belytschko, T., Stolarski, H., Liu, W. K., Carpenter, N. and Ong, J. S.-J., 1985, "Stress Projection for Membrane and Shear Locking in Shell Finite Elements," *Comp. Meth. Appl. Mech. Eng.*, Vol. 51, pp. 221–258.

Bogner, F. K., Fox, R. L., and Schmit, L. A., 1965, "The Generation of Interelement, Compatible Stiffness and Mass Matrices by the Use of Interpolation Formulas," *Proc. Conf. on Matrix Methods in Structural Mechanics*, Wright-Patterson AFB, Ohio, pp. 397–444.

Calladine, C. R., 1983, *Theory of Shell Structures*, Cambridge University Press, Cambridge.

Clough, R. W., and Felippa, C. A., 1968, "A Refined Quadrilateral Element for Analysis of Plate Bending," *The Second Proc. Conf. on Matrix Methods in Structural Mechanics*, Wright-Patterson AFB, Ohio, pp. 399–440.

Cook, R. D., 1974, "Improved Two-Dimensional Finite Element," *J. Struct. Div.*, ASCE, Vol. 100, ST6, pp. 1851–1863.

Crisfield, M. A., 1983, "A Four-Noded Thin-Plate Element Using Shear Constraints – A Modified Version of Lyons' Element," *Comp. Meth. Appl. Mech. Engr.*, Vol. 38, pp. 93–120.

Crisfield, M. A., 1984, "A Quadratic Mindlin Element Using Shear Constraints," *Comp. Meth. Appl. Mech. & Engr.*, Vol. 18, pp. 833–852.

Dvorkin, E. N., and Bathe, K. J., 1984, "A Continuum Mechanics Based Four-Node Shell Element for General Nonlinear Analysis," *Int. J. for Computer-Aided Engr. & Software*, Vol. 1, pp. 77–88.

Ergatoudis, I., Irons, B. M., and Zienkiewicz, O. C., 1968, "Curved Isoparametric Quadrilateral Elements for Finite Element Analysis," *International Journal of Solids and Structures*, Vol. 4, pp. 31–42.

Felippa, C. A., 1981, "Architecture of a Distributed Analysis Network for Computational Mechanics," *Computers and Structures*, Vol. 13, pp. 405–413.

Fraeijs de Veubeke, B., 1965, "Displacement and Equilibrium Models in the Finite Element Method," in: *Stress Analysis*, Zienkiewicz, O. C., and Holister, G., ed., Wiley, pp. 145–197.

Hrennikoff, A., 1941, "Solution of Problems of Elasticity by the Framework Method," ASME JOURNAL OF APPLIED MECHANICS, Vol. 8, pp. 169–175.

Hughes, T. J. R., Taylor, R. C., and Kanoknukulchai, W., 1977, "A Simple and Efficient Finite Element for Plate Bending," *Int. J. Num. Meth. Engr.*, Vol. 11, pp. 1529–1547.

Hughes, T. J. R., and Cohen, M., 1978, "The Heterosis Finite Element for Plate Bending," *Comp. & Struct.*, Vol. 9, pp. 445–450.

Hughes, T. J. R., and Tedzduyar, T. E., 1981, "Finite Elements Based on Mindlin Plate Theory with Particular Reference to the Four-node Bilinear Isoparametric Elements," ASME JOURNAL OF APPLIED MECHANICS, pp. 587–596.

Hughes, T. J. R., and Liu, W. K., 1981, "Nonlinear Finite Element Analysis of Shells: Part I," *Comp. Meth. Appl. Mech. Engr.*, Vol. 26, pp. 1331–1362.

Hughes, T. J. R., and Winget, J. M., 1980, "Finite Rotation Effects in Numerical Integration of Rate Constitutive Equations Arising in Large Deformation Analysis," *Int. J. Num. Meth. Eng.*, Vol. 15, pp. 1862–1867.

Irons, B. M., 1976, "The Semiloof Shell Element," in: *Finite Elements for Thin Shells and Curved Membranes*, Ashwell, D. G., and Gallagher, R. H., eds., Wiley, New York, pp. 197–222.

Irons, B., and Ahmad, S., 1980, *Techniques for Finite Elements*, Wiley, New York.

Knight, N. F. and Starnes, J. H., 1984, "Postbuckling Behavior of Axially Compressed Graphite-Epoxy Cylindrical Panels with Circular Holes," in: *Collapse Analysis of Structures*, ed. by Sobel, L. H. et al., PVP-Vol. 84, ASME, New York, N. Y., pp. 153–167.

Lee, S. W., and Pian, T. H. H., 1978, "Improvement of Plate and Shell Finite Elements by Mixed Formulations," *AIAA J.*, Vol. 16, pp. 29–34.

MacNeal, R. H., 1978, "A Simple Quadrilateral Shell Element," *Comp. & Struct.*, Vol. 8, pp. 175–183.

MacNeal, R. H., 1982, "Derivation of Element Stiffness Matrices by Assumed Strain Distribution," *Nuclear Eng. Design*, Vol. 70, pp. 3–12.

Noor, A. K., and Peters, J. M., 1981, "Mixed Models and Reduced/Selective Integration Displacement Models for Nonlinear Analysis of Curved Beams," *Int. J. Num. Meth. Eng.*, Vol. 17, pp. 615–631.

Parisch, H., 1979, "A Critical Survey of the 9-Node Degenerated Shell Element with Special Emphasis on Thin Shell Application and Reduced Integration," *Comp. Meth. Appl. Mech. Engr.*, Vol. 20, pp. 323–350.

Park, K. C., and Flaggs, D. L., 1984a, "An Operational Procedure for the Symbolic Analysis of the Finite Element Method," *Comp. Meth. Appl. Mech. Eng.*, Vol. 42, pp. 37–46.

Park, K. C., and Flaggs, D. L., 1984b, "A Fourier Analysis of Spurious

Mechanisms and Locking in the Finite Element Method," *Comp. Meth. Appl. Mech. & Engr.*, Vol. 46, pp. 65–81.

Park, K. C., and Flaggs, D. L., 1985, "A Symbolic Fourier Synthesis of a One-Point Integrated Quadrilateral Plate Element," *Comp. Meth. Appl. Mech. Engr.*, Vol. 48, pp. 203–236.

Park, K. C., 1984, "Symbolic Fourier Analysis Procedures for C^0 Finite Elements," in: *Innovative Methods for Nonlinear Analysis*, Pineridge Press, Swansea, pp. 269–293.

Park, K. C., Stanley, G. M., and Flaggs, D. L., 1985, "A Uniformly Reduced, Four-Noded C^0-Shell Element with Consistent Rank Corrections," *Comp. & Struct.*, Vol. 20, pp. 129–139.

Park, K. C., 1985, "An Improved Strain Interpolation for Curved C^0 Elements," to appear in the Bruce Irons Memorial Issue of *Int. J. Num. Meth. Engr.*

Pawsey, S. F., and Clough, R. W., 1971, "Improved Numerical Integration of Thick Shell Finite Elements," *Int. J. Num. Meth. Engr.*, Vol. 3, pp. 575–586.

Pian, T. H. H., and Sumihara, K., 1984, "Rational Approach for Assumed Stress Finite Elements," *Int. J. Num. Meth. Engr.*, Vol. 20, pp. 1685–1695.

Prager, W., 1973, *Introduction to Mechanics of Continua*, Dover Pub. Co., p. 12.

Ramm, E., and Sattele, J. M., 1981, "Elasto-Plastic Large Deformation Shell Analysis Using Degenerated Elements," in: *Nonlinear Finite Element Analysis of Plates and Shells*, Hughes, T. J. R., Pifko, A. and Jay, A., ed., ASME, AMD, Vol. 48, pp. 265–282.

Rankin, C. C., and Brogan, F. A., 1984, "An Element-Independent Corotational Procedure for the Treatment of Large Rotations," in: *Collapse Analysis of Structures*, Sobel, L. H., and Thomas, K., ed., ASME, New York, pp. 85–100.

Stanley, G. M., 1985, "Continuum-Based Shell Analysis," Ph.D. Thesis, Stanford University, Stanford, Calif., Lockheed Report LMSC-F035839.

Stolarski, H., and Belytschko, T., 1983, "Shear and Membrane Locking in Curved C^0 Elements," *Comp. Meth. Appl. Mech. Engr.*, Vol. 41, pp. 279–296.

Stolarski, H., Belytschko, T., Carpenter, N., and Kennedy, J. M., "A Simple Triangular Curved Shell Element," *Int. J. for Computer-Aided Eng. & Software*, Vol. 1, pp. 210–218.

Taig, I. C., 1961, *Structural Analysis by the Matrix Displacement Method*, English Electric Aviation Report No. S017.

Turner, M. J., Clough, R. W., Martin, H. C., and Topp, L. J., 1956, "Stiffness and Deflection Analysis of Complex Structures," *Journal of the Aeronautical Sciences*, Vol. 23, pp. 805–823.

Wempner, G. A., Oden, T. J., and Kross, D. A., 1968, "Finite Element Analysis of Thin Shells," *J. Eng. Mech. Div.*, ASCE, pp. 1273–1294.

Wempner, G., Talaslidis, D., and Huang, C.-M., 1982, "A Simple and Efficient Approximation of Shells Via Finite Quadrilateral Elements," ASME JOURNAL OF APPLIED MECHANICS, Vol. 49, pp. 115–120.

Wilson, E. L., 1963, "Finite Element Analysis of Two-Dimensional Structures," Ph.D. Thesis, University of California, Department of Civil Engineering, Berkeley, California.

Zienkiewicz, O. C., Taylor, R. C., and Too, J. M., 1971, "Reduced Integration Technique in General Analysis of Plates and Shells," *Int. J. Num. Meth. Engr.*, Vol. 3, pp. 275–290.

Zienkiewicz, O. C., 1971, *The Finite Element Method in Engineering Science*, McGraw-Hill, New York.

ERRATA

Erratum on "The Plastic Spin," by Y. F. Dafalias, and published in the December, 1985, issue of the ASME JOURNAL OF APPLIED MECHANICS, Vol. 52, pp. 865-871.

On page 865, 8th line from the bottom of the second column, should read "the second Piola – Kirchhoff stress."

On page 867, end of Section 3, should read $\mathbf{V} = |\mathbf{V}|^{1/3}\mathbf{I}$.

On page 871, in equation (*A*2), the term with the second bracket in the third member should read $\mathbf{Q}^T\left[\frac{D\mathbf{s}}{Dt}\right]$.

On page 868, in equation (29), the coefficients D, E and F should be substituted by $2D$, $2E$, and $2F$. Consequently, the following modifications must be made:

a) On page 868, first column, third line from bottom, should read $D = A + 2B$

b) On page 870, after equation (43), the quantity R should read $R = [X(B + C + (2X/F\tan^2 2\theta))]^{1/2}$

c) On page 870, after equation (46), the quantity Q should read

$$Q = [A(Q_1 - Q_2)^2 + BQ_2^2 + CQ_1^2 + 2FQ_3^2]^{1/2}$$

Accelerating Vector Iteration Methods

M. Papadrakakis
Senior Lecturer,
Institute of Structural Analysis
and Aseismic Research,
National Technical University,
Athens (147) Greece

This paper describes a technique for accelerating the convergence properties of iterative methods for the solution of large sparse symmetric linear systems that arise from the application of finite element method. The technique is called partial preconditioning process (PPR) and can be combined with pure vector iteration methods, such as the conjugate gradient, the dynamic relaxation, and the Chebyshev semi-iterative methods. The proposed triangular splitting preconditioner combines Evans' SSOR preconditioner with a drop-off tolerance criterion. The (PPR) is attractive in a FE framework because it is simple and can be implemented at the element level as opposed to incomplete Cholesky preconditioners, which require a sparse assembly. The method, despite its simplicity, is shown to be more efficient on a set of test problems for certain values of the drop-off tolerance parameter than the partial elimination method.

1 Introduction

Engeli et al. [3] introduced the general form of a three-term recursion formula for solving the linear system

$$\mathbf{A}\mathbf{x} = \mathbf{d} \tag{1.1}$$

as follows

$$\mathbf{x}^{(m+1)} = -\frac{1}{q_m}\mathbf{r}^{(m)} + \left(\frac{e_{m-1}}{q_m} + 1\right)\mathbf{x}^{(m)} - \frac{e_{m-1}}{q_m}\mathbf{x}^{(m-1)} \tag{1.2}$$

where A is symmetric positive definite of order $(n \times n)$, $\mathbf{r}^{(m)} = \mathbf{A}\mathbf{x}^{(m)} - \mathbf{d}$ is the residual vector and $e_{m-1} = 0$ for $m = 0$. The q_m and e_{m-1} are iteration coefficients. It was found [3, 5, 7] that a number of well known iterative methods for solving symmetric linear algebraic equations, such as the conjugate gradient, the dynamic relaxation and the Chebyshev semi-iterative methods, may be formulated in the unified way of the recursion formula (1.2). The only difference exists in the expressions by which the iteration coefficients are computed which are characteristic of the method. In earlier papers [10, 12] Papadrakakis evaluated the performance of these methods to linear and nonlinear systems of equations that arise from the finite element discretization method. For such problems only four vectors with dimension n need mainly be stored apart from the storage requirement for the elemental matrices which is very small compared to storing the global matrix. The multiplication $\mathbf{A}\mathbf{x}^{(m)}$ for the evaluation of the residual vector may be performed on an elemental level, thus avoiding storing or handling the coefficient matrix $\mathbf{A}$. It is for this reason that this family of methods is also called vector iteration methods.

The object of this work is to discuss a unified procedure for enhancing the covergence properties of the methods, to suggest a new acceleration technique for improving the response of the methods without having excessive storage requirements and to present comparative tests with other acceleration techniques.

It is well known that the effectiveness of iterative methods may be severely limited by the value of the condition number of the coefficient matrix $\mathbf{A}$. One basic idea for improving the convergence properties of the original method is that of preconditioning the initial equation in order to minimize the condition number and hence increasing the rate of convergence. Such a preconditioning of (1.1) may be visualized as follows

$$\bar{\mathbf{A}}\bar{\mathbf{x}} = \bar{\mathbf{d}} \tag{1.3}$$

with

$$\bar{\mathbf{A}} = \mathbf{W}^{-1}\mathbf{A}\mathbf{W}^{-T}, \quad \bar{\mathbf{x}} = \mathbf{W}^{T}\mathbf{x}, \quad \bar{\mathbf{d}} = \mathbf{W}^{-1}\mathbf{d} \tag{1.4}$$

The nonsingular matrix $\mathbf{R} = \mathbf{W}\mathbf{W}^{T}$ is called symmetrization matrix, $\bar{\mathbf{A}}$ is the preconditioned matrix and $\bar{\mathbf{x}}$, $\bar{\mathbf{d}}$ transformed quantities. The three-term recursion formula when applied to the preconditioned system (1.3) gives the generalized expression

$$\mathbf{x}^{(m+1)} = -\frac{1}{q_m}\mathbf{R}^{-1}\mathbf{r}^{(m)} + \left(\frac{e_{m-1}}{q_m} + 1\right)\mathbf{x}^{(m)} - \frac{e_{m-1}}{q_m}\mathbf{x}^{(m-1)} \tag{1.5}$$

with

$$\bar{\mathbf{r}}^{(m)} = \bar{\mathbf{A}}\bar{\mathbf{x}}^{(m)} - \bar{\mathbf{d}} = \mathbf{W}^{-1}\mathbf{r}^{(m)} \tag{1.6}$$

2 The Preconditioned Conjugate Gradient Method (PCG)

The CG method solves (1.1) through the minimization of the function

$$f(\mathbf{x}) = \frac{1}{2}\mathbf{x}^{T}\mathbf{A}\mathbf{x} - \mathbf{x}^{T}\mathbf{d} \tag{2.1}$$

Contributed by the Applied Mechanics Division for publication in the JOURNAL OF APPLIED MECHANICS.

Discussion on this paper should be addressed to the Editorial Department, ASME, United Engineering Center, 345 East 47th Street, New York, N.Y. 10017, and will be accepted until two months after final publication of the paper itself in the JOURNAL OF APPLIED MECHANICS. Manuscript received by ASME Applied Mechanics Division, December 21, 1984; final revision, October 28, 1985.

defined over an n-dimensional space, with the gradient vector corresponding to the residual

$$\frac{\partial f(\mathbf{x})}{\partial \mathbf{x}} = \mathbf{A}\mathbf{x} - \mathbf{d} = \mathbf{r} \tag{2.2}$$

The PCG algorithm is obtained by considering the transformed quantities of (1.4). Introducing them in (2.1) yields

$$f(\bar{\mathbf{x}}) = \frac{1}{2}\,\bar{\mathbf{x}}^T\bar{\mathbf{A}}\bar{\mathbf{x}} - \bar{\mathbf{x}}^T\bar{\mathbf{d}} \tag{2.3}$$

with

$$\frac{\partial f(\bar{\mathbf{x}})}{\partial \bar{\mathbf{x}}} = \bar{\mathbf{A}}\bar{\mathbf{x}} - \bar{\mathbf{d}} = \bar{\mathbf{r}} = \mathbf{W}^{-1}\mathbf{r} \tag{2.4}$$

The minimization of (2.3) with the CG method is obtained according to the following algorithm

$$\mathbf{u}^{(m)} = \bar{\mathbf{A}}\mathbf{p}^{(m)} \tag{2.5}$$

$$\alpha_m = [\bar{\mathbf{r}}^{(m)}]^T\bar{\mathbf{r}}^{(m)}/[\mathbf{p}^{(m)}]^T\mathbf{u}^{(m)} \tag{2.6}$$

$$\bar{\mathbf{x}}^{(m+1)} = \bar{\mathbf{x}}^{(m)} + \alpha_m\mathbf{p}^{(m)} \tag{2.7}$$

$$\bar{\mathbf{r}}^{(m+1)} = \bar{\mathbf{r}}^{(m)} + \alpha_m\mathbf{u}^{(m)} \tag{2.8}$$

$$\beta_m = [\bar{\mathbf{r}}^{(m+1)}]^T\bar{\mathbf{r}}^{(m+1)}/[\bar{\mathbf{r}}^{(m)}]^T\bar{\mathbf{r}}^{(m)} \tag{2.9}$$

$$\mathbf{p}^{(m+1)} = -\bar{\mathbf{r}}^{(m+1)} + \beta_m\mathbf{p}^{(m)} \tag{2.10}$$

with

$$\mathbf{p}^{(o)} = -\bar{\mathbf{r}}^{(o)} = \bar{\mathbf{d}}, \quad \text{for} \quad \mathbf{x}^{(o)} = 0 \tag{2.11}$$

Since $\bar{\mathbf{A}}$ is only involved in the multiplication of (2.5), explicit determination of the preconditioned matrix can be avoided. The product is replaced by three operations:

$$\text{Solution for } \mathbf{v}^{(m)} \;:\; \mathbf{W}^T\mathbf{v}^{(m)} = \mathbf{p}^{(m)} \tag{2.12}$$

$$\text{Multiply} \;:\; \mathbf{z}^{(m)} = \mathbf{A}\mathbf{v}^{(m)} \tag{2.13}$$

$$\text{Solution for } \mathbf{u}^{(m)} \;:\; \mathbf{W}\mathbf{u}^{(m)} = \mathbf{z}^{(m)} \tag{2.14}$$

Equations (2.7) and (2.10) may be combined [6] to form the recursive expression

$$\bar{\mathbf{x}}^{(m+1)} = -\alpha_m\bar{\mathbf{r}}^{(m)} + \left(\beta_{m-1}\frac{\alpha_m}{\alpha_{m-1}} + 1\right)\bar{\mathbf{x}}^{(m)} - \beta_{m-1}\frac{\alpha_m}{\alpha_{m-1}}\,\bar{\mathbf{x}}^{(m-1)} \tag{2.15}$$

which has the same form as (1.5).

3 The Preconditioned Dynamic Relaxation Method (PDR)

To enable us to handle the solution of (1.1) by the DR method, we may consider it as resulting from the static solution of structural mechanics problems. The DR is based on the fact that the static solution is the steady state part of the transient response of the system for a temporal-step load. The equation of motion governing structural dynamic response is given by

$$\mathbf{M}\ddot{\mathbf{x}} + \mathbf{C}\dot{\mathbf{x}} + \mathbf{A}\mathbf{x} = \mathbf{d} \tag{3.1}$$

where $\mathbf{M}$ is the mass matrix, $\mathbf{C}$ is the damping matrix, and a superimposed dot indicates a temporal derivative.

The static solution of (3.1), which is given by (1.1), is independent of the matrices $\mathbf{M}$ and $\mathbf{C}$. Therefore, the evaluation of these matrices is governed by the need to obtain the fastest convergence to the steady state condition. If we assume that $\mathbf{M}$ and $\mathbf{C}$ are proportional to the symmetrization matrix $\mathbf{R}$

$$\mathbf{M} = \rho\mathbf{W}\mathbf{W}^T, \quad \mathbf{C} = c\mathbf{W}\mathbf{W}^T, \tag{3.2}$$

then (3.1) becomes

$$\rho\ddot{\bar{\mathbf{x}}} + c\dot{\bar{\mathbf{x}}} + \bar{\mathbf{A}}\bar{\mathbf{x}} = \bar{\mathbf{d}} \tag{3.3}$$

where

$$\dot{\bar{\mathbf{x}}} = \mathbf{W}^T\dot{\mathbf{x}}, \quad \ddot{\bar{\mathbf{x}}} = \mathbf{W}^T\ddot{\mathbf{x}} \tag{3.4}$$

Using the following central difference expressions for the temporal derivatives

$$\dot{\bar{\mathbf{x}}}^{(m-1/2)} = [-\bar{\mathbf{x}}^{(m-1)} + \bar{\mathbf{x}}^{(m)}]/h \tag{3.5}$$

$$\ddot{\bar{\mathbf{x}}}^{(m)} = [-\dot{\bar{\mathbf{x}}}^{(m-1/2)} + \dot{\bar{\mathbf{x}}}^{(m+1/2)}]/h \tag{3.6}$$

$$\bar{\mathbf{x}}^{(m)} = [\bar{\mathbf{x}}^{(m-1/2)} + \bar{\mathbf{x}}^{(m+1/2)}]/2 \tag{3.7}$$

where h is a fixed time increment, (3.3) becomes

$$\bar{\mathbf{x}}^{(m+1/2)} = (2 - ch/\rho)/(2 + ch/\rho)\bar{\mathbf{x}}^{(m-1/2)} + 2h/(2 + ch/\rho)\mathbf{W}^{-1}\mathbf{r}^{(m)} \tag{3.8}$$

$$\mathbf{x}^{(m+1)} = \mathbf{x}^{(m)} + h\mathbf{W}^{-T}\bar{\mathbf{x}}^{(m+1/2)} \tag{3.9}$$

with

$$\bar{\mathbf{x}}^{(-1/2)} = \bar{\mathbf{x}}^{(1/2)} \text{ and } \mathbf{x}^{(o)} = 0 \tag{3.10}$$

Combining (3.8) and (3.9) we obtain the three-term recursive expression (1.5)

$$\mathbf{x}^{(m+1)} = -2h^2/(2 + ch/\rho)\mathbf{W}^{-T}\mathbf{W}^{-1}\mathbf{r}^{(m)} + 4/(2 + ch/\rho)\mathbf{x}^{(m)} - 2(ch/\rho)/(2 + ch/\rho)\mathbf{x}^{(m-1)} \tag{3.11}$$

The optimum values for the iteration parameters ρ, c, and h are expressed in terms of the extreme eigenvalues $\bar{a}$, $\bar{b}$ of $\bar{\mathbf{A}}$ and are given by

$$h^2/\rho = 4/(\bar{a} + \bar{b}), \quad ch/\rho = 4\sqrt{\bar{a}\bar{b}}/(\bar{a} + \bar{b}) \tag{3.12}$$

Similar expressions to (3.11) and (3.12) may be obtained with the preconditioned Chebyshev semi-iterative method (PCHSI) through a totally different approach. The original equation (1.1) is first preconditioned by premultiplying with $\mathbf{R}^{-1}$. Then the semi-iterative approach [15, 18] based on Chebyshev polynomials is applied to the first degree linear stationary iterative method which results from the preconditioned set of equations. The only difference exists in the characteristic coefficients which in the case of PCHSI are not constant as in PDR. The characteristic coefficients of PCHSI, however, converge to those of PDR for higher values of m.

The characteristic coefficients of the PCG are computed during the iteration process from the current values of the iteration vectors. In PDR and PCHSI, however, for the evaluation of the characteristic coefficients, estimates of the extreme eigenvalues of $\bar{\mathbf{A}}$ are required a priori. In order to avoid the computational difficulties of this eigenvalue problem, Papadrakakis [11] and Underwood [14] have proposed self-adaptive methods for the evaluation of the iteration parameters without the need to compute the extreme eigenvalues.

4 The Choice of W

It is evident that the choice of $\mathbf{W}$ has a profound effect on the convergence properties of the iterative method. The more $\mathbf{R}$ resembles $\mathbf{A}$, the rate of convergence increases, since most of the eigenvalues of $\bar{\mathbf{A}}$ would be clustered in the vicinity of 1. This, however, would not necessarily improve the overall efficiency of the method, which is also dependent on the amount of computation and on the computer storage requirements.

The simplest choice for $\mathbf{W}$ is a diagonal matrix. The particular choice for $\mathbf{W}$

$$W_i = (a_{ii})^{1/2} \tag{4.1}$$

which in diagonally dominant matrices works very effectively, corresponds to the diagonal scaling in which the diagonal elements of $\bar{\mathbf{A}}$ are equal to one.

A more efficient choice for $\mathbf{W}$ is a lower triangular matrix. In this case the evaluation of $\mathbf{R}^{-1}\mathbf{r}^{(m)}$ of (1.5) or the solution of (2.12) and (2.14) is performed by back and forward substitutions. Another crucial factor which affects the selec-

tion of **W** is its sparsity nature which is usually required to reflect that of **A**.

5 Partial Elimination (PEL)

The choice of **W** being the lower triangular matrix of the complete *LU* decomposition of **A** is ideal for the iteration process since apart from round-off errors only one iteration is needed. The most efficient way of transforming a symmetric positive definite matrix into two triangular matrices is the Choleski decomposition in which

$$\mathbf{A} = \tilde{\mathbf{L}}\tilde{\mathbf{L}}^T \tag{5.1}$$

For large sparse matrices the calculation of $\tilde{\mathbf{L}}$ or $\tilde{\mathbf{L}}^T$ is both time and storage consuming because the sparsing pattern of the original matrix is destroyed. In order to retain the sparsity of **A** one can do incomplete Choleski decomposition in which a previously defined sparsity pattern is enforced on $\tilde{\mathbf{L}}$ or $\tilde{\mathbf{L}}^T$. The coefficient matrix is factorized according to

$$\mathbf{A} = \mathbf{L}\mathbf{L}^T - \mathbf{E}, \text{ and } \mathbf{W} = \mathbf{L} \tag{5.2}$$

with **L** being a lower triangular matrix. The incomplete Choleski (IC) factorization was first described by Varga [16] as a method of constructing a regular splitting of certain finite difference operators. The simplest case of an IC decomposition is to force **L** to have the same sparsity pattern as **A**. Thus, the elements of **L** which correspond to zero elements of **A** are neither calculated nor stored. It was found, however, that discarding off-diagonal elements could sometimes lead to loss of positive definiteness and hence a breakdown of the factorization process. Techniques to avoid this shortcoming have been proposed by Manteuffel [9] and Wong [17].

Tuff and Jennings [13] have introduced the concept of partial elimination. This technique is an IC decomposition but the choice of which elements to retain in **L** is not made by their position in the matrix but by their magnitude. In order to retain the positive definiteness of this factorization process, Ajiz and Jennings [1] have recently proposed the robust partial elimination method in which modifications to the diagonal elements of **A** are introduced whenever the drop off tolerance criterion is activated. The elements of $\mathbf{L}^T$ are computed by the following procedure:

$$a_{ij}^* = a_{ij} - \sum_{k=1}^{i-1} l_{ki} l_{kj} \quad \text{for} \quad j = i+1, \ldots n \tag{5.3}$$

and then setting

$$l_{ii}^2 = \tilde{a}_{ii}, \quad l_{ij} = a_{ij}^*/l_{ii} \quad \text{if} \quad a_{ij}^* \text{ is large}$$

or

$$l_{ij} = 0 \qquad \text{if} \quad a_{ij}^* \text{ is small} \tag{5.4}$$

The criterion used to decide whether a_{ij}^* is large or small is to specify a drop off tolerance ψ and then to consider all elements to be small which satisfy

$$a_{ij}^{*2} < \psi \tilde{a}_{ii} \tilde{a}_{jj} \tag{5.5}$$

If this criterion is satisfied, then the diagonal elements of **A**, which correspond to i and j, are modified according to

$$\tilde{a}_{ii} = a_{ii}^* + (\tilde{a}_{ii}/\tilde{a}_{jj})^{1/2} |a_{ij}^*| \tag{5.6}$$

$$\tilde{a}_{jj} = a_{jj} + (\tilde{a}_{jj}/\tilde{a}_{ii})^{1/2} |a_{ij}^*| \tag{5.7}$$

6 Partial Preconditioning (PPR)

Under the assumption that $\mathbf{A} = \mathbf{D} - \mathbf{C}_L - \mathbf{C}_U$, where **D**, $-\mathbf{C}_L$, and $-\mathbf{C}_U$ represents, respectively, the diagonal, strictly lower and upper triangular parts of **A**, Evans' [4] transformation matrix takes the form

$$\mathbf{W} = (\mathbf{D} - \omega \mathbf{C}_L)\mathbf{D}^{-1/2} \tag{6.1}$$

in which ω is an acceleration parameter. The great advantage of this preconditioning method is its simplicity, since no alterations are needed in the original coefficient matrix **A** for the evaluation of **W**. It can also be noticed that the sparseness of **A** is retained in **W** and $\mathbf{W}^T$.

The PPR method combines the simplicity of Evans' preconditioning method with the reduced storage requirements of PEL as they appear in **W**. Evans' preconditioning, despite its simplicity in forming **W**, needs, however, storage space which is equivalent to half of matrix **A**. In this respect the application of this transformation method to the generalized three-term recursion equations (1.5) contradicts the great advantage of this family of methods, which is their vectorial nature. The same arguments are also valid for PEL in that although storage requirements are controlled through the drop-off tolerance criterion, storage space must be allowed for **A** in order for the Choleski decomposition to be performed. In PPR the transformation matrix contains elements of **A** without any modification but the choice of which elements to be retained is made, as in PEL, by their magnitude. When the drop-off tolerance

$$a_{ij}^2 < \psi a_{ii} a_{jj} \tag{6.2}$$

is not satisfied, the off-diagonal term a_{ij} is retained in **W**. The new transformation matrix is denoted by

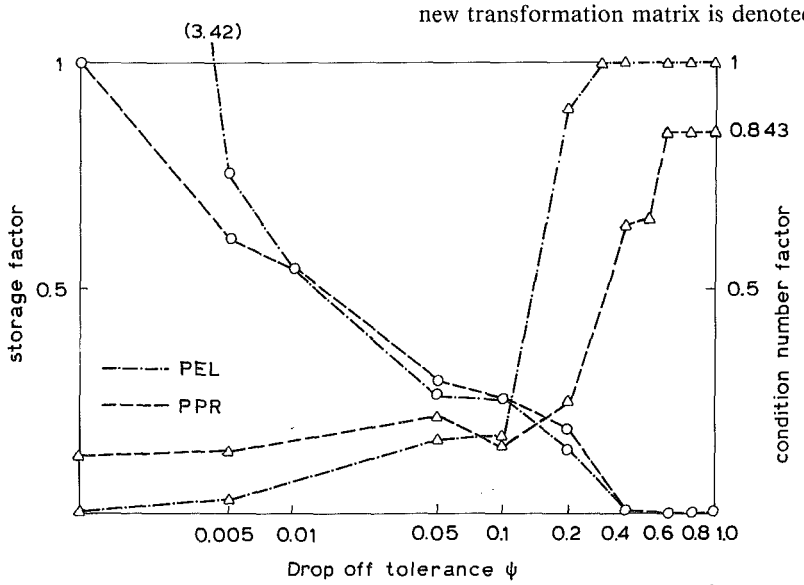

Fig. 1 Example 1: storage and condition number factors for PEL end PPR; o, storage factor relative to the off-diagonal nonzero elements of A; Δ, condition number factor of Ã relative to the diagonally scaled Ã

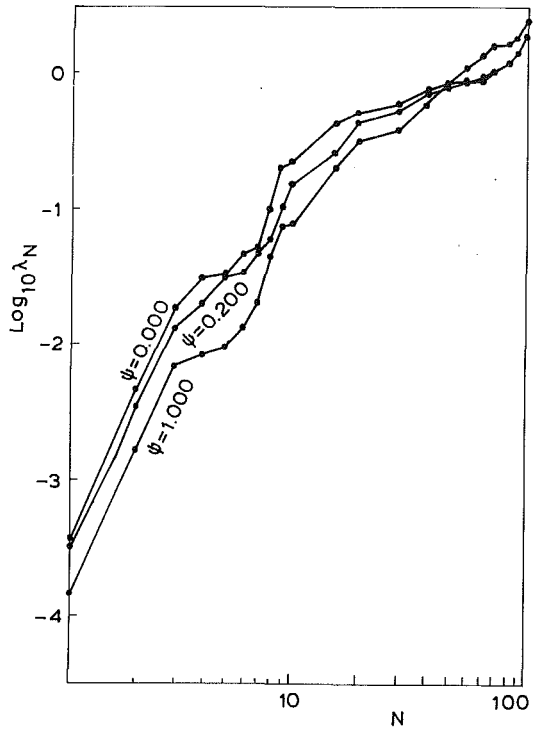

Fig. 2 Eigenvalue spectrum for PPR of example 1

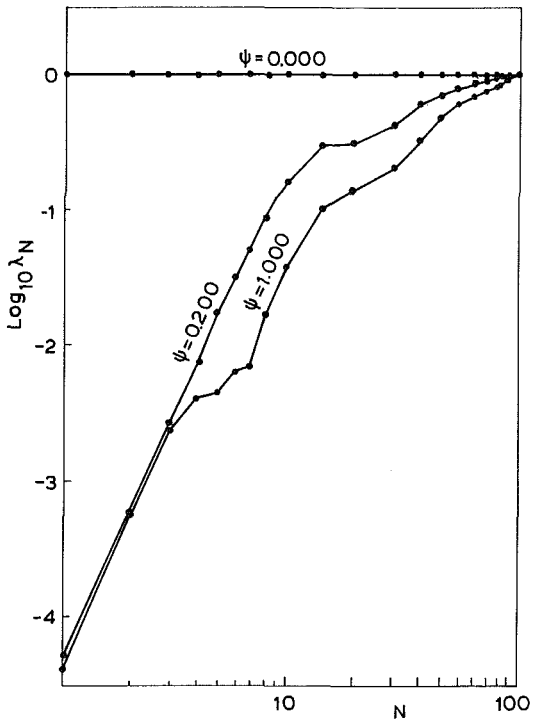

Fig. 3 Eigenvalue spectrum for PEL of example 1

$$\mathbf{W} = (\mathbf{D} - \omega \mathbf{C}_p)\mathbf{D}^{-1/2} \tag{6.3}$$

The selection of the nonzero elements of **W** does not require the formation or the storage of **A**, because for finite element discretizations, each coefficient a_{ij} may be formed on the elemental level. It is also possible, in certain types of problems, to specify a priori the elements to be retained by considering their topological origin as criterion instead of choosing a specific ψ value and checking all off-diagonal elements of **A**.

The only restriction which is placed upon the preconditioned $\bar{\mathbf{A}}$, in order for the described iterative methods to converge, is that it should be symmetric and positive definite. The first condition is satisfied automatically by the way $\bar{\mathbf{A}}$ is constructed from **A**. The second condition is easily proved as follows: if **v** is an auxiliary vector, and assuming that **W** of (6.3) is nonsingular, then

$$\mathbf{v}^T \bar{\mathbf{A}} \mathbf{v} = \mathbf{u}^T \mathbf{A} \mathbf{u} > 0 \tag{6.4}$$

in which

$$\mathbf{u} = \mathbf{W}^{-T} \mathbf{v} \tag{6.5}$$

In the very rare case that **W** of (6.3) becomes singular, an adjustment of the diagonal terms of **W**, in accordance with the robust PEL method, is employed.

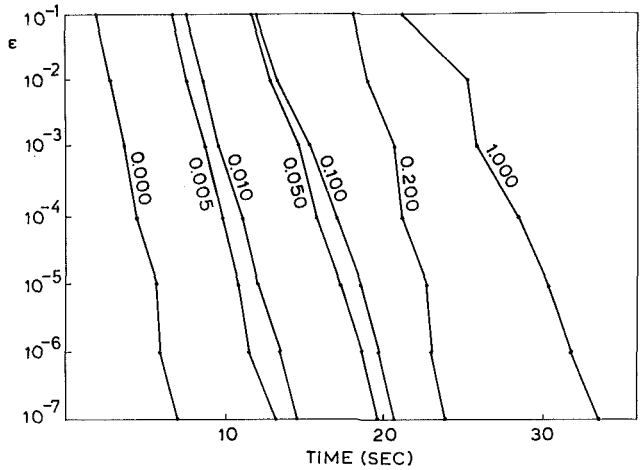

Fig. 4 Example 1: convergence paths for different ψ of PCG-PEL (PCG iterations only)

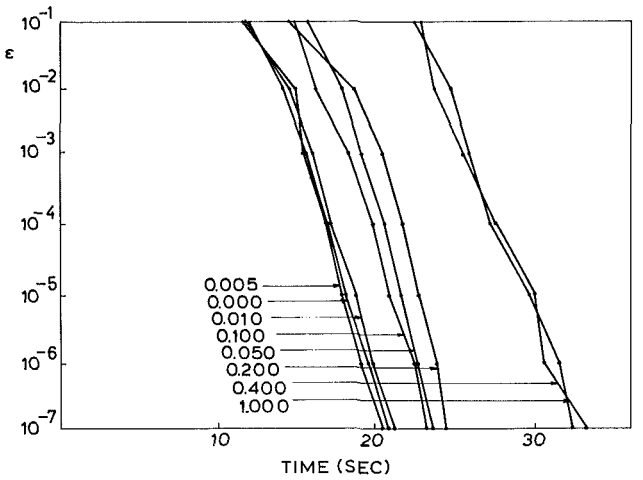

Fig. 5 Example 1: convergence paths for different ψ of PCG-PPR (PCG iterations only)

7 Numerical Experiments

Previous experiments [10] on CHSI and DR showed almost the same efficiency for the two methods with a marginal superiority for DR. For this reason numerical experiments are performed for PCG and PDR only. The iterative procedures compared in this section are denoted by abbreviated names with the second component denoting the method used for the evaluation of **W**. PEL stands for the robust PEL and in PPR the accelerating parameter was set to one. A compact storage scheme is used for W in which the nonzero components of **W** are stored in a vector which is accompanied by an auxiliary identification vector. The convergence properties of the

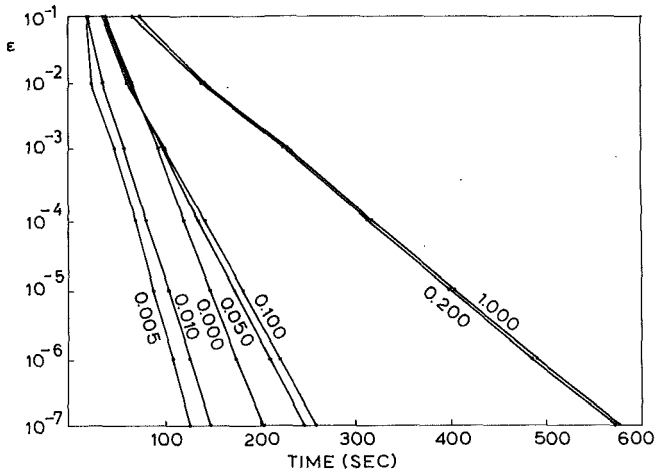

Fig. 6 Example 1: convergence paths for different ψ of PDR-PEL (PDR iterations only)

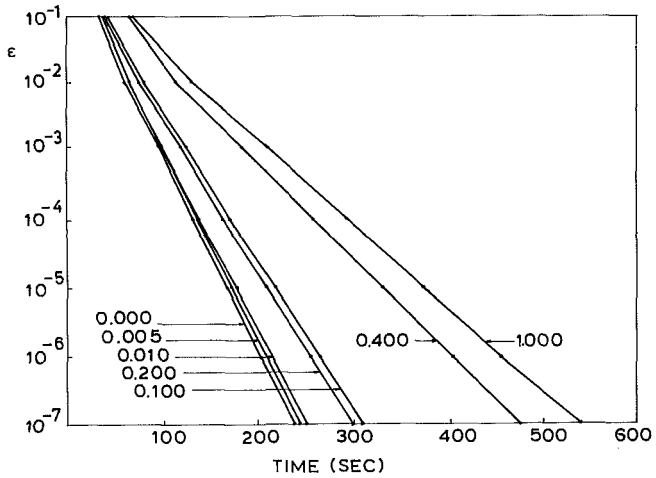

Fig. 7 Example 1: convergence paths for different ψ of PDR-PPR (PDR iterations only)

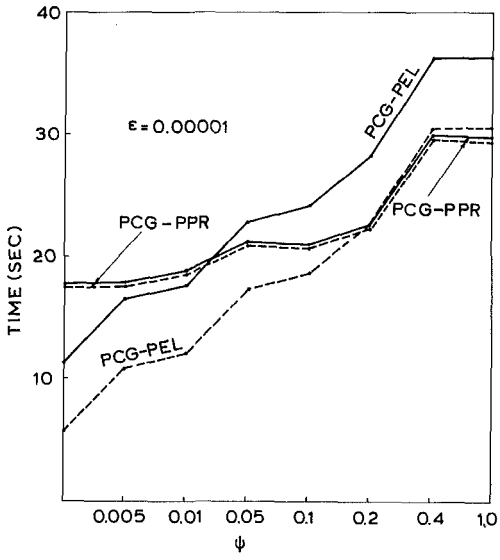

Fig. 8 Example 1: convergence study of PCG-PEL and PCG-PPR;
——— time for PCG iterations and computation of W;
- - - time for PCG iterations only

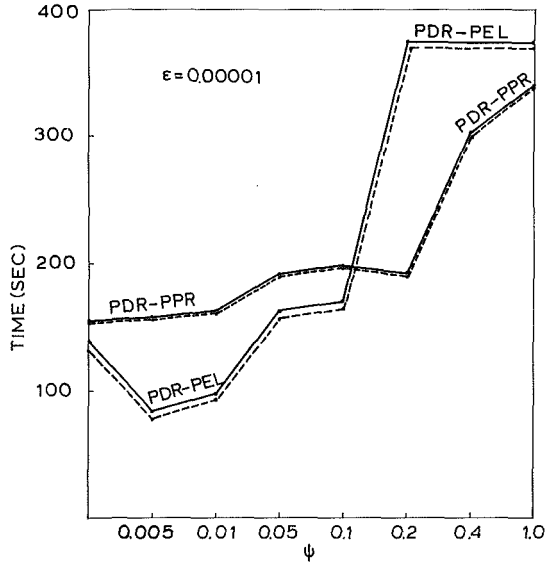

Fig. 9 Example 1: convergence study of PDR-PEL and PDR-PPR;
——— time for PDR iterations and computation of W;
- - - time for PDR iterations only

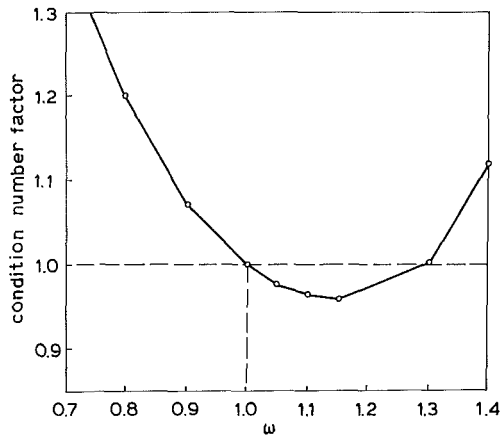

Fig. 10 Example 1: variation of condition number factor of $\bar{A}$ with ω for $\psi = 0$

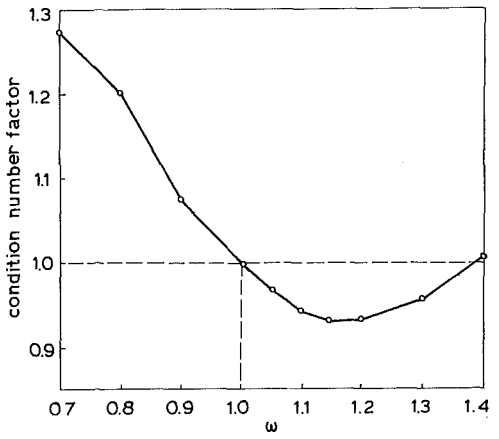

Fig. 11 Example 1: variation of condition number factor of $\bar{A}$ with ω for $\psi = 0.2$

methods have been tested on a set of rigidly jointed plane frames with shear walls. These particular examples were chosen because, in this type of problem, both sway and axial stiffnesses are present and the classical iterative methods converge very slowly on account of their poor conditioning. Examples 1 to 3 are three bay plane frames with 108, 648 and 1080 degrees of freedom and 1.78×10^5, 8.8×10^5, and 1.31×10^7, respectively, the condition number of the diagonal-

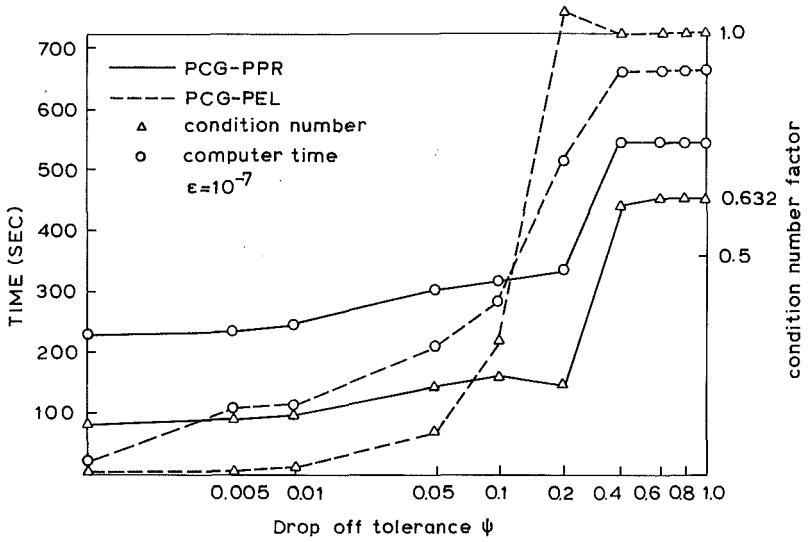

Fig. 12 Example 2: condition number factors for PEL and PPR, and total computer time to convergence for PCG-PEL and PCG-PPR

ly scaled stiffness matrices. Example 4 is a seven bay plane frame with 1071 degrees of freedom and 4.16×10^5 condition number. The semibandwidth for examples 1 to 3 is 12 and that for example 4 is 24.

Figure 1 shows for example 1 the condition number of $\bar{\mathbf{A}}$ in relation to that of the diagonally scaled $\mathbf{A}$ and the nonzero terms of $\mathbf{W}$ in relation to the off-diagonal nonzero terms of $\mathbf{A}$, with respect to the parameter ψ. In this figure and all subsequent ones, for ease of reading, the graphs have been shown as straight lines between each of the result points. It is shown that the improvement achieved by PEL on the condition number of $\mathbf{A}$ is better than the corresponding improvement achieved by PPR for small values of ψ while the opposite is happening for large values of ψ. Storage requirements, remain the same for PEL and PPR except for very small values of ψ where PEL needs much more storage. Figures 2 and 3 show the complete eigenvalue spectrum of $\bar{\mathbf{A}}$ for PPR and PEL with respect to three characteristic values of ψ. N is the number of the eigenvalue in ascending order drown in logarithmic scale and λ_N is its corresponding value. Figures 4–7 show the convergence paths of the methods for different ψ. Iterations were continued until the error tolerance criterion $\|\mathbf{r}^{(m)}\|/\|\mathbf{d}\| < \epsilon$ was satisfied. Since the number of iterations do not reflect the efficiency of the method, due to different calculations performed in each case inside an iterative loop, the computer time is used as a measure of comparison. The computational work has been carried out on the CDC Cyber 171-8 computer. From Figs. 4–7 it can be seen that in both PCG and PDR the convergence properties of the methods are improved almost invariably with the condition number of $\bar{\mathbf{A}}$. In Fig. 4 it can also be seen that the PCG-PEL with $\psi = 0$ does not converge in one iteration as would have been expected since all eigenvalues of $\bar{\mathbf{A}}$ are unity. The convergence to $\epsilon = 10^{-7}$ takes place after 27 iterations and this is attributed to round-off errors which affect considerably the performance of CG. For the same test problem, however, without the shear wall, the method converged in just one iteration.

Figures 8–9 show a comparative study of the convergence efficiency of the methods. Broken lines indicate the computing time that is taken up in the PCG or PDR part of the algorithm only, while solid lines incorporate the time required for the creation of $\mathbf{W}$ as well. From Fig. 8 it can be seen that the performance of PCG–PEL, as indicated by the broken lines, is the same as that of PCG–PPR for larger ψ despite the corresponding increase of the condition number of $\bar{\mathbf{A}}$. This phenomenon does not occur with the performance of PDR which follows in reverse order the condition number of $\bar{\mathbf{A}}$

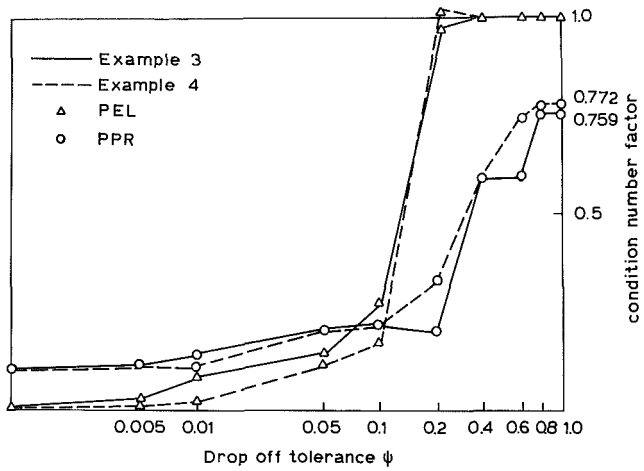

Fig. 13 Examples 3 and 4: condition number factors for PEL and PPR

(Fig. 9). In Figs. 10–11, the condition number of $\bar{\mathbf{A}}$ for different ω relative to that of $\bar{\mathbf{A}}$ when $\omega = 1$, is plotted for the PPR.

In Fig. 12 it can be seen that similar performance as previously is exhibited by PEL and PPR for example 2. Again PCG–PPR performs better for large values of ψ and PCG–PEL for small values of ψ. Due to space limitations the performance of PDR is not shown but it is qualitatively similar to that of Fig. 9. Finally, Fig. 13 reaffirms the results obtained previously and indicates that the improvement of the condition number in PPR is better for more ill-conditioned problems.

9 Concluding Remarks

Techniques for improving the convergence properties of a number of vector iterative methods are discussed and compared. The improvement of the original method is achieved by a transformation of the initial equations in order to improve the conditioning of the coefficient matrix. This achievement, however, should not violate the very nature of these methods, which is strictly vectorial, requiring the storage of a few vectors only with dimension n. In this spirit the proposed PPR is not strictly comparable with PEL. The great advantage of PPR, when finite element idealization is used, apart from its ease of implementation, is that W need not be constructed from $\mathbf{A}$. The components of $\mathbf{W}$ may be obtained by working on the elemental level rather than on the whole matrix. Packed

storage schemes could be used to decrease the storage requirements for PEL but this would result in an increase of the computing time.

From the experimental results of the previous section, the following conclusions may be drawn:

(1) PEL performs better in reducing the condition number of $\bar{\mathbf{A}}$ for low values of ψ, while PPR produces better results for values of ψ in the vicinity of 0.1 to 1.0.

(2) The convergence properties of the accelerated methods appear to improve almost monotonically with the decrease of the condition number of $\bar{\mathbf{A}}$.

(3) The results reaffirm the superiority of CG over all other iterative methods for the solution of linear problems.

(4) The value of ω_{opt} in PPR remains in the neighborhood of 1 and is constantly slightly greater than 1. The additional improvement of the condition number of $\bar{\mathbf{A}}$ is not very significant, thus justifying the a priori selection of $\omega = 1$.

(5) The proposed PPR technique proved superior to PEL, for both PCG and PDR, when the total nonzero terms in $\mathbf{W}$ are less than n. This means that by increasing the storage requirements by approximately four more vectors to provide space for the location array as well, the convergence efficiency of the simple iterative methods could be dramatically increased. Bearing in mind the ease of implementation and evaluation of $\mathbf{W}$, we may conclude that the PPR is a very powerful technique for accelerating vector iteration methods, particularly when ill-conditioned problems are considered and excessive storage space is not available.

References

1 Ajiz, M. A., and Jennings, A., 1984, "A Robust Incomplete Choleski-Conjugate Gradient Algorithm," *International Journal for Numerical Methods in Engineering*, Vol. 20, pp. 949-966.

2 Concus, P., Golub, G. H., and O'Leary, D. P., 1978, "Numerical Solution of Nonlinear Elliptic Partial Differential Equations by a Generalized Conjugate Gradient Method," *Computing*, Vol. 19, 1978, pp. 321-339.

3 Engeli, M., Ginsburg, T., Rutishauser, H., and Stiefel, E., 1959, *Refined Iterative Methods for Computation of the Solution and the Eigenvalues of Self-Adjoint Boundary Value Problems*, Birkhauser Verlag, Basel/Stuttgart.

4 Evans, D. J., 1967, "The Use of Pre-conditioning in Iterative Methods for Solving Linear Equations with Symmetric Positive Definite Matrices," *Journal of the Institute of Mathematics and its Applications*, Vol. 4, pp. 295-314.

5 Golub, G. E., and Varga, R. S., 1961, "Chebyshev Semi-iterative Methods, Successive Overrelaxation Iterative Methods, and Second Order Richardson Iterative Methods," *Numerische Mathematik*, Vol. 3, pp. 147-168.

6 Hageman, L. A., and Young, D. M., 1981, *Applied Iterative Methods*, Academic Press, p. 145.

7 Hodgins, W. R., 1967, "On the Relation Between DR and Semi-iterative Matrix Methods," *Numerische Mathematik*, Vol. 9, pp. 446-451.

8 Jennings, A., and Malik, G. M., 1977, "Partial Elimination," *Journal of the Institute of Mathematics and its Applications*, Vol. 20, pp. 307-316.

9 Manteuffel, T. A., 1980, "An Incomplete Factorization Technique for Positive Definite Linear Systems," *Mathematics of Computation*, Vol. 34, pp. 473-497.

10 Papadrakakis, M., 1982, "A Family of Methods with Three-Term Recursion Formulae," *International Journal for Numerical Methods in Engineering*, Vol. 18.

11 Papadrakakis, M., 1981, "A Method for the Automatic Evaluation of the Dynamic Relaxation Parameters," *Computer Methods in Applied Mechanics and Engineering*, Vol. 25, pp. 35-48.

12 Papadrakakis, M., 1979, "Methods with Three-Term Recursion Formulae for the Analysis of Cable Structures," *IASS, World Congress on Shell and Spatial Structures*, Madrid, pp. 3.65-3.78.

13 Tuff, A. D., and Jennings, A., 1973, "An Iterative Method for Large Systems of Linear Structural Equations," *International Journal for Numerical Methods in Engineering*, Vol. 7, pp. 175-183.

14 Underwood, P., 1983, "Dynamic Relaxation - A Review," *Computational Methods for Transient Response Analysis*, Belytschko, T., and Hughes, T. J. R., eds., North-Holland, pp. 245-265.

15 Varga, 1962, *Matrix Iterative Analysis*, Prentice-Hall, Englewood Cliffs, N.J.

16 Varga, R. S., 1960, "Factorization and Normalized Iterative Methods," *Boundary Problems in Differential Equations*, Langer, R. E., ed., Univ. of Wisconsin Press, Madison.

17 Wong, Y. S., 1979, in *Numerical Methods in Thermal Problems*, Lewis, R. W., and Morgan, K., eds., Pineridge Press, England, pp. 967-979.

18 Young, D. M., 1972, *Iterative Solution of Large Linear Systems*, Academic Press, New York.

S. Sharp
Research Associate,
Department of Civil and
Mineral Engineering,
University of Minnesota,
Minneapolis, Minn. 55455

S. L. Crouch
Professor,
Department of Civil and
Mineral Engineering,
University of Minnesota,
Minneapolis, Minn. 55455

Boundary Integral Methods for Thermoelasticity Problems

The boundary integral method for solving transient heat flow problems is extended to calculate thermally induced stresses and displacements. These results are then corrected by means of an elastostatic solution to satisfy the boundary conditions.

Introduction

In recent years several boundary integral methods [1, 2] have been proposed for solving two dimensional transient heat flow problems. In order to use these methods to calculate thermo-mechanical effects, however, it has been necessary to determine the instantaneous influence of the temperature [3, 4], requiring the evaluation of singular body integrals. In this paper we show how to extend the boundary integral method to avoid this, providing a more natural framework in which to solve linear quasi-static thermoelasticity problems.

The Problem

The classical quasi-static thermoelastic problem for a body Ω bounded by the contour S (Fig. 1) may be formulated in terms of the temperature and displacement fields θ and u_i (i = 1 or 2) as follows:

$$\theta_{,jj}(\mathbf{x},t)-\frac{1}{K}\frac{\partial\theta}{\partial t}(\mathbf{x},t)=-\frac{1}{K}f(\mathbf{x},t) \tag{1}$$

$$\mu u_{i,jj}(\mathbf{x},t)+(\mu+\lambda)u_{j,ij}(\mathbf{x},t)$$
$$=(3\lambda+2\mu)2\alpha\theta_{,i}(\mathbf{x},t)-F_i(\mathbf{x},t)\ \mathbf{x}\in\Omega,t>0 \tag{2}$$

where $\mathbf{n}$ is the unit vector in the outward normal direction from S, K is the diffusivity of the conducting material, α the coefficient of thermal expansion, f the distributed body heat source, F the distributed body mechanical force, and

$$\mu=G$$
$$\lambda=2G\frac{\nu}{(1-2\nu)}$$

where G and ν are the shear modulus and Poisson's ratio, respectively.

Solutions to equations (1) and (2) are subject to the initial condition

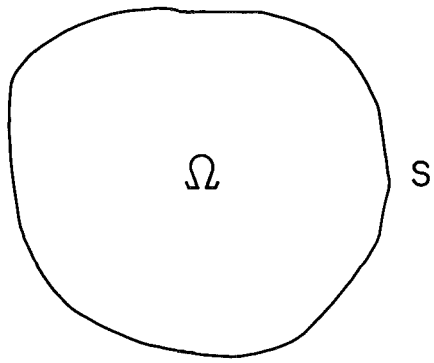

Fig. 1 The problem domain

$$\theta(\mathbf{x},0)=\theta_0(\mathbf{x})\qquad \mathbf{x}\in\Omega$$

and the thermal boundary conditions

$$\theta(\mathbf{s},t)=g(\mathbf{s},t)$$

or $\mathbf{s}\in S,t>0$

$$\frac{\partial\theta(\mathbf{s},t)}{\partial n}=d(\mathbf{s},t)$$

or compatible combinations of these two, and the mechanical constraints

$$u_i(\mathbf{s},t)=U_i(\mathbf{s},t)$$

or $\mathbf{s}\in S,t>0$

$$\sigma_i(\mathbf{s},t)=T_i(\mathbf{s},t)$$

or compatible combinations of this pair, where σ_i is the traction vector and where d, g, U_i and T_i are prescribed boundary functions.

Boundary Integral Formulae for Heat Conduction

The direct boundary integral formula for the temperature may be written [1, 2] as

$$\theta(\mathbf{x},t)=K\int_0^t\int_S\left[\tilde{\theta}(\mathbf{x},t;s,\tau)\frac{\partial\theta(\mathbf{s},\tau)}{\partial n}-\frac{\partial\tilde{\theta}(\mathbf{x},t;\mathbf{s},\tau)}{\partial n}\theta(\mathbf{s},\tau)\right]ds d\tau$$
$$+\int_\Omega[\tilde{\theta}(\mathbf{x},t;\xi,0)\theta(\xi,0)]d\xi+\int_0^t\int_\Omega[\tilde{\theta}(\mathbf{x},t;\xi,\tau)f(\xi,\tau)]d\xi d\tau \tag{3}$$

Contributed by the Applied Mechanics Division for presentation at the Winter Annual Meeting, Anaheim, CA, December 7-12, 1986, of the American Society of Mechanical Engineers.

Discussion on this paper should be addressed to the Editorial Department, ASME, United Engineering Center, 345 East 47th Street, New York, N.Y. 10017, and will be accepted until two months after final publication of the paper itself in the JOURNAL OF APPLIED MECHANICS. Manuscript received by ASME Applied Mechanics Division, December 21, 1984; final revision June 4, 1985. Paper No. 86-WA/APM-2.

where

$$\bar{\theta}(\mathbf{x},t;\xi,\tau)=\frac{1}{[4\pi K(t-\tau)]}\exp\left(\frac{-|\mathbf{x}-\xi|^2}{[4K(t-\tau)]}\right) \quad t>\tau$$
$$=0 \quad t=0 \ \ \mathbf{x}\neq\xi \qquad (4)$$
$$=0 \quad t<\tau$$

is the fundamental solution of equation (1), i.e.,

$$\bar{\theta}_{,jj}(\mathbf{x},t)-\frac{1}{K}\frac{\partial\bar{\theta}}{\partial t}(\mathbf{x},t)=-\frac{1}{K}\delta(\mathbf{x}-\xi)\delta(t-\tau)$$

where δ is the Dirac delta function. $\bar{\theta}$ may be interpreted as the temperature at point $\mathbf{x}$ in an infinite body at time t, produced by a heat pulse location at point ξ at time τ.

The unknown boundary functions can be found directly from equation (3) by allowing $\mathbf{x}$ to approach S, and by solving the resulting integral equation. An alternative formula derived from equation (3) [2] may be written as

$$\bar{\theta}(\mathbf{x},t)=K\int_0^t\int_S\left[\bar{\theta}(\mathbf{x},t;\mathbf{s},\tau)Q(\mathbf{s},\tau)\right]d\mathbf{s}\,d\tau$$
$$+\int_0^t\int_\Omega[\bar{\theta}(\mathbf{x},t;\xi,\tau)f(\xi,\tau)]d\xi d\tau+\int_\Omega[\bar{\theta}(\mathbf{x},t;\xi,0)\theta_0(\xi)]d\xi \qquad (5)$$

where $Q(\mathbf{s},\tau)$ is the strength of a single layer boundary heat source. A similar expression can be written for the case of a double layer source. Boundary element methods using these fictitious devices are known as indirect methods because the unknown boundary functions are not the direct product of the solution procedure, but must be found after the source strengths have been determined.

The Thermoelastic Calculations

The solution of equation (2) for the function u_i may be written as

$$u_i=u_i^{(\theta)}+u_i^{(F)}+u_i^{(*)}$$

where $u_i^{(F)}$ and $u_i^{(\theta)}$ are the particular solutions corresponding to the terms involving F and θ, respectively, in equation (2), and $u_i^{(*)}$ is the homogeneous solution. The latter may be dealt with by any numerical procedure (see later) while $u_i^{(F)}$ can always be written as a volume integral, or under certain conditions [5] as a boundary integral. We focus here on determining the thermal effects upon displacements and stresses, i.e., on calculating the displacement and stress terms $u_i^{(\theta)}$ and $\sigma_{ij}^{(\theta)}$, respectively.

In accordance with the development of linear quasi-static thermoelasticity theory [6], we begin by writing

$$u_i^{(\theta)}=\phi_{,i} \qquad (6)$$

where ϕ is known as the thermoelastic displacement potential. Substituting this into equation (2) (with $F = 0$) we obtain

$$\phi_{,ii}=m\theta \qquad (7)$$

where

$$m=\frac{(3\lambda+2\mu)}{(\lambda+2\mu)}\alpha$$

Since θ is given by equations (3) or (5), we may solve this equation by means of the fundamental solution

$$\eta(\mathbf{x},\xi)=\frac{1}{4\pi}Ln|\mathbf{x}-\xi|^2$$

for Laplace's equation. Thus

$$\phi(\mathbf{x},t)=m\int_\Omega\eta(\mathbf{x},\xi)\theta(\xi,t)d\xi \qquad (8)$$

Now from equations (6) and (7), and the strain-displacement relation

$$e_{ij}=\frac{1}{2}(u_{i,j}+u_{j,i})$$

we have

$$e_{ij}=\phi_{,ij} \text{ and } e_{ii}=m\theta.$$

Using the constitutive relation for quasi-static thermoelasticity

$$\sigma_{ij}=2\mu e_{ij}+[\lambda e_{kk}-(3\lambda+2\mu)\alpha\theta]\delta_{ij}$$

or

$$\sigma_{ij}=2\mu[\phi_{ij}-m\theta\delta_{ij}], \qquad (9)$$

we can find the functions $u_i^{(\theta)}$ and $\sigma_{ij}^{(\theta)}$ directly by differentiating the solution (8) of equation (7), since from equations (6) and (9) we could write

$$u_i^{(\theta)}(\mathbf{x},t)=m\left[\int_\Omega\eta(\mathbf{x},\xi)\theta(\xi,t)d\xi\right]_{,i} \qquad (10a)$$

$$\sigma_{ij}^{(\theta)}(\mathbf{x},t)=2\mu m\left[\int_\Omega\eta(\mathbf{x},\xi)\theta(\xi,t)d\xi\right]_{,ij}-2\mu m\theta\delta_{ij} \qquad (10b)$$

It is important to note that the irrotational form of the displacement in equation (6) does not imply loss of generality since the balance of the temperature effects is incorporated into the homogeneous solution $u_i^{(*)}$. Expressions in equation (10) are equivalent to those treating the temperature gradient as a distributed body force [3, 4] and provide an apparently efficient way of determining the thermomechanical response to the temperature distribution.

A Boundary Integral Approach

It is also possible to calculate the thermally induced values by means of a boundary integral. We begin by examining the thermoelastic response of an infinite elastic medium to an instantaneous heat pulse.

If we set $\theta(\mathbf{x},t) = \bar{\theta}(\mathbf{x}, t'; \mathbf{w}, \tau)$ in equation (7) we find that the thermoelastic displacement potential at time t' due to a heat pulse that occurs at time $\tau < t'$ is

$$\phi(\mathbf{x},t';\mathbf{w},\tau)=m[KE(\mathbf{x},t';\mathbf{w},\tau)+\eta(\mathbf{x},\mathbf{w})]=\bar{\phi}(\mathbf{x},t';\mathbf{w},\tau)$$

where

$$E(\mathbf{x},t';\mathbf{w},\tau)=\int_\tau^{t'}\bar{\theta}(\mathbf{x},t';\mathbf{w},\tau)dt'=-\frac{1}{(4K\pi)}E_i\left[\frac{-|\mathbf{x}-\mathbf{w}|^2}{(4K(t'-\tau))}\right]$$

and

$$E_i(-y)=\gamma+Ln(y^2)+\sum_{k=1}^{\infty}\frac{(-y)^k}{(k\ k!)}$$

is the exponential integral, with $\gamma = 0.57721$ (Euler's constant). Note that at $\mathbf{x} = \mathbf{w}$, ϕ is continuous and differentiable to the second order at least.

It follows then from equations (6) and (9) that

$$\bar{u}_i(\mathbf{x},t';\mathbf{w},\tau)=\frac{m}{2\pi}X_i h(\mathbf{x},t';\mathbf{w},\tau)$$

and

$$\bar{\sigma}_{ij}(\mathbf{x},t';\mathbf{w},\tau)=\frac{\mu m}{\pi r}\left[h(\mathbf{x},t';\mathbf{w},\tau)(\delta_{ij}-2X_iX_j)\right]$$
$$+2\mu m(X_iX_j-\delta_{ij})\theta$$

where

$$\mathbf{x}=(x_1,x_2),\mathbf{w}=(w_1,w_2),r=|\mathbf{x}-\mathbf{w}|,X_i=(x_i-w_i)/r$$

and

$$h(\mathbf{x},t';\mathbf{w},\tau)=\frac{1}{r}\left[1-\exp\left(\frac{-r^2}{[4K(t'-\tau)]}\right)\right] \quad t'>\tau$$

These expressions represent the mechanical effects of an in-

stantaneous heat pulse occurring at a point w at time τ on a point $\mathbf{x}$ at time $t' > \tau$ in an infinite medium, and are analogous to the fundamental heat solution $\bar{\theta}$ given in equation (4). Consequently, they can be used to generate solutions of the thermoelastic problem in precisely the same manner as was the function θ. By extension, they can also be generalized to comprise boundary integral formulae corresponding to equations (3) and (5).

Mathematically this can be derived by using the identity

$$\theta(\xi,t) = \int_0^t \frac{\partial\theta(\xi,t')}{\partial t}\, dt' + \theta(\xi,0)$$

in equation (8) giving

$$\phi(\mathbf{x},t) = m\int_\Omega \eta(\mathbf{x},\xi)\left[\int_0^t \frac{\partial\theta(\xi,t')}{\partial t}\, dt' + \theta(\xi,0)\right] d\xi$$

which with equation (1) becomes

$$= m\int_\Omega \eta(\mathbf{x},\xi)\left[\int_0^t [K\theta_{,jj}(\xi,t') + f(\xi,t')]dt' + \theta(\xi,0)\right] d\xi$$

Changing the order of integration, using Green's second theorem in the first term, and recognizing that

$$\eta_{,ii}(\mathbf{x},\xi) = \delta(\mathbf{x}-\xi)$$

we obtain

$$\phi(\mathbf{x},t) = mK\int_0^t\int_\Omega \left[\eta(\mathbf{x};\mathbf{s})\frac{\partial\theta(\mathbf{s},t')}{\partial n} - \frac{\partial\eta(\mathbf{x};s)}{\partial n}\theta(\mathbf{s},t')\right] ds dt'$$

$$+ m\int_0^t\int_\Omega \eta(\mathbf{x};\xi) f(\xi,t')\, d\xi dt' + m\int_\Omega \eta(\mathbf{x};\xi)\theta(\xi,0)\, d\xi$$

$$+ mK\int_0^t \theta(\mathbf{x},t')dt' \qquad (11)$$

In order to avoid the use of field temperature values we simply use expressions (3) or (5) in place of $\theta(\mathbf{x},t)$ in the final term. For example if we use the expression (3) we have that

$$\phi(\mathbf{x},t) = K\int_0^t\int_S \left[\bar{\phi}(\mathbf{x},t;\mathbf{s},\tau)\frac{\partial\theta(\mathbf{s},\tau)}{\partial n} - \frac{\partial\bar{\phi}(\mathbf{x},t;\mathbf{s},\tau)}{\partial n}\theta(\mathbf{s},\tau)\right] ds d\tau$$

$$+ \int_\Omega [\bar{\phi}(\mathbf{x},t;\xi,0)\theta(\xi,0)]d\xi + \int_0^t\int_\Omega [\bar{\phi}[\mathbf{x},t;\xi,\tau)f(\xi,\tau)]d\xi d\tau \qquad (12)$$

and that

$$u^{(\theta)}(\mathbf{x},t) =$$

$$K\int_0^t\int_S \left[\bar{u}_i(\mathbf{x},t;\mathbf{s},\tau)\frac{\partial\theta(\mathbf{s},\tau)}{\partial n} - \frac{\partial\bar{u}_i(\mathbf{x},t;\mathbf{s},\tau)}{\partial n}\theta(\mathbf{s},\tau)\right] ds d\tau$$

$$+ \int_\Omega [\bar{u}_i(\mathbf{x},t;\xi,0)\theta(\xi,0)]d\xi + \int_0^t\int_\Omega [\bar{u}_i(\mathbf{x},t;\xi,\tau)f(\xi,\tau)]d\xi d\tau \qquad (13)$$

and

$$\sigma_{ij}^{(\theta)}(\mathbf{x},t) =$$

$$K\int_0^t\int_S \left[\bar{\sigma}_{ij}(\mathbf{x},t;\mathbf{s},\tau)\frac{\partial\theta(\mathbf{s},\tau)}{\partial n} - \frac{\partial\bar{\sigma}_{ij}(\mathbf{x},t;\mathbf{s},\tau)}{\partial n}\theta(s,\tau)\right] ds d\tau$$

$$+ \int_\Omega [\bar{\sigma}_{ij}(\mathbf{x},t;\xi,0)\theta(\xi,0)]d\xi + \int_0^t\int_\Omega [\bar{\sigma}_{ij}(\mathbf{x},t;\xi,\tau)f(\xi,\tau)]d\xi d\tau \qquad (14)$$

where the kernels for these expressions represent the thermoelastic effects of a heat pulse in an infinite medium, as derived previously.

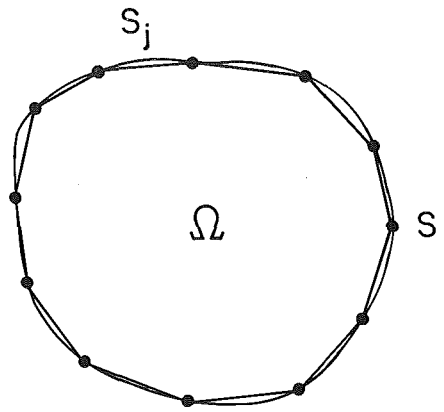

Fig. 2 Boundary discretisation using straight line segments

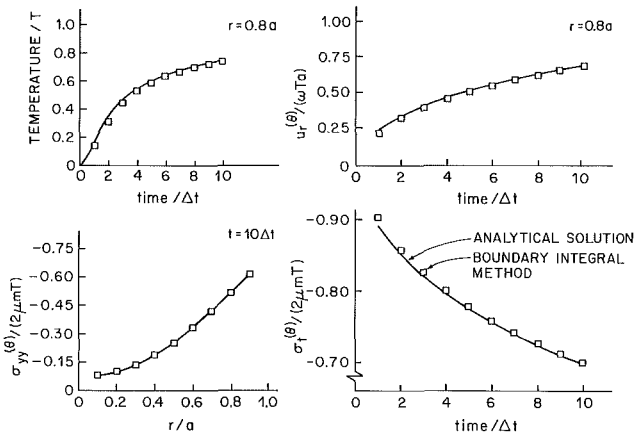

Fig. 3 Finite disc problem: results for temperature and induced stresses and displacements

Notice that the temperature, stresses, and displacements are now all calculated by means of analogous integral expressions. A similar set of boundary integral formulae can also be written for the indirect method in analogy with expression (5) or its double layer equivalent. Also, we note that equations (10) represent limiting cases of these formulae since they can be obtained by reducing the time step Δt to zero. Thus we have a general framework which incorporates several alternatives for calculating thermal stresses and displacements.

The Numerical Procedure

In order to calculate the required integral expressions over time, we will adopt a stepwise approach to generate temperatures at points over the domain, and use this distribution as the 'initial' condition for the following time step [1, 2]. Thus, for step M, we can write expressions (3), (13), and (14) as the generic recurrent relations

$$R(\mathbf{x},M\Delta t) = K\int_0^{\Delta t}\int_S \left[\bar{R}(\mathbf{x},\Delta t;\mathbf{s},\tau)\frac{\partial\theta(\mathbf{s},(M-1)\Delta t+\tau)}{\partial n}\right.$$

$$\left. - \frac{\partial\bar{R}(\mathbf{x},\Delta t;\mathbf{s},\tau)}{\partial n}\theta(\mathbf{s},(M-1)\Delta t+\tau)\right] ds d\tau$$

$$+ \int_\Omega [\bar{R}(\mathbf{x},\Delta t;\xi,0)\theta(\xi,(M-1)\Delta t)]d\xi$$

$$+ \int_0^{\Delta t}\int_\Omega [\bar{R}(\mathbf{x},\Delta t;\xi,\tau)f(\xi,(M-1)\Delta t+\tau)]d\xi d\tau \qquad (15)$$

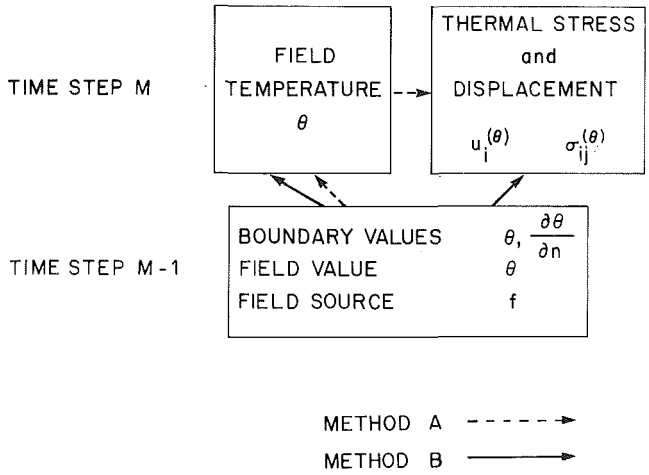

Fig. 4 Schematic comparison between alternative methods for thermomechanical calculations

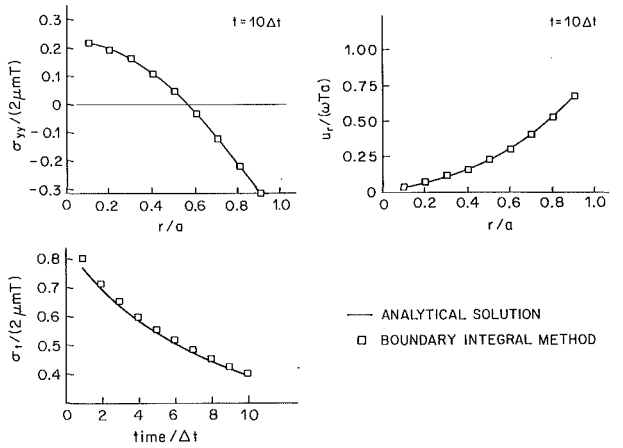

Fig. 5 Finite disc problem: Final results (i.e., including homogeneous solution)

where $\bar{R}$ and R represent $\bar{\theta}$, $\bar{u}$, $\bar{\sigma}$ and θ, $u^{(\theta)}$ and $\sigma^{(\theta)}$, respectively. The surface integrals can be evaluated by discretizing the boundary using straight line segments as shown in Fig. 2. If we assume that the boundary functions $\theta(\mathbf{s},\tau)$ and $\partial\theta/\partial n$ $(\mathbf{s},\tau)$ can be approximated by constants θ_{Mj} and q_{Mj}, respectively, over each segment S_j and over each time step M, equations (15) may be written as

$$R(\mathbf{x},M\Delta t)=\sum_j\left[\overset{j}{C}(\mathbf{x})q_{Mj}-\overset{j}{D}(\mathbf{x})\theta_{Mj}\right]+\sum_k\left[\overset{k}{W}R(\mathbf{x},\Delta t;\overset{k}{\xi},0)\theta(\overset{k}{\xi},(M-1)\Delta t))\right]+P_M(\mathbf{x})$$

where

$$\overset{j}{C}(\mathbf{x})=K\int_0^{\Delta t}\int_{S_j}\bar{R}(\mathbf{x},\Delta t;\mathbf{s},\tau)ds d\tau$$

$$\overset{j}{D}(\mathbf{x})=K\int_0^{\Delta t}\int_{S_j}\frac{\partial\bar{R}(\mathbf{x},\Delta t;\mathbf{s},\tau)}{\partial n}ds d\tau$$

$\overset{k}{\xi}$ are Gaussian points in the field

$\overset{k}{W}$ are Gaussian weights associated with field points $\overset{k}{\xi}$

and

$$P_M(\mathbf{x})=\int_0^{\Delta t}\int_\Omega\bar{R}(\mathbf{x},\Delta t;\xi,\tau)f(\xi,(M-1)\Delta t+\tau)d\xi d\tau$$

is the generic term resulting from the body heat source. The evaluation of this integral will not be attended to here.

The unknown boundary functions can be determined by solving, at each time step, the set of linear algebraic equations resulting from the case where

$$\bar{R}=\bar{\theta}\text{ and }\mathbf{x}=\mathbf{s}.$$

Thereafter these values may be used in the remaining expressions enabling the thermally induced mechanical effects $u_i^{(\theta)}$ and $\sigma_{ij}^{(\theta)}$ to be calculated.

The procedure was tested on the problem of a finite cylindrical disc of radius a, free of body sources and forces, initially void of temperature, whose surface is maintained traction free at a constant temperature T over time. The simple nature of this problem allows the analytical calculation [6] of the temperature θ and the components $u^{(\theta)}$, $\sigma_{ij}^{(\theta)}$ so that a direct comparison with the numerical solution can be made. A sample of results are shown in Fig. 3. It should be noted that the tangential stresses $\sigma_t^{(\theta)}$ at the boundary were calculated from a numerical differentiation of the displacements (equation (13)) since they are found to be more accurate than when found directly [7]. This has become standard practice in boundary element computations.

The distinction between the approach represented by equations (10) (method A) and that given by the boundary integral formula (method B) can be illustrated diagrammatically as shown in Fig. 4. By calculating the thermal and elastic quantities in series, method A appears to provide a more efficient procedure since it exploits work that has already been done. The parallel arrangement afforded by the boundary element method requires the retrieval of thermal boundary, initial and source data and the computation of stresses and displacements in direct analogy with the thermal problem. It follows also, however, that while method B for computing displacements and stresses produces expressions which are of the same order of approximation as that inherent in θ, method A necessarily compounds the error in θ, aside from introducing further uncertainty in the determining the mechanical quantities. A further distinction between the two methods involves the behavior of the kernel functions of the body integrals. In the case of A these are singular, and require careful treatment during the integration process. Method B on the other hand calculates the effect of the field temperature over a complete time step, and so produces expressions which are continuous, allowing computations to be made in a straightforward manner.

The Homogeneous Solution

It must be recalled that the values $u_i^{(\theta)}$ and $\sigma_{ij}^{(\theta)}$ calculated at each step will not in general agree with the prescribed mechanical boundary conditions. Thus at each time step we must superimpose an elastostatic solution $[u_i^{(*)}, \sigma_{ij}^{(*)}]$ which compensates for the difference between the required and calculated boundary conditions. The problem to be solved then may be formulated by the equations

$$\mu u^{(*)}{}_{i,jj}(\mathbf{x})+(\lambda+\mu)u^{(*)}{}_{j,ij}(\mathbf{x})=0$$

subject to the boundary conditions

$$u_i(\mathbf{s},M\Delta t)=U_i(\mathbf{s},M\Delta t)-u_i^{(\theta)}(\mathbf{s},M\Delta t)$$

or

$$\sigma_i(\mathbf{s},M\Delta t)=T_i(\mathbf{s},M\Delta)-\sigma_i^{(\theta)}(\mathbf{s},M\Delta t)$$

or the appropriate combination of these. This solution may be found by any numerical means, the most straightforward being a boundary element method. In this case an indirect (fictitious stress) [8] method was used. The final results for the cylindrical disc problem, obtained from the equations

$$u_i(\mathbf{x},M\Delta t) = u_i^{(\theta)}(\mathbf{x},M\Delta t) + u_i^{(*)}(\mathbf{x},M\Delta t)$$

$$\sigma_{ij}(\mathbf{x},M\Delta t) = \sigma_{ij}^{(\theta)}(\mathbf{x},M\Delta t) + \sigma_{ij}^{(*)}(\mathbf{x},M\Delta t)$$

for each time step M, are given in Fig. 5.

Conclusions

We have presented a general framework for analyzing thermo-mechanical behavior using boundary element methods when linear quasi-static conditions are assumed to hold. The thermal stresses and displacements are calculated using boundary integrals, and achieve the same order of approximation obtained for the temperature. The method obviates the need for calculating the instantaneous mechanical effects of the temperature, and therefore does not require the evaluation of singular body integrals.

Acknowledgments

This work was supported by the Office of Nuclear Waste Isolation through the Battelle Memorial Institute, Columbus, Ohio, Contact No. E512-00800, (1978–1982).

References

1 Chang, Y. P., Kang, C. S., and Chen, D. J., 1973, "The Use of Fundamental Greens Functions for the Solution of Problems of Heat Conduction in Anisotropic Media," *Journal of Heat and Mass Transfer*, Vol. 16, pp. 1905–1918.

2 Banerjee, P. K., Butterfield, R., and Tomlin, G. R., 1981, "Boundary Element Methods for Two Dimensional Problems of Transient Groundwater Flow," International Journal of Numerical and Analytical Methods in Geomechanics, Vol. 5, pp. 15–31.

3 Banerjee, P. K., and Butterfield, R., *Boundary Element Methods in Engineering Science*, McGraw-Hill, London.

4 Tanaka, M., Togoh, H., and Kikuta, M., "Fracture Mechanics Applications in Thermoelastic States," *Topics in Boundary Element Analysis*, Vol. 1, C. A. Brebbia, ed., Springer-Verlag, Berlin.

5 Rizzo, F. J., and Shippy, D. J., "An Advanced Boundary Integral Equation Method for Three Dimensional Thermoelasticity," *International Journal of Numerical Methods in Engineering*, Vol. 11, pp. 1753–1768.

6 Nowacki, W., 1962, *Thermoelasticity*, Addison-Wesley, London.

7 Cruse, T. A., and Vanburen, W., 1971, "Three Dimensional Elastic Stress Analysis of a Fracture Specimen with an Edge Crack," *International Journal of Fracture Mechanics*, Vol. 7, pp. 1–15.

8 Crouch, S. L., and Starfield, A. M., 1983, *Boundary Element Methods in Solid Mechanics*, George Allen and Unwin, London.

The Extent of the Stress Intensity Factor Field During Crack Growth Under Dynamic Loading Conditions

C. C. Ma[1]

L. B. Freund
Fellow ASME

Division of Engineering,
Brown University,
Providence, RI 02912

The phenomenon considered is fracture initiation and crack growth in a plate due to dynamic pressure loading on the faces of a pre-existing crack. The problem is formulated within the framework of two-dimensional elastodynamics, and the system is viewed as a semi-infinite crack in an otherwise unbounded body. At a certain instant of time, a spatially uniform pressure begins to act on the crack faces. The pressure magnitude increases linearly in time for a certain period (the rise time T*), and it is constant thereafter. The crack begins to extend at constant speed at some time after the pressure begins to act (the delay time* τ*). The pressure acts only over the original crack faces, and both* $\tau > T$ *and* $\tau < T$ *are considered. The ratio of the normal stress on the fracture plane to the value due to the singular term in the stress field alone is computed for some point at a small fixed distance ahead of the crack tip, with a view toward establishing the conditions under which the stress intensity factor controlled singular term accurately describes the near tip stress distribution in this highly transient process. Measured and calculated histories compare very well for relatively low crack face pressures, but there is significant disagreement beyond crack growth initiation for higher pressures. Possible reasons for the discrepancies are discussed.*

1 Introduction

The idea of an elastic stress intensity factor is a well-established concept in fracture mechanics, and it represents the cornerstone of applied linear elastic fracture mechanics. Interpretation of the stress field near the edge of a crack in a loaded solid body in terms of a stress intensity factor magnitude must always be based on the assumption that the dimensions of the body and the details of the loading are such that a stress intensity factor-controlled field does indeed exist in the equivalent elastic body and that the size of the region over which the material response is inelastic is sufficiently small compared to the size of the region over which the stress intensity factor-controlled field exists. "Standard" criteria have been adopted for determining whether or not the stress intensity factor idea can be applied in a given situation in fracture toughness testing (ASTM Standards, 1978).

If a cracked solid is subjected to stress pulse loading, the transient nature of the process adds a new dimension to the question of existence of a stress intensity factor-controlled field. Consider the most ideal case of a half plane crack in an otherwise unbounded elastic solid, and suppose that the crack faces are subjected to spatially uniform, suddenly applied pressure. The resulting plane strain field consists of plane pressure waves propagating away from each crack face, plus cylindrical longitudinal and shear waves radiating from the edge of the crack. Even though this configuration strictly meets all of the size requirements of the standard criteria, a stress intensity factor controlled field will be found only for points closer to the crack tip than about 5–10 percent of the distance to the cylindrical shear wave front. This fact complicates the interpretation of experiments concerned with fracture initiation in brittle materials under intense stress wave loads in terms of a stress intensity factor K, simply because the extent of the K field is so small at the onset of growth.

The problem is even more complicated in the case of crack growth. In the case of dynamic loading of a stationary crack, the ability to find a K-controlled field over a region of some minimal size near the crack edge may hinge only on waiting for the wavefronts to pass and the transients to die away. In the case of dynamic crack growth, however, the transients are being continuously refreshed. This may be seen by viewing the process of crack growth as the negation of traction on the prospective fracture plane. With this point of view, the internal stress in the body at a point on the prospective fracture plane gradually builds up as the crack tip approaches. This gradually accumulated stress is then *suddenly* released with the passage of the crack tip, and the resulting transient fields must radiate out continuously through the region surrounding the crack tip. There are obviously limitations on the use of the stress in-

[1]Present address: Department of Mechanical Engineering, National Taiwan University, Taipei, Republic of China.

Contributed by the Applied Mechanics Division for publication in the JOURNAL OF APPLIED MECHANICS.

Discussion on this paper should be addressed to the Editorial Department, ASME, *United Engineering Center, 345 East 47th Street, New York, N.Y.* 10017, and will be accepted until two months after final publication of the paper itself in the JOURNAL OF APPLIED MECHANICS. Manuscript received by ASME Applied Mechanics Division, July 25, 1985; final revision, January 2, 1986.

tensity factor concept in such situations, perhaps only if the crack speed is very high and/or the loading is very intense.

Interest in the stress intensity factor in considering dynamic crack growth stems from its potential as a driving force for the process. The crack tip stress distribution is extremely difficult to measure directly, and the only more or less direct measurements have been made by means of the optical methods of photoelasticity and shadow spots. In both methods, the influence of the crack tip deformation features on a particular light field is measured, and it is always the case that the crack tip deformation features are sensed over some finite region around the crack tip. Furthermore, both the experimental data and field observations are interpreted as though the crack tip stress intensity factor field is *fully established* over this entire region. The purpose of this study is to consider limitations on the assumption that the stress intensity factor field is fully established over a region of given size near the tip of a growing crack in a stress wave field.

The theoretical background that will be required to study the limitations on the usual interpretation of the shadow spot data derives from the work of Freund (1972, 1973) and Burridge (1976), and some fundamental results are reviewed in the next section. In section 3, a particular case of time-dependent crack face loading is studied which allows for direct comparison with a set of experimental data. Of special interest in this analysis is the time required for the normal stress on the fracture plane at a point near the moving crack tip to reach the value it would have if the stress field were actually given by the near-tip stress intensity factor field. In section 4, the stress intensity factor calculation is generalized to the case of a loading pulse with a finite rise time. The shadow spot method, a technique that has been used in recent years by Kalthoff et al. (1977), Ravi-Chandar and Knauss (1984), Rosakis et al. (1984), and others in dynamic crack growth experiments, is briefly described in section 5. Of particular interest is the series of experiments reported by Ravi-Chandar and Knauss (1984) which may be examined in light of the theoretical model studied in the preceding sections. Finally, in section 6, a comparison between the theoretically predicted and the experimentally measured stress intensity factors is made, including a discussion of the possible reasons for the differences observed.

2 Analysis of Crack Growth

The phenomenon considered here is the growth of a half-plane crack in an otherwise unbounded body of a homogeneous, isotropic elastic solid. The loading is uniform in the direction of the crack edge in all cases, so that the state of deformation is plane strain and the mode of crack tip opening is the plane strain opening mode, that is, mode I. The crack is assumed to extend in its own plane at speeds large enough for inertial effects to be important. Initially, the body is stress free and at rest, and the case of dynamic loading is considered. Suppose that a uniform normal pressure of magnitude σ_o begins to act on the faces of the crack at a certain instant, say time $t = 0$. The stress gradually intensifies at the crack tip, and crack propagation may be initiated only after some time has elapsed following application of the crack face pressure. It is assumed that after some finite delay time τ, the crack tip begins to move at a constant speed $v = 1/d$. The pressure does not expand over the newly-created crack faces, but it continues to act on the original crack faces. The solution can be obtained by superimposing the stress distribution that results from sudden application of the crack face normal pressure of magnitude σ_o for the stationary crack and the stress distribution that results from growth of the crack under the action of crack face tractions which exactly negate the stresses on the crack line in the first problem (Freund, 1973).

For the stationary crack, the boundary conditions on $z = 0$ are that the normal stress on the crack faces is $-\sigma_o H(t)$, the shear traction is zero, and the normal displacement is zero on the crack plane ahead of the crack tip. The complete stress distribution can be determined, but of primary interest is the distribution of normal stress on $z = 0$, $x > 0$. This stress distribution is denoted by $f(t/x)$ and it is given by Freund (1973) as

$$f(t/x) = \frac{\sigma_o \omega_o}{\pi} \int_a^{t/x} Im[\eta \omega_+^o(-\eta)]^{-1} d\eta \quad t/x > a \tag{2.1}$$

where

$$S_+(\lambda) = \exp\left(-\frac{1}{\pi}\int_a^b \tan^{-1}\frac{4\eta^2\sqrt{(\eta^2-a^2)(b^2-\eta^2)}}{(2\eta^2-b^2)^2} \frac{(1-\eta/d)^{-1}d\eta}{[\eta+\lambda(1-\eta/d)]}\right)$$

$$\omega_+(\lambda) = (1-c/d)[a+\lambda(1-a/d)]^{1/2}/[(\lambda+c-\lambda c/d)S_+(\lambda)] \tag{2.2}$$

$$\omega_+^o(\lambda) = \lim_{v\to 0}\omega_+(\lambda), \quad \omega_o = \omega_+^o(0), \quad S_+^o(\lambda) = \lim_{v\to 0} S_+(\lambda)$$

where $d = 1/v$ is the crack tip slowness, $a = 1/v_\ell$ is the longitudinal wave slowness, $b = 1/v_s$ is the shear wave slowness, and $c = 1/v_R$ is the Rayleigh wave slowness which satisfies the equation $(2c^2 - b^2)^2 - 4c^2(c^2 - a^2)^{1/2}(c^2 - b^2)^{1/2} = 0$. The subscript '+' on functions above is a remnant of the Wiener–Hopf procedure used to solve the underlying crack propagation problems.

The distribution (2.1) varies with position and time only through the ratio t/x. This implies that any fixed stress level radiates out along the x axis at the constant speed $u = x/t$. The speed u varies between zero and the longitudinal wave speed. The stress intensity factor at time t for the stationary crack tip is found to be

$$K^S(t) = \lim_{x\to 0^+}\left(\sqrt{2\pi x} f(t/x)\right) = 2\sigma_o\omega_o\sqrt{2t/\pi} \tag{2.3}$$

In order to construct the complete solution for dynamic loading, a fundamental solution is derived and the complete field is constructed by means of superposition. Suppose that the crack tip is at rest at $x = 0$ and there are no loads acting on the body for $t < 0$. At time $t = 0$, the crack tip begins to move in the x direction at speed v and simultaneously a symmetric pair of concentrated normal forces appears at the crack tip, tending to open the crack. For $t > 0$, the concentrated forces move in the x direction with speed $u < v$. The amplitude of the forces increases linearly in time. The resulting dynamic stress field is called the fundamental solution and the boundary conditions on $z = 0$ are

$$\begin{aligned} &\sigma_{zz}(x,0,t) = (mt+n)\delta(x-ut)H(t) \quad \text{for} \quad -\infty < x < vt \\ &\sigma_{xz}(x,0,t) = 0 \quad \text{for} \quad -\infty < x < \infty \\ &w(x,0,t) = 0 \quad \text{for} \quad vt < x < \infty \end{aligned} \tag{2.4}$$

where m and n are arbitrary constants. The x coordinate is eliminated in favor of the coordinate $\xi = x - v(t-\tau)$, so that the ξ, z coordinate system moves along with the crack tip. The normal stress on the plane $z = 0$ ahead of the crack tip is

$$\sigma_{zz}^F(\xi,0,t;u,m,n) = \frac{1}{2\pi i}\int_{B_1}\frac{1}{2\pi i}\int_{B_2}\left(\left[\frac{mh^2}{s\omega_+(\lambda)}\right]\left[\frac{\omega_+(h)}{(\lambda-h)}\right]_h - \left[\frac{nh\omega_+(h)}{(\lambda-h)\omega_+(\lambda)}\right]\right)e^{s(t+\lambda\xi)}d\lambda\, ds \tag{2.5}$$

where B_1 and B_2 are the inversion paths for the one-sided and two-sided Laplace transforms, and $h = 1/(v-u)$. The stress intensity factor for the fundamental solution may be extracted by examining the behavior of (2.5) as $\xi \to 0^+$, with the result

$$K^F = \lim_{\xi\to 0^+}\left(\sqrt{2\pi\xi}\sigma_{zz}^F\right) = \frac{2mh^2\omega_+'(h)\sqrt{2t}}{\sqrt{\pi}(1-a/d)^{1/2}} - \frac{\sqrt{2}nh\omega_+(h)}{(1-a/d)^{1/2}\sqrt{\pi t}} \tag{2.6}$$

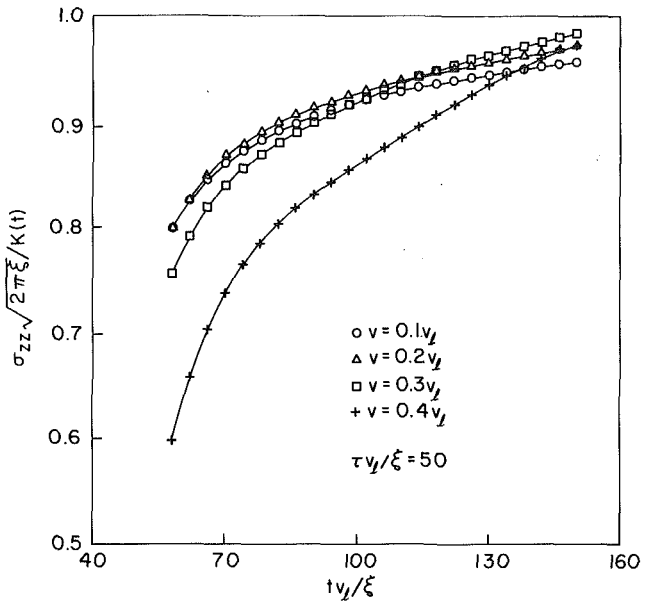

Fig. 1 The ratio of the total stress σ_{zz} to the contribution to the total stress from the singular stress intensity factor term alone versus nondimensional time at a fixed distance ξ ahead of the moving crack tip for the configuration considered in section 4. Results are shown for fixed delay time and several crack speeds.

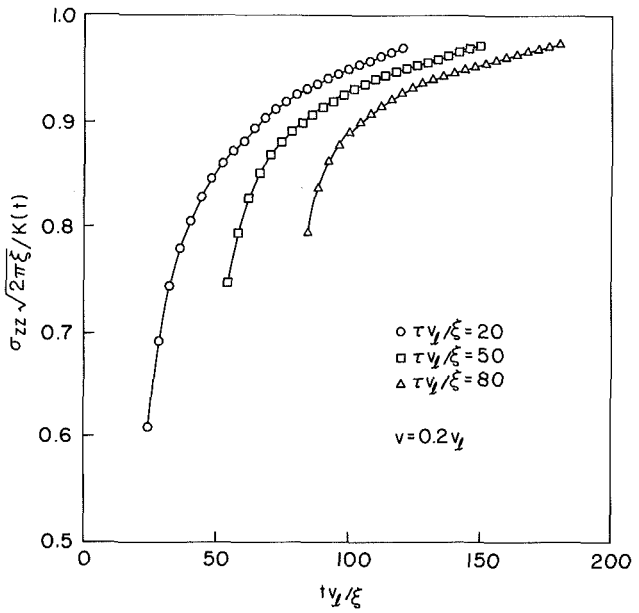

Fig. 2 Same as Fig. 1, except that results are shown for several delay times and fixed crack speed

For the crack face impact problem that was outlined earlier in this section, the stress distribution on the crack line may be obtained by superposition (Freund, 1973) as

$$\sigma_{zz}^{D}(\xi;0,t) = \int_0^{v(t-\tau)/t} \sigma_{zz}^{F}(\xi,0,t-t_o;u, -1,-t_o)f(1/u)du + f(t/x) \tag{2.7}$$

where $t_o = v\tau/(v-u) = h\tau/d$. The corresponding stress intensity factor is

$$K^D = \frac{2\sqrt{2}}{\sqrt{\pi}}\sigma_o k(d)\left(\omega_o\sqrt{t} - \sqrt{v(t-\tau)}\right) \tag{2.8}$$

where

$$k(d) = \frac{(1-c/d)}{S_+(d)(1-a/d)^{1/2}} \tag{2.9}$$

For given elastic material properties, $k(d)$ is a universal function of crack tip speed. The function $k(d)$ decreases monotonically from one at $v = 0$ to zero when the crack speed reaches the Rayleigh wave speed of the material (Freund, 1972). All subsequent numerical results have been obtained for the case of Poisson's ratio $\nu = 0.25$. The foregoing results will be useful in the subsequent discussion of experimental data obtained by means of a particular apparatus. Next, the degree to which the dominant singular stress distribution (2.8) actually represents the total stress distribution (2.7) for points very near to the crack tip is examined.

3 An Observation Concerning the Crack Tip Field

In order to examine just how the transient near tip field approaches the stress intensity factor controlled field, attention is focused on a moving point which is always a fixed distance ξ ahead of the moving crack tip. The stress component σ_{zz} at this point will exhibit some transient behavior due to the onset of crack growth. Of particular interest is the time beyond $t = \tau$ which is required for the stress level at this point to become approximately equal to the corresponding stress component computed from the crack tip singular field alone. Consequently, the ratio of the total stress σ_{zz} to the corresponding stress due to the singular term alone has been computed numerically. In the integral expression for σ_{zz}^{D}, the integrand is square root singular at each end of the integration range. Therefore, the appropriate Gaussian integration scheme based on a weight function with the same singular behavior and the Chebyshev polynomials was used (Abramowitz and Stegun, 1965).

A graph of the ratio of the total stress σ_{zz} to the singular field contribution to the stress $K/\sqrt{2\pi\xi}$ versus the nondimensional time $\tau v_l/\xi$ is shown in Fig. 1. The delay time, in nondimensional form, was taken to be $\tau v_l/\xi = 50$ for the calculations, and crack tip speeds of 10, 20, 30 and 40 percent of the longitudinal wave speed were considered. As can be seen from Fig. 1, the time required for the stress ratio to approach 0.9 is quite large. For example, if $v_l = 2000$ m/s and $\xi = 2$ mm, then the normalized time scale may be read in units of microseconds. For a delay time of 50 μs and a crack tip speed of 400 m/s, an elapsed time of about 30 μs is required after the onset of crack growth before the total stress increases to 90 percent of the singular field alone. For the other parameters used in generating the data of Fig. 1, the time required is as long or longer. While this time of 30 μs is not great in an absolute sense, it is quite a long time on the scale of many dynamic fracture phenomenon observed in the laboratory.

Data similar to that in Fig. 1 are also shown in Fig. 2. In this case, however, the crack tip speed has been fixed at 20 percent of the longitudinal wave speed of the material and the ratio of total stress to the singular stress has been computed for the nondimensional delay times of 20, 50, and 80. It appears from these results that the time required before the singular stress becomes a good estimate of the total stress decreases as the delay time increases.

4 Loading Pulse With Finite Rise Time

Up to this point in the discussion, it has been assumed that the time dependence of the loading pressure is a simple step in time. In experiments, it is impossible to produce a true step profile and, instead, the loading pulse has a finite rise time. Therefore, with a view to comparison of the theoretical results with the results of experiments, the analysis is extended to the case where the loading pulse has a finite rise time. Suppose that at time $t = 0$ the crack pressure is applied, and that the magnitude of the pressure increases according to some function of time, say $f(t)$. After some finite rise time, say T, the

magnitude of the applied pressure reaches its maximum value σ_o so that $f(T) = \sigma_o$. The magnitude of the pressure is held constant for $t > T$. Suppose for the moment that the crack propagation delay time τ is larger than the loading rise time T. In this case, the stress intensity factor can be obtained for all time in a straightforward manner, as will now be demonstrated. The procedure is similar to that used by Achenbach and Nuismer (1971) in generalizing Baker's (1962) solution and, for the case of nonuniform crack growth, by Freund (1973).

For $t < T < \tau$, the crack tip is stationary and the stress intensity factor for a unit step stress pulse applied at $t = 0$ is given in (2.3). The corresponding result for an indefinitely large number of infinitesimal jumps of magnitude $\Delta g(s) = g'(s)\Delta s$ as $\Delta s \to 0$, each applied at time $t = s$, is

$$\frac{K}{\sqrt{2\pi}} = \frac{2\omega_o}{\pi}\int_0^t g'(s)(t-s)^{1/2}ds \quad \text{for} \quad t<T \tag{4.1}$$

For $T < t < \tau$, the crack tip is still stationary and the stress intensity factor during this interval is given by

$$\frac{K}{\sqrt{2\pi}} = \frac{2\omega_o}{\pi}\int_0^T g'(s)(t-s)^{1/2}ds \quad \text{for} \quad T<t<\tau \tag{4.2}$$

For $\tau < t$, the crack is growing and the stress intensity factor for this case has already been given in (2.8) for a step applied pressure. The stress intensity factor for a crack moving at a constant speed v due to application of time $t = 0$ of an applied crack face pressure of magnitude $g(t)$ that increases to a constant level σ_o at time $t = T$ and with crack growth for $t > \tau > T$ is

$$\frac{K}{\sqrt{2\pi}} = \frac{2}{\pi}k(d)\left[\int_0^T g'(s)\omega_o(t-s)^{1/2}ds - \sigma_o[v(t-\tau)]^{1/2}\right]$$

$$\text{for} \quad t>\tau \tag{4.3}$$

For purposes of calculating specific results, the time profile of the applied loading pulse is taken to be linear between $g(0) = 0$ and $g(T) = \sigma_o$. Then, $g'(t) = \sigma_o/T$ for $0 < t < T$ and $g'(t) = 0$ for $T < t$. The stress intensity factor for $t > 0$ is given by

$$\frac{K}{\sqrt{2\pi}} =$$

$$\begin{cases} \dfrac{4\sigma_o\omega_o}{3\pi T}\, t^{3/2}, & 0<t<T \\ \dfrac{4\sigma_o\omega_o}{3\pi T}\,[t^{3/2}-(t-T)^{3/2}], & T<t<\tau \\ \dfrac{2\sigma_o k(d)}{\pi T}\left(\dfrac{2\omega_o}{3}\,[t^{3/2}-(t-T)^{3/2}]-[v(t-\tau)]^{1/2}T\right), & \tau<t<\infty \end{cases} \tag{4.4}$$

It is emphasized at this point that the above result is valid only if the delay time τ is greater than the rise time T, so that the pressure on the crack faces is constant during the entire time that the crack is growing.

For the case when the crack begins to grow before the magnitude of the applied crack face pressure reaches its maximum level σ_o, that is, when $\tau < T$, a solution in closed form does not appear to exist. The stress intensity factor may be constructed by superposition, however, leaving an integral to be evaluated numerically. If the pressure is assumed to act over the entire crack surface during growth, instead of only over the original crack surface, then an expression for the stress intensity factor may be extracted by following the steps in the previous paragraph. For an applied pressure which rises

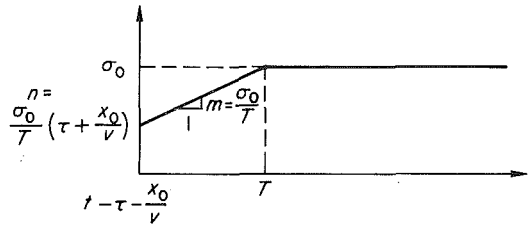

FIG. 3a

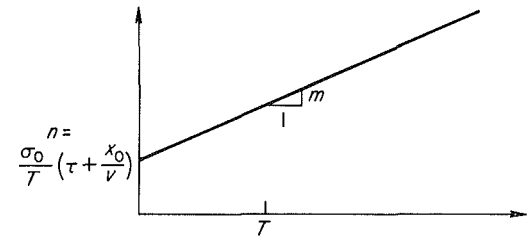

FIG. 3b

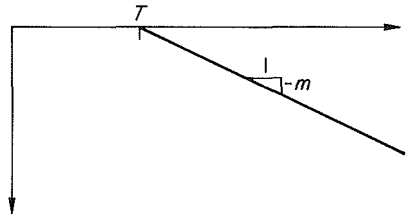

FIG. 3c

Fig. 3 The superposition scheme for the case when the crack begins to before the pressure magnitude has reached its maximum level, that is, $\tau < T$

linearly in time until $t = T$, and then remains constant thereafter, the result is

$$\frac{K^E}{\sqrt{2\pi}} = \begin{cases} \dfrac{4\sigma_o\omega_o}{3\pi T}\, t^{3/2} & \text{for} \quad 0<t<\tau \\ \dfrac{4\sigma_o\omega_o k(d)}{3\pi T}\, t^{3/2} & \text{for} \quad \tau<t<T \\ \dfrac{4\omega_o\sigma_o k(d)}{3\pi T}\,[t^{3/2}-(t-T)^{3/2}] & \text{for} \quad T<t<\infty \end{cases} \tag{4.5}$$

The stress intensity factor which results from negating the crack face pressure over $0 < x < v(t - \tau)$ must now be added to the result in (4.5). Suppose that the half-plane crack begins to grow from $x = 0$ so that at any time the amount of growth is $\ell(t)$. A symmetric pair of concentrated forces of unit magnitude begin to act on the crack faces at $x = x_o$ at time $t = t_o$, where $0 < x_o \le \ell(t_o)$. Burridge (1976) has shown that the stress intensity factor for this case is given by

$$\frac{K^B(t;x_o,t_o)}{\sqrt{2\pi}} = \frac{k(d)}{\pi^2(\ell-x_o)^{1/2}}\int_a^{\xi_o} Im\left[\frac{(a-z)^{1/2}}{(c-z)S_-^o(z)}\right]\frac{dz}{(\xi_o-z)^{1/2}} \tag{4.6}$$

for $t \ge t_o$ where

$$\xi_o = \frac{t-t_o}{\ell(t)-x_o}$$

If $\xi_o > b$, the integral in (4.6) can be evaluated by means of

contour integration methods to yield the simple form (Freund, 1974b)

$$\frac{K^B(t;x_o,t_o)}{\sqrt{2\pi}}=\frac{k(d)}{\pi^2(\ell-x_o)^{1/2}}\left[1-\frac{(c-a)^{1/2}H(c-\xi_o)}{(c-\xi_o)^{1/2}S_-^o(c)}\right] \quad (4.7)$$

The complete stress intensity factor is the sum of (4.5) and the corresponding stress intensity factor that results from negation of crack face tractions over $0 < x < v(t-\tau)$, say K^N.

The determination of K^N follows the force superposition approach introduced by Freund (1972, 1973). The details will not be included here, but the steps are indicated in the various sketches in Fig. 3. For any point x_o in the range $0 \le x_o < v(t-\tau)$, the time history of crack face traction is shown in the sketch in Fig. 3*a*. The crack tip passes this point at time $t = \tau + x_o/v$ and the magnitude of the crack face traction at that instant is $\sigma_o(\tau + x_o/v)/T$. Thereafter, the traction at that point increases linearly in time at the rate σ_o/T until $t = T$. For $t > T$, the traction has the constant value σ_o at that point. For each point x_o, this time variation is viewed as the superposition of the time variations shown in Figs. 3*b* and 3*c*. In Fig. 3*b*, the traction at x_o starts out just as in Fig. 3*a*, but it continues to increase linearly in time beyond $t = T$. In Fig. 3*c*, on the other hand, the traction at this point is zero until $t = T$, whereupon it begins to decrease linearly in time at rate σ_o/T. It is obvious that the sum of the variation shown in Figs. 3*b* and 3*c* is equal to the variation shown in Fig. 3*a*.

The solution for the time history of the stress intensity factor for crack growth with a single force pair acting on the crack faces with time variation shown in Fig. 3*b* is given by Freund (1973), and superposition over the appropriate range of x_o is a straightforward matter. The time history of the stress intensity factor for a force pair with time variation shown in Fig. 3*c* can be obtained from the result in (4.6) due to Burridge (1976), which may then also be superimposed over the appropriate range of x_o. The result is summarized as follows:

$$\frac{K^N}{\sqrt{2\pi}}=$$

$$\begin{cases} 0, \quad 0<t\le\tau \\ \dfrac{2\sigma_o d(t-\tau)^{1/2}}{3T\pi(1-a/d)^{1/2}}\,[2\omega_+'(d)(t-\tau)-\omega_+(d)(\tau v+2tv)], \\ \qquad\qquad \tau<t\le T \\ \dfrac{K^*}{\sqrt{2\pi}}+\dfrac{2\sigma_o k(d)\sqrt{v}}{3T\pi}\,[2(t-T)^{3/2}-(\tau+2t)(t-\tau)^{1/2}]- \\ -\dfrac{4\sigma_o d\omega_+'(d)}{3T\pi(1-a/d)^{1/2}}\,[(t-T)^{3/2}-(t-\tau)^{3/2}], \quad T<t\le\infty \end{cases} \quad (4.8)$$

where

$$K^*=\frac{\sigma_o}{T}\int_0^{v(T-\tau)}\int_T^t K^B(t;t_o,x_o)\,dt_o\,dx_o \quad (4.9)$$

The integral in (4.9) that defines K^* must be evaluated numerically.

The total stress intensity factor for the case $T > \tau$, given through (4.5) and (4.8), has been evaluated numerically and typical results are shown in Figs. 4 and 5 for crack tip speeds $v = 0.1\,v_\ell$ and $v = 0.2\,v_\ell$, respectively. Because the crack tip speed changes discontinuously at $t = \tau$ in each case, the stress intensity factor also changes abruptly at the same time. In all cases, the magnitude of the stress intensity factor immediately after the jump is $k(1/v)$ times the magnitude just before the jump (Freund, 1973). Numerical data for the case $\tau > T$ are also shown in the same graphs for purposes of comparison. These computed results provide a basis for analysis of certain experiments in dynamic fracture, and this is the subject of the following sections.

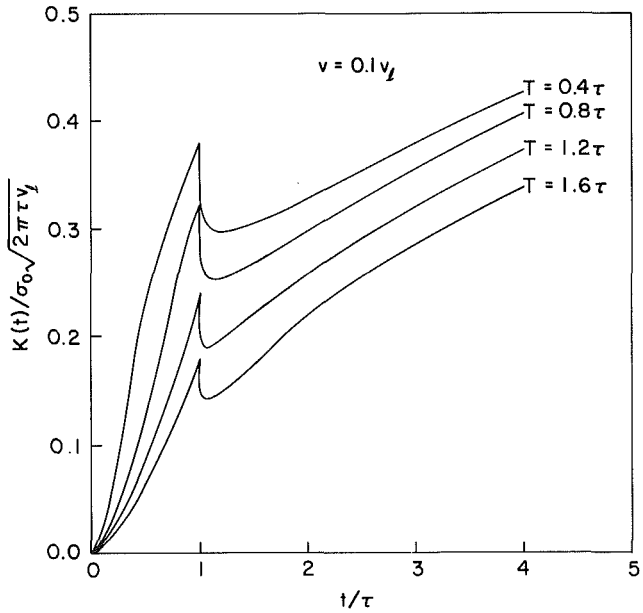

Fig. 4 The stress intensity factor history for dynamic loading of the crack faces and the onset of crack growth at constant speed v after some delay time τ

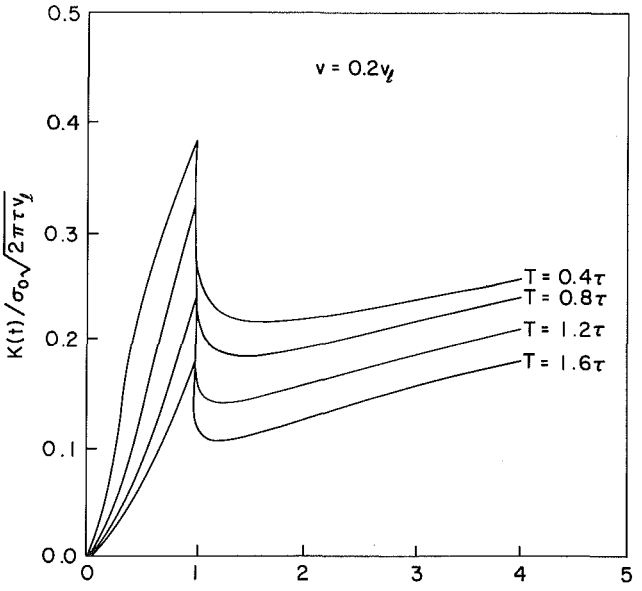

Fig. 5 Same as Fig. 4, except for different crack tip speed

5 The Shadow-Spot Measurement Technique

The use of the shadow-spot method, which is also known as the method of caustics, for measuring the intensity of crack tip stress fields is now quite common in experimental work in the fracture of brittle materials. When a large plate containing a long through-crack is loaded so that the crack opening occurs in mode I, the stress and deformation fields near the crack tip assume the familiar universal spatial distribution. The magnitude of the near tip field, which varies with load and geometry, is the elastic stress intensity factor. The method is based on the fact that the value of the stress intensity factor can be related to features of the optical field obtained by directing parallel light through a transparent specimen in the crack

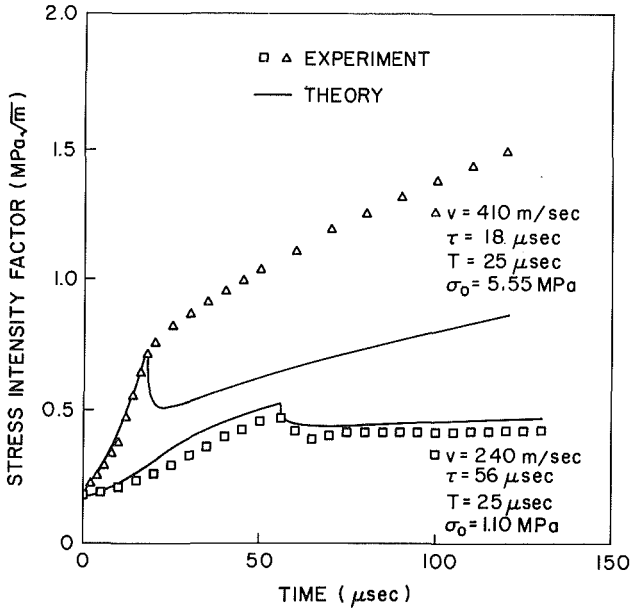

Fig. 6 The stress intensity factor history calculated from the loading and crack motion observed in the experiments on Homalite-100 by Ravi-Chandar and Knauss (1984). Also shown is the stress intensity factor history inferred from the experimental data by means of the optical shadow spot method.

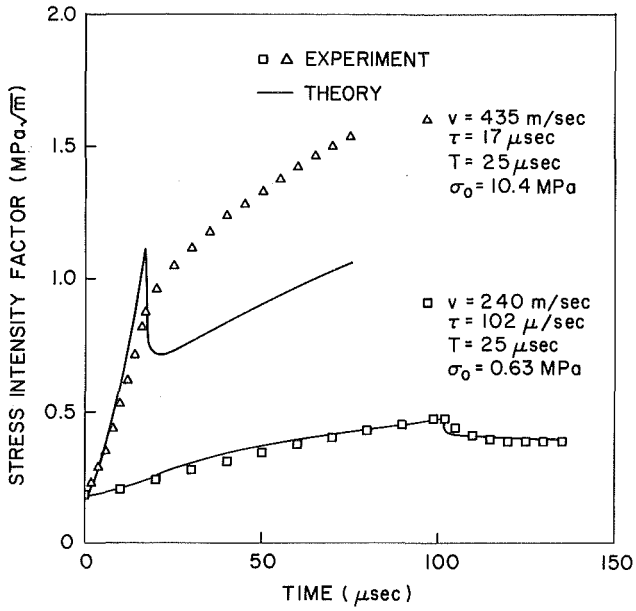

Fig. 7 Same as Fig. 6, but for data shown

tip region, or by reflecting light from the surface of an opaque specimen in the crack tip region. The interest here is in discussing experiments carried out with a transparent material, so the technique is briefly described for this application.

Consider a family of light rays, normally incident on the plane of the specimen. Upon passing through the specimen, the direction of each ray is modified. The amount of deviation for each ray depends on local conditions, in particular, on the local thinning of the specimen due to the in-plane stresses and on the change of index of refraction due to the stress optic effect. Suppose that a screen is placed at a distance z_o behind the specimen, and that the features of the transmitted light field as they appear on this screen are examined. If the plane of the specimen is the x_1, x_2 plane, then let the X_1, X_2 plane be the plane of the screen, where the screen coordinate axes are obtained by translating the specimen coordinate axes in the directional normal to the specimen. The light ray which strikes the specimen at point x_i then strikes the screen at the point X_i where

$$X_i = x_i - z_o \frac{\partial F}{\partial x_i}, \quad i = 1,2 \tag{5.1}$$

For an optically isotropic material, the so-called retardation in optical path $F(x_1, x_2)$ is given by

$$F(x_1,x_2) = [c - (n-1)\nu/E]d_o(\sigma_1 + \sigma_2) \tag{5.2}$$

where c is the stress optic constant, n is the index of refraction in the absence of stress, d_o is the undeformed plate thickness, ν and E are the isotropic elastic moduli, and σ_1 and σ_2 are the principal stresses in the plane.

Under suitable conditions, the light field on the screen will appear as a dark spot (the shadow spot) surrounded by a bright border (the caustic curve), with diminishing light intensity away from the caustic curve. The curve on the specimen which maps into the caustic curve according to (5.1) is the so-called initial curve. The light rays which strike the specimen both inside and outside the initial curve map into points on the screen which are outside of the caustic curve according to (5.1). If the stress field near the crack tip is completely characterized by the prevailing stress intensity factor, and if the initial curve is well within the region of the specimen where this is indeed the case, then the features of the optical field as observed on the screen are also known up to the value of the stress intensity factor. By means of elementary analysis, it can be shown that the value of stress intensity factor is proportional to the maximum transverse diameter of the shadow spot raised to the poewr 5/2. Furthermore, the proportionality factor can be expressed explicitly in terms of material and geometric parameters of the system. These ideas have been extended to the case of elastodynamic crack growth in recent years, and the details are presented by Beinert et al. (1978), Rosakis (1980), and Ma (1982).

The shadow-spot method has played an important role in the development of dynamic fracture mechanics. With the use of a high speed camera, many shadow-spot photographs can be taken at regular intervals during a crack propagation experiment. Each photograph shows the instantaneous stress intensity factor and the instantaneous position of the crack tip and, with a sequence of such photographs, the time history of the stress intensity factor and the crack position can be determined. The main points to be made here are that the shadow-spot photographs record light fields determined by the features of the stress field in the specimen within a certain distance of the crack tip (near and within the initial curve on the specimen, say) and that the data are interpreted as though the near tip field characterized by the instantaneous stress intensity factor is fully established over this region of finite extent. Indeed, the calculations described in the preceding sections were carried out with a view toward clarifying the matter and, in the next section, some recent experiments described by Ravi-Chandar and Knauss (1984) will be discussed in light of this analysis.

6 Comparison With Experiment

In the work reported by Ravi-Chandar and Knauss (1984), a long edge crack was cut into a large rectangular sheet of Homalite-100 along a symmetry line. The specimen was then subjected to a small tensile load in the direction perpendicular to the line of the crack, mainly to hold the specimen in place. A continuous copper ribbon of the same lateral dimension as the thickness of the plate was then doubled over and placed in the slightly open crack. The fold in the ribbon was as close to the crack tip as possible, and one side of the doubled ribbon was adjacent to each crack face. A large capacitor bank was then discharged through the ribbon. The mechanical forces in-

duced by the electrical current flowing through the copper ribbin caused the opposite sides of the ribbon to repel each other and, in so doing, applied essentially uniform normal pressure on the crack faces. The time variation of this pressure distribution was approximated very well by a linear increase in magnitude up until some time after application (the elapsed time is called the rise time T), and then constant magnitude thereafter. The dimensions of the specimen were such that the waves generated by the loading device would not be reflected back onto the crack tip for about 150 μs after application of the pressure. Therefore, for all practical purposes, the situation is that of semi-infinite crack in an unbounded body subjected to spatially uniform pressure over the initial crack faces during the early part of the experiment, and the data may be analyzed on the basis of crack analyses such as those introduced in preceding sections. The properties of Homalite-100 given by Ravi-Chandar and Knauss are $\rho = 1230$ kg/m^3, $\nu = 0.31$, and $E = 4550M$ N/m^2, which yield the wave speeds $v_\ell = 2057$ m/s, $v_s = 1176$ m/s, and $v_R = 1081$ m/s.

First, it was observed that the elapsed time between application of the crack face pressure and the onset of crack growth, which has been denoted by τ, varied with the magnitude of crack face pressure and that the magnitude of stress intensity factor at the instant of crack growth initiation $t = \tau$ varied with the value of τ. It was found that for relatively low levels of crack face pressure, corresponding to relatively long delay times, the level of stress intensity factor is independent of the level of crack face pressure, as is expected from the quasistatic theory of brittle fracture. On the other hand, as the magnitude of applied loading increased, the delay time decreased, and the observed valued of stress intensity factor at the instant of fracture initiation increased.

For times $t > \tau$, it was observed in the experiments that the crack tip *moved with constant speed* until the first reflected waves arrived from the remote boundaries. The analyses of the preceding sections, which were based on the assumption of constant crack tip speed, may also be applied to study the crack propagation phase of the experiments. From the data presented, the loading rise time T was approximately 25 μs, independent of the final magnitude of the applied pressure, and this value is used in all calculations. From the measured delay time τ, pressure magnitude σ_o, crack propagation speed v, and preload, it is possible to compute the exact stress factor as a function of time for the experiment, at least until reflected waves arrive back at the crack tip. The results for four particular experiments reported by Ravi-Chandar and Knauss are shown in Figs. 6 and 7.

The general features of the theoretical curves in Figs. 6 and 7 have already been anticipated in the foregoing analysis. The stress intensity factor starts at a level corresponding to the preload. Following application of the dynamic crack face pressure, the stress intensity factor rises rapidly until the crack begins to grow. With the sudden onset of crack growth at speed v, the stress intensity factor is reduced by a factor $k(1/v)$, that is, $K(\tau + 0) = k(1/v)K(\tau - 0)$. Thereafter, the stress intensity factor continues to vary in a continuous manner.

The experimental results corresponding to the theoretical results appear on the same graphs as the discrete data points, and the data for measured crack speed, delay time, and pressure magnitude also appear on the graphs. In all four cases, the agreement between the theoretical and experimental results is very good for $t < \tau$. Furthermore, the agreement continues to be very good for the cases with relatively low crack face pressures of 1.10 MPa and 0.63 MPa. These are also the cases with lower crack tip speeds, of course. On the other hand, for the higher crack face pressures and the higher crack tip speeds, the agreement between the observed and the calculated results is not good. Indeed, the experimental results continue smoothly through the instant of crack growth initiation $t = \tau$ and they show none of the variation in stress intensity factor history predicted through the calculations. Furthermore, the theoretical and experimental results do not seem to approach each other for $t > \tau$.

Two main reasons may be cited for the observed discrepancy. The first of these is based on the observation that the data are interpreted as though the near tip deformation field was accurately described by the stress intensity factor controlled singular field, whereas the results of section 3 suggest that this may not be the case. The crack tip speed for the experiment leading to the upper curve in Fig. 6 was about 20 percent of the longitudinal wave speed of the material. If attention is focused on a point approximately 2 mm ahead of the moving crack tip, then a delay time of 18 μs leads to a value of the dimensionless parameter $\tau\, v_\ell/\xi$ of about 20. Indeed, for this set of system parameters, the horizontal scale in Fig. 2 may be read in microseconds rather than dimensional units without significant error. Examination of the curve in this figure for $\tau\, v_\ell/\xi = 20$ shows that the stress at a distance ξ ahead of the crack tip is only 60 percent of the value due to the singular term alone just after the onset of crack growth, and it does not reach 90 percent of the singular term value until approximately 70 μs after the application of the crack face loads. While the comparison of relative stress magnitudes at just one point (with respect to the crack tip) is probably not an adequate basis for rejecting any data set, the discrepancy indicated through Fig. 2 is sufficiently large so that the data should be re-evaluated and the complete near tip stress distribution should be worked out for comparison to the stress intensity factor controlled term alone. This latter calculation can be carried out on the basis of available solutions, but the details will be very involved.

It is interesting to note that the delay effect in establishing a stress intensity factor field predicts a shift in the appropriate direction for the results in Figs. 6 and 7. According to the results in Fig. 2, the actual stress at a distance ξ ahead of the crack tip is less than the stress due to the stress intensity factor singular term alone, whereas at the crack tip the singular term is an accurate description of the stress field. Consequently, the actual gradients in stress as the observation point approaches the tip are greater than those predicted by the singular term alone. If the role played by these stress gradients in the formation of shadow spots is recalled from section 5, an immediate inference is that the observed shadow spot will be larger than that which would result from the stress intensity factor field alone. Therefore, the inferred value of stress intensity factor would also be larger than the actual value, as appears to be the case for the upper curves in Figs. 6 and 7.

A second reason for the discrepancy in the results in Figs. 6 and 7 is suggested by the results themselves which are, in a sense, paradoxical. The theoretical results in Figs. 6 and 7 are exact. That is, within the framework of linear elastodynamics, the solid curve is the stress intensity factor history for the measured values of the parameters v, τ, T and σ_o. On the other hand, the experimental data in Figs. 6 and 7 are inferred from measured quantities, also within the framework of linear elastodynamics, for the same measured values of the system parameters. If the process is indeed describable in terms of linear elastodynamics, then the experimental and the theoretical results *must be the same*, but this is obviously not the case for the higher applied load levels. This suggests that the problem may lie in the assumption of linear elastic material response. While there must always be a zone of nonlinear and/or inelastic material response near the crack tip, perhaps at the lower load levels and for a stationary crack tip is is too small to be sensed at a distance of 2–3 mm from the crack tip. For crack growth at the higher load levels, this zone of inelastic and/or nonlinear response or zone of microcracking may extend outward from the crack tip a greater distance,

on the order of the transverse dimensions of the initial curve size, in which case the assumption of linear elasticity would no longer be valid. This conjecture is consistent with the suggestion that the process of fracture is the initiation of microcracks at some fraction of distributed nucleation sites which eventually coalesce with the macroscopic crack. If the intensity of the crack tip stress field is below that necessary to sustain fracture, then there is no tendency for a zone of microcracking to expand from the crack tip. Even if the stress intensity level is at or slightly above the critical level, microcracks that contribute to macroscopic crack growth unload nearby nucleation sites as they form, so there is still no tendency to develop an expanding zone of microcracking. If the crack is highly overdriven (by stress waves, for example) then there may be insufficient time for microcracks nucleated at the most critical sites to mitigate the influence of rising loads at adjacent sites, so many more microcracks may form than are actually necessary to sustain fracture. In this case, an expanding zone of microcracking is indeed conceivable.

Finally, it is pointed out that both the present analysis and the models that underlie the interpretation of experiments are two-dimensional in nature. In either case, the three-dimensional effects that are overlooked may have too much of an influence to be neglected in considering the process. At the present time, there are no quantitative estimates of this influence, and this is an area requiring further study.

Acknowledgments

The research support of the National Science Foundation, Solid Mechanics Program (Grant MEA82-10931) and of the NSF Materials Research Laboratory at Brown University (Grant DMR83-1683) is gratefully acknowledged. We are also grateful to Professor K. Ravi-Chandar for providing us with some unpublished data and for commenting on an earlier version of this paper.

The calculations described here were performed in the VAX-11/780 Computational Mechanics Facility at Brown University. This facility was made possible by grants from the National Science Foundation (Solid Mechanics Program), the General Electric Foundation, and the Digital Equipment Corporation.

References

Abramowitz, M., and Stegun, I. A., 1965, *Handbook of Mathematical Functions*, National Bureau of Standards, Washington.

Achenbach, J. D., and Nuismer, R. J., 1971, "Fracture Generated by a Dilatational Wave," *International Journal of Fracture Mechanics*, Vol. 7, pp. 77–88.

ASTM Standards, Part 10, 1978, "E399: Plane Strain Fracture Toughness of Metallic Materials," American Society for Testing and Materials, Philadelphia, pp. 512–533.

Baker, B. R., 1962, "Dynamic Stresses Created by a Moving Crack," ASME JOURNAL OF APPLIED MECHANICS, Vol. 29, pp. 449–458.

Beinert, J., Kalthoff, J. F., and Winkler, S., 1978, "Neuere Ergebnisse zur Andwendung des Schattenfleckverfahrens auf stehende und schnell-laufende Brûche," *VDI-Berichte Nr. 313*, pp. 791–799.

Burridge, R., 1976, "An Influence Function for the Intensity Factor in Tensile Fracture," *International Journal of Engineering Science*, Vol. 14, pp. 725–734.

Freund, L. B., 1972, "Crack Propagation in an Elastic Solid Subjected to General Loading—I. Constant Rate of Extension," *Journal of the Mechanics and Physics of Solids*, Vol. 20, pp. 129–140; "II. Nonuniform Rate of Extension," ibid, pp. 141–152.

Freund, L. B., 1973, "Crack Propagation in an Elastic Solid Subjected to General Loading—III. Stress Wave Loading," *Journal of the Mechanics and Physics of Solids*, Vol. 21, pp. 47–61.

Freund, L. B., 1974a, "Crack Propagation in an Elastic Solid Subjected to General Loading—IV. Obliquely Incident Stress Pulse," *Journal of the Mechanics and Physics of Solids*, Vol. 22, pp. 137–146.

Freund, L. B., 1974b, "The Stress Intensity Factor Due to Normal Impact Loading of the Faces of a Crack," *International Journal of Engineering Sciences*, Vol. 12, pp. 179–189.

Kalthoff, J. F., Beinert, J., and Winkler, S., 1977, "Measurements of Dynamic Stress Intensity Factors for Fast Running and Arresting Cracks in Double Cantilever Beam Specimens," in *Fast Fracture and Crack Arrest*, ASTM STP 627, Hahn, G. T., and Kanninen, M. F., eds., pp. 161–176.

Ma, C. C., 1982, "Caustic Curves Obtained by Numerically Simulating Reflection of Light Rays from the Surface of Plane Stress Fracture Specimens," Sc. M. Thesis, Brown University, Providence.

Ravi-Chandar, K., and Knauss, W. G., 1984, "An Experimental Investigation into the Mechanics of Dynamic Fracture: I. Crack Initiation and Arrest," *International Journal of Fracture*, Vol. 25, pp. 247–262; "II. Microstructural Branching," Vol. 26, pp. 141–154; "IV. On the Interaction of Stress Waves with Propagating Cracks," Vol. 26, pp. 189–200.

Rosakis, A. J., 1980, "Analysis of the Optical Method of Caustics for Dynamic Crack Propagation," *Engineering Fracture Mechanics*, Vol. 13, pp. 331–347.

Rosakis, A. J., Duffy, J., and Freund, L. B., 1984, "The Determination of Dynamic Fracture Toughness of AISI 4340 Steel by the Shadow Spot Method," *Journal of the Mechanics and Physics of Solids*, Vol. 32, pp. 443–460.

J. C. Lee

L. M. Keer
Fellow ASME

Department of Civil Engineering,
Northwestern University,
Evanston, Ill. 60201

Study of a Three-Dimensional Crack Terminating at an Interface

In this study the stress intensity factors for a three-dimensional crack perpendicular to and terminating at a bimaterial interface are calculated. It is assumed that the crack is pressurized by a uniform pressure. The method of solution used here is based upon the body-force method and requires the analytical results from the elasticity point-force solution for a bimaterial interface. The solution technique leads to the reduction of the problem to a two-dimensional singular integral equation, which can be solved numerically for the crack opening displacement. Numerical examples of a semi-circular, semi-elliptical crack and growth of circular crack are given.

Introduction

Considerable research has been done to evaluate the stress intensity factor and crack opening displacement for cracks in layered media (see, e.g., Daneshy (1976), Erdogan and Aksogan (1976)); however, the literature is usually applied to two-dimensional cases. The present paper presents the three-dimensional modelling of a vertical crack terminating at a perfectly bonded interface.

Few numerical methods are available for an accurate stress analysis of irregularly shaped three-dimensional cracks. Several general treatments of the planar crack problem reduce the problem to one involving a two-dimensional integral equation with the crack opening displacement or its derivative (the dislocation density) over the crack surface as the unknown quantity. By the use of single layer and double layer potentials, Bui (1977) has numerically solved the problem of a square crack under constant normal pressure. A rectangular crack in an infinite medium under normal pressure has been analyzed by Weaver (1977) by the boundary integral method. The body force method has been extensively used by Murakami and Nemat-Nasser (1982, 1983) to analyze first semi-elliptical surface flaws and then the growth of more generally shaped cracks in a half space. Using a different technique, Mastrojannis et al. (1979) obtained an integral equation for the unknown stresses outside the crack subjected to normal pressure and estimated the stress fields associated with egg-shaped, square with rounded corner, triangular and teardrop-shaped cracks.

In the present paper the body force method is used to solve the problem of an irregularly shaped three-dimensional vertical crack terminating at a perfectly bonded interface. The key to the utilization of the body force method is the availability of the known body force-displacement relation which in the present case is obtained by Rongved (1955) and put into the present notation by Dundurs and Hetényi (1965). The resultant equation is a two-dimensional integral equation for the crack opening displacement over the crack surface. The numerical results for stress intensity factor, K_I, for semi-circular and semi-elliptical cracks and the growth of circular cracks, constrained above and below are presented.

Method of Analyses

A fixed rectangular Cartesian system x_i, $i = 1, 2, 3$, with unit base vector $\mathbf{e}_i$ is used. We consider two dissimilar elastic half-spaces bonded together along the x–z plane. Suppose that the lower half-space is occupied by an elastic medium with elastic constants C^1_{ijkl} and the upper half-space by an elastic medium with constants C^2_{ijkl}. The crack is assumed to be in a plane normal to the $\mathbf{e}_3$ direction (Fig. 1). To account for the disturbance from the crack, let Ω be the volume of the crack in the lower half-space and introduce the eigenstrains ϵ^*_{ij} in Ω in such a manner that the stresses satisfy the boundary condition and that they vanish outside of Ω. The displacements in the lower material due to these eigenstrains ϵ^*_{ij} can be expressed as

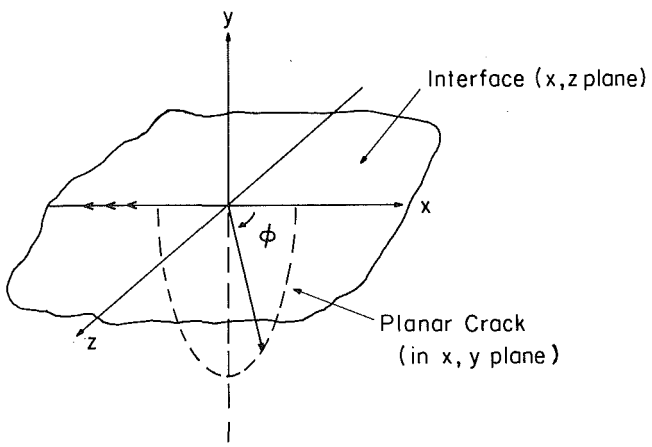

Fig. 1 Problem Configuration. Material 1 (μ_1, ν_1) is lower half-space ($y < 0$); material 2 (μ_2, ν_2) is upper half-space ($y > 0$).

Contributed by the Applied Mechanics Division for publication in the JOURNAL OF APPLIED MECHANICS.

Discussion on this paper should be addressed to the Editorial Department, ASME, United Engineering Center, 345 East 47th Street, New York, N.Y. 10017, and will be accepted until two months after final publication of the paper itself in the JOURNAL OF APPLIED MECHANICS. Manuscript received by ASME Applied Mechanics Division, April 23, 1985; final revision, August 27, 1985.

$$u_i(\mathbf{x}) = \int_\Omega C^1_{jlmn}\epsilon^*_{mn}\frac{\partial G_i^{(j)}(\mathbf{x},\xi)}{\partial\,\xi_l}\,d\xi \quad i=1,\,2,\,3 \tag{1}$$

where the Einstein summation convention is used and $G_i^{(j)}(\mathbf{x},\xi)$ represents the $\mathbf{e}_i$ direction displacement at point $\mathbf{x}$ produced by a unit load applied at point ξ in the $\mathbf{e}_j$ direction (Mura, 1982). The corresponding stress field is, therefore, given by

$$\sigma_{ij}(\mathbf{x}) = C^1_{ijkl}\int_\Omega C^1_{pqmn}\epsilon^*_{mn}\frac{\partial^2}{\partial x_l\partial\xi_q}G_k^{(p)}(\mathbf{x},\xi)d\xi \tag{2}$$

Denote by $2a_3$ the maximum direction of Ω measured in the x_3 direction. We now seek to obtain the limiting expression for equation (2), as $a_3 \to 0$ and $\Omega \to D$, i.e., as the inclusion reduces to the planar crack normal to the x_3 direction. Since only the opening mode in the $\mathbf{e}_3$ direction is involved, then ϵ^*_{33} is the only relevant eigenstrain. Let the distance to the crack faces measured along the x_3 direction be given by

$$w = \pm g(\xi),\ \xi = \xi_1\mathbf{e}_1 + \xi_2\mathbf{e}_2 \tag{3}$$

and introduce the quantity

$$b(\xi) = \int_g^g \epsilon^*_{33}(\xi)\,d\xi_3 \tag{4}$$

Then equation (2) yields

$$\begin{aligned}\sigma_{33}(\mathbf{x}) = \frac{2\mu_1\nu_1}{1-2\nu_1}\int_D \Bigg\{&\frac{2\mu_1\nu_1}{1-2\nu_1}\left[\frac{\partial^2 G_q^{(p)}}{\partial x_q\partial\xi_p}\right]_{\xi_3=0}\\ &+2\mu_1\left[\frac{\partial^2 G_q^{(3)}}{\partial x_q\partial\xi_3}\right]_{\xi_3=o}\Bigg\}b(\xi)ds\\ &+2\mu_1\int_D\Bigg\{\frac{2\mu_1\nu_1}{1-2\nu_1}\left[\frac{\partial^2 G_3^{(p)}}{\partial x_3\partial\xi_p}\right]_{\xi_3=0}\\ &+2\mu_1\left[\frac{\partial^2 G_3^{(3)}}{\partial x_3\partial\xi_3}\right]_{\xi_3=o}\Bigg\}b(\xi)ds\end{aligned} \tag{5}$$

where linear isotropic elasticity is assumed and μ_1 and ν_1 are the shear modulus and Poisson's ratio. The crack opening displacement $b(\xi)$ can be obtained from the boundary condition

$$\sigma_{33}(\mathbf{x}) = \int_D K(\mathbf{x},\xi)b(\xi)ds \equiv -p(\mathbf{x}),\quad \mathbf{x}\epsilon D \tag{6}$$

where $\mathbf{x} = x_1\mathbf{e}_1 + x_2\mathbf{e}_2$.

The Green's function $G_i^{(j)}$ can be obtained from Rongved's solution as modified by Dundurs and Hetényi (1965). The solution is given in terms of the Papkovich–Neuber potentials with Φ_i, ψ as vector and scalar potentials, respectively, which determine the displacement field through the relation

$$2\mu\,G_i^{(j)} = (\kappa+1)\Phi_i - (x_k\Phi_k + \psi)_{,i} \tag{7}$$

where $\kappa = 3-4\nu$.

The potentials for the force perpendicular to the interface ($\mathbf{e}_j = \mathbf{e}_2$) are

$$\Phi_2 = \{1/r_1 + A\kappa_1/r_2 + 2A\xi_2(x_2+\xi_2)/r_2^3\}/2\pi(\kappa_1+1) \tag{8}$$

$$\psi = \{\xi_2/r_1 + A\kappa_1\xi_2/r_2 + (A\kappa_1^2 - B)\log(r_2 - x_2 - \xi_2)/2\}/2\pi(\kappa_1+1) \tag{9}$$

where

$$r_1^2 = (x_1-\xi_1)^2 + (x_2-\xi_2)^2 + (x_3-\xi_3)^2,$$
$$r_2^2 = (x_1-\xi_1)^2 + (x_2+\xi_2)^2 + (x_3-\xi_3)^2, \tag{10}$$

$$A = (1-\Gamma)/(1+\Gamma\kappa_1),\ B = (\kappa_2 - \Gamma\kappa_1)/(\Gamma+\kappa_2) \quad \text{and } \Gamma = \mu_2/\mu_1 \tag{11}$$

The Papkovich–Neuber potentials for the parallel force ($\mathbf{e}_j = \mathbf{e}_1$) are

$$\Phi_1 = \{1/r_1 + S/r_2\}/2\pi(\kappa_1+1) \tag{12}$$

$$\Phi_2 = \{(A\kappa_1 - S)(x_1-\xi_1)/[r_2(r_2 - x_2 - \xi_2)] + 2A\xi_2(x_1-\xi_1)/r_2^3\}/2\pi(\kappa_1+1) \tag{13}$$

$$\psi = -\{(A\kappa_1^2 + B - 2S\kappa_1)(x_1-\xi_1)/[2(r_2 - x_2 - \xi_2)] + (A\kappa_1 - S)\xi_2(x_1-\xi_1)/[r_2(r_2 - x_2 - \xi_2)]\}/2\pi(\kappa_1+1) \tag{14}$$

where, in addition to the contractions defined by (11),

$$S = (1-\Gamma)/(1+\Gamma) \text{ and } T = (1-S)(\kappa_1+1)/(\kappa_2+1) \tag{15}$$

The kernel in equation (6) involves two differentiations of $G_i^{(j)}$. With the aid of the Symbolic Manipulation Package (SMP), which performs differentiation symbolically, the analytical effort is made considerably easier. The final result is given as

$$K(\mathbf{x},\xi) = \frac{\mu_1}{\pi(\kappa_1+1)}[1/r_1^3 + K_0(\mathbf{x},\xi)] \tag{16}$$

where $K_0(\mathbf{x},\xi)$ is a regular part and is of the form

$$\begin{aligned}K_0(\mathbf{x},\xi) = &\frac{2S(1+\kappa_1) - 3A(\kappa_1^2 - 2\kappa_1 + 3)}{2r_2^3}\\ &+\frac{3[12Ax_2\xi_2 - A(3-\kappa_1)(\kappa_1-1)(x_2+\xi_2)^2]}{2r_2^5}\\ &+\frac{3[B - 2S + 2A\kappa_1 + A\kappa_1^2 - 2S\kappa_1]}{2r_2(r_2 - x_2 - \xi_2)^2}\end{aligned} \tag{17}$$

If it is required to develop a solution for a crack in the upper half-space, then additional analysis must be performed. The results for such an analysis are given in the Appendix. Since the objective of this paper is to calculate growth constrained by the interface, computations only for the case shown in Fig. 1 are performed.

Numerical Procedure

To solve equation (6) numerically for a given crack contour shape, we first approximate the smooth contour ∂D by a straight line segment polygon ∂D_o and the domain D is then replaced by D_o. It is well known that the crack opening displacement vanishes in a square root sense on the smooth contour of the crack, if it is located interior to the material. The quantity $b(\xi)$, therefore is replaced by

$$b(\xi) = \sqrt{2a\epsilon - \epsilon^2}f(\xi) \tag{18}$$

where ϵ is a function whose value represents the shortest distance from the point ξ to the crack contour ∂D_o and "a" is a representative crack length (Murakami and Nemat-Nasser, 1983). The domain D_o is then divided into N triangular subdomains, $D\alpha$, $\alpha = 1, 2, \ldots N$, over each of which the unknown function $f(\xi_1, \xi_2)$ is assumed to be constant, where the point (ξ_1, ξ_2) for evaluating the function $f(\xi_1, \xi_2)$ is the center of each triangle. The integral equation (6) is now reduced to an algebraic equation

$$\sigma_{33}(\mathbf{x}^\alpha) = \sum_{\beta=1}^{N} K^{\alpha\beta}f^\beta = -p(\mathbf{x}^\alpha) \tag{19}$$

where

$$K^{\alpha\beta} = \frac{\mu_1}{4\pi(1-\nu_1)}\int_{D\beta}\sqrt{2a\epsilon - \epsilon^2}[r_1^{-3} + K_0(\mathbf{x}^\alpha,\xi)]d\xi_1 d\xi_2 \tag{20}$$

with $r_1^2 = (x_1^\alpha - \xi_1)^2 + (x_2^\alpha - \xi_2)^2$.

The integration in equation (20) is performed numerically. For the regular part, Gaussian double integration over a triangular region D_β is used directly (Cooper, 1973). If the distance $r_2 = \sqrt{(x_1^\alpha - \xi_1^\beta)^2 + (x_2^\alpha + \xi_2^\beta)^2}$ is smaller than $5\sqrt{\text{Area of } D_\beta}$, D_β is divided into four equal triangles and the procedure continues until the related distance r_2 of each triangle is greater than $5\sqrt{\text{Area of triangle}}$. Gaussian integration is then applied to each triangle.

The singular term associated with $1/r_1^3$ is evaluated by a combination of a closed form integral and numerical integration. Let ϵ_β be the minimum distance from the center of D_β to the crack edge and denote the singular integral by I as

$$I=\int_{D\beta}\frac{\sqrt{2a\epsilon-\epsilon^2}}{r_1^3}\,d\xi_1 d\xi_2 \tag{21}$$

If we let

$$I_1=\int_{D\beta}\frac{\sqrt{2a\epsilon-\epsilon^2}-\sqrt{2a\epsilon_\beta-\epsilon_\beta^2}}{r_1^3}\,d\xi_1\,d\xi_2 \tag{22}$$

$$I_2=\int_{D\beta}\frac{d\xi_1 d\xi_2}{r_1^3} \tag{23}$$

then $I = I_1 + \sqrt{2a\epsilon_\beta-\epsilon_\beta^2}\ I_2$. (24)

The integral I_2 has a closed form (Murakami and Nemat-Nasser, 1983). The procedure is as follows: rotate and shift the axes such that one of the axes is parallel to one side of triangle D_β and the origin is a point where the stress $\sigma_{33}(\mathbf{x})$ in equation (20) is to be determined. After this procedure, the integration can be performed in an ordinary sense; therefore, the detailed result is omitted.

When $\alpha \neq \beta$, the integral I_1 is not a singular one and Gaussian integration or repeated Gaussian integration can be used. However, for the case $\alpha = \beta$ a special numerical integration formula is needed. Rewrite I_1 as

$$I_1=\int_{D\beta}\frac{w(\mathbf{x}^\alpha,\xi)}{r_1^2}\,d\xi_1 d\xi_2 \tag{25}$$

with

$$w(\mathbf{x}^\alpha,\xi)=(\sqrt{2a\epsilon-\epsilon^2}-\sqrt{2a\epsilon_\beta-\epsilon_\beta^2})/r_1 \tag{26}$$

Integral I_1 is evaluated in the Cauchy principal value sense and converges if the function w is bounded and continuous (Theocaris et al., 1980). The continuity of w implies that the distance function ϵ should be differentiable at point $\mathbf{x}^\alpha$. However, the function ϵ is not differentiable everywhere unless the corresponding point can be surrounded by a circle containing neither the points of the polygon nor its separation points (Goncharyuk, 1972). The separation point is the point to which two or more points in the polygon have equal distances. For example, the point along the diagonals of square is a separation point which has equal distances from two conjunctive sides. The set of separation points forms a separation diagram. With this fact in mind, we do not triangulate the crack domain arbitrarily but first construct the separation diagram based on the scheme (Lee, 1978). Once the diagram and triangulation developed by Cavendish (1974) are constructed, the numerical scheme is applied to the integral I_1 (Theocaris et al., 1980).

To test the numerical scheme, two cases, circular and square cracks in a homogeneous material subjected to uniform pressure, were investigated. The stress intensity factor for a circular crack has 0.85 percent error in comparison with the exact solution. For the square crack, the maximum stress intensity factor has the value of $0.745\ \sigma_o\sqrt{(\pi a)}$ which is close to Mastrojannis et al. (1979) [$0.746\ \sigma_o\sqrt{(\pi a)}$] and Murakami and Nemat-Nasser (1983) [$0.736\ \sigma_o\sqrt{(\pi a)}$].

Numerical Scheme for Growth of Plane Cracks

A numerical scheme for growth of planar cracks is considered based on that developed by Mastrojannis et al. (1980) in which the material weakened by the crack was assumed to be a homogeneous and isotropic solid with zero permeability. Fluid is injected into the crack cavity at a constant rate. At any instant, the faces of the cracks are loaded with a normal pressure intensity given by the following expression:

$$p(x_1,x_2)=p_o+\Delta p(x_1,x_2) \tag{27}$$

where p_o = difference of fluid pressure and tectonic stresses at the reference point; Δp = tectonic stress differences. In equation (27), Δp is a known quantity, while the magnitude of p_o is assumed unknown. To make the problem well-posed, an additional equation is needed which comes from the equilibrium of volumes of injected fluid and crack cavity,

$$V=\int_D b(\xi_1,\xi_2)d\xi_1 d\xi_2 \tag{28}$$

The equation (26) with $p(x)$ as in equation (27) and equation (28) form a well-posed problem and the stress intensity factor K_I along the crack contour can be calculated. The crack does not grow unless K_I of part of the crack contour exceeds the critical value K_{IC}. By analogy to the crack growth law used in fatigue crack growth, we assume that the normal velocity of propagation of a point on the crack contour is given by

$$\begin{aligned} v&=C\left(\frac{K_I-K_{IC}}{K_{IC}}\right)^\gamma && \text{for } K_I > K_{IC}\\ &=0 && \text{for } K_I \le K_{IC}\end{aligned} \tag{29}$$

where C, with dimension of velocity, and γ are constants depending on the material properties. The normal distance covered by a point on a crack contour as it propagates for a time interval Δt is given by

$$\Delta u = v\Delta t \tag{30}$$

The scheme proposed for the solution of the stated problem consists of the following steps:

(1) Determine the stress intensity factor along the crack contour with the crack volume V.

(2) Using equation (29) calculate the velocity of propagation of a finite number of points on the crack contour.

(3) Allow the crack contour point with the maximum velocity to travel a short distance Δu along the normal to the crack contour at that point and determine the time interval Δt from equation (30). Then calculate the distances covered by the other points of the crack contour during the same time interval.

(4) From the coordinates of the propagated and stationary points determine the new contour shape of the crack.

(5) Start again from step 1.

The posed problem will be considered solved when a crack contour has been found, all points of which have a zero velocity of propagation.

Results

The method described in the preceding section, although sufficiently general for cracks having an arbitrary shape, will be applied specifically for the case of a semi-elliptical crack that terminates at a bimaterial interface (Fig. 1). For this case the crack is perpendicular to the plane of the interface, x-z axis, and the semi-minor axis of the ellipse is in the x direction. The crack is loaded by a uniform pressure, and it is desired to compute the value of the stress intensity factor as a function of the angle around the crack tip. The dimensions of the crack axes in the x and y directions are a and b, respectively. Figure 2 shows the mesh patterns used for a semi-circular and semi-elliptical crack. It is recalled from the previous sections that these meshes provide the means by which integration in the integral equations can be calculated.

For the circular case ($a/b = 1$) the figure shows that the dimensionless stress intensity factor remains relatively constant as a function of angle from -90 deg until about -30 deg, after which it rapidly approaches zero. The approach to zero at the interface for the materials shown in Fig. 3 will be less than 1/2. The conclusion that can be drawn from this curve is that crack growth will probably be constant along radial lines for most of the crack edge. For the semi-elliptical case ($a/b = 0.5$) the stress intensity factor is seen to reach a maximum at about -50 deg and decreases in value around this angle. Thus, it would appear that in this case further crack growth would tend to make the elliptical crack grow to become a circular crack. The conclusions for these cases are the following: the semi-circular crack will tend to grow cir-

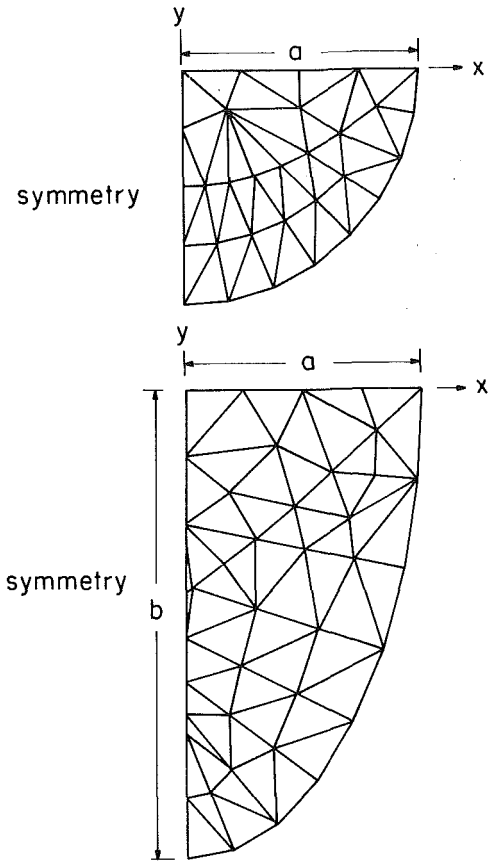

Fig. 2 Mesh pattern for semi-circular and semi-elliptical cracks

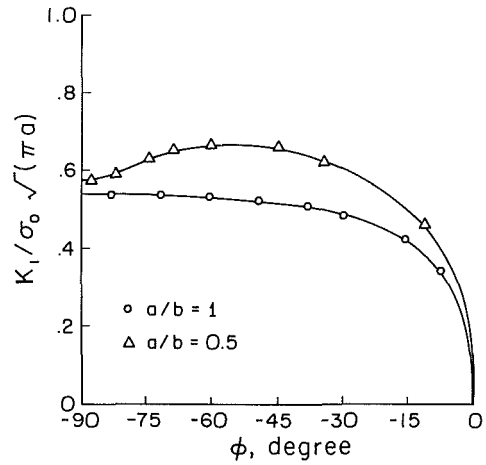

Fig. 3 Stress intensity factor for semi-circular and semi-elliptical cracks ($\mu_2/\mu_1 = 3$, $\nu_1 = \nu_2 = 0.1$)

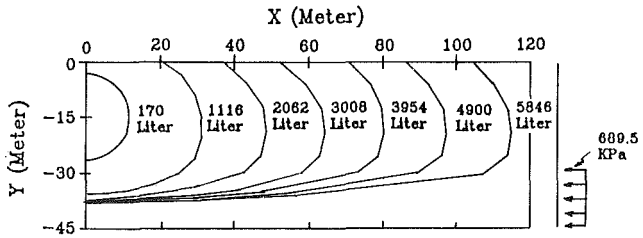

Fig. 4(a) Crack front growth with stress contrasts

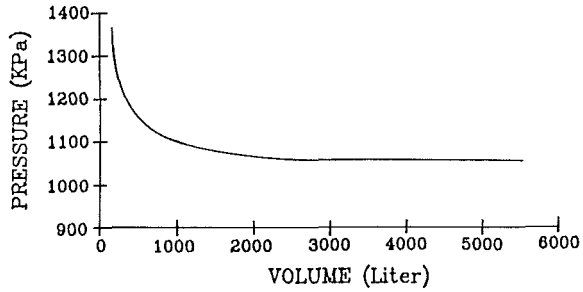

Fig. 4(b) Pressure (p_o) as a function of crack volume

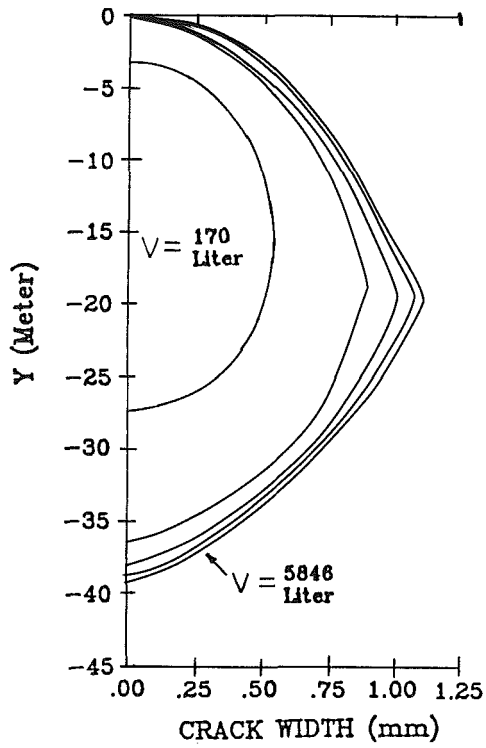

Fig. 4(c) Crack width along wellbore

cular and the semi-elliptical crack will tend to grow to become circular. It should be emphasized that these conclusions may be modified as further results are developed. Figures 4 through 5 show the results of the growth of a circular crack with a barrier at $y = -30.48$ m. The region $0 > y > -30.48$ m will be termed the "fracture zone." Tectonic stress applied to the lower barrier zone is taken to be larger than that applied to the fracture zone by 689.5 KPa and 1379 KPa, respectively. Shear moduli, μ_1 and μ_2, are 34.475 GPa and 103.425 GPa, respectively, and Poisson's ratios, ν_1 and ν_2, have the same value, $\nu_i = 0.1$, $i = 1, 2$. Fracture toughness is assumed to be 5.49 MPa$\sqrt{\text{m}}$. Figures 4(*a*) and 5(*a*) show that the crack front grows mainly in the fracture zone with some minor growth into the lower barrier. We note that the crack front near the interfacial boundary is approximated by straight lines. It seems that the crack shapes are at arrest around $y = -39$ m and $y = -33$ m. The variations of the uniform pressure term p_o are shown in Figs. 4(*b*) and 5(*b*). It is observed that during the initial phase of crack growth the magnitude of p_o decreases sharply and as crack growth continues the magnitude of p_o becomes relatively uniform. The crack opening displacements along the crack center line are shown in Figs. 4(*c*) and 5(*c*). They increase significantly at the first few steps and are rather steady thereafter. Furthermore, opening displacements show a discontinuity in slope that results from the approximation scheme used and which could be removed by smoothing. Figures 6(*a*) and 6(*b*) are plots of crack front growth and the variation of p_o for a circular crack in a homogeneous material. The crack grows farther into the upper barrier rather than the lower one, since the lower stress barrier is greater by 689.5 KPa than the upper one. The crack shape is at arrest

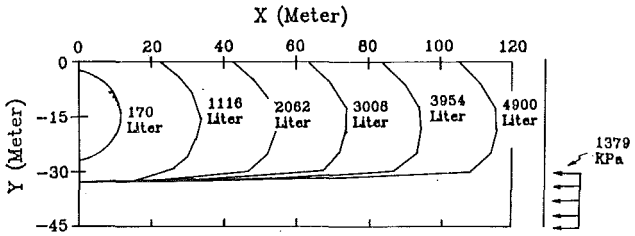

Fig. 5(*a*) Crack front growth with stress contrasts

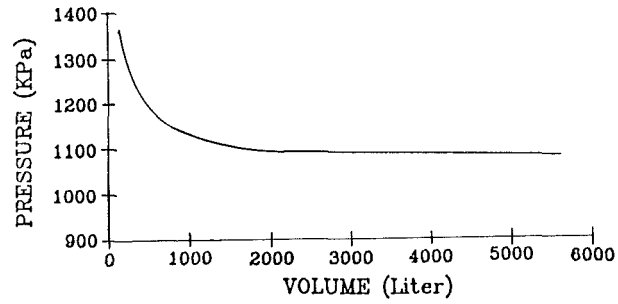

Fig. 5(*b*) Pressure (p_o) as a function of crack volume

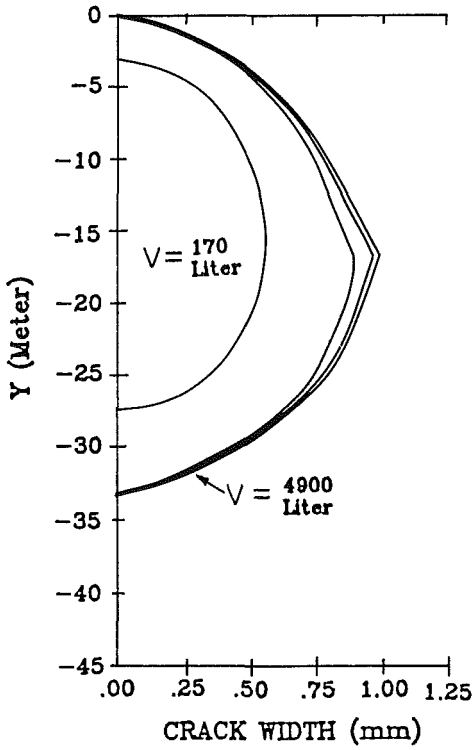

Fig. 5(*c*) Crack width along wellbore

around $y = 24$ m and $y = -18$ m for the upper and lower barriers, respectively. The crack opening displacement along the crack center line is given in Fig. 6(*c*).

Acknowledgment

The authors are grateful for support from Halliburton Services. They are also pleased to acknowledge helpful suggestions by Dr. A. A. Daneshy.

References

1 Bui, H. D., 1977, "An Integral Equations Method for Solving the Problem of Plane Crack of Arbitrary Shape," *Journal of the Mechanics and Physics of Solids*, Vol. 25, pp. 29-39.

2 Cavendish, J. C., 1974, "Automatic Triangulation of Arbitrary Planar Domains for the Finite Element Method," *International Journal for Numerical Methods in Engineering*, Vol. 8, pp. 679-696.

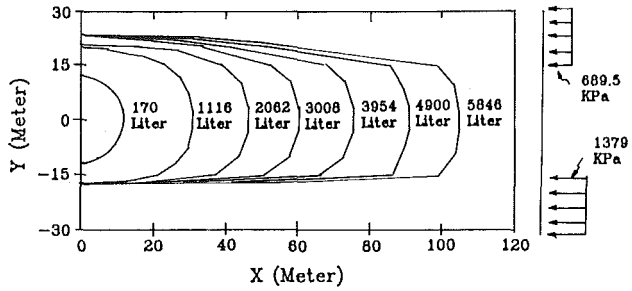

Fig. 6(*a*) Crack front growth for a circular crack in a homogeneous material with stress contrasts

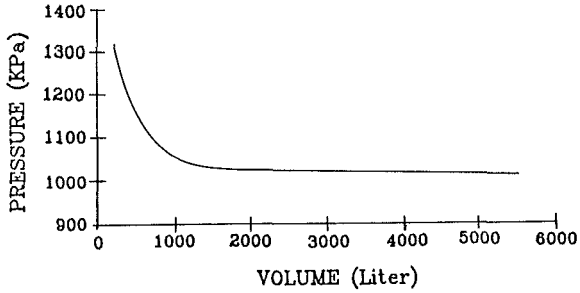

Fig. 6(*b*) Pressure (p_o) as a function of crack volume

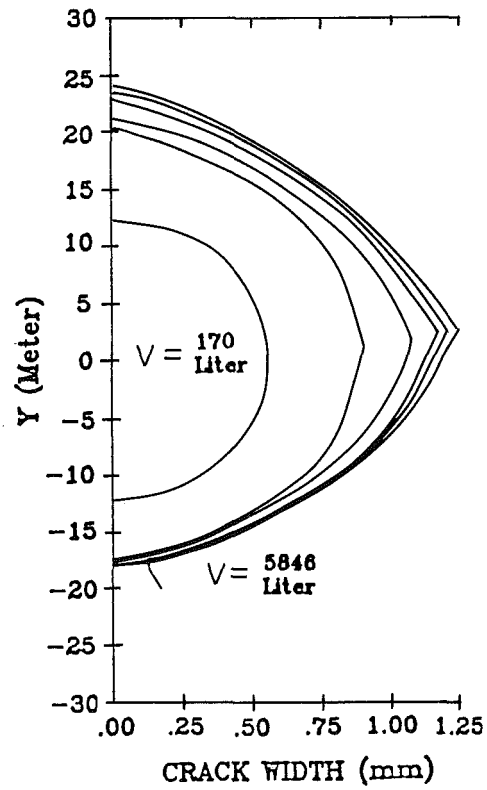

Fig. 6(*c*) Crack width along wellbore

3 Cooper, G. R., 1973, "Gaussian Quadrature Formulas for Triangles," *International Journal for Numerical Methods in Engineering*, Vol. 7, pp. 405-408.

4 Daneshy, A. A., 1976, "Hydraulic Fracture Propagation in Layered Formations," Paper SPE 6088, pp. 33-41.

5 Dundurs, J., and Hetényi, M., 1965, "Transition of Force Between Two Semi-Infinite Solids," ASME Journal of Applied Mechanics, Vol. 32, pp. 671-674.

6 Erdogan, F., and Aksogan, O., 1976, "Bonded Half-Planes Containing an Arbitrarily Oriented Crack," *International Journal Solids Structures*, Vol. 10, pp. 569-585.

7 Goncharyuk, I. V., 1972, "On the Elastic-Plastic Torsion of Rods of Complex Profile," English Translation, *Prikladnaya Mekhanika*, Vol. 8, No. 7, pp. 755-759.

8 Lee, D. T., 1978, "Proximity and Reachability in the Plane," Ph.D. Dissertation, Univ. of Ill., Urbana, Ill.

9 Mastrojannis, E. N., Keer, L. M., and Mura, T., 1979, "Stress Intensity Factor for a Plane Crack Under Normal Pressure," *International Journal of Fracture*, Vol. 15, pp. 247–258.

10 Mastrojannis, E. N., Keer, L. M., and Mura, T., 1980, "Growth of Planar Cracks Induced by Hydraulic Fracturing," *International Journal for Numerical Methods in Engineering*, Vol. 15, pp. 41–54.

11 Mura, T., 1982, *Micromechanics of Defects in Solids*, Martinus Nijhoff, pp. 104–109.

12 Murakami, Y., and Nemat-Nasser, S., 1982, "Interacting Dissimilar Semi-Elliptical Surface Flaws Under Tension and Bending," *Engineering Fracture Mechanics*, Vol. 16, pp. 373–386.

13 Murakami, Y., and Nemat-Nasser, S., 1983, "Growth and Stability of Interacting Surface Flaws of Arbitrary Shape," *Engineering Fracture Mechanics*, Vol. 17, pp. 193–210.

14 Rongved, L., 1955, "Force Interior to One of Two Joined Semi-Infinite Solids," *Proceedings of Second Midwestern Conference on Solid Mechanics*, pp. 1–13.

15 Theocaris, P. S., Ioakimidis, N. I., and Kaogantzakis, J. G., 1980, "On the Numerical Evaluation of Two-Dimensional Principal Value Integrals," *International Journal for Numerical Methods in Engineering*, Vol. 15, pp. 629–634.

16 Weaver, J., 1977, "Three-Dimensional Crack Analysis," *International Journal Solids Structure*, Vol. 13, pp. 321–330.

APPENDIX

Crack in Upper Half-Space

If crack is introduced into the upper material, then the potentials in the upper material due to the point force in the lower material are required. The potentials for the force perpendicular to the interface ($\mathbf{e}_j = \mathbf{e}_2$) are

$$\phi_2 = (1-B)/2\pi\ (\kappa_1+1)r_1 \tag{A1}$$

$$\psi = \{(1-A)\xi_2/r_1 + [(1-A)\kappa_1 - (1-B)\kappa_2]\log(r_1+x_2 - \xi_2)/2\}/2\pi\ (\kappa_1+1) \tag{A2}$$

The potentials for the parallel force ($\mathbf{e}_j = \mathbf{e}_1$) are

$$\phi_1 = T/2\pi\ (\kappa_1+1)r_1 \tag{A3}$$

$$\phi_2 = -(1-B-T)\,(x_1-\xi_1)/2\pi(\kappa_1+1)r_1(r_1+x_2-\xi_2) \tag{A4}$$

$$\psi = \{-[(1-A)\kappa_1 + (1-B-2T)\kappa_2]/2 - (1-A-T)\xi_2/r_1\}\,(x_1-\xi_1)/2\pi(\kappa_1+1)r_1(r_1+x_2-\xi_2)$$

The resulting integral equations can be expressed in the form

$$\sigma_{33}^{(i)} = \sum_{j=1}^{2}\int_{Dj} K_j^i(\mathbf{x},\,\xi)b_j(\xi)d\xi \quad \mathbf{x}\epsilon D_i,\ i=1,\,2 \tag{A5}$$

where D_1, D_2 are crack domains in the lower and upper materials, respectively. The kernel K_1^1 is shown in equation (16) and the other kernel terms are given below:

$$K_1^2 = \frac{\mu_1}{\pi(\kappa_1+1)}\{[A(\kappa_1-3)+B(\kappa_2-3)+(\kappa_1+1) - (\kappa_2-1) - 2S(1+\kappa_1)]/2r_1^3 + 3[-\kappa_1(1+A)+\kappa_2(1-B) + 2S(1+\kappa_1)]/2r_1(r_1+x_2-\xi_2)^2 - 3(A\xi_2 - Bx_2)\,[1/r_1 + 1/(r_1+x_2-\xi_2)]/r_1^2(r_1+x_2-\xi_2)\} \tag{A6}$$

$$K_2^1 = \frac{\mu_2}{\pi(\kappa_2+1)}\{[\bar{A}(\kappa_1-3)+\bar{B}(\kappa_2-3)+(\kappa_2+1) - (\kappa_1-1) + 2S(1+\kappa_2)]/2r_1^3 + 3[\kappa_1(1-\bar{A}) - \kappa_2(1+\bar{B}) - 2S(1+\kappa_2)]/2r_1(r_1-x_2+\xi_2)^2 + 3(\bar{B}\xi_2 - \bar{A}x_2)\,[1/r_1 + 1/(r_1-x_2+\xi_2)]/r_1^2(r_1-x_2+\xi_2)\} \tag{A7}$$

$$K_2^2 = \frac{\mu_2}{\pi(\kappa_2+1)}\{1/r_1^3 - [2S(1+\kappa_2)+3\bar{B}(\kappa_2^2-2\kappa_2+3)]/2r_2^3 + 3[12\bar{B}x_2\xi_2 - \bar{B}(3-\kappa_2)(\kappa_2-1)(x_2+\xi_2)^2]/2r_2^5 + 3[\bar{A}+2S(1+\kappa_2)+\bar{B}\kappa_2(\kappa_2+2)]/2r_2(r_2+x_2+\xi_2)^2\} \tag{A8}$$

where $\bar{A} = (\Gamma\kappa_1 - \kappa_2)/(1+\Gamma\kappa_1)$, $\bar{B} = (\Gamma-1)/(\Gamma+\kappa_2)$

M. J. Forrestal
Sandia National Laboratories,
Albuquerque, N. Mex. 87185
Mem. ASME

L. M. Lee

B. D. Jenrette

Ktech Corporation,
Albuquerque, N. Mex. 87110

Laboratory-Scale Penetration Experiments into Geological Targets to Impact Velocities of 2.1 km/s

We obtained forces on 3.0 and 6.0 CRH, ogival-nosed projectiles penetrating a simulated geological target. A gas gun and a powder gun accelerated foundry core targets (a simulated soft sandstone) to steady velocities between 0.6–2.1 km/s, and the targets subsequently impacted 20.6 mm diameter penetrators. Rigid-body motions of the penetrators were obtained with laser interferometry and piezoelectric accelerometers. At a penetration velocity of about 1.5 km/s, the 6.0 CRH nose shape exhibited severe, permanent deformation; whereas, the 3.0 CRH nose shape remained undeformed for penetration velocities up to 2.1 km/s.

Introduction

Backman and Goldsmith (1978) and Zukas (1982) discuss many recently developed analytical and experimental methods used to study penetration mechanics. For metal perforation and penetration, laboratory-scale experiments play a dominant role in the research required to understand penetration phenomena. However, experimental work on penetration into geological targets seems to be dominated by full-scale, field tests. Over the last two decades, Young (1969, 1971) and Patterson (see Forrestal, Longcope, and Norwood, 1981) conducted hundreds of instrumented, full-scale, field tests into soil, rock, and sea-ice targets. These penetrators usually contained on-board recording systems and measured deceleration during the penetration event. To complement these full-scale test programs, we have recently devised some laboratory-scale experiments. Forrestal et al. (1984) used gas guns to perform reverse-ballistic experiments with simulated, geological targets. Piezoelectric accelerometers measured the rigid-body acceleration of several nose shapes for impact velocities between 0.2–1.2 km/s. Since current field data are limited to impact velocities less than 0.6 km/s, laboratory-scale experiments can provide time-resolved data for much higher impact velocities.

For the present study, we measured rigid-body penetrator motions with laser interferometry and accelerometers for impact velocities from 0.6 to 2.1 km/s. As in our previous paper (Forrestal et al. 1984), the targets were foundry core samples made at the Sandia foundry. These targets had nominal density 1.8 Mg/m^3 and simulated many of the properties of the natural targets at the Sandia Tonopah Test Range, Nevada. For impact velocities less than 1.2 km/s, we used the Air Force Weapons Laboratory 102 mm bore (4.0 in.) gas gun; and for impact velocities between 1.2–2.1 km/s, we used the Sandia National Laboratories 89 mm bore (3.5 in.) powder gun. For impact velocities above 1.2 km/s, the penetrator accelerations approached the accelerometer capability (10^5 g); and for these

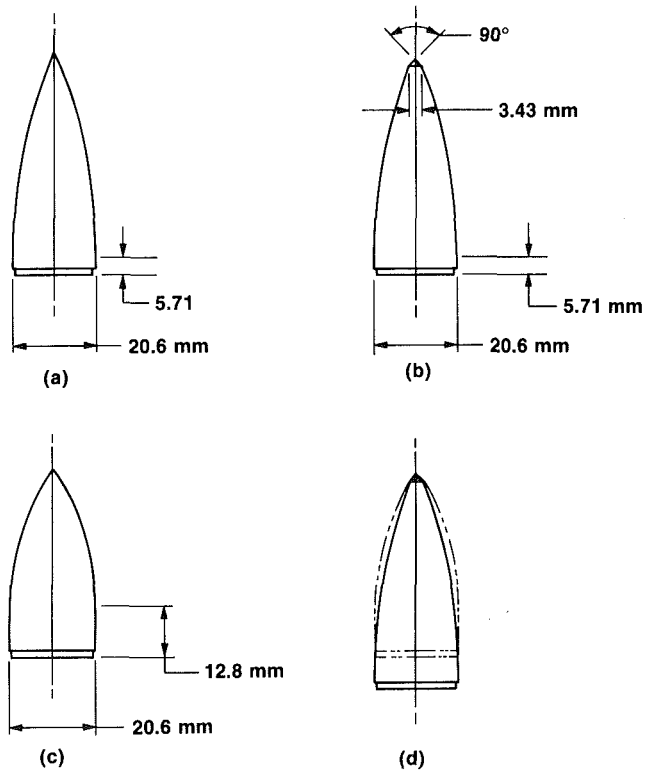

Fig. 1 Penetrator nose shapes: (*a*) 6.0 CRH; (*b*) tip-modified 6.0 CRH; (*c*) 3.0 CRH; (*d*) overlay of (*b*) and (c)

Contributed by the Applied Mechanics Division and presented at the Symposium on Mechanics of Impact Fracture—Part II, Winter Annual Meeting, Miami, Fla., November 17–21, 1985, of the AMERICAN SOCIETY OF MECHANICAL ENGINEERS.

Discussion on this paper should be addressed to the Editorial Department, ASME, United Engineering Center, 345 East 47th Street, New York, N.Y. 10017, and will be accepted until two months after final publication of the paper itself in the JOURNAL OF APPLIED MECHANICS. Manuscript received by ASME Applied Mechanics Division, February 12, 1985.

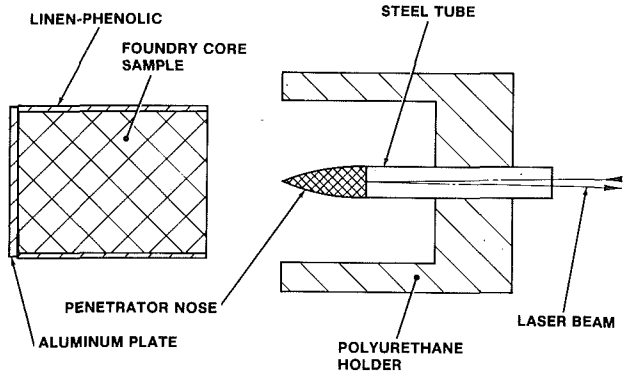

Fig. 2 Schematic for the powder-gun, reverse-ballistic experiments

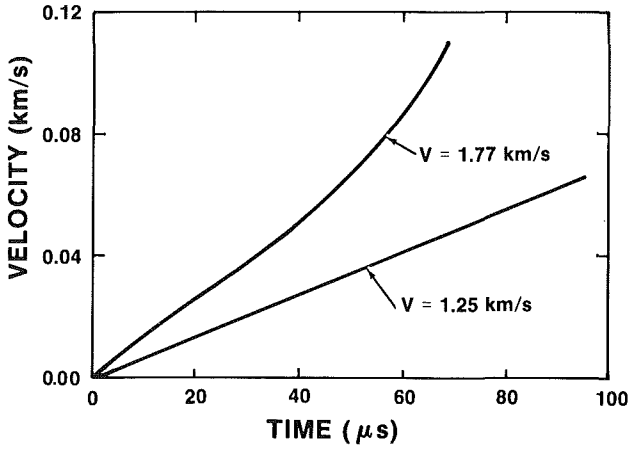

Fig. 3 Rigid-body, velocity-time responses for the 6.0 CRH nose shape. Impact velocities V = 1.25 and 1.77 km/s.

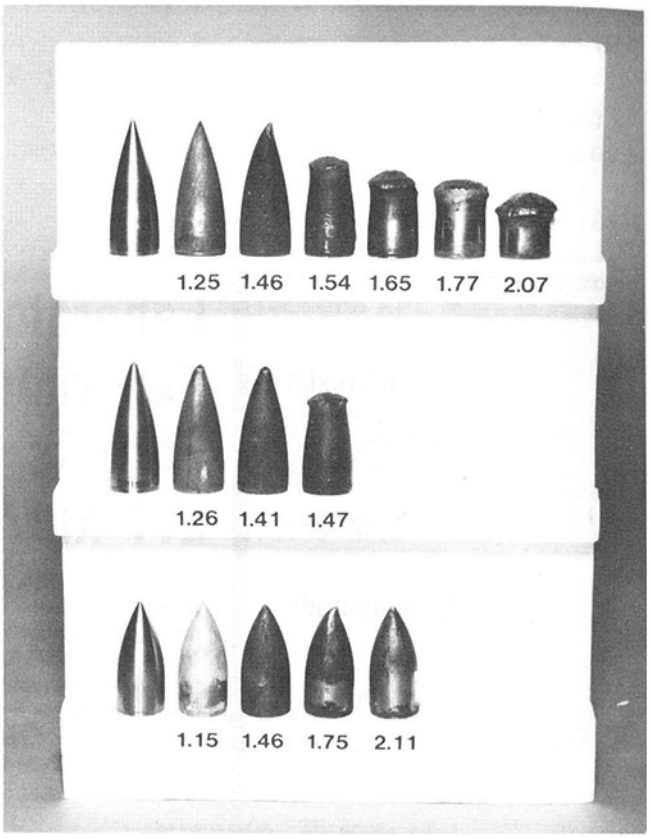

Fig. 4 Post-test nose shapes: (*a*) top, 6.0 CRH; (*b*) middle, tip-modified 6.0 CRH; (*c*) bottom, 3.0 CRH

higher impact velocity experiments, rigid-body motions were measured with laser interferometry (VISAR).

In our previous paper (Forrestal et al., 1984), we performed experiments to impact velocities of 1.2 km/s with two conical nose shapes and a 6.0 CRH ogival nose shape made from a tungsten alloy. For this study, we performed experiments on the same nose material to impact velocities of 2.1 km/s on 3.0 and 6.0 CRH ogival nose shapes. At a penetration velocity of about 1.5 km/s, the 6.0 CRH nose shape exhibited severe, permanent deformation. Brooks (1974) observed this same effect in his study on penetration into metal targets and termed this phenomenon the hydrodynamic transition velocity. By contrast, the 3.0 CRH nose shape remained undeformed for penetration velocities up to 2.1 km/s. In addition, we conducted a few experiments with the nose shape shown in Fig. 1*b*. This nose has a 6.0 CRH shape except its tip has a blunted, conical shape. The overlay in Fig. 1*d* shows that this tip-modified 6.0 CRH nose shape has nearly the same geometry as the 3.0 CRH nose shape. We hoped this design modification would avoid the hydrodynamic transition that occurred with the 6.0 CRH nose shape. However, several experiments indicated negligible differences in the motion responses and the hydrodynamic transition velocities for the 6.0 CRH nose shape and the tip-modified 6.0 CRH nose shape.

Experiments

Reverse-Ballistic Experiments. Figure 2 illustrates the reverse-ballistic experimental arrangement. Foundry core samples, contained within hollow projectiles, were accelerated to steady velocities, and the targets subsequently impacted 20.6 mm diameter (0.81 in.) penetrators. The Sandia Foundry made the targets with nearly the same process as that used for making molds for metal castings. This material is a mixture of silica sand (90 percent by weight) and binder ingredients. After the mixture is oven fired, the material resembles a low-density cemented sandstone with nominal density 1.85 Mg/m^3 and porosity 30 percent. Triaxial material tests data for this material are published (Forrestal et al., 1984). As typical for dry geologic materials, shear resistance increases significantly with increasing confining pressure.

As shown in Fig. 2, polyurethane holders, designed to ensure normal impact and offer negligible axial constraint, supported the penetrators. Thin (0.25 mm, 0.01 in.) steel tubes held the nose shapes forward of the polyurethane holders to permit full-length penetration of the foundry core targets before the projectile struck the back of the holders. These tubes were 246 mm (6.25 in.) long and were about nine percent of the total penetrator masses.

For the powder-gun experiments (impact velocity greater than 1.2 km/s), 69 mm diameter (2.7 in.), 121 mm length (4.75 in.) foundry core samples were contained in linen-phenolic projectiles with aluminum base plates. The gas-gun experiments used aluminum projectiles and 89 mm diameter, 89 mm length foundry core samples. At both facilities, impact velocities were measured to within 0.2 percent accuracy with a series of electrical contact pins.

Penetrators. The nose shapes shown in Fig. 1 were made from a dense (18.7 Mg/m^3) tungsten alloy.[1] These shapes consisted of a 6.0 CRH, a tip-modified 6.0 CRH, or a 3.0 CRH section and a stepped-cylindrical section. As illustrated in Fig. 2, the thin (0.25 mm) supporting tubes were shrunk fit to the nose shapes. All penetrators had 20.6 mm diameter afterbodies and masses of about 0.22 kg. Figure 2 illustrates the set-up for experiments that used laser interferometry to measure nose responses. As previously mentioned, some experiments were also conducted with piezoelectric ac-

[1] Kennertium W-2, Kennametal Inc., Latrobe, Pa. 15650.

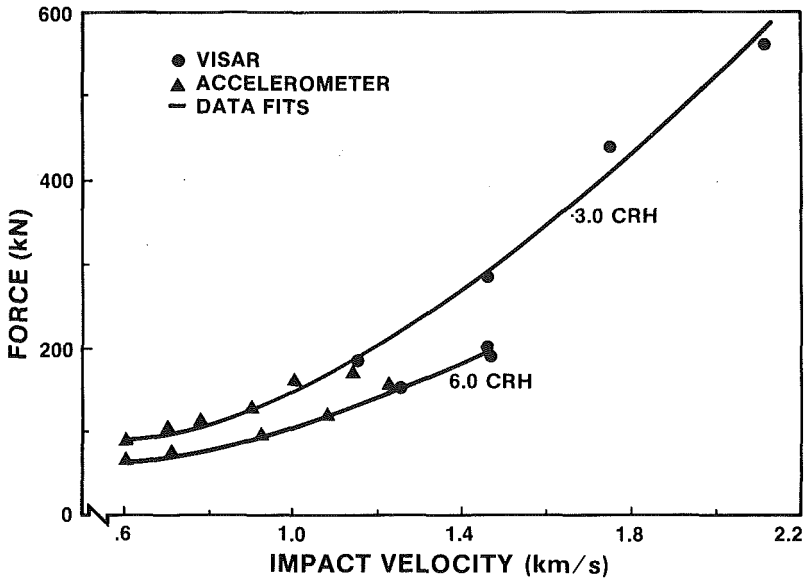

Fig. 5 Peak force versus impact velocity

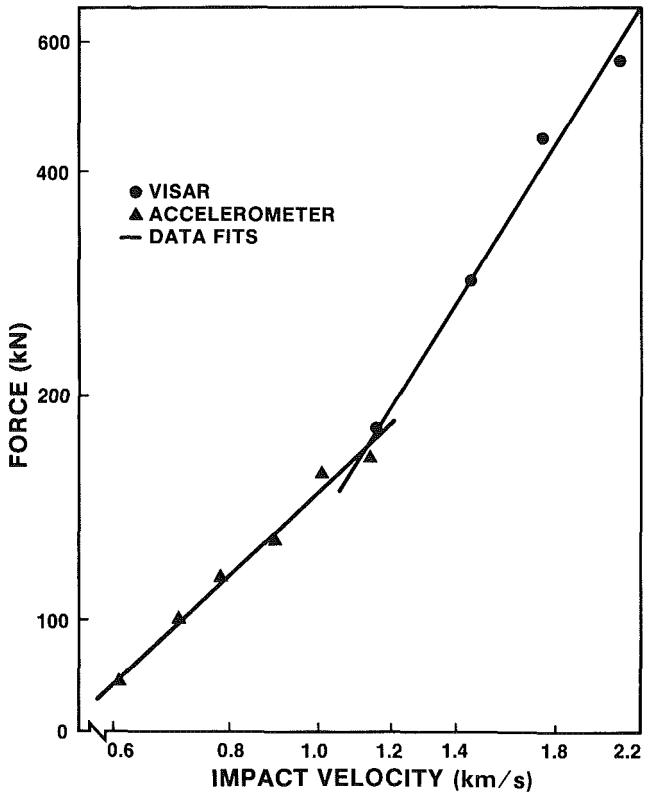

Fig. 6 Measurements and data fits for the 3.0 CRH nose shape

celerometers.[2] For these experiments the accelerometers were screwed into the back of the nose shapes (Forrestal et al., 1984).

Measurements. Rigid-body velocity and acceleration were measured with laser interferometry (VISAR) and accelerometers, respectively. Laser interferometry (VISAR, Barker and Hollenbach, 1972) was developed to measure time-resolved motion of the back surface of shocked specimen. VISAR is a widely used precision tool for shock profile measurements. However, our experiments were concerned with rigid-body motions and the back surface velocity magnitudes were much lower than those for typical shock wave studies. Therefore, for these relatively low-velocity measurements, we used an air-delay-leg VISAR (Amery, 1976, and Kusher et al., 1981) that was about five times more sensitive than VISARs used for shock wave studies and provided 3–5 fringes. Briefly, the interferometer provided a fringe signal with a fringe count proportional to the back surface velocity of the nosepiece. For the Argon-Ion laser and the delay length used for these experiments, each fringe corresponded to 0.031 km/s velocity change. Typical velocity-time data are presented in Fig. 3. Details on the acceleration measurement are contained in our previous paper (Forrestal et al., 1984).

[2]PCB Model 305A, PCB Piezotronics Inc., Depew, N.Y. 14043.

Table 1 Data summary for the 3.0 CRH ogival-nosed penetrators with cylindrical diameter 20.6 mm (0.810 in.); (GG = gas gun, PG = powder gun, A = accelerometer, V = VISAR)

Impact Velocity (km/s)	Target Density (Mg/m^3)	Facility, Measurement	Penetrator Mass (kg)	Peak Acceleration (g)	Peak Force (kN)
0.608	1.83	GG, A	228	37,000	82
0.704	1.83	GG, A	229	44,000	99
0.785	1.86	GG, A	229	50,000	113
0.895	1.85	GG, A	229	57,000	128
1.01	1.86	GG, A	228	70,000	158
1.14	1.84	GG, A	228	73,000	165
1.15	1.77	GG, V	217	85,000	181
1.46	1.85	PG, V	210	138,000	283
1.75	1.86	PG, V	220	203,000	440
2.11	1.84	PG, V	223	256,000	560

Table 2 Data summary for the 6.0 CRH ogival-nosed penetrators with cylindrical diameter 20.6 mm (0.810 in.); (GG = gas gun, PG = powder gun, V = VISAR, O = ogival tip, C = conical tip)

Impact Velocity (km/s)	Target Density (Mg/m^3)	Facility, Measurement, Nose Tip	Penetrator Mass (kg)	Peak Acceleration (g)	Peak Force (kN)
1.10	1.84	GG, V, O	214	60,000	127
1.25	1.85	PG, V, O	218	72,000	153
1.26	1.80	PG, V, C	219	73,000	156
1.41	1.81	PG, V, C	218	83,000	178
1.46	1.85	PG, V, O	223	87,000	190
1.46	1.84	PG, V, O	220	92,000	198

Experimental Results

Figures 4–6 and Tables 1 and 2 summarize the results of this study. The post-test photographs[3] shown in Fig. 4 indicate clearly that the 6.0 CRH and tip-modified 6.0 CRH nose shapes exhibit severe, permanent deformations for impact velocities larger than 1.5 km/s. Brooks (1974) observed this same effect when he conducted experiments with 6.0 CRH, tungsten-alloy penetrators and AISI 4340 steel targets. That is,

[3]We were not able to provide a soft catch for the penetrators. After impact, the penetrators interacted with a series of baffel plates.

in excess of a particular impact velocity the nose shape changed from essentially nondeforming to one that exhibited plastic flow. Brooks (1974) called this impact velocity, the hydrodynamic transition velocity. By contrast, the 3.0 CRH nose shape remained undeformed for impact velocities to 2.1 km/s.

We first conducted experiments with the 3.0 and 6.0 CRH shapes shown in Figs. 1*a* and 1*c*. The tip-modified, 6.0 CRH shape shown in Fig. 1*b* was designed with the intent of increasing the hydrodynamic transition velocity. However, subsequent experiments showed that this tip modification had no measurable effect. Figure 1*d* compares profiles of the 3.0 CRH and tip-modified 6.0 CRH nose shapes. The close similarity of these shapes indicates that the hydrodynamic transition velocity is sensitive to small geometry changes in nose shape.

Velocity-time profiles shown in Fig. 3 for the 6.0 CRH nose shapes provide additional information about the hydrodynamic transition velocity. The 1.25 km/s impact velocity was below the transition velocity, and velocity time was nearly linear after nose entry and before the end of travel through the foundry core target. However, the 1.77 km/s impact velocity was above the hydrodynamic transition velocity, and the velocity-time profile exhibited a monotonic slope increase after 40 μs. This velocity-time profile suggests that the onset time for the transition from a nondeformable nose to a plastically deformed nose shape was 40 μs.

As previously discussed, rigid-body velocity and acceleration of the nose shapes were measured with laser interferometry (VISAR) and accelerometers, respectively. Most of the experiments were conducted at impacts below the hydrodynamic transition velocity. For these experiments, velocity response was a smooth rise for about the time of nose entry followed by a nearly constant slope. This slope was measured to obtain peak acceleration and used to calculate peak force. Details of the acceleration measurements are discussed in our previous paper (Forrestal et al., 1984). Briefly, the rigid-body acceleration data show a smooth monotonic rise for about the time of nose entry followed by a nearly flat plateau. The magnitudes of the measured plateaus were used to calculate peak force. Tables 1 and 2 summarize the penetration data below the hydrodynamic transition velocity. Penetrator masses included the masses of the nose shape, supporting shell (0.02 kg), and accelerometer (0.005 kg, when applicable).

Peak force versus impact velocity data and quadratic fits to the data are shown in Fig. 5 for both the 3.0 and 6.0 CRH[4] nose shapes. The curve for the 6.0 CRH shape stops at V = 1.5 km/s, the hydrodynamic transition velocity. Data for the tip-modified, 6.0 CRH nose shape (Fig. 1*b*) are presented in Table 1, and these data show no measurable differences between the tip-modified 6.0 CRH and the 6.0 CRH nose shapes. It should also be pointed out that at V = 1.5 km/s (the transition velocity for the 6.0 CRH nose shape), the force on the 3.0 CRH nose shape was 50 percent larger than that on the 6.0 CRH nose shape. We have, at this time, no explanation for this observation.

Data and linear fits to the data for the 3.0 CRH nose shape are also presented on a log-log plot in Fig. 6. Empirical models are widely used as predictive tools (Sliter, 1980), and these data can be described conveniently in the form

$$F = KV^n$$

and K = 148 and n = 1.18 for $0.61 < V < 1.14$, K = 134 and n = 1.98 for $1.14 < V < 2.11$, and F, V have the units of kN, km/s.

Discussion

Over the last two decades, hundreds of instrumented, full-scale, field tests into geological targets have been conducted. To complement these full-scale test programs, we have devised some laboratory-scale experiments that measure penetrator motion for impact velocities to 2.1 km/s. Since data for instrumented, field tests are currently limited to impact velocities of about 0.6 km/s, only laboratory-scale experiments can currently provide time-resolved, velocity, and acceleration data for higher impact velocities.

Acknowledgment

This work was supported by the US Department of Energy.

References

Amery, B. T., 1976, "Wide Range Velocity Interferometer," *Proceedings of the Sixth Symposium on Detonation*, Office of Naval Research Report No. ACR 221, Washington, D.C., pp. 681–689.

Backman, M. E., and Goldsmith, W., 1978, "The Mechanics of Penetration of Projectiles into Targets," *International Journal of Engineering Science*, Vol. 16, pp. 1–99.

Barker, L. M., and Hollenbach, R. E., 1972, "Laser Interferometer for Measuring High Velocities of Any Reflecting Surface," *Journal of Applied Physics*, Vol. 43, No. 11, pp. 4669–4675.

Brooks, P. N., 1974, "Ballistic Impact—The Dependence of the Hydrodynamic Transition Velocity on Projectile Tip Geometry," DREV Report 4001/74, Research and Development Branch, Dept. of National Defense, Quebec, Canada.

Forrestal, M. J., Longcope, D. B., and Norwood, F. R., 1981, "A Model to Estimate Forces on Conical Penetrators Into Dry Porous Rock," ASME Journal of Applied Mechanics, Vol. 48, pp. 25–29.

Forrestal, M. J., Lee, L. M., Jenrette, B. D., and Setchell, R. E., 1984, "Gas-Gun Experiments Determine Forces on Penetrators Into Geological Targets," ASME Journal of Applied Mechanics, Vol. 51, No. 3, pp. 602–607.

Kusher, G., Hohler, V., Stilp, A., and Schneider, E., 1981, "Laser-Interferomic Investigations of Rod Deceleration During Impact Process," *Proceedings of the Sixth International Symposium on Ballistics*, Orlando, Florida.

Longcope, D. B., and Forrestal, M. J., 1983, "Penetration of Targets Described by a Mohr–Coulomb Failure Criterion With a Tension Cutoff," ASME Journal of Applied Mechanics, Vol. 50, No. 2, pp. 327–333.

Sliter, G. E., 1980, "Assessment of Empirical Concrete Impact Formulas," *Journal of the Structural Division*, ASCE, ST5, pp. 1023–1045.

Young, C. W., 1969, "Depth Prediction For Earth Penetrating Projectiles," *ASCE Journal of Soil Mechanics and Foundation*, Vol. 95, No. SM3, pp. 803–817.

Young, C. W., and Keck, L. J., 1971, "An Air-Dropped Sea Ice Penetrometer," SC-DR-71-0729, Sandia National Laboratories, Albuquerque, N.M.

Zukas, J. A., et al., 1982, *Impact Dynamics*, Wiley, New York.

[4]Accelerometer data for the 6.0 CRH nose shape were taken from our previous paper (Forrestal et al., 1984).

The Transient Field Under a Point Force Acting on an Infinite Strip

L. M. Brock
Dept. of Engineering Mechanics,
University of Kentucky,
Lexington, KY 40506

As a prelude to studying the transient stresses in a notched bar under impact, the transient stress and velocity field in the cross-section under a point force acting on one surface of an infinite elastic strip is examined. The point force is suddenly applied and normal to the surface. By transform methods, closed-form expressions for the transient field are obtained and used to study the multiple wave reflection process noticeably affects the field. In particular, the normal stress on the cross-section, tensile for the most part before the arrival of reflections, subsequently becomes essentially compressive.

Introduction

Elastic wave propagation studies in layers give insight into the dynamic response of plates, beams, and columns. While time-harmonic wave studies are often sufficient, for situations involving impulsive loadings and the possibility of rapid fracture, transient wave effects must be considered. Unfortunately, the mathematics of the multiple transient wave reflection processes which occur in layers and strips is complicated, so that asymptotic methods are often used, the results of which are accurate near wavefronts or for low or high-frequency waves (Keller, 1978).

One important transient wave problem for a strip arises in studying the dynamic tear (DT) test, a standard experiment in which a mass impacts across the width of the unnotched side of a simply-supported rectangular notched bar, causing fracture at the notch tip. Experiments (Nash and Lange, 1964) and rudimentary analysis (Brock et al., 1985) both suggest that fracture occurs after several wave reflections from the impacted and notched bar surfaces reach the notch tip. Because their number is small, the effect of each particular reflection on the solution field may be important; however, asymptotic or time-harmonic wave methods, as well as numerical solution approaches such as the finite element method, often lack specific wave signal sensitivity.

Thus, a nonasymptotic transient wave study of this test is needed. As a first step, it would be helpful to know what the stress field is in an unnotched bar in the cross-section under the impact load prior to the arrival of the wave reflections from the bar ends. It is this field which would be, in effect, removed by a notch.

This paper idealizes this first step into the two-dimensional problem of finding the transient stress and velocity field in the cross-section of an infinite strip underneath a suddenly-applied point force (line load in the out-of-plane direction). The strip is linearly elastic, isotropic and homogeneous, and is at rest prior to the point force application. This problem has been treated previously (Achenbach, 1973) by a combination of transform and asymptotic solution techniques. The present analysis will also employ transform methods, but will obtain closed-form expressions for the transient fields in the cross-section underneath the point force. These expressions are then studied, and illustrated graphically to indicate the field behavior.

Problem Formulation

Consider the infinite strip in the xy plane defined by $|y|<H$, where $2H$ is the strip width. Prior to $s=0$, where $s=$(dilatational wave speed) $\times$ (time), the strip is completely at rest. For $s>0$, a point force of magnitude F is applied normal to the strip surface $y=-H$ at $x=0$, as seen in Fig. 1. The pattern of wavefronts thus generated are indicated schematically in Fig. 2 for the first few dilatational wave strip traversal times. The governing equations for the process are

$$|y|=H: s_{xy}=0,\ y=H: s_y=0,\ y=-H: s_y=-F\delta(x) \qquad (1)$$

$$|y|<H: \nabla^2(u,v) + (m^2-1)\left(\frac{\partial}{\partial x},\frac{\partial}{\partial y}\right)\left(\frac{\partial u}{\partial x}+\frac{\partial v}{\partial y}\right)=m^2(\ddot{u},\ddot{v}) \qquad (2)$$

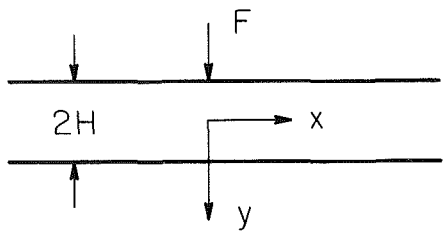

Fig. 1 Point force on strip

Contributed by the Applied Mechanics Division for presentation at the Winter Annual Meeting, Anaheim, CA, December 7-12, 1986, of The American Society of Mechanical Engineers.

Discussion on this paper should be addressed to the Editorial Department, ASME, United Engineering Center, 345 East 47th Street, New York, N.Y. 10017, and will be accepted until two months after final publication of the paper itself in the JOURNAL OF APPLIED MECHANICS. Manuscript received by ASME Applied Mechanics Division, March 28, 1985; final revision September 12, 1985. Paper No. 86-WA/APM-9.

$$\frac{1}{\mu}\, s_{xy} = \frac{\partial v}{\partial x} + \frac{\partial u}{\partial y}\,,\ \frac{1}{\mu}\,(s_x, s_y)$$

$$= m^2\left(\frac{\partial u}{\partial x}\,,\ \frac{\partial v}{\partial y}\right) + (m^2-2)\left(\frac{\partial v}{\partial y}\,,\ \frac{\partial u}{\partial x}\right) \tag{3}$$

for $s>0$, while for $s\le 0$

$$(u,v)\equiv 0 \tag{4}$$

Here (u, v) are the (x, y)-displacement components and are functions of (x, y, s), ∇^2 is the Laplacian operator, δ is the Dirac function, ($\dot{}$) denotes s-differentiation, μ is the shear modulus, and $(1, 1/m)$ are the dilatational and rotational wave speeds nondimensionalized by division by the dilatational wave speed. Thus, $m>1$. In addition to (1)-(4), appropriate radiation conditions (Stakgold, 1968) must hold as $|x|\to\infty$.

Transform Solution

The problem is attacked by introducing the Laplace and Fourier transforms (Sneddon, 1972)

$$G=\int_0^\infty g(s)e^{-ps}ds,\quad g^*=\int_{-\infty}^{\infty} g(x)e^{-ipqx}dx \tag{5a,b}$$

with respect to s and x, where p is real and positive while q is, in general, complex. Application of (5) to (2) in light of (3), (4) and the radiation conditions yields a pair of homogeneous coupled equations which can be solved to give

$$U^* = Ae^{pay} + Be^{-pay} + Ce^{pby} + De^{-pby} \tag{6}$$

$$V^* = \frac{a}{iq}\,(Be^{-pay} - Ae^{pay}) + \frac{iq}{b}(De^{-pby} - Ce^{pby}) \tag{7}$$

for $|y|<H$. Here (A,B,C,D) are arbitrary functions of (p,q) while

$$a=\sqrt{(1+q^2)},\quad b=\sqrt{(m^2+q^2)} \tag{8}$$

where the branch cuts of (a,b) are chosen so that $\mathrm{Re}(a,b)\ge 0$ in the cut q plane. Application of (5) to (1) in view of (3), (4) and the radiation conditions yields

$$|y|=H\text{: } S_{xy}^*=0,\ y=-H\text{: } S_y^*=0,\ y=-H\text{: } S_y^*=-\frac{F}{p} \tag{9}$$

where for $|y|<H$

$$\frac{1}{\mu}\,S_{xy}^* = \frac{dU^*}{dy} + ipqV^*,\ \frac{1}{\mu}(S_x^*, S_y^*)$$

$$= m^2\left(ipqU^*,\ \frac{dV^*}{dy}\right) + (m^2-2)\left(\frac{dV^*}{dy}\,,ipqU^*\right) \tag{10}$$

Substitution of (10) into (9) in view of (6)-(8) gives a matrix equation

$$\begin{bmatrix} 2ab\alpha_+ & -2ab\alpha_- & T\beta_+ & -T\beta_- \\ 2ab\alpha_- & -2ab\alpha_+ & T\beta_- & -T\beta_+ \\ T\alpha_+ & T\alpha_- & 2q^2\beta_+ & 2q^2\beta_- \\ T\alpha_- & T\alpha_+ & 2q^2\beta_- & 2q^2\beta_+ \end{bmatrix} \begin{bmatrix} A \\ B \\ C \\ D \end{bmatrix}$$

$$= \frac{Fq}{\mu p^2}\begin{bmatrix} 0 \\ 0 \\ 0 \\ 1 \end{bmatrix} \tag{11}$$

for the functions (A, B, C, D) where

$$T=2q^2+m^2,\quad S=2a^2-m^2,\quad \alpha_\pm = e^{\pm paH},\quad \beta_\pm = e^{\pm pbh} \tag{12}$$

Equation (11) is readily solved to yield

$$4PA = \frac{F}{\mu}\,\frac{qT}{p^2}\,[\alpha_-(\beta_-^2 R_+ + \beta_-^2 R_-) - 8q^2ab\alpha_+] \tag{13}$$

$$4PC = \frac{F}{\mu}\,\frac{2abq}{p^2}\,[\beta_-(\alpha_+^2 R_+ - \alpha_-^2 R_-) - 2T^2\beta_+] \tag{14}$$

where (B, D) follow from (A, C) by interchanging the subscripts $(+)$ and $(-)$, and

$$P=Q_+^2 - Q^2,\ Q=R_-\,sh\,pH(a+b),\ Q_+ = R_+\,shpH(b-a) \tag{15}$$

$$R_\pm = 4q^2ab \pm T^2 \tag{16}$$

Here, R_- is the Rayleigh function, with zeroes at $q=\pm im_R$, where $1/m_R$ is the nondimensionalized Rayleigh wave speed, and $m_R>m>1$. Indeed, since p is real and positive, it can be shown that P itself has no zeroes along the $\mathrm{Re}(q)$-axis.

Subsequently, the stress and velocity field underneath the point force, i.e., $x=0$, will be of interest. It is easily shown in view of (12)-(16) that the pertinent transforms for this field are

$$P\frac{\mu}{F}\,p\dot{V}^* = aT[Qchp(bH-ay) - Q_+\,chp(bH+ay)]$$

$$+ 2aq^2[Q_+\,chp(aH+by) - Qchp(aH-by)] \tag{17}$$

$$\frac{P}{F}\,p(S_x^*, S_y^*) = (S,-T)T[Q_+\,shp(bH+ay) + Qshp(bH-ay)]$$

$$+ (1,1)4abq^2[Q_+\,shp(aH+by) + Qshp(aH-by)] \tag{18}$$

Symmetry, of course, quarantees that $(s_{xy}, \dot{u})$ vanish along $x=0$. It should be noted that the expression corresponding to S_x^* obtained by Achenbach (1973) does not agree with equation (18) because a function corresponding to T appears in place of one corresponding to S, where S is defined in equation (12) along with T. It should also be noted that introducing the transformation $y'=H+y$ and then allowing $H\to\infty$ appropriately reduces equations (17) and (18) to the corresponding expressions for the point force on an elastic half-plane, i.e., Lamb's problem.

Manipulation of Transforms for Inversion

If the variable changes $pq=\xi$, $p=i\omega$ are made in equation (15), then setting the factors $Q_+ \pm Q$ of the denominator term P to zero gives the Rayleigh-Lamb frequency equations for, respectively, the antisymmetric and symmetric (with respect to y) vibrations of the strip. The asymptotic transient solution method described by Achenbach (1973) is based on knowing these frequencies, which can be found numerically by following Mindlin (1960).

The present analysis takes a more basic approach motivated by manipulations of equations (17) and (18) used in extracting the aforementioned Lamb's problem solution transform as a limiting case. First we write

$$2\,\frac{Q}{P} = \frac{1}{Q_+ - Q} - \frac{1}{Q_+ + Q}\,,\ 2\,\frac{Q_+}{P} = \frac{1}{Q_+ - Q} + \frac{1}{Q_+ + Q} \tag{19}$$

$$Q_+ \pm Q = \pm\,\frac{R_-}{2}\,\alpha_+\beta_+(1-C_\pm),\quad C_\pm$$

$$= (\alpha_-\beta_-)^2 \pm r(\beta_-^2 - \alpha_-^2),\quad R_-r = R_+ \tag{20}$$

and then, since p is real and positive, $\mathrm{Re}(a,b)\ge 0$ and P has no zeroes along the $\mathrm{Re}(q)$ axis, we write the terms $1/(1-C_\pm)$ as power series expansions in $C_\pm$. It is then easily shown that equation (19) can be rewritten as

$$\frac{Q}{P} = -2\,\frac{\alpha_-\beta_-}{R_-}\,D^-,\ \frac{Q_+}{P} = 2\,\frac{\alpha_-\beta_-}{R_-}\,D^+ \tag{21}$$

$$D^+ = I^+[r^{2k-2}\alpha_-^{\,2(l+n-2k)}\beta_-^{\,2(n-l)}],$$

$$D^- = I^-[r^{2k-1}\alpha_-^{\,2(l+n-2k-1)}\beta_-^{\,2(n-l)}] \tag{22}$$

$$I^+(f)=\sum_{n=1}^{\infty}(n-1)!\sum_{k=1}^{(n+1)/2}\frac{1}{(n-2k+2)!}\sum_{l=1}^{2k-1}\frac{(-1)^{l-1}f}{(l-1)!(2k-l-1)!} \tag{23}$$

$$I^-(f)=\sum_{n=1}^{\infty}(n-1)!\sum_{k=1}^{n/2}\frac{1}{(n-2k+1)!}\sum_{l=1}^{2k}\frac{(-1)^{l-1}f}{(l-1)!(2k-l)!} \tag{24}$$

Here it is understood that the summation limits on k are truncated to the nearest integer value, including zero, and that zero means that the term does not appear.

Transform Inversion

The inverse operation of equation (5*b*) is (Sneddon, 1972)

$$g(x)=\frac{p}{2\pi}\int g^*e^{ipqx}dq \tag{25}$$

where, as implied by the discussion of P, integration for equations (17) and (18) can be taken along the entire Re(q) axis. Formal application of equations (25) to (17) in view of its symmetry with respect to q yields

$$\frac{\mu}{F}\dot{V}=-2\mathrm{Re}\int\frac{\alpha_-\beta_-}{R_-}aT[D^+chp(bH-ay)+D^-chp(bH+ay)]e^{ipqx}dq+4\mathrm{Re}\int\frac{\alpha_-\beta_-}{R_-}aq^2[D^-chp(aH+by)+D^+chp(aH-by)]e^{ipqx}dq \tag{26}$$

where integration is now over the positive Re(q) axis. Equations (12), (23), and (24) show that equation (26) can be interpreted as the sum of an infinite number of integrals of the form

$$\mathrm{Re}\int_0^{\infty}f(q)e^{-p(a\xi+b\eta-iqx)}dq \tag{27}$$

The parameters (ξ, η) are linear combinations of (H, y), and the H coefficients are themselves linear combinations of the indices (k, l, n). Moreover, it is easily shown that (ξ, η) ≥ 0.

Following the Cagniard approach (deHoop, 1960), alternate integration contours in the q plane are now sought for each integral along which its exponential integrand factor assumes the form $\exp(-pt)$, $t>0$. The general properties of such Cagniard contours are well known (Brock, 1981), but explicit determination of the transformation $q(t)$ which defines the contour is difficult for the form given in equation (27). Fortunately, for the case $x=0$ which concerns us here, it is easily shown that

$$q(t)=\sqrt{\left[\left(\frac{t\xi-\eta\tau}{\xi^2-\eta^2}\right)^2-1\right]}=\sqrt{\left[\left(\frac{t\eta-\xi\tau}{\xi^2-\eta^2}\right)^2-m^2\right]},\qquad \tau(t)=\sqrt{[t^2+(m^2-1)(\xi^2-\eta^2)]} \tag{28}$$

where $t>\xi+m\eta$. Thus, the Cagniard contours for $x=0$ are simply parameterizations of the present integration path, where the t range $(\xi+m\eta,\infty)$ corresponds to the q range (0, ∞). Since equation (26) shows that the functions $f(q)$ in equation (27) are purely real along this path, introduction of equation (28) into (27) yields

$$\int_{\xi+m\eta}^{\infty}g[q(t)]\frac{e^{-pt}}{\tau(t)}dt,\quad g(q)=\frac{abf(q)}{q} \tag{29}$$

The Laplace transform of $\delta(s-t)$ is $\exp(-pt)$, so that the inverse of equation (29) is recognized as

$$\frac{g[q(s)]}{\tau(s)},\quad s>\xi+m\eta \tag{30}$$

Thus, for $x=0$, equation (26) becomes

$$\pi\frac{\mu}{F}\dot{v}=I^+[E_1(H+y,0)+E_1(H-y,2H)+E_2(0,H+y)+E_2(2H,H-y)]+I^-[E_1(H-y,0)+E_1(H+y,2H)+E_2(0,H-y)+E_2(E_2(2H,H+y)] \tag{31}$$

where

$$E_i(\alpha,\beta)=r(\alpha,\beta)^{2k-1}\frac{f_i(\alpha,\beta)}{\tau(\alpha,\beta)},\quad s>t(\alpha,\beta) \tag{32}$$

$$r(\alpha,\beta)=r[q(\alpha,\beta)],\quad f_i(\alpha,\beta)=f_i[q(\alpha,\beta)] \tag{33}$$

$$\tau(\alpha,\beta)=\tau(s),\quad t(\alpha,\beta)=\xi+m\eta \tag{34}$$

$$q(\alpha,\beta)=q(s),\quad qR_{\pm}f_1(q)=-a^2bT,\quad R_{\pm}f_2(q)=2a^2bq \tag{35}$$

In equations (32)-(35), $R_{\pm}$ corresponds to $I^{\pm}$ while the parameters (α,β) are manifested as

$$I^+:\ \xi=2(l+n-2k)H+\alpha,\quad \eta=2(n-l)H+\beta \tag{36}$$

$$I^-:\ \xi=2(l+n-2k-1)H+\alpha,\quad \eta=2(n-l)H+\beta \tag{37}$$

It should be noted that three special cases arise for the terms in equation (31):

$$\eta=0:\ q(s)=\sqrt{(z^2-1)},\quad z>1 \tag{38}$$

$$\xi=0:\ q(s)=\sqrt{(z^2-m^2)},\quad z>m \tag{39}$$

$$\xi=\eta:\ q(s)=\sqrt{\left[\frac{1}{4z^2}(z^2+1-m^2)^2-1\right]}=\sqrt{\left[\frac{1}{4z^2}(z^2+m^2-1)^2-m^2\right]},\quad z>1+m \tag{40}$$

where $z=s/\xi$ in equation (38) and $z=s/\eta$ in equations (39) and (40). For the special case (equation (38)), we have in equations (34) and (35)

$$\eta=0:\ \tau(s)=\sqrt{(s^2-\xi^2)},\quad R_{\pm}f_1(q)=-a^2T,\quad R_{\pm}f_2(q)=2a^2q \tag{41}$$

while for the special case (equation (39))

$$\xi=0:\ \tau(s)=\sqrt{(s^2-m^2\eta^2)},\quad R_{\pm}f_1(q)=-abT,\quad R_{\pm}f_2(q)=2abq^2 \tag{42}$$

Similar results hold for s_x and s_y along $x=0$:

$$\frac{\pi}{F}s_x=I^+[E_1(H-y,2H)-E_1(H+y,0)+E_2(2H,H-y)-E_2(0,H+y)]+I^-[E_1(H-y,0)-E_1(H+y,2H)+E_2(0,H-y)-E_2(2H,H-y)] \tag{43}$$

where in equations (35), (41), (42) we now have

$$qR_{\pm}f_1(q)=abST,\quad R_{\pm}f_2(q)=-4a^2b^2q \tag{44}$$

$$R_{\pm}f_1(q)=STa,\quad R_{\pm}f_2(q)=-4a^2bq^2 \tag{45}$$

$$R_{\pm}f_1(q)=STb,\quad R_{\pm}f_2(q)=-4ab^2q^2 \tag{46}$$

respectively, and the expression for s_y follows by replacing S with $-T$ and -4 with 4 in equations (44)-(46), cf. equation (18). Although not now surprising, introducing the transformation $y'=H+y$ and allowing $H\to\infty$ in equations (31) and (43) results in the corresponding Lamb's problem expressions.

General Observations

Equations (23) and (24) imply that the stress and velocity field along $x=0$ is described by an infinite series of E func-

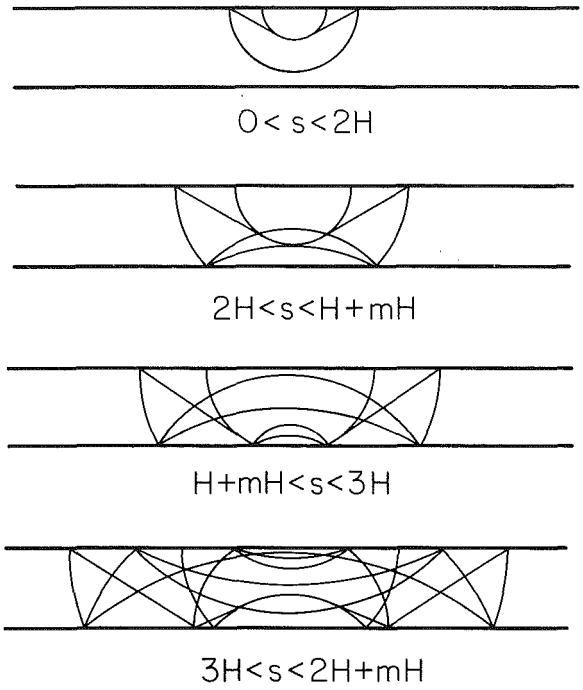

Fig. 2 Wavefront patterns due to point force on strip

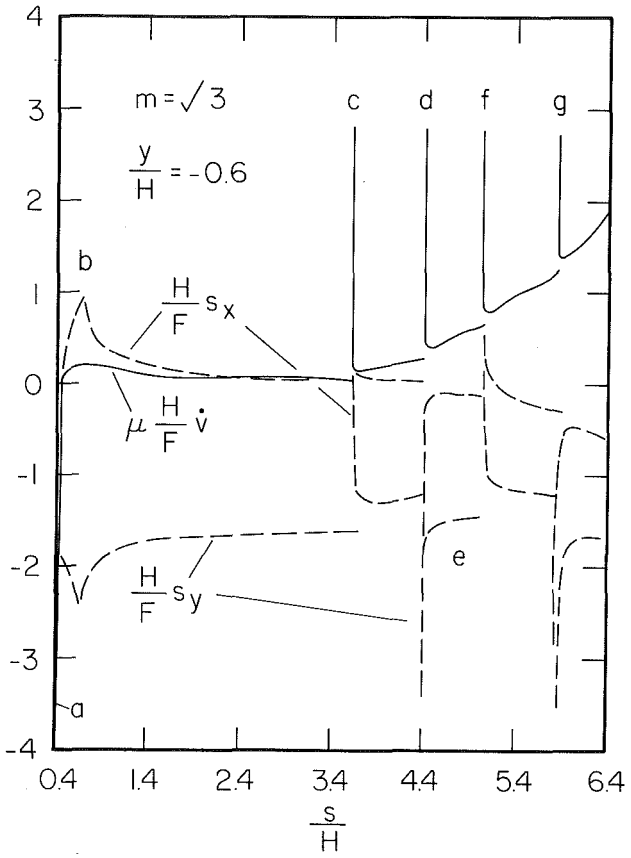

Fig. 3 Stress and velocity field on strip cross-section under point force

tions. However, equation (32) shows that a given E function actually does not appear until a specified instant $t(\alpha,\beta)$. Whenever $\alpha = H \pm y$, β does not, and equations (36) and (37) show that $t(\alpha, \beta)$ assumes the form

$$t(\alpha,\beta) = 2n_1 H + 2mn_2 H + H \pm y \geq 0 \tag{47}$$

where (n_1, n_2) are integers determined by β and the indices (k, l, n). Similarly, whenever $\beta = H \pm y$, α does not, and we have

$$t(\alpha,\beta) = 2n_1 H + 2mn_2 H + m(H \pm y) \geq 0 \tag{48}$$

Further examination of equations (36) and (37) in view of equations (31) and (43) shows that

$$I^+ : n_1 + n_2 = 2(n-k) + (1,0) \tag{49}$$

$$I^- : n_1 + n_2 = 2(n-k) - 1 + (0,1) \tag{50}$$

for $(H-y, H+y)$, respectively. That is, $n_1 + n_2$ is an odd number whenever $H-y$ appears in $t(\alpha,\beta)$, but even when $H+y$ appears. In view of Fig. 2, then, equations (47) and (48) are clearly the times of arrival at a given y of, respectively, a dilatational and rotational wave, where $H \pm y$ indicates that the waves are traveling, respectively, away from and towards the point force.

Since $2H$ is the strip width, equations (47) and (48) also show that the waves are the $n_1 + n_2$ reflections in reflection processes involving n_1 dilatational and n_2 rotational waves. It follows that the special cases (equations (38) and (39)) arise when, respectively, equation (47) holds with $n_2 = 0$, and equation (48) holds with $n_1 = 0$. That is, the reflection processes do not involve phase changes.

Further study of equations (47)–(50) shows that the smallest two values of $t(\alpha,\beta)$, i.e., the first two wave arrivals, are

$$I^+(E_1): t(\alpha,\beta) = H + y, \quad I^+(E_2): t(\alpha,\beta) = m(H+y) \tag{51}$$

This indicates that the reflection process described by the E_1 and E_2-function series arise from, respectively, the first dilatational and rotational waves, see Fig. 2, generated by the point force application. Indeed, their arguments in equations (31) and (43) show that, no matter what the reflection history is, E_1 and E_2 always describe waves which are, at the instant, dilatational and rotational, respectively.

Finally, examination of equations (28) and (38)–(46) shows

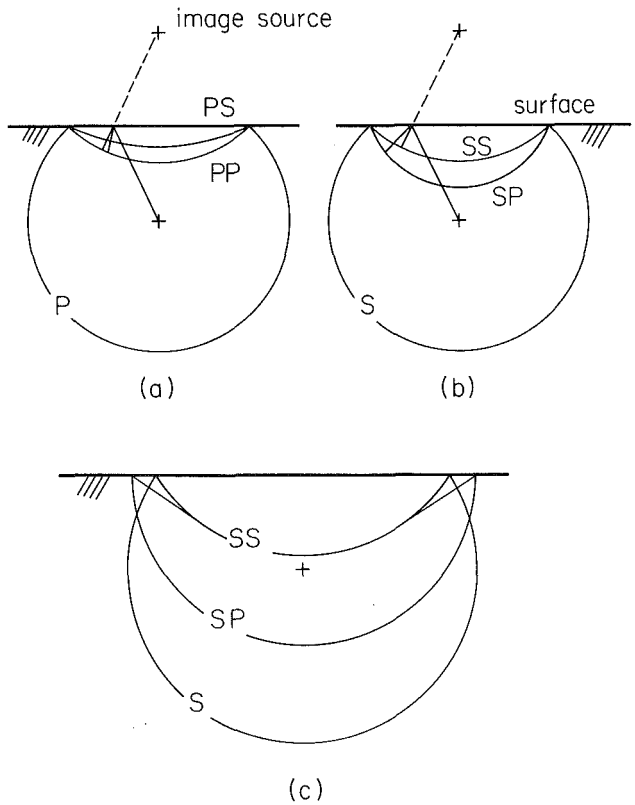

Fig. 4 (a) Schematic of dilatational wave reflection; (b) schematic of rotational wave reflection before separation; (c) schematic of rotational wave reflection after separation

that $q[t(\alpha,\beta)]=0$ in general while $\tau[t(\alpha,\beta)]=0$ for the special cases (equations (38) and (39)) which, in turn, implies that the E_2 function, i.e., rotational, waves are continuous at their wavefronts, while the E_1, i.e., dilatational, fronts exhibit square-root singularities.

In summary, the series expansions (equation (21)) allow the stress and velocity field along $x=0$ to be written as superpositions of the elastic waves generated by the multiple reflection process in the strip. This series approach is a standard (Carrier and Pearson, 1976) one in the solution of wave propagation problems.

Numerical Calculations

For insight into solution response features which are not apparent from the forms of equations (31) and (43), these expressions are plotted versus s/H for $y/H = -0.6$ and $m = \sqrt{3}$ in Fig. 3. Important aspects of Fig. 3 are, however, best viewed in terms of the wavefront pattern shown in Fig. 2. The multiple wave reflection process in Fig. 2 looks complicated, but essentially follows the scheme shown in Fig. 4:

Imagine a cylindrical dilatational (*P*) wave nearing a stress-free surface. As shown in Fig. 4*a*, the reflection of this wave by the surface generates a dilatational (*PP*) and rotational (*PS*) wave. The fronts of these waves can be defined in terms of the image of the *P*-wave source location and Snell's law (Lindsay, 1960). Similarly, as shown in Fig. 4*b*, the reflection of a cylindrical rotational (*S*) wave generates a dilatational (*SP*) and rotational (*SS*) wave. Because the *SP* wave travels faster than the *S* and *SS* waves, however, its front will eventually become perpendicular to the surface and then separate from those waves. This separation, as seen in Fig. 4*c*, leads to the formation of head waves, in keeping with Huygen's principle (Lindsay, 1960).

In view of Figs. 2 and 4, the various wave arrivals indicated by the letters in Fig. 3 are now easily identified as

a: *P* wave from surface $y=-H$
b: *S* wave from surface $y=-H$
c: *PP* wave from surface $y=H$ (reflection of *P* wave *a*)
d: *PP* wave from surface $y=-H$ (reflection of *PP* wave *c*)
e: *PS* wave from surface $y=H$ (reflection of *P* wave *a*)
f: *SP* wave from surface $y=H$ (reflection of *S* wave *b*)
g: *PP* wave from surface $y=-H$ (reflection of *SP* wave *f*)

The wavefront behavior at the arrivals confirms the observations made above. It is of interest to note that the velocity wavefront singularities do not affect the general time response as noticeably as do the stress wavefront singularities. In general, however, Fig. 3 shows that the multiple wave reflection process in the strip does have an important effect on the stress and velocity field. In particular, the process guarantees that the stress state on the strip cross-section under the point force is, except for brief periods after some dilatational wave arrivals, compressive. On the other hand, the normal stress on the cross-section become tensile very rapidly after the first wave arrival, and remains so until the arrival of dilatational waves generated by reflection. Thus, the cross-section is, for certain intervals, a good location for Mode I fracture.

Summary

Closed-form expressions for the fully transient stress and velocity field along the cross-section of an infinite strip under a suddenly-applied point force have been derived by standard transform and inversion techniques. The forms of the expressions themselves represent the multiple wave reflection process which occurs because component wave contributions can in principle be identified. Moreover, they show that the wavefront behavior of either a dilatational or rotational wave is the same, no matter what its reflection history is.

Calculations of the field expressions show that the normal stress on the cross-section is initially compressive, but rapidly becomes tensile before the arrival of wave reflections. Their arrival results in a generally compressive stress. This prereflection arrival behavior also seems to occur even when the strip contains a notch along the cross-section, as analytical results obtained by Brock et al. (1985) show. The effect suggests that the fracture plane becomes tensile without necessarily "knowing" that it is located in a strip of finite length. However, the results of Brock et al. (1985), are valid only until the arrival of the first wave reflections. Further study is obviously required to satisfactorily characterize the transient stress field at the notch tip. As indicated at the outset, it is planned that the results obtained here will be used in such a study.

Acknowledgment

This work was supported by NSF Grant MEA 8319605.

References

Achenbach, J. D., 1973, *Wave Propagation in Elastic Solids*, North-Holland, Amsterdam, pp. 331–342.

Brock, L. M., Jolles, M., and Schroedl, M., 1985, "Dynamic Impact over a Subsurface Crack: Applications to the Dynamic Tear Test," ASME JOURNAL OF APPLIED MECHANICS, Vol. 52, pp. 287–290.

Brock, L. M., 1981, "The Effects of Displacement Discontinuity Derivatives on Wave Propagation – III. Body and Point Forces," *International Journal of Engineering Science*, Vol. 19, pp. 949–957.

Carrier, G. F., and Pearson, C. E., 1976, *Partial Differential Equations*, Academic Press, New York, pp. 50–53.

deHoop, A. T., 1960, "A Modification of Cagniard's Method for Solving Seismic Pulse Problems," *Applied Scientific Research*, Vol. B8, pp. 249–256.

Keller, J. B., 1978, "Rays, Waves and Asymptotics," Bulletin of the American Mathematical Society, Vol. 84, pp. 727–750.

Lindsay, R. B., 1960, *Mechanical Radiation*, McGraw-Hill, New York, pp. 48–68.

Mindlin, R. D., 1960, "Waves and Vibration in Isotropic Elastic Plates," *Structural Mechanics*, Goodier, J. N., and Hoff, N. J., eds., Pergamon Press, New York.

Nash, G. E., and Lange, E. A., 1964, "Mechanical Aspects of the Dynamic Tear Test," ASME *Journal of Basic Engineering*, Vol. 91, pp. 535–543.

Sneddon, I. N., 1972, *The Use of Integral Transforms*, McGraw-Hill, New York.

Stakgold, I., 1968, *Boundary Value Problems of Mathematical Physics, Vol. II*, MacMillan, New York. pp. 296–299.

Elastic Wave Scattering from an Interface Crack in a Layered Half Space Submerged in Water: Part I: Applied Tractions at the Liquid-Solid Interface

S. M. Gracewski
Assistant Professor,
Department of Mechanical Engineering,
University of Rochester,
Rochester, NY 14627

D. B. Bogy
Professor,
Department of Mechanical Engineering,
University of California, Berkeley,
Berkeley, CA 94720

In Part I of this two-part paper, the analytical solution of time harmonic elastic wave scattering by an interface crack in a layered half space submerged in water is presented. The solution of the problem leads to a set of coupled singular integral equations for the jump in displacements across the crack. The kernels of these integrals are represented in terms of the Green's functions for the structure without a crack. Analysis of the integral equations yields the form of the singularities of the unknown functions at the crack tip. These singularities are taken into account to arrive at an algebraic approximation for the integral equations that can then be solved numerically.

Numerical results in the form of crack tip stress intensity factors are presented for the cases in which the incident disturbance is a harmonic uniform normal or shearing traction applied at the liquid-solid interface. These results are compared with a previously published solution for this problem in the absence of the liquid. In Part II, which immediately follows Part I in the same journal issue, the more realistic disturbances of plane waves and bounded beams incident from the liquid are considered.

I Introduction

Wave propagation in layered elastic media has been the focus of much work both in seismology and for nondestructive evaluation (NDE) applications. In much of this work, the layers are assumed to be perfectly bonded to each other. Structures are not always ideal however, and can contain flaws such as interface cracks or debonding between layers. One concern in NDE is the location and characterization of these regions of debonding. With this purpose in mind, in this paper, Part I, and the following one, Part II, we investigate the elastic wave scattering by a crack at the interface between a layer and a half space. Here we restrict the numerical results to the cases in which the incident disturbance is due to harmonic uniform normal or shearing traction applied at the liquid-solid interface. In Part II we consider more realistic incident disturbances and obtain various scattered field results that are relevant to fracture mechanics and NDE.

In many ultrasonic NDE test facilities, the solid structure under investigation is submerged in a liquid, usually water. Two pressure transducers are located above the structure, one to create a wave beam that impinges on the solid surface and the other to detect the "reflected" waves. Therefore, the layered solid half space in the present investigation is in contact above with a liquid half space. The incident wave and detected response are assumed to be in the liquid.

In Achenbach et al. [1] and Keer et al. [2], the plane strain problem of scattering by a crack parallel to the free surface of a half space was considered. The structure considered here reduces to this case when the two materials are the same and the liquid is removed. Comparison in this limiting case with results in [2] has been used as one check on the results presented here. The corresponding antiplane problem was considered in Ryan and Mall [3].

The antiplane and plane strain problems of an interface crack between a layer and half space were investigated by Neerhoff [4] and Yang and Bogy [5], respectively. Reference [5] was also used as a check on the calculations of the present work. Due to space limitations many important details are omitted here. Readers interested in a more complete development are referred to the Ph.D. Dissertation of Gracewski [6] on which these two papers are based.

II Problem Formulation

The two-dimensional plane strain structure to be considered consists of an elastic layer of thickness H bonded below to an

Contributed by the Applied Mechanics Division for presentation at the Winter Annual Meeting, Anaheim, CA, December 7–12, 1986, of the American Society of Mechanical Engineers.

Discussion on this paper should be addressed to the Editorial Department, ASME, United Engineering Center, 345 East 47th Street, New York, N.Y. 10017, and will be accepted until two months after final publication of the paper itself in the JOURNAL OF APPLIED MECHANICS. Manuscript received by ASME Applied Mechanics Division, November 15, 1984; final revision June 10, 1985. Paper No. 86-WA/APM-4.

elastic half space (substrate) and in contact above with a liquid half space (see Fig. 1). The layer is perfectly bonded to the solid half space except along the region $|x| < a$, where a stress-free crack of length $2a$ is located. We assume the crack faces remain traction free over the entire load cycle. In order to achieve this condition in reality the crack would have to be initially opened by a static preload or some other means, and our dynamical solution would be superposed on that initial state. Both solids are assumed to be isotropic, homogeneous, and linearly elastic and the liquid is compressible and inviscid.

The density, longitudinal (dilatational) wave speed, and shear wave speed of the layer are denoted by ρ, c_d, and c_s, respectively. The wave speeds are related to the Lamé constants, λ and μ, and Poisson's ratio ν by

$$c_d = [(\lambda + 2\mu)/\rho]^{1/2} \ , \ c_s = (\mu/\rho)^{1/2}, \qquad c_d/c_s = [(2-2\nu)/(1-2\nu)]^{1/2}. \tag{2.1}$$

Quantities referring to the substrate are distinguished by the addition of a prime (see Fig. 1). Quantities referring to the liquid have a subscript L. (Note that the dilatational wave speed in the liquid is simplified to c_L instead of c_{dL}. This will be the case for all variables associated with the liquid.) The corresponding wavenumbers are denoted by k_L in the liquid, k_d and k_s in the layer, and k_d' and k_s' in the half space. The wavenumber in the x direction, which must be the same for all regions, will be denoted by k. Using Snell's law, we can relate the (acute) angles between the wave vectors and the normal to the interface in terms of these wavenumbers by

$$k = k_L \sin\theta_L = k_d \sin\theta_d = k_s \sin\theta_s = k_d' \sin\theta_d' = k_s' \sin\theta_s'. \tag{2.2}$$

In plane strain, the displacement vector $\mathbf{u}$ and force vector $\mathbf{f}$ can be decomposed in terms of potentials as

$$\mathbf{u} = \nabla\phi + \nabla \times \psi \mathbf{e}_2 \ , \ \mathbf{f} = \nabla f + \nabla \times b\mathbf{e}_2 \ , \tag{2.3}$$

with

$$\mathbf{u} = u_x \mathbf{e}_1 + u_z \mathbf{e}_3 \ , \ \mathbf{f} = f_x \mathbf{e}_1 + f_z \mathbf{e}_3 \ ,$$

and

$$\nabla = \frac{\partial}{\partial x}\mathbf{e}_1 + \frac{\partial}{\partial z}\mathbf{e}_3.$$

Then the stress-potential relations for the two components of the stress tensor τ needed here become

$$\tau_{zz} = (\lambda + 2\mu)\nabla^2\phi - 2\mu\left[\frac{\partial^2\phi}{\partial x^2} - \frac{\partial^2\psi}{\partial x \partial z}\right] \ ,$$
$$\tau_{xz} = \tau_{zx} = \mu\left[2\frac{\partial^2\phi}{\partial x \partial z} + \left(\frac{\partial^2\psi}{\partial x^2} - \frac{\partial^2\psi}{\partial z^2}\right)\right] \ , \tag{2.4}$$

where

$$\nabla^2 = \frac{\partial^2}{\partial x^2} + \frac{\partial^2}{\partial z^2} \ .$$

In terms of these potentials, the equations of motion reduce to

$$(\lambda + 2\mu)\nabla^2\phi - \rho\ddot{\phi} = -f \ ,$$
$$\mu\nabla^2\psi - \rho\ddot{\psi} = -b. \tag{2.5}$$

Appropriate boundary, interface, and radiation conditions must also be satisfied. The radiation condition denies scattered waves propagating toward the interface in the substrate and in the liquid as well as interface waves propagating in from infinity. The boundary and interface conditions expressed in terms of stresses and displacements are

$$\tau_{xz} = 0, \tau_{zz} = \tau_{zz}^L, \text{ and } u_z = u_z^L \text{ at } z = 0, -\infty < x < \infty,$$
$$\tau_{xz} = \tau_{xz}', \tau_{zz} = \tau_{zz}', u_x = u_x', \text{ and } u_z = u_z' \text{ at } z = H, |x| > a, \tag{2.6}$$
$$\tau_{xz} = \tau_{xz}' = 0 \text{ and } \tau_{zz} = \tau_{zz}' = 0 \text{ at } z = H, |x| < a.$$

These conditions can also be expressed in terms of the potentials by using the stress-potential and displacement-potential relations for plane strain in equations (2.3) and (2.4).

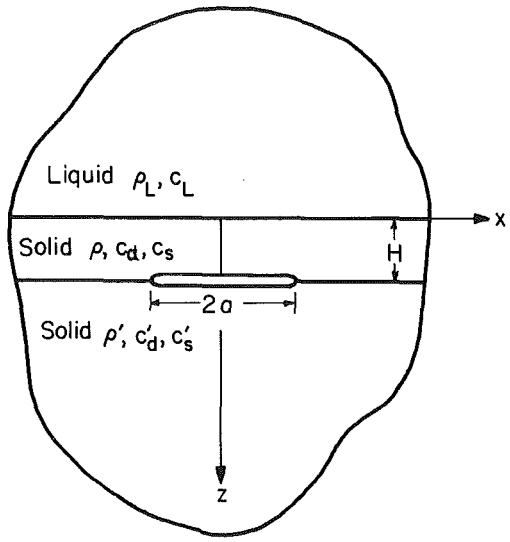

Fig. 1 Liquid-solid layer-solid structure with an interface crack of length 2a with harmonic uniform normal or shear tractions applied at the liquid-solid interface

Because of linearity, the principle of superposition can be used to reformulate the problem in a more convenient form. The total solution will be expressed as the sum of its incident and scattered parts, i.e.,

$$\tau = \tau^I + \tau^S \ , \ \mathbf{u} = \mathbf{u}^I + \mathbf{u}^S. \tag{2.7}$$

The total field (no superscript) is defined as the solution of the problem formulated above subject to a given disturbance. The incident field (superscript I) is the solution corresponding to the given disturbance on a similar structure, but without a crack. And the scattered field solution (superscript S) is the difference between the total and incident solutions. The interface conditions for the incident field are given by equations (2.6) with $a = 0$.

The boundary and interface conditions of the scattered field can be written with use of the incident field and equations (2.6) and (2.7) as

$$\tau_{xz}^S = 0, \tau_{zz}^S = \tau_{zz}^{L\,S}, \text{ and } u_z^S = u_z^{L\,S} \text{ at } z = 0, -\infty < x < \infty,$$
$$\tau_{xz}^S = \tau_{xz}'^S, \tau_{zz}^S = \tau_{zz}'^S, u_x^S = u_x'^S, u_z^S = u_z'^S \text{ at } z = H, |x| > a, \tag{2.8}$$
$$\tau_{xz}^S = \tau_{xz}'^S = -\tau_{xz}^I \text{ and } \tau_{zz}^S = \tau_{zz}'^S = -\tau_{zz}^I \text{ at } z = H, |x| < a.$$

The solution of the scattered field problem will be considered next.

III Reduction of the Problem to Integral Equations

A dynamical generalization of Betti's reciprocal theorem for plane strain and steady harmonic motion can be stated as

$$\iint_D (\mathbf{f}^A \cdot \mathbf{u}^B - \mathbf{f}^B \cdot \mathbf{u}^A) dA = \oint_{\partial D} (\tau^B \mathbf{u}^A - \tau^A \mathbf{u}^B) \cdot \mathbf{n} ds, \tag{3.1}$$

where the superscripts A and B distinguish between fields corresponding to two different sets of surface tractions and body forces (acting at the same frequency) and D is a region within the domain of the elastic body with boundary ∂D and outward unit normal $\mathbf{n}$. The quantity $\tau\mathbf{u}$ represents a vector with components $\tau_{ij}u_j$.

To derive the integral equations for the scattered field on the cracked region, let the region D be bounded externally by a circle of radius R denoted by C_R and internally by the contour $C_{\epsilon-} + \Sigma^- + C_{\epsilon+} + \Sigma^+$ that encloses the crack, as shown in Fig. 2. Also let fields A and B correspond to the scattered field solution and to the Green's function solution on the un-

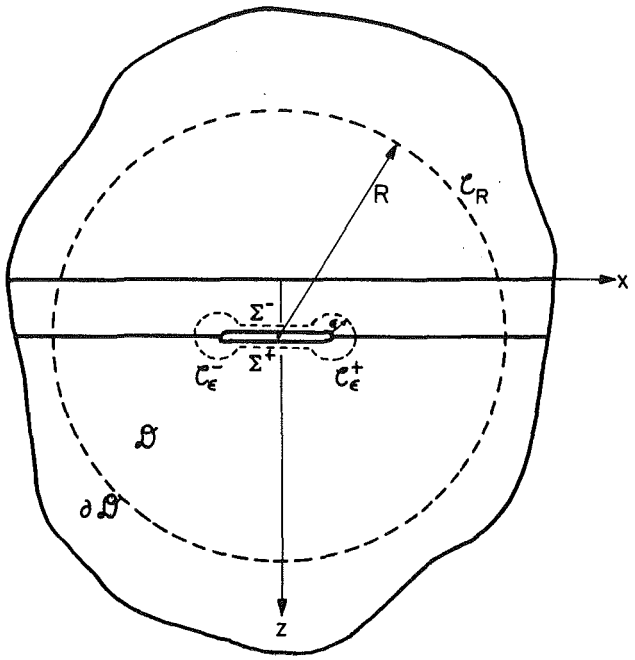

Fig. 2 Domain to which the reciprocal relation (equation (3.1)) is applied

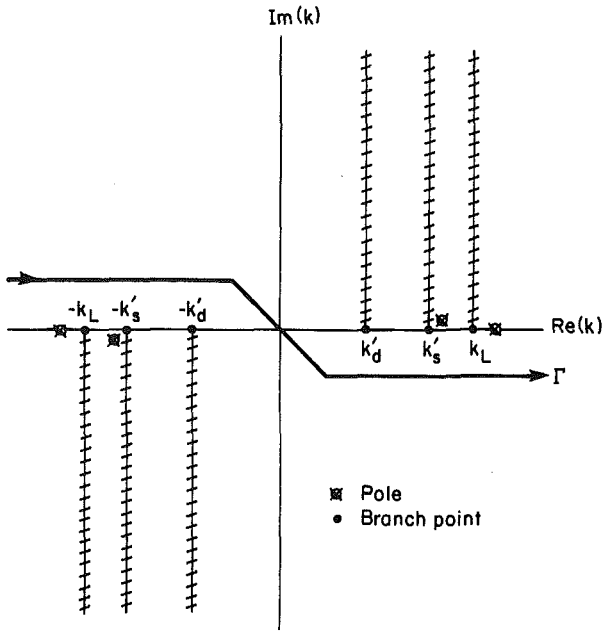

Fig. 3 Contour of intergration for the infinite integrals in equations (3.8) is along the real k axis but is considered as the limit of the path Γ as it approaches the real axis

cracked structure, respectively. The derivation of this Green's function solution is given in Appendix B of Gracewski [6].

In the layer, this choice of fields can be restated as

$$\{\mathbf{u}^A,\tau^A,\mathbf{f}^A\}=\{\bar{\mathbf{u}}^S,\bar{\tau}^S,\mathbf{0}\}e^{-i\omega t},$$
$$\{\mathbf{u}^B,\tau^B,\mathbf{f}^B\}=\{\bar{\mathbf{u}}^{G_n},\bar{\tau}^{G_n},\bar{\mathbf{f}}^{G_n}\}e^{-i\omega t}, \tag{3.2}$$

where superscript G_n denotes the Green's function solutions resulting from the following loading cases

$$\begin{aligned} n=1 &\quad \bar{f}'=\delta(\mathbf{r}-\mathbf{r}_p)\ ,\ \bar{b}=\bar{f}=\bar{b}'=0\ ,\\ n=2 &\quad \bar{b}'=\delta(\mathbf{r}-\mathbf{r}_p)\ ,\ \bar{b}=\bar{f}=\bar{f}'=0,\\ n=3 &\quad \bar{f}=\delta(\mathbf{r}-\mathbf{r}_p)\ \ ,\ \bar{b}=\bar{b}'=\bar{f}'=0,\\ n=4 &\quad \bar{b}=\delta(\mathbf{r}-\mathbf{r}_p)\ \ ,\ \bar{f}=\bar{b}'=\bar{f}'=0, \end{aligned} \tag{3.3}$$

A prime or a L added to a variable denotes the corresponding quantity for the substrate and liquid, respectively, and a superposed bar denotes time reduced harmonic functions.

With these fields so specified, the time-reduced form of equation (3.1) becomes

$$\iint_D -\bar{\mathbf{f}}^{G_n}\cdot\bar{\mathbf{u}}^S dA=\oint_{\partial D}(\bar{\tau}^{G_n}\bar{\mathbf{u}}^S-\bar{\tau}^S\bar{\mathbf{u}}^{G_n})\cdot\mathbf{n}ds. \tag{3.4}$$

The superimposed bars will be eliminated in the following to simplify notation.

Evaluating equation (3.4) as $R\to\infty$ and $\epsilon\to 0$, using the radiation condition and edge conditions at the crack tips, and defining

$$[\![u^S(x,H)]\!]\equiv \lim_{z\to H^+}\mathbf{u}^S-\lim_{z\to H^-}\mathbf{u}^S, \tag{3.5}$$

we obtain for $z_p\le H$

$$\begin{aligned} k_d^2\phi^S(\mathbf{r}_p)&=\int_{-a}^{a}\tau^{G_3}(x,H;\mathbf{r}_p)[\![\mathbf{u}^S(x,H)]\!]\cdot\mathbf{e}_3dx,\\ k_s^2\psi^S(\mathbf{r}_p)&=\int_{-a}^{a}\tau^{G_4}(x,H;\mathbf{r}_p)[\![\mathbf{u}^S(x,H)]\!]\cdot\mathbf{e}_3dx, \end{aligned} \tag{3.6}$$

and for $z_p\ge H$

$$\begin{aligned} k_d'^2\phi'^S(\mathbf{r}_p)&=\int_{-a}^{a}\tau^{G_1}(x,H;\mathbf{r}_p)[\![\mathbf{u}^S(x,H)]\!]\cdot\mathbf{e}_3dx,\\ k_s'^2\psi'^S(\mathbf{r}_p)&=\int_{-a}^{a}\tau^{G_2}(x,H;\mathbf{r}_p)[\![\mathbf{u}^S(x,H)]\!]\cdot\mathbf{e}_3dx, \end{aligned} \tag{3.7}$$

Substituting equations (3.6) into the stress-potential relations (equations (2.4)), we obtain expressions for the scattered field stresses $\tau_{zz}^S(\mathbf{r}_p)$, $\tau_{xz}^S(\mathbf{r}_p)$, in the layer. Then evaluating these expressions along the crack and making use of the last two boundary conditions in equations (2.8), we obtain the integral equations

$$\begin{aligned} -\tau_{zz}^I(x_p,H)&=\int_{-a}^{a}[\![u_1^S(x)]\!]dx\,\frac{1}{2\pi}\int_\Gamma e^{ik(x-x_p)}K_{11}(k)dk\\ &\quad+\int_{-a}^{a}[\![u_3^S(x)]\!]dx\,\frac{1}{2\pi}\int_\Gamma e^{ik(x-x_p)}K_{12}(k)dk,\\ -\tau_{zz}^I(x_p,H)&=\int_{-a}^{a}[\![u_1^S(x)]\!]dx\,\frac{1}{2\pi}\int_\Gamma e^{ik(x-x_p)}K_{21}(k)dk\\ &\quad+\int_{-a}^{a}[\![u_3^S(x)]\!]dx\,\frac{1}{2\pi}\int_\Gamma e^{ik(x-x_p)}K_{22}(k)dk. \end{aligned} \tag{3.8}$$

The contour Γ is defined by the Green's function solution and is shown in Fig. 3. The kernals $K_{ij}(k)$ are given in the Appendix.

IV Analysis of the Integral Equations

Before the integral equations can be solved, the singularities at the crack tips have to be determined. First, the equations (3.8) are integrated by parts with use of the symmetry of the kernels to obtain for $|x_p|<a$

$$\begin{aligned} &\tau_{zz}^I(x_p,H)=\\ &-\frac{i}{\pi}\int_{-a}^{a}\frac{d}{dx}[\![u_1{}^S(x)]\!]dx\oint_0^\infty\frac{K_{11}(k)}{k}\cos k(x-x_p)dk\\ &+\frac{1}{\pi}\int_{-a}^{a}\frac{d}{dx}[\![u_3{}^S(x)]\!]dx\oint_0^\infty\frac{K_{12}(k)}{k}\sin k(x-x_p)dk\\ &\tau_{xz}^I(x_p,H)= \end{aligned} \tag{4.1}$$

$$\frac{1}{\pi}\int_{-a}^{a}\frac{d}{dx}[\![u_1^S(x)]\!]dx\oint_0^\infty\frac{K_{21}(k)}{k}\sin k(x-x_p)dk$$

$$+\frac{i}{\pi}\int_{-a}^{a}\frac{d}{dx}[\![u_3^S(x)]\!]dx\oint_0^\infty\frac{K_{11}(k)}{k}\cos k(x-x_p)dk,$$

where the symbol $\oint_0^\infty$ has been used to denote that the contour of integration is the limit of the contour Γ in Fig. 3 as it collapses to the positive real axis.

To determine the singularities of the unknown functions, the kernels, i.e., the semi-infinite integrals, will be separated into regular and singular parts. It was found that the integral over any finite length will be finite and therefore the only singularity results because the integrand does not decay quickly enough at infinity.

Following Muskhelishvili [8], the singularities of the unknowns can be determined by examining the dominant part of equations (4.1). Erdogen et al. [7] show that for the one-degree-of-freedom singular integral equation of the second kind, the solution has the form

$$\phi(x)=\phi^*(x)/(a^2-x^2)^\gamma \qquad -1<\mathrm{Re}(\gamma)<1,$$

where $\phi^*(x)$ is a bounded continuous function that can always be represented by an infinite series.

For the present case, the unknown functions have integrable singularities at the end points. Both unknown functions must have the same order singularity, and therefore they can be written as

$$\frac{d}{dx}[\![u_i^S(x)]\!]=\frac{U_i(x)}{(a^2-x^2)^\gamma}, \quad \gamma=\gamma_R+i\gamma_I \qquad (4.2)$$

$$i=1,2 \qquad 0<\gamma_R<1$$

Solving the dominant part of equation (4.1) for γ, we obtain

$$\gamma=\frac{1}{2}+\frac{i}{2\pi}\ln\left(\frac{1+\beta}{1-\beta}\right) \qquad (4.3)$$

where

$$\beta=\frac{\mu(1-2\nu')-\mu'(1-2\nu)}{\mu(2-2\nu')+\mu'(2-2\nu)} \qquad (4.4)$$

which agrees with the interface crack tip singularity obtained by several authors for related static problems.

The real part of γ defines a square-root singularity, while the imaginary part results in an oscillating singularity. For the rest of this paper the material combinations will be chosen so that β is zero and only the square-root singularity will be considered. This puts the following restriction on the material parameters:

$$\frac{\mu'}{\mu}=\frac{1-2\nu'}{1-2\nu}. \qquad (4.5)$$

Since many material combinations come close to satisfying this restriction, approximate results for many real materials can be obtained. Examples of such material combinations for which this condition can be considered to hold are given in Table I, as well as in [5].

After setting $\beta = 0$, substituting the derived form of the singularities into the integral equations (equations (4.1)), we obtain

$$\tau_{zz}^I(x_p,H)=$$

$$-\frac{i}{\pi}\int_{-a}^{a}\frac{U_1(x)}{(a^2-x^2)^{1/2}}dx\oint_0^\infty\frac{K_{11}(k)}{k}\cos k(x-x_p)dk$$

$$+\frac{1}{\pi}\int_{-a}^{a}\frac{U_3(x)}{(a^2-x^2)^{1/2}}dx\oint_0^\infty\left(\frac{K_{12}(k)}{k}-\tilde{K}_2\right)\sin k(x-x_p)dk$$

Table 1 Values used for material parameters

Material	ν	ρ (g/cm^3)	c_d (km/s)	c_s (km/s)	c_R (km/s)
Iron	0.28	7.7	5.72	3.16	2.92
Nickel	0.31	8.8	5.24	2.75	2.55
Water	–	1.0	1.48	–	–

$$+\frac{\tilde{K}_2}{\pi}\int_{-a}^{a}\frac{U_3(x)}{(a^2-x^2)^{1/2}}\frac{1}{x-x_p}dx \qquad (4.6)$$

$$\tau_{xz}^I(x_p,H)=$$

$$\frac{1}{\pi}\int_{-a}^{a}\frac{U_1(x)}{(a^2-x^2)^{1/2}}dx\oint_0^\infty\left(\frac{K_{21}(k)}{k}-\tilde{K}_2\right)\sin k(x-x_p)dk$$

$$+\frac{i}{\pi}\int_{-a}^{a}\frac{U_3(x)}{(a^2-x^2)^{1/2}}dx\oint_0^\infty\frac{K_{11}(k)}{k}\cos k(x-x_p)dk$$

$$+\frac{\tilde{K}_2}{\pi}\int_{-a}^{a}\frac{U_1(x)}{(a^2-x^2)^{1/2}}\frac{1}{x-x_p}dx.$$

where

$$\tilde{K}_2\equiv\lim_{k\to\infty}K_{12}(k)/k.$$

The additional constraints that arise from (4.2) and the fact that the points $\pm a$ are crack tips are

$$\int_{-a}^{a}\frac{U_i(x)}{(a^2-x^2)^{1/2}}dx=0. \qquad (4.7)$$

V Algebraic Approximation of the Integral Equations

Before the equations are discretized, they first will be put in a nondimensional form convenient for the numerical calculations. For nondimensional parameters, we choose

$$\hat{\rho}=\frac{\rho}{\rho'}, \quad \hat{\rho}_L=\frac{\rho_L}{\rho'}, \quad \hat{\omega}=\frac{\omega H}{c_R'}$$
$$\hat{H}=\frac{H}{a}, \quad \hat{x}=\frac{x}{a}, \quad \hat{x}_p=\frac{x_p}{a}, \quad \hat{k}=\frac{k}{k_R'}, \qquad (5.1)$$

where k_R' denotes the substrate Rayleigh wave number. The dimensionless equations are similar in form to equations (4.6) and (4.7) and therefore they are not repeated here.

In [7], Erdogen et al. show that singular integrals can be approximated using a Gaussian integration formula if the weight function of the polynomial used in the integration formula has the same form as the singularity of the unknown. Therefore, for a square-root singularity, the Gauss-Chebyshev quadrature formula should be used.

The integral equations could be reduced to an $n \times n$ matrix equation by direct use of the Gauss-Chebyshev quadrature formulas. However, it is computationally more efficient to separate the equations into physically symmetric and antisymmetric pairs and take advantage of the corresponding mathematical symmetries to obtain two $n/2 \times n/2$ matrix equations. For large n, the number of evaluations of the infinite integrals needed for the separated system of equations is approximately half that needed for the full system. Because most of the computational time is spent calculating these infinite integrals, separating the system into symmetric and antisymmetric parts results in almost 50 percent savings in computer time.

The quadrature formulas are used to obtain the final set of algebraic equations, which can be solved numerically. For explicit expressions of these algebraic equations see [6].

VI Calculation of the Stress Intensity Factors and Normal Displacement at the Liquid-Solid Interface

The solution of the integral equations gives the derivative of the jump in displacements across the crack, $d/d\hat{x}_r[[\hat{u}_i^S(\hat{x}_r)]]$ at $\hat{x}_r = \cos(\pi r/n)$. By substituting these functions back into the integral expressions (3.6) and (3.7) after integrating by parts, the scattered field solution at any point in the solid can be obtained.

For use in fracture mechanics, the important quantities are the Mode I and II stress intensity factors, which are defined in nondimensional form by

$$\hat{K}_I = \frac{K_I}{\sqrt{a}\rho' c_R'^2} = \lim_{\hat{x}\to 1} [2(\hat{x}-1)]^{1/2} |\hat{\tau}_{zz}(\hat{x})|,$$
$$\hat{K}_{II} = \frac{K_{II}}{\sqrt{a}\rho' c_R'^2} = \lim_{\hat{x}\to 1} [2(\hat{x}-1)]^{1/2} |\hat{\tau}_{xz}(\hat{x})|. \tag{6.1}$$

Expressions for the stress intensity factors at the right crack tip can be determined by taking the limit as $\hat{x}\to 1^+$ of the Cauchy integrals in the equations for the scattered field stresses, following [8]. The resulting equations are

$$\hat{K}_I = |\hat{\bar{K}}_2 \hat{U}_3(1)|,$$
$$\hat{K}_{II} = |\hat{\bar{K}}_2 \hat{U}_1(1)|, \tag{6.2}$$

where $\hat{U}_i(1)$ can be calculated from the extrapolation formula

$$\hat{U}_i(1) = \frac{1}{n}\sum_{r=1}^{n} \frac{\sin\left[\left(\frac{2n-1}{4n}\right)(2r-1)\pi\right]}{\sin\left[\frac{(2r-1)}{4n}\pi\right]} \hat{U}_i(\hat{x}_r).$$

For NDE applications, the response of the receiving transducer is the quantity of interest. For this we obtain the normal displacement along the liquid-solid boundary, which is the only displacement component transmitted to the liquid since the liquid is assumed to be inviscid. Substituting equations (3.6) into the displacement-potential relation, and following a procedure similar to the calculation of the scattered field stresses, we obtain for $\hat{u}_z^S$, at $\hat{z}_p = 0$, the result

$$\hat{u}_z^S(\hat{r}_p) = \frac{i}{\pi}\int_{-1}^{1} [[\hat{u}_1^S(\hat{x})]] d\hat{x} \oint_0^\infty \frac{\hat{B}_1}{\hat{k}} \cos[\hat{k}\frac{\hat{\omega}}{\hat{H}}(\hat{x}-\hat{x}_p)] d\hat{k}$$
$$-\frac{1}{\pi}\int_{-1}^{1} [[\hat{u}_3^S(\hat{x})]] d\hat{x} \oint_0^\infty \frac{\hat{B}_2}{\hat{k}} \sin[\hat{k}\frac{\hat{\omega}}{\hat{H}}(\hat{x}-\hat{x}_p)] d\hat{k}, \tag{6.3}$$

where B_1 and B_2 are defined in the Appendix. The integrals in equation (6.3) are not singular. Therefore, the equations can be immediately discretized using the quadrature formulas for regular integrals.

VII Incident Field for Harmonic Normal or Shear Tractions Applied at the Liquid-Solid Interface.

The incident field solution for the disturbances shown in Fig. 1 are obtained in this section. As stated in Section II, the incident field is the solution corresponding to the given disturbance acting on the uncracked structure.

Expressions for the incident field tractions along the solid-solid interface for $|x| < a$ are derived first. These are needed to define the boundary conditions for the scattered field. Also, the normal displacement along the liquid-solid interface (later added to the scattered field displacement to obtain the total displacement) is calculated.

To simplify this calculation the x axis is taken along the solid-solid interface, with the Z axis vertically downward (i.e., $Z = z-H$). The potentials that satisfy the equations of motion for this case are simply

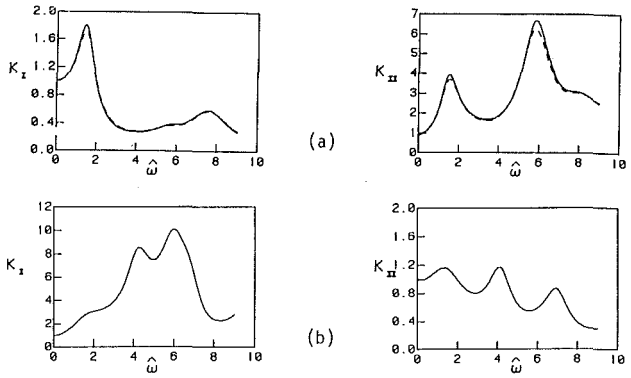

Fig. 4 Mode I (K_I) and Mode II (K_{II}) stress intensity factors versus normalized frequency for: (a) Normal traction on the upper solid surface; ——iron half space only; - - - - - - water-iron structure; (b) Shear traction on the upper solid surface, water-iron structure

$$\phi = (\check{\phi}e^{ik_d Z} + \hat{\phi}e^{-ik_d Z})e^{-i\omega t},$$
$$\phi' = (\check{\phi}' e^{ik_d' Z})e^{-i\omega t}. \tag{7.1}$$

The displacement-potential and stress-potential relations reduce to

$$u_Z = \frac{\partial\phi}{\partial Z}, \quad \tau_{ZZ} = (\lambda+2\mu)\frac{\partial^2\phi}{\partial Z^2}. \tag{7.2}$$

And the boundary and interface conditions that must be satisfied are

$$\tau_{ZZ} = A_1 e^{-i\omega t} \text{ at } Z=-H \text{ and } -\infty<x<\infty,$$
$$\tau_{ZZ} = \tau'_{ZZ},\ u_Z = u'_Z \text{ at } Z=0 \text{ and } -\infty<x<\infty. \tag{7.3}$$

Solving for the normal stress along the solid-solid interface, we obtain

$$\tau'_{ZZ} = \frac{A_1}{\cos k_d H - i\kappa \sin k_d H} e^{-i\omega t} \text{ at } z=H, \tag{7.4}$$

where

$$\kappa = \rho k_d'/\rho' k_d$$

The vertical displacement on the upper surface is

$$u_Z = \frac{-iA_1[(\kappa-1)e^{ik_d H} + (\kappa+1)e^{-ik_d H}]}{2(\lambda+2\mu)k_d(\cos k_d H - i\kappa \sin k_d H)} e^{-i\omega t} \text{ at } z=0. \tag{7.5}$$

The analogous results for applied uniform harmonic shear loading,

$$\tau_{xZ}(x, z=0) = A_2 e^{-i\omega t}, \text{ are}$$
$$\tau_{xZ} = \frac{A_2 e^{-i\omega t}}{\cos k_s H - i\bar{\kappa} \sin k_s H} \text{ at } z=H,$$
$$u_Z = 0 \text{ at } z=0$$

where

$$\bar{\kappa} \equiv \frac{\rho k_s'}{\rho' k_s}.$$

VIII Numerical Results: Mode I and II Stress Intensity Factors

The parameters for the solution of the algebraic equations derived in Section V can be separated into three categories: 1) the structure dimensions, 2) the material parameters, and 3) parameters to describe the incident disturbance. There are two structure dimensions, the layer thickness H and the crack length $2a$. In dimensionless form, these reduce to one parameter $\hat{H} = H/a$. For all the results presented here, we have used $\hat{H} = 2$.

There are eight material parameters as shown in Fig. 1. In our nondimensional form, these reduce to seven parameters—$\hat{\rho}, \hat{\rho}_L$, $\hat{k}_d$, $\hat{k}_s$, $\hat{k}_d'$, $\hat{k}_s'$, $\hat{k}_L$. Both $\hat{k}_d'$ and $\hat{k}_s'$ can be

represented as functions of ν' alone. Because of this relationship and the restriction given by equation (4.5), there are only five independent quantities which can be taken as ν', ν, $\hat{\rho}$, $\hat{\rho}_L$ and $\hat{k}_L$. To satisfy the equation (4.5), we have chosen material parameters, given in Table 1, that approximate nickel and iron. In Part I we consider only the water-iron structure. For the normal or shear loading on the upper layer surface, Fig. 1, unit amplitude is assumed so that the only additional parameter is the frequency. In nondimensional terms, this is $\hat{\omega} = \omega H/c_R'$.

The continuous curves in Figs. 4(*a*) show the Mode I and Mode II stress intensity factors for a normal harmonic loading on an iron half space, without the presence of the liquid. The curves for both K_I and K_{II} are normalized by the corresponding static stress intensity factors. These curves are in agreement with the corresponding curves in Figs. 4 and 5 of [5]. The dashed curves in Figs. 4(*a*) show the effects of the liquid. The addition of the liquid reduces the peaks slightly as some energy is evidently dissipated into the liquid.

For this normal loading, the Mode I stress intensity factor shows two peaks; one at $\hat{\omega} = 1.5$ and a weaker one at $\hat{\omega} = 7.7$. The Mode II stress intensity factor has peaks at $\hat{\omega} = 1.7$ and $\hat{\omega} = 5.8$. Achenbach et al. [1] show that the frequencies corresponding to the peaks in similar plots correlate well with resonances for simply-supported or clamped plates of length $2a$ and thickness H.

The curves in Figs. 4(*b*) present the results for a harmonic shear loading applied at the interface of the water-iron structure. There are peaks at $\hat{\omega} = 4.2$ and $\hat{\omega} = 6.0$ for the Mode I stress intensity factor. For the Mode II stress intensity factor, the peaks occur at $\hat{\omega} = 1.5$, 4.2, and 6.9.

IX Summary

In this paper, the analytical solution for scattering by an interface crack in a liquid-solid layer-solid substrate structure has been derived. Numerical results have been presented for uniform normal and shear harmonic loading applied at the liquid-solid interface for the case of identical materials for the layer and substrate. In Part II the results for plane waves and bounded beams incident from the liquid onto the solid structure will be presented. The resonances observed here for the uniform normal and shear harmonic loading will also be present in various strengths in the solutions to these more complex incidence disturbances.

References

1 Achenbach, J. D., Lin, W., and Keer, L. M., "Surface Waves Due to Scattering by a Near-Surface Parallel Crack," *IEEE Trans. Sonics and Ultrasonics*, SU-30(4), July 1983, pp. 270–276.

2 Keer, L. M., Lin, W., and Achenbach, J. D., "Resonance Effects for a Crack Near a Free Surface," ASME JOURNAL OF APPLIED MECHANICS, Vol. 51, March 1984, pp. 65–70.

3 Ryan, R. L., and Mall, S., "Scattering of Antiplane Shear Waves by a Submerged Crack," *Int. J. Solids Structures*, Vol. 18, No. 12, 1982, pp. 1145–1152.

4 Neerhoff, F. L., "Diffraction of Love Waves by a Stress-Free Crack of Finite Width in the Plane Interface of a Layered Composite," *Applied Scientific Research*, Vol. 35, 1979, pp. 265–315.

5 Yang, H.-J., and Bogy, D. B., "Elastic Wave Scattering from an Interface Crack in a Layered Half Space," ASME JOURNAL OF APPLIED MECHANICS, Vol. 52, Mar. 1985, pp. 42–50.

6 Gracewski, S. M., Ph.D. Thesis, University of California, Berkeley, 1984.

7 Erdogen, F., Gupta, G. D., and Cook, T. S., "The Numerical Solutions of Singular Integral Equations," in *Methods of Analysis and Solutions to Crack Problems*, ed., G. C. Sih, Wolters-Noordhoff Publishing, 1972.

8 Muskhelishvili, *Singular Integral Equations*, P. Noordhoff N. V., Gorningen, Holland, 1958.

APPENDIX

Kernal Functions in Equations (3.8)

$$K_{11}(k) = \frac{\mu\rho'}{\Delta}\Big[i\rho k_s^2 k_s'^2[(k_s'^2-2k^2)-2\gamma_d'\gamma_s'] \times \Big\{\frac{-[(k_s^2-2k^2)^4+16\gamma_d^2\gamma_s^2k^4]}{4\gamma_d\gamma_s k} S_dS_s + 2k(k_s^2-2k^2)^2(C_dC_s-1)\Big\} + i\rho' k_s^4\Big[\frac{(k_s'^2-2k^2)^2+4\gamma_d'\gamma_s'k^2}{2k} \times \Big\{\frac{[(k_s^2-2k^2)^3-8\gamma_d^2\gamma_s^2k^2]}{2\gamma_d\gamma_s} S_dS_s + (k_s^2-2k^2)(k_s^2-4k^2)(C_dC_s-1)\Big\} + \frac{\rho_L\rho' k_s^8}{\rho}\frac{[(k_s'^2-2k^2)^2+4\gamma_d'\gamma_s'k^2]}{4\gamma_s\gamma_L k}[-(k_s^2-2k^2)C_dS_s + 2\gamma_d\gamma_sC_sS_d] + \rho_L k_s^6 k_s'^2\frac{[(k_s'^2-2k^2)-2\gamma_d'\gamma_s']}{4\gamma_s\gamma_L k} [(k_s^2-2k^2)^2C_dS_s+4\gamma_d\gamma_sk^2C_sS_d]\Big],$$

$$K_{12}(k) = -\frac{\mu\rho'}{\Delta}\Big[\rho' k_s^6[(k_s'^2-2k^2)^2+4\gamma_d'\gamma_s'k^2] \Big[\gamma_sC_dS_s+\frac{(k_s^2-2k^2)^2}{4\gamma_dk^2}C_sS_d\Big] + i\rho k_s^2k_s'^4\gamma_s'\Big\{2(k_s^2-2k^2)^2(C_dC_s-1) - \frac{[(k_s^2-2k^2)^4+16\gamma_s^2\gamma_d^2k^4]}{4\gamma_d\gamma_sk^2}S_dS_s\Big\} + \frac{\rho_Lk_s^6k_s'^4\gamma_s'}{4\gamma_s\gamma_Lk^2}[(k_s^2-2k^2)^2C_dS_s+4\gamma_d\gamma_sk^2C_sS_d] + \frac{i\rho_L\rho' k_s^{10}}{4\rho\gamma_Lk^2}[(k_s'^2-2k^2)^2+4\gamma_d'\gamma_s'k^2]C_dC_s\Big],$$

$$K_{21}(k) = \frac{\rho'\mu}{\Delta}\Big[-\rho' k_s^6[(k_s'^2-2k^2)^2 + 4\gamma_d'\gamma_s'k^2]\Big[\frac{(k_s^2-2k^2)^2}{4\gamma_sk^2}C_dS_s+\gamma_dC_sS_d\Big] + i\rho k_s^2k_s'^4\gamma_d'\Big\{\frac{[(k_s^2-2k^2)^4+16\gamma_d^2\gamma_s^2k^4]}{4\gamma_s\gamma_dk^2}S_dS_s + 2(k_s^2-2k^2)^2(1-C_sC_d)\Big\} - \frac{\rho_Lk_s^6k_s'^4\gamma_d'}{4\gamma_L\gamma_sk^2}[(k_s^2-2k^2)^2C_dS_s+4\gamma_d\gamma_sk^2C_sS_d] + \frac{i\rho_L\rho' k_s^{10}}{4\rho\gamma_s\gamma_Lk^2}\gamma_d[(k_s'^2-2k^2)^2+4\gamma_d'\gamma_s'k^2]S_dS_s\Big],$$

$$K_{22}(k) = K_{11}(k).$$

$$\Delta = \rho'^2k_s^4[(k_s'^2-2k^2)^2+4\gamma_d'\gamma_s'k^2]\Big\{\Big[\frac{(k_s^2-2k^2)^2}{4\gamma_d\gamma_s}+\gamma_d\gamma_s\Big]S_dS_s - \Big[\frac{(k_s^2-2k^2)^2}{4k^2}+k^2\Big]C_dC_s-(k_s^2-2k^2)\Big\} - \rho\rho' k_s^2k_s'^2[(k_s'^2-2k^2)-2\gamma_d'\gamma_s']\Big\{\Big[\frac{(k_s^2-2k^2)^3}{2\gamma_d\gamma_s} - 4\gamma_d\gamma_sk^2\Big]S_dS_s+(k_s^2-2k^2)(k_s^2-4k^2)(C_dC_s-1)\Big\}$$

$$+\frac{\rho\rho' ik_s^4 k_s'^4 (k_s^2-2k^2)^2}{4\gamma_s\gamma_d k^2}\,[\gamma_d\gamma_s' C_d S_s+\gamma_d'\gamma_s C_s S_d]$$

$$+\rho\rho' ik_s^4 k_s'^4[\gamma_d'\gamma_s C_d S_s+\gamma_d\gamma_s' C_s S_d]$$

$$+\rho^2 k_s'^4(k^2+\gamma_d'\gamma_s')\left\{\left[\frac{(k_s^2-2k^2)^4}{4\gamma_d\gamma_s k^2}+4\gamma_d\gamma_s k^2\right]S_d S_s$$

$$-2(k_s^2-2k^2)^2(C_d C_s-1)\right\}$$

$$+\frac{i\rho\rho_L k_s^4 k_s'^4}{\gamma_L}\,\frac{(k^2+\gamma_d'\gamma_s')}{4\gamma_s k^2}\,[(k_s^2-2k^2)^2 C_d S_s+4\gamma_s\gamma_d k^2 C_s S_d]$$

$$+\frac{\rho'\rho_L k_s^6 k_s'^2}{4\gamma_L\gamma_s k^2}\,\{\gamma_d\gamma_s' k_s^2 k_s'^2 S_d S_s-\gamma_s\gamma_d' k_s^2 k_s'^2 C_d C_s$$

$$-2ik^2[(k_s'^2-2k^2)-2\gamma_d'\gamma_s'][(k_s^2-2k^2)C_d S_s-2\gamma_d\gamma_s C_s S_d]\}$$

$$+\frac{i\rho'^2\rho_L k_s^8}{\rho}\,\frac{[(k_s'^2-2k^2)^2+4\gamma_d'\gamma_s' k^2]}{4\gamma_L\gamma_s k^2}$$

$$[k^2 C_d S_s+\gamma_d\gamma_s S_d C_s].$$

Kernal Functions in Equations (6.3)

$$B_1=-\frac{i\rho'^2 k_s^6}{4\gamma_s k\Delta}\,[(k_s'^2-2k^2)^2+4\gamma_d'\gamma_s' k^2]$$

$$[(k_s^2-2k^2)S_s-2\gamma_d\gamma_s S_d]$$

$$+\frac{\rho\rho' k_s^4 k_s'^2}{4\gamma_s k\Delta}\{i[(k_s'^2-2k^2)-2\gamma_d'\gamma_s'][(k_s^2-2k^2)^2 S_s+4\gamma_d\gamma_s k^2 S_d]$$

$$+2k_s'^2\gamma_s\gamma_d'(k_s^2-2k^2)(C_s-C_d)\},$$

$$B_2=\frac{\rho'^2 k_s^6}{4k^2\Delta}\,[(k_s'^2-2k^2)^2+4\gamma_d'\gamma_s' k^2][(k_s^2-2k^2)C_s+2k^2 C_d]$$

$$+\frac{\rho\rho' k_s^4 k_s'^2}{4\gamma_s k^2\Delta}\,\{-i\gamma_s' k_s'^2[(k_s^2-2k^2)^2 S_s+4\gamma_d\gamma_s k^2 S_d]$$

$$+2\gamma_s k^2(k_s^2-2k^2)[(k_s'^2-2k^2)-2\gamma_d'\gamma_s'](C_s-C_d)\}.$$

The following shorthand notation for the trigonometric functions has been used:

$$C_d\equiv\cos(\gamma_d H), S_d\equiv\sin(\gamma_d H), C_s\equiv\cos(\gamma_s H), S_s\equiv\sin(\gamma_s H)$$

and

$$\gamma_d^2\equiv k_d^2-k^2\ ,\ \gamma_s^2\equiv k_s^2-k^2.$$

Elastic Wave Scattering from an Interface Crack in a Layered Half Space Submerged in Water: Part II: Incident Plane Waves and Bounded Beams

S. M. Gracewski
Assistant Professor,
Department of Mechanical Engineering,
University of Rochester,
Rochester, NY 14627

D. B. Bogy
Professor,
Department of Mechanical Engineering,
University of California, Berkeley,
Berkeley, CA 94720

This is Part II of a two part paper which analyzes time harmonic elastic wave scattering by an interface crack in a layered half space submerged in water. The analytic solution was derived in Part I. Also numerical results for uniform harmonic normal or shear traction applied to the liquid-solid interface were presented. These were compared with previously published results as a check on the computer program used to obtain the numerical results. Here in Part II, additional numerical results are presented. Plane waves incident from the liquid onto the solid structure are first considered to gain insight into the response characteristics of the structure. The solution for an incident beam of Gaussian profile is then presented since this profile approximates the output of an ultrasonic transducer.

I Introduction

In Part I of this two part paper, the problem of elastic wave scattering by an interface crack in a liquid – solid layer – solid substrate structure (LSS) was formulated and solved analytically. The solution resulted in a set of coupled singular integral equations for the scattered field along the crack. A quadrature method was used to obtain algebraic equations which approximate these integral equations and numerical solutions of these equations for uniform harmonic normal or shear traction applied at the liquid-solid interface were given. In Part II, additional numerical results will be presented for more realistic incident disturbances.

Figure 1 shows the two types of steady time-harmonic disturbances which are considered. The first is a plane wave incident from the liquid onto the solid structure at an angle θ_L with the vertical. Plots of stress intensity factor versus normalized frequency for this disturbance are analyzed to gain insight into the response characteristics of the cracked structure. The second is a Gaussian beam again incident from the liquid at an angle θ_L. This beam with a Gaussian profile approximates a beam generated by a pressure transducer. For this disturbance, results for the displacement along the liquid-solid interface are given in addition to graphs of stress intensity factor versus normalized frequency.

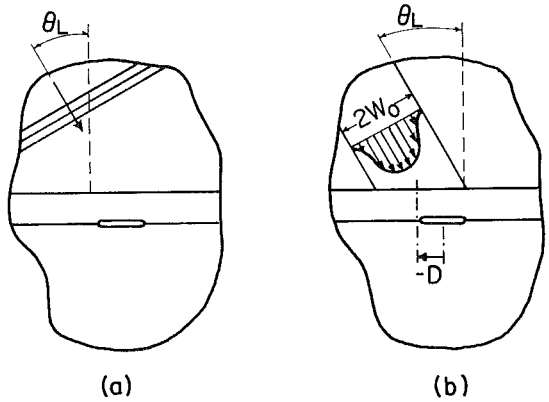

Fig. 1 Incident disturbances considered: a) Plane wave incident from the liquid at angle θ_L with the normal, b) "Bounded" beam with a Gaussian profile. *D* is the offset distance of the beam center referred to the crack center and is positive when the beam is offset to the right of the crack.

To solve the algebraic equations for the scattered field, the incident field stresses along the crack must first be known. Also, to obtain the total field displacements along the liquid-solid interface, the incident field displacements are added to the scattered field displacements. Therefore in Sections II and III of this paper, the incident field solutions for the two cases considered will be derived. In Section IV, a discussion of the numerical techniques and limitations will be given. Finally, in Section V numerical results for each case will be presented.

The notation used in this paper is explained in Part I.

II Incident Plane Longitudinal Wave in the Liquid

In this section, the incident field solution is derived for a

Contributed by the Applied Mechanics Division for presentation at the Winter Annual Meeting, Anaheim, CA, December 7–12, 1986, of The American Society of Mechanical Engineers.

Discussion on this paper should be addressed to the Editorial Department, ASME, United Engineering Center, 345 East 47th Street, New York, N.Y. 10017, and will be accepted until two months after final publication of the paper itself in the JOURNAL OF APPLIED MECHANICS. Manuscript received by ASME Applied Mechanics Division, November 15, 1984; final revision June 10, 1985. Paper No. 86-WA/APM-5.

plane longitudinal wave incident from the liquid onto the uncracked solid structure at an angle θ_L with the vertical. The longitudinal and shear wave potentials for zero body forces corresponding to this incident longitudinal wave in the liquid can be written in the form

$$\begin{aligned}\phi_L &= (A_2 e^{i\gamma_L z} + Be^{-i\gamma_L z})e^{i(kx-\omega t)},\\ \phi &= (C\cos\gamma_d z + D\sin\gamma_d z)e^{i(kx-\omega t)},\\ \psi &= (E\cos\gamma_s z + F\sin\gamma_s z)e^{i(kx-\omega t)},\\ \phi' &= Ge^{i\gamma_d'(z-H)}e^{i(kx-\omega t)},\\ \psi' &= Ie^{i\gamma_s'(z-H)}e^{i(kx-\omega t)}.\end{aligned} \tag{2.1}$$

The upward propagating waves in the substrate are ruled out by the radiation condition. Substituting these potentials into the interface conditions (equations (2.8) of Part I with $a=0$), we obtain a system of seven equations in terms of the potential amplitudes. These algebraic equations can then be solved simultaneously to obtain expressions for the coefficients $B-I$ in equations (2.1).

To calculate the stresses along the solid-solid interface, expressions for G and I must be obtained. For this purpose we used the symbol-manipulation program VAXIMA, which is the version of MAXSYMA [1] that was developed at U.C. Berkeley to run on the UNIX operating system. The results are

$$\begin{aligned}G &= \frac{A_2}{\Delta}\Big\{\frac{\rho\rho_L k_s^4 k_s'^4}{2\gamma_s k^2}[i\gamma_s'(k_s^2-2k^2)^2 S_s\\ &\quad + 4i\gamma_d\gamma_s\gamma_s' k^2 S_d - 2\gamma_s k^2(k_s^2-2k^2)C_s\\ &\quad + 2\gamma_s k^2(k_s^2-2k^2)C_d]\\ &\quad + \frac{\rho'\rho_L k_s^6 k_s'^2}{2\gamma_s k^2}[2i\gamma_s' k^2(k_s^2-2k^2)S_s\\ &\quad - 4i\gamma_d\gamma_s\gamma_s' k^2 S_d - \gamma_s(k_s^2-2k^2)(k_s'^2-2k^2)C_s\\ &\quad - 2\gamma_s k^2(k_s'^2-2k^2)C_d]\Big\},\\ I &= \frac{A_2}{\Delta}\Big\{\frac{\rho\rho_L k_s^4 k_s'^4}{2\gamma_s k}[i(k_s^2-2k^2)^2 S_s + 4i\gamma_d\gamma_s k^2 S_d\\ &\quad + 2\gamma_d'\gamma_s(k_s^2-2k^2)C_s - 2\gamma_s\gamma_d'(k_s^2-2k^2)C_d]\\ &\quad - \frac{\rho'\rho_L k_s^6 k_s'^2}{2\gamma_s k}[i(k_s^2-2k^2)(k_s'^2-2k^2)S_s\\ &\quad - 2i\gamma_d\gamma_s(k_s'^2-2k^2)S_d\\ &\quad + 2\gamma_d'\gamma_s(k_s^2-2k^2)C_s + 4\gamma_s\gamma_d' k^2 C_d]\Big\},\end{aligned} \tag{2.2}$$

where Δ is defined in the appendix of Part I.

The stress-potential relations are used to calculate the stresses along the solid-solid interface. After the differentiations are performed with use of the form of the potentials, these relations become

$$\begin{aligned}\tau_{xz}'(x,z) &= \mu'[-2k\gamma_d'\phi' + (k_s'^2-2k^2)\psi'],\\ \tau_{zz}'(x,z) &= -\mu'[(k_s'^2-2k^2)\phi' + 2k\gamma_s'\psi'].\end{aligned}$$

Substitution for the potentials from equations (2.1) and evaluation of the resulting expressions at $z=H$ results in

$$\begin{aligned}\tau_{xz}'(x,z=H) &= \mu'[-2k\gamma_d' G + (k_s'^2-2k^2)I]e^{i(kx-\omega t)},\\ \tau_{zz}'(x,z=H) &= -\mu'[(k_s'^2-2k^2)G + 2k\gamma_s' I]e^{i(kx-\omega t)},\end{aligned} \tag{2.3}$$

where G and I are as given in equations (2.2).

The normal displacement along the liquid-solid interface due to the reflected waves is

$$u_z^L = \frac{\partial\phi_{L_{\text{refl}}}}{\partial z} = -i\gamma_L B e^{i(kx-\omega t)}, \tag{2.4}$$

where B/A_2 is the reflection coefficient. This reflection coefficient was derived in algebraic form and given in equation (22) of Bogy and Gracewski [2] and therefore will not be repeated here.

III Gaussian Beam Incident From the Liquid

In this section the incident field solution for a Gaussian beam incident from the liquid onto the uncracked solid structure at an angle θ_L from the vertical will be derived. In a manner similar to Brekhovskikh [3], we assume the form of the incident potential in the liquid along the surface $z=0$ to be

$$\phi_{L_{\text{inc}}}(x,0) = F(x)e^{i(k_i x-\omega t)}. \tag{3.1}$$

For a Gaussian profile the amplitude is defined as

$$F(x) = A_3 e^{-(x/W_o)^2},$$

where W_o is the projection of the "beam half-width" on the surface $z=0$.

Because the incident beam is not simply harmonic in x, the solution can no longer be assumed harmonic in x as was done for the incident plane wave. Instead, a spatial Fourier transform will be taken with respect to the x direction. Define the Fourier transform as

$$\Phi(k,z) = \int_\Gamma \phi(x,z)e^{-ikx}dx, \tag{3.2}$$

where the path is shown in Fig. (3) of Part I. The inverse transform is then

$$\phi(x,z) = \frac{1}{2\pi}\int_\Gamma \Phi(k,z)e^{ikx}dk. \tag{3.3}$$

Taking the Fourier transform of the incident wave potential we obtain

$$\Phi_{L_{\text{inc}}}(k,0) = A_3\sqrt{\pi}W_o e^{[-(k_i-k)^2(W_o/2)^2]}e^{-i\omega t}. \tag{3.4}$$

Application of this Fourier transform to the homogeneous potential equations of motion yields

$$\Big(\frac{\partial^2}{\partial z^2} + \gamma_d^2\Big)\Phi(k,z) = 0;\ \gamma_d^2 = k_d^2 - k^2,$$

$$\Big(\frac{\partial^2}{\partial z^2} + \gamma_s^2\Big)\Psi(k,z) = 0;\ \gamma_s^2 = k_s^2 - k^2. \tag{3.5}$$

Convenient forms of the potentials that satisfy the transformed equations of motion are

$$\begin{aligned}\Phi_L &= (Ae^{i\gamma_L z} + Be^{-i\gamma_L z})e^{-i\omega t},\\ \Phi &= (C\cos\gamma_d z + D\sin\gamma_d z)e^{-i\omega t},\\ \Psi &= (E\cos\gamma_s z + F\sin\gamma_s z)e^{-i\omega t},\\ \Phi' &= Ge^{i\gamma_d'(z-H)}e^{-i\omega t},\\ \Psi' &= Ie^{i\gamma_s'(z-H)}e^{-i\omega t},\end{aligned} \tag{3.6}$$

where

$$A = A_3\sqrt{\pi}W_o e^{[-(k_i-k)^2(W_o/2)^2]},$$

which satisfies equation (3.4).

Note the similarity of the potentials in equations (3.6) and (2.1). After the Fourier transform is applied to the boundary conditions and the potentials are substituted into the resulting equations, the final equations are identical to the system of seven simultaneous equations discussed in Section II for the incident plane wave solution. The expressions for G and I are therefore identical to those in equations (2.2) with A_2 replaced by A.

The inverse Fourier transform must be applied to obtain solutions for the potentials as functions of x and z. First define the two transmission coefficients and the reflection coefficient as

$$T_d'(k) = \frac{G(k)}{A(k)},\ T_s'(k) = \frac{I(k)}{A(k)},\ R(k) = \frac{B(k)}{A(k)}. \tag{3.7}$$

After applying the inverse Fourier transform to $\Phi_{L_{\text{refl}}}$, Φ', and Ψ', we obtain for the potentials

$$\phi_{L_{\text{refl}}} = \frac{1}{2\pi}\int_\Gamma A(k)R(k)e^{i(kx-\gamma_L z)}e^{-i\omega t}dk,$$

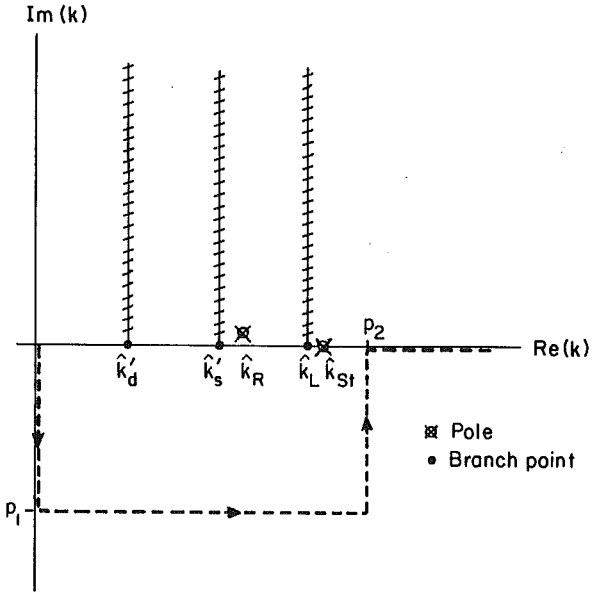

Fig. 2 Path for the numerical integration

$$\phi' = \frac{1}{2\pi}\int_\Gamma A(k)T'_d(k)e^{i(kx+\gamma'_d(z-H))}e^{-i\omega t}dk,$$

$$\psi' = \frac{1}{2\pi}\int_\Gamma A(k)T'_s(k)e^{i(kx+\gamma'_s(z-H))}e^{-i\omega t}dk. \tag{3.8}$$

Using these potentials and interchanging the order of differentiation and integration, we obtain for the stress-potential relations evaluated at $z = H$

$$\tau'_{xz}(x,H) = \frac{\mu'}{2\pi}\left\{2\int_\Gamma(-k\gamma'_d)T'_d(k)A(k)e^{i(kx-\omega t)}dk + \int_\Gamma(k'^2_s - 2k^2)T'_s(k)A(k)e^{i(kx-\omega t)}dk\right\},$$

$$\tau'_{zz}(x,H) = -\frac{\mu'}{2\pi}\left\{\int_\Gamma(k'^2_s - 2k^2)T'_d(k)A(k)e^{i(kx-\omega t)}dk + 2\int_\Gamma k\gamma'_s T'_s(k)A(k)e^{i(kx-\omega t)}dk\right\}. \tag{3.9}$$

Use of equations (3.8) in the displacement-potential relations yields

$$u^L_{z_{\text{refl}}}(x,0) = \frac{1}{2\pi}\int_\Gamma(-i\gamma_L)R(k)A(k)e^{i(kx-\omega t)}dk \tag{3.10}$$

for the normal displacement along the liquid-solid interface.

IV Numerical Techniques and Limitations

The solution of the discretized equations derived in Part I of this paper consists of two parts: evaluation of the matrix and vector elements and solution of the resulting matrix equations. The matrix equations are solved using a method based on elimination and back substitution. This part of the computation takes only a fraction of the total computer time and does not introduce any significant numerical inaccuracies. Evaluation of the matrix elements involves the evaluation of the infinite integrals. To calculate the infinite integrals numerically, the location of the branch cuts and poles along the real axis must first be determined.

The branch points result from the multivalued square-root

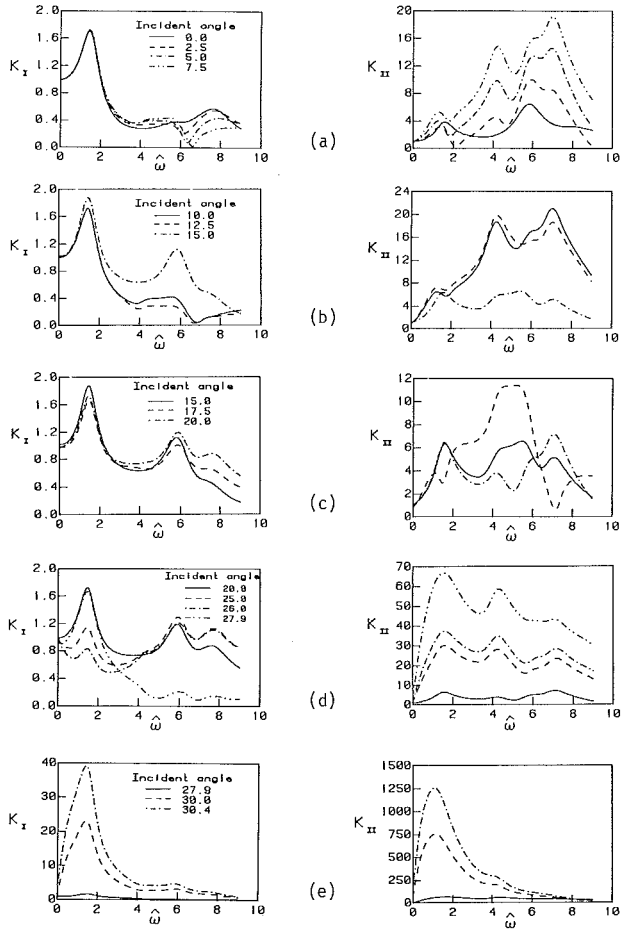

Fig. 3 Mode I and Mode II stress intensity factors versus normalized frequency for a plane wave incident from the water onto an iron layer-iron half space structure for various values of incident angle θ_L

quantities γ'_d γ'_s and γ_L and occur at $k = \pm k'_d, \pm k'_s, \pm k_L$. In the derivation of the Green's function solution, branch cuts were chosen extending into the first or third quadrants beginning at the positive and negative branch points, respectively. The path of integration for the infinite integrals was chosen so that it would not cross these branch cuts.

Poles correspond to interface waves. For each combination of materials we find one root on the real axis that corresponds to a wave at the liquid-solid interface with a velocity slightly less than the longitudinal wave speed of the liquid. For a liquid on a homogeneous solid half space, this interface wave is sometimes referred to as a Stoneley wave [3] since the Stoneley wave equation reduces to this result when one material is a liquid. Poles corresponding to the leaky Rayleigh-like and Lamb-like waves are all off the real axis in the first and third quadrants. No roots were found in the second or fourth quadrants for the materials considered.

Only the Stoneley wave pole is on the integration contour. Since there are no poles in the fourth quadrant, the integration path for the semi-infinite integral can be deformed so that it goes around this pole, as shown in Fig. 2. The values of $p1$ and $p2$ which define this contour are chosen to minimize computation time for a given accuracy requirement.

Sources of error in the computation include the discretization of the integral equations, the numerical calculation of the infinite integrals, and the round-off error that occurs in all calculations. For any finite n, the algebraic equations are only an approximation of the integral equations. We found that eight points along half the crack gave results that were accurate to about four significant figures. The accuracy of the infinite integrals is checked by changing the contour of in-

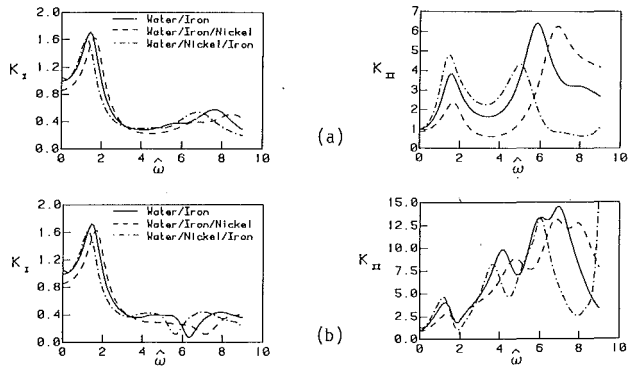

Fig. 4 Mode I and Mode II stress intensity factors versus normalized frequency for a plane wave incident from the water onto a layered structure (a) $\theta_L = 0.0$ deg; (b) $\theta_L = 5.0$ deg

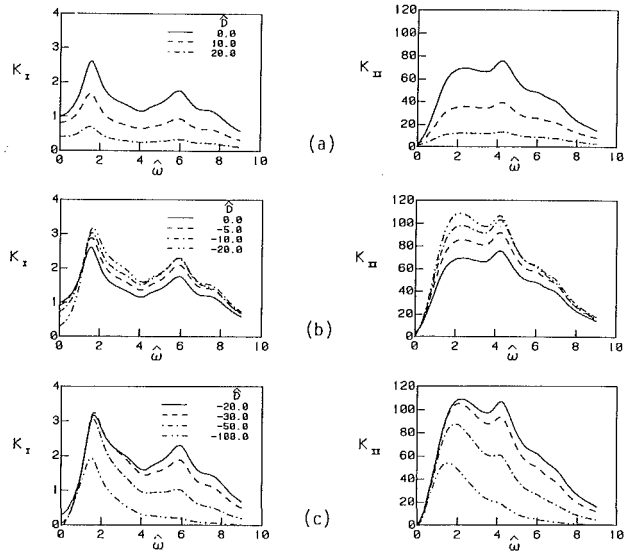

Fig. 5 Mode I and Mode II stress intensity factors versus normalized frequency for a beam with Gaussian profile incident from the liquid at the Rayleigh angle, $\theta_L = 30.42$ deg, with $\hat{W}_o = 20.0$ and for various values of D

tegration and by adding more points along the path of integration.

Computer round-off error becomes significant in the evaluation of the kernels and of the other infinite integrals only in certain regions of the complex k plane. Overflow errors occur for values of k close to the Stoneley wave pole and for values of k with large imaginary parts. Also, we found that for values of k with large real parts, these kernel functions become inaccurate. The calculation of the kernels is inaccurate even using double precision, for $\mathrm{Re}(k) > 100$, because the magnitudes of the terms within each function increase as the limit of their combination decreases to zero. Round-off error is minimized by choosing the integration contour to avoid these regions.

V Results and Conclusions

The independent material parameters and structural dimensions were discussed in Section VIII of Part I. We again choose $\hat{H} = 2.0$ and material parameters that approximate nickel and iron as given in Table 1 of Part I. The three combinations used are a nickel layer on an iron substrate, an iron layer on a nickel substrate, and the case where both the layer and half space are iron. The liquid is water in all cases.

Two additional independent parameters are introduced by the incident plane wave shown in Fig. 1(*a*). These are the nondimensional frequency $\hat{\omega}$ and the incident angle θ_L. The two other parameters, the beam half-width W_o and the horizontal distance from the crack center to the beam center D are introduced when the Gaussian beam is considered, Fig. 1(*b*). In dimensionless terms these can be written as $\hat{W}_o = W_o/a$, $\hat{D} = D/a$. Therefore, at most four parameters are introduced by the incident disturbance if unit amplitude is assumed.

In Figs. 3 and 4 the left column of plots shows the Mode I stress intensity factor K_I versus $\hat{\omega}$ and the right column of plots shows the Mode II stress intensity factor K_{II} versus $\hat{\omega}$ for the crack tip at $\hat{x} = 1.0$. The range of $\hat{\omega}$ used is from 0 to 9.

Figures 3(*a*)–(*e*) show the two stress intensity factors for plane waves incident from the water onto the iron layer-iron half space at various angles (case (*a*) in Fig. 1). The resonances that occur in this case appear to be combinations of the resonances that occur for incident shear and normal tractions as found in Part I.

In Fig. 3(*a*), results are presented for incident angles between $\theta_L = 0.0$ and 7.5 degrees. The continuous curves are identical to the dashed curve in Fig. 4(*a*) of Part I. The first peak in K_I is almost independent of incident angle for this range of angles. The second peak decreases as the angle of incidence increases. Also a dip appears between $\hat{\omega} = 6.0$ and $\hat{\omega} = 7.0$.

The curves for the Mode II stress intensity factor in Fig. 3(*a*) are more strongly dependent on the incident angle for this range of incident angles. For $\theta_L = 0.0$ degrees, only the two peaks displayed in Fig. 4(*a*) of Part I for the normal loading appear. As the angle increases, peaks also appear at the same values of $\hat{\omega}$ as they did for the shear loading case (shown in Fig. 4(*b*) of Part I). In this range of incident angles, the peaks corresponding to the shear loading case become more dominant as the angle increases.

The results presented in Figs. 3(*b*) represent a continuation of Fig. 3(*a*) to higher incident angles between $\theta_L = 10.0$ deg and the longitudinal critical angle $\theta_L = 15.0$ deg. The curves for $\theta_L = 10.0$ deg and $\theta_L = 12.5$ deg are similar to the curves in Fig. 3(*a*) for nonnormal incidence, but the solution for an incident wave at $\theta_L = 15.0$ deg does not follow this pattern. For the Mode I stress intensity factor, the first peak shows a slight increase, and a pronounced second peak occurs at $\hat{\omega} = 5.9$. This is close to the value of $\hat{\omega}$ of the second peak of K_I for a shear loading as shown in Fig. 4(*b*) of Part I. This curve also shows a slight bump at $\omega \simeq 7.5$. The curve in Fig. 3(*b*) for K_{II} at the longitudinal critical angle of $\theta_L = 15.0$ deg has, in general, a much smaller magnitude than the curves for angles below this critical angle. Also the strength of those peaks identifiable with the shear harmonic loading becomes much less at this angle.

Figures 3(*c*) show additional results for the incident angles $\theta_L = 15.0$, 17.5, and 20.0 deg. The continuous curves, corresponding to $\theta_L = 15.0$ deg, are identical to the dot-dash curves of Fig. 3(*b*). Peaks occur in each K_I curve in Fig. 3(*c*) at values of $\hat{\omega} = 1.5$, 5.8, and 7.7, but the relative magnitudes of the peaks do not keep the same order. The corresponding curves in Fig. 3(*c*) for K_{II} in this range of incident angle are more complex and change radically as the angle changes. No general statement can be made regarding these curves.

In Fig. 3(*d*), the incident angles vary between $\theta_L = 20.0$ deg and the shear critical angle, $\theta_L = 27.9$ deg. Peaks occur at the same three values of $\hat{\omega}$ in all the curves for the Mode I stress intensity factor. As in Fig. 3(*c*), the relative magnitudes of these peaks do not maintain fixed ordering. The first peak decreases as the angle increases, up to $\theta_L = 26.0$ deg, but is strong again at the shear critical angle. The magnitude of K_I at this critical angle for $\hat{\omega} > 4$ is less than one fourth of that for the angles between 20.0 deg and 26.0 deg. The magnitude of the Mode II stress intensity factor in Fig. 3(*d*) monotonically increases with angle for this range of incident angles. Three peaks occur at about the same values of $\hat{\omega}$ for which K_{II} resonances occur in Fig. 4(*b*) of Part I for the shear loading. Comparing the responses of K_I and K_{II} at the shear and

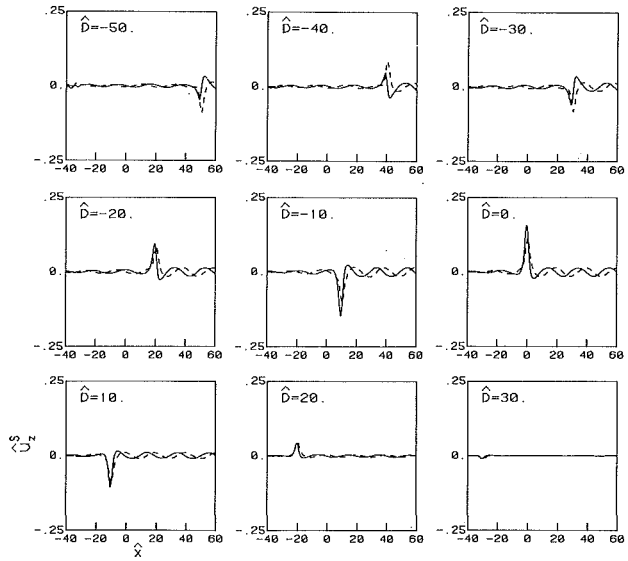

Fig. 6(*a*) Real (———) and imaginary (- - - - -) parts of the scattered field normal displacement versus normalized distance #x along the liquid-solid interface for a Gaussian beam incident from the water onto an iron layer-iron structure with $W_o = 20.0$, $\hat{\omega} = 0.6$, and $\theta_L = 30.4$ deg

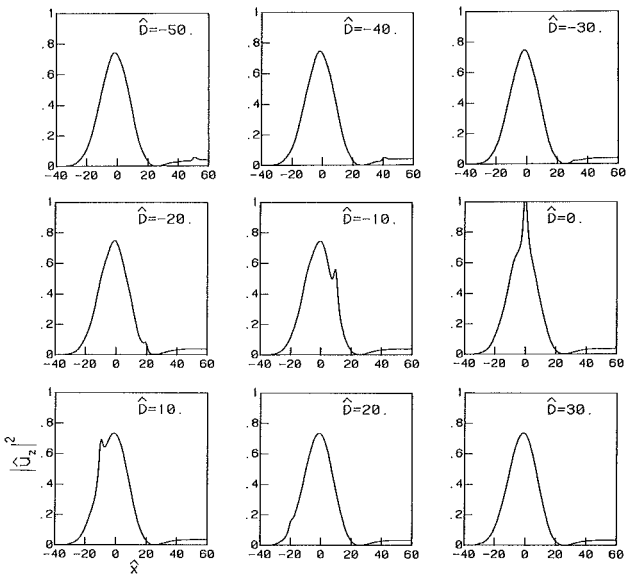

Fig. 6(*b*) Total field intensity versus normalized distance $\hat{x}$ along the liquid-solid interface for a Gaussian beam incident from the water onto an iron layer-iron structure with $\hat{W}_o = 20.0$, $\hat{\omega} = 0.6$, and $\theta_L = 30.4$ deg

longitudinal critical angles, it is evident that at the shear critical angle more energy is going into shearing the crack whereas at the longitudinal critical angle, more energy is going into pulling the crack apart. This indicates that the best incident angle for testing shear and normal bond strength may be the shear and longitudinal critical angles, respectively.

Finally in Fig. 3(*e*), the incident angle increases from the shear critical angle of 27.9 deg to the Rayleigh critical angle of 30.4 deg. The level of the first peaks in both the Mode I and Mode II stress intensity factors increases by an order of magnitude in this range. At the Rayleigh angle, the incident field stresses decay exponentially with depth, and become negligible within a few wavelengths below the surface. Therefore, one would expect a strong decrease in the scattered field, and hence in K_I and K_{II}, as $\hat{\omega}$ increases, as shown in Fig. 3(*e*).

In Figs. 4(*a*), (*b*) the stress intensity factors for the water-iron-nickel structure (dashed) and water-nickel-iron structure

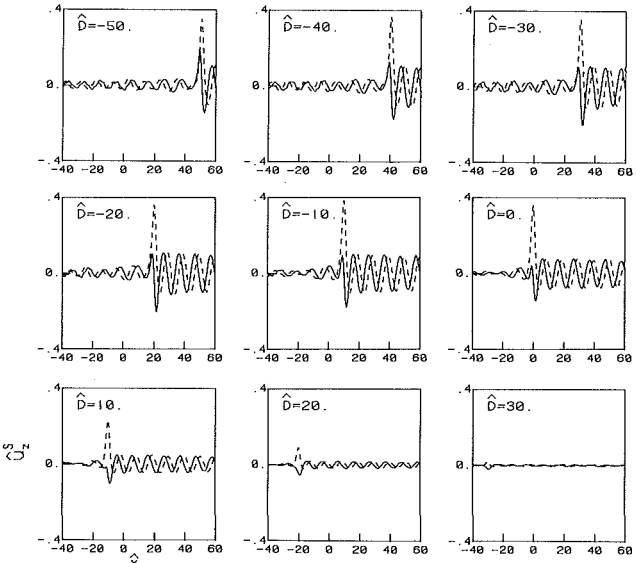

Fig. 7(a) Same as Fig. 6(*a*) except for $\hat{W}_o = 20.0$ and $\hat{\omega} = 1.2$

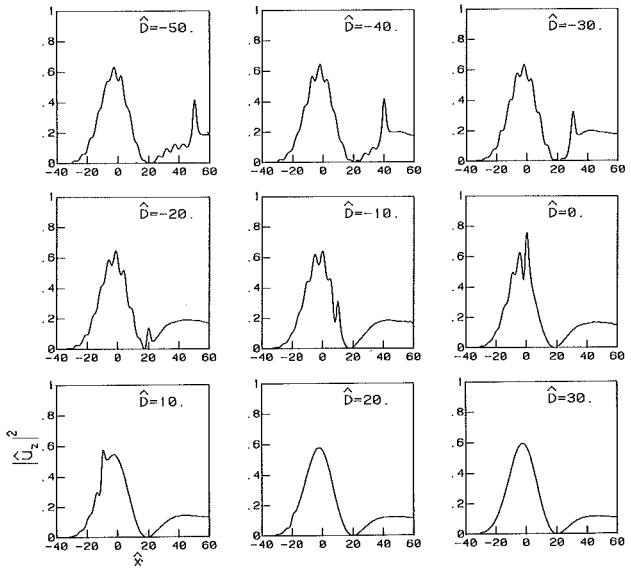

Fig. 7(b) Same as Fig. 6(*b*) except for $\hat{W}_o = 20.0$ and $\hat{\omega} = 1.2$

(dot-dashed) are compared with the results for the water-iron-iron structure (solid). The incident disturbance is a plane wave with incident angles of 0.0 and 5.0 deg, respectively. For both K_I and K_{II}, the water-iron-nickel structure has slightly higher resonance frequences and the water-nickel-iron structure has slightly lower resonance frequencies than those for the water-iron-iron structure examined in Fig. 3. The amplitudes also vary with the material parameters.

Figure 5 shows the two stress intensity factors at $\hat{x} = 1.0$ for a Gaussian beam (the case in Fig. 1(*b*)) incident from the water at the Rayleigh critical angle, $\theta_L = 30.4$ deg, onto an iron-iron structure as the beam is moved across the crack. The dimensionless beam half-width is $\hat{W}_o = 20.0$ for all cases. The maximum scattered field response occurs at the frequencies that correspond to maximum heights in these graphs. A comparison of these graphs for the range of crack sizes of interest could be used to predict the range of frequencies that will give the maximum response in an NDE test.

The beam is centered on the crack for the continuous curves in Fig. 5(*a*). The dashed and dot-dash curves in Fig. 5(*a*) correspond to an incident beam that is displaced 10 and 20 crack half-lengths, respectively, past the crack center. As expected, the magnitude of the response decreases as the beam center is

moved away from the center of the crack. The peaks in the curves remain at the same frequencies.

Figures 5(*b*) and 5(*c*) present the results for the incident Gaussian beam for various beam positions ahead of the crack. In Fig. 5(*b*), $\hat{D}$ varies from 0.0 to -20.0 while in Fig. 5(*c*), $\hat{D}$ varies from -20.0 to -100.0. Again, the continuous curve in Fig. 5(*b*) corresponds to an incident beam centered on the crack. The magnitude of all peaks in both K_I and K_{II} increase until $\hat{D}=-20.0$. Above this value the profiles of the curves begin to decrease.

In Fig. 5(*c*), the continuous curve corresponds to $\hat{D}=-20.0$. The first peak in K_I for $\hat{D}=-30.0$ is greater than the corresponding peak for $\hat{D}=-20.0$. All other peaks for $\hat{D}=-30.0$ have smaller magnitudes than those for $\hat{D}=-20.0$. As the incident beam moves farther away from the crack, all peaks decrease; however the second peak decreases faster than the first peak in both K_I and K_{II}.

Figures 6 and 7 show the response at the liquid-solid interface due to an incident Gaussian beam for various values of the parameters $\hat{W}_o$, $\hat{\omega}$ and $\hat{D}$. Part (*a*) of each figure shows the real and imaginary parts of the scattered field normal displacement along the liquid-solid interface. Part (*b*) of each figure shows the total reflected field intensity profile along the liquid-solid interface. These figures present results for frequencies $\hat{\omega}=0.6$ and $\hat{\omega}=1.2$, respectively, and beam half-width $\hat{W}_o=20.0$. Each figure contains nine graphs that correspond to nine values of the beam off-set $\hat{D}$ ranging from $-5\hat{W}_o/2$ to $3\hat{W}_o/2$, at equal increments.

In plots of the scattered field normal displacements, the largest peaks occur near the crack center. The heights of the peaks increase as $\hat{D}$ increases from $\hat{D}=-5\hat{W}_o/2$ and reaches a maximum for $\hat{D}$ in the range $\hat{W}_o/2<\hat{D}<0$. After this maximum height is reached, the heights of the peaks decrease as $\hat{D}$ increases, becoming almost zero at $\hat{D}=3\hat{W}_o/2$. The magnitudes of these peaks also depend on $\hat{\omega}$ and $\hat{W}_o$, with the largest response occurring for $\hat{\omega}=1.2$, $\hat{W}_o=20$.

These figures show that the oscillation to the right of the location of the crack has a wavelength equal to the Rayleigh wavelength, which can be expressed as

$$\hat{\lambda}_R=2\pi\hat{H}/\hat{\omega}$$

in nondimensional form. The magnitudes of the peaks of this oscillation slowly decay as the distance from the crack increases, therefore we conclude that the oscillation is the result of forward scattered leaky Rayleigh waves. The oscillations to the left of the crack also have the same wavelength, so they must be the result of a back-scattered leaky Rayleigh wave. This back-scattered leaky Rayleigh wave has smaller magnitude than the forward scattered wave. The oscillations become less smooth at large distances from the crack, indicating some numerical inaccuracy in this region.

In part (*b*) of Figs. 6 and 7, the total field intensity at the liquid-solid interface plotted against $\hat{x}$ is given for the parameters corresponding to each graph in part (*a*) of these figures. The total field intensity is calculated using the expression

$$|\hat{u}_z|^2=|\hat{u}_z^S+\hat{u}_{z_{\text{refl}}}^I|^2.$$

The curve corresponding to $\hat{D}=3\hat{W}_o/2$ in each of these figures essentially shows the response in the absence of the crack, since for this value of $\hat{D}$, the effect of the scattered field is negligible.

The plots of intensity in Figs. 6(*b*) are affected by the scattered field only by the addition of a small bump above the location of the crack. This bump has the largest magnitude when the Gaussian beam is centered above the crack ($\hat{D}=0.0$).

In Figs. 7(*b*), the bump again appears above the location of the crack, but at this frequency the bumps are larger than the corresponding bumps in Figs. 6(*b*). Also, the forward scattered and back-scattered leaky Rayleigh waves are large enough in amplitude to affect the intensity profile.

The graphs of total field intensity show the response that would affect a transducer that is on the upper solid surface. The effect of the crack on the total field intensity is greater for some values of the parameters than for others. Graphs of this type could be used to predict the response of a transducer for a certain structure and crack size or to predict whether a crack of a certain length will be detected by a transducer. Comparison with experimental data is needed to determine how close this model approximates an actual NDE test.

Results given here are for a limited range of the parameters. More work needs to be done to categorize results for other material combinations, thickness-to-crack-length ratios, and incident beam widths. This analysis could also easily be extended to other incident disturbances. The amount of computer time required to obtain this kind of result is not inconsequential, however. For example, about nine hours of CPU time on a VAX 11-780 was required to produce each of Figs. 6 and 7.

References

1 MACSYMA Reference Manual, The Math Lab Group, Laboratory for Computer Science, Massachusetts Institute of Technology, 1983.

2 Bogy, D. B., and Gracewski, S. M., "Reflection Coefficient for Plane Waves in a Fluid Incident on a Layered Elastic Half-Space," ASME JOURNAL OF APPLIED MECHANICS, Vol. 50, 1983, pp. 405–415.

3 Brekhovskikh, L. M., *Waves in Layered Media*, Academic Press, New York, 1960.

Mechanics of Fatigue Damage and Degradation in Random Short-Fiber Composites, Part I—Damage Evolution and Accumulation

S. S. Wang
Professor of Theoretical & Applied Mechanics, and of Aeronautical & Astronautical Engineering. Mem. ASME

E. S.-M. Chim[1]
Graduate Research Assistant.

H. Suemasu
Visiting Research Assistant Professor.

Department of Theoretical and Applied Mechanics, University of Illinois, Urbana, IL 61801

Cyclic fatigue damage in random short-fiber composites is studied experimentally and analytically. In the experimental phase of the study, the fatigue damage is observed to involve various forms of microcracking, originated from microscopic stress concentrators in the highly heterogeneous microstructure. In the analytical portion of the study, a probabilistic treatment of the microcracks is conducted to evaluate the statistical nature of the microscopic fatigue damage. The density and the cumulative distribution of microcrack lengths are found to follow the well known Weibull-form function, and the microcrack orientation density and cumulative distribution have expressions of a fourth-order power form of the cosθ function. Fatigue damage evolution and accumulation in the random short-fiber composite are analyzed in detail through the development of probabilistic microcrack density and distribution functions during the cyclic loading history.

1 Introduction

Recent advances in basic science and manufacturing technology of high-modulus, high-strength fibers and polymers have made short-fiber composites attractive materials for engineering applications due to advantages in processibility, high-volume production, parts consolidation, lowering tooling costs, and increased flexibility in design. The short-fiber composite, for example, the sheet molding compound (SMC) now being considered for automotive structural parts (Heimbuch and Sanders, 1978; Riegner and Sanders, 1979; Riegner and Hsu, 1982), is anticipated to experience repeated loading during service. Thus, clear understanding of the fatigue behavior is essential in the proper use of the composite material. Specifically, quantitative information on damage evolution and accumulation, and accompanying property degradation is necessary in the analysis, design and life prediction to insure structural integrity and reliability.

Owing to the inherently heterogeneous microstructure of the random short-fiber composite, various kinds of microscopic stress concentrators such as fiber ends, fiber-matrix interfaces, filler material, and process-induced defects play important roles in fatigue failure. In conjunction with relatively weak strengths of the resin matrix and the fiber-matrix interface, the microscopic stress concentrators introduce cyclic fatigue damage of various forms such as fiber-end cracking, interface debonding, matrix cracking, and separation of inclusions from the matrix. As will be discussed

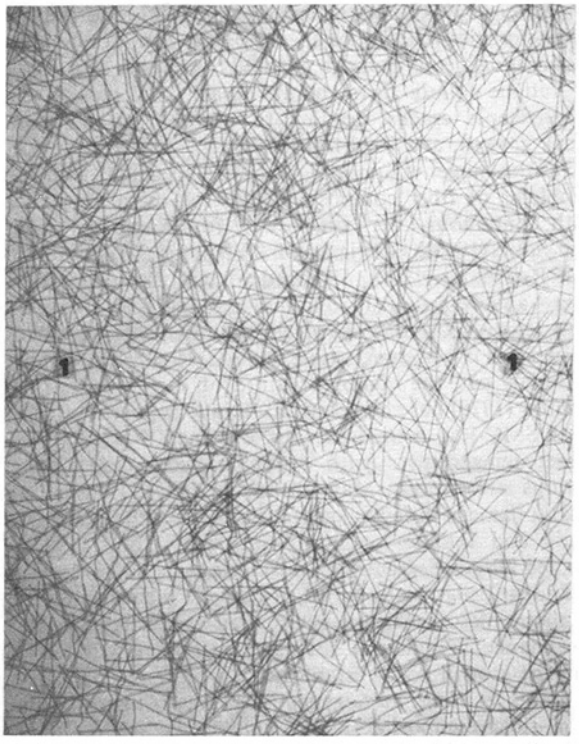

Fig. 1 X-ray radiograph of a random short-fiber SMC composite (with 1.5 percent high-lead-content glass fibers and without $CaCO_3$ fillers)

[1] Presently Advanced Engineer, Owens-Corning Fiberglas Corporation.

Contributed by this Applied Mechanics Division for presentation at the Winter Annual Meeting, Anaheim, CA, December 7–12, 1986, of The American Society of Mechanical Engineers.

Discussion on this paper should be addressed to the Editorial Department, ASME, United Engineering Center, 345 East 47th Street, New York, N.Y. 10017, and will be accepted until two months after final publication of the paper itself in the JOURNAL OF APPLIED MECHANICS. Manuscript received by ASME Applied Mechanics Division, December 7, 1984; final revision July 2, 1985. Paper No. 86-WA/APM-6.

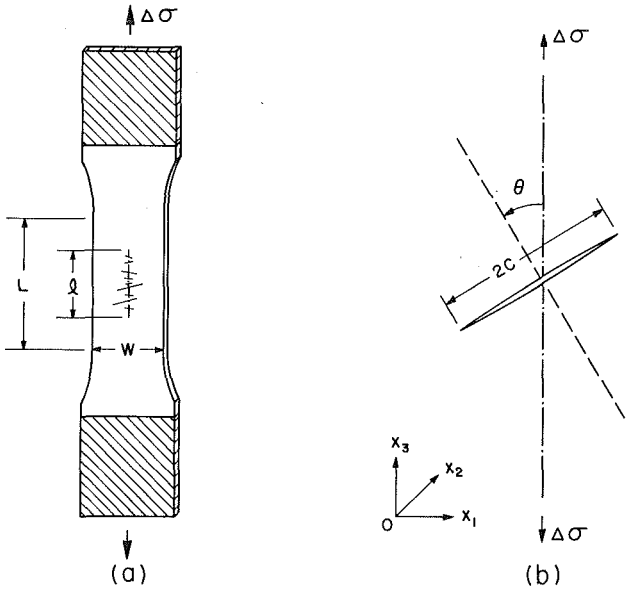

Fig. 2 *(a)* **Short-fiber SMC-R50 composite fatigue specimen and a sampling line, *l*, for damage evaluation; *(b)* definitions of microcrack length, 2c, and orientation, θ, along the sampling line**

later, for most part of the fatigue life, the microcracks distribute uniformly in the composite due to the random fiber orientation and the microstructure. Thus, the damage can be viewed as being macroscopically homogeneous. The state of the homogeneous damage is generally affected by loading parameters, material variables, and environmental conditions. Direct consequences of the homogeneous fatigue damage are loss of structural integrity and destruction of load-transfer mechanisms. Hence, appreciable changes in macroscopic structural responses such as material stiffness (Riegner and Sanders, 1979; Riegner and Hsu, 1982) and vibrational characteristics (Gibson et al., 1981) are commonly observed. Nonhomogeneous damage generally occurs at the final stage of fatigue failure through microcrack coalescence to form macroscopic cracks, leading to nonuniform deformation, crack growth, and final fracture.

In the huge volume of literature dealing with fatigue problems of fiber composites, most of them are concerned with continuous-fiber composites, for example, Broutman and Sahu (1969), O'Brien and Reifsnider (1977), Stinchomb and Reifsnider (1979), DiBenedetto and Salee (1979), Hertzberg and Manson (1980), and Hahn (1979). Research on fatigue damage and property degradation of short-fiber composites has not been extensive due to late entry of this class of materials and the complex nature of their microstructures. Denton (1979) has characterized fatigue properties of a short-fiber SMC-R50 composite, and obtained S-N curves at different temperatures with modulus decay being noted at various stress levels. Mandell and Lee (1982) have observed matrix damage in several short-fiber composite systems under static and fatigue loading. Wang and Chim (1983) have studied fatigue degradation in a random short-fiber composite and identified various forms of damage mechanisms. Effects of these microcracks are determined experimentally through the change in material stiffness, and an empirical fatigue damage-growth law is established.

In this research, homogeneous fatigue damage in a random short-fiber composite subjected to cyclic tensile loading is studied in detail. The basic nature of damage development, fundamental to the understanding of cyclic degradation and failure behavior, is discussed. In the next section, an experimental program is conducted first to provide information on microcrack initiation, growth and associated characteristics for the subsequent analysis. A probabilistic treatment of density and cumulative distributions of microcrack lengths and orientations is discussed in Section 3. Results obtained from the experiment and the analysis on fatigue damage evolution and accumulation in the composite are presented in Section 4. Several conclusions obtained from this study are given in Section 5. The probabilistic fatigue damage functions are used later (Wang et al., 1986) in conjunction with a micromechanics theory, based on the self-consistent mechanics scheme, to derive constitutive equations for damage-induced anisotropic degradation and effective elastic properties of the random short-fiber composite.

2 Experiment

2.1 Material. The material used in the experiments was a short-fiber SMC-R50 composite. (The letter *R* refers to randomly oriented, chopped fiber strands, and the number following indicates the weight percent of reinforcing fibers.) This particular material system was used because its mechanical properties were well characterized and readily available in the literature (Denton, 1979). The reinforcement was OCF 433AB-114 roving-glass filaments, chopped to a length of 25.4 mm. The resin matrix was OCF E980 polyester, a medium viscosity, highly reactive isophthalic polymer designed for structural applications. In addition, calcium carbonate filler, resin inhibitor and catalyst, alkaline earth oxide thickening agent, and mold release agent were contained. Detailed formulation of the composite, molding temperature and pressure, and charge size and pattern in the fabrication process are given in (Denton, 1979). Figure 1 is an X-ray radiograph of the short-fiber SMC composite with high-lead-content glass fibers to illustrate general characteristics of the random microstructure of the material.

2.2 Fatigue Experiment and Surface Replica Technique for Monitoring Damage. Tensile fatigue tests on the SMC-R50 composite were conducted on smooth-coupon specimens. The geometry of these specimens is shown in Fig. 2. The specimen had a total length of 254 mm. The gage length was 76.2 mm and the free length between grips was 152.4 mm. The specimen had a width of 38.1 mm in the gage section. All tests were conducted in an MTS servohydraulic test system under a load-control condition at a frequency of 2 Hz. Both stress and strain were recorded at selected intervals during the entire history of the fatigue test.

In order to monitor the initiation and subsequent developments of fatigue damage in the composite during tensile cyclic loading, a nondestructive evaluation method, employing a surface replica technique, was used. The surface replica technique has been applied successfully in monitoring fatigue crack growth in metals (Waill, 1983) and delaminations in advanced fiber-composite laminates (Masters, 1981). The advantages of this technique are that a quick and reliable permanent record of microdamage can be made and that it can be performed nondestructively on specimens under loading in a testing machine. With this method, it was possible to monitor microcrack developments during fatigue by making records at selected intervals throughout the test history. The replicas were then sputtered and later examined under a scanning electron microscope. The detailed procedure and the validity of the replica technique for fatigue damage assessment are given in (Masters, 1981; Waill, 1983; Chim, 1984).

3 Probabilistic Treatment of Damage Development

3.1 Statistical Properties of Microcracks. The state of the fatigue damage is related to the development of microcracks in the random short-fiber composite. Owing to the heterogeneous microstructure and the random distribution of fiber orientations, the statistical nature of microcracks may be described quantitatively with suitable probabilistic expressions. In the development of homogeneous fatigue damage,

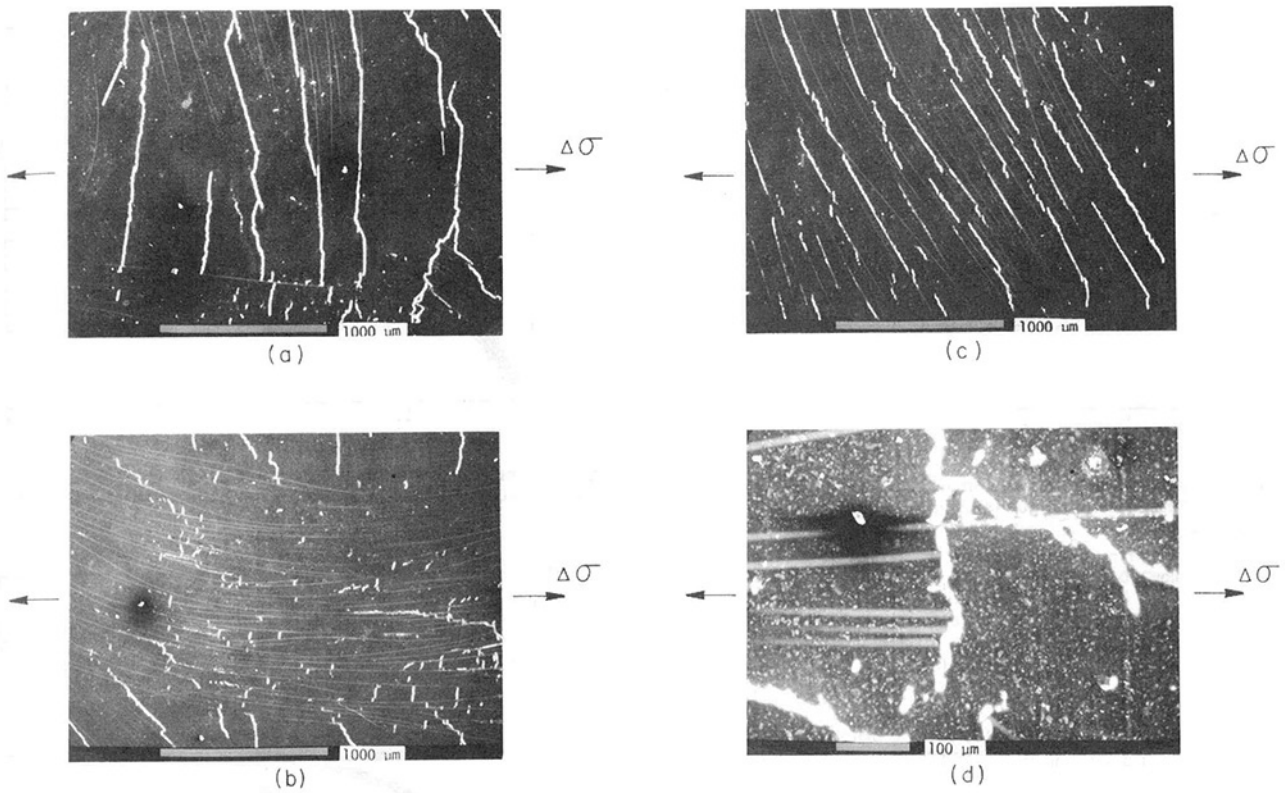

Fig. 3 Fatigue damage in short-fiber SMC-R50 composite ($\sigma_{max} = 0.6\sigma_{UTS}$, $N \simeq N_f$); microcracks (*a*) in a matrix-dominant area with sparsely dispersed fibers, (*b*) in a fiber-dominant area with fibers parallel to the loading direction, (*c*) in a matrix-dominant area with fibers oriented at an angle to the loading direction, and (*d*) at fiber ends

microcrack density and cumulative distribution functions can be thought of as being probabilistically uniform; that is, probabilistic properties of microcracks do not vary spatially in the composite. Denote the microcrack density, i.e., the total number of cracks per unit volume, by $\tilde{\lambda}$. $\tilde{\lambda}$ is generally related to the size A and the orientation vector ν of a microcrack. In practice, it is very difficult to measure $\tilde{\lambda}(A, \nu)$ nondestructively. Based on microscopic observations, planes of microcracks are generally normal to the mid-plane of the composite plate; thus, the orientation of a microcrack can be indentified with an angle θ relative to the loading direction. For simplicity and without loss of generality, the cracks are assumed to be elliptic in shape with their minor axis $2b$ equal to the thickness dimension of fiber strands. Therefore, each microcrack can be defined by two variables c and θ (Fig. 2(*b*)), and $\tilde{\lambda}(A,\nu)$ can be rewritten as $\tilde{\lambda}(c, \theta)$ $(0 \le 2c \le 2c_f, -\pi/2 \le \theta \le \pi/2)$, where $2c$ is the crack length and $2c_f$ is a finite value equal to the dimension of the specimen. It is further assumed that $\tilde{\lambda}(c,\theta)$ is constant through the thickness direction of the composite. Thus, one can introduce the expected microcrack number density function per unit area, $\tilde{\lambda}(c,\theta)$ $(0 \le 2c \le 2c_f, -\pi/2 \le \theta \le \pi/2)$, by

$$\tilde{\lambda}(c,\theta) = \lim_{\Delta c \to 0} \lim_{\Delta\theta \to 0} \lim_{S \to \infty} \frac{1}{S\, 2\Delta c\, \Delta\theta} \tilde{\Gamma}[2c \le \text{microcrack length} \le 2(c+\Delta c), \quad \theta \le \text{microcrack orientation} \le (\theta+\Delta\theta)\,|S] \tag{1}$$

where $\tilde{\Gamma}$ denotes the number of cracks which satisfy the constraints in the bracket, and S is the area in which microcracks are counted. We note that $\tilde{\lambda}(c,\theta)$ and $\tilde{\lambda}(c,\theta)$ are related by

$$\tilde{\lambda}(c,\theta) = \frac{1}{2h}\, \tilde{\lambda}(c,\theta) \tag{2}$$

where $2h$ is a characteristic width of the microcracks.

For the convenience of later developments, an expected number density function of microcracks per unit length, $\lambda(c,\theta)$, is introduced as follows:

$$\lambda(c,\theta) = \lim_{\Delta c \to 0} \lim_{\Delta\theta \to 0} \lim_{l \to \infty} \frac{1}{l\, 2\Delta c\, \Delta\theta} \Gamma[2c \le \text{microcrack length} \le 2(c+\Delta c), \quad \theta \le \text{microcrack orientation} \le (\theta+\Delta\theta)\,|l] \tag{3}$$

where l is the total length of a sampling line. We note that $\lambda(c,\theta)$ can be directly determined in the experiment by counting the number of cracks that intersect a sampling line parallel to the loading direction. Moreover, it can be easily shown that $\lambda(c,\theta)$ and $\tilde{\lambda}(c,\theta)$ are related by the expression

$$\tilde{\lambda}(c,\theta) = \frac{1}{2c\, \cos\theta}\, \lambda(c,\theta) \tag{4}$$

Once $\lambda(c,\theta)$ is determined, $\tilde{\lambda}(c,\theta)$ can be evaluated by

$$\tilde{\lambda}(c,\theta) = \frac{1}{4ch\, \cos\theta}\, \lambda(c,\theta) \tag{5}$$

Owing to the random nature of the heterogeneous material microstructure, the variables c and θ are assumed to be probabilistically independent. Thus the microcrack density function $\lambda(c,\theta)$ may be expressed as

$$\lambda(c,\theta) = \frac{1}{M_o}\, f_c(c) g_\theta(\theta) \tag{6}$$

where $f_c(c)$ and $g_\theta(\theta)$ are expected number density functions of c and θ, respectively, and M_o is the expected number of microcracks per unit length intersecting the sampling line. The $f_c(c)$ and $g_\theta(\theta)$ are determined by direct differentiation of cumulative distribution functions of microcrack length and orientation, $F_c(c)$ and $G_\theta(\theta)$, i.e.,

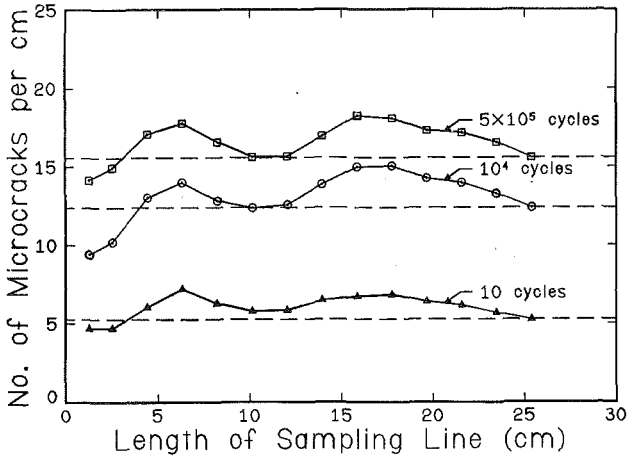

Fig. 4 Variations of microcrack density as a function of the length of a sampling line at several fatigue loading cycles (σ_{max} = 0.4 σ_{UTS}, R = 0.05, f = 2 Hz)

$$f_c(c) = \frac{dF_c(c)}{dc} \tag{7}$$

$$g_\theta(\theta) = \frac{dG_\theta(c)}{d\theta} \tag{8}$$

We remark that $F_c(c)$ and $G_\theta(\theta)$ can be obtained directly from experiments and will be discussed in the next section.

4 Results and Discussion

4.1 Microscopic Fatigue Damage. The fatigue damage was observed to appear prevalently in different forms of microcracking, such as matrix cracking (Figs. 3(*a*) and 3(*b*)), fiber-matrix interface debonding (Fig. 3(*c*)), and fiber-end cracking (Fig. 3(*d*)). The microscopic cracks in the composite possessed strong directionality relative to fatigue loading. In general, in a matrix-dominant area with sparsely dispersed fibers, almost all microcracks were formed nearly normal to the loading direction (Fig. 3(*a*)). In a fiber-dominant region with fibers oriented parallel to the loading, microcracks were developed mainly in the matrix, also normal to the loading, but had rather small crack lengths limited by the interfiber spacing (Fig. 3(*b*)). In a fiber strand oriented with an angle to the loading direction, microcracks generally grew along the interface between the fiber and matrix (Fig. 3(*c*)). Fiber-bundle (or ligament) fracture, which is commonly observed in fatigue of continuous filamentary composites (Mandell, 1982), was rarely observed in the random short-fiber composite.

To obtain the microcrack density functions, lengths and orientations (Fig. 2(*b*)) of all microcracks that intersected the selected sampling line were recorded directly, using the aforementioned surface replica technique. For example, in the case of σ_{max} = 0.4 σ_{UTS} the total sampling-line length is 25.6 cm, taken from four specimens, 3.2 cm from each surface. Variations of the number of microcracks per unit sampling length at three stages in the fatigue life are shown in Fig. 4 for this case. The effect of increasing the sampling-line length is clearly seen. The dotted lines represent averages of measurements along the total sampling-line length at different loading cycles. Moreover, the characteristic length of microcracks which will be discussed later is found to be several orders of magnitude smaller than the sampling-line length selected here and the fiber length in the composite. Thus, the present data are considered to be representative enough for further statistical analysis of the microcracks. We note that the pattern of increase in the number of cracks with loading cycles is consistent from specimen to specimen.

4.2 Cumulative Distribution Functions of Microcracks, $F_c(c)$ and $G_\theta(\theta)$. Cumulative distribution functions of microcrack length and orientation can be determined directly from the probabilistic treatment of crack measurements. For illustration, experimenal data for the cumulative distribution function $F_c(c)$ are given in Figs. 5 and 6 for the cases of σ_{max} = 0.8 σ_{UTS} and 0.4 σ_{UTS}. ($F_c(c)$ represents the total number of microcracks per unit length of the sampling line, that have length less than or equal to a certain crack length.) In general $F_c(c)$ increases rapidly with c between 0 and 1 mm, and reaches a plateau beyond 2 mm, indicating a high concentration of small microcracks of length less than 1 mm. Also, $F_c(c)$ increases with the number of load cycles, revealing that the total number of microcracks increases during the course of fatigue. However, the rate of increase in the total crack number decreases with the loading cycle and rapidly approaches a saturation state – a phenomenon similar to the transverse cracking development in continuous-fiber composites (Reifsnider, 1980).

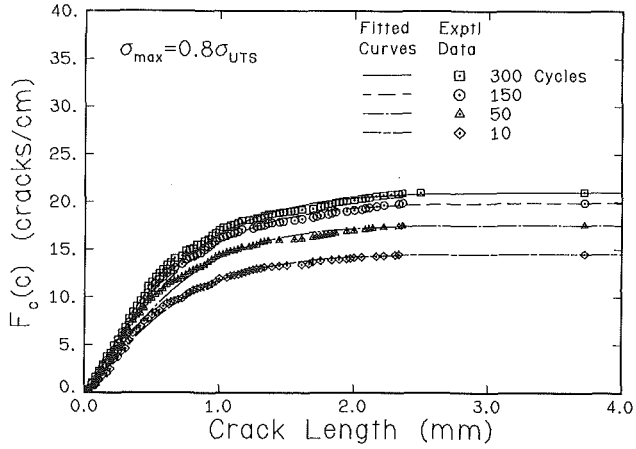

Fig. 5 Cumulative distribution function, F_c, versus microcrack length, 2c, at several fatigue loading cycles for σ_{max} = 0.8σ_{UTS} (R = 0.05, f = 2 Hz)

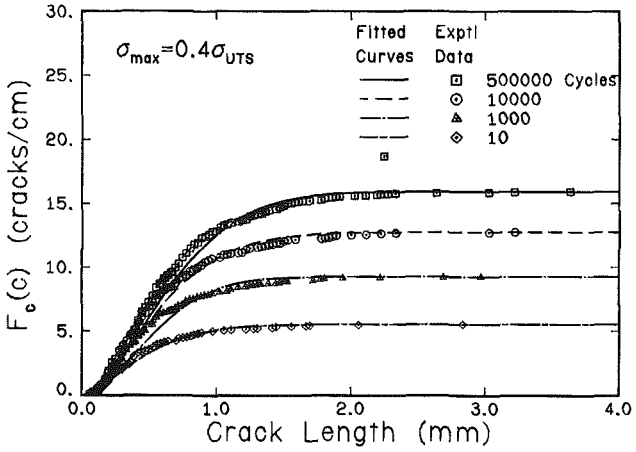

Fig. 6 Cumulative distribution function, F_c, versus microcrack length, 2c, at several fatigue loading cycles for σ_{max} = 0.4σ_{UTS} (R = 0.05, f = 2 Hz)

The Weibull-type function (Weibull, 1951) is found to describe very well the experimental data of cumulative distribution of microcrack lengths, i.e.,

$$F_c(c) = M_o\left\{1 - \exp\left[-\left(\frac{c}{c_o}\right)^\gamma\right]\right\}, \quad 0 \le c \le c_f \tag{9}$$

where M_o is defined in equation (6); $2c_o$ is a measure of the average crack length, and γ is a shape parameter, depicting deviation or variance of crack lengths from the average value. These curves are obtained by a least-square curve-fitting

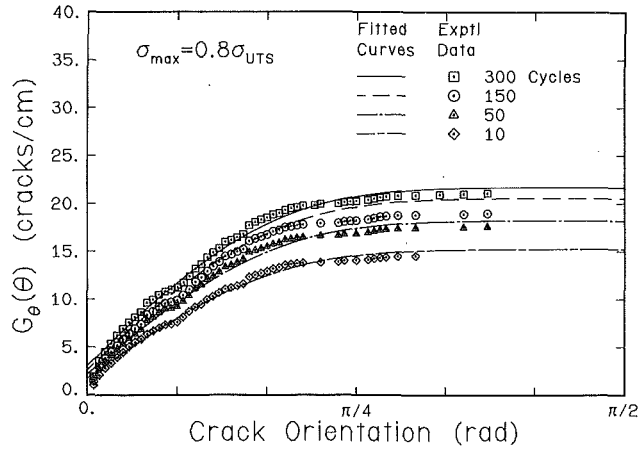

Fig. 7 Cumulative distribution function, G_θ, versus microcrack orientation, θ, at several fatigue loading cycles for $\sigma_{max} = 0.8\sigma_{UTS}$ ($R = 0.05$, $f = 2$ Hz)

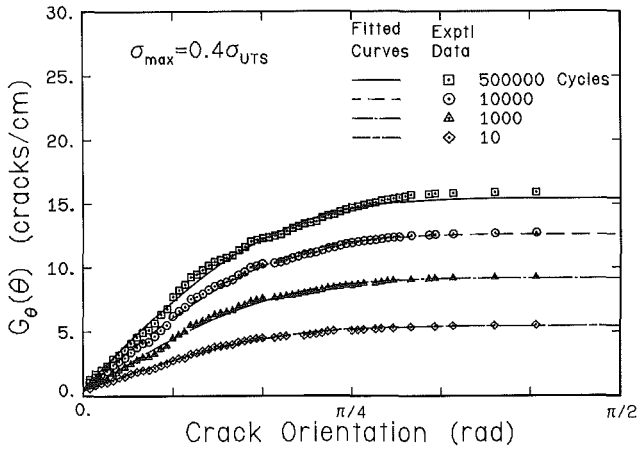

Fig. 8 Cumulative distribution function, G_θ, versus microcrack orientation, θ, at several fatigue loading cycles for $\sigma_{max} = 0.4\sigma_{UTS}$ ($R = 0.05$, $f = 2$ Hz)

method. Relationships between the parameters, M_o, c_o, and γ, and fatigue loading variables are discussed in the next section.

While microcrack lengths increased with fatigue cycles, orientations of these cracks were observed to remain almost unchanged. Few exceptions occurred such as microcracks approaching a fiber bundle and then being deflected along the fiber direction. Experimental data for cumulative distribution of microcrack orientations, $G_\theta(\theta)$, are shown in Figs. 7 and 8, where probabilistic symmetry about $\theta = 0$ deg is assumed. The $G_\theta(\theta)$ increases between $\theta = 0$ deg and 45 deg and reaches a plateau beyond 45 deg, indicating that the microcracks have strongly preferred orientations. Thus damage-induced anisotropy of macroscopic property degradation is anticipated in the fatigued short-fiber composite.

The experimental data of microcrack orientations are fitted with the following equation to obtain the cumulative distribution function $G_\theta(\theta)$:

$$G_\theta(\theta) = \alpha_o + \int_0^\theta (\alpha_1 \cos^4\tilde{\theta} + \alpha_2 \cos^2\tilde{\theta} \sin^2\tilde{\theta}) \cos\tilde{\theta}\, d\tilde{\theta},$$

$$0 \le \theta \le \frac{\pi}{2} \tag{10}$$

The rationale of adopting this expression results from statistical brittle fracture mechanics considerations (Wang and Yu, 1982) of microcracks in the short-fiber composite with orientations θ relative to the loading direction. Fracture initiation driving forces or strain energy releases rates for self-similar microcrack growth can be expressed as

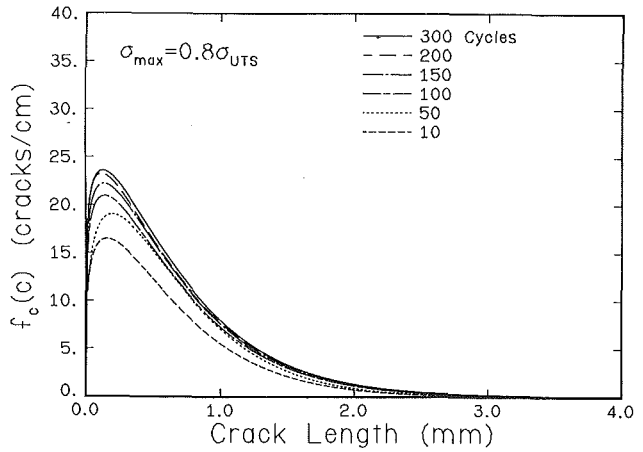

Fig. 9 Microcrack density function, f_c, versus crack length, 2c, at several fatigue loading cycles for $\sigma_{max} = 0.8\sigma_{UTS}$ ($R = 0.05$, $f = 2$ Hz)

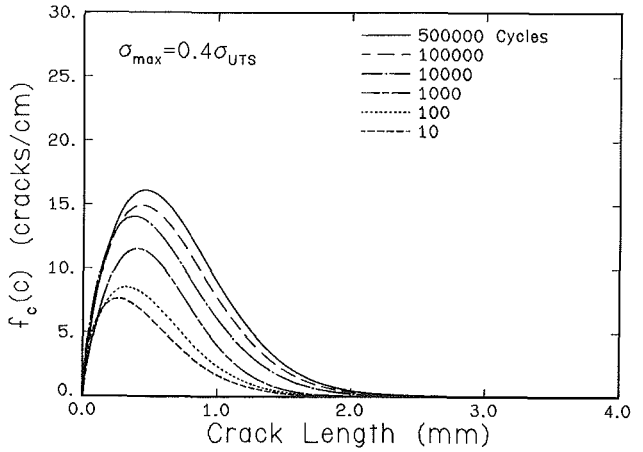

Fig. 10 Microcrack density function, f_c, versus crack length, 2c, at several fatigue loading cycles for $\sigma_{max} = 0.4\sigma_{UTS}$ ($R = 0.05$, $f = 2$ Hz)

$$\mathcal{G}_I = \xi_1 \cos^4\theta \tag{11}$$

$$\mathcal{G}_{II} = \xi_2 \cos^2\theta \sin^2\theta \tag{12}$$

where ξ_1 and ξ_2 are parameters related to material constants, and loading and geometric variables. If the microcrack orientation density $g_\theta(\theta)$ is assumed to be related to the driving forces $\mathcal{G}_I$ and $\mathcal{G}_{II}$, then we can write

$$g_\theta(\theta) \sim (\eta_1 \cos^4\theta + \eta_2 \cos^2\theta \sin^2\theta) \cos\theta \tag{13}$$

where η_1 and η_2 are constants to be determined. The $\cos\theta$ term is introduced into equation (13) by considering the relationship between $\tilde{\lambda}(c,\theta)$ and $\lambda(c,\theta)$ through equation (4). A direct integration leads to the exact form of the cumulative microcrack-orientation distribution function $G_\theta(\theta)$ in equation (10). Variations of α_0, α_1, and α_2 with fatigue loading variables are studied in the next section.

4.3 Microcrack Density Functions, $f_c(c)$ and $g_\theta(\theta)$. The microcrack density function $f_c(c)$ is obtained by direct differentiation of equation (9) with respect to crack length and has the following form:

$$f_c(c) = \frac{M_o \gamma}{c_o}\left(\frac{c}{c_o}\right)^{\gamma-1} \exp\left[-\left(\frac{c}{c_o}\right)^\gamma\right], \quad 0 \le c \le c_f \tag{14}$$

Distributions of $f_c(c)$ for two fatigue-stress levels at several different loading cycles are shown in Figs. 9 and 10. As can be clearly seen in the figures, lengths of the microcracks developed during fatigue are generally very small compared to the fiber length. The majority of the cracks are less than 1 mm. The density distribution of microcrack lengths changes

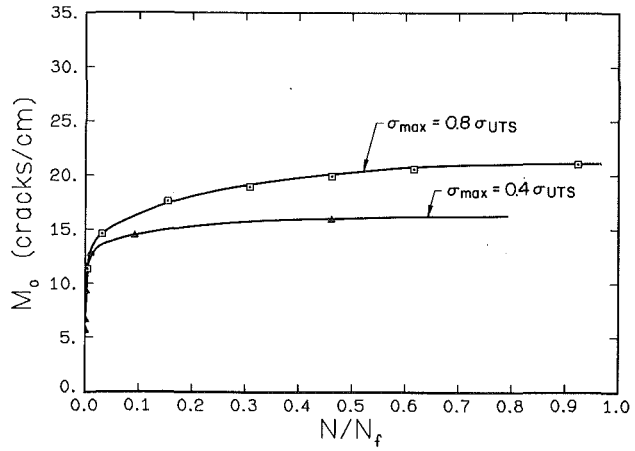

Fig. 11 Variations of M_o as a function of fatigue cycles N/N_f at different cyclic stress levels σ_{max} ($R = 0.05$, $f = 2$ Hz)

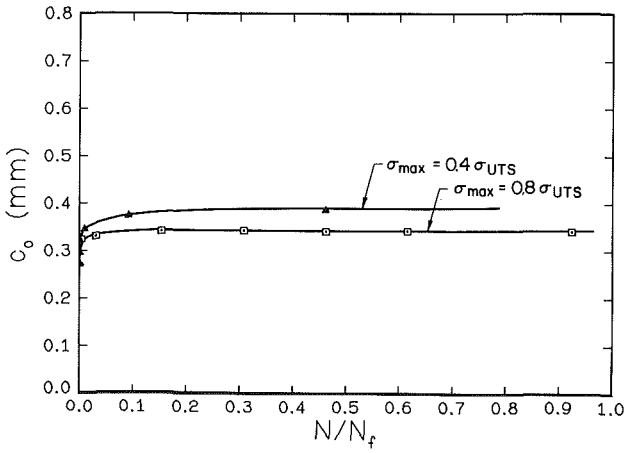

Fig. 12 Variations of c_o as a function of fatigue cycles N/N_f at different cyclic stress levels σ_{max} ($R = 0.05$, $f = 2$ Hz)

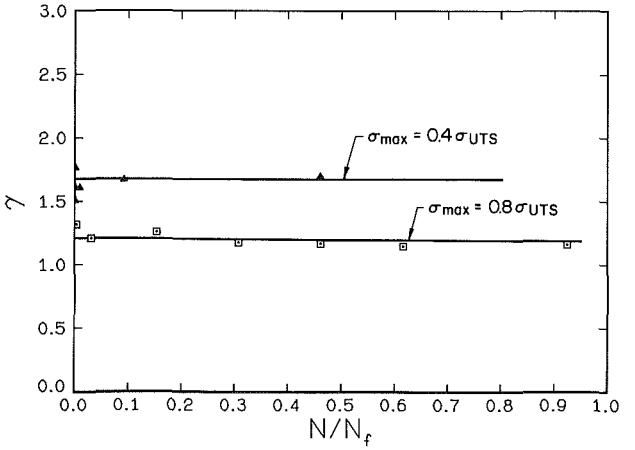

Fig. 13 Variations of γ as a function of fatigue cycles N/N_f at different cyclic stress levels σ_{max} ($R = 0.05$, $f = 2$ Hz)

with the number of load cycles. However, the average microcrack length remains approximately the same during fatigue, as evidenced by the relatively unchanged peak position of each curve along the horizontal axis.

Variations of M_o, c_o and γ with fatigue stress σ_{max} and loading cycles N are shown in Figs. 11, 12, and 13. At a given σ_{max}, M_o rapidly increases initially with the number of load cycles and then the rate of increase gradually decreases for the rest of fatigue life. As expected, increasing the fatigue stress

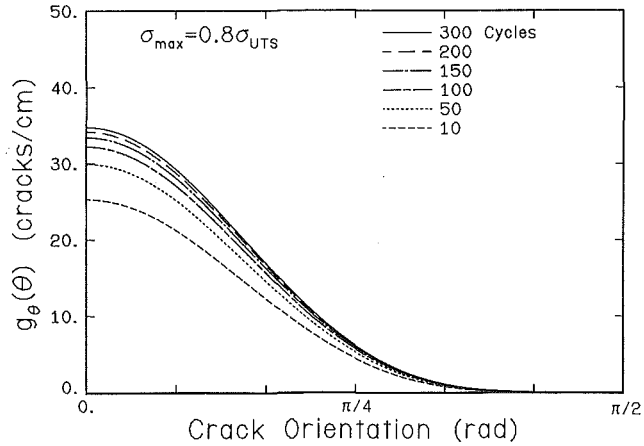

Fig. 14 Microcrack density function, g_θ, versus crack orientation, θ, at several fatigue loading cycles for $\sigma_{max} = 0.8\sigma_{UTS}$ ($R = 0.05$, $f = 2$ Hz)

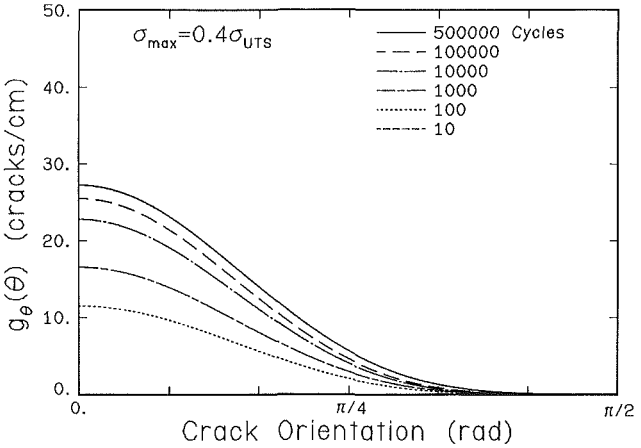

Fig. 15 Microcrack density function, g_θ, versus crack orientation, θ, at several fatigue loading cycles for $\sigma_{max} = 0.4\sigma_{UTS}$ ($R = 0.05$, $f = 2$ Hz)

also increases M_o, indicating that more microcracks are initiated at a higher stress than at a lower one. The value of c_o increases slightly at the very early stage of fatigue cycles and becomes almost constant thereafter. Thus, under a given cyclic stress, the average microcrack size remains approximately unchanged during fatigue. However, the constant value of c_o decreases with increasing cyclic stress, suggesting that the higher the stress, the shorter the average crack length. The behavior of M_o and c_o obtained from the microcrack statistics illustrates the most important characteristics of fatigue damage evolution and accumulation: at the same N/N_f, more microcracks but with a shorter average length would appear in the composite subjected to a higher fatigue stress, whereas the composite under a lower cyclic stress does the opposite. This phenomenon may be attributed to the fact that under higher cyclic loading, fatigue life of the composite was generally shorter, and the microcracks did not have sufficient time to grow into full sizes prior to final failure, as compared with those under a lower cyclic stress, and thereby possessed shorter lengths. Variations of γ with N/N_f and σ_{max} are given in Fig. 13. Besides the small fluctuation in the very beginning, the value of γ is virtually constant during fatigue. We note that γ decreases with increase in fatigue stress σ_{max}. Apparently, microcracks initiated at a higher stress did not have sufficient time to grow, leading to a higher concentraton of shorter cracks, which gives a $f_c(c)$ curve with a smaller γ. But at a lower stress level, microcracks had ample time to develop themselves fully; therefore, the $f_c(c)$ curve generally spreads wider with a larger value of γ.

The density function $g_\theta(\theta)$ of microcrack orientation is obtained by differentiating equation (10) and has the form,

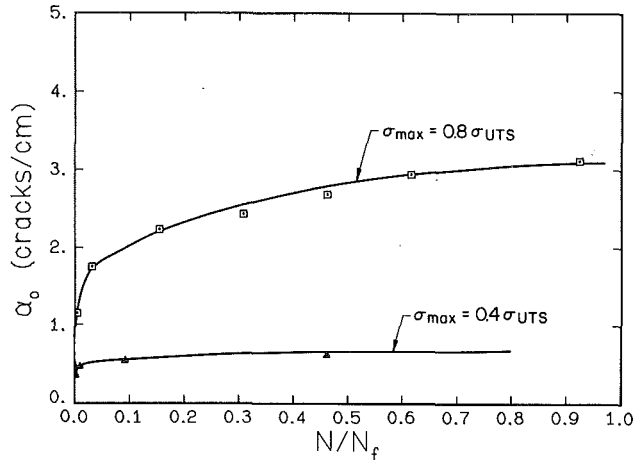

Fig. 16 Variations of α_o as a function of fatigue loading cycles N/N_f at different cyclic stress levels σ_{max} ($R = 0.05$, $f = 2$ Hz)

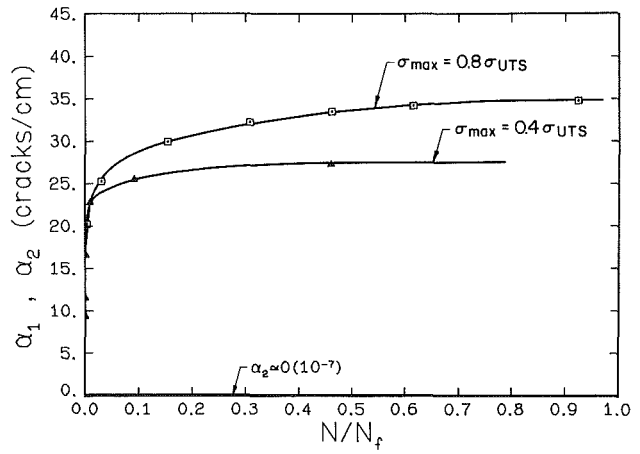

Fig. 17 Variations of α_1 and α_2 as a function of fatigue loading cycles N/N_f at different cyclic stress levels σ_{max} ($R = 0.05$, $f = 2$ Hz)

$$g_\theta(\theta) = \alpha_o \delta(\theta) + [\alpha_1 \cos^4\theta + \alpha_2 \cos^2\theta \sin^2\theta]\cos\theta \qquad (15)$$

where $\delta(\ )$ is a Dirac delta function. At any fatigue cycles, $g_\theta(\theta)$ (Figs. 14 and 15) has a peak at $\theta = 0$ deg and then decreases rapidly with θ, indicating that the majority of the microcracks are within 30 deg of the normal to the loading axis. As the number of load cycles increases, $g_\theta(\theta)$ at $\theta = 0$ deg increases in both magnitude and rate larger than those at any other θ, revealing that microcrack formation is more preferred along the direction perpendicular to the fatigue loading.

Variations of α_o, α_1, and α_2 with N/N_f and σ_{max} are given in Figs. 16 and 17. Both α_o and α_1 increase with load cycles and fatigue stress levels, and gradually approach approximately constant values as the microcracks become saturated. α_2 is found to be practically zero [i.e., $\alpha_2 \sim 0(10^{-8})$] in all cases studied, indicating that formation of microcracks is more closely related to the local stress normal to the defects than the shear component. This is consistent with experimental observations and brittle fracture statistics in (Owen, 1974; Wang and Yu, 1982) that microcracks are initiated predominantly by tensile loading perpendicular to the reinforcing fibers.

6 Conclusions

Fatigue damage evolution and accumulation in random short-fiber composites are studied. A probabilistic treatment of microcrack developments is conducted. Quantitative information on damage statistics in the form of cumulative distribution and density functions of microcrack length and orientation is obtained. Based on the results obtained from this study, the following conclusions may be reached:

(1) On a macroscopic scale, fatigue damage distributed homogeneously in the random short-fiber composite during the most part of fatigue life. Mechanisms of the fatigue damage involved continuous initiation and growth of various kinds of microcracks. The homogeneous fatigue damage was characterized by the density or the cumulative distribution functions of microcrack length and orientation.

(2) Both the loading amplitude and the cyclic stress history affected the fatigue damage significantly. At the same fatigue cycle N/N_f, high cyclic stress introduced fatigue damage with a high microcrack density but short characteristic crack length; low cyclic stress did the opposite.

(3) While the virgin random short-fiber composite may be viewed as being macroscopically isotropic, the homogeneous fatigue damage had preferred orientations relative to the cyclic loading direction, as evidenced by the development of directionally dependent microcracks, leading to damage-induced anisotropy of material property degradation.

(4) Experimental data on damage developments indicate that the cumulative distribution and the density of microcrack lengths may be expressed by the well known Weibull-form function. The majority of the fatigue microcracks were less than 1 mm in length.

(5) The parameter M_o in the density function of microcrack length increases gradually with the number of load cycles. Except at the very early stage of the cyclic loading, values of c_o and γ virtually remain constant during fatigue. An increase in fatigue stress increases the value of M_o but decreases those of c_o and γ.

(6) The microcrack-orientation density function follows a fourth-order power form of the $\cos\theta$ function. The majority of the microcracks were oriented within 30 deg of the normal to the loading direction.

(7) In the density and cumulative distribution functions of microcrack orientation, α_0 and α_1 increase gradually with increasing load cycles. An increase in fatigue stress increases both values of α_0 and α_1. The value of α_2 is practically zero in all cases studied owing to the nature of brittle fracture in the random short-fiber composite.

Acknowledgments

The work reported in this paper was supported in part by research grants from Office of Naval Research (N00014-79-C-0579) and Owens-Corning Fiberglas Corporation to the University of Illinois at Urbana-Champaign. The authors gratefully acknowledge the constant support and encouragement from Dr. Y. Rajapakase of ONR and Drs. G. N. Hartt and D. L. Denton of OCF. Numerical computations were conducted in Digital Computer Laboratory at the University of Illinois.

References

Broutman, L. J., and Sahu, S., 1969, "Progressive Damage of a Glass Reinforced Plastic during Fatigue," *Proceedings of the 24th Annual Technical Conference of the Society of the Plastic Industry*, Sec. 11-D, Washington, D.C., pp. 1-12.

Chim, E. S.-M., 1984, "Tensile Fatigue Damage and Degradation of Random Short-Fiber SMC Composite," Ph.D. Thesis, Department of Theoretical and Applied Mechanics, University of Illinois, Urbana, Ill.

Denton, D. L., 1979, *The Mechanical Properties of an SMC-R50 Composite*, Owens-Corning Fiberglas Technical Center, Granville, Ohio.

DiBenedetto, A. T., and Salee, G., 1979, "Fatigue Crack Propagation in Graphite Fiber Reinforced Nylon 66," *Polymer Engineering and Science*, Vol. 19, No. 7, pp. 512-518.

Gibson, R. F., Yau, A., and Reigner, D. A., 1981, "The Influence of Environmental Conditions on Vibrational Characteristics of Chopped-Fiber Reinforced Composite Material," *Proceedings of the 22nd AIAA/ASME/ASCE/AHS Structures, Structural Dynamics and Materials Conference*, American Institute of Aeronautics and Astronautics, New York, pp. 333-340.

Hahn, H. T., 1979, "Fatigue Behavior and Life Prediction of Composite

Laminates," *Composite Materials: Testing and Design (Fifth Conference), ASTM STP 674*, S. W. Tsai, Ed., American Society for Testing and Materials, Philadelphia, PA, pp. 383–417.

Heimbuch, R. A., and Sanders, B. A., 1978, "Mechanical Properties of Chopped Fiber Reinforced Plastics," in *Composite Materials in the Automotive Industry*, S. V. Kulkarni and R. B. Pipes, Eds., American Society of Mechanical Engineers, New York, pp. 111–139.

Hertzberg, R. H., and Manson, J. A., 1980, *Fatigue of Engineering Plastics*, Academic Press, New York.

Mandell, J. F., 1982, "Fatigue Behavior of Fiber-Reinforced Composites," in *Developments in Reinforced Plastics—2*, G. Pritchard, Ed., Applied Science Publisher, London, pp. 67–107.

Mandell, F. J., and Lee, B. L., 1982, "Matrix Cracking in Short Fiber Reinforced Composites Under Static and Fatigue Loading," *Composite Materials: Testing and Design (Sixth Conference), ASTM STP 787*, I. M. Denial, Ed., American Society for Testing and Materials, Philadelphia, PA, pp. 200–222.

Masters, J. E., Jr., 1981, "An Experimental Investigation of Cumulative Damage Development in Graphite-Epoxy Laminates," Ph.D. Thesis, Department of Engineering Science and Mechanics, Virginia Polytechnic Institute and State University, Blacksburg, VA.

O'Brien, T. K., and Reifsnider, K. L., 1977, "Fatigue Damage: Stiffness/Strength Comparisons for Composite Materials," *Journal of Materials Testing and Evaluation*, Vol. 5, No. 5, pp. 384–393.

Owen, M. J., 1974, "Fatigue Damage in Glass-Fiber-Reinforced Plastics," Chapter 7, *Composite Materials*, Vol. 5, L. J. Broutman and R. H. Krock, Eds., Academic Press, New York, pp. 313–340.

Reifsnider, K. L., 1980, "Fatigue Behavior of Composite Material," *International Journal of Fracture*, Vol. 16, No. 6, pp. 563–583.

Riegner, D. A., and Sanders, B. A., 1979, "A Characterization Study of Automotive Continuous and Random Glass Fiber Composites," Technical Report GMMD 79-023, GM Manufacturing Development, General Motors Technical Center, Warren, Mich.

Riegner, D. A., and Hsu, J. C., 1982, "Fatigue Considerations for FRP Composites," *Proceedings of the SAE Fatigue Conference*, P-109, Society of Automotive Engineers, Detroit, Mich., pp. 237–247.

Stinchomb, W. W., and Reifsnider, K. L., 1979, "Fatigue Damage Mechanisms in Composite Materials: A Review," *Fatigue Mechanisms, ASTM STP 675*, J. Fong, Ed., American Society for Testing and Materials, Philadelphia, PA, pp. 762–787.

Waill, L. E., 1983, "Crack Observations in Biaxial Fatigue," M.S. Thesis, Department of Mechanical and Industrial Engineering, University of Illinois, Urbana, Ill.

Wang, S. S., and Yu, T. P., 1982, "Statistical Fracture Initiation in Randomly Oriented Chopped-Mat Fiber Composites Subjected to Biaxial Thermomechanical Loading," *Short Fiber Reinforced Composite Materials, ASTM/STP 722*, B. A. Sanders, Ed., American Society for Testing and Materials, Philadelphia, PA, pp. 151–166.

Wang, S. S., and Chim, E. S.-M., 1983, "Fatigue Damage and Degradation in Random Short-Fiber SMC Composite," *Journal of Composite Materials*, Vol. 17, No. 2, pp. 114–134.

Wang, S. S., Chim, E. S.-M., and Suemasu, H., 1986, "Mechanics of Fatigue Damage and Degradation in Random Short-Fiber Composites, Part II—Analysis of Anisotropic Property Degradation," ASME JOURNAL OF APPLIED MECHANICS, Vol. 53, No. 2, pp. 347–353.

Weibull, W., 1951, "A Statistical Distribution Function of Wide Applicability," ASME JOURNAL OF APPLIED MECHANICS, Vol. 18, No. 3, pp. 293–297.

Mechanics of Fatigue Damage and Degradation in Random Short-Fiber Composites, Part II—Analysis of Anisotropic Property Degradation

S. S. Wang
Professor of Theoretical & Applied Mechanics, and of Aeronautical & Astronautical Engineering. Mem. ASME

E. S.-M. Chim[1]
Graduate Research Assistant.

H. Suemasu
Visiting Research Assistant Professor.

Department of Theoretical and Applied Mechanics, University of Illinois, Urbana, IL 61801

Based on the microcrack density and cumulative distribution functions obtained in (Wang et al., 1986), cyclic fatigue degradation and associated damage-induced anisotropy of elastic properties of random short-fiber composites are studied. Constitutive equations of the fatigue-damaged composite are derived on the basis of the well-known self-consistent mechanics scheme in conjunction with a three-dimensional elliptic crack theory and the probabilistic functions of microcrack density and cumulative distribution. The anisotropic stiffness degradation is determined as a function of microcrack evolution and accumulation in the damaged composite. Theoretical predictions and experimental data of effective modulus decay during fatigue are in excellent agreement. A damage parameter is introduced to depict quantitatively the degree of homogeneous fatigue damage. The tensorial nature of anisotropic stiffness degradation and fatigue damage is examined in detail. A power-law relationship is established between the rate of damage development and the fatigue loading cycle. The rate of fatigue damage growth is found to decrease exponentially with the loading cycle—a phenomenon unique to the random short-fiber composite. The fundamental mechanics of composite fatigue damage and associated property degradation is elucidated in this paper.

1 Introduction

In an associated paper (Wang et al., 1986), mechanical damage in a random short-fiber composite subjected to cyclic fatigue loading has been studied. The fatigue damage involves continuous initiation and growth of distributed microcracks during the loading history. Owing to the heterogeneous microstructure and random fiber orientations, the damage introduced in the material is statistically homogeneous on a macroscopic scale for the most part of the fatigue life. However, on a microscopic scale, electron-microscopic observations reveal that the distributed cracks possess well-behaved characteristics in orientation and length distributions during fatigue. A probabilistic treatment of the damage leads to the establishment of proper microcrack density and cumulative distribution functions. The density and cumulative distribution of microcrack lengths during fatigue are found to follow a Weibull-form function. The microcrack-orientation density and cumulative distribution functions have expressions in the power-law form of a $\cos\theta$ function. The fundamental fatigue damage mechanisms are investigated, and effects of cyclic stress and fatigue loading history on damage evolution and accumulation are examined.

Since the microcracks have preferred orientation and well-defined length distributions, the homogeneous fatigue damage is generally anisotropic in nature. The degree of anisotropy depends on the loading mode, stress level, and material microstructure. The damage apparently changes the macroscopic mechanical response of the composite such as stiffness or compliance, introducing the important problem of damage-induced property degradation. Equally important is the anisotropy of the degraded material properties during fatigue. Thus, the tensorial nature of damage evolution and accumulation and the associated property degradation are of fundamental concern in studying the fatigue behavior of random short-fiber composites. The purposes of this paper are to: (1) derive constitutive equations for effective elastic properties of the damaged composite subjected to cyclic loading, (2) determine the relationship between the microscopic damage development and macroscopic material degradation, (3) introduce a macroscopic tensorial parameter to describe the state of damage in the material, and (4)

[1] Presently Advanced Engineer, Owens-Corning Fiberglas Corporation

Contributed by the Applied Mechanics Division for presentation at the Winter Annual Meeting, Anaheim, CA, December 7–12, 1986, of The American Society of Mechanical Engineers.

Discussion of this paper should be addressed to the Editorial Department, ASME, United Engineering Center, 345 East 47th Street, New York, N.Y. 10017, and will be accepted until two months after final publication of the paper itself in the JOURNAL OF APPLIED MECHANICS. Manuscript received by ASME Applied Mechanics Division, December 7, 1984; final revision July 2, 1985. Paper No. 86-WA/APM-7.

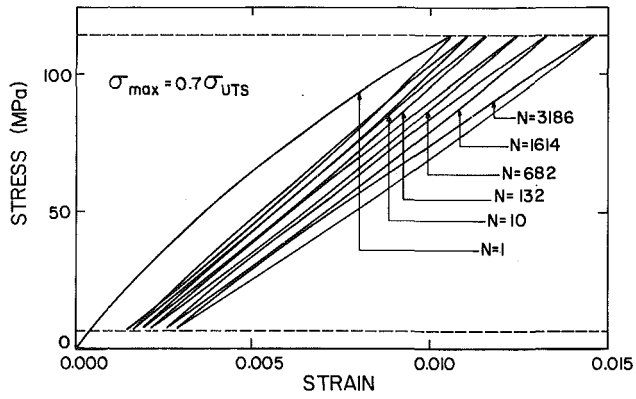

Fig. 1 Stress-strain response of a short-fiber SMC-R50 composite subjected to stress-controlled cyclic fatigue loading, $\sigma_{max} = 0.7\sigma_{UTS}$

establish a fatigue damage growth law to evaluate the evolution and accumulation of microcracks.

The overall or effective elastic properties of solids containing distributed inhomogeneities such as inclusions and voids have been a subject of considerable research; extensive lists of references can be found, for example, in Kröner (1967), Christensen (1979), Willis (1981), Mura (1982), and Hashin (1983). Among various theories and methods of approach proposed, the self-consistent mechanics analysis (Hershey, 1954, and Kröner, 1958) has attracted significant attention. Applications of this method to fiber composites have been made by many researchers, for instance, Hill (1965), Hermans (1967), Christensen and Waals (1972), and Chou et al. (1980). Also, the self-consistent scheme has been used to study the overall moduli of isotropic elastic solids containing randomly oriented cracks by Budiansky and O'Connell (1976) and aligned cracks by Hoenig (1979). Recently, Horii and Nemat-Nasser (1983) have taken the same approach to examine an elastic body containing randomly distributed cracks that may be closed or undergo frictional sliding. In this paper, the self-consistent mechanics analysis is employed in conjunction with the probabilistic microcrack distribution functions introduced in the composite under cyclic fatigue. The constitutive behavior of effective stiffness properties and the tensorial nature of fatigue damage are determined for the random short-fiber composite having homogeneously distributed microcracks.

In the next section, an experimental program is conducted to evaluate stiffness degradation in a random short-fiber SMC-R50 composite subject to cyclic tensile fatigue. The basic solution scheme of the self-consistent analysis is briefly described in Section 3 for the damaged composite. Probabilistic density functions of crack orientation and length developed during fatigue are incorporated in the formulation with the aid of a three-dimensional elliptic crack theory. A tensorial fatigue-damage parameter is introduced in Section 4, based on the anisotropic cyclic stiffness degradation of the composite. Experimental results are compared with theoretical predictions in Section 5. The rate of fatigue degradation is determined, and a cyclic damage-growth law is established for the random short-fiber composite system. The tensorial nature of damage development and the rate of change in the damage tensor are examined. This study has established the fundamental mechanics of cyclic fatigue damage and property degradation in random short-fiber composites. Important conclusions obtained from the study are given in Section 6.

2 Fatigue Degradation Experiment

Cyclic fatigue tests were performed on the short-fiber SMC-R50 composite to study the effect of microscopic fatigue damage on macroscopic property degradation. The geometry of the specimens is shown in Fig. 2 of Wang et al. (1986). The specimens had a total length of 254 mm with a gage section of 76.2 mm and a free length between grips of 152.4 mm. The width in the gage section was 38.1 mm. All specimens were machined from composite plates of 533 mm × 610 mm × 2.54 mm as received. During machining, care was taken to insure that all cut edges were smooth and free from visible defects. The microscopic damage development was monitored continuously during cyclic fatigue, using a replica technique discussed in the associated paper (Wang et al., 1986). The experiments were conducted at room temperature in a 20-kip MTS servohydraulic system interfaced with a multi-user PDP digital computer. Constant-amplitude stress-controlled fatigue tests were performed at a frequency of 2 Hz. A minimum stress of about 5 percent of the ultimate tensile strength σ_{UTS} was employed to prevent the specimens from being subjected to any compressive loads. The tests were controlled by the computer through preprogrammed software. Cyclic stress levels were monitored continuously, and corresponding strains were measured with a clip-gage extensometer of 63.5 mm gage length during the entire history of the fatigue test. Both stress and strain data were digitized and stored on floppy disks through a data acquisition system for later analyses.

3 Self-Consistent Mechanics Analysis and Solution Procedure for Damaged Composite

In the present study, the virgin random short-fiber composite is considered to be macroscopically homogeneous and planarly isotropic. The damage introduced by the fatigue loading takes various forms of microcracks with preferred orientation and length distributions, leading to macroscopic, anisotropic property degradation. The density functions of microcrack length and orientation determined in Wang et al. (1986) are now incorporated in a self-consistent mechanics analysis to obtain overall constitutive properties of the damaged composite.

Consider a random short-fiber composite of volume V with an exterior surface B, containing microcracks of total surface area $B^{(d)}$. Effective strains and stresses, $\bar{\epsilon}_{ij}$ and $\bar{\sigma}_{ij}$, in the solid with homogeneously distributed cracks are related by the effective compliance tensor S_{ijkl} of the damaged composite as

$$\bar{\epsilon}_{ij} = S_{ijkl}\bar{\sigma}_{kl} \tag{1}$$

Components of the effective compliance tensor display the usual symmetry, i.e., $S_{ijkl} = S_{ijlk} = S_{jikl} = S_{klij}$, etc.

The effective strains in the damaged body can be defined as

$$\bar{\epsilon}_{ij} = \frac{1}{V}\int_V \epsilon_{ij} dv, \qquad \text{with } \epsilon_{ij} = \frac{1}{2}(u_{i,j} + u_{j,i}) \tag{2}$$

where u_i are displacements, and the comma following by an index denotes partial differentiation with respect to the corresponding coordinate. Using the divergence theorem, $\bar{\epsilon}_{ij}$ can be rewritten as

$$\bar{\epsilon}_{ij} = \frac{1}{V}\int_B (u_i n_j + u_j n_i) ds \tag{3}$$

where n_j are unit outward normals on B. Similarly, the average stresses $\bar{\sigma}_{ij}$ are written as

$$\bar{\sigma}_{ij} = \frac{1}{V}\int_V \sigma_{ij} dv \tag{4}$$

and $\bar{\sigma}_{ij}$ are related to self-equilibrating overall tractions $\bar{T}_i$ prescribed on B by

$$\bar{T}_i = \bar{\sigma}_{ij} n_j \tag{5}$$

The average strains $\bar{\epsilon}_{ij}^{(c)}$ in the portion $V^{(c)}$ exterior to the cracks in the damaged composite can be rewritten in terms of displacements u_i as

$$\bar{\epsilon}_{ij}^{(c)} = \frac{1}{V^{(c)}}\int_{V^{(c)}} \epsilon_{ij} dv = \frac{1}{V}\left[\int_B \frac{1}{2}(u_i n_j + u_j n_i) ds + \int_{B^{(d)}} \frac{1}{2}(u_i n_j + u_j n_i) ds\right] \tag{6}$$

Since the material in $V^{(c)}$ is undamaged, the average strains $\bar{\epsilon}_{ij}^{(c)}$ can be written as

$$\bar{\epsilon}_{ij}^{(c)} = S^o_{ijkl}\bar{\sigma}_{kl}^{(c)} \tag{7}$$

where S^o_{ijkl} is the elastic compliance tensor of the undamaged composite. Substituting equation (3) into equation (6) and using equation (7), one obtains

$$\bar{\epsilon}_{ij} = S^o_{ijkl}\bar{\sigma}_{kl} + \frac{1}{V}\int_{B^{(d)}} \frac{1}{2}(u_i n_j + u_j n_i) ds \tag{8}$$

where the expression $\bar{\sigma}_{kl} = \bar{\sigma}_{kl}^{(c)}$ is used. We note that n_j are taken here and hereafter as unit inward normals to the material along $B^{(d)}$.

Let $G_{ij}(\mathbf{x},\xi)$ be the displacement component in the x_i direction at a point $\mathbf{x}$ due to a unit load applied at point ξ on B in the x_j direction. The displacements at $\mathbf{x}$ are

$$u_i(\mathbf{x}) = \int_B G_{ij}(\mathbf{x},\xi)\bar{T}_j ds = \bar{\sigma}_{jk}\int_B G_{ij}(\mathbf{x},\xi) n_k(\xi) ds \tag{9}$$

where $G_{ij}(\mathbf{x},\xi)$ are actually Green's functions of the problem. The second term on the right hand side of equation (8) can be written as

$$\frac{1}{V}\int_{B^{(d)}} \frac{1}{2}(u_i n_j + u_j n_i) ds = H_{ijkl}\bar{\sigma}_{kl} \tag{10}$$

where

$$H_{ijkl} = \frac{1}{V}\int_{B^{(d)}}\int_B \frac{1}{2}[G_{ik}(\mathbf{x},\xi) n_j(\mathbf{x}) n_l(\xi) + G_{jk}(\mathbf{x},\xi) n_i(\mathbf{x}) n_l(\xi)] ds\, ds^{(d)} \tag{11}$$

The average strains $\bar{\epsilon}_{ij}$ in the damaged composite are now expressed in terms of the average stresses $\bar{\sigma}_{ij}$ as

$$\bar{\epsilon}_{ij} = (S^o_{ijkl} + H_{ijkl})\bar{\sigma}_{kl} \tag{12}$$

Hence, the effective compliance S_{ijkl} can be determined by

$$S_{ijkl} = S^o_{ijkl} + H_{ijkl}(S_{pqrs}) \tag{13}$$

In the present study, H_{ijkl} can be obtained directly from equation (10) provided that u_i in the damaged composite are known.

To apply the self-consistent mechanics analysis, the problem of an elliptic crack embedded in the homogeneously damaged composite is considered first. The effect of the crack on overall elastic behavior of the composite is calculated from equation (10). Total effects of all microcracks are determined by summation of all of the contributions from each individual crack. Then equation (13) is used to estimate the effective elastic properties of the damaged fiber composite.

Based on experimental observations of the microstructure and the damage in the random short-fiber composite, several assumptions are introduced to simplify the analysis of the problem: (*i*) probabilistic properties of microcrack density functions are homogeneous in the damaged composite, (*ii*) all microcracks are elliptic in shape and each crack plane is perpendicular to the plane of the composite, and (*iii*) the length of the minor axis of each crack is equal to the thickness of a fiber strand in the composite.

To evaluate H_{ijkl} in equation (10) for the embedded elliptic crack, the following information on displacements of the crack surface in an anisotropic elastic solid is required (Hoenig, 1979):

$$u_i' = L_{ij}^{-1}\bar{\sigma}_{3j}'\sqrt{cb\left(1 - \frac{x_1'^2}{c^2} - \frac{x_2'^2}{b^2}\right)} \quad (i,j = 1,2,3) \tag{14}$$

where x_i' are local coordinates, and the influence coefficients L_{ij} are defined as

$$L_{ij} = -\frac{1}{4}\sqrt{c/b}\int_0^{2\pi} Q_{kl} R_{ki} R_{lj} d\phi \tag{15}$$

in which Q_{ij} are functions of material constants of the composite with damage; $[R_{ij}]$ is a transformation matrix, and c and b are major and minor semi-axes of the elliptical crack. Explicit expressions for Q_{ij} and R_{ij} can be found in Chim (1984).

For a flat elliptic crack, equation (14) can be evaluated by taking the integration over the platform area S of the crack and replacing the displacements with displacement jumps across the crack surface. Hence, the influence of one single crack on the effective compliance tensor is determined by

$$\int_S \frac{1}{2}([u_i']n_j' + [u_j']n_i') ds = K_{ijkl}'\bar{\sigma}_{kl}' \tag{16}$$

where the bracket [ ] denotes a displacement discontinuity, and the quantity with a prime (′) is referred to the local coordinates. For the convenience of later developments, contracted notation is used hereafter, i.e., $\sigma_{11} = \sigma_1$, $\sigma_{22} = \sigma_2$, . . . , . . . , $\sigma_{12} = \sigma_6$. Substituting equation (14) into (16) yields explicit expressions for K_{ij}' as

$$[K_{ij}'] = \frac{4}{3}\pi(cb)^{3/2}\begin{bmatrix} 0 & 0 & 0 & 0 & 0 & 0 \\ 0 & 0 & 0 & 0 & 0 & 0 \\ 0 & 0 & L_{33}^{-1} & L_{32}^{-1} & L_{31}^{-1} & 0 \\ 0 & 0 & L_{23}^{-1} & L_{22}^{-1} & L_{21}^{-1} & 0 \\ 0 & 0 & L_{13}^{-1} & L_{12}^{-1} & L_{11}^{-1} & 0 \\ 0 & 0 & 0 & 0 & 0 & 0 \end{bmatrix} \tag{17}$$

since $n_1' = n_2' = 0$ and $n_3' = 1$, and L_{ij}^{-1} are components of the inversed $[L_{ij}]$ matrix. The effect is transformed into the principal material coordinates as

$$K_{ij}(c,\theta\,|S_{pq}) = T_{im}T_{jn}K_{mn}' \tag{18}$$

where $K_{ij}(c,\theta\,|S_{pq})$ are defined as the influence functions of a microcrack with length $2c$ and orientation θ on the effective compliance S_{pq}, and $[T_{mn}]$ is a transformation matrix between local and material coordinates, involving $\cos\theta$ and $\sin\theta$ terms only.

Total effects of all microcracks on $H_{ij}(S_{pq})$ can be obtained by summing up the contributions of each individual microcrack as

$$H_{ij}(S_{pq}) = \frac{1}{V}\sum_n K_{ij}(c_n,\theta_n\,|S_{pq}) \tag{19}$$

When the volume of the composite becomes large enough to include many homogeneously distributed microcracks, the summation in equation (19) can be replaced with an integration weighted by the aforementioned microcrack density function $\lambda(c,\theta)$, i.e.,

$$H_{ij}(S_{pq}) = \int_0^\infty\int_{-\pi/2}^{\pi/2} K_{ij}(c,\theta\,|S_{pq})\lambda(c,\theta) dc\, d\theta \tag{20}$$

We remark that the kernels K_{ij} in equation (20) involve the unknowns S_{pq}; thus $H_{ij}(S_{pq})$ may be solved numerically by an iterative solution scheme. Once H_{ij} are determined, the effective compliance tensor of the damaged composite can be obtained immediately.

4 Fatigue Damage Evolution and Accumulation

Based on the experimental results obtained and the

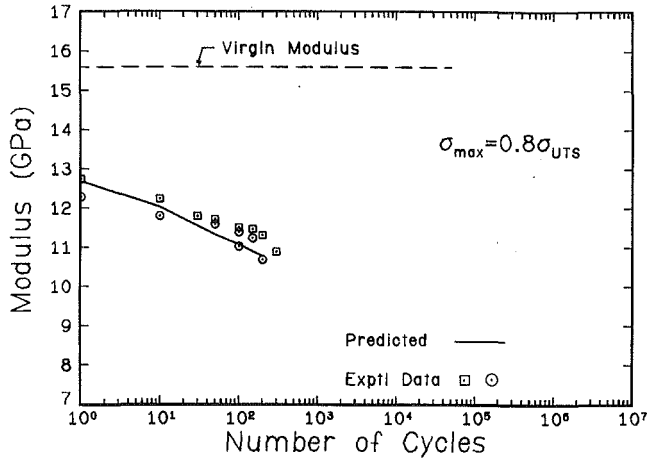

Fig. 2 Theoretical predictions and experimental data of axial stiffness degradation in short-fiber SMC-R50 composite during fatigue ($\sigma_{max}=0.8\sigma_{UTS}$; $R=0.05$, $f=2$ Hz)

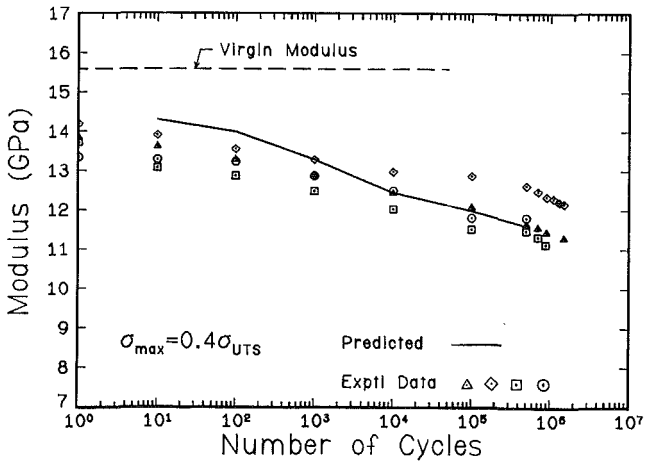

Fig. 3 Theoretical predictions and experimental data of axial stiffness degradation in short-fiber SMC-R50 composite during fatigue ($\sigma_{max}=0.4\sigma_{UTS}$; $R=0.05$, $f=2$ Hz)

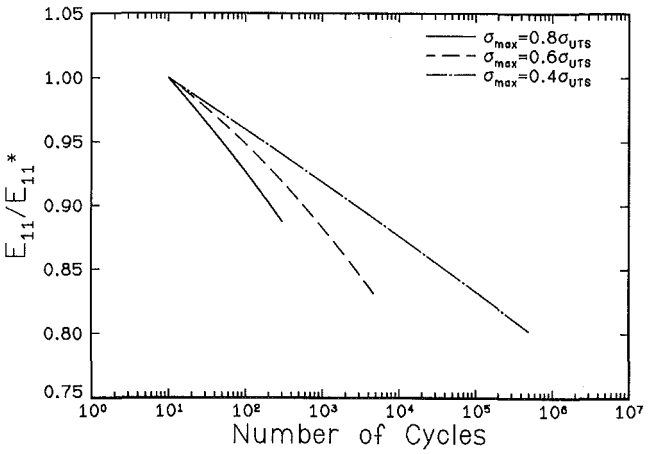

Fig. 4 Changes of Young's modulus, E_{11}, in short-fiber SMC-R50 composite during fatigue at several cyclic stress levels σ_{max} ($R=0.05$, $f=2$ Hz)

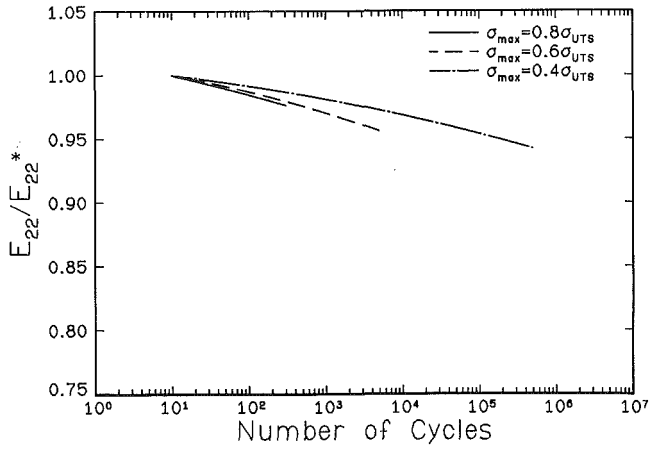

Fig. 5 Changes of Young's modulus, E_{22}, in short-fiber SMC-R50 composite during fatigue at several cyclic stress levels σ_{max} ($R=0.05$, $f=2$ Hz)

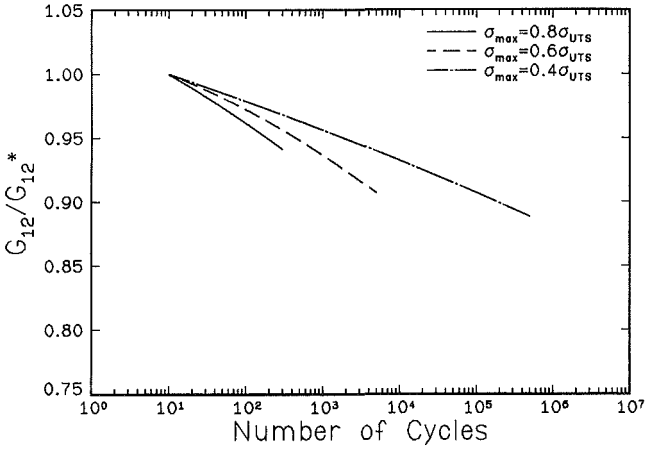

Fig. 6 Changes of shear modulus, G_{12}, in short-fiber SMC-R50 composite during fatigue at several cyclic stress levels σ_{max} ($R=0.05$, $f=2$ Hz)

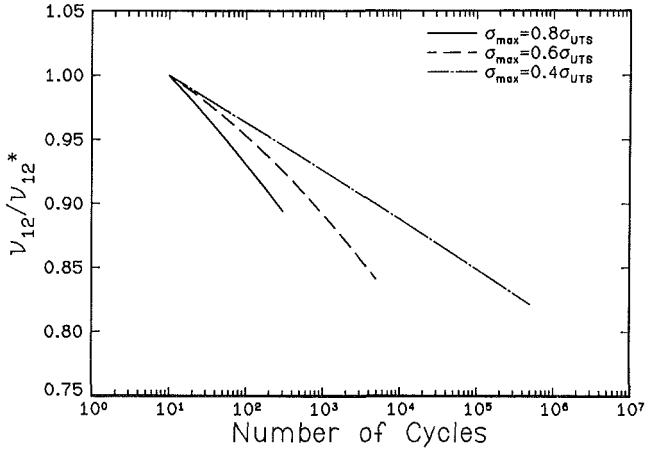

Fig. 7 Changes of Poisson's ratio, ν_{12}, in short-fiber SMC-R50 composite during fatigue at several cyclic stress levels σ_{max} ($R=0.05$, $f=2$ Hz)

theoretical analysis developed, a damage parameter is introduced to provide a quantitative measure of the anisotropic nature of fatigue damage in the composite. In this study, the damage parameter D_{ij} is defined as relative tensorial stiffness changes in the composite,

$$D_{ij}=1-\frac{C_{ij}}{C_{ij}^*} \quad (i,j=1,2,3,\ldots,6; \text{ no summation on } i \text{ and } j) \tag{21}$$

where C_{ij} are the stiffness components of the damaged material, and the superscript (*) refers to a reference state. The C_{ij} are obtained directly from inversion of the S_{ij} matrix determined in the previous section. The instantaneous stiffness and the fatigue damage are functions of cyclic stress variables, fatigue loading cycles, and environmental conditions as

$$C_{ij}=C_{ij}(\sigma_{max}, s, N, \alpha, T, \ldots), \tag{22}$$

Table 1 Elastic material properties of short-fiber SMC-R50 composite at the tenth fatigue cycle

$\frac{\sigma_{max}}{\sigma_{UTS}}$	E_{11}^* (GPa)	E_{22}^* (GPa)	G_{12}^* (GPa)	ν_{12}^*
0.4	14.1	15.4	5.70	.286
0.6	13.6	15.2	5.57	.273
0.8	12.0	14.8	5.21	.243

$$D_{ij} = D_{ij}(\sigma_{max}, \mathbf{s}, N, \alpha, T, \ldots), \quad (23)$$

where s is the state of cyclic stress (i.e., tensile, compressive, or multiaxial), and α is a microstructural parameter of the composite.

5 Results and Discussion

The typical stress-strain response of a short-fiber SMC-R50 composite at different fatigue loading cycles is shown in Fig. 1 for the case of $\sigma_{max} = 0.7\ \sigma_{UTS}$. The material clearly changed with load cycles and became less resistant to the applied stress. The size of the hysteresis loop of the first load excursion was much larger than the subsequent ones due to growth of existing defects and initiation of a large number of microcracks at various microscopic stress concentrators (Wang and Chim, 1983). As a result, a nonlinear, transient first-cycle (or monotonic) stress-strain relationship was observed. The next few loading cycles resulted in arrest of most of the initially growing cracks and rapid depletion of favorable microcrack nucleation sites (Wang and Chim, 1983; Wang et al., 1986). Thus energy dissipation and the degradation rate in the composite dropped sharply, leading to reduced sizes of hysteresis loops with approximately linear stress-strain relationships. Subsequent cyclic loading initiated further microdamage and grew existing microcracks but with rapidly decreasing rates, as discussed by Wang and Chim (1983) and Wang et al. (1986). This further development of homogeneous damage is reflected by a continuous decrease in stiffness of the composite and by an increase in size of the hysteresis loops.

5.1 Comparison Between Theoretical Predictions and Experimental Results. To illustrate the experimentally measured Young's modulus and theoretically predicted values, typical results of axial stiffness degradation during fatigue are shown in Figs. 2 and 3 for the SMC-R50 composite at two cyclic stress levels, $\sigma_{max} = 0.8\ \sigma_{UTS}$ and $0.4\ \sigma_{UTS}$, respectively. The vertical axis in the figures represents the actual value of the modulus along the loading direction. The experimental data shown in the figures were taken from specimens on which microcrack density measurements were made. The theoretical predictions are obtained numerically by the use of an iterative scheme. In the computation, the microcrack density functions, $f_c(c)$ and $g_\theta(\theta)$, obtained from Wang et al. (1986) are used. Comparing the experimental data with the theoretical predictions, excellent agreement is observed. Similar agreement between experimental results and theoretical predictions of stiffness changes in the composite under other cyclic fatigue stress levels is also obtained in this study, and these additional results are not reported here because of space limitation. (Note here that in the self-consistent mechanics analysis, the microcrack width, i.e., the minor axis of the elliptic crack, is taken to have the fiber-strand thickness as discussed in the previous section. However, from cross-sectional micrographs of the damaged SMC composite (Wang et al., 1987), some microcracks were observed to develop into a dimension of several fiber-strand thicknesses.) Based on these results, the present self-consistent mechanics analysis in conjunction with the probabilistic treatment of microcracks appears to provide good predictions of material property degradation in a fatigue-damaged short-fiber composite.

5.2 Anisotropic Stiffness Degradation in Damaged Composite. As discussed in Wang et al. (1986), the microscopic damage has a preferred orientation distribution, leading to damage-induced anisotropy of material properties; thus, changes in all independent material constants during fatigue are required to be examined. Since degradation of in-plane stiffness properties is of major concern in this study, only four elastic constants, namely, E_{11}, E_{22}, G_{12}, and ν_{12}, are reported here. (E_{22} is the Young's modulus normal to the loading direction, and G_{12} is the in-plane shear modulus.) The predicted values of E_{11}, E_{22}, G_{12} and ν_{12} of the composite during fatigue with $\sigma_{max} = 0.8\ \sigma_{UTS}$, $0.6\ \sigma_{UTS}$, and $0.4\ \sigma_{UTS}$ are shown in Figs. 4–7, respectively. These quantities are normalized with their corresponding reference values at the tenth cycle (Table 1). It is clear that all these material constants change with load cycles; only degrees of the relative changes are different. Magnitudes and rates of changes in E_{11} and ν_{12} are most significant, and E_{22} has the least amount of degradation. The self-consistent mechanics analysis clearly provides an effective means of predicting all components of anisotropic material stiffness degradation in the composite during its fatigue life.

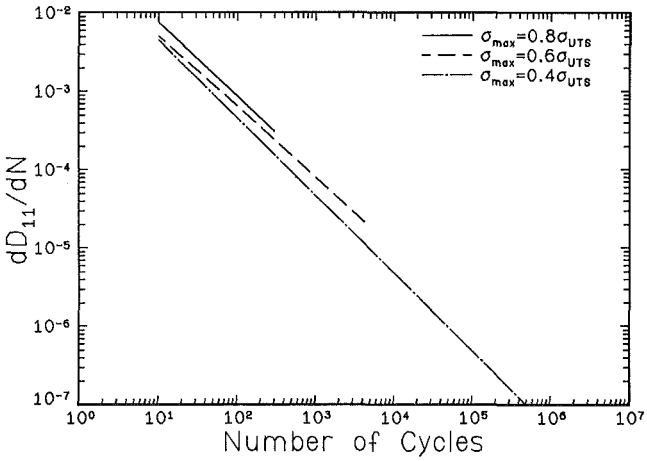

Fig. 8 The rate of change of homogeneous damage component, dD_{11}/dN, in short-fiber SMC-R50 composite during fatigue at several cyclic stress levels σ_{max} ($R = 0.05$, $f = 2$ Hz)

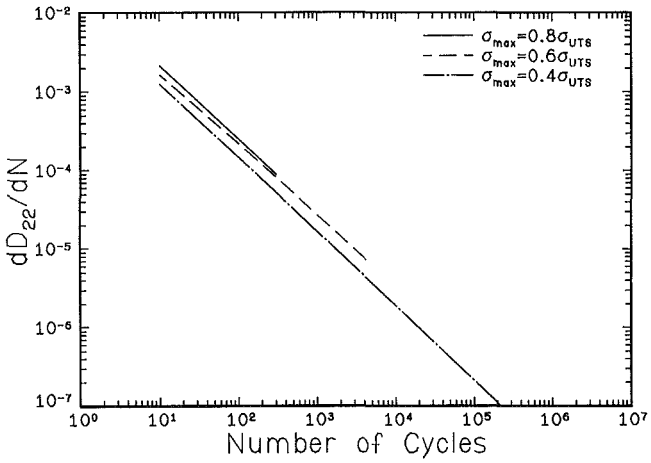

Fig. 9 The rate of change of homogeneous damage component, dD_{22}/dN, in short-fiber SMC-R50 composite during fatigue at several cyclic stress levels σ_{max} ($R = 0.05$, $f = 2$ Hz)

5.3 The Rate of Fatigue Damage Evolution and Accumulation. The rates of change of fatigue damage, dD_{ij}/dN, are quantities of primary interest in evaluation of damage evolution and accumulation. The development of dD_{ij}/dN during fatigue can be determined directly from degradation of the stiffness tensor. For illustration, values of dD_{ij}/dN for the short-fiber SMC-R50 composite at three

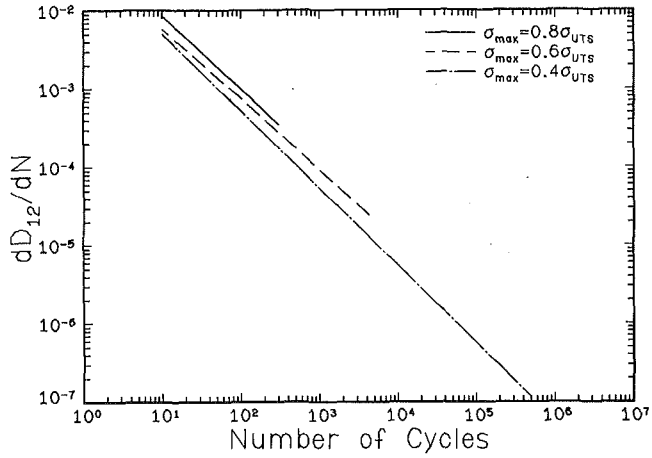

Fig. 10 The rate of change of homogeneous damage component, dD_{12}/dN, in short-fiber SMC-R50 composite during fatigue at several cyclic stress levels σ_{max} ($R=0.05$, $f=2$ Hz)

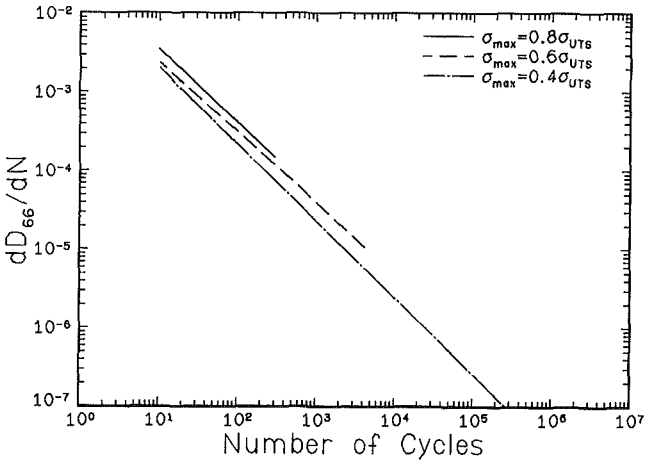

Fig. 11 The rate of change of homogeneous damage component, dD_{66}/dN, in short-fiber SMC-R50 composite during fatigue at several cyclic stress levels σ_{max} ($R=0.05$, $f=2$ Hz)

fatigue stress levels are shown in Figs. 8–11. As anticipated, at any given number of fatigue cycles, the higher the fatigue stress σ_{max}, the higher the dD_{ij}/dN. This is apparently caused by a larger number of microcracks being initiated and the higher rate of microcrack growth, as clearly evidenced by the cumulative crack distribution function $F_c(c)$ in Wang et al. (1986). However, at a given fatigue stress level, the rate of change in damage decreases exponentially with the number of loading cycles. This is the most unique characteristic of fatigue damage developments in the short-fiber composite. From the present theoretical and experimental results, the exponential decrease in dD_{ij}/dN can be clearly attributed to: (1) the rapid decrease in the rate of formation of new microcracks, as demonstrated in the evaluation of the cumulative crack distribution function $F_c(c)$ in Wang et al. (1986), (2) the very slow growth of relatively long microcracks, as indicated in the evolution of the microcrack-length density function $f_c(c)$ in Wang et al. (1986), and (3) the presence of various microcrack arrest mechanisms in the heterogeneous short-fiber composite, as illustrated in Wang and Chim (1983). An apparently linear relationship between dD_{ij}/dN and N with a common slope is found in all logarithmic plots of dD_{ij}/dN versus N (Figs. 8–11), leading to the following power-law damage-rate equation:

$$\frac{dD_{ij}}{dN}=A_{ij}(D_{ij})N^{-B}, \quad (i,j=1,2,3,\ldots,6; \text{ no summation on } i \text{ and } j) \tag{24}$$

where A_{ij} are functions of D_{ij}, and $-B$ is the slope of each line in the log-log plot. The functions $A_{ij}(D_{ij})$ are related to the damage rate in a reference state at a given cyclic stress, the fatigue loading history, the amplitude of fatigue stress, and the state of cyclic stress. Based on the definition of damage, the total fatigue life may be determined, for example, by a direct integration of equation (24),

$$N_f=\left\{\int_0^{\mathbf{D}_f}\frac{(1-B)}{\mathbf{A}}d\mathbf{D}\right\}^{\frac{1}{1-B}} \tag{25}$$

where $\mathbf{D}=0$ indicates a reference state and $\mathbf{D}=\mathbf{D}_f$ refers to the final failure state which is in general determined from a stiffness-based failure criterion.

6 Conclusion

Based on the probabilistic treatment of microcrack developments discussed in Wang et al. (1986) and the self-consistent mechanics analysis of a random short-fiber composite containing distributed microcracks with well-defined density functions of crack length and orientation, damage-induced anisotropy and degradation of effective elastic properties of the composite during cyclic fatigue are studied in detail. Experimental and theoretical results are obtained for evaluating the microcrack evolution and accumulation as well as the associated property degradation. The basic mechanics and mechanisms of fatigue damage in the random short-fiber composite are elucidated. A power-law type relationship for fatigue damage growth is established for the random short-fiber composite under cyclic loading. The following conclusions may be reached, based on the current theoretical and experimental results:

(1) Constitutive equations for effective elastic properties of the damaged composite are derivable from a self-consistent mechanics scheme. Three-dimensional elliptic crack theory for anisotropic solids and probabilistic treatment of distributed microcracks are essential in formulating a proper SCS analysis of fatigue damage and degradation in the random short-fiber composite.

(2) Excellent agreement is observed between theoretical predictions and experimental data of tensile stiffness changes in the loading direction. The present theory and analysis appear to provide an effective means to predict all of the components of the anisotropic stiffness degradation in the composite during cyclic fatigue.

(3) Severity of the magnitude and the rate of fatigue degradation for in-plane material constants is ranked in the order of E_{11}, ν_{12}, G_{12} and E_{22} for the random short-fiber composite under uniaxial tensile fatigue. The maximum degradation of approximately 20–25 percent is observed for E_{11} during the cyclic homogeneous fatigue damage of the composite.

(4) The parameter D_{ij}, introduced to describe quantitatively the degree of homogeneous fatigue damage, is defined by the change of material stiffness tensor relative to a reference state. Microcrack evolution and accumulation during cyclic fatigue are expressed by the rate of change of the damage tensor, dD_{ij}/dN.

(5) A power-law relationship is found between the rate of damage development and the fatigue cycle. The rate of change of the homogeneous fatigue damage, dD_{ij}/dN, in the random short-fiber SMC composite decreases exponentially with fatigue loading cycles owing to rapid depletion of new crack initiation sites, slow growth of existing microcracks, and presence of various crack-arrest mechanisms.

(6) The exponent B in the damage-growth law is the same for all components of the damage rate tensor dD_{ij}/dN and can be related to the cyclic tensile fatigue stress σ_{max}.

Acknowledgments

The work reported in this paper was supported in part by

research grants from Office of Naval Research (N00014-79-C-0579) and Owens-Corning Fiberglas Corporation to the University of Illinois at Urbana-Champaign. The authors gratefully acknowledge the constant support and encouragement from Dr. Y. Rajapakase of ONR and Drs. G. N. Hartt and D. L. Denton of OCF. Numerical computations were conducted in Digital Computer Laboratory at the University of Illinois.

References

Budiansky, B., and O'Connell, R. J., 1976, "Elastic Moduli of a Cracked Solid," *International Journal of Solids and Structures*, Vol. 12, pp. 81–97.

Chim, E. S.-M., 1984, "Tensile Fatigue Damage and Degradation of Random Short-Fiber Composites," Ph.D. Dissertation, Department of Theoretical and Applied Mechanics, University of Illinois, Urbana, Ill.

Christensen, R. M., and Waals, F. M., 1972, "Effective Stiffness of Randomly Oriented Fiber-Reinforced Composites," *Journal of Composite Materials*, Vol. 6, pp. 518–532.

Christensen, R. M., 1979, *Mechanics of Composite Materials*, Wiley-Interscience, New York.

Chou, T. W., Nomura, S., and Taya, M., 1980, "A Self-Consistent Approach to Elastic Stiffness of Short-Fiber Composites," *Journal of Composite Materials*, Vol. 14, pp. 178–188.

Hashin, Z., 1983, "Analysis of Composite Materials – A Survey," ASME JOURNAL OF APPLIED MECHANICS, Vol. 50, No. 3, pp. 481–505.

Hermans, J. J., 1967, "The Elastic Properties of Fiber-Reinforced Materials when the Fibers are Aligned," *Proceedings Koninklijke Nederlandse Ackademie van Wetenschappen*, Series B, Vol. 70, pp. 1–9.

Hershey, A. V., 1954, "The Elasticity of an Isotropic Aggregate of Anisotropic Cubic Crystals," ASME JOURNAL OF APPLIED MECHANICS, Vol. 21, pp. 236–240.

Hill, R., 1965, "Theory of Mechanical Properties of Fiber-Strengthened Materials – III. Self-Consistent Model," *Journal of the Mechanics and Physics of Solids*, Vol. 13, pp. 189–198.

Hoenig, A., 1979, "Elastic Moduli of Non-Randomly Cracked Bodies," *International Journal of Solids and Structures*, Vol. 15, pp. 137–154.

Horri, H., and Nemat-Nasser, S., 1983, "Overall Moduli of Solids with Microcracks: Load-Induced Anisotropy," *Journal of the Mechanics and Physics of Solids*, Vol. 31, No. 2, pp. 155–171.

Kröner, E., 1958, "Berechnung der Elastischen Konstanten des Vielkristalls aus der Konstanten des Einkristalls," *Zeitschrift für Physik*, Vol. 151, pp. 504–518.

Kröner, E., 1967, "Elastic Moduli of Perfectly Disordered Materials," *Journal of the Mechanics and Physics of Solids*, Vol. 15, pp. 319–329.

Mura, T., 1982, *Micromechanics of Defects in Solids*, Martinus Nijhoff Publisher, The Hague.

Wang, S. S., and Chim, E. S.-M., 1983, "Fatigue Damage and Degradation in Random Short-Fiber SMC Composite," *Journal of Composite Materials*, Vol. 17, No. 2, pp. 114–134.

Wang, S. S., Chim, E. S.-M., and Suemasu, H., 1986, "Mechanics of Fatigue Damage and Degradation in Random Short-Fiber Composites, Part I – Damage Evolution and Accumulation," *ASME Journal of Applied Mechanics*, Vol. 53, No. 2, pp. 339–346.

Wang, S. S., Suemasu, H., and Chim, E. S.-M., 1987, "Analysis of Fatigue Damage Evolution and Property Degradation in Random Short-Fiber Composites," *Journal of Composite Materials*, Vol. 21, No. 1.

Willis, J. R., 1981, "Variational and Related Methods for the Overall Properties of Composites," in *Advances in Applied Mechanics*, Vol. 21, Academic Press, pp. 1–81.

M. Kaneta
Professor.

M. Suetsugu
Graduate Student.

Department of Mechanical Engineering,
Kyushu Institute of Technology,
Tobata, Kitakyushu, 804, Japan

Y. Murakami
Professor,
Department of Mechanics and
Strength of Solids,
Faculty of Engineering,
Kyushu University,
Hakozaki, Fukuoka, 812, Japan

Mechanism of Surface Crack Growth in Lubricated Rolling/Sliding Spherical Contact

A possible mechanism of the crack growth is described by calculating stress intensity factors for a semicircular surface crack under a spherical Hertzian contact moving over a cracked elastic half-space surface. In the analysis the crack is assumed to be inclined at an angle of 45 deg from the surface. In particular, the effects of surface traction, frictional force between crack faces, and oil hydraulic pressure caused by oil penetrated into the crack are discussed.

1 Introduction

Cracks initiating at/in the contact surface propagate due to the cyclic loading, and, as a result, surface damage may be brought about. Recently, in order to elucidate the rolling and/or sliding contact fatigue phenomenon, fracture mechanics has been utilized because the phenomenon is related to the growth of cracks.

Fracture mechanics was first utilized by Fleming and Suh (1977) to characterize the driving force for a subsurface crack growth. Such a subsurface crack has been examined by various workers (Hills and Ashelby, 1980; Rosenfield, 1981; Keer et al., 1982; Chang et al., 1984; Sin and Suh, 1984; Yoshimura et al., 1984; Hearle and Johnson, 1985). For an inclined two-dimensional surface crack Keer and Bryant (1983) have calculated the stress intensity factors and have estimated the fatigue life. Yamashita et al. (1985) have proposed a mechanism for the initiation of surface pitting through their analytical method. The authors have also analyzed in previous papers (Murakami et al., 1985; Kaneta et al., 1985) the growth mechanism of surface cracks formed on lubricated rolling/sliding line-contact surfaces on the basis of fracture mechanics, and have clarified the following points. A microcrack initiated at a comparatively early stage in the cyclic loading extends nearly along the original crack plane by shear mode fatigue crack growth. As the crack extends, the growth mode is altered to the tensile mode, which is caused by the influence of the fluid pressure by lubricant oil which has penetrated into the crack interior. Finally, the crack may be expected to grow into a pit. In these processes the surface traction plays an important role.

The purpose of this paper is to elucidate analytically a possible growth mechanism of surface cracks formed on lubricated rolling/sliding spherical contact surfaces by the same method as the previous paper (Murakami et al., 1985; Kaneta et al., 1985). To make the crack growth phenomenon tractable mathematically, the Hertzian contact pressure distribution is used instead of the pressure distribution obtained by the elastohydrodynamic lubrication theory. Moreover, the changes of material properties and surface topography induced by the rolling contact fatigue process, a solidification phenomenon of lubricant oil due to high contact pressure, etc., are ignored, though they must be considered in a more exact treatment of the crack growth behavior. In the current level of three-dimensional stress analyses and experimental techniques, it is almost impossible to solve this problem completely considering all factors strictly. Even if some analytical methods and experimental techniques are available, such an approach will not necessarily reveal the important factors which influence this complicated contact problem. This is the reason why the authors make a simple assumption.

2 Method of Analysis

2.1 Analytical Model and Method of Calculation. Figure 1 shows the analytical model used in this study. The elastic half-space containing a surface crack inclined at an angle (90 deg $-\alpha$) to the surface is loaded by normal and tangential stresses. Strictly speaking, the pressure distribution in the lubricated rolling and/or sliding contact spherical surface should be determined by the elastohydrodynamic lubrication theory, and it varies with oil viscosity, surface velocity, etc. Moreover, the existence of a surface crack may alter the pressure distribution. However, in this investigation, it is assumed that the normal stress arises from the Hertzian contact pressure and the surface shear stress is given by multiplying the Hertzian pressure by a mean frictional coefficient, f, between contact surfaces. Although a simple model is assumed because of the difficulties in three-dimensional stress analysis and experimental techniques, we may expect that the simple model helps us to understand the main factors which control this complicated problem.

Contributed by the Applied Mechanics Division for publication in the JOURNAL OF APPLIED MECHANICS.

Discussion on this paper should be addressed to the Editorial Department, ASME, United Engineering Center, 345 East 47th Street, New York, N.Y. 10017, and will be accepted until two months after final publication of the paper itself in the JOURNAL OF APPLIED MECHANICS. Manuscript received by ASME Applied Mechanics Division, February 7, 1985; final revision, August 2, 1985.

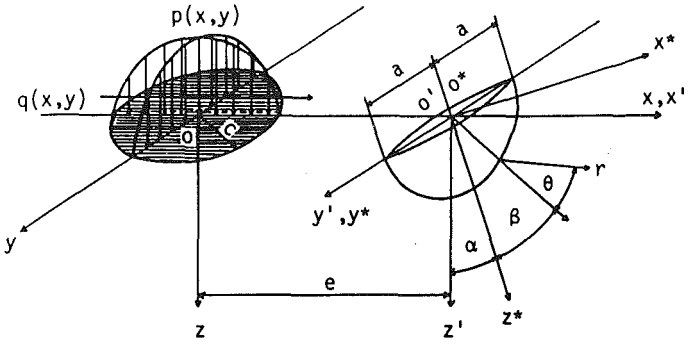

Fig. 1 Analytical model and coordinate system
$p(x,y)$ = Hertzian contact pressure
$q(x,y)$ = shear surface stress
a = radius of semi-circular crack
c = radius of Hertzian contact
e = distance between crack mouth and center of Hertzian contact
α = crack inclination angle
β = angle from deepest crack tip of crack front
(r,θ) = polar coordinates with origin at crack tip
(x,y,z) = rectangular coordinate system based on semi-infinite body
(x',y',z') = rectangular coordinates with origin at center of crack mouth
(x^*,y^*,x^*) = rectangular coordinate system based on crack face

Thus, the stress distributions on the elastic half-space are given by the following equations:

$$p(x,y) = p_o\sqrt{1-(x^2+y^2)/c^2} \tag{1}$$

$$q(x,y) = fp(x,y) \tag{2}$$

where p_o and c are the maximum Hertzian pressure and the Hertzian radius, respectively. The surface crack was assumed to be a semi-circle with radius a, and to be in the y^*-z^* plane. One cycle of rolling process can be viewed by shifting the location of the contact pressure along the surface of the cracked half-space in a direction opposite to that of rolling.

Way (1935) suggested that crack propagation will be accelerated if the oil hydraulic pressure caused by oil seepage into the crack is applied on the crack faces. This hypothesis has been evoked to explain oil viscosity effect in surface damage (Dawson, 1961). In addition, oil seepage into the crack has been observed experimentally (Michau et al., 1974). The pressure at the mouth of the crack, caused by the contact pressure sweeping over the crack mouth, may be transmitted down the deepest crack tip. However, if the pressure is only applied for a very short time, the full contact pressure will not be felt at the end of the crack instantaneously because of viscosity, compressibility, and inertia of the oil in the crack (Foord et al., 1969). Therefore, in this work, the fluid pressure, p_f, applied on the crack faces by lubricant oil entering the crack is assumed to decrease linearly from the crack mouth to the crack front. The motion of fluid in the crack interior was neglected for the sake of simplicity. Namely, the fluid pressure in the crack is expressed in the region of $|e| \leqq c$ as

$$p_f(z^*,y^*) = p(e,y)(1-z^*/a) \tag{3}$$

where e is the distance between the center of Hertzian contact pressure and the mouth of the crack.

When some or whole parts of crack faces are closed or sustain the compressive stresses, the frictional force acting on those parts may restrain the shear mode fatigue crack growth. In order to investigate its influence, the mean frictional coefficient, f_c, between the contacting crack faces was assumed as 0.2 or 0.5. We denote by τ^* and σ^* the shearing and compressive stresses (Hamilton, 1983) which act on the crack face imagined in a semi-infinite body without a crack under the contact pressure. It was assumed that the net shear stress τ_{net} acting on the crack faces was obtained as

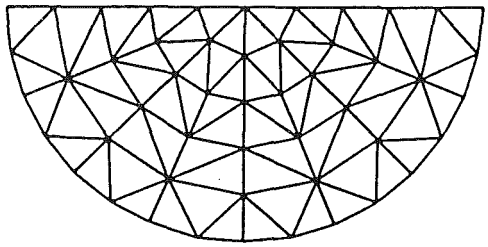

Fig. 2 Mesh pattern of crack face

$$\tau_{\text{net}} = \begin{cases} 0 & \text{if } |\tau^*| \leqq |f_c\sigma^*| \\ \tau^* + f_c\,\text{sgn}(\tau^*)\sigma^* & \text{if } |\tau^*| > |f_c\sigma^*| \end{cases} \tag{4}$$

where $\text{sgn}(\tau^*)$ is the sign function for τ^*. Equation (4) is valid only when the crack faces receive the compressive stress, i.e., $\sigma^*<0$. At the location where $\sigma^*>0$ on the parts of crack, a boundary condition was enforced so as to satisfy the free surface condition.

These simplifications may lead to results at some variance with the actual tendencies of crack growth and the related problems. However, such assumptions seem quite adequate for understanding complicated rolling contact fatigue phenomena qualitatively. Similar assumptions were also adopted by Keer and Bryant (1983) for treating the growth problem of two-dimensional surface crack under a line-contact pressure condition.

The stress intensity factors (SIFs) were obtained by the body force method. The details of the method were described in a previous paper (Murakami et al., 1985). The problem is essentially a three-dimensional boundary value problem and it can be described with the integral equations. However, it is difficult to solve the integral equations analytically and, therefore, the semicircular crack assumed in this study was divided into 72 triangular subregions as shown in Fig. 2 in order to solve the integral equations numerically. The value of weighting functions, F_{Ij}, F_{IIj} and F_{IIIj}, indicating the magnitude of body forces at each subregion was determined so as to satisfy the boundary conditions for the crack under the contact stress field. In this procedure, each main triangular subregion in Fig. 2 was subdivided into four equal triangles in order to improve the accuracy of analysis. The average of the values evaluated at the centers of gravity of the four triangles was regarded as the representative value of the main triangular subregion. The values of weighting functions at the crack contour become the dimensionless SIFs F_I, F_{II} and F_{III}. They are related to the nominal SIFs as follows:

$K_I = F_I p_o\sqrt{\pi a}$, $K_{II} = F_{II}p_o\sqrt{\pi a}$,

and

$$K_{III} = F_{III}p_o\sqrt{\pi a} \tag{5}$$

The Poisson's ratio used was 0.3.

The crack opening displacement (COD) at the j triangular subregion can be given by

$$\text{COD} = 4(1-\nu^2)p_o F_{Ij}\sqrt{2a\epsilon_j - \epsilon_j^2}/E \tag{6}$$

where ν is the Poisson's ratio, E is the elastic modulus, and ϵ_j is the minimum distance between the center of main triangular subregion and the crack contour.

2.2 Condition of Fatigue Crack Growth. Taking a crack tip as the origin of the polar coordinate system (r, θ), as shown in Fig. 1, we can express the SIFs representing the intensities of the fields of shearing stress, $\tau_{r\theta}$, and tangential stress, σ_θ, in the neighborhood of the crack tip as follows (Erdogan and Sih, 1963):

$$K_\tau(\theta) = \tau_{r\theta}\sqrt{2\pi r} = \frac{1}{2}\cos\frac{\theta}{2}[K_I\sin\theta + K_{II}(3\cos\theta - 1)] \tag{7}$$

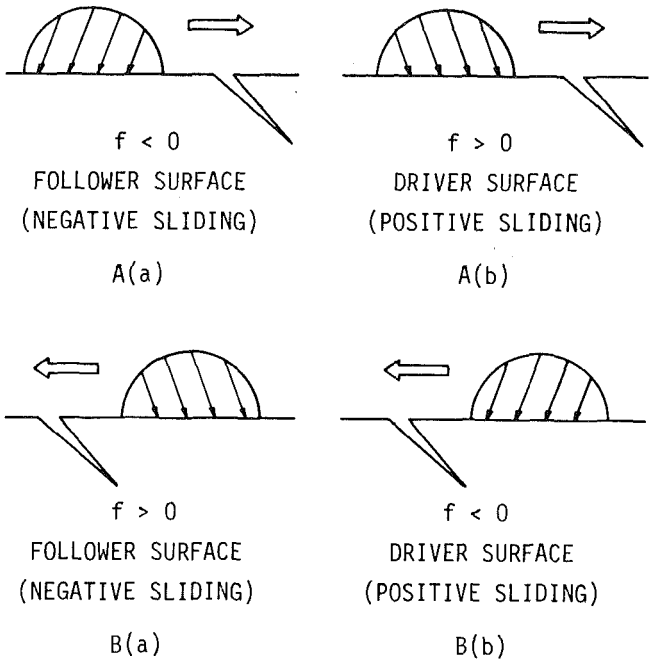

Fig. 3 Relations among directions of crack inclination, surface traction, and movement of contact pressure

$$K_\sigma(\theta)=\sigma_\theta\sqrt{2\pi r}=\cos\frac{\theta}{2}\left[K_I\cos^2\frac{\theta}{2}-\frac{3}{2}K_{II}\sin\theta\right] \tag{8}$$

In the above, $K_\tau(\theta)$ and $K_\sigma(\theta)$ are related to the dimensionless SIFs $F_\tau(\theta)$ and $F_\sigma(\theta)$ as follows:

$$K_\tau(\theta)=F_\tau(\theta)p_o\sqrt{\pi a} \text{ and } K_\sigma(\theta)=F_\sigma(\theta)p_o\sqrt{\pi a} \tag{9}$$

Both the critical condition and the direction of crack growth were determined by the same criterions as the previous paper (Murakami et al., 1985). Namely, the shear mode fatigue crack growth occurs macroscopically in the direction along which $K_\tau(\theta)$ is the maximum ($K_\tau(\theta)_{\max}=K_{\tau\max}$) when $K_{\tau\max}$ is larger than the threshold SIF, i.e., $\Delta K_{\tau th}$. Also the crack extension angle for the tensile mode fatigue crack growth is macroscopically given by θ_o which makes $K_\sigma(\theta)$ the maximum ($K_\sigma(\theta)_{\max}=K_{\sigma\max}$). The critical conditions both of the tensile mode growth and of the transition from the shear mode growth to the tensile mode growth are given by $K_{\sigma\max}\geqq\Delta K_{\sigma th}$, where $\Delta K_{\sigma th}$ is the threshold SIF for the tensile mode growth.

Otsuka et al. (1975) have shown that $\Delta K_{\tau th}\fallingdotseq 1.5\text{MPa}\cdot\text{m}^{1/2}$ and $\Delta K_{\sigma th}\fallingdotseq 6\text{MPa}\cdot\text{m}^{1/2}$ for low carbon steels.

3 Results and Discussion

3.1 Variations of SIFs Caused by Movement of Contact. The relationship between the directions of the crack inclination and the movement of the contact pressure differs depending on the direction of surface traction. In this analysis the direction of the crack inclination was fixed to the positive x direction in Fig. 1, and its angle was assumed to be 45 deg. The direction of surface traction was changed as $f>0$ and $f<0$. When the contact pressure moves from the left side of the crack mouth to the right side over the surface of the semi-infinite body, the condition $f>0$ corresponds to the driver surface, i.e., the positive sliding surface, and that of $f<0$ corresponds to the follower surface, i.e., the negative sliding surface (see Fig. 3(*A*)). On the contrary, when the contact pressure moves from right to left, the conditions $f>0$ and $f<0$ correspond to the follower and the driver surface, respectively (see Fig. 3(B)).

The variations of F_I and F_{II} at the deepest point of the crack tip caused by the movement of the contact pressure are shown

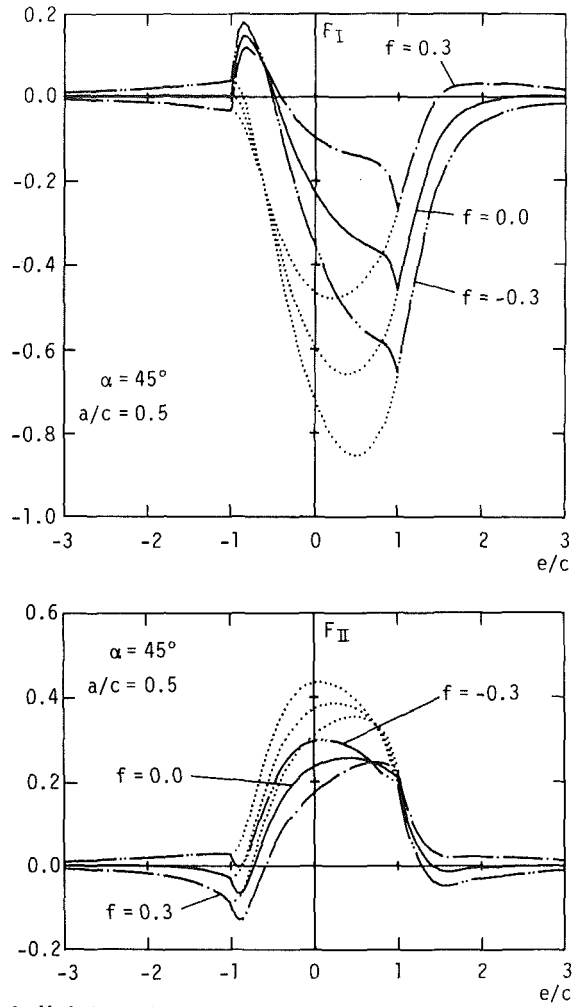

Fig. 4 Variations of dimensionless stress intensity factors F_I and F_{II} at the deepest crack tip during a loading cycle (Dotted lines denote no *oil hydraulic pressure case*)

in Figs. 4 and 5, where it is assumed that the crack faces are subject to the fluid pressure due to lubricant oil which penetrated into the crack. In the region of $|e/c|\leqq 1$, the fluid pressure corresponding to equation (3) acts on the crack faces. However, the dotted lines in the figures are the results for the cases of no fluid pressure. The tendencies of these results are similar to the case of the line-contact (Murakami et al., 1985; Kaneta et al., 1985). When the contact pressure moves from left to right, F_I for the negative sliding surface ($f<0$) has a positive value in the region $e/c\leqq -1$, and its magnitude increases with increasing surface traction. The crack with the size of $a/c=0.5$ on the positive sliding surface ($f>0$) is closed ($F_I<0$) in the whole region of $e/c<-1$ under the condition of high surface traction of $f=0.3$. These trends become predominant with decreasing crack size, because the effect of surface traction increases.

The states of crack opening/closure at the position of $e/c=-1$ are illustrated in Fig. 6 for the cases of $a/c=0.1$, 0.5, and 2.0 under the condition of $f=0.1$. These figures show half of the crack face. From equation (6) we can recognize that when $F_{Ij}>0$ the crack faces at the j subregion are separated from each other, i.e., they are open, and when $F_{Ij}<0$, they are closed. The condition $F_{Ij}<0$ is never achieved in the actual situation, because it corresponds to the negative displacement. Similar kinds of separation and slip problems were treated by Comninou et al. (1983). They treated the problem of a two-dimensional subsurface layer which is parallel to the surface of a semi-infinite plate and is subjected to tangential and normal forces. They stated that the iteration procedure which specifies

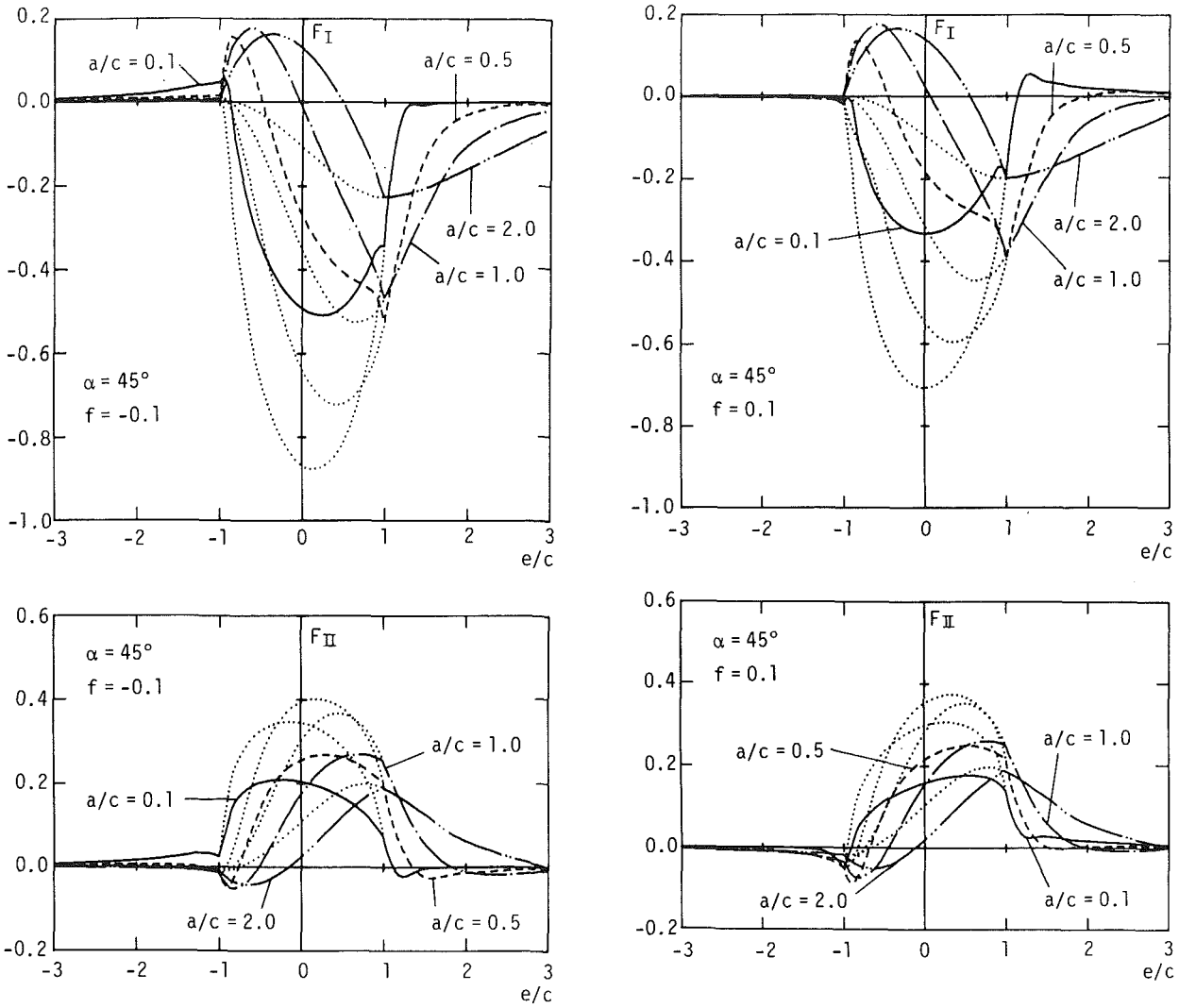

Fig. 5 Relation between crack size and dimensionless stress intensity factors F_I and F_{II} (Dotted lines denote no oil hydraulic pressure case) (a) $f = -0.1$; (b) $f = 0.1$

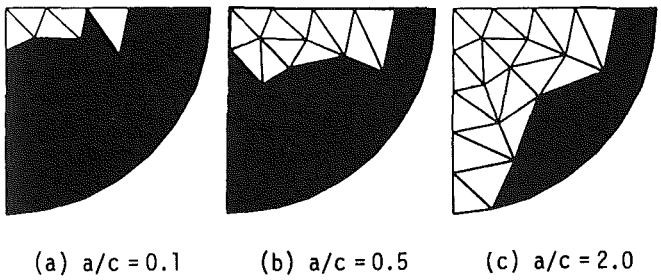

Fig. 6 States of crack opening/closure at $e/c \simeq -1$; $f = 0.1$; (a) a/c = 0.1; (b) a/c = 0.5; (c) a/c = 2.0.

the extent and location of the slip and separation zones is very complicated. The situation in the present model is the same as Comninou et al.'s.

The final correct configuration of the semi-circular crack in the present problem can be obtained only by the iteration procedure. Now, suppose that we adopt the iteration procedure. Then, as the first iteration we must apply the reactions on the crack surface where F_{Ij} have negative values. These reactions induce tensile stress at the regions of positive F_{Ij} and, accordingly, increase crack opening at the already opened crack tip. However, this procedure breaks the boundary conditions at the regions of positive F_{Ij}. Then as the second iteration we need to decrease the intensity of the pairs of positive body forces (Murakami et al., 1985) at the regions of positive F_{Ij}. The first and second iterations are thus likely to cancel each other. Therefore, we may finally expect, with a high degree of plausibility, that $F_{Ij} < 0$ indicates the closed states of crack faces and $F_{Ij} > 0$ can be approximately the measure of the separation.

This prediction was recently verified by the comparison between the analyses and experimental measurements on the subsurface crack under contact loading (Kaneta et al., 1985). Therefore, in this study we regarded the values of F_{Ij} as the measure of crack opening and closure, i.e., $F_{Ij} > 0$ indicates crack opening and $F_{Ij} < 0$ indicates no crack opening displacement and the intensity of compressive stress between crack faces.

In Fig. 6 the black area indicates the closed part. It is to be noticed from these results that, even if the crack is on the positive sliding surface, the crack is open at least in the neighborhood of the contacting surface under the condition of $f \leqq 0.1$, which includes the case of pure rolling ($f = 0$) because the tensile stress exists in the neighborhood of the circular region of spherical contact (Hamilton, 1983). This phenomenon was never found in the case of line-contact (Murakami et al., 1985; Kaneta et al., 1985). The opening

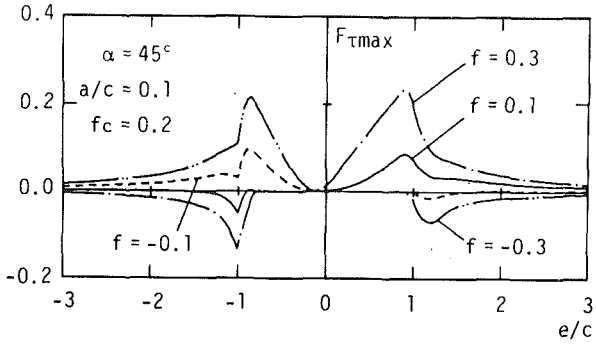

(a) $f_c = 0.2$

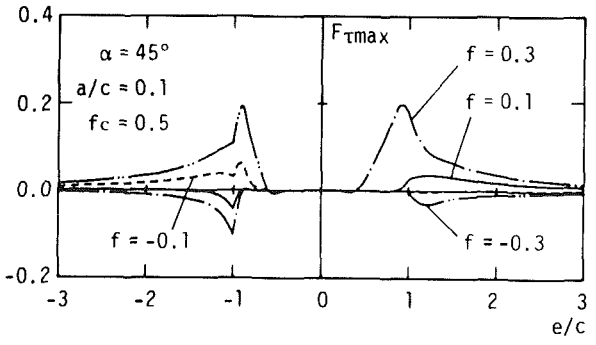

(b) $f_c = 0.5$

Fig. 7 Variation of $F_{\tau max}$ during a loading cycle; (a) $f_c = 0.2$; (b) $f_c = 0.5$.

region of the crack is enlarged with increasing crack size and with decreasing f, since the surface traction corresponding to $f>0$ acts so as to close the crack faces in $e/c<-1$.

However, when the contact pressure moves over the cracked surface from right to left, the crack is completely closed from its deepest point as the contact approaches to $e/c=1$ even if the crack is open in a certain region of $e/c>1$. The same phenomenon was already pointed out in the case of the line contact (Murakami et al., 1985; Kaneta et al., 1985).

Now, as shown in Figs. 4 and 5, when the crack interior is filled with oil, F_I takes positive value in a certain region of $|e/c|<1$ because of the oil hydraulic effect. In the case of a tiny crack, however, the magnitude of F_I is small and the region showing $F_I>0$ is also narrow. It should be noticed that if the crack is closed in $|e/c| \geqq 1$, the oil hydraulic action in $|e/c|<1$ is never produced since the oil cannot enter the crack.

From the above discussion it may be concluded that the possibility of oil seepage into the crack is highest in the case shown in Fig. 3*A* (*a*), and the case of pure rolling follows. The oil may enter the crack shown in Fig. 3*A* (*b*), only when the surface traction is low. In the cases of Fig. 3(*B*), however, it may be difficult to assume the oil hydraulic action, because the oil which entered the crack may be excluded due to the crack closure from its deepest point. Moreover, as has been already described, if there is no oil in the crack and, accordingly, if the oil hydraulic action does not exist, F_I in $|e/c|<1$ has a negative value under the compressive stress field of contact pressure.

3.2 Fatigue Crack Growth in Shear Mode. Figures 7(*a*) and 7(*b*) show the variations of $F_{\tau max}$ at the deepest point of the crack tip during a loading cycle for tiny cracks ($a/c=0.1$) with $f_c=0.2$ and 0.5. In these calculations, the oil hydraulic pressure is not considered in order to put emphasis on the effect of the frictional coefficient between the crack faces. $F_{\tau max}$ is calculated by assuming $F_I=0$ when $F_I<0$, because $F_I<0$ never occurs in the real phenomenon. Then in this case the crack growth angle, θ_o, becomes zero. The crack growth angle corresponding to the maximum value of $|F_{\tau max}|$, which controls the shear mode crack growth, is mostly in the range of -3 deg $<\theta_o<0$ deg even in the case of $F_I>0$, because F_I is small in comparison with F_{II}. Therefore, we shall assume $\theta_o=0$ deg in the following discussion when the crack extends by the shear mode with the growth angle of the above range. On this occasion, the crack growth by shear mode occurs along the original crack plane when $\Delta K_{\tau max}$ exceeds $\Delta K_{\tau th}$.

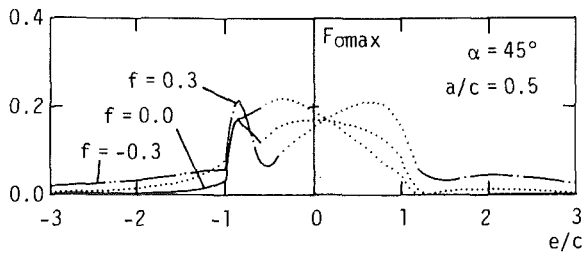

Fig. 8 Variation of $F_{\sigma max}$ during a loading cycle (Dotted lines correspond to $F_I<0$ in Fig. 4)

$|F_{\tau max}|$ achieves the maximum value at near points of $e/c=\pm 1$, where the right and left edges of the contact pressure are just on the mouth of the crack. When the contact pressure covers the mouth of the crack, $F_{\tau max}$ becomes zero over most of $|e/c|<1$, because the frictional stress between the crack faces supports the shear stress applied on the crack faces by the contact load. Accordingly, the slip between the crack faces never occurs in this region. It can be seen from Fig. 7 that $\Delta F_{\tau max}$ increases with the increase in f and with the decrease in f_c. These tendencies coincide with the case of line contact. For example, assuming $p_o=1$GPa or 3GPa for $c=0.5$ mm and considering $\Delta F_{\tau max} \fallingdotseq 0.065$ under the conditions $a/c=0.1$, $f=-0.1$ and $f_c=0.5$, we obtain $\Delta K_{\tau max} \fallingdotseq 0.81MPa\cdot$m$^{1/2}$ or 2.4MPa$\cdot$m$^{1/2}$. This shows that the fatigue crack growth in shear mode may possibly occur for $p_o=3$GPa but unlikely for $p_o=1$GPa. As the surface traction increases, however, we can expect the possibility of the crack growth even in the case of $p_o=1$GPa. On the other hand, the crack growth under the condition of pure rolling ($f=0$) is unlikely to occur even in the case of $p_o=3$GPa.

If the oil containing a good boundary lubricant additive enters the crack while the mouth of the crack is open, the crack growth rate by shear mode may be accelerated because of the decrease in the frictional coefficient between the crack faces. In this occasion, however, we must consider that the crack growth may be retarded by the decrease in the surface traction.

The increase in crack size brings on the decrease in the frictional force between the crack faces, because the compressive stress due to the contact load decreases with the depth measured from the contact surface. Accordingly, the value of $\Delta F_{\tau max}$ increases somewhat with the increase in the crack size. For example, under the conditions of $f=-0.1$ and $f_c=0.2$, we have $\Delta F_{\tau max} \fallingdotseq 0.108$ for $a/c=0.1$ and 0.122 for $a/c=0.5$. From equation (9), however, it should be noted that $K_{\tau max}$ is proportional to $F_{\tau max}\sqrt{a/c}$ if p_o and c are constant.

3.3 Fatigue Crack Growth in Tensile Mode. Figure 8 shows the variations of $F_{\sigma max}$ during a loading cycle. These values are calculated from Fig. 4. The dotted lines in this figure correspond to the case of $F_I<0$ in Fig. 4. As pointed out, the state of $F_I<0$ never happens in the actual situation. Moreover, the values of $F_{\sigma max}$ corresponding to $F_I<0$ are overestimated because the frictional force between the crack faces is not considered in this analysis. Therefore, Fig. 8 gives a correct value only in the case of $F_I>0$. We shall focus our attention on the value of $F_{\sigma max}$ obtained for $F_I>0$ in the following discussion.

Table 1 Relations among the crack size, the maximum value of $F_{\sigma max}$ and the crack growth angle

f		-0.1			0.1	
a/c	e/c	θ_o deg	$F_{\sigma max}$	e/c	θ_0 deg	$F_{\sigma max}$
0.1	−0.9	−62.7	0.1309	1.2	−51.3	0.0627
0.3	−0.9	14.2	0.1356	−0.9	48.3	0.1502
0.5	−0.8	22.5	0.1553	−0.9	48.6	0.1741
1.0	−0.7	23.8	0.1830	−0.6	27.1	0.1936
2.0	−0.4	20.7	0.1712	−0.4	24.6	0.1776

In general, the maximum value of $F_{\sigma max}$, as seen from Fig. 8, occurs in the region of $|e/c|<1$ ($F_I>0$), where the crack faces receive the oil hydraulic pressure. The crack growth angle θ_o in the tensile mode for $a/c=0.5$ in Fig. 8 is about -60 deg ($F_{\sigma max} \fallingdotseq 0.20$) with $f=-0.3$, and about 41 deg ($F_{\sigma max} \fallingdotseq 0.163$) with $f=0$. This means that the maximum value of $F_{\sigma max}$ increases and the crack extends into the material with increasing surface traction. In other words, it may be said that the higher the surface traction, the deeper the pit.

Relations among the crack size, the maximum value of $F_{\sigma max}$ and the crack growth angle are shown in Table 1. Under the conditions of $f=0.1$ and $a/c=0.1$, $F_{\sigma max}$ takes its maximum at $e/c \fallingdotseq 1.2$, where there is no oil hydraulic effect. On the other hand, in the case of $f=-0.1$ for $a/c=0.1$, $F_{\sigma max}$ obtains the maximum at $e/c \fallingdotseq -0.9$ and its value is larger than the case of $f=0.1$. Assuming $c=0.5$ mm, $a/c=0.1$ and the crack growth criterion as $\Delta K_{\sigma th} \geqq 6\text{MPa}\cdot\text{m}^{1/2}$, and having $F_{\sigma max} \geqq 0.48$ for $p_o=1$GPa and $F_{\sigma max} \geqq 0.16$ for $p_o=3$GPa, we can expect crack growth. Comparing these results with Table 1, we may arrive at the conclusion that the possibility of the fatigue crack growth in the tensile mode of a tiny crack is extremely low. The increase in crack size brings on the increase in the maximum value of $F_{\sigma max}$. The maximum values of $F_{\sigma max}$ corresponding to $\Delta K_{\sigma th}=6\text{MPa}\cdot\text{m}^{1/2}$ under the above conditions are 0.214 for $p_o=1$GPa and 0.071 for $p_o=3$GPa when $a/c=0.5$. Therefore, the crack growth by tensile mode becomes likely to occur as the crack size increases. It should also be noted that the growth angle in a large crack is always positive, and its value is greater for $f>0$ than for $f<0$. This means that a pit produced on the driver surface may be shallow as compared with that on the follower surface. However, we must consider that the crack on the driver surface with high surface traction, say $f=0.3$, is unlikely to propagate by the tensile mode, because the oil seepage into the crack is unlikely to be expected.

Figures 4 and 5 indicate that as the contact pressure moves from the left of the crack mouth to the right (this case corresponds to Fig. 3(*A*)), the value of F_I attains positive peak due to the oil hydraulic pressure effect, and then decreases and takes negative value. When a/c is relatively small as $a/c \leqq 1$, the deepest point of the crack tip is closed before the center of the contact pressure reaches the mouth of the crack. On this occasion, the crack formed on the follower surface ($f<0$) closes from the mouth of the crack as shown in Fig. 9, though that on the driver surface ($f>0$) closes from the deepest point of the crack. When the center of the contact pressure is to the left of the crack mouth, the stress state in the neighborhood of the deepest point of the crack tip is tensile for $f<0$, and compressive for $f>0$ due to the action of surface traction. This is the main reason for the difference of the crack closure behavior for $f<0$ and $f>0$.

With the increase in crack size, say $a/c=2.0$, the deepest point of the crack tip is closed after the center of the contact pressure passes over the crack mouth, as shown in Fig. 10, both for $f<0$ and for $f>0$, because the contact pressure presses down the upper part of the crack faces. If the oil is sealed in the crack interior as shown in Fig. 9(*c*) or Fig. 10, extremely high hydraulic oil pressure is exerted on the crack faces and subsequently the tensile mode crack growth may further be accelerated.

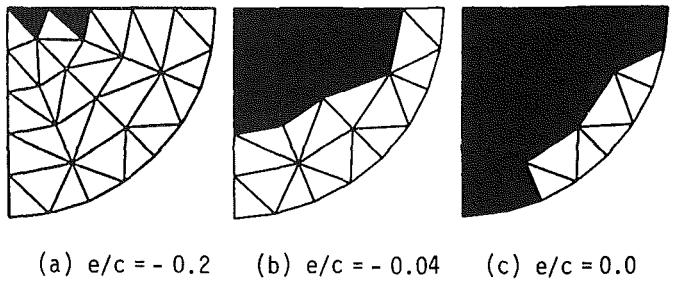

Fig. 9 Oil blockade phenomenon caused by movement of contact pressure; $f=-0.1$, $a/c=1.0$; (a) $e/c=-0.2$; (b) $e/c=-0.04$; (c) $e/c=0.0$.

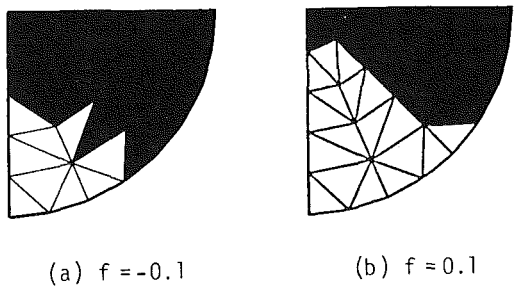

Fig. 10 Oil blockade action for extended crack; $a/c=2.0$, $e/c=0.4$; (a) $f=-0.1$; (b) $f=0.1$.

In the case of a tiny crack as $a/c=0.1$, however, such an oil blockade action is unlikely to occur even for the crack formed on the follower surface. Furthermore, when the contact condition is like Fig. 3(*B*) or Fig. 3*A* (*b*) and yet the surface traction is high, the oil blockade action is scarcely induced because the possibility of the oil seepage into the crack is unlikely to occur.

4 Conclusions

Growth mechanism of an inclined crack formed on the rolling/sliding spherical contact surfaces was clarified analytically by applying the fracture mechanics. The results obtained in this study give not only the reasonable explanations for experimental facts but also the predictions for several possible phenomena. The conclusions are summarized as follows:

(1) The possible growth mechanism of a tiny crack is propagated by the shear mode (Mode II) along nearly the original crack plane. The higher the surface traction, the faster the growth rate.

(2) The tensile mode (Mode I) fatigue crack growth is induced by the oil hydraulic action due to the oil which entered the crack. Transition from a crack to a pit seems to be triggered by the tensile mode growth.

(3) A tiny crack is unlikely to fulfill the criterion of tensile mode crack growth.

(4) The possibility of oil seepage into the crack is highest in the case of Fig. 3*A* (*a*). If the surface traction is low, say $0 \leq f \leq 0.1$, the oil may enter the crack even in the case of Fig. 3*A* (*b*). In other cases the oil seepage into the crack is unlikely to occur.

(5) The oil hydraulic pressure acting on the crack faces is

induced by two kinds of mechanisms. One is due to the contact pressure transmitted directly by the oil to the crack faces when the crack mouth is kept open. The other is due to the oil blockade action caused by the closure of the crack mouth and by squeezing the oil contained in the crack interior.

References

Chang, F.-K., Comninou, M., Sheppard, S., and Barber, J. R., 1984, "The Subsurface Crack Under Conditions of Slip and Stick Caused by a Surface Normal Force," ASME JOURNAL OF APPLIED MECHANICS, Vol. 51, pp. 311-316.

Comninou, M., Barber, J. R., and Dundurs, J., 1983, "Interface Slip Caused by a Surface Load Moving at Constant Speed," INTERNATIONAL JOURNAL OF MECHANICAL SCIENCES, Vol. 25, pp. 41-46.

Dawson, P. H., 1961, "The Pitting of Lubricated Gear Teeth and Rollers," *Power-Transmission*, London, Vol. 30, pp. 208-217 and pp. 286-290.

Erdogan, F., and Sih, G. C., 1963, "On the Crack Extension in Plates Under Plane Loading and Transverse Shear," *ASME Journal of Basic Engineering*, Vol. 85, pp. 519-527.

Fleming, J. R., and Suh, N. P., 1977, "Mechanism of Crack Propagation in Delamination Wear," *Wear*, Vol. 44, pp. 39-56.

Foord, C. A., Hingley, C. G., and Cameron, A., 1969, "Pitting of Steel Under Varying Speeds and Combined Stresses," ASME *Journal of Lubrication Technology*, Vol. 91, pp. 282-293.

Hamilton, G. M., 1983, "Explicit Equations for the Stresses Beneath a Sliding Spherical Contact," *Proceedings of the Institution of Mechanical Engineers*, Vol. 197C, pp. 53-59.

Hearle, A. D., and Johnson, K. L., 1985, "Mode II Stress Intensity Factors for a Crack Parallel to the Surface of an Elastic Half-Space Subjected to a Moving Point Load," *Journal of Mechanics and Physics of Solids*, Vol. 33, pp. 61-81.

Hills, D. A., and Ashelby, D. W., 1980, "On the Determination of Stress Intensification Factors for a Wearing Half-Space," *Engineering Fracture Mechanics*, Vol. 13, pp. 69-78.

Kaneta, M., Murakami, Y., and Yatsuzuka, H., 1985, "Mechanism of Crack Growth in Lubricated Rolling/Sliding Contact," *ASLE Transactions*, Vol. 28, pp. 407-414.

Kaneta, M., Murakami, Y., and Okazaki, T., 1985, "Mechanism of Opening/Closure of a Subsurface Crack Due to a Moving Hertzian Loading," *Proceedings of the 12th Leeds-Lyon Symposium on Tribology*, to appear.

Keer, L. M., Bryant, M. D., and Haritos, G. K., 1982, "Subsurface and Surface Cracking Due to Hertzian Contact," ASME *Journal of Lubrication Technology*, Vol. 104, pp. 347-351.

Keer, L. M., and Bryant, M. D., 1983, "A Pitting Model for Rolling Contact Fatigue," ASME *Journal of Lubrication Technology*, Vol. 105, pp. 198-205.

Michau, B., Berthe, D., and Godet, M., 1974, "Observations of Oil Pressure Effects in Surface Crack Development," *Tribology International*, Vol. 7, pp. 119-122.

Murakami, Y., Kaneta, M., and Yatsuzuka, H., 1985, "Analysis of Surface Crack Propagation in Lubricated Rolling Contact," *ASLE Transactions*, Vol. 28, pp. 60-68.

Otsuka, A., Mori, K., and Miyata, T., 1975, "The Condition of Fatigue Crack Growth in Mixed Mode Condition," *Engineering Fracture Mechanics*, Vol. 7, pp. 429-439.

Rosenfield, A. R., 1981, "Elastic-Plastic Fracture Mechanics and Wear," *Wear*, Vol. 72, pp. 245-254.

Sin, H.-C., and Suh, N. P., 1984, "Subsurface Crack Propagation Due to Surface Traction in Sliding Wear," ASME JOURNAL OF APPLIED MECHANICS, Vol. 51, pp. 317-323.

Yamashita, N., Mura, T., and Cheng, H. S., 1985, "Effect of Stresses Induced by a Spherical Asperity on Surface Pitting in Elastohydrodynamic Contacts," *ASLE Transactions*, Vol. 28, pp. 11-20.

Yoshimura, H., Rubin, C. A., and Hahn, G. T., 1984, "A Technique for Studying Crack Growth under Repeated Rolling Contact," *Wear*, Vol. 95, pp. 29-34.

Way, S., 1935, "Pitting Due to Rolling Contact," ASME JOURNAL OF APPLIED MECHANICS, Vol. 2, pp. A49-A58.

A Model for the Flow of a Chopped Fiber Reinforced Polymer Compound in Compression Molding

M. R. Barone
Mem. ASME

D. A. Caulk
Mem. ASME

Engineering Mechanics Department,
General Motors Research Laboratories,
Warren, MI 48090

The flow of a chopped fiber reinforced polymer compound in compression molding is modelled as a two-dimensional membrane-like sheet which extends uniformly through the cavity thickness with slip at the mold surface. The model is consistent with both the kinematic mechanisms observed in actual flow and the three-dimensional anisotropy caused by the arrangement of fibers in the sheet. The material resistance to extension is expressed in a constitutive equation for the two-dimensional stress resultant formed by integrating the planar stress components through the thickness of the cavity. This stress resultant is assumed to be a linear function of the corresponding planar rate of deformation in the molding compound. Through a mechanism of fiber-resin interaction, the material resistance to extension can be characterized by a single scalar function of the transverse temperature distribution. Three alternatives are considered for the friction response at the cavity surface: (i) constant magnitude, (ii) proportional to the relative velocity (hydrodynamic), and (iii) proportional to the normal component of the stress vector (Coulomb). These three assumptions are compared by considering their general implications on the flow-front progression. The latter two are examined in some detail for thin charges in which the material resistance to extension is negligible compared to the effect of friction. Analytical solutions for an elliptical charge are obtained for both hydrodynamic and Coulomb friction. By comparing these solutions with experimental results, we conclude that the hydrodynamic model for the friction response is the best of the three proposed alternatives.

Introduction

As compression molding of chopped fiber reinforced thermosetting compounds has grown in commercial importance in recent years, a need has developed for a model describing the flow of such materials as they are formed in the mold cavity. Most efforts to date in this area have been motivated by successful models for the flow of thermoplastic melts in injection molding. Although the molding compound is squeezed between cavity surfaces in compression molding rather than forced through a gate onto a fixed cavity as in injection molding, the flow in both cases is confined to a relatively narrow cavity, which suggests a similar approach. However, the sheet molding compounds (SMC) typically used in compression molding have a distinguishing characteristic which dramatically influences the qualitative aspects of their flow. These compounds are filled with a relatively large volume fraction of chopped fibers (at least 25 percent) which are arranged in a randomly woven network in the plane of the sheet. This arrangement of fibers makes the material anisotropic, so that its mechanical response is substantially different from that of a polymer melt.

All existing models for the flow of SMC assume it to be an incompressible isotropic fluid. Inertia is neglected and a no-slip boundary condition is imposed at the cavity surface. Silva-Nieto, Fisher, and Birley (1980) were the first to propose a model under these assumptions, based on isothermal, Newtonian lubrication theory. Tucker and Folgar (1983) later used this model with a finite element method to calculate the flow-front progression in a rectangular charge. These calculations correlated well with their experiments on modelling clay and single-layer charges of SMC. In a later paper, Lee, Folgar, and Tucker (1984) generalized this model to include a power-law viscous response, but showed (again by means of finite element calculations) that the flow-front progression is insensitive to the value of the power-law exponent. In the same paper, they reported experimental results that showed a significant change in the flow-front progression as the initial charge thickness was increased. This observation is not consistent with the isothermal lubrication model, which predicts that the flow-front progression is independent of the instantaneous cavity thickness. The authors reasoned that this difference

Contributed by the Applied Mechanics Division for publication in the JOURNAL OF APPLIED MECHANICS.
Discussion on this paper should be addressed to the Editorial Department, ASME, United Engineering Center, 345 East 47th Street, New York, N.Y. 10017, and will be accepted until two months after final publication of the paper itself in the JOURNAL OF APPLIED MECHANICS. Manuscript received by ASME Applied Mechanics Division, February 7, 1985.

may be due to increasing importance of non-isothermal effects in thicker charges. On the surface, this conjecture appears to be supported by the analytical work of Lee et al. (1982) who simulated the effect of heat conduction from the mold surface by analyzing squeezing flow of a three-layer fluid with lower viscosity in the layers near the mold surface. Lee and Tucker (1983) generalized this approach somewhat by considering eight separate layers with different viscosities in each layer obtained by combining a transverse temperature gradient with a power-law dependence of viscosity on temperature.[1] Both papers showed that a preferential shearing motion in the lower viscosity outer layers can occur together with a predominantly extensional flow in the higher viscosity core whenever the transverse viscosity gradient or the thickness-to-length ratio of the charge is sufficiently large. Lee and Tucker (1983) also showed that this mechanism produces a flow-front progression that has features similar to those observed experimentally in increasingly thicker charges.

Although the above approach has led to some encouraging results, it has at least two fundamental difficulties: (1) SMC is not isotropic and (2) the transverse velocity distribution is inconsistent with observations of actual flow (Barone and Caulk, 1985). In the present paper, we depart from the approach of previous work and directly account for the material anisotropy caused by the presence of the fibers in the SMC. Recent experimental results revealing the influence of the fiber structure on the kinematics of flow in SMC are used to motivate a model for the material as a two-dimensional membrane-like sheet which extends uniformly through the cavity thickness with slip at the mold surface. The material resistance to extension is expressed in a constitutive equation for the two-dimensional stress resultant formed by integrating the planar stress components through the thickness of the cavity. This stress resultant is assumed to be a linear function of the corresponding planar rate of deformation in the SMC. By considering a mechanism of fiber-resin interaction, we show how this response can be characterized entirely by one scalar function of the transverse temperature distribution. Three alternative assumptions are explored for describing the friction response at the cavity surface: (*i*) constant magnitude friction, (*ii*) hydrodynamic friction in which the friction force is proportional to the relative velocity at the mold surface, and (*iii*) Coulomb friction in which the friction force is proportional to the normal component of the stress vector at the mold surface. The first alternative is eliminated based on its general implications about the flow progression. The other two assumptions are compared in more detail by considering an approximation (suitable for thin charges) in which the material response to extension is neglected relative to the effect of friction. The equations corresponding to this approximation are solved analytically for both hydrodynamic and Coulomb friction in the case of an initially elliptical charge. By comparing these solutions with experimental results for the progression of the flow front in one and four-layer charges, we conclude that hydrodynamic friction is the only assumption of those considered which is consistent with the limiting behavior observed in thin charges. When the assumption of hydrodynamic friction is combined with the thin-charge approximation, the reduced equations become formally equivalent to those of isothermal lubrication theory. For thicker charges, when the in-plane extensional resistance is no longer negligible, the deformation of the charge is more equibiaxial, which is consistent with experimental results and is obtained without appealing to the influence of heat conduction.

In summary, the present approach is faithful to the anisotropy of the material, consistent with its observed kinematics, and, in the limit of small cavity thickness, formally reduces to the equations of isothermal lubrication theory, which have already been shown to adequately predict the flow-front progression in thin charges (Lee et al., 1984).

Fig. 1 Fiber structure of SMC

The Material

Sheet molding compound (SMC) is a generic name given to a wide class of chopped-fiber reinforced thermosetting compounds used in compression molding. Uncured material is produced in sheets approximately 5 mm thick containing fibers which are typically 25 mm long. These fibers, which are actually bundles of individual filaments, are randomly oriented in the plane of the sheet and distributed uniformly throughout its volume. The fibers usually occupy from 20–50 percent of the material volume, resin about 30 percent, and the remainder is usually a powdered filler such as calcium carbonate.

The most important feature affecting the mechanical response of SMC during molding is its fiber structure. A photograph of this structure is shown in Fig. 1. The first thing we observe from this picture is that the material is inhomogeneous on a relatively large scale. Since the fiber bundles are widely separated in any given plane, there is probably a minimum length scale over which the "averaging" influence of their random orientation is effective. Thus any model representing SMC as a homogeneous continuum should be relevant only for problems in which the characteristic dimension, both parallel and transverse to the plane of the sheet, is sufficiently large. When this is the case, SMC may be regarded as transversely isotropic. The characteristic transverse dimension in the mold is the instantaneous separation between the cavity surfaces, which is usually quite small (2–10 mm). This raises a legitimate concern over the applicability of a *three-dimensional* continuum model describing the flow of such a material.

A second thing we can observe in Fig. 1 is that the fiber bundles do not simply lie on top of each other in the sheet, but form a randomly woven network. This network exerts a significant influence on the kinematics of flow in the mold as will become apparent in the next section. It also gives the sheet a mild transverse elasticity which makes it very difficult to

[1] It is important to emphasize that Lee et al. (1982) and Lee and Tucker (1983) only *simulate* the effect of heat conduction by imposing a *static* variation in viscosity through the thickness. Strictly speaking, the analysis in both cases is isothermal.

eliminate the air which is introduced in the sheet as it is compounded. Typically, the uncompressed volume fraction of air is about 30 percent. This void fraction is reduced to about 1 percent at molding pressures, however, and as long as sufficient pressure is maintained on the material as it cures, the finished part does not show any visible evidence of porosity.

The Nature of the Flow

A compression mold is usually charged with 2–4 layers of SMC covering from 30–70 percent of the cavity surface area (Fig. 2). As the charge is pressed between the surfaces of the mold, the volume of air in the SMC is reduced until sufficient pressure builds to cause the material to flow. Once flow begins, it takes only a few seconds for the material to fill the cavity, after which the rising force of the press is balanced by increasing hydrostatic pressure in the SMC. Contact with the warm mold raises the temperature of the SMC, which causes the resin to cure. After the resin has cured sufficiently, the mold can be opened and the finished part removed.

In an earlier study, Barone and Caulk (1985) investigated the qualitative nature of the kinematics in SMC by assembling charges from black and white material and observing the motion of distinct regions at various stages during flow. Circular charges 300 mm in diameter were constructed in two different ways (Fig. 3): (*a*) otherwise identical charge layers were made of alternating colors, and (*b*) a concentric circle 200 mm in diameter was cut from an entirely black charge and replaced by white material. By inserting different thicknesses of steel shims between the mold stops, the flow in these charges was allowed to progress to various stages, short of filling the cavity. Cross sections from these short moldings were examined to determine the nature of the transverse kinematics at two different closing speeds. Selected results are shown in Figs. 4 and 5. In general, the SMC flowed in uniform extension through the thickness of each layer, with slip at the mold surfaces and, for the slower closing speed on the thicker charges, also between the outer layers of SMC. The latter case corresponds to the observations of Marker and Ford (1977). At the rapid closing speed, the entire charge extended uniformly through its thickness, regardless of the number of layers, with all slip concentrated at the mold surface. This boundary slip is especially evident in the samples molded from the second charge arrangement (Fig. 5). These results demonstrate the significant influence of the random fiber network in constraining transverse shearing motion within the sheet.

Further experience with short moldings indicates that during flow the flow front develops in a very repeatable manner, considering the nature of the material. Random variations in the boundary profile usually occur on the scale of about one centimeter. This is no doubt a consequence of the random inhomogeneous material structure discussed in the previous section. The magnitude of such random variations may suggest the appropriate length scale on which a continuum model would be suitable for such a material.

Basic Theory

For simplicity in developing the basic theory we assume that the cavity surfaces are plane and parallel. Let x_i be rectangular Cartesian coordinates[2] with associated unit base vectors $\mathbf{e}_i$, such that the x_3 axis is perpendicular to the cavity surfaces. The motion of these surfaces is described by

$$x_3 = \pm h(t)/2, \tag{1}$$

where the instantaneous separation $h(t)$ is a specified function of time. We assume that SMC occupies a region bounded by the mold surfaces (1) and a closed cylinder defined by[3]

[2] In this paper Latin subscripts take the values 1, 2, 3 and Greek subscripts 1, 2. Summation is implied over a repeated index in the usual manner.

[3] The absence of x_3 in (2) is justified by the assumption (3) following.

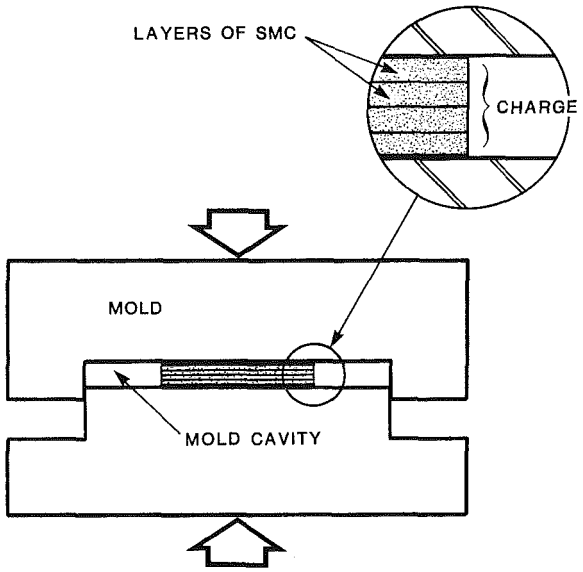

Fig. 2 Compression molding

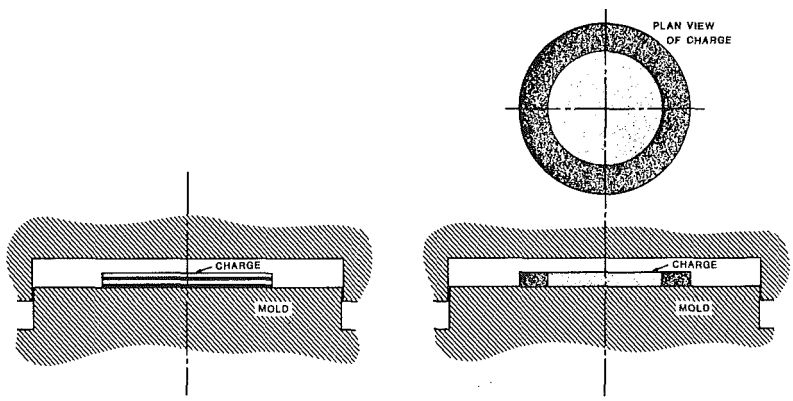

Fig. 3 Black and white charges used to investigate the kinematics of flow; (*a*) alternate black and white layers, and (*b*) separate black and white regions (from Barone and Caulk, 1985)

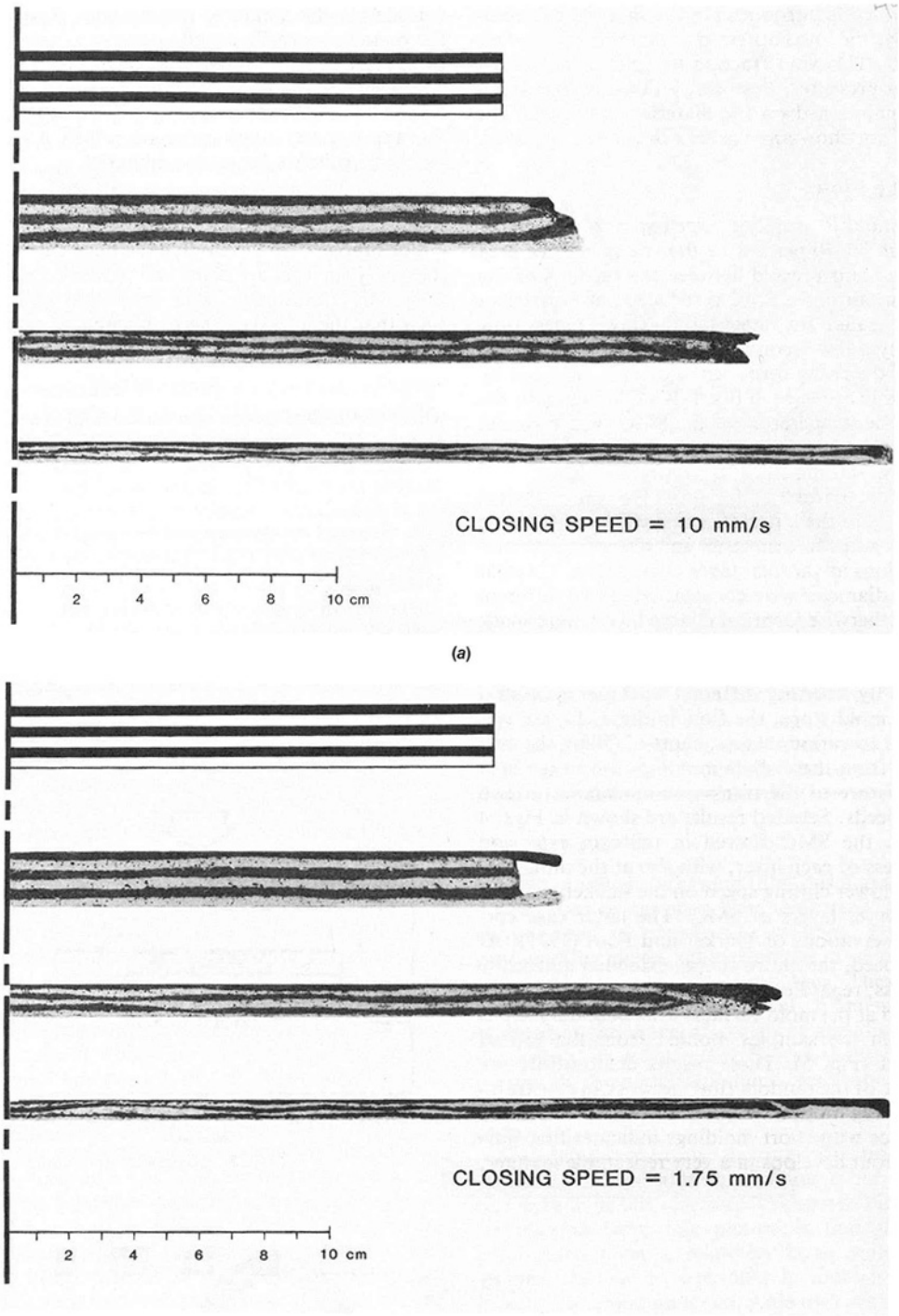

Fig. 4 Stages of deformation at two different closing speeds for a six-layer charge with alternate black and white layers (from Barone and Caulk, 1985)

$$g(x_\alpha, t) = 0, \tag{2}$$

which forms the perimeter of the material region in the $x_1 - x_2$ plane. Sections of this boundary are either fixed, corresponding to the edge of the cavity, or free, corresponding to the developing flow front.

For the present time, we regard the SMC as a transversely isotropic continuum with its principal symmetry axis parallel to $\mathbf{e}_3$ and let v_i be the components of its velocity vector. Based on the experimental results discussed in the previous section, we assume that the in-plane velocity components v_α satisfy

$$v_{\alpha,3} = 0, \tag{3}$$

where a comma denotes partial differentiation. We also neglect any volume change during flow, so that

$$v_{i,i} = 0. \tag{4}$$

From (3) and (4) it follows that

$$v_{3,33} = 0, \tag{5}$$

which can be integrated with the kinematic boundary condition $\dot{x}_3 = v_3 = \pm \dot{h}/2$ on the cavity surfaces to yield

$$v_3 = (\dot{h}/h)x_3. \tag{6}$$

The other two velocity components have the general form

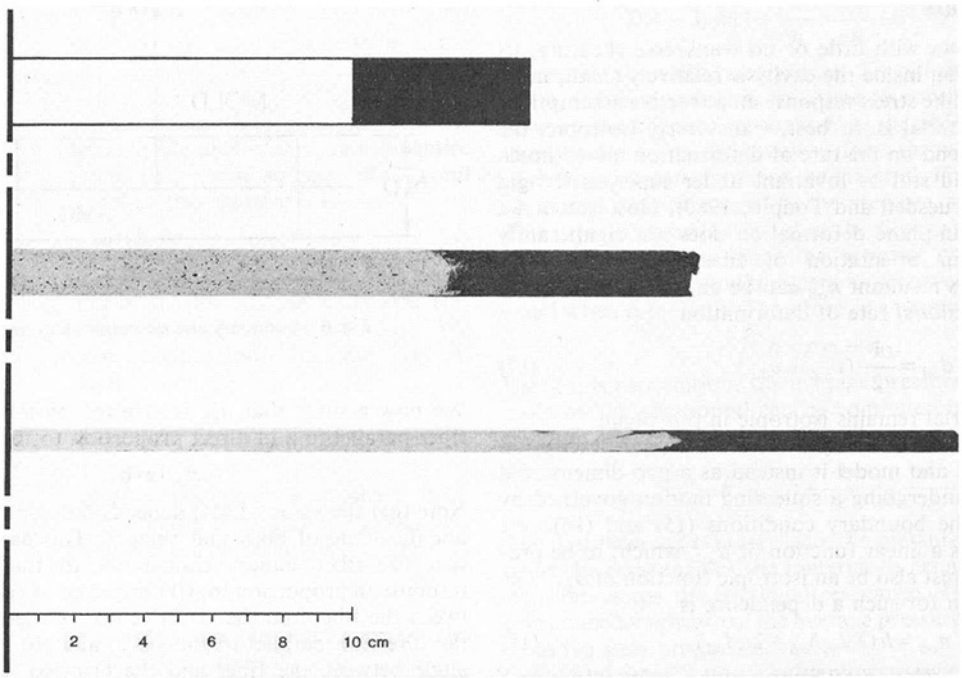

Fig. 5 Stages of deformation at a closing speed of 10 mm/s in a six-layer charge with separate black and white regions (from Barone and Caulk, 1985)

$$v_\alpha = v_\alpha(x_\beta, t). \tag{7}$$

Since v_3 is determined entirely from $h(t)$, and v_α is independent of x_3, the in-plane velocity field may be determined by merely satisfying an integrated form of the momentum equations, as in elastic membrane theory. Certain details of the three-dimensional stress distribution are lost in this approach, but this is compensated later by significant advantages in characterizing the material response. With this as motivation, we impose the following statement of equilibrium (neglecting inertia)

$$\int_{-h/2}^{h/2} \tau_{ij,j}\, dx_3 = 0, \tag{8}$$

where τ_{ij} are the components of stress. Since the compound is incompressible, τ_{ij} can be decomposed in the form

$$\tau_{ij} = -p\delta_{ij} + \sigma_{ij}, \tag{9}$$

where p is the pressure, δ_{ij} is the Kronecker symbol, and σ_{ij} is the determinate part of the stress response.[4] Using this representation for τ_{ij}, (8) can be expanded in the form

$$-\left[\int_{-h/2}^{h/2} p\, dx_3\right]_{,\alpha} + \left[\int_{-h/2}^{h/2} \sigma_{\alpha\beta}\, dx_3\right]_{,\beta} + [\sigma_{\alpha 3}]_{-h/2}^{h/2} = 0,$$
$$\left[\int_{-h/2}^{h/2} \sigma_{3\beta}\, dx_3\right]_{,\beta} + [-p + \sigma_{33}]_{-h/2}^{h/2} = 0. \tag{10}$$

The second of these is trivially satisfied by the symmetry of the problem. With the additional definitions

$$P = \int_{-h/2}^{h/2} p\, dx_3\ ,\quad n_{\alpha\beta} = \int_{-h/2}^{h/2} \sigma_{\alpha\beta}\, dx_3,$$
$$f_\alpha = \sigma_{\alpha 3}\Big|_{x_3 = h/2} = \sigma_{\alpha 3}\Big|_{x_3 = -h/2}, \tag{11}$$

the first equation in (10) reduces to

$$-P_{,\alpha} + n_{\alpha\beta,\beta} + 2f_\alpha = 0. \tag{12}$$

Each of the quantities defined in (11) has a simple physical interpretation: P is a pressure resultant through the cavity thickness, $n_{\alpha\beta}$ is a planar stress resultant, and f_α are the components of the friction force at the cavity surface. The equilibrium equation (12) must be supplemented by the incompressibility condition (4), which, for the velocity field represented by (6) and (7), reduces to

$$v_{\alpha,\alpha} + \dot{h}/h = 0. \tag{13}$$

To solve (12) and (13) for the unknown velocity components v_α, we need to supply constitutive equations for the stress resultant $n_{\alpha\beta}$, which measures the extensional response of the SMC, and the surface traction f_α, which measures the frictional response at the interface between the cavity surface and the SMC.

Since v_α is a two-dimensional field, boundary conditions are specified only on the perimeter $g(x_\alpha, t) = 0$. Let Γ_0 designate the advancing free boundary of the compound and let Γ_1 designate that portion of the perimeter (2) in contact with the edge of the mold cavity. The outward unit normal ν_α to the perimeter is defined by

$$\nu_\alpha = g_{,\alpha}/(g_{,\beta}g_{,\beta})^{1/2} \tag{14}$$

and the unit tangent vector λ_α by $\nu_\alpha\lambda_\alpha = 0$ and $\lambda_\alpha\lambda_\alpha = 1$. On a free boundary, we require that the stress resultant vanish and that $g(x_\alpha, t)$ represent the motion of a material surface. These conditions may be expressed as

$$\left.\begin{aligned}(-P\delta_{\alpha\beta} + n_{\alpha\beta})\nu_\beta = 0,\\ g_{,t} + v_\alpha g_{,\alpha} = 0.\end{aligned}\right\} \text{on } \Gamma_0 \tag{15}$$

On a fixed boundary, the normal velocity vanishes and we assume that the resultant shear caused by friction with the vertical edge of the cavity may be neglected. These two conditions are expressed by

$$\left.\begin{aligned}v_\alpha\nu_\alpha = 0,\\ n_{\alpha\beta}\nu_\alpha\lambda_\beta = 0.\end{aligned}\right\} \text{on } \Gamma_1 \tag{16}$$

[4] Actually $\sigma_{\alpha 3}$ will also be a constraint response because of the condition (3), but for reasons that will become evident later, it is not necessary to consider these components separately.

Material Response

Since SMC flows with little or no transverse shearing, its rate of deformation inside the cavity is relatively small, making a Newtonian-like stress response an attractive assumption. But since the material is, at best, transversely isotropic, the stress cannot depend on the rate of deformation alone (much less be linear) and still be invariant under superposed rigid body motions (Truesdell and Toupin, 1960). However, if we assume that the in-plane deformation does not significantly alter the random orientation of fibers, then the *two-dimensional* stress resultant $n_{\alpha\beta}$ can be an invariant function of the *two-dimensional* rate of deformation

$$d_{\alpha\beta}=\frac{1}{2}(v_{\alpha,\beta}+v_{\beta,\alpha}) \tag{17}$$

because the material remains isotropic in this plane.

Therefore, we abandon any three-dimensional description of the compound and model it instead as a two-dimensional extensible sheet undergoing a squeezing motion governed by (12), (13), and the boundary conditions (15) and (16). We assume that $n_{\alpha\beta}$ is a linear function of $d_{\alpha\beta}$, which, to be properly invariant, must also be an isotropic function of $d_{\alpha\beta}$. The most general form for such a dependence is

$$n_{\alpha\beta}=h(\lambda d_{\gamma\gamma}\delta_{\alpha\beta}+2\mu d_{\alpha\beta}), \tag{18}$$

where λ and μ are scalar coefficients and the cavity thickness h is introduced in (18) to give λ and μ units of viscosity. In general, λ and μ depend on the transverse temperature distribution, which, because of the condition (3), is independent of x_α. This temperature solution is available (Barone and Caulk, 1979), but we do not make explicit use of it in this paper.

It is interesting to note that although the stress response for an incompressible linear viscous fluid is expressed in terms of a single viscosity coefficient, the representation (18) for the two-dimensional stress resultant may in general have two. This is because the planar dilatation $d_{\alpha\alpha}$ is never zero during flow, a fact which follows from the incompressibility condition (13) expressed as

$$d_{\alpha\alpha}+\dot{h}/h=0. \tag{19}$$

But this expression also implies that $d_{\alpha\alpha,\beta}=0$, so that when the constitutive equation (18) is substituted in the equilibrium equation (12), the resulting expression

$$-P_{,\alpha}+\mu h v_{\alpha,\beta\beta}+2f_\alpha=0 \tag{20}$$

does not include λ. The only other place that λ appears in the governing equations is in the boundary condition $(15)_1$ on the advancing flow front. With (18) and (19), this boundary condition reduces to

$$-(P+\lambda\dot{h})+2\mu h d_{\alpha\beta}\nu_\alpha\nu_\beta=0 \quad \text{on } \Gamma_0. \tag{21}$$

Now since $(P+\lambda\dot{h})_{,\alpha}=P_{,\alpha}$, the coefficient λ may be absorbed into the definition of the pressure resultant and the solution for v_α determined independent of λ. One must still reckon with λ, however, since the other coefficient μ is determined by measuring the pressure exerted on the SMC during flow. In the remainder of this section we motivate a relationship between λ and μ by considering the principal mechanism that produces the resultant stress response $n_{\alpha\beta}$.

Consider a single fiber bundle oriented parallel to a given direction in the x_1-x_2 plane specified by the unit vector $\mathbf{a}=a_\alpha\mathbf{e}_\alpha$. Now define

$$d_{aa}=a_\alpha d_{\alpha\beta}a_\beta \tag{22}$$

as the extensional rate of deformation parallel to the fiber. Next, consider the extensional component of the stress resultant along one of its principal directions specified by the unit vector $\mathbf{b}=b_\alpha\mathbf{e}_\alpha$, i.e.,

$$n_{bb}=b_\alpha n_{\alpha\beta}b_\beta. \tag{23}$$

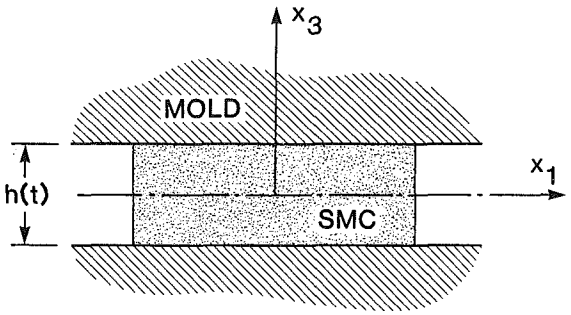

Fig. 6 Geometry and coordinates in mold cavity

We now assume that n_{bb} is affected by the presence of the fiber parallel to $\mathbf{a}$ in direct proportion to the product

$$d_{aa}|\mathbf{a}\cdot\mathbf{b}|. \tag{24}$$

Note that the value of (24) depends only on the direction and not the sense of both unit vectors. This assumption implies that the fiber bundle contributes to the principal stress response in proportion to: (*i*) the degree of relative motion between the fiber and the effective homogeneous continuum in the direction parallel to the fiber, and (*ii*) the cosine of the angle between the fiber and the principal directions of the stress resultant $n_{\alpha\beta}$. In addition, we assume that this mechanism accounts for the entire material response represented by the constitutive equation (18).

We now return to the actual compound with its random distribution of fibers and assume that the principal stress response n_{bb} at any point x_α is given by a simple average over all directions $\mathbf{a}$ in the plane. Accordingly, we assume that

$$n_{bb}=\frac{\alpha}{\pi}\int_0^\pi d_{aa}|\mathbf{a}\cdot\mathbf{b}|\,d\theta, \tag{25}$$

where

$$\mathbf{a}=\cos\theta\mathbf{e}_1+\sin\theta\mathbf{e}_2, \tag{26}$$

and α depends on the resin properties and the volume fraction of fiber.

Consider two simple cases for $d_{\alpha\beta}$:

$$d^{(1)}_{\alpha\beta}=-(\dot{h}/2h)\delta_{\alpha\beta}, \tag{27}$$

$$d^{(2)}_{\alpha\beta}=\begin{cases}-\dot{h}/h & ;\ \alpha=\beta=1,\\ 0 & ;\ \alpha,\beta\neq 1,\end{cases} \tag{28}$$

which both satisfy the incompressibility condition (19). The first is an equibiaxial deformation in the x_1-x_2 plane and the second is a one-dimensional deformation parallel to the x_1 axis. In both instances $\mathbf{e}_1$ is a principal direction and from (22) and (26)–(28)

$$d^{(1)}_{aa}=-(\dot{h}/2h)\ ,\ d^{(2)}_{aa}=-(\dot{h}/h)\cos^2\theta. \tag{29}$$

From a combination of (18) with (25)–(29), we obtain

$$n^{(1)}_{11}=-\frac{2\alpha}{\pi}\int_0^{\pi/2}(\dot{h}/2h)\cos\theta\,d\theta=-(\lambda+\mu)\dot{h}, \tag{30}$$

$$n^{(2)}_{11}=-\frac{2\alpha}{\pi}\int_0^{\pi/2}(\dot{h}/h)\cos^3\theta\,d\theta=-(\lambda+2\mu)\dot{h}. \tag{31}$$

The first term in both (30) and (31) comes from the assumed response mechanism (25) and the second term from the constitutive equation (18). By performing the integration in (30) and (31), and then eliminating α between the two equations, we determine the simple relationship between λ and μ:

$$\lambda=2\mu. \tag{32}$$

Substituting this relationship in the constitutive equation (18), we obtain

$$n_{\alpha\beta} = 2\mu h(d_{\gamma\gamma}\delta_{\alpha\beta} + d_{\alpha\beta}). \tag{33}$$

It is interesting to note that (33) now has the same form as the constitutive equation for an incompressible elastic membrane (Naghdi, 1972).

Before closing this section, we consider the case when the friction at the cavity surface is identically zero and the entire boundary is free. In this case the general solution of (12) and (13), regardless of the shape of the boundary, is

$$v_\alpha = (\dot{h}/2h)x_\alpha. \tag{34}$$

Therefore, the material expands in equibiaxial, homogeneous deformation. The presence of friction will generally alter this symmetry, depending on the shape of the free boundary. We consider some alternative assumptions for the friction response in the next section.

Friction Response

The appropriate constitutive assumption for f_α depends on the mechanism responsible for the fiction at the cavity surface. In this section we examine the implications of three simple assumptions.

Constant Friction. The simplest possible assumption is to let f_α be constant in magnitude, say κ_o, so that

$$f_\alpha = -\kappa_o u_\alpha, \tag{35}$$

where u_α is the velocity direction vector defined by

$$u_\alpha = v_\alpha/(v_\beta v_\beta)^{1/2}. \tag{36}$$

Substituting (35) into the equilibrium equation (20) yields

$$-P_{,\alpha} + \mu h v_{\alpha,\beta\beta} - 2\kappa_o u_\alpha = 0. \tag{37}$$

The velocity field for this case is determined by solving (37) together with the incompressibility condition (13), subject to the boundary conditions (15) and (16). It is easy to see from these equations that the solution for (hv_α) is independent of h. This means that the instantaneous cavity separation only affects the overall magnitude of the velocity, and not its distribution. Therefore, two charges with identical shape but different thickness will have identical flow patterns for the same closing speed $-\dot{h}$. Since this result contradicts the experimental observations of Lee et al. (1984) as well as those discussed later in this paper, we do not consider this case further.

Hydrodynamic Friction. The next assumption we consider is motivated by the existence of a very thin resin-rich boundary layer adjacent to the cavity surface. This thin layer of fluid may serve to lubricate the relative motion between the SMC and the mold. Since the mold velocity is perpendicular to the cavity surface, this friction mechanism can be characterized by

$$f_\alpha = -\kappa_H v_\alpha, \tag{38}$$

where κ_H depends on the surface resin properties and the boundary layer thickness. We assume that the layer has a uniform thickness and temperature so that it is reasonable to assume that κ_H is constant. With this assumption for f_α, the equilibrium equation (20) becomes

$$-P_{,\alpha} + \mu h v_{\alpha,\beta\beta} - 2\kappa_H v_\alpha = 0. \tag{39}$$

As an example, consider a circular region with an entirely free boundary of radius $R(t)$. In this case

$$g(x_\alpha, t) = x_1^2 + x_2^2 - R^2(t) \tag{40}$$

and the velocity field, which follows directly from (13) and the circular symmetry, is

$$v_\alpha = -(\dot{h}/2h)x_\alpha. \tag{41}$$

The corresponding pressure distribution follows by integrating (39) with the boundary condition (15), to yield

$$P = -3\mu\dot{h}\left[1 + \frac{1}{6}\frac{\kappa_H}{\mu h}(R^2 - r^2)\right], \tag{42}$$

where r is the radial coordinate. To aid in interpreting this result, it is convenient at this time to consider a relationship between the pressure resultant P in the SMC and the normal stress vector τ_{33} on the cavity surface, through which the load of the press is transmitted to the material. First we assume that σ_{33} is negligible compared to the pressure, so that $\tau_{33} = -p$. This is justified by the fact that the fibers are aligned perpendicular to x_3. Then, since the pressure must be symmetric about $x_3 = 0$, we would expect its transverse gradient to be small when h is small. Therefore, we assume that

$$P/h = p = -\tau_{33}. \tag{43}$$

Using this assumption, the average pressure $\bar{p}$ exerted by the mold on the compound can be computed by integrating (42) over the region defined by (40). The result is

$$\bar{p} = -\dot{h}\left(3\mu/h + \frac{1}{4}\kappa_H\frac{R^2}{h^2}\right). \tag{44}$$

The first term in (44) represents the pressure required to overcome the resistance of the material to extension. The second term represents the frictional resistance. Therefore, the friction contributes more to the average pressure as R/h increases, or as the flow progresses.

To understand the relative importance of the material resistance and the friction in a more general context, consider the following dimensionless variables motivated by the above solution

$$\hat{x}_\alpha = x_\alpha/L\ ,\ \hat{t} = \log[h_o/h(t)]\ ,\ \hat{P} = -P/\mu\dot{h}, \tag{45}$$

where $h_o = h(0)$ is the mold separation at the beginning of flow and L is a characteristic planar dimension. In terms of these variables, the equilibrium equation (39) becomes

$$-\hat{P}_{,\alpha} + \hat{v}_{\alpha,\beta\beta} - 2\left(\frac{\kappa_H L^2}{\mu h}\right)\hat{v}_\alpha = 0. \tag{46}$$

Therefore, the friction term becomes more important as the region becomes larger, and thinner, and as μ decreases due to heat conduction from the mold. All these trends occur as the flow progresses.

Coulomb Friction. Next we assume that the friction arises from direct fiber-to-metal contact without significant resin lubrication. The friction force f_α is taken proportional to the normal stress vector at the cavity surface, so that with (43)

$$f_\alpha = -\kappa_C(P/h)u_\alpha. \tag{47}$$

In this case the equilibrium equation becomes

$$-P_{,\alpha} + \mu h v_{\alpha,\beta\beta} - 2\kappa_C(P/h)u_\alpha = 0. \tag{48}$$

Corresponding to (42), the pressure resultant over an expanding circular region is

$$P = -3\mu\dot{h}\exp\left[\frac{2\kappa_C}{h}(R - r)\right] \tag{49}$$

and the average pressure at the cavity surface is

$$\bar{p} = -3\mu\frac{\dot{h}}{h}\left[1 + 2\sum_{n=1}^{\infty}\frac{(2\kappa_C R/h)^n}{(n+2)!}\right]. \tag{50}$$

Here again, friction contributes more to the average pressure as the flow progresses. The dimensionless form of (48) corresponding to (46) is just

$$-\hat{P}_{,\alpha} + \hat{v}_{\alpha,\beta\beta} - 2\left(\frac{\kappa_C L}{h}\right)\hat{P}u_\alpha = 0. \tag{51}$$

Here the important dimensionless group is $\kappa_C L/h$, which does not include μ and only has L to the first power. Therefore, the importance of friction may not increase as rapidly in this case as the flow progresses.

Since Coulomb and hydrodynamic friction influence the developing flow in a similar qualitative manner, they must be further examined in light of quantitative experimental results. This is pursued in the next two sections.

Thin Charge Approximation

To further compare the different constitutive assumptions for the friction response, it is useful to consider the case when the material resistance may be neglected relative to friction. Based on the nondimensional equations (46) and (51) in the previous section, this approximation would be appropriate for very thin charges. For simplicity, we also confine attention in this section to the case when the entire boundary is free.

Hydrodynamic Friction. Neglecting the material resistance, the governing equations for hydrodynamic friction reduce to

$$\begin{aligned} \nabla P + 2\kappa_H \mathbf{v} &= 0, \\ \nabla \cdot \mathbf{v} + \dot{h}/h &= 0, \end{aligned} \tag{52}$$

subject to the condition $P = 0$ on the free boundary (2). Taking the divergence of $(52)_1$ and combining the result with $(52)_2$ yields for P

$$\nabla^2 P = 2\kappa_H \dot{h}/h. \tag{53}$$

Therefore, the pressure resultant satisfies Poisson's equation and vanishes on the boundary. The velocity field can be computed by substituting the solution for P into $(52)_1$. It is interesting to note that the specific values κ_H, h, or $\dot{h}$ do not affect this velocity field apart from a change in time scale; hence the deformation history resulting from the solution to (52) depends only on the initial geometry of the charge.

Consider an elliptical charge with major and minor axes $2a$ and $2b$, respectively. Then the initial boundary of the region is specified by

$$g(x_\alpha, 0) = \left(\frac{x_1}{a}\right)^2 + \left(\frac{x_2}{b}\right)^2 - 1. \tag{54}$$

The solution of (53) which satisfies $P = 0$ on (54) is

$$P = \kappa_H \left(\frac{\dot{h}}{h}\right) \frac{a^2 b^2}{a^2 + b^2} \left(\frac{x_1^2}{a^2} + \frac{x_2^2}{b^2} - 1\right), \tag{55}$$

so that from $(52)_1$

$$v_1 = -\left(\frac{\dot{h}}{h}\right) \frac{x_1 b^2}{a^2 + b^2}, \quad v_2 = -\left(\frac{\dot{h}}{h}\right) \frac{x_2 a^2}{a^2 + b^2}. \tag{56}$$

The solution is not valid for $t > 0$ unless the region remains elliptical as the flow progresses. If this is true, then a and b must be functions of time with rates consistent with (56), i.e.,

$$\dot{a} = -\left(\frac{\dot{h}}{h}\right) \frac{ab^2}{a^2 + b^2}, \quad \dot{b} = -\left(\frac{\dot{h}}{h}\right) \frac{ba^2}{a^2 + b^2}. \tag{57}$$

But the entire boundary $g(x_\alpha, t)$ based on these functions must also satisfy the material surface condition $(15)_2$. This can be verified by a straightforward calculation. Therefore, the boundary does remain elliptical and the progression of the flow front is obtained by integrating $(57)_{1,2}$ for $a(t)$ and $b(t)$. One integral follows immediately from conservation of volume:

$$abh = \text{constant} = a_o b_o h_o, \tag{58}$$

where $a_o = a(0)$, $b_o = b(0)$, and $h_o = h(0)$. The other can be obtained by combining $(57)_{1,2}$ in the form

$$\dot{a}a - \dot{b}b = 0 \tag{59}$$

and then integrating to obtain

$$a^2 - b^2 = \text{constant} = a_o^2 - b_o^2. \tag{60}$$

In terms of the instantaneous eccentricity $e(t)$ of the ellipse, this integral may be expressed in the compact form

$$ae = \text{constant}, \tag{61}$$

which says the boundary of the region approaches a circle ($e \to 0$) as the flow progresses. The explicit solutions for a and b in terms of h_o/h follow from a simultaneous solution of (58) and (60).

Coulomb Friction. In the absence of material resistance, the governing equations for Coulomb friction become

$$\begin{aligned} \nabla P + 2(\kappa_C/h) P\mathbf{u} &= 0, \\ \nabla \cdot \mathbf{v} + \dot{h}/h &= 0. \end{aligned} \tag{62}$$

By taking the curl of $(62)_1$, it is easy to show that

$$\nabla \times \mathbf{u} = 0 \quad \text{or} \quad u_{1,2} - u_{2,1} = 0. \tag{63}$$

Let s be a measure of arc length along a streamline. Then since $\mathbf{u}$ is the unit tangent vector to the streamline,

$$\frac{\partial u_\alpha}{\partial s} = u_{\alpha,\beta} u_\beta = u_{\beta,\alpha} u_\beta = \frac{1}{2}(u_\beta u_\beta)_{,\alpha} = 0, \tag{64}$$

so that every streamline must be straight. From $(62)_1$ the pressure gradient is always parallel to the streamlines, and since the boundary is a line of constant pressure,[5] the streamlines must intersect the boundary at right angles. Hence the streamlines are uniquely determined by the geometry of the region. The magnitude of the velocity along these streamlines may be found by integrating $(62)_2$. Again, the deformation history turns out to be independent of κ_C, h, and $\dot{h}$. The details of this analysis are given in the Appendix, where we again obtain an analytical solution for an ellipse. In this case, the result is simply

$$a(a^2 - b^2)^{1/2} = a^2 e = \text{constant}. \tag{65}$$

By comparing (61) with (65), it is clear that Coulomb friction causes the ellipse to approach a circle more rapidly than hydrodynamic friction.

Experiments With Elliptical Charges

To experimentally evaluate the alternative assumptions for the friction response, we examined the developing shape of an initially elliptical charge at various stages of deformation. We used a sheet molding compound consisting of (by weight) 30 percent chopped glass fibers about 25 mm long, 30 percent polyester resin, and 40 percent powdered calcium carbonate filler. The sheet had a nominal weight specification of 16 oz/ft^2 (4.9 kg/m^2) and measured approximately 2.6 mm thick, devoid of air. The mold had a plane rectangular cavity measuring 530 mm by 610 mm, but the flow front never reached the edges of the cavity in the experiments. The mold was mounted in a 500 ton hydraulic press and heated to a nominal surface temperature of 160°C. Any intrinsic nonparallelism between the press platens was corrected by using the mounting procedure discussed by Barone and Caulk (1985). Parallelism during the actual flow was monitored by LVDT's at each corner of the mold. In all cases these measurements showed no more than 0.1 mm deviation from parallel across the cavity surface.

We first checked the material for random fiber orientation by making short moldings from initially circular, single-layer charges. Any systematic deviation from randomness in the fiber orientation would introduce asymmetry in the developing flow front. A typical result from this test is shown in Fig. 7, where the deformation was about 160 percent. The flow front shows random deviations from a circle on a scale less

[5] This follows from the boundary condition $(15)_1$, after the material resistance has been neglected. Note, however, that since ∇P always vanishes with P, only a trivial solution for the pressure resultant will satisfy $P = 0$ on the boundary. Therefore, it is necessary to retain the material resistance in $(15)_1$, however small, when solving for the pressure resultant. This apparent inconsistency is reconciled by the fact that in this case the velocity field may be determined independently of P (see Appendix).

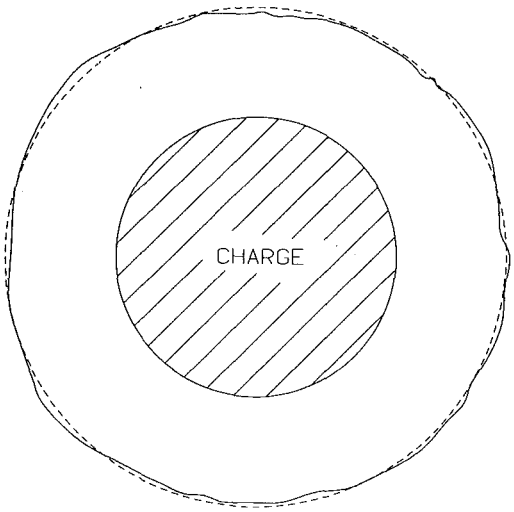

Fig. 7 Flow-front configuration after a thickness reduction of 2.6 to 1.0 mm on a single-layer circular charge

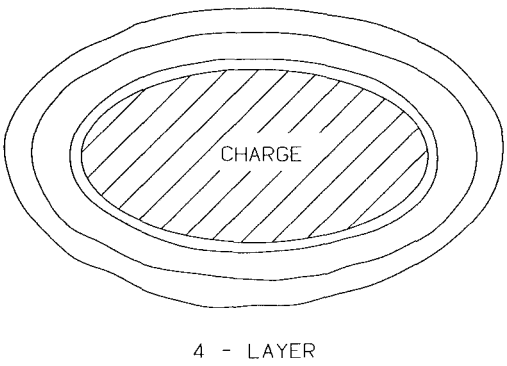

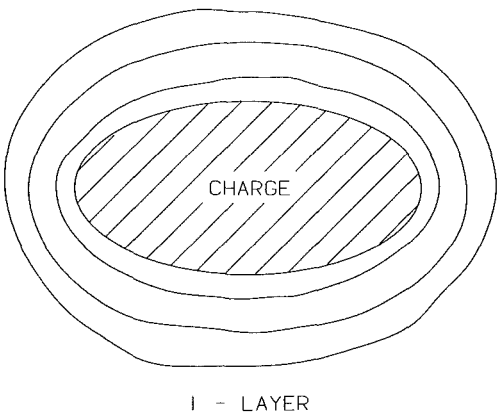

Fig. 8 Flow-front progression from identical elliptical charges made from one and four layers of SMC

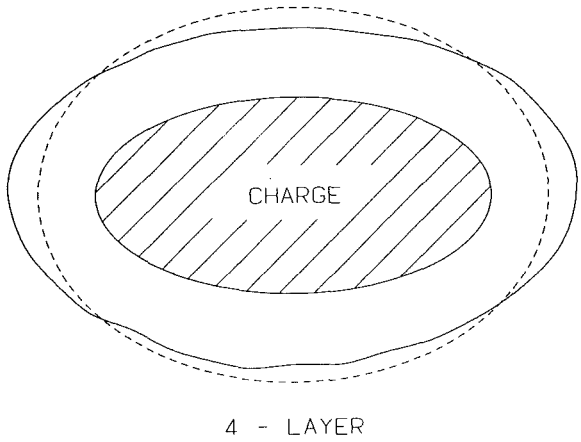

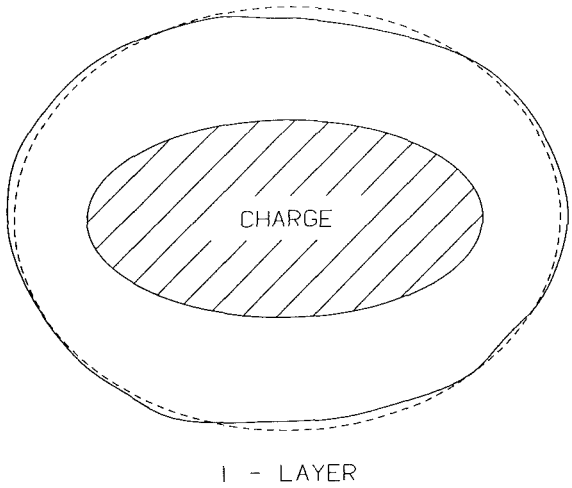

Fig. 9 Comparison of experimental flow-front progression (————) in one and four-layer elliptical charges with the analytical result (---), given by (61), which was obtained for hydrodynamic friction, neglecting material resistance

than 1 cm. Based on this result, we can be confident that our later conclusions are not affected by initial anisotropy of the material.

To evaluate the analytical solutions in the previous section, we made short moldings from elliptical charges measuring 400 mm by 200 mm along the major and minor axes. Assuming that the inertia and elasticity of the SMC are negligible, these short moldings should give an accurate picture of the developing boundary profile during flow. The mold was closed at the relatively rapid rate of $\dot{h} = 10$ mm/s to minimize the influence of any heat conduction on the results. Flow times at this speed ranged from 0.16 s to 0.64 s, depending on the charge thickness. Repeatability in the resulting flow fronts was remarkable, considering the nature of the material; after more than 100 percent deformation, differences in corresponding samples occurred randomly on a scale less than 1 cm.

Figure 8 displays typical results obtained with one and four-layer charges at three different stages of flow. The single-layer charge clearly shows greater proportional extension of the minor axis relative to the major axis than the four-layer charge. Since the constant friction assumption implies that the deformation history is independent of charge thickness, these results confirm the earlier elimination of that alternative.

In a previous section we noted that in the absence of friction, the material undergoes a homogeneous, equibiaxial deformation given by (34). This causes an ellipse to deform into a larger ellipse with the same ratio of major to minor axes. When friction is present, this symmetry is lost, and the ellipse approaches a more circular shape as the flow progresses. Both hydrodynamic and Coulomb friction imply that the effect of friction increases as the charge thickness decreases. Therefore, we would expect to see a thinner ellipse approaching a circle faster than a thicker one. This result is consistent with the qualitative trends evident in Fig. 8.

The analytical solutions for elliptical charges obtained in the previous section were based on the assumption of a negligible

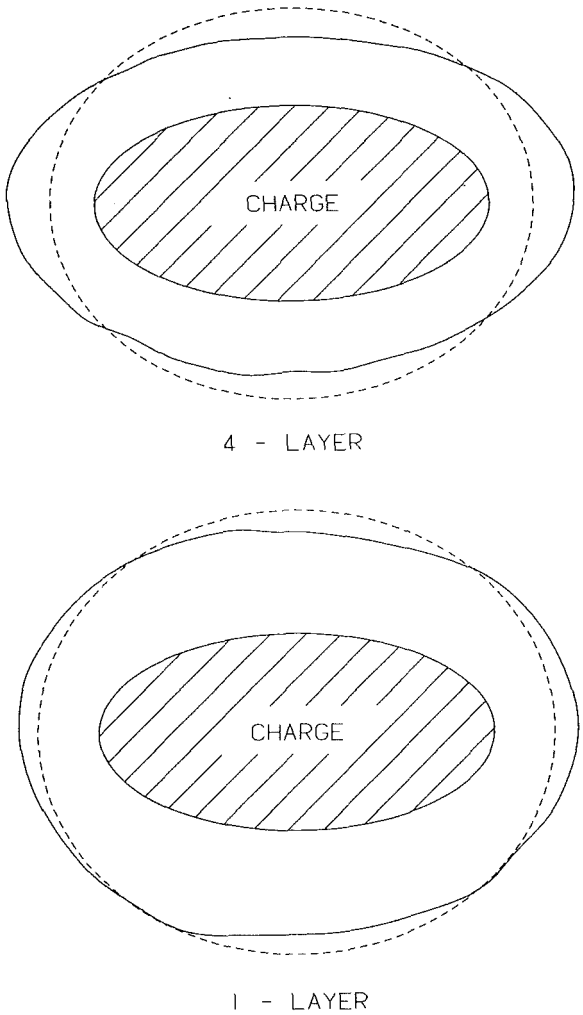

Fig. 10 Comparison of the experimental flow-front progression (————) in one and four-layer elliptical charges with the analytical result (---), given by (65), which was obtained for Coulomb friction, neglecting material resistance

material resistance, which should be appropriate, at best, for very thin charges. The analytical solution (61) for hydrodynamic friction is compared to the experimental results in Fig. 9 and the corresponding solution (65) for Coulomb friction is compared to the same results in Fig. 10. Since the degree of approximation in these solutions is directly proportional to the value of h, we should see a relatively rapid convergence of the experimental results to the analytical solution as the material thickness is reduced by a factor of four. This seems to be true only for hydrodynamic friction (Fig. 9). Therefore, we conclude from this evidence that hydrodynamic friction is the best assumption among the alternatives considered.

Discussion

In this section we discuss the relationship between certain results obtained as part of this work and previous analysis of the flow of SMC by Tucker and Folgar (1983). These authors modelled SMC as an isotropic Newtonian fluid using the usual lubrication approximations, which neglect inertia and normal stresses. This approach gives a parabolic velocity profile through the thickness of the cavity and yields for the governing equations:

$$\nabla^2 p = 12\mu\dot{h}/h^3 \ , \ \bar{\mathbf{v}} = -\frac{h^2}{12\mu}\nabla p, \tag{66}$$

where μ is the viscosity and $\bar{\mathbf{v}}$ is the average velocity through the cavity thickness. The pressure p vanishes on a free boundary and its normal derivative is assumed to be zero when the boundary is fixed. It is a simple matter to show that the history of deformation satisfying (66) does not depend on μ or on the instantaneous values of h or $\dot{h}$. It depends only on the shape of the cavity and the initial geometry of the charge. If we identify

$$6\mu/h^2 = \kappa_H, \tag{67}$$

then $(66)_{1,2}$ become formally equivalent to (53) and $(52)_1$, which correspond to the thin charge approximation with hydrodynamic friction. This explains why Tucker and Folgar (1983) obtained successful correlation between numerical solutions based on (66) and their own experiments on single-layer rectangular (75 × 150 mm) charges. In a subsequent paper Lee et al. (1984) showed that this correlation breaks down when the same charge is made from three layers of SMC. These observations are both confirmed by our own experimental work and consistent with the present model. Although Lee and Tucker (1983) later attempted to explain the different behavior in thicker charges by imposing a static variation in the fluid viscosity through the cavity thickness, their basic model of SMC as a classical fluid is still not consistent with the observed kinematics of the flow (Barone and Caulk, 1985) or the obvious anisotropy of the material.

Acknowledgment

Thanks are extended to Ronald Henderson from General Motors Advanced Engineering Staff for preparing the charges and molding the samples used in this study.

References

Barone, M. R., and Caulk, D. A., 1979, "Effect of Deformation and Thermoset Cure on Heat Conduction in a Chopped Fiber Reinforced Polyester During Compressing Molding," *Int. J. Heat Mass Transfer*, Vol. 22, pp. 1021–1032.

Barone, M. R., and Caulk, D. A., 1985, "Kinematics of Flow in SMC," *Polymer Composites*, Vol. 6, pp. 105–109.

Lee, C. C., Folgar, F., and Tucker, C. L., 1984, "Simulation of Compression Molding for Fiber-Reinforced Thermosetting Polymers," *Journal of Engineering for Industry*, Vol. 106, pp. 114–125.

Lee, C. C., and Tucker, C. L., 1983, "A Simulation of Nonisothermal Compression Molding," Society of Plastics Engineers ANTEC.

Lee, S. J., Denn, M. M., Crochet, M. J., and Metzner, A. B., 1982, "Compressive Flow Between Parallel Disks: I. Newtonian Fluid with Transverse Viscosity Gradient," *Journal of Non-Newtonian Fluid Mechanics*, Vol. 10, pp. 3–10.

Marker, L. F., and Ford, B., 1977, "Flow and Curing Behavior of SMC During Molding," *Modern Plastics*, Vol. 54, pp. 64–70.

Naghdi, P. M., 1972, "The Theory of Shells and Plates," *Handbuch der Physik*, Truesdell, C., ed., Springer Verlag, Berlin, pp. 425–640.

Silva-Nieto, R. J., Fisher, B. C., and Birley, A. W., 1980, "Predicting Mold Flow for Unsaturated Polyester Sheet Molding Compounds," *Polymer Composites*, Vol. 1, pp. 14–23.

Truesdell, C., and Toupin, R. A., 1960, "The Classical Field Theories," *Handbuch der Physik*, Vol. III/A, Flügge, A., ed., Springer Verlag, Berlin, pp. 226–902.

Tucker, C. L., and Folgar, F., 1983, "A Model of Compression Mold Filling," *Polymer Engineering and Science*, Vol. 23, pp. 69–73.

APPENDIX

In this appendix, we determine the general solution to the approximate equations (62), which are valid for Coulomb friction with negligible material resistance. We also obtain an explicit solution for an elliptical free boundary.

Recall that the streamlines corresponding to (62) must be straight and intersect the free boundary at right angles. Each streamline emanates from a stagnation point inside the region located by its intersection with one or more other streamlines. In general, the locus of these stagnation points will be a connected curve which may have one or more branches.

To construct a general solution, we introduce a system of

normal coordinates s_α in the region, where s_1 is the arc length along the free boundary and s_2 is the distance inward from the boundary along the streamline $\mathbf{u}(s_1)$. Let $\mathbf{r}(s_1)$ denote the position vector to a point s_1 on the boundary and let $\mathbf{p}(s_\alpha)$ be the position vector to any point s_α inside the region. Then

$$\mathbf{p}(s_\alpha)=\mathbf{r}(s_1)-s_2\mathbf{u}(s_1), \tag{A1}$$

where the minus sign occurs because s_2 increases in the direction opposite to flow. The base vectors associated with s_α are simply

$$\mathbf{g}_1=\partial\mathbf{p}/\partial s_1=(1-\kappa s_2)\underset{\sim}{\lambda}(s_1), \tag{A2}$$

$$\mathbf{g}_2=\partial\mathbf{p}/\partial s_2=-\mathbf{u}(s_1), \tag{A3}$$

where $\kappa(s_1)$ is the boundary curvature and $\underset{\sim}{\lambda}=\partial\mathbf{r}/\partial s_1$ is the unit tangent to the boundary. If $v(s_\alpha)$ is the magnitude of the velocity vector, then in these coordinates the contravariant components of $\mathbf{v}$ are

$$v^1=0\ ,\ v^2=-v, \tag{A4}$$

so that

$$\nabla\cdot\mathbf{v}=v^\alpha|_\alpha=-\frac{\partial v}{\partial s_2}-\Gamma^\alpha_{2\alpha}v, \tag{A5}$$

where a vertical bar denotes the covariant derivative and $\Gamma^\alpha_{\beta\gamma}$ are the Christoffel symbols, defined by

$$\Gamma^\alpha_{\beta\gamma}=\mathbf{g}^\alpha\cdot\mathbf{g}_{\beta,\gamma}. \tag{A6}$$

From (A2) and (A3), it is easy to show that in this case

$$\Gamma^\alpha_{2\alpha}=\frac{-\kappa}{1-\kappa s_2}, \tag{A7}$$

so that the incompressibility equation may be written in the form

$$\nabla\cdot\mathbf{v}+\dot{h}/h=-\frac{\partial v}{\partial s_2}+\frac{\kappa v}{1-\kappa s_2}+\frac{\dot{h}}{h}=0 \tag{A8}$$

or

$$\frac{\partial}{\partial s_2}[v(1-\kappa s_2)]=\frac{\dot{h}}{h}(1-\kappa s_2). \tag{A9}$$

The solution to this equation is

$$v(s_\alpha)=-\frac{\dot{h}}{2\kappa h}(1-\kappa s_2)\left[1-\left(\frac{1-\kappa s^*}{1-\kappa s_2}\right)^2\right], \tag{A10}$$

where $s^*=s^*(s_1)$ is the length of the streamline s_1. Since $s_2=0$ on the boundary, the normal velocity of the flow front is simply

$$v_\nu=v(s_1,0)=-\frac{\dot{h}s^*}{h}\left(1-\frac{1}{2}\kappa s^*\right). \tag{A11}$$

The solution (A10) is valid for any region where the entire boundary is free.

Consider now the elliptical region defined by (54) and let the position vector $\mathbf{r}$ be written in terms of the polar angle θ. Then

$$\mathbf{r}=a\cos\theta\ \mathbf{e}_1+b\sin\theta\ \mathbf{e}_2, \tag{A12}$$

and the outward unit normal to this boundary is given by

$$\nu=\beta^{-1}(b\cos\theta\ \mathbf{e}_1+a\sin\theta\ \mathbf{e}_2), \tag{A13}$$

where

$$\beta^2=a^2\sin^2\theta+b^2\cos^2\theta. \tag{A14}$$

The stagnation points for this region all lie along the major axis of the ellipse, and from the geometry of the problem, it is easy to show that the length of each streamline is

$$s^*=(b/a)\beta \tag{A15}$$

and the curvature at any point on the boundary is given by

$$\kappa=ab/\beta^3. \tag{A16}$$

The velocity of the flow front now follows from (A11), (A15), and (A16):

$$v=\frac{\dot{h}}{h}(b/a)\beta\left[1-\frac{1}{2}(b/\beta)^2\right]. \tag{A17}$$

This solution will not be valid for $t>0$ unless the region remains elliptical as the flow progresses. For this to be true, the boundary velocity (A17) must identically satisfy $(15)_2$ when the major and minor axes extend consistent with (A17):

$$\dot{a}=-\frac{1}{2}\left(\frac{\dot{h}}{h}\right)\frac{b^2}{a}\ ,\ \dot{b}=-\left(\frac{\dot{h}}{h}\right)b\left[1-\frac{1}{2}\left(\frac{b^2}{a^2}\right)\right]. \tag{A18}$$

This can be verified by a straightforward calculation. Now from (58) and (A18)

$$\frac{d}{dt}(a^4)=4a^3\dot{a}=-2\frac{\dot{h}}{h}a^2b^2=-2\frac{\dot{h}}{h^3}a_o^2b_o^2h_o^2$$

$$=\frac{d}{dt}(h^{-2})a_o^2b_o^2h_o^2, \tag{A19}$$

which may be integrated to yield the desired result:

$$a^4-a_o^2b_o^2h_o^2/h^2=a^4-a^2b^2=a^2(a^2-b^2)=\text{constant}. \tag{A20}$$

The Stress Field Induced by a Twisting Sphere

D. A. Hills
Department of Engineering Science,
Oxford University,
Oxford, England OX1 3PJ

A. Sackfield
Department of Mathematics,
Statistics and Operations Research,
Trent Polytechnic,
Nottingham, England NG1 4BU

Analytical solutions are presented for the stress field induced in an elastic half space by a sphere pressed normally into its surface, and twisted. It is found that the stresses decay rapidly with depth, and that the severest stress state occurs in the surface. Cases of both partial slip, i.e., where there is a central disk where no relative rotation occurs, surrounded by a slip annulus, and full slip where the disk degenerates to a point, are considered. The largest tensile stress, associated with brittle fracture and cracking, occurs on the edge of the contact circle, while the greatest tendency to yield, by von Mises criterion, occurs somewhere within the slip annulus, depending on the coefficient of friction. Twisting has a first order effect on the strength of contact as measured by each of these criteria.

Introduction

Stresses induced by Hertzian contact have been found for all configurations of the contacting bodies, due to both a normal load, and the effect of a tangential force sufficient to cause sliding (Bryant and Keer, 1982, Sackfield and Hills, 1983a, 1983b, 1983c). However, there are comparatively few solutions in the literature for the case of a Hertzian contact which is undergoing a relative twist. In this paper, we restrict ourselves to a study of circular contacts, formed by the pressing of a sphere into a half space, since this is the only axisymmetric configuration which leads to a static, constant stress field in the contacting bodies. Besides their fundamental significance, the results should be of interest to an understanding of the strength of rolling contact involving a spin component, such as is found beneath a railway carriage wheel, or in balldrive mechanisms, although their application to these cases involves further approximation. However, the results as presented may be used to analyze fretting and wear tests where the geometry of test is exactly that described above, and which is currently in vogue (Kennedy and Peterson, 1982, 1983).

If a linear elastic sphere is pressed normally on to a half space with the same elastic constants, the resulting contact is a classic Hertzian configuration (Timoshenko and Goodier, 1951). The stresses in the neighborhood of contact are identical in each body, and hence the radial displacement of surface particles is also identical, so that no shear tractions develop. The prior determination of the contact radius follows standard lines, and throughout the paper we shall nondimensionalize the coordinates with respect to this contact radius, a. The surface tractions in this case are given by (Fig. 1)

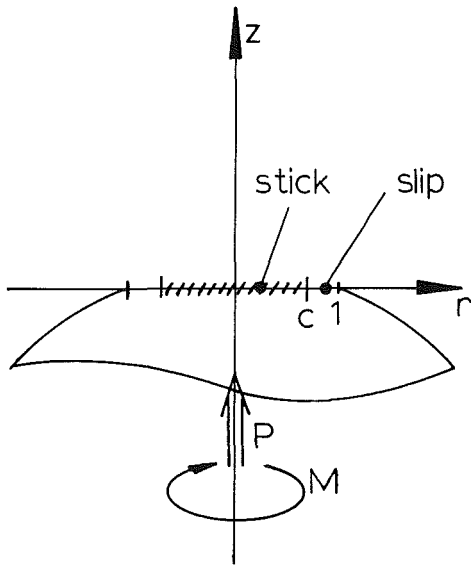

Fig. 1 Coordinate set used

$$\sigma_{rz} = 0$$
$$\sigma_{zz} = 0 \qquad r > 1 \qquad (1)$$
$$\frac{\sigma_{zz}}{p_o} = -\sqrt{1-r^2} \qquad r \le 1$$

where p_o is the peak Hertzian contact pressure.

A couple of magnitude M is now applied, and shear tractions $\sigma_{z\theta}$ will arise. If it is assumed that the contacting faces remain adhered over the entire disk $r \le 1$, infinite shear tractions arise at the periphery of contact, as shown by Mindlin (1949). It is clear that the direct traction here is insufficient to maintain stick, and that there will be an annulus where the shear traction is limited by friction, while the central disk remains adhered. Therefore, we have a mixed boundary value problem, where, in addition to conditions (1)

Contributed by the Applied Mechanics Division for publication in the JOURNAL OF APPLIED MECHANICS.

Discussion on this paper should be addressed to the Editorial Department, ASME, United Engineering Center, 345 East 47th Street, New York, N.Y. 10017, and will be accepted until two months after final publication of the paper itself in the JOURNAL OF APPLIED MECHANICS. Manuscript received by ASME Applied Mechanics Division, September 5, 1985; final revision, December 6, 1985.

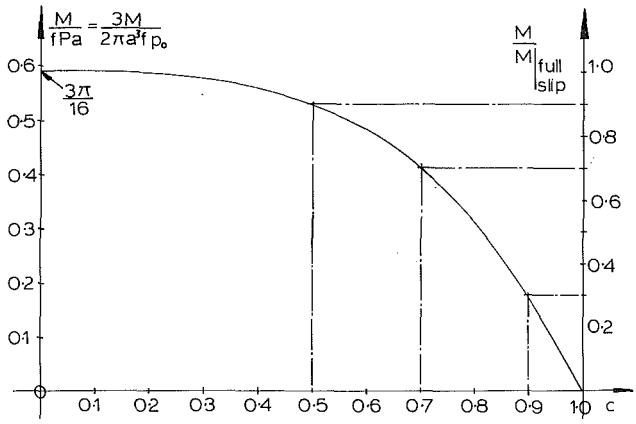

Fig. 2 Penetration of slip band with increasing applied moment

$$u_\theta = \text{constant} \times r \quad r<c \tag{2a}$$

$$\frac{\sigma_{\theta z}}{fp_o} = \sqrt{1-r^2} \quad c\le r\le 1 \tag{2b}$$

$$\sigma_{\theta z} = 0 \quad r>1 \tag{2c}$$

where f is the coefficient of friction, and c is the radius of the stick/slip boundary. Lubkin (1951) considered this problem further and obtained closed forms for the surface traction corresponding to equation (2*a*)

$$\frac{\sigma_{\theta z}}{fp_o} = \sqrt{1-r^2}\left\{1+\frac{2}{\pi}\left[K(k)[F(c,\phi)-E(c,\phi)] - E(k)F(c,\phi)\right]\right\} \tag{3}$$

$$0<r<c$$

$$\text{where} \quad \sin\phi = \frac{1}{c}\sqrt{\frac{c^2-r^2}{1-r^2}} \quad k^2 = 1-c^2$$

and $F(x,\theta)$, $E(x,\theta)$ are incomplete integrals of the first and second kinds, respectively, whose complete counterparts are $K(x)$,$E(x)$, all tabulated by Abramowitz and Stegun (1972). Lubkin also determined the relationship between the applied couple and the size of the stick zone, with the result (Fig. 2)

$$\frac{M}{fpa} = \frac{1}{4\pi}\left\{\frac{3\pi^2}{4} + c^2k^2\left[6\,K(k) + \frac{(4c^2-3)}{k^2}\left\{K(k)-E(k)\right\}\right]\right.$$

$$-3\,k\,K(k)\sin^{-1}(c) - 3\,k^2K(k)\int_o^{\pi/2}\frac{\sin^{-1}(c\,\sin\alpha)d\alpha}{(1-c^2\,\sin^2\alpha)^{3/2}} +$$

$$\left.+3\{K(k)-E(k)\}\int_o^{\pi/2}\frac{\sin^{-1}(c\,\sin\alpha)d\alpha}{(1-c^2\,\sin^2\alpha)^{1/2}}\right\} \tag{4}$$

It may be noted that as $c \to 0$ the above reduces to

$$\frac{M}{fpa} = \frac{3\pi}{16} \tag{5}$$

This is the moment sustained by friction under "spin" conditions, where the relative rotation between the two contacting bodies may take any value.

Equations (1, 2*b*, 2*c*, 3) constitute a well posed problem of the first kind in the theory of linear elasticity, and it is the object of this paper to derive the complete stress fields generated, and to determine the effect of torsion on the contact strength. It may be noted that direct loading gives rise to displacements in the r and z directions alone, while, from Michell's theorem, torsional loading gives rise to only a θ direction displacement (Michell, 1899). Therefore, the two problems are uncoupled, and results for stresses induced under the "spin" conditions are valid whether or not the elastic constants of the bodies are similar, since, in the steady state, the shear traction is directed precisely in the θ direction. A determination of the interfacial tractions for dissimilar elastic bodies undergoing torsion less than the limiting value, and which may be thought of as the corresponding transient problem, is not attempted.

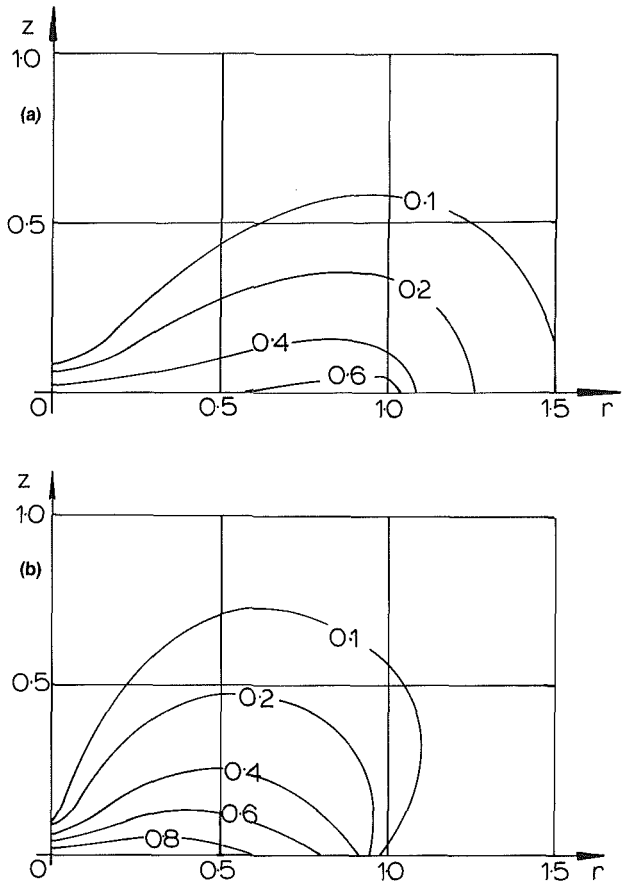

Fig. 3 Stresses generated under full-slip conditions: (a) $\sigma_{r\theta}/fp_o$; (b) $\sigma_{\theta z}/fp_o$

Full Slip Solution

Derivations of the stress field corresponding to axisymmetric Hertzian contact are treated extensively in the literature, and will not be reproduced here (see e.g., Sackfield and Hills, 1983c, Huber, 1904). The problem posed is, therefore, given by boundary conditions (2*b*, *c*), with $c = 0$. This has been treated before, by Hetenyi and McDonald (1958).

Since there is only one nonzero displacement, an examination of the equilibrium equations in cylindrical coordinates reveals that the only nonzero stresses are $\sigma_{\theta z}$, $\sigma_{r\theta}$. Hetenyi and McDonald solve the problem by expressing the equilibrium conditions in terms of Bessel functions, with the result

$$\frac{\sigma_{r\theta}}{fp_o} = -\frac{\pi}{2}\int_o^\infty e^{-zt}J_2(rt)J_1^2(\tfrac{1}{2}t)dt \tag{6}$$

$$\frac{\sigma_{\theta z}}{fp_o} = \frac{\pi}{2}\int_o^\infty e^{-zt}J_1(rt)J_1^2(\tfrac{1}{2}t)dt \tag{7}$$

where J_1, J_2 are Bessel functions of the first kind. Numerical evaluation of the integrals in equations (6, 7) presents great difficulty, since the Bessel functions are of course, oscillatory, and the magnitude of the integrand will decay only slowly for small z. Therefore, this method was not adopted, and an alternative scheme due to Green and Collins, recently reported by Barber (1983), was adopted.

Since $u_r = u_z = 0$, we require a potential to represent u_θ alone. Letting

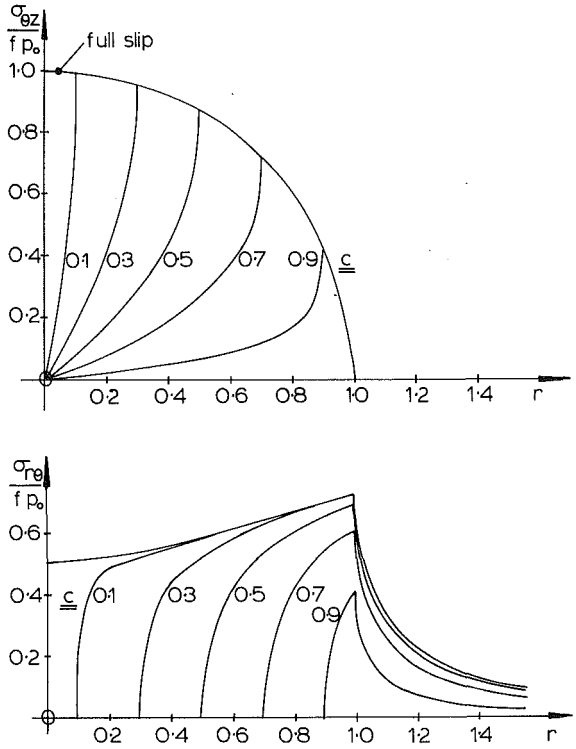

Fig. 4 Surface tractions induced by full or partial slip

$$u_\theta = \frac{1}{\mu}\frac{d\psi}{dr} \tag{8}$$

where μ is the modulus of rigidity, enables us to write the stress components as

$$\sigma_{r\theta} = r\frac{\partial}{\partial r}\left[\frac{1}{r}\frac{\partial \psi}{\partial r}\right] \tag{9}$$

$$\sigma_{\theta z} = \frac{\partial^2 \psi}{\partial r \partial z} \tag{10}$$

Now let (Barber, 1983)

$$\psi = fp_o Im\int_o^1 g(t)\ln\left\{(r^2+(z+it)^2)^{1/2}+z+it\right\}dt \tag{11}$$

so that

$$\frac{\partial \psi}{\partial z} = fp_o Im\int_o^1 \frac{g(t)dt}{\sqrt{r^2+(z+it)^2}} \tag{12}$$

Differentiating again

$$\frac{\sigma_{\theta z}}{fp_o} = \frac{1}{fp_o}\frac{\partial^2 \psi}{\partial r \partial z} = \frac{\partial}{\partial r} Im\int_o^1 \frac{g(t)dt}{\sqrt{r^2+(z+it)^2}} \tag{13}$$

It is clear that provided $g(t)$ is real, the integral has no imaginary part on $z = 0$ for $r > 1$, so that (2*c*) is satisfied automatically; while on $z = 0$ for $r \le 1$, the following Abel type integral equation results, from 2(*b*)

$$-\frac{\partial}{\partial r}\int_r^1 \frac{g(t)dt}{\sqrt{t^2-r^2}} = \sqrt{1-r^2} \tag{14}$$

which may be inverted (Barber, 1983, Table 2) to give

$$g(t) = \frac{2t}{\pi}\left\{K(t') - E(t')\right\} \tag{15}$$

where $t' = \sqrt{1-t^2}$

With the potential established, determination of the stress

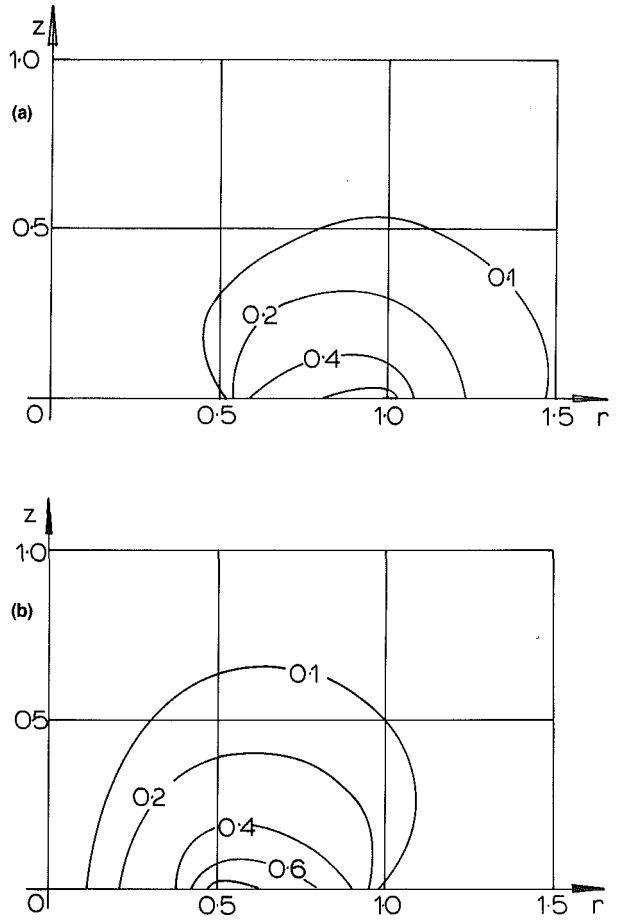

Fig. 5 Stresses generated under partial slip conditions, c = 0.5; *(a)* $\sigma_{r\theta}/fp_o$; *(b)* $\sigma_{\theta z}/fp_o$

field follows Green and Zerna's method (Green and Zerna, 1968). From (9, 10)

$$\sigma_{\theta z} = r\int_o^1 \frac{g(t)\sin(3\alpha/2)dt}{\rho^3} \tag{16}$$

$$\sigma_{r\theta} = 2\int_o^1 g(t)\,\frac{\{\rho\sin\alpha + z\sin(\alpha/2) + t\cos(\alpha/2)\}dt}{\rho\{(\rho\cos(\alpha/2)+z)^2+(\rho\sin(\alpha/2)+t)^2\}}$$
$$-\int_o^1 \frac{g(t)}{\rho^3}\left\{z\sin(3\alpha/2) - t\cos(3\alpha/2)\right\}dt \tag{17}$$

where $\rho^4(t) = (r^2+z^2-t^2)^2 + 4z^2t^2 \quad \rho > 0$

$$\tan\alpha(t) = \frac{2zt}{r^2+z^2-t^2} \qquad 0 \le \alpha \le \pi$$

The intergrals (16, 17) are both well behaved and readily converge numerically with the kernel given by (15). Contours of the stresses $\sigma_{r\theta}$, $\sigma_{\theta z}$ under full slip conditions are shown in Fig. 3. They fall off rapidly with depth and hence some attention will be focused on the surface where the effect of twist predominates. $\sigma_{\theta z}$ is, of course, fully specified by boundary conditions (2*b*, *c*) so that only $\sigma_{r\theta}$ remains to be found.

Setting $\frac{\partial \psi}{\partial r} = -fp_o\phi$ (18)

we see from (9) that $\frac{\sigma_{r\theta}}{fp_o} = \frac{\phi}{r} - \frac{d\phi}{dr}$ (19)

From (11, 18)

$$\phi = \frac{1}{r}\int_0^s g'(t)\sqrt{r^2-t^2}dt \tag{20}$$

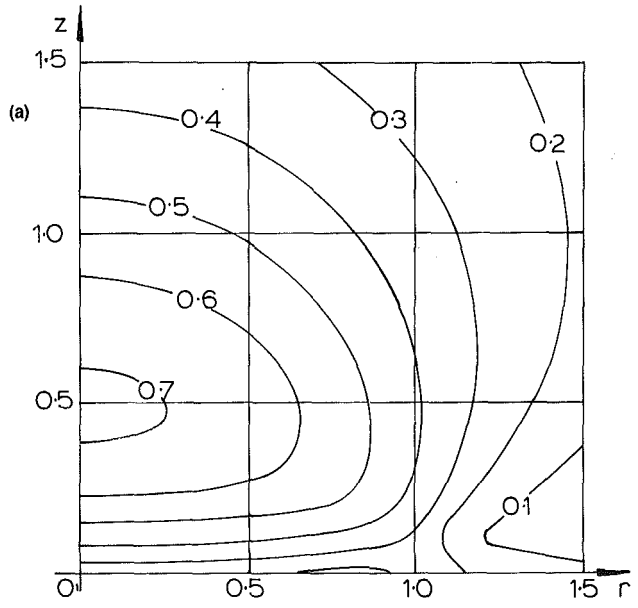

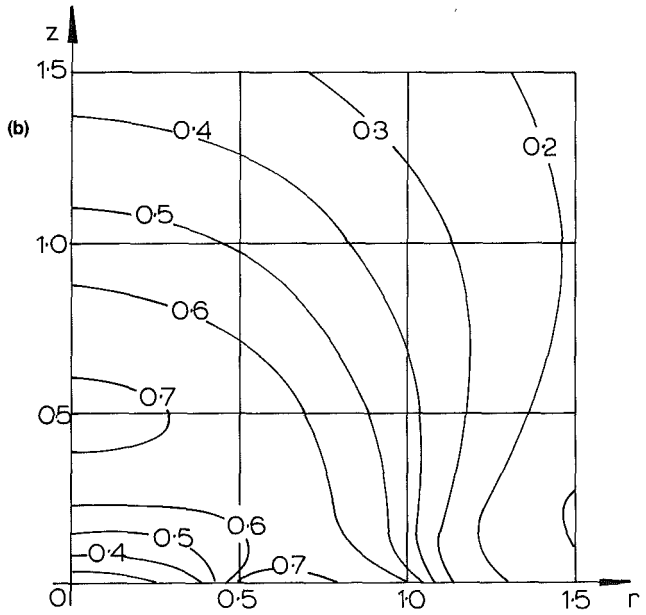

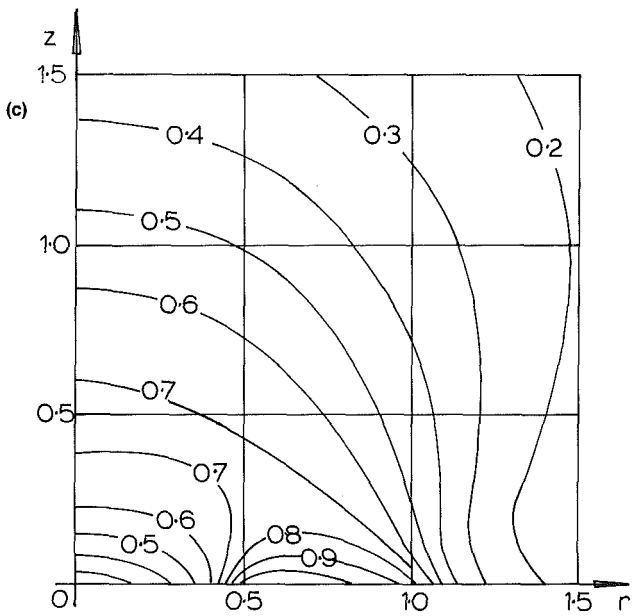

Fig. 6 von Mises yield contours; *(a)* normal load alone; *(b)* $c = 0.5$, $f = 0.4$; *(c)* $c = 0.5$, $f = 0.6$

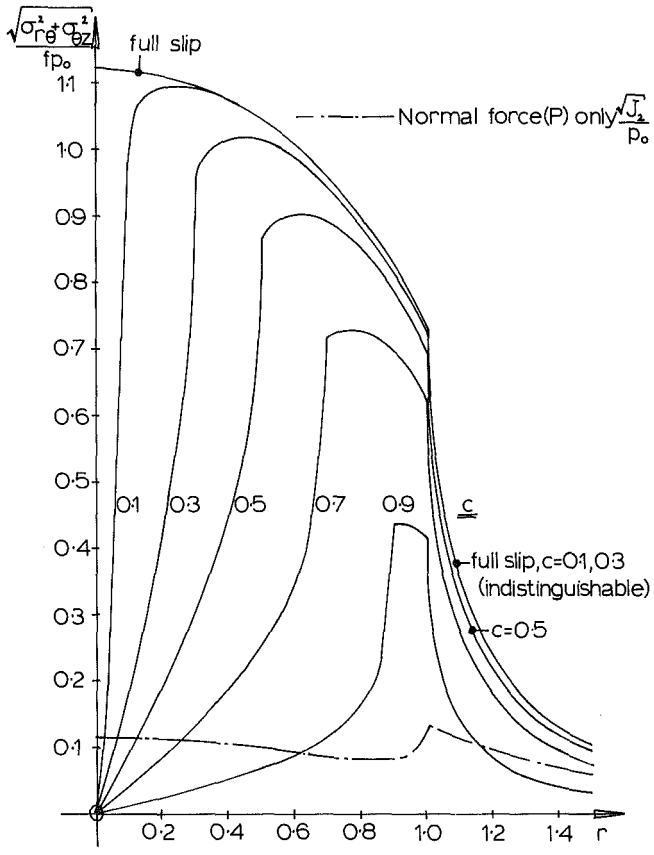

Fig. 7 Contributions of normal and twist loading to second deviatoric stress invariant

where $s = 1$ if $r \geq 1$

$s = r$ if $r < 1$

and $g'(t) = \frac{2}{\pi}\{K(t') - 2E(t')\}$

$t' = \sqrt{1 - t^2}$

Combining $\frac{\sigma_{r\theta}}{fp_o} = \frac{2}{\pi r^2}\int_0^s \frac{t^2 E(t')dt}{\sqrt{r^2 - t^2}}$ (21)

This integral, though improper if $r < 1$, is readily evaluated numerically by Gauss-Chebyshev quadrature (Conte and de Boor, 1972). As noted by Hetenyi and McDonald, the surface shear tractions given by (2*b*, 21) remains finite as

$$r \to 0, \text{ i.e., } \frac{\sigma_{r\theta}}{fp_o} \to \frac{1}{2} \qquad \frac{\sigma_{\theta z}}{fp_o} \to 1$$

wheras both are required to vanish at all z along the axis of symmetry. This doubled valuedness was mentioned by Deresiewicz (1959), who also shows that for $r < 1$ (only), equation (21) may be written in terms of a hypogeometric function thus

$$\frac{\sigma_{r\theta}}{fp_o} = -\frac{3\pi}{16r^3}\left[{}_2F_1\left\{\frac{1}{2}, \frac{5}{2}; 2; \frac{1}{2} - \frac{1}{2}\sqrt{1 - 1/r^2}\right\}\right]^2 \quad (22)$$

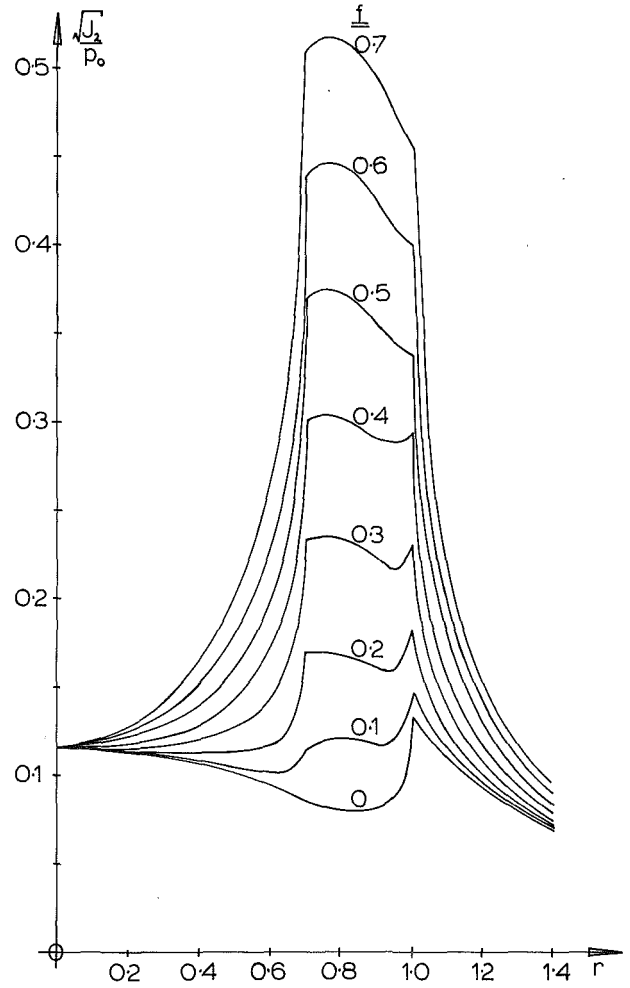

Fig. 8 Development of surface yield parameter with increasing friction, $c = 0.7$

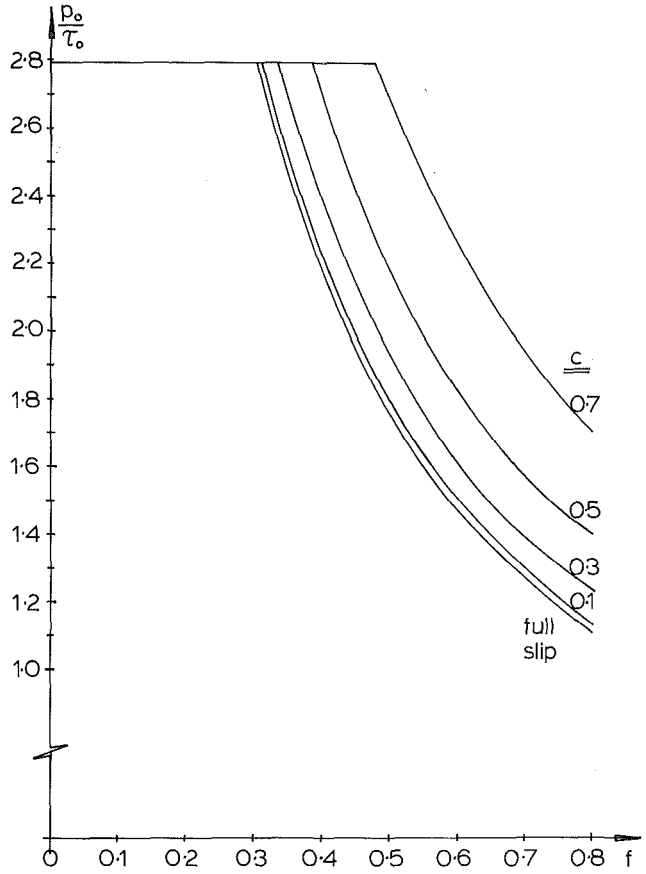

Fig. 9 Elastic limit according to von Mises criterion

Partial Slip Solution

Under partial slip conditions, a solution corresponding to boundary conditions (2), $c > 0$, is obtained by superposition. First, assuming full slip ($c = 0$), the stress field given in the above section is found. Then, a "core" of shear traction

$$\frac{\sigma^o_{\theta z}}{fp_o} = -\sqrt{1-r^2} \quad 0<r<c \tag{23}$$

is added to cancel the full-slip solution, and a further traction equivalent to (3) added. It transpires that another form of (3), given by Deresiewicz (1954), is more suitable in subsequent computations, viz,

$$\frac{\sigma^1_{\theta z}}{fp_o} = \frac{2}{\pi} r\sqrt{c^2-r^2}\int_o^{\pi/2} \frac{k^2\sin^2\alpha/(1-r^2)d\alpha}{\{1-k^2\sin^2\alpha/(1-r^2)\}\sqrt{1-k^2\sin^2\alpha}} \tag{24}$$

$0<r<c$

Determination of the stress fields induced by (23, 24) follows a generally similar recipe to that described in the previous section, where we seek functions $g_o(t)$, corresponding to (23), and $g_1(t)$, corresponding to (24). These are determined by inverting Abel type integral equations similar to (14), viz

$$\frac{\partial}{\partial r}\int_r^c \frac{g_i(t)dt}{\sqrt{t^2-r^2}} = \frac{\sigma^i_{\theta z}}{fp_o} \qquad i=0,1 \tag{25}$$

giving $g_o(t) = -\frac{2}{\pi}t\left\{F(\chi, t') - E(\chi, t') + \frac{k}{c}\sqrt{c^2-t^2}\right\}$ (26)

$$g_1(t) = \frac{2}{\pi}t\left\{\left[K(k)-E(k)\right] - \left[F(\eta, t')-E(\eta, t')\right]\right\} \tag{27}$$

where $\sin\chi = \frac{1}{c}\sqrt{\frac{c^2-t^2}{1-t^2}}$, $\sin\eta = \frac{k}{t'}$,

Stresses are given by (16, 17), mutatis mutandis.

Again of particular interest are the surface stresses, and, since $\sigma_{\theta z}$ is specified by (2*b*, 2*c*, 3) attention is concentrated on $\sigma_{r\theta}$. Within the disk $0 < r < c$ each body undergoes a rigid body rotation, since all corresponding particles are assumed stuck. Therefore, there are no displacement gradients in the r direction, and $\sigma_{r\theta} \equiv 0$. Outside this disk the same method is used as for full slip, with which it is superimposed, where, in equation (20), $g'(t)$ is replaced by $g'_0(t) + g'_1(t)$ and s is set to c. After considerable manipulation, some details of which are given in the appendix, this yields

$$\frac{\sigma_{r\theta}}{fp_o} = \frac{2}{3\pi}\frac{k}{rc}\{2(c^2-r^2)K(c/r) + (2r^2-c^2)E(c/r)\}$$
$$-\frac{2}{\pi r^2}\int_0^c \frac{t^2}{\sqrt{r^2-t^2}}\{E(\eta, t')+E(\chi, t')\}dt \tag{28}$$
$$r \geq c$$

The integral is proper for $r < c$ and readily evaluated numerically, while on the stick/slip boundary $r = c$ Gauss-Chebyshev quadrature may again be used, and the first term in the equation simplifies yielding

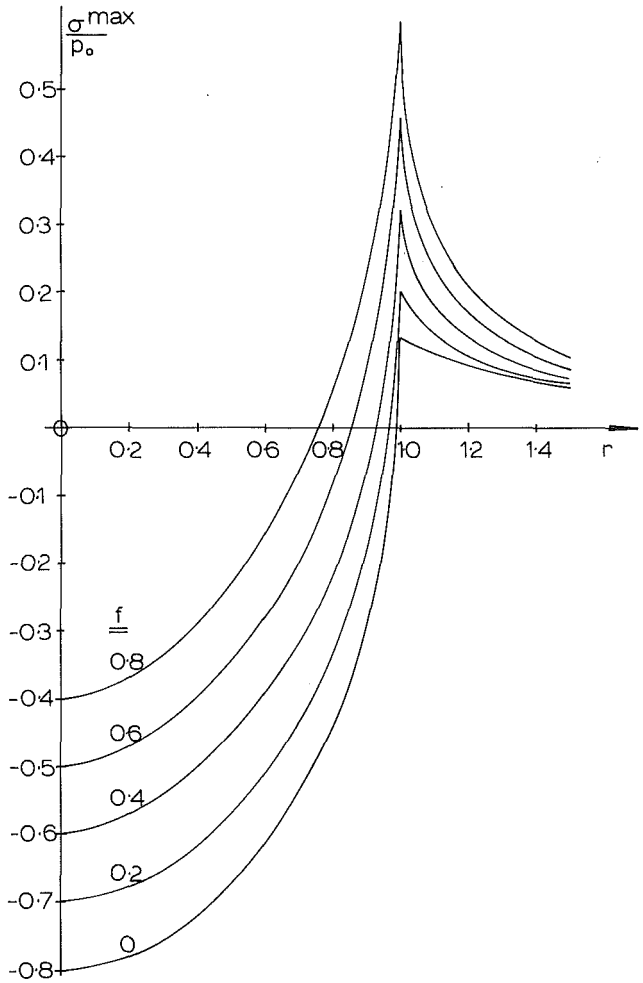

Fig. 10 Variation in more positive principal stress with radius, full slip

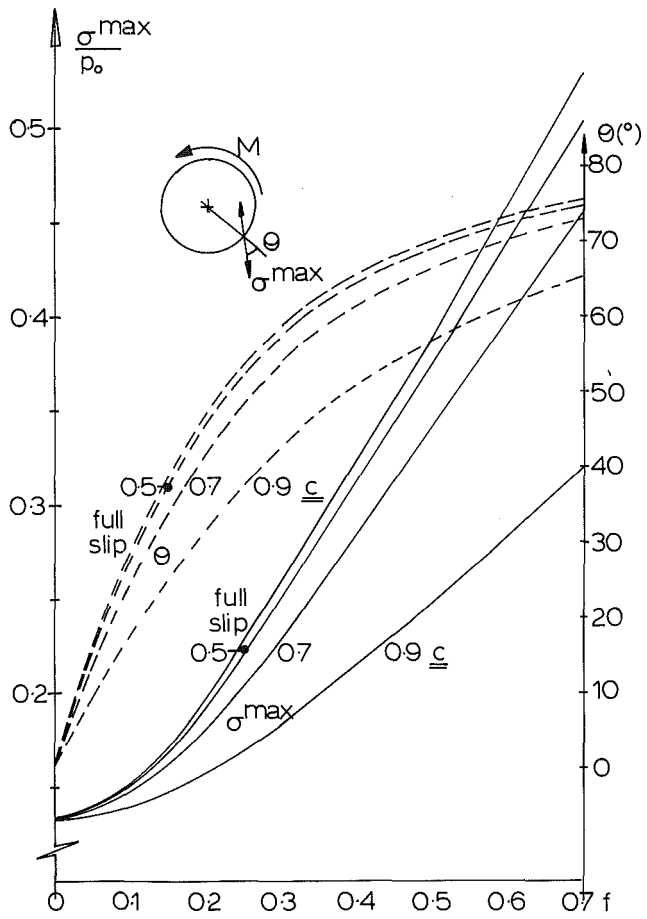

Fig. 11 Magnitude and orientation of more positive principal stress, full or partial slip

$$\frac{\sigma_{r\theta}}{rp_o}=\frac{2}{3\pi}\sqrt{1-c^2}-\frac{2}{\pi c^2}\int_o^c\frac{t^2}{\sqrt{c^2-t^2}}\{E(\eta,t')+E(\chi,t')\}dt \qquad (29)$$

$$r=c$$

It may be noted that equation (29) yields a value of $\sigma_{r\theta}$ identical in magnitude (but of opposite sign) to that obtained under full slip conditions. Therefore, $\sigma_{r\theta}$ falls continuously to zero as r tends to c from above. Surface values of the stresses are given in Fig. 4, while in Fig. 5 contours of $\sigma_{r\theta}$, $\sigma_{\theta z}$ are shown for a specimen value of c, viz 0.5. It may be noted that there are no difficulties in double valuedness at the origin, providing $c > 0$.

Elastic Limit

Resistance to yielding is assumed by von Mises criterion, i.e.,

$$J_2=\frac{1}{6}\{(\sigma_{rr}-\sigma_{\theta\theta})^2+(\sigma_{\theta\theta}-\sigma_{zz})^2+(\sigma_{zz}-\sigma_{rr})^2\}+$$
$$+\sigma_{r\theta}^2+\sigma_{\theta z}^2+\sigma_{rz}^2\le\tau_o^2 \qquad (30)$$

where τ_o is the yield stress in pure shear. Contours of the yield parameter $\sqrt{J_2}/p_o$ are plotted in Fig. 6 for f = 0.0, 0.4, 0.6, and c = 0.5. It is clear that the well-known subsurface maximum found under twist-free conditions is not affected (since $\sigma_{r\theta}$, $\sigma_{\theta z} \to 0$ as $r \to 0$), and the deviatoric component due to those stresses does not build up as quickly as that due to normal loading falls off, in the neighborhood of this maximum.

A comprehensive range of plots has been made, and all lead to the same conclusion. Therefore, the primary effect of twist is on the surface strength.

Since normal loading contributes only to the direct stresses together with σ_{rz}, while twist contributes only to the other two shear terms, there is some merit in plotting each component separately, for different c, so that the relative contributions of each form can be visualized for different coefficients of friction, Fig. 7. In every case the severest state of stress occurs within the slip annulus, though its exact location depends on the coefficient of friction, Fig. 8; for low coefficients of friction the maximum is near the edge of contact, but moves inwards as f is increased.

A summary of the elastic limit, i.e., the largest pressure which may be sustained without yielding, is given in Fig. 9. The contact strength is not influenced below a coefficient of friction of about 0.3, and the maximum reduction in strength occurs under full slip conditions. For full slip, surface-controlled yielding, the elastic limit is first reached at the origin and takes a very simple form. Equation (30) becomes

$$\frac{J_2}{p_o^2}=\frac{1}{3}\left(\frac{1}{2}-\nu\right)^2+\frac{5}{4}f^2\le\left[\frac{\tau_o}{p_o}\right]^2 \qquad (31)$$

where ν is Poisson's ratio.

Therefore, under spinning conditions the point of first contact and a subsurface point on the axis of symmetry are the two controlling points.

Brittle Failure

While spin may not always influence yielding appreciably, it does have a significant effect on the maximum tension generated in the surface, even at modest coefficients of fric-

tion. Figure 10 shows the variation in the more positive principal stress with radius, for full slip, and it may be noted that the region of tension is confined to a narrow annulus at the edge of contact. It is found that the greatest tension is always at the periphery of contact, and its value and orientation are shown for both full/partial slip conditions in Fig. 11. For full slip the magnitude of the maximum tension is given by

$$\frac{\sigma^{\max}}{p_o}=\sqrt{\left\{\frac{(1-2\nu)^2}{9}+\frac{4}{\pi^2}\left[\int_o^1 t'E(t)dt\right]^2\right\}} \tag{32}$$

Summary

The complete stress field beneath an axisymmetric Hertzian contact undergoing twist has been found. It is revealed that stresses due to torque decay very rapidly with depth, and, since they also vanish both on the axis of symmetry and for large r, their influence is confined to a near-surface zone, principally within the slip annulus beneath contact. The tendency of the contact to yield is influenced only for large coefficients of friction ($f > 0.3$), but there is a steady increase in the magnitude of the maximum surface tensile stress with f.

References

Abramowitz, M., and Stegun, I. A., 1972, *Handbook of Mathematical Functions with Formulas, Graphs and Mathematical Tables*, Wiley, New York.

Barber, J. R., 1983, "The Solution of Elasticity Problems for the Half Space by the Method of Green and Collins," *Appl. Scientific Res.*, Vol. 40, pp. 135–157.

Bryant, M. D., and Keer, L. M., 1982, "Rough Contact Between Elastically and Geometrically Identical Bodies," ASME JOURNAL OF APPLIED MECHANICS, Vol. 49, pp. 345–352.

Conte, S. D., and de Boor, C., 1972, *Elementary Numerical Analysis*, 2nd ed., McGraw-Hill, New York.

Deresiewicz, H., 1954, "Contact of Elastic Spheres Under an Oscillating Torsional Couple," ASME JOURNAL OF APPLIED MECHANICS, Vol. 21, pp. 52–56.

Deresiewicz, H., 1959, "Contact Stress Under Combined Pressure and Twist," ASME JOURNAL OF APPLIED MECHANICS, Vol. 26, pp. 305–306.

Green, A. E., and Zerna, W., 1968, *Theoretical Elasticity*, O.U.P. 2nd ed.

Hetenyi, M., and McDonald, P. H., 1958, "Contact Stresses Under Combined Pressure and Twist," ASME JOURNAL OF APPLIED MECHANICS, Vol. 25, pp. 396–401.

Huber, M. T., 1904, Zur Theorie der Beruhrung fester elasticher Korper, *Ann. der Phys.*, Vol. 14, pp. 153–163.

Kennedy, P. J., Peterson, M. B., and Stallings, L., 1982, "An Evaluation of Fretting at Small Amplitudes," *ASTM STP*, Vol. 780, pp. 30–48.

Kennedy, P. J., Stallings, L., and Peterson, M. B., 1983, "A Study of Surface Damage at Low Amplitude Slip," ASLE-ASME Conf., Hartford, Conn., 18–20 Oct., 1983.

Lubkin, J. L., 1951, "The Torsion of Elastic Spheres in Contact," ASME JOURNAL OF APPLIED MECHANICS, Vol. 73, pp. 183–187.

Michell, J. H., 1899, "The Transmission of Stress Across a Plane of Discontinuity in an Isotropic Elastic Body," *Proc. London Math. Soc.*, Vol. 31, pp. 183–192.

Mindlin, R. D., 1949, "Compliance of Elastic Bodies in Contact," ASME JOURNAL OF APPLIED MECHANICS, Vol. 16, pp. 259–268.

Sackfield, A., and Hills, D. A., 1983a, "Some Useful Results in the Classical Hertz Contact Problems," *Jnl. Strain Anal.*, Vol. 18, pp. 101–105.

Sackfield, A., and Hills, D. A., 1983b, "Some Useful Results in the Tangentially Loaded Hertz Contact Problem," *Jnl. Strain Anal.*, Vol. 18, pp. 107–110.

Sackfield, A., and Hills, D. A., 1983c, "A Note on the Hertz Contact Problem: A Correlation of Standard Formulae," *Jnl. Strain Anal.*, Vol. 18, pp. 195–197.

Timoshenko, S., and Goodier, J. N., 1951, *Theory of Elasticity*, 3rd. ed., New York, pp. 409–414.

APPENDIX

Some intermediate steps in the determination of equation (28) are as follows. Combining equations (19) and (20), and specializing s to c gives

$$\frac{\sigma_{r\theta}^o}{fp_o}=\frac{1}{r^2}\int_o^c \frac{g(t)t\,dt}{\sqrt{r^2-t^2}}-\frac{1}{r^2}\int_o^c \frac{g'(t)t^2dt}{\sqrt{r^2-t^2}}$$

$$=\frac{1}{r^2}\int_o^c \frac{t^3}{\sqrt{r^2-t^2}}\left[\frac{t}{t'}\right]\frac{d}{dt'}\left\{\frac{g(t)}{t}\right\}dt \tag{33}$$

where $g(t)=g_o'(t)+g_1'(t)$

And

$$-\frac{d}{dt'}\left\{\frac{g(t)}{t}\right\}=\frac{2}{\pi}\left\{\frac{t'}{t^2}E(\eta,t')-\frac{kt'c}{t^2\sqrt{t'^2-k^2}}\right.$$

$$\left.+\frac{t'}{t^2}E(\chi,t')+\frac{k}{c}\,\frac{t'}{\sqrt{t'^2-k^2}}\right\}$$

$$=\frac{2t'}{\pi t^2}\left[E(\eta,t')+E(\chi,t')-\frac{k}{c}\sqrt{t'^2-k^2}\right] \tag{34}$$

Substituting equation (34) into (33) and carrying out the integration yields (28) directly.

Surface Waves Guided by the Exterior of a Rectangular Elastic Solid

A. K. Gautesen
Ames Laboratory and
Department of Mathematics,
Iowa State University,
Ames, IA 50011

We show that surface waves can be guided on the exterior of an isotropic elastic bar with a rectangular cross section. We assume that the dimensionless wavenumber is sufficiently large that elastodynamic ray theory is valid. Dispersion relations are obtained and representative curves for various cross sections are shown.

1 Introduction

The study of surface waves guided by elastic solids is of interest in ultrasonics, geophysics, the design of mechanical devices for electronic circuitry, and other areas. White (1970) has discussed applications for electronic circuitry; Tiersten (1969) has considered elastic surface waves guided by thin films; and Freund (1972) has shown that surface waves can be guided by a slit in an elastic solid.

We show that an isotropic elastic solid with a rectangular cross section and infinite length can guide surface waves on its exterior. Our results are presented from the point of view of elastodynamic ray theory. The application of this theory to the scattering of waves by cracks in elastic solids is discussed by Achenbach, Gautesen and McMaken (1982). We make the assumption that the corners of the rectangular solid are sufficiently far apart that they can be treated independently.

This assumption implies that the wavenumber times the smallest dimension of the rectangular cross section should be large. Experience (e.g., see Achenbach et al., 1982) has shown that this number need not be very large to obtain good results. This assumption also requires knowledge of the problem of the scattering of obliquely incident surface waves in an elastic quarterspace (the canonical problem). Gautesen (1986) has recently studied this problem. From the discussion presented herein, it is clear that surface waves can also be guided by a rectangular solid whose cross section is a polygon. However, the lack of knowledge of the associated canonical problem(s) prevents one from obtaining dispersion relations.

In the next section we discuss ray theory for the canonical problem. In Section 3 we derive the dispersion relations, and in Section 4 we discuss our results.

2 The Associated Canonical Problem

We begin with a discussion of ray theory for the associated canonical problem. We refer the reader to Achenbach et al. (1982) for a summary of ray theory for elastodynamic diffraction by cracks. All field quantities contain a common factor of $\exp[-i\omega t]$, where ω is the circular frequency. This factor is hereafter suppressed.

Consider a homogeneous, isotropic, linearly elastic quarterspace. Let the z axis coincide with the corner. Let the incident wave be a Rayleigh surface wave propagating on one of the free surfaces, and let the direction of propagation make an acute angle ϕ with respect to the z axis. This problem has been treated by Gautesen (1986).

When an incident surface-wave ray intersects the corner, it (1) reflects a surface-wave ray on the same free surface and transmits a surface-wave ray to the other free surface, and (2) diffracts two (quarter) cones of body-wave rays corresponding to longitudinal and transverse motions. Energy propagates into the elastic medium via the body-wave rays. The half angles ϕ_L and ϕ_T of these diffracted cones of rays are related to the incident angle ϕ by

$$\cos\phi_\alpha = (c_\alpha/c_R)\cos\phi, \quad \alpha = L, T \tag{2.1}$$

where c_L, c_T and c_R denote the speeds of longitudinal, transverse and Rayleigh waves, respectively. When

$$\phi < \phi_{cr} \equiv \cos^{-1}(c_R/c_T) \tag{2.2}$$

both ϕ_L and ϕ_T are imaginary angles and the body-wave rays are nonpropagating. For this case, the sum of the energies carried by the reflected and transmitted surface waves equals the energy carried by the incident wave.

The reflected and transmitted surface-wave rays each make an angle ϕ with respect to the z axis. The amplitude and phase of the reflected (u_r) and transmitted (u_t) surface-wave rays are related to the amplitude and phase of the incident $u_i(P)$ surface-wave rays evaluated at the point of intersection (P) with the corner by

$$u_\alpha = u_i(P) D_\alpha \exp[ik_R d_\alpha], \quad \alpha = r, t \tag{2.3}$$

where $k_R = \omega/c_R$, D_r and D_t are the reflection and transmission coefficients, respectively, and d_r and d_t denote distance measured from P along the reflected and transmitted surface-wave rays, respectively. When ϕ satisfies (2.2), D_r and D_t satisfy $|D_t \pm D_r| = 1$ (see Gautesen, 1986). Thus

$$D_r = Re^{i\theta} \tag{2.4}$$

$$D_t = \pm iTe^{i\theta} \tag{2.5}$$

where R, T, θ are real nonnegative numbers and

$$R^2 + T^2 = 1. \tag{2.6}$$

Contributed by the Applied Mechanics Division for publication in the JOURNAL OF APPLIED MECHANICS.

Discussion on this paper should be addressed to the Editorial Department, ASME, United Engineering Center, 345 East 47th Street, New York, N.Y. 10017, and will be accepted until two months after final publication of the paper itself in the JOURNAL OF APPLIED MECHANICS. Manuscript received by ASME Applied Mechanics Division, October 3, 1985; final revision, November 21, 1985.

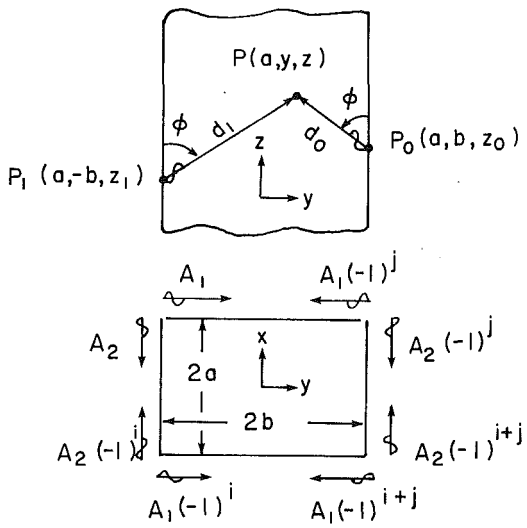

Fig. 1 Geometry and coordinate systems

3 Dispersion Relations for Waveguide

In this section we derive the dispersion relations for surface waves guided on the exterior of a homogeneous, isotropic, linearly elastic, rectangular solid which extends to infinity in the z direction. We find it convenient to divide the modes into modes whose displacements are symmetric ($j=0$) and antisymmetric ($j=1$) with respect to the xz plane, and symmetric ($i=0$) and antisymmetric ($i=1$) with respect to the yz plane. We regard the surface waves propagating over each of the free surfaces as being comprised of surface-wave rays such that a given surface-wave ray propagates away from the corners at an angle $\phi < \phi_{cr}$ with respect to the z axis and is normalized so that the amplitude and phase at a point of emanation ($\pm a$, $\pm b$, z_0) is given by the factor shown in Fig. 1 times $\exp[ik_R z_0 \cos\phi]$. Thus, for example, the displacements of surface waves on the top free surface can be expressed as

$$\mathbf{u}(a,y,z) = u_1 \mathbf{e}_1 + u_0 \mathbf{e}_0 \tag{3.1}$$

where

$$\mathbf{e}_k = (-\cos\eta, -(-1)^k \sin\phi \sin\eta, \cos\phi \sin\eta)/\cos^{1/2}(2\eta)$$

$$\eta = 2i \cosh^{-1}(c_T/c_R) \tag{3.2}$$

$$u_k = (-1)^{j(k+1)} A_1 e^{ik_R(z_k \cos\phi + d_k)} \tag{3.3}$$

and z_k and d_k follow from Fig. 1 as

$$z_k = z - d_k \cos\phi \tag{3.4}$$

$$d_k = (b - (-1)^k y)/\sin\phi \tag{3.5}$$

When (3.4) and (3.5) are substituted into (3.3) we find that

$$u_k = A_1(-1)^{j(k+1)} \exp[ik_R\{(b-(-1)^k y)\sin\phi + z\cos\phi\}] \tag{3.6}$$

Upon substitution of (3.6) into (3.1), we see that $\mathbf{u}$ takes on the appearance of a standing wave. Also, we note that

$$\mathbf{e}_k \cdot \mathbf{e}_k^* = 1 \tag{3.7}$$

where the asterisk denotes the complex conjugate. Thus u_k represents the amplitude and phase of the surface-wave ray on the top free surface which emanates from the point (a, $(-1)^k b$, z_k).

We now obtain the dispersion relations. In Fig. 2, we have drawn the top and left free surfaces side by side. The ray on the top free surface emanating from the point P_0 is generated by reflection of the ray emanating from P_1 and by transmission of the ray emanating from P_2. Thus the amplitude and phase of u_1 defined by (3.3) at P_0 must equal the sum of the amplitude and phases of the rays emanating from P_1 and P_2 evaluated at P_0 times the appropriate reflection or transmission coefficient, and we have

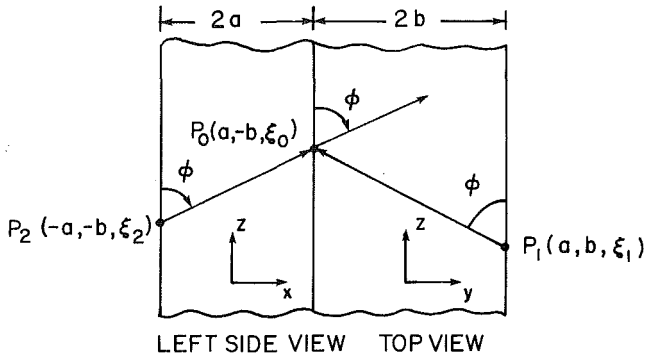

Fig. 2 Reflection and transmission of surface-wave rays at a corner

$$A_1 \exp[ik_R \xi_0 \cos\phi] = (-1)^j A_1 \exp[ik_R(\xi_1 \cos\phi + r_1)] D_r + (-1)^i A_2 \exp[ik_R(\xi_2 \cos\phi + r_2)] D_t \tag{3.8}$$

where

$$r_1 = 2b/\sin\phi \tag{3.9}$$

and

$$r_2 = 2a/\sin\phi \tag{3.10}$$

represent the distance traversed by a ray.

At this point, we assume that the corners are sufficiently far apart that the interaction of the corners is negligible. Therefore, in (3.8) we can use the reflection and transmission coefficients corresponding to the canonical problem discussed in Section 2. This assumption requires that $k_R a >> 1$ and $k_R b >> 1$. We remark that Achenbach, Gautesen, and McMaken (1982) have shown that, for some crack problems, diffraction theory yields results which compare well with numerical results at moderate values of the dimensionless wavenumber.

Again, with respect to the notation of Fig. 2, the ray emanating from the P_0 on the left free surface (not shown in Fig. 2) is generated by transmission of the ray emanating from P_1 and by reflection of the ray emanating from P_2. Thus,

$$A_2 \exp[ik_R \xi_0 \cos\phi] = (-1)^j A_1 \exp[ik_R(\xi_1 \cos\phi + r_1)] D_t + (-1)^i A_2 \exp[ik_R(\xi_2 \cos\phi + r_2)] D_r \tag{3.11}$$

If a similar procedure is repeated at any of the other corners, we would again arrive at (3.8) and (3.11). These equations represent a homogeneous, linear system of equations for the amplitudes A_1 and A_2. For this system to have nontrivial solutions, its determinant must vanish. Thus,

$$\cos[k_r(a+b)\sin\phi + \theta + (i+j)\pi/2] - R\cos[k_R(b-a)\sin\phi + (j-i)\pi/2] = 0 \tag{3.12}$$

are dispersion relations, where $i = 0, 1$ and $j = 0, 1$ determines the relative symmetry. In arriving at (3.12), we have used (2.4)–(2.6), (3.9), (3.10) and the relations $\xi_k = \xi_0 - r_k \cos\phi$. The apparent speed of the guided wave in the z direction is

$$v = c_R/\cos\phi \tag{3.13}$$

4 Discussion

In Fig. 3 we have plotted v/c_R versus $k_R(a+b)$ for each of the lowest modes for $b/a = 1, 3, 5, 7$, and for Poisson's ratio $\nu = 1/4$. The solid curve represents the mode whose displacements are symmetric with respect to both the xz and yz planes. As the speed of the guided wave v approaches c_R, the wavenumber is asymptotically $0((v-c_R)^{-1/2})$. In contrast, the mode whose displacements are antisymmetric with respect to both the xz and yz planes (the dotted curves) has a finite limit as v approaches c_R.

The modes whose displacements have different symmetries

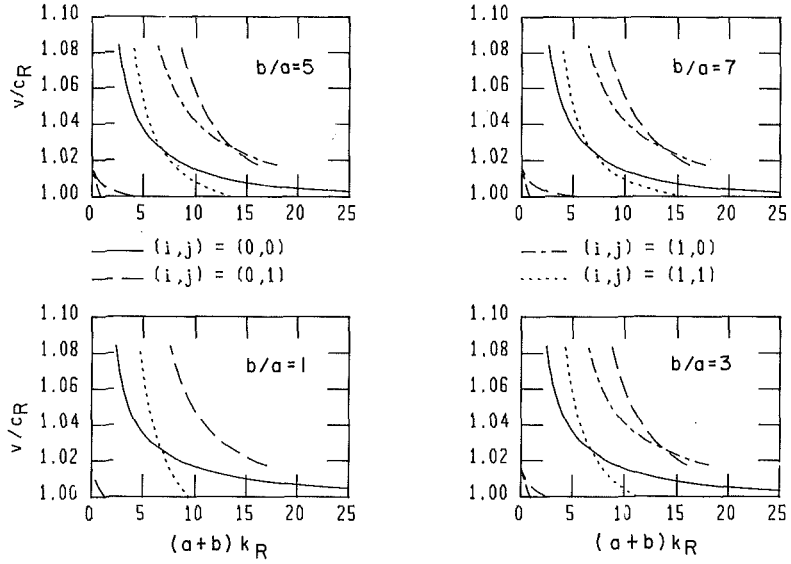

Fig. 3 Dispersion curves for the lowest modes for *b/a* = 1, 3, 5, 7

with respect to the xz and yz planes are represented in Fig. 3 by the dashed and dot-dashed curves. For $b/a = 1$, these curves coincide. We observe that when the speed v of the guided wave becomes smaller than a critical speed $v_{cr} \approx 1.018\, c_R$, the wave number k_R jumps to zero and then increases again as v decreases. Recall that for this theory to be valid, $k_R(a+b) >> 1$. Thus, we have no guarantee that this jump actually exists.

Acknowledgment

This work was supported (in part) by the Applied Mathematical Sciences subprogram of the Office of Energy Research, US Department of Energy, under Contract No. W-7405-ENG-82.

References

Achenbach, J. D., Gautesen, A. K., and McMaken, H., 1982, *Ray Methods for Waves on Elastic Solids*, Pitman, Boston.

Freund, L. B., 1972, "Surface Waves Guided by a Slit in an Elastic Solid," ASME JOURNAL OF APPLIED MECHANICS, Vol. 39, pp. 1027–1032.

Gautesen, A. K., 1986, "Scattering of an Obliquely Incident Rayleigh Wave by an Elastic Quarterspace," *Wave Motion*, Vol. 8, pp. 27–41.

Tiersten, H. F., 1969, "Elastic Surface Waves Guided by Thin Films," *Journal of Applied Physics*, Vol. 40, pp. 770–789.

White, R. M., 1970, "Surface Elastic Waves," *Proceedings of the IEEE*, Vol. 58, pp. 1238–1276.

M. H. Santare
Student Mem. ASME

L. M. Keer
Fellow ASME

Department of Civil Engineering,
Northwestern University,
Evanston, IL 60201

Interaction Between an Edge Dislocation and a Rigid Elliptical Inclusion

A solution is presented for the two-dimensional elastic field created by the interaction of an edge dislocation with a rigid elliptical inclusion. The complex potential approach by Muskhelishvili is used and a closed-form solution is obtained. Contour plots for the glide component of the Peach–Koehler forces are presented. Particular attention is paid to the rigid body of the inclusion with respect to the dislocation.

Introduction

Interactions between dislocations and inhomogeneities have been a topic of considerable research. Greater understanding of material defects can be gained through the solution of suitable elasticity problems. These solutions can be used to study phenomena such as crack growth in composites and strain hardening in metal alloys.

The problem of a circular elastic inhomogeneity near an edge dislocation was solved in terms of Airy's stress potentials by Dundurs and Mura (1964). Later, Dundurs and Sendeckyj (1965) solved the allied problem where the dislocation is within the circular inhomogeneity. The interaction between a dislocation and a crack was investigated by Lo (1978) for a flat crack and Vitek (1975) and Vitek and Hirth (1977) for the elliptical crack with a finite root radius.

Recently, the solution for a dislocation inside an elastic elliptical inhomogeneity has been solved in the form of an infinite series by Warren (1983). The same technique was used by Stagni and Lizzio (1983) for the dislocation located outside an elastic elliptical inhomogeneity. While these solutions are perfectly general in geometry and material parameters, the infinite series form of the solution may prove to be cumbersome in applications.

In crack problems, the dislocation solution must be integrated over the path of the crack and computational complexity may become an important issue. A closed-form solution is preferable in such problems to reduce the number of iterations necessary to obtain convergence. In an earlier paper, Stagni (1982) mentions the proper integral expressions that are required to find the closed-form solution for a rigid inclusion under a general loading, but does not solve them for the dislocational case nor does he include the rigid body motion of the inclusion.

In the following, the closed-form solution is obtained for a dislocation near a rigid elliptical inclusion. The analysis is in two dimensions and employs complex potentials. The elastic matrix is infinite with no stresses and no rotation of infinity. Particular attention is paid to the rigid body motion of the inclusion relative to the dislocation.

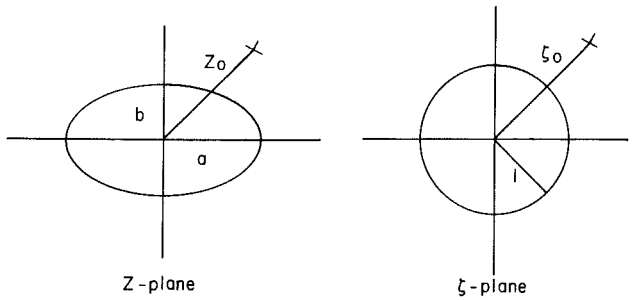

Fig. 1 Geometry of problem; *a*) physical; *b*) mapped plane

Problem Formulation

To solve the problem in terms of complex potentials, the methods of Muskhelishvili (1954) are used. The stresses and displacements are expressed in terms of two complex functions ϕ and ψ such that

$$\sigma_{xx}+\sigma_{yy}=2[\phi'(z)+\overline{\phi'(z)}] \tag{1}$$

$$\sigma_{yy}-\sigma_{xx}+2i\sigma_{xy}=2[\bar{z}\phi''(z)+\psi'(z)] \tag{2}$$

$$2\mu(u+iv)=\kappa\phi(z)-z\overline{\phi'(z)}-\overline{\psi(z)} \tag{3}$$

where $z=x+iy$, μ is the shear modulus of the matrix, $\kappa=3-4\nu$ for the plane strain problem, $\kappa=(3-\nu)/(1+\nu)$ for plane stress, where ν is Poisson's ratio of the matrix. Primes denote differentiation with respect to z and a superimposed bar denotes the complex conjugate.

The boundary condition along the surface of the rigid inclusion is

$$u+iv=u_o+iv_o+i\epsilon_o z \quad z\in \text{inclusion surface} \tag{4}$$

where u_o and v_o are rigid body translations and ϵ_o is a rigid body rotation. The boundary condition at infinity is that the stresses must vanish

$$\sigma_{xx}\to 0,\sigma_{yy}\to 0,\sigma_{xy}\to 0 \quad z\to\infty \tag{5}$$

This condition will be satisfied automatically as a consequence of the solution procedure. At the dislocation, $z=z_o$,

Contributed by the Applied Mechanics Division for publication in the JOURNAL OF APPLIED MECHANICS.

Discussion on this paper should be addressed to the Editorial Department, ASME, United Engineering Center, 345 East 47th Street, New York, N. Y. 10017, and will be accepted until two months after final publication of the paper itself in the JOURNAL OF APPLIED MECHANICS. Manuscript received by ASME Applied Mechanics Division, September 16, 1985.

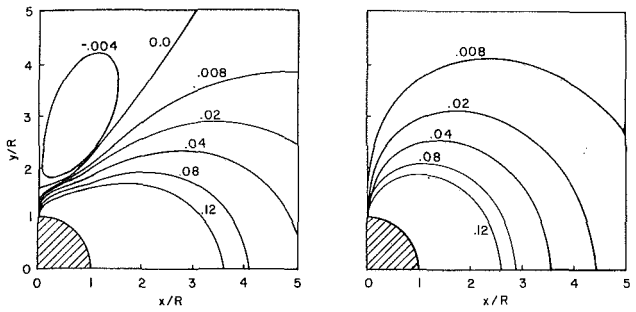

Fig. 2 Contour plots of the dimensionless glide force for $m = 0$, $b_y = 0$, $\kappa = 2.6$; *a*) $\epsilon_o = 0$; *b*) $\epsilon_o \neq 0$

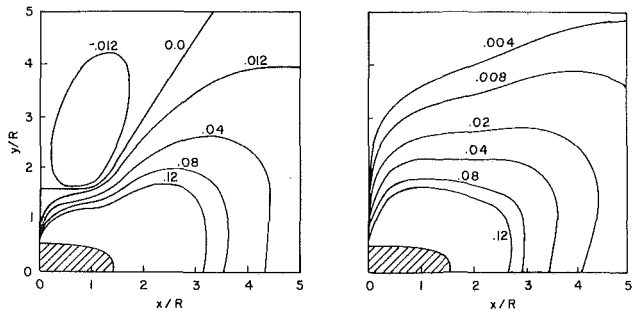

Fig. 3 Contour plots of the dimensionless glide force for $m = 0.5$, $b_y = 0$, $\kappa = 2.6$; *a*) $\epsilon_o = 0$; *b*) $\epsilon_o \neq 0$

the solution should have a singularity of the proper form, namely,

$$\phi_d(z) = \gamma \log (z - z_o) \qquad (6)$$

$$\psi_d(z) = \bar{\gamma} \log (z - z_o) - \gamma \bar{z}_o/(z - z_o) \qquad (7)$$

where $\gamma = \mu\, \mathbf{b}/i\pi(\kappa+1)$, $\mathbf{b} = b_x + ib_y$, and b_x and b_y are the cartesian components of the Burgers vector.

The resultant force along an arc AB acting on the material to the left of the arc is given by Muskhelishvili (1954) as

$$F = -i[\phi(z) + z\overline{\phi'(z)} + \overline{\psi(z)}]_A^B. \qquad (8)$$

Similarly, the resultant moment about the origin due to this force is

$$M = \mathrm{Re}[\textstyle\int \psi(z)dz - z\psi(z) - z\bar{z}\phi'(z)]_A^B \qquad (9)$$

An additional condition of the solution is that expressions (8) and (9) are zero when arc AB is taken to be the elliptical surface. This condition is equivalent to requiring that the inclusion be in equilibrium.

Method of Solution

The geometry of the problem is shown in Fig. 1. The problem can be simplified by mapping the elastic region onto a region of simpler geometry. The function

$$z = \omega(\zeta) = R\left(\zeta + \frac{m}{\zeta}\right) \qquad (10)$$

where

$$R = \frac{a+b}{2}, \quad m = \frac{a-b}{a+b} \qquad (11),(12)$$

maps the region outside an ellipse with major axis a and minor axis b onto the region outside the unit circle $|\zeta| = 1$. Equations (1)–(9), valid on the physical z plane, can be rewritten to apply on the transformed plane by the substitutions

$$z = \omega(\zeta) \qquad (13)$$

$$z_o = \omega(\zeta_o) \qquad (14)$$

$$\phi'(z) = \phi'(\zeta)/\omega'(\zeta) \qquad (15)$$

$$\psi'(z) = \psi'(\zeta)/\omega'(\zeta) \qquad (16)$$

where it is understood that $\phi(\zeta)$ implies $\phi(\omega(\zeta))$. Consider the problem of an edge dislocation in a homogeneous infinite body. The stresses and displacements are defined by the potentials in equations (6) and (7). The displacement of the points forming an ellipse centered at the origin can be obtained by substituting equations (6) and (7) into equation (3) and using equations (13)–(16) to find

$$2\mu(u_d + iv_d) = \kappa\gamma \log[R(\zeta - \zeta_o + m/\zeta - m/\zeta_o)] - \gamma \log[R(m\zeta - \bar{\zeta}_o + 1/\zeta - m/\bar{\zeta}_o)] - \bar{\gamma}\,\frac{\zeta - \zeta_o + m/\zeta - m/\zeta_o}{m\zeta - \bar{\zeta}_o + 1/\zeta - m/\bar{\zeta}_o} \quad |\zeta_o| > |\zeta| = 1 \qquad (17)$$

The solution for the rigid inclusion now consists of finding a set of potentials ϕ_* and ψ_*, so that

$$\phi(\zeta) = \phi_d(\zeta) + \phi_*(\zeta) \qquad (18)$$

$$\psi(\zeta) = \psi_d(\zeta) + \psi_*(\zeta) \qquad (19)$$

satisfy the conditions (4)–(7); thus ϕ^* and ψ^* should be regular in the region $|\zeta| > 1$, produce stresses that vanish at $|\zeta| \to \infty$ and satisfy the displacement boundary condition

$$u^* + iv^* = u_o + iv_o + i\epsilon_o R\left(\zeta + \frac{m}{\zeta}\right) - (u_d + iv_d) \quad |\zeta| = 1. \qquad (20)$$

Potentials that satisfy all of the above conditions can be calculated through the evaluation of two Cauchy integrals, see Muskhelishvili (1954). The solution can be written,

$$\phi(\zeta) = \gamma \log [R(\zeta - \zeta_o + m/\zeta - m/\zeta_o)] + \frac{1}{\kappa}\gamma\log[(\zeta - 1/\bar{\zeta}_o)/\zeta] - \gamma\log[(\zeta - m/\zeta_o)/\zeta] - \kappa\,\frac{\bar{\gamma}}{m}\,\frac{(1/\bar{\zeta}_o - m/\zeta_o)(1/\bar{\zeta}_o - \zeta_o)}{(1/\bar{\zeta}_o - \bar{\zeta}_o/m)(1/\bar{\zeta}_o - \zeta)} + 2\mu i\epsilon_o R m/\kappa\zeta \qquad (21)$$

$$\psi(\zeta) = \bar{\gamma}\log[R(\zeta - \zeta_o + m/\zeta - m/\zeta_o)] - \gamma\,\frac{\bar{\zeta}_o + m/\bar{\zeta}_o}{\zeta - \zeta_o + m/\zeta - m/\zeta_o} + \kappa\bar{\gamma}\log[(\zeta - 1/\bar{\zeta}_o)/\zeta] - \bar{\gamma}\log[(\zeta - m/\zeta_o)/\zeta] + \gamma m\,\frac{(m/\zeta_o - 1/\bar{\zeta}_o)(m/\zeta_o - \bar{\zeta}_o/m)}{(m/\zeta_o - \zeta_o)(m/\zeta_o - \zeta)} + 2\mu i\epsilon_o R/\zeta - \zeta\,\frac{1 + m\zeta^2}{\zeta^2 - m}\,\phi'^*(\zeta) \qquad (22)$$

These potentials have the proper singular behavior at the point $\zeta = \zeta_o$, and the stresses they define through (1) and (2) vanish as $\zeta \to \infty$. The only conditions that remain to be satisfied are the equilibrium conditions on the inclusion. Since the ellipse was mapped onto the unit circle, arc AB is taken as $|\zeta| = 1$ in equations (8) and (9).

Because arc AB is a closed contour, the only terms that will contribute to the force and moment along AB are multivalued terms in which the branch cut crosses the contour. No such terms exist in the expression (8) and the condition

$$\left[\phi(\zeta) + \frac{\omega(\zeta)}{\overline{\omega'(\zeta)}}\,\overline{\phi'(\zeta)} + \psi(\zeta)\right]_{|\zeta|=1} = 0 \qquad (23)$$

is satisfied. In expression (9), however, the integral term contributes to the net moment. The condition

$$\left[\textstyle\int \psi(\zeta)\omega'(\zeta)d\zeta - \omega(\zeta)\psi(\zeta) - \dfrac{\omega(\zeta)\overline{\omega(\zeta)}}{\overline{\omega'(\zeta)}}\,\overline{\phi'(\zeta)}\right]_{|\zeta|=1} = 0 \qquad (24)$$

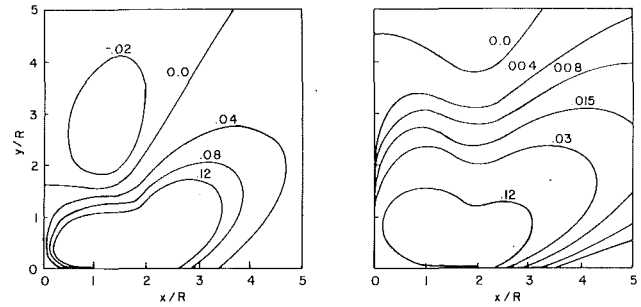

Fig. 4 Contour plots of the dimensionless glide force for $m = 1$, $b_y = 0$, $\kappa = 2.6$; a) $\epsilon_o = 0$; b) $\epsilon_o \neq 0$

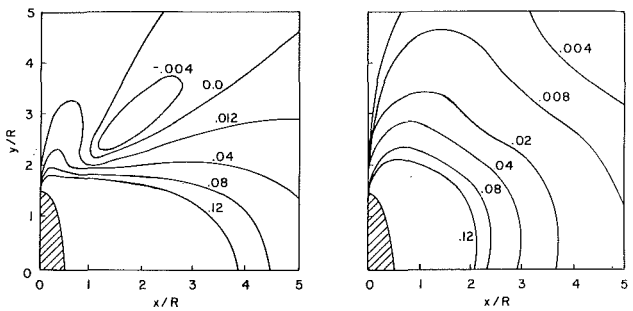

Fig. 5 Contour plots of the dimensionless glide force for $m = -0.5$, $b_y = 0$, $\kappa = 2.6$; a) $\epsilon_o = 0$; b) $\epsilon_o \neq 0$

can only be satisfied by an appropriate choice of ϵ_o, the rigid body rotation. By substituting (24) into (26) and solving, it is found that

$$\epsilon_o = \mathrm{Re}\Big\{ i[-\kappa\tilde{\gamma}/\bar{\zeta}_o + \tilde{\gamma}m/\zeta_o + \gamma m^2/\zeta_o - \gamma m/\kappa\bar{\zeta}_o - \gamma m \frac{(m/\zeta_o - 1/\bar{\zeta}_o)(m/\gamma_o - \bar{\zeta}_o/m)}{(m/\zeta_o - \zeta_o)} + \frac{\tilde{\gamma}}{\kappa} \frac{(1/\bar{\zeta}_o - m/\zeta_o)(1/\zeta_o - \zeta_o)}{(1/\bar{\zeta}_o - \bar{\zeta}_o/m)} \Big\} / 2\mu R\left(1 + \frac{m^2}{\kappa}\right). \quad (25)$$

Of particular interest in dislocation interaction problems is the effect of the stress field on the dislocation. A common measure of this effect is the Peach-Koehler force which can be written in terms of complex potentials

$$F_x + iF_y = i\left[\bar{\mathbf{b}}\left(\frac{\omega(\zeta)}{\overline{\omega'(\zeta)}}\left[\frac{\overline{\phi_*'(\zeta)}}{\omega'(\zeta)}\right]' + \frac{\overline{\psi_*'(\zeta)}}{\overline{\omega'(\zeta)}}\right) - \mathbf{b}\left(\frac{\phi_*'(\zeta)}{\omega'(\zeta)} + \frac{\overline{\phi_*'(\zeta)}}{\overline{\omega'(\zeta)}}\right)\right]_{\zeta=\zeta_o} \quad (26)$$

where F_x and F_y are the cartesian components of the Peach-Koehler force.

Results and Conclusions

In general, stresses will be produced by both the rigid body translation and rotation of the inclusion with respect to the dislocation. It is interesting that the force equilibrium condition was satisfied trivially, while the moment equilibrium was not. The displacement defined in equation (17), in general, consists of three parts: deformation, rigid body rotation, and rigid body translation. The potentials ϕ_* and ψ_* were calculated to remove the entire displacement along the contour $|\zeta| = 1$. However, as noted by Muskhelishvili (1954), these potentials can only solve the problem within a rigid body translation. Therefore, ϕ_* and ψ_* remove the deformation and the rigid body rotation only.

Under the influence of the potentials ϕ_d and ψ_d alone, the infinite medium is in a state of equilibrium. Therefore, the portion of the medium outlined by the elliptic contour is also in equilibrium. Indeed this can be shown through equations (8) and (9). When the displacement boundary condition is enforced through the addition of ϕ_* and ψ_*, additional forces are imposed along the contour. The forces imposed by the elimination of the deformation are self equilibrating and, therefore, do not effect equilibrium. The forces imposed by the elimination of the rigid body rotation, however, impose a net moment on the contour. To satisfy moment equilibrium

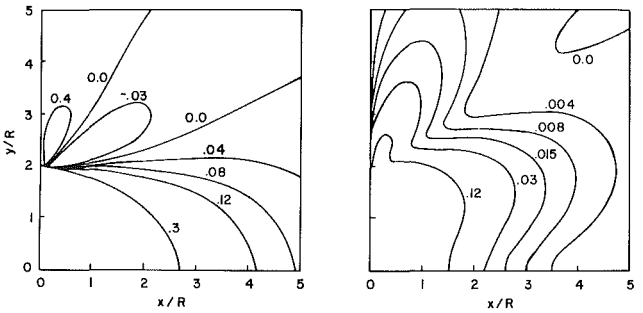

Fig. 6 Contour plots of the dimensionless glide force for $m = -1$, $b_y = 0$, $\kappa = 2.6$; a) $\epsilon_o = 0$; b) $\epsilon_o \neq 0$

(equation (9)) an additional rigid body rotation must be imposed, namely ϵ_o.

Through the inclusion or exclusion of the rigid body rotation ϵ_o, two different problems are solved. If $\epsilon_o = 0$, the inhomogeneity is not allowed to rotate with respect to the dislocation. This corresponds physically to an inclusion that is kept from rotating by some external moment. If ϵ_o is calculated so that the inclusion is in equilibrium, the problem corresponds to the physical case where no external moment acts on the inclusion.

Figures 2-6 shows that there is a significant difference between the two problems. Each figure shows the glide component of the Peach-Koehler force, $\mathbf{F}\cdot\mathbf{b}/|\mathbf{b}|$, for a specific geometry. The force is nondimensionalized by dividing through by $\mathbf{b}|\gamma|$, and in all cases $b_y = 0$ and $\kappa = 2.6$. The first plot in each figure corresponds to the case when $\epsilon_o = 0$; these results agree with those found by Stagni and Lizzio (1983). The second plot in each figure corresponds to the case where the inclusion is in equilibrium, $\epsilon_o \neq 0$. In all the plots, the y axis is a line of zero glide force.

In regions where the glide components of the Peach-Koehler force are negative, the dislocation is attracted to the y axis. A positive value indicates that the dislocation is repelled from the y axis. Therefore, when the glide force is zero, the position can be thought of as an equilibrium position for the dislocation. Observations regarding the cases where $\epsilon_o = 0$ are made in Stagni and Lizzio (1983) and, therefore, only the effect of the rigid body rotation will be discussed here.

The rigid body rotation most profoundly effects the regions of negative glide force and the loci of equilibrium positions. In Figs. 2, 3, and 5 the negative glide force regions are eliminated altogether when the rigid body rotation is included. Consequently, the only equilibrium positions, are the y axis and in each of these the equilibrium is unstable. Figures 4 and 6 show that including the rigid body rotation pushes the line of equilibrium positions away from the inclusion. In these cases there can be both stable and unstable equilibria.

Acknowledgment

The authors are grateful for support of this research through the National Science Foundation, Grant MEA-8117106, and the National Institute of Handicap Research, Grant G008300070.

References

Dundurs, J., and Mura, T., 1964, "Interaction Between an Edge Dislocation and a Circular Inclusion," *J. Mech. Phys. Sol.*, Vol. 12, pp. 177–189.

Dundurs, J., and Sendeckyj, G. P., 1965, "Edge Dislocation Inside a Circular Inclusion," *J. Mech. Phys. Sol.*, Vol. 13, pp. 141–147.

Lo, K. K., 1978, "Analysis of Branched Cracks," ASME JOURNAL OF APPLIED MECHANICS, Vol. 45, pp. 797–802.

Muskhelishvili, N. I., 1954, *Some Basic Problems in the Theory of Elasticity*, 4th ed., Noordhoff, Leyden, The Netherlands.

Stagni, L., 1982, "On the Elastic Field Perturbation by Inhomogeneities in Plane Elasticity," *ZAMP*, Vol. 33, pp. 315–325.

Stagni, L., and Lizzio, R., 1983, "Shape Effects in the Interaction Between an Edge Dislocation and an Elliptical Inhomogeneity," *Appl Phys.*, Vol. A30, pp. 217–221.

Vitek, V., 1975, "Yielding from a Crack with Finite Root-Radius Loaded in Uniform Tension," *J. Mech. Phys. Sol.*, Vol. 24, pp. 67–76.

Vitek, V., and Hirth, J. P., 1977, "Line Singularity Fields in the Presence of a Crack of Elliptical Cross-Section," *Scripta Metall.*, Vol. 11, pp. 339–340.

Warren, W. E., 1983, "The Edge Dislocation Inside an Elliptical Inclusion," *Mech. Materials*, Vol. 2, pp. 319–330.

A Green's Function Solution for Plane Anisotropic Contact Problems

G. R. Miller
Assistant Professor of Civil Engineering,
University of Washington,
Seattle, Washington 98195

An analytical expression for the stresses in contacting anisotropic cylinders containing a singularity is derived, including the effects of sliding friction. The solution is obtained using complex variables, and is expressed in terms of piecewise analytic functions. Concentrated force and edge dislocation type singularities are both considered, providing a solution useful for various boundary integral applications.

1 Introduction

This paper presents the development of a general Green's function solution for use in plane contact interaction problems. Two anisotropic cylinders are considered to be in contact. A concentrated force or an edge dislocation singularity exists in one of the bodies (see Fig. 1), and an analytical expression for the stresses in either body is obtained including the effects of sliding friction. The method of solution is based on complex variable techniques, and in this respect is similar to the work of Chen (1969), who developed his work based on results presented by Green and Zerna (1954). In addition to including fundamental singularities, however, the solution derived here also differs from that of Chen in the manner in which friction is treated. For simplicity Chen considered a single anisotropic body indented by a rigid punch, and he assumed that the tangential and normal load effects could be decoupled. This is approximately true, but in this paper the two effects are allowed to remain coupled, and the expressions obtained consider both indenting bodies to be elastic.

The usefulness of the solution derived here lies in the fact that it provides a means of solving a variety of contact interaction problems using boundary integrals. This type of approach already has been used in a series of papers dealing with the behavior of cracks and inclusions near contacts in the case of rigid indenters indenting isotropic bodies (Miller and Keer, 1983, Bryant et al., 1985, and Miller et al., 1985). The advantage of this technique is that it allows the crucial interactions to be modeled analytically, and requires numerical evaluation along a reduced number of boundaries. The purpose of the present paper is to provide the necessary analytical framework to enable the extension of such analyses to the case of anisotropic bodies.

2 Formulation

The stresses and displacements in an anisotropic elastic body may be expressed as follows in the case of planar deformation or loading:

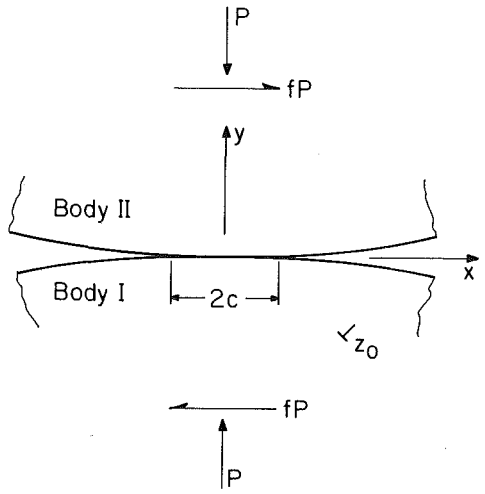

Fig. 1 Problem geometry showing two anisotropic cylinders in contact, one of which contains a singularity located at the point z_0

$$\sigma_{xx} = \lambda_1^2\phi_1'(z_1) + \bar{\lambda}_1^2\bar{\phi}_1'(\bar{z}_1) + \lambda_2^2\phi_2'(z_2) + \bar{\lambda}_2^2\bar{\phi}_2'(\bar{z}_2) \quad (1)$$

$$\sigma_{yy} = \phi_1'(z_1) + \bar{\phi}_1'(\bar{z}_1) + \phi_2'(z_2) + \bar{\phi}_2'(\bar{z}_2) \quad (2)$$

$$\tau_{xy} = -\lambda_1\phi_1'(z_1) - \bar{\lambda}_1\bar{\phi}_1'(\bar{z}_1) - \lambda_2\phi_2'(z_2) - \bar{\lambda}_2\bar{\phi}_2'(\bar{z}_2) \quad (3)$$

$$u + iv = p(\lambda_1)\phi_1(z_1) + p(\bar{\lambda}_1)\bar{\phi}_1(\bar{z}_1) + p(\lambda_2)\phi(z_2) + p(\bar{\lambda}_2)\bar{\phi}_2(\bar{z}_2) \quad (4)$$

These expressions are derived by both Green and Zerna (1954) and Milne-Thomson (1960); the notation here follows more closely that of Milne-Thomson. In particular, z_1 and z_2 are complex variables defined as

$$z_1 = x + \lambda_1 y$$
$$z_2 = x + \lambda_2 y \quad (5)$$

in which λ_1, λ_2, and their conjugates (denoted by an overbar) are the roots of the following characteristic equation, which is dependent on the elastic constants:

$$s_{11}\lambda^4 - 2s_{16}\lambda^3 + (2s_{12} + s_{66})\lambda^2 - 2s_{26}\lambda + s_{22} = 0 \quad (6)$$

In terms of these constants, Hooke's relations are:

Contributed by the Applied Mechanics Division for publication in the JOURNAL OF APPLIED MECHANICS.
Discussion on this paper should be addressed to the Editorial Department, ASME, United Engineering Center, 345 East 47th Street, New York, N.Y. 10017, and will be accepted until two months after final publication of the paper itself in the JOURNAL OF APPLIED MECHANICS. Manuscript received by ASME Applied Mechanics Division, October 23, 1985; final revision, January 2, 1986.

$$\epsilon_{xx} = s_{11}\sigma_{xx} + s_{12}\sigma_{yy} + s_{16}\tau_{xy}$$
$$\epsilon_{yy} = s_{12}\sigma_{xx} + s_{22}\sigma_{yy} + s_{26}\tau_{xy}$$
$$\epsilon_{xy} = s_{16}\sigma_{xx} + s_{26}\sigma_{yy} + s_{66}\tau_{xy} \quad (7)$$

The functions $\phi_1(z_1)$ and $\phi_2(z_2)$ are complex valued in general and analytic within the body. The expression $p(\lambda_i)$ is introduced merely for algebraic convenience; it is given by

$$p(\lambda_i) \equiv (s_{12} - s_{16}\lambda_i + s_{11}\lambda_i^2) + i(s_{22} - s_{26}\lambda_i + s_{12}\lambda_i^2)/\lambda_i \quad (8)$$

The nature of the roots of equation (6) are discussed in some detail by Green and Zerna (1954) and this topic will not be pursued here. It will be noted, however, that the above formulation does not reduce directly to the isotropic case, due to the behavior of the roots under the assumption of isotropy.

The problem to be solved is depicted in Fig. 1, which shows two anisotropic cylinders in contact, one of which contains a dislocation or concentrated force singularity at the point (x_o, y_o). In terms of the complex variable formulation outlined above, this problem may thus be viewed as one of determining for each body the functions $\phi_1(z_1)$ and $\phi_2(z_2)$ such that the proper singular behavior is exhibited at the point (x_o, y_o), and the following boundary conditions are satisfied on the line $y = o$:

$$\left.\begin{aligned} \sigma_{yy}^I + i\tau_{xy}^I &= \sigma_{yy}^{II} + i\tau_{xy}^{II} \\ \tau_{xy}^I &= f\sigma_{yy}^I \\ \tau_{xy}^{II} &= f\sigma_{yy}^{II} \end{aligned}\right\} \quad |x| < \infty \quad (9)$$

$$\sigma_{yy}^I = \sigma_{yy}^{II} = 0 \qquad |x| > c \quad (10)$$

$$\frac{\partial v^I}{\partial x} - \frac{\partial v^{II}}{\partial x} = g(x) \qquad |x| < c \quad (11)$$

Here the superscripts I and II refer to bodies I and II, respectively. The conditions (9) arise from the requirement of continuity of traction between the bodies, and from the presence of Mohr-Coulomb sliding friction with a coefficient of friction between the two bodies defined by the parameter f. The remaining conditions (10) and (11) express the necessity of vanishing tractions outside the contact region coupled with specified displacements inside the region. It is thus a mixed boundary value problem that is to be solved. The function $g(x)$ is known; the actual expression for it will be given later in the analysis.

3 Solution

To solve the problem formulated in the previous section, the following approach is taken. First, a singular solution corresponding to a concentrated force or edge dislocation in an anisotropic half plane is developed. Second, the mixed boundary value problem corresponding to the contact between two anisotropic bodies is solved, including the displacement effects due to the singular solution. The total solution then will consist of a singular and a regular part.

3.1 Singular Part. In this section the expressions corresponding to a dislocation or concentrated force acting in an anisotropic half plane are developed. This is accomplished through combining singular solutions valid for the whole plane with solutions appropriate to the half plane using continuation techniques.

The singular potentials modeling either a dislocation or a concentrated force acting at a point $z_o = x_o + iy_o$ in an infinite plane may be written as (See Green and Zerna, 1954, or Milne-Thomson, 1960):

$$_o\phi_1(z_1) = A_1 \log (z_1 - z_1^*)$$
$$_o\phi_2(z_2) = A_2 \log (z_2 - z_2^*) \quad (12)$$

in which

$$z_1^* = \frac{1}{2}[(1 - i\lambda_1)z_o + (1 + i\lambda_1)\bar{z}_o]$$
$$z_2^* = \frac{1}{2}[(1 - i\lambda_2)z_o + (1 + i\lambda_2)\bar{z}_o] \quad (13)$$

The complex constants A_1 and A_2 are to be determined from the following equations:

$$[u + iv] = 2\pi i[p(\lambda_1)A_1 - p(\bar{\lambda}_1)\bar{A}_1 + p(\lambda_2)A_2 - p(\bar{\lambda}_2)\bar{A}_2] \quad (14)$$

$$X + iY = \frac{-\pi}{2}[(1 + i\lambda_1)A_1 - (1 + i\bar{\lambda}_1)\bar{A}_1 + (1 + i\lambda_2)A_2 - (1 + \bar{\lambda}_2)\bar{A}_2] \quad (15)$$

The left-hand side of equation (14) represents the specified dislocation or displacement jump in completing a circuit about the point z_o, and likewise the left-hand side of (15) contains the specified net force obtained by integrating the tractions around a similar circuit. For a given material, the real and imaginary parts of equations (14) and (15) may be used to determine A_1 and A_2 in terms of the specified quantities.

To arrive at a half-plane solution, it is necessary to remove the tractions due to the potentials in (12) on the surface $y = 0$. Assuming that $z_o \epsilon S^-$ (i.e. $Im\{z_o\} < 0$) this may be accomplished by introducing two new piecewise analytic functions as follows:

$$\Phi_1(z_1) = \begin{cases} (1 - i\lambda_1)\phi_1'(z_1) & z_1 \epsilon S^- \\ -(1 - i\bar{\lambda}_1)\bar{\phi}_1'(z_1) & z_1 \epsilon S^+ \end{cases} \quad (16)$$

$$\Phi_2(z_2) = \begin{cases} (1 - i\lambda_2)\phi_2'(z_2) & z_2 \epsilon S^- \\ -(1 - i\bar{\lambda}_2)\bar{\phi}_2'(z_2) & z_2 \epsilon S^+ \end{cases} \quad (17)$$

Referring back to equations (2) and (3), it can be seen that for $z_1, z_2 \epsilon S^-$ the stresses may be written in terms of Φ_1 and Φ_2 as

$$\sigma_{yy} + i\tau_{xy} = \Phi_1(z_1) - \Phi_1(\bar{z}_1) + \Phi_2(z_2) - \Phi_2(\bar{z}_2) \quad (18)$$

which becomes on the boundary $y \to 0^-$:

$$\sigma_{yy} + i\tau_{xy} = \Phi_1^-(x) - \Phi_1^+(x) + \Phi_2^-(x) - \Phi_2^+(x) \quad (19)$$

By choosing Φ_1 and Φ_2 properly in terms of $_o\phi_1$ and $_o\phi_2'$ the zero traction condition can be satisfied identically. Specifically, we take

$$\Phi_1(z_1) = (1 - i\lambda_1)_o\phi_1'(z_1) - (1 - i\bar{\lambda}_1)_o\phi_1'(z_1)$$
$$\Phi_2(z_2) = (1 - i\lambda_2)_o\phi_2'(z_2) - (1 - i\bar{\lambda}_2)_o\phi_2'(z_2) \quad (20)$$

These functions exhibit the proper singular behavior at the point z_o, and in addition give rise to zero traction on $y = 0$, both of which may be verified by substitution into (18) and (19). This method of constructing half plane solutions (essentially an image approach) is discussed for the isotropic case by Green and Zerna (1954) and England (1960).

The final step necessary in this section is to calculate the displacement effects due to the potentials in (20) on the surface $y = 0$. Since no tractions are induced by Φ_1 and Φ_2 on the boundary, it can be seen that the boundary conditions (9) and (10) will be insensitive to the presence of the singularity. Thus the influence will only be felt through the displacement condition (11). Evaluating equation (4) in terms of Φ_1 and Φ_2 with $y = 0$ leads then to

$$2i\frac{\partial v_0}{\partial x} = [G(\lambda_1) + G(\bar{\lambda}_1)]\frac{A_1}{(x - z_1^*)} - [\bar{G}(\bar{\lambda}_1) + \bar{G}(\lambda_1)]\frac{\bar{A}_1}{(x - \bar{z}_1^*)}$$

$$+ [G(\lambda_2)+G(\bar{\lambda}_2)]\frac{A_2}{(x-z_2^*)}$$

$$- [\bar{G}(\bar{\lambda}_2)+\bar{G}(\lambda_2)]\frac{\bar{A}_2}{(x-\bar{z}_2^*)} \tag{21}$$

in which

$$G(\lambda_i)\equiv p(\lambda_i)-\frac{1-i\lambda_i}{1-i\bar{\lambda}_i}p(\bar{\lambda}_i) \tag{22}$$

3.2 Contact Solution. This section presents the development of the complex potentials satisfying the conditions (9)–(11) on the boundaries of the two contacting bodies. Considering first body I, note that the following definition for ϕ_1 and ϕ_2 automatically satisfies the friction condition (9):

$$\begin{aligned}\phi_1'(z) &= -\frac{f-\lambda_2^I}{\lambda_2^I-\lambda_1^I}\phi_I'(z)\\ \phi_2'(z) &= \frac{f-\lambda_1^I}{\lambda_2^I-\lambda_1^I}\phi_I'(z)\end{aligned} \tag{23}$$

Here, $\phi_I(z)$ is a function of the complex variable $z=x+iy$, analytic for $z\epsilon S^-$. Substituting the expressions in (23) into equation (2) enables the stress σ_{yy} on $y=0$ to be written as

$$\sigma_{yy}=\phi_I'(x)+\bar{\phi}_I'(x) \tag{24}$$

Next define a new potential Φ_I such that ϕ_I may be continued into S^+ in the following manner:

$$\Phi_I(z)\equiv\begin{cases}\phi_I'(z) & z\epsilon S^-\\ -\bar{\phi}_I'(z) & z\epsilon S^+\end{cases} \tag{25}$$

The normal stress may be written in terms of Φ_I as

$$\sigma_{yy}=\frac{f-\lambda_2^I}{\lambda_1^I-\lambda_2^I}\Phi_I(z_1)-\frac{f-\bar{\lambda}_2^I}{\bar{\lambda}_1^I-\bar{\lambda}_2^I}\Phi_1(\bar{z}_1)$$

$$+\frac{f-\lambda_1^I}{\lambda_2^I-\lambda_1^I}\Phi_I(z_2)-\frac{f-\bar{\lambda}_1^I}{\bar{\lambda}_2^I-\bar{\lambda}_1^I}\Phi_I(\bar{z}_2) \tag{26}$$

which becomes on the boundary $y=0^-$:

$$\sigma_{yy}^I=\Phi_I^-(x)-\Phi_I^+(x) \tag{27}$$

Proceeding with the above substitutions for the displacement expression (4) leads in similar fashion to the following for $y=0^-$:

$$\frac{\partial v_I}{\partial x}=Q_I\Phi_I^-(x)-\bar{Q}_I\Phi_I^+(x) \tag{28}$$

The complex constant Q_I contains the material constants and the coefficient of friction and is given by

$$Q_I=q(\lambda_1^I)\frac{f-\lambda_2^I}{\lambda_1^I-\lambda_2^I}+q(\lambda_2^I)\frac{f-\lambda_1^I}{\lambda_2^I-\lambda_1^I} \tag{29}$$

with

$$q(\lambda)=(s_{22}-s_{26}\lambda+s_{12}\lambda^2)/\lambda \tag{30}$$

It is not difficult to see that performing analogous manipulations and definitions for body II will lead to similar expressions for the normal traction and displacement on its boundary $y=0^+$. These are as follows:

$$\sigma_{yy}^{II}=\Phi_{II}^+(x)-\Phi_{II}^-(x) \tag{31}$$

$$\frac{\partial v_{II}}{\partial x}=Q_{II}\Phi_{II}^+(x)-\bar{Q}_{II}\Phi_{II}^-(x) \tag{32}$$

Consider now the traction continuity condition expressed by the first of equation (9). In terms of the potentials Φ_I and Φ_{II} this condition may be rewritten using equations (27) and (31) as follows:

$$[\Phi_I(x)+\Phi_{II}(x)]^- - [\Phi_I(x)+\Phi_{II}(x)]^+ = 0 \tag{33}$$

Since this condition is to hold for all x, and since the stresses should vanish at infinity, it may be inferred from Liouville's theorem that

$$\Phi_I(z)+\Phi_{II}(z)=0 \tag{34}$$

Using this result in combination with equations (29) and (32) it is possible to express the displacement condition (11) as a Hilbert problem in terms of either Φ_I or Φ_{II}. Choosing Φ_I leads to the form

$$(Q_I-\bar{Q}_{II})\bar{\Phi}_I^-(x)-(\bar{Q}_I-Q_{II})\Phi_I^+(x)=g(x)\,|x|<c \tag{35}$$

The solutions to Hilbert problems of this type are well known (Muskhelishvili, 1953) and may be written in the present case as

$$\Phi_I(z)=\frac{X(z)}{2\pi i}\int_{-c}^{c}\frac{\hat{g}(x)dx}{X^+(x)(x-z)} \tag{36}$$

Subject to the condition

$$\int_{-c}^{c}\frac{g(x)dx}{X^+(x)}=0 \tag{37}$$

This ensures proper behavior (i.e., vanishing stresses) at infinity. The function $X(z)$ is given by

$$X(z)=(z+c)^{1-\theta/\pi}(z-c)^{\theta/\pi} \tag{38}$$

with

$$\theta=-arg\{Q_I-\bar{Q}_{II}\} \tag{39}$$

The function $\hat{g}(x)$ is simply

$$\hat{g}(x)=g(x)/(Q_I-\bar{Q}_{II}) \tag{40}$$

The remaining tasks are to define $g(x)$ explicitly, and then evaluate the resulting integrals (35) and (36). To this end consider the following form for $g(x)$:

$$g(x)=\frac{x-x_o}{R}-\frac{\partial v_o}{\partial x} \tag{41}$$

Here, the first term in the right-hand side of equation (39) represents the usual Hertzian assumption of a parabolic displacement with compound radius of curvature $R(1/R=1/R_I+1/R_{II}$ in which R_I and R_{II} are the initial local radii of curvatures of the two bodies), with the additional quantity x_o included to represent the translational displacement due to the horizontal component of the load. The value of x_o must be determined as part of the solution process.

The second term on the right-hand side of equation (39) accounts for the displacement effects due to the singular solution derived in the previous section. Thus, the combination of the solution represented in equation (35) and the singular solution developed previously will satisfy the required Hertzian boundary conditions. The influence of the singularity will be reflected in the resulting contact stress distribution existing beneath the indenter.

To determine an explicit expression for Φ_I, the integrals of equations (35) and (36) can be evaluated using contour integration. Using equations (39) and (21), this gives for the condition (36):

$$2c\left(\frac{\theta}{\pi}-\frac{1}{2}\right)-\frac{x_o}{R}-\frac{1}{2i}\Bigg\{[G(\lambda_1^I)+G(\bar{\lambda}_1^I)]\frac{A_1}{X(z_1^*)}$$

$$-[\bar{G}(\bar{\lambda}_1^I)+\bar{G}(\lambda_1^I)]\frac{A_1}{X(\bar{z}_1^*)}$$

$$+[G(\lambda_2^I)+G(\bar{\lambda}_2^I)]\frac{A_2}{X(z_2^*)}-[\bar{G}(\bar{\lambda}_2^I+\bar{G}(\lambda_2^I)]\frac{A_2}{X(\bar{z}_2^*)}\Bigg\}=0 \tag{42}$$

The value of x_o may be determined from this equation. Similarly, integration of equation (35) gives ϕ_I:

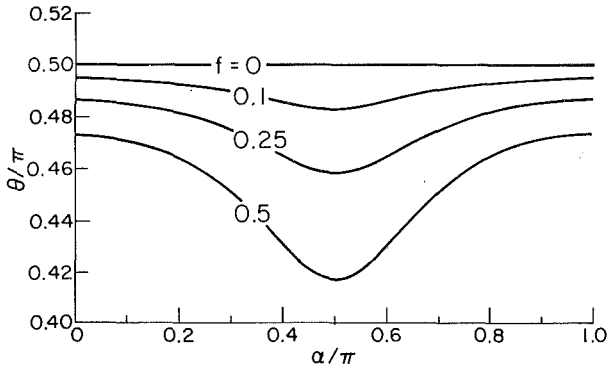

Fig. 2 Contact stress parameter θ/π as a function of material principal direction orientation angle α

$$\Phi_I(z)=\frac{1}{2iIm[Q_I+Q_{II}]}\left\{\frac{1}{R}\left[z-2c\left(\frac{\theta}{\pi}-\frac{1}{2}\right)-X(z)\right]\right.$$

$$-\frac{1}{2i}\left[[G(\lambda_1^I)+G(\bar{\lambda}_1^I)]\hat{F}(z;\,z_1^*)-[\bar{G}(\bar{\lambda}_1^I)+\bar{G}(\lambda_1^I)]\hat{F}(z;\,\bar{z}_1^*)\right.$$

$$\left.\left.+[G(\lambda_2^I)+G(\bar{\lambda}_2^I)]\hat{F}(z,\,z_2^*)-[\bar{G}(\bar{\lambda}_2^I)+\bar{G}(\lambda_2^I)]\hat{F}(z;\,\bar{z}_2^*)\right]\right\} \quad (43)$$

in which

$$\hat{F}(z;\,\zeta)=\frac{1}{z-\zeta}\left[1-\frac{X(z)}{X(\zeta)}\right]+\frac{1}{X(\zeta)}$$

The function $\hat{F}(z,\,\zeta)$ is analogous to those obtained by Lo (1978) with an additional term to ensure the proper behavior at infinity. This additional term comes from the condition equation (36), and the result (40) has been used in writing equation (41).

Thus, equation (41) provides the desired expression, allowing the stresses throughout the body to be calculated. In particular, the traction inside the contact region may be evaluated from equation (32), using the fact that Φ_1 takes on different values inside the contact region depending on whether the approach is from S^+ or S^-. This leads to

$$\sigma_{yy}(x)=-\frac{\sin\theta}{Im[Q_I+Q_{II}]}\left\{\frac{1}{R}+Im\left[(G(\lambda_1^I)\right.\right.$$

$$+G(\bar{\lambda}_1^I))\frac{A_1}{(x-z_1^*)X(z_1^*)}$$

$$\left.\left.+(G(\lambda_2^I)+G(\bar{\lambda}_2^I))\frac{A_2}{(x-z_2^*)X(z_2^*)}\right]\right\}(c-x)^{\theta/\pi}(c+x)^{1-\theta/\pi} \quad (44)$$

The first term in the curly bracket represents the Hertzian solution, while the additional terms are due to the singularity. The affects of both friction and the anisotropy are contained implicitly in the degree to which the stress distribution is skewed away from elliptical, as well as in the overall magnitude of the stresses.

In particular, Fig. 2 shows the variation in the characteristic exponent, θ/π, as a function of principal direction orientation for several coefficients of friction. Body *II* has been taken as being perfectly rigid (and so $Q_{II}=0$), while body *I* has been given material properties corresponding to a typical transversely isotropic graphite-epoxy composite with $S_{11}=1.71\times10^{-6}$/MPa, $S_{22}=6.90\times10^{-5}$/MPa, $S_{12}=1.52\times10^{-6}$/MPa, and $S_{66}=1.71\times10^{-6}$/MPa. Here the capital *S*'s denote the principal material constants for the case in which the principal material axes are aligned with the coordinate axes, x and y. In the absence of friction the characteristic exponent is equal to 1/2 regardless of the material orientation relative to the coordinate axes. This result was presented by Chen (1969) and shows that the contact stress distribution remains symmetric and elliptical for both isotropic and anisotropic materials undergoing frictionless Hertzian contact. In the presence of friction, however, the stress distribution is skewed and depends on the relative orientation between the material and coordinate axes defined by the angle α. Thus Fig. 2 gives an idea of the error involved in assuming the tangential and normal loading components are decoupled, which is equivalent to using $\theta/\pi=1/2$ for all cases. Note again, however, that Fig. 2 was obtained by making body *II* rigid. For both bodies elastic the skewing effect is diminished, and in the case of identical transversely isotropic materials it is interesting that the effect is found to disappear entirely, regardless of the relative orientation of the material axes in the two bodies.

As a final result we note that considering the behavior of Φ_I at infinity, the relation between the applied load P and the contact size c is given by

$$P=\frac{\pi}{Im[Q_I+Q_{II}]}\left\{2\,\frac{\theta}{\pi}\left(1-\frac{\theta}{\pi}\right)\frac{c^2}{R}\right.$$

$$-Im\left[(G(\lambda_1^I)+G(\bar{\lambda}_1^I))A_1\left(1+\frac{c(2\theta-\pi)}{\pi X(z_1^*)}\right)\right.$$

$$\left.\left.+(G(\lambda_2^I)+G(\bar{\lambda}_2^I))A_2\left(1+\frac{c(2\theta-\pi)}{\pi X(z_2^*)}\right)\right]\right\} \quad (45)$$

4 Closing Remarks

We note in closing that the expressions obtained above may be reduced to correspond to those given by Chen (1969) by taking $A_1=A_2=f=0$, and that the discussion concerning the value of the exponent θ/π is independent of the presence of the singularity. The total solution giving the desired Green's function is obtained by summing the contributions from the potentials defined by equations (12), (20), and (41).

Acknowledgment

This material is based upon work partially supported by the National Science Foundation under Grant No. MSM-8415489.

References

Bryant, M. D., Miller, G. R., and Keer, L. M., 1985, "Line Contact Between a Rigid Indenter and Damaged Elastic Body," *Quarterly Journal of Mechanics and Applied Mathematics*, Vol. 37, pp. 467-478.

Chen, W. T., 1969, "Stresses in Some Anisotropic Materials Due to Indentation and Sliding," *International Journal of Solids and Structures*, Vol. 5, pp. 191-214.

England, A. H., 1960, *Complex Variable Methods in Elasticity*, Wiley-Interscience, London.

Green, A. E., and Zerna, W., 1954, *Theoretical Elasticity*, Clarendon Press, London.

Lo, K. K., 1978, "Analysis of Branched Cracks," ASME JOURNAL OF APPLIED MECHANICS, Vol. 45, pp. 797-802.

Miller, G. R., and Keer, L. M., 1983, "Interaction Between a Rigid Indenter and a Near-Surface Void or Inclusion," ASME JOURNAL OF APPLIED MECHANICS, Vol. 105, pp. 615-620.

Miller, G. R., Keer, L. M., and Cheng, H. S., 1985, "On the Mechanics of Fatigue Crack Growth Due to Contact Loading," *Proceedings of the Royal Society of London*, Series A, Vol. 397, pp. 197-209.

Milne-Thomson, L. M., *Plane Elastic Systems*, Springer-Verlag, Berlin.

Muskhelishvili, N. I., 1953, *Singular Integral Equations*, Noordhoff, Leyden.

Several Elliptical Punches on an Elastic Half Space

V. I. Fabrikant
Department of Mechanical Engineering,
Concordia University,
Montreal, H3G 1M8, Canada

A general theorem is established which relates the resulting forces, acting on a set of arbitrary punches, with their generalized displacements through a system of linear algebraic equations. The theorem is applied to the case of arbitrarily located elliptical punches. Several specific examples are considered.

Introduction

The interaction between two or more circular punches was considered by several authors. A list of references can be found in Gladwell and Fabrikant (1982). A system of circular punches on a nonhomogeneous half space was investigated by Fabrikant and Keer (1983) where simple approximate relationships were established between the applied forces and the displacements of the punches. We are not aware of any publication treating the interaction between elliptical punches.

Here, a general theorem is established which is valid for arbitrary punches, and relates the total forces applied to the punches with their displacements through a system of linear algebraic equations. Since the coefficients of these equations depend on the displacements outside a flat punch of arbitrary planform, the theorem can be used effectively for elliptical punches only, as there seems to be no publication giving the displacements outside a nonelliptical punch. The exact values of the coefficients are not known but, since their variation is quite limited, the established theorem allows to obtain the upper and the lower bounds for the parameters sought. There is no need to know the stress distribution under the punches which presents a significant advantage for the user. Several examples are considered to show that these bounds may be so close that they provide, in fact, a reasonably accurate solution to the problem. A comparison is made with the only known numerical solution by Kobayashi (1939) which claims to be accurate. The problem he considered is equivalent to the case of two equal coplanar circular punches on an elastic half space. The discrepancy between our solution and the one by Kobayashi does not exceed 0.4 percent in the whole range of distances between the punches from 2 to ∞.

Theory

Consider a set of N arbitrary punches acting upon an elastic half space $z \geq 0$. Let S_n be the domain of contact for the nth punch, and P_n be the normal force acting on the nth punch. The friction forces between the punches and the half space are neglected. The problem is to find the relationships between the generalized displacements of the punches and the acting forces. The boundary conditions for the problem are

$$w = w_n(M) \text{ for } M \in S_n,$$
$$\sigma_n(M) = 0 \quad \text{for } M \notin S_n,\ n = 1,2,\ \ldots\ ,N \tag{1}$$

where w denote the normal displacement of a point at the boundary $z=0$, and σ stands for the normal stress distribution; w_n is defined by the punch face. By using the known solution of the Boussinesque problem and the principle of superposition, one can write

$$w(Q) = H \sum_{n=1}^{N} \int\int_{S_n} \frac{\sigma_n(T_n)}{R(T_n,Q)} dS_n \tag{2}$$

where H is an elastic constant which reduces to $H=(1-\nu^2)/\pi E$ when the half space is an isotropic medium with the Poisson's ratio ν and the elastic modulus E. In the case of a transversely isotropic medium, an appropriate expression for H can be found in Fabrikant (1971). Substitution of the boundary conditions (1) in (2) leads to a set of N integral equations. The exact solutions of these equations are not known at the present time even for the case of several circles. Here, we are to show that we do not really need to know these solutions. We can single out, without loss of generality, the first punch, and consider the related integral equation

$$w_1(Q_1) = H \int\int_{S_1} \frac{\sigma_1(T_1)}{R(T_1,Q_1)} dS_1 + H \sum_{n=2}^{N} \int\int_{S_n} \frac{\sigma_n(T_n)}{R(T_n,Q_1)} dS_n \tag{3}$$

Suppose that the functions σ_0, σ_x, and σ_y are known, satisfying, respectively, the following integral equations inside S_1

$$\int\int_{S_1} \frac{\sigma_0(Q_1)}{R(T_1,Q_1)} dS_1 = 1, \tag{4}$$

$$\int\int_{S_1} \frac{\sigma_x(Q_1)}{R(T_1,Q_1)} dS_1 = x \tag{5}$$

$$\int\int_{S_1} \frac{\sigma_y(Q_1)}{R(T_1,Q_1)} dS = y \tag{6}$$

Multiplication of both sides of (3) by $\sigma_0(Q_1)$ and integration over the area S_1 yields

Contributed by the Applied Mechanics Division for publication in the JOURNAL OF APPLIED MECHANICS.
Discussion on this paper should be addressed to the Editorial Department, ASME, United Engineering Center, 345 East 47th Street, New York, N.Y. 10017, and will be accepted until two months after final publication of the paper itself in the JOURNAL OF APPLIED MECHANICS. Manuscript received by ASME Applied Mechanics Division, July 24, 1985.

$$\int\int_{S_1} \sigma_0(Q_1)w_1(Q_1)dS_1$$

$$= H\int\int_{S_1} \sigma_0(Q_1)dS_1 \int\int_{S_1} \frac{\sigma_1(T_1)}{R(T_1,Q_1)}dS_1 +$$

$$+ H\sum_{n=2}^{N} \int\int_{S_1} \sigma_0(Q_1)dS_1 \int\int_{S_n} \frac{\sigma_n(T_n)}{R(T_n,Q_1)}\, dS_n \qquad (7)$$

By changing the order of integration in (7) and taking into consideration that σ_0 satisfies (4), the following result can be obtained

$$\int\int_{S_1} \sigma_0(Q_1)w_1(Q_1)dS_1 = H\Big[P_1$$

$$+ \sum_{n=2}^{N} \int\int_{S_n} w_{1n}(T_n)\sigma_n(T_n)dS_n\Big] \qquad (8)$$

where P_1 is the total force acting on the first punch, and

$$w_{1n}(T_n) = \int\int_{S_1} \frac{\sigma_0(Q_1)}{R(T_n,Q_1)}\, dS_1 \qquad (9)$$

which is proportional to the normal displacement in the domain S_n due to a flat punch in S_1 under the action of a force producing a unit displacement. By evoking the theorem about the mean which is valid when σ_n does not change sign, we come to the linear algebraic equation

$$\int\int_{S_1} \sigma_0(Q_1)w_1(Q_1)dS_1 = H\Big[P_1 + \sum_{n=2}^{N} w_{1n}(C_n)P_n\Big] \qquad (10)$$

The exact location of the point C_n is not known but the fact that $C_n \in S_n$ allows only limited variation within S_n, and in many cases provides sufficiently close upper and lower bounds for the parameters sought. By using the same logic, $N-1$ additional linear algebriac equations can be derived for the remaining punches. This set of equations provides the necessary relationships between the normal displacements of the punches and the applied forces.

Let us derive similar relationships for the angular displacements. Multiplication of both sides of (3) by $\sigma_x(Q_1)$ and integration over the area S_1 yields

$$\int\int_{S_1} \sigma_x(Q_1)w_1(Q_1)dS_1$$

$$= H\int\int_{S_1} \sigma_x(Q_1)dS_1 \int\int_{S_1} \frac{\sigma_1(T_1)}{R(T_1,Q_1)}\, dS_1 +$$

$$+ H\sum_{n=2}^{N} \int\int_{S_1} \sigma_x(Q_1)dS_1 \int\int_{S_n} \frac{\sigma_n(T_n)}{R(T_n,Q_1)}\, dS_n \qquad (11)$$

By changing the order of integration in (11) and taking into consideration that σ_x satisfies (5), the following result can be obtained

$$\int\int_{S_1} \sigma_x(Q_1)w_1(Q_1)dS_1 = H\Big[-M_{1y}$$

$$+ \sum_{n=2}^{N} \int\int_{S_n} x\alpha_{1n}(T_n)\sigma_n(T_n)dS_n\Big] \qquad (12)$$

where M_{1y} is the tilting moment acting on the first punch about the axis Oy, and

$$\alpha_{1n}(T_n) = \frac{1}{x}\int\int_{S_1} \frac{\sigma_x(Q_1)}{R(T_n,Q_1)}\, dS_1 \qquad (13)$$

If σ_n does not change sign, we can again use the theorem about the mean to yield

$$\int\int_{S_1} \sigma_x(Q_1)w_1(Q_1)dS_1 = H\Big[-M_{1y}$$

$$+ \sum_{n=2}^{N} \alpha_{1n}(A_n)x_nP_n\Big] \qquad (14)$$

where $A_n(x_n, y_n) \in S_n$. The additional $N-1$ equations relating the punch rotations about the axis Oy with the corresponding tilting moments can be obtained in a similar way. Multiply both sides of (3) by $\sigma_y(Q_1)$ and integrate over S_1. Using the same logic as before, we come to the equation

$$\int\int_{S_1} \sigma_y(Q_1)w_1(Q_1)dS_1 = H\Big[M_{1x}$$

$$+ \sum_{n=2}^{N} \int\int_{S_n} y\beta_{1n}(T_n)\sigma_n(T_n)dS_n\Big] \qquad (15)$$

where M_{1x} is the tilting moment about the axis Ox acting on the first punch, and

$$\beta_{1n}(T_n) = \frac{1}{y}\int\int_{S_1} \frac{\sigma_y(Q_1)}{R(T_n,Q_1)}dS_1 \qquad (16)$$

And again, application of the theorem about the mean gives

$$\int\int_{S_1} \sigma_y(Q_1)w_1(Q_1)dS_1 = H\Big[M_{1x}$$

$$+ \sum_{n=2}^{N} \beta_{1n}(B_n)y_nP_n\Big] \qquad (17)$$

Three sets of linear algebraic equations of the type (10), (14), and (17) are the main results of the paper. It is quite clear that each equation can be interpreted in terms of the reciprocal work. In order to use them, one needs to know the normal displacements outside every punch in the system due to three types of loading which, at the moment, is available for the elliptical punches only. This particular case is considered in the next Section.

Application to Elliptical Punches

Consider the interaction of a set of N flat elliptical punches arbitrarily located on an elastic half space. Let a_n and b_n be the major and the minor semi-axes of the nth ellipse; X_n and Y_n be its center, and θ_n be the angle between the axis Ox and the major semi-axis a_n; P_n is the normal force acting upon the nth punch. The boundary condition (1) in this case will take the form

$$w_n = \delta_n - \alpha_n x + \beta_n y \quad \text{for} \quad n = 1,2, \ldots, N \qquad (18)$$

Substitution of (18) into (10), (14), and (17) yields, respectively,

$$\frac{a_1}{K(k_1)}\delta_1 = H\Big[P_1 + \sum_{n=2}^{N} \frac{F(\phi_{1n},k_1)}{K(k_1)}\, P_n\Big], \qquad (19)$$

$$\frac{a_1{}^3}{3D(k_1)}\, \alpha_1 = H\Big[M_{1y} - \sum_{n=2}^{N} \alpha_{1n}x_nP_n\Big], \qquad (20)$$

$$\frac{a_1b_1{}^2}{3B(k_1)}\, \beta_1 = H\Big[M_{1x} + \sum_{n=2}^{N} \beta_{1n}y_nP_n\Big], \qquad (21)$$

where

$$a_{1n} = \frac{F(\phi_{1n},k_1) - E(\phi_{1n},k_1)}{K(k_1) - E(k_1)}, \qquad (22)$$

$$\beta_{1n} = \frac{E(\phi_{1n},k_1) - (1-k_1^2)F(\phi_{1n},k_1) - k_1{}^2(\rho_{1n}{}^2-1)^{1/2}/\rho_{1n}(\rho_{1n}{}^2-k_1^2)^{1/2}}{E(k_1) - (1-k_1^2)K(k_1)} \qquad (23)$$

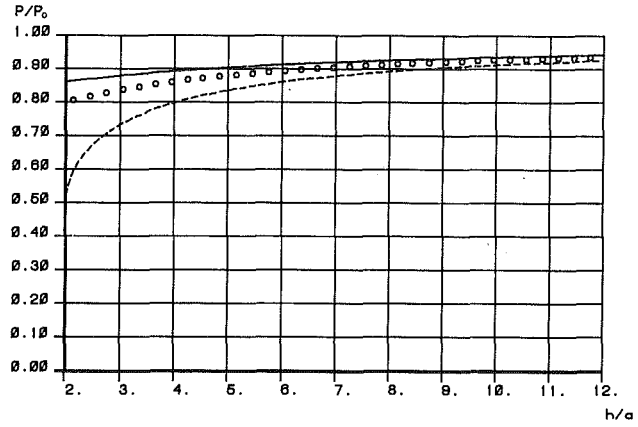

Fig. 1 The case of two equal elliptical punches

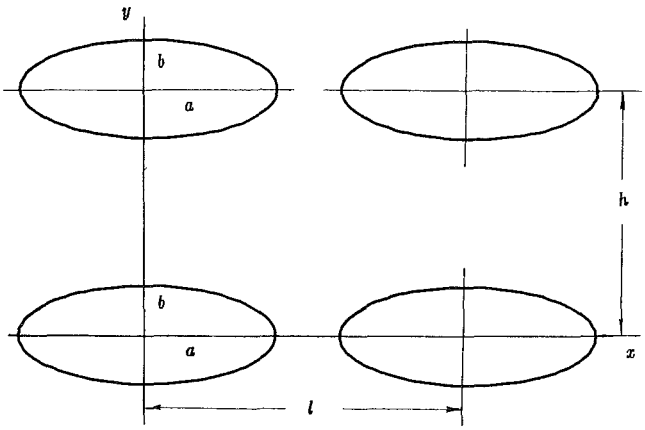

Fig. 2 The geometry of four elliptical punches

$$B(k_1)=\frac{E(k_1)-(1-k_1^2)K(k_1)}{k_1^2}, \tag{24}$$

$$D(k_1)=\frac{K(k_1)-E(k_1)}{k_1^2}, \tag{25}$$

and $K(k_1)$, $F(\phi_{1n},k_1)$, $E(k_1)$, $E(\phi_{1n},k_1)$ stand for the complete and the incomplete elliptic integrals of the first and second kind, respectively; ρ_{1n} and ϕ_{1n} are defined according to (A9) and (A10); formulae (A1–A8) from the Appendix were used in the derivation of (19–25); k_1 is the eccentricity of the first ellipse

$$k_1=\sqrt{1-b_1^2/a_1^2}$$

Equations (19), (20), and (21) each represent the first of the set of N equations. When the acting forces are known, the three sets of equations define the normal and the angular displacements of the punches. In the case when the displacements are known, the three sets of linear algebraic equations have to be solved with respect to P_n, M_{nx} and M_{ny}. It is also important to notice that each equation in the set is valid in the local system of the coordinates realted to the center of the ellipse.

Examples

Two Equal Elliptical Punches. Consider the case $N = 2$, $a_1 = a_2 = a$, $b_1 = b_2 = b$, $X_1 = Y_1 = 0$, $X_2 = h$, $Y_2 = 0$, $\theta_1 = \theta_2 = 0$. If also $P_1 = P_2 = P$, then, due to the symmetry of the system, the set of equations which are equivalent to (19), reduces to just one equation, namely

$$\frac{a}{K(k)}\delta=H\left[P+\frac{F(\phi,k)}{K(k)}P\right], \tag{26}$$

Table 1 Comparison of two solutions

d	upper bound	lower bound	central estimation	result by Kobayashi	Error %
2.0	0.8221338	0.5000000	0.7500000	0.75272	0.36
2.2	0.8317164	0.6145749	0.7689962	0.77014	0.15
2.4	0.8402998	0.6637918	0.7851738	0.78545	0.04
2.6	0.8480356	0.6993975	0.7991486	0.79898	-0.02
2.8	0.8550458	0.7272786	0.8113602	0.81096	-0.05
3.0	0.8614294	0.7500000	0.8221338	0.82102	-0.06
3.5	0.8751494	0.7924057	0.8442654	0.84370	-0.07
4.0	0.8863767	0.8221338	0.8614294	0.86093	-0.06
5.0	0.9036083	0.8614294	0.8863767	0.88602	-0.04
7.0	0.9261093	0.9036083	0.9163737	0.91619	-0.02
10.0	0.9452202	0.9338098	0.9400541	0.93999	-0.007
∞	1.	1.	1.		0

with an immediate result

$$P=\frac{P_0}{1+\dfrac{F(\phi,k)}{K(k)}} \tag{27}$$

where $P_0 = \delta a/HK(k)$ indicates the force which produces the punch settlement equal to δ when acting on a solitary punch. Equation (27) shows that the interaction between the punches decreases the value of the force necessary to produce the required settlement. The upper and the lower bounds for P can be obtained from (27) by taking

$$\phi=\sin^{-1}\left[\frac{a}{h-a}\right] \text{ and } \phi=\sin^{-1}\left[\frac{a}{h+a}\right] \tag{28}$$

respectively. We shall also consider the central estimation for P defined by

$$\phi=\sin^{-1}\left[\frac{a}{h}\right] \tag{29}$$

Figure 1 plots the ratio P/P_0 versus h/a for $a=2$, $b=1$. The solid line gives the upper bound, the dashed line gives the lower one, and the circles represent the central estimation. As one can see, the maximum possible error of the central estimation is less than 9 percent for $h/a>3.5$, it is less than 5 percent for $h/a>5$, it is less than 2 percent for $h/a>8$, and it is less than 1 percent for $h/a>12$. Since there is no accurate solution available for this case, it is difficult to say how great the real error of the central estimation is, but there is a reason to believe that it is much less than the one indicated above. The reason for such belief gives a comparison of the central estimation for two equal circular punches with a numerical solution by Kobayashi (1939). The values of the ratio P/P_0 for various $d=h/a$ are given in Table 1. If one takes Kobayashi's solution as exact, then the maximum error of the central estimation does not exceed 0.4 percent in the whole range of $2\le d<\infty$. Even if one assumes the accuracy in the case of two elliptical punches being ten times worse than the accuracy of the central estimation for two circular punches, this still would give the maximum error at 4 percent, which is not bad. Having this in mind, we shall evaluate the central estimation only in the examples to follow.

If the normal forces are applied centrally, then the angles of inclination of the punches will be defined by (20) and (21) as

$$\alpha_1 = -\alpha_2 = -\frac{3D(k)}{a_1^3} H\alpha_{12} hP,\ \beta_1 = \beta_2 = 0 \tag{30}$$

where

$$\alpha_{12} = \frac{F(\phi,k) - E(\phi,k)}{K(k) - E(k)},$$

$$k = \sqrt{1 - b^2/a^2}, \tag{31}$$

and ϕ is defined by (29).

In the case $\alpha_1 = \alpha_2 = 0$ there should be tilting moments applied to the punches whose value can be defined by (20) as

$$M_{1y} = -M_{2y} = \alpha_{12} hP \tag{32}$$

Four Equal Elliptical Punches. Consider the configuration given in Fig. 2. Let equal vertical forces P be applied to each punch. The punches are numbered in the clockwise direction starting from the one at the coordinate system origin. Due to the symmetry of the system, it is sufficient to consider just one equation of each of the sets (19–21). The result is

$$\frac{a}{K(k)}\delta = HP\left[1 + \frac{F(\phi_{12},k)}{K(k)} + \frac{F(\phi_{13},k)}{K(k)} + \frac{F(\phi_{14},k)}{K(k)}\right], \tag{33}$$

$$\frac{a^3}{3D(k)}\alpha_1 = H[M_{1y} - Pl(\alpha_{13} + \alpha_{14})] \tag{34}$$

$$\frac{ab^2}{3B(k)}\beta_1 = H[M_{1x} + Ph(\beta_{12} + \beta_{13})] \tag{35}$$

where α_{1n} and β_{1n} are defined by (22) and (23), respectively, and

$$\phi_{1n} = \sin^{-1}\frac{1}{\rho_{1n}}, \text{ for } n = 2,3,4; \tag{36}$$

$$\rho_{12} = [1 + (h^2 - b^2)/a^2]^{1/2},\ \rho_{14} = \frac{l}{a}$$

$$\rho_{13} = [L + (L^2 - k^2 l^2/a^2)^{1/2}]^{1/2},$$

$$L = \frac{1}{2}[k^2 + (l^2 + h^2)/a^2], \tag{37}$$

When the forces and the tilting moments are known, equations (33–35) define the normal and the angular displacements of the punches. If the punches are not allowed to tilt, then the tilting moments are

$$M_{1x} = -Ph(\alpha_{12} + \alpha_{13}),\ M_{1y} = Ph(\alpha_{13} + \alpha_{14}) \tag{38}$$

Discussion

The results of this paper can be considered as a generalization of those by Mossakovskii (1953) who considered the case of a solitary punch. It is also necessary to indicate certain limiting cases. In the case of a circular punch the eccentricity $k_1 \to 0$, and formulae (22–25) give

$$\alpha_{1n} \to \beta_{1n} \to \frac{2}{\pi}\left\{\sin^{-1}\left[\frac{a_1}{r_{1n}}\right] - \frac{a_1}{r_{1n}}\left[1 - \frac{a_1^2}{r_{1n}^2}\right]^{1/2}\right\} \tag{39}$$

$$B(k_1) \to D(k_1) \to \pi/4,\ \frac{F(\phi_{1n},k_1)}{K(k_1)} \to \frac{2}{\pi}\sin^{-1}\left[\frac{a_1}{r_{1n}}\right] \tag{40}$$

and the equations (19–21) will take the form

$$\frac{2}{\pi}a_1\delta_1 = H\left[P_1 + \frac{2}{\pi}\sum_{n=2}^{N} P_n \sin^{-1}\frac{a_1}{r_{1n}}\right], \tag{41}$$

$$\frac{4a_1^3}{3\pi}\alpha_1 = H\left[M_{1y} - \sum_{n=2}^{N}\alpha_{1n} x_n P_n\right], \tag{42}$$

$$\frac{4a_1^3}{3\pi}\beta_1 = H\left[M_{1x} + \sum_{n=2}^{N}\beta_{1n} y_n P_n\right], \tag{43}$$

where a_1 is the radius of the punch number one and r_{1n} is the polar radius of the system of coordinates related to the center of the punch. Formulae (41–43) are in agreement with the results by Gladwell and Fabrikant (1982).

Consider the procedure of shrinking the areas S_n, $n = 2,3, \ldots, N$. The accuracy of equations (19–21) will increase. In the limiting case $S_n \to 0$ formulae (19–21) give an *exact* solution to the problem of several concentrated forces acting outside an elliptical punch.

References

Fabrikant, V. I., 1971, "Effect of Shearing Force and Tilting Moment on a Cylindrical Punch Attached to a Transversely Isotropic Half Space," *Journal of Applied Mathematics and Mechanics* (PMM), Vol. 35, pp. 147–151.

Fabrikant, V. I., and Keer, L. M., 1983, "The Interaction Between a System of Circular Punches on a Nonhomogeneous Half Space," *International Journal of Mechanical Science*, Vol. 25, pp. 513–518.

Gladwell, G. M. L., and Fabrikant, V. I., 1982, "The Interaction Between a System of Circular Punches on an Elastic Half Space," ASME JOURNAL OF APPLIED MECHANICS, Vol. 49, pp. 341–344.

Kobayashi, I., 1939, "Das electrostatische Potential um zwei auf derselben Ebene liegende und sich nicht schneidende gleichgrobe Kreisscheiben," *Sc. Rep. Tôhoku Imp. Univ.*, Vol. 27, pp. 365–391.

Lur'e, A. I., 1964, *Three-Dimensional Problems of the Theory of Elasticity*, Interscience, New York.

Mossakovskii, V. I., 1953, "Application of the Reciprocity Theorem to the Determination of the Resultant Forces and Moments in Three-Dimensional Contact Problems," in Russian, *Journal of Applied Mathematics and Mechanics* (PMM), Vol. 17, pp. 477–482.

APPENDIX

Here are some results implicitly given by Lur'e (1964) which are used for the derivation of (19–25). The functions σ_0, σ_x, and σ_y have the form

$$\sigma_0 = \frac{1}{2\pi b_1 K(k_1)}\left[1 - \frac{x^2}{a_1^2} - \frac{y^2}{b_1^2}\right]^{-1/2} \tag{A1}$$

$$\sigma_x = \frac{x}{2\pi b_1 D(k_1)}\left[1 - \frac{x^2}{a_1^2} - \frac{y^2}{b_1^2}\right]^{-1/2} \tag{A2}$$

$$\sigma_y = \frac{y}{2\pi b_1 B(k_1)}\left[1 - \frac{x^2}{a_1^2} - \frac{y^2}{b_1^2}\right]^{-1/2} \tag{A3}$$

where

$$B(k_1) = \frac{E(k_1) - (1 - k_1^2)K(k_1)}{k_1^2}, \tag{A4}$$

$$D(k_1) = \frac{K(k_1) - E(k_1)}{k_1^2}, \tag{A5}$$

and $K(k_1)$ and $E(k_1)$ stand for the complete elliptic integrals of the first and second type, respectively.

Introduce the notation

$$R = [(x - x_0)^2 + (y - y_0)^2]^{1/2}$$

$$Z_0 = \left[1 - \frac{x_0^2}{a_1^2} - \frac{y_0^2}{b_1^2}\right]^{1/2}$$

The following integrals are valid

$$\int\int_{S_1} \frac{dx_0 dy_0}{RZ_0} = \begin{cases} 2\pi b_1 K(k_1) & \text{for } (x,y) \in S_1 \\ 2\pi b_1 F(\phi_1,k_1) & \text{for } (x,y) \notin S_1 \end{cases} \tag{A6}$$

$$\int\int_{S_1} \frac{x_0 dx_0 dy_0}{RZ_0} = \begin{cases} 2\pi b_1 \dfrac{K(k_1)-E(k_1)}{k_1^2} x \\ \text{for } (x,y) \in S_1 \\ \\ 2\pi b_1 \dfrac{F(\phi_1,k_1)-E(\phi_1,k_1)}{k_1^2} x \\ \text{for } (x,y) \notin S_1 \end{cases} \tag{A7}$$

where

$$\phi_1 = \sin^{-1}\left[\frac{1}{\rho_1}\right], \tag{A9}$$

$$\rho_1 = [L + (L^2 - k_1^2 x^2/a_1^2)^{1/2}]^{1/2},$$

$$L = \frac{1}{2}[k_1^2 + (x^2+y^2)/a_1^2] \tag{A10}$$

The remaining integrals are elementary

$$\int\int_{S_1} \left[1 - \frac{x^2}{a_1^2} - \frac{y^2}{b_1^2}\right]^{-1/2} dxdy = 2\pi a_1 b_1 \tag{A11}$$

$$\int\int_{S_1} \frac{y_0 dx_0 dy_0}{RZ_0} = \begin{cases} 2\pi b_1 \dfrac{E(k_1)-(1-k_1^2)K(k_1)}{k_1^2} y \quad \text{for } (x,y) \in S_1 \\ \\ 2\pi b_1 \left\{ \dfrac{E(\phi_1,k_1)-(1-k_1^2)F(\phi_1,k_1)}{k_1^2} - \dfrac{1}{\rho_1}\left[\dfrac{\rho_1^2-1}{\rho_1^2-k_1^2}\right]^{1/2} \right\} y \quad \text{for } (x,y) \notin S_1 \end{cases} \tag{A8}$$

$$\int\int_{S_1} \left[1 - \frac{x^2}{a_1^2} - \frac{y^2}{b_1^2}\right]^{-1/2} x^2 dx\, dy = \frac{2}{3}\pi a_1^3 b_1 \tag{A12}$$

$$\int\int_{S_1} \left[1 - \frac{x^2}{a_1^2} - \frac{y^2}{b_1^2}\right]^{-1/2} y^2 dx\, dy = \frac{2}{3}\pi a_1 b_1^3 \tag{A13}$$

A Constitutive Model of Cyclic Plasticity for Nonlinear Hardening Materials

N. Ohno
Department of Energy Engineering,
Toyohashi University of Technology,
Tempaku-cho, Toyohashi,440 Japan

Y. Kachi
Sumitomo Electric Industries, Ltd.,
Shimaya, Konohana-ku,
Osaka, 554 Japan

A constitutive model is proposed for cyclic plasticity of nonlinear hardening materials. The concept of a cyclic nonhardening range, which enables us to describe the dependence of cyclic hardening on the amplitude of cyclic straining or stressing, is employed together with the idea of a two-surface plasticity model. Results of the proposed model are compared with experiments of 304 and 316 stainless steels in several cases of cyclic loading in which mean strain is zero or nonzero and strain limits are fixed or variable. Thus, it is shown that the model successfully describes both the cyclic hardening phenomenon and the transient elastoplastic behavior after initial and reverse yields of these materials. The capability of the model to provide nonlinear cyclic stress-strain curves is also discussed.

Introduction

For detailed inelastic analysis of structural components subjected to cyclic loading, we need a constitutive model which can describe cyclic plastic behavior of materials accurately. Since cyclic hardening or softening is one of the most fundamental characteristics in cyclic plasticity of metals, the constitutive model must describe this phenomenon by any means. However, it is not sufficient for the model to be valid for one specific cyclic strain or stress range only, because generally strain and stress ranges distribute nonuniformly in structural components. The constitutive model, therefore, must be valid for any cyclic strain or stress range occurring in the component to be analyzed. The dependence of cyclic hardening on the size of cyclic strain or stress range is significant especially in 304 and 316 stainless steels, as seen later in Figs. 5 and 10.

Ohno [1] proposed a constitutive model of cyclic plasticity by introducing the concept of a cyclic nonhardening range, which enabled us to describe the dependence of cyclic hardening mentioned above. He postulated that a plastic strain range called the cyclic nonhardening range develops as cyclic straining proceeds, and that the plastic strain increment inside this range does not contribute to cyclic hardening. Some details of the concept will be reviewed later. The validity of the model was ascertained for 304 stainless steel subjected to cyclic straining between variable, as well as fixed, strain limits at room temperature [1].

However, the model above has a limitation that it cannot describe transient elastoplastic behavior observed just after initial yielding and reyielding under reverse loading.

The transient elastoplastic behavior can be expressed successfully by two-surface plasticity models [2–6], in which an imaginary stress surface called the bounding surface is introduced to specify a stress region for the translation and expansion of a yield surface. It must be noticed, however, that, without appropriate evolution equations of the bounding surface, the two-surface models cannot describe cyclic hardening or softening of materials well. Dafalias [7] proposed one type of such evolution equations on the basis of the maximum plastic strain range, which Chaboche et al. [8] originally used to describe cyclic plastic behavior of 316L stainless steel.

Another idea to express the transient elastoplastic behavior is to take account of a memory erasure term (a recovery term) in the evolution equation of a kinematic hardening variable [9]. However, this idea and that of two-surface plasticity models are not completely different from each other, because a mathematical equivalence can be shown between them in a special case [10], as quoted in [11].

In the present paper, by applying the concept of a cyclic nonhardening range to the evolution equations of the bounding surface in a two-surface model, we construct a constitutive model of cyclic plasticity which can describe both the cyclic hardening phenomenon and the transient elastoplastic behavior after yielding. The validity of the resulting model is verified on the basis of experiments of 304 and 316L stainless steels subjected to several kinds of cyclic straining at room temperature. Besides, we discuss the capability of the proposed model to provide nonlinear cyclic stress-strain curves.

Previous Model Based on Cyclic Nonhardening Range (Model I)

First let us review the constitutive model proposed by Ohno [1] in order to explain the description of cyclic hardening based on the cyclic nonhardening range. We consider here for simplciity uniaxial loading of stress σ, strain ϵ, and plastic strain ϵ^p.

Cyclic Nonhardening Range. We assume that isotropic hardening of materials does not develop, while the plastic

Contributed by the Applied Mechanics Division for publication in the JOURNAL OF APPLIED MECHANICS.
Discussion on this paper should be addressed to the Editorial Department, ASME, United Engineering Center, 345 East 47th Street, New York, N.Y. 10017, and will be accepted until two months after final publication of the paper itself in the JOURNAL OF APPLIED MECHANICS. Manuscript received by ASME Applied Mechanics Division, August 8, 1984; final revision, September 5, 1985.

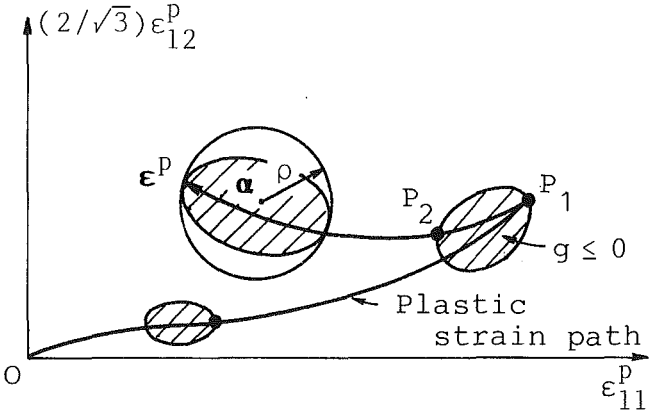

Fig. 1 Evolution of cyclic nonhardening region $g \le 0$ in plastic strain space

strain point moves inside a certain plastic strain range after a reversal of the straining direction, for example, the range $[P_1, P_2]$ along the strain path in Fig. 1. We refer to this plastic strain range as the *cyclic nonhardening range*, because *the plastic strain increment inside it does not contribute to the accumulation of cyclic hardening*. It is possible to interpret such a plastic strain range from the microscopic point of view [1]; dislocations piled up to obstacles may be remobilized under reverse straining, and thus a certain amount of plastic strain may proceed without marked increase of the dislocation density after a reversal of the straining direction.

The evolution of the cyclic nonhardening range, which can be a plastic strain region under multiaxial loading, is illustrated in Fig. 1. Under monotonic or near-monotonic straining as along the path OP_1, the region expands and translates progressively under the condition that the plastic strain point remains on the boundary of the region and moves in an outward direction. Under reverse straining, on the other hand, the region is assumed to remain unchanged as long as the plastic strain point moves inside it (i.e., along the path P_1P_2). But it starts to expand and translate again, when the plastic strain point reaches the bound (i.e., the point P_2).

In the case of uniaxial loading, the cyclic nonhardening range is represented as follows:

$$g = (\epsilon^p - \alpha)^2 - \rho^2 \le 0 \tag{1}$$

where α and ρ denote the center and half the size of this range. As assumed in the above, the range $g \le 0$ expands and translates, only when the plastic strain point ϵ^p is located on the bound $g = 0$ and moves outward:

$$\dot{\rho} = c\Gamma|\dot{\epsilon}^p|, \qquad \rho(0) = \rho_0 \tag{2}$$

$$\dot{\alpha} = (1-c)\Gamma\dot{\epsilon}^p \tag{3}$$

where c is a constant specifying the expansion rate of the range $g \le 0$, and Γ represents the evolution condition of this range:

$$\Gamma = \begin{cases} 1, & g = 0 \text{ and } (\partial g/\partial \epsilon^p)\dot{\epsilon}^p > 0 \\ 0, & g < 0 \text{ or } (\partial g/\partial \epsilon^p)\dot{\epsilon}^p \le 0 \end{cases} \tag{4}$$

The initial value of ρ is taken to be ρ_0, whereas that of α is zero. Here and from now on, $\dot{(\ )}$ stands for the derivative with respect to a certain loading parameter. It is ascertained that when $g = 0$ and $(\partial g/\partial \epsilon^p)\dot{\epsilon}^p > 0$ (i.e., $\Gamma = 1$), equations (2) and (3) satisfy the consistency condition $\dot{g} = 0$.

Under cyclic straining between fixed strain limits $\epsilon^p_{\min}$ and $\epsilon^p_{\max}$, the cyclic nonhardening range $g \le 0$ develops progressively with an increase of the number of cycles, n (see Appendix A). Eventually, the range $g \le 0$ occupies the cyclic range of plastic strain $[\epsilon^p_{\min}, \epsilon^p_{\max}]$, and the condition $g < 0$ becomes satisfied in a *whole* cycle. Then, equation (4) gives Γ the value of zero only, so that the range $g \le 0$ ceases from developing. Therefore, 2ρ increases to $\Delta\epsilon^p$ $(= \epsilon^p_{\max} - \epsilon^p_{\min})$. The increase of ρ as a function of n is obtained as equation (A4) in the Appendix.

It is seen from equation (A4) that when c is a constant as in the present paper, the number of cycles for the saturation of progressive development of the range $g \le 0$ does not depend on $\Delta\epsilon^p$. If c is a function of ρ and so on, however, it will depend on $\Delta\epsilon^p$.

A special case of the range $g \le 0$ with $c = 1/2$ respresents the maximum plastic strain range, which was originally used by Chaboche et al. [8], and subsequently by Dafalias [7], for the description of strain-controlled cyclic plastic behavior of 316 stainless steel. However, it was pointed out that the use of this special case is not always appropriate even under strain-controlled cyclic loading [1], see also [12]. Moreover, Ohno and Kachi [13] recently showed that the progressive development of the cyclic nonhardening range, i.e.,, $c << 1/2$, is important for the description of stress-controlled cyclic plasticity. Incidentally, constitutive models of creep with the range $g \le 0$ were proposed by Murakami and Ohno [14] and Ohno et al. [15].

Model I. Assuming combined isotropic-kinematic hardening of materials, we consider the following constitutive relations incorporating Γ defined by equation (4):

$$f = (\sigma - \eta)^2 - \kappa^2 = 0 \tag{5}$$

$$\kappa = \kappa(q), \quad \dot{q} = \Gamma|\dot{\epsilon}^p| \tag{6}$$

$$\dot{\eta} = [K + (1-\Gamma)d\kappa/dq]\dot{\epsilon}^p \tag{7a}$$

$$\dot{\epsilon}^p = (K + d\kappa/dq)^{-1}\dot{\sigma} \tag{8a}$$

where $f = 0$ is the yield condition, κ and η denote half the size and the center of the elastic stress range $f < 0$, q is an isotropic hardening variable, and K is a constant for kinematic hardening.

The concept of the cyclic nonhardening range is embodied through Γ in equations (6) and (7*a*) as follows:

$\Gamma = 1$: When the plastic strain point ϵ^p is located on the bound $g = 0$ and moves outward, equations (5)–(8) represent the *combined hardening model* of isotropic hardening modulus $d\kappa/dq$ and kinematic hardening modulus K.

$\Gamma = 0$: On the other hand, when ϵ^p moves inside the range $g \le 0$, the isotropic hardening variable q does not change, and equations (5)–(8) are reduced to those for the *kinematic hardening model* of hardening modulus $K + d\kappa/dq$.

It is seen from equation (8*a*) that the plastic tangent modulus is equal to $K + d\kappa/dq$ independently of the value of Γ, and hence it is not disturbed by the discrete change of Γ in equation (4). It is because the change of the isotropic hardening modulus from $d\kappa/dq$ to zero due to Γ in equation (6) is compensated with the change of the kinematic hardening modulus expressed in terms of $(1-\Gamma)d\kappa/dq$ in equation (7*a*).

Figure 2 illustrates the response of equations (5)–(8). In this figure, $d\kappa/dq$ is taken to be a constant. The evolution of the cyclic nonhardening range $g \le 0$ is also shown by hatched ranges on the axis of ϵ^p, and it occupies the ranges R_A, R_B, and R_C when plastic deformation proceeds to A, B, and C on the $\sigma - \epsilon^p$ diagram, respectively. (It is assumed that the range $g \le 0$ is initially reduced to the origin of the axis of ϵ^p, i.e., $\rho_0 = 0$). Then, the model gives the following cyclic response:

i) Under the incipient tensile loading to B, $\Gamma = 1$. Therefore, the range $g \le 0$ expands and translates continuously, and stress σ increases owing to the expansion and translation of the yield surface.

ii) Under the unloading and reverse loading from B to $\bar{B}$, ϵ^p moves inside the range R_B, and hence $\Gamma = 0$. Therefore, the range $g \le 0$ remains unchanged, and the yield surface does not expand but simply translates. This translation of the yield surface is accompanied with an increase of the kinematic hardening modulus expressed by $(1 - \Gamma)d\kappa/dq$ in equation

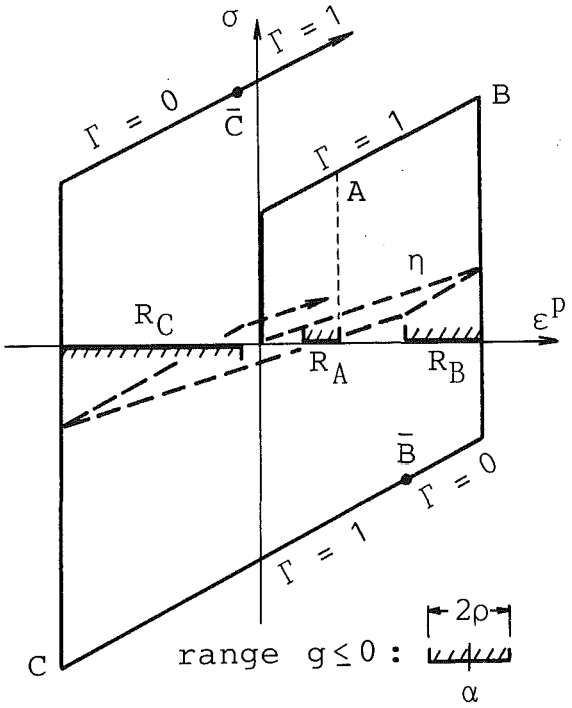

Fig. 2 Stress-strain diagram by Model I, together with evolution of cyclic nonhardening range $g \leq 0$

(7*a*), as mentioned already (see the dashed line in the figure).

iii) Under the reverse loading from $\bar{B}$ to C, ϵ^p keeps located on the bound $g = 0$ and moves outward ($\Gamma = 1$). Thus the development of the range $g \leq 0$ and the expansion of the yield surface occur in the same manner as under the incipient loading.

iv) The response under the second reverse loading is the same as under the first, except that the plastic strain range of $\Gamma = 0$ under the second reverse loading, R_C, is larger than the first, R_B.

The model describes the saturation of cyclic hardening which depends on the amplitude of cyclic straining as follows: As cyclic straining proceeds between fixed plastic strain limits, the cyclic nonhardening range eventually occupies the cyclic range of plastic strain, so that the condition $g < 0$ for $\Gamma = 0$ becomes satisfied in a whole cycle, as was mentioned earlier and will be seen from Fig. 2. Then, the yield surface ceases from expanding and only translates. The saturated size of the yield surface is given by $2\kappa(q_s)$, where q_s, the saturated value of q, is expressed as $q_s = (1/c)(\Delta\epsilon^p/2 - \rho_0)$ (see equation (*A*7) in Appendix). Therefore, Model I describes the dependence of cyclic hardening on the size of cyclic strain range. If $\kappa(q)$ is a dcreasing function of q, Model I expresses cyclic softening.

By taking account of the recovery of kinematic hardening [9], we can generalize the kinematic hardening equation (7*a*) to

$$\dot{\eta} = [K + (1-\Gamma)d\kappa/dq]\dot{\epsilon}^p - K_r\eta\,|\,\dot{\epsilon}^p\,| \qquad (7b)$$

where K_r is a constant. Then, by use of the condition $\dot{f} = 0$, equation (8*a*) is modified as

$$\dot{\epsilon}^p = \{K + d\kappa/dq - \mathrm{sgn}[\sigma-\eta]K_r\eta\}^{-1}\dot{\sigma} \qquad (8b)$$

Introduction of such a recovery term seems to give a general model which can describe nonlinear hardening of materials, cyclic relaxation of mean stress, and cyclic creep at least qualitatively. Nevertheless, we will employ a two-surface plasticity model, because this model has an advantage that transient elastoplastic behavior after yielding can be described separately from cyclic hardening behavior by means of bounding and yield surfaces, as explained below. Moreover, it will be discussed later that when the coefficient K_r in the recovery term in equation (7*b*) is determined from the data of cyclic recovery of mean stress, this term has only a small effect on the transient elastoplastic behavior after yielding.

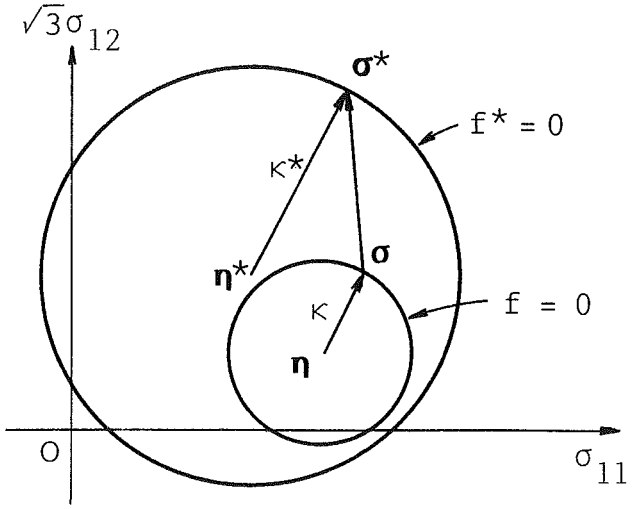

Fig. 3 Bounding surface $f^* = 0$ and yield surface $f = 0$

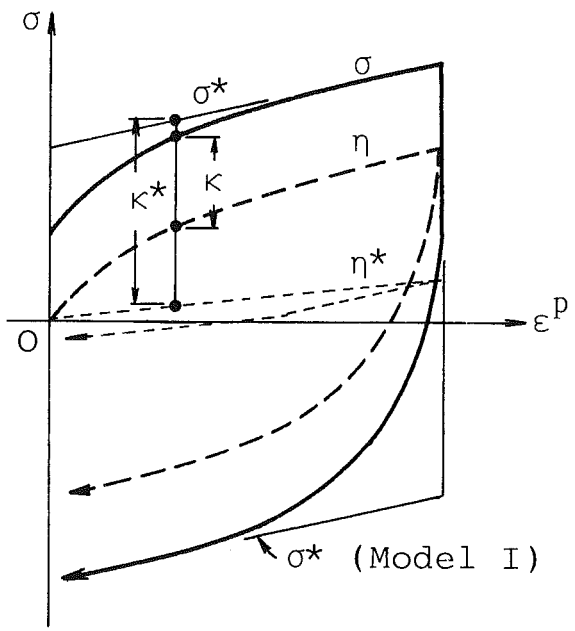

Fig. 4 Stress-strain diagram by Model II

Two-Surface Plasticity Model

A two-surface model is briefly explained by following Krieg [3] and Dafalais and Popov [4, 5] based on Mróz [16].

In order to describe the transient elastoplastic behavior of materials observed just after initial and reverse yieldings, a bounding surface $f^* = 0$ is introduced inside which a yield surface $f = 0$ is allowed to translate and expand, as schematically shown in Fig. 3, where η_{ij}^* and η_{ij} denote the centers of these surfaces, κ^* and κ being their radii. After the onset of yielding, the yield surface is assumed to translate so that stress σ_{ij} approaches the stress point σ_{ij}^* on $f^* = 0$ at which $\partial f^*/\partial\sigma_{ij}^*$ is codirectional with $\partial f/\partial\sigma_{ij}$. In this change of the yield surface, the plastic tangent modulus is taken to be larger when σ_{ij} is more distant from σ_{ij}^*, and it gets to depend on the evolution of the bounding surface as σ_{ij} comes near σ_{ij}^*. In other words, the change of the yield surface within the bounding surface describes the transient elastoplastic behavior after yielding, while the evolution of the bounding surface is responsible for the plastic behavior succeeding this transient one.

Formulation of New Constitutive Model (Model II)

We are in a position to formulate a new constitutive model of cyclic plasticity, Model II, by combining the cyclic nonhardening range model with the two-surface model.

Let us specify evolution equations of the bounding surface on the basis of the cyclic nonhardening range; i.e., we regard the yield surface in Model I as the boundary surface (Fig. 4). Then the radius and center of the bounding surface, κ^* and η^*, change as in equations (6) and (7):

$$\kappa^* = \kappa^*(q), \quad \dot{q} = \Gamma |\dot{\epsilon}^p| \tag{9}$$

$$\dot{\eta}^* = [K + (1-\Gamma) d\kappa^*/dq] \dot{\epsilon}^p - K_r \eta^* |\dot{\epsilon}^p| \tag{10}$$

where Γ is given by equations (1)–(4). The recovery term in equation (10) plays a role in describing cyclic recovery of mean stress.

Next let us specify the evolution of the yield surface for Model II. We assume for simplicity the yield surface of constant size

$$f = (\sigma - \eta)^2 - \kappa^2 = 0, \quad \kappa = \kappa_0 \tag{11}$$

where κ_0 is a constant. In regards to the translation of the yield surface inside the bounding surface, let us employ the rule [3]

$$\left.\begin{aligned} \dot{\eta} &= A(\sigma^* - \sigma)|\dot{\epsilon}^p| \\ \sigma^* &= \eta^* + \mathrm{sgn}[\sigma - \eta]\kappa^* \end{aligned}\right\} \tag{12}$$

where σ^* is the stress state on the bounding surface which stress σ approaches (Fig. 4), and A is a constant, possibly a function of σ^*, σ and so on. The above equation is a simple example, and it is possible to use other translation rules, e.g., [4, 5].

Then, using the consistency condition $\dot{f} = 0$ together with equations $(11)_2$ and (12), we obtain

$$\dot{\epsilon}^p = \mathrm{sgn}[\sigma - \eta]\{A(\sigma^* - \sigma)\}^{-1}\dot{\sigma} \tag{13}$$

Extension of Model II to Multiaxial States

The new constitutive model expressed by equations (9)–(13) together with (1)–(4) is extended to multiaxial stress states.

Cyclic Nonhardening Region. Restricting our concerns to radial or near-radial loading, we approximate the cyclic nonhardening region by the hyper-sphere of radius ρ and center α_{ij} (Fig. 1). Then, equations (1)–(4) are extended as follows [1]:

$$g = (2/3)(\epsilon^p_{ij} - \alpha_{ij})(\epsilon^p_{ij} - \alpha_{ij}) - \rho^2 \le 0 \tag{14}$$

$$\dot{\rho} = c\Gamma\dot{\epsilon}^p \tag{15}$$

$$\dot{\alpha}_{ij} = (3/2)^{1/2}(1-c)\Gamma\dot{\epsilon}^p \nu_{ij} \tag{16}$$

$$\Gamma = \begin{cases} \nu_{ij}\dot{\epsilon}^p_{ij}/\|\dot{\epsilon}^p\|, & g = 0 \text{ and } \nu_{ij}\dot{\epsilon}^p_{ij} > 0 \\ 0, & g < 0 \text{ or } \nu_{ij}\dot{\epsilon}^p_{ij} \le 0 \end{cases} \tag{17}$$

where $\dot{\epsilon}^p = [(2/3)\dot{\epsilon}^p_{ij}\dot{\epsilon}^p_{ij}]^{1/2}$, $\nu_{ij} = (\partial g/\partial \epsilon^p_{ij})/\|\partial g/\partial \epsilon^p\|$, and $\|t\| = (t_{ij}t_{ij})^{1/2}$ for a second rank tensor t_{ij}. It is seen from equation (17) that Γ is equal to the cosine of the angle between the vectors ν_{ij} and $\dot{\epsilon}^p_{ij}$ when $g = 0$ and $\nu_{ij}\dot{\epsilon}^p_{ij} > 0$, and thus $0 \le \Gamma \le 1$.

Bounding and Yield Surfaces. We consider the following multiaxial forms of the bounding and yield surfaces:

$$f^* = (3/2)(s^*_{ij} - \eta^*_{ij})(s^*_{ij} - \eta^*_{ij}) - \kappa^{*2} = 0 \tag{18}$$

$$f = (3/2)(s_{ij} - \eta_{ij})(s_{ij} - \eta_{ij}) - \kappa^2 = 0, \quad \kappa = \kappa_0 \tag{19}$$

where s^*_{ij} and s_{ij} are the deviators of σ^*_{ij} and σ_{ij}, respectively. The centers η^*_{ij} and η_{ij} are assumed to be in the deviatoric stress space, and thus the axial components in uniaxial stress states, η^*_{11} and η_{11}, are related with η^* and η in uniaxial equations (10) and (12) as follows:

$$\eta^*_{11} = (2/3)\eta^*, \quad \eta_{11} = (2/3)\eta.$$

Then, the uniaxial evolution equations of the bounding surface, (9) and (10), can be generalized as

$$\kappa^* = \kappa^*(q), \quad \dot{q} = \Gamma\dot{\epsilon}^p \tag{20}$$

$$\dot{\eta}^*_{ij} = (2/3)\{K + (1-\Gamma)d\kappa^*/dq\}\dot{\epsilon}^p_{ij} - K_r\eta^*_{ij}\dot{\epsilon}^p \tag{21}$$

Similary, the translation equation of the yield surface, (12), can be extended as

$$\left.\begin{aligned} \dot{\eta}_{ij} &= A(s^*_{ij} - s_{ij})\dot{\epsilon}^p \\ s^*_{ij} &= \eta^*_{ij} + (\kappa^*/\kappa)(s_{ij} - \eta_{ij}) \end{aligned}\right\} \tag{22a}$$

Assuming the normality of $\dot{\epsilon}^p_{ij}$ to the yield surface, and using the consistency condition $\dot{f} = 0$ together with equations $(19)_2$ and (22a), we obtain

$$\dot{\epsilon}^p_{ij} = (3/2)n_{ij}n_{kl}\dot{s}_{kl}/H \tag{23}$$

$$H = (3/2)^{1/2}A(s^*_{ij} - s_{ij})n_{ij} \tag{24a}$$

where $n_{ij} = (\partial f/\partial \sigma_{ij})/\|\partial f/\partial \sigma\|$ and H denotes the plastic tangent modulus.

Elimination of s^*_{ij}. Although we have completed the formulation of the model, we eliminate s^*_{ij} from the constitutive relations, i.e., equations (22a) and (24a). Equations $(22a)_2$ and (23) give, respectively,

$$s^*_{ij} - s_{ij} = \eta^*_{ij} - \eta_{ij} + (\kappa^*/\kappa - 1)(s_{ij} - \eta_{ij}) \tag{25}$$

$$\dot{\epsilon}^p_{ij}/\dot{\epsilon}^p = (3/2)(s_{ij} - \eta_{ij})/\kappa \tag{26}$$

Then, equations $(22a)_1$ and (24a) are rewritten as

$$\dot{\eta}_{ij} = A[(2/3)(\kappa^* - \kappa)\dot{\epsilon}^p_{ij} - (\eta_{ij} - \eta^*_{ij})\dot{\epsilon}^p] \tag{22b}$$

$$H = A[\kappa^* - \kappa - (3/2)^{1/2}(\eta_{ij} - \eta^*_{ij})n_{ij}] \tag{24b}$$

It is seen from equation (22b) that the translation equation of the yield surface of Model II has a recovery term. Since it has the form $(\eta_{ij} - \eta^*_{ij})\dot{\epsilon}^p$, the recovery of η_{ij} takes place around the center of the boundary surface. It is obvious from the character of Model II that this recovery term describes the transient elastoplastic behavior of materials just after yielding.

Comparison With Experiments and Discussion

Cyclic Torsional Tests of 304 Stainless Steel. Let us discuss the validity of the proposed model, Model II, on the basis of cyclic torsional tests of 304 stainless steel at room temperature [1]. Total (engineering) shear strain γ is assumed to be the sum

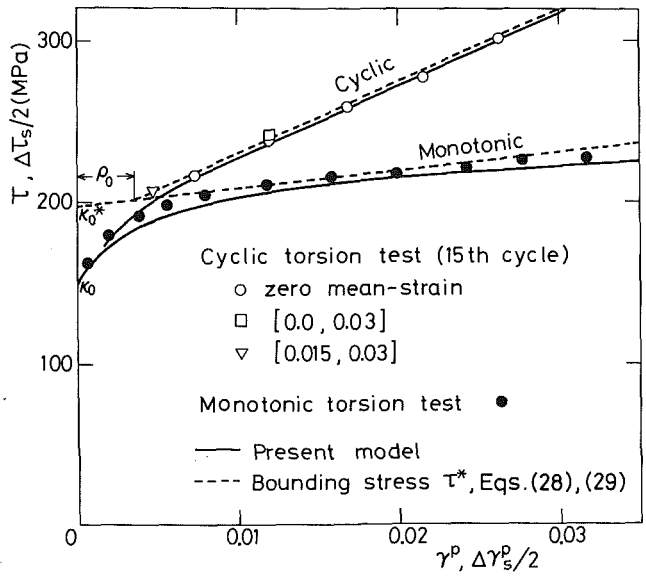

Fig. 5 Torsional cyclic and monotonic curves of stress versus plastic strain (304 stainless steel [1])

of elastic and plastic components claculated by Hooke's law and equations (9)–(13) together with (1)–(4), respectively. Equations (9)–(13) and (1)–(4) are used by simply replacing σ and ϵ^p with shear stress τ and shear plastic strain γ^p. The rate-dependence is disregarded, which this material shows at room temperature [17, 18], although the present model can be extened to viscoplastic deformations (see Concluding Remarks).

Let us choose the form of $\kappa^*(q)$ as

$$\kappa^*(q) = \kappa_0^* + Lq \quad (\kappa_0^*, L: \text{constants}) \tag{27}$$

Then, if the recovery term in equation (10) is negligibly small, equations ($A9$) and ($A10$) in the Appendix give the following relations for monotonic loading and cyclic loading between fixed strain limits, respectively:

$$\tau^* = \kappa_0^* + (K+L)\gamma^p \tag{28}$$

$$\frac{\Delta\tau_s^*}{2} = \kappa_0^* + (K+L)\rho_0 + \left\{K + \left(1+\frac{1}{c}\right)L\right\}\left(\frac{\Delta\gamma_s^p}{2} - \rho_0\right) \tag{29}$$

where Δ designates the sizes of cylic ranges, and the subscript s stands for the stabilized state of stress-strain hysteresis loops. Moreover, the monotonic stress-strain relation is obtained as equation ($A11$). These relations helped us obtain the following values of material constants from the experimental data in Figs. 5 and 6 (see Appendix D): $\kappa_0^* = 197$ MPa, $\kappa_0 = 150$ MPa, $A = 350$, $K = 900$ MPa, $L = 265$ MPa, $K_r = 7.0$, $\rho_0 = 0.0036$, and $c = 0.08$.

Figures 7(a)–7(c) show the stress-strain hysteresis loops for cyclic strain ranges [−0.03, 0.03], [0.0, 0.3], and [0.015, 0.03], respectively. The changes of peak stresses during the tests are shown in Fig. 6. The 15th loops can be regarded as stabilized (Fig. 6).

It is seen in Figs. 7(a)–7(c) that the proposed model simulates fairly well the stress-strain hysteresis loops obtained from the experiments. In regards to Fig. 7(a), however, the Bauschinger effect does not become so large in the calculation as in the experiment, as cyclic hardening proceeds. A better description may be obtained by letting the coefficient A in equation (12) be a function of κ^*, for example, as $A = A_0[\mu + (1-\mu)\kappa_0^*/\kappa^*]$ (A_0, μ: constants). Then, since A becomes smaller with increase of κ^*, larger Bauschinger effect will be calculated as cyclic hardening proceeds.

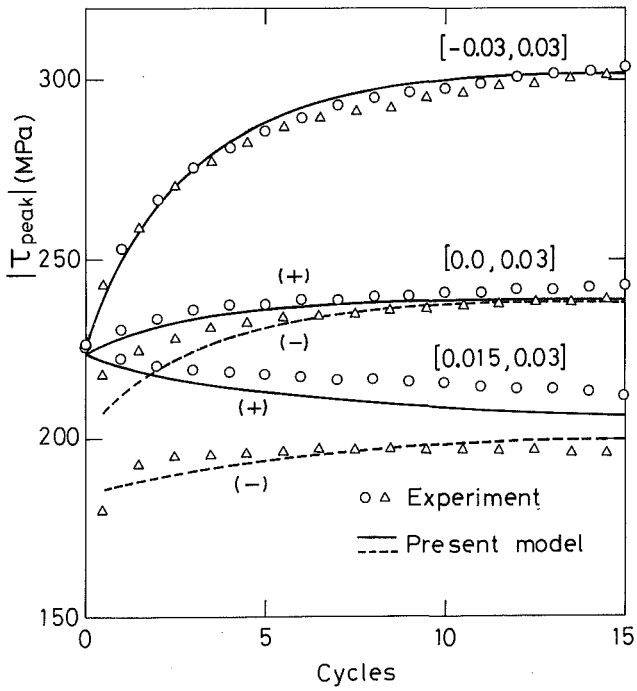

Fig. 6 Changes of positive and negative peak stresses, τ^+_{peak} and τ^-_{peak}, (304 stainless steel [1])

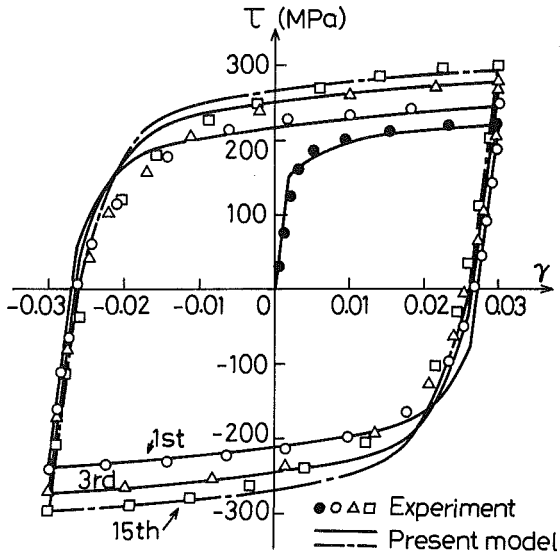

Fig. 7(a)

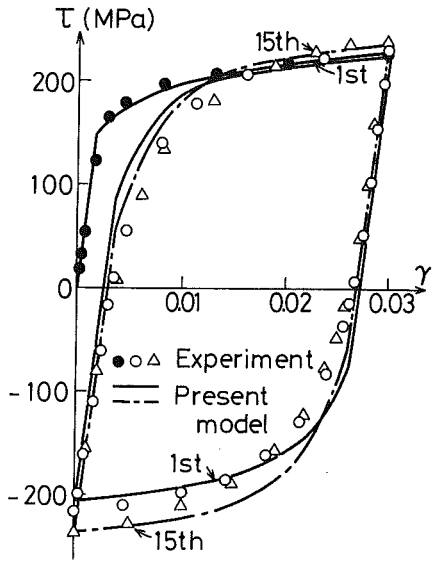

Fig. 7(b)

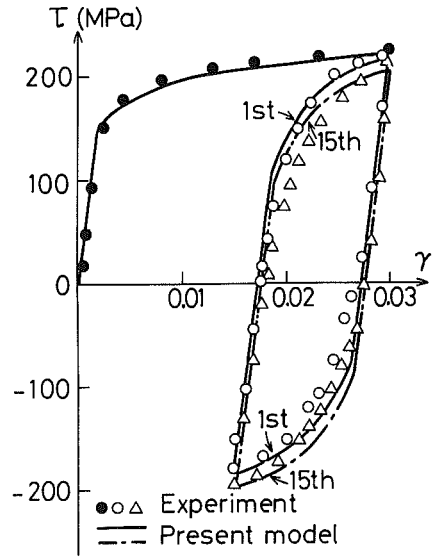

Fig. 7(c)

Fig. 7 Stress-strain loops for constant cyclic strain ranges (304 stainless steel [1]): (a) cyclic strain range [−0.03, 0.03]; (b) cyclic strain range [0.0, 0.03]; (c) cylic strain range [0.015, 0.03]

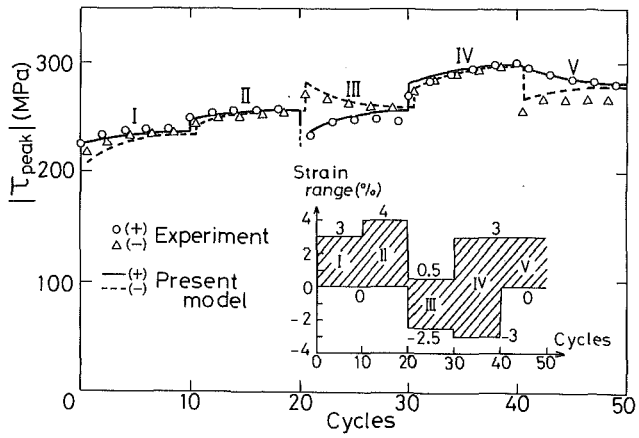

Fig. 8 Changes of peak stresses under variation of cyclic strain range (304 stainless steel [1])

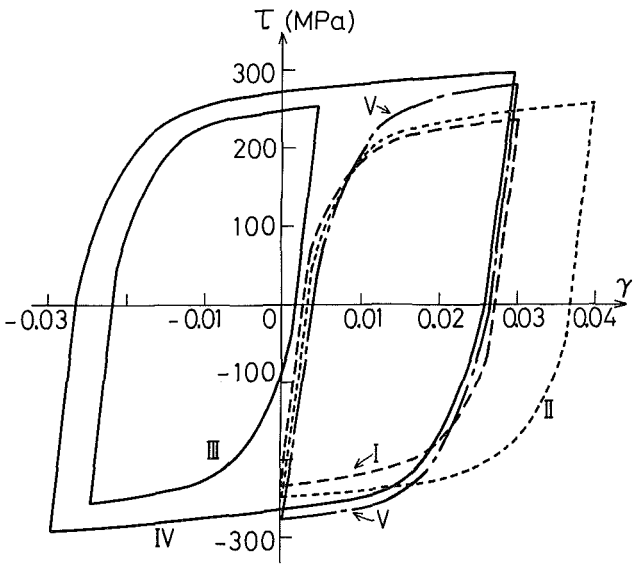

Fig. 9(a)

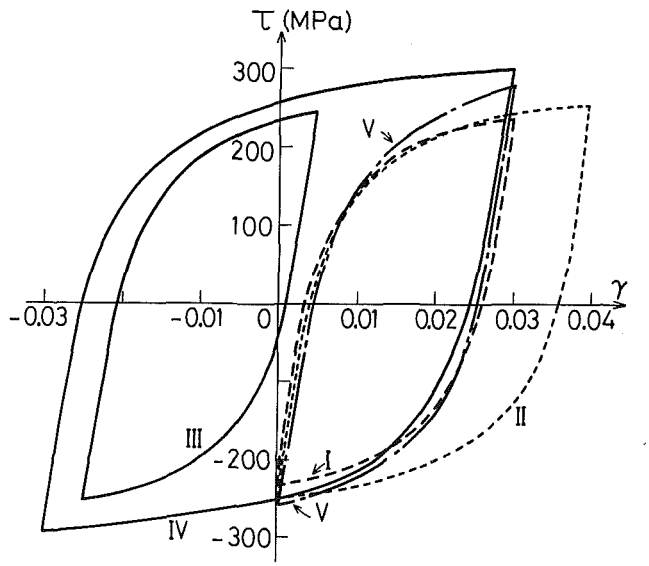

Fig. 9(b)

Fig. 9 Stress-strain loops at the last cycles in Step I through V: (a) present model; (b) experiment (304 stainless steel [1])

The values of $\Delta\tau_s/2$ and $\Delta\gamma_s^p/2$ in the experiments for the strain ranges [0.0, 0.03] and [0.015, 0.03] shown in Figs. 7(*b*) and 7(*c*) are plotted in Fig. 5, too. Noting that mean strain is not zero in these experiments, we see that the saturated level of cyclic hardening is expressed as a function of strain amplitude and hence does not depend on mean strain. This tendency was observed for 2017 aluminum alloy, too, subjected to several kinds of plastic prestrain, up to 10.0 percent, followed by cyclic straining of plastic strain range 1.0 or 2.0 percent [19].

The experimental tendency above is described by the present model as follows: We have assumed that the expansion of the bounding surface is controlled by the development of the cyclic nonhardening range $g \leq 0$. Since the range $g \leq 0$ with $c << 1/2$ develops little by little with increase of the number of cycles, it eventually occupies the cyclic range of plastic strain irrespective of the value of mean strain. Thus, equations (*A*10) and (*A*7) in the Appendix are valid in this case, too. Therefore, mean strain does not affect the saturated level of cyclic hardening.

Chaboche et al. [18] proposed a model of cyclic plasticity by representing isotropic hardening in terms of the maximum plastic strain range given by a special case of equations (1)–(4) with $c = 1/2$. However, their model is not supported by the experimental observation above: It can be shown that for cyclic straining between ϵ^p_{min} and ϵ^p_{max} ($0 \leq \epsilon^p_{min} < \epsilon^p_{max}$), this maximum plastic strain range takes [0, ϵ^p_{max}]. Therefore, according to their model, cyclic hardening in this case depends on ϵ^p_{max} rather than $\Delta\epsilon^p$ ($= \epsilon^p_{max} - \epsilon^p_{min}$), no matter how small $\Delta\epsilon^p$ is. It does not agree with the experimental results shown in Figs. 7(*b*) and 7(*c*) for the cyclic strain ranges [0.0, 0.03] and [0.015, 0.03], where ϵ^p_{max} is the same.

We now discuss the recovery term in the translation rule (10) of the bounding surface, i.e., the term $K_r\eta^*|\dot{\epsilon}^p|$. When $K_r = 0$, this rule is essentially a linear one and similar to Prager's rule; hence, the present model does not describe cyclic relaxation of mean stress under nonzero mean strain. But, for a positive value of K_r, it describes the cyclic relaxation, which becomes rapid with increase of K_r. Therefore, the value of K_r was determined from the best fitting of the data of cyclic relaxation (cyclic equlaization of positive and negative peak stresses) obtained from the experiments of [0.0, 0.03] and [0.015, 0.03] (see Fig. 6). Then, it was found in equation (10) that the magnitude of the recovery term is at most about twenty percent of that of the hardening term. In other words, when the recovery term in equation (10), or (7*b*) for Model I, is determined from the data of cyclic relaxation of mean stress, it is not large enough to describe the transient elastoplastic behavior appearing just after yielding.

Figures 8 and 9 show predicted and experimental results under cyclic straining between varying strain limits. The cyclic history consists of Step I through V with ten cycles each, as shown in Fig. 8. The stress-strain loops in Fig. 9 are the ones at the last cycles in these steps.

It is seen in Fig. 9 that the predicted peak stresses coincide well with the experimental ones. The degree of coincidence is nearly the same as that in the previous paper [1]. It is because the bounding surface in the present model is just the yield surface of Model I proposed in [1]. In regards to the description of the transient response after yielding, on the other hand, the present model is definitely better than Model I and simulates the experimental stress-strain loops fairly well (Fig. 9).

Incidentally, the test results in Fig. 8 shows weak cyclic softening after the reduction of the strain range size from Step IV to V, but the present model does not describe it. This phenomenon may be described by adding a memory erasure term to equation (2), see [30].

Cyclic Uniaxial Tests of 316L Stainless Steel. The cyclic stress-strain curve of 316L stainless steel at room temperature [8] shown in Fig. 10 is considerably nonlinear, in contrast with

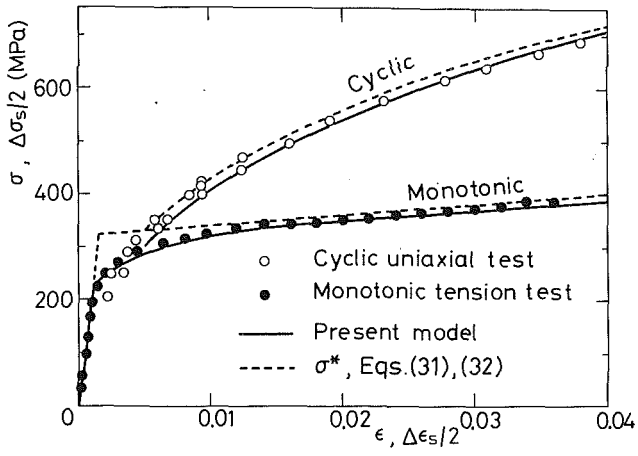

Fig. 10 Uniaxial cyclic and monotonic curves of stress versus strain (316L stainless steel [8])

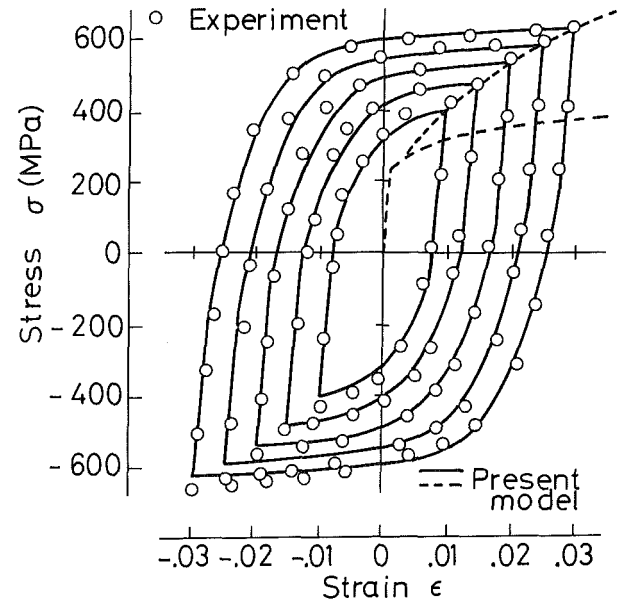

Fig. 11 Stabilized stress-strain loops under stepwise expanding of strain range as Δϵ/2 = 1.0 → 1.5 → • • • • → 3.0 percent (316L stainless steel [8])

that in Fig. 5, although this cyclic curve up to $\Delta\epsilon/2 = 0.01$ or 0.02 can be approximated by a linear relation as in Fig. 5.

Let us describe the nonlinearity mentioned above by assuming $\kappa(q)$ as

$$\kappa^*(q) = \kappa_0^*[1 + Lq/(m\kappa_0^*)]^m \quad (\kappa_0^*, L, \text{m: constants}) \tag{30}$$

which is reduced to equation (27) when $m = 1$ or q is sufficiently small. Since we are not concerned with cyclic relaxation of mean stress under nonzero mean strain here, we neglect the recovery term for $\dot{\eta}^*$, i.e., $K_r = 0$ in equation (10). Then the monotonic and cyclic relations between σ^* and ϵ^p are obtained from equations (A9) and (A10), respectively, as follows:

$$\sigma^* \simeq \kappa_0^* + (K+L)\epsilon^p \ (\text{for } \epsilon^p << m\kappa_0^*/L) \tag{31}$$

$$\frac{\Delta\sigma_s^*}{2} = \left\{K + L\left[\omega\left(\frac{\Delta\epsilon_s^p}{2} - \rho_0\right) + 1\right]^{m-1}\right\}\frac{\Delta\epsilon_s^p}{2} + \kappa_0^*\left[\omega\left(\frac{\Delta\epsilon_s^p}{2} - \rho_0\right) + 1\right]^m \tag{32}$$

where $\omega = L/(mc\kappa_0^*)$. Using the above relations and the monotonic $\sigma - \epsilon^p$ relation (A11), we determined the material constants as explained in the Appendix D; $\kappa_0^* = 325$ MPa, $\kappa_0 = 230$ MPa, $A = 230$, $K = 350$ MPa, $L = 1750$ MPa, $m = 0.40$, $\rho_0 = 0.0034$, and $c = 0.08$, where the value of c was determined from the observation that the $\sigma - \epsilon$ loop for $\Delta\epsilon/2 = 0.01$ becomes nearly stabilized after about ten cycles [8]. It is seen in Fig. 10 that the present model simulates well the experimental results.

Figure 11 shows the stabilized $\sigma - \epsilon$ loops under stepwise expanding of strain range. It is seen that the present model describes very well the transient response after yielding observed in the experiment. It is also seen that the nearly-elastic stress range of large plastic stiffness expands with increase of the strain range size, although we have assumed no expansion of the yield surface, i.e., equation $(11)_2$.

Concluding Remarks

We proposed a constitutive model of cyclic plasticity, Model II, by combining Model I based on the cyclic nonhardening range with a two-surface model. It was shown that the resulting model describes well the cyclic hardening phenomenon and the transient elastoplastic behavior after yielding of 304 and 316 stainless steels in several cases where mean strain is zero or nonzero and strain limits are fixed or variable.

Recently, Ohno and Kachi [13] applied the present constitutive model to stress-controlled cyclic loading, and showed that the cyclic stress-strain curve calculated for constant stress ranges coincides with that for constant strain ranges, as observed experimentally for 304 and 316 stainless steels. Therefore, they pointed out the importance of the progressive development of the cyclic nonhardening range under stress-controlled cyclic loading.

The present model can be extended to viscoplastic deformations in the same way as in [20, 9]: Regarding the yield surface in the rate-independent model as the quasi-static yield surface, we replace equation (23) with

$$d\epsilon_{ij}^p/dt = \mu < \tilde{\sigma} > \partial\tilde{\sigma}/\partial\sigma_{ij} \tag{33}$$

$$\tilde{\sigma} = \{(3/2)(s_{ij} - \eta_{ij})(s_{ij} - \eta_{ij})\}^{1/2} - \kappa \tag{34}$$

where $\tilde{\sigma}$ denotes the overstress measured from the quasi-static yield surface $\tilde{\sigma} = 0$, t denotes the time, and $\mu < x >$ is $\mu(x)$ if $x \geq 0$, and zero if $x < 0$. Equation (22b) is appropriate as the translation rule of the quasi-static yield surface. On the other hand, when equation (22a) is used, s_{ij} in this equation should be replaced with the projection of s_{ij} onto the quasi-static yield surface, $s'_{ij} = \eta_{ij} + (s_{ij} - \eta_{ij})\kappa/(\kappa + \tilde{\sigma})$. We notice that the bounding surface is defined for the quasi-static yield surface.

Cyclic hardening of 304 and 316 stainless steels is more significant under nonproportional cyclic loading than under proportional one [21-25], see also [26] for OFHC copper and [27] for 1 percent Cr-Mo-V steel. Recently, Tanaka et al. [28] showed an extension of the present model to the case of nonproportional cyclic loading. Nouailhas et al. [29] discussed this case on the basis of the cyclic nonhardening region and the Baltov-Sawczuk yield surface. McDowell [30] proposed a measure of nonproportional cyclic straining and formulated a constitutive model of cyclic plasticity.

Acknowledgment

The authors are grateful to Professor S. Murakami of Nagoya University for his encouragement and discussion. The second author, Y. Kachi, was associated with the present work while studying as a graduate student at Toyohashi University of Technology.

References

1 Ohno, N., "A Constitutive Model of Cyclic Plasticity With a Nonhardening Strain Region," ASME JOURNAL OF APPLIED MECHANICS, Vol. 49, 1982, pp. 721-727.

2 Mróz, Z., "An Attempt to Describe the Behavior of Metals Under Cyclic Loads Using a More General Workhardening Model," *Acta Mechanica*, Vol. 7, 1969, pp. 199-212.

3 Kreig, R. D., "A Practical Two Surface Plasticity Theory," ASME JOURNAL OF APPLIED MECHANICS, Vol. 42, 1975, pp. 641-646.

4 Dafalias, Y. F., and Popov, E. P., "A Model of Nonlinearly Hardening Materials for Complex Loading," *Acta Mechanica*, Vol. 21, 1975, pp. 173-192.

5 Dafalias, Y. F., and Popov, E. P., "Plastic Internal Variables Formalism of Cyclic Plasticity," ASME JOURNAL OF APPLIED MECHANICS, Vol. 43, 1976, pp. 645-651.

6 Hashiguchi, K., "Constitutive Equations of Elastoplastic Materials With Anisotropic Hardening and Elastic-Plastic Transition," ASME JOURNAL OF APPLIED MECHANICS, Vol. 48, 1981, pp. 297-301.

7 Dafalias, Y. F., "A Novel Bounding Surface Constitutive Law for the Monotonic and Cyclic Hardening Response of Metals," *Transactions of the 6th International Conference on Structural Mechanics in Reactor Technology*, Paper No. L 3/4, Vol. L, Paris, Aug. 1981.

8 Chaboche, J. L., Dang Van, K., and Cordier, G., "Modelization of the Strain Memory Effect on the Cyclic Hardening of 316 Stainless Steel," *Transactions of the 5th International Conference on Structural Mechanics in Reactor Technology*, Paper No. L 11/3, Vol. L, Berlin, Aug. 1979.

9 Chaboche, J. L., "Viscoplastic Constitutive Equations for the Description of Cyclic and Anisotropic Behaviour of Metals," *Bulletin de l'Academie Polonaise des Sciences*, Série des Sciences and Techniques, Vol. 25, 1977, pp. 33-42.

10 Marquis, D., "Etude Théorique et Vérification Expérimentale d'un Modèle de Plasticité Cyclique," Thèse Paris, VI, 1979.

11 Chaboche, J. L., and Rousselier, G., "On the Plastic and Viscoplastic Constitutive Equations—Part I: Rules Developed With Internal Variable Concept—Part II: Application of Internal Variable Concepts to the 316 Stainless Steel," *ASME Journal of Pressure Vessel Technology*, Vol. 105, 1983, pp. 153-164.

12 Dafalias, Y. F., "Modeling Cyclic Plasticity: Simplicity Versus Sophistication," *Mechanics of Engineering Materials*, ed. by Desai, C. S., and Gallagher, R. H., Wiley, 1984, pp. 153-178.

13 Ohno, N., and Kachi, Y., "Description of Stress- and Strain-Controlled Cyclic Plasticity Using the Cyclic Nonhardening Region Model," *Transactions of the 8th International Conference on Structural Mechanics in Reactor Technology*, Vol. L, Brussels, Aug. 1985, pp. 57-64; *Res Mechanica* (in print).

14 Murakami, S, and Ohno, N., "A Constitutive Equation of Creep Based on the Concept of a Creep-Hardening Surface," *International Journal of Solids and Structures*, Vol. 18, 1982, p. 597-609.

15 Ohno, N., Murakami, S., and Ueno, T., "A Constitutive Model of Creep Describing Ceep Recovery and Material Softening Caused by Stress Reversals," *ASME Journal of Engineering Materials and Technology*, Vol. 107, 1985, pp. 1-6.

16 Mróz, Z., "On the Description of Anisotropic Workhardening," *Journal of the Mechanics and Physics of Solids*, Vol. 15, 1967, pp. 163-175.

17 Krempl, E., "An Experimental Study of Room-Temperature Rate Sensitivity, Creep and Relaxation of Type 304 Stainless Steel," *Journal of the Mechanics and Physics of Solids*, Vol. 27, 1979, pp. 363-375.

18 Ikegami, K., and Nittsu, Y., "Experimental Evaluation of the Interaction Effect Between Plastic and Creep Deformation," *Engineering Fracture Mechanics*, Vol. 21, 1985, pp. 897-907.

19 Kawashima, K., and Yoshida, T., "Cycle-Dependent Change in Plastic Stress-Strain Curves," *Proceedings of the 1982 Joint Confeence on Experimental Mechanics*, Part I, SESA and JSME, Hawaii, May 1982, pp. 371-376.

20 Perzyna, P., "Thermodynamic Theory of Viscoplasticity," *Advances in Applied Mechanics*, ed. by Yih, C. S., Vol. 11, 1971, pp. 313-354.

21 Nouailhas, D., Policella, H., and Kaczmarek, H., "On the Description of Cyclic Hardening Under Complex Loading Histories," *Proceedings of International Conference on Constitutive Laws for Engineering Materials*, ed. by Desai, C. S., and Gallagher, R. H., Tucson, Arizona, Jan. 1983, p. 45-49.

22 McDowell, D. L., "On the Path Dependence of Transient Hardening and Softening to Stable States Under Complex Biaxial Cyclic Loading," *Proceedings of International Conference on Constitutive Laws for Engineering Materials*, ed. by Desai, C. S., and Gallagher, R. H., Tuscson, Arizona, Jan. 1983, p. 125-132.

23 Krempl, E., and Lu, H., "The Hardening and Rate-Dependent Behavior of Fully Annealed AISI Type 304 Stainless Steel Under Biaxial In-Phase and Out-of-Phase Strain Cycling at Room Temperature," *ASME Journal of Engineering Materials and Technology*, Vol. 106, 1984, pp. 376-382.

24 Ohashi, Y., Kawai, M., and Kaito, T., "Inelastic Behaviour of Type 316 Stainless Steel Under Multiaxial Nonproportional Cyclic Stressings at Elevated Temperature," *ASME Journal of Engineering Materials and Technology*, Vol. 107, 1985, pp. 101-109.

25 Tanaka, E., Murakami, S., and Ooka, M., "Effects of Plastic Strain Amplitudes on Non-Proportional Cyclic Plasticity," *Acta Mechanica*, Vol. 57, 1985, pp. 167-182.

26 Lamba, H. S., and Sidebottom, O. M., "Cyclic Plasticity for Nonproportional Paths: Part 1—Cyclic Hardening, Erasure of Memory, and Subsequent Strain Hardening Experiments: Part 2—Comparison With Predictions of Three Incremental Plasticity Models," *ASME Journal of Engineering Materials and Technology*, Vol. 100, 1978, pp. 96-111.

27 Kanazawa, K., Miller, K. J., and Brown, M. W., "Cyclic Deformation of 1% Cr-Mo-V Steel Under Out-of-Phase Loads," *Fatigue of Engineering Materials and Structures*, Vol. 2, 1979, pp. 217-228.

28 Tanaka, E., Murakami, S., and Ooka, M., "A Constitutive Model of Cyclic Plasticity in Multiaxial Non-Proportional Loading," *Transactions of the 8th International Conference on Structural Mechanics in Reactor Technology*, Vol. L, Brussels, Aug. 1985, pp. 71-77.

29 Nouailhas, D., Chaboche, J. L., Savalle, S., and Cailletaud, G., "On the Constitutive Equations of Cyclic Plasticity Under Non-Proportional Loading," *International Journal of Plasticity*, Vol. 1, 1985, pp. 317-330.

30 McDowell, D. L., "A Two Surface Model for Transient Nonproportional Cyclic Plasticity: Part 1—Development of Appropriate Equations: Part 2—Comparison of Theory With Experiments," ASME JOURNAL OF APPLIED MECHANICS, Vol. 52, 1985, pp. 298-308.

APPENDIX

A Evolution of Cyclic Nonhardening Range. Let us consider cyclic straining between fixed limits $\epsilon^p_{\min}$ and $\epsilon^p_{\max}$. The range $g \le 0$ at the beginning of the nth cycle is $[\epsilon^p_{\max} - 2\rho_{n-1}, \epsilon^p_{\max}]$. (In Fig. 2, R_B is the range $g \le 0$ at the beginning of the first cycle.) Then, in the first half of the nth cycle where ϵ^p changes from $\epsilon^p_{\max}$ to $\epsilon^p_{\min}$, equation (2) becomes

$$\dot{\rho} = \begin{cases} 0, & \epsilon^p_{\max} - 2\rho_{n-1} < \epsilon^p \le \epsilon^p_{\max} \\ c\,|\,\dot{\epsilon}^p\,|, & \epsilon^p_{\min} \le \epsilon^p \le \epsilon^p_{\max} - 2\rho_{n-1} \end{cases} \tag{A1}$$

With $\Delta\epsilon^p = \epsilon^p_{\max} - \epsilon^p_{\min}$, the above equation is rewritten as

$$\rho_{n-0.5} - \rho_{n-1} = c(\Delta\epsilon^p - 2\rho_{n-1}) \tag{A2}$$

In (A1) and (A2), ρ_{n-1} and $\rho_{n-0.5}$ denote the values of ρ at the beginning and end of this first half cycle. For the latter half, we have

$$\rho_n - \rho_{n-0.5} = c(\Delta\epsilon^p - 2\rho_{n-0.5}) \tag{A3}$$

If $0 < c << 1$, we obtain from (A2) and (A3) the approximation $d\rho/dn = \rho_n - \rho_{n-1} \simeq 2c(\Delta\epsilon^p - 2\rho)$. Thus, assuming $\rho_{n=0} \simeq 0$, we have

$$2\rho/\Delta\epsilon^p \simeq 1 - \exp(-4cn) \tag{A4}$$

B Monotonic and Cyclic Relations (Model I). Under monotonic tensile loading, equation $(6)_2$ together with (1)–(4) gives $q = 0$ for $\epsilon^p \le \rho_0$ and $q = \epsilon^p - \rho_0$ for $\epsilon^p > \rho_0$. Therefore, if $K_r = 0$, we obtain from equation (8) the montonic tensile relation of Model I:

$$\sigma = \begin{cases} \kappa(0) + [K + (d\kappa/dq)_0]\epsilon^p, & \epsilon^p \le \rho_0 \\ K\epsilon^p + (d\kappa/dq)_0\rho_0 + \kappa(q), & \epsilon^p > \rho_0 \end{cases} \tag{A5}$$

where $(d\kappa/dq)_0$ denotes the value of $d\kappa/dq$ at $q = 0$.

Let us consider cyclic straining between fixed strain limits. The stabilized size of cyclic stress range is expressed as

$$\Delta\sigma_s = \Delta\eta_s + 2\kappa(q_s) \tag{A6}$$

where the subscript s denotes the stabilized state. Using (2) and $(6)_2$, we have $\dot{q} = \dot{\rho}/c$, i.e., $q = (\rho - \rho_0)/c$. In the stabilized state, the range $g \le 0$ occupies the cyclic range of plastic strain, i.e., $2\rho_s = \Delta\epsilon^p_s$, as seen from (A4). Therefore,

$$q_s = (1/c)\,(\Delta\epsilon^p_s/2 - \rho_0) \tag{A7}$$

Noting that $\Gamma = 0$ in a whole cycle in the stabilized state, we obtain $\Delta\eta_s$ from (7a) as

$$\Delta\eta_s = [K + (d\kappa/dq)_s]\Delta\epsilon^p_s \tag{A8}$$

where $(d\kappa/dq)_s$ denotes the value of $d\kappa/dq$ with respect to q_s.

C Monotonic and Cyclic Relations (Model II). Since the yield surface in Model I is regarded as the bounding surface in Model II, equations (A5)–(A8) for Model I result in the relations for the bounding stress σ^* in Model II by replacing σ, κ, and η with σ^*, κ^*, and η^*, respectively. Therefore, for monotonic tensile loading,

$$\sigma^* = \begin{cases} \kappa^*(0) + [K + (d\kappa^*/dq)_0]\epsilon^p, & \epsilon^p \le \rho_0 \\ K\epsilon^p + (d\kappa^*/dq)_0\rho_0 + \kappa^*(q), & \epsilon^p > \rho_0 \end{cases} \tag{A9}$$

and for cyclic straining between fixed strain limits,

$$\Delta\sigma^*_s = [K + (d\kappa^*/dq)_s]\Delta\epsilon^p_s + 2\kappa^*(q_s) \tag{A10}$$

where q_s is given by (A7).

Under monotonic tensile loading, we have $\eta = \sigma - \kappa_0$ from (11), so that $(12)_1$ results in $d\sigma/d\epsilon^p = A(\sigma^* - \sigma)$. Therefore,

for the linear $\sigma^* - \epsilon^p$ relation (28) or (31), we obtain the monotonic $\sigma - \epsilon^p$ relation

$$\sigma = \kappa_0 + (K+L)\epsilon^p + [\kappa_0^* - \kappa_0 - (K+L)A^{-1}][1 - \exp(-A\epsilon^p)] \quad (A11)$$

D Determination of Material Constants. Constitutive relations (9)–(13) together with (1)–(4) have a material function $\kappa^*(q)$ and constants c, ρ_0, K, κ_0, A, and K_r.

The function and constants above, except K_r, can be determined from monotonic and cyclic stress-strain curves together with n_s, the number of cycles for the saturation of strain-controlled cyclic hardening. By using (A4), the value of c was first estimated from the data of n_s (Fig. 6). Then, supposing $K_r = 0$ tentatively, we determined $\kappa^*(q)$, ρ_0, and K by approximating the experimental data of monotonic and cyclic stress-strain curves with the bounding stress relations (28) and (29), or (31) and (32), (dashed lines in Fig. 5 or 10). The values of κ_0 and A were obtained by simulating the transient elastoplastic deformation after initial yielding with (A11) (Fig. 5 or 10).

Finally, the value of K_r was adjusted so that (9)–(13) together with (1)–(4) gave the best fitting of the experimental data of cyclic equalization of positive and negative peak stresses under nonzero mean strain (Fig. 6). Incidentally, it was found that the tentative assumption $K_r = 0$ influenced little on the values of the other constants as far as the data in Figs. 5 and 6 were concerned.

A Reduction Method for Nonhomogeneous Boundary Conditions

J. M. Sloss
Department of Mathematics,
University of California,
Santa Barbara, CA 93106

I. Sadek
Mathematical Science Department,
University of North Carolina at Wilmington,
Wilmington, N.C. 28403

J. C. Bruch Jr.
Department of Mechanical
and Environmental Engineering,
University of California,
Santa Barbara, CA 93106

A procedure is described for reducing dynamical equations in two-space variables defined in a rectangle with nonhomogeneous time dependent boundary data to equations with homogeneous boundary data. The procedure applies not only to a single equation but to systems of equations with systems of boundary conditions. One-space dimensional problems are treated separately and a condition for applicability is developed in this case.

Examples are presented in which dynamical equations in one and two-space variables with nonhomogeneous time dependent boundary data are reduced to equations with homogeneous boundary data. Specific applications to problems in one-space variable include a simple beam, a laminated composite plate, and a Timoshenko beam. For two-space variable problems defined in a rectangle, the application of the procedure is made to an antisymmetric angle-ply circular cylindrical panel.

Introduction

In many dynamical problems, it is advantageous to reduce a problem with nonhomogeneous boundary conditions to an equivalent problem with homogeneous boundary conditions. This is useful when seeking solutions in terms of eigenfunction expansions.

Mindlin–Goodman [1] have given a procedure for reducing time dependent nonhomogeneous boundary value problems to equivalent homogeneous boundary value problems. They applied their method to beams while Yu [2] used it on sandwich plates and Sun and Whitney [3] on laminated composite plates. All these references treat essentially only one-space dimensional problems. In the Mindlin–Goodman method, as in this paper, separation of variables is used. However, their method basically involves solving a system of equations several times, whereas to apply the method of this paper requires solving a system of equations once. For one-dimensional problems a Theorem giving conditions sufficient for the method to be applicable is proved herein.

Three example problems in one-space variable and one problem in two-space variables are presented and an illustration of the application of the procedure to each is worked out for at least one specific set of nonhomogeneous boundary conditions. In Example One, which deals with a simple Bernoulli-Euler beam, it is sufficient to satisfy four conditions; this contrasts with 16 conditions in the Mindlin–Goodman method [1]. In each one-space dimensional problem, the condition of the Theorem is shown to be satisfied and hence the applicability of the method is assured.

Contributed by the Applied Mechanics Division for publication in the JOURNAL OF APPLIED MECHANICS.

Discussion on this paper should be addressed to the Editorial Department, ASME, United Engineering Center, 345 East 47th Street, New York, N.Y. 10017, and will be accepted until two months after final publication of the paper itself in the JOURNAL OF APPLIED MECHANICS. Manuscript received by ASME Applied Mechanics Division, September 27, 1984; final revision, June 3, 1985.

Two-Dimensional Problems

Given a linear system of partial differential equations

$$L[U]=F(x,y,t) \quad \text{for} \quad 0<x<a, \quad 0<y<b, \quad 0<t<T \tag{1}$$

in which L can be a matrix of linear partial differential operators of second order in time and higher order in space, U an $(n\times 1)$ column vector of functions and F a vector of functions. U satisfies the initial conditions

$$\begin{aligned} U(x,y,0)&=\Phi(x,y),\\ U_t(x,y,0)&=\Psi(x,y) \end{aligned} \tag{2}$$

and boundary conditions

$$\begin{aligned} B^1[U]&=G^1(y,t) \quad \text{along} \quad x=a,\\ B^2[U]&=G^2(x,t) \quad \text{along} \quad y=b,\\ B^3[U]&=G^3(y,t) \quad \text{along} \quad x=0,\\ B^4[U]&=G^4(x,t) \quad \text{along} \quad y=0. \end{aligned} \tag{3}$$

It is the purpose of this paper to describe a procedure for reducing the above problem to an equivalent problem, in which the boundary conditions are homogeneous. The procedure involves looking for a vector function

$$W=W_1+W_2+W_3+W_4 \tag{4}$$

in which

$$B^i[W_j]=G^i\delta_{ij}, \quad \delta_{ij}=\begin{cases}1 \text{ if } i=j\\ 0 \text{ if } i\neq j\end{cases} \tag{5}$$

and

$$\begin{aligned} W_i(x,y,t)&=A_i(x,t)P_i(y) \quad i=2,4\\ W_i(x,y,t)&=A_i(y,t)P_i(x) \quad i=1,3, \end{aligned} \tag{6}$$

where A_i are matrices of unknowns and P_i are vectors of given functions.

The conditions

$$B^i[W_i] = G^i \tag{7}$$

serve to determine A_i, whereas $B^i[W_j] = 0$, $i \neq j$, are compatibility conditions at the corners setting conditions on G^i at the corners. In general, the determination of A_i leads to a linear system of ordinary differential equations with constant coefficients to be solved. However, as is illustrated later with an example, this system of ordinary differential equations reduces to a system of linear algebraic equations.

Once such a W has been found, then set

$$V = U - W. \tag{8}$$

An equivalent problem to the original problem becomes:

$$L[V] = F - L[W] = \bar{F}(x,y,t) \tag{9}$$

with initial conditions

$$V(x,y,0) = \Phi(x,y) - W(x,y,0) = \tilde{\Phi}(x,y)$$
$$V_t(x,y,0) = \Psi(x,y) - W_t(x,y,0) = \tilde{\Psi}(x,y) \tag{10}$$

and boundary conditions

$$B^i[V] = 0 \quad \text{on} \quad x = 0,a;\ y = 0,b. \tag{11}$$

An illustration of the method is given later to an antisymmetric angle-ply laminated circular cylindrical panel [5]. In this case there is a system of three partial differential equations in three unknown functions involving fourth partial derivatives and there are four boundary conditions given on each edge.

Reduction of Nonhomogeneous Boundary Conditions

By means of an affine transformation the problem can be transformed to a problem on a square region of side 2, $-1 \leq x \leq 1$, $-1 \leq y \leq 1$, and the boundary conditions:

$$B^1[W] = G^1(y,t) \quad \text{along} \quad x = 1; \tag{12}$$
$$B^2[W] = G^2(x,t) \quad \text{along} \quad y = 1; \tag{13}$$
$$B^3[W] = G^3(y,t) \quad \text{along} \quad x = -1; \tag{14}$$
$$B^4[W] = G^4(x,t) \quad \text{along} \quad y = -1, \tag{15}$$

where

$$W = (w_1, \ldots, w_n)^T \; G^i = (g_{i1}, \ldots, g_{im})^T,$$
$$m \geq n, \; i = 1, \ldots, 4$$
$$B^i[W] = M^i_{00} W + M^i_{10} D_x W + M^i_{01} D_y W + \ldots + M^i_{k_i l_i} D_x^{k_i} D_y^{l_i} W. \tag{16}$$

Note that the highest x derivative $= k_i <$ the highest order x derivative in the differential equation and the highest y derivative $= l_i <$ the highest order y derivative in the differential equation. $M^i_{\sigma\tau}$ are matrices of size m × n

with

$$M^i_{\sigma\tau} = \begin{cases} M^i_{\sigma\tau}(x,t) \text{ for } i = 2,4, \\ M^i_{\sigma\tau}(y,t) \text{ for } i = 1,3. \end{cases}$$

A W is sought that satisfies equations (12)–(15) and is of the form

$$W = W_1 + W_2 + W_3 + W_4: \tag{17}$$
$$W_1 = A_1(y,t) P_1(x), \tag{18}$$

where

$$A_1(y,t) = \begin{bmatrix} a_{11}(y,t) & a_{12} \ldots & a_{1n-1} & a_{1n} \ldots & a_{1m} \\ 0 & a_{12} \ldots & a_{1n-1} & a_{1n} \ldots & a_{1m} \\ 0 & 0 \ldots & a_{1n-1} & a_{1n} \ldots & a_{1m} \\ \cdot & \cdot & \cdot & \cdot & \cdot \\ \cdot & \cdot & \cdot & \cdot & \cdot \\ \cdot & \cdot & \cdot & \cdot & \cdot \\ 0 & 0 \ldots & 0 & a_{1n} \ldots & a_{1m} \end{bmatrix} n \times m$$

with

$$P_1(x) = \begin{bmatrix} p_1(x) \\ \cdot \\ \cdot \\ \cdot \\ \cdot \\ \cdot \\ p_m(x) \end{bmatrix}$$

in which $p_1(x), \ldots, p_m(x)$ are linearly independent functions and

$$D_x^\mu P_1(x) = 0 \quad \text{at} \quad x = -1, \mu \leq k_3, \tag{19}$$
$$B^2[W_1] = 0 \quad \text{at} \quad y = 1, B^4[W_1] = 0 \quad \text{at} \quad y = -1; \tag{20}$$
$$W_2 = A_2(x,t) P_2(y), \tag{21}$$

where A_2 is an $n \times m$ matrix similar in form to A_1 and $P_2(y)$ is an $m \times 1$ vector with

$$D_y^\mu P_2(y) = 0 \quad \text{at} \quad y = -1, \mu \leq l_4, \tag{22}$$
$$B^1[W_2] = 0 \quad \text{at} \quad x = 1, \quad B^3[W_2] = 0 \quad \text{at} \quad x = -1; \tag{23}$$
$$W_3 = A_3(y,t) P_3(x), \tag{24}$$

where A_3 is a $n \times m$ matrix similar in form to A_1 and $P_3(x)$ is an $m \times 1$ vector with

$$D_x^\mu P_3(x) = 0 \quad \text{at} \quad x = 1, \quad \mu \leq k_1; \tag{25}$$
$$B^2[W_3] = 0 \quad \text{at} \quad y = 1, \quad B^4[W_3] = 0 \quad \text{at} \quad y = -1; \tag{26}$$

and finally

$$W_4 = A_4(x,t) P_4(y), \tag{27}$$

where A_4 is an $n \times m$ matrix similar in form to A_1 and $P_4(y)$ is an $m \times 1$ vector with

$$D_y^\mu P_4(y) = 0 \quad \text{at} \quad y = 1, \quad \mu \leq l_2, \tag{28}$$
$$B^1[W_4] = 0 \text{ at } x = 1, \; B^3[W_4] = 0 \text{ at } x = -1. \tag{29}$$

Procedure for Determining W_1. Note that from equation (19)

$$B^3[W_1] = 0 \quad \text{at} \quad x = -1,$$

i.e.,

$$B^3[W_1] = M^3_{00} W_1 + M^3_{10} D_x W_1 + \ldots + M^3_{k_3 l_3} D_x^{k_3} D_y^{l_3} W_1$$
$$= M^3_{00} A_1 P_1 + M^3_{10} A_1 D_x P_1 + \ldots + M^3_{k_3 l_3} D_y^{l_3} A_1 D_x^{k_3} P_1$$
$$= 0$$

since

$$P_1(x), D_x P_1(x), \ldots, D_x^{k_3} P_1(x) = 0 \text{ at } x = -1.$$

Consider on $x = 1$

$$B^1[W_1] = M^1_{00} W_1 + M^1_{10} D_x W_1 + \ldots + M^1_{k_1 l_1} D_x^{k_1} D_y^{l_1} W_1$$
$$= M^1_{00}(A_1 P_1) + M^1_{10}(A_1 D_x P_1) + \ldots + M^1_{k_1 l_1}(D_y^{l_1} A_1 D_x^{k_1} P_1). \tag{30}$$

Equation (30) is a linear system of ordinary differential equations with independent variable y of order l_1 in m unknowns, $a_{11}, a_{12}, \ldots, a_{1m}$. Once the a's are determined, W_1 is given by equation (18). Once W_1 is determined in this way, equations (20) become compatibility conditions on $G^1(-1, t)$ and $G^1(1,t)$. W_2, W_3 and W_4 are determined in a similar manner and hence W of equation (17) is determined which, when combined with equations (8)–(10), yields an equivalent problem having homogeneous boundary conditions. In the event that $M^i_{\sigma\tau}$ are independent of x and y then the system has essentially constant coefficients (t = parameter).

One-Dimensional Problems

Given a linear system of partial differential equations

$$\mathcal{L}[U] = F(x,t) \quad \text{for} \quad 0 < x < L, \; 0 < t < T \tag{31}$$

in which $\mathcal{L}$ can be a matrix of linear differential operators se-

cond order in time and higher order in space, U, a column $(n\times 1)$ vector of functions, and F, a vector of functions with initial conditions

$$U(x,0)=\Phi(x),$$
$$U_t(x,0)=\Psi(x) \tag{32}$$

and $2m$ boundary conditions:

$$B_\iota^0[U]=g_\iota^0(t) \text{ at } x=0,\ \iota=1,\ \ldots,m \tag{33}$$

$$B_\iota^L[U]=g_\iota^L(t) \text{ at } x=L,\ \iota=1,\ \ldots,m \tag{34}$$

where

$$B_\iota^0[U]=\alpha_{\iota k}^0(t)D_x^kU+\alpha_{\iota k-1}^0D_x^{k-1}U+\ \ldots\ +\alpha_{\iota 0}^0U$$
$$\text{at } x=0,\ \iota=1,\ \ldots,m \tag{35}$$

$$B_\iota^L[U]=\alpha_{\iota k}^L(t)D_x^kU+\alpha_{\iota k-1}^LD_x^{k-1}U+\ \ldots\ +\alpha_{\iota 0}^LU$$
$$\text{at } x=L,\ \iota=1,\ \ldots,m \tag{36}$$

with $\alpha_{\iota\sigma}^0$ and $\alpha_{\iota\sigma}^L$ are row vectors with n components and $k+1=$ highest order derivative occurring in the system. Assume

$$n=\frac{(2m)}{(k+1)}=\text{integer}. \tag{37}$$

Reduction of Nonhomogeneous Boundary Conditions

Set

$$w_j(x,t)=p_0(x)a_{j0}(t)+p_1(x)a_{j1}(t)+\ \ldots\ .$$
$$+p_k(x)a_{jk}(t),j=1,\ \ldots,n, \tag{38}$$

i.e.,

$$W(x,t)=A(t)P(x), \tag{39}$$

where

$$P(x)=[p_0(x),\ p_1(x),\ \ldots,p_k(x)]^T$$

with $p_\sigma(x)=$ general sufficiently smooth functions, $\sigma=0,\ \ldots,\ k$; and

$$A(t)=\begin{bmatrix} a_{10} & a_{11} & \ldots & a_{1k}\\ a_{20} & a_{21} & \ldots & a_{2k}\\ \cdot & \cdot & & \cdot\\ \cdot & \cdot & & \cdot\\ \cdot & \cdot & & \cdot\\ \cdot & \cdot & & \cdot\\ a_{n0} & a_{n1} & \ldots & a_{nk}\end{bmatrix},$$

in which $a_{j\sigma}$ are functions of t, $j=1,\ \ldots,\ n$, $\sigma=0,\ \ldots,\ k$.

Inserting W into equations (35) and (36) gives

$$B_\iota^\nu[W]=\alpha_{\iota k}^\nu(t)D_x^kW(x,t)+\alpha_{\iota k-1}^\nu D_x^{k-1}W(x,t)$$
$$+\ \ldots\ .+\alpha_{\iota 0}^\nu W(x,t), \tag{40}$$

where $k=(2m/n)-1$ and $\nu=0,\ L$. Introducing equation (39) into equation (40) yields

$$B_\iota^\nu[W]=\alpha_{\iota k}^\nu(t)\ \ [A(t)D_x^kP(\nu)]+\alpha_{\iota k-1}^\nu(t)[A(t)D_x^{k-1}P(\nu)]+$$
$$\ldots\ .+\alpha_{\iota 0}^\nu(t)\ \ \ [A(t)P(\nu)],\ \iota=1,\ \ldots,m,\ \nu=0,L, \tag{41}$$

i.e., $2m$ conditions to determine the $n(k+1)=2m$ constants $a_{j\sigma}$.

In order to determine the applicability of the method, it is useful to have a general criterion..

Theorem. The above method can always be used provided the following $2m$ vectors, $2m=n(k+1)$,

$$(\Gamma_{\iota 1}^\nu,\Gamma_{\iota 2}^\nu,\ \ldots,\Gamma_{\iota n}^\nu),\ \nu=0,L,\ \iota=1,\ \ldots,m$$

are linearly independent, where

$$\Gamma_{ij}^\nu=\alpha_{\iota k,j}^\nu D_x^kP(\nu)+\alpha_{\iota k-1,j}^\nu D_x^{k-1}P(\nu)+\ \ldots\ .+\alpha_{\iota 0,j}^\nu P(\nu), \tag{42}$$

and

$$\alpha_{\iota k,j}^\nu=\text{the } j^{th} \text{ component of the } n \text{ vector } \alpha_{\iota k}^\nu.$$

Proof. With the notation

$A=[A_1,\ \ldots,A_n]^T$, $A_j=j^{th}$ row, equation (41) can be written:

$$B_\iota^\nu[W]=[A_1,\ A_2,\ \ldots,A_n]\begin{bmatrix}\Gamma_{\iota 1}^\nu\\ \Gamma_{\iota 2}^\nu\\ \cdot\\ \cdot\\ \cdot\\ \Gamma_{\iota n}^\nu\end{bmatrix}$$

in which Γ_{ij}^ν is a $(k+1)$ column vector for $\iota=1,\ \ldots,\ m$, and $\nu=0,\ L$. Thus there are $2m$ conditions to solve for $n(k+1)=2m$ unknowns $a_{j\sigma}$, $j=1,\ \ldots,\ n$ and $\sigma=0,\ \ldots,\ k$. Thus a necessary and sufficient condition for solubility is that the $2m$ row vectors $B_\iota^\nu[W]$ be linearly independent and the Theorem is proved.

Examples of One-Space Dimensional Problems

Example 1. Consider the simple Bernoulli-Euler beam governed by the fourth order equation in one unknown function u

$$\rho A(x)\frac{\partial^2u}{\partial t^2}+\frac{\partial^2}{\partial x^2}\left[EI(x)\frac{\partial^2u}{\partial x^2}\right]=F(x,t). \tag{43}$$

For this example $n=1$, $m=2$, $k=3$. Since it is the boundary conditions with which we are concerned, we give several examples of possible pairs of boundary conditions, in which each set holds at $\nu=0$ and/or at $\nu=L$:

$$\left.\begin{aligned} B_1^\nu[u]&=u(\nu,t)=g_1^\nu(t)\\ B_2^\nu[u]&=u_x(\nu,t)=g_2^\nu(t);\end{aligned}\right\} \tag{44a}$$

$$\left.\begin{aligned} B_1^\nu[u]&=u(\nu,t)=g_3^\nu(t)\\ B_2^\nu[u]&=u_{xx}(\nu,t)=g_4^\nu(t);\end{aligned}\right\} \tag{44b}$$

$$\left.\begin{aligned} B_1^\nu[u]&=u_{xx}(\nu,t)=g_5^\nu(t)\\ B_2^\nu[u]&=(EI(x)u_{xx})_x\Big|_{x=\nu}=(EI)_xu_{xx}+EIu_{xxx}=g_6^\nu(t);\end{aligned}\right\} \tag{44c}$$

$$\left.\begin{aligned} B_1^\nu[u]&=u_{xx}(\nu,t)=g_7^\nu(t)\\ B_2^\nu[u]&=(EI(x)u_{xx})_x\Big|_{x=\nu}-S_0k_0u(\nu,t)=g_8^\nu(t),\end{aligned}\right\} \tag{44d}$$

where $S_0=+1$ at $x=L$, $S_0=-1$ at $x=0$;

$$\left.\begin{aligned} B_1^\nu[u]&=u_x(\nu,t)=g_9^\nu(t)\\ B_2^\nu[u]&=(EI(x)u_{xx})_x\Big|_{x=\nu}=g_{10}^\nu(t);\end{aligned}\right\} \tag{44e}$$

$$\left.\begin{aligned} B_1^\nu[u]&=(EI(x)u_{xx})_x\Big|_{x=\nu}=g_{11}^\nu(t)\\ B_2^\nu[u]&=EI(x)u_{xx}(\nu,t)-S_0'\bar\beta_0u_x(\nu,t)=g_{12}^\nu(t),\end{aligned}\right\} \tag{44f}$$

where $S_0'=-S_0$ and $\bar\beta_0=$ constant.

Illustration of Example 1. As an illustration of the method of reduction, consider equations (44*a*) at $x=0$ and equations (44*d*) at $x=L$, and take $p_0(x)=1$, $p_1(x)=x$, $p_2(x)=x^2$, $p_3(x)=x^3$. Since $n=1$, $W=w_1=w$, and equation (40) becomes

$$B_\iota^\nu[w]=\alpha_{\iota 3}^\nu w_{xxx}+\alpha_{\iota 2}^\nu w_{xx}+\alpha_{\iota 1}^\nu w_x+\alpha_{\iota 0}^\nu w,\ \nu=0,\ L;\ \iota=1,2 \tag{45}$$

where

$$\alpha_{13}^0=0,\qquad \alpha_{12}^0=0,\qquad \alpha_{11}^0=0,\qquad \alpha_{10}^0=1$$

$$\alpha_{23}^0=0,\qquad \alpha_{22}^0=0,\qquad \alpha_{21}^0=1,\qquad \alpha_{20}^0=0$$

$$\alpha_{13}^L=0, \qquad \alpha_{12}^L=1, \qquad \alpha_{11}^L=0, \quad \alpha_{10}^L=0$$

$$\alpha_{23}^L=EI(L), \quad \alpha_{22}^L=(EI)_x, \quad \alpha_{21}^L=0, \quad \alpha_{20}^L=-k_0.$$

With

$$w(x,t)=A(t)P(x)=\begin{bmatrix}a_{10} & a_{11} & a_{12} & a_{13}\end{bmatrix}\begin{bmatrix}1\\ x\\ x^2\\ x^3\end{bmatrix} \tag{46}$$

equation (45) becomes in component from

$$a_{10}=g_1^0(t), \tag{47}$$

$$a_{11}=g_2^L(t), \tag{48}$$

$$2a_{12}+6La_{13}=g_7^L(t), \tag{49}$$

$$6EI(L)a_{13}+(EI(x))_x(L)[2a_{12}+6La_{13}]-k_0a_{10}$$
$$-k_0La_{11}-k_0L^2a_{12}-k_0L^3a_{13}=g_8^L(t). \tag{50}$$

Equations (49) and (50) can be rewritten in the following convenient manner using equations (47) and (48):

$$2a_{12}+6La_{13}=g_7^L(t), \tag{51}$$

$$A_1a_{12}+A_2a_{13}=A_3(t), \tag{52}$$

where

$$A_1=2(EI(x))_x(L)-k_0L^2,$$
$$A_2=6EI(L)+6L(EI(x))_x(L)-k_0L^3,$$

and

$$A_3(t)=g_8^L(t)+k_0g_1^0(t)+k_0Lg_2^0(t).$$

The determinant of the coefficient matrix of equations (51) and (52) is $[12EI(L)+4k_0L^3]>0$. Thus, by the Theorem the method is applicable. Solving for a_{12} and a_{13} from equations (51) and (52) and using equations (47) and (48) gives for W of equation (39)

$$W(x,t)=[a_{10},a_{11},a_{12},a_{13}][p_0,p_1,p_2,p_3]^T$$
$$=a_{10}+a_{11}x+a_{12}x^2+a_{13}x^3.$$

As another illustration of Example 1, use boundary condition equations (44*a*) at $x=0$ and equations (44*b*) at $x=L$. Then $a_{10}=g_1^0$, $a_{11}=g_2^0$, $L^2a_{12}+L^3a_{13}=g_3^L-g_1^0-Lg_2^0$, and $2a_{12}+6La_{13}=g_4^L$, with determinant $4L^3>0$ and as before the method is applicable.

Example 2. As an example of one-space dimensional problem in which there are five unknown functions $U=[u_1, u_2, u_3, u_4, u_5]^T$, and five boundary conditions at each end consider the case of laminated composite plates dealt with by Sun and Whitney [3]. For this example $m=5$, $n=5$, and $k=1$. The boundary conditions can be expressed as $B_i^\nu[u_1, u_2, u_3, u_4, u_5]=B_i^\nu$, $\nu=0, L$; $i=1, \ldots, 5$. Special cases of boundary conditions are given by:

$$B_1^\nu=A_{11}u_{1,x}(\nu,t)+A_{16}u_{2,x}+B_{11}u_{4,x}+B_{16}u_{5,x}=g_1^\nu(t) \tag{53a}$$

or

$$B_1^\nu=u_1(\nu,t) \qquad =g_1^\nu(t); \tag{53b}$$

$$B_2^\nu=A_{16}u_{1,x}+A_{66}u_{2,x}+B_{16}u_{4,x}+B_{66}u_{5,x}$$
$$=g_2^\nu(t) \tag{54a}$$

or

$$B_2^\nu=u_2 \qquad =g_2^\nu(t) \tag{54b}$$

$$B_3^\nu=\bar{k}(A_{45}u_5+A_{55}u_{3,x}+A_{55}u_4) \qquad =g_3^\nu(t) \tag{55a}$$

or

$$B_3^\nu=u_3 \qquad =g_3^\nu(t); \tag{55b}$$

$$B_4^\nu=B_{11}u_{1,x}+B_{16}u_{2,x}+D_{11}u_{4,x}+D_{16}u_{5,x} \qquad =g_4^\nu(t) \tag{56a}$$

or

$$B_4^\nu=u_4 \qquad =g_4^\nu(t); \tag{56b}$$

$$B_5^\nu=B_{16}u_{1,x}+B_{66}u_{2,x}+D_{16}u_{4,x}+D_{66}u_{5,x} \qquad =g_5^\nu(t) \tag{57a}$$

or

$$B_5^\nu=u_5 \qquad =g_5^\nu(t), \tag{57b}$$

where A's, B's, D's and $\bar{k}$ are constants (See Sun and Whitney [3]).

These boundary conditions can be written in the following compact form:

$$B_i^\nu[U]=\alpha_{i1}^\nu U_x+\alpha_{i0}^\nu U=g_i^\nu(t), \quad \nu=0,L; \iota=1, \ldots, 5, \tag{58}$$

where

$$\left\{\begin{matrix}\alpha_1^\nu=(A_{11},A_{16},0,B_{11},B_{16})\\ \alpha_{10}^\nu=(0,0,0,0,0)\end{matrix}\right\} \text{ or } \left\{\begin{matrix}\alpha_1^\nu=(0,0,0,0,0)\\ \alpha_{10}^\nu=(1,0,0,0,0)\end{matrix}\right\}$$

$$\left\{\begin{matrix}\alpha_{21}^\nu=(A_{16},B_{66},0,B_{16},B_{66})\\ \alpha_{20}^\nu=(0,0,0,0,0)\end{matrix}\right\} \text{ or } \left\{\begin{matrix}\alpha_{21}^\nu=(0,0,0,0,0)\\ \alpha_{20}^\nu=(0,1,0,0,0)\end{matrix}\right\}$$

$$\left\{\begin{matrix}\alpha_{31}^\nu=\bar{k}(0,0,A_{55},0,0)\\ \alpha_{30}^\nu=\bar{k}(0,0,0,A_{55},A_{45})\end{matrix}\right\} \text{ or } \left\{\begin{matrix}\alpha_{31}^\nu=(0,0,0,0,0)\\ \alpha_{30}^\nu=(0,0,1,0,0)\end{matrix}\right\},$$

$$\left\{\begin{matrix}\alpha_{41}^\nu=(B_{11},B_{16},0,D_{11},D_{16})\\ \alpha_{40}^\nu=(0,0,0,0,0)\end{matrix}\right\} \text{ or } \left\{\begin{matrix}\alpha_{41}^\nu=(0,0,0,0,0)\\ \alpha_{40}^\nu=(0,0,0,1,0)\end{matrix}\right\}$$

$$\left\{\begin{matrix}\alpha_{51}^\nu=(B_{16},B_{66},0,D_{16},D_{66})\\ \alpha_{50}^\nu=(0,0,0,0,0)\end{matrix}\right\} \text{ or } \left\{\begin{matrix}\alpha_{51}^\nu=(0,0,0,0,0)\\ \alpha_{50}^\nu=(0,0,0,0,1)\end{matrix}\right\}.$$

Illustration of Example 2. Consider as boundary conditions equations (53*a*), (54*b*), (55*b*), (56*b*), and (57*b*) at $\nu=0$ and equations (53*b*), (54*b*), (55*b*), (56*b*), and (57*b*) at $\nu=L$.

Set

$$W(x,t)=A(t)P(x)=\begin{bmatrix}a_{10} & a_{20} & a_{30} & a_{40} & a_{50}\\ a_{11} & a_{21} & a_{31} & a_{41} & a_{51}\end{bmatrix}^T\begin{bmatrix}p_0(x)\\ p_1(x)\end{bmatrix}. \tag{59}$$

Choose $p_0(x)=1$ and $p_1(x)=x$.

Then according to the Theorem it is necessary to verify that the rows of the following matrix are linearly independent.

$$M=\begin{bmatrix}(0,A_{11}) & (0,A_{16}) & (0,0) & (0,B_{11}) & (0,B_{16})\\ (1,L) & (0,0) & (0,0) & (0,0) & (0,0)\\ (0,0) & (1,0) & (0,0) & (0,0) & (0,0)\\ (0,0) & (1,L) & (0,0) & (0,0) & (0,0)\\ (0,0) & (0,0) & (1,0) & (0.0) & (0.0)\\ (0,0) & (0,0) & (1,L) & (0,0) & (0,0)\\ (0,0) & (0,0) & (0,0) & (1,0) & (0,0)\\ (0,0) & (0,0) & (0.0) & (1,L) & (0,0)\\ (0,0) & (0,0) & (0,0) & (0,0) & (1,0)\\ (0,0) & (0,0) & (0,0) & (0,0) & (1,L)\end{bmatrix}$$

However, it is clear by inspection that the rows are linearly independent and hence the method is applicable.

To find W, it is necessary to solve the 10 equations in the 10 unknowns $a_{10}, a_{11}, \ldots, a_{51}$.

$$Ma^T=g^T, \tag{60}$$

where $a=[a_{10}, a_{11}, a_{20}, a_{21}, a_{30}, a_{31}, a_{40}, a_{41}, a_{50}, a_{51}]$

and

$$g=[g_1^0(t),g_1^L(t),g_2^0(t),g_2^L(t),g_3^0(t),g_3^L(t),g_4^0(t),g_4^L(t),g_5^0(t),g_5^L(t)].$$

Equation (60) has the following solution:

$$a_{11}=A_{11}^{-1}[g_1^0(t)-A_{16}a_{21}-B_{11}a_{41}-B_{16}a_{51}],$$

$$a_{10}=g_1^L(t)-La_{11},$$

$a_{i0}=g^0_{i(t)}$ and $a_{i1}=L^{-1}[g_i^L(t)-g_i^0(t)]$, $i=2,\ldots,5$.

This information combined with equation (59) gives $W(x,t)=[w_1, w_2, w_3, w_4, w_5]^T$.

Example 3 With Illustration. Consider the case of the Timoshenko beam having two unknown functions, $U=[u, \psi]^T$ and the following example time dependent boundary conditions (see Magrab [4]).

$$B_1^0[u,\psi]=u(0,t)=g_1^0(t), B_1^L[u,\psi]=u(L,t)=g_1^L(t),$$

$$B_2^0[u,\psi]=EI\psi_x(0,t)=g_2^0(t), B_2^L[u,\psi]=EI\psi_x(L,t)=g_2^L(t),$$

in which $m=2$, $n=2$, $k=1$. For $P(x)=[p_0(x), p_1(x)]^T$ with $p_0(x)=1$, $p_1(x)=x$ the method can be shown not to be applicable, since in this case the system of equations to be solved is linearly dependent.

However, for $p_0(x)=1+x$, $p_1(x)=x+x^2$, the method is applicable and results in the following solution: $W=[w, \bar{\psi}]^T$, where

$$w=(1+x)g_1^0(t)+(x+x^2)(L+L^2)^{-1}[g_1^L(t)-(1+L)g_1^0(t)]$$

and

$$\bar{\psi}=(1+x)(EI)^{-1}[g_2^0(t)-(2L)^{-1}(g_2^L(t)-g_2^0(t))]+(x+x^2)(EI2L)^{-1}[g_2^L(t)-g_2^0(t)].$$

Example of a Two-Space Dimensional Problem

Application: Antisymmetric Angle-Ply Laminated Circular Cylindrical Panel. The displacement components $U=[u, v, w]^T$ for an antisymmetric angle-ply laminated panel are assumed (Soldatos [5]) to satisfy the system of partial differential equations of the form

$$L[U]\equiv\begin{bmatrix}L_1 & L_2 & L_3\\ L_2 & L_4 & L_5\\ L_3 & L_5 & L_6\end{bmatrix}\begin{bmatrix}u\\ v\\ w\end{bmatrix}=\begin{bmatrix}0\\ 0\\ 0\end{bmatrix}\quad -1<x<1,\ -1<s<1, \tag{61}$$

in which $L_{\bar{i}}$, $\bar{i}=1,\ldots,6$, are linear partial differential operators involving up to fourth-order derivatives in the spatial variables and up to second order in the time variable. Here $n=3$ and $m=4$. Initial conditions are of the form

$$U(x,s,0)=\Phi(x,s) \tag{62}$$

$$U_t(x,s,0)=\Psi(x,s), \tag{63}$$

where

$$\Phi=[\phi_1,\phi_2,\phi_3]^T, \text{ and } \Psi=[\psi_1,\psi_2,\psi_3]^T.$$

The sixteen boundary conditions for the problem are for $\kappa=-1,1$:

$$\underline{\text{on } x=\kappa:}\qquad u(\kappa,s,t)=g_{\kappa1}(s,t); \tag{64}$$

$$N_{xs}=A_{66}\left(\frac{2}{L_x}v_x+\frac{2}{L_s}u_s\right)-\left[B_{16}\left(\frac{2}{L_x}\right)^2 w_{xx}+B_{26}\left(\frac{2}{L_s}\right)^2 w_{ss}\right]=g_{\kappa2}(s,t); \tag{65}$$

$$w(\kappa,s,t)=g_{\kappa3}(s,t); \tag{66}$$

$$M_x=B_{16}\left[\frac{2}{L_x}v_x+\frac{2}{L_s}u_s\right]-\left[D_{11}\left(\frac{2}{L_x}\right)^2 w_{xx}+D_{12}\left(\frac{2}{L_s}\right)^2 w_{ss}\right]=g_{\kappa4}(s,t); \tag{67}$$

$$\underline{\text{on } s=\kappa:}\qquad v=g_{\kappa5}(x,t); \tag{68}$$

$$N_{xs}=A_{66}\left(\frac{2}{L_x}v_x+\frac{2}{L_s}u_s\right)-\left[B_{16}\left(\frac{2}{L_x}\right)^2 w_{xx}+B_{26}\left(\frac{2}{L_s}\right)^2 w_{ss}\right]=g_{\kappa6}(x,t); \tag{69}$$

$$w=g_{\kappa7}(x,t); \tag{70}$$

$$M_s=B_{26}\left[\frac{2}{L_x}v_x+\frac{2}{L_s}u_s\right]-\left[D_{12}\left(\frac{2}{L_x}\right)^2 w_{xx}+D_{22}\left(\frac{2}{L_s}\right)^2 w_{ss}\right]=g_{\kappa8}(x,t). \tag{71}$$

Writing the boundary operators in the form

$$B^i[U]=\sum_{\sigma=0}^{k_i}\sum_{\tau=0}^{l_i}M^i_{\sigma\tau}D_x^\sigma D_y^\tau U,\ i=1,\ldots,4,$$

gives:

$$B^1[U]=\begin{bmatrix}1&0&0\\0&0&1\\0&0&0\\0&0&0\end{bmatrix}\begin{bmatrix}u\\v\\w\end{bmatrix}+\left(\frac{2}{L_x}\right)\begin{bmatrix}0&0&0\\0&0&0\\0&A_{66}&0\\0&B_{16}&0\end{bmatrix}\begin{bmatrix}u\\v\\w\end{bmatrix}_x+$$

$$+\left(\frac{2}{L_s}\right)\begin{bmatrix}0&0&0\\0&0&0\\A_{66}&0&0\\B_{16}&0&0\end{bmatrix}\begin{bmatrix}u\\v\\w\end{bmatrix}_s+[0]\begin{bmatrix}u\\v\\w\end{bmatrix}_{xs}$$

$$+\left(\frac{2}{L_x}\right)^2\begin{bmatrix}0&0&0\\0&0&0\\0&0&-B_{16}\\0&0&-D_{11}\end{bmatrix}\begin{bmatrix}u\\v\\w\end{bmatrix}_{xx}$$

$$+\left(\frac{2}{L_s}\right)^2\begin{bmatrix}0&0&0\\0&0&0\\0&0&-B_{26}\\0&0&-D_{12}\end{bmatrix}\begin{bmatrix}u\\v\\w\end{bmatrix}_{ss} \tag{72}$$

with

$$B^1[U]=B^3[U]; \tag{73}$$

$$B^2[U]=\begin{bmatrix}0&1&0\\0&0&0\\0&0&1\\0&0&0\end{bmatrix}\begin{bmatrix}u\\v\\w\end{bmatrix}+\left(\frac{2}{L_x}\right)\begin{bmatrix}0&0&0\\0&A_{66}&0\\0&0&0\\0&B_{26}&0\end{bmatrix}\begin{bmatrix}u\\v\\w\end{bmatrix}_x$$

$$+\left(\frac{2}{L_s}\right)\begin{bmatrix}0&0&0\\A_{66}&0&0\\0&0&0\\B_{26}&0&0\end{bmatrix}\begin{bmatrix}u\\v\\w\end{bmatrix}_s+[0]\begin{bmatrix}u\\v\\w\end{bmatrix}_{xs}$$

$$+\left(\frac{2}{L_x}\right)^2\begin{bmatrix}0&0&0\\0&0&-B_{16}\\0&0&0\\0&0&-D_{12}\end{bmatrix}\begin{bmatrix}u\\v\\w\end{bmatrix}_{xx}$$

$$+\left(\frac{2}{L_s}\right)^2\begin{bmatrix}0&0&0\\0&0&-B_{26}\\0&0&0\\0&0&-D_{22}\end{bmatrix}\begin{bmatrix}u\\v\\w\end{bmatrix}_{ss} \tag{74}$$

with

$$B^2[U]=B^4[U]. \tag{75}$$

Note that the subscripts x and s on the vector U in equations (72) and (74) indicate partial derivatives. The boundary conditions are:

$$B^1[U]=\begin{bmatrix}g_{11}\\g_{12}\\g_{13}\\g_{14}\end{bmatrix}(s,t)\text{ at }x=1;$$

$$B^3[U]=\begin{bmatrix}g_{-11}\\g_{-12}\\g_{-13}\\g_{-14}\end{bmatrix}(s,t)\text{ at }x=-1; \tag{76}$$

$$B^2[U]=\begin{bmatrix}g_{15}\\g_{16}\\g_{17}\\g_{18}\end{bmatrix}(x,t)\text{ at }s=1;$$

$$B^4[U]=\begin{bmatrix}g_{-15}\\g_{-16}\\g_{-17}\\g_{-18}\end{bmatrix}(x,t)\text{ at }s=-1 \tag{77}$$

Next a W is sought that will satisfy the boundary conditions, but not necessarily the differential equations. Toward this end set

$$W=W_1+W_2+W_3+W_4. \tag{78}$$

As a special case to illustrate the method take $B^2[W]=0$ at $s=1$, $B^3[W]=0$ at $x=-1$, and $B^4[W]=0$ at $s=-1$. Let

$$W_1=[u_1,v_1,w_1]^T=A_1(s,t)P_1(x). \tag{79}$$

Since it is only W_1 that is sought, set $u_1=u$, $v_1=v$, $w_1=w$,

$$P_1(x)=[p_1(x),p_2(x),p_3(x),p_4(x)]^T,$$

$$A_1(s,t)=\begin{bmatrix}a_{11}&a_{12}&a_{13}&a_{14}\\0&a_{12}&a_{13}&a_{14}\\0&0&a_{13}&a_{14}\end{bmatrix}(s,t). \tag{80}$$

By choosing

$$P_1(x)=[(x+1)^3,(x+1)^4,(x+1)^5,(x+1)^6]^T, \tag{81}$$

it follows that $D_x^\mu P_1(x)=0$ at $x=-1$, for $\mu\le k_3$ where $k_3=2$ and hence $B^3[W]=0$ at $x=-1$.

Next consider

$$B^1[W_1]=\begin{bmatrix}1&0&0\\0&0&1\\0&0&0\\0&0&0\end{bmatrix}A_1\begin{bmatrix}2^3\\2^4\\2^5\\2^6\end{bmatrix}$$

$$+\frac{2}{L_x}\begin{bmatrix}0&0&0\\0&0&0\\0&A_{66}&0\\0&B_{16}&0\end{bmatrix}A_1\begin{bmatrix}3(2^2)\\4(2^3)\\5(2^4)\\6(2^5)\end{bmatrix}$$

$$+\left(\frac{2}{L_x}\right)^2\begin{bmatrix}0&0&0\\0&0&0\\0&0&-B_{16}\\0&0&-D_{11}\end{bmatrix}A_1\begin{bmatrix}3(2)2\\4(3)2^2\\5(4)2^3\\6(5)2^4\end{bmatrix}$$

$$+\frac{2}{L_s}\begin{bmatrix}0&0&0\\0&0&0\\A_{66}&0&0\\B_{16}&0&0\end{bmatrix}A_{1,s}\begin{bmatrix}2^3\\2^4\\2^5\\2^6\end{bmatrix}$$

$$+\left(\frac{2}{L_s}\right)^2\begin{bmatrix}0&0&0\\0&0&0\\0&0&-B_{26}\\0&0&-D_{12}\end{bmatrix}A_{1,ss}\begin{bmatrix}2^3\\2^4\\2^5\\2^6\end{bmatrix}=\begin{bmatrix}g_{11}\\g_{12}\\g_{13}\\g_{14}\end{bmatrix} \tag{82}$$

Equation (82) in component form becomes four linear algebraic equations in four unknowns.

$$2^3a_{11}+2^4a_{12}+2^5a_{13}+2^6a_{14}=g_{11}, \tag{83}$$

$$2^5a_{13}+2^6a_{14}=g_{12}, \tag{84}$$

$$\frac{2}{L_x}A_{66}(4\cdot2^3a_{12}+5\cdot2^4a_{13}+6\cdot2^5a_{14})-\left(\frac{2}{L_x}\right)^2B_{16}(5\cdot4\cdot2^3a_{13}+6\cdot5\cdot2^4a_{14})+\frac{2}{L_s}A_{66}g_{11,s}-\left(\frac{2}{L_s}\right)^2B_{26}g_{12,ss}=g_{13}, \tag{85}$$

$$\frac{2}{L_x}B_{16}(4\cdot2^3a_{12}+5\cdot2^4a_{13}+6\cdot2^5a_{14})$$

$$-\left(\frac{2}{L_x}\right)^2 D_{11}(5\cdot4\cdot2^3 a_{13}+6\cdot5\cdot2^4 a_{14})$$

$$+\frac{2}{L_s}B_{16}g_{11,s}-\left(\frac{2}{L_s}\right)^2 D_{12}g_{12,ss} \qquad =g_{14}. \quad (86)$$

Unique solubility of equations (83)–(86) is always assured provided

$$A_{66}D_{11}-B_{16}^2\neq 0. \quad (87)$$

In the event

$$A_{66}D_{11}-B_{16}^2=0 \quad (88)$$

the solubility is assured only if

$$D_{11}\tilde{g}_{13}-B_{16}\tilde{g}_{14}=D_{11}g_{13}-B_{16}g_{14}$$
$$+\left(\frac{2}{L_s}\right)^2 g_{12,ss}(D_{11}B_{26}-B_{16}D_{12})=0, \quad (89)$$

where

$$\tilde{g}_{13}=g_{13}-\left(\frac{2}{L_s}\right)A_{66}g_{11,s}+\left(\frac{2}{L_s}\right)^2 B_{26}g_{12,ss},$$

$$\tilde{g}_{14}=g_{14}-\left(\frac{2}{L_s}\right)B_{16}g_{11,s}+\left(\frac{2}{L_s}\right)^2 D_{12}g_{12,ss}.$$

The compatibility conditions are:

$$B^2[W](x,1,t)=0 \text{ and } B^4[W](x,-1,t)$$
$$=B^2[W](x,-1,t)=0.$$

From equation (74) with $s=1$

$$a_{12}(x+1)^4+a_{13}(x+1)^5+a_{14}(x+1)^6=0, \quad (90)$$

$$A_{66}\left(\frac{2}{L_x}\right)[a_{12}(4)(x+1)^3+a_{13}(5)(x+1)^4+a_{14}(6)(x+1)^5]$$

$$+A_{66}\left(\frac{2}{L_s}\right)[a_{11,s}(x+1)^3+a_{12,s}(x+1)^4$$
$$+a_{13,s}(x+1)^5+a_{14,s}(x+1)^6]$$

$$-B_{16}\left(\frac{2}{L_x}\right)^2[a_{13}(5)(4)(x+1)^3+a_{14}(6)(5)(x+1)^4]$$

$$-B_{26}\left(\frac{2}{L_s}\right)^2[a_{13,ss}(x+1)^5+a_{14,ss}(x+1)^6]=0, \quad (91)$$

$$a_{13}(x+1)^5+a_{14}(x+1)^6=0, \quad (92)$$

$$B_{26}\left(\frac{2}{L_x}\right)[a_{12}(4)(x+1)^3+a_{13}(5)(x+1)^5+a_{14}(6)(x+1)^6]$$

$$+B_{26}\left(\frac{2}{L_s}\right)[a_{11,s}(x+1)^3+a_{12,s}(x+1)^4+a_{13,s}(x+1)^5$$
$$+a_{14,s}(x+1)^6]$$

$$-D_{12}\left(\frac{2}{L_x}\right)^2[a_{13}(5)(4)(x+1)^3+a_{14}(6)(5)(x+1)^4]$$

$$-D_{22}\left(\frac{2}{L_s}\right)^2[a_{13,ss}(x+1)^5+a_{14,ss}(x+1)^6]=0. \quad (93)$$

If it is assumed

$$A_{66}D_{22}-B_{26}^2\neq 0, \quad (94)$$

then the compatibility conditions, equations (90)–(93) become

$$\left.\begin{aligned}
&a_{11,s}(1,t)=0,\\
&a_{12}(1,t)=a_{12,s}(1,t)=0,\\
&a_{13}(1,t)=a_{13,s}(1,t)=a_{13,ss}(1,t)=0,\\
&a_{14}(1,t)=a_{14,s}(1,t)=a_{14,ss}(1,t)=0.
\end{aligned}\right\} \quad (95)$$

Comparing equations (83)–(86) with equations (95), it is seen that sufficient conditions for compatibility are:

$$\left.\begin{aligned}
&\frac{d^\mu}{ds^\mu}g_{1j}(s,t)=0,\ s=\kappa=\pm1,\ \mu=0,1,\ldots,4;\ j=1,2,\\
&\frac{d^\mu}{ds^\mu}g_{1j}(s,t)=0,\ s=\kappa=\pm1,\ \mu=0,1,2;\ j=3,4.
\end{aligned}\right\} \quad (96)$$

Summarizing. In order to solve equations (61) for U satisfying equations (62)–(71) with the boundary conditions homogeneous on $s=\pm1$ and $x=-1$ it is sufficient to solve:

$$L[V]=L[W_1],$$

where

$$V=U-W_1$$

subject to the initial conditions:

$$V(x,s,0)=\Phi(x,s)+W_1(x,s,0),$$
$$V_t(x,s,0)=\Psi(x,s)+W_{1,t}(x,s,0)$$

with *all boundary conditions homogeneous* provided equations (87) and (94) hold and provided W_1 is given by equation (79) in which $P_1(x)$ is given by equation (81) and $A_1(s,t)$ is given by equation (80) with its components given by solving equations (83)–(86).

Conclusions

In the two-space dimensional case the method of this paper reduces in general to a problem of solving a linear system of ordinary differential equations. However, in practice the system often reduces to a system of linear algebraic equations. In the one-space dimensional case, the method reduces to a problem of solving a linear system of algebraic equations. A general criterion to determine the applicability of the method is given for the one-space dimensional case.

The method used in this paper to reduce a problem with nonhomogeneous boundary conditions to one with homogeneous boundary conditions requires prescribing m independent polynomials for $2m$ nonhomogeneous boundary conditions and determining an $n\times m$ coefficient matrix which is a function of time. This method, as shown, is equally applicable to one and two (rectangle) space dimensional problems. In the Mindlin–Goodman method [1], polynomials are to be determined, the number of which is the number of nonhomogeneous boundary conditions. Coefficients of the I^{th} polynomial are determined from the $2m$ boundary conditions by applying the J^{th} boundary operator to the I^{th} polynomial such that the result is the Kronecker delta function δ_{IJ}.

To contrast the method of this paper with that of the Mindlin–Goodman method [1], it is of interest to note that the Mindlin–Goodman method requires, in general, solving four equations ($2m$) in four unknowns (n) four times for an Euler beam whereas by the method of this paper it is only necessary to solve four equations in four unknowns once. When the number of unknowns increases, the contrast is even greater. For example, in Sun and Whitney [3] where the number of equations is five ($n=5$) and the order is 2 ($k+1=2$) and there are five boundary conditions ($m=5$) on each edge, the Mindlin–Goodman method requires, in general, solving ten equations in ten unknowns ten times, whereas by the method of this paper it is only necessary to solve ten equations in ten unknowns.

Specific examples illustrating the method for the reduction

of nonhomogeneous boundary conditions to homogeneous boundary conditions are given. In Example 1, boundary conditions for a Bernoulli–Euler beam are treated in which there is one unknown function and two boundary conditions at each end and an illustration of the method for boundary conditions of order zero, one, two, and three are worked out. In Example 2, a one-space dimensional problem with five unknown functions and five boundary conditions at each end, representing a laminated composite plate, was treated with a specific illustration of representative boundary conditions. The final one-space dimensional example dealt with a Timoshenko beam in which there are two unknown functions and two boundary conditions at each end. For this case the importance of carefully choosing the polynomial is demonstrated. Finally an application to a two-space dimensional problem is given for an antisymmetric angle-ply laminated circular cylindrical panel. This problem has three unknown functions and four boundary conditions for the three functions on each side of the rectangular domain considered.

References

1 Mindlin, R. D., and Goodman, L. E., "Beam Vibrations With Time-Dependent Boundary Conditions," ASME JOURNAL OF APPLIED MECHANICS, Vol. 17, No. 4, 1950, pp. 377–380.

2 Yu, Yi-Yuan, "Forced Flexural Vibrations of Sandwich Plates in Plane Strain," ASME JOURNAL OF APPLIED MECHANICS, Vol. 27, Series E, No. 3, 1960, pp. 535–540.

3 Sun, C. T., and Whitney, J. M., "Forced Vibrations of Laminated Composite Plates in Cylindrical Bending," *J. Acoust. Soc. Am.*, Vol. 55, No. 5, 1974, pp. 1003–1008.

4 Magrab, E. B., *Vibrations of Elastic Structural Membranes*, Sijthoff and Noordhoff, 1979.

5 Soldatos, K., "On the Buckling and Vibration of Antisymmetric Angle-Ply Laminated Circular Cylindrical Shells," *Int. J. Eng. Sci.*, Vol. 21, No. 3, 1983, pp. 217–222.

S. L. Hendricks
Associate Professor,
Engineering Science and Mechanics,
Virginia Polytechnic Institute
and State University,
Blacksburg, VA 24061

The Effect of Viscoelasticity on the Vibration of a Rotor

This paper analyzes the dynamics of a simple rotor mounted on a shaft constructed from a viscoelastic material. The equations are solved using a perturbation technique that is valid whenever viscoelastic time constants are much larger than elastic time constants. Regions of stable and unstable motion are discovered analytically. Several time histories for the rotor motion are presented.

I Introduction

Since the early days of the development of the steam turbine, rotating flexible shafts have received much attention (see for example Bolotin, 1963). Historically, most of the rotor dynamic work has involved rotors constructed from elastic materials. Recently people have become interested in the dynamics of rotors made from materials which exhibit viscoelastic behavior (Crandall, 1980, and Pyrz, 1982). The interest stems from the increasing use of Composite Materials in structures. Recent papers report on the effect that viscoelasticity has on: helicopter rotor blades (Rosen, 1983, Pak, 1982); squeeze film bearing forces (Tichy, 1982); spacecraft (Tkachenko, 1978); gas turbine disks (Bokhberg, 1976); flywheels (Cuccuru et al., 1980); and continuous beams (Norwood, 1980, and Schweitzer, 1975). This paper examines the dynamics of a simple disk mounted in the middle of a flexible shaft.

If a shaft is constructed from elastic materials, then there will exist certain critical speeds of rotation at which the transverse displacement of the shaft (due to mass imbalance) reaches a maximum amplitude. These rotational speeds are known as critical speeds and correspond to the natural frequencies of vibration of the nonrotating shaft. If the rotational speed is held constant, the shaft vibrations will damp out and the shaft will bow out to a steady amplitude that depends on the location of the center of mass. If the shaft is constructed from viscoelastic materials, then in addition to an "elastic" vibration behavior, there will be a slower "viscoelastic" motion as the shaft material relaxes under stress. This viscoelastic motion can be unstable under certain conditions that are developed in the paper. Section II reviews briefly the analysis for a simple elastic shaft. Section III analyzes the dynamics if the shaft is viscoelastic.

II Elastic Shaft

Consider a single rotor (disk of mass m) in the middle of a massless elastic shaft (Fig. 1). The center of mass of the rotor

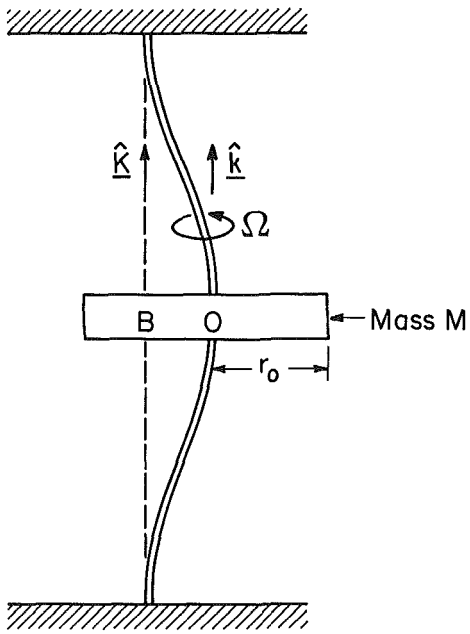

Fig. 1 Single mass rotor

G is offset a distance δ from the center of the rotor 0. Let $(\hat{I}, \hat{J}, \hat{K})$ be a coordinate system fixed in the laboratory and let $(\hat{\mathbf{i}}, \hat{\mathbf{j}}, \hat{\mathbf{k}})$ be a coordinate system attached to and spinning with the rotor with an angular velocity Ω (Fig. 2). The elastic shaft provides a restoring force which is linearly proportional to the distance between the rotor center 0 and the nominal location of the rotor center B. The effect of this force is modeled by a spring of constant k. In addition to the spring force, an external damper is added to the system. This damper adds a force that is linearly proportional to the velocity of point 0 as measured from the laboratory fixed reference frame. The damper is modeled as a linear dashpot of constant c. Note that the dashpot in Fig. 2 always opposes the velocity of point 0 and is not only a radial damper.

The rotor disk is allowed to translate in two directions but it is not allowed to tilt in this simple model. The runout of the rotor (the distance from B to 0) is defined by the coordinates x and y which are distances measured with respect to the rotating coordinate system $(\hat{\mathbf{i}}, \hat{\mathbf{j}}, \hat{\mathbf{k}})$.

Contributed by the Applied Mechanics Division for publication in the JOURNAL OF APPLIED MECHANICS.
Discussion on this paper should be addressed to the Editorial Department, ASME, United Engineering Center, 345 East 47th Street, New York, N.Y. 10017, and will be accepted until two months after final publication of the paper itself in the JOURNAL OF APPLIED MECHANICS. Manuscript received by ASME Applied Mechanics Division, January 29, 1985; final revision, September 15, 1985.

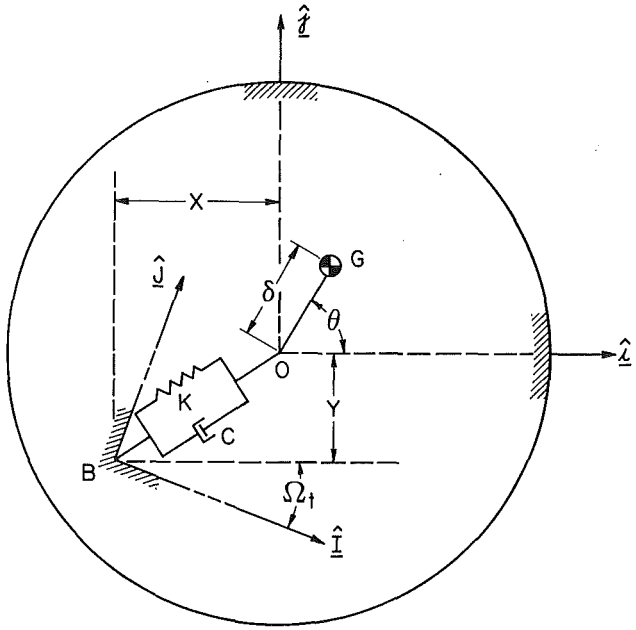

Fig. 2 Configuration for elastic rotor

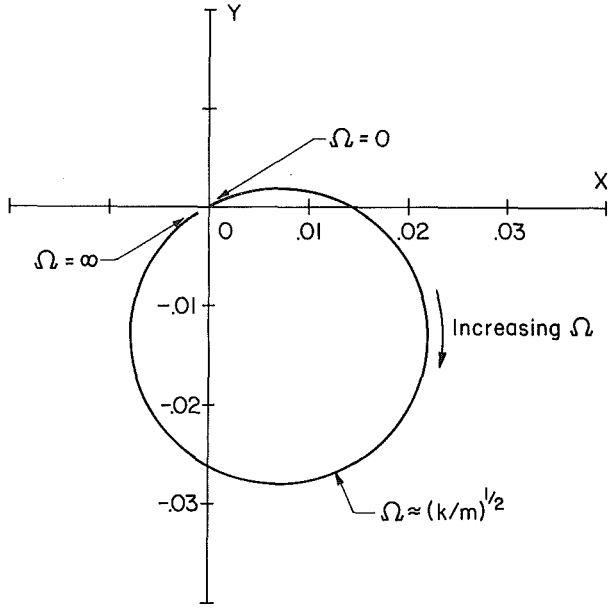

Fig. 3 Elastic polar plot

The position, velocity, and acceleration of the center of mass (G) are:

$$\mathbf{R}_G = (x+\delta\cos\theta)\hat{\mathbf{i}} + (y+\delta\sin\theta)\hat{\mathbf{j}} \tag{1a}$$

$$\dot{\mathbf{R}}_G = (\dot{x}-\Omega y-\Omega\delta\sin\theta)\hat{\mathbf{i}} + (\dot{y}+\Omega x+\Omega\delta\cos\theta)\hat{\mathbf{j}} \tag{1b}$$

$$\ddot{\mathrm{R}}_G = (\ddot{x}-2\Omega\dot{y}-\Omega^2[x+\delta\cos\theta])\hat{\mathbf{i}} + (\ddot{y}+2\Omega\dot{x}-\Omega^2[y+\delta\sin\theta])\hat{\mathbf{j}} \tag{1c}$$

The position and velocity of point 0 are

$$\mathbf{R}_0 = x\hat{\mathbf{i}} + y\hat{\mathbf{j}} \tag{2a}$$

$$\dot{R}_0 = (\dot{x}-\Omega y)\hat{\mathbf{i}} + (\dot{y}+\Omega x)\hat{\mathbf{j}} \tag{2b}$$

The equations of motion for the rotor can now be written

$$m\ddot{\mathbf{R}}_G + c\dot{\mathbf{R}}_o + k\mathbf{R}_o = 0 \tag{3}$$

In scalar form equation (3) is

$$m\ddot{x} + c\dot{x} - 2m\Omega\dot{y} + (k-m\Omega^2)x - c\Omega y = m\Omega^2\delta\cos\theta \tag{4a}$$

$$m\ddot{y} + c\dot{y} + 2m\Omega\dot{x} + (k-m\Omega^2)y + c\Omega x = m\Omega^2\delta\sin\theta \tag{4b}$$

In terms of the complex quantity $\eta = x + iy$, the two real equations (4a,b) can be expressed in terms of the one complex equation

$$m\ddot{\eta} + (c+2im\Omega)\dot{\eta} + (k-m\Omega^2+ic\Omega)\eta = m\Omega^2\delta e^{i\theta} \tag{5}$$

To determine the stability of equation (5), the eigenvalues of the homogeneous equation (δ = 0) are checked. The characteristic equation associated with equation (5) is

$$m\lambda^2 + (c+2im\Omega)\lambda + (k-m\Omega^2+ic\Omega) = 0 \tag{6}$$

where λ is the eigenvalue. The two roots of equation (6) are

$$\lambda = -\frac{c}{2m} - i\left(\Omega \pm \left[\frac{k}{m} - \left(\frac{c}{2m}\right)^2\right]^{1/2}\right) \tag{7}$$

Since the real part is always negative, any motion in the system will be damped out and the solution will decay to the equilibrium configuration. This equilibrium position will not be at the origin (pt. B, Fig. 2) because the rotor center of mass is not located at point 0. The equilibrium position is found by solving the steady state (time derivatives = 0) version of equation (5)

$$(k-m\Omega^2+ic\Omega)\eta = m\Omega^2\delta e^{i\theta} \tag{8}$$

Thus

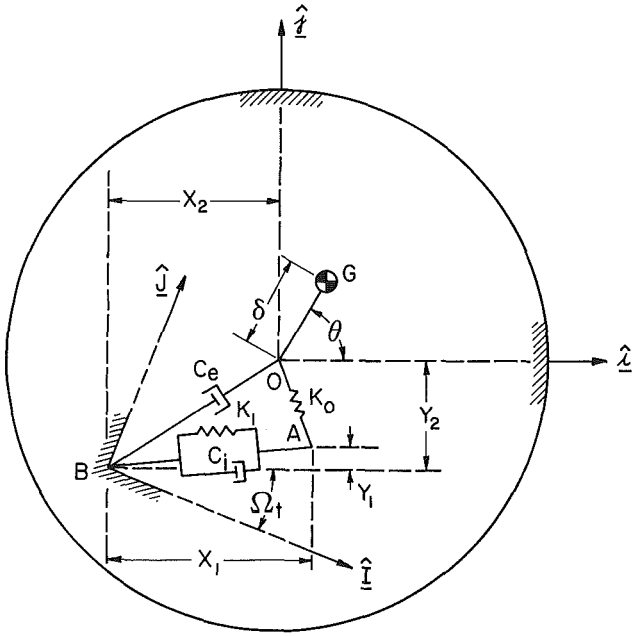

Fig. 4 Configuration for viscoelastic rotor

$$\eta_{eq} = \frac{m\Omega^2\delta e^{i\theta}}{k-m\Omega^2+ic\Omega} \tag{9}$$

where η_{eq} is the equilibrium position in complex form.

A plot of x (Real [η_{eq}]) versus y (Imaginary [η_{eq}]) as a function of the parameter Ω provides the locus of equilibrium positions for the rotor. This graph is known as a polar plot. For example, if m = 0.25 kg, k = 2,000 N/m, c = 0.75 kg/s, δ = 0.001 m, θ = 30 deg, then Fig. 3 gives the polar plot. At a particular constant spin speed, the time history of the motion consists of oscillations that decay to the equilibrium position (one point on the polar plot) at that spin speed. For times $t \gg c/2m$ there would be no motion relative to the rotating axes.

III Viscoelastic Shaft

This section explores the ramifications of replacing the elastic shaft (Fig. 1) with a shaft made of viscoelastic material.

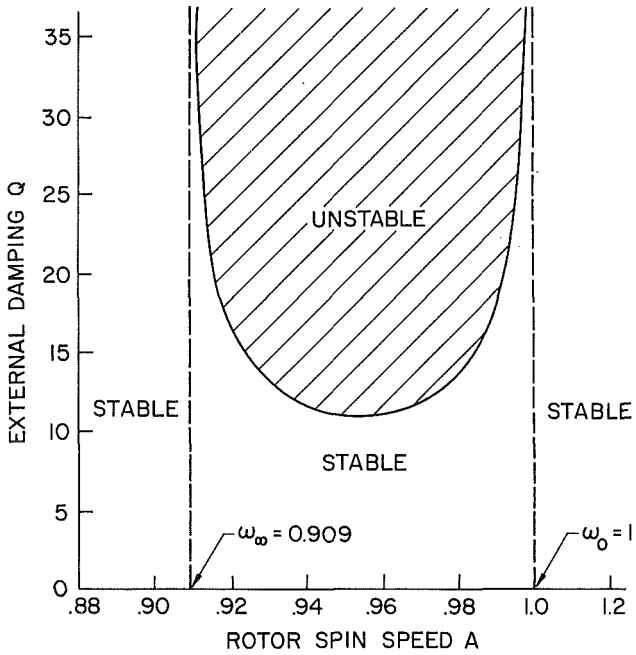

Fig. 5 Viscoelastic stability map

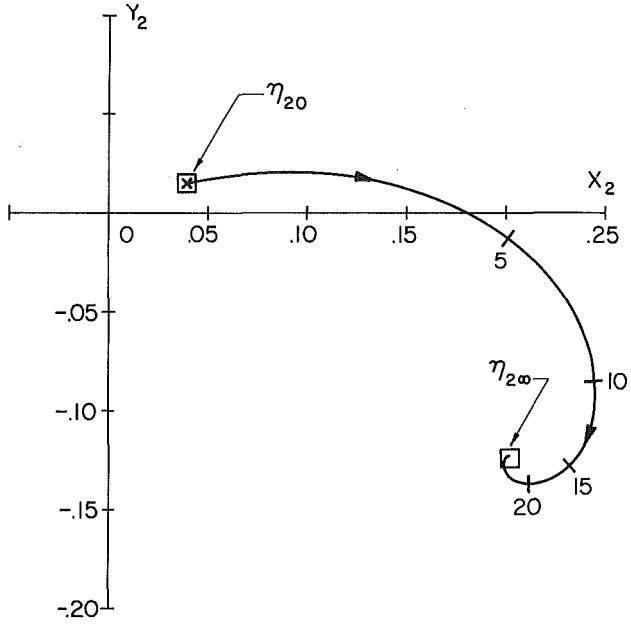

Fig. 6 Time history (stable); $A = 0.90$; $\lambda_V = (-0.017 + 0.022i) \times 10^{-6}$

The viscoelastic material will be modeled as a standard 3 parameter solid (Fig. 4) consisting of 2 springs (spring constants k_o and k_1) and one dashpot (damping constant c_i). The dynamics of the viscoelastic shaft can be incorporated by introducing an extra degree of freedom in both the x direction and the y direction. This extra degree of freedom is represented schematically in Fig. 4 by the point A. Point A has no mass associates with it and is used only as a convenient stepping stone to determine the motion of the center of the rotor (point 0). In addition to the viscoelastic element, an external damper (damping constant c_e) is added to the rotor. The two dashpots (c_i, c_e) in Fig. 4 do not act in the same manner. The external damper (c_e) provides a force that is linearly proportional to the velocity of point 0 *as measured from a laboratory fixed (I, J, K) reference frame.* The internal damper that is part of the viscoelastic element provides a force that is linearly proportional to the velocity of point A *as measured from a rotating (i, j, k) frame of reference.* This is an important distinction that has significant effects.

The position, velocity, and acceleration of the mass center G are:

$$\mathbf{R}_G = (x_2 + \delta\cos\theta)\hat{\mathbf{i}} + (y_2 + \delta\sin\theta)\hat{\mathbf{j}} \tag{10a}$$

$$\dot{\mathbf{R}}_G = (\dot{x}_2 - \Omega y_2 - \Omega\delta\sin\theta)\hat{\mathbf{i}} + (\dot{y}_2 + \Omega x_2 + \Omega\delta\cos\theta)\hat{\mathbf{j}} \tag{10b}$$

$$\ddot{\mathbf{R}}_G = (\ddot{x}_2 - 2\Omega\dot{y}_2 - \Omega^2[x_2 + \delta\cos\theta]\mathrm{k})\hat{\mathbf{i}} + (\ddot{y}_2 + 2\Omega\dot{x}_2 - \Omega^2[y_2 + \delta\sin\theta])\hat{\mathbf{j}} \tag{10c}$$

The position and velocity of point 0 are:

$$\mathbf{R}_0 = x_2\hat{\mathbf{i}} + y_2\hat{\mathbf{j}} \tag{11a}$$

$$\dot{\mathbf{R}}_0 = (\dot{x}_2 - \Omega y_2)\hat{\mathbf{i}} + (\dot{y}_2 + \Omega x_2)\hat{\mathbf{j}} \tag{11b}$$

The position and velocity (taken with respect to rotating axes) of point A are:

$$\mathbf{R}_A = x_1\hat{\mathbf{i}} + y_1\hat{\mathbf{j}} \tag{12a}$$

$$\dot{\mathbf{R}}_A = \dot{x}_1\hat{\mathbf{i}} + \dot{y}_1\hat{\mathbf{j}} \tag{12b}$$

The equations of motion in vector form are:

$$m\ddot{\mathbf{R}}_G + c_e\dot{\mathbf{R}}_o + k_o(\mathbf{R}_o - \mathbf{R}_A) = 0 \tag{13a}$$

$$c_i\dot{\mathbf{R}}_A + k_o(\mathbf{R}_A - \mathbf{R}_o) + k_1\mathbf{R}_A = 0 \tag{13b}$$

Equations (13) represent four scalar equation (two second order and two first order) which can be expressed in terms of the two complex quantities $\eta_2 = x_2 + iy_2$ and $\eta_1 = x_1 + iy_1$ as

$$m\ddot{\eta}_2 + (c_e + 2im\Omega)\dot{\eta}_2 + (k_o - m\Omega^2 + ic_e\Omega)\eta_2 - k_0\eta_1 = m\Omega^2\delta e^{i\theta} \tag{14a}$$

$$c_i\dot{\eta}_1 + (k_o + k_1)\eta_1 - k_o\eta_2 = 0 \tag{14b}$$

Equation (14) describes the motion of this rotor. For stability, the eigenvalues of the characteristic equation

$$[m\lambda^2 + (c_e + 2im\Omega)\lambda + k_o - m\Omega^2 + ic_e\Omega][c_i\lambda + k_o + k_1] - k_o^2 = 0 \tag{15}$$

must all have negative real parts. A Routh-Hurwitz analysis provides the following stability information:

(*a*) If $c_i = 0$, $c_e \neq 0$ then the rotor is always stable. This is not surprising since in this case the viscoelastic material is equivalent to an elastic spring of spring constant

$$k_\infty = \frac{k_o k_1}{k_o + k_1}.$$

(*b*) If $c_i \neq 0$, $c_e = 0$ then the rotor becomes unstable if $\Omega > (k_\infty/m)^{1/2}$. This is a fairly well known result showing that internal damping is destabilizing if the rotor spin exceeds the lowest natural frequency (Kimball, 1923).

(*c*) If $c_i \neq 0$, $c_e \neq 0$ then the algebra is too involved to yield a useful stability criteria.

To proceed further analytically it is helpful to nondimensionalize the problem so as to highlight the important terms. Using $\omega_o = (k_o/m)^{1/2}$, m, and r_o = disk radius, as the characteristic frequency, mass and length, the following nondimensional parameters are introduced: $A = \Omega/\omega_o$ = spin speed; $Q = m\omega_o/c_e$ = external damping (quality factor); $\omega_\infty = [k_1/(k_o + k_1)]^{1/2}$ = relaxation frequency; $\tau = c_i\omega_o/k_1$ = relaxation time constant; $\epsilon = \delta/r_o$ = imbalance distance.

In terms of the nondimensional parameters, equations (14) become

$$\ddot{\eta}_2 + \left(\frac{1}{Q} + 2iA\right)\dot{\eta}_2 + (1 - A^2 + iA/Q)\eta_2 - \eta_1 = \epsilon A^2 e^{i\theta} \tag{16a}$$

$$\tau\omega_\infty^2\dot{\eta}_1 + \eta_1 + (\omega_\infty^2 - 1)\eta_2 = 0 \tag{16b}$$

where η_1 and η_2 are now nondimensional variables. As an example consider the following dimensional parameters: m =

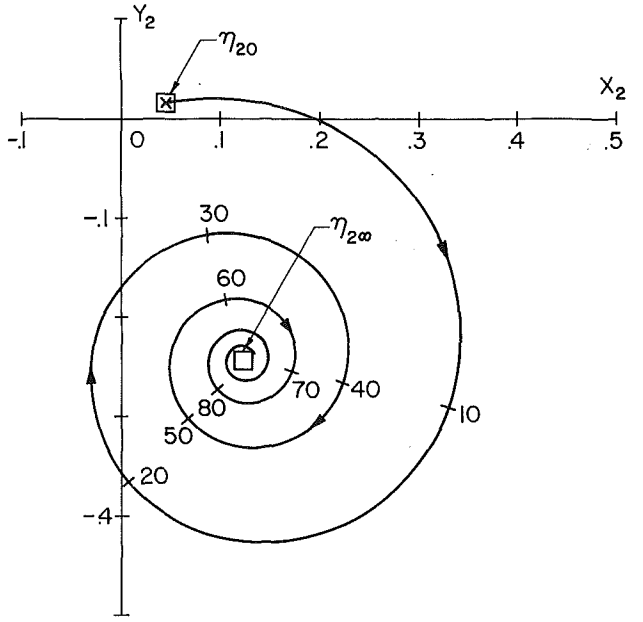

Fig. 7 Time history (stable); $A = 0.91$; $\lambda_v = (-0.003 + 0.027i) \times 10^{-6}$

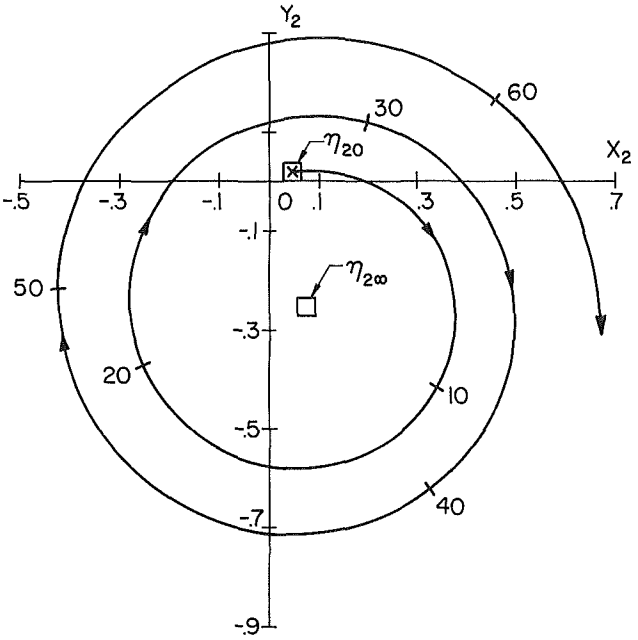

Fig. 8 Time history (unstable); $A = 0.913$; $\lambda_v = (-0.002 + 0.029i) \times 10^{-6}$

0.25 kg; $c_i/k_1 = 1$ day; $k_o = 2{,}000$ N/m; $r_o = 0.1$ m; $c_e = 0.75$ kg/s; $\delta = 0.001$ m; $k_1 = 9500$ N/m; $\theta = 30$ deg. The characteristic frequency is $\omega_o = 89.4$ rad/s. The important nondimensional parameters are then $Q = 30$; $\omega_\infty = 0.909$; $\tau = 7.73 \times 10^6$; $\epsilon = 0.01$. The numbers chosen in this example correspond to a viscoelastic relaxation time constant (c_i/k_1) of one day. The elastic vibration time constant ($1/\omega_o$) is ~ 0.01 s. The disparity between these two time constants is manifested in the nondimensional parameter τ which in this case is five orders of magnitude larger than any other parameter. A perturbation approach can be used to solve equations (16) whenever viscoelastic time constants are long compared to elastic time constants.

The nondimensional characteristic equation associated with equations (16*a*,*b*) is

$$\left[\lambda^2 + \left(\frac{1}{Q} + 2iA\right)\lambda + 1 - A^2 + iA/Q\right]\left[\omega_\infty^2\lambda + \frac{1}{\tau}\right] + (\omega_\infty^2 - 1)/\tau = 0 \tag{17}$$

To take advantage of the small parameter ($1/\tau$) let

$$\lambda = \lambda_o + \frac{\lambda_1}{\tau} + \frac{\lambda_2}{\tau^2} + \ldots \tag{18}$$

and solve for the 3 roots of equation (17) accurate to the lowest nonvanishing term. The result is two 0(1) eigenvalues and one $0(1/\tau)$ eigenvalue.

a) 0(1) eigenvalues (elastic)

$$\lambda_e = -\frac{1}{2Q} - i\left[A \pm \left(1 - \frac{1}{4Q^2}\right)^{1/2}\right] \tag{19}$$

These two roots are labeled the elastic roots since equation (19) is the nondimensional equivalent of equation (7). Since the error in equation (19) is $0(1/\tau)$, the elastic roots will always be stable (real parts less than zero) provided $1/2Q \gg 1/\tau$.

b) $0(1/\tau)$ eigenvalue (viscoelastic)

$$\lambda_v = -\frac{1}{\tau\omega_\infty^2}\left(\frac{\omega_\infty^2 - A^2 + iA/Q}{1 - A^2 + iA/Q}\right) \tag{20}$$

This root is labeled viscoelastic since it corresponds to a slow $0(1/\tau)$ motion that is not present in the elastic shaft. The viscoelastic motion will be unstable (real part of $\lambda_v > 0$) if

$$A^4 + \left(\frac{1}{Q^2} - \omega_\infty^2 - 1\right)A^2 + \omega_\infty^2 < 0 \tag{21}$$

Figure 5 shows the stability map based on equation (21). If the rotor spin speed $A < \omega_\infty$ or if $A > \omega_o$, the motion is always stable. If Q is large (external damping is small) then the motion becomes unstable when $\omega_\infty < A < \omega_o$. As Q decreases (the external damping increases) the unstable region narrows. If $Q < 1/(1 - \omega_\infty)$ the motion is always stable. Note that the boundaries of the unstable region do not depend on the value of τ (the nondimensional relaxation time constant). Equation (21) is valid for any value of τ, provided only that τ is large enough to make the perturbation approach valid.

It is sometimes useful to know the complete time history of the rotor motion. If the shaft is made of a viscoelastic material then the position of the center of the rotor will change slowly with time as the viscoelastic dashpot relaxes. To track the time history, equations (16*a*,*b*) could be integrated over time using numerical integration. However even for this simple rotor the numerical integration would be expensive since equations (16*a*,*b*) are stiff. The equations are stiff because both the fast 0(1) elastic motion and the slow $0(1/\tau)$ viscoelastic motion are included. Any time step that is small enough to discern the 0(1) motion would be so small compared to the $0(1/\tau)$ motion that an inordinate number of steps would be required to complete the integration.

A perturbation expansion of equations (16*a*,*b*) shows that motion occurs on two different time scales. There is a fast elastic motion associated with the 0(1) eigenvalues. The elastic vibrations damp out at the beginning of the motion in a time that is very short compared to the viscoelastic motion. Once the elastic transients have died out there is a slow $0(1/\tau)$ viscoelastic motion given by

$$(1 - A^2 + iA/Q)\eta_2 - \eta_1 = \epsilon A^2 e^{i\theta} \tag{22a}$$

$$\tau\omega_\infty^2\dot{\eta}_1 + \eta_1 + (\omega_\infty^2 - 1)\eta_2 = 0 \tag{22b}$$

Eliminating η_1 produces the single differential equation that describes the time history of the center of the rotor.

$$\tau\omega_\infty^2(1 - A^2 + iA/Q)\dot{\eta}_2 + (\omega_\infty^2 - A^2 + iA/Q)\eta_2 = \epsilon A^2 e^{-i\theta} \tag{23}$$

For times $1/\omega_o \ll t \ll \tau/\omega_o$ the elastic motion has died out but the viscoelastic element has not yet begun to yield. This means that $\eta_1 = 0$ and equation (22*a*) gives

$$\eta_{2o} = \frac{\epsilon A^2 e^{i\theta}}{1 - A^2 + iA/Q} \tag{24}$$

where the subscript o means the beginning of the viscoelastic motion. η_{2o} is the initial condition for equation (23). The solution to equation (23) is

$$\eta_2(t) = (\eta_{2o} - \eta_{2\infty}) e^{\lambda_v t} + \eta_{2\infty} \tag{25}$$

where

$$\eta_{2\infty} = \frac{\epsilon A^2 e^{i\theta}}{\omega_\infty^2 - A^2 + iA/Q} \tag{26}$$

and λ_v is given in equation (20). Note that η_{2o} is just the equilibrium position (point on a polar plot) of an equivalent elastic shaft using k_o as the spring constant while $\eta_{2\infty}$ is the equilibrium point of an elastic shaft using k_∞ as the spring constant.

Equation (25) is the equation of a spiral centered at $\eta_{2\infty}$ and beginning at η_{2o}. If the real part of $\lambda_v < 0$ then the motion spirals in, asymptotically approaching $\eta_{2\infty}$. If the real part of $\lambda_v > 0$, then the motion spirals out diverging from $\eta_{2\infty}$.

For the following rotor parameters the stability boundaries occur at $A = 0.912$ and $A = 0.997$: $Q = 30$; $\omega_\infty = 0.909$; $\tau = 7.73 \times 10^6$; $\epsilon = 0.01$; $\theta = 30$ deg.

Figure 6 shows the time history for this rotor with a spin speed of $A = 0.90$. Note that the motion occurs in the stable region and quickly (on a viscoelastic time scale) decays to $\eta_{2\infty}$. The numbers at the tick marks along the trajectory signify time measured in days.

Figure 7 shows the time history for the same rotor with a spin speed of $A = 0.91$. This is still in the stable region but much closer to the stability boundary. The decay is, therefore, slower, allowing more encirclements.

Figure 8 shows the same rotor with a spin speed of $A = 0.913$. The motion is now unstable and the distance from $\eta_{2\infty}$ grows with time. Note that when the motion is unstable, $\eta_{2\infty}$ is not the final position of the rotor, but should be thought of as the center of a growing spiral.

IV Conclusions

When a rotating shaft is constructed from viscoelastic material, the motion of the rotor occurs on two different time scales. If the two time scales differ by several orders of magnitude, the problem is amenable to a perturbation solution. The perturbation solution reveals a region of instability for the rotor motion. In the unstable region the center of the rotor moves in an exponentially growing spiral. If the motion occurs in the stable region, the rotor moves in an exponentially decaying spiral and the rotor center will reach a final fixed position. The spiral motion evolves on a long time scale governed by the viscoelastic time constant.

References

Bolotin, V. V., *Nonconservative Problems of the Theory of Elastic Stability*, Pergamon Press, 1963.

Crandall, S. H., "Physical Explanations of the Destabilizing Effects of Damping in Rotating Parts," in *Rotordynamic Instability Problems in High Performance Turbomachinery*, NASA CP 2133, May 1980, pp. 369–382.

Cuccuru, G. A., Ginesu, F., Picasso, B., and Priolo, P., "Characterization of Composite Materials for Filament Wound Flywheels," *Journal of Composite Materials*, Vol. 14, Jan. 1980, pp. 31–41.

Danfelt, E. L., Hewes, S. A., and Chou, T. W., "Optimization of Composite Flywheel Design," *International Journal of Mechanical Sciences*, Vol. 19, Feb. 1977, pp. 69–78.

Gokhberg, V. E., Ivanov, I. A., and Sadakov, O. S., "Use of the Structural Model of a Viscoelastic-Plastic Material for Calculating the Deformation Kinetics of Structural Elements," *Teplovye Napriazheniia v Elementakh Konstruktsii*, No. 16, 1976, pp. 89–93.

Kimball, A. L., Jr., "Internal Friction Theory of Shaft Whirling," *Phys. Rev.*, Vol. 2, No. 21, 1923, p. 703.

Norwood, R. L., "Studies on the Motion of Continuous Viscoelastic Rotors," Ph.D. Thesis, University of Illinois at Urbana-Champaign, 1980.

Pak, E. G., Stekolnikov, V. N., Ganiushkin, I. P., Ivannikova, R. V., and Kestelman, V. N., "The Effect of Hybrid Composite Materials on the Dynamic Characteristics of Helicopter Rotor Blades," *Mekhanika Kompozitnykh Materialov*, May–June 1982, pp. 475–479.

Pyrz, R., "Stability of Motion of a Viscoelastic Rotating Shaft," Report No. 237, Danish Center for Applied Mathematics and Mechanics, April 1982.

Rosen, A., "Equivalent G/E of Helicopter Rotor Blades—Shear Modulus to Young's Modulus Ratio," *AIAA Journal*, Vol. 21, Mar. 1983, pp. 478–479.

Schweitzer, G., "Stabilization of Self-Excited Rotor Vibrations by an Active Damper," *Dynamics of Rotors*, Proceedings of the Symposium, Lyngby, Denmark, August 12–16, 1974, Springer-Verlag, 1975, pp. 472–493.

Tichy, J. A., "Effects of Fluid Inertia and Viscoelasticity on Squeeze-Film Bearing Forces," *ASLE Transactions*, Vol. 25, Jan. 1982, pp. 125–132.

Tkachenko, V. A., "Dynamical Analysis of the Precision of a Spacecraft With a Powered Flywheel in a Cardan Suspension With Viscoelastic Dampers in Uniaxial Correction," *Cosmic Research*, Vol. 16, No. 3, Nov. 1978, pp. 284–290.

Transient Response of a Support Structure Excited by an Accelerating Unbalanced Rotor

F. Ellyin
Mem. ASME

Z. Wolanski

Department of Mechanical Engineering,
The University of Alberta,
Edmonton, Alberta,
Canada, T6G 2G8

The transient vibration of a beam supporting an unbalanced rotor is investigated using finite element discretization techniques. The rotor speed is time dependent to simulate transients at startup. The beam is low-tuned relative to the rotor operating speed. A rigid rotor shaft mounted in an oil-film bearing is considered. The "short-bearing" approximation and nonlinear performance of the journal bearing are assumed. The method of solution for transient response is based on direct integration of the system equations of motion using finite element in time formulation. The results of numerical anlaysis are presented in graphical form and discussed. One notes significant effects of the journal bearing on the system response.

Introduction

There is a trend to support rotating machinery on flexible foundation blocks which are low-tuned relative to the machine speed. In such cases, the machine service speed is higher than at least the first natural frequency of the supporting structure. Consequently, as the rotor is brought up to speed during start-up operation, the frequency of the forcing function[1] passes through one or more resonant frequencies of the system. In practice, the large foundation blocks are constructed from simple beam and frame elements constituting the main load transfer members of the structure (Ellyin, 1982). Therefore, to appreciate the dynamic response of the whole system, it is of great importance to fully understand the dynamic behavior of these simple elements. While there is an abundance of literature on steady-state modal vibration analysis of beam and frame models, in contrast very few works are published on their transient analysis.

The response of a beam excited by an unbalanced accelerating rotor mounted in a rigid bearing has been studied by Victor and Ellyin (1981). An analytical approach to solving equations of motion enabled the authors to carry out thorough parametric studies, and to draw conclusions regarding the effects of rotor acceleration rate, shear deformation, rotary inertia and damping on the system response. However, extension of the proposed method of solution to other structures proved difficult.

This paper attempts to fill a gap by providing a method of solution based on a finite element technique, which makes it more general and, therefore, suitable for vibration analysis of complex structures subjected to any type of forcing function. First, the method of solution and the computer program developed are verified by performing numerical analysis on the model investigated by Victor and Ellyin (1981). Then, an analysis is undertaken to determine the effect of oil-film bearings on the forcing function and, consequently, on the dynamic behavior of a simply supported beam subjected to this excitation.

Method of Solution

The transient response analysis of continuous physical structures generally involves discretization yielding an approximate n-degree of freedom model of the structure. Regardless of the spatial discretization scheme employed, the resulting set of system dynamic equations of motion becomes:

$$[M]\{\ddot{q}\} + [C]\{\dot{q}\} + [K]\{q\} = \{F\} \tag{1}$$

where $[M]$,[2] $[C]$, and $[K]$ are the $(n \times n)$ system mass, damping and stiffness matrices; $\{F\}$ is the $(n \times 1)$ external load vector, and $\{\ddot{q}\}$, $\{\dot{q}\}$, and $\{q\}$ are the $(n \times 1)$ nodal acceleration, velocity and displacement vectors, respectively.

The set of ordinary differential equations (1) can be integrated forward in time to generate a transient solution. The integration scheme used in this analysis is based on a finite element in time approximation. A "finite time element" consists simply of a fixed time interval, Δt, which can be treated as a standard one-dimensional finite element with two nodes at $t = t_1$ and $t = t_2$ ($\Delta t = \tau = t_2 - t_1$).

Finite Time Formulation (Recurrence Formulae). Consider a finite time element with three degrees of freedom per node:

[1] The sources of exciting force are numerous. Only the most common one (due to rotor unbalance) is considered in this study.

Contributed by the Applied Mechanics Division for presentation at the Winter Annual Meeting, Anaheim, CA, December 7–12, 1986, of The American Society of Mechanical Engineers.

Discussion on this paper should be addressed to the Editorial Department, ASME, United Engineering Center, 345 East 47th Street, New York, N.Y. 10017, and will be accepted until two months after final publication of the paper itself in the JOURNAL OF APPLIED MECHANICS. Manuscript received by ASME Applied Mechanics Division, July 30, 1985; final revision December 5, 1985. Paper No. 86-WA/APM-12.

[2] Throughout the text two notations for matrices and vectors are used interchangeably, e.g., $[M] \equiv \mathbf{M}$, $\{\dot{q}\} \equiv \dot{\mathbf{q}}$.

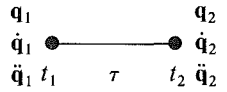

This gives six "time-wise" degrees of freedom per element. The problem now is to find an approximation for vector function $\mathbf{q}(t)$ which satisfies boundary conditions, as follows:

$$\begin{aligned} \mathbf{q}(t_1)&=\mathbf{q}_1 \quad \dot{\mathbf{q}}(t_1)=\dot{\mathbf{q}}_1 \quad \ddot{\mathbf{q}}(t_1)=\ddot{\mathbf{q}}_1 \\ \mathbf{q}(t_2)&=\mathbf{q}_2 \quad \dot{\mathbf{q}}(t_2)=\dot{\mathbf{q}}_2 \quad \ddot{\mathbf{q}}(t_2)=\ddot{\mathbf{q}}_2 \end{aligned} \tag{2}$$

This requires each component $q_i(t)$ of $\mathbf{q}(t)$ to be approximated by at least a fifth-order polynomial in time. Thus

$$\begin{aligned} q_i(t)&=\alpha_1+\alpha_2 t+\alpha_3 t^2+\alpha_4 t^3+\alpha_5 t^4+\alpha_6 t^5 \\ &=[1\ t\ t^2\ t^3\ t^4\ t^5]\{\alpha\} \end{aligned} \tag{3}$$

and

$$\mathbf{q}(t)=[I \quad tI \quad t^2I \quad t^3I \quad t^4I \quad t^5I]\{a\}=[\Phi]^T\{a\} \tag{4}$$

where I is the $(n\times n)$ identity matrix, $[\Phi]$ is the $(6n\times n)$ matrix of time terms and $\{a\}$ is the $(6n\times 1)$ vector of undetermined coefficients. The first and second derivatives of $\mathbf{q}(t)$ are obtained from equation (4):

$$\begin{aligned} \dot{\mathbf{q}}(t)&=[0\ I\ 2tI\ 3t^2I\ 4t^3I\ 5t^4I]\{a\}=[\dot{\Phi}]^T\{a\} \\ \ddot{\mathbf{q}}(t)&=[0\ 0\ 2I\ 6tI\ 12t^2I\ 20t^3I]\{a\}=[\ddot{\Phi}]^T\{a\} \end{aligned} \tag{5}$$

The $(6n\times 1)$ coefficients $\{a\}$ can be evaluated in terms of nodal variables by matching the displacements, velocities and accelerations at the nodal points $t_1 = 0$ and $t_2 = \tau$, which yields:

$$\underset{(6n\times 1)}{\{q_n\}}=\begin{bmatrix} \{q_1\} \\ \{\dot{q}_1\} \\ \{\ddot{q}_1\} \\ \{q_2\} \\ \{\dot{q}_2\} \\ \{\ddot{q}_2\} \end{bmatrix}=\underset{(6n\times 6n)}{\begin{bmatrix} I & 0 & 0 & 0 & 0 & 0 \\ 0 & I & 0 & 0 & 0 & 0 \\ 0 & 0 & 2I & 0 & 0 & 0 \\ I & \tau I & \tau^2 I & \tau^3 I & \tau^4 I & \tau^5 I \\ 0 & I & 2\tau I & 3\tau^2 I & 4\tau^3 I & 5\tau^4 I \\ 0 & 0 & 2I & 6\tau I & 12\tau^2 I & 20\tau^3 I \end{bmatrix}}\underset{(6n\times 1)}{\begin{bmatrix} \{a_1\} \\ \{a_2\} \\ \{a_3\} \\ \{a_4\} \\ \{a_5\} \\ \{a_6\} \end{bmatrix}} \tag{6}$$

or

$$\{q_n\}=[T]\{a\} \tag{7}$$

and

$$\{a\}=[T]^{-1}\{q_n\} \tag{8}$$

Substituting equation (8) into equations (4), (5) gives an approximation for $\mathbf{q}(t)$, $\dot{\mathbf{q}}(t)$ and $\ddot{\mathbf{q}}(t)$ in terms of nodal variables $\{q_n\}$:

$$\begin{aligned} \mathbf{q}(t)&\simeq[\Phi]^T[T]^{-1}\{q_n\}=[N]\{q_n\} \\ \dot{\mathbf{q}}(t)&\simeq[\dot{\Phi}]^T[T]^{-1}\{q_n\}=[\dot{N}]\{q_n\} \\ \ddot{\mathbf{q}}(t)&\simeq[\ddot{\Phi}]^T[T]^{-1}\{q_n\}=[\ddot{N}]\{q_n\} \end{aligned} \tag{9}$$

where $[N]=[\Phi]^T[T]^{-1}=[N_1\ N_2\ N_3\ N_4\ N_5\ N_6]$ is a matrix of interpolation functions (here the fifth-order Hermitian polynomials). Substituting equation (9) into the equations of motion (1) gives:

$$\begin{aligned} &[M][\ddot{N}]\{q_n\}+[C][\dot{N}]\{q_n\} \\ &\quad+[K][N]\{q_n\}-\{F\}=\{R\}\neq 0 \end{aligned} \tag{10}$$

Note that upon substitution of the approximated functions (equation (9)) the equations of motion will generally not be satisfied. In fact there is some residual $\{R\}$ left. The residual can be minimized with respect to the shape functions $[N]$ over the entire finite time element domain, i.e., over time interval $\Delta t = \tau$. This minimization process (Galerkin approach) can be expressed in the form of integral equation, as:

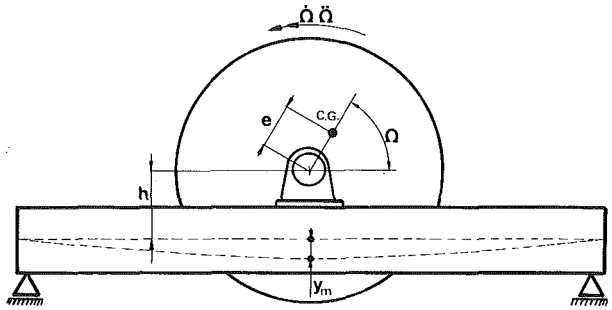

Fig. 1 Beam supporting an unbalanced rotor

$$\int_0^\tau [N]^T\{R\}dt=\mathbf{0} \tag{11}$$

Substituting equations (9), (10) into (11) and carrying out integration and matrix multiplication yields:

$$[Z]\{q_n\}=\{P\}$$

or

$$\underset{(6n\times 6n)}{\left[\begin{array}{c:c} & \\ [Z_{11}] & [Z_{12}] \\ & \\ \hdashline & \\ [Z_{21}] & [Z_{22}] \\ & \end{array}\right]}\underset{(6n\times 1)}{\left[\begin{array}{c} \{q_1\} \\ \{\dot{q}_1\} \\ \{\ddot{q}_1\} \\ \hdashline \{q_2\} \\ \{\dot{q}_2\} \\ \{\ddot{q}_2\} \end{array}\right]}=\underset{(6n\times 1)}{\left[\begin{array}{c} \{P_1\} \\ \{P_2\} \\ \{P_3\} \\ \hdashline \{P_4\} \\ \{P_5\} \\ \{P_6\} \end{array}\right]} \tag{12}$$

where

$$\{P_i\}=\int_0^\tau t^{(i-1)}[I]\{F\}dt \quad i=1,2,\ldots 6 \tag{13}$$

and

$$[Z]=\int_0^\tau([\Phi][M][\ddot{\Phi}]^T+[\Phi][C][\dot{\Phi}]^T+[\Phi][K][\Phi]^T)[T]^{-1}dt \tag{14}$$

For an initial value problem, only part of the general time formulation (equation (12)) is required to determine $\mathbf{q}_2$, $\dot{\mathbf{q}}_2$ and $\ddot{\mathbf{q}}_2$. Hence, applying simple matrix algebra and rearranging terms gives:

$$\begin{bmatrix} \{q_2\} \\ \{\dot{q}_2\} \\ \{\ddot{q}_2\} \end{bmatrix}=[Z_{12}]^{-1}\left\{\begin{bmatrix} \{P_1\} \\ \{P_2\} \\ \{P_3\} \end{bmatrix}-[Z_{11}]\begin{bmatrix} \{q_1\} \\ \{\dot{q}_1\} \\ \{\ddot{q}_1\} \end{bmatrix}\right\} \tag{15}$$

The above formulae represents a recurrence relation between displacement, velocity, and acceleration vectors at two successive nodes of time element, i.e., at time $t + \Delta t$ and t. This relationship is employed in a computer program for a sequence of time intervals to advance the solution in time in a step-by-step manner. Matrix $[Z_{12}]$ has to be inverted only once and then, for each time step, only integration to evaluate components P_i and simple matrix multiplication is involved.

The recurrence scheme just derived is conditionally stable. For numerical stability (convergence of solution) it requires time step $\Delta t = \tau$ to be less than some critical value which, in general, is "controlled" by the system's highest natural frequency. Due to the high order approximation used, components of matrices $[Z_{11}]$ and $[Z_{12}]$ contain multipliers τ^k with the exponent varying from 0 to 5 ($1, \tau, \ldots \tau^5$). For $\tau \ll 1.0$, it

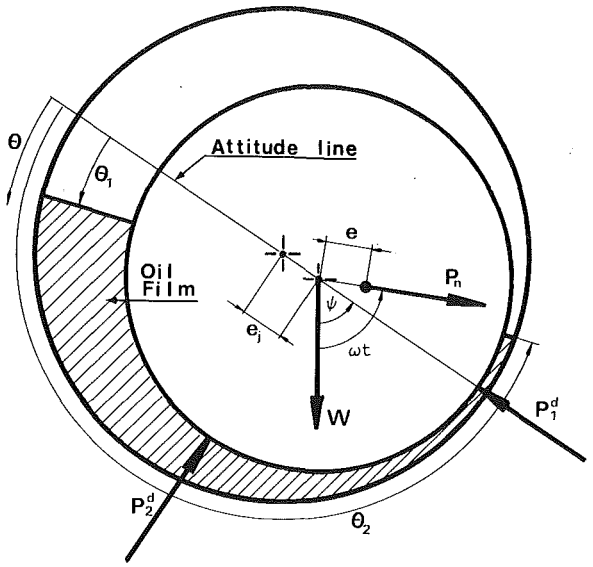

Fig. 2 Journal-bearing system

tends to give high upper bounds for a solution error estimation. To test the scheme accuracy, the transient response of the same system was obtained using double and quadruple precision and, additionally, using an independent computer code (Addison and Gladwell, 1984). All these results were in complete agreement.

Forcing Function. A force transmitted from an unbalanced rotor to its foundation depends on rotor geometry and flexibility, and on mounting details, such as: characteristics of bearings, bearing seals, bearing pedestals, etc. To simplify the analysis, highly idealized systems are examined in this study. A symmetric rigid rotor, represented by a lumped mass ($2m_r$), is located centrally between two identical bearings. This leads to consideration of only one plane with a bearing supporting a load equal to half the rotor weight (Fig. 1). If, further, a rigid bearing is assumed the forcing function becomes (Victor and Ellyin, 1981):

$$F(t) = m_r e(\dot{\Omega}^2 \sin\Omega - \ddot{\Omega}\cos\Omega) - m_r \ddot{y}_m = F_t(t) - m_r \ddot{y}_m(t) \quad (16)$$

where e is the rotor mass eccentricity, F_t is the vertical component of the inertia force due to rotor unbalance, $m_r\ddot{y}_m$ is the inertia force due to rotor acceleration in its linear motion. The rotor angular travel, Ω, is assumed to vary with time according to:

$$\Omega = \begin{cases} \omega_s T_1(3t^2/T_1^2 - t^3/T_1^3)/3 & \text{for} \quad 0 < t \le T_1 \\ \omega_s(t - T_1/3) & \text{for} \quad t > T_1 \end{cases} \quad (17)$$

where ω_s and T_1 are the rotor service speed and acceleration time, respectively. The forcing function cannot be expressed analytically if an oil-film bearing (Fig. 2) is assumed.

Consider first the case when shaft angular velocity ω is constant. The journal is in motion due to the action of four external forces, i.e., static load (weight) W, centrifugal force due to rotor unbalance P_n, and hydrodynamic oil-film forces P_1^d and P_2^d. In analyzing the motion of the journal, it is convenient to employ polar coordinates, i.e., the attitude angle ψ and the eccentricity ratio $\epsilon = e_j/C$ (where C is bearing radial clearance). Assuming the force P_1^d acts in the positive ϵ-direction (i.e., opposite to that in Fig. 2), the equations of the journal center motion may be written as:

$$\begin{aligned} P_1^d + W\cos\psi + P_n\cos(\omega t - \psi) &= m_r C(\ddot{\epsilon} - \dot{\psi}^2\epsilon) \\ P_2^d - W\sin\psi + P_n\sin(\omega t - \psi) &= m_r C(\epsilon\ddot{\psi} + 2\dot{\epsilon}\dot{\psi}) \end{aligned} \quad (18)$$

The only problem in solving these equations is to decide on functions describing the dynamic film forces (P_1^d, P_2^d). Holmes (1970) analyzed a nonlinear performance of modern turbine bearings, using a "short-bearing" approximation due to Ocvirk (1953), and reported the results to be in good agreement with his experimental works. This approach yields expressions:

$$\begin{aligned} P_1^d &= -(\mu L^3 R/2C^2)[\pi(1+2\epsilon^2)\dot{\epsilon} \\ &\quad + 2(\omega - 2\dot{\psi})\epsilon^2(1-\epsilon^2)^{1/2}](1-\epsilon^2)^{-5/2} \\ P_2^d &= (\mu L^3 R/2C^2)[4\epsilon\dot{\epsilon} \\ &\quad + \pi\epsilon(\omega - 2\dot{\psi})(1-\epsilon^2)^{1/2}/2](1-\epsilon^2)^{-2} \end{aligned} \quad (19)$$

where μ is lubricant viscosity, and L and R are bearing length and radius, respectively.

Under static conditions (i.e., in an ideal case of perfectly balanced rotor), the journal center takes a unique equilibrium position (ϵ_0, ψ_0) given by the well known relationships (Pinkus and Sternlicht, 1961):

$$\begin{aligned} S_m &= (1-\epsilon_0^2)^2[\epsilon_0\{16\epsilon_0^2 + \pi^2(1-\epsilon_0^2)\}^{1/2}]^{-1} \\ \psi_0 &= \tan^{-1}[\pi(1-\epsilon_0^2)^{1/2}/4\epsilon_0] \end{aligned} \quad (20)$$

where $S_m = \mu L^3 R\omega/4C^2 W$ is the modified Sommerfeld Number. Hence, P_1^d and P_2^d are functions of ϵ_0, ϵ, $\dot{\epsilon}$, ψ and $\dot{\psi}$. By nondimensionalizing equations (18) it can be shown (Holmes, 1970) that, for given rotor unbalance and constant angular velocity, the shaft center motion is governed by three independent dimensionless parameters, namely: ϵ_0, e/C and $g/C\omega^2$.

During transients at start-up operation, there is always tangential acceleration of the rotor shaft. Therefore, for such a case, the equations of motion for the journal center include an additional term, i.e., the inertia force due to circumferential acceleration of an unbalanced rotor. Hence

$$\begin{aligned} P_1^d + W\cos\psi + m_r e\dot{\Omega}^2\cos(\Omega - \psi) \\ + m_r e\ddot{\Omega}\sin(\Omega - \psi) = m_r C(\ddot{\epsilon} - \dot{\psi}^2\epsilon) \\ P_2^d - W\sin\psi + m_r e\dot{\Omega}^2\sin(\Omega - \psi) \\ - m_r e\ddot{\Omega}\cos(\Omega - \psi) = m_r C(\epsilon\ddot{\psi} + 2\dot{\epsilon}\dot{\psi}) \end{aligned} \quad (21)$$

The Reynolds' lubrication equation, used in deriving equation (19), neglects inertia of lubricant. Consequently, the inertia terms due to unsteady velocity (acceleration) of the journal surface were ignored. The effect of this acceleration tends to reduce the magnitude of the oil-film pressure and, therefore, the load carrying capacity of the journal bearing. This reduction can be significant for high acceleration rates. However, use of a more accurate model, to account for this effect, would be extremely complicated. Therefore, in the present work, at each instant a pseudo-steady state for rotor speed is assumed so that equations (19) can be used to calculate forces P_1^d and P_2^d. After that equations (21) are solved, using the fourth-order Runge-Kutta step procedure. These calculations are repeated in a time stepping manner to advance solutions (for the shaft center motion, dynamic film forces and their resultant in vertical direction) in time. A force equal to this resultant in magnitude and opposite in sign is considered in the original problem as component F_d of the forcing function (transmitted through bearing to foundation). Thus

$$F(t) = F_d(t) - m_r \ddot{y}_m(t) \quad (22)$$

In order to avoid metal to metal friction at the early stage of start-up operation, a rotor is lifted up by pressurized oil supplied into bearing. The pressure is dropped when rotor speed is high enough to secure sufficient load carrying capacity of the bearing film. Therefore, transient analysis of this model always starts with a rotor having some initial speed ω_i and, consequently, rotor angular travel is assumed to vary with time according to:

$$\Omega = \begin{cases} (\omega_s - \omega_i) T_1 (3t^2/T_1^2 - t^3/T_1^3)/3 + \omega_i t & \text{for} \quad 0 < t \le T_1 \\ \omega_s t - (\omega_s - \omega_i) T_1/3 & \text{for} \quad t > T_1 \end{cases} \tag{23}$$

Structure Modeling. The eight degree of freedom Timoshenko beam element TM544, proposed by Akella and Craggs (1982), is chosen to model distributed inertial and elastic properties of the supporting structure. The element four nodal variables represent transverse displacement, bending slope, shear force, and moment. In deriving the element consistent mass and stiffness matrices the centroidal displacement and bending slope are approximated by the fourth and the third order polynomials, respectively. The high order approximation used makes this element suitable for dynamic analysis of "deep" beams (with radius of gyration to length ratio $\kappa > 0.05$), i.e., when the effects of shear deformation and rotary inertia become significant.

A standard finite element assemblage process is employed to form global mass and stiffness matrices of the discretized beam, which are then modified to incorporate system constraints and boundary conditions. Upon completion of this process, a continuous beam is approximated by a spatially discrete n-degree of freedom model with the $(n \times n)$ $[M]$ and $[K]$ matrices.

The exact form of damping for structural elements is unknown. However, to take advantage of the direct time stepping integration scheme, it is necessary to evaluate the damping matrix explicitly. In the present analysis a particular form of proportional damping (Rayleigh damping) is used. Thus

$$[C] = a[M] + b[K], \tag{24}$$

where a and b are proportionality constants (Bathe, 1982).

Synthesis and Implementation. In order to implement the recurrence formulae (equation (15)) in a computer program, components of generalized load vector $\{P\}$ have to be evaluated at each time step according to equation (13).

Consider first the model with the forcing funtion given by equations (16) and (17). The component $m_r \ddot{y}_m$ can be transferred to the left hand side of the system equations of motion (equation (1)), by adding lumped rotor mass (m_r) to appropriate term in matrix $[M]$. The component $F_t(t)$ is a known function of time, therefore, the integration to obtain vectors $\{P_1\}$, $\{P_2\}$ and $\{P_3\}$ of equation (13) is straightforward. The 4-point Gaussian quadrature integration scheme is employed in the computer program.

In the second case, i.e., for the model with the journal bearing and the forcing function given by equation (22), matrix $[M]$ is modified in exactly the same way. However, the components of vector $\{P\}$ are obtained differently, since the term $F_d(t)$ in the forcing function is not given by analytical expression. The procedure used in this case can be summarized as follows:

(1) The time interval τ is divided into "j" sub-intervals $\bar{\tau}$.

(2) At each sub-interval $\bar{\tau}$, the dynamic force F_d^j is determined according to the procedure outlined before, equations (19), (21).

(3) At the same time, two additional functions are generated, namely: $\bar{\tau} F_d^j$ and $\bar{\tau}^2 F_d^j$.

(4) Then, the "j" discrete values of these functions, i.e., F_d, tF_d, and $t^2 F_d$ are integrated numerically over the interval τ to give components of vector $\{P\}$. The cubic spline method of numerical integration is used in this process.

Numerical Analysis and Discussion

To generalize discussion of the results, additional dimensionless parameters are introduced, namely: $\alpha = \omega_s/\omega_0$; $\beta = T_1/\tau_0$; rotor to beam mass ratio η and damping factor in the first mode of vibration ζ (where ω_0 and τ_0 are the system first natural frequency and period, respectively). The results presented apply to reinforced concrete beams (Poisson's ratio $\nu = 0.15$) with rectangular cross-sections (shear factor $\chi = 0.85$). For the sake of simplicity, the dynamic response of the model is examined by analyzing only displacement envelopes at the structure driving point, i.e., at the midspan of the beam.

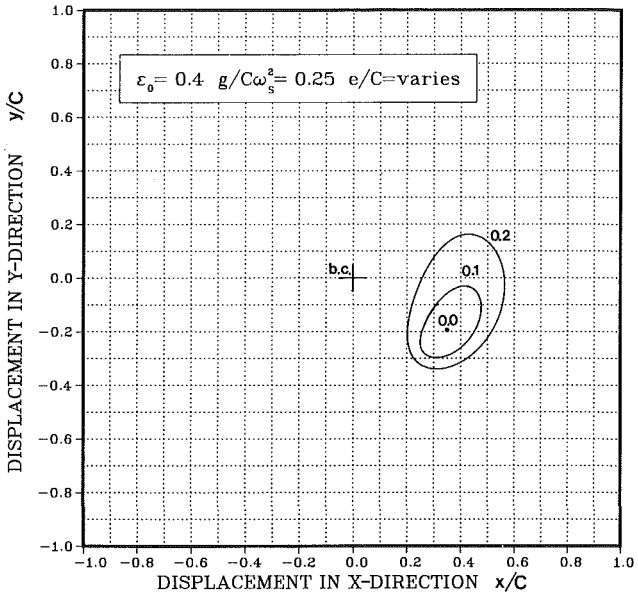

Fig. 3 Effect of rotor unbalance on steady-state whirl orbit of journal center

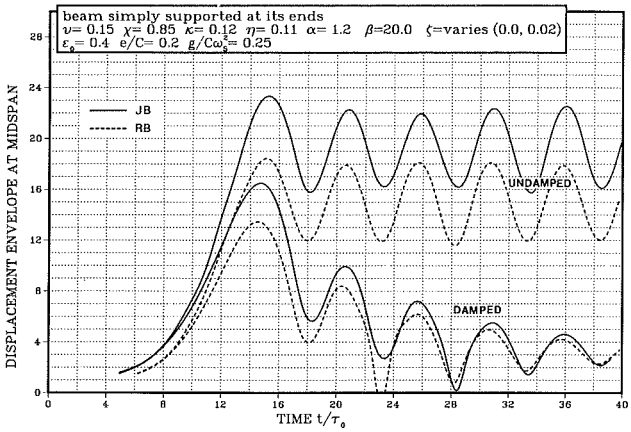

Fig. 4 Comparison of system responses for model with: journal bearing (JB), and rigid bearing (RB)

In the case of an ideal perfectly balanced rotor, for any given constant speed, the journal center is in a stationary equilibrium and the total oil-film pressure force equals the static load on the bearing. However, when the rotor has an unbalance, the center of the rotating journal is in motion describing a closed orbit about this equilibrium position. Due to this motion, additional pressures are set up in the lubricant film which act on the journal as dynamic forces over and above the static force. These dynamic forces depend on the journal center orbit.

Figure 3 shows whirl loci of the journal center for $\epsilon_0 = 0.4$ and $g/C\omega_s^2 = 0.25$, being typical for a rotor-bearing system of a relatively small high-speed turbogenerator. The orbits are obtained by integrating equations of motion (18) for two different values of the rotor unbalance parameter e/C (0.1, 0.2). The pronounced effect of rotor unbalance on the journal center motion and, consequently, on the oil-film dynamic forces is obvious from this figure. The magnitude of the rotor unbalance is insignificant in analyzing rigid bearing model

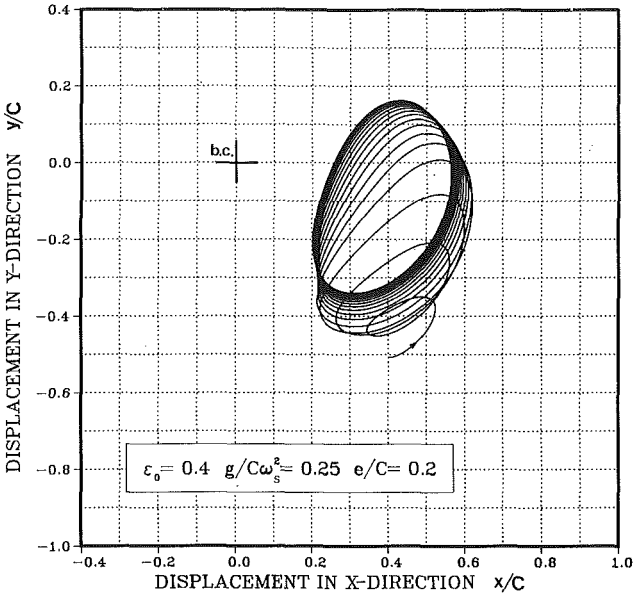

Fig. 5 Transient orbits of journal center due to rotor acceleration

since it has no effect on the normalized displacement envelopes.[3] The results shown in Fig. 3 indicate, however, that this magnitude will play a very important role in the analysis of the present model.

Under dynamic conditions the bearing oil film behaves as a dashpot system. By employing a conventional linear analysis[4] of the journal bearing, it can be shown that the oil-film "stiffness" and "damping" properties depend on the bearing geometry, the lubricant viscosity, the static load on the bearing and, most importantly, on the rotor speed. As a result of these dynamic properties, the oil-film plays a dominant role in attenuating or amplifying the excitation force due to the rotor unbalance. These effects are complex in nature, involving a great number of independent parameters, and their detailed discussion is beyond the scope of this paper.[5]

Figure 4 shows the relationship between displacement envelope and time for the model with: (1) journal bearing, and (2) rigid bearing. Except for parameters associated with the bearing, all other system parameters are identical for both cases. The supporting beam and the rotor speed chosen for analysis give $\alpha = 1.2$. The rotor acceleration time is set so that the service speed is reached at nondimensional time equal to 20.0, ($\beta = 20.0$). The curve indicates the same general character of the system response regardless of the bearing model. However, magnitudes of the maximum amplitude of vibration and levels of envelope oscillation differ considerably. Since the absolute value of the rotor unbalance is identical for both models, it is concluded that the force due to the rotor unbalance is magnified when transmitted to foundation through an oil-film bearing. It is also noted that the peak-to-peak amplitude of the envelope oscillation, after the rotor speed has stabilized at the operating level, is almost the same for both cases. This suggests the transmissibility of the journal bearing at the rotor operating speed is close to 1.0 in this case and, consequently, that the force magnification occurs during the transient period.

Figure 5 shows transient orbits of the journal center as they

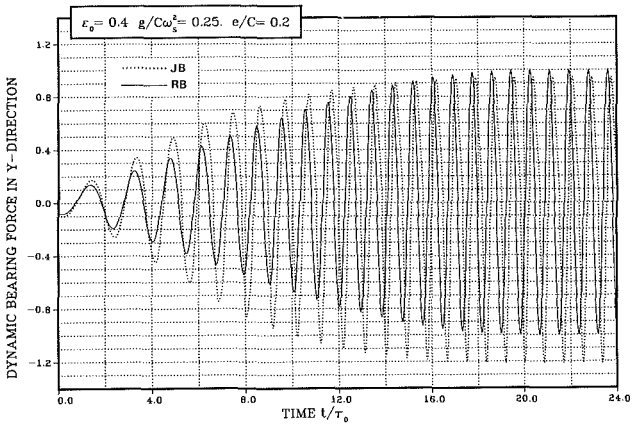

Fig. 6 Comparison of dynamic bearing force for: journal bearing (JB), and rigid bearing (RB)

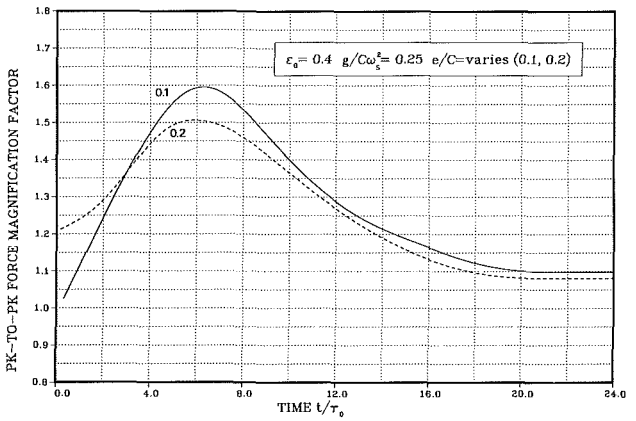

Fig. 7 Effect of rotor unbalance on oil-film force magnification factor

change with rotor velocity coming up from the initial to the operating speed. High rotor acceleration rate at the beginning of the motion causes rapid increase in the rotor speed and, accordingly, fast growth of the orbit amplitude. With the steadily decreasing acceleration rate these changes become smaller for each consecutive cycle of journal motion and, eventually, the journal center describes the steady-state orbit. From the remarks made earlier, it follows that the dynamic bearing force, the oil-film flexibility and damping have to change accordingly.

For the particular case studied, the change of bearing dynamic forces with time is depicted in Fig. 6. These forces are normalized with respect to the same value, $m_r e\omega_s^2$. Both nonlinearity of the oil-film force, and the change of transmissibility with time is observed. To better visualize the dynamic transmissibility of the oil-film, a force magnification factor is defined as a peak-to-peak magnitude ratio of a journal bearing force to a rigid bearing force. This magnification factor versus time, for $e/C = 0.1$ and 0.2, is plotted in Fig. 7. The relationship manifests full agreement with the conclusions drawn from the analysis of the system response presented in Fig. 4. A fifty percent magnification (for $e/C = 0.2$) is observed during the acceleration which decreases to about eight percent when a steady-state is obtained. The results demonstrate that for a given rotor-bearing system parameters the oil-film transmissibility depends not only on the rotor instantaneous speed but also on the rotor unbalance.

The effect of structural damping on the system response is demonstrated in Fig. 4. The displacement envelopes for the model with the journal bearing and that of rigid bearing are compared for the ideal and damped systems. It is noted that

[3] Note that the displacement envelopes are normalized with respect to static deflections due to centrifugal force $m_r e\omega_s^2$.

[4] Linear analysis of the journal-bearing system is well documented. See, for example, Holmes (1960).

[5] An interested reader is referred to papers concerned with stability of the rotor-bearing system, e.g., Hahn (1975).

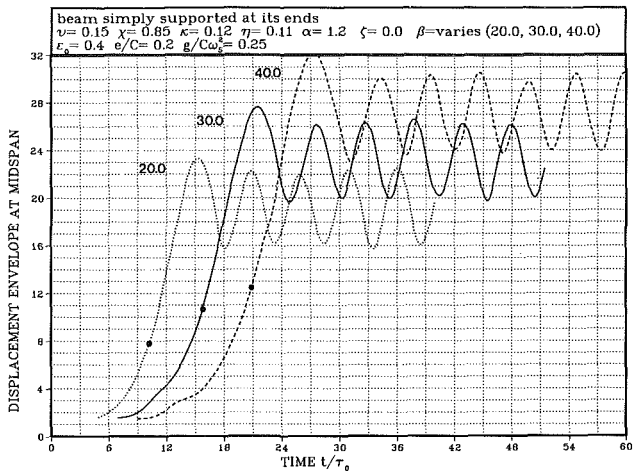

Fig. 8 Displacement envelope versus time for different values of rotor acceleration time parameter β

the levels of the damped transient envelope oscillation for both these models lie close to each other after operating speed is reached. This can be expected, since the oil-film force magnification factor is equal to ~ 1.08 after rotor speed has stabilized at its operating level, as shown in Fig. 7.

Figure 8 shows the results of the analysis carried out while varying acceleration time parameter β (β = 20.0, 30.0, 40.0) and keeping all other system parameters fixed. The time when the instantaneous rotor speed passes the first natural frequency of the support system is indicated on the curves by " ● ". The results illustrate that the maximum amplitude of vibration and its shift from the system critical frequency are both dependent on the rotor acceleration time, thus also on the rotor acceleration rate through the critical frequency. It is noted that the character of this relationship is similar to that of the rigid bearing model (Victor and Ellyin, 1981). This implies that the conclusions regarding the dependency of the system response on the rotor acceleration rate through the critical frequency and on the rotor operating speed are general, regardless of the type of bearing in the system.

The numerical analysis carried out so far dealt with the bearing-rotor system parameters typical of a relatively small turbogenerator. Larger units operate generally at lower speeds and with higher static loads on bearings. Both these parameters, as discussed before, have a fundamental effect on the dynamic performance of the journal bearing. Parametric studies were carried out for $\epsilon_0 = 0.7$ and $g/C\omega_s^2 = 1.0$, being typical of a medium-sized turbogenerator rotor (Holmes, 1970). It will suffice to mention that while the general character and trends in the system response remained the same, the nonlinear effects of journal bearing on the forcing function are more pronounced for this case. This is well illustrated by the transient journal orbits shown in Fig. 9. Considerable increase in a journal bearing force magnification (with respect to a rigid bearing) was observed, with its maximum being at the rotor operating speed, see Fig. 10.

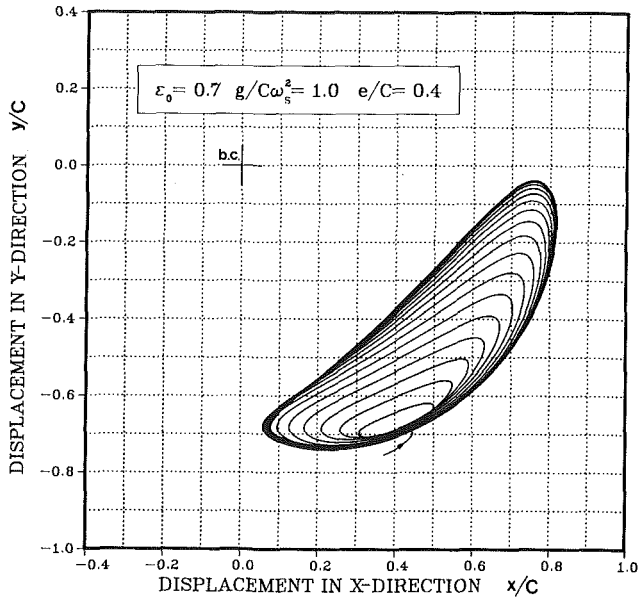

Fig. 9 Transient orbit of journal center due to rotor acceleration

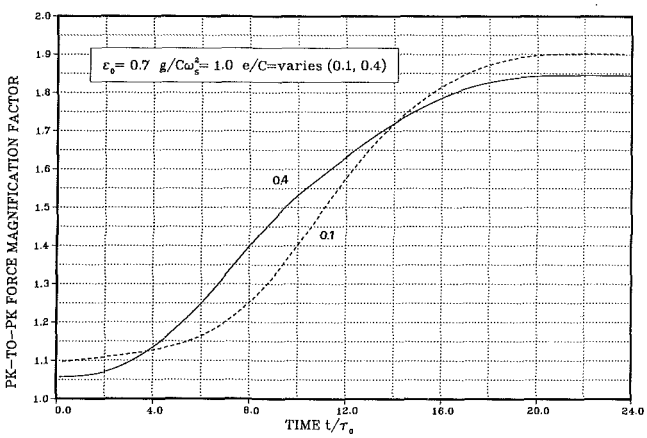

Fig. 10 Oil-film force magnification factor versus time

Conclusions

The following major conclusions are drawn from the results of the present analysis:

(1) The proposed method of solution for the transient response analysis of structures supporting rotating machinery is readily adaptable to complex models of the forcing function.

(2) The dynamic response of the system is highly dependent on the rotor-bearing system parameters.

(3) A generalization of the overall trends in the system response as a result of change in the system parameters, e.g., lubricant viscosity, static load, radial clearance, etc., is rather difficult due to a large number of independent parameters involved.

(4) Dynamic properties of a journal bearing depend on the region of bearing operation on design maps (ϵ_0, g/C_s^2) and they change during transient period with rotor speed.

(5) The magnitude of the rotor unbalance has a significant effect on the system response. This effect is dependent on a specific rotor-bearing system and varies with the instantaneous rotor speed.

(6) For any given system parameters, the dynamic response is dependent on the level of the rotor operating speed and its acceleration rate through the system critical frequency. All conclusions drawn from the previous study (rigid bearing), are general regardless of the type of bearing in the system.

To summarize, the two most important conclusions drawn from this study are: (*a*) the oil-film journal bearings have very significant and rather complex effects on the dynamic behavior of the system, and (*b*) the maximum amplitude of vibration of low-tuned structures supporting rotating machinery occurs during the transient period of the rotor speed build-up and is highly dependent on the rotor acceleration rate through the critical frequency of the support system. This maximum amplitude cannot be predicted by the classical steady-state analysis. Therefore, the transient response analysis, as the most inclusive approach to the system dynamic analysis, should be employed in the present-day design practices of low-tuned foundations.

Acknowledgment

The work presented is part of a general investigation in rotor dynamics and machine-foundation interaction. This research is supported, in part, by the Natural Sciences and Engineering Research Council of Canada (NSERC Grant No. A3808).

References

Addison, C. A., and Gladwell, I., 1984, "Second Derivative Methods Applied to Implicit First- and Second-Order Systems," *International Journal for Numerical Methods in Engineering*, Vol. 20, pp. 1211–1231.

Akella, S., and Craggs, A., 1982, "An Accurate Timoshenko Beam Element," Department of Mechanical Engineering Report No. 32, The University of Alberta, Edmonton.

Bathe, K. J., 1982, *Finite Element Procedures in Engineering Analysis*, Prentice-Hall, Englewood Cliffs, N.J., pp. 527–532.

Dubois, G. B., and Ocvirk, F. W., 1953, "Short Bearing Approximation for Full Journal Bearings," N.A.C.A. Report 1157.

Ellyin, F., 1982, "Dynamic Behavior and Design of Turbo-Generator Support System," *Proc. Seventh Machinery Dynamics Seminar*, National Research Council Canada, pp. 3.1–3.15.

Hahn, E. J., 1975, "The Excitability of Flexible Rotors in Short Sleeve Bearings," ASME *Journal of Lubrication Technology*, Vol. 97, pp. 105–115.

Holmes, R., 1960, "The Vibration of a Rigid Shaft on Short Sleeve Bearings," *Journal of Mechanical Engineering Science*, Vol. 2, No. 4, pp. 337–341.

Holmes, R., 1970, "Non-Linear Performance of Turbine Bearing," *Journal of Mechanical Engineering Science*, Vol. 12, No. 6, pp. 377–380.

Holmes, R., 1974, "Vibration and Its Control in Rotating Systems," *Dynamics of Rotors*, IUTAM Symposium, Springer-Verlag, Berlin, pp. 156–181.

Pinkus, O., and Sternlicht, B., 1961, *Theory of Hydrodynamic Lubrication*, McGraw-Hill, New York, pp. 48–49.

Victor, F., and Ellyin, F., 1981, "Acceleration of Unbalanced Rotor Through the Resonance of Supporting Structure," ASME JOURNAL OF APPLIED MECHANICS, Vol. 48, pp. 419–424.

W. Zhang
Associate Professor,
Department of Applied Mechanics,
Fudan University,
Shanghai, People's Republic of China
201 903

F. H. Ling
Professor,
Department of Engineering Mechanics,
Shanghai Jiao Tong University,
Shanghai, People's Republic of China
200 030

Dynamic Stability of the Rotating Shaft Made of Boltzmann Viscoelastic Solid[1]

A general theory is developed in this paper for studying the dynamic stability of high-speed nonuniform rotating shafts made of a Boltzmann viscoelastic solid. The equation of motion of the shaft is deduced. The stability criteria are derived by using this equation. The unstable regions for a nonhomogeneous viscoelastic shaft are worked out numerically. Analytical formulas are also given in this paper for determining the planar deflection of the shaft and its inclined angle due to a planar static load. The conclusions for special cases given in the literature known to the authors are all covered by the results in this paper.

1 Introduction

New materials are now widely used in industry. Many of them, such as plastics and composite materials, do not obey Hooke's law. Coleman and Noll (1960) proved that the simple isotropic material under small deformations can be modeled only by the integral or the differential type linear viscoelastic models. The one-dimensional constitutive equation of an integral type material (called Boltzmann material) is given by (Fung, 1965)

$$\sigma(t)=\int_{-\infty}^{t} K(t-\tau)\,\frac{d\epsilon}{d\tau}\,d\tau, \tag{1.1}$$

where K is the stress relaxation function of the material, and the differential type material (called Rivlin material) obeys the relation

$$\sum_{j=0}^{R}\alpha_j\frac{d^j\sigma}{dt^j}=\sum_{j=0}^{P}\beta_j\,\frac{d^j\epsilon}{dt^j}\quad(\beta_0\neq 0,\ \alpha_0=1). \tag{1.2}$$

While there is much research work on the strength and vibrations of the material obeying equations (1.1) or (1.2) (Flügge, 1975, Pipkin, 1972, and Timoshenko, 1955), only a few articles are available on the dynamic behavior of a high-speed rotating shaft made of viscoelastic material. However, some features of the motion of the high spinning viscoelastic shaft have been noticed for a long time. For instance, the deflection plane of a weighty viscoelastic shaft installed horizontally would deviate from the vertical plane when the shaft is spinning (Timoshenko, 1955). Another phenomenon which attracts attention among engineers consists in the dynamic instability of the viscoelastic shaft in certain rotation speed regions (Tondl, 1965, Torby, 1979, Ehrich, 1964, Huseyin, 1977, and Thomson et al., 1977). But so far the quantitative analysis of these phenomena are only limited to the simplest Voigt linear viscoelastic model and to the simple rotor system such as a Jeffcoat rotor and a uniform shaft. The main difficulty probably lies in setting up the general equation of motion for a complex viscoelastic rotor system. Thomson et al. (1977) tried to avoid this trouble and phrased the stability criterion from the energy viewpoint. But recently Bucciarelli (1982) pointed out that this result is wrong. Therefore, it is necessary to establish the equation of motion, and indeed, it is imperative to study the dynamic instability of a nonconservative system by using the equation of motion.

Recently, a general theory to treat the rotor system made of Voigt material or metal type viscoelastic materials was put forward (Zhang, 1984). But there are still quite a lot of rotor systems in practice which could not be modeled by the above two models. The high-speed spindle is a simple example. The spindle shaft is made of plastic, and the internal friction between cotton yarn must be considered too. So it is useful to set up a general theory based on the constitutive equations (1.1) or (1.2). This serves as the subject of our paper.

2 Equation of Motion

Let us introduce a fixed cooordinate system o-xyz, where the x axis is the undeformed neutral axis of the shaft. The deformed neutral axis is described by $y=y(x,t)$ and $z=z(x,t)$. In addition, introduce a local system c-y_1 z_1 on the cross-section normal to the deformed neutral axis, where c is the intersection of the neutral axis to the cross-section and the y_1 axis and z_1 axis are parallel to the y axis and z axis, respectively (Fig. 1).

The tensile strain of the longitudinal fibre at (y_1, z_1) is given by

$$\epsilon_x=-(y''y_1+z''z_1), \tag{2.1}$$

where the double primes denote second-order partial differentiation with respect to x.

[1]Projects supported by the Science Fund of the Chinese Academy of Sciences.
Contributed by the Applied Mechanics Division for presentation at the Winter Annual Meeting, Anaheim, CA, December 7-12, 1986, of The American Society of Mechanical Engineers.
Discussion on this paper should be addressed to the Editorial Department, ASME, United Engineering Center, 345 East 47th Street, New York, N.Y. 10017, and will be accepted until two months after final publication of the paper itself in the JOURNAL OF APPLIED MECHANICS. Manuscript received by ASME Applied Mechanics Division, January 23, 1985; final revision October 25, 1985. Paper No. 86-WA/APM-11.

Let Ω denote the rotating angular speed. We have

$$y_1 = r\cos\Omega t, \quad z_1 = r\sin\Omega t, \tag{2.2}$$

where r is the radial distance of the fibre from the origin c. Substituting equation (2.2) into (2.1), we obtain

$$\epsilon_x = -r(y''\cos\Omega t + z''\sin\Omega t), \tag{2.3}$$

Substituting equation (2.3) into (1.1) with some manipulations, we obtain the tensile stress of the fibre as

$$\begin{aligned}\sigma_x = &-\int_0^\infty K(\xi)[y''(x,\ t-\xi)+\Omega z''(x,\ t-\xi)]\\ &(y_1\cos\Omega\xi + z_1\sin\Omega\xi)d\xi\\ &-\int_0^\infty K(\xi)[z''(x,\ t-\xi)-\Omega y''(x,\ t-\xi)]\\ &(z_1\cos\Omega\xi - y_1\sin\Omega\xi)d\xi.\end{aligned}$$

Notice that

$$\int_A y_1\,dA = \int_A y_1 z_1\,dA = \int_A z_1\,dA = 0,$$

Thus we find that the resultant moment generated by σ_x over the whole cross-section has its components in the y and z directions, respectively, as

$$\begin{aligned}M_z = -\int_A \sigma_x y_1\,dA &= I(x)\int_0^\infty K(\xi)[\dot y''(x,\ t-\xi)\\ &\quad +\Omega z''(x,\ t-\xi)]\cos\Omega\xi\,d\xi\\ &\quad -I(x)\int_0^\infty K(\xi)[\dot z''(x,\ t-\xi)\\ &\quad -\Omega y''(x,\ t-\xi)]\sin\Omega\xi\,d\xi,\\ M_y = \int_A \sigma_x z_1\,dA &= -I(x)\int_0^\infty K(\xi)[\dot y''(x,\ t-\xi)\\ &\quad +\Omega z''(x,\ t-\xi)]\sin\Omega\xi\,d\xi\\ &\quad -I(x)\int_0^\infty K(\xi)[\dot z''(x,\ t-\xi)\\ &\quad -\Omega y''(x,\ t-\xi)]\cos\Omega\xi\,d\xi,\end{aligned} \tag{2.4}$$

where $I(x)$ is the moment of inertia of the cross-section.

Let $m(x)$, $c(x)$, $f_y(x)$ and $f_z(x)$ denote, respectively, the mass per unit length, the external damping coefficient per unit length, and the external load distribution along the y and z directions. We then have

$$\begin{aligned}M_z'' &= -m\ddot y - c\dot y + f_y,\\ M_y'' &= m\ddot z + c\dot z - f_z.\end{aligned} \tag{2.5}$$

Substituting equation (2.4) into (2.5) and defining the complex deflection, complex bending moment, complex shear force, and complex external force, respectively, as

$$\begin{aligned}q &= y + iz, \quad M = M_z - iM_y,\\ Q &= Q_y + iQ_z, \quad F = f_y + if_z,\end{aligned} \tag{2.6}$$

we obtain

$$\left\{I(x)\int_0^\infty K(\xi)e^{i\Omega\xi}[\dot q''(x,\ t-\xi) - i\Omega q''(x,\ t-\xi)]d\xi\right\}'' + m\ddot q + c\dot q = F \tag{2.7}$$

and

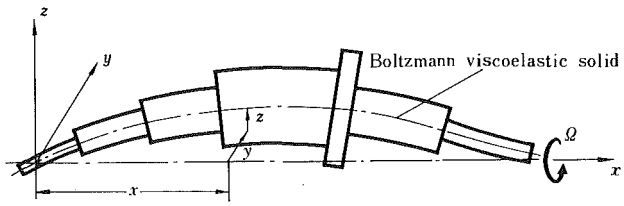

(a)

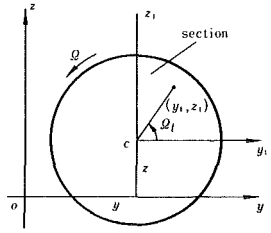

(b)

Fig. 1 The coordinate systems

$$\begin{aligned}M &= I(x)\int_0^\infty K(\xi)e^{i\Omega\xi}[\dot q''(x,\ t-\xi) - i\Omega q''(x,\ t-\xi)]d\xi,\\ Q &= \left\{I(x)\int_0^\infty K(\xi)e^{i\Omega\xi}[\dot q''(x,\ t-\xi) - i\Omega q''(x,\ t-\xi)]d\xi\right\}'.\end{aligned} \tag{2.8}$$

Equation (2.7) is the equation of motion for a nonuniform rotating shaft made of a Boltzmann viscoelastic solid.

3 Eigensolutions of the Equation of Motion

Assume that there are no external forces, i.e., $F=0$, and let $q=\tilde q(x)e^{\lambda t}$. Equations (2.7) and (2.8) are reduced to

$$(\lambda - i\Omega)\bar K(\lambda - i\Omega)(I\tilde q'')'' + (m\lambda^2 + c\lambda)\tilde q = 0 \tag{3.1}$$

$$\begin{aligned}M &= (\lambda - i\Omega)\bar K(\lambda - i\Omega)I\tilde q''e^{\lambda t},\\ Q &= (\lambda - i\Omega)\bar K(\lambda - i\Omega)(I\tilde q'')'e^{\lambda t},\end{aligned} \tag{3.2}$$

where $\bar K(s)$ is the Laplace transformation of $K(t)$,

$$\bar K(s) = \int_0^\infty K(\tau)e^{-s\tau}d\tau.$$

It is remarkable that equation (3.1) is also applicable to the differential type material (equation (1.2)) provided that the expression of K is available.

The usual boundary conditions for the complex displacement $\tilde q(x)$ are as follows:

$$\begin{aligned}&\text{The deflection at } x_0 \quad \tilde q|_{x_0} = 0\\ &\text{The slope at } x_0 \quad \tilde q'|_{x_0} = 0\\ &\text{The moment at } x_0 \quad \tilde q''|_{x_0} = 0\\ &\text{The shear force at } x_0 \quad (I\tilde q'')'|_{x_0} = 0\end{aligned} \tag{3.3}$$

If the shaft is made of a Hookean material, $\bar K(s) = E/S$, and no external damping exists, i.e., $c=0$, equation (3.1) is then reduced further (by taking $\lambda = i\omega$) to the following well-known free vibration equation of motion for an elastic shaft:

$$(EI\tilde q'')' - m\omega^2\tilde q = 0. \tag{3.4}$$

With the same boundary conditions as in the equation (3.1), the eigensolutions of equation (3.4) are denoted by ω_j and $q_j(x)$, which correspond to the jth critical speed and the jth whirling mode of this elastic shaft and we have the following orthogonality relations:

$$\int_0^1 EIq_j''q_k''dx=\omega_j{}^2\delta_{jk},\quad \int_0^1 mq_jq_kdx=\delta_{jk}. \tag{3.5}$$

Now let us expand the solution of equation (3.1), $\tilde{q}(x)$, in a series of $q_j(x)$:

$$\tilde{q}(x)=\sum_{k=1}^{\infty} a_kq_k(x), \tag{3.6}$$

where a_k are complex coefficients.

Substituting equation (3.6) into (3.1) and using equation (3.5), we have

$$\left[\frac{(\lambda-i\Omega)\bar{K}(\lambda-i\Omega)}{E}\omega_j^2 + \lambda^2\right]a_j+\lambda\sum_{k=1}^{\infty}c_{jk}a_k=0 \quad (j=1,\ 2,\ \ldots), \tag{3.7}$$

where

$$c_{jk}=\int_0^1 c(x)q_jq_kdx. \tag{3.8}$$

Now let us to solve the discrete eigenvalue problem (equation (3.7)) for two special cases.

(1) Rayleigh Proportional Damping. In this case

$$c_{jk}=c_{jj}\delta_{jk} \tag{3.9}$$

equation (3.7) is decoupled to

$$\begin{cases}\lambda^2+c_{jj}\lambda+\dfrac{(\lambda-i\Omega)\bar{K}(\lambda-i\Omega)}{E}\omega_j^2=0 \\ \qquad\qquad\qquad\qquad\qquad\qquad (j=1,\ 2,\ \ldots), \\ a_j=1,\quad a_k=0\quad (k\neq j).\end{cases} \tag{3.10}$$

The eigenvalues λ can be evaluated directly from equation (3.10). The corresponding eigenfunctions q_j are the same as those in equation (3.4).

(2) Small External and Internal Damping. In this case $\bar{K}(s)$ should be represented as

$$\bar{K}(s)=\frac{E}{S}+\bar{K}^*(s), \tag{3.11}$$

where $\bar{K}^*$ as well as c_{jk} is a small quantity. Most practical rotor systems have this property, so the perturbation method can be used. The perturbed solution of equation (3.7) may be written as

$$\begin{cases}\lambda=\omega_ji+\delta_j, \\ a_k=\delta_{jk}+(1-\delta_{jk})\Delta_{jk} \qquad (k=1,\ 2,\ \ldots),\end{cases} \tag{3.12}$$

where δ_j and Δ_{jk} are small quantities of the same order as $\bar{K}^*$ and c_{jk}. Substituting equation (3.12) into (3.7) and neglecting all the higher order terms, we have

$$\delta_j = -\frac{c_{jj}}{2}-\frac{\omega_j(\omega_j-\Omega)\bar{K}^*[(\omega_j-\Omega)i]}{2E}$$

$$\Delta_{jk} = i\frac{c_{jk}}{\omega_j^2-\omega_k^2}\omega_j\ (k\neq j).$$

The approximate eigensolutions of equation (3.7) are then obtained as

$$\begin{cases}\lambda_j=\omega_ji-\dfrac{c_{jj}}{2}-\dfrac{\omega_j(\omega_j-\Omega)\bar{K}^*[(\omega_j-\Omega)i]}{2E} \\ \qquad\qquad\qquad\qquad\qquad\qquad (j=1,2,\ \ldots). \\ \tilde{q}_j(x)=q_j(x)+i\displaystyle\sum_{k=1,k\neq j}^{\infty}\frac{c_{jk}\omega_j}{\omega_j^2-\omega_k^2}q_k(x)\end{cases} \tag{3.13}$$

4 Stability Criteria

According to the stability theory, the system is asymptotically stable if and only if the real parts of the eigenvalues of equation (3.7) are all negative. Furthermore, it is unstable if at least one of them is positive. The function $\bar{K}(s)$ usually takes the form of a rational fraction, so the characteristic equation (3.10) can be reduced to an algebraic equation of λ with real coefficients. By use of the Routh-Hurwitz criterion the stability of the system can be determined.

Let the characteristic equation be of the form

$$f(\lambda)=\lambda^n+a_1\lambda^{n-1}+a_2\lambda^{n-2}+\ \ldots\ +a_n=0, \tag{4.1}$$

the necessary and sufficient condition for $f(\lambda)$ to have the roots only with negative real parts is that all the principal minors $\Delta_i(i=1,2\ \ldots\ n)$ of the Hurwitz matrix

$$H=\begin{bmatrix} a_1 & 1 & 0 & 0 & \ldots & & 0 \\ a_3 & a_2 & a_1 & 1 & \ldots & & 0 \\ a_5 & a_4 & a_3 & a_2 & a_1 & 1\ \ldots & 0 \\ & & \ldots & & & & \\ \ldots & \ldots & \ldots & \ldots & \ldots & & a_n \end{bmatrix}$$

are positive, i.e.,

$$\Delta_1=a_1>0,\qquad \Delta_2=\begin{vmatrix} a_1 & 1 \\ a_3 & a_2 \end{vmatrix}>0,\ \ldots,$$
$$\Delta_n=a_n\Delta_{n-1}>0, \tag{4.3}$$

where $a_k=0$, if $k>n$.

For small external and internal damping, on the other hand, the eigenvalues may be given approximately by equation (3.13). In this case, the stability criterion is obtained directly as

$$c_{jj}+\frac{\omega_j(\omega_j-\Omega)}{E}R_e\bar{K}^*[(\omega_j-\Omega)i]>0 \quad (j=1,2,\ \ldots). \tag{4.4}$$

We consider now some typical viscoelastic materials.

(1) Voigt Model. This is the most frequently adopted viscoelastic model, for which

$$K(t)=E(H(t)+\mu\delta(t)),$$

where $H(t)$ is the unit step function and $\delta(t)$ is the unit impulse function. It is easily deduced that $\bar{K}(s)=E(1/s+\mu)$. Substituting it into equation (3.10), we have

$$\lambda^2+c_{jj}\lambda+(1+\mu\lambda)\omega_j^2=i\Omega\mu\omega_j^2\quad (j=1,2,\ \ldots).$$

Squaring both sides of this equation and making some rearrangements, we obtain

$$\lambda^4+2(c_{jj}+\mu\omega_j^2)\lambda^3+[(c_{jj}+\mu\omega_j^2)^2+2\omega_j^2]\lambda^2 + 2\omega_j^2(c_{jj}+\mu\omega_j^2)\lambda+\omega_j^4(1+\mu^2\Omega^2)=0.$$

Substituting it into equation (4.3), we obtain

$$\Delta_1 = 2(c_{jj}+\mu\omega_j^2),$$
$$\Delta_2 = 2(c_{jj}+\mu\omega_j^2)[(c_{jj}+\mu\omega_j^2)^2+\omega_j^2],$$
$$\Delta_3 = 4(c_{jj}+\mu\omega_j^2)^2\omega_j^2[(c_{jj}+\mu\omega_j^2)^2-\omega_j^2\Omega^2\mu^2],$$
$$\Delta_4 = \omega_j^2(1+\mu^2\Omega^2)\Delta_3.$$

Obviously, Δ_1 and Δ_2 are both always positive. From $\Delta_3 > 0$, we have

$$\Omega < \frac{c_{jj}}{\mu\omega_j} + \omega_j \quad (j = 1,2, \ldots),$$

or equivalently

$$\Omega < \Omega_0 = \min_j \left(\frac{c_{jj}}{\mu\omega_j} + \omega_j \right). \tag{4.5}$$

This is the stability criterion for a rotor system made of a Voigt solid under the Rayleigh proportional external damping. From equation (4.5) it is clear that there exists a maximum stable rotation speed Ω_0. If $\Omega > \Omega_0$, the system will be unstable and the excited whirling mode is q_j, where j is the subscript of the minimum term in equation (4.5). Obviously, Ω_0 is larger than the first critical speed ω_1 unless the external damping is zero. In the later case $\Omega_0 = \omega_1$, and the first mode is excited. Therefore, the external damping delays the instability.

If the Voigt solid is with small internal loss, $\mu \ll 1$, and hence $\bar{K}^* = E\mu$, then from equation (4.4) we have

$$c_{jj} + \omega_j(\omega_j - \Omega)\mu > 0 \quad (j = 1,2, \ldots),$$

i.e.,

$$\Omega < \frac{c_{jj}}{\mu\omega_j} + \omega_j \quad (j = 1,2, \ldots).$$

Therefore, the stability criterion (equation (4.5)) for a proportional external damping is also valid for a small external and internal damping.

It should be pointed out that the criterion (equation (4.5)) is not the most general stability criterion for a Voigt solid shaft because it is not proved yet to be suitable for the case of a nonproportional external damping or for the case of a large loss. Nevertheless, equation (4.5) is a quite general stability criterion applicable to the general nonuniform shaft. This criterion covers all the special results available in the literature (Timoshenko, 1955, Ehrich, 1964, Torby, 1979).

Example. A uniform Voigt solid shaft is simply supported at its two ends. It is well known that

$$\omega_j = j^2\omega_1, \quad \omega_1 = \frac{\pi^2}{1^2}\sqrt{\frac{EI}{m}}, \qquad (j = 1,2, \ldots, n)$$

$$q_j(x) = \sin\frac{j\pi x}{1}.$$

Substituting them into equation (4.5), we obtain

$$\Omega \le \min_j \left(j^2 + \frac{a}{j^2} \right)\omega_1, \tag{4.6}$$

where

$$a = \frac{c}{m\mu\omega_1^2}.$$

For a given value of a, the right-hand side of equation (4.6) is satisfied by $(j-1)^2\, j^2 < a \le j^2(j+1)^2$. So for $0 < a \le 4$, the instability occurs when $\Omega \ge (1+a)\omega_1$ and the first whirling mode $\sin \pi x/1$ is excited; for $4 \le a \le 36$, the instability occurs when $\Omega \ge (4 + a/4)\omega_1$ and the second mode $\sin 2\pi x/1$ is excited; for $36 \le a \le 144$, the instability occurs when $\Omega \ge (9 + a/9)\omega_1$ and the third mode is excited, and so on.

(2) Standard Linear Solid (Fung, 1965). In this model we have

$$K(t) = E_R\left[1 + \left(\frac{\tau_\sigma}{\tau_\epsilon} - 1\right)e^{\frac{t}{\tau_\epsilon}}\right]H(t),$$

where $\tau_\sigma > \tau_\epsilon$. If τ_σ and τ_ϵ are both very large, the solid approximates a Hookean material with small internal damping:

$$\bar{K}^*(s) \approx \frac{E}{s} - \frac{E_R(\tau_\sigma/\tau_\epsilon - 1)}{\tau_\epsilon s^2}$$

where

$$E = E_R\,\frac{\tau_\sigma}{\tau_\epsilon}.$$

Substituting it into equation (4.4), the stability criterion is given by

$$c_{jj} + \left(\frac{1}{\tau_\epsilon} - \frac{1}{\tau_\sigma}\right)\frac{\omega_j}{\omega_j - \Omega} > 0 \quad (j = 1,2, \ldots), \tag{4.7}$$

which is equivalent to

$$\begin{cases} \Omega < \omega_j \\ \Omega > \omega_j^* \end{cases} \quad (j = 1,2, \ldots),$$

where

$$\omega_j^* = \left[1 + \left(\frac{1}{\tau_\epsilon} - \frac{1}{\tau_\sigma}\right)\frac{1}{c_{jj}}\right]\omega_j \quad (j = 1,2, \ldots). \tag{4.8}$$

So the shaft will be stable provided that Ω satisfies following conditions:

$$\begin{cases} 0 < \Omega < \omega_1 \\ \omega_j^* < \Omega < \omega_{j+1} \end{cases} \qquad (j = 1,2, \ldots, n). \tag{4.9}$$

Obviously, the stable and unstable intervals appear alternatively until $\omega_n^* > \omega_{n+1}$. After that, the unstable regions will overlap each other and stable region fully disappears. This dynamic behavior is not exhibited for the Voigt solid shaft. For a uniform simply supported shaft, the integer n is determined as

$$n = \min_k \left\{ k, \left| \left(\frac{k+1}{k}\right)^2 < 1 + \frac{m}{c}\left(\frac{1}{\tau_\epsilon} - \frac{1}{\tau_\sigma}\right) \right\}. \tag{4.10}$$

(3) Differential Type Viscoelastic Material (Rivlin Solid). As already mentioned, its one-dimensional constitutive equation is (1.2). Assuming $\epsilon = H(t)$ and substituting it into equation (1.2), and taking the Laplace transformation for both sides, we obtain

$$\bar{K}(s) = \sum_{k=0}^{R} \beta_k s^k / s \sum_{k=0}^{P} \alpha_n s^k. \tag{4.11}$$

Substituting it into equation (3.10), we obtain the characteristic equation for proportional external damping:

$$(\lambda^2 + c_{jj}\lambda)\sum_{k=0}^{R} \alpha_k(\lambda - i\Omega)^k + \frac{\omega_j^2}{E}\sum_{k=0}^{P} \beta_k(\lambda - i\Omega)^k = 0. \tag{4.12}$$

For small internal loss, $\alpha_k (k = 1, \ldots, R)$ and $\beta_k (k = 1, \ldots, P)$ should be small quantities. So we have

$$\bar{K}^*(s) = \frac{\beta_0}{s}\sum_{k=1}^{\max(P,R)} \left(\frac{\beta_k}{\beta_0} - \alpha_k\right)s^k. \tag{4.13}$$

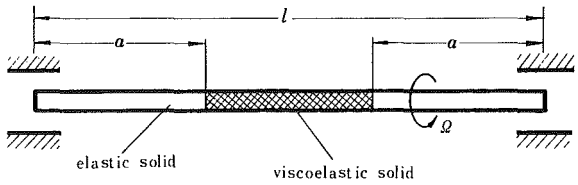

Fig. 2 A simply supported shaft partially made of viscoelastic solid.

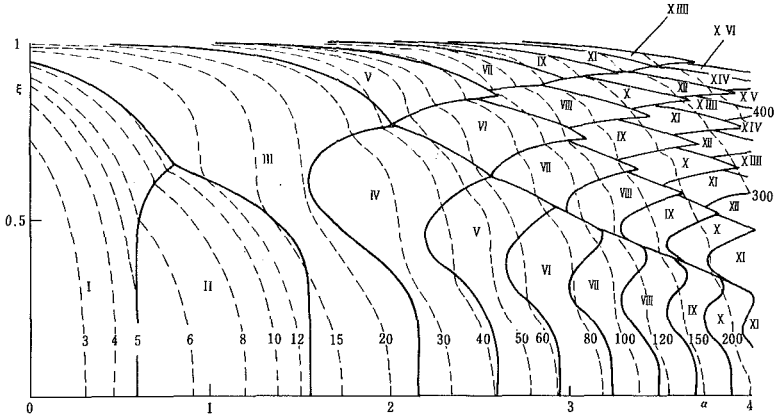

Fig. 3 The boundaries of excited whirling modes on α-ξ plane and its instability threshold speed of a simply supported shaft with its middle part consisting of a Voigt solid

Substituting equation (4.13) into (4.4), we obtain the stability criterion for this material

$$c_{jj}+\omega_j\sum_{k=odd}\left(\frac{\beta_k}{\beta_0}-\alpha_k\right)(\omega_j-\Omega)^k(-1)^{\frac{k-1}{2}}$$

$$>0\ (j=1,2,\ldots). \tag{4.14}$$

Example: Four-Parameter Solid (*Flügge, 1975*). This model is characterized by

$$\sigma+\alpha_1\dot{\sigma}=E\epsilon+\beta_1\dot{\epsilon}+\beta_2\ddot{\epsilon},$$

where

$$\beta_1{}^2>4E\beta_2,\ \beta_1-\alpha_1E>\frac{\beta_2}{\alpha_1}>0.$$

Substituting them into equation (4.14), we obtain

$$c_{jj}+\omega_j\left(\frac{\beta_1}{E}-\alpha_1\right)(\omega_j-\Omega)>0\ (j=1,2,\ldots).$$

Then the stability criterion is given by

$$\Omega<\min_j\left[\omega_j+\frac{c_{jj}}{\left(\frac{\beta_1}{E}-\alpha_1\right)\omega_j}\right]. \tag{4.15}$$

This criterion is similar to that for a Voigt solid, equation (4.5).

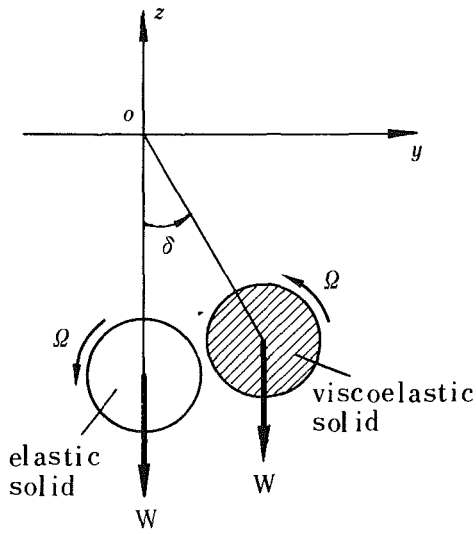

Fig. 4 The inclined angle δ

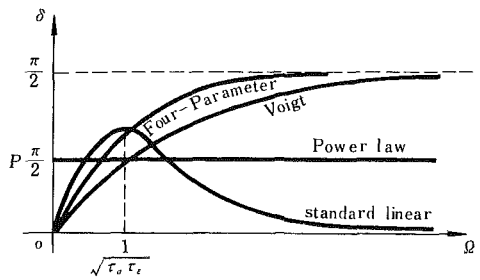

Fig. 5 The relations between δ and Ω for some viscoelastic materials

5 Nonhomogeneous Viscoelastic Shaft

For a nonhomogeneous viscoelastic shaft, we have

$$K=K(x,t)$$

equation (3.1) is altered to

$$(\lambda-i\Omega)[\bar{K}(x,\lambda-i\Omega)I\tilde{q}'']''+(m\lambda^2+c\lambda)\tilde{q}=0 \tag{5.1}$$

The equation of motion of the relevant elastic shaft is given by

$$(E(x)I\tilde{q}'')''-m(x)\omega^2\tilde{q}=0, \tag{5.2}$$

whose eigensolutions are still denoted by ω_j and $q_j(x)$.

Considering now only the material with small loss:

$$\bar{K}(x,s)=\frac{E(x)}{s}+\bar{K}^*(x,s), \tag{5.3}$$

we obtain the perturbed solution of (5.1) as follows:

$$\begin{cases}\lambda_j=i\omega_j-\dfrac{c_{jj}}{2}-\dfrac{\omega_j-\Omega}{2\omega_j}\mu_{jj}^*,\\[2ex] \tilde{q}_j(x)=q_j(x)+i\displaystyle\sum_{\substack{k=1\\k\neq j}}^{\infty}\frac{\omega_jc_{jk}+(\omega_j-\Omega)\mu_{jk}^*}{\omega_j^2-\omega_k^2}q_j(x)\end{cases} \tag{5.4}$$

where

$$c_{jk}=\int_0^1 c(x)q_jq_k\,dx, \tag{5.5}$$

$$\mu_{jk}^{*}=\int_0^1 q_j\{\bar{K}[x,(\omega_j-\Omega)i]Iq_j''\}''\,dx. \tag{5.6}$$

Then the stability criterion is given by

$$c_{jj}+\frac{\omega_j-\Omega}{\omega_j}\,\mathrm{Re}\mu_{jj}^{*}>0\ \ (j=1,2,\ldots). \tag{5.7}$$

Example: A Simply Supported Viscoelastic Shaft Whose Segment (a, 1-a), is made of Voigt Solid (Fig. 2). From equation (5.7), the stability range is given by

$$\frac{\Omega}{\omega_1}<\frac{\Omega_0}{\omega_1}=\min_j\left[j^2+\frac{\alpha}{j^2\left(1-\xi+\frac{1}{j\pi}\sin j\pi\xi\right)}\right] \tag{5.8}$$

where

$$\alpha=\frac{C}{m\mu\omega_1^2},\quad \xi=\frac{2a}{1}.$$

The solid lines in Fig. 3 are the boundaries of different excited whirling modes on the $\alpha-\xi$ parameter plane. And the dashed lines represent the isolines of the nondimensional instability threshold speed Ω_0/ω_1.

6 Planar Deflection and Inclined Angle of the Rotating Viscoelastic Shaft Due to a Planar Static Load

Assuming a static planar load $F(x)=f_z(x)i$, from equation (2.7) the static deflection q_0 of the viscoelastic shaft is governed by

$$(Iq_0'')''=-\frac{f_z}{\Omega}\,\frac{1}{\bar{K}(-i\Omega)}. \tag{6.1}$$

The deflection Z_0 of the relevant elastic shaft with the same boundary conditions should satisfy

$$(EIZ_0'')''=f_z. \tag{6.2}$$

By comparing these two equations, it is obvious that the solution q_0 of equation (6.1) takes the form

$$q_0(x)=y(x)+iz(x)=-\frac{E}{\Omega\bar{K}(-i\Omega)}\,Z_0(x),$$

or

$$\begin{cases} y(x)=-\dfrac{E}{\Omega}\,\mathrm{Re}\left[\dfrac{1}{\bar{K}(-i\Omega)}\right]Z_0(x), \\ z(x)=-\dfrac{E}{\Omega}\,Im\left[\dfrac{1}{\bar{K}(-i\Omega)}\right]Z_0(x). \end{cases} \tag{6.3}$$

The the inclined angle δ of the deflection plane of the shaft (see Fig. 4) is given by

$$\mathrm{tg}\delta=-\frac{y}{z}=\frac{\mathrm{Re}\bar{K}(-i\Omega)}{Im\bar{K}(-i\Omega)}. \tag{6.4}$$

Equation (6.4) is the general formula for the inclined angle δ under a static load.

For the Voigt shaft, $\mathrm{tg}\delta=\mu\Omega$. For the standard linear model,

$$\mathrm{tg}\delta=\frac{(\tau_\sigma-\tau_\epsilon)\Omega}{1+\tau_0\tau_\epsilon\Omega^2},$$

which reaches its maximum

$$\mathrm{tg}\delta_m=\frac{\tau_\sigma-\tau_\epsilon}{2\sqrt{\tau_\sigma\tau_\epsilon}}\ \text{ at }\ \Omega=\frac{1}{\sqrt{\tau_\sigma\tau_\epsilon}}.$$

For the power law viscoelastic solid (Pipkin, 1972), $\bar{K}(s)=as^{p-1}$. $\delta=\pi p/2$, which is independent of Ω. For the four-parameter solid,

$$\bar{K}(s)=\frac{E+\beta_1 s+\beta_2 s^2}{s(1+\alpha_1 s)},$$

we have

$$\mathrm{tg}\delta=\frac{\beta_1-\alpha_1 E+\alpha_1\beta_2\Omega^2}{E+(\alpha_1\beta_1-\beta_2)\Omega^2}\,\Omega$$

and it can be expanded to

$$\mathrm{tg}\delta\approx\left(\frac{\beta_1}{E}-\alpha_1\right)\left(1+\frac{\beta_2}{E}\,\Omega^2\right)\Omega$$

when α_1, β_1, and β_2 are all small.

From equation (6.4) we see that δ depends on the material and Ω, but not on the shape of the shaft. For various viscoelastic materials, the $\delta\sim\Omega$ relations are quite different (Fig. 5). This relation offers us an experimental method for selecting the viscoelastic model closest to the actual material by measuring the inclined angle of the deflection plane of the rotating shaft due to its own weight.

References

Bucciarelli, L. L., 1982, "On the Instability of Rotating Shafts Due to Internal Damping," ASME Journal of Applied Mechanics, Vol. 49, pp. 425–428.

Coleman, B. D., Noll, W., 1960, "An Approximation Theorem for Functionals With Application in Continuum Mechanics," *Archive for Rational Mechanics and Analysis*, Vol. 6, pp. 355–370.

Ehrich, F. F., 1964, "Shaft Whirl Induced by Rotor Internal Damping," ASME Journal of Applied Mechanics, Vol. 31, pp. 279–282.

Flügge, W., 1975, *Viscoelasticity*, Springer, New York, pp. 22, 95–120.

Fung, Y. C., 1965, *Foundations of Solid Mechanics*, Prentice-Hall, New Jersey, pp. 20–30.

Huseyin, K., 1977, "The Effect of Damping On the Flutter Boundary of Rotating Systems," *Vibration in Rotating Machinery*, Mechanical Engineering Publication, England, pp. 133–138.

Huseyin, K., 1978, *Vibration and Stability of Multiple Parameter Systems*, Noordhoff International Publishing, Netherlands, pp. 51–53.

Pipkin, A. C., 1972, *Lectures on Viscoelasticity Theory*, Springer-Verlag, New York, pp. 48–71.

Thomson, W. T., Younger, F. C., and Gordon, H. S., 1977, "Whirl Stability of the Pendulously Supported Flywheel System," ASME Journal of Applied Mechanics, Vol. 44, pp. 322–328.

Timoshenko, S., 1955, *Vibration Problems in Engineering*, D. Van Nostrand Company, New York, pp. 227–232.

Tondl, A., 1965, *Some Problems of Rotor Dynamics*, Publishing House of the Czechoslovak Academy of Sciences, Prague, pp. 17–69.

Torby, J., 1979, *"The Effect of Structural Damping Upon the Whirling of Rotors," ASME* Journal of Applied Mechanics, Vol. 46, pp. 469–470.

Zhang, Wen, 1984, "Dynamic Stability of Rotating Viscoelastic Shafts," (in Chinese), *Fudan Journal* (Natural Science), Vol. 23, pp. 425–433.

J. Brindley

L. Elliott

J. T. McKay

Department of Applied Mathematical Studies,
University of Leeds,
Leeds, LS2 9JT, England

Whirl Instabilities in Pressure Step Bearings

The effect on the stability of a dynamically loaded journal bearing of introducing a pressure step is examined by calculating numerically the whirl orbits described by the journal for a range of values of physical effects. In all full film cases the configuration is unstable in that the orbits spiral outwards to the bearing case; the tightness of the spiral is, however, much influenced by parameter values. The presence of appropriate cavitation permits a degree of stability, with the existence of stable whirl orbits. Cavity position and extent are vitally important to the stability characteristics, a result one would expect to be true of more realistic cavitation models than the single one used here.

1 Introduction

Instability of a plain journal bearing may often be avoided by changing the operating conditions, (i.e., varying the oil supply conditions, altering the running speed) but it is sometimes advantageous to operate with an alternatively designed bearing (e.g., elliptical or orthogonally displaced).

The effect on stability of grooving the bearing surface and hence creating a build up of pressure in the unloaded upper half of the bearing was discussed by Newkirk and Grobel [1]. Since then several investigations have been performed in order to determine the stability characteristics of bearings of various geometrical shapes. Pinkus [2] found that cylindrical bearings were the least stable, but that when they were externally pressurized this situation was reversed. Wilcock [3] concluded that orthogonally displaced bearings introduced a stiffness effect, while Akers and Cameron [4], using a finite difference model for the journal bearing with a stepped housing (i.e., a geometry with one or more "steps" on the bearing at which the gap changes discontinuously) were able to show and confirm experimentally that this modification enabled the rotational frequency to be more than doubled before whirling arose. Allaire [5] also examined the stability aspects of pressure step bearings, neglecting the inertia effects due to the step, but including those due to turbulence; he found that the step size and its position could greatly influence the bearing stability.

The majority of the above bearings have complicated geometries, hence the only avenue available to investigate their performances has been that of numerical modelling; although useful information is provided, the basic dynamics of the problem are often obscured by this approach. In the case of the stepped bearing, however, we expect the main dynamical consequence of the step to be a local steep azimuthal pressure gradient. The experiments of Constantinescu and Galeteuse [6], which explored the behavior of the pressure as a function of gap width ratio across the step, bear out our expectation; depending on the ratio, either rises or falls in pressure may occur.

In this paper we represent the steep pressure gradient, caused by the step, by a pressure *discontinuity* or jump from p_1 to p_2 at the position of the step ($\theta = \theta_1$), permitting the pressure to vary smoothly with azimuth elsewhere. We then ignore the step in a geometrical sense, and assume a smoothly varying gap width throughout the whole circumference of the bearing. This device enables us to proceed analytically and gain insight into the dynamics of the problem; at the same

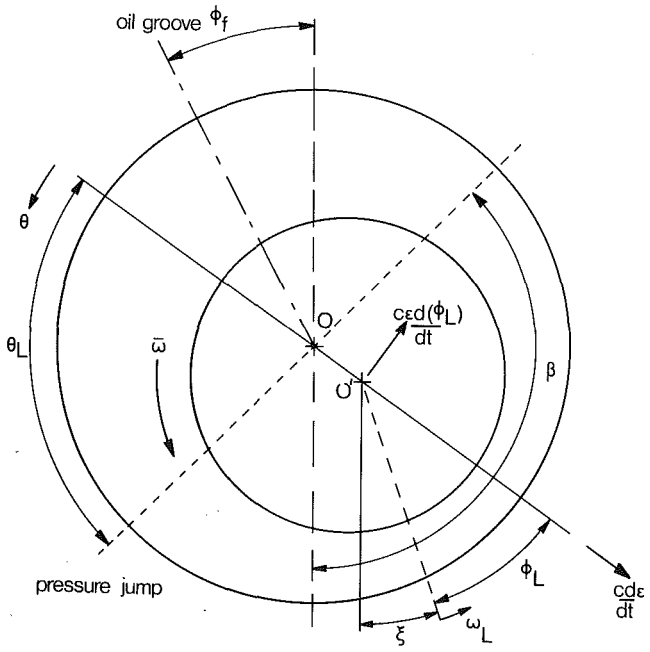

Fig. 1 Coordinate system used

Contributed by the Applied Mechanics Division for presentation at the Winter Annual Meeting, Anaheim, CA, December 7–12, 1986, of the American Society of Mechanical Engineers.

Discussion on this paper should be addressed to the Editorial Department, ASME, United Engineering Center, 345 East 47th Street, New York, N.Y. 10017, and will be accepted until two months after final publication of the paper itself in the JOURNAL OF APPLIED MECHANICS. Manuscript received by ASME Applied Mechanics Division, November 15, 1983; final revision October 23, 1984. Paper No. 86-WA/APM-3.

time the results of Constantinescu and Galateuse [6], and also those of Constantinescu [7] and Ruddy [8] give some credence to the model as representative of real bearings with one or more steps on the bearing case.

In practice, cavitation of some form usually arises, and this influences stability by introducing an asymmetry into the pressure distribution, which implies the existence of a radial "stiffness" in the equation of motion for the journal center. In this exploratory paper we consider a model in which cavitation is associated with an oil feed at angular position ϕ_f on bearing case; the size of cavity is determined by the region of subambient pressure (difficulties arise with the half film model since it requires $p(0)=p(\pi)=0$, in addition to the pressure jump condition.

For both the full and cavitated lubrication films, force expressions are derived from the calculated pressure distributions; on substitution into the dynamical equations of motion the whirl trajectories may be calculated for a variety of positions of oil groove, inlet pressure, Sommerfeld number, and normalized angular speed.

2 Pressure Distribution and Fluid Forces

For an infinitely long journal bearing (see Fig. 1), the pressure as shown by Brindley, Elliott, and McKay [9], is expressible as

$$\frac{d}{d\theta}\left(h^3\frac{dp}{d\theta}\right)=6\mu R^2\left[(\bar{\omega}-2\omega_L-2\frac{d\phi_L}{dt})\frac{dh}{d\theta}+2c\frac{d\epsilon}{dt}\cos\theta\right] \tag{2.1}$$

The long bearing approximation is not a true representation of what happens in reality, but it does lend itself to analysis which should show the trends in bearings of finite length. The pressure jump is built into the model via the boundary conditions

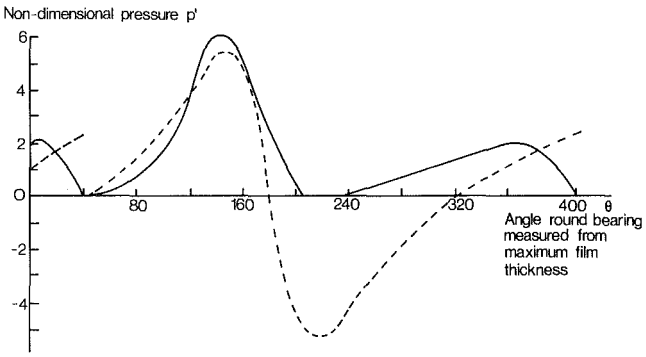

Fig. 2 Pressure distributions: dashed line denotes pressure given by equation (2.4); solid line is distribution found by Ruddy [8]

$$\begin{aligned} p&=p_1 \text{ at } \theta=\theta_1,\\ p&=p_2 \text{ at } \theta=2\pi+\theta_1, \end{aligned} \tag{2.2}$$

where θ_1 is the angle between the maximum film thickness and the pressure jump. (With $p_2>p_1$ a pressure drop occurs, while for $p_2<p_1$ a pressure rise is present.)

Applying the Sommerfeld transformation

$$(1+\epsilon\cos\theta)=\frac{1-\epsilon^2}{1-\epsilon\cos\phi} \tag{2.3}$$

to equation (2.1) enables the pressure distribution to be expressed as

$$p=\frac{6\mu R^2}{c^2}\left[(\bar{\omega}-2\omega_L-2\frac{d\phi_L}{dt})\left(\frac{\sin\phi_1-\sin\phi}{(1-\epsilon^2)^{3/2}}\right)\epsilon + \frac{1}{\epsilon}\frac{d\epsilon}{dt}\left[\left(\frac{1-\epsilon\cos\phi}{1-\epsilon^2}\right)^2-\left(\frac{1-\epsilon\cos\phi_1}{1-\epsilon^2}\right)^2\right]\right]$$

Nomenclature

$c=R_o-R$ = radial clearance
h = gap width
k = external stiffness of journal
p = dimensional pressure
p_f = inlet pressure at the oil groove
p_1 = pressure at $\theta=\theta_1$
p_2 = pressure at $\theta=\theta_2$
$p/(\mu R^2\bar{\omega}/c^2)$ = dimensionless pressure
$\Delta p=p_1-p_2$ = pressure jump due to step at $\theta=\theta_1$
$\Delta p^1=\Delta p/(\mu R^2\bar{\omega}/c^2)$ = dimensionless pressure jump
r = radial distance between centres of journal and bearing
t = time
$\beta=\theta_1+(\theta_L+\xi)$ = angle (anticlockwise) from upward vertical to pressure jump
ϵ = eccentricity ratio
ϵ_o = static eccentricity ratio
ξ = angle between vertical and rotating loadline
θ = polar angle
θ_f = position of the oil groove from line of maximum film thickness
θ_1 = position of pressure jump from line of maximum film thickness
ϕ = transformed coordinate using $1+\epsilon\cos\theta=\frac{1-\epsilon^2}{1-\epsilon\cos\phi}$
$\phi_f=\theta_f+(\theta_L+\xi)$ = position of the oil groove from upward vertical
ϕ_1 = position of pressure jump from maximum film thickness in the transformed coordinates
ϕ_L = attitude angle
ϕ_{L_o} = static attitude angle
μ = viscosity
$\omega_L=\frac{d\xi}{dt}$ = frequency of rotation of applied load
$\bar{\omega}$ = angular speed of journal
$\bar{\omega}_1=\bar{\omega}\left(\frac{2Mc}{W}\right)^{1/2}$ = normalized angular speed
D = journal diameter
(F_r,F_n) = radial and tangential force components exerted on the journal
L = bearing length
M = mass of journal
N = angular speed of journal
$P_w=\frac{W}{LD}$ = unit load
R = journal radius
R_o = bearing radius
$S=\frac{\mu N}{P_W}\left(\frac{D}{2c}\right)^2$ = Sommerfeld number
$T=t\left(\frac{W}{2Mc}\right)^{1/2}$ = normalized time
W = bearing load

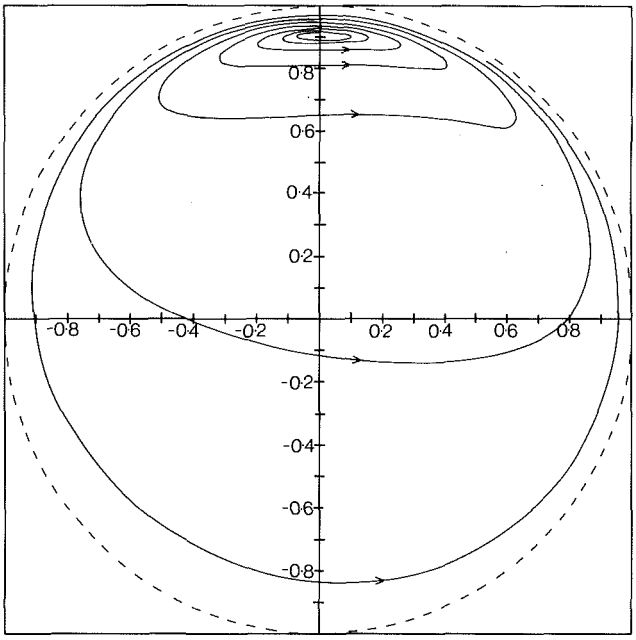

Fig. 3(*a*) $S = 0.01685$; $\bar{\omega}_1 = 1.6$; $\Delta p^1 = 5$

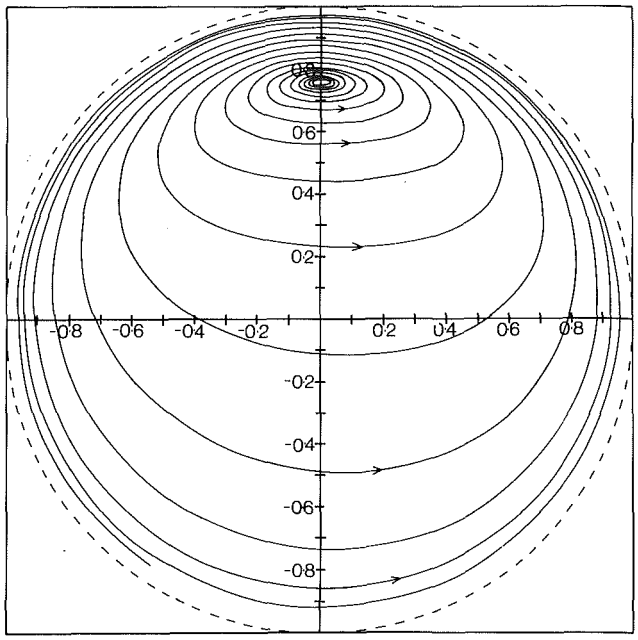

Fig. 4 $S = 0.0421$; $\bar{\omega}_1 = 1.6$; $\Delta p^1 = 5$

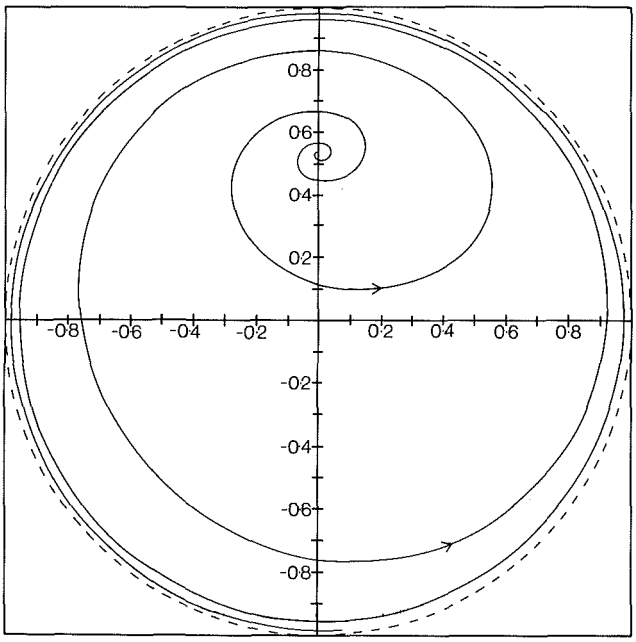

Fig. 3(*b*) $S = 0.01685$; $\bar{\omega}_1 = 1.6$; $\Delta p^1 = -5$

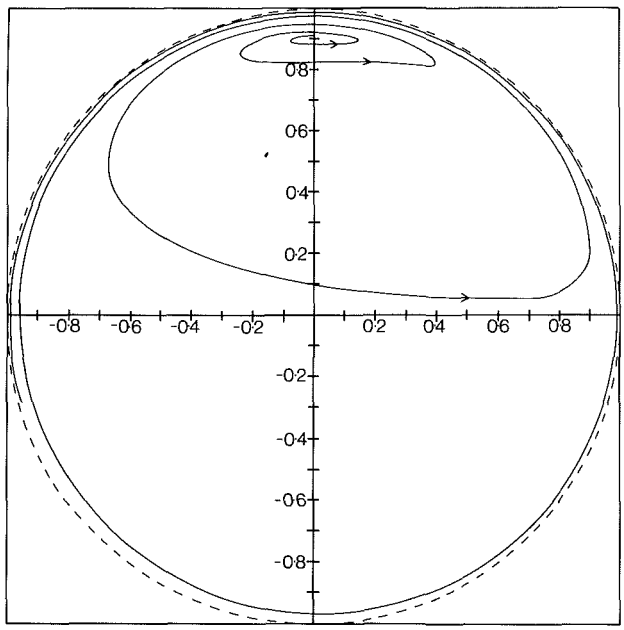

Fig. 5 $S = 0.01685$; $\bar{\omega}_1 = 2.5$; $\Delta p^1 = 5$

$$+\frac{\Delta p}{\pi(2+\epsilon^2)}\left[(\phi-\phi_1)\left(1+\frac{\epsilon^2}{2}\right)+2(\sin\phi_1-\sin\phi)\epsilon\right. \tag{2.4}$$

$$\left.+(\sin 2\phi-\sin 2\phi_1)\frac{\epsilon^2}{4}\right]-\frac{12\mu R^2}{c^2(2+\epsilon^2)(1+\epsilon^2)^{3/2}}$$

$$\left[\left(\bar{\omega}-2\omega_L-2\frac{d\phi_L}{dt}\right)(2(\sin\phi_1-\sin\phi)\epsilon+(\sin 2\phi\right.$$

$$\left.-\sin 2\phi_1)\frac{\epsilon^2}{4}\right)\Bigg]+p_1,$$

where $\Delta p = p_2 - p_1$ and ϕ_1 is the angle in the transformed coordinates corresponding to θ_1. As no directly equivalent pressure distributions are available from observation of real bearings, the results are compared with those from a numerical study of orthogonally displaced bearings by Ruddy [8], who assumed zero pressure at the displacement points with each half of the journal at its own equilibrium point. The present model used for comparison had a nondimensional pressure jump $\Delta p^1 = 2.23$ at an angle $\pi/4$ from the maximum film thickness (see Fig. 2). Both distributions possess (*i*) region of large positive pressure in the lower half of the bearing and (*ii*) rapid falls of pressure around the offset positions, even though the present model has only a single pressure discontinuity, compared with the two offset positions in Ruddy's model at which the pressure was assumed continuous and atmospheric. Further similarities between the two distributions are observed when the subambient pressure in the present model is set to atmospheric. (N. B. Ruddy's distribution itself is only a rough approximation to the real situation.)

Since an oil groove is present at ϕ_f, (Fig. 1), it is necessary to introduce this effect into expression (2.4). This is effected by evaluating the pressure at the groove, adjusting it to the

prescribed value p_f and then modifying the pressure appropriately throughout the bearing.

The fluid force components are calculated from

$$F_r = LR\int_{\text{FLUID}} p\cos\theta d\theta,\ F_n = LR\int_{\text{FLUID}} p\sin\theta d\theta. \tag{2.5}$$

Evaluation of the integrals, (assuming a full film), gives

$$F_r = \frac{12\pi\mu R^3 L}{c^2(1-\epsilon^2)^{3/2}}\frac{d\epsilon}{dt} + RL\Delta p\sin\theta_1,$$

$$F_n = \frac{12\pi\mu R^3 L}{c^2(2+\epsilon^2)(1-\epsilon^2)^{1/2}}\epsilon\left(\bar{\omega} - 2\omega_L - 2\frac{d\phi_L}{dt}\right) \tag{2.6}$$

$$- RL\Delta p\left(\cos\theta_1 + \frac{3\epsilon}{2+\epsilon^2}\right).$$

As the journal whirls, the pressure discontinuity remains fixed on the bearing case; hence θ_1 is replaced by

$$\theta_1 = \beta - (\phi_L + \xi), \tag{2.7}$$

where β is a constant angle measured anticlockwise from the upward vertical (see Fig. 1). To simplify the numerical calculations the following restrictions are imposed

(*i*) load direction fixed along downward vertical ($\xi = 0$),

(*ii*) pressure jump situated at $\beta = \pi/2$.

When required, cavitation zones were determined by the subambient pressure region, for which we adopted the simplest model of ambient pressure; other cavitation algorithms would merit inquiry. This approach provided an adequate description of the pressure distribution provided the pressure jump remained in the lubricant. Unfortunately, situations arose where this was not the case; in such circumstances the pressure distribution is identical to that occurring without a jump, and is available from expression (2.4), (with the appropriate modifications to bring both the pressure at the groove to p_f and that in the cavity to its ambient value). With the pressure distribution available irrespective of whether the jump is in the lubricant or the cavity the fluid force components may be calculated from expression (2.5). As the cavity size is continually changing, the pressure within this expression needs modifying as the jump is within the cavity or the lubricant.

It is impossible to present an analytic form for the force components, (regardless of whether cavitation is considered). Numerical integration techniques are, therefore, employed to evaluate F_r and F_n and the resulting answers substituted into the equations of motion to calculate the whirl trajectories.

3 Equations of Motion

The motion of the rotor, of mass M situated at O′ (Fig. 1), is related to a fixed inertial frame, whose origin coincides with the center of the bearing O. Then if the position of O′ relative to O is specified by polar coordinates (r, ϕ_L), we can write the equations of motion in radial and transverse directions as

$$\begin{aligned} M(\ddot{r} - r\dot{\phi}_L^2) &= F_r + W\cos\phi_L, \\ M(r\ddot{\phi}_L + 2\dot{r}\dot{\phi}_L) &= F_n - W\sin\phi_L, \end{aligned} \tag{3.1}$$

Thus, nondimensionalizing equations (2.1) by writing $r = c\epsilon$, together with

$$T = t\left(\frac{W}{2Mc}\right),\ \bar{\omega}_1 = \omega\left(\frac{2Mc}{W}\right)^{1/2} = 2\pi N\left(\frac{2Mc}{W}\right)^{1/2},$$

$$\Delta p^1 = \Delta p\left(\frac{\mu R^2\bar{\omega}}{c^2}\right), \tag{3.2}$$

substituting for F_r and F_n from (2.5), with Sommerfeld number

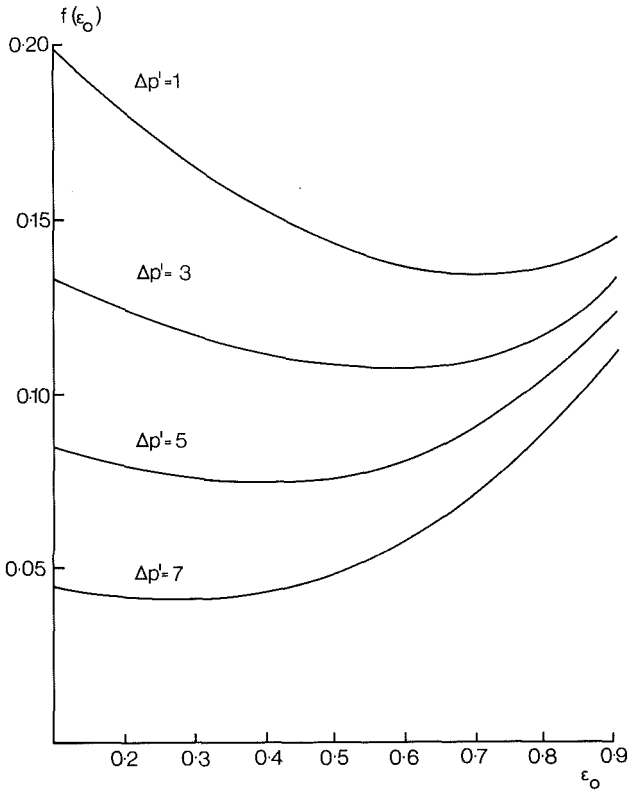

Fig. 6 Static equilibrium point v $f(\epsilon_o)$

$$S = \frac{\mu N}{P_w}\left(\frac{D}{2c}\right),\ \text{where } P_w = \frac{W}{LD},$$

we have

$$\ddot{\epsilon} - \epsilon\dot{\phi}_L^2 = \frac{-24\pi S\dot{\epsilon}}{\bar{\omega}_1(1-\epsilon^2)^{3/2}} + 2\cos\phi_L + 2\pi S\Delta p^1\cos\phi_L,$$

$$\epsilon\ddot{\phi}_L + 2\dot{\epsilon}\dot{\phi}_L = \frac{24\pi^2 S\epsilon}{(2+\epsilon^2)(1-\epsilon^2)^{1/2}}\left(1 - \frac{2}{\bar{\omega}_1}\dot{\phi}_L\right) - 2\sin\phi_L \tag{3.3}$$

$$- 2\pi S\Delta p^1\left(\sin\phi_L + \frac{3\epsilon}{2+\epsilon^2}\right).$$

At the static equilibrium point ϵ_o, ϕ_{L_o},

$$\dot{\epsilon} = \dot{\phi}_L = \ddot{\epsilon} = \ddot{\phi}_L = 0$$

hence

$$\frac{1}{12\pi}\left[\frac{1}{\pi S} + \Delta p^1\right] = \frac{\epsilon_o}{(2+\epsilon_o^2)(1-\epsilon_o^2)^{1/2}} - \frac{3\Delta p^1\epsilon_o}{12\pi(2+\epsilon_o^2)},$$

$$\phi_{L_o} = \frac{\pi}{2}. \tag{3.5}$$

4 Numerical Computation of Orbits

Numerical computations of the whirl orbits have been carried out for a number of pressure jumps, Sommerfeld numbers and normalized angular speeds, using an algorithm based on Krugh's variable order method. This method involves the reduction of the two second order differential equations (3.3) into four first order equations, from which we compute data for the whirl trajectories.

In the presence of cavitation the values of ϵ_o and ϕ_{L_o} referred to are those corresponding to a π-film situation in the absence of a pressure discontinuity. (These are preferred because of the closer similarity with a simple cavitated model then with a full film, where ϕ_{L_o} is always $\pi/2$.) Typical orbits are present in Figs. 3(*a*), 3(*b*), 4, and 5.

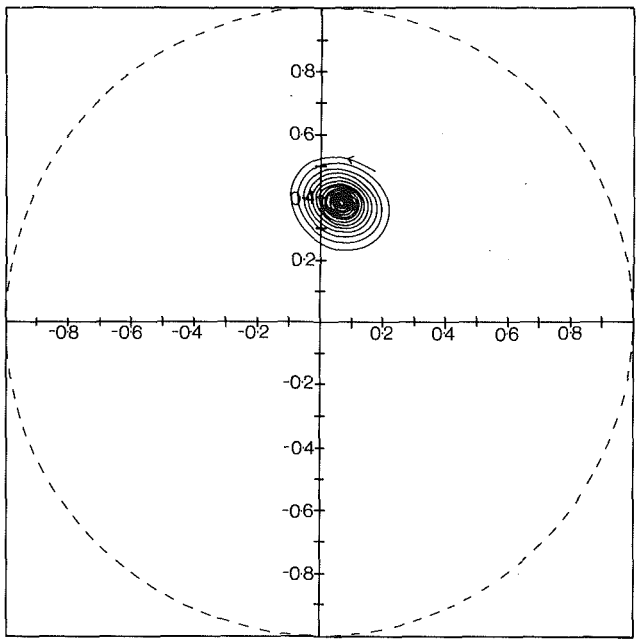

Fig. 7(*a*) $S = 0.06177$; $\bar{\omega}_1 = 2.5$; $\phi_f = 3\pi/2$; $\Delta p^1 = 0$

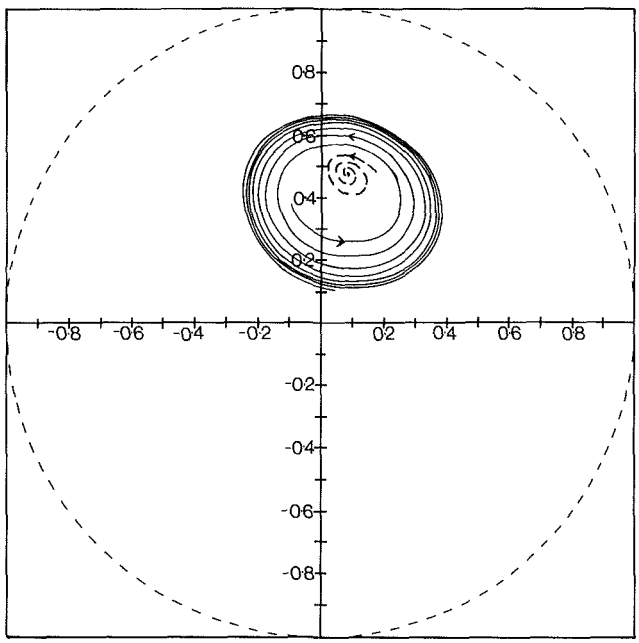

Fig. 7(*b*) $S = 0.06177$; $\bar{\omega}_1 = 2.5$; $\phi_f = 3\pi/2$; $\Delta p^1 = 1$, _____; $\Delta p^1 = 2$, — — —

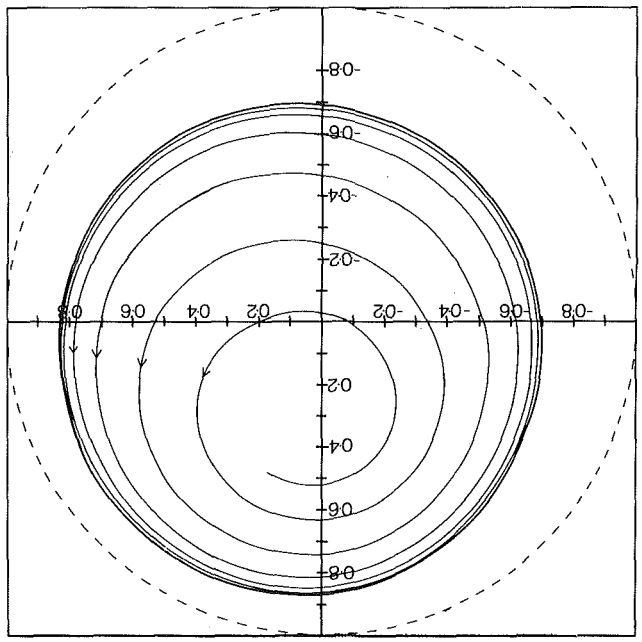

Fig. 8 $S = 0.06177$; $\bar{\omega}_1 = 2.5$; $\phi_f = \pi/6$; $\Delta p^1 = 0$. [NB. $\Delta p^1 = 0.5^1$ produces different initial trajectory but indentical final limit cycle.]

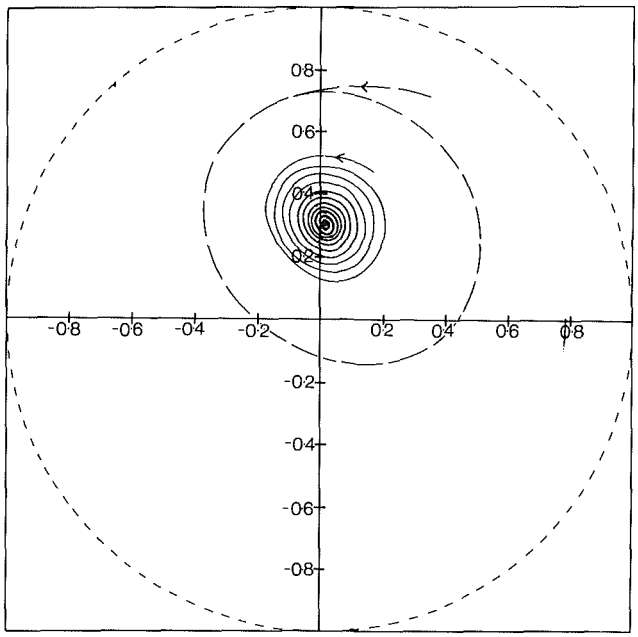

Fig. 9 $S = 0.06177$; $\bar{\omega}_1 = 2.5$; $\Delta p^1 = 0$; $\phi_f = 11\pi/24$, _____; $\phi_f = \pi/4$, — — —

(*a*) **Full film.** The most important result to emerge is that for all parameters tested the whirl trajectory spiralled to the bearing case and no closed orbit could be found. Other features may be summarized as follows:

(*i*) The larger the positive pressure jump the greater the number of loops around the static equilibrium point and the more their elongation in the direction of the load. (Figs. 3(*a*), 3(*b*).) N.B. via equation (3.5) it is easily seen that positive pressure jumps move static equilibrium points closer to the bearing case.

(*ii*) Increasing the Sommerfeld number indicates the number of loops around the static equilibrium point and their shape becomes more circular. (Figs. 3(*a*), 4.)

(*iii*) Increasing $\bar{\omega}_1$ results in fewer loops around the static equilibrium point. (Figs. 3(*a*), 5.)

(*iv*) Whirl speed approaches half shaft speed as the journal nears the bearing case.

A linear stability analysis similar to that developed by Holmes [10] substantiated the fact that closed orbits were impossible, but produced the stability criterion

$$\frac{k}{M\bar{\omega}^2} > f(\epsilon_o) = \left[\frac{12\pi(1-\epsilon_o^2)^{1/2} - 3\Delta p^1(1-\epsilon_o^2)^2}{288\pi^2(2+\epsilon_o^2)}\right] \times \left[\frac{12\pi(2-\epsilon_o^2+2\epsilon_o^4) - 3\Delta p^1(2-\epsilon_o^2)(1-\epsilon_o^2)^{3/2}}{(2+\epsilon_o^2)(1-\epsilon_o^2)^{3/2}}\right] \tag{4.1}$$

when applied to the more realistic model involving some form

of external stiffness, represented by k. Graphical representation of the right-hand side of the above inequality is shown in Fig. 6. This reinforces the idea that increasing Δp^1, which in turn increases the number of loops around the equilibrium point, produces a less unstable situation since it appears that a smaller value of the stiffness parameter is required to produce a stable situation. To find the modification in stiffness required to stabilize the journal after a given change in Δp^1 it is necessary not only to utilize Fig. 6 but also to adjust the value of the ϵ_o, which for fixed Sommerfeld number changes with Δp^1 according to equation (3.5).

A phenomenon of particular interest is the elongation of trajectories and eventual formation of crescent shape loops for increases in the magnitude of the positive pressure jump, a feature predicted by analysis for a massless rotor (unpublished). A similar pattern occurred in [9] and was noted by Mitchell, Holmes, and Byrne [11], when the Sommerfeld number was decreased. A possible explanation of these crescent shaped trajectories is to be found in Brindley, Elliott, and McKay [12], where graphs of F_r and F_n indicate $F_r << F_n$ and that both increase rapidly as ϵ_o approaches unity. This suggests that small disturbances of the rotor from its equilibrium position will produce increasingly large unbalanced contributions from F_n the closer ϵ_o is to unity, with the result that the rotor will be displaced further towards the bearing wall in the direction of the load.

So it would appear that the inclusion of a positive pressure jump has an effect similar to that of a decrease in Sommerfeld number; however, this is obviously not the complete answer as increasing Δp^1 produces more loops around the static equilibrium position whereas decreasing the Sommerfeld number for a plain journal bearing decreases this number. Hence the effect of increasing Δp^1 appears to be more akin to a combination of decreasing *both S and* $\bar{\omega}_1$.

(*b*) **Cavitation.** The main features are summarized as follows:

(*i*) The introduction of some form of cavitation in pressure jump bearings permits the existence of both stable, and unstable trajectories.

(*ii*) Two regions of stability are detected as in [9].

(*iii*) Variations in the sign and magnitude of the pressure discontinuity affect the stability borderlines, some jumps increasing, some decreasing the extent of the stable regions.

(*iv*) The introduction of a pressure discontinuity may produce limit cycles, or pole behavior different from that predicted with the jump absent. (Figs. 7(*a*), 7(*b*).)

(*v*) As in the plain journal model changes in Sommerfeld number for a fixed jump Δp^1 may result in a destabilization or a stabilization according to the groove position.

(*vi*) Increases in the value of the normalized speed $\bar{\omega}_1$ always destabilize the trajectories irrespective of groove position, Sommerfeld number and sign and magnitude of jump.

(*vii*) Changes in the supply pressure may for a fixed jump value either stabilize or destabilize compared with the no jump case, depending on groove position.

(*viii*) Increases in the magnitude of the jump or changes in its sign may either stabilize or destabilize according to position of groove. Figs. 7(*a*), 7(*b*).)

Result (*i*) taken in conjunction with the findings of the full film analysis (which show that irrespective of the sign or magnitude of Δp^1 no closed orbits exist) suggest that the influence of the pressure jump on stability is of a secondary importance compared with that exerted by the position of the groove and the cavitation zone it induces. (Figs. 8, 9).

5 Conclusion

In general the results are similar (but for slight modifications due to the pressure jump) to those in [9], involving highly complex relationships between all the parameters affecting stability; the only universal effect, regardless of the values of the other parameters, is the destabilization that occurs when the normalized angular speed is increased.

The effects produced by pressure discontinuity in a cavitated flow may be most easily understood by a comparison of the pressure distribution in the present situation with its corresponding form in the absence of a jump. It appears that the pressure discontinuity may slightly increase or decrease the size of the cavity, hence for those groove positions on the stability border it could provide the change in cavity size needed to stabilize or destabilize the resulting trajectory. However for those positions well removed from this critical region the perturbations to the size of cavity are insufficient to have any major effect on the trajectory (Fig. 8) and hence its form corresponds to that in the absence of a jump.

In summary, the results obtained indicate the great importance of cavity size and position in determining the stability characteristics of journal bearings. It seems appropriate to end with a plea that systematic laboratory experiments be undertaken to assess the degree of realism of the various cavitation models available. Other, more sophisticated models exist (see, e.g., Dowson and Taylor [13] which should be amenable to investigation along the lines followed here).

References

1 Newkirk, B. L., and Grobel, L. P., "Oil Film Whirl – A Nonwhirling Bearing," *Transactions ASME*, Vol. 56, No. 8, 1934, pp. 607–615.

2 Pinkus, O., "Experimental Investigation of Resonant Whip," *Transactions ASME*, Vol. 78, 1956, pp. 975–983.

3 Wilcock, D. F., "Orthogonally Displaced Bearing I," *Transactions ASLE*, Vol. 4, 1961, pp. 117–123.

4 Akers, A., and Cameron, A., "Use of Journal Bearing with Stepped Housings," *Proceedings of Tribology Convention* (*Institution of Mechanical Engineers*), 1971, pp. 9–17.

5 Allaire, P. E., "Design of Journal Bearings for High Speed Rotating Machinery," *Fundamentals of the Design of Fluid Film Bearings*, ASME, 1978, pp. 45–84.

6 Constantinescu, V. N., and Galateuse, S., "Pressure Drop Due to Inertia Forces in Step Bearings," ASME *Journal of Lubrication Technology*, Vol. 98 (i), 1976, pp. 167–174.

7 Constantinescu, V. N., "Special Problems Concerning Lubrication Phenomena at Large Reynolds Numbers," 2nd Leeds-Lyon Symposium, Superlaminar flow in bearings, Mechanical Engineering Publications Limited, London, New York, 1977, pp. 77–84.

8 Ruddy, A. V., "The Dynamics of Rotor Bearing Systems with Particular Reference to the Influence of Fluid Film Journal Bearings and the Modelling of Flexible Rotors," Ph.D. Thesis, Leeds University, England, 1979.

9 Brindley, J., Elliott, L., and McKay, J., "The Role of Cavitation in Whirl Instability in a Rotor Bearing," ASME JOURNAL OF APPLIED MECHANICS, Vol. 50 (iva), 1983, pp. 877–890.

10 Holmes, R., "Oil Whirl Characteristics of a Rigid Rotor in 360° Journal Bearings," *Proceedings of the Institution of Mechanical Engineers*, Vol. 177 (ii), 1963, pp. 291–307.

11 Mitchell, J. R., Holmes, R., and Byrne, J., "Oil Whirl of a Rigid Rotor in 360° Journal Bearings: Further Characteristics," *Proceedings of the Institution of Mechanical Engineers*," Vol. 180, 1966, pp. 593–610.

12 Brindley, J., Elliott, L., and McKay, J., "Flow in a Whirling Rotor Bearing," ASME JOURNAL OF APPLIED MECHANICS, Vol. 46 (iv), 1979, pp. 767–771.

13 Dowson, D., and Taylor, C. M., "Cavitation in Bearings," *Annual Review of Fluid Mechanics*, Vol. 11, 1979, pp. 35–66.

J. J. Blech
Faculty of Mechanical Engineering.

I. Green
Faculty of Mechanical Engineering.

J. Kopelman
Department of Food Engineering and Biotechnology.

Technion,
Israel Institute of Technology,
Haifa 32000, Israel

Transient Temperature Distribution in Partially Filled Rotating Horizontal Cylinders

The transient temperature distribution in an infinitely long horizontal rotating cylinder which is partially filled by a viscous fluid is calculated. Thermal boundary and initial conditions are such that the fluid starts from a uniform temperature, and that the outer boundary (cylinder surface) is isothermal at a different temperature. Nondimensional analysis shows that the problem can be fully described by a properly defined Fourier modulus and a normalized bubble eccentricity.

Introduction

The internal temperature distribution in a partially filled cylinder rotating about its axis and being exposed to an external heat source has several applications, one of those being in the food processing industry where liquid canned foods may be pasteurized while rotating horizontally and moved by some conveyor through a steam chamber. The liquids partially fill the can, and there exists a headspace with trapped air. During rotation of the can about its axis, the air bubble mixes the contents of the can, thus accelerating the heating process. In spite of the wide usage of induced convection heating in the food industry, the theoretical analysis of flow and heat, useful for a systematic design of sterilization processes, is quite limited (Lenz and Lund, 1978). Gavish et al. (1978) attacked the flow problem in the can, but due to the complexity of the problem they had to restrict their analysis to infinitely long cylinders with cylindrical bubbles, as opposed to the actual problem of finite cylinders with bubbles resembling an airfoil in their cross section. The purpose of this analysis is to extend the flow problem, which was attacked in Gavish et al. (1978), and determine the transient temperature field in this configuration.

Analysis

The incompressible viscous flow in a partially filled rotating horizontal cylinder was studied both experimentally and theoretically by Gavish et al. (1978). Here we propose to study the transient temperature distribution in that field under the assumption that both fields are decoupled.

Maintaining only convection-conduction terms in the energy equation leads to:

$$\frac{\partial T}{\partial t} + \mathrm{Pe}\vec{U}\cdot\nabla\bar{T} = \nabla^2 T \tag{1}$$

where T, $\vec{U}$, and α are the fluid temperature, velocity, and thermal diffusivity, respectively. Pe is the Peclet number, $r_2^2\Omega/\alpha$, with r_2 and Ω being the cylinder outer radius and its angular velocity, respectively.

A typical time scale is of order $0(r_2{}^2/\alpha)$. The Peclet number gives a measure of the ratio between typical times for convection and conduction. In the problem of our interest it turns out that Pe >> 1 (Pe$\sim 10^5$). Such a large Peclet number discards the possibility of solving equation (1) by an ordinary finite difference scheme since the norm of the grid must be 1/Pe approximately, making it necessary to work with enormously large matrices. We make use, therefore, of the Peclet number being so large by resorting to asymptotic approximations of equation (1).

The solution of the flow problem was given in Gavish et al. (1978), assuming two-dimensional creeping flow. (The variation of the Reynolds number, $\Omega r_1^2/\nu$, in the experiments was in the range 0.20–20.) It is most naturally expressed in Bipolar coordinates. For our purpose, however, there exists a more natural system of coordinates (r,s), r being perpendicular to streamlines and s measured along streamlines.

With respect to the transformations between the Cartesian and natural systems $x(r,s)$, $y(r,s)$, the heat transport equation (1) in the natural coordinate system is:

$$\frac{\partial T}{\partial t} + \mathrm{Pe}\,\frac{U(r,s)}{h_2(r,s)}\,\frac{\partial T}{\partial s} = \frac{1}{h_1 h_2}\left[\frac{\partial}{\partial r}\left(\frac{h_2}{h_1}\,\frac{\partial T}{\partial r}\right) + \frac{\partial}{\partial s}\left(\frac{h_1}{h_2}\,\frac{\partial T}{\partial s}\right)\right] \tag{2}$$

where h_1 and h_2 are the metrics of the transformation.

We expand the temperature in a series:

$$T = T_o + \frac{1}{\mathrm{Pe}}\,T_1 + \ldots . \tag{3}$$

Inserting the expansion into equation (2) and equating coefficients of like powers of Pe gives for the first order:

$$\frac{U}{h_2}\,\frac{\partial T_o}{\partial s} = 0;\quad \frac{\partial T_i}{\partial t} + \frac{U}{h_2}\,\frac{\partial T_{i+1}}{\partial s} = L[T_i];\quad i = 0,1,2,\ldots \tag{4}$$

From equation (4) we have:

$$T_o = T_o(r,t) \tag{5}$$

where L is the operator which acts on the right-hand side of equation (2). Integrating equation (4) along streamlines, for $i=0$, and noting that conduction times are much larger than convection times, we get:

Contributed by the Applied Mechanics Division for publication in the JOURNAL OF APPLIED MECHANICS.

Discussion on this paper should be addressed to the Editorial Department, ASME, United Engineering Center, 345 East 47th Street, New York, N.Y. 10017, and will be accepted until two months after final publication of the paper itself in the JOURNAL OF APPLIED MECHANICS. Manuscript received by ASME Applied Mechanics Division, December 11, 1984; final revision, October 9, 1985.

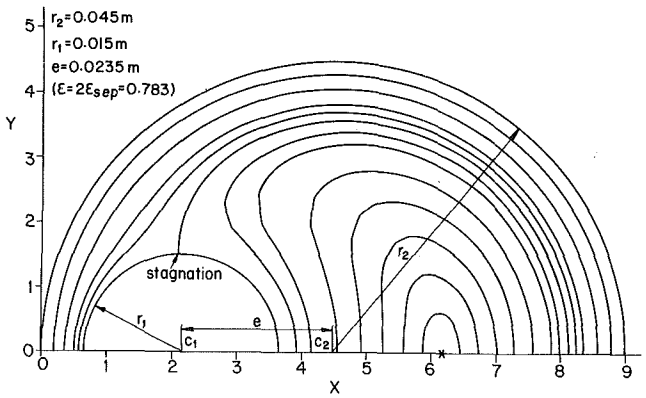

Fig. 1 Streamlines of the separated flow field for $r_1 = 0.015$ m, $r_2 = 0.045$ m, and $e = 0.0235$ m

$$\frac{\partial T_o}{\partial t} = \mu_2 \frac{\partial T_o}{\partial r} + \mu_3 \frac{\partial^2 T_o}{\partial r^2} \tag{6}$$

where:

$$\mu_2 = \frac{\gamma_2(r)}{\gamma_1(r)};\ \mu_3 = \frac{\gamma_3(r)}{\gamma_1(r)} \tag{7}$$

and

$$\gamma_1(r) = \int_\psi \frac{h_2}{U} d\sigma;\ \gamma_2(r) = \int_\psi \frac{1}{Uh_1} \frac{\partial}{\partial r}\left(\frac{h_2}{h_1}\right) d\sigma;$$

$$\gamma_3(r) = \int_\psi \frac{h_2}{Uh_1^2}\, d\sigma. \tag{8}$$

Equation (6) is the governing equation in the zeroth order temperature T_o. Its physical interpretation is intuitively clear. The temperature distribution T_o is identical to the temperature distribution in a layered solid, its layers being the streamlines. The thermal conductivity of this solid along streamlines is infinite, so that heat flows only in the r direction. The streamlines themselves are isotherms.

Numerical Formulation

The governing equation (6) is a time dependent partial differential equation in the natural coordinate r only. The complicated dependence of μ_2 and μ_3 on r requires that a numerical method of solution be used. The solution consists of two stages.

(*a*) Determination of the Flow Field. The flow field is evaluated by the equations given in Gavish et al. (1978). The simplifying assumptions which were made in Gavish et al. (1978) are summarized below: (*a*) the bubble remains continuous while the cylinder is rotated; (*b*) the cross-sectional shape of the bubble is circular; (*c*) the flow field inside the bubble is negligible, thus the shear stress on the interface is zero; (*d*) the flow is assumed to be a two-dimensional creeping flow. Therefore, the two-dimensional Stokes equations are solved for a bubble location which depends on the angular velocity of the can. At low rotating speeds, the bubble is set far apart from the can center, thus having a high eccentricity, ϵ. The eccentricity is defined by

$$\epsilon = \frac{e}{r_2 - r_1} \tag{9}$$

where e is the distance between the two centers. A typical description of such flow regimes is given in Fig. 1 (streamlines are separated similar to creeping flows around solid cylinders). As the speed increases, the bubble moves toward the can center thus attaining small eccentricities, as described, for example, in Fig. 2, where streamlines are not separated – all of them surround the bubble. Therefore, at small eccentricities, the fluid rotates on one region (see also Fig. 6(*a*) of Gavish et al., 1978). At high eccentricities, the passage between the bubble and the cylinder wall becomes narrow, not permitting all of the fluid to pass through it and thus the fluid engulfs the bubble, forming two rotational regions (see also Figs. 6(*b*), 6(*c*), and 6(*d*) of Gavish et al., 1978).

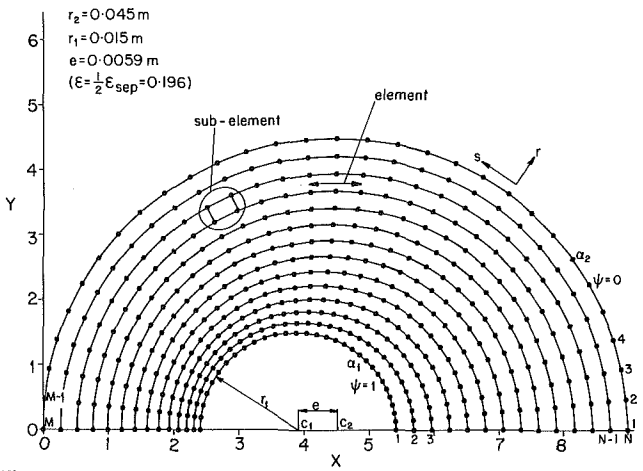

Fig. 2 Streamlines of the unseparated flow field for $r_1 = 0.015$ m, $r_2 = 0.045$ m, and $e = 0.0059$ m

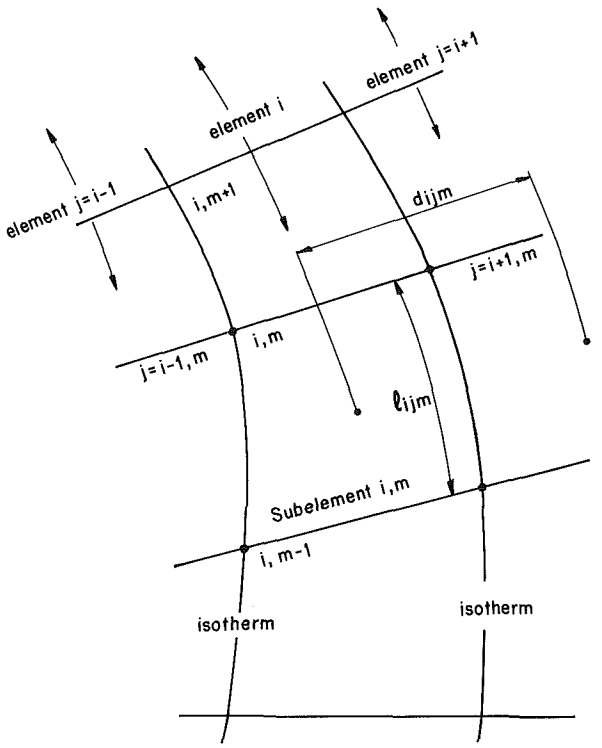

Fig. 3 Division and nomenclature of elements and subelements

(*b*) Determination of the Transient Temperature Field. To solve equation (6), a lumped parameters approach is taken, where an energy balance equation is written for each element i, which is bounded by two isotherms (streamlines). The resultant equation is

$$T_i^{p+1} = a_i \sum_j S_{ij} T_j^p + b_i T_i^p \tag{10}$$

For the determination of the transient temperature field, the radial and the azimuthal directions are divided into $N-1$ and $M-1$ intervals, respectively. Every four points construct a subelement, and every $M-1$ subelements in the s direction, tangent to streamlines, construct a layer, thus forming $N-1$ layers (elements) in the r direction (see Fig. 2).

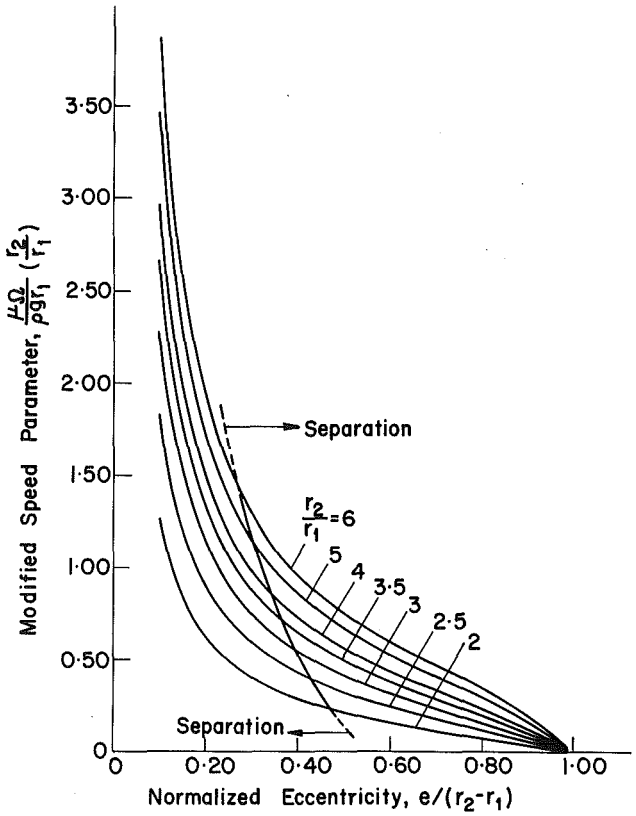

Fig. 4 Modified speed parameter versus the normalized eccentricity, ϵ, for various radii ratios, r_2/r_1

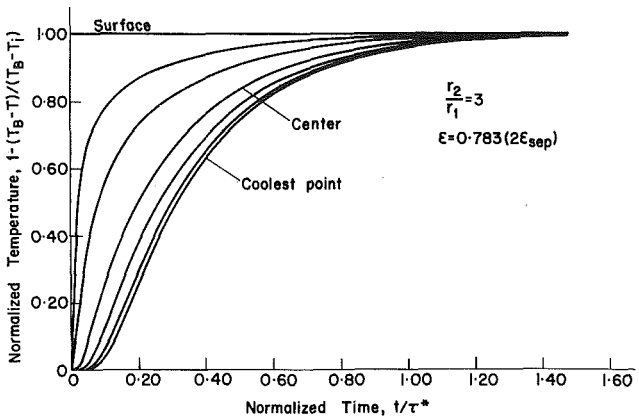

Fig. 5 Normalized temperature, θ, versus normalized time, τ, for different locations, at $r_2/r_1 = 3$, and $\epsilon = 2\epsilon_{sep}$

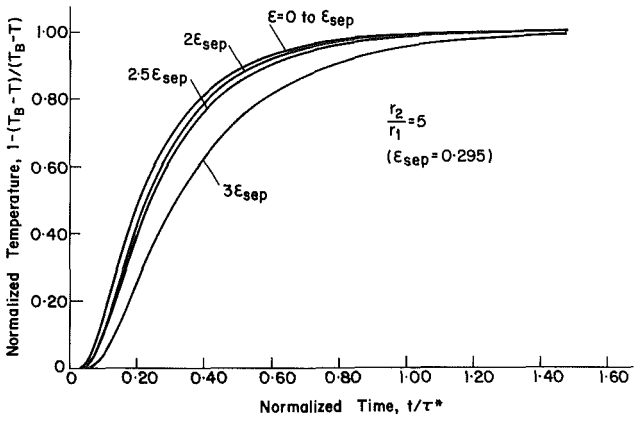

Fig. 6 Normalized temperature, θ, versus normalized time, τ, for various normalized eccentricities, ϵ, at $r_2/r_1 = 5$

where the subscripts on T locate the element and the superscripts refer to time, and

$$a_i = \frac{\Delta t}{C_i};\ b_i = 1 - \frac{\Delta t}{C_i}\sum_j S_{ij};\ C_i = \rho c_p \Delta A_i \tag{11}$$

ρ, c_p are the fluid mass density and specific heat, respectively. ΔA_i is the area of each element. S_{ij} is the so-called "shape factor" for two adjacent elements, i and j:

$$S_{ij} = k \sum_{m=1}^{M-1} \frac{l_{ijm}}{d_{ijm}} \tag{12}$$

where l_{ijm} is the common boundary length of two subelements m, located in two adjacent elements i and j (see Fig. 3), and d_{ijm} is the distance between the "centers" of these two subelements.

Numerical stability is guaranteed by requiring $b_i \geq 0$ (thermodynamic reasoning), hence,

$$\Delta t \leq \min\left(\frac{C_i}{\sum_j S_{ij}}\right)_i \quad i = 1,2,\ldots,N-1 \tag{13}$$

and time steps where chosen, accordingly, in the program. Based on the above formulation the computer program evaluates first the flow field and divides it into subelements and elements. The program distinguishes between the two flow regimes and identifies all the geometric variables. Then, the temperature in each layer (element) is determined at every time step, subjected to the boundary conditions, $T = T_B$ on the outer surface and $\partial T/\partial r = 0$ on the bubble surface. The initial condition for the entire field (excluding the outer boundary) is $T = T_i$.

To obtain a general solution it is necessary to state the problem in a dimensionless form. The governing dimensionless groups which were introduced in Gavish et al. (1978) were regrouped here for more convenience. Figure 4 gives the dependence between the normalized eccentricity, $e/(r_2 - r_1)$, and the modified speed parameter, $\mu\Omega(r_2/t_1)/\rho g r_1$, for different r_2/r_1 ratios. That figure also gives the eccentricity, ϵ_{sep}, at which separation takes place.

Similarity is also achieved in the temperature field. Let us introduce a time constant, τ^*, based on cylindrical heat transfer, by

$$\tau^* = \frac{r_2^2 - r_1^2}{2\alpha}\, \ell n\left(\frac{r_2}{r_1}\right) \tag{14}$$

Defining the Fourier modulus, Fo, by

$$\mathrm{Fo} = \frac{\alpha \tau^*}{{r_2}^2} \tag{15}$$

and substituting (14) in (15) yields:

$$F_0 = \frac{1}{2}\left[1 - \left(\frac{r_1}{r_2}\right)^2\right] \ell n\left(\frac{r_2}{r_1}\right) \tag{16}$$

Nondimensionalysing further, time, temperature, and the normal coordinate as follows:

$$\tau = \frac{t}{\tau^*};\ \theta = 1 - \frac{T_B - T}{T_B - T_i};\ R = \frac{r}{r_2} \tag{17}$$

and substituting the above relations in the unidirectional heat conduction equation, which applies here normal to streamlines, results in

$$\frac{\partial \theta}{\partial \tau} = \mathrm{Fo}\, \frac{\partial^2 \theta}{\partial R^2} \tag{18}$$

along with the boundary conditions

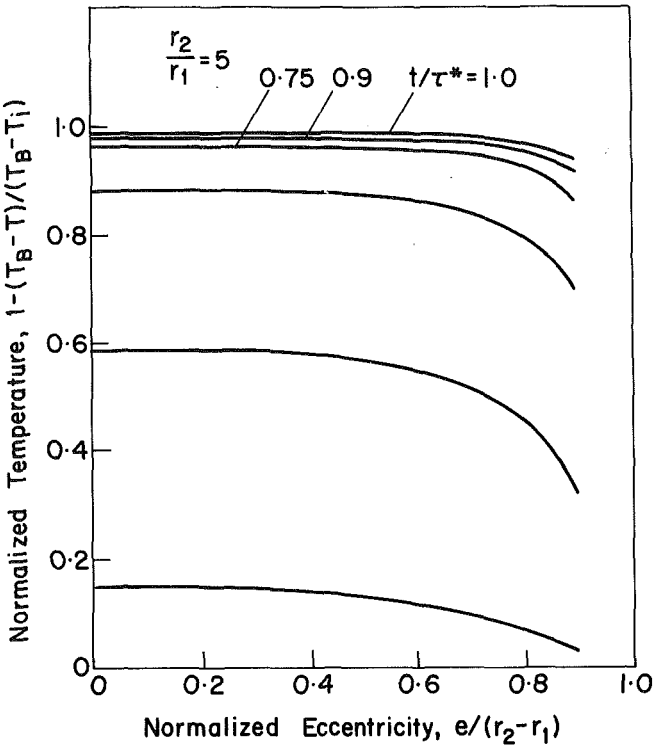

Fig. 7 Normalized temperature, θ, versus normalized eccentricity, ϵ, for various normalized times, τ, at $r_2/r_1=5$

$$\theta=1 \ @ \ \alpha=\alpha_2 \text{ (outer surface)}$$

$$\frac{\partial\theta}{\partial R}=0 \ @ \ \alpha=\alpha_1 \text{ (bubble surface)}$$

and the initial condition

$$\theta=0 \ @ \ \tau=0$$

Now, since the flow field is "similar" for the normalized geometric groups, $e/(r_2-r_1)$ and r_2/r_1, and the temperature field is also governed by the same groups according to equations (26) and (18), it is concluded that these groups preserve overall similarity.

Results and Discussion

The results appearing here were extracted from the computer program. Usually a mesh of $M=31$ by $N=14$ (as described in Fig. 2) gave good results at low and moderate eccentricities. The numerical solution for $\epsilon=0$ converged exactly to the analytical solution for two concentric cylinders (Ozisik, 1980). At higher eccentricity values, which cause a separated flow regime, a finer mesh was required because of the overcrowding of the streamlines at the left part of the horizontal diameter (see Fig. 1). At $\epsilon=0.95$ a mesh of $M=99$ and $N=91$ was needed for a correct computation and division of the flow field. But, such a fine mesh requires a very small time increment.

Before discussing the results, one should pay attention to the fact that the coolest point in the fluid is not at the center of the can. In the separated flow regimes the coolest temperature is at the point about which the separated flow rotates. In Fig. 1 this point is marked by an asterisk (*). In the unseparated flow regime the coolest temperature is always at the bubble. In Fig. 5 the transient temperature field is presented for the flow described in Fig. 1. It can be seen that there is a considerable difference between the temperatures of the center and the coolest point.

Figure 6 shows the effect of the bubble location on the coolest temperature point for radii ratio $r_2/r_1=5$. It can be seen from the figure that eccentricities ranging from zero (infinite rotating speed) up to ϵ_{sep}, result in the same normalized temperature, θ, as a function of normalized time, τ. Only a drastic increase of the eccentricity causes a lower temperature in the coolest point. This behavior is even more enhanced in the cross-plot shown in Fig. 7, where the normalized temperature is plotted versus the normalized eccentricity at prescribed normalized times. It is obvious that only high eccentricities (0.6 and above) have a pronounced effect on the coolest temperature. It is also clear that the case $\epsilon=0$ can serve as the upper bound for the temperature at various times.

It is noted that the results in Fig. 7 are presented only up to $\epsilon=0.9$. Analyzing high eccentricities is costly in computer time, as mentioned earlier, and results may turn out to be meaningless. This is mainly because of the limitation, of the solution given in Gavish et al. (1978), to predict correctly the flow field at high eccentricities, i.e., low rotating speeds. Another limitation of the present analysis is the assumption that the flow and temperature fields are decoupled. This is of course not so since the viscosity is drastically affected by temperature. However, this fact is not very restrictive since a time dependent viscosity results in a time dependent eccentricity. It has been shown, however, that the eccentricity has a weak effect on the temperature (unless the eccentricity reaches high values).

Consider the numerical examples presented in Figs. 1-7:

Outer radius, r_2, m	0.045
Bubble radius, r_1, m	0.009
Fluid viscosity, μ, mPa•s	10^3
Density, ρ, kg/m^3	900
Specific heat, c_p, kJ/kg•°C	2.0
Thermal conductivity, k, W/m•°C	0.15
Fourier modulus, Fo,	0.77
Time constant, τ^*, s	19555
Separation eccentricity, e,m,	0.0107
(Prandtl number, Pr, 13333)	

It can be seen in Fig. 7 that when $t/\tau^*=1$, the temperature at the coolest point is just a few percent lower than the surface temperature. Therefore, τ^*, is the time required to reach "almost" steady state.

Similar results, which are not presented here, were generated for the case $r_2/r_1=3$. The time constant for $r_2/r_1=3$ is about two thirds of that for $r_2/r_1=5$, thus requiring much less time to reach steady state.

Concluding Remarks

A numerical solution is given for the transient temperature distribution in a viscous fluid which fills partially an infinitely long horizontal rotating cylinder. It was found that the coolest temperature is not at the cylinder center, but depends on the flow regime. For unseparated flow it will be on the bubble surface. The bubble eccentricity does not affect considerably the temperature-time dependence. Only at high eccentricity ratios this eccentricity has a profound influence on the temperature – time dependence. The case of $\epsilon=0$ (no eccentricity, and thus infinitely high rotational speed) is an upper bound for the temperature-time curves.

The results of this analysis were useful in locating the coolest point in the experimental program. The times to reach steady state predicted by the analysis are much larger than those obtained by experiment. This is due to better mixing, which occurs in reality; the model used here is still far from reality, which is much more complex.

References

Gavish, J., Chadwick, R. S., and Gutfinger, C., 1978, "Viscous Flow in a Partially Filled Rotating Horizontal Cylinder," *Israel Journal of Technology*, Vol. 16, pp. 264-272.

Lenz, M. K., and Lund, D. B., 1978, "The Lethality Fourier Number-Method – Heating Rate Variation and Lethality Confidence Intervals for Forced Convection Heated Food in Containers," *Journal of Food Process Engineering*, Vol. 2, p. 227.

Ozisik, N. N., 1980, *Heat Conduction*, Wiley, New York.

Kuo-Kuang Chen
Mathematics Department.

D. C. Sun
Fluid Mechanics Department.
Mem. ASME

General Motors Research Laboratories,
Warren, Mich. 48090

Hydrodynamic Lubrication in Hemispherical Punch Stretch Forming

The existence and consequence of hydrodynamic lubrication in sheet metal forming is demonstrated using a model problem of hemispherical punch stretch forming. The problem is solved by incorporating a lubrication analysis into an incremental plasticity analysis. The sheet material is assumed to be elastic plastic with strain hardening, and the lubricant is assumed isoviscous. The study identifies two dimensionless parameters controlling the condition of lubrication. The resulting variable friction at the punch-sheet interface is found to affect significantly the distribution of strains in the sheet metal and its formability.

1 Introduction

Analysis of sheet metal forming (SMF) is best made with the incremental theory (Hill, 1950), which describes the path dependence of plastic deformation. Currently three problem areas confront the modeling work. These are modeling the sheet material, developing efficient computational methods, and modeling the punch-sheet interfacial friction. On the question of material modeling, elaborate yield criteria (Mendelson, 1968), strain hardening laws (Koiter, 1953; Drucker, 1951), and strain rate hardening laws (Cristescu, 1967) have been developed to describe the material behavior under large strain conditions. The mechanics of SMF is usually described by a variational principle written in rate form (Budiansky, 1968) and its equivalent finite element stiffness equations. To improve the efficiency of the incremental computation, advanced numerical methods (Cavendish et al., to appear) and better equation solvers (Arlinghaus et al., 1986) are being studied. On the question of modeling the interfacial friction, however, progress has been slow (Wilson, 1978). The current practice is to assume that Coulomb's law of friction applies, and to adopt a constant coefficient of friction over the contact region in such a way that the computed peak strains match the measured ones (Wang and Budiansky, 1978). But the distribution of strains is sensitive to the magnitude as well as the variation of the coefficient of friction over the contact region. Moreover, the distribution of strains has a profound implication on forming limits (Ghosh, 1978). Therefore, this simplistic treatment of the punch-sheet interfacial friction is inadequate in modeling SMF (Wilson, 1978).

The interfacial friction can be computed accurately if the contact region is lubricated hydrodynamically, i.e., a thin film of liquid lubricant separates the punch and the sheet surfaces completely. The existence of hydrodynamic lubrication (HL) is determined by several competing mechanisms: Suppose that initially there is a sufficiently thick lubricant film on the sheet surface. The advance of the punch against the sheet generates a high pressure in the contact region, which generates a flow of the lubricant. In the meantime, the stretching motion of the sheet tends to carry the lubricant away from the contact region. On the other hand, the viscosity of the lubricant retards its flow. If the punch advances sufficiently rapidly to complete the forming process before the lubricant thins out, then the condition of HL prevails. Therefore, besides geometric variables and sheet material properties, the parameters controlling the condition of HL are the punch velocity, the viscosity of the lubricant, the initial film thickness, and the composite roughness of the two solid surfaces. The last parameter defines the lower limit of the lubricant film thickness, below which the concept of HL does not apply. A right combination of these parameters ensures the existence of HL. The present work is aimed at (1) establishing the criteria for HL to exist; (2) computing the fluid friction on the sheet metal exerted by the lubricant film; and (3) studying the effects of variable friction on the distribution of strains in the sheet metal.

The application of HL to SMF has been previously considered. Fogg and Owais (1978) considered the lubrication of the punch-sheet interface by means of external pressurization, and studied the oil film thickness under various operating conditions and arrangements of orifice locations. Wilson and Wang (1984) derived a film thickness formula based on the interplay between punch advancing and sheet stretching. Their proposed mechanisms, method of analysis, and results are, however, substantially different from those of the present work. These differences will be discussed in Section 5. None of these earlier works studied the influence of HL on the distribution of strains in the sheet metal. The present work combines the squeeze film and sheet deformation mechanisms in treating the evolution of the lubricant film. By incorporating the lubrication analysis into the incremental plasticity

Contributed by the Applied Mechanics Division for presentation at the Winter Annual Meeting, Anaheim, CA, December 7-12, 1986, of The American Society of Mechanical Engineers.

Discussion on this paper should be addressed to the Editorial Department, ASME, United Engineering Center, 345 East 47th Street, New York, N.Y. 10017, and will be accepted until two months after final publication of the paper itself in the JOURNAL OF APPLIED MECHANICS. Manuscript received by ASME Applied Mechanics Division, February 12, 1985; final revision August 9, 1985. Paper No. 86-WA/APM-10.

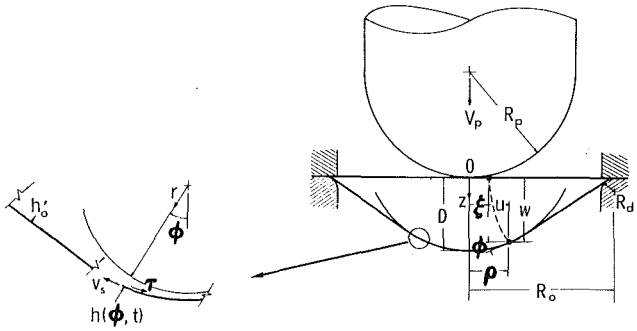

Fig. 1 Geometry and notation

analysis, the present work reveals the spatial distribution, as well as the time variation, of the lubricant film thickness and friction in the contact region, and the strains in the sheet metal throughout the forming process.

The model problem studied is the stretch forming of sheet metal with a hemispherical punch. In this initial phase of SMF lubrication studies, the material is assumed to be elastic plastic with strain hardening and the lubricant is assumed isoviscous. The plasticity analysis is outlined in Section 2 and the lubrication analysis given in Section 3. The computational scheme interfacing the two analyses is described in Section 4. Results of computation and discussion are contained in Section 5.

2 Mechanics of Hemispherical Punch Stretch Forming

The theoretical fundamentals of a finite element analysis of SMF have been outlined by Wang and Budiansky (1978), based on a nonlinear theory of membrane shells (Budiansky, 1968). The model treats plastic flow by a modified von Mises flow rule, and takes into account finite deformation, work hardening and normal anisotropy. The effect of punch-sheet interfacial friction is included with the use of a Coulomb type coefficient of friction. The computation of sheet deformation, stresses and strains is then implemented with an incremental integration scheme. This method has been applied to hemispherical punch stretch forming, taking advantage of the axisymmetric properties of the problem (Wang and Wenner, 1982). The present work expands this analysis to include a study of HL effects. The lubrication and plasticity analyses are interfaced through an effective coefficient of friction. In the following the plasticity analysis is briefly outlined and attention is paid to obtaining the contact pressure and the sheet sliding velocity relative to the punch, which are needed in the lubrication analysis.

A schematic diagram of hemispherical punch stretch forming is shown in Fig. 1. The configuration of the die set is specified by the punch radius R_p, the die radius R_d, and the undeformed sheet radius R_o. In this work, axisymmetric conditions are assumed. At time $t = 0$, the sheet lies in the $z = 0$ plane and is tangent to the punch. At time t, the punch has traveled, with a constant velocity V_p, a distance D. A material point with coordinates $(\xi, 0)$ initially is displaced by (u, w) to a current coordinate (ρ, w). The principal logarithmic strains in the radial and circumferential directions, ϵ_1 and ϵ_2, respectively, are

$$\{\epsilon\} = \begin{Bmatrix} \epsilon_1 \\ \epsilon_2 \end{Bmatrix} = \begin{Bmatrix} \ln\left[\left(1+\frac{du}{d\xi}\right)^2 + \left(\frac{dw}{d\xi}\right)^2\right]^{1/2} \\ \ln\left(1+\frac{u}{\xi}\right) \end{Bmatrix}. \quad (1)$$

The strain rates $\{\dot{\epsilon}\}$ (as a convention, a dot above a quantity denotes time rate) are assumed to consist of an elastic part $\{\dot{\epsilon}^{(e)}\}$ and a plastic part $\{\dot{\epsilon}^{(p)}\}$, given by

$$\{\dot{\epsilon}\} = \{\dot{\epsilon}^{(e)}\} + \{\dot{\epsilon}^{(p)}\}, \quad (2)$$

where

$$\{\dot{\epsilon}^{(e)}\} = \begin{Bmatrix} \dot{\epsilon}_1^{(e)} \\ \dot{\epsilon}_2^{(e)} \end{Bmatrix} = \frac{1}{E} \begin{bmatrix} 1 & -\nu \\ -\nu & 1 \end{bmatrix} \begin{Bmatrix} \dot{\tau}_1 \\ \dot{\tau}_2 \end{Bmatrix}, \quad (3)$$

$$\{\dot{\epsilon}^{(p)}\} = \begin{Bmatrix} \dot{\epsilon}_1^{(p)} \\ \dot{\epsilon}_2^{(p)} \end{Bmatrix} = \frac{\dot{\tau}_e}{\tau_e} \cdot \frac{E-E_t}{EE_t} \begin{bmatrix} 1 & -\frac{R}{1+R} \\ -\frac{R}{1+R} & 1 \end{bmatrix} \begin{Bmatrix} \tau_1 \\ \tau_2 \end{Bmatrix}, \quad (4)$$

Nomenclature

A_o = area on undeformed sheet
D = punch travel distance
E = Young's modulus
E_t = tangent modulus
f_1 = horizontal force component per unit undeformed sheet area
f_2 = vertical force component per unit undeformed sheet area
$\{\dot{F}\}$ = nodal force rate vector, $\{\dot{F}\}^T = [\dot{R}_1, \dot{Z}_1, \dot{R}_2, \dot{Z}_2, \ldots, \dot{R}_N, \dot{Z}_N]$
h = lubricant film thickness
h_o = initial lubricant film thickness
h_s = initial sheet thickness
H = dimensionless lubricant film thickness, $= h/h_o$
K = strength coefficient in the strain hardening relation
$[K]$ = global stiffness matrix
n = strain hardening exponent of sheet material
N = number of nodes
p = pressure in the lubricant film
P_i = pressure at the ith node
P_i^e = pressure under the ith element
Q_i = normal component of force at the ith node
Q_{fi} = tangential component of force at the ith node
$\dot{Q}_i$ = normal component of force rate at the ith node
r = radial coordinate in spherical polar coordinate system
R = anisotropy constant of sheet material
R_d = die radius
R_p = punch radius
R_o = radius of undeformed sheet
R_i = horizontal component of force at the ith node
$\dot{R}_i$ = horizontal component of force rate at the ith node
t = time
T = dimensionless time, $= V_p t/R_p$
u = horizontal component of displacement
$\{\dot{U}\}$ = nodal displacement rate vector, $\{\dot{U}\}^T = [\dot{U}_1, \dot{W}_1, \dot{U}_2, \dot{W}_2, \ldots, \dot{U}_N, \dot{W}_N]$
$\dot{U}_i$ = horizontal component of displacement rate at the ith node
v_r = r-component of film flow velocity
v_ϕ = ϕ-component of film flow velocity
v_s = sheet sliding velocity relative to punch
V_p = punch velocity
V_i = sheet sliding velocity at the ith node relative to punch
w = vertical component of displacement
$\dot{W}_i$ = vertical component of displacement rate at the ith node

and

$$\tau_e = \left(\tau_1^2 + \tau_2^2 - \frac{2R}{1+R}\,\tau_1\tau_2\right)^{1/2}. \tag{5}$$

In the above, E, E_t, ν and R are the Young's modulus, tangent modulus, Poisson's ratio and anisotropy constant, respectively, of the sheet mateiral. τ_1 and τ_2 are the radial and circumferential components of Kirchhoff stress. τ_e is the effective stress. In this work, the material is assumed rate independent and its uniaxial Kirchhoff stress, $\tau^{(u)}$, versus uniaxial logarithmic strain, $\epsilon^{(u)}$, curve is assumed to satisfy the Ramberg-Osgood relation

$$\epsilon^{(u)} = \frac{\tau^{(u)}}{E} + \left[\frac{\tau^{(u)}}{K}\right]^{1/n}, \tag{6}$$

where K is the strength coefficient and n is the strain hardening exponent of the sheet material. The tangent modulus E_t is then the slope of this curve,

$$E_t = \frac{d\tau^{(u)}}{d\epsilon^{(u)}}. \tag{7}$$

The principle of virtual work for membrane shells in rate form can be written as (Budiansky, 1968)

$$h_s\int_{A_o}(\dot\tau_1\delta\dot\epsilon_1 + \dot\tau_2\delta\dot\epsilon_2)dA_o - 2\,h_s\int_{A_o}(\tau_1\dot\epsilon_1\delta\dot\epsilon_1 + \tau_2\dot\epsilon_2\delta\dot\epsilon_2)dA_o$$
$$+ h_s\int_{A_o}\left\{\tau_1\frac{\dot u_\xi\delta\dot u_\xi + \dot w_\xi\delta\dot w_\xi}{[(1+u_\xi)^2 + w_\xi{}^2]} + \tau_2\frac{\dot u\delta\dot u}{(\xi+u)^2}\right\}dA_o$$
$$= \int_{A_o}(\dot f_1\delta\dot u + \dot f_2\delta\dot w)dA_o, \tag{8}$$

where

$$u_\xi = \frac{du}{d\xi}, \qquad w_\xi = \frac{dw}{d\xi},$$

h_s is the initial sheet thickness, A_o is the area of undeformed sheet, f_1 and f_2 are the horizontal and vertical force components per unit undeformed sheet area, and δ denotes variation. Using axisymmetric ring elements to discretize the initially flat sheet, linear interpolation functions for the displacement fields in the elements, and following standard procedures in finite element analysis, a global stiffness matrix equation is obtained (Wang and Wenner, 1982),

$$[K]\{\dot U\} = \{\dot F\}, \tag{9}$$

where

$$\{U\}^T = \lfloor U_1, W_1, U_2, W_2, \ldots, U_N, W_N\rfloor,$$
$$\{F\}^T = \lfloor R_1, Z_1, R_2, Z_2, \ldots, R_N, Z_N\rfloor,$$

$[K]$ is the global stiffness matrix, N is the number of nodes, and U_i and W_i are the horizontal and vertical components of displacement of the ith node, R_i and Z_i are the horizontal and vertical components of force of the ith node.

The nodal force rates $\dot F$ are obtained as follows: For a node not in contact with the punch, $\dot R_i = \dot Z_i = 0$. For nodes which contact the punch and slide relative to it, the contact force may be decomposed into a normal component Q_i and a tangential component Q_{fi}; the latter is the friction and is related to the former by

$$Q_{fi} = \mu(\phi, t)Q_i, \tag{10}$$

where μ is the effective coefficient of friction, and ϕ is the conical coordinate of the node in spherical polar coordinate system. Note that the angle ϕ is only used in the contact region. The contact force may also be decomposed into a horizontal and a vertical components, which are given as

$$\begin{Bmatrix} R_i \\ Z_i \end{Bmatrix} = \begin{Bmatrix} \sin\phi - \mu\cos\phi \\ \cos\phi + \mu\sin\phi \end{Bmatrix} Q_i. \tag{11}$$

The rates of these force components are then

$$\begin{Bmatrix} \dot R_i \\ \dot Z_i \end{Bmatrix} = \begin{Bmatrix} \sin\phi - \mu\cos\phi \\ \cos\phi + \mu\sin\phi \end{Bmatrix}\dot Q_i + \frac{Q_i}{R_p}\begin{Bmatrix} 1+\mu\tan\phi \\ \mu - \tan\phi \end{Bmatrix}\dot U_i$$
$$+ Q_i\begin{Bmatrix} -\cos\phi \\ \sin\phi \end{Bmatrix}\left(\frac{\partial\mu}{\partial t} + \frac{\partial\mu}{\partial\phi}\frac{1}{R_p\cos\phi}\dot U_i\right). \tag{12}$$

In the differentiation process an additional unknown $\dot Q_i$ is introduced. This is offset by the constraining equation

$$\dot W_i + \dot U_i\tan\phi = V_p. \tag{13}$$

The quantities needed in the lubrication analysis are obtained next. The sliding velocity of the sheet, at node i, relative to the punch, V_i, is evaluated by

Nomenclature (cont.)

z = vertical coordinate
Z_i = vertical component of force at the ith node
$\dot Z_i$ = vertical component of force rate at the ith node
$\{\epsilon\}$ = logarithmic principal strain vector, $= \begin{Bmatrix}\epsilon_1\\ \epsilon_2\end{Bmatrix}$
ϵ_1 = radial component of logarithmic strain
ϵ_2 = circumferential component of logarithmic strain
$\epsilon^{(u)}$ = uniaxial logarithmic strain in tensile test
$\{\dot\epsilon\}$ = stain rate vector, $= \begin{Bmatrix}\dot\epsilon_1\\ \dot\epsilon_2\end{Bmatrix}$
$\{\dot\epsilon^{(e)}\}$ = elastic strain rate vector, $= \begin{Bmatrix}\dot\epsilon_1^{(e)}\\ \dot\epsilon_2^{(e)}\end{Bmatrix}$
$\{\dot\epsilon^{(p)}\}$ = plastic strain rate vector, $= \begin{Bmatrix}\dot\epsilon_1^{(p)}\\ \dot\epsilon_2^{(p)}\end{Bmatrix}$
$\dot\epsilon_1^{(e)}$ = radial component of elastic strain rate
$\dot\epsilon_2^{(e)}$ = circumferential component of elastic strain rate
$\dot\epsilon_1^{(p)}$ = radial component of plastic strain rate
$\dot\epsilon_2^{(p)}$ = circumferential component of plastic strain rate
η = lubricant viscosity
θ = azimuthal coordinate in spherical polar coordinate system
Λ = dimensionless lubrication parameter, $= (\eta V_p R_p^2)/(Kh_s h_o^2)$
μ = effective coefficient of friction
ν = Poisson's ratio
ξ = horizontal coordinate of a material point on undeformed sheet
Π = dimensionless pressure, $= (R_p p)/(Kh_s)$
ρ = current horizontal coordinate of a material point on sheet
σ = characteristic surface roughness height
Σ = dimensionless roughness parameter, $= \sigma/h_o$
τ = shear stress acting on sheet by lubricant film
$\{\tau\}$ = Kirchhoff stress vector, $= \begin{Bmatrix}\tau_1\\ \tau_2\end{Bmatrix}$
τ_1 = radial component of Kirchhoff stress
τ_2 = circumferential component of Kirchhoff stress
τ_e = effective stress
$\tau^{(u)}$ = uniaxial Kirchhoff stress in tensile test
$\dot\tau_1$ = radial component of Kirchhoff stress rate
$\dot\tau_2$ = circumferential component of Kirchhoff stress rate
Υ_s = dimensionless sheet sliding velocity, $= v_s/V_p$
ϕ = conical coordinate in spherical polar coordinate system

$$V_i(\phi,t) = \dot{U}_i \cos\phi + (\dot{W}_i - V_p)\sin\phi. \tag{14}$$

The pressure between the punch and the sheet in each element, P_i^e, is evaluated from equilibrium considerations,

$$P_i^e = \frac{h_s}{R_p} e^{-\epsilon_1-\epsilon_2}(\tau_1+\tau_2). \tag{15}$$

The pressure at a node, P_i, is then taken to be the average of the pressures of adjacent elements,[1]

$$P_i(\phi,t) = \frac{1}{2}(P_{i-1}^e + P_i^e). \tag{16}$$

3 Formulation and Solution of the Hydrodynamic Lubrication Problem

The central feature of the HL theory is the thin film approximation (Reynolds, 1886). Because the thickness of the lubricant film is several orders smaller than the other dimensions involved in a lubrication problem, the dominant viscous stresses in the film are due to the normal gradients of the tangential components of the flow velocity, and the pressure variation in the normal direction may be neglected. Besides, the small film thickness, in conjunction with a moderate flow velocity, also renders the inertia of the flow negligibly small. By using the thin film approximation, and two simplifying assumptions that the density and viscosity of the lubricant are constant, the axisymmetric film flow in the contact region is formulated as follows:

Continuity Equation

$$\frac{1}{r^2}\frac{\partial}{\partial r}(r^2 v_r) + \frac{1}{r\sin\phi}\frac{\partial}{\partial\phi}(v_\phi \sin\phi) = 0, \tag{17}$$

r-Momentum Equation

$$\frac{\partial p}{\partial r} = 0, \tag{18}$$

ϕ-Momentum Equation

$$\frac{1}{r}\frac{\partial p}{\partial \phi} = \frac{\eta}{r^2}\frac{\partial}{\partial r}\left(r^2\frac{\partial v_\phi}{\partial r}\right). \tag{19}$$

In the above, a spherical polar coordinate system (r, ϕ, θ) with its origin fixed to the center of the punch is used. See Fig. 1. p is the pressure in the lubricant film, η is the lubricant viscosity, and v_r is the r component and v_ϕ is the ϕ component of the film flow velocity. The velocity boundary conditions are

$$v_r = v_\phi = 0 \text{ at } r = R_p, \tag{20}$$

and

$$v_r = \frac{\partial h}{\partial t} + \frac{v_s}{R_p+h}\frac{\partial h}{\partial\phi},\ v_\phi = v_s(\phi,t) \text{ at } r = R_p + h, \tag{21}$$

where h is the lubricant film thickness, and v_s is the sheet sliding velocity relative to punch. The shear stress, τ, acting on the sheet surface by the lubricant film is given by

$$\tau = \eta\left[r\frac{\partial}{\partial r}\left(\frac{v_\phi}{r}\right)\right]_{r=R_p+h}. \tag{22}$$

The sign of τ is positive if it acts toward the center of the contact region.

By equation (18) the pressure is not a function of r, which allows equation (19) to be easily integrated. With the use of boundary conditions (20) and (21), v_ϕ is found to be

$$v_\phi = -\frac{(r-R_p)(R_p+h-r)}{2\eta r}\frac{\partial p}{\partial\phi} + \frac{(R_p+h)(r-R_p)}{hr}v_s. \tag{23}$$

[1]The pressure can also be obtained from Q_i and an effective area. But when a node just comes into contact with the punch, it is difficult to determine the effective area. Therefore, the pressure calculated by the present method is more accurate.

The integration of equation (17) with respect to r, with the aid of boundary conditions (20) and (21), yields

$$(R_p+h)^2\frac{\partial h}{\partial t} + \frac{1}{\sin\phi}\frac{\partial}{\partial\phi}\left[(\sin\phi)\int_{R_p}^{R_p+h} v_\phi r dr\right] = 0. \tag{24}$$

By substituting v_ϕ as given in equation (23) into equation (24) and performing the integration, the following equation is obtained after neglecting terms of $O(h/R_p)$,

$$\frac{1}{\sin\phi}\frac{\partial}{\partial\phi}\left[(\sin\phi)h^3\frac{\partial p}{\partial\phi}\right] = 12\eta R_p^2\frac{\partial h}{\partial t} + \frac{6\eta R_p}{\sin\phi}\frac{\partial}{\partial\phi}[(\sin\phi)v_s h], \tag{25}$$

which relates the pressure in the film with the film thickness function and the sheet sliding velocity.

By substituting v_ϕ from equation (23) into equation (22), the expression for the shear stress becomes, after neglecting terms of $O(h/R_p)$,

$$\tau = \frac{\eta v_s}{h} + \frac{h}{2R_p}\frac{\partial p}{\partial\phi}. \tag{26}$$

The shear stress is seen to consist of two terms: One from sheet stretching and the other from the pressure gradient. The first term is always positive because the sheet is stretched in the outward direction. The second term may be either positive or negative, depending on the flow direction in the squeeze film.

Since $p(\phi, t)$ and $v_s(\phi, t)$ can be obtained from equations (16) and (14), they are treated as known. Then, equation (25) may be solved for h. By rearranging terms, equation (25) becomes

$$\frac{\partial h}{\partial t} + \frac{1}{12\eta R_p^2}\left(6\eta R_p v_s - 3h^2\frac{\partial p}{\partial\phi}\right)\frac{\partial h}{\partial\phi} = \frac{1}{12\eta R_p^2\sin\phi}\left\{h^3\frac{\partial}{\partial\phi}\left[(\sin\phi)\frac{\partial p}{\partial\phi}\right] - 6\eta R_p h\frac{\partial}{\partial\phi}(v_s\sin\phi)\right\}. \tag{27}$$

Define a characteristic direction by

$$\frac{d\phi}{dt} = \frac{v_s}{2R_p} - \frac{h^2}{4\eta R_p^2}\frac{\partial p}{\partial\phi}. \tag{28}$$

Along the characteristic direction, equation (27) transforms into

$$\frac{dh}{dt} = \frac{h^3}{12\eta R_p^2\sin\phi}\frac{\partial}{\partial\phi}\left[(\sin\phi)\frac{\partial p}{\partial\phi}\right] - \frac{h}{2R_p\sin\phi}\frac{\partial}{\partial\phi}(v_s\sin\phi) \tag{29}$$

and may be integrated from a prescribed initial condition.

When the computed h falls below an appropriate characteristic surface roughness height, σ, the film thickness is considered too small for HL to exist. This value of σ is usually taken to be five times the sum of the arithmetic average roughness heights of the two surfaces (Neale, 1973).

By introducing the following dimensionless variables and parameters

$$\left.\begin{aligned} &T = \frac{V_p t}{R_p},\ H = \frac{h}{h_o},\ \Pi = \frac{R_p p}{K h_s} \\ &\Upsilon_s = \frac{v_s}{V_p},\ \Lambda = \frac{\eta V_p}{K h_s}\left(\frac{R_p}{h_o}\right)^2,\ \Sigma = \frac{\sigma}{h_o}, \end{aligned}\right\} \tag{30}$$

where h_o is the initial lubricant film thickness, equations (28) and (29) are put in the form

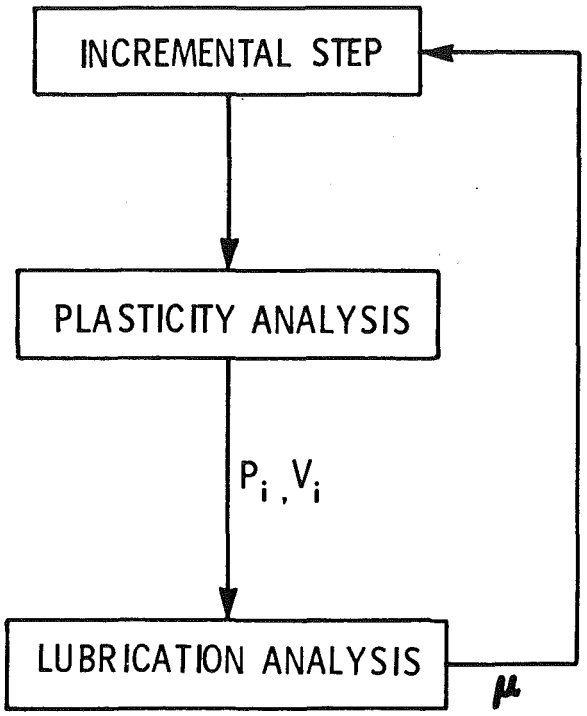

Fig. 2 Flow chart of computation

$$\frac{d\phi}{dT}=\frac{\Upsilon_s}{2}-\frac{H^2}{4\Lambda}\frac{\partial\Pi}{\partial\phi}, \tag{31}$$

$$\frac{dH}{dT}=\frac{H^3}{12\Lambda\sin\phi}\frac{\partial}{\partial\phi}\left[(\sin\phi)\frac{\partial\Pi}{\partial\phi}\right]$$

$$-\frac{H}{2\sin\phi}\frac{\partial}{\partial\phi}(\Upsilon_s\sin\phi). \tag{32}$$

They apply when

$$H\geq\Sigma \tag{33}$$

Thus, the HL of stretch forming is controlled by the dimensionless lubrication parameters Λ and roughness parameter Σ.

The shear stress obtained in the lubrication analysis can be used to define an effective coefficient of friction μ,

$$\mu=\frac{\tau}{p}. \tag{34}$$

With the use of equation (26) and the dimensionless variables introduced in equation (30), one obtains

$$\left(\frac{R_p}{h_o}\right)\mu=\frac{\Lambda\Upsilon_s}{H\Pi}+\frac{H}{2\Pi}\frac{\partial\Pi}{\partial\phi}. \tag{35}$$

4 Method of Calculation

The plasticity and lubrication analyses are linked in each step of the incremental computation as shown by the flow chart in Fig. 2. The plasticity computation yields, among other things, P_i and V_i, which are converted into

$$\Pi(\phi,t)=\frac{R_pP_i(\phi,t)}{Kh_s}, \tag{36}$$

$$\Upsilon_s(\phi,t)=\frac{V_i(\phi,t)}{V_p} \tag{37}$$

The derivatives $\partial\Pi/\partial\phi$, $\partial^2\Pi/\partial\phi^2$ and $\partial\Upsilon_s/\partial\phi$ are approximated by central differences for interior nodes, and by backward differences for the boundary node. These quantities are used in the lubrication computation to yield μ, which is then used in the next incremental step.

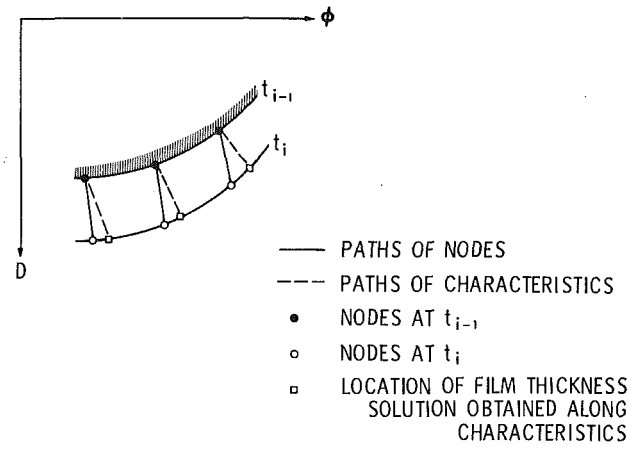

Fig. 3 Paths of characteristics and paths of nodes

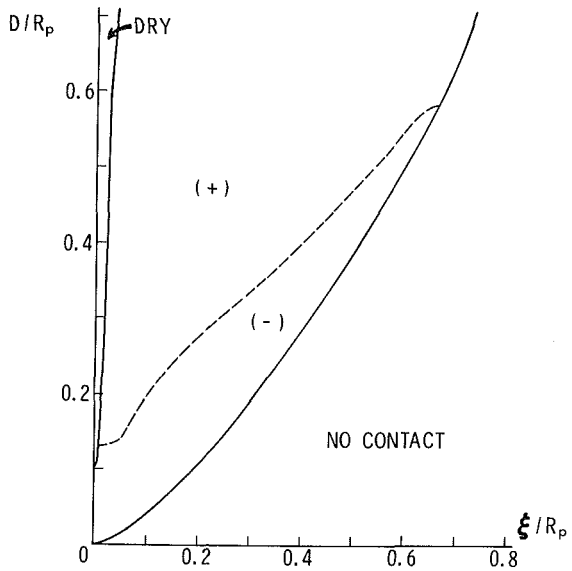

Fig. 4 Condition of lubrication in contact region (Λ = 0.02, Σ = 0.1)

The lubrication analysis is based on Eulerian formulation, while the plasticity analysis is based on Lagrangian formulation. Suppose at time t_{i-1} equations (31) and (32) are integrated from a node (a material point). At t_i the end point of the characteristic path no longer coincides with the same node. See Fig. 3. Likewise, the film thickness value obtained is not that at the node. Therefore, the film thickness values obtained by integration along the characteristics must be transferred to the nodes at the end of each incremental step. This is done by interpolation.

It is assumed that the film thickness at a node when it first comes into contact with the punch is $H = 1$, which serves as the initial value in the integration of equation (32). When the H value at a node falls to the preassigned Σ value, the lubrication computation is terminated. From then on the node is considered dry and a constant coefficient of friction, $\mu = 0.17$, is assigned to the node. This value is appropriate for A-K steel (Wang and Budiansky, 1978), a material used in the present calculation.

5 An Example

The material constants (typical to A-K steel), dimensions and range of parameters used in the present calculation are as follows:

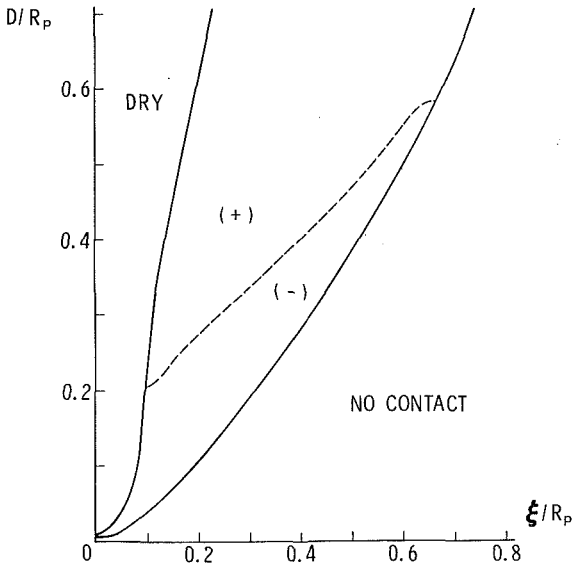

Fig. 5 Condition of lubrication in contact region ($\Lambda = 0.02$, $\Sigma = 0.15$)

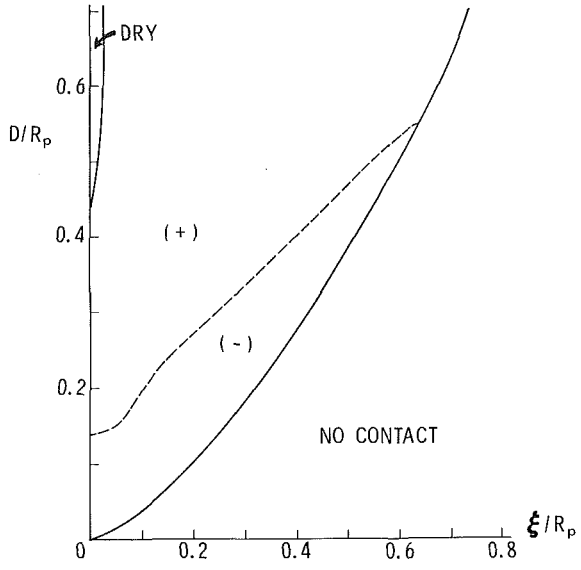

Fig. 7 Condition of lubrication in contact region ($\Lambda = 0.1$, $\Sigma = 0.2$)

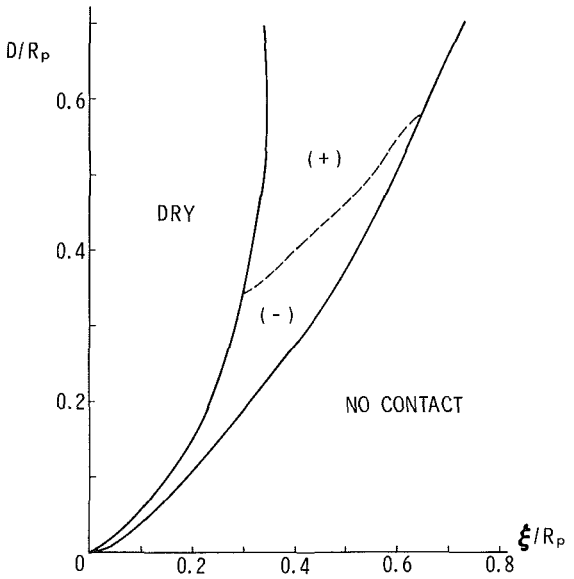

Fig. 6 Condition of lubrication in contact region ($\Lambda = 0.02$, $\Sigma = 0.2$)

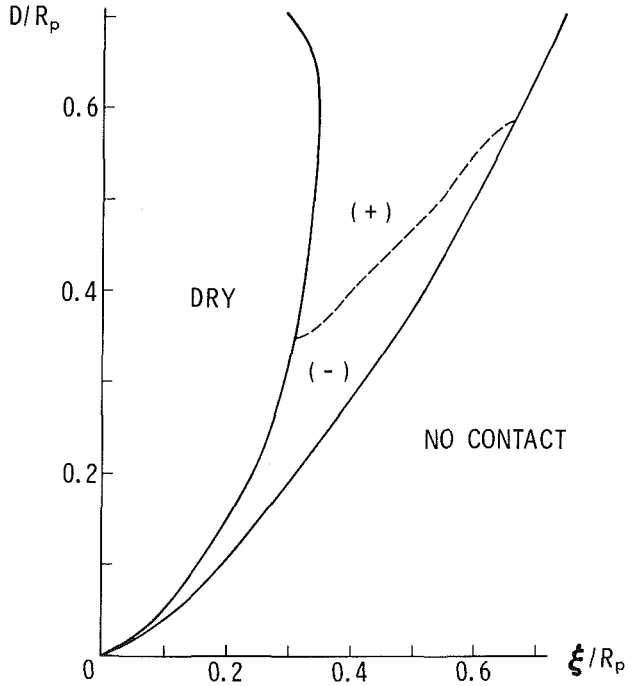

Fig. 8 Condition of lubrication in contact region ($\Lambda = 0.005$, $\Sigma = 0.1$)

$E = 207$ GPa, $K = 523$ MPa,
$n = 0.21$, $R = 1.7$, $h_s = 1$ mm,
$R_p = 50.8$ mm, $R_o = 59.26$ mm, $R_d = 6.35$ mm,
$\Lambda = 0.005 - 0.1$, $\Sigma = 0.04 - 0.5$.

The contact condition for a given set of (Λ, Σ) values is displayed in Fig. 4, where the abscissa represents the horizontal coordinate on the undeformed sheet and the ordinate the punch travel (distance), both normalized by the punch radius. The solid curve on the right is the boundary of the contact region, which is divided into two parts by the solid curve near the vertical axis. The part labeled as *DRY* is the region where $H \leq \Sigma$. The part between the dry boundary and the contact boundary is the region where HL prevails. The lubricated region is further divided into two parts by the dashed curve. The lower part, labeled as (−), is characterized by a negative shear stress. In this region a negative pressure gradient dominates the influence of sheet stretching. In the upper part, which is labeled as (+), the opposite is true.

The variation of contact condition with increasing Σ values is shown in Figs. 4 to 6. As can be seen, the central part of the contact region becomes dry sooner with increasing Σ values. Figures 7 and 8 exhibit the contact conditions for two other sets of (Λ, Σ) values, and should be compared with Figs. 6 and 4, respectively. They show that, for the same Σ value, increasing the value of Λ enlarges the lubricated region. These figures reveal that the contact condition for a given punch travel is generally heterogeneous, i.e., the central region is dry and the region surrounding it hydrodynamically lubricated. The dry central region vanishes only when Λ is sufficiently large or Σ is sufficiently small. Figure 8 also exhibits a trend of the dry boundary to shift inward as the punch travel becomes large, which will be explained later.

The detailed spatial variation in the contact region of the pressure, the sheet sliding velocity, the film thickness and the effective coefficient of friction, for the case of $\Lambda = 0.02$, $\Sigma =$

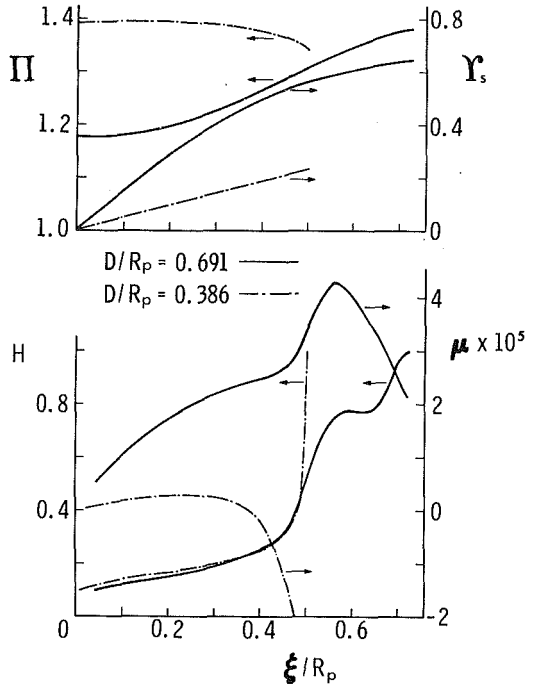

Fig. 9 Distribution of pressure, sheet sliding velocity, film thickness and coefficient of friction in contact region ($\Lambda = 0.02$, $\Sigma = 0.1$)

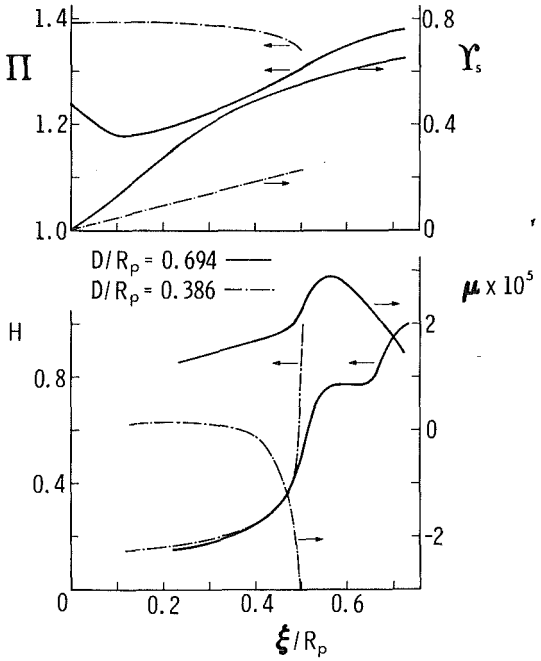

Fig. 11 Distribution of pressure, sheet sliding velocity, film thickness and coefficient of friction in contact region ($\Lambda = 0.02$, $\Sigma = 0.15$)

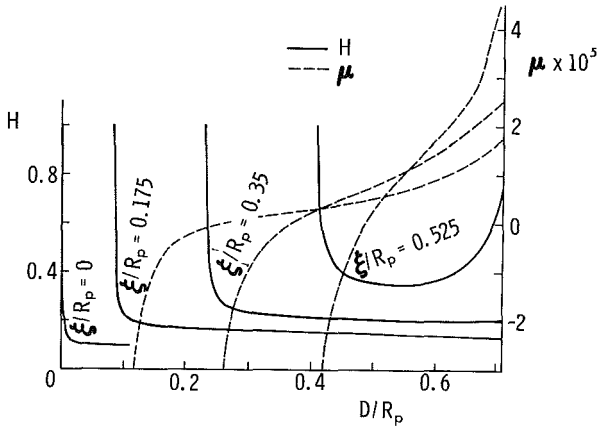

Fig. 10 Film thickness and friction coefficient versus punch travel ($\Lambda = 0.02$, $\Sigma = 0.1$)

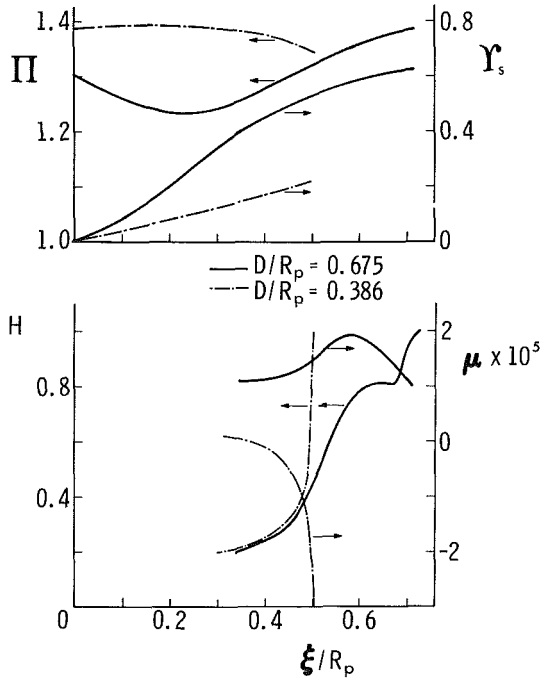

Fig. 12 Distribution of pressure, sheet sliding velocity, film thickness and coefficient of friction in contact region ($\Lambda = 0.02$, $\Sigma = 0.2$)

0.1, are plotted in Fig. 9 for two punch travel distances. At the smaller punch travel, high contact pressure occurs in the interior, and the pressure decreases with increasing distance from the contact center. The negative pressure gradient, combined with the outward sliding velocity, causes the lubricant to flow away from the contact region. This results in a film thickness distribution that is low in the interior, but rises rapidly toward the edge. The relatively rapid pressure drop near the contact edge also causes the coefficient of friction to descend to negative values. At the larger punch travel, low contact pressure occurs in the interior, and the pressure rises toward the edge. This is because the sheet becomes progressively thinner with the advance of the punch, while the tensile stresses are limited in magnitude as prescribed by the strain hardening law. The resulting smaller tensile forces can only be balanced by a smaller contact pressure. Thus, the lowest pressure always occurs where the thickness strain is the largest. The positive pressure gradient competes with the influence of sheet stretching, and a more varied film thickness distribution results. The corresponding distribution of the coefficient of friction is also more varied; it remains positive in this case over the entire contact region. The film thickness and the coefficient of friction are further plotted in Fig. 10, for a few selected ξ values, as functions of the punch travel. It is revealed in this case that, except in a region very close to the contact center, the lubricant film can remain in existence for a large punch travel distance. In fact, the film thickness near the contact edge can even decrease first and then increase again as the punch advances. This is the result of reverse flow due to the positive pressure gradient mentioned earlier.

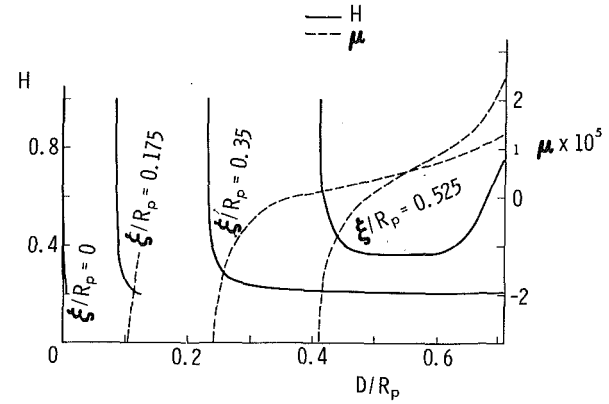

Fig. 13 Film thickness and friction coefficient versus punch travel ($\Lambda = 0.02$, $\Sigma = 0.2$)

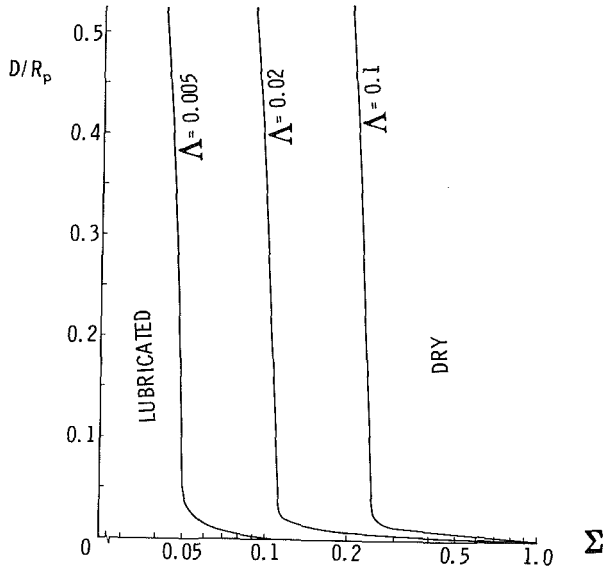

Fig. 14 Typical condition of lubrication at a node ($\xi/R_p = 0.01$)

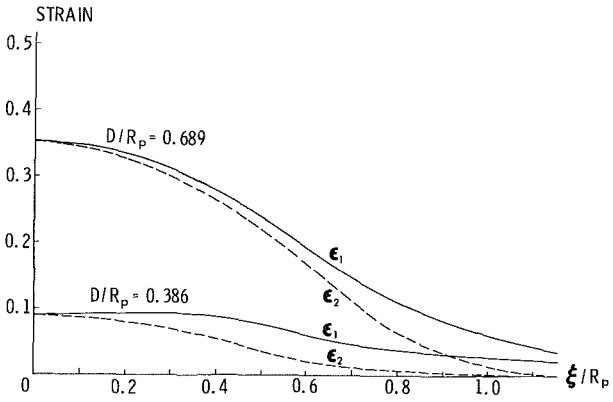

Fig. 15 Distribution of strains in frictionless contact ($\mu = 0$)

The case of $\Lambda = 0.02$, $\Sigma = 0.15$ is plotted in Fig. 11; the case of $\Lambda = 0.02$, $\Sigma = 0.2$ is plotted in Figs. 12 and 13. It is seen that, as Σ increases, the main features of these lubrication-related quantities at both small and large punch travel distances remain as described in the previous paragraph. However, the influence of reverse flow becomes greater, because at a larger Σ value the dry boundary lies closer to where the reverse flow occurs. This explains why the dry boundary tends to shift inward in Fig. 8.

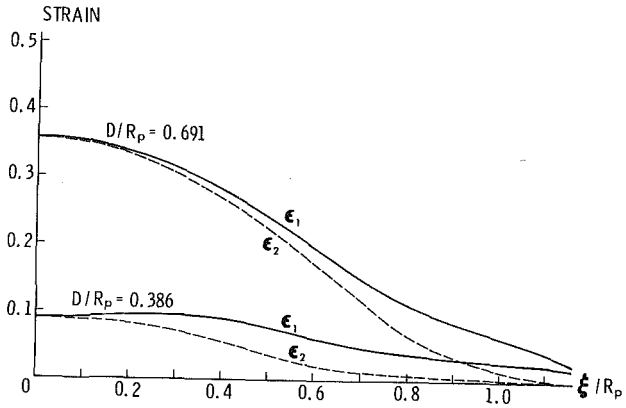

Fig. 16 Distribution of strains ($\Lambda = 0.02$, $\Sigma = 0.1$)

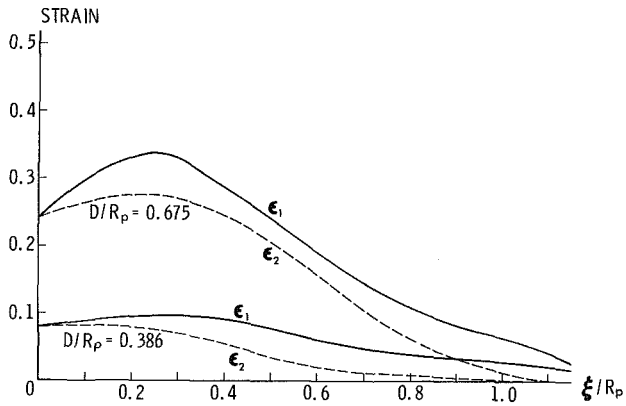

Fig. 17 Distribution of strains ($\Lambda = 0.02$, $\Sigma = 0.2$)

The contact condition at any specified location can be summaried in terms of Λ, Σ and the punch travel distance by a chart such as given in Fig. 14. The chart shows that, for a given Λ value, there is a critical Σ value, below which this location remains hydrodynamically lubricated throughout the stretch forming process.

The film thickness results described above are diametrically opposed to those obtained by Wilson and Wang (1984), who found that the film was the thickest near the punch center, decreased toward the contact edge, and eventually broke down there. While the ultimate check for correctness should come from careful experimentation, the following comparison of the two analyses might help to explain the discrepancies:

(1) Wilson and Wang analyzed the evolution of the lubricant film in two steps. The first step dealt with the formation of an "initial" film thickness ("initial" in the sense that the second step would start here) due to the wrapping motion of the sheet around the punch. This was treated as a steady state foil bearing problem, and the analysis tacitly assumed that unlimited amount of oil was originally placed on the sheet surface. In contrast, the present analysis deals with the unsteady squeeze film problem exactly, and it assumes that a finite oil film thickness is initially given on the sheet surface.

(2) The second step of their analysis dealt with the subsequent evolution of the oil film, once the "initial" film thickness was formed. This was analyzed by considering only the "transport" effect, i.e., the pressure gradient term in equation (25) was neglected. Clearly, for such a simplification to be valid, the pressure gradient effect must be small compared with the sheet stretching effect. The present calculation

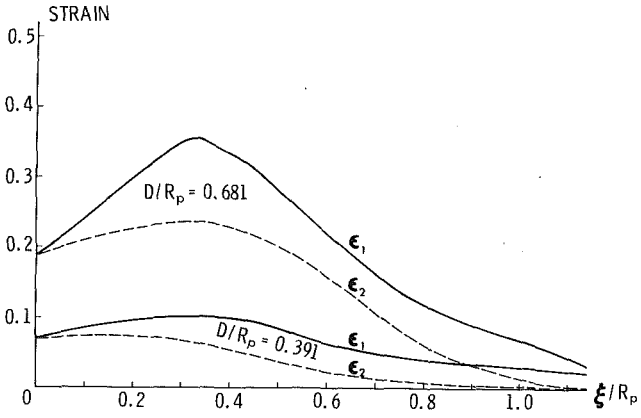

Fig. 18 Distribution of strains ($\Lambda = 0.02$, $\Sigma = 0.5$)

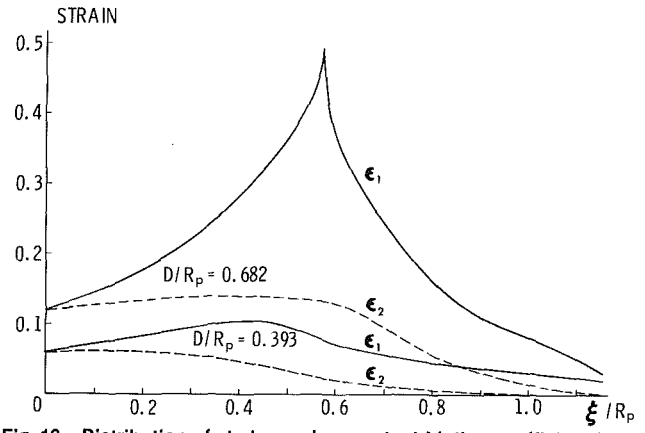

Fig. 19 Distribution of strains under constant friction coefficient ($\mu = 0.17$)

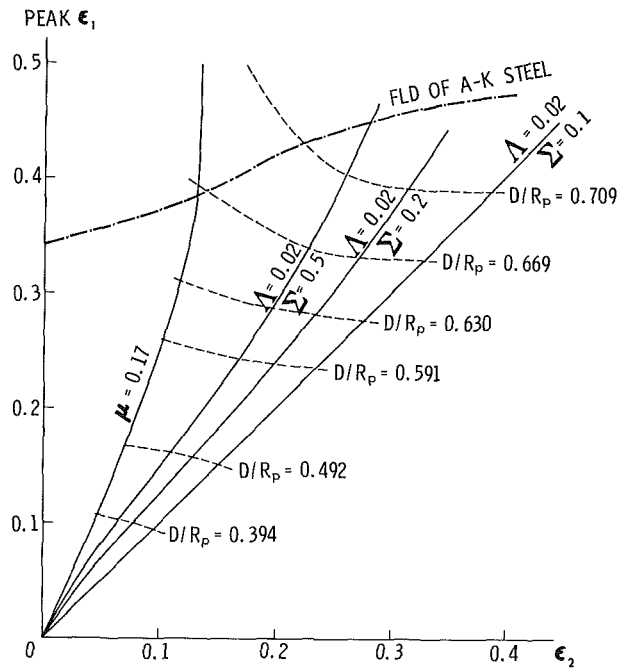

Fig. 20 Effect of lubrication on peak radial strain with punch travel distances and an empirical FLD superimposed

shows almost invariably that the opposite is true. In fact, the rather varied shapes of the film thickness distribution in Figs. 9–13 are principally determined by the pressure distribution.

The distribution of strains for several sets of (Λ, Σ) values are shown in Figs. 16 to 18. For the purpose of comparison, the distribution of strains at constant values of the coefficient of friction, $\mu = 0$ and $\mu = 0.17$, is shown in Figs. 15 and 19. It is seen that the case of $\Sigma = 0.1$, where HL prevails in most of the contact region, is indistinguishable from the frictionless case, $\mu = 0$. As Σ increases, the difference between radial and circumferential strains becomes more pronounced in the contact region. Besides, the locations of peak strains gradually shift outward and approach the case of dry contact with the larger coefficient of friction, $\mu = 0.17$. In this latter case, the radial strain peaks around $\xi/R_p = 0.57$, signaling fracture at this location. The peaking of strains has a profound implication on forming limits. Figure 20 is a plot of peak radial strain versus the circumferential strain at the location of the peak radial strain. These curves represent the typical cases studied. Superimposed on these curves is an empirical forming limit diagram (FLD) for A-K steel (Ghosh, 1978) above which fracture occurs. It is seen that the presence of HL improves the biaxiality of the strain state, which in turn allows a larger punch travel distance without failure in the stretch forming process.

6 Summary

Hydrodynamic lubrication in the stretch forming of sheet metal with a hemispherical punch is investigated by incorporating a lubrication analysis into an incremental plasticity analysis. The sheet material is assumed to be elastic plastic with strain hardening, and the lubricant is assumed isoviscous. Two dimensionless parameters controlling the condition of lubrication are identified. The spatial distribution, as well as the time variation, of the lubricant film thickness and friction in the contact region, and the strains in the sheet metal are calculated for a range of these parameters. The results of the example considered reveal the following:

(1) The condition of lubrication at the punch-sheet interface is generally heterogeneous, with the central part of the contact region dry and the region surrounding it hydrodynamically lubricated. This finding differs substantially from that of an earlier published analysis.

(2) The heterogeneous nature of the contact condition results in an interfacial friction which varies both in the contact region and during the forming process.

(3) The variable friction affects significantly the distribution of strains in the sheet metal. In the case of hemispherical punch stretch forming, the presence of hydrodynamic lubrication enhances the biaxiality of the strain state and improves the formability.

Acknowledgments

This study was initiated when one of the authors, D. C. Sun, was under the supervision of Mr. Arnold O. DeHart. D. C. Sun wishes to express sincere gratitude to Mr. DeHart for his strong support of the study.

References

Arlinghaus, F. J., Stoughton, T. B., Frey, W. H., and Murphy, B. K., "Finite Element Modeling of a Stretch-Formed Production Panel," *Computer Modeling of Sheet Metal Forming Process*, Wang, N.-M., and Tang, S. C., eds., The Metallurgical Society, pp. 51–64.

Budiansky, B., 1968, "Notes on Nonlinear Shell Theory," ASME JOURNAL OF APPLIED MECHANICS, Vol. 90. pp. 393–401.

Cavendish, J. C., Wenner, M. L., Hall, C. A., and Rheinboldt, W. C., "DEM: A New Computational Approach to Sheet Metal Forming Problems," *Int. J. Num. Eng'g*, (to appear).

Cristescu, N., 1967, *Dynamic Plasticity*, North-Holland.

Drucker, D. C., 1951, "A More Fundamental Approach to Plastic Stress-Strain Solutions," *Proc. 1st U.S. Natn. Cong. Appl. Mech.*, pp. 487–491.

Fogg, B., Owais, M. K. A., 1978, "Calculation of Pressure Distribution and Oil Flow and Film Thickness in Externally Pressurized Lubrication in Sheet Metal Forming," *CIRP Annalen*, Vol. 27, No. 1, pp. 183–188.

Ghosh, A. K., 1978, "Plastic Flow Properties in Relation to Localized Necking in Sheets," *Mechanics of Sheet Metal Forming*, Koistinen, D. P., and Wang, N. M., eds., Plenum Press.

Hill, R., 1950, *The Mathematical Theory of Plasticity*, Oxford University Press.

Koiter, W. T., 1953, "Stress-Strain Relations, Uniqueness and Variational Theorems for Elastic-Plastic Materials with a Single Yield Surface," *Q. J. Appl. Math.*, Vol. 11, pp. 350–354.

Mendelson, A., 1968, *Plasticity: Theory and Application*, Macmillan.

Neale, M. J., 1973, *Tribology Handbook*, John Wiley, Part F5.

Reynolds, O., 1886, "On the Theory of Lubrication and Its Application to Mr. Beauchamp Tower's Experiments Including an Experimental Determination of the Viscosity of Olive Oil," *Philosophical Transactions of the Royal Society*, Vol. 177, Pt. 1, pp. 157–234.

Wang, N. M., and Budiansky, B., 1978, "Analysis of Sheet Metal Stamping by a Finite Element Method," ASME JOURNAL OF APPLIED MECHANICS, Vol. 100, pp. 73–82.

Wang, N. M., and Wenner, M. L., 1982, "Effects of Strain-Hardening Representation in Sheet Metal Forming Calculations of 2036-T4 Aluminum," *Formability of Metallic Materials—2000 A.D.*, ASTM STP 753, Newby, J. R., and Niemeier, B. A., eds., ASTM, pp. 84–104.

Wilson, W. R. D., 1978, "Friction and Lubrication in Sheet Metal Forming," *Mechanics of Sheet Metal Forming*, Koistinen, D. P., and Wang, N. M., eds., Plenum Press.

Wilson, W. R. D., and Wang, J. J., 1984, "Hydrodynamic Lubrication in Simple Stretch Forming Processes," ASME *Journal of Tribology*, Vol. 106, pp. 70–77.

Analytic Solution of a Finite-Width Rough Surface Hydrodynamic Bearing

J. W. White
Professor,
Department of Mechanical and Aerospace Engineering,
The University of Tennessee,
Knoxville, Tenn. 37996-2210
Mem. ASME

An analytic solution of the full incompressible unaveraged Reynolds equation is obtained by regular perturbation expansion for the case of a finite width bearing with transverse roughness. Results show that the unaveraged pressure is first influenced by the roughness statistics at the 0 (ϵ^2) level and is negligibly affected by the details of the roughness distribution. Through second order effects, it is shown that the closure assumption utilized by Christensen and Tϕnder in developing their theory for striated roughness effects on incompressible lubrication is correct. That is, for transverse roughness [h = h(x)], h^3 *and* $\partial P/\partial y$ *are statistically independent. Due to the linearity of the incompressible Reynolds equation, it is likely that a similar approach can be used for the study of fully three-dimensional roughness effects on lubrication in order to reveal the detailed relationship between clearance and pressure.*

Introduction

In one of the early treatments of the effect of striated surface roughness on the load carrying capacity of incompressible lubricants, Christensen and Tϕnder (1969) made a plausible but untested assumption as to the statistical relationship between clearance and pressure gradient. To be specific, the pressure gradient in the direction of striations was assumed to be statistically independent of h^3 (where h is the bearing clearance). This assumption was required in order to close their theoretical model. Since this early work, the approach taken by Christensen and Tϕnder has been extended and generalized (Christensen, 1969; Christensen et al., 1971) but neither a detailed experimental nor theoretical verification of their closure model has appeared. Other approaches to the study of surface roughness effects on lubrication have been developed in the past ten years, such as the multiscale analysis of Elrod (1973) and the use of flow factors by Patir and Cheng (1978). Recently, Tripp (1983) extended and generalized the average flow model of Patir and Cheng.

In studies of surface roughness effects on very thin film gas bearings, White (1980, 1983) developed analytical solutions for the detailed (unaveraged) pressure distribution for several simple geometric bearings. From these analytic solutions, the statistical relationship between clearance and pressure was revealed, allowing the ensemble average of the Reynolds equation. For the case of transverse surface roughness, the transverse pressure gradient and h^3 were found to be highly coupled. This is in contradiction to the Christensen/Tϕnder theory for incompressible lubricants and indicates how differently roughness affects the load carrying capacity of incompressible and very low clearance gas bearings. It is expected that the statistical relationship of clearance and pressure found from the simple geometry cases can be applied to a rather wide range of bearing geometries, since the role of roughness occurs at such a short length scale. The motivation for this approach is much the same that one would have for the study of turbulent boundary layers if it were possible to find even one analytic solution for turbulent flow. The mixing length theory of turbulent boundary layers which is valid for a rather wide range of flow conditions could probably have been discovered from a single exact analytic solution, such as turbulent flow over a flat plate. Instead, since no exact solution of turbulence has been found, the mixing-length theory developed through much experimental work. The analytic treatment of surface roughness effects on incompressible lubrication is more tractable than that of turbulence, allowing unaveraged analytic solutions to some simple bearing geometries. It is likely that such analytical solutions will allow one to discover universal properties of this short wavelength phenomenon which can be applied to a wide range of bearing geometries and operating conditions.

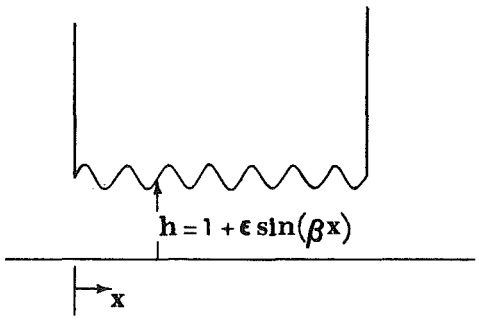

Fig. 1 The rough plane bearing geometry

Contributed by the Applied Mechanics Division for publication in the JOURNAL OF APPLIED MECHANICS.
Discussion on this paper should be addressed to the Editorial Department, ASME, United Engineering Center, 345 East 47th Street, New York, N.Y. 10017, and will be accepted until two months after final publication of the paper itself in the JOURNAL OF APPLIED MECHANICS. Manuscript received by ASME Applied Mechanics Division, February 12, 1985.

The remainder of this paper reports findings of an analytical study of the effects of striated transverse surface roughness on the load carrying capacity of incompressible fluid bearings. The approach taken is similar to that used earlier for the study of gas films by White (1980, 1983). However, in the earlier work, a model lubrication equation was used to avoid the inherent nonlinearity of gas bearings. In the present work, the full Reynolds equation is utilized and the unaveraged solution is obtained analytically by regular perturbation expansion through second order effects. It will be shown by a straightforward analysis of the unaveraged results of a parallel surface bearing that the closure assumption used by Christensen and Tønder is correct.

The Analytical Solution

Consider a finite-width parallel surface bearing with transverse sine wave roughness on the stationary surface as shown on Fig. 1. The bearing length is L_x while the width is L_y, and the roughness wave length is L_w. The roughness distribution appears in dimensionless form as

$$h(x) = 1 + \epsilon \sin(\beta x) \tag{1}$$

and is assumed to be such that the Reynolds equation of lubrication is valid. The Reynolds equation appears in dimensionless form as

$$\frac{\partial}{\partial x}\left(h^3 \frac{\partial P}{\partial x}\right) + \left(\frac{Lx}{Ly}\right)^2 \frac{\partial}{\partial y}\left(h^3 \frac{\partial P}{\partial y}\right) = \Lambda \frac{\partial h}{\partial x} \tag{2}$$

where

$$\Lambda = \frac{6\mu V L_x}{P_o h_o^2}$$

Bearing clearance and pressure are normalized on h_o and P_o, respectively. The translational velocity is denoted by V, and the Newtonian fluid viscosity is μ. The dimensionless boundary conditions that will be satisfied on Fig. 1 are given by

$$\begin{aligned} &x = 0,\ P = 1 \\ &x = 1,\ P = 0 \\ &y = 0,\ \frac{\partial P}{\partial y} = 0 \text{ (centerline)} \\ &y = 1,\ P = 0 \end{aligned} \tag{3}$$

The solution of equation (2) is initially divided into two parts as

$$P(x,y) = P_1(x) + P_2(x,y) \tag{4}$$

where

$$\frac{\partial}{\partial x}\left(h^3 \frac{\partial P_1}{\partial x}\right) = \Lambda \frac{\partial h}{\partial x} \tag{5}$$

and

$$\frac{\partial}{\partial x}\left(h^3 \frac{\partial P_2}{\partial x}\right) + \left(\frac{L_x}{L_y}\right)^2 \frac{\partial}{\partial y}\left(h^3 \frac{\partial P_2}{\partial y}\right) = 0 \tag{6}$$

The solution of equation (5) is found subject to the boundary conditions

$$\begin{aligned} &x = 0,\ P_1 = 1 \\ &x = 1,\ P_1 = 0 \end{aligned} \tag{7}$$

while equation (6) willl be solved subject to

$$\begin{aligned} &x = 0, \quad P_2 = 0 \\ &x = 1, \quad P_2 = 0 \\ &y = 0, \quad \frac{\partial P_2}{\partial y} = 0 \\ &y = 1, \quad P_2 = -P_1(x) \end{aligned} \tag{8}$$

Using expansions of the form

$$\frac{1}{h^2} = 1 - 2\,\epsilon\sin(\beta x) + 3\,\epsilon^2 \sin^2(\beta x) - \ldots$$

and

$$\frac{1}{h^3} = 1 - 3\,\epsilon\,\sin(\beta x) + 6\,\epsilon^2\,\sin^2(\beta x) - \ldots$$

the solution of equation (5) appears as

$$P_1(x) = 1 - x + 0\left(\frac{1}{\beta}\right) \tag{9}$$

The surface roughness of interest will be restricted to very short wavelength or more specifically

$$\beta = 2\pi \frac{L_x}{L_w} >> 1$$
$$L_w << L_x \tag{10}$$

Equation (9) represents the solution to a wide parallel plate bearing and indicates that for such a geometry, the short wavelength roughness has a negligible influence on pressure.

The solution to equation (6) and boundary condition (8) is obtained by a regular perturbation expansion. First, the pressure is written as

$$P_2(x,y) = f(x)g(y) \tag{11}$$

and equation (6) is then expressed by

$$\left(\frac{L_x}{L_y}\right)^2 \frac{g''}{g} = -\frac{f''}{f} - \frac{3\epsilon\beta\cos(\beta x)}{[1 + \epsilon\sin(\beta x)]}\frac{f'}{f} = \lambda_0^2 + \epsilon\lambda_1^2 + \ldots \tag{12}$$

The solution for $g(y)$ follows:

$$g'' - \left(\frac{L_y}{L_x}\right)^2 [\lambda_o^2 + \epsilon\lambda_1^2 + \ldots]g = 0 \tag{13}$$

$$g(y) = C_3 \sinh\left[\frac{L_y}{L_x}\, y[\lambda_o^2 + \epsilon\lambda_1^2 + \ldots]^{1/2}\right] +$$

$$C_4 \cosh\left[\frac{L_y}{L_x}\, y[\lambda_o^2 + \epsilon\lambda^2 + \ldots]^{1/2}\right] \tag{14}$$

The boundary condition ($y = 0$, $\partial P_2/\partial y = 0$) can be satisfied by setting $g'(0) = 0$. Therefore, equation (14) reduces to

$$g(y) = C_4 \cosh\left[\frac{L_y}{L_x}\, y[\lambda_o^2 + \epsilon\lambda_1^2 + \ldots]^{1/2}\right] \tag{15}$$

The differential equation for $f(x)$ is given by

$$f'' + 3\epsilon\beta\cos(\beta x)[1 - \epsilon\sin(\beta x) + \ldots]f' + [\lambda_o^2 + \epsilon\lambda_1^2 + \ldots]f = 0 \tag{16}$$

and the solution to equation (16) will be expressed in the form

$$f(x) = f_o(x) + \epsilon f_1(x) + \epsilon^2 f_2(x) + \ldots$$

The zeroth order term is governed by

$$f_o'' + \lambda_o^2 f_o = 0 \tag{17}$$

$$\begin{aligned} &x = 0, f_o = 0 \\ &x = 1, f_o = 0 \end{aligned} \tag{18}$$

The second boundary condition of (18) requires λ_o to be of the form

$$\lambda_o = n\pi \tag{19}$$

and f_o appears with one arbitrary constant as

$$f_o = C_1 \sin(n\pi x) \tag{20}$$

We could at this point satisfy the condition along $y = 1$; however, it will be shown that we can proceed to compute $f_1(x)$ and $f_2(x)$ with the satisfaction of

$$P_2(x,1) = -P_1(x)$$

appearing as the last step. The solution for $f_1(x)$ and $f_2(x)$ follows:

$$0(\epsilon): f_1'' + \lambda_o^2 f_1 + 3\beta\cos(\beta x) f_0' + \lambda_1^2 f_o = 0 \tag{21}$$

$$x = 0, f_1 = 0$$

$$x = 1, f_1 = 0$$

$$f_{1_c} = \hat{C}_1 \sin(n\pi x) + \hat{C}_2 \cos(n\pi x) \tag{22}$$

$$f_{1_p} = A\cos[(\beta + n\pi)x] + B\cos[(\beta - n\pi)x] + Cx\sin(n\pi x) + Dx\cos(n\pi x) \tag{23}$$

The undetermined coefficients are found to appear as

$$A = \frac{\frac{3}{2}\beta C_1 n\pi}{(\beta + n\pi)^2 - (n\pi)^2} \qquad B = \frac{\frac{3}{2}\beta C_1 n\pi}{(\beta - n\pi)^2 - (n\pi)^2}$$

$$C = 0 \qquad D = \frac{\lambda_1^2 C_1}{2\pi n} \tag{24}$$

At this point, for convenience, we require $\beta = 2\pi N$; N = integer. The boundary condition at $x = 0$ requires $A + B + \hat{C}_2 = 0$ while the conditions at $x = 1$ gives

$$A + B + \hat{C}_2 + \frac{\lambda_1^2 C_1}{2\pi n} = 0$$

Therefore, the eigenvalue λ_1 is zero.

$$f_1(x) = \hat{C}_1 \sin(n\pi x) + A\cos[(\beta + n\pi)x] + B\cos[(\beta - n\pi)x] - (A + B)\cos(n\pi x) \tag{25}$$

$0(\epsilon^2)$:

$$f_2'' + \lambda_o^2 f_2 + 3\beta\cos(\beta x) f_1' - 3\beta\cos(\beta x)\sin(\beta x) f_o' + \lambda_1^2 f_1 + \lambda_2^2 f_o = 0 \tag{26}$$

$$x = 0, f_2 = 0$$

$$x = 1, f_2 = 0$$

$$f_{2_C} = \bar{C}_1 \sin(n\pi x) + \bar{C}_2 \cos(n\pi x) \tag{27}$$

$$f_{2_p} = k_1\sin[(2\beta + n\pi)x] + k_2\cos[(2\beta + n\pi)x] + k_3\sin[(2\beta - n\pi)x] + k_4\cos[(2\beta - n\pi)x] + k_5\sin[(\beta + n\pi)x] + k_6\cos[(\beta + n\pi)x] + k_7\sin[(\beta - n\pi)x] + k_8\cos[(\beta - n\pi)x] + k_9 x\sin[n\pi x] + k_{10} x\cos[n\pi x] \tag{28}$$

Upon substituting equation (28) into (26), we obtain

$$k_1 = \frac{-\frac{3}{4}C_1\beta n\pi - \frac{3}{2}A\beta(\beta + n\pi)}{(2\beta + n\pi)^2 - n^2\pi^2}$$

$$k_2 = 0$$

$$k_3 = \frac{-\frac{3}{4}C_1\beta n\pi - \frac{3}{2}B\beta(\beta - n\pi)}{(2\beta - n\pi)^2 - n^2\pi^2}$$

$$k_4 = 0$$

$$k_5 = \frac{\frac{3}{2}\beta(A + B)n\pi}{(\beta + n\pi)^2 - n^2\pi^2}$$

$$k_6 = \frac{\frac{3}{2}\beta\hat{C}_1 n\pi}{(\beta + n\pi)^2 - n^2\pi^2}$$

$$k_7 = \frac{\frac{3}{2}\beta(A + B)n\pi}{(\beta - n\pi)^2 - n^2\pi^2}$$

$$k_8 = \frac{\frac{3}{2}\beta\hat{C}_1 n\pi}{(\beta - n\pi)^2 - n^2\pi^2}$$

$$k_9 = 0$$

$$k_{10} = \left[-\frac{3}{2}\beta A(\beta + n\pi) + \frac{3}{2}\beta B(\beta - n\pi) + \lambda_2^2 C_1\right]/(2\pi n) \tag{29}$$

Satisfaction of the $x = 0$ condition by f_2 requires

$$\bar{C}_2 + k_6 + k_8 = 0$$

while the boundary condition at $x = 1$ produces

$$\bar{C}_2 + k_6 + k_8 + k_{10} = 0$$

Therefore, we see that k_{10} must be zero. This allows λ_2 to be expressed as

$$\lambda_2^2 = \left[\frac{3}{2}\beta A(\beta + n\pi) - \frac{3}{2}\beta B(\beta - n\pi)\right]/C_1$$

or

$$\lambda_2^2 = -\frac{9n^2\pi^2\beta^4}{2\{(\beta + n\pi)^2 - n^2\pi^2\}\{(\beta - n\pi)^2 - n^2\pi^2\}} \tag{30}$$

At this point, it is convenient to take the limit of λ_2^2 for extremely short roughness wavelength

$$\lim_{\beta \to \infty} \lambda_2^2 = -\frac{9}{2} n^2 \pi^2 \tag{31}$$

The solution for $P_2(x, y)$ then appears as

$$P_2 = [C_1 + \epsilon\hat{C}_1 + \epsilon^2\overline{C_2} + 0(\epsilon^3)]\sin(n\pi x) C_4 \cdot \cosh\left[\frac{L_y}{L_x}\left\{n\pi\left(1 - \frac{9}{2}\epsilon^2 + \ldots\right)^{1/2} y\right\}\right] + 0\left(\frac{1}{\beta}\right)$$

or

$$P_2 = \sum_{n=1}^{\infty} C_n \cosh\left\{\frac{L_y}{L_x} \cdot y \cdot n\pi\left[1 - \frac{9}{2}\epsilon^2 + \ldots\right]^{1/2}\right\} \sin(n\pi x) + 0\left(\frac{1}{\beta}\right) \tag{32}$$

Satisfaction of the final boundary condition along $y = 1$ requires

$$C_n = \frac{-2}{n\pi\cosh\left[n\pi\frac{L_y}{L_x}\left[1 - \frac{9}{2}\epsilon^2 + \ldots\right]^{1/2}\right]} \tag{33}$$

and the final expression for lubricant pressure is then given by

$$P=1-x-\frac{2}{\pi}\sum_{n=1}^{\infty}$$

$$\frac{\cosh\left[n\pi\frac{L_y}{L_x}y\left[1-\frac{9}{2}\epsilon^2+\ldots\right]^{1/2}\right]\sin(n\pi x)}{\cosh\left[n\pi\frac{L_y}{L_x}\left[1-\frac{9}{2}\epsilon^2+\ldots\right]^{1/2}\right]n}$$

$$+0\left(\frac{1}{\beta}\right) \tag{34}$$

A dimensionless load is expressed as

$$W=\int_o^1\int_o^1 P(x,y)dx\,dy=\frac{1}{2}-\frac{4}{\pi^3}$$

$$\sum_{n=\text{odd}}^{\infty}\frac{\sinh\left[n\pi\frac{L_y}{L_x}\left[1-\frac{9}{2}\epsilon^2+\ldots\right]^{1/2}\right]}{n^3\frac{L_y}{L_x}\left[1-\frac{9}{2}\epsilon^2+\ldots\right]^{1/2}\cosh\left[n\pi\frac{L_y}{L_x}\left[1-\frac{9}{2}\epsilon^2+\ldots\right]^{1/2}\right]}+0\left(\frac{1}{\beta}\right) \tag{35}$$

Transverse roughness influences the pressure distribution but only through the roughness statistics and is seen to decrease the load carrying capacity of this bearing. The details of the roughness appear only through the asymptotically small $0(1/\beta)$ terms. However, the pressure gradient in the direction of ripples ($\partial P/\partial x$) is a function of the roughness details (for the case of a sine wave roughness, the term "details" refers to the wavelength or β). This is because the x derivatives of asymptotically small terms such as $\cos[(\beta+n\pi)x]/\beta$ in equation (34) is of order unity. The y derivative of pressure is seen not to be a function of the roughness details, after examination of the terms contributing to the order 0 ($1/\beta$) expression.

The pressure boundary conditions used in this study were chosen to expedite the analytical solution, however, it is expected that any reasonable set of Dirichlet and Neumann boundary conditions would produce the statistical independence of h^3 and $\partial P/\partial y$ for transverse roughness. White (1980) showed that two different sets of transverse pressure boundary conditions for the very low clearance gas bearing with transverse roughness produce the same conclusion for the statistical dependence of pressure and clearance.

The fact that $\partial P/\partial y$ as calculated from equation (34) is independent of the roughness details then allowed an ensemble-averaged Reynolds equation to be developed. The ensemble-averaged Reynolds equation as derived by Christensen and Tϕnder (1969) for transverse roughness appears as

$$\frac{\partial}{\partial x}\left[\frac{1}{E(1/h^3)}\frac{\partial\bar{P}}{\partial x}\right]+\left(\frac{L_x}{L_y}\right)^2\frac{\partial}{\partial y}\left[E(h^3)\frac{\partial\bar{P}}{\partial y}\right]$$

$$=\Lambda\frac{\partial}{\partial x}\left[\frac{E(1/h^2)}{E(1/h^3)}\right] \tag{36}$$

where $\bar{P}$ represents the ensemble-averaged pressure and $E(\ )$ indicates the averaging process. Since the detailed solution for the parallel plate bearing (equation 34) is for practical purposes independent of roughness details, we would expect to recover the same solution from the ensemble-averaged equation (but with much less effort). To demonstrate this, consider the solution for P_2 given earlier and which appears as equations (32) and (33). The ensemble-averaged expressions appear as follows:

$$E\left(\frac{1}{h^2}\right)=1+\frac{3}{2}\epsilon^2+\ldots;\quad E\left(\frac{1}{h^3}\right)=1+3\epsilon^2+\ldots;$$

$$E(h^3)=1+\frac{3}{2}\epsilon^2$$

The ensemble averaged lubrication equation for the parallel plate bearing is then given by

$$\frac{\partial^2\bar{P}_2}{\partial x^2}+\left(\frac{L_x}{L_y}\right)^2\left(1+\frac{9}{2}\epsilon^2+\ldots\right)\frac{\partial^2\bar{P}_2}{\partial y^2}=0 \tag{37}$$

Boundary conditions are the same as before and appear as equations (8). A simple separation of variables solution to equation (37) provides

$$\bar{P}_2(x,y)=\sum_{n=1}^{\infty}C_n\cosh\left[\frac{L_y}{L_x}n\pi y\left(1-\frac{9}{4}\epsilon^2+\ldots\right)\right]\sin(n\pi x) \tag{38}$$

When the factor $(1-9/2\,\epsilon^2+\ldots)^{1/2}$ of equation (32) is expanded into series form, the results through second order are identical to those of equation (38). Therefore, the ensemble-averaged pressure solution due to the Christensen/Tϕnder theory is identical to the averaged exact solution. Also of interest is the fact that the solution of the ensemble-averaged lubrication equation is identical to the unaveraged exact solution to within the asymptotically small 0 ($1/\beta$) "roughness detail" terms.

From this exact solution of this parallel plate bearing, we see that the transverse pressure gradient is statistically independent of the details of h^3, thus satisfying the closure assumptions of the Christensen/Tϕnder theory. Since the influence of surface roughness on lubricant pressure is such a localized phenomenon, it is expected that the properties uncovered by this solution are universal and can be applied to all realistic bearing geometries.

Conclusions

By employing a finite-width parallel plate bearing with transverse sine wave roughness on the stationary surface, the unaveraged analytic solution for incompressible lubricant pressure was obtained by perturbation. The solution reveals that the pressure is influenced by the statistics (ϵ^2) of the roughness but is negligibly influenced by the roughness details (β). For the case of random surface roughness, this implies that the unaveraged pressure is affected by the variance of the roughness pattern but is only negligibly dependent on the precise description of the roughness over the surface. Because of the very localized influence of roughness on the fluid properties, it is fully expected that the characteristics observed for this case apply also to other bearings of realistic geometric contour. The closure assumption used by Christensen and Tϕnder in their early work on roughness effects in incompressible lubrication is thus shown to be valid.

The approach of using simple geometry exact analytic solutions of the unaveraged Reynolds equation to reveal the detailed relationship of pressure and transverse roughness has now been demontrated for both very low clearance gas films (White, 1980, 1983) and in the present work for incompressible lubricants. The fact that the present work confirms the validity of the widely accepted Christensen/Tϕnder theory for the incompressible case adds confidence to this approach. Analysis of the much more difficult case of fully three-dimensional roughness effects on incompressible fluid lubrication should also yield to this approach since the governing Reynolds equation is linear.

References

1 Christensen, H., and Tϕnder, K., 1969, "Tribilogy of Rough Surfaces. Stochastic Models of Hydrodynamic Lubrication," Report No. 10/69-18. SINTEF, Trondheim.

2 Christensen, H., 1969, "Stochastic Models for Hydrodynamic Lubrication of Rough Surfaces," *Proc. Instn. Mech. Engrs.*, Vol. 184, Part 1, pp. 1013–1025.

3 Christensen, H., and Tϕnder, K., 1971, "The Hydrodynamic Lubrication of Rough Bearing Surfaces of Finite Width," *ASME Journal of Lubrication Technology*, Vol. 93, pp. 324–330.

4 Elrod, H. G., 1973, "Thin-Film Lubrication Theory for Newtonian Fluids with Surfaces Possessing Striated Roughness or Grooving," *ASME Journal of Lubrication Technology*, Vol. 95, pp. 484–489.

5 Patir, N., and Cheng, H., 1978, "An Average Flow Model for Determining Effects of Three-Dimensional Roughness on Partial Lubrication," *ASME Journal of Lubrication Technology*, Vol. 100, pp. 12–17.

6 Tripp, J. H., 1983, "Surface Roughness Effects in Hydrodynamic Lubrication: The Flow Factor Method," *ASME Journal of Lubrication Technology*, Vol. 105,

7 White, J. W., 1980, "Surface Roughness Effects on the Load Carrying Capacity of Very Thin Compressible Lubricating Films," *ASME Journal of Lubrication Technology*, Vol. 102, pp. 445–451.

8 White, J. W., 1983, "The Effect of Two-Sided Surface Roughness on Ultra-Thin Gas Films," *ASME Journal of Lubrication Technology*, Vol. 105, pp. 131–137.

Journal of Applied Mechanics

Brief Notes

A Brief Note is a short paper that presents a specific solution of technical interest in mechanics but which does not necessarily contain new general methods or results. A Brief Note should not exceed 1500 words *or equivalent* (a typical one-column figure or table is equivalent to 250 words; a one line equation to 30 words). Brief Notes will be subject to the usual review procedures prior to publication. After approval such Notes will be published as soon as possible. The Notes should be submitted to the Technical Editor of the JOURNAL OF APPLIED MECHANICS. Discussions on the Brief Notes should be addressed to the Editorial Department, ASME, United Engineering Center, 345 East 47th Street, New York, N. Y. 10017, or to the Technical Editor of the JOURNAL OF APPLIED MECHANICS. Discussions on Brief Notes appearing in this issue will be accepted until two months after publication. Readers who need more time to prepare a Discussion should request an extension of the deadline from the Editorial Department.

On the Equivalence of the Incremental Harmonic Balance Method and the Harmonic Balance-Newton Raphson Method

A. A. Ferri[1]

Recently, the Incremental Harmonic Balance Method (IHB) has been applied to several problems in nonlinear dynamics; for example, Lau and Cheung (1981), Lau, Cheung, and Wu (1982), Pierre and Dowell (1985), and Pierre, Ferri, and Dowell (1985). The method possesses advantages in studying systems with severe nonlinearities and is easily applied to systems with harmonic (or, more generally, periodic) excitation. Some insight into the solution method is lost, however, since the problem of solving the original governing differential equations is replaced with that of solving a second, "simpler" set of equations involving increments in the motion, exciting force and/or frequency of excitation. Here it is shown that the IHB method is exactly equivalent to the Harmonic Balance Newton Raphson Method (HBNR); for example, Tamura, Tsuda, and Sueoka (1981), and Tongue (1984). By showing the equivalence of these two methods, it is felt that a better understanding of the IHB method is obtained.

A second order, ordinary, nonlinear differential equation of the following form is considered:

$$D(x,\dot{x},\ddot{x},\Omega,\tau)=F\cos\tau$$

or simply

$$f(x,\dot{x},\ddot{x},F,\Omega,\tau)=0 \tag{1}$$

Here $x=x(\tau)$ is the motion, or in general, the dependent variable; $\cdot$ indicates a derivative with respect to τ; F is the amplitude of harmonic forcing; and Ω represents a normalized frequency of excitation.

The unknowns in this equation may be x, F, or Ω or any combination thereof. For example, knowing F and Ω, $x(\tau)$ could be determined, or knowing the amplitude of x and F, Ω could be calculated. The solution of (1) can be taken to be $x^*(\tau),F^*,\Omega^*$.

The first step in applying the IHB method is to increment from some initial guess of the solution of (1) – x_o, F_o, Ω_o – to the actual solution – x^*, F^*, Ω^*. In other words, an increment in x, F, and Ω is sought which when added to the initial state, x_o, F_o, Ω_o, produces the desired solution to (1), x^*, F^*, Ω^*. Using Taylor series yields

$$\begin{aligned}&f(x_o+\Delta x,\dot{x}_o+\Delta\dot{x},\ddot{x}_o+\Delta\ddot{x},F_o+\Delta F,\Omega_o+\Delta\Omega,\tau)\\&=f_o+\frac{\partial f}{\partial x}\bigg|_o\Delta x+\frac{\partial f}{\partial\dot{x}}\bigg|_o\Delta\dot{x}+\frac{\partial f}{\partial\ddot{x}}\bigg|_o\Delta\ddot{x}+\frac{\partial f}{\partial F}\bigg|_o\Delta F\\&\quad+\frac{\partial f}{\partial\Omega}\bigg|_o\Delta\Omega\\&\quad+\text{Higher Order Terms}=0\end{aligned} \tag{2}$$

Neglecting Higher Order Terms (HOT) yields the incremental equation:

$$\begin{aligned}&f_o+\frac{\partial f}{\partial x}\bigg|_o\Delta x+\frac{\partial f}{\partial\dot{x}}\bigg|_o\Delta\dot{x}+\frac{\partial f}{\partial\ddot{x}}\bigg|_o\Delta\ddot{x}+\frac{\partial f}{\partial F}\bigg|_o\Delta F\\&\quad+\frac{\partial f}{\partial\Omega}\bigg|_o\Delta\Omega=0\end{aligned} \tag{3}$$

Note that since the derivative terms

$$\frac{\partial f}{\partial x}\bigg|_o,\frac{\partial f}{\partial\dot{x}}\bigg|_o,\frac{\partial f}{\partial\ddot{x}}\bigg|_o,\frac{\partial f}{\partial F}\bigg|_o\text{ and}\frac{\partial f}{\partial\Omega}\bigg|_o$$

are, in general, time varying, (3) represents a linear, second order, nonconstant coefficient, ordinary differential equation. Note also that as x_o, F_o, $\Omega_o\to x^*$, F^*, Ω^*, $f_o\to 0$.

An approximate solution is obtained for (3) by assuming periodic response and applying Galerkin's procedure. x is expanded in a finite Fourier series:

$$x=b_o+\sum_{i=1}^{N}(a_i\sin i\tau+b_i\cos i\tau) \tag{4}$$

Since (4) represents an expansion of x in terms of temporal harmonics, the Galerkin procedure will yield results identical to those found using the harmonic balance method. It should be noted that both the Galerkin and harmonic balance methods find *equilibrium* solutions. The stability and uniqueness of these solutions must be determined separately. In fact, stable periodic solutions for (1) need not exist.

The increment, Δx, is found to be

[1] Visiting Scholar, Duke University, Durham, NC 27706. Presently: Assistant Professor, School of Mechanical Engineering, Georgia Institute of Technology, Atlanta, GA 30332.

Manuscript received by ASME Applied Mechanics Division, December, 1984; final revision, September, 1985.

$$\Delta x = \frac{\partial x}{\partial b_o}\Delta b_o + \sum_{i=1}^{N}\frac{\partial x}{\partial a_i}\Delta a_i + \frac{\partial x}{\partial b_i}\Delta b_i$$

$$= \Delta b_o + \sum_{i=1}^{N}(\Delta a_i \sin i\tau + \Delta b_i \cos i\tau) \tag{5}$$

For simplicity, the constant or "bias" terms, b_o and Δb_o, will be neglected. Including them in the subsequent analysis is straightforward. Equations (4) and (5) are substituted into (3). Since they represent only approximate solutions for x and Δx, the right-hand side of (3) will not be zero, but some time varying quantity, $\epsilon(\tau)$. The Galerkin method requires that the increments Δa_i, Δb_i, ΔF, $\Delta\Omega$ be chosen so as to minimize $\epsilon(\tau)$, by making $\epsilon(\tau)$ orthogonal to each term in the expansion (4), i.e.,

$$\int_0^{2\pi}\epsilon(\tau)\begin{Bmatrix}\sin i\tau\\ \cos i\tau\end{Bmatrix}d\tau = 0 \quad i = 1,2\ldots,N \tag{6}$$

Equation (6) represents $2N$ algebraic linear equations in $\Delta\mathbf{a}$, ΔF, and $\Delta\Omega$ where $\Delta\mathbf{a} = [\Delta a_1, \Delta a_2, \ldots, \Delta a_N, \Delta b_1, \ldots, \Delta b_N]^T$. Equation (6) can be written in matrix form as

$$\mathbf{R} = \left[\begin{array}{c|c} C^{11} & C^{12} \\ \hline C^{21} & C^{22}\end{array}\right]\Delta\mathbf{a} + \begin{bmatrix}\mathbf{P}_1\\ \hline \mathbf{P}_2\end{bmatrix}\Delta F + \begin{bmatrix}\mathbf{Q}_1\\ \hline \mathbf{Q}_2\end{bmatrix}\Delta\Omega \tag{7}$$

or

$$\mathbf{R} = [C]\Delta\mathbf{a} + \mathbf{P}\Delta F + \mathbf{Q}\Delta\Omega \tag{8}$$

where

$$C_{ij}^{11} = \int_o^{2\pi}\left\{\frac{\partial f}{\partial x}\Big|_o \sin j\tau + \frac{\partial f}{\partial \dot{x}}\Big|_o j\cos j\tau - \frac{\partial f}{\partial \ddot{x}}\Big|_o j^2\sin j\tau\right\}\sin i\tau d\tau$$

$$C_{ij}^{12} = \int_o^{2\pi}\left\{\frac{\partial f}{\partial x}\Big|_o \cos j\tau - \frac{\partial f}{\partial \dot{x}}\Big|_o j\sin j\tau - \frac{\partial f}{\partial \ddot{x}}\Big|_o j^2\cos j\tau\right\}\sin i\tau d\tau$$

$$C_{ij}^{21} = \int_o^{2\pi}\left\{\frac{\partial f}{\partial x}\Big|_o \sin j\tau + \frac{\partial f}{\partial \dot{x}}\Big|_o j\cos j\tau - \frac{\partial f}{\partial \ddot{x}}\Big|_o j^2\sin j\tau\right\}\cos i\tau d\tau$$

$$C_{ij}^{22} = \int_o^{2\pi}\left\{\frac{\partial f}{\partial x}\Big|_o \cos j\tau - \frac{\partial f}{\partial \dot{x}}\Big|_o j\sin j\tau - \frac{\partial f}{\partial \ddot{x}}\Big|_o j^2\cos j\tau\right\}\cos i\tau d\tau$$

$$P_{1_i} = \int_o^{2\pi}\frac{\partial f}{\partial F}\Big|_o \sin i\tau d\tau \qquad P_{2_i} = \int_o^{2\pi}\frac{\partial f}{\partial F}\Big|_o \cos i\tau d\tau$$

$$Q_{1_i} = \int_o^{2\pi}\frac{\partial f}{\partial \Omega}\Big|_o \sin i\tau d\tau \qquad Q_{2_i} = \int_o^{2\pi}\frac{\partial f}{\partial \Omega}\Big|_o \cos i\tau d\tau$$

$$R_{1_i} = -\int_o^{2\pi} f_o \sin i\tau d\tau \qquad R_{2_i} = -\int_o^{2\pi} f_o \cos i\tau d\tau$$

Equation (8) defines an iterative solution algorithm for equation (2). After each iteration x_o, F_o, Ω_o are updated to $x_o + \Delta x$, $F_o + \Delta F$, $\Omega_o + \Delta\Omega$. Convergence is indicated by the magnitude of $\mathbf{R}$ since $\mathbf{R}\to\mathbf{O}$ as $x_o, F_o, \Omega_o \to x^*, F^*, \Omega^*$.

The HBNR method differs from IHB only in the order in which the Galerkin method and incrementation are applied. Here, the Galerkin method is applied first and incrementation (with subsequent removal of HOT) is performed second. Again, the objective is to solve (1):

$$f(x,\dot{x},\ddot{x},F,\Omega,\tau) = 0 \tag{9}$$

A multi-harmonic solution for x is assumed identical to (4) with constant term suppressed:

$$x = \sum_{i=1}^{N}(a_i \sin i\tau + b_i \cos i\tau) \tag{10}$$

Substituting (10) into (9) gives

$$\hat{f}(\mathbf{a},F,\Omega,\tau) = \epsilon(\tau) \tag{11}$$

where $\mathbf{a} = [a_1, a_2, \ldots, a_N, b_1, \ldots, b_N]^T$ and $\epsilon(\tau)$ is a time varying term which arises because (10) satisfies (9) only approximately.

Galerkin's method applied to (11) yields

$$\int_o^{2\pi}\epsilon(\tau)\begin{Bmatrix}\sin i\tau\\ \cos i\tau\end{Bmatrix}d\tau = 0 \quad i = 1,2,\ldots,N \tag{12}$$

or, in vector form,

$$\mathbf{G}(\mathbf{a},F,\Omega) = \begin{bmatrix}\mathbf{G}^s\\ \hline \mathbf{G}^c\end{bmatrix} = \mathbf{O} \tag{13}$$

where the elements of $\mathbf{G}$ are given by

$$G_i^s = \int_0^{2\pi}\epsilon(\tau)\sin i\tau d\tau$$

$$G_i^c = \int_0^{2\pi}\epsilon(\tau)\cos i\tau d\tau \tag{14}$$

From an initial state, $\mathbf{a}_o$, F_o, Ω_o, an incarement to the solution of (13) is sought, i.e., find $\Delta\mathbf{a}$, ΔF, $\Delta\Omega$ such that

$$\mathbf{G}(\mathbf{a}_o + \Delta\mathbf{a}, F_o + \Delta F, \Omega_o + \Delta\Omega) = \mathbf{G}_o + \frac{\partial\mathbf{G}}{\partial\mathbf{a}}\Big|_o \Delta\mathbf{a} + \frac{\partial\mathbf{G}}{\partial F}\Big|_o \Delta F + \frac{\partial\mathbf{G}}{\partial\Omega}\Big|_o \Delta\Omega + \text{HOT} = \mathbf{O} \tag{15}$$

Dropping HOT yields

$$-\mathbf{G}_o = \frac{\partial\mathbf{G}}{\partial\mathbf{a}}\Big|_o \Delta\mathbf{a} + \frac{\partial\mathbf{G}}{\partial F}\Big|_o \Delta F + \frac{\partial\mathbf{G}}{\partial\Omega}\Big|_o \Delta\Omega \tag{16}$$

Comparing (16) with (8), it is seen that in order for both methods to be exactly equivalent, it must be shown that

$$-\mathbf{G}_o = \mathbf{R}, \quad \frac{\partial\mathbf{G}}{\partial\mathbf{a}}\Big|_o = [C], \quad \frac{\partial\mathbf{G}}{\partial F}\Big|_o = \mathbf{P}, \quad \frac{\partial\mathbf{G}}{\partial\Omega}\Big|_o = \mathbf{Q}$$

These terms can be compared one by one:

$$\text{(I)} \quad \mathbf{G}_o = \begin{bmatrix}\mathbf{G}^s\\ \hline \mathbf{G}^c\end{bmatrix}_o = \frac{\displaystyle\int_o^{2\pi}\hat{f}(\mathbf{a}_o,F_o,\Omega_o,\tau)\begin{Bmatrix}\vdots\\ \sin i\tau\\ \vdots\end{Bmatrix}d\tau}{\displaystyle\int_o^{2\pi}\hat{f}(\mathbf{a}_o,F_o,\Omega_o,\tau)\begin{Bmatrix}\vdots\\ \cos i\tau\\ \vdots\end{Bmatrix}d\tau}$$

$$= \frac{\int_o^{2\pi} f_o \begin{Bmatrix} \vdots \\ \sin i\tau \\ \vdots \end{Bmatrix} d\tau}{\int_o^{2\pi} f_o \begin{Bmatrix} \vdots \\ \cos i\tau \\ \vdots \end{Bmatrix} d\tau} = -\mathbf{R}$$

(II) $$\left.\frac{\partial \mathbf{G}}{\partial \mathbf{a}}\right|_o = \left[\begin{array}{c|c} G^{11} & G^{12} \\ \hline G^{21} & G^{22} \end{array}\right]$$

(II) $$G_{ij}^{11} = \left.\frac{\partial G_i^s}{\partial a_j}\right|_o ; G_{ij}^{12} = \left.\frac{\partial G_i^s}{\partial b_j}\right|_o ; G_{ij}^{21} = \left.\frac{\partial G_i^c}{\partial a_j}\right|_o ;$$

$$G_{ij}^{22} = \left.\frac{\partial G_i^c}{\partial b_j}\right|_o$$

$$G_{ij}^{11} = \left.\frac{\partial}{\partial a_j}\int_o^{2\pi} \hat{f}(\mathbf{a},F,\Omega,\tau)\sin i\tau d\tau\right|_o$$

$$= \left.\frac{\partial}{\partial a_j}\int_o^{2\pi} f\Big(x = \sum_{i=1}^{N}(a_i \sin i\tau + b_i \cos i\tau),\right.$$

$$\left.\dot{x} = \sum_{i=1}^{N}(a_i i\cos i\tau - b_i i\sin i\tau), \ldots\Big)\sin i\tau d\tau\right|_o$$

$$= \int_o^{2\pi}\left\{\frac{\partial f}{\partial x}\frac{\partial x}{\partial a_j} + \frac{\partial f}{\partial \dot{x}}\frac{\partial \dot{x}}{\partial a_j}\right.$$

$$\left. + \frac{\partial f}{\partial \ddot{x}}\frac{\partial \ddot{x}}{\partial a_j}\right\}\sin i\tau \, d\tau\Big|_o$$

$$= \int_o^{2\pi}\left\{\left.\frac{\partial f}{\partial x}\right|_o \sin j\tau + \left.\frac{\partial f}{\partial \dot{x}}\right|_o j\cos j\tau\right.$$

$$\left. - \left.\frac{\partial f}{\partial \ddot{x}}\right|_o j^2 \sin j\tau\right\}\sin i\tau d\tau = C_{ij}^{11}$$

Similarly, it is found that $G^{12} = C^{12}$, $G^{21} = C^{21}$, $G^{22} = C^{22}$ or

$$\left.\frac{\partial \mathbf{G}}{\partial \mathbf{a}}\right|_o = [\mathbf{C}]$$

(III and IV)

$$\left.\frac{\partial \mathbf{G}}{\partial F}\right|_o = \left[\begin{array}{c} \dfrac{\partial \mathbf{G}^s}{\partial F} \\ \hline \dfrac{\partial \mathbf{G}^c}{\partial F} \end{array}\right]_o$$

$$\left.\frac{\partial G_i^s}{\partial F}\right|_o = \left.\frac{\partial}{\partial F}\int_o^{2\pi} f\Big(x = \sum \ldots, \dot{x} = \sum \ldots, \ddot{x}\right.$$

$$\left. = \sum \ldots, F, \Omega, \tau\Big)\sin i\tau d\tau\right.$$

$$= \left.\int_o^{2\pi} \frac{\partial f}{\partial F}\right|_o \sin i\tau d\tau = P_{1_i}$$

Similarly, $\left.\frac{\partial G_i^c}{\partial F}\right|_o = P_{2_i}, \left.\frac{\partial G_i^s}{\partial \Omega}\right|_o = Q_{1_i}, \left.\frac{\partial G_i^c}{\partial \Omega}\right|_o = Q_{2_i}$

or

$$\left.\frac{\partial \mathbf{G}}{\partial F}\right|_o = \mathbf{P} \text{ and } \left.\frac{\partial \mathbf{G}}{\partial \Omega}\right|_o = \mathbf{Q}$$

Therefore, both the IHB and HBNR methods produce the same linear system of equations (8) and (16). Both systems must be solved iteratively. As mentioned previously, iteration continues until x_o, F_o, and Ω_o, or $\mathbf{a}_o$, F_o, Ω_o produce acceptably small elements in the vectors $\mathbf{R}$ or $\mathbf{G}_o$. In practice, we might minimize the vector norm of $\mathbf{R}$ or $\mathbf{G}_o$, or perhaps the maximum element of $\mathbf{R}$ or $\mathbf{G}_o$.

In some cases, the expansion in (2) is easier to perform than the expansion in (15) since the chain rule must be used to evaluate $\partial \mathbf{G}/\partial \mathbf{a}|_o$. In those cases, (8) would be easier to generate than (16) and the IHB method would have a slight advantage over the HBNR method. The equivalence of the two methods provides a better understanding of the solution mechanism of the IHB method.

Acknowledgment

This work was supported by NASA Lewis Research Center, Grant No. NAG3-516. Mr. Gerald Brown is the technical monitor. The author is grateful to Professor Earl Dowell and Christophe Pierre for their helpful comments and suggestions.

References

Lau, S. L., and Cheung, Y. K., 1981, "Amplitude Incremental Variational Principle for Nonlinear Vibration of Elastic Systems," ASME JOURNAL OF APPLIED MECHANICS, Vol. 48, pp. 959–964.

Lau, S. L., Cheung, Y. K., and Wu, S. Y., 1982, "A Variable Parameter Incrementation Method for Dynamic Instability of Linear and Nonlinear Elastic Systems," ASME JOURNAL OF APPLIED MECHANICS, Vol. 49, pp. 849–853.

Pierre, C. and Dowell, E. H., 1985, "A Study of Dynamic Instability of Plates by an Extended Incremental Harmonic Balance Method," ASME JOURNAL OF APPLIED MECHANICS, Vol. 52, pp. 693–697.

Pierre, C., Ferri, A. A., and Dowell, E. H., 1985, "Multi-Harmonic Analysis of Dry Friction Damped Systems Using an Incremental Harmonic Balance Method," ASME JOURNAL OF APPLIED MECHANICS, Vol. 52, pp. 958–964.

Tamura, H., Tsuda, Y., and Sueoka, A., 1981, "Higher Approximation of Steady Oscillations in Nonlinear Systems with Single Degree of Freedom (Suggested Multi-Harmonic Balance Method)," *Bulletin of the JSME*, Vol. 24, No. 195, pp. 1616–1625.

Tongue, B. H., 1984, "Limit Cycle Oscillations of a Nonlinear Rotorcraft Model," *AIAA Journal*, Vol. 22, No. 7, pp. 967–974.

On the Relation Between Kinematic Mappings of Planar and Spherical Displacements

J. M. McCarthy[1]

Kinematic mappings, which transform the parameters specifying a rigid displacement into a point in a higher dimensional space, have been the focus of recent study for the purpose of classifying rigid motion, aiding mechanism design, and automating robot task planning. Presented here is the procedure which demonstrates that the particular mapping introduced by Blaschke and Müller (1956) to study planar kinematics, and used subsequently by other researchers, is a limiting case of a mapping based on the Euler parameters of an orthogonal matrix used by Ravani (1982) for spherical kinematics.

Introduction

The *planar displacement* of rigid body is represented by the

[1]Department of Mechanical Engineering and Applied Mechanics, University of Pennsylvania, Philadelphia, PA 19104.

Manuscript received by ASME Applied Mechanics Division, June, 1985; final revision, October, 1985.

$$= \frac{\int_o^{2\pi} f_o \begin{Bmatrix} \vdots \\ \sin i\tau \\ \vdots \end{Bmatrix} d\tau}{\int_o^{2\pi} f_o \begin{Bmatrix} \vdots \\ \cos i\tau \\ \vdots \end{Bmatrix} d\tau} = -\mathbf{R}$$

(II) $$\left.\frac{\partial \mathbf{G}}{\partial \mathbf{a}}\right|_o = \left[\begin{array}{c|c} G^{11} & G^{12} \\ \hline G^{21} & G^{22} \end{array}\right]$$

(II) $$G_{ij}^{11} = \left.\frac{\partial G_i^s}{\partial a_j}\right|_o ; G_{ij}^{12} = \left.\frac{\partial G_i^s}{\partial b_j}\right|_o ; G_{ij}^{21} = \left.\frac{\partial G_i^c}{\partial a_j}\right|_o ;$$

$$G_{ij}^{22} = \left.\frac{\partial G_i^c}{\partial b_j}\right|_o$$

$$G_{ij}^{11} = \left.\frac{\partial}{\partial a_j}\int_o^{2\pi} \hat{f}(\mathbf{a},F,\Omega,\tau)\sin i\tau d\tau\right|_o$$

$$= \left.\frac{\partial}{\partial a_j}\int_o^{2\pi} f\Big(x = \sum_{i=1}^{N}(a_i\sin i\tau + b_i\cos i\tau),$$

$$\dot{x} = \sum_{i=1}^{N}(a_i i\cos i\tau - b_i i\sin i\tau), \ldots\Big)\sin i\tau d\tau\right|_o$$

$$= \int_o^{2\pi}\left\{\frac{\partial f}{\partial x}\frac{\partial x}{\partial a_j} + \frac{\partial f}{\partial \dot{x}}\frac{\partial \dot{x}}{\partial a_j}\right.$$

$$\left. + \frac{\partial f}{\partial \ddot{x}}\frac{\partial \ddot{x}}{\partial a_j}\right\}\sin i\tau\, d\tau\Big|_o$$

$$= \int_o^{2\pi}\left\{\left.\frac{\partial f}{\partial x}\right|_o \sin j\tau + \left.\frac{\partial f}{\partial \dot{x}}\right|_o j\cos j\tau\right.$$

$$\left. - \left.\frac{\partial f}{\partial \ddot{x}}\right|_o j^2\sin j\tau\right\}\sin i\tau d\tau = C_{ij}^{11}$$

Similarly, it is found that $G^{12} = C^{12}$, $G^{21} = C^{21}$, $G^{22} = C^{22}$ or

$$\left.\frac{\partial \mathbf{G}}{\partial \mathbf{a}}\right|_o = [\mathbf{C}]$$

(III and IV)

$$\left.\frac{\partial \mathbf{G}}{\partial F}\right|_o = \left[\begin{array}{c} \dfrac{\partial \mathbf{G}^s}{\partial F} \\ \hline \dfrac{\partial \mathbf{G}^c}{\partial F} \end{array}\right]_o$$

$$\left.\frac{\partial G_i^s}{\partial F}\right|_o = \frac{\partial}{\partial F}\int_o^{2\pi} f\Big(x = \sum \ldots, \dot{x} = \sum \ldots, \ddot{x}$$

$$= \sum \ldots, F, \Omega, \tau\Big)\sin i\tau d\tau$$

$$= \int_o^{2\pi}\left.\frac{\partial f}{\partial F}\right|_o \sin i\tau d\tau = P_{1_i}$$

Similarly, $\left.\frac{\partial G_i^c}{\partial F}\right|_o = P_{2_i}, \left.\frac{\partial G_i^s}{\partial \Omega}\right|_o = Q_{1_i}, \left.\frac{\partial G_i^c}{\partial \Omega}\right|_o = Q_{2_i}$

or

$$\left.\frac{\partial \mathbf{G}}{\partial F}\right|_o = \mathbf{P} \text{ and } \left.\frac{\partial \mathbf{G}}{\partial \Omega}\right|_o = \mathbf{Q}$$

Therefore, both the IHB and HBNR methods produce the same linear system of equations (8) and (16). Both systems must be solved iteratively. As mentioned previously, iteration continues until x_o, F_o, and Ω_o, or $\mathbf{a}_o$, F_o, Ω_o produce acceptably small elements in the vectors $\mathbf{R}$ or $\mathbf{G}_o$. In practice, we might minimize the vector norm of $\mathbf{R}$ or $\mathbf{G}_o$, or perhaps the maximum element of $\mathbf{R}$ or $\mathbf{G}_o$.

In some cases, the expansion in (2) is easier to perform than the expansion in (15) since the chain rule must be used to evaluate $\partial \mathbf{G}/\partial \mathbf{a}|_o$. In those cases, (8) would be easier to generate than (16) and the IHB method would have a slight advantage over the HBNR method. The equivalence of the two methods provides a better understanding of the solution mechanism of the IHB method.

Acknowledgment

This work was supported by NASA Lewis Research Center, Grant No. NAG3-516. Mr. Gerald Brown is the technical monitor. The author is grateful to Professor Earl Dowell and Christophe Pierre for their helpful comments and suggestions.

References

Lau, S. L., and Cheung, Y. K., 1981, "Amplitude Incremental Variational Principle for Nonlinear Vibration of Elastic Systems," ASME JOURNAL OF APPLIED MECHANICS, Vol. 48, pp. 959–964.

Lau, S. L., Cheung, Y. K., and Wu, S. Y., 1982, "A Variable Parameter Incrementation Method for Dynamic Instability of Linear and Nonlinear Elastic Systems," ASME JOURNAL OF APPLIED MECHANICS, Vol. 49, pp. 849–853.

Pierre, C. and Dowell, E. H., 1985, "A Study of Dynamic Instability of Plates by an Extended Incremental Harmonic Balance Method," ASME JOURNAL OF APPLIED MECHANICS, Vol. 52, pp. 693–697.

Pierre, C., Ferri, A. A., and Dowell, E. H., 1985, "Multi-Harmonic Analysis of Dry Friction Damped Systems Using an Incremental Harmonic Balance Method," ASME JOURNAL OF APPLIED MECHANICS, Vol. 52, pp. 958–964.

Tamura, H., Tsuda, Y., and Sueoka, A., 1981, "Higher Approximation of Steady Oscillations in Nonlinear Systems with Single Degree of Freedom (Suggested Multi-Harmonic Balance Method)," *Bulletin of the JSME*, Vol. 24, No. 195, pp. 1616–1625.

Tongue, B. H., 1984, "Limit Cycle Oscillations of a Nonlinear Rotorcraft Model," *AIAA Journal*, Vol. 22, No. 7, pp. 967–974.

On the Relation Between Kinematic Mappings of Planar and Spherical Displacements

J. M. McCarthy[1]

Kinematic mappings, which transform the parameters specifying a rigid displacement into a point in a higher dimensional space, have been the focus of recent study for the purpose of classifying rigid motion, aiding mechanism design, and automating robot task planning. Presented here is the procedure which demonstrates that the particular mapping introduced by Blaschke and Müller (1956) to study planar kinematics, and used subsequently by other researchers, is a limiting case of a mapping based on the Euler parameters of an orthogonal matrix used by Ravani (1982) for spherical kinematics.

Introduction

The *planar displacement* of rigid body is represented by the

[1]Department of Mechanical Engineering and Applied Mechanics, University of Pennsylvania, Philadelphia, PA 19104.

Manuscript received by ASME Applied Mechanics Division, June, 1985; final revision, October, 1985.

coordinate transformation equation which relates points in a displaced reference frame M to those in a fixed reference frame F, given by

$$\begin{bmatrix} X \\ Y \end{bmatrix} = \begin{bmatrix} \cos\theta & -\sin\theta \\ \sin\theta & \cos\theta \end{bmatrix} \begin{bmatrix} x \\ y \end{bmatrix} + \begin{bmatrix} a \\ b \end{bmatrix}. \quad (1)$$

The coordinate vectors $\mathbf{X} = (X, Y)$, and $\mathbf{x} = (x, y)$ represents points in the planar reference frames F and M, respectively. The parameters θ, a, and b specify a particular planar displacement of M relative to F. The triples $\mathbf{D} = (a, b, \theta)$ are considered points in a three-dimensional *configuration space* (Lozano-Perez and Wesley, 1979). Blaschke and Müller (1956) introduced a mapping of this configuration space to a three-dimensional projective space to facilitate the study of planar kinematics (see also DeSa and Roth, 1981).

In a similar way the rotation in space of a rigid body about a fixed point, termed a *spherical displacement*, is represented by a coordinate transformation between three dimensional reference frames M and F:

$$\begin{Bmatrix} X \\ Y \\ Z \end{Bmatrix} = \begin{bmatrix} a_{11} & a_{12} & a_{13} \\ a_{21} & a_{22} & a_{23} \\ a_{31} & a_{32} & a_{33} \end{bmatrix} \begin{Bmatrix} x \\ y \\ z \end{Bmatrix}. \quad (2)$$

The vectors $\mathbf{X} = (X, Y, Z)$ and $\mathbf{x} = (x, y, z)$ represents points in F and M, respectively. The matrix $[A] = a_{ij}$, $i, it = 1, 2, 3$, is orthogonal and depends on three parameters. There are many ways to choose these parameters, we use the following form for $[A]$:

$$[A] = \begin{bmatrix} \cos\alpha & 0 & \sin\alpha \\ 0 & 1 & 0 \\ -\sin\alpha & 0 & \cos\alpha \end{bmatrix} \begin{bmatrix} 1 & 0 & 0 \\ 0 & \cos\beta & \sin\beta \\ 0 & -\sin\beta & \cos\beta \end{bmatrix} \begin{bmatrix} \cos\theta & -\sin\theta & 0 \\ \sin\theta & \cos\theta & 0 \\ 0 & 0 & 1 \end{bmatrix}. \quad (3)$$

from which we see a spherical displacement may be represented as the triple $\mathbf{S} = (\alpha, \beta, \theta)$. Ravani (1982) used the Euler parameters of an orthogonal matrix to define a mapping of the matrix to a three-dimensional projective space to study spherical kinematics (see also Ravani and Roth, 1984, and McCarthy and Ravani, 1985).

Here we show that the Euler parameters of $[A]$ define a map on the set of triples $\mathbf{S}$ which becomes the mapping of Blaschke and Müller in the limit of small angular displacements α and β. The device we use consists of replacing the angular measures by the ratio of arc-length along the surface of a sphere to its radius. As the radius of the sphere is increased a finite region of the sphere in the vicinity of the Z-axis shrinks in angular measure and its geometry approaches that of the tangent plane at the point the Z-axis pierces the sphere (see McCarthy, 1983).

Blaschke's Mapping

Following Bottema and Roth (1979) we define Blaschke's mapping of the displacement $\mathbf{D}$ to a three-dimensional projective space as given by the four dimensional homogeneous vector function $\mathbf{X}(a, b, \theta) = (X_1, X_2, X_3, X_4)$, where

$$X_1 = x_p\tan(\theta/2),\ X_2 = y_p\tan(\theta/2),\ X_3 = \tan(\theta/2),\ X_4 = 1. \quad (4)$$

The point $\mathbf{x}_p = (x_p, y_p)$ is the *pole of the displacement* $\mathbf{D}$, and is given by

$$x_p = (a\sin(\theta/2) - b\cos(\theta/2))/(2\sin(\theta/2)),$$
$$y_p = (a\cos(\theta/2) + b\sin(\theta/2))/(2\sin(\theta/2)). \quad (5)$$

Substituting (5) into (4) and multiplying each of the components by $\cos(\theta/2)$ we obtain the desired map

$$X_1 = (a\sin(\theta/2) - b\cos(\theta/2))/2,$$
$$X_2 = (a\cos(\theta/2) + b\sin(\theta/2))/2,$$
$$X_3 = \sin(\theta/2),$$
$$X_4 = \cos(\theta/2). \quad (6)$$

Euler Parameters

The Euler parameters of an orthogonal matrix can be defined (see Bottema and Roth, 1979) as the set of four homogenous parameters c_0, c_1, c_2, and c_3 given by

$$c_0 = s_x\sin(\varphi/2),\ c_1 = s_y\sin(\varphi/2),\ c_2 = s_z\sin(\varphi/2),\ c_3 = \cos(\varphi/2). \quad (7)$$

The vector $\mathbf{s} = (s_x, s_y, s_z)$ is the axis of the rotational displacement represented by $[A]$ and φ is the rotation angle about $\mathbf{s}$ which carries the reference frame F into M. $\mathbf{s}$ and φ are obtained from the components a_{ij}, $i, j = 1, 2, 3$, of $[A]$ by the following relations

$$\varphi = \arccos\{(a_{11} + a_{22} + a_{33} - 1)/2\}, \quad (8a)$$

and

$$s_x = (a_{32} - a_{23})/(2\sin\varphi),$$
$$s_y = (a_{13} - a_{31})/(2\sin\varphi),$$
$$s_z = (a_{21} - a_{12})/(2\sin\varphi). \quad (8b)$$

By choosing the set of angles $\mathbf{S} = (\alpha, \beta, \theta)$ given in equation (3) to specify an orthogonal matrix, we obtain a standard form for $[A]$

$$[A] = \begin{bmatrix} c\alpha c\theta - s\alpha s\beta s\theta & -c\alpha s\theta - s\alpha s\beta c\theta & s\alpha c\beta \\ c\beta s\theta & c\beta c\theta & s\beta \\ -s\alpha c\theta - c\alpha s\beta s\theta & s\alpha s\theta - c\alpha s\beta c\theta & c\alpha c\beta \end{bmatrix}. \quad (9)$$

where s and c represent the sine and cosine functions. Substituting the elements of this matrix (9) into (8) we obtain

$$\varphi = \arccos\{(c\alpha c\theta - s\alpha s\beta s\theta + c\beta c\theta + c\alpha c\beta - 1)/2\} \quad (10a)$$

and

$$s_x = (s\alpha s\theta - c\alpha s\beta c\theta - s\beta)/(2\sin\varphi),$$
$$s_y = (s\alpha c\beta + s\alpha c\theta + c\alpha s\beta s\theta)/(2\sin\varphi),$$
$$s_z = (c\beta s\theta + c\alpha s\theta + s\alpha s\beta c\theta)/(2\sin\varphi). \quad (10b)$$

Substitute (10) into (7) and replace $\sin\varphi$ by $2\sin(\varphi/2)\cos(\varphi/2)$ to obtain a mapping of the spherical displacement $\mathbf{S} = (\alpha, \beta, \theta)$ to a point in a three-dimensional projective space which is an explicit form of that used by Ravani (1982). We write it as $\mathbf{X}(\alpha, \beta, \theta) = (X_1, X_2, X_3, X_4) = (c_1, c_2, c_3, c_0)$, where

$$X_1 = (s\alpha s\theta - c\alpha s\beta c\theta - s\beta)/(4c(\varphi/2)),$$
$$X_2 = (s\alpha c\beta + s\alpha c\theta + c\alpha s\beta s\theta)/(4(c\varphi/2)),$$
$$X_3 = (c\beta s\theta + c\alpha s\theta + s\alpha s\beta c\theta)/(4c(\varphi/2)),$$
$$X_4 = c(\varphi/2), \quad (11)$$

note φ is defined by (10a).

Small Displacements on a Sphere

Before exhibiting Blaschke's mapping (6) as a limiting case of (11) we demonstrate the procedure by showing how (1) is obtained as a limiting case of (2). Introduce the arc-lengths $\tilde{a}$ and $\tilde{b}$ measured along a sphere of radius R and replace the angles α and β in (3) by the expressions

$$\alpha = \tilde{a}/R, \quad \text{and} \quad \beta = \tilde{b}/R. \quad (12)$$

α and β are the yaw and pitch angles of the attitude of the reference frame M relative to F.

Now introduce the angles $\xi = \tilde{x}/R$ and $\eta = \tilde{y}/r$ as the spherical coordinates for $\mathbf{x}$ in M, defined in the same way as α and β, so we have:

$$\mathbf{x} = (R\sin\xi\cos\eta,\ R\sin\eta,\ R\cos\xi\cos\eta),$$

$$\text{or}\quad \mathbf{x} = (R\sin(\tilde{x}/R)\cos(\tilde{y}/R),\ R\sin(\tilde{y}/R),\ R\cos(\tilde{x}/R)\cos(\tilde{y}/r)), \tag{13}$$

$\tilde{x}$ and $\tilde{y}$ are arc-lengths measured along the surface of a sphere of radius R.

Substitute (12) and (13) into (2) and compute the series expansions of the sine and cosine functions to obtain

$$\begin{Bmatrix} X \\ Y \\ Z \end{Bmatrix} = \begin{bmatrix} \cos\theta & -\sin\theta & \tilde{a}/R \\ \sin\theta & \cos\theta & \tilde{b}/R \\ 0 & 0 & 1 \end{bmatrix} \begin{Bmatrix} \tilde{x} \\ \tilde{y} \\ R \end{Bmatrix} + (1/R)$$

$$\begin{bmatrix} 0 & 0 & 0 \\ 0 & 0 & 0 \\ (-\tilde{a}\cos\theta + \tilde{b}\sin\theta) & (\tilde{a}\sin\theta + \tilde{b}\cos\theta) & -(\tilde{a}^2 + \tilde{b}^2)/R \end{bmatrix} \begin{Bmatrix} \tilde{x} \\ \tilde{y} \\ R \end{Bmatrix} + O(1/R^2). \tag{14}$$

The zeroth order term in (14) is the equation of a planar displacement in the $Z = R$ plane, parallel to the $X-Y$ coordinate plane of F. Also notice that the first order term consists only of a component in the Z direction. We conclude that the planar displacement (1) is the limiting case of the spherical displacement (2) for which the angles α, β, ξ and η are small such that the terms $\alpha^2 = (\tilde{a}/R)^2$, $\beta^2 = (\tilde{b}/R)^2$, $\xi^2 = (\tilde{x}/R)^2$ and $\eta^2 = (\tilde{y}/R)^2$ are negligible.

Blaschke's mapping is obtained as a limiting case of (11) by following the same procedure. Substitute $\alpha = \tilde{a}/R$ and $\beta = \tilde{b}/R$ into (11), compute the series expansion of the sine and cosine functions, and collect terms in $1/R$. The result is

$$X_1 = (\tilde{a}\sin(\theta/2) - \tilde{b}\cos(\theta/2))/2R + O(1/R^3),$$

$$X_2 = (\tilde{a}\cos(\theta/2) + \tilde{b}\sin(\theta/2))/2R + O(1/R^3),$$

$$X_3 = \sin(\theta/2) + O(1/R^2),$$

$$X_4 = \cos(\theta/2) + O(1/R^2). \tag{15}$$

These computations were facilitated using the symbolic computation software MACSYMA. The similarities between (15) and (6) are clear and we conclude that Blaschke's map is the limiting case of Ravani's for which the terms $\alpha^2 = (\tilde{a}/R)^2$ and $\beta^2 = (\tilde{b}/R)^2$ are negligible.

Conclusion

This note demonstrates that Blaschke's map of planar displacements is closely related to Ravani's map of spherical displacements which is based on Euler parameters. This result is of interest because it suggests a way to extend recent results on the differential geometry of the image space of spherical kinematics under Ravani's map (McCarthy and Ravani, 1985) to the image space of planar kinematics under Blaschke's map.

References

Blaschke, W., and Müller, H. R., 1956, *Ebene Kinematik*, R. Oldenbourg Verlag, Munich.

Bottema, O., and Roth, B., 1979, *Theoretical Kinematics*, North-Holland, New York.

DeSa, S., and Roth, B., 1981, "Kinematic Mappings, Part 1: Classification of Algebraic Motions in the Plane," ASME *Journal of Mechanical Design*, Vol. 103, No. 3, pp. 585–591.

Lozano-Perez, T., 1981, "Automatic Planning of Manipulator Transfer Movements," *IEEE Trans. on Systems, Man, and Cybernetics*, Vol. SMC-11, No. 10.

McCarthy, J. M., 1983, "Planar and Spatial Rigid Body Motion as Special Cases of Spherical and 3-Spherical Motion," ASME *Journal of Mechanisms, Transmissions, and Automation in Design*, Vol. 105, No. 3, pp. 569–575.

McCarthy, J. M., and Ravani, B., 1985, "Differential Kinematics of Spherical and Spatial Motions Using Kinematic Mapping," accepted for publication, ASME JOURNAL OF APPLIED MECHANICS.

Ravani, B., 1982, "Kinematic Mapping Applied to Motion Approximation and Mechanism Synthesis," doctoral dissertation, Stanford University, Calif.

Ravani, B., and Roth, B., 1984, "Mappings of Spatial Kinematics," ASME *Journal of Mechanisms, Transmissions, and Automation in Design*, Vol. 106, pp. 341–347.

Stress Singularity at the Tip of a Rigid Line Inhomogeneity Under Antiplane Shear Loading

Z. Y. Wang,[1] H. T. Zhang,[1] and Y. T. Chou[1]

1 Introduction

It has been shown (Chou and Wang, 1983; Wang et al., 1985) that under an inplane tensile loading, a plane elastic body containing a rigid line inhomogeneity would generate a square-root stress singularity at the tip of the line segment, a situation similar to the case of a slit crack (Broek, 1982). However, if the applied stress is an inplane shear, the inhomogeneity and the matrix become elastically compatible and no stress singularity exists, which is different from the case of a crack.

In the present work we investigate a similar inhomogeneity system in which the applied stress is an antiplane shear. This system is analyzed by two different methods: the complex variable method of Muskhelishvili and the equivalent inclusion method of Eshelby. The present analysis, together with the analysis reported earlier for the inplane elastic system (Chou and Wang, 1983; Wang et al., 1985), thus provides a complete description for the rigid line inhomogeneity problem in plane elasticity.

2 Analysis

We consider an antiplane strain deformation in which a rigid flat inhomogeneity of width $2a$ is embedded in an infinite elastic body along the x axis of a Cartesian coordinate system xyz (Fig. 1). The dependent variables of the system are the displacement $u_z(x,y)$ and the stress components σ_{xz} and σ_{yz}, related by

$$\sigma_{xz} = G\frac{\partial u_z}{\partial x},\ \sigma_{yz} = G\frac{\partial u_z}{\partial y} \tag{1}$$

where G is the shear modulus of the matrix. Under the condition of equilibrium, the governing partial differential equation is

$$\frac{\partial^2 u_z}{\partial x^2} + \frac{\partial^2 u_z}{\partial y^2} = 0 \tag{2}$$

with the boundary conditions

$$u_z = 0 \quad \text{for } -a \leqq x \leqq a \text{ and } y = 0 \tag{3}$$

and

$$\sigma_{xz} = \sigma_{xz}^A,\ \sigma_{yz} = \sigma_{yz}^A \quad \text{at infinity} \tag{4}$$

where σ_{xz}^A and σ_{yz}^A are the uniform applied stresses. Equation (2) can be solved according to the position of the loading.

[1]Department of Metallurgy and Materials Engineering, Lehigh University, Bethlehem, PA 18015.

Manuscript received by ASME Applied Mechanics Division, August, 1985; final revision, October, 1985.

α and β are the yaw and pitch angles of the attitude of the reference frame M relative to F.

Now introduce the angles $\xi = \tilde{x}/R$ and $\eta = \tilde{y}/r$ as the spherical coordinates for $\mathbf{x}$ in M, defined in the same way as α and β, so we have:

$$\mathbf{x} = (R\sin\xi\cos\eta,\ R\sin\eta,\ R\cos\xi\cos\eta),$$

$$\text{or}\quad \mathbf{x} = (R\sin(\tilde{x}/R)\cos(\tilde{y}/R),\ R\sin(\tilde{y}/R),\ R\cos(\tilde{x}/R)\cos(\tilde{y}/r)), \tag{13}$$

$\tilde{x}$ and $\tilde{y}$ are arc-lengths measured along the surface of a sphere of radius R.

Substitute (12) and (13) into (2) and compute the series expansions of the sine and cosine functions to obtain

$$\begin{Bmatrix} X \\ Y \\ Z \end{Bmatrix} = \begin{bmatrix} \cos\theta & -\sin\theta & \tilde{a}/R \\ \sin\theta & \cos\theta & \tilde{b}/R \\ 0 & 0 & 1 \end{bmatrix} \begin{Bmatrix} \tilde{x} \\ \tilde{y} \\ R \end{Bmatrix} + (1/R)$$

$$\begin{bmatrix} 0 & 0 & 0 \\ 0 & 0 & 0 \\ (-\tilde{a}\cos\theta + \tilde{b}\sin\theta) & (\tilde{a}\sin\theta + \tilde{b}\cos\theta) & -(\tilde{a}^2 + \tilde{b}^2)/R \end{bmatrix} \begin{Bmatrix} \tilde{x} \\ \tilde{y} \\ R \end{Bmatrix} + O(1/R^2). \tag{14}$$

The zeroth order term in (14) is the equation of a planar displacement in the $Z = R$ plane, parallel to the $X-Y$ coordinate plane of F. Also notice that the first order term consists only of a component in the Z direction. We conclude that the planar displacement (1) is the limiting case of the spherical displacement (2) for which the angles α, β, ξ and η are small such that the terms $\alpha^2 = (\tilde{a}/R)^2$, $\beta^2 = (\tilde{b}/R)^2$, $\xi^2 = (\tilde{x}/R)^2$ and $\eta^2 = (\tilde{y}/R)^2$ are negligible.

Blaschke's mapping is obtained as a limiting case of (11) by following the same procedure. Substitute $\alpha = \tilde{a}/R$ and $\beta = \tilde{b}/R$ into (11), compute the series expansion of the sine and cosine functions, and collect terms in $1/R$. The result is

$$X_1 = (\tilde{a}\sin(\theta/2) - \tilde{b}\cos(\theta/2))/2R + O(1/R^3),$$

$$X_2 = (\tilde{a}\cos(\theta/2) + \tilde{b}\sin(\theta/2))/2R + O(1/R^3),$$

$$X_3 = \sin(\theta/2) + O(1/R^2),$$

$$X_4 = \cos(\theta/2) + O(1/R^2). \tag{15}$$

These computations were facilitated using the symbolic computation software MACSYMA. The similarities between (15) and (6) are clear and we conclude that Blaschke's map is the limiting case of Ravani's for which the terms $\alpha^2 = (\tilde{a}/R)^2$ and $\beta^2 = (\tilde{b}/R)^2$ are negligible.

Conclusion

This note demonstrates that Blaschke's map of planar displacements is closely related to Ravani's map of spherical displacements which is based on Euler parameters. This result is of interest because it suggests a way to extend recent results on the differential geometry of the image space of spherical kinematics under Ravani's map (McCarthy and Ravani, 1985) to the image space of planar kinematics under Blaschke's map.

References

Blaschke, W., and Müller, H. R., 1956, *Ebene Kinematik*, R. Oldenbourg Verlag, Munich.

Bottema, O., and Roth, B., 1979, *Theoretical Kinematics*, North-Holland, New York.

DeSa, S., and Roth, B., 1981, "Kinematic Mappings, Part 1: Classification of Algebraic Motions in the Plane," ASME *Journal of Mechanical Design*, Vol. 103, No. 3, pp. 585–591.

Lozano-Perez, T., 1981, "Automatic Planning of Manipulator Transfer Movements," *IEEE Trans. on Systems, Man, and Cybernetics*, Vol. SMC-11, No. 10.

McCarthy, J. M., 1983, "Planar and Spatial Rigid Body Motion as Special Cases of Spherical and 3-Spherical Motion," ASME *Journal of Mechanisms, Transmissions, and Automation in Design*, Vol. 105, No. 3, pp. 569–575.

McCarthy, J. M., and Ravani, B., 1985, "Differential Kinematics of Spherical and Spatial Motions Using Kinematic Mapping," accepted for publication, ASME JOURNAL OF APPLIED MECHANICS.

Ravani, B., 1982, "Kinematic Mapping Applied to Motion Approximation and Mechanism Synthesis," doctoral dissertation, Stanford University, Calif.

Ravani, B., and Roth, B., 1984, "Mappings of Spatial Kinematics," ASME *Journal of Mechanisms, Transmissions, and Automation in Design*, Vol. 106, pp. 341–347.

Stress Singularity at the Tip of a Rigid Line Inhomogeneity Under Antiplane Shear Loading

Z. Y. Wang,[1] H. T. Zhang,[1] and Y. T. Chou[1]

1 Introduction

It has been shown (Chou and Wang, 1983; Wang et al., 1985) that under an inplane tensile loading, a plane elastic body containing a rigid line inhomogeneity would generate a square-root stress singularity at the tip of the line segment, a situation similar to the case of a slit crack (Broek, 1982). However, if the applied stress is an inplane shear, the inhomogeneity and the matrix become elastically compatible and no stress singularity exists, which is different from the case of a crack.

In the present work we investigate a similar inhomogeneity system in which the applied stress is an antiplane shear. This system is analyzed by two different methods: the complex variable method of Muskhelishvili and the equivalent inclusion method of Eshelby. The present analysis, together with the analysis reported earlier for the inplane elastic system (Chou and Wang, 1983; Wang et al., 1985), thus provides a complete description for the rigid line inhomogeneity problem in plane elasticity.

2 Analysis

We consider an antiplane strain deformation in which a rigid flat inhomogeneity of width $2a$ is embedded in an infinite elastic body along the x axis of a Cartesian coordinate system xyz (Fig. 1). The dependent variables of the system are the displacement $u_z(x,y)$ and the stress components σ_{xz} and σ_{yz}, related by

$$\sigma_{xz} = G\frac{\partial u_z}{\partial x},\ \sigma_{yz} = G\frac{\partial u_z}{\partial y} \tag{1}$$

where G is the shear modulus of the matrix. Under the condition of equilibrium, the governing partial differential equation is

$$\frac{\partial^2 u_z}{\partial x^2} + \frac{\partial^2 u_z}{\partial y^2} = 0 \tag{2}$$

with the boundary conditions

$$u_z = 0 \quad \text{for } -a \leqq x \leqq a \text{ and } y = 0 \tag{3}$$

and

$$\sigma_{xz} = \sigma_{xz}^A,\ \sigma_{yz} = \sigma_{yz}^A \quad \text{at infinity} \tag{4}$$

where σ_{xz}^A and σ_{yz}^A are the uniform applied stresses. Equation (2) can be solved according to the position of the loading.

[1]Department of Metallurgy and Materials Engineering, Lehigh University, Bethlehem, PA 18015.

Manuscript received by ASME Applied Mechanics Division, August, 1985; final revision, October, 1985.

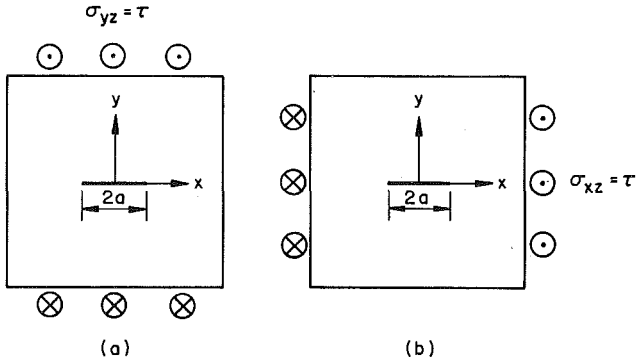

Fig. 1 A rigid line inhomogeneity under the action of an antiplane shear loading. (a) $\sigma^A_{xz} = o$, $\sigma^A_{yz} = \tau$, (b) $\sigma^A_{xz} = \tau$, $\sigma^A_{yz} = o$.

There are two distinct cases. In the first case (Fig. 1*a*) where the applied stress is acting parallel to the rigid inhomogeneity, $\sigma^A_{xz} = 0$ and $\sigma^A_{yz} = \tau$, and the solution of (2) is simply

$$u_z = \frac{\tau}{G} y \tag{5}$$

which satisfies both the boundary conditions (3) and (4). The corresponding stresses in the matrix are $\sigma_{xz} = 0$ and $\sigma_{yz} = \tau$. The inhomogeneity is, therefore, compatible with the matrix and no stress singularity exists.

In the second case (Fig. 1*b*) where the applied stress is acting perpendicular to the rigid inhomogeneity, $\sigma^A_{xz} = \tau$ and $\sigma^A_{yz} = 0$. A suggested solution of (2) is

$$u^s_z = \frac{\tau}{G} x \tag{6}$$

which satisfies the boundary condition (4) but not (3). For a valid solution, a perturbation field must be added with the following boundary conditions:

$$u^P_z = -\frac{\tau}{G} x \quad \text{for } -a \leqq x \leqq a \text{ and } y = 0 \tag{7}$$

and

$$\sigma^P_{xy} = \sigma^P_{yz} = 0 \quad \text{at infinity} \tag{8}$$

For solving the above boundary value problem, it is convenient to use the complex variable method of Muskhelishvili (1953). Consider the mapping function

$$z = \omega(\zeta) = \frac{a}{2}\left(\zeta + \frac{1}{\zeta}\right) \tag{9}$$

which maps the rigid line in the z plane ($z = x + iy$) onto a unit circle in the ζ plane ($\zeta = \rho\, e^{i\psi}$). The entire z plane, excluding the rigid line, is then mapped onto the region exterior to the unit circle in the ζ plane. With the value of u^P_z given by (7) in the z plane, the corresponding value on the unit circle in the ζ plane can be determined. The problem is, therefore, a Dirichlet problem. The displacement function which is harmonic in the region exterior to the unit circle in the ζ plane can be represented by the Poisson's formula

$$\delta^P(\zeta) = \frac{1}{2\pi}\int_0^{2\pi} \frac{(\rho^2 - 1)\delta^P(\phi)\, d\phi}{1 - 2\rho\cos(\phi - \psi) + \rho^2}, \quad \rho > 1 \tag{10}$$

where $\delta^P(\phi)$ is the value of $\delta^P(\zeta)$ on the unit circle $t = e^{i\phi}$ in the ζ plane. From equations (7) and (9), we have

$$\delta^P(\phi) = -\frac{\tau}{G} a \cos\phi \tag{11}$$

which is also the boundary condition for the displacement function in the ζ plane. Equation (10) can then be evaluated by the contour integration to yield

$$\delta^P(\zeta) = -\frac{\tau a}{G}\frac{1}{\rho}\cos\psi = -\frac{\tau a}{G}\frac{\mathrm{Re}\zeta}{|\zeta|^2} \tag{12}$$

where $\mathrm{Re}\zeta$ represents the real part of ζ. Equation (12) reduces to (11) at $\rho = 1$ and $\psi = \phi$, i.e., on the unit circle in the ζ plane.

To determine the displacement function in the z plane, we use the inverse function of (9)

$$\zeta = \omega^{-1}(z) = \frac{z + \sqrt{z^2 - a^2}}{a} \tag{13}$$

Since we are interested in the field near the tip of the rigid line, it is convenient to choose a local polar coordinate system (r, θ) with the origin at a, i.e.,

$$z = a + r\, e^{i\theta} \tag{14}$$

Substituting equation (14) in equation (13) and assuming $r \ll a$ yield

$$\zeta = 1 + \left(\frac{2r}{a}\right)^{1/2} e^{i\theta/2} + \frac{r}{a} e^{i\theta} \tag{15}$$

where the terms of $(r/a)^{3/2}$ and higher were dropped. Subsequently, from equation (12) one obtains

$$u^P_z = -\frac{\tau a}{G}\left[1 - \left(\frac{2r}{a}\right)^{1/2}\cos\frac{\theta}{2} + \frac{r}{a}\cos\theta\right] \tag{16}$$

which reduces to (7) at $\theta = \pi$.

Now, in reexamining equation (6) near the tip region, we have

$$u^s_z = \frac{\tau a}{G}\left(1 + \frac{r}{a}\cos\theta\right) \tag{17}$$

The local displacement field which satisfies (3) is then the combination of (16) and (17),

$$u_z = u^s_z + u^P_z = \frac{\tau a}{G}\left(\frac{2r}{a}\right)^{1/2}\cos\frac{\theta}{2} \tag{18}$$

The corresponding stress components of the system are derived from (18),

$$\sigma_{xz} = \frac{\tau(\pi a)^{1/2}}{(2\pi r)^{1/2}}\cos\frac{\theta}{2} \tag{19a}$$

$$\sigma_{yz} = \frac{\tau(\pi a)^{1/2}}{(2\pi r)^{1/2}}\sin\frac{\theta}{2} \tag{19b}$$

It is clear that the system has a stress singularity at the tip of the inhomogeneity similar to the case of a slit crack. It is worth noting that, in the case of a rigid inhomogeneity, the applied shear stress is acting perpendicular to the inhomogeneity segment, whereas in the case of a crack, it is parallel to the crack line.

The above results can also be obtained by the equivalent inclusion method of Eshelby (1957). A rigid line can be considered as a limit case of an elliptic inhomogeneity. Following Yang and Chou (1977), the equivalent eigenstrains for a rigid inhomogeneity (with shear modulus $G_1 \to \infty$) are obtained from the following equations

$$\epsilon^c_{ij} = -\epsilon^A_{ij} \tag{20}$$

where ϵ^c_{ij} are the constrained strains and ϵ^A_{ij} the applied strains.

The constrained strains, ϵ^c_{xz} and ϵ^c_{yz}, can be expressed in terms of the eigenstrains of the equivalent inclusion, ϵ^*_{xz} and ϵ^*_{yz}, i.e.,

$$\epsilon^c_{xz} = \frac{e}{1+e}\epsilon^*_{xz} \tag{21a}$$

$$\epsilon^c_{yz} = \frac{1}{1+e}\epsilon^*_{yz} \tag{21b}$$

where $e = b/a$ is the ratio of the semi-axes, a and b, of the ellipse (Zhang and Zhe, 1981). For a rigid line inhomogeneity $e \to o$ and

$$\epsilon^*_{xz} = -\epsilon^A_{xz}/e = -\sigma^A_{xz}/2Ge \tag{22a}$$

$$\epsilon^*_{yz} = -\epsilon^A_{yz} = -\sigma^A_{yz}/2G \tag{22b}$$

where G is the shear modulus of the inclusion. From equations (22) it is seen that only ϵ^A_{xz} or σ^A_{xz} would induce the stress singularity, in accordance with the results obtained by the complex variable method.

The stress field due to the eigenstrain component ϵ^*_{xz} can be written as (Zhang and Zhe, 1981)

$$\sigma_{xz} = 2\,G\,e\,\epsilon^*_{xz}\left[1+\frac{1}{R}(x\sin\eta - y\cos\eta)\right] \tag{23a}$$

$$\sigma_{yz} = -2\,G\,e\,\epsilon^*_{xz}\,\frac{1}{R}(x\cos\eta - y\sin\eta) \tag{23b}$$

where

$$R\,e^{i\eta} = \sqrt{a^2 - z^2}, \quad z = x + iy \tag{24}$$

Near the tip of the flat inclusion, equations (23) reduce to

$$\sigma_{xz} = -2\,G\,e\,\epsilon^*_{xz}\left(\frac{\pi a}{2\pi r}\right)^{1/2}\cos\frac{\theta}{2} \tag{25a}$$

$$\sigma_{yz} = -2\,G\,e\,\epsilon^*_{xz}\left(\frac{\pi a}{2\pi r}\right)^{1/2}\sin\frac{\theta}{2} \tag{25b}$$

where r and θ are defined in (14). By substituting (22) into (25) and taking $\sigma^A_{xz} = \tau$, one obtains the sames results as (19).

3 Discussion of the Results

As in the previous paper (Wang et al., 1985), we propose a stress singularity coefficient for the present system,

$$S_{\mathrm{III}} = \lim_{r\to o}\,(2\pi r)^{1/2}\sigma_{xz}(\theta = o)$$

$$= \tau\sqrt{\pi a} \tag{26}$$

This mode of deformation is designated as mode III deformation for a rigid line inhomogeneity. The J integral or the inhomogeneity extension force may also be calculated by using the equivalent inclusion method.

The increase of the elastic energy in the body due to the rigid line inclusion is

$$\Delta W = \pi\,a^2 e\,\sigma^A_{xz}\epsilon^*_{xz}$$

$$= -\frac{\pi\,a^2}{2G}(\sigma^A_{xz})^2 \tag{27}$$

However, the total increase in free energy of the system (the elastic energy in the body and the potential energy of the loading mechanism) is

$$E_{\mathrm{int}} = -\Delta W \tag{28}$$

The J integral is then given by

$$J_{\mathrm{III}} = -\frac{\partial E_{\mathrm{int}}}{\partial\,(2a)} = \frac{\partial\,(\Delta W)}{\partial\,(2a)}$$

$$= -\frac{\pi\,a}{2\,G}(\sigma^A_{xz})^2 = -\frac{\pi a}{2\,G}\,\tau^2 \tag{29}$$

which is related to S_{III} by

$$J_{\mathrm{III}} = -\frac{1}{2G}\,S^2_{\mathrm{III}} \tag{30}$$

The negative sign in (29) indicates that the driving force on the rigid line favors a contraction in the length of the segment. This is consistent with the results derived previously for the in-plane system (Wang et al., 1985).

To summarize, we have analyzed the stress and displacement fields near the tip of a rigid line inhomogeneity in a two-dimensional elastic system subject to an antiplane shear loading. Similar to the case of the inplane deformation, a square-root stress singularity is identified; the singularity exists only if the shear loading is acting perpendicular to the inhomogeneity segment. In conjunction with the mode I and mode II deformation, a mode III antiplane deformation is defined and the inhomogeneity extensin force is calculated.

References

Broek, D., 1982, *Elementary Engineering Fracture Mechanics*, Martinus Nijhoff Publishers, Hague, Netherlands, pp. 3–23.

Chou, Y. T., and Wang, Z. Y., 1983, "Stress Singularity at the Tip of a Rigid Flat Inclusion," in *Recent Developments in Applied Mathematics*, Ling, F. F., and Tadjbaklish, I. G., eds., Rensselaer Press, Troy, pp. 21–30.

Eshelby, J. D., 1957, "The Determination of the Elastic Field of an Ellipsoid Inclusion, and Related Problems," *Proceedings of the Royal Society*, Series A, Vol. 241, pp. 376–396.

Muskhelishvili, N. I., 1953, *Some Basic Problems of Mathematical Theory of Elasticity*, Noordhoff Ltd., Groningen, pp. 104–161.

Wang, Z. Y., Zhang, H. T., and Chou, Y. T., 1985, "Characteristics of the Elastic Field of a Rigid Line Inhomogeneity," ASME JOURNAL OF APPLIED MECHANICS, Vol. 52, pp. 818–822.

Yang, H. C., and Chou, Y. T., 1977, "Antiplane Strain Problems of an Elliptic Inclusion in an Anisotropic Medium," ASME JOURNAL OF APPLIED MECHANICS, *Vol. 44*, pp. 437–441.

Zhang, H. T., and Zhe, X. L., 1981, "Theory of Inclusion and Applications in the Study of Fracture," *Acta Physica Sinica*, Vol. 30, pp. 761–774.

Asymptotic Integration Applied to the Differential Equation for Thin Elastic Toroidal Shells

O. Jenssen[1]

The second order differential equation in question is

$$W'' - [i\mu f_1(\phi) + f_2(\phi)]W = \mu F(\phi) \tag{1}$$

where μ is a large parameter and

$$f_1(\phi) = \frac{\sin\phi}{1+\lambda\sin\phi}, \quad f_2(\phi) = \frac{3}{4}\left(\frac{\lambda\cos\phi}{1+\lambda\sin\phi}\right)^2$$

$$F(\phi) = \Omega(\phi)\cos\phi(1+\lambda\sin\phi)^{-1/2} \tag{2}$$

with $\Omega(\phi)$ as an expression for the axial load. A solution of this equation was given by Wei (1944). The homogeneous equation was solved by a method similar to Langers (1931) and the the inhomogeneous equation was solved by the standard formula using an approximation for $F(\phi)$. Clarke (1950) presents a simple particular solution which is widely used, but which is not as accurate as the Langer solution of the homogeneous equation. This particular integral was developed jointly with E. Reissner.

This author presented a more exact solution (Jenssen 1960) which, however, is laborious and has later used the following simplified version:

The solution W is approximated by the function

$$Y = Q(\phi)h(z) + \mu^{1/3}F(o)QT(z) + Y_m \tag{3}$$

where Y_m is the membrane solution

$$Y_m = -i[Q^{-3}F(o) - F(\phi)]\,\frac{1}{f_1} \tag{4}$$

The functions $h(z)$ and $T(z)$ are solutions of the equations

$$\frac{d^2h}{dz^2} + zh = 0, \quad \frac{d^2T}{dz^2} + zT = -1 \tag{5}$$

[1] Universitetet I Trondheim, Norges Tekniske Hogskole, Trondheim, Norway 7034.

Manuscript received by ASME Applied Mechanics Division, October 28, 1985.

$$\epsilon^*_{xz} = -\epsilon^A_{xz}/e = -\sigma^A_{xz}/2Ge \tag{22a}$$

$$\epsilon^*_{yz} = -\epsilon^A_{yz} = -\sigma^A_{yz}/2G \tag{22b}$$

where G is the shear modulus of the inclusion. From equations (22) it is seen that only ϵ^A_{xz} or σ^A_{xz} would induce the stress singularity, in accordance with the results obtained by the complex variable method.

The stress field due to the eigenstrain component ϵ^*_{xz} can be written as (Zhang and Zhe, 1981)

$$\sigma_{xz} = 2\,G\,e\,\epsilon^*_{xz}\left[1+\frac{1}{R}(x\sin\eta - y\cos\eta)\right] \tag{23a}$$

$$\sigma_{yz} = -2\,G\,e\,\epsilon^*_{xz}\,\frac{1}{R}(x\cos\eta - y\sin\eta) \tag{23b}$$

where

$$R\,e^{i\eta} = \sqrt{a^2 - z^2}, \quad z = x + iy \tag{24}$$

Near the tip of the flat inclusion, equations (23) reduce to

$$\sigma_{xz} = -2\,G\,e\,\epsilon^*_{xz}\left(\frac{\pi a}{2\pi r}\right)^{1/2}\cos\frac{\theta}{2} \tag{25a}$$

$$\sigma_{yz} = -2\,G\,e\,\epsilon^*_{xz}\left(\frac{\pi a}{2\pi r}\right)^{1/2}\sin\frac{\theta}{2} \tag{25b}$$

where r and θ are defined in (14). By substituting (22) into (25) and taking $\sigma^A_{xz} = \tau$, one obtains the sames results as (19).

3 Discussion of the Results

As in the previous paper (Wang et al., 1985), we propose a stress singularity coefficient for the present system,

$$S_{\mathrm{III}} = \lim_{r\to o}\,(2\pi r)^{1/2}\sigma_{xz}(\theta = o)$$

$$= \tau\sqrt{\pi a} \tag{26}$$

This mode of deformation is designated as mode III deformation for a rigid line inhomogeneity. The J integral or the inhomogeneity extension force may also be calculated by using the equivalent inclusion method.

The increase of the elastic energy in the body due to the rigid line inclusion is

$$\Delta W = \pi\,a^2 e\,\sigma^A_{xz}\epsilon^*_{xz}$$

$$= -\frac{\pi\,a^2}{2G}(\sigma^A_{xz})^2 \tag{27}$$

However, the total increase in free energy of the system (the elastic energy in the body and the potential energy of the loading mechanism) is

$$E_{\mathrm{int}} = -\Delta W \tag{28}$$

The J integral is then given by

$$J_{\mathrm{III}} = -\frac{\partial E_{\mathrm{int}}}{\partial\,(2a)} = \frac{\partial\,(\Delta W)}{\partial\,(2a)}$$

$$= -\frac{\pi\,a}{2\,G}(\sigma^A_{xz})^2 = -\frac{\pi a}{2\,G}\,\tau^2 \tag{29}$$

which is related to S_{III} by

$$J_{\mathrm{III}} = -\frac{1}{2G}\,S^2_{\mathrm{III}} \tag{30}$$

The negative sign in (29) indicates that the driving force on the rigid line favors a contraction in the length of the segment. This is consistent with the results derived previously for the in-plane system (Wang et al., 1985).

To summarize, we have analyzed the stress and displacement fields near the tip of a rigid line inhomogeneity in a two-dimensional elastic system subject to an antiplane shear loading. Similar to the case of the inplane deformation, a square-root stress singularity is identified; the singularity exists only if the shear loading is acting perpendicular to the inhomogeneity segment. In conjunction with the mode I and mode II deformation, a mode III antiplane deformation is defined and the inhomogeneity extensin force is calculated.

References

Broek, D., 1982, *Elementary Engineering Fracture Mechanics*, Martinus Nijhoff Publishers, Hague, Netherlands, pp. 3–23.

Chou, Y. T., and Wang, Z. Y., 1983, "Stress Singularity at the Tip of a Rigid Flat Inclusion," in *Recent Developments in Applied Mathematics*, Ling, F. F., and Tadjbaklish, I. G., eds., Rensselaer Press, Troy, pp. 21–30.

Eshelby, J. D., 1957, "The Determination of the Elastic Field of an Ellipsoid Inclusion, and Related Problems," *Proceedings of the Royal Society*, Series A, Vol. 241, pp. 376–396.

Muskhelishvili, N. I., 1953, *Some Basic Problems of Mathematical Theory of Elasticity*, Noordhoff Ltd., Groningen, pp. 104–161.

Wang, Z. Y., Zhang, H. T., and Chou, Y. T., 1985, "Characteristics of the Elastic Field of a Rigid Line Inhomogeneity," ASME Journal of Applied Mechanics, Vol. 52, pp. 818–822.

Yang, H. C., and Chou, Y. T., 1977, "Antiplane Strain Problems of an Elliptic Inclusion in an Anisotropic Medium," ASME Journal of Applied Mechanics, *Vol. 44*, pp. 437–441.

Zhang, H. T., and Zhe, X. L., 1981, "Theory of Inclusion and Applications in the Study of Fracture," *Acta Physica Sinica*, Vol. 30, pp. 761–774.

Asymptotic Integration Applied to the Differential Equation for Thin Elastic Toroidal Shells

O. Jenssen[1]

The second order differential equation in question is

$$W'' - [i\mu f_1(\phi) + f_2(\phi)]W = \mu F(\phi) \tag{1}$$

where μ is a large parameter and

$$f_1(\phi) = \frac{\sin\phi}{1+\lambda\sin\phi}, \quad f_2(\phi) = \frac{3}{4}\left(\frac{\lambda\cos\phi}{1+\lambda\sin\phi}\right)^2$$

$$F(\phi) = \Omega(\phi)\cos\phi(1+\lambda\sin\phi)^{-1/2} \tag{2}$$

with $\Omega(\phi)$ as an expression for the axial load. A solution of this equation was given by Wei (1944). The homogeneous equation was solved by a method similar to Langers (1931) and the the inhomogeneous equation was solved by the standard formula using an approximation for $F(\phi)$. Clarke (1950) presents a simple particular solution which is widely used, but which is not as accurate as the Langer solution of the homogeneous equation. This particular integral was developed jointly with E. Reissner.

This author presented a more exact solution (Jenssen 1960) which, however, is laborious and has later used the following simplified version:

The solution W is approximated by the function

$$Y = Q(\phi)h(z) + \mu^{1/3}F(o)QT(z) + Y_m \tag{3}$$

where Y_m is the membrane solution

$$Y_m = -i[Q^{-3}F(o) - F(\phi)]\,\frac{1}{f_1} \tag{4}$$

The functions $h(z)$ and $T(z)$ are solutions of the equations

$$\frac{d^2h}{dz^2} + zh = 0, \quad \frac{d^2T}{dz^2} + zT = -1 \tag{5}$$

[1] Universitetet I Trondheim, Norges Tekniske Hogskole, Trondheim, Norway 7034.

Manuscript received by ASME Applied Mechanics Division, October 28, 1985.

and $z = ix = i\mu^{1/3}\left(\frac{3}{2}\omega\right)^{2/3}$,

$$\omega = \int_0^{\phi} f_1(\phi)^{1/2} d\phi, \quad Q = \left(\frac{3}{2}\omega\right)^{1/6} (\omega')^{-1/2} \tag{6}$$

It should be noted that $Q(o) = 1$. The expression (3) satisfies the following differential equation

$$Y'' - \left[i\mu f_1(\phi) + \frac{Q''}{Q}\right] Y = \mu F(\phi) + 0(1) \tag{7}$$

The homogeneous solution of equation (7) is the Langer solution (1931) used by Clarke (1950) and is equal to the first term on the right-hand side of the expression (3).

Therefore, solution (3) seems to be a natural extension of the solution by Langer (1931) to include particular integrals for equations with a transition point.

References

Clark, R. A., 1950, "On the Theory of Thin Elastic Toroidal Shells," *Journal of Mathematics and Physics*, Vol. 29, pp. L149–178.

Jenssen, O., 1960, (Received 1956), "Asymptotic Integration of the Differential Equation for a Special Case of Symmetrically Loaded Toroidal Shells," *Journal of Mathematics and Physics*, Vol. 39, pp. 1–17.

Langer, R. E., 1931, "On the Asymptotic Solution of Ordinary Differential Equations," *Trans. Am. Math. Soc.*, Vol. 33, pp. 23–64.

Wei, C., 1944, "Der Spannungszustand in Kreisringschalen und Ähnlichen Schalen mit Scheitelkreisringen unter Drehsymmetrisher Belastnung," Ph.D. Thesis, Technischen Hochschule, Berlin; 1949, The Science Reports of National Tsing Hua University. Series A, Vol. V, pp. 289–349.

Explicit Approximate Solutions Associated With the Mechanics of Hydraulic Fracturing

S. H. Advani,[1] J. S. Torok,[1] and J. K. Lee[1]

Governing equations, based on a Lagrangian formulation, for the assumed case of a hydraulically induced vertial elliptic fracture propagating in a uniformly confined, linear, elastic, homogeneous medium are derived. Explicit solutions for the generalized coordinates designating the time-dependent crack width, major axis, and minor axis are obtained for one-dimensional fracture fluid flow with and without leak-off effects.

[1]Department of Engineering Mechanics, Ohio State University, Columbus, Ohio 43210.

Manuscript received by ASME Applied Mechanics Division, October 16, 1984; final revision, November 21, 1985.

Introduction

The mechanics of hydraulic fracturing generally entails the controlled pumping of the selected proppant laden fracture fluid in a bore hole and subsequent initiation and sustained vertical extension of the induced fracture in the formation pay zone. This technique is commercially used for stimulating oil and gas reservoirs. Potential applications to geothermal energy extraction, nuclear waste management, and underground coal gasification have also been explored. In view of the importance of this problem, considerable research on the prediction of the induced fracture geometry and fracture fluid leak-off has been conducted (Clifton and Abou-Sayed, 1982; Settari and Cleary, 1984; Advani et al., 1984).

In this note, the governing nonlinear equations for the assumed propagation of an elliptic fracture in a uniformly confined, linear elastic, homogeneous medium are derived. A Lagrangian formulation with strain energy, fracture fluid energy dissipation, and generalized force terms incorporating Griffith crack separation energy contributions is utilized. The time dependent crack width, minor axis, and major axis are chosen as generalized coordinates (Fig. 1) with $c \ll a$, b for the flat ellipsoid geometry. The variational formulation is consistent with the two-dimensional methodology presented by Biot et al. (1982) in terms of fracture width and length. Explicit solutions for the generalized coordinates, for one-dimensional fracture fluid flow, are derived in the absence of leak-off and with leak-off effects.

Problem Formulation

The classical form of Lagrange's equations, in terms of the Lagrangian, L, are

$$\frac{d}{dt}\left(\frac{\partial L}{\partial \dot{q}_i}\right) - \frac{\partial L}{\partial q_i} = F_i \quad i = 1,2,3 \tag{1}$$

where the generalized coordinates, q_i, represent the major axis ($q_1 = a$), minor axis ($q_2 = b$), and fracture width ($q_3 = c$). In the analysis, the kinetic energy of the system and the effects due to gravity are ignored. The generalized forces, F_i, include the effects of the viscous fracture fluid dissipation and other forces not derivable from a potential, (V), or a dissipation function, (D), (i.e., forces increasing fracture volume and surface area). Therefore,

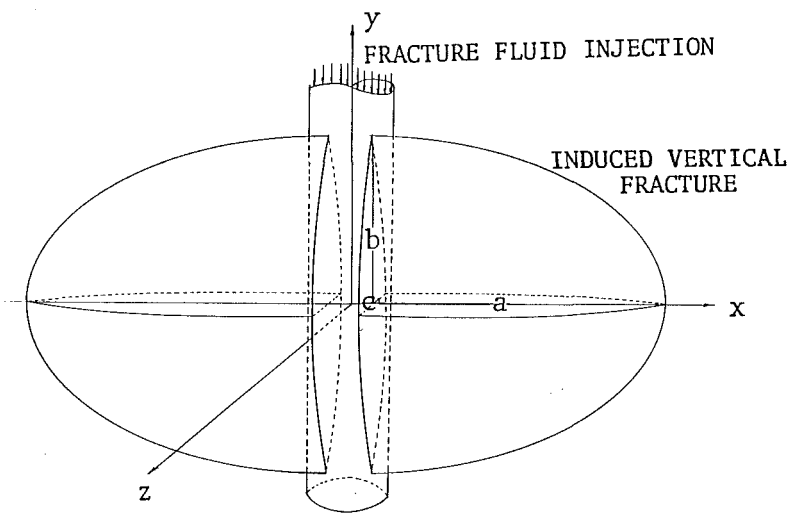

Fig. 1 Assumed vertical elliptic crack model

and $z = ix = i\mu^{1/3}\left(\frac{3}{2}\omega\right)^{2/3}$,

$$\omega = \int_0^{\phi} f_1(\phi)^{1/2} d\phi, \quad Q = \left(\frac{3}{2}\omega\right)^{1/6} (\omega')^{-1/2} \tag{6}$$

It should be noted that $Q(o) = 1$. The expression (3) satisfies the following differential equation

$$Y'' - \left[i\mu f_1(\phi) + \frac{Q''}{Q}\right] Y = \mu F(\phi) + 0(1) \tag{7}$$

The homogeneous solution of equation (7) is the Langer solution (1931) used by Clarke (1950) and is equal to the first term on the right-hand side of the expression (3).

Therefore, solution (3) seems to be a natural extension of the solution by Langer (1931) to include particular integrals for equations with a transition point.

References

Clark, R. A., 1950, "On the Theory of Thin Elastic Toroidal Shells," *Journal of Mathematics and Physics*, Vol. 29, pp. L149–178.

Jenssen, O., 1960, (Received 1956), "Asymptotic Integration of the Differential Equation for a Special Case of Symmetrically Loaded Toroidal Shells," *Journal of Mathematics and Physics*, Vol. 39, pp. 1–17.

Langer, R. E., 1931, "On the Asymptotic Solution of Ordinary Differential Equations," *Trans. Am. Math. Soc.*, Vol. 33, pp. 23–64.

Wei, C., 1944, "Der Spannungszustand in Kreisringschalen und Ähnlichen Schalen mit Scheitelkreisringen unter Drehsymmetrisher Belastnung," Ph.D. Thesis, Technischen Hochschule, Berlin; 1949, The Science Reports of National Tsing Hua University. Series A, Vol. V, pp. 289–349.

Explicit Approximate Solutions Associated With the Mechanics of Hydraulic Fracturing

S. H. Advani,[1] J. S. Torok,[1] and J. K. Lee[1]

Governing equations, based on a Lagrangian formulation, for the assumed case of a hydraulically induced vertial elliptic fracture propagating in a uniformly confined, linear, elastic, homogeneous medium are derived. Explicit solutions for the generalized coordinates designating the time-dependent crack width, major axis, and minor axis are obtained for one-dimensional fracture fluid flow with and without leak-off effects.

[1]Department of Engineering Mechanics, Ohio State University, Columbus, Ohio 43210.

Manuscript received by ASME Applied Mechanics Division, October 16, 1984; final revision, November 21, 1985.

Introduction

The mechanics of hydraulic fracturing generally entails the controlled pumping of the selected proppant laden fracture fluid in a bore hole and subsequent initiation and sustained vertical extension of the induced fracture in the formation pay zone. This technique is commercially used for stimulating oil and gas reservoirs. Potential applications to geothermal energy extraction, nuclear waste management, and underground coal gasification have also been explored. In view of the importance of this problem, considerable research on the prediction of the induced fracture geometry and fracture fluid leak-off has been conducted (Clifton and Abou-Sayed, 1982; Settari and Cleary, 1984; Advani et al., 1984).

In this note, the governing nonlinear equations for the assumed propagation of an elliptic fracture in a uniformly confined, linear elastic, homogeneous medium are derived. A Lagrangian formulation with strain energy, fracture fluid energy dissipation, and generalized force terms incorporating Griffith crack separation energy contributions is utilized. The time dependent crack width, minor axis, and major axis are chosen as generalized coordinates (Fig. 1) with $c \ll a$, b for the flat ellipsoid geometry. The variational formulation is consistent with the two-dimensional methodology presented by Biot et al. (1982) in terms of fracture width and length. Explicit solutions for the generalized coordinates, for one-dimensional fracture fluid flow, are derived in the absence of leak-off and with leak-off effects.

Problem Formulation

The classical form of Lagrange's equations, in terms of the Lagrangian, L, are

$$\frac{d}{dt}\left(\frac{\partial L}{\partial \dot{q}_i}\right) - \frac{\partial L}{\partial q_i} = F_i \quad i = 1,2,3 \tag{1}$$

where the generalized coordinates, q_i, represent the major axis ($q_1 = a$), minor axis ($q_2 = b$), and fracture width ($q_3 = c$). In the analysis, the kinetic energy of the system and the effects due to gravity are ignored. The generalized forces, F_i, include the effects of the viscous fracture fluid dissipation and other forces not derivable from a potential, (V), or a dissipation function, (D), (i.e., forces increasing fracture volume and surface area). Therefore,

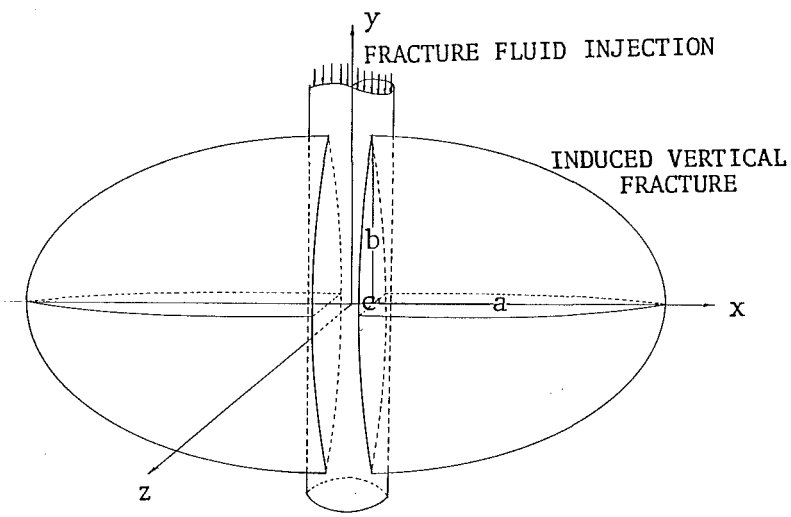

Fig. 1 Assumed vertical elliptic crack model

$$F_i = -\frac{\partial D}{\partial \dot{q}_i} + Q_i$$

and equation (1) can now be rewritten in the form

$$\frac{\partial V}{\partial q_i} + \frac{\partial D}{\partial \dot{q}_i} = Q_i \tag{2}$$

The Lagrangian formulation presented here provides an attractive methodology for including dissipation and leak-off effects associated with fracture fluid flow. It is noteworthy that this variational formulation, for a constant fracture height, yields expressions for fracture width (Biot et al., 1982) which are physically compatible with the solutions presented by Geertsma and Haafkens (1979). In the following analysis, we define the nondimensional major and minor axes coordinate variables by:

$$\alpha = x/a, \quad \beta = y/b$$

and consider symmetric flow in one quadrant of the elliptical fracture surface, A.

Potential Function. The potential function, V, is given as the work done by the fracture fluid pressure, $p(x, y, t)$ in generating the fracture geometry, i.e.,

$$V = \iint_A p(x,y,t)\, w(x,y,t)\, dx\, dy \tag{3}$$

where $w(x, y, t) = 2c\, f(\alpha, \beta)$ is the fracture width with the shape function $f(\alpha, \beta) = 0$ on the fracture boundary.

The corresponding pressure-width relation, from elastostatics, has the general form

$$p(x,y,t) = \frac{G}{1-\nu} P(a,b,c) g_n(\alpha,\beta), \quad 0 \le \alpha, \beta \le 1 \tag{4}$$

where G and ν are the formation shear modulus and Poisson's ratio, respectively, and $g_n(\alpha, \beta)$ is a polynomial of degree n in α and β, obtained to match the specified displacement shape function, $f(\alpha, \beta)$ (Segedin, 1968). The coefficients of $g_n(\alpha, \beta)$ are computed in terms of elliptic integrals. For an elongated ellipsoidal fracture surface, $f(\alpha, \beta) = (1 - \alpha^2 - \beta^2)^{1/2}$ and the corresponding polynomial for the pressure distribution $g_0(\alpha, \beta)$ is equal to unity.

The potential function is given by

$$V = Iabc P(a,b,c) \tag{5}$$

where

$$I = \frac{2G}{1-\nu} \int_0^1 \int_0^{(1-\alpha^2)^{1/2}} f(\alpha,\beta) g_n(\alpha,\beta)\, d\beta\, d\alpha = \frac{\pi G}{3(1-\nu)}$$

Dissipation Function. Energy dissipation arises from flow of the viscous fracture fluid. Assuming Poiseuille flow in each cross section normal to the fracture surfaces, the flow rate, $\vec{q}$, in the fracture can be shown to be

$$\vec{q} = -\frac{w^3}{12\mu} \vec{\nabla} p \tag{6}$$

where μ is the viscosity of the Newtonian frac fluid. The dissipation, D, is defined by

$$D = -\frac{1}{2} \iint_A \vec{q} \cdot \vec{\nabla} p\, dA \tag{7}$$

Substituting equation (6) in equation (7) yields

$$D = 6\mu \iint_A \frac{(\vec{q})^2}{w^3}\, dA$$

The flow rate, $\vec{q}$, is related to the fracture width, w, by mass conservation. For an incompressible fluid, the local continuity equation is

$$\frac{\partial q_x}{\partial x} + \frac{\partial q_y}{\partial y} + q_L + \frac{\partial w}{\partial t} = 0 \tag{8}$$

where q_L, the fluid leak-off rate into the reservoir, is governed by the traditionally accepted relation

$$q_L = \frac{2\bar{C}}{\sqrt{t - \tau(x,y)}} \tag{9}$$

with $\bar{C}$ being the overall leak-off coefficient, and $\tau(x, y)$ being the elapsed time of arrival of the fracture fluid (as well as fracture surface) to the coordinate point (x, y).

The global continuity equation is obtained by integrating equation (8) over the fracture surface, from which the local flow rate is computed. The derivation of the dissipation function in terms of the generalized coordinates is the most difficult task in the model response evaluation.

Generalized Forces. The generalized forces, Q_i, are derived from virtual work analysis, i.e.,

$$dW = Q_1 da + Q_2 db + Q_3 dc \tag{10}$$

The virtual work, incorporating associated contributions relating to fracture volume and surface increase, can be expressed in the form

$$\begin{aligned} Q_1 &= M p_f bc - \frac{\pi}{4} E_s b \\ Q_2 &= M p_f ac - \frac{\pi}{4} E_s a \\ Q_3 &= M p_f ab \end{aligned} \tag{11}$$

where $M = \pi/3$ for the selected ellipsoid configuration, p_f is the effective bore hole pressure, the E_s is the Griffith type separation energy.

Governing Equations and Special Solutions

The above expressions for V, D, and Q_i are in terms of the generalized displacements and velocities. The governing equations are obtained by substitution in Lagrange's equations for nonconservative systems (equations 2). As expected, the differential equations are coupled and highly nonlinear. However, depending on the physical assumptions, solutions for selected special cases can be derived.

We consider, for example, one-dimensional flow in the absence of leak-off, i.e.,

$$q_x = q(x,t), \quad q_y = 0, \quad \text{and} \quad q_L = 0$$

Conservation of mass requires that

$$q(x,t)\left(b^2 - \frac{b^2 x^2}{a^2}\right)^{1/2} = \frac{d}{dt}\left[2abc \int_\alpha^1 \int_0^{\sqrt{1-\alpha^2}} f(\alpha,\beta)\, d\beta\, d\alpha\right] \tag{12}$$

With $P(a, b, c) = c/b$, the potential function $V = Iac^2$. This form of $P(a, b, c)$ corresponds to an approximation of the constant pressure-width relation for an elliptic crack ($a > b$). The governing equations for this case are:

$$\begin{aligned} 12Ic^4 + 3\mu D_1 a\dot{a}bc + 3\mu D_2 a^2 (bc)^{\cdot} &= 4\pi p_f bc^3 - 3\pi E_s bc^2 \\ 3\mu D_2 a\dot{a}bc + 3\mu D_3 a^2 (bc)^{\cdot} &= 4\pi p_f bc^3 - 3\pi E_s bc^2 \\ 24Ic^4 + 3\mu D_2 a\dot{a}bc + 3\mu D_3 a^2 (bc)^{\cdot} &= 4\pi p_f bc^3 \end{aligned} \tag{13}$$

where D_1, D_2, and D_3 are constants defined by

$$\begin{aligned} D_1 &= \frac{1536}{\pi^3} \int_0^1 \frac{[F(\alpha) + G(\alpha)]^2}{(1-\alpha^2)^2}\, d\alpha \\ D_2 &= \frac{1536}{\pi^3} \int_0^1 \frac{F(\alpha)[F(\alpha) + G(\alpha)]}{(1-\alpha^2)^2}\, d\alpha \\ D_3 &= \frac{1536}{\pi^3} \int_0^1 \frac{[F(\alpha)]^2}{(1-\alpha^2)^2}\, d\alpha \end{aligned} \tag{13a}$$

with $F(\alpha) = \int_{\alpha}^{1}\int_{0}^{\sqrt{1-\alpha^2}} f(\alpha,\beta)d\beta d\alpha = \frac{\pi}{12}(2-3\alpha+\alpha^3)$

and $G(\alpha) = \alpha\int_{0}^{\sqrt{1-\alpha^2}} f(\alpha,\beta)d\beta = \frac{\pi}{4}\alpha(1-\alpha^2)$

To solve the above equations, we set

$$a = C_1 t^l,\ b = C_2 t^m,\ c = C_3 t^n, \text{ and } P_f = C_4 t^k$$

in equations (13) to obtain

$$(l,m,n,k) = (1+\xi, 2+4\xi, 1+2\xi, -1-2\xi),\ \xi \epsilon R$$

Conservation of mass (equation 12) yields $\xi = -3/7$. Therefore,

$$a = C_1 t^{4/7},\ b = C_2 t^{2/7},\ c = C_3 t^{1/7},$$
$$\text{and}\quad p_f = C_4 t^{-1/7} \tag{14}$$

Solution (14) corresponds to a constant bore hole flow rate Q. The constants C_i can be determined by substitution of equation (14) into equations (12) and (13), resulting in the following expressions for the fracture dimensions and borehole pressure

$$a(t) = 0.34\left[\frac{QE_s^4(1-\nu)}{\mu^3 G}\right]^{1/7} t^{4/7}$$

$$b(t) = 1.09\left[\frac{Q^4\mu^2 G^3}{(1-\nu)^3 E_s^5}\right]^{1/7} t^{2/7} \tag{15a}$$

$$c(t) = 0.64\left[\frac{Q^2 E_s(1-\nu)^2\mu}{G^2}\right]^{1/7} t^{1/7}$$

$$p_f(t) = 0.58\left[\frac{E_s^6 G^2}{Q^2\mu(1-\nu)^2}\right]^{1/7} t^{-1/7}$$

or alternatively

$$a(t) = 0.63\left[\frac{Q^3 G}{\mu(1-\nu)(2b)^4}\right]^{1/5} t^{4/5}$$

$$w(0,0,t) = 1.49\left[\frac{Q^2(1-\nu)\mu}{G(2b)}\right]^{1/5} t^{1/5} \tag{15b}$$

$$p_f(t) = \frac{1.67}{2b}\left[\frac{Q\mu G^3 a}{(1-\nu)^3}\right]^{1/4}$$

The fracture dimensions (15*b*) are comparable to the solutions derived by Perkins and Kern and Nordgren (PKN), presented in the comparative study done by Geertsma and Haafkens (1979). The fundamental difference between the two models is that the PKN solutions presume an elliptical vertical cross section while maintaining a constant height H both in space and time. The presented formulation is developed on the premise that the induced fracture has an elliptical configuration, with all the deduced dimensions varying in time.

For a more general case with leak-off, the fluid leak-off expression equation (9), is assumed with $\bar{C}$ proportional to $t^{-\gamma}$. The governing equations, for one-dimensional flow q_x, with $P(a, b, c) = c/b$ are:

$$12Ic^4 + 3\mu D^{11}\frac{a^2 b}{t^{1/2+\gamma}} + 3\mu D_1 a\dot{a}bc + 3\mu D_2 a^2(bc)^{\cdot} = 4\pi p_f bc^3 - 3\pi E_s bc^2$$

$$3\mu D^{21}\frac{a^2 b}{t^{1/2+\gamma}} + 3\mu D_2 a\dot{a}bc + 3\mu D_3 a^2(bc)^{\cdot} = 4\pi p_f bc^3 - 3\pi E_s bc \tag{16}$$

$$24Ic^4 + 3\mu D^{21}\frac{a^2 b}{t^{1/2+\gamma}} + 3\mu D_2 a\dot{a}bc + 3\mu D_3 a^2(bc)^{\cdot} = 4\mu p_f bc^3$$

where the constants D^{ij} are similar in form to those presented in equations (13*a*).

A solution to the preceding set of equations is

$$a = \tilde{C}_1 t^{3/4-\gamma/2},\ b = \tilde{C}_2 t^{1-2\gamma},\ c = \tilde{C}_3 t^{1/2-\gamma}$$
$$\text{and}\quad p_f = \tilde{C}_4 t^{\gamma-1/2} \tag{17}$$

All physically relevant values of γ for solution (17) yield a time dependent bore hole flow rate, based on mass balance requirements. For $\gamma = 1/6$, the leak-off coefficient $\bar{C}$ is proportional to $(p_f)^{1/2}$.

It is noteworthy that the results are sensitive to the selected expression for $P(a, b, c)$. For example, with $P(a, b, c) = c/a$, we obtain $V = Ibc^2$. In the absence of leak-off, the derived solutions with this assumed form are:

$$a(t) = 0.60\left[\frac{Q^3 G}{8b_0^3(1-\nu)\mu}\right]^{1/6} t^{2/3}$$

$$b(t) = b_0 \tag{18}$$

$$w(0,0,t) = 2c(t) = 1.58\left[\frac{Q^3(1-\nu)\mu}{8b_0^3 G}\right]^{1/6} t^{1/3}$$

$$p_f(t) = 1.29\left[\frac{\mu G^2}{(1-\nu)^2}\right]^{1/3} t^{-1/3}$$
$$= \frac{2.05}{4b_0}\left[\frac{QG^3\mu(2b_o)^3}{(1-\nu)^3 a^2}\right]^{1/4}$$

The time dependent solutions (18) model the propagation of a vertical elliptical fracture with constant height $2b_0$ at the wellbore and qualitatively agree with Geertsma and de Klerk (GdK) solutions presented by Geertsma and Haafkens (1979). The difference in the numerical coefficients stems from the assumed geometry of the GdK model, which is a constant height model with uniform fracture width over a vertical cross section.

For the more general case involving fluid leak-off, the fracture dimensions and effective borehole pressure, analogous to equations (17) can be shown to have the form

$$a = \tilde{C}_1 t^{2/3}\quad b = \tilde{C}_2 t^0\quad C = \tilde{C}_3 t^{1/3}\quad p_f = \tilde{C}_4 t^{-1/3} \tag{19}$$

Concluding Remarks

Although the presented explicit solutions are based on the hypothetical case of a propagating elliptic fracture configuration, with unidirectional fracture fluid flow, they can provide response calibration of sophisticated numerical codes under the prescribed model limitations. The results can also be used for parameter sensitivity evaluations and theory comparisons, in a manner similar to the fracture width and length trends presented by Geertsma and Haafkens (1979). The variational formulation associated with the dissipation function, D, for two-dimensional fracture fluid flow ($\bar{q}(x, y, t)$) presents considerable difficulty and seemingly does not yield explicit solutions.

Acknowledgment

This research was supported by the U.S. Department of Energy under Contract No. DE-AC21-83MC20338 and the National Science Foundation under Grant No. MSM-8311643.

References

1 Advani, S. H., Lee, J. K., and Khattab, H., 1984, "Fluid Flow and Associated Response Modeling of Hydraulic Stimulation Processes," *Finite Elements in Fluids*, Vol. 5, Wiley, pp. 299–309.

2 Biot, M. A., Masse, L., and Medlin, W. L., 1982, "A Two-Dimensional Theory of Fracture Propagation," SPE 11067, Society of Petroleum Engineers of AIME, pp. 1–19.

3 Clifton, R. J., and Abou-Sayed, A. S., 1982, "On the Mechanics of Hydraulic Fracturing," *Proceedings of the Ninth U.S. National Congress of Applied Mechanics*, pp. 443–451.

4 Geertsma, J., and Haafkens, R., 1979, "A Comparison of the Theories Predicting Width and Extent of Vertical Hydraulically Induced Fractures," ASME *Journal of Energy Resources Technology*, Vol. 101, pp. 8–17.

5 Segedin, C. M., 1968, "A Note on Geometric Discontinuities in Elastostatics," *International Journal of Engineering Sciences*, pp. 309–312.

6 Settari, A., and Cleary, M. P., 1984, "Three-Dimensional Simulation of Hydraulic Fracturing," *Journal of Petroleum Technology*, pp. 1177–1190.

Incremental Hamilton's Principle With Multiple Time Scales for Nonlinear Aperiodic Vibrations of Shells

S. L. Lau[1] and Y. K. Cheung[2]

Paper [1] provided an extension of the Incremental Harmonic Balance (IHB) Method [2, 3] to aperiodic vibrations of nonlinear systems by introducing the concept of multiple time scales (dimensions), where the solution is assumed to be a combination of sinusoidal terms of incommensurable frequencies. This extended numerical technique is of practical significance as in many cases only the aperiodic vibrations exist in a nonlinear system.

To illustrate the wide applicability of the method and also for later use, this note will present an incremental Hamilton's principle with multiple time scales for thin plates and shallow shells. Based on this principle, a discrete incremental formulation for computing nonlinear vibrations can be deduced directly in conjunction with various approximate procedures such as the finite element method, etc.

Consider the plate problem first. Let $\{d\}$ denote the middle plane displacement vector, such that

$$\{d\} = [u, v, w]^T \tag{1}$$

where u, v are the in-plane displacements and w the deflection of the middle plane. The curvature vector $\{\chi\}$ and in-plane strain vector $\{e\}$ are defined as

$$\{\chi\} = \left[-\frac{\partial^2 w}{\partial x^2}, -\frac{\partial^2 w}{\partial y^2}, -2\frac{\partial^2 w}{\partial x \partial y}\right]^T \tag{2}$$

$$\{e\} = \{\epsilon\} + \tfrac{1}{2}[A]\{\theta\}$$

in which

$$\{\epsilon\} = \left[\frac{\partial u}{\partial x}, \frac{\partial y}{\partial y}, \frac{\partial v}{\partial x} + \frac{\partial u}{\partial y}\right]^T \tag{3}$$

$$[A] = \begin{bmatrix} \frac{\partial w}{\partial x} & 0 \\ 0 & \frac{\partial w}{\partial y} \\ \frac{\partial w}{\partial y} & \frac{\partial w}{\partial x} \end{bmatrix}, \quad \{\theta\} = \begin{Bmatrix} \frac{\partial w}{\partial x} \\ \frac{\partial w}{\partial y} \end{Bmatrix} \tag{4}$$

The Hamilton's principle for thin plates under periodic motion can be written in the form

$$\delta \int_0^T \iint_A \frac{1}{2}\Big[\{e\}^T[D_p]\{e\} + \{\chi\}^T[D_b]\{\chi\} - \rho h \frac{\partial\{d\}^T}{\partial t}\frac{\partial\{d\}}{\partial t} - 2\{d\}^T\{q\}\Big] dxdydt = 0 \tag{5}$$

where ρ = density, h = thickness of plate, t = time, T = period of vibration, A = area of middle plane, $\{q\} = [q_x, q_y, q_z]^T$ = the load intensity vector and

$$[D_p] = \frac{Eh}{1-\nu^2}\begin{bmatrix} 1 & \nu & 0 \\ \nu & 1 & 0 \\ 0 & 0 & \frac{1-\nu}{2} \end{bmatrix},$$

$$[D_b] = \frac{Eh^3}{12(1-\nu)^2}\begin{bmatrix} 1 & \nu & 0 \\ \nu & 1 & 0 \\ 0 & 0 & \frac{1-\nu}{2} \end{bmatrix} \tag{6}$$

with E = Young's modulus, ν = Poisson's ratio.

When the concept of multiple time scales is introduced, the Hamilton's principle given by (5) can easily be generalized (by considering equations (5), (9) of paper [1]) to the following form

$$\underbrace{\delta \int_0^{2\pi}\int_0^{2\pi}\cdots\int_0^{2\pi}}_{m} \iint_A \frac{1}{2}\Big[\{e\}^T[D_p]\{e\} + \{\chi\}^T[D_b]\{\chi\} - \rho h\Big(\sum_j \omega_j \frac{\partial\{d\}^T}{\partial\tau_j}\Big)\Big(\sum_k \omega_k \frac{\partial\{d\}}{\partial\tau_k}\Big) - 2\{d\}^T\{q\}\Big] dxdyd\tau_1 d\tau_2 \ldots d\tau_m = 0 \tag{7}$$

Using similar incrementation procedure as given in [2] and assuming a neighboring state of motion represented by $\{d'\}$, $\{q'\}$ and ω_j' such that

$$\left.\begin{aligned} \{d'\} &= \{d\} + \{\Delta d\} \\ \{q'\} &= \{q\} + \{\Delta q\} \\ \omega_j' &= \omega_j + \Delta\omega_j \qquad (j = 1,2,\ldots,m) \end{aligned}\right\} \tag{8}$$

where $\{\Delta d\}$, $\{\Delta q\}$ and $\Delta\omega_j$ are corresponding increments. Substituting equation (8) into equation (7) and noting that (*i*) only the increments are subjected to variation and (*ii*) small quantities containing the products of over two increments are to be neglected, the incremental Hamilton's principle with multiple time scales for aperiodic vibration of thin plates can be obtained, after some manipulations, in the following form

$$\underbrace{\delta \int_0^{2\pi}\int_0^{2\pi}\cdots\int_0^{2\pi}}_{m}\Big(\iint_A \Big[\tfrac{1}{2}\{\Delta\epsilon\}^T[D_p]\{\Delta\epsilon\} + \tfrac{1}{2}\{\Delta\chi\}^T[D_b]\{\Delta\chi\} + \tfrac{1}{2}\{\Delta\theta\}^T([S] + [S^*])\{\Delta\theta\} + \{\Delta\epsilon\}^T[D_p][A]\{\Delta\theta\} - \tfrac{1}{2}\rho h\Big(\sum_j \omega_j \frac{\partial\{\Delta d\}^T}{\partial\tau_j}\Big)\Big(\sum_j \omega_j \frac{\partial\{\Delta d\}}{\partial\tau_j}\Big)\Big] dxdy - \iint_A \rho h\Big[\Big(\sum_j \omega_j \frac{\partial\{\Delta d\}^T}{\partial\tau_j}\Big)\Big(\sum_j \Delta\omega_j \frac{\partial\{d\}}{\partial\tau_j}\Big) + \Big(\sum_j \Delta\omega_j \frac{\partial\{\Delta d\}^T}{\partial\tau_j}\Big)\Big(\sum_j \omega_j \frac{\partial\{d\}}{\partial\tau_j}\Big)\Big] dxdy - \iint_A \{\Delta d\}^T\{\Delta q\} dxdy$$

[1]Senior Lecturer, Department of Civil and Structural Engineering, Hong Kong Polytechnic, Hong Kong. Member ASME.

[2]Professor and Head, Department of Civil Engineering, University of Hong Kong, Hong Kong.

Manuscript received by ASME Applied Mechanics Division, August, 1985; final revision, November, 1985.

4 Geertsma, J., and Haafkens, R., 1979, "A Comparison of the Theories Predicting Width and Extent of Vertical Hydraulically Induced Fractures," ASME *Journal of Energy Resources Technology*, Vol. 101, pp. 8–17.

5 Segedin, C. M., 1968, "A Note on Geometric Discontinuities in Elastostatics," *International Journal of Engineering Sciences*, pp. 309–312.

6 Settari, A., and Cleary, M. P., 1984, "Three-Dimensional Simulation of Hydraulic Fracturing," *Journal of Petroleum Technology*, pp. 1177–1190.

Incremental Hamilton's Principle With Multiple Time Scales for Nonlinear Aperiodic Vibrations of Shells

S. L. Lau[1] and Y. K. Cheung[2]

Paper [1] provided an extension of the Incremental Harmonic Balance (IHB) Method [2, 3] to aperiodic vibrations of nonlinear systems by introducing the concept of multiple time scales (dimensions), where the solution is assumed to be a combination of sinusoidal terms of incommensurable frequencies. This extended numerical technique is of practical significance as in many cases only the aperiodic vibrations exist in a nonlinear system.

To illustrate the wide applicability of the method and also for later use, this note will present an incremental Hamilton's principle with multiple time scales for thin plates and shallow shells. Based on this principle, a discrete incremental formulation for computing nonlinear vibrations can be deduced directly in conjunction with various approximate procedures such as the finite element method, etc.

Consider the plate problem first. Let $\{d\}$ denote the middle plane displacement vector, such that

$$\{d\} = [u, v, w]^T \tag{1}$$

where u, v are the in-plane displacements and w the deflection of the middle plane. The curvature vector $\{\chi\}$ and in-plane strain vector $\{e\}$ are defined as

$$\{\chi\} = \left[-\frac{\partial^2 w}{\partial x^2}, -\frac{\partial^2 w}{\partial y^2}, -2\frac{\partial^2 w}{\partial x \partial y}\right]^T \tag{2}$$

$$\{e\} = \{\epsilon\} + \tfrac{1}{2}[A]\{\theta\}$$

in which

$$\{\epsilon\} = \left[\frac{\partial u}{\partial x}, \frac{\partial y}{\partial y}, \frac{\partial v}{\partial x} + \frac{\partial u}{\partial y}\right]^T \tag{3}$$

$$[A] = \begin{bmatrix} \frac{\partial w}{\partial x} & 0 \\ 0 & \frac{\partial w}{\partial y} \\ \frac{\partial w}{\partial y} & \frac{\partial w}{\partial x} \end{bmatrix}, \quad \{\theta\} = \begin{Bmatrix} \frac{\partial w}{\partial x} \\ \frac{\partial w}{\partial y} \end{Bmatrix} \tag{4}$$

The Hamilton's principle for thin plates under periodic motion can be written in the form

$$\delta \int_0^T \iint_A \frac{1}{2}\Big[\{e\}^T[D_p]\{e\} + \{\chi\}^T[D_b]\{\chi\} - \rho h \frac{\partial\{d\}^T}{\partial t}\frac{\partial\{d\}}{\partial t} - 2\{d\}^T\{q\}\Big] dxdydt = 0 \tag{5}$$

where ρ = density, h = thickness of plate, t = time, T = period of vibration, A = area of middle plane, $\{q\} = [q_x, q_y, q_z]^T$ = the load intensity vector and

$$[D_p] = \frac{Eh}{1-\nu^2}\begin{bmatrix} 1 & \nu & 0 \\ \nu & 1 & 0 \\ 0 & 0 & \frac{1-\nu}{2} \end{bmatrix},$$

$$[D_b] = \frac{Eh^3}{12(1-\nu)^2}\begin{bmatrix} 1 & \nu & 0 \\ \nu & 1 & 0 \\ 0 & 0 & \frac{1-\nu}{2} \end{bmatrix} \tag{6}$$

with E = Young's modulus, ν = Poisson's ratio.

When the concept of multiple time scales is introduced, the Hamilton's principle given by (5) can easily be generalized (by considering equations (5), (9) of paper [1]) to the following form

$$\underbrace{\delta \int_0^{2\pi}\int_0^{2\pi}\int_0^{2\pi}}_{m} \iint_A \frac{1}{2}\Big[\{e\}^T[D_p]\{e\} + \{\chi\}^T[D_b]\{\chi\} - \rho h\Big(\sum_j \omega_j \frac{\partial\{d\}^T}{\partial\tau_j}\Big)\Big(\sum_k \omega_k \frac{\partial\{d\}}{\partial\tau_k}\Big) - 2\{d\}^T\{q\}\Big] dxdyd\tau_1 d\tau_2 \ldots d\tau_m = 0 \tag{7}$$

Using similar incrementation procedure as given in [2] and assuming a neighboring state of motion represented by $\{d'\}$, $\{q'\}$ and ω_j' such that

$$\left.\begin{aligned} \{d'\} &= \{d\} + \{\Delta d\} \\ \{q'\} &= \{q\} + \{\Delta q\} \\ \omega_j' &= \omega_j + \Delta\omega_j \qquad (j = 1,2,\ldots,m) \end{aligned}\right\} \tag{8}$$

where $\{\Delta d\}$, $\{\Delta q\}$ and $\Delta\omega_j$ are corresponding increments. Substituting equation (8) into equation (7) and noting that (*i*) only the increments are subjected to variation and (*ii*) small quantities containing the products of over two increments are to be neglected, the incremental Hamilton's principle with multiple time scales for aperiodic vibration of thin plates can be obtained, after some manipulations, in the following form

$$\underbrace{\delta \int_0^{2\pi}\int_0^{2\pi}\cdots\int_0^{2\pi}}_{m}\Big(\iint_A \Big[\tfrac{1}{2}\{\Delta\epsilon\}^T[D_p]\{\Delta\epsilon\} + \tfrac{1}{2}\{\Delta\chi\}^T[D_b]\{\Delta\chi\} + \tfrac{1}{2}\{\Delta\theta\}^T([S] + [S^*])\{\Delta\theta\} + \{\Delta\epsilon\}^T[D_p][A]\{\Delta\theta\} - \tfrac{1}{2}\rho h\Big(\sum_j \omega_j \frac{\partial\{\Delta d\}^T}{\partial\tau_j}\Big)\Big(\sum_j \omega_j \frac{\partial\{\Delta d\}}{\partial\tau_j}\Big)\Big] dxdy - \iint_A \rho h\Big[\Big(\sum_j \omega_j \frac{\partial\{\Delta d\}^T}{\partial\tau_j}\Big)\Big(\sum_j \Delta\omega_j \frac{\partial\{d\}}{\partial\tau_j}\Big) + \Big(\sum_j \Delta\omega_j \frac{\partial\{\Delta d\}^T}{\partial\tau_j}\Big)\Big(\sum_j \omega_j \frac{\partial\{d\}}{\partial\tau_j}\Big)\Big] dxdy - \iint_A \{\Delta d\}^T\{\Delta q\} dxdy$$

[1]Senior Lecturer, Department of Civil and Structural Engineering, Hong Kong Polytechnic, Hong Kong. Member ASME.

[2]Professor and Head, Department of Civil Engineering, University of Hong Kong, Hong Kong.

Manuscript received by ASME Applied Mechanics Division, August, 1985; final revision, November, 1985.

$$+\iint_A \Big[\{\Delta\epsilon\}^T\{S\}+\{\Delta\theta\}^T[S]\{\theta\}+\{\Delta\chi\}^T[D_b]\{\chi\}$$

$$-\rho h\Big(\sum_j \omega_j \frac{\partial\{\Delta d\}^T}{\partial\tau_j}\Big)\Big(\sum_j \omega_j \frac{\partial\{d\}^T}{\partial\tau_j}\Big)$$

$$-\{\Delta d\}^T\{q\}\Big]dxdy\Big)d\tau_1 d\tau_2 \ldots d\tau_m = 0 \tag{9}$$

where $\{S\}$ is in the in-plane resultant force vector of the current state and is given by

$$\{S\}=[S_x, S_y, S_{xy}]^T=[D_p]\{e\} \tag{10}$$

$[S]$ is a square matrix consisting of components of $\{S\}$, i.e.,

$$[S]=\begin{bmatrix} S_x & S_{xy} \\ S_{xy} & S_y \end{bmatrix} \tag{11}$$

and $[S^*]$ is defined as

$$[S^*]=\begin{bmatrix} S_x^* & S_{xy}^* \\ S_{xy}^* & S_y^* \end{bmatrix}=[A]^T[D_p][A] \tag{12}$$

This relation can be rewritten as

$$\{S^*\}=[S_x^*,S_y^*,S_{xy}^*]^T=[D_p^*][A]\{\theta\} \tag{13}$$

in which

$$[D_p^*]=\frac{Eh}{1-\nu^2}\begin{bmatrix} 1 & \frac{1-\nu}{2} & 0 \\ \frac{1-\nu}{2} & 1 & 0 \\ \nu & 0 & \frac{1+\nu}{2} \end{bmatrix} \tag{14}$$

The last area integral in equation (9) gives the correction term which is useful in the process of incrementation for preventing the solution from drifting away.

For the case of thin shallow shell, it is obvious that equation (9) is still valid if the definition of $\{\epsilon\}$ is modified to become

$$\{\epsilon\}=\Big[\frac{\partial u}{\partial x}-k_x w, \frac{\partial v}{\partial y}-k_y w, \frac{\partial v}{\partial x}+\frac{\partial u}{\partial y}-2k_{xy}w\Big]^T \tag{15}$$

where k_x, k_y and k_{xy} denote the curvatures and twist of the middle surface of the shallow shell.

References

Lau, S. L., and Cheung, Y. K., 1981, "Amplitude Incremental Variational Principle for Nonlinear Vibration of Elastic Systems," ASME JOURNAL OF APPLIED MECHANICS, Vol. 48, pp. 959–964.

Lau, S. L., Cheung, Y. K., and Wu, S. Y., 1982, "Variable Parameter Incrementation Method for Dynamic Instability of Linear and Nonlinear Elastic Systems," ASME JOURNAL OF APPLIED MECHANICS, Vol. 49, pp. 849–853.

Lau, S. L., Cheung, Y. K., and Wu, S. Y., 1983, "Incremental Harmonic Balance Method With Multiple Time Scales for Aperiodic Vibration of Nonlinear Systems," ASME JOURNAL OF APPLIED MECHANICS, Vol. 50, pp. 871–876.

A Simply Supported Column Under a Tangential Follower Force as a Self-Adjoint System

B. L. Ly[1]

[1]Atomic Energy of Canada Limited, Mississauga, Ontario, Canada L5K 1B2.

Manuscript received by ASME Applied Mechanics Division, May 17, 1985; final revision August 28, 1985.

Introduction

In spite of the presence of the polygenetic force, some nonconservative systems lose their stability by divergence. When buckled, they assume a nontrivial equilibrium configuration. The Pfluger column (Pfluger, 1964; Leipholz, 1970) is such a system. Stability of a nonconservative system of the divergence type can be studied from a consideration of static equilibrium. The buckling load can be estimated with the use of the Galerkin method or the generalized Rayleigh quotient.

This paper shows that a simply supported column which is under the action of a distributed tangential follower force can be treated like a self-adjoint system, with the buckling load determined via the upperbound principle. Such a column includes the Pfluger column as a special case. A variational method is presented, in which a functional and a Rayleigh quotient are formulated in terms of the bending moment rather than the deflection of the column. The functional and the Rayleigh quotient can be evaluated by using the Ritz method. A better estimate of the buckling load, however, can be obtained by means of the Schmidt technique (Schmidt, 1982 and 1983; Bert, 1984).

The Governing Differential Equation

The lateral deflection $w(x)$ of a column which is subjected to a distributed tangential follower force and is simply supported at both ends satisfies the differential equation

$$EI\frac{d^4w}{dx^4}+qf(x)\frac{d^2w}{dx^2}=0, \qquad x\in[0,L] \tag{1}$$

and the boundary conditions: $w = d^2w/dx^2 = 0$ at $x = 0$ and $x = L$. EI is the flexural rigidity of the column, q is the intensity of the follower force, and $f(x)$, a positive function, defines the distribution of the polygenetic force. For a uniform distribution, $f(x) = L-x$, L being the length of the column.

With $EI\, d^2w/dx^2 = -M$, the bending moment in the column, and $z = 1-x/L$, equation (1) and the boundary conditions are rewritten as

$$M''+pg(z)M=0, \tag{2}$$

and

$$M(0)=M(1)=0,$$

where $M'' = d^2M/dz^2$ and $p = qL^3/EI$.

Equation (2) in M is self-adjoint, whereas equation (1) in w is not. In the ensuing analysis, equation (2) is to be considered.

Variational Method for the Buckling Load

A functional H is chosen for equation (2) in the form of

$$H=\int_0^1 [(M')^2-pgM^2]dz. \tag{3}$$

A Rayleigh quotient for the buckling load is formulated from equation (3) as

$$p_{cr}=\int (M')^2dz/\int gM^2dz$$

$$=\inf_y \Big[\int (y')^2dz/\int gy^2dz\Big], \tag{4}$$

where $y(z)$ is an admissible function which possesses a first derivative and satisfies the boundary conditions $y(0) = y(1) = 0$. H is positive definite when $p<p_{cr}$. Furthermore, if $p<p_{cr}$, when H approaches zero it implies that M and M' also approach zero.

H is stationary in the neighborhood of the eigenfunction because

$$\frac{1}{2}\delta H=M'\delta M\Big]_0^1-\int (M''+pgM)\delta M\, dz=0, \tag{5}$$

in view of the boundary conditions and the differential equa-

$$+\iint_A \Big[\{\Delta\epsilon\}^T\{S\}+\{\Delta\theta\}^T[S]\{\theta\}+\{\Delta\chi\}^T[D_b]\{\chi\}$$

$$-\rho h\Big(\sum_j \omega_j \frac{\partial\{\Delta d\}^T}{\partial\tau_j}\Big)\Big(\sum_j \omega_j \frac{\partial\{d\}^T}{\partial\tau_j}\Big)$$

$$-\{\Delta d\}^T\{q\}\Big]dxdy\Big)d\tau_1 d\tau_2 \ldots d\tau_m = 0 \tag{9}$$

where $\{S\}$ is in the in-plane resultant force vector of the current state and is given by

$$\{S\}=[S_x, S_y, S_{xy}]^T=[D_p]\{e\} \tag{10}$$

$[S]$ is a square matrix consisting of components of $\{S\}$, i.e.,

$$[S]=\begin{bmatrix} S_x & S_{xy} \\ S_{xy} & S_y \end{bmatrix} \tag{11}$$

and $[S^*]$ is defined as

$$[S^*]=\begin{bmatrix} S_x^* & S_{xy}^* \\ S_{xy}^* & S_y^* \end{bmatrix}=[A]^T[D_p][A] \tag{12}$$

This relation can be rewritten as

$$\{S^*\}=[S_x^*,S_y^*,S_{xy}^*]^T=[D_p^*][A]\{\theta\} \tag{13}$$

in which

$$[D_p^*]=\frac{Eh}{1-\nu^2}\begin{bmatrix} 1 & \frac{1-\nu}{2} & 0 \\ \frac{1-\nu}{2} & 1 & 0 \\ \nu & 0 & \frac{1+\nu}{2} \end{bmatrix} \tag{14}$$

The last area integral in equation (9) gives the correction term which is useful in the process of incrementation for preventing the solution from drifting away.

For the case of thin shallow shell, it is obvious that equation (9) is still valid if the definition of $\{\epsilon\}$ is modified to become

$$\{\epsilon\}=\Big[\frac{\partial u}{\partial x}-k_x w, \frac{\partial v}{\partial y}-k_y w, \frac{\partial v}{\partial x}+\frac{\partial u}{\partial y}-2k_{xy}w\Big]^T \tag{15}$$

where k_x, k_y and k_{xy} denote the curvatures and twist of the middle surface of the shallow shell.

References

Lau, S. L., and Cheung, Y. K., 1981, "Amplitude Incremental Variational Principle for Nonlinear Vibration of Elastic Systems," ASME JOURNAL OF APPLIED MECHANICS, Vol. 48, pp. 959–964.

Lau, S. L., Cheung, Y. K., and Wu, S. Y., 1982, "Variable Parameter Incrementation Method for Dynamic Instability of Linear and Nonlinear Elastic Systems," ASME JOURNAL OF APPLIED MECHANICS, Vol. 49, pp. 849–853.

Lau, S. L., Cheung, Y. K., and Wu, S. Y., 1983, "Incremental Harmonic Balance Method With Multiple Time Scales for Aperiodic Vibration of Nonlinear Systems," ASME JOURNAL OF APPLIED MECHANICS, Vol. 50, pp. 871–876.

A Simply Supported Column Under a Tangential Follower Force as a Self-Adjoint System

B. L. Ly[1]

[1]Atomic Energy of Canada Limited, Mississauga, Ontario, Canada L5K 1B2.

Manuscript received by ASME Applied Mechanics Division, May 17, 1985; final revision August 28, 1985.

Introduction

In spite of the presence of the polygenetic force, some nonconservative systems lose their stability by divergence. When buckled, they assume a nontrivial equilibrium configuration. The Pfluger column (Pfluger, 1964; Leipholz, 1970) is such a system. Stability of a nonconservative system of the divergence type can be studied from a consideration of static equilibrium. The buckling load can be estimated with the use of the Galerkin method or the generalized Rayleigh quotient.

This paper shows that a simply supported column which is under the action of a distributed tangential follower force can be treated like a self-adjoint system, with the buckling load determined via the upperbound principle. Such a column includes the Pfluger column as a special case. A variational method is presented, in which a functional and a Rayleigh quotient are formulated in terms of the bending moment rather than the deflection of the column. The functional and the Rayleigh quotient can be evaluated by using the Ritz method. A better estimate of the buckling load, however, can be obtained by means of the Schmidt technique (Schmidt, 1982 and 1983; Bert, 1984).

The Governing Differential Equation

The lateral deflection $w(x)$ of a column which is subjected to a distributed tangential follower force and is simply supported at both ends satisfies the differential equation

$$EI\frac{d^4w}{dx^4}+qf(x)\frac{d^2w}{dx^2}=0, \qquad x\in[0,L] \tag{1}$$

and the boundary conditions: $w = d^2w/dx^2 = 0$ at $x = 0$ and $x = L$. EI is the flexural rigidity of the column, q is the intensity of the follower force, and $f(x)$, a positive function, defines the distribution of the polygenetic force. For a uniform distribution, $f(x) = L-x$, L being the length of the column.

With $EI\, d^2w/dx^2 = -M$, the bending moment in the column, and $z = 1-x/L$, equation (1) and the boundary conditions are rewritten as

$$M''+pg(z)M=0, \tag{2}$$

and

$$M(0)=M(1)=0,$$

where $M'' = d^2M/dz^2$ and $p = qL^3/EI$.

Equation (2) in M is self-adjoint, whereas equation (1) in w is not. In the ensuing analysis, equation (2) is to be considered.

Variational Method for the Buckling Load

A functional H is chosen for equation (2) in the form of

$$H=\int_0^1 [(M')^2-pgM^2]dz. \tag{3}$$

A Rayleigh quotient for the buckling load is formulated from equation (3) as

$$p_{cr}=\int (M')^2dz/\int gM^2dz$$

$$=\inf_y \Big[\int (y')^2dz/\int gy^2dz\Big], \tag{4}$$

where $y(z)$ is an admissible function which possesses a first derivative and satisfies the boundary conditions $y(0) = y(1) = 0$. H is positive definite when $p<p_{cr}$. Furthermore, if $p<p_{cr}$, when H approaches zero it implies that M and M' also approach zero.

H is stationary in the neighborhood of the eigenfunction because

$$\frac{1}{2}\delta H=M'\delta M\Big]_0^1-\int (M''+pgM)\delta M\, dz=0, \tag{5}$$

in view of the boundary conditions and the differential equa-

tion. Likewise, the Rayleigh quotient is also stationary in the neighborhood of the eigenfunction because of the stationary property of the functional.

As can be seen, the preceding variational formulation is the same as that for a self-adjoint system. The Rayleigh quotient can be evaluated by using the Ritz method to yield an upper-bound estimate of the buckling load. However, the Schmidt technique can be used to obtain a better estimate. In the Schmidt technqiue, the coordinate function contains terms with nonintegral powers. These powers are not predetermined but are treated as variables to be optimized. Because such coordinate functions include polynomials as a special case and the nonintegral powers are determined as a result of optimization, naturally the Schmidt technique would yield a better estimate of the eigenvalue than the Ritz method.

To apply the Schmidt technique, the static deflected shape of a transversally loaded simply supported beam is chosen as the coordinate function. In this regard, the Schmidt technique may be viewed as being equivalent to the determination of the optimum transverse loading that optimizes the functional H or the Rayleigh quotient.

Examples

For illustration of the method, consider the Pfluger column and the Hauger problem where the tangential force varies in a linear fashion, that is, $f(x) = 1/2\,(L-x)^2$.

The coordinate function which approximates the bending moment is assumed to be in the form of

$$y(z) = z - z^r, \tag{6}$$

where $r > 2$ is a power to be determined so as to minimize the buckling load. It is easy to show that equation (6) represents the bending moment of a simply supported beam under a transverse loading cz^{r-2}, c being a scale factor.

(*A*) The Pfluger Column. In this case, $g(z) = z$. Substitution of the expression in equation (6) into equation (4) yields

$$p_{cr} = \frac{\dfrac{(r-1)^2}{2r-1}}{\dfrac{1}{4} + \dfrac{1}{2r+2} - \dfrac{2}{r+3}}. \tag{7}$$

The buckling load is obtained as the smallest value of the expression on the right-hand-side of equation (7), which is equal to 19.165 when $r = 2.79016$. This estimate of the buckling load is only 1.1 percent higher than the exact value of 18.957 (see Appendix). A still better estimate is equal to $p_{cr} = 19.148$ when the coordinate function is chosen as

$$y(z) = z^{1.0449} - z^{2.79015}. \tag{8}$$

(*B*) The Hauger Problem. In this case, $g(z) = Lz^2/2$. With use made of equation (6), the Rayleigh quotient yields

$$p_{cr}L = \frac{\dfrac{2(r-1)^2}{2r-1}}{\dfrac{1}{5} - \dfrac{2}{r+4} + \dfrac{1}{2r+3}}. \tag{9}$$

The smallest value of $p_{cr}L$ is found to be equal to 62.5 when r is equal to 3.5. This estimate is only 0.35 percent higher than the value of 62.28 given by Hauger.

Conclusion

The differential equation that governs the bending moment in a simply supported column which is subjected to a polygenetic force is self-adjoint. From this differential equation a functional and a Rayleigh quotient are formulated in terms of the bending moment. This allows the nonconservative system to be treated like a self-adjoint system. It is also shown that a very good estimate of the buckling load can be obtained if the Rayleigh quotient is evaluated by means of the Schmidt technique.

References

Bert, C. W., "Improved Technique for Estimating Buckling Loads," *Journal of Engineering Mechanics*, Vol. 110, No. 12, Dec. 1984.

Leipholz, H., *Stability Theory*, Academic Press, New York, 1970.

Pfluger, A., *Stability Problems of Elastostatic*, Springer, Berlin, 1964.

Schmidt, R., "Technique for Estimating Natural Frequencies," *Journal of Engineering Mechanics*, Vol. 109, 1983, pp. 654–657.

Schmidt, R., "Estimation of Buckling Loads and Other Eigenvalues Via a Modification of the Rayleigh-Ritz Method," ASME JOURNAL OF APPLIED MECHANICS, Vol. 49, 1982, pp. 639–640.

APPENDIX

The exact solution of the buckling load of the Pfluger column is given here. With $g(z) = z$, equation (2) is a Bessel differential equation. Its solution is a linear combination of Bessel functions:

$$M = z^{1/2}\left[AJ_{-1/3}\left(\frac{2}{3}p^{1/2}z^{3/2}\right) + BJ_{1/3}\left(\frac{2}{3}p^{1/2}z^{3/2}\right)\right],$$

where A and B are arbitrary constants, and $J_n(z)$ are Bessel functions of order n. The above equation is widely known as the "Airy Integral."

The boundary condition $M(0) = 0$ yields $A = 0$ because

$$z^{1/2}J_{-1/3}\left(\frac{2}{3}p^{1/2}z^{3/2}\right) = 1 - \frac{pz^3}{6} + \frac{p^2z^6}{180} - \frac{p^3z^9}{12960} + \cdots\cdots,$$

whereas

$$z^{1/2}J_{1/3}\left(\frac{2}{3}p^{1/2}z^{3/2}\right) = z\left(1 - \frac{pz^3}{12} + \frac{p^2z^6}{504} - \frac{p^3z^9}{45360} + \cdots\right).$$

The other boundary condition $M(1) = 0$ yields

$$J_{1/3}\left(\frac{2}{3}p^{1/2}\right) = 0,$$

assuming that $B \neq 0$ otherwise the solution is trivial.

The above equation is the characteristic equation from which the buckling load p_{cr} is calculated. The first zero of $J_{1/3}(z) = 0$ is $z = 2.90262$. Therefore, the buckling load is found to be

$$p_{cr} = 18.957.$$

Optimal Forms of Shallow Arches With Respect to Deflection

R. H. Plaut[1] and L. W. Johnson[2]

Formulation

We consider a shallow elastic arch with uniform cross section. It is subjected to a uniformly distributed load of given intensity, and its ends are either simply supported or clamped. The cross section, material, span, and length of the arch are specified. Our objective is the determination of the arch form which will minimize a measure of the deflection under the given load.

A similar problem involving the central deflection of a simply supported arch was treated by Stadler (1977) using con-

[1]Professor, Department of Civil Engineering, Virginia Polytechnic Institute and State University, Blacksburg, VA 24061. Mem. ASME.

[2]Professor, Department of Mathematics, Virginia Polytechnic Institute and State University, Blacksburg, VA 24061.

Manuscript received by ASME Applied Mechanics Division, July 2, 1985; final revision, October 25, 1985.

tion. Likewise, the Rayleigh quotient is also stationary in the neighborhood of the eigenfunction because of the stationary property of the functional.

As can be seen, the preceding variational formulation is the same as that for a self-adjoint system. The Rayleigh quotient can be evaluated by using the Ritz method to yield an upper-bound estimate of the buckling load. However, the Schmidt technique can be used to obtain a better estimate. In the Schmidt technqiue, the coordinate function contains terms with nonintegral powers. These powers are not predetermined but are treated as variables to be optimized. Because such coordinate functions include polynomials as a special case and the nonintegral powers are determined as a result of optimization, naturally the Schmidt technique would yield a better estimate of the eigenvalue than the Ritz method.

To apply the Schmidt technique, the static deflected shape of a transversally loaded simply supported beam is chosen as the coordinate function. In this regard, the Schmidt technique may be viewed as being equivalent to the determination of the optimum transverse loading that optimizes the functional H or the Rayleigh quotient.

Examples

For illustration of the method, consider the Pfluger column and the Hauger problem where the tangential force varies in a linear fashion, that is, $f(x) = 1/2\,(L-x)^2$.

The coordinate function which approximates the bending moment is assumed to be in the form of

$$y(z) = z - z^r, \tag{6}$$

where $r > 2$ is a power to be determined so as to minimize the buckling load. It is easy to show that equation (6) represents the bending moment of a simply supported beam under a transverse loading cz^{r-2}, c being a scale factor.

(*A*) The Pfluger Column. In this case, $g(z) = z$. Substitution of the expression in equation (6) into equation (4) yields

$$p_{cr} = \frac{\dfrac{(r-1)^2}{2r-1}}{\dfrac{1}{4} + \dfrac{1}{2r+2} - \dfrac{2}{r+3}}. \tag{7}$$

The buckling load is obtained as the smallest value of the expression on the right-hand-side of equation (7), which is equal to 19.165 when $r = 2.79016$. This estimate of the buckling load is only 1.1 percent higher than the exact value of 18.957 (see Appendix). A still better estimate is equal to $p_{cr} = 19.148$ when the coordinate function is chosen as

$$y(z) = z^{1.0449} - z^{2.79015}. \tag{8}$$

(*B*) The Hauger Problem. In this case, $g(z) = Lz^2/2$. With use made of equation (6), the Rayleigh quotient yields

$$p_{cr}L = \frac{\dfrac{2(r-1)^2}{2r-1}}{\dfrac{1}{5} - \dfrac{2}{r+4} + \dfrac{1}{2r+3}}. \tag{9}$$

The smallest value of $p_{cr}L$ is found to be equal to 62.5 when r is equal to 3.5. This estimate is only 0.35 percent higher than the value of 62.28 given by Hauger.

Conclusion

The differential equation that governs the bending moment in a simply supported column which is subjected to a polygenetic force is self-adjoint. From this differential equation a functional and a Rayleigh quotient are formulated in terms of the bending moment. This allows the nonconservative system to be treated like a self-adjoint system. It is also shown that a very good estimate of the buckling load can be obtained if the Rayleigh quotient is evaluated by means of the Schmidt technique.

References

Bert, C. W., "Improved Technique for Estimating Buckling Loads," *Journal of Engineering Mechanics*, Vol. 110, No. 12, Dec. 1984.

Leipholz, H., *Stability Theory*, Academic Press, New York, 1970.

Pfluger, A., *Stability Problems of Elastostatic*, Springer, Berlin, 1964.

Schmidt, R., "Technique for Estimating Natural Frequencies," *Journal of Engineering Mechanics*, Vol. 109, 1983, pp. 654–657.

Schmidt, R., "Estimation of Buckling Loads and Other Eigenvalues Via a Modification of the Rayleigh-Ritz Method," ASME JOURNAL OF APPLIED MECHANICS, Vol. 49, 1982, pp. 639–640.

APPENDIX

The exact solution of the buckling load of the Pfluger column is given here. With $g(z) = z$, equation (2) is a Bessel differential equation. Its solution is a linear combination of Bessel functions:

$$M = z^{1/2}\left[AJ_{-1/3}\left(\frac{2}{3}p^{1/2}z^{3/2}\right) + BJ_{1/3}\left(\frac{2}{3}p^{1/2}z^{3/2}\right)\right],$$

where A and B are arbitrary constants, and $J_n(z)$ are Bessel functions of order n. The above equation is widely known as the "Airy Integral."

The boundary condition $M(0) = 0$ yields $A = 0$ because

$$z^{1/2}J_{-1/3}\left(\frac{2}{3}p^{1/2}z^{3/2}\right) = 1 - \frac{pz^3}{6} + \frac{p^2z^6}{180} - \frac{p^3z^9}{12960} + \cdots\cdots,$$

whereas

$$z^{1/2}J_{1/3}\left(\frac{2}{3}p^{1/2}z^{3/2}\right) = z\left(1 - \frac{pz^3}{12} + \frac{p^2z^6}{504} - \frac{p^3z^9}{45360} + \cdots\right).$$

The other boundary condition $M(1) = 0$ yields

$$J_{1/3}\left(\frac{2}{3}p^{1/2}\right) = 0,$$

assuming that $B \neq 0$ otherwise the solution is trivial.

The above equation is the characteristic equation from which the buckling load p_{cr} is calculated. The first zero of $J_{1/3}(z) = 0$ is $z = 2.90262$. Therefore, the buckling load is found to be

$$p_{cr} = 18.957.$$

Optimal Forms of Shallow Arches With Respect to Deflection

R. H. Plaut[1] and L. W. Johnson[2]

Formulation

We consider a shallow elastic arch with uniform cross section. It is subjected to a uniformly distributed load of given intensity, and its ends are either simply supported or clamped. The cross section, material, span, and length of the arch are specified. Our objective is the determination of the arch form which will minimize a measure of the deflection under the given load.

A similar problem involving the central deflection of a simply supported arch was treated by Stadler (1977) using con-

[1]Professor, Department of Civil Engineering, Virginia Polytechnic Institute and State University, Blacksburg, VA 24061. Mem. ASME.

[2]Professor, Department of Mathematics, Virginia Polytechnic Institute and State University, Blacksburg, VA 24061.

Manuscript received by ASME Applied Mechanics Division, July 2, 1985; final revision, October 25, 1985.

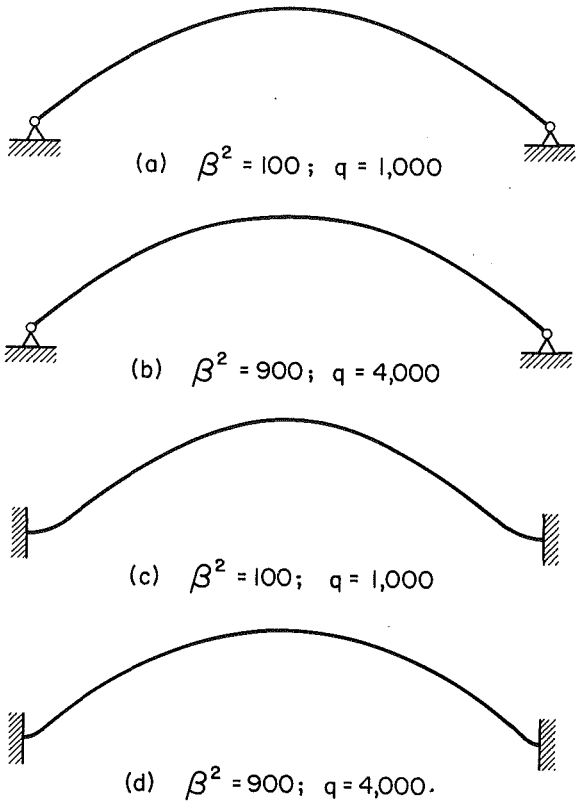

Fig. 1 Optimal arch forms ($p = 10$)

trol theory. Here, the calculus of variations is utilized and the formulation is similar to that used by Plaut and Olhoff (1983) and Plaut (1983) for optimization with respect to vibration or stability. When the arch ends are clamped, we also find in the present results that the optimal forms have zero slope at the ends.

The arch has cross-sectional area A, moment of inertia I, Young's modulus E, total arc length S, and span L. The horizontal coordinate is denoted X, with $0 \le X \le L$. The unloaded configuration of the arch is given by the vertical coordinate $Y_o(X)$, and the downward deflection under a uniformly distributed load Q is denoted $W(X)$. We introduce the nondimensional quantities

$$x = X/L, y_o = Y_o/(2r), w = W/(2r), q = QL^4/(2EIr),$$
$$r = \sqrt{I/A}, \quad \beta^2 = (S-L)AL/(2I), \tag{1}$$

where β^2 is an arch length parameter.

The equilibrium equation is given by

$$w'''' (x) - \alpha w'' (x) = \alpha y_o'' (x) - q \tag{2}$$

where the induced axial thrust α is defined as

$$\alpha = 2\int_0^1 [(w')^2 + 2w' y_o'] dx. \tag{3}$$

The boundary conditions are $w = w'' = 0$ at simply supported ends and $w = w' = 0$ at clamped ends. For shallow arches, the length parameter satisfies the equation

$$\int_0^1 (y_o')^2 dx = \beta^2. \tag{4}$$

As an objective function, we adopt the deflection measure

$$f = \left\{ \int_0^1 w^p dx \right\}^{1/p} \tag{5}$$

where p is an even, positive integer (Olhoff and Taylor, 1983). As p gets large, the function f approaches the maximum deflection of the arch.

For given load intensity q, arch length parameter β^2, and value of p in (5), we want to find the arch form $y_o(x)$ that minimizes f subject to (2) and (4). Therefore, we define the functional

$$\mathcal{L} = \int_0^1 w^p dx - \int_0^1 \phi [w'''' - \alpha (w'' + y_o'') + q] dx$$
$$- \mu \left[\int_0^1 (y_o')^2 dx - \beta^2 \right] \tag{6}$$

where $\phi(x)$ and μ are Lagrange multipliers. Stationarity of $\mathcal{L}$ with respect to w leads to the adjoint equation

$$\phi'''' (x) - \alpha \phi'' (x) + 2\eta [w'' (x) + y_o'' (x)] = p[w(x)]^{p-1} \tag{7}$$

where

$$\eta = 2\int_0^1 (w'' + y_o'') \phi dx \tag{8}$$

and $\phi(x)$ satisfies the same boundary conditions as $w(x)$. Stationarity of $\mathcal{L}$ with respect to y_o' leads to the optimality condition

$$\mu y_o' (x) = \eta w' (x) - (\alpha/2) \phi' (x) \tag{9}$$

where α is defined in (3) and η in (8). From (9), we note that $y_o' = 0$ at clamped ends.

Results

Equations (2), (7), and (9) are discretized using the finite difference method. Equation (9) is then solved at the mesh points using a quasi-Newton method.

Optimal arch forms $y_o(x)$ were computed for two combinations of the arch length parameter β^2 and the load intensity q: $\beta^2 = 100$, $q = 1{,}000$, and $\beta^2 = 900$, $q = 4{,}000$. In the objective function f, defined in (5), values $p = 2$ and $p = 10$ were used. The results, normalized by β, are depicted in Fig. 1 for $p = 10$ and the two sets of boundary conditions. The optimal form in Fig. 1(*a*) is lower near the ends, and higher in the middle, than the form in Fig. 1(*b*). The same is true for Fig. 1(*c*) in relation to Fig. 1(*d*). In comparison to the value of the objective function f for a corresponding circular arch, the value of the objective function f for the optimal forms in Fig. 1(*a*)-(*d*) is lower by 11 percent, 19 percent, 32 percent, and 26 percent, respectively.

For the case $p = 2$, the optimal forms are almost identical to those for $p = 10$. They tend to be slightly lower near the ends, and higher in the middle, than the forms in Fig. 1. The decreases in the objective function for the results corresponding to Fig. 1(*a*)-(*d*) when $p = 2$ are 3 percent, 5 percent, 23 percent, and 19 percent, respectively, in comparison to a circular arch.

Acknowledgment

The first author was supported by the National Science Foundation under Grant CEE-8210222.

References

Olhoff, N., and Taylor, J. E., 1983, "On Structural Optimization," ASME JOURNAL OF APPLIED MECHANICS, Vol. 50, pp. 1139-1151.

Plaut, R. H., 1983, "Optimal Arch Form for Stability Under End Moments," *Developments in Mechanics*, Vol. 12, Proceedings of the 18th Midwestern Mechanics Conference, University of Iowa, pp. 87-89.

Plaut, R. H., and Olhoff, N., 1983, "Optimal Forms of Shallow Arches with Respect to Vibration and Stability," *Journal of Structural Mechanics*, Vol. 11, pp. 81-100.

Stadler, W., 1977, "Uniform Shallow Arches of Minimum Weight and Minimum Maximum Deflection," *Journal of Optimization Theory and Applications*, Vol. 23, pp. 137-165.

Vibration Analysis of a Rectangular Plate Resting on Line Supports by the Lagrange Multiplier-Fourier Expansion Approach

Y. Narita[1]

Introduction

Although use of Lagrange multipliers in variational problems has been well known, its application to vibration analysis of elastic structural elements has received sparse treatment after the pioneering works of Dowell (1971 and 1972). Recently, the Ritz–Lagrange multiplier method has been extensively used for vibrations of point supported flat plates (Narita, 1984 and 1985) and shallow shells (Narita and Leissa, 1984), and it is noted that this approach yields quite accurate results for problems involving point supports.

In the present note, an extension of this method is made to deal with vibration of plates resting on continuous line supports. For this purpose, the constraint equation is written as a line integral along the support and the Lagrange multiplier of a function of the line coordinates is expanded into the Fourier sine series. The resulting functional is then minimized with respect to coefficients both in a trial function and in the Fourier series. The analysis is applied in the numerical examples to determination of natural frequencies for square plates having partial line supports. Convergence of the method is demonstrated, and comparison with exact solutions is made for a special case.

Analysis

Consider the free transverse vibration of a flat plate resting on line supports of arbitrary location, as shown in Figure 1(*a*). The functional for the system may be written as

$$F = U - T + \int_S \tilde{W}(s)\lambda(s)ds \tag{1}$$

where the maximum strain and kinetic energies stored in the plate are defined by U and T, respectively (Leissa, 1969). A constraint condition along the support is expressed as a line integral, where λ is a Lagrange multiplier and $\tilde{W}$ is the quantity associated with deflection of the plate. Unlike the case of point supports, however, the present Lagrange multiplier is a function of the line coordinates and is, therefore, expanded into the Fourier (sine) series as

$$\lambda(s) = \sum_{i=1}^{I} C_i \sin \frac{i\pi s}{\ell} \tag{2}$$

where the C_i are Fourier coefficients and ℓ is the length of the support. For a trial function denoting deflection of the unconstrained plate, it is convenient to use double power series

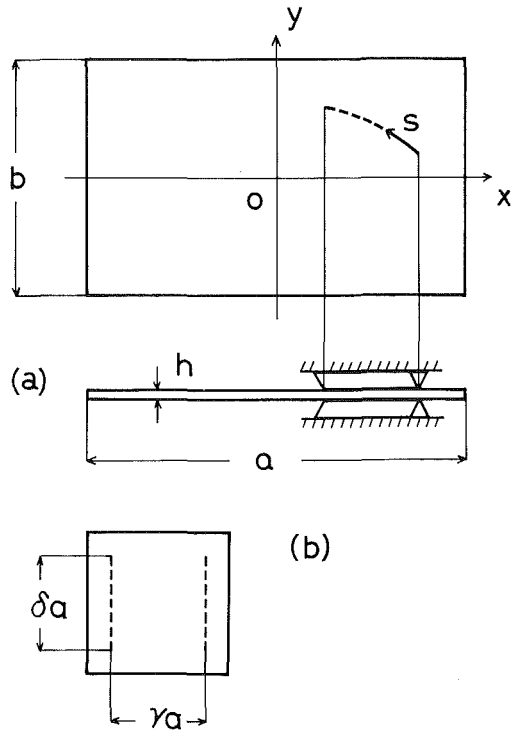

Fig. 1 (*a*) Rectangular plate resting on continuous line supports, (*b*) numerical example

$$W(x,y) = \sum_{m=0}^{M} \sum_{n=0}^{N} A_{mn} x^m y^n \tag{3}$$

Equations (2) and (3) are substituted into equation (1), and the functional is minimized with respect to coefficients A_{mn} and Fourier coefficients C_i in the Ritz minimizing process. This procedure yields a frequency equation in the coefficients $\{A_{mn}\ C_i\}$, the eigenvalues of which are frequency parameters for the plate.

Numerical Examples and Discussions

Figure 1(*b*) illustrates a numerical example a square plate supported on a pair of partial straight lines. Because of the two-fold symmetry of the plate, four types of vibration modes exist: *SS*, *SA*, *AS*, *AA* modes (*S*: symmetric, *A*: antisymmetric), and in the frequency equation m and n take on odd or even integer values, depending upon the mode in question. For example, for the *SA* mode the mode shape is symmetric about the y axis and antisymmetric about the x axis, with $m = 0, 2, 4, \ldots$ and $n = 1, 3, 5, \ldots$. The constraints are placed only in the first quarter plane to express the complete support shape. The frequency parameter is defined by $\Omega = \omega a^2(\rho h/D)^{1/2}$ (ω: natural radian frequency, ρ: mass density per unit volume, D

Table 1 Convergence of frequency parameters Ω with the number of Fourier terms ($\gamma = \delta = 0.8$, $m \times n = 7 \times 7$, $\nu = 0.3$)

		Mode				
		SS−1	*SS*−2	*SA*−1	AS−1	*AA*−1
I	4	14.811	44.832	23.445	57.125	66.974
	5	14.900	46.190	23.868	57.635	68.215
	6	14.940	46.760	24.032	57.866	68.676
	7	14.944	46.782	24.038	57.899	68.731

[1]Associate Professor, Department of Mechanical Engineering, Hokkaido Institute of Technology, Sapporo 006, Japan.

Manuscript received by ASME Applied Mechanics Division, June 5, 1985; final revision, August 7, 1985.

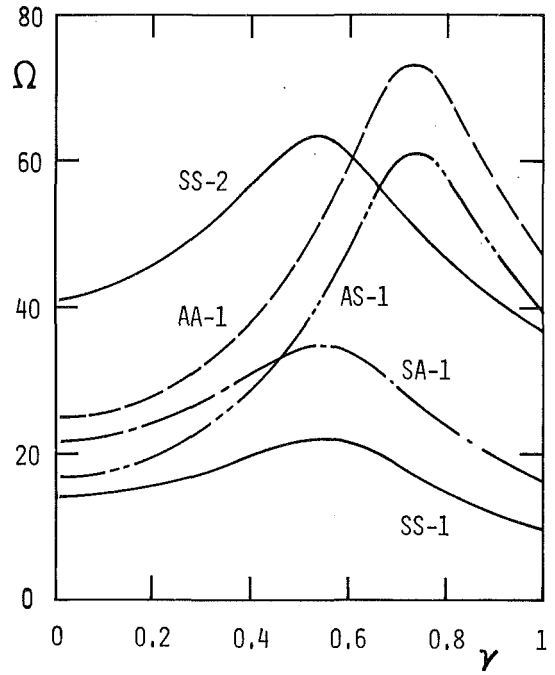

Fig. 2 Variation of frequency parameters with distance of a pair of partial line supports ($\delta = 0.6$)

$= Eh^3/12(1-\nu^2)$: flexural rigidity, E: Young's modulus, ν: Poisson's ratio).

Table 1 presents a convergence study with the number of Fourier terms I in the case of internal supports ($\gamma = \delta = 0.8$). As more Fourier terms are used, the frequency values tend to converge, yielding accurate values, e.g., at $I = 7$. These lowest five frequencies are calculated for the fixed number of $m = n = 7$, which are sufficiently converged in m and n (Narita, 1984). Furthermore, the present results were compared to exact values (Leissa, 1973) for a special case of the two opposite edges simply supported ($\gamma = \delta = 1$), and agreement was found to five significant figures.

In Figure 2, the variation of frequencies is illustrated for the example as a function of the support distance γ. The length of the supports is taken as $\delta = 0.6$. It is seen here that each frequency curve for the *SS*-1, 2, and *SA*-1 mode has a peak around $\gamma = 0.55$, while the frequency peaks of the *AS*-1 and *AA*-1 mode are found around $\gamma = 0.75$. Apparently, there exists an optimal distance of the two line supports for each mode, which causes the natural frequency to be a maximum value.

The present method may be used to analyze the problem of mixed boundary conditions simply by locating supports along parts of the edges. One also notes that the clamping support can be introduced by using an additional constraint in rotation.

References

Dowell, E. H., 1971, "Free Vibrations of a Linear Structure with Arbitrary Support Conditions," ASME JOURNAL OF APPLIED MECHANICS, Vol. 38, pp. 595-600.

Dowell,. E. H., 1972, "Free Vibrations of an Arbitrary Structure in Terms of Component Modes," ASME JOURNAL OF APPLIED MECHANICS, Vol. 39, pp. 727-731.

Leissa, A. W., 1969, *Vibration of Plates*, U.S. Government Printing Office, Washington, D.C.

Leissa, A. W., 1973, "The Free Vibration of Rectangular Plates," *Journal of Sound and Vibration*, Vol. 31, pp. 257-293.

Narita, Y., 1984, "Note on Vibrations of Point Supported Rectangular Plates," *Journal of Sound and Vibration*, Vol. 93, pp. 593-597.

Narita, Y., 1985, "Free Vibration of Polar-Orthotropic Sector Plates Resting on Point Supports," *ASME Journal of Vibration, Acoustics, Stress and Reliability in Design*, Vol. 107, pp. 334-338.

Narita, Y., and Leissa, A. W., 1984, "Vibrations of Corner Point Supported Shallow Shells of Rectangular Planform," *Earthquake Engineering and Structural Dynamics*, Vol. 12, pp. 651-661.

A Note on the Propagation of Finite Amplitude Shear Waves in a Hyperelastic Solid

J. B. Haddow[1] and R. J. Tait[2]

Currie and Hayes (1969) have shown that, for hyperelastic Hadamard solids, two finite amplitude transverse waves without coupled longitudinal waves can propagate in every direction when the material is homogeneously deformed. We show that there is a class of strain energy function for compressible solids which admit the propagation of finite amplitude plane transverse waves without coupled longitudinal waves in an undeformed medium. The hyperelastic Hadamard material is a subclass of this class. Another subclass also admits the propagation of finite amplitude telescopic shear waves without coupled longitudinal waves in an undeformed material.

Plane Shear Waves

The position vector of a material point at time t is given by $\bar{x}(\bar{X},t)$, where $\bar{X}$ is the position vector at $t=0$ when the material is in the unstrained reference configuration. The components of $\bar{x}$ and $\bar{X}$, referred to the same rectangular Cartesian coordinate system are denoted by x_i and X_i, respectively, with $i=1,2,3$.

The isochoric deformation field for propagation in the X_1 direction of a plane shear wave, polarized in the X_3 direction, is

$$x_1 = X_1, x_2 = X_2, x_3 = X_3 + w(X_1,t), \tag{1}$$

and the physical components of the deformation gradient tensor $\mathbf{F}$ and the left Cauchy Green tensor $\mathbf{B}$ are given by

$$[\mathbf{F}] = \begin{bmatrix} 1 & 0 & 0 \\ 0 & 1 & 0 \\ K & 0 & 1 \end{bmatrix}, \quad [\mathbf{B}] = \begin{bmatrix} 1 & 0 & K \\ 0 & 1 & 0 \\ K & 0 & 1+K^2 \end{bmatrix}, \tag{2}$$

where $K(x_1,t) = \partial w(x_1,t)/\partial x_1$.

The strain energy function per unit volume of the undeformed reference configuration may be expressed as a function $W(I_1,I_2,I_3)$ of the basic invariants of $\mathbf{B}$, which are

$$I_1 = I_2 = 3 + K^2, I_3 = 1, \tag{3}$$

for the deformation field (1), and the Cauchy stress is given (Atkin and Fox, 1980) by

$$\sigma = 2I_3^{-1/2}\{(I_2 W_2 + I_3 W_3)\mathbf{I} + W_1 \mathbf{B} - I_3 W_2 \mathbf{B}^{-1}\}, \tag{4}$$

where $W_i = \partial W/\partial I_i$ $(i=1,2,3)$, and $\mathbf{I}$ is the unit tensor.

Nonzero components of stress obtained from equations (2), (3), and (4) are

$$\sigma_{11} = 2\{W_1 + 2W_2 + W_3\}, \quad \sigma_{22} = 2\{(2+K^2)W_2 + W_3 + W_1\},$$
$$\sigma_{33} = 2\{(2+K^2)W_2 + W_3 + W_1(1+K^2)\}, \quad \sigma_{13} = 2(W_1 + W_2)K, \tag{5}$$

[1]Department of Mechanical Engineering, University of Alberta, Edmonton, Alberta, Canada T6G 2G8. Mem. ASME.

[2]Department of Mathematics, University of Alberta, Edmonton, Alberta, Canada T6G 2G8.

Manuscript received by ASME Applied Mechanics Division, May 3, 1985; final revision, August 6, 1985.

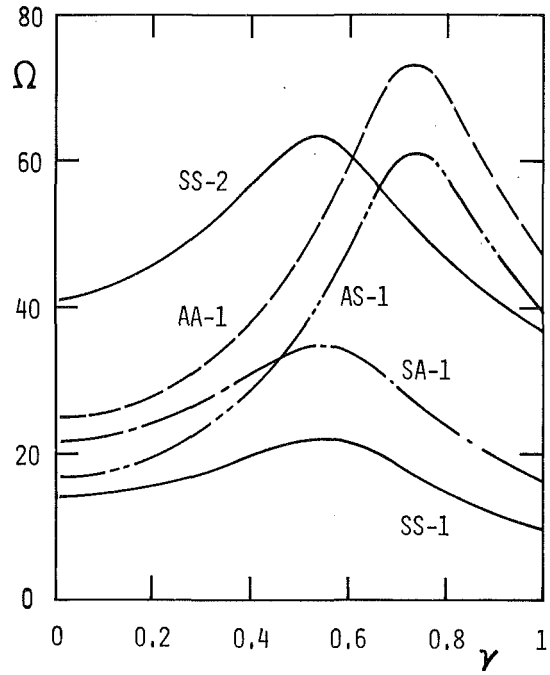

Fig. 2 Variation of frequency parameters with distance of a pair of partial line supports ($\delta = 0.6$)

$= Eh^3/12(1-\nu^2)$: flexural rigidity, E: Young's modulus, ν: Poisson's ratio).

Table 1 presents a convergence study with the number of Fourier terms I in the case of internal supports ($\gamma = \delta = 0.8$). As more Fourier terms are used, the frequency values tend to converge, yielding accurate values, e.g., at $I = 7$. These lowest five frequencies are calculated for the fixed number of $m = n = 7$, which are sufficiently converged in m and n (Narita, 1984). Furthermore, the present results were compared to exact values (Leissa, 1973) for a special case of the two opposite edges simply supported ($\gamma = \delta = 1$), and agreement was found to five significant figures.

In Figure 2, the variation of frequencies is illustrated for the example as a function of the support distance γ. The length of the supports is taken as $\delta = 0.6$. It is seen here that each frequency curve for the *SS*-1, 2, and *SA*-1 mode has a peak around $\gamma = 0.55$, while the frequency peaks of the *AS*-1 and *AA*-1 mode are found around $\gamma = 0.75$. Apparently, there exists an optimal distance of the two line supports for each mode, which causes the natural frequency to be a maximum value.

The present method may be used to analyze the problem of mixed boundary conditions simply by locating supports along parts of the edges. One also notes that the clamping support can be introduced by using an additional constraint in rotation.

References

Dowell, E. H., 1971, "Free Vibrations of a Linear Structure with Arbitrary Support Conditions," ASME JOURNAL OF APPLIED MECHANICS, Vol. 38, pp. 595–600.

Dowell,. E. H., 1972, "Free Vibrations of an Arbitrary Structure in Terms of Component Modes," ASME JOURNAL OF APPLIED MECHANICS, Vol. 39, pp. 727–731.

Leissa, A. W., 1969, *Vibration of Plates*, U.S. Government Printing Office, Washington, D.C.

Leissa, A. W., 1973, "The Free Vibration of Rectangular Plates," *Journal of Sound and Vibration*, Vol. 31, pp. 257–293.

Narita, Y., 1984, "Note on Vibrations of Point Supported Rectangular Plates," *Journal of Sound and Vibration*, Vol. 93, pp. 593–597.

Narita, Y., 1985, "Free Vibration of Polar-Orthotropic Sector Plates Resting on Point Supports," *ASME Journal of Vibration, Acoustics, Stress and Reliability in Design*, Vol. 107, pp. 334–338.

Narita, Y., and Leissa, A. W., 1984, "Vibrations of Corner Point Supported Shallow Shells of Rectangular Planform," *Earthquake Engineering and Structural Dynamics*, Vol. 12, pp. 651–661.

A Note on the Propagation of Finite Amplitude Shear Waves in a Hyperelastic Solid

J. B. Haddow[1] and R. J. Tait[2]

Currie and Hayes (1969) have shown that, for hyperelastic Hadamard solids, two finite amplitude transverse waves without coupled longitudinal waves can propagate in every direction when the material is homogeneously deformed. We show that there is a class of strain energy function for compressible solids which admit the propagation of finite amplitude plane transverse waves without coupled longitudinal waves in an undeformed medium. The hyperelastic Hadamard material is a subclass of this class. Another subclass also admits the propagation of finite amplitude telescopic shear waves without coupled longitudinal waves in an undeformed material.

Plane Shear Waves

The position vector of a material point at time t is given by $\bar{x}(\bar{X},t)$, where $\bar{X}$ is the position vector at $t=0$ when the material is in the unstrained reference configuration. The components of $\bar{x}$ and $\bar{X}$, referred to the same rectangular Cartesian coordinate system are denoted by x_i and X_i, respectively, with $i=1,2,3$.

The isochoric deformation field for propagation in the X_1 direction of a plane shear wave, polarized in the X_3 direction, is

$$x_1 = X_1, x_2 = X_2, x_3 = X_3 + w(X_1,t), \tag{1}$$

and the physical components of the deformation gradient tensor $\mathbf{F}$ and the left Cauchy Green tensor $\mathbf{B}$ are given by

$$[\mathbf{F}] = \begin{bmatrix} 1 & 0 & 0 \\ 0 & 1 & 0 \\ K & 0 & 1 \end{bmatrix}, \quad [\mathbf{B}] = \begin{bmatrix} 1 & 0 & K \\ 0 & 1 & 0 \\ K & 0 & 1+K^2 \end{bmatrix}, \tag{2}$$

where $K(x_1,t) = \partial w(x_1,t)/\partial x_1$.

The strain energy function per unit volume of the undeformed reference configuration may be expressed as a function $W(I_1,I_2,I_3)$ of the basic invariants of $\mathbf{B}$, which are

$$I_1 = I_2 = 3 + K^2, I_3 = 1, \tag{3}$$

for the deformation field (1), and the Cauchy stress is given (Atkin and Fox, 1980) by

$$\sigma = 2I_3^{-1/2}\{(I_2W_2 + I_3W_3)\mathbf{I} + W_1\mathbf{B} - I_3W_2\mathbf{B}^{-1}\}, \tag{4}$$

where $W_i = \partial W/\partial I_i$ $(i=1,2,3)$, and $\mathbf{I}$ is the unit tensor.

Nonzero components of stress obtained from equations (2), (3), and (4) are

$$\sigma_{11} = 2\{W_1 + 2W_2 + W_3\}, \quad \sigma_{22} = 2\{(2+K^2)W_2 + W_3 + W_1\},$$
$$\sigma_{33} = 2\{(2+K^2)W_2 + W_3 + W_1(1+K^2)\}, \quad \sigma_{13} = 2(W_1 + W_2)K, \tag{5}$$

[1]Department of Mechanical Engineering, University of Alberta, Edmonton, Alberta, Canada T6G 2G8. Mem. ASME.

[2]Department of Mathematics, University of Alberta, Edmonton, Alberta, Canada T6G 2G8.

Manuscript received by ASME Applied Mechanics Division, May 3, 1985; final revision, August 6, 1985.

where the I_i are given by equation (3), so that the W_i are either constants or functions of K^2 and σ_{13} is an odd function of K.

Since $K=K(x_1,t)$, the stresses (5) depend only on x_1 and t; consequently the nontrivial equations of motion

$$\frac{\partial \sigma_{11}}{\partial x_1}=0,\ \frac{\partial \sigma_{13}}{\partial x_1}=\rho\frac{\partial^2 w}{\partial t^2} \tag{6}$$

must be satisfied if the deformation field (1) is possible without body forces. Since we consider propagation into an undeformed region, equation $(6)_1$ implies that $\sigma_{11}=0$ and it follows from equation $(5)_1$ that this condition is satisfied if

$$W_1+2W_2+W_3=0, \tag{7}$$

with the I_i given by equation (3).

A class of strain energy function which satisfies (7) is

$$W=p(I_3)F(I_1-3)+q(I_3)G(I_2-3)$$
$$+r(I_3)H((I_1-3),\ (I_2-3))+s(I_3)\frac{dF}{dI_1} \tag{8}$$
$$+2u(I_3)\frac{dG}{dI_2}+v(I_3)\left(\frac{\partial H}{\partial I_1}+2\frac{\partial H}{\partial I_2}\right), \tag{8}$$

where

$$p(1)=q(1)=r(1)=1,\ s(1)=u(1)=v(1)=0,$$
$$p'(1)=q'(1)=r'(1)=0,$$
$$s'(1)=u'(1)=v'(1)=-1, \tag{9}$$

and a prime denotes differentiation with respect to the arguments.

Strain energy functions of the class (8) admit the propagation of finite amplitude plane shear waves into an undeformed medium without coupled longitudinal waves provided σ_{13}, given by equation $(5)_4$, is a monotonically increasing function of K, so that the wave equation obtained from equations $(5)_4$, (6) and $K=\partial w/\partial x_1$ is hyperbolic. This wave equation is nonlinear unless $H=0$, $F(I_1-3)=\alpha_1(I_1-3)$ and $G(I_2-3)=\alpha_2(I_2-3)$, where α_1 and α_2 are constants. The linear wave equation

$$\rho\frac{\partial^2 w}{\partial t^2}=\mu\frac{\partial^2 w}{\partial x^2},$$

is then obtained, where $\mu=(\alpha_1+\alpha_2)/2$ is the shear modulus for infinitesimal deformation from the ground state. An example of this is the hyperelastic Hadamard material

$$W=\alpha_1(I_1-3)+\alpha_2(I_2-3)+h(I_3). \tag{10}$$

Telescopic Shear Wave

The coordinates of a material point referred to a system of cylindrical polar coordinates are denoted by (R,θ,Z) and (r,θ,z) in the undeformed reference and spatial configurations, respectively, and the isochoric deformation field for propagation of a telescopic shear wave propagating in the R direction without a coupled longitudinal wave is

$$r=R,\ \theta=\theta,\ z=w(R,t)+Z. \tag{11}$$

The physical components of the deformation gradient tensor and the left Cauchy Green tensor are again given by equations (2) and the invariants of **B** by equations (3), with K now given by $K(r,t)=\partial w/\partial r$. Nonzero components of stress are given by equations (5) with σ_{11}, σ_{22}, σ_{33}, σ_{13}, replaced by σ_r, σ_θ, σ_z and τ_{rz} with the usual notation for cylindrical polar components of stress.

Since the stresses depend only on r and t, the nontrivial equations of motion

$$\frac{\partial \sigma_r}{\partial r}+\frac{\sigma_r-\sigma_\theta}{r}=0,\ \frac{\partial \tau_{rz}}{\partial r}+\frac{\tau_{rz}}{r}=\rho\frac{\partial^2 w}{\partial t^2} \tag{12}$$

must be satisfied if the deformation field (11) is possible without body forces. Equation $(12)_1$ is satisfied if $\sigma_r=\sigma_\theta=0$ and this condition is satisfied if the stresses given by equations $(5)_{1,2}$ are obtained from a strain energy function of the class

$$W=p(I_3)F(I_1-3)+s(I_3)\frac{dF}{dI_1}, \tag{13}$$

which is a subclass of class (8). In equation (13), $p(I_3)$ and $S(I_3)$ satisfy the conditions (9). Strain energy functions of class (13) admit the propagation of finite amplitude telescopic shear waves into an undeformed medium without coupled longitudinal waves provided τ_{rz}, given by equation $(5)_4$, is a monotonically increasing function of K, so that the wave equation obtained from equations $(5)_4$, $(12)_2$, and K is hyperbolic. This wave equation is linear if $F(I_1-3)=\alpha_1(I_1-3)$ where, as before, α_1 is constant.

Concluding Remarks

Blatz and Ko (1962) have proposed a class of strain energy function, for slightly compressible solids, which is similar in form to class (10) with I_2 replaced by I_2/I_3. Experimental data for slightly compressible solids can be modelled equally well by strain energy functions of class (10). In addition a strain energy function proposed earlier by Blatz (1960) is a special case of (10) with $\alpha_2=0$ and is also a special case of class (13). Further work needs to be done to determine if strain energy functions exist which admit uncoupled telescopic shear waves in a homogeneously deformed compressible solid.

References

Atkin, R. J., and Fox, N., 1980, *An Introduction to the Theory of Elasticity*, Longman, London and New York, pp. 65-67.

Blatz, P. J., 1960, "Application of Finite Elastic Theory in Predicting the Performance of Solid Propellant Rocket Motors," CALCIT SM60-25, California Institute of Technology.

Blatz, P. J., and Ko, W. L., 1962, "Application of Finite Elastic Theory to the Deformation of Rubbery Materials," *Transactions of the Society of Rheology*, Vol. 6, pp. 140-161.

Currie, P., and Hayes, M., 1969, "Longitudinal and Transverse Waves in Finite Elastic Strain. Hadamard and Green Materials," *Journal of the Institute of Mathematics and its Applications*, Vol. 5, pp. 140-161.

On the Effects of Nonlinear Elastic Foundation on Free Vibration of Beams

V. Birman[1]

Introduction

Nonlinear free vibration of simply supported elastic beams with fixed distance between pin-ends was studied by Woinowsky-Krieger (1950) and Burgreen (1951). The nonlinearity was due to the nonlinear stretching of the elastic curve. The solution was represented as a product of a time function and the sinusoidal vibrational mode corresponding to linear motion. A Galerkin procedure yielded the nonlinear differential equation for the time function which was solved exactly in terms of elliptic functions. The experiments of Burgreen (1951) and Ray and Bert (1969) confirmed the

[1]Assistant Professor, School of Naval Architecture and Marine Engineering, University of New Orleans, New Orleans, LA 70148. Mem. ASME.

Manuscript received by ASME Applied Mechanics Division, August 5, 1985; final revision November 11, 1985.

where the I_i are given by equation (3), so that the W_i are either constants or functions of K^2 and σ_{13} is an odd function of K.

Since $K=K(x_1,t)$, the stresses (5) depend only on x_1 and t; consequently the nontrivial equations of motion

$$\frac{\partial \sigma_{11}}{\partial x_1}=0,\ \frac{\partial \sigma_{13}}{\partial x_1}=\rho\frac{\partial^2 w}{\partial t^2} \tag{6}$$

must be satisfied if the deformation field (1) is possible without body forces. Since we consider propagation into an undeformed region, equation $(6)_1$ implies that $\sigma_{11}=0$ and it follows from equation $(5)_1$ that this condition is satisfied if

$$W_1+2W_2+W_3=0, \tag{7}$$

with the I_i given by equation (3).

A class of strain energy function which satisfies (7) is

$$W=p(I_3)F(I_1-3)+q(I_3)G(I_2-3)$$

$$+r(I_3)H((I_1-3),\ (I_2-3))+s(I_3)\frac{dF}{dI_1} \tag{8}$$

$$+2u(I_3)\frac{dG}{dI_2}+v(I_3)\left(\frac{\partial H}{\partial I_1}+2\frac{\partial H}{\partial I_2}\right), \tag{8}$$

where

$$p(1)=q(1)=r(1)=1,\ s(1)=u(1)=v(1)=0,$$
$$p'(1)=q'(1)=r'(1)=0,$$
$$s'(1)=u'(1)=v'(1)=-1, \tag{9}$$

and a prime denotes differentiation with respect to the arguments.

Strain energy functions of the class (8) admit the propagation of finite amplitude plane shear waves into an undeformed medium without coupled longitudinal waves provided σ_{13}, given by equation $(5)_4$, is a monotonically increasing function of K, so that the wave equation obtained from equations $(5)_4$, (6) and $K=\partial w/\partial x_1$ is hyperbolic. This wave equation is nonlinear unless $H=0$, $F(I_1-3)=\alpha_1(I_1-3)$ and $G(I_2-3)=\alpha_2(I_2-3)$, where α_1 and α_2 are constants. The linear wave equation

$$\rho\frac{\partial^2 w}{\partial t^2}=\mu\frac{\partial^2 w}{\partial x^2},$$

is then obtained, where $\mu=(\alpha_1+\alpha_2)/2$ is the shear modulus for infinitesimal deformation from the ground state. An example of this is the hyperelastic Hadamard material

$$W=\alpha_1(I_1-3)+\alpha_2(I_2-3)+h(I_3). \tag{10}$$

Telescopic Shear Wave

The coordinates of a material point referred to a system of cylindrical polar coordinates are denoted by (R,θ,Z) and (r,θ,z) in the undeformed reference and spatial configurations, respectively, and the isochoric deformation field for propagation of a telescopic shear wave propagating in the R direction without a coupled longitudinal wave is

$$r=R,\ \theta=\theta,\ z=w(R,t)+Z. \tag{11}$$

The physical components of the deformation gradient tensor and the left Cauchy Green tensor are again given by equations (2) and the invariants of **B** by equations (3), with K now given by $K(r,t)=\partial w/\partial r$. Nonzero components of stress are given by equations (5) with σ_{11}, σ_{22}, σ_{33}, σ_{13}, replaced by σ_r, σ_θ, σ_z and τ_{rz} with the usual notation for cylindrical polar components of stress.

Since the stresses depend only on r and t, the nontrivial equations of motion

$$\frac{\partial \sigma_r}{\partial r}+\frac{\sigma_r-\sigma_\theta}{r}=0,\ \frac{\partial \tau_{rz}}{\partial r}+\frac{\tau_{rz}}{r}=\rho\frac{\partial^2 w}{\partial t^2} \tag{12}$$

must be satisfied if the deformation field (11) is possible without body forces. Equation $(12)_1$ is satisfied if $\sigma_r=\sigma_\theta=0$ and this condition is satisfied if the stresses given by equations $(5)_{1,2}$ are obtained from a strain energy function of the class

$$W=p(I_3)F(I_1-3)+s(I_3)\frac{dF}{dI_1}, \tag{13}$$

which is a subclass of class (8). In equation (13), $p(I_3)$ and $S(I_3)$ satisfy the conditions (9). Strain energy functions of class (13) admit the propagation of finite amplitude telescopic shear waves into an undeformed medium without coupled longitudinal waves provided τ_{rz}, given by equation $(5)_4$, is a monotonically increasing function of K, so that the wave equation obtained from equations $(5)_4$, $(12)_2$, and K is hyperbolic. This wave equation is linear if $F(I_1-3)=\alpha_1(I_1-3)$ where, as before, α_1 is constant.

Concluding Remarks

Blatz and Ko (1962) have proposed a class of strain energy function, for slightly compressible solids, which is similar in form to class (10) with I_2 replaced by I_2/I_3. Experimental data for slightly compressible solids can be modelled equally well by strain energy functions of class (10). In addition a strain energy function proposed earlier by Blatz (1960) is a special case of (10) with $\alpha_2=0$ and is also a special case of class (13). Further work needs to be done to determine if strain energy functions exist which admit uncoupled telescopic shear waves in a homogeneously deformed compressible solid.

References

Atkin, R. J., and Fox, N., 1980, *An Introduction to the Theory of Elasticity*, Longman, London and New York, pp. 65-67.

Blatz, P. J., 1960, "Application of Finite Elastic Theory in Predicting the Performance of Solid Propellant Rocket Motors," CALCIT SM60-25, California Institute of Technology.

Blatz, P. J., and Ko, W. L., 1962, "Application of Finite Elastic Theory to the Deformation of Rubbery Materials," *Transactions of the Society of Rheology*, Vol. 6, pp. 140-161.

Currie, P., and Hayes, M., 1969, "Longitudinal and Transverse Waves in Finite Elastic Strain. Hadamard and Green Materials," *Journal of the Institute of Mathematics and its Applications*, Vol. 5, pp. 140-161.

On the Effects of Nonlinear Elastic Foundation on Free Vibration of Beams

V. Birman[1]

Introduction

Nonlinear free vibration of simply supported elastic beams with fixed distance between pin-ends was studied by Woinowsky-Krieger (1950) and Burgreen (1951). The nonlinearity was due to the nonlinear stretching of the elastic curve. The solution was represented as a product of a time function and the sinusoidal vibrational mode corresponding to linear motion. A Galerkin procedure yielded the nonlinear differential equation for the time function which was solved exactly in terms of elliptic functions. The experiments of Burgreen (1951) and Ray and Bert (1969) confirmed the

[1]Assistant Professor, School of Naval Architecture and Marine Engineering, University of New Orleans, New Orleans, LA 70148. Mem. ASME.

Manuscript received by ASME Applied Mechanics Division, August 5, 1985; final revision November 11, 1985.

theoretical solutions. An approximate solution obtained by Rehfield (1973) by a perturbation procedure was also in complete agreement with an asymptotic approximation of the solution given by Woinowsky-Krieger (1950) and Burgreen (1951). The influence of initial imperfections on nonlinear free motion of simply supported beams was investigated by Elishakoff et al. (1985).

Buckling of structures on a nonlinear elastic foundation was considered by Reissner (1970, 1971), Keener (1974), and Hui and Hansen (1980a). The probabilistic approach to the stability of such structures is discussed by Elishakoff (1979, 1985).

In this paper we consider the nonlinear free vibration of statically compressed hinged beams supported by a nonlinear cubic elastic foundation. Contrary to the previous works the ends are not necessarily restricted in the axial direction.

Analysis

Consider a simply supported beam on the nonlinear elastic foundation subjected to a constant compressive force P_o. The reaction of the foundation per unit length is

$$R(y) = K_1 y \pm K_3 y^3 \tag{1}$$

where K_1 and K_3 are the foundation constants. The positive nonlinear term in (1) corresponds to a hardening foundation. The softening foundation is represented by (1) with a negative nonlinear term. The equation of motion is

$$\mu\ddot{y} + EIy^{IV} + \left[P_o - u\frac{AE}{2L}\int_0^L (y')^2 dx\right]y'' + K_1 y \pm K_3 y^3 = 0 \tag{2}$$

where the axial stretching term contributes to nonlinearity (Woinowsky-Krieger, 1950).

In (2) μ is the mass of the beam per unit length, EI is the bending stiffness, A is the cross sectional area and L is the length of the beam. The coefficient u represents the restraint of the beam ends in the axial direction. The unrestrained beam corresponds to $u=0$; in this case the only nonlinear effect is due to elastic foundation. If $u=1$ the distance between the ends is fixed and the additional nonlinearity is due to the stretching. Equation (2) corresponds to the accuracy accepted in the previously cited references. Note that a more complete formulation can be derived based on the paper by Hui and Hansen (1980 b).

Following the standard procedure, the motion is represented by

$$y = f(t)\sin\frac{n\pi x}{L} \tag{3}$$

The substitution of (3) into (2) and the Galerkin procedure yield the equation which can be represented in the nondimensional form

$$\frac{d^2F}{d\tau^2} + \frac{1}{\bar{\omega}^2}(1 - \bar{P} + n_1)F + \frac{us \pm n_3}{\bar{\omega}^2}F^3 = 0 \tag{4}$$

where

$$F = f/L \qquad \tau = \omega t$$

$$\bar{\omega} = \omega/\omega_o \qquad \bar{P} = P_o/P_{cr}$$

$$\omega_o^2 = \left(\frac{n\pi}{L}\right)^4 \frac{EI}{\mu} \qquad P_{cr} = \left(\frac{n\pi}{L}\right)^2 EI$$

$$n_1 = \frac{K_1}{\mu\omega_o^2} \qquad n_3 = \frac{3K_3L^2}{4\mu\omega_o^2} \qquad s = \frac{AL^2}{4I} \tag{5}$$

Multiplication of (4) by dF and integration give

$$\left(\frac{dF}{d\tau}\right)^2 = -\frac{1}{\bar{\omega}^2}(1 - \bar{P} + n_1)F^2 - \frac{1}{2\bar{\omega}^2}(us \pm n_3)F^4 + C \tag{6}$$

where C is a constant determined from the condition that the velocity corresponding to the maximum displacement $F_{\max}$ is zero. Introducing the ratio

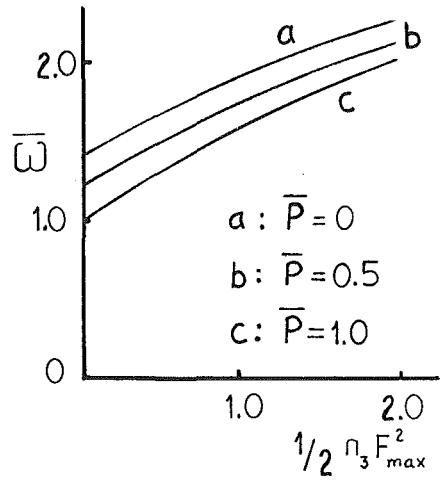

Fig. 1 Influence of nonlinear foundation on frequencies ($n_1 = 1.0$, $u = 0$, $n = 1$)

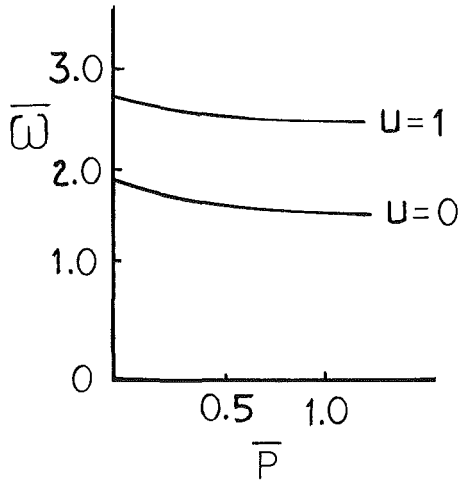

Fig. 2 Influence of end restraint on frequencies ($n_1 = 1.0$, $n_3 = 20{,}000$, $s = 50{,}000$, $F_{max} = 0.01$, $n = 1$)

$$\xi = F/F_{\max} \tag{7}$$

and substituting the value of C into (6), we obtain

$$\frac{d\xi}{d\tau} = \frac{1}{\bar{\omega}}\left[(1 - \bar{P} + n_1)(1 - \xi^2) + \frac{1}{2}(us \pm n_3)F_{\max}{}^2(1 - \xi^4)\right]^{1/2} \tag{8}$$

The solution of equations similar to (8) is an elliptic function (Woinowsky-Krieger, 1950). Note that the restoring force in (8) is an odd function of displacements. Therefore, a quarter of the period of vibration corresponds to the motion from $\xi = 0$ to $\xi = 1$. If the initial time $\tau = 0$ is chosen so that $\xi(0) = 0$, the nondimensional period is

$$T = 4\bar{\omega}[1 - \bar{P} + n_1 + \tfrac{1}{2}(us \pm n_3)F_{\max}{}^2]^{-1/2}K(m) \tag{9}$$

where $K(m)$ is a complete elliptic integral of the first kind (Abramovitz and Stegun, 1964), and

$$m = -\frac{(us \pm n_3)F_{\max}{}^2}{2(1 - \bar{P} + n_1) + (us \pm n_3)F_{\max}{}^2} \tag{10}$$

If the parameter m is negative, the complete elliptic integral is calculated (Abramovitz and Stegun, 1964):

$$K(m) = (1 + |m|)^{-1/2} K(|m|/(1 + |m|)) \tag{11}$$

The period of linear vibrations of the beam without an elastic foundation and the compressive force, obtained in terms of nondimensional time from (4) or (9), is $2\pi\bar{\omega}$. Therefore,

$$\bar{\omega} = \frac{\pi}{2}[1 - \bar{P} + n_1 + \frac{1}{2}(us \pm n_3)F_{\max}{}^2]^{1/2}[K(m)]^{-1} \tag{12}$$

The influence of a hardening elastic foundation on the frequencies of the beam with the ends free to move in the axial direction is shown in Fig. 1. When the parameter $\frac{1}{2} n_3 F_{\max}{}^2$ (which characterizes the cubic hardening nonlinearity) increases, the frequencies increase as well. Compressive forces decrease the frequency of motion. The effect of the restraint in the axial direction is illustrated in Fig. 2 where the order of the coefficient s is typical for slender beams. The axial restraint increasing the stiffness of the beam is shown to increase the frequencies of vibration.

References

Ambramovitz, M., and Stegun, I. A., 1964, *Handbook of Mathematical Functions*, National Bureau of Standards, New York, Ch. 17.

Burgreen, D., 1951, "Free Vibrations of Pin-Ended Column with Constant Distance Between Pin-Ends," ASME JOURNAL OF APPLIED MECHANICS, Vol. 18, pp. 135–139.

Elishakoff, I., 1979, "Buckling of Stochastically Imperfect Finite Column on a Nonlinear Elastic Foundation," ASME JOURNAL OF APPLIED MECHANICS, Vol. 46, pp. 411–416.

Elishakoff, I., 1985, "Reliability Approach to the Random Imperfection Sensitivity of Columns," *Acta Mechanica*, Vol. 55, pp. 151–170.

Elishakoff, I., Birman, V., and Singer, J., 1985, "Influence of Initial Imperfections on Nonlinear Free Vibration of Elastic Bars," *Acta Mechanica*, Vol. 55, pp. 191–202.

Hui, D., and Hansen, J. S., 1980a, "Two-Mode Buckling of an Elastically Supported Plate and its Relation to Catastrophe Theory," ASME JOURNAL OF APPLIED MECHANICS, Vol. 47, pp. 607–612.

Hui, D., and Hansen, J. S., 1980b, "The Swallowtail and Butterfly Cuspoids and Their Application in the Initial Post-Buckling of Single-Mode Structural Systems," *Quarterly of Applied Mathematics*, April, pp. 17–36.

Keener, J. P., 1974, "Buckling Imperfection Sensitivity of Columns and Spherical Caps," *Quarterly of Applied Mathematics*, Vol. 32, pp. 173–199.

Ray, J. D., and Bert, C. W., 1969, "Nonlinear Vibrations of a Beam with Pinned Ends," *ASME Journal of Engineering for Industry*, Vol. 91, pp. 997–1104.

Rehfield, L. W., 1973, "Nonlinear Free Vibrations of Elastic Structures," *International Journal of Solids and Structures*, Vol. 9, pp. 581–590.

Reissner, E., 1970, "On Postbuckling Behavior and Imperfection Sensitivity of Thin Plates on a Non-Linear Elastic Foundation," *Studies Appl. Mathematics*, Vol. XLIV, No. 1, pp. 45–47.

Reissner, E., 1971, "A Note on Imperfection Sensitivity of Thin Plates on a Non-Linear Elastic Foundation," *Instability of Continuous Systems*, Leipholz, H. E., ed., Proceedings of IUTAM Symposium held at Herrenalb, Sept. 1969, Springer-Verlag, Berlin-Heidelberg-New York, pp. 15–18.

Woinowsky-Krieger, S., 1950, "The Effect of an Axial Force on the Vibration of Hinged Bars," ASME JOURNAL OF APPLIED MECHANICS, Vol. 17, pp. 35–36.

The Plane Problem of Orthotropic Elastic Contact

D. J. Steigmann[1]

Consider symmetric frictionless contact of circular regions $S_\alpha (\alpha = 1,2)$ (Fig. 1) over $-a < x < a$, where "a" is determined by the contact force per unit length F. In light of the assumption of infinitesimal deformation we assume $a \ll R$, where R is the smaller of the radii of curvature of the S_α. Then, provided attention is restricted to the neighborhood of the contact line, the S_α can be approximated by half-planes. Therefore, if the S_α are cylindrically orthotropic (Lekhnitskii, 1981), it is consistent to assume uniform rectilinear orthotropy. For the plane problem we adopt the notation of Pipkin (1979):

$$G\left(\frac{\partial u}{\partial y} + \frac{\partial v}{\partial x}\right) = \sigma_{xy},$$

$$G\frac{\partial u}{\partial x} = A\sigma_{xx} - B\sigma_{yy},\ G\frac{\partial v}{\partial y} = -B\sigma_{xx} + C\sigma_{yy}. \tag{1}$$

The coefficients in (1) can be expressed in terms of the usual engineering constants for plane stress and plane strain (Christensen, 1979). Eliminating u and v results in

$$A\frac{\partial^4 \chi}{\partial y^4} + D\frac{\partial^4 \chi}{\partial y^2 dx^2} + C\frac{\partial^4 \chi}{\partial x^4} = 0;\ D \equiv 1 - 2B$$

where χ is the Airy function defined by the relations $\sigma_{xx} = G\partial^2\chi/\partial y^2$, $\sigma_{yy} = G\partial^2\chi/\partial x^2$, and $\sigma_{xy} = -G\partial^2\chi/\partial x\partial y$. A solution of the form $\chi(x + \mu y)$ exists for constant μ provided

$$\mu^2 = -\frac{D}{2A}[1 \pm (1 - 4AC/D^2)^{1/2}].$$

We require the undeformed material to be stable against kinematically admissible small displacements. Hence the plane displacement equations of equilibrium are strongly elliptic. Following Hill (1979) it can then be shown that the roots μ are complex. We denote these by $\lambda = |\lambda| e^{i\beta}$, $\gamma = -|\lambda| e^{-i\beta}$, $\bar{\lambda}$, $\bar{\gamma}$ and take $Im\lambda > 0$ without loss of generality.
For $(x, y) \in S_\alpha$ we find

$$\chi = \mathrm{Re}[f_\alpha(\zeta_\alpha) + g_\alpha(\omega_\alpha)];\ \zeta_\alpha = x + \lambda_\alpha y,\ \omega_\alpha = x + \gamma_\alpha y$$

$$\sigma_{xx}/G_\alpha = \mathrm{Re}[\lambda_\alpha^2 f_\alpha''(\zeta_\alpha) + \gamma_\alpha^2 g_\alpha''(\omega_\alpha)] \tag{2}$$

$$2(\sigma_{yy} - i\sigma_{xy})/G_\alpha = (1 + \Lambda_\alpha)f_\alpha''(\zeta_\alpha) + (1 - \bar{\Lambda}_\alpha)\bar{f}_\alpha''(\bar{\zeta}_\alpha)$$
$$+ (1 + \Gamma_\alpha)g_\alpha''(\omega_\alpha) + (1 - \bar{\Gamma}_\alpha)\bar{g}_\alpha''(\bar{\omega}_\alpha);\ \Lambda_\alpha \equiv i\lambda_\alpha,\ \Gamma_\alpha \equiv i\gamma_\alpha$$

where $f_\alpha(\zeta_\alpha)$, $g_\alpha(\omega_\alpha)$ are holomorphic for $(x, y) \in S_\alpha$ and S_1, S_2 have different elastic constants in general. Substituting (2) into (1) and making use of properties of the roots λ and γ leads to the displacements

$$u = \mathrm{Re}[(\kappa_\alpha - 1)g_\alpha'(\omega_\alpha) - \kappa_\alpha f_\alpha'(\zeta_\alpha)],$$
$$v = \mathrm{Re}[(\kappa_\alpha - 1)\lambda_\alpha f'{}_\alpha(\zeta_\alpha) - \kappa_\alpha \gamma_\alpha g_\alpha'(\omega_\alpha)];$$
$$\kappa_\alpha \equiv B_\alpha - A_\alpha\lambda_\alpha^2 = B_\alpha - C_\alpha/\gamma_\alpha^2,$$
$$1 - \kappa_\alpha = B_\alpha - A_\alpha\gamma_\alpha^2 = B_\alpha - C_\alpha/\lambda_\alpha^2 \tag{3}$$

apart from rigid-body terms. Define functions $h_\alpha(z)$, $k_\alpha(z)$ by

$$2h_\alpha(z)/G_\alpha \equiv (1 + \Lambda_\alpha)f_\alpha(z) + (1 + \Gamma_\alpha)g_\alpha(z),$$
$$2k_\alpha(z)/G_\alpha \equiv (1 - \Lambda_\alpha)f_\alpha(z) + (1 - \Gamma_\alpha)g_\alpha(z);\ z = x + iy.$$

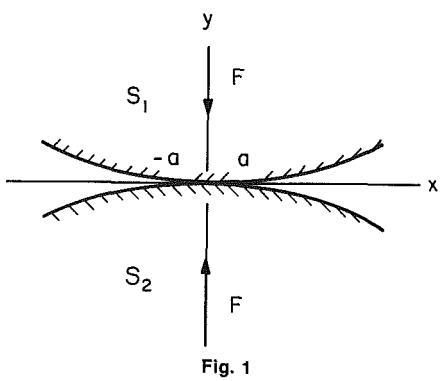

Fig. 1

[1] Graduate Student, Division of Engineering, Brown University, Providence, RI 02912.

Manuscript received by ASME Applied Mechanics Division, July 26, 1984; final revision November 10, 1985.

$$K(m) = (1 + |m|)^{-1/2} K(|m|/(1 + |m|)) \tag{11}$$

The period of linear vibrations of the beam without an elastic foundation and the compressive force, obtained in terms of nondimensional time from (4) or (9), is $2\pi\bar{\omega}$. Therefore,

$$\bar{\omega} = \frac{\pi}{2}[1 - \bar{P} + n_1 + \frac{1}{2}(us \pm n_3)F_{\max}{}^2]^{1/2}[K(m)]^{-1} \tag{12}$$

The influence of a hardening elastic foundation on the frequencies of the beam with the ends free to move in the axial direction is shown in Fig. 1. When the parameter $\frac{1}{2} n_3 F_{\max}{}^2$ (which characterizes the cubic hardening nonlinearity) increases, the frequencies increase as well. Compressive forces decrease the frequency of motion. The effect of the restraint in the axial direction is illustrated in Fig. 2 where the order of the coefficient s is typical for slender beams. The axial restraint increasing the stiffness of the beam is shown to increase the frequencies of vibration.

References

Ambramovitz, M., and Stegun, I. A., 1964, *Handbook of Mathematical Functions*, National Bureau of Standards, New York, Ch. 17.

Burgreen, D., 1951, "Free Vibrations of Pin-Ended Column with Constant Distance Between Pin-Ends," ASME JOURNAL OF APPLIED MECHANICS, Vol. 18, pp. 135–139.

Elishakoff, I., 1979, "Buckling of Stochastically Imperfect Finite Column on a Nonlinear Elastic Foundation," ASME JOURNAL OF APPLIED MECHANICS, Vol. 46, pp. 411–416.

Elishakoff, I., 1985, "Reliability Approach to the Random Imperfection Sensitivity of Columns," *Acta Mechanica*, Vol. 55, pp. 151–170.

Elishakoff, I., Birman, V., and Singer, J., 1985, "Influence of Initial Imperfections on Nonlinear Free Vibration of Elastic Bars," *Acta Mechanica*, Vol. 55, pp. 191–202.

Hui, D., and Hansen, J. S., 1980a, "Two-Mode Buckling of an Elastically Supported Plate and its Relation to Catastrophe Theory," ASME JOURNAL OF APPLIED MECHANICS, Vol. 47, pp. 607–612.

Hui, D., and Hansen, J. S., 1980b, "The Swallowtail and Butterfly Cuspoids and Their Application in the Initial Post-Buckling of Single-Mode Structural Systems," *Quarterly of Applied Mathematics*, April, pp. 17–36.

Keener, J. P., 1974, "Buckling Imperfection Sensitivity of Columns and Spherical Caps," *Quarterly of Applied Mathematics*, Vol. 32, pp. 173–199.

Ray, J. D., and Bert, C. W., 1969, "Nonlinear Vibrations of a Beam with Pinned Ends," *ASME Journal of Engineering for Industry*, Vol. 91, pp. 997–1104.

Rehfield, L. W., 1973, "Nonlinear Free Vibrations of Elastic Structures," *International Journal of Solids and Structures*, Vol. 9, pp. 581–590.

Reissner, E., 1970, "On Postbuckling Behavior and Imperfection Sensitivity of Thin Plates on a Non-Linear Elastic Foundation," *Studies Appl. Mathematics*, Vol. XLIV, No. 1, pp. 45–47.

Reissner, E., 1971, "A Note on Imperfection Sensitivity of Thin Plates on a Non-Linear Elastic Foundation," *Instability of Continuous Systems*, Leipholz, H. E., ed., Proceedings of IUTAM Symposium held at Herrenalb, Sept. 1969, Springer-Verlag, Berlin-Heidelberg-New York, pp. 15–18.

Woinowsky-Krieger, S., 1950, "The Effect of an Axial Force on the Vibration of Hinged Bars," ASME JOURNAL OF APPLIED MECHANICS, Vol. 17, pp. 35–36.

The Plane Problem of Orthotropic Elastic Contact

D. J. Steigmann[1]

Consider symmetric frictionless contact of circular regions $S_\alpha (\alpha = 1,2)$ (Fig. 1) over $-a < x < a$, where "a" is determined by the contact force per unit length F. In light of the assumption of infinitesimal deformation we assume $a \ll R$, where R is the smaller of the radii of curvature of the S_α. Then, provided attention is restricted to the neighborhood of the contact line, the S_α can be approximated by half-planes. Therefore, if the S_α are cylindrically orthotropic (Lekhnitskii, 1981), it is consistent to assume uniform rectilinear orthotropy. For the plane problem we adopt the notation of Pipkin (1979):

$$G\left(\frac{\partial u}{\partial y} + \frac{\partial v}{\partial x}\right) = \sigma_{xy},$$

$$G\frac{\partial u}{\partial x} = A\sigma_{xx} - B\sigma_{yy},\ G\frac{\partial v}{\partial y} = -B\sigma_{xx} + C\sigma_{yy}. \tag{1}$$

The coefficients in (1) can be expressed in terms of the usual engineering constants for plane stress and plane strain (Christensen, 1979). Eliminating u and v results in

$$A\frac{\partial^4 \chi}{\partial y^4} + D\frac{\partial^4 \chi}{\partial y^2 dx^2} + C\frac{\partial^4 \chi}{\partial x^4} = 0;\ D \equiv 1 - 2B$$

where χ is the Airy function defined by the relations $\sigma_{xx} = G\partial^2\chi/\partial y^2$, $\sigma_{yy} = G\partial^2\chi/\partial x^2$, and $\sigma_{xy} = -G\partial^2\chi/\partial x\partial y$. A solution of the form $\chi(x + \mu y)$ exists for constant μ provided

$$\mu^2 = -\frac{D}{2A}[1 \pm (1 - 4AC/D^2)^{1/2}].$$

We require the undeformed material to be stable against kinematically admissible small displacements. Hence the plane displacement equations of equilibrium are strongly elliptic. Following Hill (1979) it can then be shown that the roots μ are complex. We denote these by $\lambda = |\lambda| e^{i\beta}$, $\gamma = -|\lambda| e^{-i\beta}$, $\bar{\lambda}$, $\bar{\gamma}$ and take $Im\lambda > 0$ without loss of generality.
For $(x, y) \in S_\alpha$ we find

$$\chi = \mathrm{Re}[f_\alpha(\zeta_\alpha) + g_\alpha(\omega_\alpha)];\ \zeta_\alpha = x + \lambda_\alpha y,\ \omega_\alpha = x + \gamma_\alpha y$$

$$\sigma_{xx}/G_\alpha = \mathrm{Re}[\lambda_\alpha^2 f_\alpha''(\zeta_\alpha) + \gamma_\alpha^2 g_\alpha''(\omega_\alpha)] \tag{2}$$

$$2(\sigma_{yy} - i\sigma_{xy})/G_\alpha = (1 + \Lambda_\alpha)f_\alpha''(\zeta_\alpha) + (1 - \bar{\Lambda}_\alpha)\bar{f}_\alpha''(\bar{\zeta}_\alpha)$$
$$+ (1 + \Gamma_\alpha)g_\alpha''(\omega_\alpha) + (1 - \bar{\Gamma}_\alpha)\bar{g}_\alpha''(\bar{\omega}_\alpha);\ \Lambda_\alpha \equiv i\lambda_\alpha,\ \Gamma_\alpha \equiv i\gamma_\alpha$$

where $f_\alpha(\zeta_\alpha)$, $g_\alpha(\omega_\alpha)$ are holomorphic for $(x, y) \in S_\alpha$ and S_1, S_2 have different elastic constants in general. Substituting (2) into (1) and making use of properties of the roots λ and γ leads to the displacements

$$u = \mathrm{Re}[(\kappa_\alpha - 1)g_\alpha'(\omega_\alpha) - \kappa_\alpha f_\alpha'(\zeta_\alpha)],$$
$$v = \mathrm{Re}[(\kappa_\alpha - 1)\lambda_\alpha f'{}_\alpha(\zeta_\alpha) - \kappa_\alpha \gamma_\alpha g_\alpha'(\omega_\alpha)];$$
$$\kappa_\alpha \equiv B_\alpha - A_\alpha\lambda_\alpha^2 = B_\alpha - C_\alpha/\gamma_\alpha^2,$$
$$1 - \kappa_\alpha = B_\alpha - A_\alpha\gamma_\alpha^2 = B_\alpha - C_\alpha/\lambda_\alpha^2 \tag{3}$$

apart from rigid-body terms. Define functions $h_\alpha(z)$, $k_\alpha(z)$ by

$$2h_\alpha(z)/G_\alpha \equiv (1 + \Lambda_\alpha)f_\alpha(z) + (1 + \Gamma_\alpha)g_\alpha(z),$$
$$2k_\alpha(z)/G_\alpha \equiv (1 - \Lambda_\alpha)f_\alpha(z) + (1 - \Gamma_\alpha)g_\alpha(z);\ z = x + iy.$$

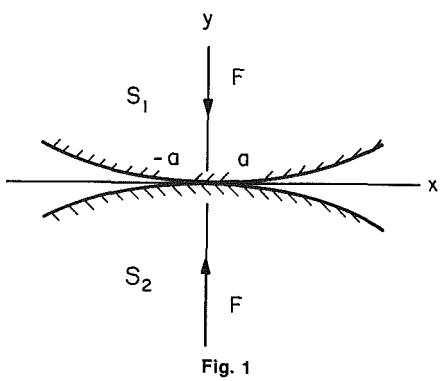

Fig. 1

[1] Graduate Student, Division of Engineering, Brown University, Providence, RI 02912.

Manuscript received by ASME Applied Mechanics Division, July 26, 1984; final revision November 10, 1985.

Then

$$G_\alpha(\Lambda_\alpha-\Gamma_\alpha)f_\alpha(z) = (1-\Gamma_\alpha)h_\alpha(z)-(1+\Gamma_\alpha)k_\alpha(z),$$
$$G_\alpha(\Lambda_\alpha-\Gamma_\alpha)g_\alpha(z) = (1+\Lambda_\alpha)k_\alpha(z)-(1-\Lambda_\alpha)h_\alpha(z). \quad (4)$$

Substituting into (2c) and its conjugate and evaluating the resulting expressions in the limit $y\to 0^+$ leads to the conclusion that the condition of frictionless contact ($\sigma_{xy}(x, y=0)=0$) is satisfied by the choice

$$k_\alpha(z)=h_\alpha(z) \quad (5)$$

while

$$\sigma_{yy}(x, y=0)=[h_1''(x)]_+ + [\bar{h}_1''(x)]_- = [h_2''(x)]_- + [\bar{h}_2''(x)]_+,$$

where subscripts $+$, $-$ correspond to the limits $y=0\pm$. The functions $h_\alpha(z)$ are defined and holomorphic for $z\in S_\alpha$. Define the continuations $h_1(z)=-\bar{h}_1(z)$ for $y<0$ and $h_2(z)=-\bar{h}_2(z)$ for $y>0$. Then

$$\bar{h}_1(\bar{z})=-h_1(\bar{z}), y>0;\ \bar{h}_2(\bar{z})=-h_2(\bar{z}), y<0 \quad (6)$$

and

$$\sigma_{yy}(x, y=0)=[h_1''(x)]_+ - [h_1''(x)]_- = [h_2''(x)]_- - [h_2''(x)]_+. \quad (7)$$

Thus $h_\alpha''(z)$ are continuous across $y=0$, $|x|>a$ and $[h_1''(x)+h_2''(x)]_+ = [h_1''(x)+h_2''(x)]_-$, $-\infty<x<\infty$. Then the conditions $\sigma_{\alpha\beta}\to 0$ as $|z|\to\infty$ and Liouville's theorem (Carrier et al., 1966) require $h_2(z)=-h_1(z)$.

Let $v_+(x)$, $v_-(x)$ be the limits of $v(x, y)$ as $y\to 0\pm$ in S_1, S_2. Then (3)–(6) lead to the Hilbert problem

$$if'(x)=(N_1+N_2)\{[h_1''(x)]_+ + [h_1''(x)]_-\}$$

where

$$f(x)\equiv v_+(x)-v_-(x),\ N_\alpha\equiv -|\lambda_\alpha|^2 Im\kappa_\alpha/(G_\alpha Re\lambda_\alpha).$$

The solution which complies with (6a) is (Muskhelishvili, 1953)

$$h_1''(z)=\frac{i}{2\pi(N_1+N_2)\sqrt{(z^2-a^2)}}\int_{-a}^{a}\frac{f'(x)\sqrt{(a^2-x^2)}}{x-z}\,dx + \frac{iP}{\sqrt{(z^2-a^2)}}$$

where P is a real constant and the branch cut is the arc $y=0$, $|x|<a$. If $y=f_\pm(x)$ are the equations of the boundaries of S_1, S_2 before deformation then for $|x|<a$, $f_+(x)+v_+(x)=f_-(x)+v_-(x)$ and $f(x)=f_-(x)-f_+(x)$. If the S_α are circular regions of radii R_α then $f'(x)\equiv -x(R_1+R_2)/R_1R_2$ and

$$h_1''(z)=-iQ[z-(z^2-a^2/2)/\sqrt{(z^2-a^2)}]+iP/\sqrt{(z^2-a^2)};$$
$$Q\equiv\frac{R_1+R_2}{2R_1R_2(N_1+N_2)}. \quad (8)$$

Boundedness of $\sigma_{\alpha\beta}$ at $z=\pm a$ requires $P+Qa^2/2=0$. Then (7) gives $\sigma_{yy}(x, y=0)=4P\sqrt{(a^2-x^2)}/a^2$, $|x|<a$, and the equilibrium condition

$$F = -\int_{-a}^{a}\sigma_{yy}(x, y=0)dx$$

yields

$$P = -F/2\pi,\ a^2=F/\pi Q. \quad (9)$$

From (8), (9) we find the stress functions

$$h_1''(z) = -h_2''(z)=\frac{iF}{\pi a^2}(\sqrt{(z^2-a^2)}-z);$$
$$Re h_1''(z) = -Re h_2''(z)=\frac{F}{\pi a^2}(y-\Delta(z)\sin\delta(z)), \quad (10)$$
$$Im h_1''(z) = -Im h_2''(z)=\frac{F}{\pi a^2}(\Delta(z)\cos\delta(z)-x)$$

where

$$2\delta(z) \equiv \tan^{-1}\frac{y}{x-a}+\tan^{-1}\frac{y}{x+a},\ \Delta(z)\equiv|z^2-a^2|^{1/2}, \quad (11)$$
$$|z^2-a^2| = [(x^2-y^2-a^2)^2+(2xy)^2]^{1/2},\ x=Re z,\ y=Im z.$$

We note that (10) has the same form as the stress function for the isotropic problem. A similar result was found by Chen (1969) in an application of the analysis of Green and Zerna (1968) to the problem of indentation of a half-space by a rigid punch.

From (2), (4), (5), (10) and (11) we find the stresses for $(x, y)\in S_\alpha$:

$$(Re\lambda_\alpha/|\lambda_\alpha|^2)\sigma_{xx}=(Re\lambda_\alpha)Re[h_\alpha''(\zeta_\alpha)+h_\alpha''(\omega_\alpha)] + (Im\lambda_\alpha)Im[h_\alpha''(\omega_\alpha)-h_\alpha''(\zeta_\alpha)]$$
$$(Re\lambda_\alpha)\sigma_{yy}=(Re\lambda_\alpha)Re[h''_\alpha(\zeta_\alpha)+h_\alpha''(\omega_\alpha)] - (Im\lambda_\alpha)Im[h_\alpha''(\omega_\alpha)-h_\alpha''(\zeta_\alpha)]$$
$$(Re\lambda_\alpha/|\lambda_\alpha|^2)\sigma_{xy}=Re[h_\alpha''(\omega_\alpha)-h_\alpha''(\zeta_\alpha)]; \quad (12)$$
$$Re\zeta_\alpha=x+yRe\lambda_\alpha,\ Re\omega_\alpha=x-yRe\lambda_\alpha,\ Im\zeta_\alpha=Im\omega_\alpha=yIm\lambda_\alpha.$$

To find displacements we impose the conditions $u=0$ at $x=0$, $y=0\pm$ and $v_+(0)-v_-(0)=f(0)=0$ (e.g., $v_+(0)=0$). Then (3)–(5) and (10) lead to the results

$$(2G_\alpha Re\lambda_\alpha)u=(Re(\gamma_\alpha\kappa_\alpha))Re[\phi_\alpha(\zeta_\alpha)+\phi_\alpha(\omega_\alpha)-F] + (Im(\gamma_\alpha\kappa_\alpha))Im[\phi_\alpha(\omega_\alpha)-\phi_\alpha(\zeta_\alpha)]$$
$$(2G_\alpha Re\lambda_\alpha/|\lambda_\alpha|^2)v=(Re\kappa_\alpha)Re[\phi_\alpha(\omega_\alpha)-\phi_\alpha(\zeta_\alpha)] + (Im\kappa_\alpha)\left\{(-)^\alpha\frac{F}{\pi}\log a^2-Im[\phi_\alpha(\zeta_\alpha)+\phi_\alpha(\omega_\alpha)]\right\}$$

where

$$\phi_1(z)=-\phi_2(z)=\frac{iF}{\pi a^2}z(\sqrt{(z^2-a^2)}-z) - \frac{iF}{\pi}\log(z+\sqrt{(z^2-a^2)}),$$
$$Re\phi_1(z)=-Re\phi_2(z)=\frac{F}{\pi a^2}\Big[2xy-\Delta(z)(x\sin\delta(z) + y\cos\delta(z))+a^2\tan^{-1}\left(\frac{y+\Delta(z)\sin\delta(z)}{x+\Delta(z)\cos\delta(z)}\right)\Big], \quad (14)$$
$$Im\phi_1(z)=-Im\phi_2(z)=\frac{F}{\pi a^2}\{y^2-x^2+\Delta(z)(x\cos\delta(z)-y\sin\delta(z)) - a^2\log[(x+\Delta(z)\cos\delta(z))^2+(y+\Delta(z)\sin\delta(z))^2]^{1/2}\}.$$

Acknowledgment

The support of the Division of Engineering at Brown University is gratefully acknowledged.

References

Carrier, G. F., Krook, M., and Pearson, C. E., 1966, *Functions of a Complex Variable*, McGraw-Hill, New York.

Chen, W. T., 1969, "Stresses in Some Anisotropic Materials due to Indentation and Sliding," *Int. J. Solids Structures*, Vol. 5, pp. 191–214.

Christensen, R. M., 1979, *Mechanics of Composite Materials*, Wiley, New York.

Green, A. E., Zerna, W., 1968, *Theoretical Elasticity*, 2nd ed., Oxford University Press.

Hill, R., 1979, "On the Theory of Plane Strain in Finitely Deformed Compressible Materials," *Math. Proc. Camb. Phil. Soc.*, Vol. 86, pp. 161–178.

Lekhnitskii, S. G., 1981, *Theory of Elasticity of an Anisotropic Body*, 2nd ed., Mir Publishers, Moscow.

Muskhelishvili, N. J., 1953, *Singular Integral Equations*, J. R. M. Radok, transl. ed., P. Nordhoff Ltd., Groningen.

Pipkin, A. C., 1979, "Stress Analysis for Fiber-Reinforced Materials," in *Advances in Applied Mechanics*, Vol. 19, C.-S. Yih, ed., Academic Press, pp. 1-51.

Asymmetric Buckling of Ring Stiffened Circular Plates

J. N. Rossettos[1,3] and G. Yang[2,3]

Introduction

The symmetric buckling of a circular plate which is stiffened by a single concentric ring was studied by Rossettos and Miller (1984). It was shown how the buckling load was dependent on the ring radius, r_1, and the parameter $\alpha = EI/aD$, which is a measure of the ring stiffness relative to that of the plate. The quantity, I, is the moment of inertia of the ring cross section about the plate midsurface, while a and D are the plate radius and bending stiffness, respectively. It is noted that α can be increased by either increasing I or decreasing the plate thickness (and therefore, D). It was shown by Yang (1984) that for sufficiently large values of α, asymmetric buckling can occur. The present note treats the asymmetric buckling problem, and indicates a coalescence of the lowest symmetric and asymmetric mode eigenvalues for certian values of α, r_1, and the parameter $\beta = GJ/EI$ which involves the ring torsional stiffness.

Analysis

The governing differential equation for the deflection, w, is given by

$$\nabla^4 w + (N_r/D)\nabla^2 w = 0 \tag{1}$$

where

$$\nabla^2 = \partial^2/\partial r^2 + \partial/r\partial r + \partial^2/r^2\partial\theta^2$$

The general solutions which are valid in the two plate regions separated by the ring are

$$w(r,\theta) = [C_1 r^n + C_2 J_n(\lambda r)]\cos n\theta \qquad (0 \le r \le r_1) \tag{2}$$

$$w(r,\theta) = [C_3 r^n + C_4 r^{-n} + C_5 J_n(\lambda r) + C_6 Y_n(\lambda r)]\cos n\theta \qquad (r_1 \le r \le a) \tag{3}$$

where $n = 1, 2, \ldots$, and $\lambda^2 = N_r/D$. Equation (1) assumes that the state of stress in the primary state is constant and given by $N_{rr} = N_{\theta\theta} = N_r$, $N_{r\theta} = 0$, so that any r dependence of the stress resultants in the annular region, in cases where the ring extensional stiffness is different from that of the plate, is not considered.

The constants $C_1, C_2, \ldots C_6$ can be accomodated by two boundary conditions at the outer edge of the plate and four continuity conditions at the ring. It turns out that the first antisymmetric mode ($n = 1$) gives the lowest critical load, and separation of variables can be carried out by $w(r,\theta) = W(r)\cos\theta$. The boundary conditions are then given as follows. For a clamped plate we have

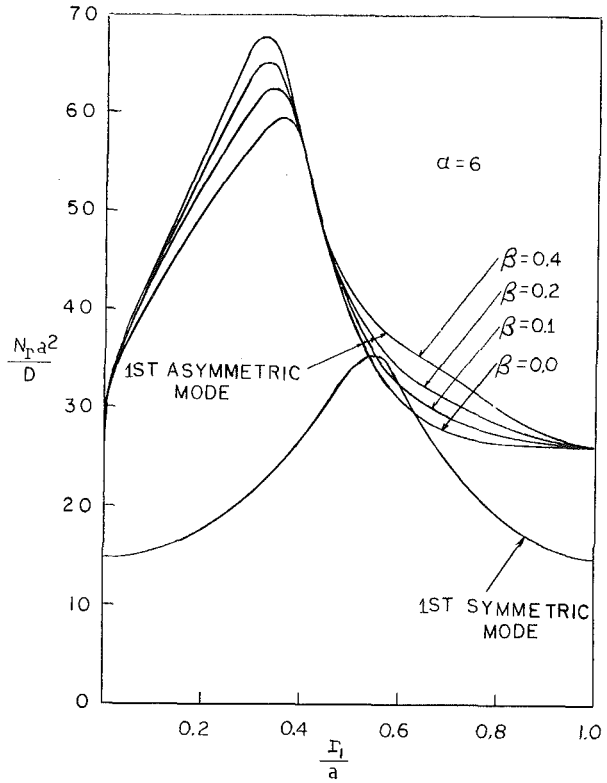

Fig. 1 Buckling load parameter, $N_r a^2/D$, versus nondimensional ring radius, r_1/a, for $\alpha = 6$ and various values of β; clamped plate

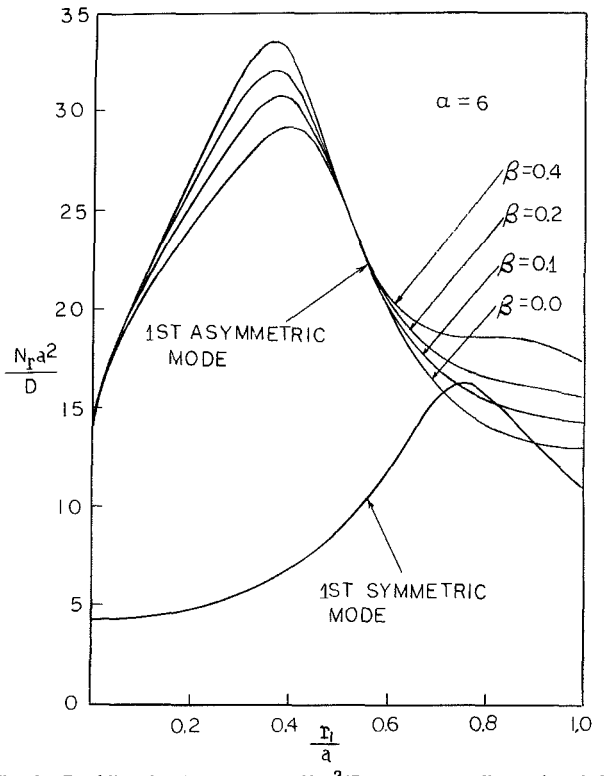

Fig. 2 Buckling load parameter, $N_r a^2/D$, versus nondimensional ring radius, r_1/a, for $\alpha = 6$ and various values of β; simply supported plate

$$W(a) = dW(a)/dr = 0 \tag{4a, b}$$

and for a simply supported plate, we have

$$W(a) = d^2 W(a)/dr^2 + \nu[W(a)/a^2 - dW(a)/adr] = 0 \tag{5a, b}$$

[1]Professor, Mem. ASME.
[2]Graduate student.
[3]Department of Mechanical Engineering, Northeastern University, Boston, MA 02115.

Manuscript received by ASME Applied Mechanics Division, July 24, 1985; fianl revision December 16, 1985.

Muskhelishvili, N. J., 1953, *Singular Integral Equations*, J. R. M. Radok, transl. ed., P. Nordhoff Ltd., Groningen.

Pipkin, A. C., 1979, "Stress Analysis for Fiber-Reinforced Materials," in *Advances in Applied Mechanics*, Vol. 19, C.-S. Yih, ed., Academic Press, pp. 1-51.

Asymmetric Buckling of Ring Stiffened Circular Plates

J. N. Rossettos[1,3] and G. Yang[2,3]

Introduction

The symmetric buckling of a circular plate which is stiffened by a single concentric ring was studied by Rossettos and Miller (1984). It was shown how the buckling load was dependent on the ring radius, r_1, and the parameter $\alpha = EI/aD$, which is a measure of the ring stiffness relative to that of the plate. The quantity, I, is the moment of inertia of the ring cross section about the plate midsurface, while a and D are the plate radius and bending stiffness, respectively. It is noted that α can be increased by either increasing I or decreasing the plate thickness (and therefore, D). It was shown by Yang (1984) that for sufficiently large values of α, asymmetric buckling can occur. The present note treats the asymmetric buckling problem, and indicates a coalescence of the lowest symmetric and asymmetric mode eigenvalues for certian values of α, r_1, and the parameter $\beta = GJ/EI$ which involves the ring torsional stiffness.

Analysis

The governing differential equation for the deflection, w, is given by

$$\nabla^4 w + (N_r/D)\nabla^2 w = 0 \tag{1}$$

where

$$\nabla^2 = \partial^2/\partial r^2 + \partial/r\partial r + \partial^2/r^2\partial\theta^2$$

The general solutions which are valid in the two plate regions separated by the ring are

$$w(r,\theta) = [C_1 r^n + C_2 J_n(\lambda r)]\cos n\theta \qquad (0 \le r \le r_1) \tag{2}$$

$$w(r,\theta) = [C_3 r^n + C_4 r^{-n} + C_5 J_n(\lambda r) + C_6 Y_n(\lambda r)]\cos n\theta \qquad (r_1 \le r \le a) \tag{3}$$

where $n = 1, 2, \ldots$, and $\lambda^2 = N_r/D$. Equation (1) assumes that the state of stress in the primary state is constant and given by $N_{rr} = N_{\theta\theta} = N_r$, $N_{r\theta} = 0$, so that any r dependence of the stress resultants in the annular region, in cases where the ring extensional stiffness is different from that of the plate, is not considered.

The constants $C_1, C_2, \ldots C_6$ can be accomodated by two boundary conditions at the outer edge of the plate and four continuity conditions at the ring. It turns out that the first antisymmetric mode ($n = 1$) gives the lowest critical load, and separation of variables can be carried out by $w(r,\theta) = W(r)\cos\theta$. The boundary conditions are then given as follows. For a clamped plate we have

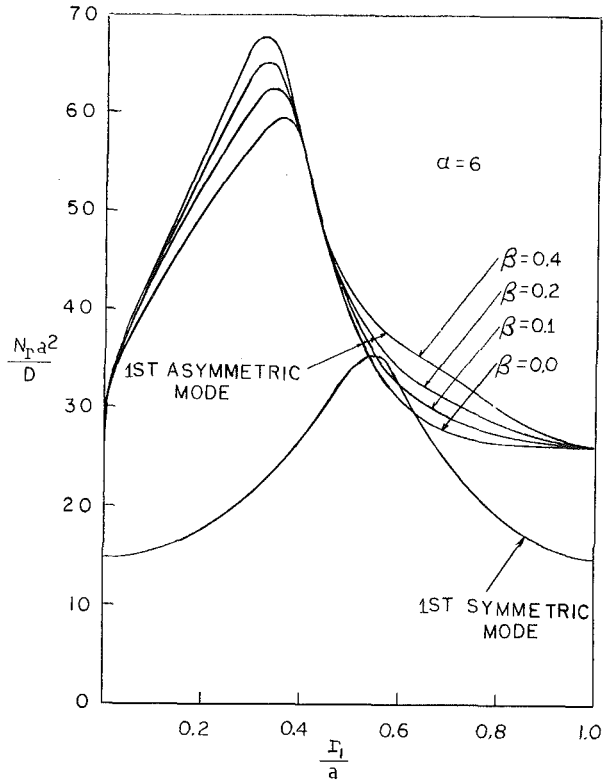

Fig. 1 Buckling load parameter, $N_r a^2/D$, versus nondimensional ring radius, r_1/a, for $\alpha = 6$ and various values of β; clamped plate

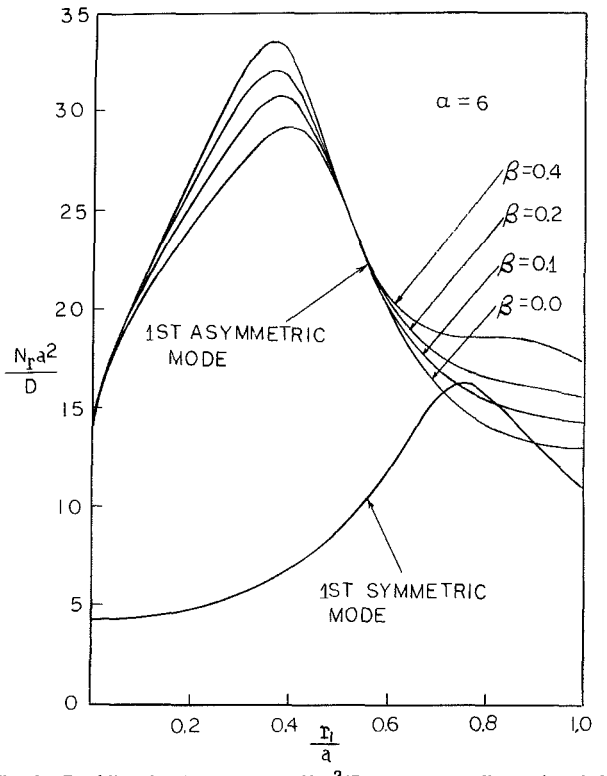

Fig. 2 Buckling load parameter, $N_r a^2/D$, versus nondimensional ring radius, r_1/a, for $\alpha = 6$ and various values of β; simply supported plate

$$W(a) = dW(a)/dr = 0 \tag{4a, b}$$

and for a simply supported plate, we have

$$W(a) = d^2 W(a)/dr^2 + \nu[W(a)/a^2 - dW(a)/adr] = 0 \tag{5a, b}$$

[1]Professor, Mem. ASME.
[2]Graduate student.
[3]Department of Mechanical Engineering, Northeastern University, Boston, MA 02115.

Manuscript received by ASME Applied Mechanics Division, July 24, 1985; fianl revision December 16, 1985.

Appropriate continuity or transition conditions at the ring are derived (Yang, 1984) as natural boundary conditions using a variational approach, where stationary values of $\pi = U_p + U_r - V$ are sought. The plate bending energy, U_p, is given by Timoshenko (1959). The ring energy, U_r, to be used for asymmetric buckling, contains bending and twisting terms, while ring stretching and eccentricty effects have been neglected. Similar energy expressions have been employed extensively in the literature, such as the paper by McElman et al. (1966). V is the work done by N_r. To obtain the continuity conditions, integration is carried out in the region from r_1^- to r_1^+ which also contains the ring, and by this device boundary terms at the so-called cut edges (r_1^-, r_1^+) can be found by integration by parts. We have

$$U_p = \frac{D}{2}\int_0^{2\pi}\int_{r_1^-}^{r_1^+} [(w_{,rr} + w_{,r}/r + w_{,\theta\theta}/r^2)^2 - 2(1-\nu)\, w_{,rr}(w_{,r}/r + w_{,\theta\theta}/r^2) + 2(1+\nu)(w_{,r\theta}/r + w_{,\theta}/r^2)^2]\, r dr d\theta \tag{6}$$

$$U_r = \frac{EI}{2}\int_0^{2\pi} (w_{,\theta\theta}/r_1^2)^2 r_1 d\theta + \frac{GJ}{2}\int_0^{2\pi} (w_{,\theta r}/r_1)^2 r_1 d\theta \tag{7}$$

$$V = \frac{N_r}{2}\int_0^{2\pi}\int_{r_1^-}^{r_1^+} \nabla w \cdot \nabla w\, r dr d\theta \tag{8}$$

With $w = W(r)\cos\theta$, the operation $\delta\pi = 0$ is carried out. Then, by combining the integrated terms with the ring terms, the following transition conditions are obtained

$$D[d^2W/dr^2 + \nu(dW/rdr - W/r^2)]_{r_1^-}^{r_1^+} = (-GJ/r_1^2)dW(r_1)/dr \tag{9}$$

$$D[d^3W/dr^3 + d^2W/rdr^2 - (N_r + (3-\nu)/r^2)dW/dr + (3-\nu)W/r^3]_{r_1^-}^{r_1^+} = (EI/r_1^4)W(r_1) \tag{10}$$

Equations (9) and (10) together with the continuity of displacement and slope

$$W(r_1^-) = W(r_1^+) \text{ and } dW(r_1^-)/dr = dW(r_1^+)/dr \tag{11a, b}$$

yield the four additional conditions at the ring. It is noted that equations (11*a*, *b*) allow simplification of equations (9) and (10) so that the last two terms on the left hand side of these equations vanish identically.

Results and Discussion

The conditions given by equations (9), (10), (11*a*, *b*), and either (4*a*, *b*) or (5*a*, *b*) lead to a characteristic determinant for asymmetric buckling (Yang, 1984). In Figs. 1 and 2 the buckling parameter, $N_r a^2/D$, is plotted against r_1/a for a given value of α and several values of β. The symmetric buckling curve for the given α is also indicated. It is noted that for certain values of β the buckling loads for the lowest symmetric and anti-symmetric modes are equal (coalesce) at two distinct values of r_1/a. Other values of α have been treated (Yang, 1984) and coalescence occurs provided α is greater than 3.95 for the clamped case and 4.85 for the simply supported case. In all the cases considered, coalescence will occur for sufficiently small values of β, in a range covering values up to about 0.2. Since $\beta = GJ/EI$, such values can be shown to be practical and will easily be obtained for typical open section rings for which J is much smaller than I.

References

McElman, J. A., Mikulas, M. M., Jr., and Stein, M., 1966, "Static and Dynamic Effects of Eccentric Stiffening on Plates and Shells," *AIAA Journal*, Vol. 4, pp. 877–895.

Rossettos, J. N., and Miller,W. H., 1984, "On the Buckling on Ring-Stiffened Circular Plates," ASME JOURNAL OF APPLIED MECHANICS, Vol. 51, pp. 689–691.

Yang, G., 1984, "The Asymmetric Buckling of a Ring-Stiffened Circular Plate," M.S. Thesis, Northeastern University, Boston, MA.

Timoshenko, S., and Woinowsky-Kreiger, S., 1959, *Theory of Plates and Shells*, 2nd ed., McGraw-Hill, New York, p. 346.

Journal of Applied Mechanics

Book Reviews

Fracture Mechanics of Concrete: Material Characterization and Testing. Edited by A. Carpinteri and A. R. Ingraffea. Martinus Nijhoff Publishers, The Hague, 1984. 202 pages.

REVIEWED BY Z. P. BAŽANT[1]

Concrete structures are normally full of cracks, more so than structures of any other material, and the typical mode of failure of concrete is fracture rather than plasticity. Yet, fracture mechanics so far has not been introduced in standard specifications for concrete design. Its applicability has been doubted by concrete engineers, due to the fact that the linear elastic fracture mechanics was shown long ago to disagree with tests of brittle failures almost as much as the plastic limit analysis. Recent research, however, has shown that fracture mechanics formulations which take into account the nonlinear behavior in the fracture process zone and the distributed nature of cracking can be brought in good agreement with the test results. This has led in recent years to a tremendous surge of interest and intensification of research in the fracture mechanics of concrete. The present volume, which summarizes the recent research results, is thus a very welcome addition to the literature.

The book consists of six chapters. Chapter 1, written by G. C. Sih, deals with the mechanics of material damage in concrete, which is characterized chiefly by the material strain energy density function. Chapter 2, prepared by A. DiTommaso, discusses the evaluation of concrete fracture, its microscopic aspects as well as the consequences of cracking for stress-strain relations. Chapter 3, authored by S. Mindess, is the largest chapter which treats fracture testing of cement and concrete and discusses the physical phenomena involved in fracture, the rate of loading effects, notch sensitivity, the fracture toughness parameters and their measurement techniques, and the effect of specimen size. A valuable aspect of this chapter is an extensive and detailed summary of the concrete fracture test data available in the literature. An excellent historical review, documented by a set of 175 references, is also given in this chapter. Chapter 4, written by S. P. Shah, analyzes the dependence of concrete fracture toughness on specimen geometry and composition. This chapter presents a lucid and thorough discussion of the resistance curves and their measurement techniques, proposes a theoretical model for the nonlinear fracture process zone, and gives many comparisons with test data. Fracture of fiber reinforced concrete is also discussed and a new model is presented. Chapter 5, by F. O. Slate and K. C. Hover, deals with microcracking in concrete, discussing the microscopic observations of microcracks as well as their effect on the properties of concrete, with particular attention to the differences between high strength and low strength concretes. Finally, Chapter 6, prepared by P. Jacquot, addresses the specialized field of interferometry measurements in scattered coherent light, which has emerged as an important technique for observing the deformations in the cracking zones. Fracture analysis of structures and numerical calculations are not covered in the present volume, since they are treated in a subsequent companion volume written by another set of experts under the editorship of G. C. Sih and A. DiTommaso.

The book represents a collection of very valuable authoritative articles on various aspects of material characterization and fracture testing, rather than a unified and coherent treatise. The individual chapters sometimes overlap in the subject matter covered, and sometimes offer different opinions on the same subject, which might leave a student bewildered. This is, however, inevitable when individual chapters are prepared by different authors. The book, nevertheless, presents an outstanding exposition of the current research and the latest results. It is a reference volume which is highly recommended to researchers, teachers, and graduate students in the field of fracture mechanics, and it should prove useful to concrete engineers as well.

Dynamics of Rotors – Stability and System Identification. Edited by O. Mahrenholtz. Springer-Verlag, Wien New York, 1984. 511 pages. Price $37.40.

REVIEWED BY S. L. HENDRICKS[2]

This book contains the lecture notes presented at the course *Dynamics of Rotors* held at the International Center for Mechanical Sciences (CISM), Udine, in October, 1980. Contributors include: J. Drechsler; L. Gaul, B. Grabowski; O. Mahrenholtz; R. Nordmann; Z. A. Parszewski; N. F. Rieger; V. Schlegel; and H. Springer. As a collection of lectures, the book is tutorial in nature and is presented without trying to intimidate, although some familiarity with the equations of rotor dynamics is assumed. The book begins with a lucid discussion of Modal Analysis. Later topics include: various types of bearings; sources of instabilities; rotor-support interactions; balancing; vibration measurement; parameter identification; crack effects; turbine blades; and torsional vibrations.

Part I – Modal Analysis in Rotor Dynamics. This section contains one paper which introduces the study of rotor dynamics via modal analysis. The matrices which describe the motion of rotating machinery are asymmetric and speed dependent. To decouple the equations of motion requires complex eigenvalues and eigenvectors. These are developed and the author gives a qualitative feel for their interpretation.

Part II – Dynamic Behavior of Rotors. The ten papers

[1]Department of Civil Engineering, Northwestern University, Evanston, Ill. 60201.

[2]Associate Professor, Engineering Science and Mechanics Department, Virginia Polytechnic Institute & State University, Blacksburg, VA 24061.

presented in this section begin with two papers which sketch how to calculate the forces in hydrodynamic journal bearings and tilting pad bearings. Six papers then address instabilities due to: internal energy dissipation; asymmetries (such as bearing stiffnesses or inertias) which introduce time dependent parameters (solution by Floquet theory); fluid film bearings; gas seals; transverse-torsional coupling; and internal fluid flow. Particularly helpful are the two papers by Rieger (Ch. 2.5 and 2.6) which give a concise history of these stability problems, explain quantitatively the physics of the instabilities using a simple rotor, and describe methods for suppression of instabilities. The section concludes with two papers on the interaction of rotating machinery with the surrounding support structure/ground.

Part III – Balancing of Flexible Rotors. This section consists of a single paper which overviews the two methods for balancing: the modal approach; and the influence coefficient method.

Part IV – Measurement and Identification. The six papers in this section begin with one on common vibration instruments and their uses on rotating machinery. The remaining papers deal with various aspects of the identification problem (how to deduce from measurements what the hard to predict rotor parameters are).

Part V – Miscellaneous Topics. This section contains the last three (unrelated) papers. The first deals with the dynamics of a rotor containing a crack. The question of how to recognize the existence of a crack from vibration measurements is addressed. The second gives a good summary of the complex problem of analysis of rotating turbine blades. The last paper deals with the problem of torsional vibrations.

The tone of the whole book is one of instruction. The papers attempt to (and for the most part do) provide enough detail to serve as a quick reference to those working in one area of rotor dynamics who wish to familiarize themselves with some other aspect of this large field. It would also serve as an excellent primer for a vibrations engineer who wishes to learn rotor dynamics. Each paper contains adequate references for those wishing to delve deeper.

Magneto-Solid Mechanics. By F. C. Moon. John Wiley, New York, 1984. 436 Pages. Price: $59.95.

REVIEWED BY S. CHATTOPADHYAY[3]

This is the first book of its kind that treats the engineering aspects of magnetic forces in deformable solids and structures. A number of magnetomechanical devices, such as superconducting magnets, levitated vehicles, magnetic mass drivers, and electromagnets have been considered. Traditional treatment of this subject splits the analysis into a magnetic field solution and then into a structural mechanics problem. In this mode of design process, the interaction problem, such as magnetoelastic instabilities, is overlooked. This book adequately meets that need and presents a comprehensive treatment of the problem in monograph form. An essential contribution of this book is to address the magnetoelastic instabilities in magnets and magnetic devices – to understand their origins and how to analyze them.

The book has a total of nine chapters. Chapter 1 is the introductory chapter in which the essential physical concepts are introduced. The potential applications of magneto-solid mechanics to magnetic forming, fusion and MHD magnets and magnetic levitation are indicated. The chapter ends with a brief historical review of the subject which is fairly comprehensive. In Chapter 2 the concepts of electromagnetic theory are reviewed. Basic equations of magneto-solid mechanics are presented in Chapter 3. After reviewing the electromagnetic forces in discrete circuits and on magnetized materials, the chapter moves on to a rational continuum approach. The equations of nonmagnetic elastic conductors are derived as a special constitutive assumption. The author comes up with a particularly interesting concept of magnetomechanical virial theorem, stated simply: depending on the structural failure criterion, there exists a lower bound on structural mass required to contain stored magnetic energy.

Chapter 4 covers stress analysis of current-carrying structures. The methods of determination of magnetic fields and forces are presented. This is followed by various stress analysis techniques for solenoid magnets due to magnetic forces. The chapter ends with the concept of magnetic stiffness which depicts the dependence of magnetic forces on structural stiffness. Chapter 5 presents a discussion of various magnetomechanical instabilities. Examples of static instabilities such as buckling or divergence have been highlighted and the implications of Earnshaw's theorem for the design of magnet structures have been indicated. Chapter 6 deals with the mechanics of superconducting structures. A notable feature is the treatment of the stored energy versus mass comparisons for a number of existing designs of MHD and fusion magnets. These comparisons are based on a magnetomechanical virial theorem developed in Chapter 3 and could lead to improved structural design of such magnets.

Specific problems involving mechanics of ferromagnetic structures appear in Chapter 7. Included in this chapter are forces in electromagnet and permanent magnet circuits and the bending of ferroelastic plates and shells. Chapter 8 is involved with the response of electrically conducting structures to time varying electromagnetic fields. Some important applications, such as the magnetic levitation of vehicles, linear induction motors, fusion reactors, and magnetic forming are presented. The final chapter provides good background information on experimental techniques in magneto-solid mechanics.

This book is definitely a great benefit to the engineering community. It is of particular interest to the designers of magnetomechanical devices, who have traditionally neglected the mutual interaction of electromagnetic theory and solid mechanics. This book illustrates how catastrophic some of the instabilities can be, unless some adequate measures are taken during the design process. Most of the material presented is based on the author's pioneering research in this area spanning two decades and reflects his original scholarly contribution in this very important interdisciplinary field. This is an exreference book for engineers and researchers involved with the analysis of magnetic forces and stress related problems in various electromagnetic devices. The material is presented in a lucid style, and a large number of illustrations add to the clarity of presentation. There is an invaluable collection of formulas, tables, and examples on magnetoelastic systems in this book. This book is highly recommended for researchers in magneto-solid mechanics as well as for engineers and applied physicists in peripheral disciplines.

Finite Element Analysis of Shells of Revolution. By P.L. Gould. Pitman Publishing Inc., Marshfield, Mass., 1985. 210 Pages. Price: $34.95.

REVIEWED BY A. W. LEISSA[4]

This book is aimed at those who desire to use finite element

[3]Department of Mechanical Engineering, Villanova University, Villanova, PA 19085.

[4]Visiting Professor, Department of Engineering Mechanics, United States Air Force Academy.

methods to analyze the behavior of shells of revolution and, at the same time, wish to have a clear understanding of the methods. It is one of those books, too rarely seen, which simultaneously presents the fundamentals with sufficient rigor and clarity, and applies them to problems of unquestionable practical value.

After a brief Introduction given in the first chapter, Chapter 2 is devoted to laying out the basics of surface geometry; midsurface strains and curvature changes; stress resultants and moments; kinematic conditions; constitutive equations; boundary conditions; and variational principles. All this is done in a format of matrix equations which is directly applicable to the finite element approach. Some practical considerations for subsequent application (e.g., the advantages of *not* employing the classical Kirchhoff hypothesis, even for thin shells) are also described.

Chapter 3 is devoted to static displacement and stress analysis. First, stiffness matrices for shell ring elements are derived. Then global equilibrium equations are assembled in a standard manner. Methods of accommodating stiffness or interrupting lattice frameworks ("open type elements") are discussed. The method is subsequently applied to a number of examples, such as: (1) hyperboloidal shells subjected either to seventh or one-hundredth harmonic (cos 7θ and cos 100θ) normal pressure loading, or wind loading; (2) cylindrical shells subjected to edge ring loads, thermal stressing or hydrostatic loading; (3) a cantilevered parabolic shell carrying its own weight; and (4) a pressurized cylindrical shell having a torospherical head.

Chapters 4 and 5 continue with numerous other examples of dynamic and buckling analyses, respectively. Consistent mass and viscous damping element matrices are derived for the dynamic problems. Solutions are presented for free vibrations, earthquake dynamic response, and wind load buckling, particularly of hyperboloidal cooling towers. Chapter 6 describes how local irregularities (e.g., bulges, cutouts, pipe connections) which destroy the axisymmetric geometry of a shell of revolution, may be accommodated in the analysis.

The finite element code, SHORE III, developed by the author and his students and used to obtain the above mentioned numerical results, along with the BOSOR code developed by Bushnell and others, are both described in Chapter 7. Additional results for cooling tower problems are presented.

In the opinion of the reviewer this short (210 page) book is very useful for those who are involved in the analysis of the static, dynamic and buckling behavior of shells of revolution, such as cooling towers. For the more theoretically oriented person, it serves as a useful bridge to understand how shell theory may be applied in a reasonably rational manner to geometrically complicated problems.

Shell Theory. By F. I. Niordson. North-Holland, Amsterdam, 1985. 408 Pages. Price: $49.00.

REVIEWED BY J. G. SIMMONDS[5]

This is a first-rate book: comprehensive, authoritative, well-written with a nice mixture of theory and practice, and timely (with one exception to be mentioned later). Each of its 17 chapters, from "Tensor analysis" to the "Buckling of plates and shells," has an introduction and summary; this is good pedagogy.

The first two chapters are concise but adequate summaries of the requisite tensor analysis needed in modern shell theory. (Beware: Niordson denotes the coefficients of the second fundamental form of a surface by $d_{\alpha\beta}$, though he is not the first shell theorist – for no explicable reason – to tinker with the conventional symbol $b_{\alpha\beta}$.) Next comes a chapter on the kinematics of large deformation. Extensional and bending strains are defined, first, in terms of the differences between the first and second fundamental forms of the deformed and undeformed midsurface and then in terms of displacements; the discussion of rotations is limited to infinitesimal deformations. This is followed by a derivation of the equilibrium equations for a shell in which the integral equations of equilibrium of a three-dimensional, shell-like body are integrated through its deformed thickness. (To do so Niordson uses a set of normal coordinates that consist of material surface coordinates plus a spatial coordinate that measures distance along a normal to the deformed midsurface of the shell.) Here, as in the preceding chapters, Niordson follows a common practice and defines tensors in terms of their components, sometimes identifying the two. For example, on p. 79 he refers to σ^{ij} as the components of the three-dimensional stress tensor but on p. 81 calls $N^{\alpha\gamma}$ the membrane stress tensor. A potential error in failing to maintain the logical distinction between a tensor and its components – an error that Niordson avoids – is to infer that a tensor must be symmetric if its components are. A good counter-example is the matrix of components of the *unsymmetric* first Piola-Kirchhoff stress tensor, which is *symmetric* if referred to a naturally occurring basis consisting of the tensor products of the deformed and undeformed base vectors of a set of material coordinates.

Chapters 5 and 6, in my opinion, contain the clearest statement in the literature of the role of the famous Kirchhoff hypothesis in shell theory. After formulating the Principle of Virtual Work for a three-dimensional continuum, Niordson imposes the Kirchhoff hypothesis *on the virtual displacement field*. As he says, ". . . it should be stressed that by introducing these virtual displacements we make no assumption whatsoever regarding the true displacements." This produces a two-dimensional Virtual Work Principle in which the only strains that appear are the aforementioned extensional and bending strains. Conjugate to these strains are *symmetric, modified* stress resultants and couples that satisfy an exact set of equilibrium equations and boundary conditions. (In deriving boundary conditions, Niordson makes the tacit approximation that the deformed edge of a shell-like body is a normal section to the deformed midsurface; unless fixed in a special way, an edge is usually regarded as the deformed image of a normal section to the *undeformed* midsurface.)

The link between kinematics and kinetics is the constitutive relations. Niordson confines himself to shells that, from a three-dimensional viewpoint, are elastically isotropic and obey Hooke's Law. In an analysis admirable for its simplicity and persuasiveness, Niordson shows that the strain-energy density can be taken to be an uncoupled, quadratic function of the extensional and bending strains to within an error of $O(h/R + h^2/L^2)$, where h is the shell thickness, R is the smallest principle radius of curvature of the undeformed midsurface, and L is the characteristic wavelength of the deformation pattern. Here, I would have liked to have seen reference to the pioneering work of Hildebrand, Reissner, and Thomas (1949), Koiter (1959), and John (1965). Niordson completes his theoretical development of first-approximation shell theory with a chapter on the static-geometric analogy (valid only if the field equations are linearized).

Chapters 9 and 14 and half of chapter 15 treat the linear theory of plates, membranes, shells of revolution, and shallow shells. Although much of this material may be found in other texts such as Kraus (1967), Novozhilov (1970, 2nd ed.), Flügge (1973, 2nd ed.), or Seide (1975), Niordson's coverage is crisp and sprinkled with useful, illuminating calculations. His treatment of the unsymmetrical vibrations of spherical shells is new and thorough and contains some beautiful pictures of mode shapes. I am also happy to see at last, in a textbook, the en-

[5]Professor of Applied Mathematics, University of Virginia, Charlottesville, VA 22903.

shrinement of the Morley-Koiter equations for the bending of circular cylindrical shells; without a doubt, these are the simplest possible *displacement* equations consistent with the inherent errors in first-approximation theory. (There are, for static problems, even simpler, alternative *displacement-stress function* equations that, thanks to the static-geometric duality, can be written in a compact, complex-valued form, as explained in a recent survey by Sanders (1983).) My only disappointment in this middle part of the book is with the treatment of the axisymmetric bending of shells of revolution: it is out of date. E. Reissner's work (1950 onward) has superceded that of Meissner (1913) and the application of Langer's method (1935) of uniform asymptotic approximation by Clark (1950, 1964), Naghdi and DeSilva (1954, 1955), Baker and Cline (1962), and Steele (1962 onward) has superceded the work of Geckeler (1926).

The last part of the book touches on nonlinear problems. In the last half of Chapter 15 the nonlinear Donnell-Mushtari-Vlasov equations are derived via order-of-magnitude arguments, but no examples are worked out. Chapter 16 applies the von Karman equations to several static and dynamic problems involving plates and membranes of rectangular and circular planform. The final chapter derives buckling equations for a general shell, assuming a membrane prebuckling state and using the method of adjacent equilibrium. The resulting equations are applied to a circular cylindrical shell under axial compression, and the important role of imperfections is discussed briefly.

In summary, this book contains the best introduction to first-approximation shell theory that I know of and covers diverse applications in a clean, straightforward way. It would be an excellent text for a first-year graduate course.

Elastic-Plastic Fracture Mechanics. Edited by L. H. Larsson. D. Riedel Publshing Company, Dordrecht, Holland, 1985. 527 Pages. Price: $64.00.

REVIEWED BY A. S. DOUGLAS[6]

This volume contains the edited proceedings of the 4th Advanced Seminar on Fracture Mechanics, held at the Joint Research Center, Ispra, Italy, in October, 1983. The authors can all be considered among Europe's foremost researchers in the area of ductile fracture, and Dr. Larsson has put together a good balance of relevant work which constitutes excellent material for both researchers and practitioners in this field. There are 13 technical papers, some of which include particulary good reviews of that author's previous work, four workshops (on the applications of different fracture evaluation methods) and the introduction and conclusion. These articles represent the (then) state of the art in the basis and use of fracture criteria (including J and COD), micromechanisms of ductile growth and of ductile fracture design methodology.

The article by Nilsson and Brikstad on dynamic fracture is a particulary well researched and referenced paper dealing with both impact loading and rapidly propagating cracks in ductile materials. The shadow optical method of caustics and its application to dynamic fracture is well described in the article by Kalthoff, who also provides a good review of his excellent past work.

The four workshops detail the background to, and use of, four different fracture evaluation techniques. The first is the CEGB procedure, which cites six illustrative examples, followed by the EPRI method, the COD method and the EnJ criterion. All have at least one case study or example problem with discussion to illustrate the use of the method and the results (such as sensitivity studies) which can be drawn therefrom.

Introduction to Applied Mathematics. By G. Strang. Wellesley-Cambridge Press, Wellesley, MA, 1986. 758 Pages. Price: $39.00.

REVIEWED BY L. B. FREUND[7]

This book is intended to serve as a text for a course dealing with methods of applied mathematics at the advanced undergraduate or introductory graduate level. The general subject matter covered is usually taught under the heading of methods of applied mathematics or advanced calculus or engineering analysis. Professor Strang opens the Preface of his book with the statement. "I believe that the teaching of applied matematics needs a fresh approach." He argues that the way in which mathematical concepts are applied to solve physical problems continues to change, due to the availability of computers and the types of problems being addressed. He succeeds admirably in conveying the vitality of applied mathematics, as well as his own enthusiasm for the subject.

Most of the topics normally identified with the subject at this level have been included, such as linear algebra and matrix theory, ordinary differential equations, introductory partial differential equations, calculus of variations, Fourier series and orthogonal functions, functions of a complex variable and complex integration, and so on. In addition, some not-so-traditional topics have been included, such as the finite element method, fast Fourier transforms, network theory, shock waves and solitons, chaotic motion of dynamic systems, and linear programming and optimization. The common theme through all topics is the development of either differential equations or matrix equations as models for physical systems, along with the means of using mathematics to draw conclusions of consequence about these systems. The many parallels between the differential equations and matrix equations are emphasized to great advantage, and geometrical arguments are used effectively to make certain points or to illustrate certain ideas.

The book includes eight chapters with the following titles: Symmetric Linear Systems, Equilibrium Equations, Equilibrium in the Continuous Case, Analytical Methods, Numerical Methods, Initial-Value Problems, Network Flows and Combinatorics, and Optimization. Each section (there are five or six sections per chapter) is followed by an extensive list of exercises, and answers to selected exercises are listed at the back of the book. The topics introduced are treated quite thoroughly, and there is more than enough material for a full year course. Overall, the book is highly recommended, both as a text and as a general introduction to the topics covered.

[6]Assistant Professor, Department of Mechanical Engineering, The Johns Hopkins University, Baltimore MD 21218.

[7]Professor of Engineering, Brown University, Providence, RI 02912. Fellow ASME.

shrinement of the Morley-Koiter equations for the bending of circular cylindrical shells; without a doubt, these are the simplest possible *displacement* equations consistent with the inherent errors in first-approximation theory. (There are, for static problems, even simpler, alternative *displacement-stress function* equations that, thanks to the static-geometric duality, can be written in a compact, complex-valued form, as explained in a recent survey by Sanders (1983).) My only disappointment in this middle part of the book is with the treatment of the axisymmetric bending of shells of revolution: it is out of date. E. Reissner's work (1950 onward) has superceded that of Meissner (1913) and the application of Langer's method (1935) of uniform asymptotic approximation by Clark (1950, 1964), Naghdi and DeSilva (1954, 1955), Baker and Cline (1962), and Steele (1962 onward) has superceded the work of Geckeler (1926).

The last part of the book touches on nonlinear problems. In the last half of Chapter 15 the nonlinear Donnell-Mushtari-Vlasov equations are derived via order-of-magnitude arguments, but no examples are worked out. Chapter 16 applies the von Karman equations to several static and dynamic problems involving plates and membranes of rectangular and circular planform. The final chapter derives buckling equations for a general shell, assuming a membrane prebuckling state and using the method of adjacent equilibrium. The resulting equations are applied to a circular cylindrical shell under axial compression, and the important role of imperfections is discussed briefly.

In summary, this book contains the best introduction to first-approximation shell theory that I know of and covers diverse applications in a clean, straightforward way. It would be an excellent text for a first-year graduate course.

Elastic-Plastic Fracture Mechanics. Edited by L. H. Larsson. D. Riedel Publshing Company, Dordrecht, Holland, 1985. 527 Pages. Price: $64.00.

REVIEWED BY A. S. DOUGLAS[6]

This volume contains the edited proceedings of the 4th Advanced Seminar on Fracture Mechanics, held at the Joint Research Center, Ispra, Italy, in October, 1983. The authors can all be considered among Europe's foremost researchers in the area of ductile fracture, and Dr. Larsson has put together a good balance of relevant work which constitutes excellent material for both researchers and practitioners in this field. There are 13 technical papers, some of which include particulary good reviews of that author's previous work, four workshops (on the applications of different fracture evaluation methods) and the introduction and conclusion. These articles represent the (then) state of the art in the basis and use of fracture criteria (including J and COD), micromechanisms of ductile growth and of ductile fracture design methodology.

The article by Nilsson and Brikstad on dynamic fracture is a particulary well researched and referenced paper dealing with both impact loading and rapidly propagating cracks in ductile materials. The shadow optical method of caustics and its application to dynamic fracture is well described in the article by Kalthoff, who also provides a good review of his excellent past work.

The four workshops detail the background to, and use of, four different fracture evaluation techniques. The first is the CEGB procedure, which cites six illustrative examples, followed by the EPRI method, the COD method and the EnJ criterion. All have at least one case study or example problem with discussion to illustrate the use of the method and the results (such as sensitivity studies) which can be drawn therefrom.

Introduction to Applied Mathematics. By G. Strang. Wellesley-Cambridge Press, Wellesley, MA, 1986. 758 Pages. Price: $39.00.

REVIEWED BY L. B. FREUND[7]

This book is intended to serve as a text for a course dealing with methods of applied mathematics at the advanced undergraduate or introductory graduate level. The general subject matter covered is usually taught under the heading of methods of applied mathematics or advanced calculus or engineering analysis. Professor Strang opens the Preface of his book with the statement. "I believe that the teaching of applied matematics needs a fresh approach." He argues that the way in which mathematical concepts are applied to solve physical problems continues to change, due to the availability of computers and the types of problems being addressed. He succeeds admirably in conveying the vitality of applied mathematics, as well as his own enthusiasm for the subject.

Most of the topics normally identified with the subject at this level have been included, such as linear algebra and matrix theory, ordinary differential equations, introductory partial differential equations, calculus of variations, Fourier series and orthogonal functions, functions of a complex variable and complex integration, and so on. In addition, some not-so-traditional topics have been included, such as the finite element method, fast Fourier transforms, network theory, shock waves and solitons, chaotic motion of dynamic systems, and linear programming and optimization. The common theme through all topics is the development of either differential equations or matrix equations as models for physical systems, along with the means of using mathematics to draw conclusions of consequence about these systems. The many parallels between the differential equations and matrix equations are emphasized to great advantage, and geometrical arguments are used effectively to make certain points or to illustrate certain ideas.

The book includes eight chapters with the following titles: Symmetric Linear Systems, Equilibrium Equations, Equilibrium in the Continuous Case, Analytical Methods, Numerical Methods, Initial-Value Problems, Network Flows and Combinatorics, and Optimization. Each section (there are five or six sections per chapter) is followed by an extensive list of exercises, and answers to selected exercises are listed at the back of the book. The topics introduced are treated quite thoroughly, and there is more than enough material for a full year course. Overall, the book is highly recommended, both as a text and as a general introduction to the topics covered.

[6]Assistant Professor, Department of Mechanical Engineering, The Johns Hopkins University, Baltimore MD 21218.

[7]Professor of Engineering, Brown University, Providence, RI 02912. Fellow ASME.